frontiers | Research Topics

Glaciation and climate change in the andean cordillera

Edited by
Jacob M. Bendle, Bethan Joan Davies, Michael R. Kaplan, Juan-Luis García and Neil Franklin Glasser

Published in
Frontiers in Earth Science
Frontiers in Environmental Science

ISSN 1664-8714
ISBN 978-2-83251-552-5
DOI 10.3389/978-2-83251-552-5

About Frontiers

Frontiers is more than just an open access publisher of scholarly articles: it is a pioneering approach to the world of academia, radically improving the way scholarly research is managed. The grand vision of Frontiers is a world where all people have an equal opportunity to seek, share and generate knowledge. Frontiers provides immediate and permanent online open access to all its publications, but this alone is not enough to realize our grand goals.

Frontiers journal series

The Frontiers journal series is a multi-tier and interdisciplinary set of open-access, online journals, promising a paradigm shift from the current review, selection and dissemination processes in academic publishing. All Frontiers journals are driven by researchers for researchers; therefore, they constitute a service to the scholarly community. At the same time, the *Frontiers journal series* operates on a revolutionary invention, the tiered publishing system, initially addressing specific communities of scholars, and gradually climbing up to broader public understanding, thus serving the interests of the lay society, too.

Dedication to quality

Each Frontiers article is a landmark of the highest quality, thanks to genuinely collaborative interactions between authors and review editors, who include some of the world's best academicians. Research must be certified by peers before entering a stream of knowledge that may eventually reach the public - and shape society; therefore, Frontiers only applies the most rigorous and unbiased reviews. Frontiers revolutionizes research publishing by freely delivering the most outstanding research, evaluated with no bias from both the academic and social point of view. By applying the most advanced information technologies, Frontiers is catapulting scholarly publishing into a new generation.

What are Frontiers Research Topics?

Frontiers Research Topics are very popular trademarks of the *Frontiers journals series*: they are collections of at least ten articles, all centered on a particular subject. With their unique mix of varied contributions from Original Research to Review Articles, Frontiers Research Topics unify the most influential researchers, the latest key findings and historical advances in a hot research area.

Find out more on how to host your own Frontiers Research Topic or contribute to one as an author by contacting the Frontiers editorial office: frontiersin.org/about/contact

Glaciation and climate change in the andean cordillera

Topic editors

Jacob M. Bendle — Geological Survey of Norway, Norway
Bethan Joan Davies — Newcastle University, United Kingdom
Michael R. Kaplan — Columbia University, United States
Juan-Luis García — Pontificia Universidad Católica de Chile, Chile
Neil Franklin Glasser — Aberystwyth University, United Kingdom

Citation

Bendle, J. M., Davies, B. J., Kaplan, M. R., García, J.-L., Glasser, N. F., eds. (2023). *Glaciation and climate change in the andean cordillera*. Lausanne: Frontiers Media SA. doi: 10.3389/978-2-83251-552-5

Table of contents

frontiers | Frontiers in Earth Science

TYPE Editorial
PUBLISHED 19 January 2023
DOI 10.3389/feart.2023.1129795

OPEN ACCESS

EDITED AND REVIEWED BY
Michael Lehning,
Swiss Federal Institute of Technology Lausanne, Switzerland

*CORRESPONDENCE
Bethan Davies,
bethan.davies@newcastle.ac.uk

SPECIALTY SECTION
This article was submitted to Cryospheric Sciences, a section of the journal Frontiers in Earth Science

RECEIVED 22 December 2022
ACCEPTED 11 January 2023
PUBLISHED 19 January 2023

CITATION
Davies B, Bendle J, Glasser N, García J-L and Kaplan M (2023), Editorial: Glaciation and climate change in the Andean Cordillera.
Front. Earth Sci. 11:1129795.
doi: 10.3389/feart.2023.1129795

Editorial: Glaciation and climate change in the Andean Cordillera

Bethan Davies[1]*, Jacob Bendle[2], Neil Glasser[3], Juan-Luis García[4] and Michael Kaplan[5]

[1]School of Geography, Politics and Sociology, Newcastle University, Newcastle upon Tyne, United Kingdom, [2]Geological Survey of Norway, Trondheim, Sør-Trøndelag, Norway, [3]Faculty of Earth and Life Sciences, Aberystwyth University, Aberystwyth, United Kingdom, [4]College of Pontifical Catholic University of Chile, Santiago, Santiago Metropolitan Region (RM), Chile, [5]Lamont Doherty Earth Observatory, Columbia Climate School, Columbia University, Palisades, NY, United States

KEYWORDS

andes (South America), quaternary, cosmogenic, glaciology, ecology, PALAEO, palaeoclimate

Editorial on the Research Topic
Glaciation and climate change in the Andean Cordillera

Introduction

The Andean Cordillera runs the length of South America (~10° S to 56° S) and incorporates a wide variety of topographic and climatic zones, and the largest concentration of glacial ice in the southern hemisphere outside of Antarctica. The Andean Cordillera is cryospherically diverse, ranging from high mountain glaciation in the arid north, to large temperate icefields in the humid south. Recent work has indicated that Andean glaciers are among the fastest changing on Earth, posing a threat for regional water security and power generation, ecosystem stability, the prevalence of geohazards, and a potentially substantial contribution to global sea level rise. The region is also subject to changing patterns of large-scale ocean-atmosphere systems, such as the sub-decadal El Niño Southern Oscillation and the Southern Annular Mode, with uncertain future impacts on glaciated basins. Studies on the climate and cryosphere of the Andean Cordillera, both past and present, are thus needed to better understand the sensitivity of these systems to future change.

Despite growing interest, assessments of cryosphere and climate change are currently too limited (both spatially and temporally) to constrain past or future ice mass variability with a high degree of confidence across this diverse mountain range. Data-model comparisons are also rare, which limit the ability to establish the regional drivers (e.g., climatic, topographic) of glacier change. With this Research Topic, we draw together knowledge from the fields of climatology, glaciology, and geomorphology, as well as other disciplines, to build towards an improved understanding of the variability in, and interactions between, the climate-cryosphere system across the Andean Cordillera, and to promote new links between researchers working in this area.

This Research Topic brings together 16 articles from a diverse and multinational authorship that includes researchers from Chile, Argentina, Germany, France, the United States, Ireland, Austria, Switzerland, Canada, Belgium, Germany and Italy, with multiple examples of international collaborations, including between European, North American and South American countries. We are also pleased that at least 50% of the publications in this

Research Topic were led by early career researchers. However, only three of the 16 publications were led by female scientists, and several had entirely male co-author lists. We strongly believe that more work needs to be done to improve the gender balance of research in this field, and we encourage authors to reflect on this, and to seek gender balance in future publications.

The articles in this Research Topic generally fall into three broad categories; 1) modern day glaciology and climate; 2) palaeoglaciology and glacier reconstruction; and 3) ecological and environmental reconstruction. The articles herein represent a range of disciplines and include state of the art chronological and modelling methods, such as machine learning approaches to understanding glacier behaviour and their potential responses to future climate change. Many articles also make use of traditional and essential approaches, including glacial and geomorphological mapping, geodetic mass balance analyses, chronological methods, and numerical simulations of glacier behaviour. The articles within this Research Topic refine and build on the works of pioneering early researchers who studied past ice sheet fluctuations, including Nordenskjold (1899), Caldenius (1932) and Lliboutry (1956), and expand into new areas where little or no research has been carried out. Geographically, the articles span almost the full extent of the Andean chain, from tropical Peru in the low latitudes to Tierra del Fuego in the high latitudes.

Modern day glaciology and climate

Modern-day glaciological and climate studies are well-represented (approximately one-third of the articles) in this issue. The research encompasses state-of the-art approaches to determining glacier mass balance, glacier dynamics, and sensitivity to climate. The manuscripts focus on areas where data are sparse, and address important problems to understand better Andean cryology. The papers have glaciers playing active (in terms of hydrology, hazards) and passive roles (as a paleoclimate proxy) in Andean (paleo)environments.

In the north of the Andes, Taylor et al. focus on the tropical glaciers of the southern Peruvian Andes, including the Cordilleras Vilcanota, Vilcabamba, and Urubamba. Using Landsat and ASTER archives, they document ice losses of >50% since the 1970s. These glaciated mountains provide the primary water resource for local populations and larger urban areas, such as the Cusco region. Taylor et al. suggest that recent and future changes will lead to increased hazards on destabilizing slopes, in addition to increased pressure on fresh water availability.

Staying in Peru, dos Reis et al. investigate dust concentration in an ice core from the Quelccaya Ice Cap to assess seasonality and climate (wet/dry conditions), including the Pacific Ocean influence and regional dust transport. They observed an association between snow accumulation and Quelccaya dust variability, and suspended sediment load and runoff in the Madeira River system, the largest contributor to the Amazon River. dos Reis et al. infer linkages between regional atmospheric patterns and climates, tropical ice core records and snow accumulation, and ultimately larger Amazon basin rivers.

Further south, in Patagonia (47°S), Martin et al. used the state-of-the-art Parallel Ice Sheet Model to study current and past glacier-climates around the Monte San Lorenzo massif, an ice cap east of the Patagonian Icefields. They quantified present-day physical glacier properties, ice dynamics and surface mass balance. Then, they quantified the paleoclimatic ranges of temperature and precipitation that may have caused glacier advances during late glacial and Holocene times, likely caused by shifts in the westerlies and associated air masses. Martin et al. infer the sensitivity of present-day and past ice masses in Patagonia to climatic and model parameters.

McDonnell et al. use declassified Hexagon imagery and remotely-sensed data to estimate mass balance for subsets of the Northern and Southern Patagonian Icefields, since the 1970s. They found an acceleration of ice loss by a factor of 1.2–2.4 for the icefields since 2000, with lake-terminating glaciers showing the most significant increase in mass loss rate. Spatial heterogeneity in geodetic mass balance trends for glaciers of all terminus environments suggests that sensitivity to climate change is dependent on a multitude of morphological and climatological factors.

Moving to the Southern Patagonian Icefield, Irarrazaval et al. integrate geomorphological and ice-dynamic information to assess proglacial lake development adjacent to Exploradores Glacier. Using field based (including uncrewed aerial vehicles) and satellite imagery to study 20 years of history, they improved understanding of glacier lake dynamics and development. Such efforts are essential to incorporate the influence of lakes in numerical models, which may inform glacier response to future climate scenarios, and understand hazards such as outburst floods.

Taking a broader perspective across the Andean Cordillera, Caro et al. use a machine learning approach to study the role of climatic and morphometric variables (e.g., elevation and aspect, or glacier surface area and slope) on the variance of glacier surface area between 8°S and 55°S. Focusing on the period 1980–2019, they show that spatial variability in climate is the leading driver of spatial variance in glacier changes, and go on to evaluate the relative roles of precipitation and temperature on glacier changes from the outer Tropics and Dry Andes to the wet southern Andes, respectively. They also documented 12 glaciological zones based on clustering analysis, which considers different seasonal climate and the morphometric characteristics of glaciers. Such efforts will be important for regional hydro-glaciological simulations along the Andes.

Palaeoglaciology and glacial reconstruction

Six articles in this Research Topic tackle the task of reconstructing former glaciers. A high latitudinal range is represented, ranging from northern Peru (Lee et al.), northern Chile (Aguilar et al.), central Chile (Price et al.), northern and central Patagonia (Leger et al.; Sagredo et al.), through to southern Patagonia (Lira et al.). This group of publications applies remote sensing and field surveys of glacial geomorphology, in some cases together with cosmogenic nuclide dating, to reconstruct glacier behaviour during the Last Glacial Maximum, Late Glacial and Holocene. These papers provide therefore an important contribution to understanding how the timing and climatic drivers of glacial advances and periods of rapid recession vary along this enormous latitudinal gradient, shedding light into changes in large scale atmospheric and oceanic circulation systems, and the likely reach of climatic features such as the Antarctic Cold Reversal, Southern Westerly Winds and the Southern Annular Mode.

Starting farthest north, Lee et al. analyse tropical mountain glaciers in the northern highlands of Peru (5°S), an area presently without glaciers. The authors characterise the glacial geomorphology, mapping cirques, moraines and ice-sculpted bedrock. The authors assume that the moraines were deposited during the local Last Glacial Maximum (21.2–23.5 ka). They reconstructed 29 glaciers using these geomorphological data, and reconstructed ice-surface contours and the equilibrium line altitude (ELA) for these palaeoglaciers, following the method of Pellitero et al. (2015).

In the southern Atacama Desert of Chile, Aguilar et al. mapped glacial landforms in the Encierro River Valley (29.1°S). They used these data and new ^{10}Be exposure ages to reconstruct the extent and timing of palaeoglaciation. The outermost moraines yielded an exposure age of approximately 40 ka. Inboard of this, moraine arcs yielded exposure ages of 25–33 ka (the local Last Glacial Maximum). The glacier had receded from the valley before 18 ka. Higher up-valley, a smaller readvance was recorded at 17–20 ka, coincident with Heinrich Stadial Event 1. A main implication of this ^{10}Be moraine record is that no major late-glacial advance occurred after the c.18 ka deglaciation of this valley that is located in the tropic to extra-tropic geographic transition.

Focusing on the Holocene, Price et al. use novel ^{36}Cl exposure ages on basaltic boulders, dendrochronology, and glacier mass balance modelling to constrain Late Holocene glacial fluctuations at Monte Sierra Nevada (38°S), in the Central-South Chilean Andes. The outermost moraine in the valley yielded an exposure age of 4.2 ka. A series of moraines further up-valley yielded ages from 2.5 to 0.8 ka, suggesting multiple readvances of the glacier during this period. A large readvance resulted in the glacier re-occupying the outermost moraine at 0.7 ka. The glacier then formed a series of nested moraines dating 0.45 to 0.30 ka, with pulsed ice recession during the latest Holocene. Glacier modelling suggests that the conditions were around 1.5°C colder and 20% wetter during the Holocene maximum neoglaciations, relative to modern.

Moving to northeast Patagonia, Leger et al. present geomorphological mapping, terrestrial cosmogenic nuclide exposure dating and glacial numerical modelling to reconstruct the late-Last Glacial Maximum behaviour of two mountain glaciers at 43°S. In both these valleys, Leger et al. find evidence for glacial readvances that occurred after the onset of main deglaciation, with the readvances centred at 18.0 ± 1.15 ka, coincident with readvances observed further north, in the Encierro River Valley (Aguilar et al.). A numerical model, forced to match these Late Glacial moraine extents, suggests that annual temperatures were 1.9°C–2.8°C cooler than today, with precipitation 50%–380% higher. This implicates an equatorward migration of the precipitation-bearing Southern Westerly Winds at this time (19.5–18 ka), bringing increased precipitation and higher humidity to the northern Patagonian Ice Sheet before widespread deglaciation across these mountains.

At Monte San Lorenzo (47°S), Sagredo et al. analyse the Holocene fluctuations of Río Tranquillo Glacier. They apply 24 new ^{10}Be ages, together with published ages, to constrain the dynamics of this glacier. Sagredo et al. find that the glacier approached its maximum Holocene extent, possibly several times, between 9.8 and 6.7 ka. This was followed by smaller readvances at ~5.4, ~4.3, ~3.5, ~1.4 ka, with Late Holocene readvances at about 670, 430, and 390 years ago. The pattern of multiple moraine-building events, with slightly decreasing extent each time, is mirrored in other parts of the Southern Hemisphere, and is starkly different to the pattern of Holocene glacier behaviour in the Northern Hemisphere. The authors suggest that the difference in Holocene glacier behaviour between the Northern and Southern hemispheres (e.g., the difference between Patagonia and the European Alps) may be due to natural forcing that has now been overwhelmed by anthropogenic greenhouse gas-driven warming. In contrast, now, interhemispheric synchronous retreat seems unprecedented during the Holocene.

In southern Patagonia, Lira et al. attempts to tackle the timing of glacial advances for Seno Skyring Lobe (52°S), one of the few main ice lobes draining the former Patagonian Ice Sheet whose glacial history had remained mostly undocumented until now. Two outer Laguna Blanca moraines yielded mean ^{10}Be exposure ages of 26.3 ± 2.3 ka and 24.3 ± 0.9 ka. Inboard of these, the inner Río Verde moraines yielded mean ages of 18.7 ± 1.5 ka, with deglaciation from this moraine already underway by 16.4 cal yr BP. The authors also used ^{10}Be exposure ages and optically stimulated luminescence dating to constrain lake levels for the palaeolake Laguna Blanca, revealing a drainage event at 22 ± 3 ka. The work by Lira et al. exposes that none of the main southernmost Patagonian ice lobes embrace the complete record of former ice fluctuations, but altogether they uncover full glacial conditions at different times during the last glacial period, including the Marine Isotope Stage (MIS) 4, 3 and 2.

Ecological and environmental reconstruction

Four contributions in this Research Topic illustrate how palaeoecological methods and associated geochronology can be used to understand better the changes in Late glacial and Holocene glacial environments of the Andean Cordillera.

The northernmost contribution from Mayta and Maldonado describes the climate–vegetation dynamics of the last 4,500 years in the high subtropical Andes of Chile (30°S). Using fossil pollen and macroscopic carbon obtained from sediment cores from two lakes they recognise three contrasting periods in the paleoclimate. From the beginning of the sequences until ~1,900 cal yr BP, relatively dry climatic conditions are suggested, with a slight trend toward more humid conditions after 2,700 cal yr BP. Pollen records from ~1,900 to ~600 cal yr BP suggest wetter conditions than today. Finally, relatively arid conditions have reappeared in the last ~600 years.

Maldonado et al. present the first pollen and charcoal records from the Lago Cochrane/Pueyrredón valley in Patagonia, spanning the last 11,650 cal yrs BP. Using records from two separate sites at Laguna Maldonado and Laguna Anónima they reconstruct changes in Holocene vegetation dynamics in the period after the drainage of the proglacial lake associated with the Lago Cochrane/Pueyrredón ice lobe. These records show the progression from open forest and scattered patches of forest of variable size in a steppe matrix, through to a closed Nothofagus forest. Their records indicate that after 3,800 cal yrs BP, a highly dynamic open forest or forest patches scattered in a grass/shrub–grass steppe matrix developed around Laguna Anónima. There was a higher fire occurrence synchronous with the presence of hunter-gatherers during the last 3,000 years.

Vásquez et al. also worked at Lago Cochrane/Pueyrredón. They study the spatial and temporal evolution and associated palaeoenvironments of the large ice-dammed lakes that developed along the eastern margin of the Patagonian Ice Sheet during the Last Glacial Termination. Using the distribution and age of shoreline

features associated with Glacial Lake Cochrane, they identified five clusters of lake terraces, shorelines, and deltas between elevations ~600–500 (N5), ~470–400 (N4), ~360–300 (N3), ~230–220 (N2), and ~180–170 m asl (N1) in the basin. A chronology, based principally on radiocarbon dates from lake sediment cores and new OSL dating, suggests that these phases developed between ~20.7–19.3 ka (N5), ~19.3–14.8 ka (N4), ~14.8–11.3 ka (N3), and shortly thereafter (N2 and N1). They were also able to relate phases of lake stabilization to former temperature and precipitation regimes.

In Southern Patagonia, Roberts et al. undertook multi-proxy analyses on two sediment cores from Lago Pato in Torres del Paine to provide insights into glacier dynamics and paleolake-level change in the Última Esperanza region over the last ~30,000 cal a BP (30 ka). The results show that a deep ice-dammed and enlarged paleolake developed ~30–20 ka after the ice had retreated from local-Last Glacial Maximum limits at c. 48–34 ka and during the build-up to the global-Last Glacial Maximum, ~26–19 ka. Gaps in the sediment records between ~20–13.4 ka and ~20–10 ka suggest hiatuses in sediment accumulation during the global-Last Glacial Maximum and Antarctic Cold Reversal readvances and/or removal by lake lowering or flushing during the Late Glacial–early Holocene. They relate these environmental changes to millennial-scale changes in the precipitation-bearing Southern Hemisphere Westerly Winds.

Summary

The 16 articles in this Research Topic provide an exciting insight into how the dynamics of glaciers and climate vary across the diverse Andean Cordillera, both at present and in the past. The articles consider glaciers as taking both active (e.g., hydrology and hazards) and passive roles (e.g., as a paleoclimate proxy) in their Andean environments. These new data are enabling a better understanding of the (a)synchronicity of the timing of glacial advances, and how this can be driven by wind systems (such as the Southern Westerly Winds) or large-scale climate patterns. The research collected in this topic also addresses fundamental problems in the timing of the end of the last glaciation, the structure of the last glacial to interglacial transition, and the patterns of Holocene climate and glacier dynamics. These insights into past climates and past glacier behaviour is critical to help understand how glaciers are behaving today, and how they will behave in the future.

Author contributions

All authors listed have made a substantial, direct, and intellectual contribution to the work and approved it for publication.

Conflict of interest

The authors declare that the research was conducted in the absence of any commercial or financial relationships that could be construed as a potential conflict of interest.

Publisher's note

References

Caldenius, C. C. Z. (1932). Las glaciaciones cuaternarias en la Patagonia y Tierra del Fuego: Una investigación regional, estratigráfica y geocronológica.—una comparación con la escala geocronológica sueca. *Geografiska Annaler*. 14 (1-2), 1–164. doi:10.1080/20014422.1932.11880545

Lliboutry, L. (1956). *Nieves y glaciares de Chile Fundamentos de glaciologia*. Santiago, Chile: Universidad de Chile, 471.

Nordenskiöld, E. (1899). Om Skifferbitar, som träffats flytande på hafsytan i sydvestra Patagonien. *Geologiska Föreningen i Stockholm Förhandlingar*. 21 (5), 536–538. doi:10.1080/11035899909442246

Pellitero, R., Rea, B. R., Spagnolo, M., Bakke, J., Hughes, P., Ivy-Ochs, S., et al. (2015). A GIS tool for automatic calculation of glacier equilibrium-line altitudes. *Computers & Geosciences*. 82, 55–62. doi:10.1016/j.cageo.2015.05.005

frontiers in Earth Science

ORIGINAL RESEARCH
published: 09 November 2021
doi: 10.3389/feart.2021.751987

Northeastern Patagonian Glacier Advances (43°S) Reflect Northward Migration of the Southern Westerlies Towards the End of the Last Glaciation

Tancrède P. M. Leger[1]†, Andrew S. Hein[1]†, Daniel Goldberg[1]†, Irene Schimmelpfennig[2]†, Maximillian S. Van Wyk de Vries[3]† Robert G. Bingham[1]† and ASTER Team[2]*

[1]School of GeoSciences, University of Edinburgh, Edinburgh, United Kingdom, [2]Aix-Marseille Université, CNRS, IRD, INRAE, CEREGE, Aix-en-Provence, France, [3]Department of Earth and Environmental Sciences and Saint Anthony Falls Laboratory, University of Minnesota, Minneapolis, MN, United States

OPEN ACCESS

Edited by:
Bethan Joan Davies,
University of London, United Kingdom

Reviewed by:
Jacob M. Bendle,
University of Northern British Columbia, Canada
Stephen J. A. Jennings,
Masaryk University, Czechia

***Correspondence:**
Tancrède P. M. Leger
Tancrede.leger@ed.ac.uk

†ORCID:
Tancrède P. M. Leger
orcid.org/0000-0001-9098-8312
Andrew S. Hein
orcid.org/0000-0003-3397-3813
Daniel Goldberg
orcid.org/0000-0003-1843-7422
Irene Schimmelpfennig
orcid.org/0000-0001-8145-9160
Maximillian S. Van Wyk de Vries
orcid.org/0000-0001-7752-8813
Robert G. Bingham
orcid.org/0000-0002-0630-2021

Specialty section:
This article was submitted to Cryospheric Sciences, a section of the journal Frontiers in Earth Science

Received: 02 August 2021
Accepted: 20 September 2021
Published: 09 November 2021

Citation:
Leger TPM, Hein AS, Goldberg D, Schimmelpfennig I, Van Wyk de Vries MS, Bingham RG and ASTER Team (2021) Northeastern Patagonian Glacier Advances (43°S) Reflect Northward Migration of the Southern Westerlies Towards the End of the Last Glaciation. Front. Earth Sci. 9:751987. doi: 10.3389/feart.2021.751987

The last glacial termination was a key event during Earth's Quaternary history that was associated with rapid, high-magnitude environmental and climatic change. Identifying its trigger mechanisms is critical for understanding Earth's modern climate system over millennial timescales. It has been proposed that latitudinal shifts of the Southern Hemisphere Westerly Wind belt and the coupled Subtropical Front are important components of the changes leading to global deglaciation, making them essential to investigate and reconstruct empirically. The Patagonian Andes are part of the only continental landmass that fully intersects the Southern Westerly Winds, and thus present an opportunity to study their former latitudinal migrations through time and to constrain southern mid-latitude palaeo-climates. Here we use a combination of geomorphological mapping, terrestrial cosmogenic nuclide exposure dating and glacial numerical modelling to reconstruct the late-Last Glacial Maximum (LGM) behaviour and surface mass balance of two mountain glaciers of northeastern Patagonia (43°S, 71°W), the El Loro and Río Comisario palaeo-glaciers. In both valleys, we find geomorphological evidence of glacier advances that occurred after the retreat of the main ice-sheet outlet glacier from its LGM margins. We date the outermost moraine in the El Loro valley to 18.0 ± 1.15 ka. Moreover, a series of moraine-matching simulations were run for both glaciers using a spatially-distributed ice-flow model coupled with a positive degree-day surface mass balance parameterisation. Following a correction for cumulative local surface uplift resulting from glacial isostatic adjustment since ~18 ka, which we estimate to be ~130 m, the glacier model suggests that regional mean annual temperatures were between 1.9 and 2.8°C lower than present at around 18.0 ± 1.15 ka, while precipitation was between ~50 and ~380% higher than today. Our findings support the proposed equatorward migration of the precipitation-bearing Southern Westerly Wind belt towards the end of the LGM, between ~19.5 and ~18 ka, which caused more humid conditions towards the eastern margins of the northern Patagonian Ice Sheet a few centuries ahead of widespread deglaciation across the cordillera.

Keywords: Patagonia, glaciers and climate, last glacial termination, cosmogenic nuclide surface exposure dating, glacier modelling, southern westerly winds, Quaternary, palaeoclimates

1 INTRODUCTION

The mechanisms contributing to the globally synchronous termination of the last glacial cycle remain a subject of great discussion and interest (Putnam et al., 2013). The main source of debate revolves around "Mercer's paradox", the phenomenon that ice sheets reached maxima and then demised synchronously in both hemispheres despite summer insolation intensity being anti-phased (Mercer, 1984). Indeed, in recent decades, an increasing number of detailed glacier chronologies from Patagonia and New Zealand have demonstrated that southern mid-latitude glacier volume fluctuations were not influenced directly by orbitally-controlled local summer insolation intensity during the last glacial cycle, in contrast to northern hemispheric glaciers (Denton et al., 1999; Hein et al., 2010; Doughty et al., 2015; Darvill et al., 2016; Shulmeister et al., 2019; Denton et al., 2021). Denton et al. (2021) proposed that the widespread deglaciation towards the end of the Last Glacial Maximum (LGM), at ~18 ka (ka: thousand years before present), was instead triggered by an insolation-induced poleward shift of the Southern Westerly Winds (SWW) and the coupled Subtropical Front (STF). Tracking the movement of the SWW during the last glacial termination (LGT; ~18 ka) is therefore important for improving our understanding of sudden global climate change during the Quaternary.

Located close to the northern edge of the precipitation-bearing SWW belt and STF, the northern Patagonian Andes are ideally suited for assessing interhemispheric phasing of climate change and for investigating the precise timing of millennial-scale latitudinal shifts in the SWW during the LGT (Mercer, 1972, 1976, 1984; Clapperton, 1990, 1993; Denton et al., 1999). However, the northeastern region of the Patagonian cordillera currently lacks empirical palaeo-climate data covering this key period of rapid environmental change (García et al., 2019). Palaeo-climate proxy data from northwestern Patagonia suggest a return to colder, wetter conditions in the late LGM, between ~19.5 and ~18 ka, during which it is hypothesised that the SWW locally reached their maximum LGM influence (Denton et al., 1999; Moreno et al., 2018). Moreover, numerous late-LGM expansion and/or stabilisation events have been reported for several Patagonian and New Zealand glaciers at ~17–18 ka (e.g., Denton et al., 1999; Kaplan et al., 2007, 2008; Shulmeister et al., 2010, 2019; Murray et al., 2012; Putnam et al., 2013; Moreno et al., 2015; Mendelová et al., 2020a; Davies et al., 2020; Peltier et al., 2021), which suggest a somewhat synchronous late-LGM glacial response across the southern mid-latitudes. However, recent geochronological evidence from the northeastern sector of the former Patagonian Ice Sheet (PIS) does not fit this pattern. Instead, major outlet glaciers experienced relatively early (~19–20 ka) deglaciation from LGM margins, approximately 1.5 kyr prior to outlet glaciers of the northwestern, central eastern and southeastern Patagonian regions (García et al., 2019; Leger et al., 2021), where rapid glacial demise was instead found to occur shortly after ~18 ka (Darvill et al., 2016; Davies et al., 2020). It remains unclear whether the cooler, wetter late-LGM conditions experienced in northwestern Patagonia extended to northeastern Patagonia, and whether early deglaciation of the northeastern PIS outlet glaciers was driven primarily by a difference in climate, or by other negative mass-balance inducing factors.

Here, we reconstruct the behaviour of two independent, climate-sensitive mountain glaciers in northeastern Patagonia to shed light on regional climatic conditions around the last glacial termination and to help unravel the causes of asynchronous PIS deglaciation. We focus our investigation on the El Loro and Río Comisario valleys, two adjacent glaciated mountain valleys of the Poncho Moro massif (**Figure 1**). Both valleys display geomorphological evidence of glacier expansion following the retreat of the Río Corcovado glacier, a major former outlet of the PIS (Leger et al., 2020; 2021). We combine geomorphological mapping and ^{10}Be terrestrial cosmogenic nuclide (TCN) dating of moraine boulders to reconstruct the extent and timing of these glacier advances/still-stands, and employ a spatially-distributed ice-flow model coupled with a positive degree-day surface mass balance parameterisation to evaluate possible climatic conditions at the time of glacier resurgence. Our analysis takes into account a correction of local topographic elevation change caused by glacial isostatic adjustment (GIA) since the time of glacier advance. We find the mountain glaciers re-advanced during the late LGM, at around ~18 ka, partly in response to increased precipitation that we propose reflects an increased influence of the SWW. Our results support the hypothesis of an equatorward migration of the SWW belt over Patagonia towards the end of the last glaciation, between ~19.5 and ~18 ka, a few centuries prior to widespread glacial demise and the onset of the LGT after 18 ka.

2 STUDY LOCATION

This study focuses on the mountain valleys and land-terminating palaeo-glaciers of the Poncho Moro massif, which is located on the eastern edge of the northern Patagonian Andes (**Figure 1**). The Poncho Moro massif today is characterised by maximum summit elevations of ~2,100 m a.s.l., and is mostly ice-free, with the exception of one small glacier (~0.1 km^2) perched in the El Loro upper catchment (**Figures 2**, **3A**). The current climate is classified as cool-temperate, due to the combined effects of the Peru-Chile current offshore from the Chilean Pacific coast and the SWW (Denton et al., 1999; Kaiser et al., 2007). However, due to the strong zonal orographic effect of the Patagonian Andes, total annual precipitation at the study site is reduced by ~60% relative to the centre of the cordillera at ~43°S. Consequently, the eastern valleys of the Poncho Moro massif are located at the western edge of the semi-arid Patagonian steppe climate zone (Garreaud et al., 2013; Fick and Hijmans, 2017). The massif is delineated to the north and east by the Río Corcovado valley, formerly host to a major topographically-controlled outlet glacier (Río Corcovado glacier) of the Patagonian Ice Sheet (PIS), which flowed eastwards from the ice-sheet divide during major Quaternary glaciations (Caldenius, 1932; Haller et al.,2003; Martínez et al., 2011; Leger et al., 2020). To the southeast of the Poncho Moro massif, the former Río Corcovado outlet glacier deposited a series of at least eight distinct moraine complexes (RC

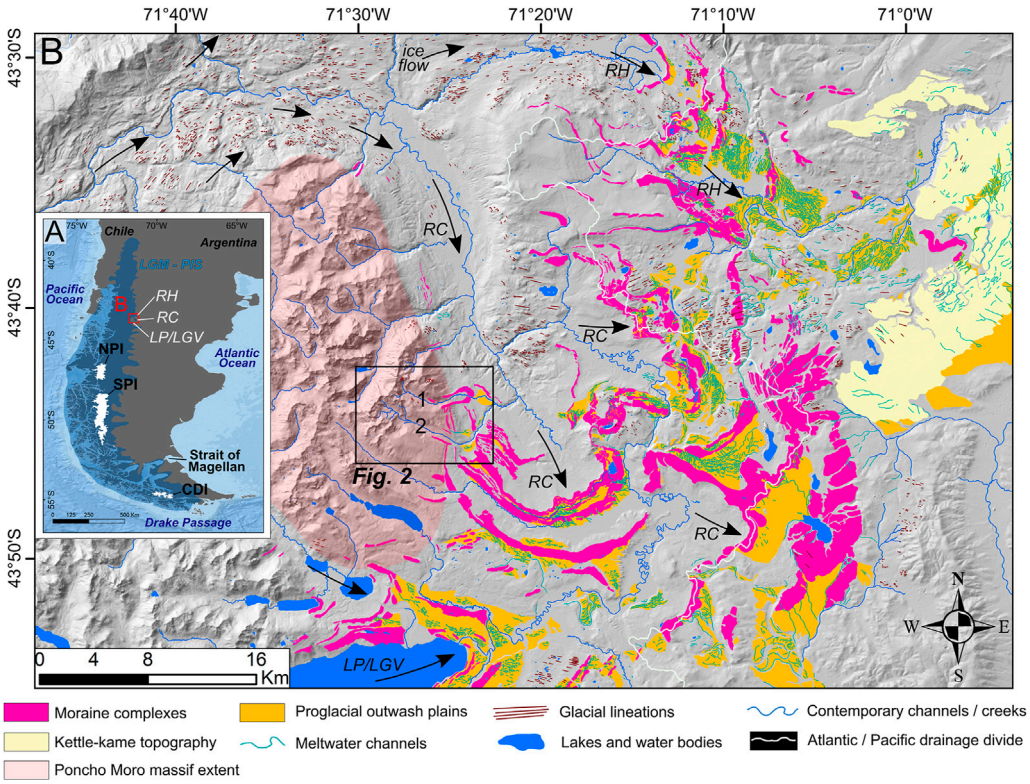

FIGURE 1 | Location of study area. **(A)** Approximate former extent of the Patagonian Ice Sheet (PIS) during the Last Glacial Maximum (LGM), modified from Glasser *et al.* (2008) (dark blue polygon). Modern extents of the North Patagonian (NPI), South Patagonian Icefield (SPI), and Cordillera Darwin (CDI) Icefields are displayed in white. Bathymetric data from General Bathymetric Chart of the Oceans (GEBCO). Outlet glaciers that formerly occupied the study region are designated: RC: Río Corcovado, RH: Río Huemul, LP/LGV: Lago Palena/General Vintter glaciers. Spatial data are displayed in WGS84. **(B)** Shaded relief map (light azimuth: 315°, incline: 45°) based on the AW3D30 Digital Elevation Model (DEM) with overlaid glacial geomorphological data, adapted from Leger *et al.* (2020). Geomorphological data focus on the RC, RH and LP/LGV lateral and terminal glaciogenic deposits. The black box highlights the location of the El Loro (EL; 1) and Río Comisario (RCO; 2) valleys **(Figure 2)**. Black arrows denote former ice-flow direction. The light red, transparent polygon highlights the geographical extent of the Poncho Moro massif. Spatial data are displayed in WGS84 and projected to UTM zone 19S.

0–VII) preserved across large expanses of the Argentinian foreland, five of which (RC III–VII) mark the local LGM and have been dated to marine isotope stage 2 (Leger et al., 2021). The Poncho Moro massif is therefore located towards the former eastern extremity of the PIS during the global LGM. Many valleys of the Poncho Moro massif display well-preserved sequences of lateral and terminal moraine complexes which enable the reconstruction of former mountain glacier extents (Leger et al., 2020, **Figures 1**, **2**). We targeted two adjacent valleys for our investigation; the El Loro (EL) and Río Comisario (RCO) valleys (**Figure 2**), which are both oriented broadly northwest-southeast and were formerly host to western tributary glaciers of the Río Corcovado glacier. We chose these valleys because they both exhibit geomorphological evidence of glacier advances that locally cross-cut the RC III-VI margins, indicating younger moraine deposition occurred after the retreat of the Río Corcovado glacier from its LGM margins. These distinct lateral and terminal moraine complexes located near the EL and RCO valley mouths share similar distance-to-headwall properties (EL: 6.1 km; RCO: 7.1 km) (**Figure 2**). When reaching their respective outermost moraines, the former EL and RCO glaciers covered elevation ranges of between 2,100-890 m a.s.l. and 2050–1,100 m a.s.l., respectively.

The Poncho Moro massif surface geology is characterised by numerous lithologies including volcanic extrusives and sedimentary assemblages, and the EL and RCO catchments are dominated by the mid-cretaceous Río Hielo formation of granites with vein and dyke intrusions (Haller et al., 2003). Moraine boulders located on the outermost EL moraines are almost exclusively granitic and quartz-abundant, making these moraine deposits suitable for ^{10}Be terrestrial cosmogenic nuclide (TCN) dating (**Figure 3C,E,F**).

3 MATERIALS AND METHODS

3.1 Geomorphological Mapping

Major landforms and topographic features were initially identified using the freely available ALOS WORLD 3D - 30 m resolution (AW3D30: Japan Aerospace Exploration Agency) Digital Elevation Model (DEM). All mapped landforms were manually digitised in the WGS84 reference coordinate system

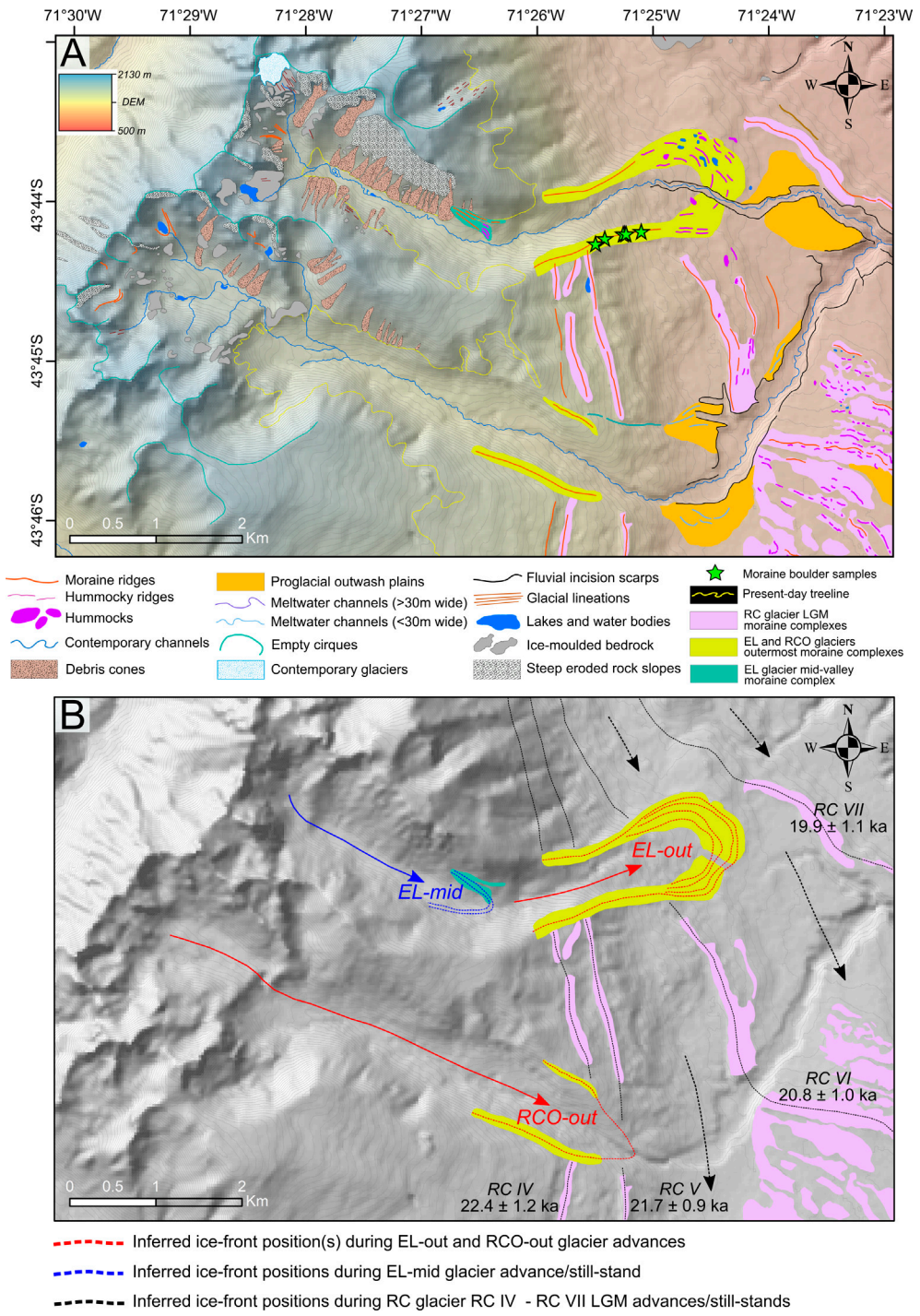

FIGURE 2 | Geomorphological map of the EL and RCO valleys, northeastern Patagonia (see location in wider context, **Figure 1**). **(A)** DEM hillshade (AW3D30 DEM, light azimuth: 315°, incline: 45°) and geomorphological map of the EL and RCO valleys. Locations of moraine boulders sampled for TCN dating are indicated by green star symbols. The variable colouring of moraine complexes (pink/yellow/green) highlights the stratigraphic order of distinct palaeo-glacier advances/stillstands according to our geomorphological interpretations. **(B)** DEM hillshade, inferred moraine-complex stratigraphic relationships and former ice-flow directions of the Río Corcovado outlet glacier LGM advances/still-stands (black arrows), EL-mid advance/still-stand (blue arrow), EL-out and RCO-out advances (red arrows). The ages of the Río Corcovado LGM advances/still-stands are arithmetic mean ± 1σ standard deviations of moraine boulder exposure age populations reported by Leger *et al.* (2021) following Bayesian age model correction. Spatial data are displayed in WGS84 and projected to UTM zone 19S.

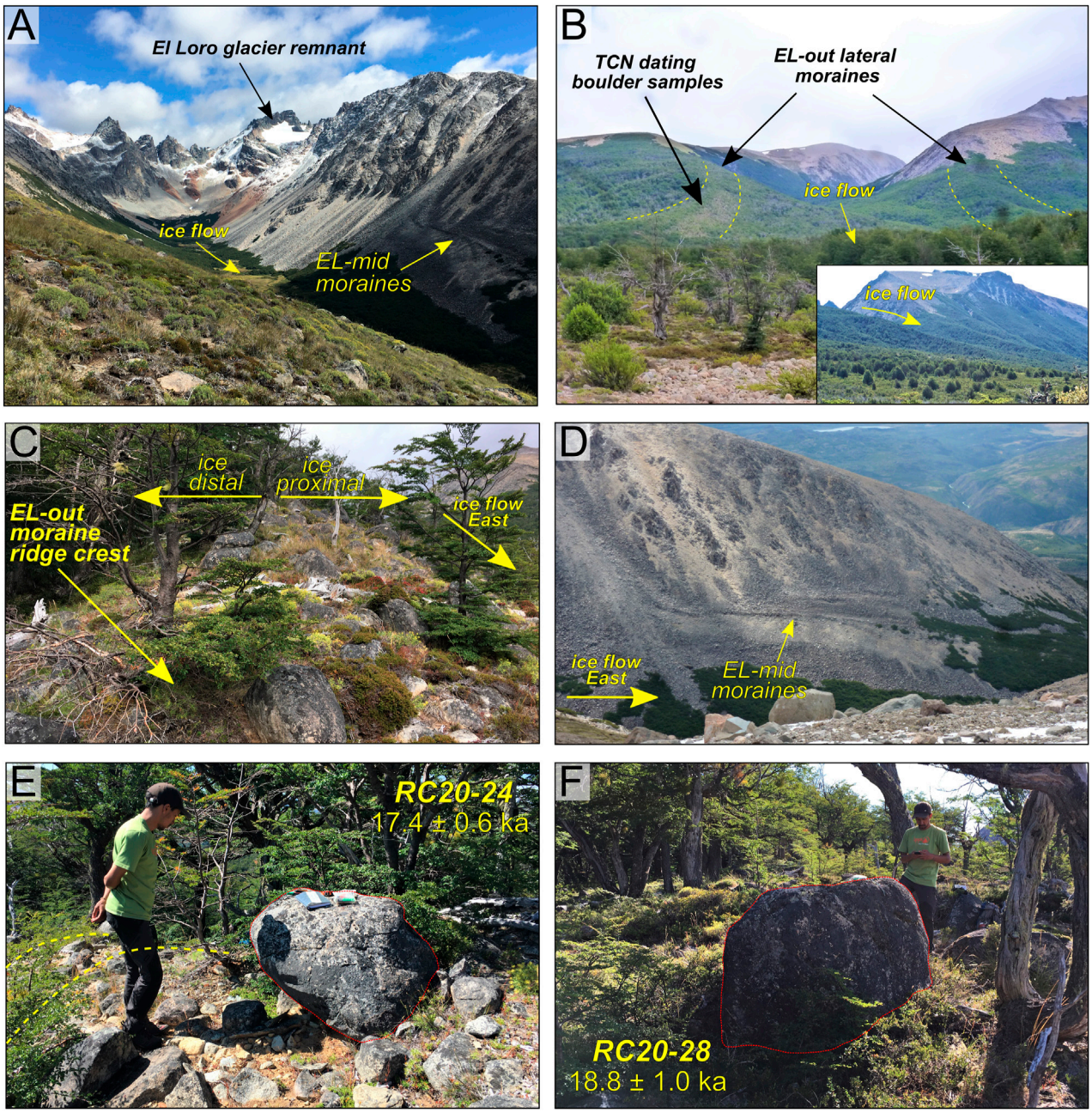

FIGURE 3 | Field photographs of the EL valley, moraines and sampled boulders. **(A)** Northwest-facing photograph of the EL valley and its upper catchment displaying the EL-mid moraine ridges nested on the northern valley side. **(B)** Westward view of the EL valley mouth from the provincial road 44 (RP44). The EL-out lateral northern and southern (targeted for sampling) moraine ridges are highlighted by yellow dashed lines. The inset panel provides another, northward view of the same features from further afield. **(C)** Westward-facing photograph captured from the EL-out southern lateral moraine crest (targeted for sampling), illustrating moraine crest sharpness, ice-proximal and ice-distal moraine-slope angles, moraine-surface boulder sizes, rough lithologies and concentration. **(D)** Northward view of the portion of the northern EL valley side displaying the preserved EL-mid moraine ridges. **(E)** South-facing photograph of an erratic granite boulder (sample RC20-24, highlighted by red line) deposited on the crest of the EL-out southern lateral moraine ridge and sampled for TCN dating. The curvature of the moraine crest is highlighted by yellow dashed lines **(F)** West-facing photograph of an erratic granite boulder (sample RC20-28, highlighted by red line) sampled for TCN dating.

projected to UTM zone 19S using the ESRI^{TM} World Imagery layer, characterized by ~1.0 m resolution images from DigitalGlobe (GeoEye, IKONOS, 2000–2011) at the study site. In areas with dense vegetation and/or cloud cover, we undertook different colour-rendering comparisons using 10 m resolution Sentinel 2A true colour (TCI) and false colour (bands 8,4,3) products (available from https://scihub.copernicus.eu/). Detailed geomorphological mapping criteria along with the complete geomorphological map of the area are presented by Leger *et al.* (2020). Field-based mapping, ground-truthing and

TABLE 1 | Sample details and nuclide concentrations.

Sample ID	Latitude (DD)	Longitude (DD)	Elevation (m a.s.l)	Boulder height (m)	Thickness (cm)	Shielding correction	Qtz mass dissolved (g)	$^{10}Be/^{9}Be$ ratio	±1σ	^{10}Be atoms g^{-1} (SiO_2)	±1σ atoms g^{-1} (SiO_2)	Aster cathode code
El Loro southern lateral moraine boulders												
RC20-23	−43.73891	−71.42438	1,130	0.75	2.0	0.995836	19.9409	1.229E−13	3.987E−15	1.812E+05	5.943E+03	CHJE
RC20-24	−43.73847	−71.42151	1,062	0.57	3.5	0.997264	20.6879	1.167E−13	3.665E−15	1.586E+05	5.042E+03	CHJF
RC20-25	−43.73849	−71.42172	1,066	0.90	3.5	0.997264	20.5538	1.068E−13	3.344E−15	1.492E+05	4.732E+03	CHJG
RC20-26	−43.73944	−71.42575	1,167	0.70	2.0	0.994171	19.0499	1.325E−13	4.080E−15	1.978E+05	6.154E+03	CHJH
RC20-27	−43.73849	−71.42128	1,058	0.75	2.8	0.995988	19.4417	1.085E−13	3.463E−15	1.583E+05	5.114E+03	CHJI
RC20-28	−43.73828	−71.41911	1,005	0.89	4.0	0.996217	19.4481	1.112E−13	5.998E−15	1.639E+05	8.934E+03	CHJJ

Rock density is assumed to be 2.65 g cm^{-3}. Samples were collected in January 2020.

corrections of preliminary landform interpretations in the EL valley were conducted during the austral summer of 2020.

3.2 ^{10}Be Terrestrial Cosmogenic Nuclide Dating

3.2.1 Dating Approach and Sampling

To establish the timing of local mountain glacier re-advances following initial PIS retreat, we targeted the outermost EL lateral moraines (**Figures 2**, **3**), and sampled moraine boulders for ^{10}Be surface exposure dating (e.g. Gosse and Phillips, 2001; Hein et al., 2010; Heyman et al., 2011). The selected granodiorite boulders (60–90 cm in height) resting directly on the moraine crest exhibited glacial polish and, in some cases, preserved striations, indicating minimal post-depositional surface erosion (e.g., **Figure 3E,F**). 1–2 kg samples were collected by hammer, chisel and angle grinder from the central section of the uppermost boulder surface, to a depth of 2–5 cm. Six boulders were sampled along a single continuous lateral moraine ridge (**Table 1**; **Figures 2**, **3**). Collecting this number of samples from one landform aims to reduce potential uncertainties resulting from geological scatter and post-depositional processes (Putkonen and Swanson, 2003; Applegate et al., 2010; Heyman et al., 2011). Exposure ages were interpreted as dating moraine stabilisation following ice-front retreat and/or glacier tongue thinning, hence providing a minimum age for the glacier advance.

3.2.2 Sample Preparation, Wet Chemistry and Exposure-age Calculations

Samples were prepared at two cosmogenic nuclide laboratories: 1) the University of Edinburgh's Cosmogenic Nuclide Laboratory for sample crushing/sieving and quartz purification/isolation; and 2) the National laboratory for Cosmogenic Nuclides (LN_2C) of CEREGE, Aix-en-Provence, France for post-purification wet chemistry. All $^{10}Be/^{9}Be$ ratios were measured by accelerator mass spectrometry at ASTER-CEREGE.

The samples were crushed in their entirety and sieved to isolate the 250–500 μm grain-size fractions. One to three treatments in *HCl* and H_2SiF_6 on a shaker table, which lasted up to 7 days per treatment, was performed to remove as much non-quartz minerals as possible (Bourlès, 1988). Pure quartz was obtained by repeated etching in a 2% *HF* and 1% HNO_3 solution for 24 h in a heated ultrasonic bath, with a sample to acid ratio of about 12 g L^{-1}. At least three etches were subsequently performed to remove atmospheric ^{10}Be. The purified quartz samples were dissolved in concentrated *HF* and each sample, as well as one process blank, were spiked with between 0.42 and 0.46 mg of ^{9}Be, in the form of an in-house carrier solution made from phenakite. After dissolution, the *HF* was evaporated off, and the solid residue was dissolved in *HCl* (10.2 mol L^{-1}), followed by $Be(OH)_2$ precipitation at pH ~9 through the addition of NH_3 and re-dissolution in *HCl*. The solutions were first passed through anion exchange chromatography columns to remove *Fe, Ti* and *Mn*. After another evaporation and $Be(OH)_2$ precipitation step, *HCl* of lower concentration (1 mol L^{-1}) was added to dissolve the *Be* prior to passing the solution through cation exchange chromatography columns to isolate *Be* from *B* and *Al*. The *Be*

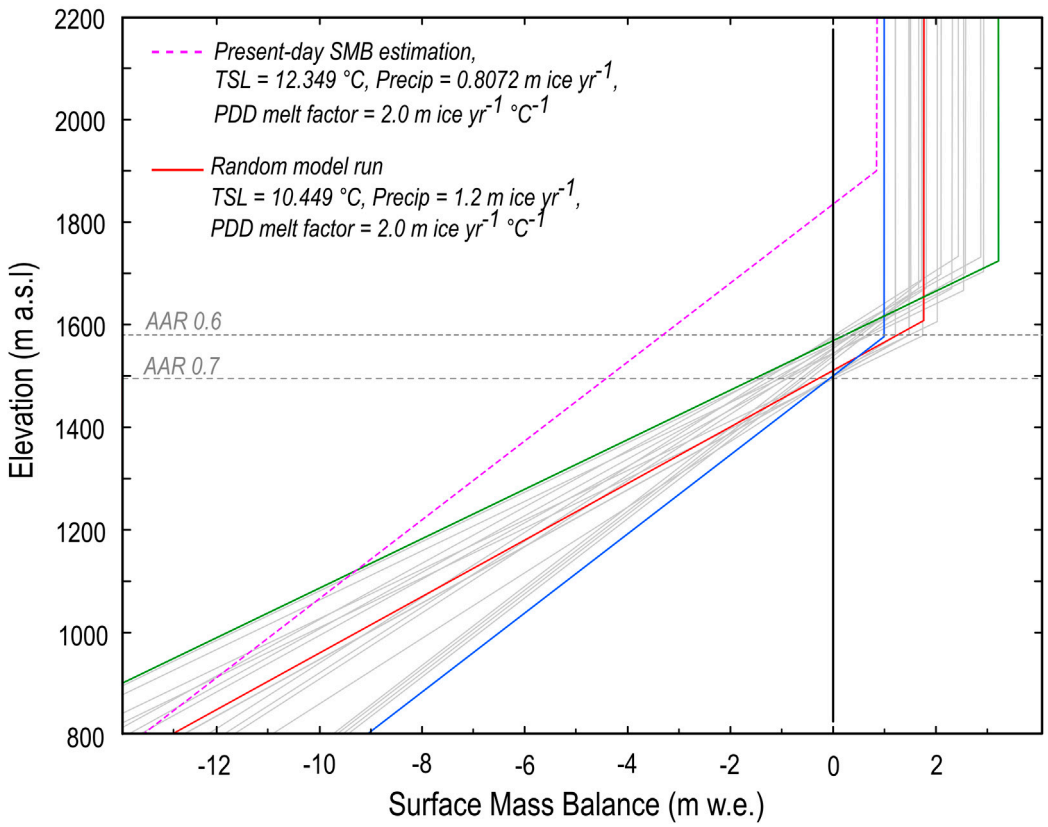

FIGURE 4 | A sample (n = 20) of Surface Mass Balance (SMB) profiles (grey and coloured lines) of the EL-out ice-flow model simulations using a positive degree-day SMB parameterisation. The pink dashed line is a surface mass balance profile representative of our modern-day climate estimation, according to our assessment of modern local atmospheric temperature and precipitation (section *Modern Climate*), when using a *PDD* value of 5 mm *w.e.* $d^{-1}°C^{-1}$. Note that the SMB profiles for EL-out model runs intersect the 0 SMB value (i.e., the glacier equilibrium line) at elevations associated with AAR values of between 0.6 (green line) and 0.7 (blue line), which are used as threshold values to constrain our model simulations.

fractions were then precipitated again as hydroxides and oxidised at ~700°C. The resulting *BeO* samples were mixed with *Nb* powder and pressed into nickel cathodes for AMS measurements. Measurements are based on the in-house standard STD-11 with a $^{10}Be/^{9}Be$ ratio of (1.191 ± 0.013) 10^{-11} (Braucher et al., 2015) and a ^{10}Be half-life of (1.387 ± 0.0012) 10^{6} years (Chmeleff et al., 2010; Korschinek et al., 2010). Analytical uncertainties include ASTER counting statistics and stability (~5%; Arnold et al., 2010) and machine blank correction. Process blank corrections ranged between 0.83 and 1.01% of calculated sample ^{10}Be atoms.

Exposure ages were calculated using the online calculator formerly known as the CRONUS-Earth online calculator version 3 (Balco et al., 2008) with the ^{10}Be Patagonian production rate of 3.71 ± 0.11 atoms g^{-1} (SiO_2) yr^{-1} (original value: Kaplan et al., 2007) obtained and re-calculated from the ICE-D online database (http://calibration.ice-d.org/). In this study, exposure ages were calculated using the time-dependent LSDn scaling scheme of Lifton *et al.* (2014) with 1σ analytical uncertainties. These ages assume no boulder surface erosion post-deposition and present no correction for shielding by snow, soil, or vegetation, following the rationale described in detail by Leger et al., 2021.

3.3 GIA-Related Uplift Estimates

The former PIS covered much of the study area during several Quaternary glaciations, resulting in glacial isostatic adjustment (GIA) of the land surface (Davies et al., 2020). Modern GPS station data from the region (Nevada Geodetic Laboratory data[1]) report uplift rates of less than 1 mm yr^{-1}. If assumed to be constant through the period of exposure, such uplift rates would have an insignificant impact on ^{10}Be production rates and numerical modelling outputs. However, the study area is located at the eastern limit of the Patagonian Andes and a significant amount of GIA-related surface uplift is expected to have occurred there during the Last Glacial–Holocene transition. Ice-sheet-wide glacial geomorphological mapping and palaeo-glacial reconstructions (Glasser et al., 2008; Davies et al., 2020) suggest that the PIS was ~240 km wide at around 43°S during the local LGM, while data

[1]http://geodesy.unr.edu/NGLStationPages/gpsnetmap/GPSNetMap_MAG.html

from the PaleoMIST global ice-sheet reconstruction dataset (Gowan et al., 2021) estimate that maximum PIS thickness during the global LGM reached approximately 1,650 m at these latitudes. In this region of Patagonia, the majority of the ice mass is thought to have melted between 19 and 15–16 ka (Moreno et al., 2015; Leger et al., 2021), with crustal unloading leading to GIA and to significant surface uplift. To estimate the effect of local GIA on ^{10}Be production and palaeo-climate outputs from glacial numerical modelling, we evaluated former time-varying isostatic uplift and subsidence rates using the ~5 km resolution PaleoMIST global ice-sheet reconstruction dataset (ice-thickness data: Gowan et al., 2021) and the gFlex lithospheric flexure model (Wickert, 2015). We calculated the GIA signal for three spatially-invariant lithospheric elastic thickness values (30, 35 and 40 km; after Lange et al., 2014). As estimates of local mantle viscosity (Ivins and James, 2004; Lange et al., 2014) indicate isostatic response timescales shorter than PaleoMIST's 2.5-kyr temporal resolution, we consider isostatic adjustment to be fully completed within each time step. With this analysis, we produced a paleo-elevation change time series and corrected palaeo-topography at the study site from 25 ka to present.

3.4 Numerical Modelling of the EL and RCO Palaeo-Glaciers

In order to investigate the interaction between climate and the dynamics of the former EL and RCO glaciers, we employed a spatially-distributed ice-flow model, coupled with a positive degree-day (PDD) surface mass balance (SMB) parameterisation. Model parameters were tuned to fit best the simulated ice extent with the observed geomorphological moraine record. Similar models have been used elsewhere to investigate glacier response to climate change (e.g., Adhikari and Marshall, 2012; Jouvet and Funk, 2014; Wijngaard et al., 2019). The ice-flow model used here follows standard equations of the Shallow Ice Approximation (SIA; Hutter, 1983). While this approximation does not resolve all of the terms of the nonlinear glacial stress balance (i.e., longitudinal and transverse stresses), it is much faster to run than higher-order or Stokes models, allowing for ensembles of multi-century simulations exploring a comprehensive range of SMB and ice-dynamical parameters (see below). Other studies have shown this to be an appropriate approximation for modelling small mountain glaciers with small aspect ratios (Wijngaard et al., 2019). We implemented the model over a ~30-m resolution topographic grid derived from the AW3D30 DEM.

3.4.1 Ice Flux

In our model, ice flux was calculated recurrently at a given time-step interval, set to 0.1 years, for each ~900 m^2 grid cell, and accounted for both internal deformation and basal sliding. Internal deformation is controlled by the interaction of the glacier's surface slope and combined weight. In this study we used a uniform ice density value of 916.7 kg m^{-3}. Ice flow occurs when basal shear stress (τ), defined by Glen's flow law (**Eq. 1**), exceeds a given yield stress value (Cuffey and Paterson, 2010):

$$\varepsilon = A\tau^n \tag{1}$$

where ε is the horizontal shear strain, τ is basal shear stress (Pa) and n and A are constants representing the combined rheological impacts of ice temperature and ice crystal orientation. n and A were here set to values of 3.0 and 1.0×10^{-16} Pa^{-3} yr^{-1} (Hubbard et al., 2005), respectively. Such values are commonly used to account for irregularities in glacier-ice structure such as crevasse fields, meltwater pockets and other impurities (Cuffey and Paterson, 2010).

As geomorphological evidence of subglacial lineations and ice-moulded bedrock outcrops suggests the EL and RCO glaciers were at least partly warm-based, modelled ice flux therefore also needed to incorporate basal sliding, which is defined by **Eq. 2** based on Weertman's law (Weertman, 1957):

$$u_s = A_s \tau_d{}^{\rho} \tag{2}$$

where u_s is basal sliding velocity (m yr^{-1}), A_s and ρ are constants, and τ_d (Pa) is a given value for driving stress. In this study, $\rho = 3$, which is within the range observed in laboratory and field-based investigations (Budd et al., 1979; Bindschadler, 1983). Based on empirical measurements of sliding velocity obtained for similarly-sized, mid-latitude temperate mountain glaciers (e.g., Engelhardt et al., 1978; Blake et al., 1994; Cohen et al., 2000), we use a uniform value of 5.0×10^{-15} $Pa^{-1/3}$ m yr^{-1} for A_s, which yields a sliding rate of 5.0 m yr^{-1} where driving stress (τ_d) is 1 bar. For the EL-outermost advance reconstruction, this parameterisation of basal sliding increased the mean glacier surface velocity by ~6.2 m yr^{-1} relative to simulations implementing no basal sliding. Such a contribution represents ~18% of mean steady-state glacier surface velocity; a ratio that is close to those reported by empirical measurements of sliding speed versus surface speed of glaciers sharing similar properties (e.g., Cohen et al., 2000; 16%). However, it is important to note that estimating a meaningful value for basal sliding velocity is amongst the most challenging and uncertain components of modelling warm-based glaciers (Cohen et al., 2005). Moreover, asuming that the modelled glaciers were warm-based across their entire area and not polythermal is subject to debate and yields uncertainties further addressed in the discussion section of this paper.

3.4.2 Surface Mass Balance

Modelled ice thickness for a given grid cell controls the modelled glacier profile and is defined by the sum of ice flux and SMB. Here we parameterised SMB (b: m w.e.) using a PDD model, defined, at a given elevation (z), by **Eqs 3–5**:

$$b = Pr - (PDD)T, \quad T > 0 \tag{3}$$

$$b = Pr, \quad T < 0 \tag{4}$$

$$T = zELA\frac{\gamma}{1000} + TSL \tag{5}$$

where Pr is precipitation (m ice yr^{-1}), PDD is the positive degree-day melt factor (m ice $^{\circ}C^{-1}$ yr^{-1}), and γ is an adiabatic lapse rate (ALR; $^{\circ}C\,km^{-1}$), which enables interpolating atmospheric temperature T ($^{\circ}C$) at an elevation z (m a.s.l.) using a given value for temperature at sea level (TSL: $^{\circ}C$). We use an ALR of 6.5$^{\circ}C\,km^{-1}$ (e.g., Wallace and Hobbs, 2006; Roe and O'Neal., 2009). As shown by the above equations, PDD only causes surface

TABLE 2 | Coupled ice-flow and positive degree-day SMB model input parameters.

Model parameter	Unit	Initial value/range	Test range
Time step	Yr	0.1	0.05–0.1
Ice softness (A)	Pa^{-3} yr^{-1}	1.0×10^{-16}	0.5×10^{-16}–1.5×10^{-16}
Ice-flow law exponent	Constant	3.0	n/a
Ice density	kg m^{-3}	917	n/a
DEM spatial resolution	M	27.15	12.5–30
Atmospheric lapse rate	°C km^{-1}	6.5	n/a
Weertman's law constant A_s	Pa-1/3 m yr^{-1}	5.0×10^{-15}	$0–10.0^{-14}$
Weertman's law constant ρ	Constant	3.0	n/a
Degree-day melt factor (PDD)	mm w.e $d^{-1}°C^{-1}$	5.0–9.0	5.0–9.0
Glacier AAR	n/a	0.6–0.7	0.6–0.7

melt when atmospheric temperature exceeds 0°C (**Figure 4**). A constant precipitation rate is applied and normally distributed across the domain (e.g., Roe and O'Neal, 2009; Roe, 2011), thus assuming little geographical and altitudinal variation across the relatively small EL and RCO valley catchments (~7.5 and ~10.3 km^2, respectively). This simple SMB model does not independently consider ablation caused by sublimation or ice-front breakoff, nor does it take into account other sources of accumulation such as avalanches. It also neglects the percolation and refreezing of meltwater and assumes that all melting ends up as runoff (after Roe and O'Neal, 2009).

3.4.3 Modern Climate

Investigating former climate change from palaeo-glacier SMB requires the determination of base values for precipitation and temperature that are representative of average modern local climate. Mean annual temperature data were acquired from five different weather stations located in the towns of Corcovado (n = 1, 43°54′S; 71°46′W), Trevelin (n = 3, 43°5′S; 71°27′W) and Río Pico (n = 1, 44°10′S; 71°22′W). These data were obtained from the Argentinian National Agricultural Technology Institute (www.argentina.gob.ar/inta). *TSL* values were extrapolated from mean annual temperatures using an ALR of 6.5°C km^{-1}, for the years between 1982 and 2015 (depending on the weather station). The values ranged between 12.06 and 12.65°C. Given these data, a mean *TSL* value of 12.35°C was here considered representative of modern regional atmospheric mean annual temperature. Using a 6.5°C km^{-1} ALR, this is equivalent to a mean annual 0°C isotherm elevation of 1900 m a.s.l. As measured precipitation data was unavailable, local modern precipitation was obtained from the 1-km spatial resolution global-land WorldClim 2 dataset (WC2; Fick and Hijmans., 2017), which spatially interpolates available weather station data and provides monthly climate data averaged over 1970–2000. From this dataset, modern-time total annual precipitation was averaged over the simulated steady-state surface area of the EL (16 data points) and RCO (19 data points) palaeo-glaciers to derive estimates of 740 mm *w.e.* and 722 mm *w.e.*, respectively. Using an ice density of 916.7 kg m^{-3}, and assuming that all precipitation is accumulated as ice, these values are equivalent to 0.8072 and 0.7876 m^3 ice m^{-2} yr^{-1} of accumulation, respectively. Consequently, for each simulation, we calculated precipitation and temperature variations relative to modern-day base values of Pr_{EL} = 0.8072 m ice yr^{-1}, Pr_{RCO} = 0.7876 m ice yr^{-1}, *TSL* = 12.35°C.

3.4.4 Model Simulations

The model was used to simulate two distinct former advances/still-stands of the EL palaeo-glacier (EL-out and EL-mid) and one advance of the RCO palaeo-glacier (RCO-out), each relating to well-defined moraine complexes observed in the field (**Figures 2**, **3**). Model simulations were constrained by PDD melt factor thresholds of 5.0 and 9.0 mm *w.e.* $d^{-1}°C^{-1}$, consistent with values reported from stack measurements on mid-latitude mountain glaciers from different regions of the world (Braithwaite and Zhang, 2000; Hock, 2003). This is also consistent with PDD melt factors measured on Patagonian glaciers, which typically range from 5.0 to 7.5 mm *w.e.* $d^{-1}°C^{-1}$ (De Angelis, 2014). Accumulation area ratios (AAR) of 0.6 and 0.7 were also implemented as additional constraints for our simulations. Such values are based on worldwide observations that AARs >0.7 or <0.6 have produced less realistic SMB profiles for debris-free, mid-latitude temperate mountain glaciers in a state of mass-balance equilibrium, and >4 km^2 in surface area (Benn et al., 2005; Kern & László, 2010; Pellitero et al., 2015). However, this assumption yields significant uncertainties as it is challenging to estimate former glacier debris cover evolution, which, if sufficiently thick, could substantially lower the AAR through glacial surface insulation (Osmaston, 2005). Moreover, surface debris cover is likely to fluctuate through time as glacier retreat and thinning causes valley-side destabilisation. The AAR was calculated for each simulated ice extent deemed to match the sampled moraines using model-output ice-thickness raster data and the SurfaceVolume_3D ArcGIS tool (following Pellitero et al., 2015). Ice-front to moraine fit was assessed by producing modelled ice-surface longitudinal cross-section profiles along the glacier centre flowline for each simulation and comparing ice-front location with terminal moraines. ArcGIS 10.8 software was subsequently employed to digitize ELA polylines and total glacier and accumulation zone polygons using ice-surface topographic contour lines, prior to computing AARs using polygon 3D surface areas. Therefore, within such PDD melt factor and AAR constraints, a minimum of thirty to forty simulations were adjusted for each of the EL and RCO glaciers and for each reconstructed glacier-front position (EL = 2

positions, RCO = 1 position) to determine ranges of ideal precipitation and temperature parameter combinations producing moraine-matching glacier extents. In total, near one hundred multi-century model simulations with differing SMB parameters were adjusted to fit the geomorphological record, excluding model sensitivity test runs (see *Model Sensitivity Test* section below) and multi-century simulations that correlated poorly with observed moraine locations. For each given round-number PDD melt factor (5–9), a second order polynomial regression equation with a R^2 value greater than 0.99 was calculated to provide a relationship between ideal precipitation and temperature parameter combinations.

In contrast to Stokes or high-order numerical glacier models, our model does not require high computational speeds and enables comparing numerous simulations against the geomorphological record using a wide range of SMB parameter values. It also enables palaeo-temperature and palaeo-precipitation estimations even in the absence of a modern active glacier at the study site, although the lack of studied modern glaciers in the Poncho Moro massif makes calibrating the model against present-day glaciological and meteorological conditions challenging, leading to larger uncertainties in SMB parameter range estimates. Unlike palaeo-climate estimations relying on ΔELA comparisons (e.g., Sagredo et al., 2018; Sun et al., 2020), our method does not require a modern ELA value to derive palaeo-temperature estimates. Furthermore, it does not assume that precipitation was identical to the present at the time of the reconstructed glacier advance/still-stand, because accumulation is already taken into account in our SMB parameterisation. We thus consider SMB model outputs as more realistic palaeo-climate indicators and chose not to compare our results with an estimated modern ELA, as in the absence of active glaciers in the study area, this would be highly subjective.

3.4.5 Model Sensitivity Tests

In order to test confidence in using our SMB parameter combinations as potential palaeo-climate indicators, we tested the model by running simulations with different ice softness parameters (constant A in Glen's flow law; **Eq. 1**) to simulate different ice-temperature regimes. While the default value chosen is $1.0 \times 10^{-16}\,Pa^{-3}\,yr^{-1}$, which corresponds approximately to a mean glacier-ice temperature of −2°C, we also conducted model runs with boundary values of 0.5×10^{-16} and $1.5 \times 10^{-16}\,Pa^{-3}\,yr^{-1}$, corresponding to ice temperatures of approximately −5 and 0°C (Cuffey and Paterson, 2010), respectively (**Table 2**). The results generated a maximum glacier volume increase ($A = 0.5 \times 10^{-16}$) of 16% and a maximum decrease ($A = 1.5 \times 10^{-16}$) of 7%. Such fluctuations in ice thickness are mostly confined to the accumulation zone of the glacier, and therefore they have minimal impact on the extent and thickness of the glacier tongue. The greatest change observed in glacier-front location as a result of sensitivity to fluctuations in A values was a retreat of 94 m, which represents a 2.5% decrease in glacier extent. For most other simulations, maximum glacier extent remained within a 1% fluctuation to the original ($A = 1.0 \times 10^{-16}$). Therefore, modifying the glacier-ice temperature regime within a −5–0°C range has little impact on the model's ability to match the geomorphological moraine record.

Note that our adjustment of the ice-softness parameter is equivalent to the consideration of a correction factor in Wijngaard *et al.* (2019) -- i.e., a factor meant to represent the inaccuracies inherent in the SIA. In this sense, the low sensitivity to Glen's flow constant suggests a wide range of correction factors, or equivalently that the assumptions of the SIA have a relatively small impact on steady glacier geometry and length.

We also conducted test model runs by removing the effect of basal sliding (**Table 2**). The results showed that although the glacier took up to 30 years longer to build up, steady-state glacier extent and thickness were identical to runs conducted with basal sliding, indicating that changing the basal sliding velocity within a realistic range had little impact on steady-state ice thickness, ice-front location and glacier surface profile. However, we do note that doubling of the baseline sliding parameter described in *Ice flux section* caused a noticeable reduction in simulated ice-thickness and augmentation in ice-front extent.

We also tested the model's sensitivity to DEM spatial resolution by running a series of simulations using the ALOS PALSAR DEM product (Dataset[2]) which, in the studied region, uses radiometric terrain correction to re-sample the AW3D30 DEM product to 12.5 m spatial resolution. Despite a 2.4 times greater spatial resolution, the simulated ice thickness, glacier extent, surface velocity and years required to reach steady-volume were all identical to simulations conducted using a ~30 m spatial resolution DEM.

To compare our model outputs to the more commonly-used method of land-terminating glacier surface reconstruction using a simple flowline model (e.g., Huss et al., 2007; Banerjee and Shankar, 2013), we conducted simulations using GlaRe (Pellitero et al., 2016) and included the associated methodology and results in the **Supplementary Material**.

To assess variability in PDD melt factor values from different palaeo-glaciers of the region, and to obtain further local climatic constraints during the late-glacial period, we compared SMB parameters required for moraine-matching simulation of both the EL and RCO glaciers. We considered it reasonable to assume that climatic conditions are and were likely very similar between the two adjacent valleys. This is supported by WC2 total annual precipitation data, indicating a 1970–2000 mean of 722 mm *w.e.* over the simulated RCO glacier surface area (Fick and Hijmans., 2017), representing a 2.4% decrease relative to the adjacent EL valley (740 mm *w.e.*). Using identical AAR and PDD melt factor constraints for the SMB model as for the EL glacier simulations, we adjusted thirty model runs with a simulated ice-front extent that matches the RCO valley moraine system in order to analyse input SMB parameter combinations required. Assuming that this advance was contemporaneous with the EL late-glacial advance sampled for TCN dating, analysing the overlap in the resulting climate constraints from the two sets of

[2]Dataset: ASF DAAC 2015, ALOS PALSAR_Radiometric_Terrain_Corrected_low_res; Includes Material © JAXA/METI 2007. Accessed through https://asf.alaska.edu on 20th September 2018.

TABLE 3 | Exposure ages and summary statistics.

Sample ID	Kaplan et al. (2011) production rate									Outlier
	LSDn: Lifton et al. (2014)			St: Lal (1991) and Stone (2000)			Lm: Lal (1991) and Stone (2000)			
	Age	Internal	External	Age	Internal	External	Age	Internal	External	
	Cal Yr BP			Cal Yr BP			Cal Yr BP			
El Loro southern lateral moraine boulders										
RC20-23	18,462	608	1,628	18,636	614	1,653	18,365	605	1,628	no
RC20-24	17,373	555	1,525	17,397	555	1,536	17,201	549	1,518	no
RC20-25	16,358	521	1,435	16,307	519	1,439	16,177	515	1,427	no
RC20-26	19,483	609	1,706	19,796	619	1,744	19,441	608	1,712	no
RC20-27	17,318	562	1,523	17,333	563	1,533	17,142	556	1,516	no
RC20-28	18,811	1,031	1,852	18,907	1,036	1,870	18,614	1,020	1,840	no
Mean (n = 6): **17.97** ka; 1σ std: **1.15** ka; 1σ internal: 1.64 ka; 1σ internal + PR%: 2.20 ka										
Uncertainty weighted mean (n = 6): 17.85 ka; 1σ std: 1.07 ka										
MSWD: 3.78 > k: 2.26 (n = 6); Peak age (n = 6): 17.42 ka										

Scaling schemes: St is the time-independent version of Lal (1991) and Stone (2000), Lm is the time dependent version of Lal (1991) and Stone (2000), and LSDn is the time-dependent scheme of Lifton et al. (2014). External uncertainties include production rate (PR%) and scaling uncertainties. Elevation flag is std. Landform summary age and standard deviation reported in results and discussion sections are here highlighted in bold.

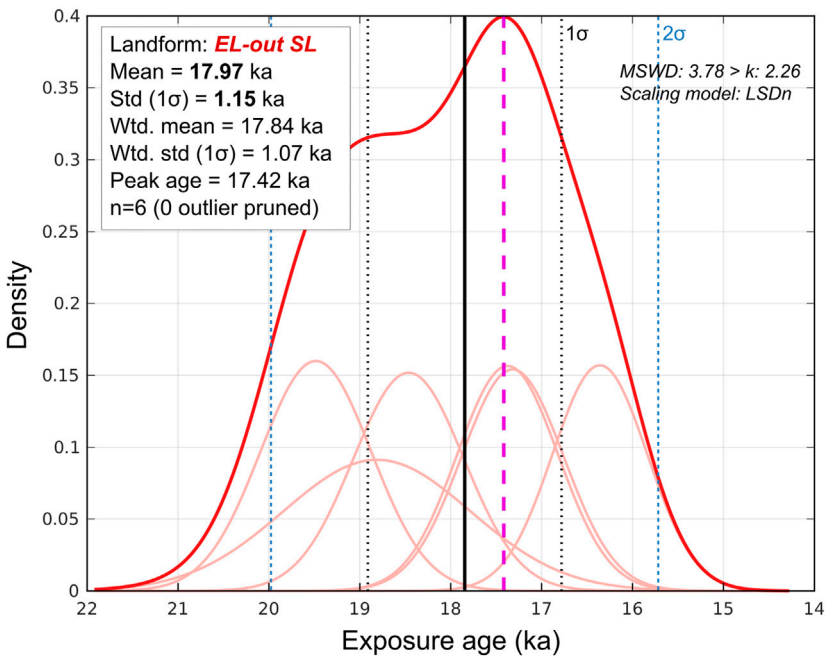

FIGURE 5 | Kernel density plot, adapted from plots produced using the iceTEA tools for exposure dating (Jones et al., 2019a; http://ice-tea.org/en/) and TCN dating summary statistics for the EL-out southern lateral (EL-out SL) moraine boulder samples (n = 6). Thick red curve represents the summed probability distribution for the age population while thin red curves depict Gaussian curves for individual samples. Vertical black lines denote the arithmetic mean, while thin black and blue vertical dashed lines denote the 1 σ and 2 σ confidence intervals of the mean, respectively. Thick purple and dashed vertical line highlights the peak age associated with the summed probability distribution. *Std*: standard deviation, *Wtd. mean*: uncertainty-weighted mean, *Wtd. std*: uncertainty-weighted standard deviation.

simulations can provide better confidence in resulting temperature and precipitation ranges required for moraine-matching simulations, and enables assessment of surface melt-rate variability between the two glaciers. Indeed, it is feasible and has been observed in other modern glaciated massifs (e.g., Glacier d'Arsine and Glacier Blanc, Ecrins massif, France; Vivian, 1967; Vivian and Volle, 1967), that two proximal mountain glaciers with similar elevation ranges and climatic conditions can display substantially different surface debris covers, mainly as a result of contrasting susceptibility of upper catchment slopes to rockfall and rock-slope failures (Benn et al., 2003). Therefore, some variability in former surface melt rates between the two glaciers may be expected, which may hinder the quality of overlaps in SMB

TABLE 4 | gFlex GIA-related surface elevation and PaleoMIST ice-thickness data.

Age (ka)	Cumulative GIA-related uplift (m)			Uplift per 2.5 ka interval (m)			Ice thickness (m)
	Elastic thickness						PaleoMIST 1.0 data
	30 km	35 km	40 km	30 km	35 km	40 km	Gowan et al. (2021)
25	–0.362	–0.362	–0.362	0	0	0	592.541
22.5	–0.146	–0.135	–0.135	0.216	0.227	0.227	601.949
20	–0.350	–0.330	–0.330	–0.204	–0.195	–0.195	573.919
17.5	22.721	23.072	23.072	23.071	23.402	23.402	617.747
15	121.657	121.257	121.257	98.936	98.185	98.185	264.197
12.5	150.980	148.053	148.053	29.323	26.797	26.797	0
10	150.974	148.049	148.049	–0.005	-0.005	–0.005	0
7.5	150.982	148.056	148.056	0.007	0.007	0.007	0
5	150.983	148.057	148.057	0.001	0.001	0.001	0
2.5	150.975	148.049	148.049	–0.008	–0.008	–0.008	0
0	150.974	148.048	148.048	–0.001	–0.001	–0.001	0

Data reported here are based on ice-thickness data for coordinates of the EL valley study site: 43°43′55″S; 71°27′38″W.

parameter ranges required for the moraine-matching simulations of both glacier advances, in the hypothetical case of these advances being triggered by the same climatic event.

4 RESULTS

4.1 Geomorphology

4.1.1 Valley Geomorphology

In the upper EL and RCO catchments, above the treeline (1,400–1,500 m a.s.l.), the valley floors are characterised by thick glacial debris cover and patterned ground displaying polygonal structures that are characteristic of periglacial environments and indicative of cryoturbation and frost heaving following ice retreat. These debris accumulations are interspersed in the steeper portions of the valley bottom by outcrops of ice-moulded and striated bedrock (**Figure 2A**). The upper EL and RCO catchments contain numerous empty cirques, while the EL valley still features one glacier remnant (~0.05 km^2) perched below its highest summit (~2095 m a.s.l.; **Figure 2A**). Debris cones and rock talus mantle the steep valley sides and indicate frost shattering of cliffs and local catchment ridges. Consequently, substantial volumes of rockfall debris partly obscure the palaeo-glacier bed topography.

4.1.2 Glacial Moraines

Geomorphological mapping from field and remotely-sensed observations reveals the preservation of three distinct moraine complexes deposited by glacier-ice confined within the EL valley, two of which are also present in the RCO valley (**Figure 2**).

In the EL valley, the outermost set of moraine ridges (*EL-out*) is located towards the eastern edge of the Poncho Moro massif, 1.5–2 km to the east of the valley mouth, and indicates a northeastward advance of the EL glacier. This complex can be linked to well-defined, ~1.5 km long, single-crested and prominent (30–35 m above the valley floor) lateral moraines preserved on both valley flanks (mean crest-surface slope: 13°; **Figure 3**). Both of these lateral ridges bifurcate downstream into a series of cross-valley arcuate ridges and hummocks spreading at least 1 km across a gently-sloping surface, which is suggestive of numerous episodes of terminus extent fluctuation and/or re-advances of the EL glacier (**Figure 2A**). The geometry of these terminal ridges and mounds suggest a piedmont-style former EL glacier terminus. The lateral moraine complex cross-cuts at right angles the RC III-VI moraines previously deposited by the Río Corcovado outlet glacier (**Figure 2**). Consequently, the advance of the EL glacier must post-date the RC VI moraine, which has been dated using ^{10}Be TCN dating to 20.7 ± 1.0 ka (Leger et al., 2021). Moreover, directly downstream of the terminal moraines, a broad (0.85 km^2 in area) low-gradient (2°) and homogeneous surface composed of fluvial sand and gravel progrades eastwards (43°43′59″S; 71°23′53″W). This terrace deposit, which was incised by the EL river post-deposition (~10–15 m incision), is interpreted as a proglacial outwash plain. It thus provides further evidence of a former glacier margin stabilised directly upstream from its location. The location of this deposit indicates that former proglacial rivers were constrained towards the north by the previously-deposited RC VII moraine. Such stratigraphic relationship further suggest that the EL-out advance is younger or similar-in-age to the deposition of the RC VII moraine, previously dated to 19.9 ± 1.1 ka (Leger et al., 2021). We targeted the prominent, sharp-crested southern lateral moraine ridge for TCN dating based on the assumption that it highlights maximum palaeo-glacier thickness and thus the most extensive, morphostratigraphically-oldest advance of the EL glacier into this moraine complex.

The RCO valley contains an analogous set of single-crested and prominent lateral moraine ridges nested on both valley flanks, which are located towards the mouth of the valley (**Figure 2**). These moraines exhibit curved geometries towards their distal ends, enabling a rough extrapolation of the former ice-front position during this advance. However, the exact position of the terminal moraine is uncertain as a consequence of local erosion by post-retreat fluvial incision. This moraine complex and associated advance are termed *RCO-out* and we consider it morphostratigraphically-equivalent to the *EL-out* moraine complex.

A second, younger complex of latero-terminal moraine ridges are evident in the EL valley, located approximately 3.8 km from

TABLE 5 | Numerical model output statistics and ranges.

Glacier advance/ still-stand simulated	Temperature depression (ΔTSL, °C)	Palaeo-precipitation (m ice yr^{-1})	% Of modern precipitation	ELA range (m a.s.l)	Steady-state glacier volume (km^3)	Steady-state glacier surface area (km^2)	Years required for steady-state	Glacier length (km)	Maximum glacier thickness (m)	Mean steady-state glacier surface velocity (m yr^{-1})	GIA-corrected temperature depression (°C)	GIA-corrected ELA range (m a.s.l)
EL-out	−1.0—1.9	1.20–3.90	149–483	1,515–1,604	0.614–0.769	7.154–7.234	100–170	6.10	272–315	31.9–61.0	−1.85—2.75	1384–1473
RCO-out	−0.7—1.6	0.95–3.45	126–438	1,579–1,645	1.110–1.500	11.060–11.430	240–400	7.12	261–291	25.4–48.0	−1.55—2.45[a]	1448–1514[a]
EL-mid (YD?)	−1.1—1.6	0.30–1.30	37–161	1,625–1,670	0.284–0.330	4.830–4.930	600–700	3.86	225–231	13.2–19.8	−1.10—1.60[b]	1625–1670[b]
EL-out (ACR?)	−1.0—1.9	1.20–3.90	149–483	1,515–1,604	0.614–0.769	7.154–7.234	100–170	6.10	272–315	31.9–61.0	−1.12—2.02[c]	1497–1586[c]

All model output ranges result from SMB constrains of PDD melt factors of between 5.0 and 9.0 mm we d^{-1} $°C^{-1}$ and AAR values of between 0.6 and 0.7.

[a]*Values rely on assumption that the RCO-out glacier advance/still-stand is coeval with the dated EL-out glacier advance/still-stand (~18 ka).*

[b]*Values rely on hypothetical assumption that EL-mid moraine date to the Younger Dryas stadial (~12 ka).*

[c]*Values rely on hypothetical assumption that ACR (~14 ka) advances/still stands of the EL glacier occured, with similar extent as EL-out.*

the valley headwall. These moraines demarcate a former glacier front positioned ~2.4 km upstream (~40% glacier-extent decrease) from the EL-out margins. This younger complex is composed of three adjacent ridges that extend for ~500 m, are curved towards their distal ends, and reach an elevation of ~1,300 m a.s.l. The ridges are relatively low in relief (2–5 m), with less well defined crests, and are only discernible on the northern valley flank (**Figure 3A,D**). Their proximal end seems to have been buried by the post-glacial accretion of rock talus. Their geomorphology is suggestive of a significantly lower sediment volume delivery and/or ice-front residence time than the EL-out moraine sequence. We refer to these deposits as the *EL-mid* moraine complex and associated glacier advance/still-stand. We did not identify geomorphic evidence of a similar mid-valley moraine complex in the RCO valley.

Finally, in both the EL and RCO valleys, smaller moraine ridges can be discerned in the upper catchment limits, near the downstream edge of isolated eastward-facing (down-wind) cirques, nested at elevations of between 1,500 and 1800 m a.s.l. (**Figure 2**). We only observed a single set of these moraines in the EL valley while the RCO catchment displays at least four cirques where such ridges are preserved. They highlight the former stabilisation/re-advance of small glaciers nested on the catchment's highest, wind-sheltered slopes. We hypothesise these deposits to be relatively young, perhaps late-Holocene or Neoglacial in age, given the late-Holocene relative glacier-extent loss observed in other Patagonian mountain valleys (e.g. Nimick et al., 2016; Reynhout et al., 2019).

4.2 ^{10}*Be* Surface Exposure Ages

The six boulders from the southern lateral moraine of the EL valley range in age from 16.4 ± 0.5 to 19.5 ± 0.6 ka and yield an arithmetic mean exposure age of 18.0 ± 1.15 ka. The age population demonstrates a relatively high and >1 mean square weighted deviation (MSWD) value of 3.78, thus suggestive of greater age scatter than can be predicted solely by 1σ analytical uncertainties (**Table 3**; **Figure 5**). Furthermore, the MSWD value exceeds the criterion *k*, which is dependent on the degree of freedom, and is equal to 2.26 given the number of samples (n = 6; Wendt and Carl, 1991; Jones et al., 2019a). Statistically, a MSWD > *k* suggests that the probability that the age population is representative of a single landform is <95% and thus the weighted mean cannot be used as an estimate of the average exposure age for the moraine (Jones et al., 2019a). Despite significant geological scatter, we do not identify obvious outliers as all ages fall within the population's 2σ envelope (**Figure 5**).

4.3 GIA-Related Uplift

Output from the gFlex lithospheric flexure model (Wickert, 2015) suggests that the surface elevation of the study site at 20 ka was between 148 m (40 km elastic thickness) and 151 m (30 km elastic thickness) lower than modern elevations measured in the field (**Table 4**). These cumulative uplift values are close to the estimate of 113.9 m obtained from the global ICE-6G model (Peltier et al., 2015) and a three-layer approximation of the VM2 Earth model implemented in the IceTEA tools for exposure ages (Jones et al., 2019b). GIA-related uplift modelling using gFlex suggests that

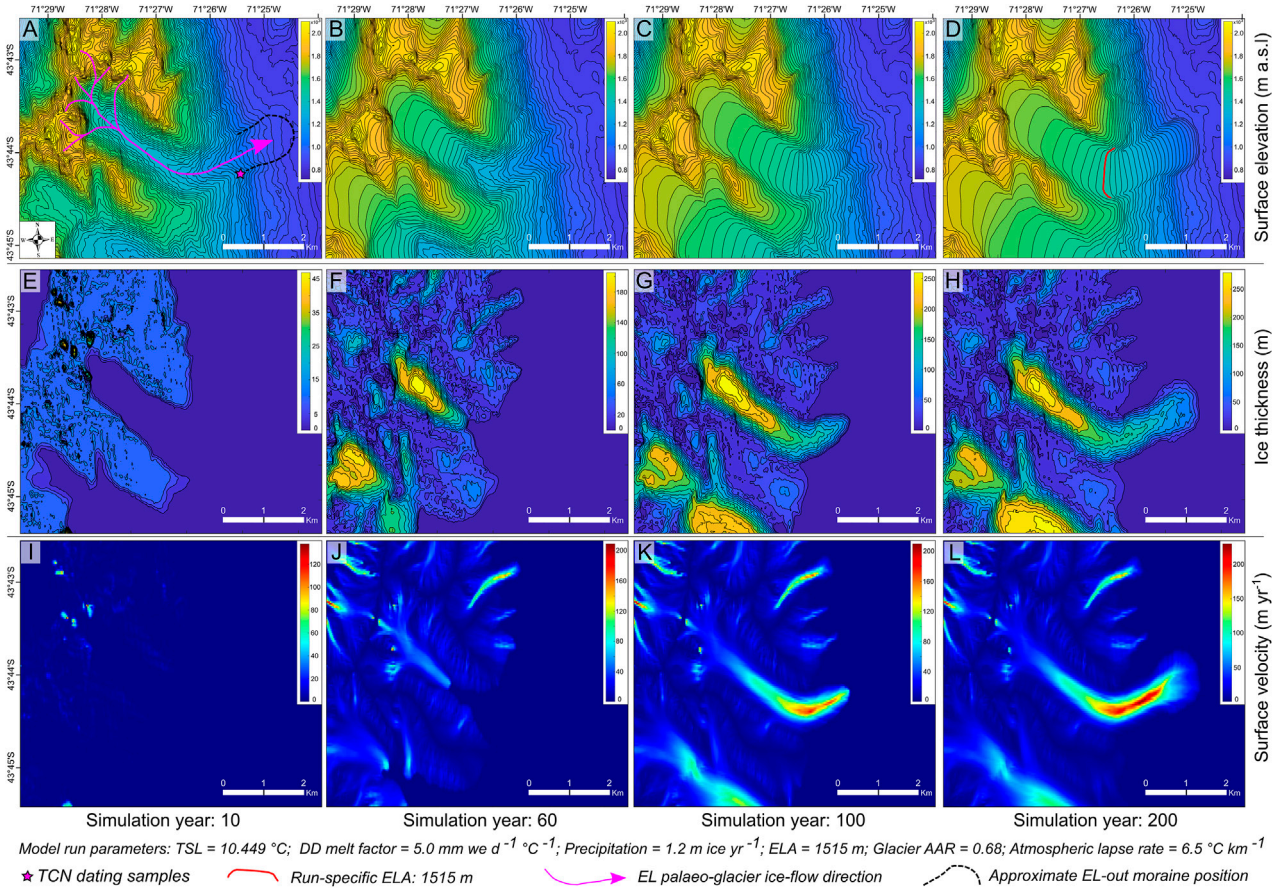

FIGURE 6 | Ice-flow model output data (~30 × ~30 m grid-cell spatial resolution) for one selected model simulation of the EL-out advance. **(A–D)** Surface elevation data (m a.s.l.) including AW3D30 DEM data plus simulated ice thickness, **(E–H)** ice thickness data (m), and **(I–L)** ice-surface velocity data (m yr^{-1}); for simulation years 10 (panels A, E, I), 60 (panels B, F, J), 100 (panels C, G, K) and 200 (steady-state volume, panels D, H, L). Note that colorbar values and scaling are panel-specific. Equivalent figures specific to the RCO-out and EL-mid advances/still-stands model simulations can be found in the **Supplementary Figures S1,2**.

over 99% of post-LGT uplift occurred between 20 and 12.5 ka in response to local ice-sheet disintegration (**Table 4**). The 2.5 kyr temporal resolution of the PaleoMIST dataset (Gowan et al., 2021) provides local, time-varying GIA-related uplift rates approximating 9.1, 39.4 and 11.6 mm yr^{-1} between 20–17.5, 17.5–15, and 15–12.5 ka, respectively. Using such uplift rates, a mean elastic thickness of 35 km, and a mean age of 18.0 ka for the EL-out advance based on our exposure age population, we estimate GIA to have caused approximately 131 m of surface uplift since the time of the EL-out glacier advance. The impact of such surface elevation change on former ^{10}Be production rates and exposure ages is inferior or equivalent to 1σ analytical uncertainties (between 0.47 and 0.74 ka; <4% age corrections), and is thus not considered applicable here. However, the inferred mean uplift of 131 m since 18 ka, the approximate time of the EL-out glacier advance, requires taking into account 0.85°C of local atmospheric temperature adjustment when applying an ALR of 6.5°C km^{-1}. Consequently, we adjusted our modelling ELA and temperature outputs using 131 m of surface uplift and 0.85°C of relative temperature lowering for a given model simulation in order to account for GIA-related uplift since the time of the reconstructed advance. These reconstructed uplift rates are inherently subject to uncertainties associated in part with the assessment of parameters such as regional palaeo-ice thicknesses, lithospheric thickness and mantle viscosity (Peltier et al., 2015; Wickert, 2015; Gowan et al., 2021). However, our estimates are similar in magnitude to modern uplift rates observed for regions of Patagonia currently experiencing rapid isostatic uplift due to present-day glacial retreat and ice-sheet thinning. For instance, Lange *et al.* (2014) reported modern uplift rates from geodetic GNSS observations of up to 41 ± 3 mm yr^{-1} near the centre of the South Patagonian Icefield (SPI), and of approximately 20 mm yr^{-1} towards the margins of the SPI. Although regional tectonic uplift may also contribute a small part of this uplift (Richter et al., 2016), these modern rates suggest that our post-LGT GIA-uplift estimates are comparable and relatively realistic for Patagonia.

4.4 Numerical Modelling Results

4.4.1 Glacier Geometry

Our spatially-distributed ice-flow model generated simulated glacier surfaces that match lateral and terminal moraine complexes well for

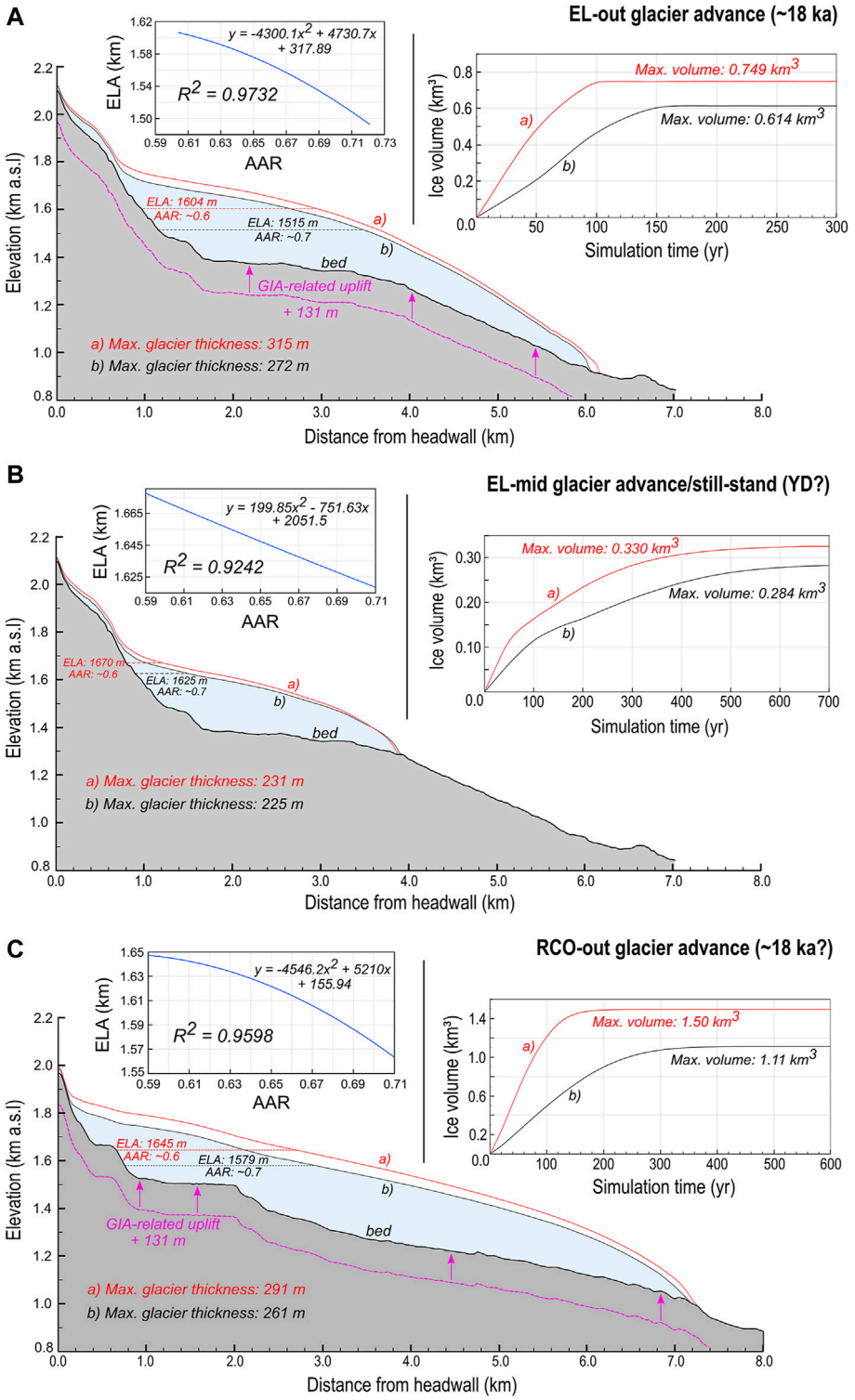

FIGURE 7 | Elevation profile graphs (above present-day sea level) of bedrock topography (AW3D30 DEM data) and simulated steady-state ice thickness along the central glacier flowline for the EL-out **(A)**, EL-mid **(B)** and RCO-out **(C)** simulations. The purple dashed lines denote the estimated former bed surface elevation at the time of the EL-out advance, prior to GIA-related uplift (131 m). For each profile graph, the two ice-surface profiles highlighting maximum and minimum simulated ice-thicknesses for a given advance/still-stand are represented. These two profiles also represent boundary AAR values (0.6 vs. 0.7). Each panel also features an ice-volume time series line graph for minimum and maximum ice-volume simulations, as well as a standard regression analysis establishing the best-fit second-degree polynomial relationship between ELAs (km a.s.l.) and AARs for all simulations of a given glacier reconstruction.

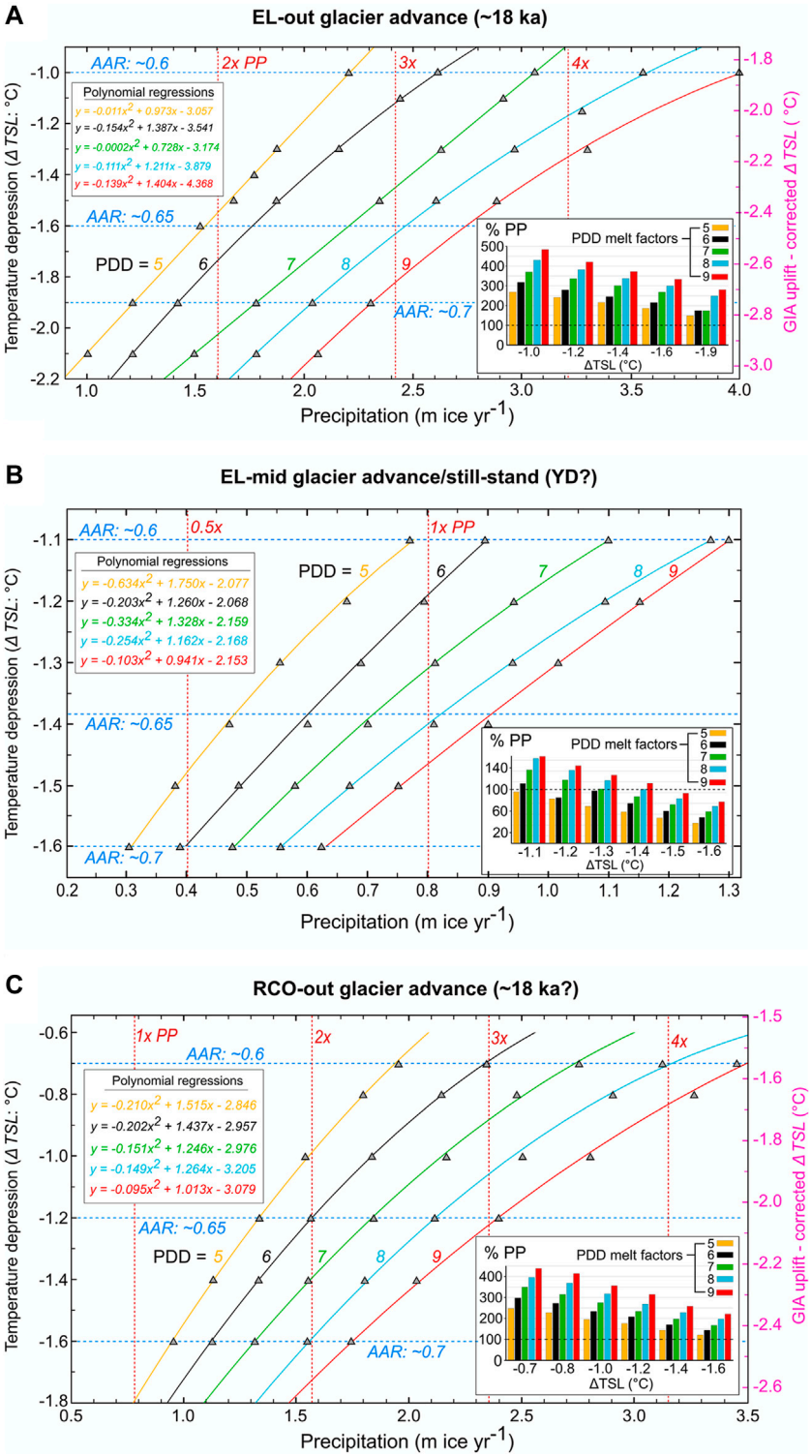

FIGURE 8 | Ice-flow model temperature depression and precipitation parameter combinations for each moraine-matching simulation (grey triangles) of the EL-out advance **(A)**, the EL-mid advance/still-stand **(B)** and the RCO-out advance **(C)**, for a given round-number positive degree-day melt factor value between 5.0 and 9.0 mm *w.e.* $d^{-1}{}^{\circ}C^{-1}$. Each graph displays colour-coded second-degree polynomial regression curves and equations for each round-number positive degree-day melt factor (n = 5). All regression equations are associated with R^2 values >0.99. Each diagram also display histograms indicating the % precipitation associated with each simulation relative to present precipitations (% PP) values, for a given temperature depression value and degree-day melt factor (colour-coded bars). The horizontal dashed line represents modern precipitation (100%). Note that GIA-corrected temperature depressions include the hypothetical assumptions that the EL-mid advance/still-stand dates to the YD (~12 ka), and that the RCO-out advance is coeval with the EL-out advance (~18 ka).

a given advance/still-stand. However, while steady-state simulated ice-fronts matched the terminal moraine record for the EL-mid and RCO-out simulations, the simulated EL-out ice front stabilised ~100 m upstream from the moraine complex. Further ELA lowering did not generate significant ice-front advances, instead inducing a wider piedmont-style ice front overrunning the lateral moraine ridges. There are numerous possible reasons for such a misfit, including, for instance, the model's inability to capture spatially-varying basal sliding conditions and ice temperature properties, and the possibility of post-advance debris accumulations near the former glacier terminus, which could have caused a decrease in basal slope gradient. Therefore, for the EL-out simulations, we based our moraine-fit quality assessment on the location of the ice margin relative to the prominent EL-out lateral moraine ridges. Simulated steady-state glacier volume for the EL-out glacier advance ranged between 0.614 km^3 (0.563 Gt) and 0.769 km^3 (0.705 Gt) depending on SMB parameter combinations, while steady-state surface area ranged between 7.154 and 7.234 km^2 (**Table 5**; **Figures 6**, **7**). Simulations took between 100 and 170 years to reach steady volume from a no-ice initial state. Maximum ice thickness ranged between 272 and 315 m and glacier length along the central flowline approximated 6.1 km from the valley headwall. Mean steady-state glacier-surface velocity, which is positively correlated to accumulation rates and thereby ice flux, ranged between 31.9 m yr^{-1} (run with lowest precipitation) and 61.0 m yr^{-1} (run with highest precipitation) (**Table 5**; **Figure 6**). These surface velocities are consistent with average surface velocities measured in the field and through remote sensing of land-terminating and similarly-sized glaciers from northern Patagonia (Rivera et al., 2012) and other mid-latitude alpine massifs (e.g., New Zealand Southern Alps, Mont-Blanc massif; Millan et al., 2019). Corresponding glacier geometry statistics for the RCO-out and EL-mid advances/still-stands are compiled in **Table 5**.

4.4.2 Palaeo-Temperature

For the EL-out glacier advance, here dated to 18.0 ± 1.15 ka, simulations constrained by PDD melt factor values ranging between 5.0 and 9.0 mm *w.e.* $d^{-1}°C^{-1}$ and by AAR values of between 0.6 and 0.7 required a range of temperature depression values relative to our present-day mean annual atmospheric temperature estimation (section *Modern Climate*) of between −1.0 and −1.9°C (**Table 5**; **Figure 8A**). Including correction for cumulative GIA-related surface uplift relative to today (−0.85°C; **Table 4**) causes temperature depression values to range between −1.85 and −2.75°C. Moraine-matching simulations conducted using a temperature depression that is greater than 2.75°C caused the ELA to increase and the glacier's accumulation zone to expand so that the AAR becomes greater than 0.7, a ratio that is rare for a mid-latitude, land-terminating mountain valley glacier in a state of mass-balance equilibrium (Braithwaite and Müller, 1980; Kern and László, 2010), and is here assumed unlikely (**Table 5**; **Figure 8A**).

4.4.3 Palaeo-Precipitation

The model simulations required precipitation values ranging between ~1.2 and ~3.9 m ice yr^{-1}, which, since we are assuming that all precipitation accumulates as glacier ice, translates to total annual precipitation values of 1,100 and 3,575 mm *w.e.* yr^{-1}, respectively, using an ice density of 916.7 kg m^{-3} (**Figure 8A**). These precipitation values represent increases of between 49 and 383% relative to modern precipitation (742 mm *w.e.* yr^{-1}; WC2 data; Fick and Hijmans., 2017), respectively. Conducting moraine-matching simulations with similar to, or smaller than, modern-day precipitation caused the simulated glacier AAR to be greater than 0.7. Therefore, our model outputs suggest that local precipitation was greater than present during this late-LGM glacier advance (**Table 5**; **Figure 8A**). Our results also showed that, when using a minimum PDD melt factor of 5.0 mm *w.e.* $d^{-1}°C^{-1}$, simulations conducted with temperature depressions that are between −1.0 and −1.5°C (−1.85°C: −2.35°C with GIA-related uplift correction) required at least twice more and up to four times more precipitation relative to modern values.

Corresponding ice-flow model output statistics for reconstructions of: 1) the RCO-out glacier advance, and 2) the EL-mid glacier advance/still-stand; are compiled in **Table 5** and **Figures 7**, **8**.

5 DISCUSSION

5.1 Geomorphological Considerations and Age Interpretation

The distribution of exposure ages from the EL southern lateral moraine boulders display greater age scatter than can be predicted by 1σ analytical uncertainties alone (MSWD = 3.78; **Table 3** and **Figure 5**). This suggests that pre- and/or post-depositional processes likely played an important role in causing exposure age under- and/or over-estimations. Rock surface erosion is not thought to contribute to this age scatter because we observed limited boulder surface erosion pitting (<1 cm), and the erosion rate of 0.2 mm ka^{-1} estimated for semi-arid central Patagonia (46°S; Douglass et al., 2007; Hein et al., 2017) would increase ages by less than 1%, which is less than the 1σ analytical uncertainties (~3–5%). We here consider two scenarios for such a spread in exposure ages.

The first scenario is based on the assumption that boulders nested on the EL southern lateral moraine were deposited by a single glacier advance, and the exposure-age scatter arose from a combination of ^{10}Be inheritance and post-deposition boulder exhumation. Nuclide inheritance may occur, for example, where sediment is sourced from a rockfall onto the glacier. A 350 m-high and 1.3 km-wide granite cliff on the northern EL valley flank, situated ~2–3.3 km from the location of sampling, is a potential source of rockfall (**Figures 2A**, **3A**). Post-depositional boulder exhumation may also have occurred given the steep slopes (>25°) of the single-crested moraine, which make it susceptible to disturbance *via* gravitational mass wasting (**Figure 3C**). Our mapping reveals the occurrence of numerous subtle ridges bifurcating towards their distal ends further downstream, towards the palaeo-glacier's latero-frontal and frontal environments (**Figure 2**). According to this hypothesis, the lateral moraine crest targeted for TCN dating, deposited by thicker ice, would relate to the outermost and oldest of several advances and/or still-stands of the EL glacier.

Alternatively, the sampled moraine boulders may have been deposited by several glacier advances/still-stands causing the sampled ridge to be a composite moraine. Indeed, the EL glacier may have reached a similar, confined position at its southern lateral margin during several advances/still-stands highlighted by the multiple terminal moraine ridges preserved down-valley (**Figure 2A**). In this eventuality, several advances/still-stands of the EL glacier could have potentially reworked previously-deposited moraine boulders, eroded moraine-crests, and caused boulder exhumation, as well as possibly incorporating younger material in the lateral moraine crest, thus generating scatter in the exposure ages. Such disturbance would predominantly cause the exposure ages to under-estimate the true age of moraine formation, which would hence be more appropriately estimated by the population's oldest exposure age, i.e., 19.5 ± 0.6 ka.

As field investigations of the southern lateral moraine, near to the sample location, revealed a well preserved single, sharp moraine crest, thus presenting a lack of a multi-ridge moraine complex, we consider the first scenario as more likely. We therefore propose that the EL southern lateral moraine crest is representative of the outermost advance, and any lateral moraine ridges deposited inside the EL southern lateral moraine during younger advances/still-stands were likely not preserved. Consequently, we consider the arithmetic mean sample age (18.0 ± 1.15 ka) as the most appropriate minimum age for the EL-out advance. Furthermore, this approximate age fits the wider chronology established for the Río Corcovado outlet glacier, as it is younger than the 20.7 ± 1.0 ka age of the RC VI moraine that it cross-cuts, and it is either younger or similar in age to the 19.9 ± 1.1 ka age of the RC VII moraine that abuts its proglacial outwash deposit (Leger et al., 2020; 2021).

5.2 Palaeo-Climate

5.2.1 PIS Context and the Late-LGM Cold/Wet Episode

The geochronological reconstruction of LGM expansions of the PIS Río Corcovado outlet glacier (Leger et al., 2021) suggests that local PIS outlets were sensitive to regional warming and drying during the Varas interstade (22–19.2 ka BP; Denton et al., 1999; Mercer, 1972), which caused the retreat of northeastern PIS outlet glaciers from LGM margins to be initiated relatively early, between ~19 and ~20 ka BP (as argued by García et al., 2019). However, palaeo-ecological data from the Chilean Lake District (Lago Pichilaguna record; Moreno et al., 2018) demonstrate sharp positive anomalies in *Poaceae* and *Isoetes savatieri* pollen concentrations between 19.3 and 17.8 kcal yrs BP. These data suggest the Varas interstade preceded a return to colder, wetter conditions between ~19.5 and ~18 ka, during which the SWW are proposed to have migrated equatorward and reached their maximum LGM influence in northern Patagonia (Moreno et al., 2018). Shortly after 18 ka, a period of rapid drying and atmospheric and oceanic warming drove widespread deglaciation throughout the southern hemisphere (Mashiotta et al., 1999; Kaiser et al., 2007; Caniupán et al., 2011; Lopes dos Santos et al., 2013), often interpreted as the timing of the LGT in Patagonia and New Zealand (Lamy et al., 2004; 2007; Putnam et al., 2013; Hall et al., 2013; Davies et al., 2020). This proposed ~1.5 kyr-long late-LGM interval of cooling and increased precipitation coincides with the timing of numerous late-LGM PIS expansion and/or stabilisation events reported for several Patagonian and New Zealand outlet glaciers around 18–17 ka (e.g., Denton et al., 1999; Kaplan et al., 2007; 2008; Murray et al., 2012; Putnam et al., 2013; Moreno et al., 2015; Darvill et al., 2016; Shulmeister et al., 2010; 2019; Davies et al., 2020; Mendelová et al., 2020a). Moraine boulder exposure ages from the EL southern lateral moraine (**Table 3**; **Figure 5**), with a mean age of 18.0 ± 1.15 ka, along with the observations of morphostratigraphically similar moraines nested in local mountain valleys (Leger et al., 2020), suggest that sensitive mountain glaciers of northeastern Patagonia (e.g. the EL and RCO palaeo-glaciers) advanced in response to this late-LGM climatic event. The geomorphological record, by featuring moraines of similar sizes, with comparable preservation levels and distance-to-headwall properties, suggests the EL-out and RCO-out advances are possibly age-equivalent, and thus reflect a response to the same climatic event. The significant overlap between temperature (67%) and precipitation (83%) ranges required for moraine-matching simulations of the EL-out and RCO-out advances (**Figure 9**; **Table 5**) support this interpretation. Moreover, ice-flow model output suggests time intervals of 100–170 years and 240–400 years for building steady-state ice volume from ice-free initial states during the EL-out and RCO-out advances (**Figures 6**, **7**). Even when considering cold-bedded glacier conditions (no basal sliding: average build-up time increase by 30 years), and moraine formation time (thought to be <50 years for moraines <40 m in height; Anderson et al., 2014), estimated maximum glacier build-up times remain <500 years. We thus argue that a 1.5 kyr cold/wet episode would have been long enough for local mountain glaciers to build up and stabilise, even from an ice-free initial state.

However, our ^{10}Be Río Corcovado moraine chronology suggest the Río Corcovado outlet glacier started to retreat from its LGM margins approximately 1.5–2 ka prior to this late-LGM return to colder/wetter conditions. Furthermore, our reconstruction of deglacial proglacial lake-level evolution and the timing of glaciolacustrine drainage shifts following the initial retreat of the Río Corcovado glacier front implies that the outlet glacier did not experience a significant re-advance towards its LGM margins during the late-LGM climatic event, at around ~18 ka (Leger et al., 2021). The relatively short-lived (~1.5 ka) nature of the late-LGM cooling and high precipitation event could perhaps explain the lack of a major outlet glacier re-advance, as the extensive Río Corcovado outlet glacier may require a longer duration before adjusting its geometry and advancing up a reversed slope. Alternatively, one could argue that, in this region, a negative-mass-balance-inducing feedback mechanism prevented the ice-sheet outlets from being sensitive to a late-LGM colder/wetter episode following earlier initial retreat. Based on recent investigations modelling lake-terminating mountain glaciers (e.g., Sutherland et al., 2020), we propose that the enhanced calving rates caused by large and deep proglacial lakes formed in overdeepened eastern Patagonian

valleys during deglaciation were likely responsible for this glacier-climate de-coupling effect. Sensitive mountain glaciers (e.g., the EL and RCO glaciers) perched on higher massifs of the region, however, were not affected by these proglacial lakes, and were thus able to advance/stabilise in response to this late LGM cold/wet event.

5.2.2 Palaeo-Precipitation

Our numerical modelling simulations of the EL-out advance suggest a precipitation increase of between ~50 and ~380% greater than present at around 18.0 ± 1.15 ka (**Table 5**; **Figures 8**, **9**). Furthermore, all of the RCO-out simulations also require higher-than-today precipitation (up to 338% higher than today) when constrained by PDD melt factors of between 5.0 and 9.0 mm *w.e.* $d^{-1}°C^{-1}$ and AAR values of between 0.6 and 0.7 (**Table 5**; **Figures 8**, **9**). These findings evidence a positive precipitation anomaly at around 18 ka relative to today. By assuming that both glaciers were responding to the same climatic event, we can constrain the estimated precipitation range to 49–338% increases relative to the present, which represents the overlap between the EL-out and RCO-out palaeo-glacier simulations when constraining SMB identically (**Figure 9**). Based on comparisons with results from Patagonian LGM palaeo-precipitation proxy data and palaeo-climate models (e.g., Galloway et al., 1988; Cartwright et al., 2011; Berman et al., 2016), we consider the lower-end estimates of our resulting palaeo-precipitation range the most likely (i.e., ~50–200% increases). Even with an equatorward-migrated SWW belt, with its core located towards 43°S, the orographic effect associated with the Patagonian Andes would still cause a rain-shadow effect, effectively starving the eastern side of the mountain front of moisture. In comparison, present-day climate displays total annual precipitation increases of more than 50% between 43°S and 49–50°S (the modern core of the SWW belt) only towards the western margin of the cordillera. Towards the centre of the Andes, this latitudinal precipitation increase is reduced to ~20% (Garreaud et al., 2013; Fick and Hijmans., 2017). Given these known orographic effects and the location of our study site towards the eastern margin of the mountain front (71°S; **Figure 1**), we consider model outputs suggesting precipitation increases > ~200%, to be less likely.

Despite the wide range of possible values that would simulate moraine-matching glacier advances, our results suggest that a local positive precipitation anomaly relative to today was required during the late-LGM. While the breakdown of the PIS and the reduction of its orographic effect may be expected to contribute to local precipitation increases, we do not consider this a primary driver because significant local ice-sheet disintegration did not occur until much later, at 16.3 ± 0.8 ka (Leger et al., 2021). Hence, we suggest that the positive precipitation anomaly identified here is consistent with the proposed hypothesis of high local SWW influence and equatorward migration of the wind belt during the late-LGM (19.5–18 ka). This latitudinal shift potentially induced positive glacier mass balances and reduced summer temperatures in northern Patagonia at the time (Denton et al., 1999; Heusser, 1983; Heusser et al., 1999; Moreno et al., 2015; 2018).

5.2.3 Palaeo-Temperatures

Our results from the EL-out simulations suggest that, after accommodating local GIA-related uplift corrections, local temperatures at around 18.0 ± 1.15 ka were between 1.9 and

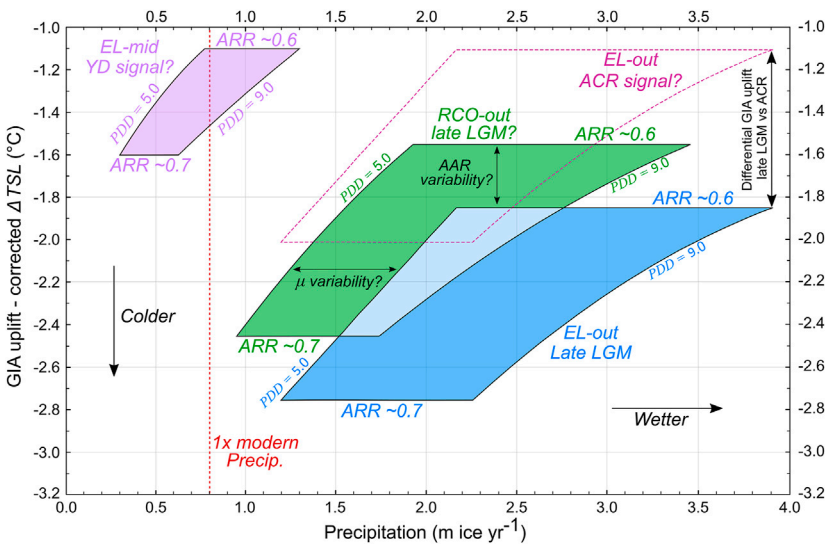

FIGURE 9 | Ice-flow model temperature depression and precipitation parameter combinations for moraine-matching simulations of the EL-out (blue), EL-mid (purple) and RCO-out (green) advances/still-stands. Temperature depression values are corrected for modelled GIA-related uplift since time of advance/still-stand. Note that GIA-corrected temperature depressions include the hypothetical assumptions that the EL-mid advance/still-stand dates to the YD (~12 ka), and the RCO-out and EL-out advances are coeval (~18 ka). The dashed purple "SMB parameter box" denotes a hypothetical advance/still-stand of the EL glacier reaching a similar ice-front position to the EL-out advance, but dating to the ACR (~14 ka) and thus associated with less GIA-related uplift (17.7 m).

2.8°C colder than today (**Tables 4**, **5**; **Figures 8**, **9**). The RCO-out simulations suggest a similar cooling signal of between −1.6 and −2.5°C. By validating the EL-out and RCO-out moraines to be age-equivalent, one could reduce the envelope of former temperatures to the overlap between the two simulations, resulting in a cooling of between −1.9 and −2.5°C. These figures should be treated with caution, however, as numerous assumptions and sources of uncertainty exist (*Limitations and Future Work section*). Firstly, we were unable to calibrate ice extents and thicknesses simulated with our modern climate estimation against modern glaciers as these do not exist in the study area. Furthermore, the lack of localised weather station data makes chosing a method for estimating atmospheric temperatures and ALR values representative of modern-day climate challenging, and this uncertainty is enhanced by the assumption that the ALR was constant over the past 18 ka, which is currently implausible to determine for certain. While we here acknowledge such uncertainties, we consider our method for estimating modern-day climate (*Modern climate section*) to be appropriate, and thus propose that local atmospheric temperatures were between ~1.9 and ~2.8°C lower than present during the late-LGM (19.5–18 ka), as suggested by our model results. This estimation overlaps the LGM mean annual temperature depression range of 2.3–4.4°C proposed for eastern Patagonia by palaeo-climate proxy data compilation and modelling using the PMIP3 model (Berman et al., 2016).

5.2.4 Younger Late-Glacial Advances/Still-Stands

There is widespread empirical evidence for glacial advances/still-stands occurring after the final disintegration of the PIS, during the Antarctic Cold Reversal (ACR) across Patagonia (Clapperton et al., 1995; Ackert et al., 2008; Glasser et al., 2011; García et al., 2012; Nimick et al., 2016; Davies et al., 2018; Sagredo et al., 2018; Reynhout et al., 2019; Mendelová et al., 2020b), New Zealand (e.g., Putnam et al., 2010), and other glacierised regions of the southern mid-latitudes such as the Kerguelen Archipelago (e.g., Jomelli et al., 2017; Charton et al., 2020). A new comprehensive ^{10}Be moraine chronology (Soteres *et al.*, personal communication) from the Nikita valley (43°57′48″S; 71°38′11″W), located 30 km south of the EL valley, provides robust geochronological evidence for an advance of the Nikita palaeo-glacier during the ACR (14.7–13.0 ka; Pedro et al., 2016). This re-advance reached a similar, but slightly less extensive (<500 m) glacier extent than an older advance/still-stand associated with the outermost ridges of the terminal moraine complex, which is argued to have occurred around ~16 ka (Soteres *et al.*, personal communication). Similarly to the EL valley, the Nikita valley also contains a smaller set of mid-valley, more subtle latero-frontal moraines located ~1.7 km further upstream from the outermost moraines. The authors propose that these ridges were likely deposited during the Younger Dryas stadial (YD: 12.9–11.7 ka) based on TCN dating results. Such a pattern of extensive ACR moraines and more subtle but distinct YD moraines located up-valley was also observed in central Patagonia (47–48°S; Sagredo et al., 2018; Mendelová et al., 2020b). According to the geomorphological similarity and proximity of the Nikita and EL moraine records, one could speculate that the innermost terminal ridges of the EL-out moraine complex may also have been deposited during the ACR, while the smaller, mid-valley latero-frontal moraines (EL-mid) observed further up-valley could perhaps date to the YD stadial.

If those hypothetical assumptions, based solely on cross-valley morphostratigraphic comparisons, are valid, our glacier numerical modelling results could be utilised to infer that regional precipitation was likely between 50 and 380% higher than present during the ACR, and between 60% lower and 60% higher (~40–160% of modern values) than present during the YD (**Table 5**; **Figure 9**). Such contrasting results would be in agreement with findings from regional palaeo-ecological proxy data that suggest late-glacial millennial-scale latitudinal shifts of the SWW belt induced increased and then decreased SWW influences in the southern mid-latitudes during the ACR and YD stadials, respectively (Siani et al., 2010; De Porras et al., 2012, 2014; Villa-Martínez et al., 2012; Montade et al., 2013; Moreno et al., 2018, 2019; Vilanova et al., 2019). Recent work by Skirrow *et al.* (2021) supports a poleward latitudinal shift of the SWW during the YD through Optically Simulated Luminescence dating of a reduction in the water supply of Río Chubut, in northeastern Patagonia. When using the modern climate estimation described in section *Modern Climate.* exclusively, and after including GIA-related surface uplift corrections of 17.7 and 0 m associated with EL glacier advances hypothetically timed at ~14 ka (ACR) and ~12 ka (YD), as suggested by the gFlex model output data (**Table 4**), our modelling results would suggest that local temperatures were between 1.1–2.0°C and 1.1–1.6°C lower than today during the ACR and YD stadials, respectively (**Table 5**; **Figure 9**). These inferences are close to findings reported by Sagredo *et al.* (2018) using ΔELA depression estimates for the extant Río Tranquilo glacier (47°S), suggesting a minimum cooling for the outermost ACR advance (13.9 ± 0.7 ka) of between 1.6 and 1.8°C. A scenario of northward SWW belt migration and local precipitation increase is also proposed by Sagredo *et al.* (2018) to help explain the widespread trans-Pacific and trans-latitudinal positive mass balance signal of sensitive Patagonian mountain glaciers during the ACR.

According to our model simulations, the EL-mid advance, which we speculate to date to the YD stadial, represents a ~54% ice-volume loss and ~37% ice-extent decrease relative to the EL-out advance dated to 18.0 ± 1.15 ka and perhaps also associated with an ACR re-advance. Given the large overlap in the estimated local palaeo-temperature ranges required during the ACR and YD scenarios, the majority of this significant ice loss would possibly have been caused by a decrease in precipitation during the YD stadial. This suggests that mountain glaciers in northeastern Patagonia were highly sensitive to variations in precipitation, most likely associated with latitudinal shifts of the SWW belt. Model simulations of the EL-mid advance require between 600 and 700 years to reach steady glacier volume (**Table 5**). Given the YD stadial was ~1.2 kyr long, such inferences presume that the EL-mid moraines were potentially deposited by either a small re-advance, or a still-stand. This hypothesis is also supported by the smaller, more subtle geomorphology of the EL-mid moraines relative to the EL-out moraine complex.

It is however essential to stress that the above discussion (*Younger Late-Glacial Advances/Still-Stands section*) is not based on any chronological evidence, but is instead exclusively based on cross-valley comparisons and mostly aims at encouraging further work in the study region. The speculative results presented here thus await either confirmation or disproof by future glacier chronological reconstructions.

5.3 Positive Degree-Day Melt Factor Variability

Simulations of the RCO-out glacier advance suggest that, using identical SMB parameters as for simulations of the EL-out glacier advance, PDD melt factor values need to be between 1.4 and 1.7 times greater to produce moraine-matching simulations. Using identical PDD melt factors instead causes the RCO ice-front to overrun the RCO-out lateral moraines. We consider such a former glacier-front position as unlikely, as it would have caused much greater erosion of the RC III-V LGM moraine record than can be observed in the field. Assuming that both advances were most likely coeval and that climatic conditions were similar in both adjacent catchments, this offset in former ice-front extents might therefore suggest a notable difference in former surface melt rates between the two palaeo-glaciers. Geomorphological analyses reveal that, relative to the RCO valley, the EL valley is narrower, its valley slopes are steeper, and it contains a higher concentration of eroded rock slopes with large debris cones and evidence of substantial talus accretion towards their base (**Figures 2**, **3**). We therefore suggest that former supraglacial debris cover might have been more substantial for the EL glacier than for the RCO glacier, thus potentially causing ice-surface insulation, lower surface melt-rates, and greater relative ice-extent in the ablation zone. The larger size of the EL-out relative to the RCO-out lateral moraines is potentially indicative of greater debris delivery, despite the EL glacier being smaller in surface area. Heavily debris-covered mountain glaciers are also often characterised by relatively low AARs (Benn et al., 2005). If both advances were synchronous and debris cover on the EL glacier was greater, then the AAR value associated with the RCO-out advance was likely greater than for the EL-out advance. This could explain, if excluding the hypothesis that both advances were not triggered by the same climatic event, why the two palaeo-glacier simulation sets, both constrained with AAR values of 0.6 and 0.7, do not produce identical palaeo-temperature ranges (**Figure 9**).

5.4 Limitations and Future Work

The outputs of our coupled SMB and ice-flow model simulations are subject to several limiting assumptions, which are as follows: 1) the SIA is appropriate for simulating the former extent of the EL and RCO glaciers. 2) The EL and RCO palaeo-glaciers were climate-sensitive and in a state of mass-balance equilibrium at the time of the reconstructed advances/still-stands. 3) All precipitation was accumulated as glacier ice, 4) the contribution of avalanching to glacier accumulation was negligible, 5) the ice was at its pressure-melting point uniformly across the glacier domain, and 6) ablation caused by sublimation or ice-front breakoff is not significant enough to be considered by our SMB parameterisation. 7) The EL and RCO glaciers were mostly free of supraglacial debris cover, and 8) the removal of valley-fill debris deposited after glacier retreat would not cause significant impacts on simulated glacier geometries and extent.

In future work, the utilisation of a high-order or Stokes model, along with a more complex SMB model, could enable revisiting and testing the impact of assumptions 1), 3), and 6), although such an approach would require significantly more computational power. Assumption 2) could be re-assessed by dating the RCO-out moraines and by generating glacier-moraine chronologies in other mountain valleys of the region. Uncertainties associated with assumption 7) and 8) could potentially be reduced in future investigations by conducting thorough sedimentological and geomorphological analyses of glaciogenic and debris deposits. Assumptions 4), and 5) however, are likely to be problematic to resolve further. SMB-derived palaeo-climate ranges could potentially be refined by improving future estimations of catchment-specific atmospheric temperatures, ALR, as well as annual and seasonal precipitation representative of modern-day climate. Finally, the dating of the innermost EL-out moraines and the EL-mid moraines is required to assess our assumption that they reflect glacial advances occurring during the ACR and YD cold intervals, respectively.

6 CONCLUSION

Geomorphological mapping of preserved glacial moraine complexes near the mouths of the El Loro and Río Comisario mountain valleys, northeastern Patagonia (43°S; 71°W), has evidenced former advances/still-stands of local mountain glaciers that are younger than the dated LGM advances/still-stands of the local Patagonian Ice Sheet outlet glacier, the Río Corcovado glacier.

In the El Loro valley, ^{10}Be surface exposure dating of the inferred outermost advance of the moraine complex suggests a minimum age of 18.0 ± 1.15 ka, while another, undated moraine complex is evident further upstream, indicative of a mid-valley re-advance and/or stabilisation of the EL palaeo-glacier front.

Our findings suggest that while PIS outlet glaciers in northeastern Patagonia experienced a relatively early initial deglaciation from their LGM margins (~19–20 ka) and no substantial late-LGM re-advances, local sensitive mountain glaciers re-advanced during the late-LGM. We propose that this glacier expansion event was triggered by the late-LGM, 1.5 kyr-long cold and wet interval (~19.5–18 ka) recorded in other regions of Patagonia which followed the Varas Interstade (22–19.2 ka), and which preceded widespread Patagonian deglaciation (17.9–15 ka). We thus hypothesise that climatic conditions during the late-LGM were suitable for glacier expansion in northeastern Patagonia, and that the earlier onset of local PIS outlet glacier retreat at around ~19–20 ka was likely exacerbated by non-climatic factors, such as proglacial lake formation.

We estimate site-specific cumulative surface uplift caused by Glacial Isostatic Adjustment over the past 18 ka to be

approximately 130 m, while time-varying uplift rates are estimated at 9.1, 39.4 and 11.6 mm yr^{-1} between 20–17.5, 17.5–15, and 15–12.5 ka, respectively. The impact of such uplift on ^{10}Be production rates is less than exposure-age 1σ analytical uncertainties. Nevertheless, it requires modification of our surface mass balance-driven temperature and ELA reconstructions by −0.85°C and −131 m, respectively. Our investigation highlights that GIA-related surface elevation change is an important factor to consider in palaeo-climate investigations using glacier reconstructions. This uplift is particularly relevant in Patagonia, where low mantle viscosities drive rapid uplift following deglaciation.

Ice-flow model surface mass balance analyses suggest that regional mean annual temperatures were between 1.9 and 2.8°C lower than present at around 18.0 ± 1.15 ka, while precipitation was between ~50 and ~380% higher than today. Our results thus support the hypothesis of increased Southern Westerly Winds influence in northern Patagonia between ~19.5 and ~18 ka, resulting from an equatorward migration of the wind belt, which may have induced positive glacial mass balances across the region.

ASTER TEAM

Georges Aumaitre, Aix-Marseille Université, CNRS, IRD, INRAE, CEREGE, Aix-en-Provence, France; **Karim Keddadouche**, Aix-Marseille Université, CNRS, IRD, INRAE, CEREGE, Aix-en-Provence, France; **Fawzi Zaidi**, Aix-Marseille Université, CNRS, IRD, INRAE, CEREGE, Aix-en-Provence, France

DATA AVAILABILITY STATEMENT

The original contributions presented in the study are included in the article/**Supplementary Material**, further inquiries can be directed to the corresponding author.

ETHICS STATEMENT

Written informed consent was obtained from the individual(s) for the publication of any potentially identifiable images or data included in this article.

AUTHOR CONTRIBUTIONS

TPML: Conceptualization, Data curation, Formal analysis, Funding acquisition, Investigation, Methodology, Project administration, Software, Visualization, Writing (original draft and review and editing). ASH: Conceptualization, Methodology, Project administration, Supervision, Validation, Writing (original draft and review and editing). DG: Data curation, Investigation, Methodology, Software, Writing (original draft and review and editing). IS: Data curation, Supervision, Writing (review and editing). MV: Data curation, Methodology, Writing (review and editing). RB: Supervision, Writing (review and editing). All authors have approved the final version of the manuscript prior to submission.

FUNDING

This investigation is part of a University of Edinburgh E3 Doctoral Training Partnership Ph.D. studentship (award code: NE/L002558/1) awarded by the National Environment Research Council (NERC) to TPML. Our 2020 field expedition was supported by a crowd-funding campaign through the Crowd.Science fundraising platform (https://crowd.science) and a British Society for Geomorphology Postgraduate Research Grant award (BSG-2019-04) awarded to TPML in October 2019. TCN dating laboratory analyses and AMS measurements were partly funded by a Scottish Alliance for Geoscience, Environment and Society (SAGES) small grant scheme awarded to TPML in August 2020.

ACKNOWLEDGMENTS

We express our most sincere gratitude towards all individuals who contributed to the https://crowd.science/crowdfunding campaign facilitating a 2020 field trip to the study site. We also thank all local landowners who authorized access and work on their properties, in particular, the Estancia Tecka (Chubut, Argentina) for enabling access to their land and private roads. Moreover, we are thankful to Pablo Tapia Gonzalez for his presence and assistance in the field. We thank Juan Luis García, María Paz Lira-Bahamonde, Mateo A. Martini and Rodrigo Soteres for their help, advice and logistical support with the overall project. We are grateful for the help of Richard S. Jones in obtaining and interpreting GIA uplift data from the iceTEA tools for exposure ages (http://ice-tea.org/en/). We thank Elaine McDougall for her preciouswork enabling efficient rock sample quartz purification and isolation. We also wish to thank Maxime Vergez for his invaluable help towards model output coding analyses and Emeritus Professor David E. Sugden for providing indispensable advice and guidance on the final manuscript. Finally, we thank the two reviewers for their thoughtful comments allowing us to improve the quality of the manuscript.

SUPPLEMENTARY MATERIAL

The Supplementary Material for this article can be found online at: https://www.frontiersin.org/articles/10.3389/feart.2021.751987/full#supplementary-material

REFERENCES

Ackert, R. P., Becker, R. A., Singer, B. S., Kurz, M. D., Caffee, M. W., and Mickelson, D. M. (2008). Patagonian Glacier Response during the Late Glacial-Holocene Transition. *Science* 321 (5887), 392–395. doi:10.1126/science.1157215

Adhikari, S., and Marshall, S. J. (2012). Glacier Volume-Area Relation for High-Order Mechanics and Transient Glacier States. *Geophys. Res. Lett.* 39 (16), a–n. doi:10.1029/2012GL052712

Anderson, L. S., Roe, G. H., and Anderson, R. S. (2014). The Effects of Interannual Climate Variability on the Moraine Record. *Geology* 42 (1), 55–58. doi:10.1130/G34791.1

Applegate, P. J., Urban, N. M., Laabs, B. J. C., Keller, K., and Alley, R. B. (2010). Modeling the Statistical Distributions of Cosmogenic Exposure Dates from Moraines. *Geosci. Model. Dev.* 3 (1), 293–307. doi:10.5194/gmd-3-293-2010

Arnold, M., Merchel, S., Bourlès, D. L., Braucher, R., Benedetti, L., Finkel, R. C., et al. (2010). The French Accelerator Mass Spectrometry Facility ASTER: Improved Performance and Developments. *Nucl. Instr. Methods Phys. Res. Section B: Beam Interactions Mater. Atoms* 268 (11-12), 1954–1959. doi:10.1016/j.nimb.2010.02.107

Balco, G., Stone, J. O., Lifton, N. A., and Dunai, T. J. (2008). A Complete and Easily Accessible Means of Calculating Surface Exposure Ages or Erosion Rates from 10Be and 26Al Measurements. *Quat. Geochronol.* 3 (3), 174–195. doi:10.1016/j.quageo.2007.12.001

Banerjee, A., and Shankar, R. (2013). On the Response of Himalayan Glaciers to Climate Change. *J. Glaciol.* 59 (215), 480–490. doi:10.3189/2013JoG12J130

Benn, D. I., Kirkbride, M. P., Owen, L. A., and Brazier, V. (2003). *Glaciated valley Landsystems. Glacial Landsystems*. chapter 15, 372–406.

Benn, D. I., Owen, L. A., Osmaston, H. A., Seltzer, G. O., Porter, S. C., and Mark, B. (2005). Reconstruction of Equilibrium-Line Altitudes for Tropical and Sub-tropical Glaciers. *Quat. Int.* 138-139, 8–21. doi:10.1016/j.quaint.2005.02.003

Berman, A. L., Silvestri, G. E., and Tonello, M. S. (2016). Differences between Last Glacial Maximum and Present-Day Temperature and Precipitation in Southern South America. *Quat. Sci. Rev.* 150, 221–233. doi:10.1016/j.quascirev.2016.08.025

Bindschadler, R. (1983). The Importance of Pressurized Subglacial Water in Separation and Sliding at the Glacier Bed. *J. Glaciol.* 29 (101), 3–19. doi:10.3189/S0022143000005104

Blake, W., Fischer, U. H., Bentley, C. R., and Clarke, G. K. G. (1994). Instruments and Methods: Direct Measurement of Sliding at the Glacier Bed. *J. Glaciol.* 40 (136), 595–599. doi:10.3189/S002214300001248X

Bourlès, D. (1988). *Etude de la géochimies de l'isotope cosmogénique ^{10}Be et de son isotope stable ^{9}Be en milieu océanique. Application à la datation des sédiments marins*. Paris XI: Univ. Ph.D. thesis.

Braithwaite, R. J., and Müller, F. (1980). On the Parameterization of Glacier Equilibrium Line Altitude. *IAHS Publ.* 126, 263–271.

Braithwaite, R. J., and Zhang, Y. (2000). Sensitivity of Mass Balance of Five Swiss Glaciers to Temperature Changes Assessed by Tuning a Degree-Day Model. *J. Glaciol.* 46 (152), 7–14. doi:10.3189/172756500781833511

Braucher, R., Guillou, V., Bourlès, D. L., Arnold, M., Aumaître, G., Keddadouche, K., et al. (2015). Preparation of ASTER In-House 10Be/9Be Standard Solutions. *Nucl. Instr. Methods Phys. Res. Section B: Beam Interactions Mater. Atoms* 361, 335–340. doi:10.1016/j.nimb.2015.06.012

Budd, W. F., Keage, P. L., and Blundy, N. A. (1979). Empirical Studies of Ice Sliding. *J. Glaciol.* 23 (89), 157–170. doi:10.3189/S0022143000029804

Caldenius, C. C. Z. (1932). Las glaciaciones cuaternarias en la patagonia y tierra del fuego. *Geografiska Annaler* 14, 1–164. doi:10.1080/20014422.1932.11880545

Caniupán, M., Lamy, F., Lange, C. B., Kaiser, J., Arz, H., Kilian, R., et al. (2011). Millennial-scale Sea Surface Temperature and Patagonian Ice Sheet Changes off Southernmost Chile (53°S) over the Past ~60 Kyr. *Paleoceanography* 26 (3), a–n. doi:10.1029/2010PA002049

Cartwright, A., Quade, J., Stine, S., Adams, K. D., Broecker, W., and Cheng, H. (2011). Chronostratigraphy and lake-level Changes of Laguna Cari-Laufquén, Río Negro, Argentina. *Quat. Res.* 76 (3), 430–440. doi:10.1016/j.yqres.2011.07.002

Charton, J., Jomelli, V., Schimmelpfennig, I., Verfaillie, D., Favier, V., Mokadem, F., et al. (2021). A Debris-Covered Glacier at Kerguelen (49° S, 69° E) Over the Past 15 000 years. *Antarctic Sci.* 33 (1), 103–115. doi:10.1017/S0954102020000541

Chmeleff, J., von Blanckenburg, F., Kossert, K., and Jakob, D. (2010). Determination of the 10Be Half-Life by Multicollector ICP-MS and Liquid Scintillation Counting. *Nucl. Instr. Methods Phys. Res. Section B: Beam Interactions Mater. Atoms* 268 (2), 192–199. doi:10.1016/j.nimb.2009.09.012

Clapperton, C. M. (1993). *Quaternary Geology and Geomorphology of South America*, 25. Amsterdam etc: Elsevier.

Clapperton, C. M. (1990). Quaternary Glaciations in the Southern Hemisphere: an Overview. *Quat. Sci. Rev.* 9 (2-3), 299–304. doi:10.1016/0277-3791(90)90024-5

Clapperton, C. M., Sugden, D. E., Kaufman, D. S., and McCulloch, R. D. (1995). The Last Glaciation in central Magellan Strait, Southernmost Chile. *Quat. Res.* 44 (2), 133–148. doi:10.1006/qres.1995.1058

Cohen, D., Hooke, R. L., Iverson, N. R., and Kohler, J. (2000). Sliding of Ice Past an Obstacle at Engabreen, Norway. *J. Glaciol.* 46 (155), 599–610. doi:10.3189/172756500781832747

Cohen, D., Iverson, N. R., Hooyer, T. S., Fischer, U. H., Jackson, M., and Moore, P. L. (2005). Debris-bed Friction of Hard-Bedded Glaciers. *J. Geophys. Res.* 110 (F2). doi:10.1029/2004JF000228

Cuffey, K., and Paterson, W. S. B. (2010). *The Physics of Glaciers*. Burlington, MA, USA: Elsevier, Butterworth-Heineman, 704.

Darvill, C. M., Bentley, M. J., Stokes, C. R., and Shulmeister, J. (2016). The Timing and Cause of Glacial Advances in the Southern Mid-latitudes during the Last Glacial Cycle Based on a Synthesis of Exposure Ages from Patagonia and New Zealand. *Quat. Sci. Rev.* 149, 200–214. doi:10.1016/j.quascirev.2016.07.024

Davies, B. J., Darvill, C. M., Lovell, H., Bendle, J. M., Dowdeswell, J. A., Fabel, D., et al. (2020). The Evolution of the Patagonian Ice Sheet from 35 Ka to the Present Day (PATICE). *Earth-Science Rev.* 204, 103152. doi:10.1016/j.earscirev.2020.103152

Davies, B. J., Thorndycraft, V. R., Fabel, D., and Martin, J. R. V. (2018). Asynchronous Glacier Dynamics during the Antarctic Cold Reversal in central Patagonia. *Quat. Sci. Rev.* 200, 287–312. doi:10.1016/J.QUASCIREV.2018.09.025

De Angelis, H. (2014). Hypsometry and Sensitivity of the Mass Balance to Changes in Equilibrium-Line Altitude: the Case of the Southern Patagonia Icefield. *J. Glaciol.* 60 (219), 14–28. doi:10.3189/2014JoG13J127

De Porras, M. E., Maldonado, A., Abarzúa, A. M., Cárdenas, M. L., Francois, J. P., Martel-Cea, A., et al. (2012). Postglacial Vegetation, Fire and Climate Dynamics at Central Chilean Patagonia (Lake Shaman, 44°S). *Quat. Sci. Rev.* 50, 71–85. doi:10.1016/j.quascirev.2012.06.015

De Porras, M. E., Maldonado, A., Quintana, F. A., Martel-Cea, A., Reyes, O., and Méndez, C. (2014). Environmental and Climatic Changes in central Chilean Patagonia since the Late Glacial (Mallín El Embudo, 44° S). *Clim. Past* 10 (3), 1063–1078. doi:10.5194/cp-10-1063-2014

Denton, G. H., Lowell, T. V., Heusser, C. J., Schlüchter, C., Andersen, B. G., Heusser, L. E., et al. (1999). Geomorphology, Stratigraphy, and Radiocarbon Chronology of LlanquihueDrift in the Area of the Southern Lake District, Seno Reloncavi, and Isla Grande de Chiloe, Chile. *Geografiska Annaler A* 81 (2), 167–229. doi:10.1111/j.0435-3676.1999.00057.x

Denton, G. H., Putnam, A. E., Russell, J. L., Barrell, D. J. A., Schaefer, J. M., Kaplan, M. R., et al. (2021). The Zealandia Switch: Ice Age Climate Shifts Viewed from Southern Hemisphere Moraines. *Quat. Sci. Rev.* 257, 106771. doi:10.1016/j.quascirev.2020.106771

Doughty, A. M., Schaefer, J. M., Putnam, A. E., Denton, G. H., Kaplan, M. R., Barrell, D. J. A., et al. (2015). Mismatch of Glacier Extent and Summer Insolation in Southern Hemisphere Mid-latitudes. *Geology* 43 (5), 407–410. doi:10.1130/G36477.1

Douglass, D. C., Singer, B., Ackert, R. P., Kaplan, M. R., and Caffee, M. W. (2007). "Constraining Boulder Erosion Rates and Ages of Mid-pleistocene Moraines in Lago Buenos Aires, Argentina," in GSA Abstracts and Programs Northeastern Section 42nd Annual Meeting, Lago Buenos Aires, Argentina.

Engelhardt, H. F., Harrison, W. D., and Kamb, B. (1978). Basal Sliding and Conditions at the Glacier Bed as Revealed by Bore-Hole Photography. *J. Glaciol.* 20 (84), 469–508. doi:10.3189/S002214300002089X

Fick, S. E., and Hijmans, R. J. (2017). WorldClim 2: New 1-km Spatial Resolution Climate Surfaces for Global Land Areas. *Int. J. Climatol* 37 (12), 4302–4315. doi:10.1002/joc.5086

Galloway, R. W., Markgraf, V., and Bradbury, J. P. (1988). Dating Shorelines of Lakes in Patagonia, Argentina. *J. South Am. Earth Sci.* 1 (2), 195–198. doi:10.1016/0895-9811(88)90037-5

García, J.-L., Maldonado, A., de Porras, M. E., Nuevo Delaunay, A., Reyes, O., Ebensperger, C. A., et al. (2019). Early Deglaciation and Paleolake History of Río Cisnes Glacier, Patagonian Ice Sheet (44°S). *Quat. Res.* 91 (1), 194–217. doi:10.1016/10.1017/qua.2018.93

García, J. L., Kaplan, M. R., Hall, B. L., Schaefer, J. M., Vega, R. M., Schwartz, R., et al. (2012). Glacier Expansion in Southern Patagonia throughout the Antarctic Cold Reversal. *Geology* 40 (9), 859–862. doi:10.1130/G33164.1

Garreaud, R., Lopez, P., Minvielle, M., and Rojas, M. (2013). Large-scale Control on the Patagonian Climate. *J. Clim.* 26 (1), 215–230. doi:10.1175/JCLI-D-12-00001.1

Glasser, N. F., Jansson, K. N., Goodfellow, B. W., De Angelis, H., Rodnight, H., and Rood, D. H. (2011). Cosmogenic Nuclide Exposure Ages for Moraines in the Lago San Martin Valley, Argentina. *Quat. Res.* 75 (3), 636–646. doi:10.1016/j.yqres.2010.11.005

Glasser, N. F., Jansson, K. N., Harrison, S., and Kleman, J. (2008). The Glacial Geomorphology and Pleistocene History of South America between 38°S and 56°S. *Quat. Sci. Rev.* 27 (3-4), 365–390. doi:10.1016/10.1016/j.quascirev.2007.11.011

Gosse, J. C., and Phillips, F. M. (2001). Terrestrial *In Situ* Cosmogenic Nuclides: Theory and Application. *Quat. Sci. Rev.* 20 (14), 1475–1560. doi:10.1016/S0277-3791(00)00171-2

Gowan, E. J., Zhang, X., Khosravi, S., Rovere, A., Stocchi, P., Hughes, A. L. C., et al. (2021). A New Global Ice Sheet Reconstruction for the Past 80 000 Years. *Nat. Commun.* 12 (1), 1–9. doi:10.1038/s41467-021-21469-w

Hall, B. L., Porter, C. T., Denton, G. H., Lowell, T. V., and Bromley, G. R. M. (2013). Extensive Recession of Cordillera Darwin Glaciers in Southernmost South America during Heinrich Stadial 1. *Quat. Sci. Rev.* 62, 49–55. doi:10.1016/j.quascirev.2012.11.026

Haller, M., Lech, R. R., Martinez, O. A., Meister, C. M., and Page, S. M. (2003). *Hoja Geologica 4373IV/III, Trevelin, Provincia del Chubut. Programa Nacional de Cartas Geologicas de la Republica Argentina, 1:250.000*. Buenos Aires: Servicio Geologico Nacional.

Hein, A. S., Cogez, A., Darvill, C. M., Mendelová, M., Kaplan, M. R., Herman, F., et al. (2017). Regional Mid-pleistocene Glaciation in central Patagonia. *Quat. Sci. Rev.* 164, 77–94. doi:10.1016/j.quascirev.2017.03.023

Hein, A. S., Hulton, N. R. J., Dunai, T. J., Sugden, D. E., Kaplan, M. R., and Xu, S. (2010). The Chronology of the Last Glacial Maximum and Deglacial Events in central Argentine Patagonia. *Quat. Sci. Rev.* 29 (9-10), 1212–1227. doi:10.1016/j.quascirev.2010.01.020

Heusser, C. J., Heusser, L. E., and Lowell, T. V. (1999). Paleoecology of The Southern Chilean Lake District-Isla Grande de Chiloe During Middle-late Llanquihue Glaciation and Deglaciation. *Geografiska Annaler A* 81, 231–284. doi:10.1111/j.0435-3676.1999.00058.x

Heusser, C. J. (1983). Quaternary pollen record from laguna de Tagua Tagua, Chile. *Science* 219 (4591), 1429–1432. doi:10.1126/science.219.4591.1429

Heyman, J., Stroeven, A. P., Harbor, J. M., and Caffee, M. W. (2011). Too Young or Too Old: Evaluating Cosmogenic Exposure Dating Based on an Analysis of Compiled boulder Exposure Ages. *Earth Planet. Sci. Lett.* 302 (1-2), 71–80. doi:10.1016/j.epsl.2010.11.040

Hock, R. (2003). Temperature index Melt Modelling in Mountain Areas. *J. Hydrol.* 282 (1-4), 104–115. doi:10.1016/S0022-1694(03)00257-9

Hubbard, A., Hein, A. S., Kaplan, M. R., Hulton, N. R. j., and Glasser, N. (2005). A Modelling Reconstruction of the Last Glacial Maximum Ice Sheet and its Deglaciation in the Vicinity of the Northern Patagonian Icefield, South America. *Geografiska Annaler: Ser. A, Phys. Geogr.* 87 (2), 375–391. doi:10.1111/j.0435-3676.2005.00264.x

Huss, M., Sugiyama, S., Bauder, A., and Funk, M. (2007). Retreat Scenarios of Unteraargletscher, Switzerland, Using a Combined Ice-Flow Mass-Balance Model. *Arctic, Antarctic, Alpine Res.* 39 (3), 422–431. doi:10.1657/1523-0430(06-036)[HUSS]2.0.CO;2

Hutter, K. (1983). *Theoretical Glaciology: Material Science of Ice and the Mechanics of Glaciers and Ice Sheets*. Dordrecht, Netherlands: Kluwer Academic Publishers.

Ivins, E. R., and James, T. S. (2004). Bedrock Response to Llanquihue Holocene and Present-Day Glaciation in Southernmost South America. *Geophys. Res. Lett.* 31 (24). doi:10.1029/2004GL021500

Jomelli, V., Mokadem, F., Schimmelpfennig, I., Chapron, E., Rinterknecht, V., Favier, V., et al. (2017). Sub-Antarctic Glacier Extensions in the Kerguelen Region (49°S, Indian Ocean) over the Past 24,000 Years Constrained by 36 Cl Moraine Dating. *Quat. Sci. Rev.* 162, 128–144. doi:10.1016/j.quascirev.2017.03.010

Jones, R. S., Small, D., Cahill, N., Bentley, M. J., and Whitehouse, P. L. (2019a). iceTEA: Tools for Plotting and Analysing Cosmogenic-Nuclide Surface-Exposure Data from Former Ice Margins. *Quat. Geochronol.* 51, 72–86. doi:10.1016/j.quageo.2019.01.001

Jones, R. S., Whitehouse, P. L., Bentley, M. J., Small, D., and Dalton, A. S. (2019b). Impact of Glacial Isostatic Adjustment on Cosmogenic Surface-Exposure Dating. *Quat. Sci. Rev.* 212, 206–212. doi:10.1016/j.quascirev.2019.03.012

Jouvet, G., and Funk, M. (2014). Modelling the Trajectory of the Corpses of Mountaineers Who Disappeared in 1926 on Aletschgletscher, Switzerland. *J. Glaciol.* 60 (220), 255–261. doi:10.3189/2014JoG13J156

Kaiser, J., Lamy, F., Arz, H. W., and Hebbeln, D. (2007). Dynamics of the Millennial-Scale Sea Surface Temperature and Patagonian Ice Sheet Fluctuations in Southern Chile during the Last 70kyr (ODP Site 1233). *Quat. Int.* 161 (1), 77–89. doi:10.1016/j.quaint.2006.10.024

Kaplan, M. R., Coronato, A., Hulton, N. R. J., Rabassa, J. O., Kubik, P. W., and Freeman, S. P. H. T. (2007). Cosmogenic Nuclide Measurements in Southernmost South America and Implications for Landscape Change. *Geomorphology* 87 (4), 284–301. doi:10.1016/j.geomorph.2006.10.005

Kaplan, M. R., Fogwill, C. J., Sugden, D. E., Hulton, N. R. J., Kubik, P. W., and Freeman, S. P. H. T. (2008). Southern Patagonian Glacial Chronology for the Last Glacial Period and Implications for Southern Ocean Climate. *Quat. Sci. Rev.* 27 (3-4), 284–294. doi:10.1016/j.quascirev.2007.09.013

Kern, Z., and László, P. (2010). Size Specific Steady-State Accumulation-Area Ratio: an Improvement for Equilibrium-Line Estimation of Small Palaeoglaciers. *Quat. Sci. Rev.* 29 (19-20), 2781–2787. doi:10.1016/j.quascirev.2010.06.033

Korschinek, G., Bergmaier, A., Faestermann, T., Gerstmann, U. C., Knie, K., Rugel, G., et al. (2010). A New Value for the Half-Life of 10Be by Heavy-Ion Elastic Recoil Detection and Liquid Scintillation Counting. *Nucl. Instr. Methods Phys. Res. Section B: Beam Interactions Mater. Atoms* 268 (2), 187–191. doi:10.1016/j.nimb.2009.09.020

Lal, D. (1991). Cosmic ray Labeling of Erosion Surfaces: *In Situ* Nuclide Production Rates and Erosion Models. *Earth Planet. Sci. Lett.* 104, 424–439. doi:10.1016/0012-821X(91)90220-C

Lamy, F., Kaiser, J., Arz, H. W., Hebbeln, D., Ninnemann, U., Timm, O., et al. (2007). Modulation of the Bipolar Seesaw in the Southeast Pacific during Termination 1. *Earth Planet. Sci. Lett.* 259, 400–413. doi:10.1016/j.epsl.2007.04.040

Lamy, F., Kaiser, J., Ninnemann, U., Hebbeln, D., Arz, H. W., and Stoner, J. (2004). Antarctic Timing of Surface Water Changes off Chile and Patagonian Ice Sheet Response. *Science* 304 (5679), 1959–1962. doi:10.1126/science.1097863

Lange, H., Casassa, G., Ivins, E. R., Schröder, L., Fritsche, M., Richter, A., et al. (2014). Observed Crustal Uplift Near the Southern Patagonian Icefield Constrains Improved Viscoelastic Earth Models. *Geophys. Res. Lett.* 41 (3), 805–812. doi:10.1002/2013GL058419

Leger, T. P. M., Hein, A. S., Bingham, R. G., Martini, M. A., Soteres, R. L., Sagredo, E. A., et al. (2020). The Glacial Geomorphology of the Río Corcovado, Río Huemul and Lago Palena/General Vintter Valleys, Northeastern Patagonia (43°S, 71°W). *J. Maps* 16 (2), 651–668. doi:10.1080/17445647.2020.1794990

Leger, T. P., Hein, A. S., Bingham, R. G., Rodés, Á., Fabel, D., and Smedley, R. K. (2021). Geomorphology and ^{10}Be Chronology of the Last Glacial Maximum and Deglaciation in NORTHEASTERN PATAGONIA, 43°S–71°W. *Quat. Sci. Rev.* 272, 107194. doi:10.1016/j.quascirev.2021.107194

Lifton, N., Sato, T., and Dunai, T. J. (2014). Scaling *In Situ* Cosmogenic Nuclide Production Rates Using Analytical Approximations to Atmospheric Cosmic-ray Fluxes. *Earth Planet. Sci. Lett.* 386, 149–160. doi:10.1016/j.epsl.2013.10.052

Lopes dos Santos, R. A., Spooner, M. I., Barrows, T. T., De Deckker, P., Sinninghe Damsté, J. S., and Schouten, S. (2013). Comparison of Organic (UK'37, TEXH86, LDI) and Faunal Proxies (Foraminiferal Assemblages) for Reconstruction of Late Quaternary Sea Surface Temperature Variability from Offshore southeastern Australia. *Paleoceanography* 28 (3), 377–387. doi:10.1002/palo.20035

Martínez, O., Coronato, A., and Rabassa, J. (2011). "Pleistocene Glaciations in Northern Patagonia, Argentina: an Updated Review," in *Developments in Quaternary Sciences* (Elsevier), 15, 729–734. doi:10.1016/b978-0-444-53447-7.00052-0

Mashiotta, T. A., Lea, D. W., and Spero, H. J. (1999). Glacial-interglacial Changes in Subantarctic Sea Surface Temperature and δ18O-water Using Foraminiferal Mg. *Earth Planet. Sci. Lett.* 170 (4), 417–432. doi:10.1016/S0012-821X(99)00116-8

Mendelová, M., Hein, A. S., Rodés, Á., Smedley, R. K., and Xu, S. (2020b). Glacier Expansion in central Patagonia during the Antarctic Cold Reversal Followed by Retreat and Stabilisation during the Younger Dryas. *Quat. Sci. Rev.* 227, 106047. doi:10.1016/j.quascirev.2019.106047

Mendelová, M., Hein, A. S., Rodés, Á., and Xu, S. (2020a). Extensive Mountain Glaciation in central Patagonia during Marine Isotope Stage 5. *Quat. Sci. Rev.* 227, 105996. doi:10.1016/j.quascirev.2019.105996

Mercer, J. H. (1972). Chilean Glacial Chronology 20,000 to 11,000 Carbon-14 Years Ago: Some Global Comparisons. *Science* 176 (4039), 1118–1120. doi:10.1210/jcem-10-10-136110.1126/science.176.4039.1118

Mercer, J. H. (1976). Glacial History of Southernmost South America. *Quat. Res.* 6 (2), 125–166. doi:10.1016/0033-5894(76)90047-8

Mercer, J. H. (1984). Simultaneous Climatic Change in Both Hemispheres and Similar Bipolar Interglacial Warming: Evidence and Implications. *Clim. Process. Clim. sensitivity* 29, 307–313. doi:10.1029/GM029p0307

Millan, R., Mouginot, J., Rabatel, A., Jeong, S., Cusicanqui, D., Derkacheva, A., et al. (2019). Mapping Surface Flow Velocity of Glaciers at Regional Scale Using a Multiple Sensors Approach. *Remote Sensing* 11 (21), 2498. doi:10.3390/rs11212498

Montade, V., Combourieu Nebout, N., Kissel, C., Haberle, S. G., Siani, G., and Michel, E. (2013). Vegetation and Climate Changes during the Last 22,000yr from a marine Core Near Taitao Peninsula, Southern Chile. *Palaeogeogr. Palaeoclimatol. Palaeoecol.* 369, 335–348. doi:10.1016/j.palaeo.2012.11.001

Moreno, P. I., Denton, G. H., Moreno, H., Lowell, T. V., Putnam, A. E., and Kaplan, M. R. (2015). Radiocarbon Chronology of the Last Glacial Maximum and its Termination in Northwestern Patagonia. *Quat. Sci. Rev.* 122, 233–249. doi:10.1016/j.quascirev.2015.05.027

Moreno, P. I., Simi, E., Villa-Martínez, R. P., and Vilanova, I. (2019). Early Arboreal Colonization, Postglacial Resilience of Deciduous Nothofagus Forests, and the Southern Westerly Wind Influence in central-east Andean Patagonia. *Quat. Sci. Rev.* 218, 61–74. doi:10.1016/j.quascirev.2019.06.004

Moreno, P. I., Videla, J., Valero-Garcés, B., Alloway, B. V., and Heusser, L. E. (2018). A Continuous Record of Vegetation, Fire-Regime and Climatic Changes in Northwestern Patagonia Spanning the Last 25,000 Years. *Quat. Sci. Rev.* 198, 15–36. doi:10.1016/j.quascirev.2018.08.013

Murray, D. S., Carlson, A. E., Singer, B. S., Anslow, F. S., He, F., Caffee, M., et al. (2012). Northern Hemisphere Forcing of the Last Deglaciation in Southern Patagonia. *Geology* 40 (7), 631–634. doi:10.1130/G32836.1

Nimick, D. A., McGrath, D., Mahan, S. A., Friesen, B. A., and Leidich, J. (2016). Latest Pleistocene and Holocene Glacial Events in the Colonia valley, Northern Patagonia Icefield, Southern Chile. *J. Quat. Sci.* 31 (6), 551–564. doi:10.1002/jqs.2847

Osmaston, H. (2005). Estimates of Glacier Equilibrium Line Altitudes by the Area×Altitude, the Area×Altitude Balance Ratio and the Area×Altitude Balance Index Methods and Their Validation. *Quat. Int.* 138-139, 22–31. doi:10.1016/j.quaint.2005.02.004

Pedro, J. B., Bostock, H. C., Bitz, C. M., He, F., Vandergoes, M. J., Steig, E. J., et al. (2016). The Spatial Extent and Dynamics of the Antarctic Cold Reversal. *Nat. Geosci* 9 (1), 51–55. doi:10.1038/ngeo2580

Pellitero, R., Rea, B. R., Spagnolo, M., Bakke, J., Hughes, P., Ivy-Ochs, S., et al. (2015). A GIS Tool for Automatic Calculation of Glacier Equilibrium-Line Altitudes. *Comput. Geosciences* 82, 55–62. doi:10.1016/j.cageo.2015.05.005

Pellitero, R., Rea, B. R., Spagnolo, M., Bakke, J., Ivy-Ochs, S., Frew, C. R., et al. (2016). GlaRe, a GIS Tool to Reconstruct the 3D Surface of Palaeoglaciers. *Comput. Geosciences* 94, 77–85. doi:10.1016/j.cageo.2016.06.008

Peltier, C., Kaplan, M. R., Birkel, S. D., Soteres, R. L., Sagredo, E. A., Aravena, J. C., et al. (2021). The Large MIS 4 and Long MIS 2 Glacier Maxima on the Southern Tip of South America. *Quat. Sci. Rev.* 262, 106858. doi:10.1016/j.quascirev.2021.106858

Peltier, W. R., Argus, D. F., and Drummond, R. (2015). Space Geodesy Constrains Ice Age Terminal Deglaciation: The Global ICE-6G_C (VM5a) Model. *J. Geophys. Res. Solid Earth* 120 (1), 450–487. doi:10.1002/2014JB011176

Putkonen, J., and Swanson, T. (2003). Accuracy of Cosmogenic Ages for Moraines. *Quat. Res.* 59 (2), 255–261. doi:10.1016/S0033-5894(03)00006-1

Putnam, A. E., Denton, G. H., Schaefer, J. M., Barrell, D. J. A., Andersen, B. G., Finkel, R. C., et al. (2010). Glacier advance in Southern Middle-Latitudes during the Antarctic Cold Reversal. *Nat. Geosci* 3 (10), 700–704. doi:10.1038/ngeo962

Putnam, A. E., Schaefer, J. M., Denton, G. H., Barrell, D. J. A., Andersen, B. G., Koffman, T. N. B., et al. (2013). Warming and Glacier Recession in the Rakaia valley, Southern Alps of New Zealand, during Heinrich Stadial 1. *Earth Planet. Sci. Lett.* 382, 98–110. doi:10.1016/j.epsl.2013.09.005

Reynhout, S. A., Sagredo, E. A., Kaplan, M. R., Aravena, J. C., Martini, M. A., Moreno, P. I., et al. (2019). Holocene Glacier Fluctuations in Patagonia Are Modulated by Summer Insolation Intensity and Paced by Southern Annular Mode-like Variability. *Quat. Sci. Rev.* 220, 178–187. doi:10.1016/j.quascirev.2019.05.029

Richter, A., Ivins, E., Lange, H., Mendoza, L., Schröder, L., Hormaechea, J. L., et al. (2016). Crustal Deformation across the Southern Patagonian Icefield Observed by GNSS. *Earth Planet. Sci. Lett.* 452, 206–215. doi:10.1016/j.epsl.2016.07.042

Rivera, A., Bown, F., Carrión, D., and Zenteno, P. (2012). Glacier Responses to Recent Volcanic Activity in Southern Chile. *Environ. Res. Lett.* 7 (1), 014036. doi:10.1088/1748-9326/7/1/014036

Roe, G. H., and O'Neal, M. A. (2009). The Response of Glaciers to Intrinsic Climate Variability: Observations and Models of Late-Holocene Variations in the Pacific Northwest. *J. Glaciol.* 55 (193), 839–854. doi:10.3189/002214309790152438

Roe, G. H. (2011). What Do Glaciers Tell Us about Climate Variability and Climate Change. *J. Glaciol.* 57 (203), 567–578. doi:10.3189/002214311796905640

Sagredo, E. A., Kaplan, M. R., Araya, P. S., Lowell, T. V., Aravena, J. C., Moreno, P. I., et al. (2018). Trans-pacific Glacial Response to the Antarctic Cold Reversal in the Southern Mid-latitudes. *Quat. Sci. Rev.* 188, 160–166. doi:10.1016/j.quascirev.2018.01.011

Shulmeister, J., Fink, D., Hyatt, O. M., Thackray, G. D., and Rother, H. (2010). Cosmogenic 10Be and 26Al Exposure Ages of Moraines in the Rakaia Valley, New Zealand and the Nature of the Last Termination in New Zealand Glacial Systems. *Earth Planet. Sci. Lett.* 297 (3-4), 558–566. doi:10.1016/j.epsl.2010.07.007

Shulmeister, J., Thackray, G. D., Rittenour, T. M., Fink, D., and Patton, N. R. (2019). The Timing and Nature of the Last Glacial Cycle in New Zealand. *Quat. Sci. Rev.* 206, 1–20. doi:10.1016/j.quascirev.2018.12.020

Siani, G., Colin, C., Michel, E., Carel, M., Richter, T., Kissel, C., et al. (2010). Late Glacial to Holocene Terrigenous Sediment Record in the Northern Patagonian Margin: Paleoclimate Implications. *Palaeogeogr. Palaeoclimatol. Palaeoecol.* 297 (1), 26–36. doi:10.1016/j.palaeo.2010.07.011

Skirrow, G. K., Smedley, R. K., Chiverrell, R. C., and Hooke, J. M. (2021). Planform Change of the Río Chubut (~42°S, ~70°W, Argentina) in Response to Climate Drivers in the Southern Andes. *Geomorphology* 393, 107924. doi:10.1016/j.geomorph.2021.107924

Stone, J. O. (2000). Air Pressure and Cosmogenic Isotope Production. *J. Geophys. Res.* 105 (B10), 23753–23759. doi:10.1029/2000jb900181

Sun, Y., Xu, X., Zhang, L., Liu, J., Zhang, X., Li, J., et al. (2020). Numerical Reconstruction of Three Holocene Glacial Events in Qiangyong Valley, Southern Tibetan Plateau and Their Implication for Holocene Climate Changes. *Water* 12 (11), 3205. doi:10.3390/w12113205

Sutherland, J. L., Carrivick, J. L., Gandy, N., Shulmeister, J., Quincey, D. J., and Cornford, S. L. (2020). Proglacial Lakes Control Glacier Geometry and Behavior during Recession. *Geophys. Res. Lett.* 47, e2020GL088865. doi:10.1029/2020gl088865

Vilanova, I., Moreno, P. I., Miranda, C. G., and Villa-Martínez, R. P. (2019). The Last Glacial Termination in the Coyhaique Sector of central Patagonia. *Quat. Sci. Rev.* 224, 105976. doi:10.1016/j.quascirev.2019.105976

Villa-Martínez, R., Moreno, P. I., and Valenzuela, M. A. (2012). Deglacial and Postglacial Vegetation Changes on the Eastern Slopes of the central Patagonian Andes (47°S). *Quat. Sci. Rev.* 32, 86–99. doi:10.1016/j.quascirev.2011.11.008

Vivian, R. (1967). Le Glacier Blanc. *rga* 55 (4), 729–732. doi:10.3406/rga.1967.3351

Vivian, R., and Volle, L. (1967). Le Glacier d'Arsine. *rga* 55 (2), 396–400. doi:10.3406/rga.1967.3325

Wallace, J. M., and Hobbs, P. V. (2006). *Atmospheric Science: An Introductory Survey*, 92. Elsevier.

Weertman, J. (1957). On the Sliding of Glaciers. *J. Glaciol.* 3 (21), 33–38. doi:10.3189/s0022143000024709

Wendt, I., and Carl, C. (1991). The Statistical Distribution of the Mean Squared Weighted Deviation. *Chem. Geology. Isotope Geosci. Section* 86 (4), 275–285. doi:10.1016/0168-9622(91)90010-T

Wickert, A. D. (2015). Open-source Modular Solutions for Flexural Isostasy: gFlex v1.0. *Geosci. Model. Dev.* 9 (6), 997–1017. doi:10.5194/gmd-9-997-2016

Wijngaard, R. R., Steiner, J. F., Kraaijenbrink, P. D. A., Klug, C., Adhikari, S., Banerjee, A., et al. (2019). Modeling the Response of the Langtang Glacier and

the Hintereisferner to a Changing Climate since the Little Ice Age. *Front. Earth Sci.* 7, 143. doi:10.3389/feart.2019.00143

Conflict of Interest: The authors declare that the research was conducted in the absence of any commercial or financial relationships that could be construed as a potential conflict of interest.

The handling editor declared a past co-authorship with one of the authors ASH.

Publisher's Note: All claims expressed in this article are solely those of the authors and do not necessarily represent those of their affiliated organizations, or those of the publisher, the editors and the reviewers. Any product that may be evaluated in this article, or claim that may be made by its manufacturer, is not guaranteed or endorsed by the publisher.

frontiers in Earth Science

ORIGINAL RESEARCH
published: 22 December 2021
doi: 10.3389/feart.2021.813433

Holocene History of Río Tranquilo Glacier, Monte San Lorenzo (47°S), Central Patagonia

Esteban A. Sagredo[1,2,3†], Scott A. Reynhout[2,4†], Michael R. Kaplan[5†], Juan C. Aravena[6], Paola S. Araya[7], Brian H. Luckman[8], Roseanne Schwartz[5] and Joerg M. Schaefer[5,9]*

[1]Instituto de Geografía, Pontificia Universidad Católica de Chile, Santiago, Chile, [2]Núcleo Milenio Paleoclima, Santiago, Chile, [3]Estación Patagonia de Investigaciones Interdisciplinarias UC, Pontificia Universidad Católica de Chile, Santiago, Chile, [4]Departamento de Geología, Universidad de Chile, Santiago, Chile, [5]Lamont-Doherty Earth Observatory, Columbia University, Palisades, NY, United States, [6]Gaia-Antártica, Universidad de Magallanes, Punta Arenas, Chile, [7]Departamento de Geofísica, Universidad de Chile, Santiago, Chile, [8]Department of Geography and Environment, University of Western Ontario, London, ON, Canada, [9]Department of Earth and Environmental Sciences, Columbia University, New York, NY, United States

OPEN ACCESS

Edited by:
Daniel Nývlt, Masaryk University, Czechia

Reviewed by:
Stephen J. A. Jennings, Masaryk University, Czechia
Stephen John Roberts, British Antarctic Survey (BAS), United Kingdom

***Correspondence:**
Esteban A. Sagredo
esagredo@uc.cl

[†]*These authors share first authorship*

Specialty section:
This article was submitted to Quaternary Science, Geomorphology and Paleoenvironment, a section of the journal Frontiers in Earth Science

Received: *11 November 2021*
Accepted: *07 December 2021*
Published: *22 December 2021*

Citation:
Sagredo EA, Reynhout SA, Kaplan MR, Aravena JC, Araya PS, Luckman BH, Schwartz R and Schaefer JM (2021) Holocene History of Río Tranquilo Glacier, Monte San Lorenzo (47°S), Central Patagonia. Front. Earth Sci. 9:813433. doi: 10.3389/feart.2021.813433

The causes underlying Holocene glacier fluctuations remain elusive, despite decades of research efforts. Cosmogenic nuclide dating has allowed systematic study and thus improved knowledge of glacier-climate dynamics during this time frame, in part by filling in geographical gaps in both hemispheres. Here we present a new comprehensive Holocene moraine chronology from Mt. San Lorenzo (47°S) in central Patagonia, Southern Hemisphere. Twenty-four new ^{10}Be ages, together with three published ages, indicate that the Río Tranquilo glacier approached its Holocene maximum position sometime, or possibly on multiple occasions, between 9,860 ± 180 and 6,730 ± 130 years. This event(s) was followed by a sequence of slightly smaller advances at 5,750 ± 220, 4,290 ± 100 (?), 3,490 ± 140, 1,440 ± 60, between 670 ± 20 and 430 ± 20, and at 390 ± 10 years ago. The Tranquilo record documents centennial to millennial-scale glacier advances throughout the Holocene, and is consistent with recent glacier chronologies from central and southern Patagonia. This pattern correlates well with that of multiple moraine-building events with slightly decreasing net extent, as is observed at other sites in the Southern Hemisphere (i.e., Patagonia, New Zealand and Antarctic Peninsula) throughout the early, middle and late Holocene. This is in stark contrast to the typical Holocene mountain glacier pattern in the Northern Hemisphere, as documented in the European Alps, Scandinavia and Canada, where small glaciers in the early-to-mid Holocene gave way to more-extensive glacier advances during the late Holocene, culminating in the Little Ice Age expansion. We posit that this past asymmetry between the Southern and Northern hemisphere glacier patterns is due to natural forcing that has been recently overwhelmed by anthropogenic greenhouse gas driven warming, which is causing interhemispherically synchronized glacier retreat unprecedented during the Holocene.

Keywords: Patagonia, Holocene, glacier fluctuations, ^{10}Be dating, Southern Annular Mode, Neoglaciation, Paleoclimate, South America

INTRODUCTION

Following an early Holocene glacier minimum, most of the glacierised areas around the world experienced a phase of renewed glacier advances, a phenomenon commonly known as Neoglaciation (Porter and Denton 1967). Since their recognition by the middle of the last century, numerous studies have attempted to decipher the causes underlying these glacier fluctuations (e.g., Grove 2004) by comparing the sequence and temporal phasing of advances in disparate regions of the world with terrestrial or extraterrestrial climate-forcing mechanisms (e.g., Denton and Karlen 1973; Bond et al., 2001; Denton and Broecker 2008). Such an understanding is crucial, as it may provide key insights into the mechanisms governing abrupt climate changes and any corresponding cryospheric response. However, further advances in these efforts have been limited by the lack of a well-distributed global network of high-resolution glacier chronologies.

In the case of Patagonia (South America between 40° and 54°S), several chronological models of Holocene glacier fluctuations have been proposed (Mercer 1982; Clapperton and Sugden 1988; Aniya 1995; Aniya 2013). These models—relaying predominantly on radiocarbon dating—differ significantly from each other and more recent studies, and make difficult any effort to understand the recent glacial history of southern South America. The apparent differences between chronological models can be attributed to: i) the reliance on minimum (maximum)-limiting ages, which tend to underestimate (overestimate) the true age of the landforms; ii) the incompleteness of the chronologies due to the limited availability of datable organic matter to conduct radiocarbon analysis; and iii) the fragmentary nature of the surficial glacial record (i.e., due to erosional censoring typical for glaciers, few sites are able to preserve the evidence of every glacier advance that occurred in the area) (Glasser et al., 2005; Strelin et al., 2011; Reynhout et al., 2019). As a consequence, significant gaps remain in our knowledge of centennial- and millennial-scale glacier responses under natural climate variability.

Advances in surface exposure dating techniques, involving both sample processing (e.g., low process blanks) and AMS measurements, have opened new horizons for the development of high-resolution Holocene glacier chronologies based on the analysis of low $^{10}Be/^{9}Be$ ratios (Schaefer et al., 2009) (e.g., ~10^{14-15} in **Table 1**). These improvements, combined with the establishment of a Patagonian ^{10}Be production rate (Kaplan et al., 2011), have recently allowed the emergence of a new generation of comprehensive moraine chronologies from southern South America spanning much or all of the Holocene (i.e., Strelin et al., 2014; Kaplan et al., 2016; Reynhout et al., 2019; García et al., 2020). These ^{10}Be chronologies have been for the most part, developed within a narrow latitudinal band at around 49–51°S in southern Patagonia, and they indicate that in this locale glaciers underwent a series of progressively less extensive advances throughout most of the Holocene.

TABLE 1 | Geographical and analytical data for samples from the Río Tranquilo valley.

Sample	CAMS #	Latitude (°)	Longitude (°)	Elevation (m a.s.l.)	Thickness (cm)	Shielding	Quartz wt (g)	^{9}Be carrier (mg)	$^{10}Be/^{9}Be$ (10^{-14})	^{10}Be (10^{4} atoms g^{-1})
PC13-01-13	BE49281	−47.5314	−72.3897	1,350	1.4	0.9821	30.0566	0.1015	7.3287 ± 0.2415	1.6801 ± 0.056
PC13-01-14	BE46329	−47.5305	−72.3905	1,332	1.5	0.9750	39.1895	0.1821	5.6108 ± 0.1270	1.7743 ± 0.041
PC13-01-18	BE49279	−47.5263	−72.3921	1,258	2.3	0.9815	60.0041	0.1806	2.3305 ± 0.0880	0.4702 ± 0.018
PC13-01-19 *	BE38777	−47.5258	−72.3904	1,236	2.4	0.9770	15.1244	0.1825	10.1541 ± 0.1921	8.4684 ± 0.16
PC13-01-23	BE46458	−47.5135	−72.3935	968	2.2	0.9590	41.0145	0.1819	1.1336 ± 0.0522	0.2949 ± 0.015
PC13-01-24	BE46459	−47.5129	−72.3927	938	2.0	0.9660	62.6149	0.1811	1.7508 ± 0.1107	0.3149 ± 0.02
PC14-01-33	BE46336	−47.5228	−72.3893	1,181	1.4	0.9820	10.0743	0.1822	5.9373 ± 0.1491	7.2577 ± 0.184
PC14-01-34	BE46337	−47.5215	−72.3885	1,157	1.7	0.9840	10.029	0.1812	7.2295 ± 0.2159	8.8565 ± 0.266
PC14-01-35	BE49286	−47.5195	−72.3875	1,107	1.9	0.9840	15.159	0.1808	12.2390 ± 0.2279	10.0182 ± 0.187
RTV16-01-03	BE49287	−47.5232	−72.3895	1,194	1.5	0.9799	15.0128	0.1814	8.7750 ± 0.1633	7.2613 ± 0.136
RTV16-01-04	BE46330	−47.5262	−72.3916	1,253	1.6	0.9660	40.4318	0.1818	15.8400 ± 0.2939	4.8823 ± 0.091
RTV16-01-05	BE49284	−47.5279	−72.3917	1,315	1.8	0.9783	20.8781	0.1813	7.3116 ± 0.1491	4.3415 ± 0.089
RTV16-01-06	BE49285	−47.5280	−72.3917	1,303	3.6	0.9865	21.8359	0.1830	7.4771 ± 0.1482	4.2861 ± 0.085
RTV16-01-07	BE49280	−47.5294	−72.3912	1,335	2.0	0.9845	37.7023	0.1802	5.4173 ± 0.1123	1.7647 ± 0.037
RTV16-01-08	BE49288	−47.5282	−72.3912	1,313	2.1	0.9863	15.0778	0.1815	8.7084 ± 0.1704	7.1787 ± 0.141
RTV16-01-09	BE46453	−47.5279	−72.3921	1,301	2.0	0.9840	70.7804	0.1825	4.2715 ± 0.1105	0.7277 ± 0.019
RTV16-01-10	BE46454	−47.5276	−72.3921	1,287	1.4	0.9090	38.1763	0.1821	1.8539 ± 0.1002	0.5534 ± 0.031
RTV16-01-12	BE46455	−47.5270	−72.3922	1,272	3.1	0.9870	70.4651	0.1835	2.6276 ± 0.1020	0.4409 ± 0.017
RTV16-01-13	BE46331	−47.5224	−72.3901	1,166	1.5	0.9800	43.1031	0.1824	12.6946 ± 0.2356	3.6789 ± 0.069
RTV16-01-15	BE46332	−47.5186	−72.3996	1,149	1.7	0.9860	27.8859	0.1821	7.6896 ± 0.1595	3.4278 ± 0.072
RTV16-01-16	BE49282	−47.5179	−72.3988	1,136	1.9	0.9876	20.0446	0.1019	9.5665 ± 0.2737	3.3145 ± 0.095
RTV16-01-17	BE46333	−47.5172	−72.3981	1,112	2.2	0.9830	45.2772	0.1813	12.2140 ± 0.2267	3.3486 ± 0.062
RTV16-01-18	BE46334	−47.5170	−72.3981	1,112	1.7	0.9780	15.0336	0.1818	5.2897 ± 0.1187	4.3137 ± 0.098
RTV16-01-19	BE46457	−47.5143	−72.3947	1,012	2.9	0.9810	64.0671	0.1805	1.7906 ± 0.0705	0.3143 ± 0.013

AMS ratios presented as boron-corrected values measured against the 07KNSTD standard material with a reported $^{10}Be/^{9}Be$ value of 2.85 × 10^{-12} (Nishiizumi et al., 2007; ^{10}Be half-life = 1.36 Myr). 1σ analytical or internal AMS uncertainties are shown. Rock density = 2.65 g/cm^3. Carrier concentrations used are 1,037 ppm (*) and 1,030 ppm for all others. We processed procedural blanks associated with each sample set, and their total ^{10}Be ranged from ~6,600 to ~26,000 atoms; these were subtracted respectively from sample concentrations.

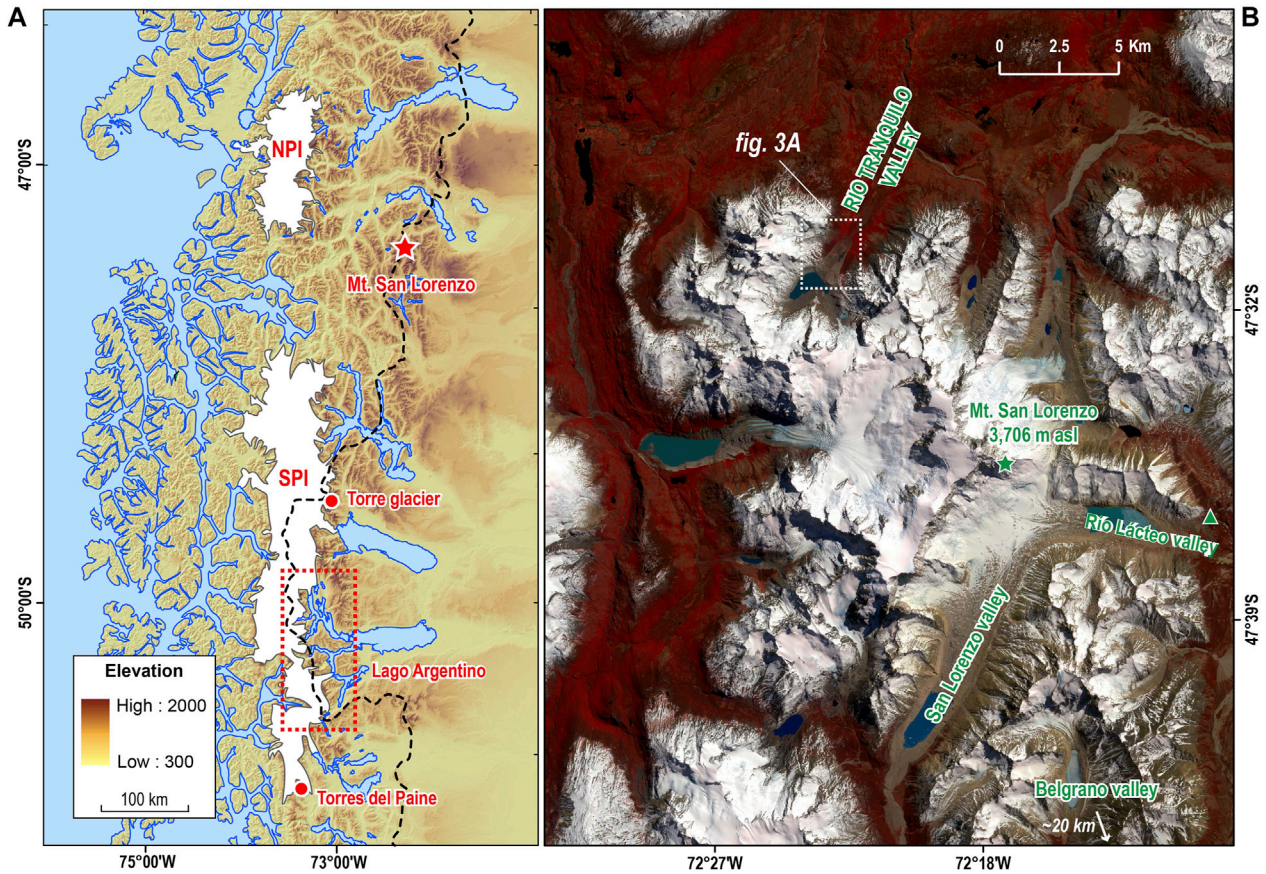

FIGURE 1 | Geographic setting of this and prior studies. **(A)** Regional overview of the Patagonian Icefields and surrounding area. ALOS PALSAR composition (m asl) NPI, Northern Patagonian Icefield; SPI, Southern Patagonia Icefield. **(B)** Río Tranquilo valley, Mt. San Lorenzo. Sentinel 2 false color image (Infrared, 2016) showing the entire San Lorenzo massif and all the glaciers draining from its headwalls. Green star indicates Mt. San Lorenzo summit. Green triangle shows the approximated location of the available Holocene radiocarbon date (Mercer, 1968). Other sites discussed in the text are also shown.

Recently published glacier chronologies, moreover, show promising consistency with pollen-inferred changes in the intensity of the Southern Westerly Winds (SWW) (Moreno et al., 2018). Modern SWW intensity is positively correlated with annual precipitation, and negatively correlated with summer temperatures throughout western Patagonia (see Figures 5, 8 in Garreaud et al., 2013). Accordingly, strong westerlies are associated with the cold and wet conditions ideal for glacier expansion; weaker westerlies, on the other hand, are associated with warmer and drier conditions, promoting glacier withdrawal. Based on the apparent relationship with past Westerlies behavior, it has been hypothesized that Holocene glacier fluctuations in southern Patagonia were paced by centennial-scale temperature and precipitation anomalies associated with changes in the SWW intensity (Moreno et al., 2018; Reynhout et al., 2019). To test and validate this hypothesis across the whole of Patagonia requires expanding the spatial network of study sites, to assess the regional representativeness of emerging ^{10}Be chronologies.

Here, we set out to refine the structure and timing of Holocene glacier fluctuations of southern South America by developing a new comprehensive ^{10}Be moraine chronology in the Río Tranquilo valley, on the northern flank of Mt. San Lorenzo (47°35′ S; 72°19′ W). Located roughly in central Patagonia, Mt. San Lorenzo is located to the east of a tectonic depression that breaks the Andes (and separates the Patagonian Ice Fields), and despite being more than 160 km from the Pacific Ocean, it is the first major orographic barrier to the moisture-laden SWW (Mendelová et al., 2020b). Consequently, Mt. San Lorenzo is ideally located to track the position of the Westerlies and assess their role in pacing Holocene glacier fluctuations in Patagonia (Moreno et al., 2018; Reynhout et al., 2019).

STUDY AREA

Mt. San Lorenzo (47°35′S, 72° 21′W) is an isolated granodiorite massif astride the border between Chile and Argentina, 80 km to the east of the topographic divide of the Andes (**Figure 1**). Mt. San Lorenzo exhibits a transitional maritime to continental climate, with a wide annual thermal amplitude and a narrow range of mean monthly precipitation (Falaschi et al., 2019). At

TABLE 2 | All the new ^{10}Be were ages calculated using CRONUS v. 3 (Balco et al., 2008) and are reported with 1σ internal (analytical) error.

Sample	St		Lm		LSDn	
	Age	±1σ	Age	±1σ	Age	±1σ
PC13-01-13	1,330	40	**1,370**	**50**	1,310	40
PC13-01-14	1,440	30	**1,480**	**30**	1,420	30
PC13-01-18	400	20	**460**	**20**	480	20
PC13-01-19	7,460	140	**7,600**	**140**	7,490	140
PC13-01-23	330	20	**380**	**20**	400	20
PC13-01-24	360	20	**400**	**30**	430	30
PC14-01-33	6,590	170	**6,770**	**170**	6,760	170
PC14-01-34	8,200	250	**8,370**	**250**	8,290	250
PC14-01-35	9,680	180	**9,860**	**180**	9,790	180
RTV16-01-03	6,540	120	**6,730**	**130**	6,720	130
RTV16-01-04	4,260	80	**4,390**	**80**	4,370	80
RTV16-01-05	3,570	70	**3,730**	**80**	3,700	80
RTV16-01-06	3,570	70	**3,740**	**80**	3,710	70
RTV16-01-07	1,420	30	**1,460**	**30**	1,400	30
RTV16-01-08	5,870	120	**6,090**	**120**	6,050	120
RTV16-01-09	600	20	**670**	**20**	670	20
RTV16-01-10	500	30	**560**	**30**	570	30
RTV16-01-12	380	20	**430**	**20**	450	20
RTV16-01-13	3,390	60	**3,540**	**70**	3,530	70
RTV16-01-15	3,190	70	**3,320**	**70**	3,300	70
RTV16-01-16	3,110	90	**3,240**	**90**	3,230	90
RTV16-01-17	3,230	60	**3,360**	**60**	3,350	60
RTV16-01-18	4,160	100	**4,290**	**100**	4,300	100
RTV16-01-19	330	10	**380**	**20**	410	20

"St" is the non-time-dependent scaling from the Lal (1991)/(Stone et al., 2000) scheme; "Lm" is the time dependent version of Lal (1991)/(Stone et al., 2000); LSDn is the time dependent version of Lifton et al. (2014). We use the "Lm" scaling scheme (in bold letters), but this choice does not change our conclusions given the overlap at 1σ. All ages calculated using a ^{10}Be production rate measured at Lago Argentino, south Patagonia (50°S) (Kaplan et al., 2011).

3,706 m a.s.l., Mt. San Lorenzo is one of the most extensively glacierized mountains in the region, with an ice-covered area of ca. 139 km^2. For the years 2005/2008, Falaschi et al. (2013) estimated the snowline to be ~1,700–1,750 m a.s.l. on the western sector of the massif and ~1,800 m asl on the eastern side. This study focuses on the Rio Tranquilo valley, a north-south oriented valley on the northern flank of Mt. San Lorenzo. The headwall of this valley is home to 16 small glaciers <5 km^2 which collectively cover an estimated area of 15 km^2 (Falaschi et al., 2013).

PREVIOUS STUDIES

Nearly all studies that have reconstructed the extent and timing of glacier events on Mt. San Lorenzo have focused on the last glacial-interglacial transition (Wenzens 2005; Glasser et al., 2012; Horta et al., 2017; Davies et al., 2018; Sagredo et al., 2018; Martin et al., 2019; Mendelová et al., 2020a; Mendelová et al., 2020b). Among these studies, Sagredo et al. (2018) addressed the deglacial history specifically of the Tranquilo valley, where they identified major glacier advances during the Antarctic Cold Reversal (ACR; 13,680 ± 460 and 13,490 ± 430 years), followed by a minor stabilization during the Younger Dryas (YD; sometime in between 12,330 ± 410 and 11,460 ± 390 years). These findings are consistent with Mendelová et al. (2020a), who found glacier advances at 13,100 ± 600 and 12,400 ± 300 to the east, in the Belgrano area.

Studies regarding the Holocene glacier history of Mt. San Lorenzo are scarcer, and the available information mostly comprises minimum ^{14}C ages, and other bracketing estimates produced by dendrochronology and lichenometry. Mercer (1968) obtained a minimum age of 5,210 ± 344 cal year BP for the most extensive Holocene glacier advance of the Río Lácteo glacier (**Figure 1**), based on a radiocarbon date of a tree stump buried in a moraine-dammed lagoon. This chronology was extended by Garibotti and Villalba (2017) who estimated the ages of the entire moraine sequence of the Río Lácteo valley using lichenometry, identifying glacier advances at 5,250 ± 360 years, 2,180 ± 50 years, 1,490 ± 20 years, and two advances during the last hundred years. Using the same approach, Garibotti and Villalba (2017) identified advances of the San Lorenzo glacier at 5,750 ± 430 years, 3,880 ± 180 years, 2,470 ± 70 years, as well as several glacier advances/stabilizations during the last few hundreds of years.

In the Tranquilo valley, using dendrochronology, Aravena (2007) dated a group of moraines in the upper section of the valley. Based on the oldest tree growing atop the ridges, he concluded that the entire sequence of moraines was deposited around or before AD 1670. However, the author also acknowledged the possibility that these moraines could be much older, arguing that their age estimate may be limited by the maximum biological ages that can be attained by *Nothofagus pumilio* (targeted species). Later on, Sagredo et al. (2017) partially confirmed this hypothesis by obtaining three coherent ^{10}Be ages of 5,450 ± 100 years, 5,640 ± 110 years and 5,800 ± 150 years (recalculated here) from a single ridge in the middle of the same moraine sequence study by Aravena (2007).

MATERIALS AND METHODS

To constrain the age of former Holocene glacier fluctuations in the Tranquilo valley, we mapped and directly dated seven moraine crests using ^{10}Be surface exposure dating. Detailed geomorphological mapping built upon previous work by Sagredo et al. (2018). In addition to field observations, we used analyses of satellite imagery from Google Earth (2021 Cnes/SPOT, ~15 m spatial resolution), aerial photographs (GEOTEC 1:70,000) and digital elevation models (ALOS Palsar). For exposure dating, we collected samples (~1 kg) from boulders embedded in or resting on stable positions atop the moraine ridges in the upper section of the Tranquilo valley. We selected tall boulders (preferably >1 m) that did not show evidence of post-depositional movement, surface erosion, or exhumation. Samples were taken from the upper ~5 cm of the boulder surface using a hammer and chisel, and the blast method of Kelly (2003). We recorded topographic skylines, as well as surficial strike and dip measurements, using a handheld transit and clinometer. We measured the coordinates and altitude of

FIGURE 2 | Photographs of the moraines and settings in the Río Tranquilo valley. **(A)** Late glacial (RT1-RT5) and Holocene (RT6) moraines. Note the difference in the magnitude between the glacier advances (Photo: Horacio Parraguez). **(B)** Left lateral moraines. Along the proximal slope it is possible to find remnants of younger recessional ridges. **(C)** Right lateral moraines (facing upstream). In this sector, the ~3,500 years ridge was over-printed by the younger moraine. **(D)** Right lateral moraines (facing downstream). Note the difference in appearance between the younger and older ridges.

samples using a handheld commercial GPS (WGS84) with an assumed uncertainty of <10 m. **Table 1** provides geographical and analytical data of the samples. Quartz isolation and beryllium extraction were performed at the Cosmogenic Nuclide Laboratory at the Lamont-Doherty Earth Observatory (LDEO), Columbia University (NY, United States), following Schaefer et al. (2009). ^{10}Be/Be isotope ratios were measured at the Center for Accelerator Mass Spectrometry at Lawrence Livermore National Laboratory (CAMS LLNL). We used version 3 of the CRONUS-Earth online calculator (Balco et al., 2008), along with a regional nuclide production rate developed at Lago Argentino, Patagonia (50°S; Kaplan et al., 2011), assuming zero erosion. Ages discussed here are based on the time dependent version of Stone/Lal's scaling protocol scheme (Lm) (Lal 1991; Stone 2000); however, the choice of scheme does not impact our main conclusions (**Table 2**). We report individual ^{10}Be ages with 1σ analytical uncertainty. We calculate the arithmetic mean ages for moraines and present them with the standard error of the mean and a 3% propagated production rate error (Peltier et al., 2021). Given the sampled boulders were sitting atop the moraines, we assume they were likely deposited at the end of moraine construction episodes; therefore, we interpret the ^{10}Be dates as most likely representing close minimum ages for the culmination of a glacier advance.^{10}Be ages from previous studies were recalculated following the same procedures as above. Previously published radiocarbon ages were recalibrated (cal yr BP) using the SHCal 20 curve (Hogg et al., 2020) in OxCal v. 4.4 (Ramsey 2009).

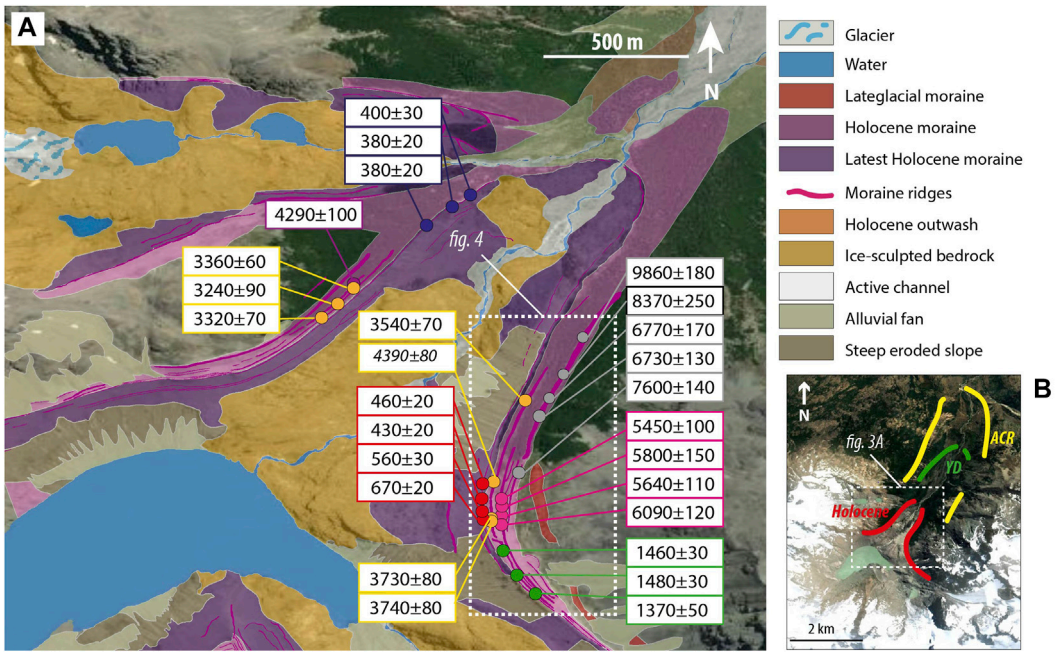

FIGURE 3 | (A) Glacial geomorphologic map of the Río Tranquilo valley with new ^{10}Be ages. Circles with the same color correspond to samples on the same moraine ridge or on correlated ridges on opposite sides of the valley. Individual ^{10}Be ages are provided with 1σ analytical uncertainty **(Table 2)**. One outlier is shown in italics. **(B)** Relative position of the Antarctic Cold Reversal (RT1-4 margins), Younger Dryas (RT5 margin) and Holocene margins (RT6) (Sagredo et al. 2017).

RESULTS

Sagredo et al. (2018) mapped and dated five late-glacial moraines (dubbed RT1-RT5) in the lower reaches of the Tranquilo valley. Upstream, on both sides of the valley, between five and seven well-defined lateral moraine crests were identified (RT6 moraines) (**Figure 2**). RT6 moraine ridges crosscut each other in multiple places documenting readvances of the glacier front (**Figures 3**, **4**). Given the frontal sections of all of the RT6 moraines are not preserved, we cannot precisely determine the maximum glacier extent during these events; however, based on the geometry and slope of the lateral ridges, we infer that the Río Tranquilo glacier reached an extent of between 6 and 7 km from the headwall. Poorly-preserved moraine/glacial drift was found beyond (i.e., distal) RT6, while inward (proximal) of RT6 remnants of small, degraded ridges are occasionally preserved (Sagredo et al., 2017) (**Figure 2**). To avoid error associated with post-depositional disturbances of these poorly-preserved landforms, our chronology focuses on the relatively intact RT6 moraine ridges. Here, we present 24 new ages, which constrain the history of glacier advances in the Tranquilo valley during the Holocene (**Figures 3**, **4**; **Table 2**). Hereafter, when referring to the right (left) moraine or side of the valley, we always mean the true-right (true-left); in other words, the location is identified in relation to an observer looking in the direction of the ice-flow (i.e., down-valley).

Right Lateral Moraines

The outermost RT6 ridge forms a continuous, well-defined ridge rising over 30 m in height downvalley. It gradually loses topographic relief upvalley before it disappears under the inner moraines (**Figure 3**). We collected five samples from boulders along the outermost RT6 ridge crest, yielding ^{10}Be ages of 6,730 ± 130, 6,770 ± 170, 7,600 ± 140, 8,370 ± 250, and 9,860 ± 180 years.

The next prominent moraine as you move inward corresponds to the same ridges previously dated by Sagredo et al. (2017) (*Previous Studies*). A new sample collected from this ridge yielded an age of 6,090 ± 120 years, which is statistically indistinguishable from the existing ages. Our new date, combined with the ages in Sagredo et al. (2017) results in a mean age of 5,750 ± 220 years.

Immediately inward, we found a 5–10 m in high, sharp-crested moraine ridge that can be traced continuously for almost 1 km. We collected four samples from this ridge. Three of them yielded coherent ages of 3,540 ± 70, 3,730 ± 80 and 3,740 ± 80 years (mean of 3,670 ± 130 years). The fourth sample (RTV16-01–04) affords an age of 4,390 ± 80 years, which is excluded from the moraine mean age because it does not overlap with the three ages at 2σ.

In the upper section of the right lateral system (**Figures 3**, **4**), the ~3,700 years ridge has been destroyed by a glacier advance that deposited a small (2-m high) ridge that can be traced to the proximity of the present glacier margin. Three samples collected from boulders atop this ~2-m high ridge provide ages of 1,370 ± 50, 1,460 ± 30 and 1,480 ± 30 years, with a mean age of 1,440 ± 60 years.

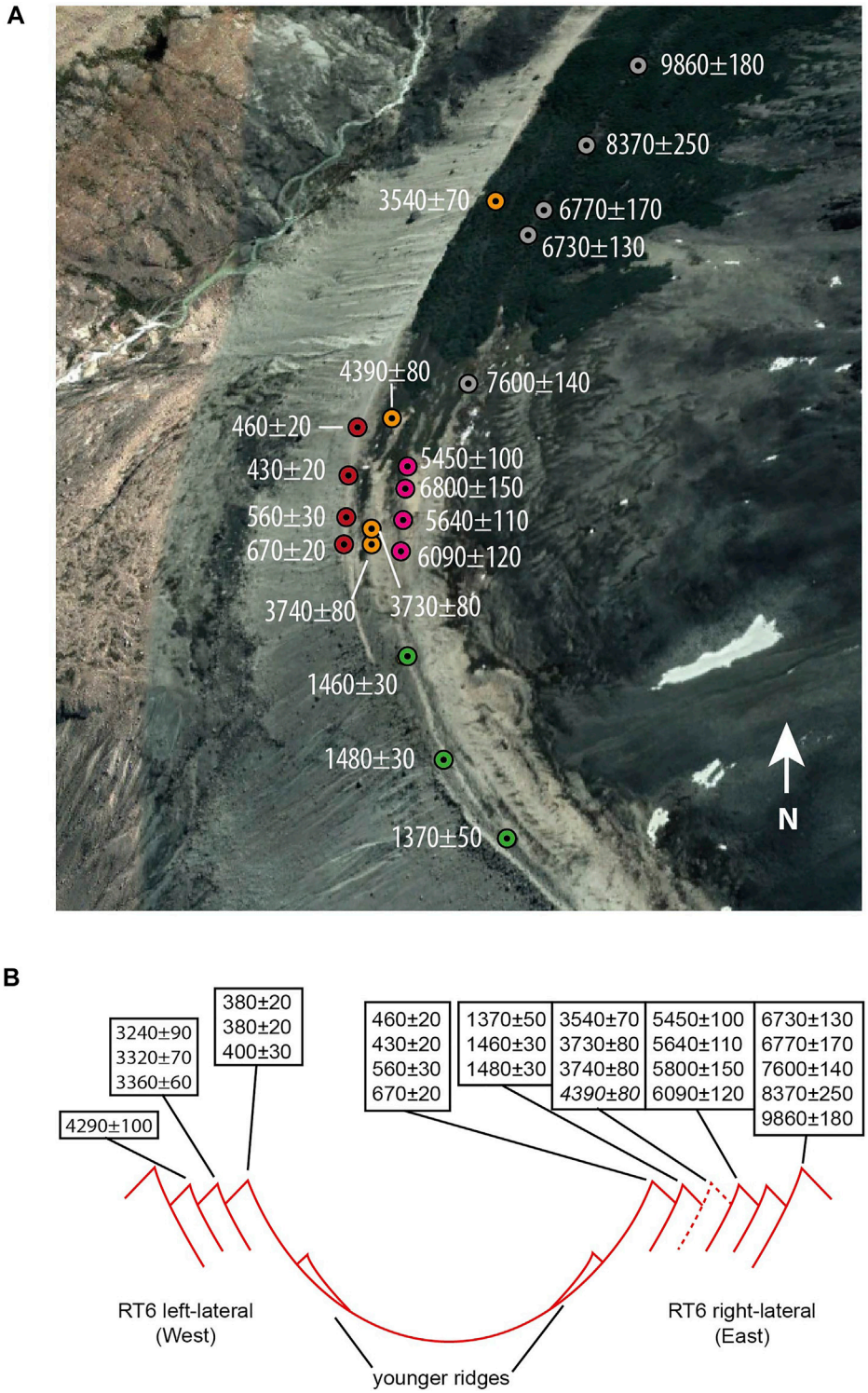

FIGURE 4 | Glacier chronology of Río Tranquilo glacier. **(A)** ^{10}Be ages obtained from the right lateral moraines (oblique perspective) on Google Earth image. **(B)** Schematic cross section of the valley. Notice that the ~3,700 years ridge was destroyed by the ~1,440 years advance in the upper right side of the valley (as represented by the dotted line) (Sagredo et al., 2017).

Finally, the innermost RT6 moraines correspond to a very sharp ridge (**Figure 2**) with a steep postglacially modified proximal slope that reaches the bottom of the valley. Four samples collected on this moraine yield ages ranging from 430 ± 20 to 670 ± 20 years with a mean age of 530 ± 60 years.

Left Lateral Moraines

We did not find any boulders from which to collect suitable samples for surface exposure dating on the two outermost ridges of the moraine suite on the left side of the valley. The outermost moraine dated from this area corresponds to the third-outermost crest, which rises ~10 m above the surrounding topography and is intermittently continuous over about 1 km. A single boulder on this ridge yielded an age of 4,290 ± 100 years.

Immediately inward, we collected three samples from a continuous ~1 km long sharp ridge, which provided ages of 3,240 ± 90, 3,320 ± 70 and 3,360 ± 60 years (mean: 3,310 ± 110 years). Finally, three samples from the steep innermost ridge provided statistically indistinguishable ages of 380 ± 20, 380 ± 20 and 400 ± 30 years (mean: 390 ± 10 years).

DISCUSSION

The glacier chronology at Río Tranquilo shows a clear pattern of multiple progressively less-extensive advances through the Holocene. We found evidence that the Tranquilo glacier reached its maximum extent sometime - or possibly at multiple occasions - during the first half of the Holocene between 9,860 ± 180 and 6,730 ± 130 years (n = 4). Our data suggest that during this Holocene glacier maximum, the Río Tranquilo ice lobe was 30–40% smaller (less extensive) than during the ACR accounting for slight uncertainties in frontal positions. Next, Tranquilo glacier readvanced around 5,750 ± 220 years (n = 4) and 3,490 ± 140 years (n = 6). The later advance is recorded and dated on both sides of the valley by moraines with statistically indistinguishable ages of 3,670 ± 130 (right lateral) and 3,310 ± 110 years (left lateral). A single date from a left lateral ridge outside this landform suggests that Tranquilo glacier may have experienced another glacier advance in between the two advances described above, at around 4,290 ± 100 years; notably, this age is statistically indistinguishable from RTV16-01-04 (4,390 ± 80 years), which was considered an outlier specifically on the ~3,700 years moraine (right lateral side of the valley). The next advance recorded in the area is dated to 1,440 ± 60 years (n = 3). Over the last millennium, we infer that the Tranquilo glacier advanced and lingered in an extended position between 670 ± 20 and 430 ± 20 years (n = 4) and underwent a final major advance ~390 ± 10 years (n = 3). After, the Tranquilo glacier retreated towards the headwall, depositing the minor ridges in the process. Continuing retreat ultimately separated the Río Tranquilo glacier into smaller ice bodies, as observed at present.

The Río Tranquilo valley provides a comprehensive chronology of the glacier history of Mt. San Lorenzo and the adjacent areas. Despite methodological differences, the new ^{10}Be chronology of Holocene glacier advances from Tranquilo valley is consistent with published chronologies (**Figure 1**) from the Río Lácteo (Mercer 1968; Garibotti and Villalba 2017: radiocarbon dating and lichenometry, respectively) and San Lorenzo valleys (Garibotti and Villalba 2017: lichenometry). The Tranquilo chronology encompasses most of the events recorded in these adjacent valleys, except for the glacier advances constrained by a minimum date of 2,470–2,180 years and another during the last 200 years. Additionally, the Tranquilo chronology captures an early Holocene glacier advance not recorded in these other valleys. We speculate that these differences may reflect the strengths and limitations of different dating approaches (cf., cosmogenic dating compared with lichenometry). However, immediately to the south of Mt. San Lorenzo, Wenzens 2005) identified at least three moraine ridges and based on ^{14}C minimum-limiting ages from kettles he inferred they were deposited sometime between 9,620 ± 120 and 7,500 ± 80 cal year BP. It is unclear if the southern glaciers of Mt. San Lorenzo were tributaries of the lobe that deposited those moraines, but interestingly the inferred timeframe for their deposition overlaps with the possible deposition (n = 2 ^{10}Be ages) of the outermost moraine in Río Tranquilo valley.

At a regional level, there are remarkable similarities between the Holocene record at Mt. San Lorenzo and other ^{10}Be (and ^{14}C)-based chronologies to the south (**Figure 5**). Records from southwestern Patagonia show evidence for early Holocene advances that coincide with the range of ages captured by the outermost RT6 moraine. At Lago Argentino (49.8°–50.7°S), based on stratigraphic evidence, Strelin et al. (2014) ^{14}C dated a glacier advance between 7,740 and 7,220 cal year BP in the Agassiz Este valley, which was less extensive than the subsequent maximum Holocene limits after 7 ka; at Torre valley (49.3°S), Reynhout et al. (2019) dated two outermost limits to 9,620 ± 340 and 6,790 ± 210 years. Although the Tranquilo record does not allow us to pinpoint the exact timing of the early Holocene events, we suggest that, collectively, these three sites offer mounting evidence to suggest that expanded glaciers were commonplace in Patagonia during the first half of the epoch. At Tranquilo and the Glacier Torre sites, the early to mid-Holocene expansions represent the Holocene glacier maximum. At Lago Argentino, on the other hand, the maximum Holocene frontal (cf., lateral) limits were reached after 7 ka and by 6 ka.

During the middle Holocene, the Tranquilo record features glacier expansions at 5,750 ± 220, 3,490 ± 140 and 1,440 ± 60 years; within uncertainties, these events may be consistent with an advance at nearby Lago Colonia (47.3°S) at 5,055 ± 190 years (Nimick et al., 2016), and they are statistically indistinguishable from those at Lago Argentino at 5,970 ± 110 and 1,380 ± 50 years (Kaplan et al., 2016), and at Torre valley at 6,030 ± 230 years (Reynhout et al., 2019). Moreover, at Lago Argentino, three ^{10}Be ages of 5,500 ± 200 (n = 2) and 5,700 ± 200 years on different crests within the maximum ~6 ka Holocene limits (e.g., at Frias valley) overlap with ages in the Tranquilo record. An additional glacier advance, preliminary dated at ~4,300 years at Tranquilo valley, is consistent with

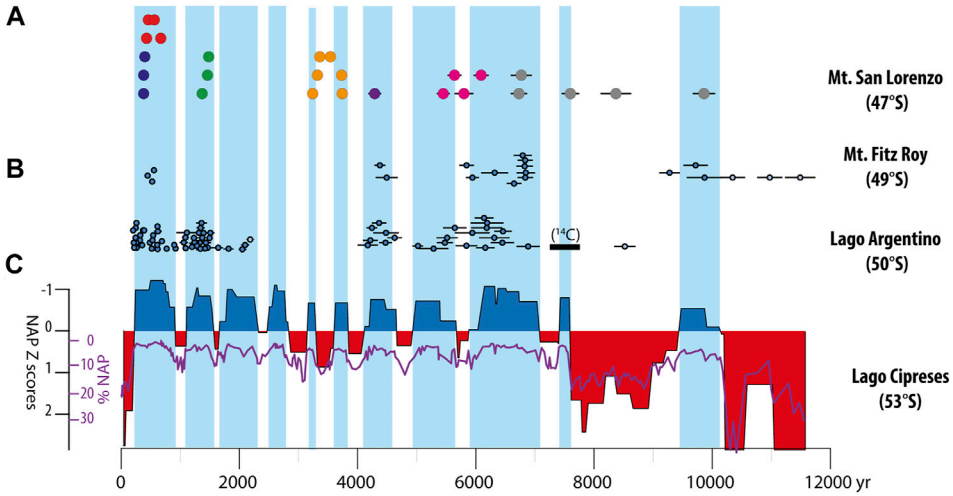

FIGURE 5 | Holocene glacier ^{10}Be chronologies from Patagonia. **(A)** Individual ages (±1σ) on moraine ridges in the Río Tranquillo valley; circles with the same color correspond to samples on the same moraine ridge, including correlated crests between right and left laterals on either side of the valley (same color as in **Figures 3**,**4**). For samples <4,000 years, the error is smaller than the symbol. Events are found between 9,860 ± 180 and 6,730 ± 130, at 5,750 ± 220, 4,290 ± 100 (?), 3,490 ± 140, 1,440 ± 60, between 670 ± 20 and 430 ± 20 and finally at 390 ± 10 years **(B)** Individual ages (±1σ) on moraine ridges in the Torre valley (Reynhout et al., 2019) and Lago Argentino basin (Strelin et al., 2014; Kaplan et al., 2016). Also, we show a glacier advance between 7.7 and 7.2 ka, detected with ^{14}C dating of wood in a stratigraphic section (Strelin et al., 2014) but not with ^{10}Be ages for the moraine record. **(C)** Cold and wet (blue) and warm and dry periods (red) as shown by regime shift detection analysis of non-arboreal pollen (NAP) record from Lago Cipreses at 51°S (Moreno et al., 2018). Negative (positive) values correspond to periods of strong (weak) and northward (southward) displaced SWW. We also included the percent of NAP (purple line). To facilitate comparisons with the glacier records, we included **blue vertical shading** representing the cold and wet periods.

the 4,440 ± 180 years advance at Lago Argentino and the 4,440 ± 140 years advance at Torre valley.

On the other hand, Lago Argentino also preserves advances at ~2,100–2000 and ~1,200–1,000 years that are not present in the chronology at Tranquilo valley, although undated moraine fragments in our study area may reflect these events. We also note that the Río Tranquilo record contains a prominent glacier advance at 3,490 ± 140 years (n = 6) not found in the chronologies at either Lago Argentino or Glacier Torre; however, evidence of this advance has been inferred elsewhere in Southern Patagonia (Wenzens 1999) and Tierra del Fuego (Kuylenstierna et al., 1996; Strelin et al., 2008; Hall et al., 2019). Future efforts will help define better similarities and potential differences between the glacier histories of central and Southern Patagonia.

Finally, during the last millennium, Tranquilo glacier underwent advances between 670 ± 20 and 430 ± 20 years, and at 390 ± 10 years. Statistically indistinguishable ^{10}Be-dated glacier advances have been documented in other sites in Patagonia: Lago Argentino basin (630–480 and 350 ± 20 years BP; Kaplan et al., 2016), Torre valley (510 ± 40 years; Reynhout et al., 2019), and Torres del Paine (51.2°S) (<600 ± 70 years BP and 340 ± 20 years BP; García et al., 2020). We acknowledge that younger glacier advances have been also documented at Lago Argentino (240 ± 10 years) and Torres del Paine (<190 years); we presume that these events correspond to the undated and poorly preserved ridges/drift inward of RT6 (**Figure 2**). Overall, we posit that our findings at Rio Tranquilo are strongly consistent with the onset and timing of expanded glaciers on the southern side of the SPI over the last 1,000 years.

The chronology of glacier fluctuations at the Río Tranquilo valley correlates well with changes in the strength of the SWW, as reconstructed in the pollen record at Lago Cipreses (51°S), in southern Patagonia (**Figure 5**) (Moreno et al., 2018). Thus, glacier advances at Río Tranquilo occurred during inferred periods of SWW maximum strength, which are associated with negative anomalies of temperature and positive anomalies of precipitations throughout western Patagonia (Moreno et al., 2018). The lower latitudinal position of Tranquilo relative to other sites demands that westerlies must have been stronger across the entirety of southern Patagonia reaching towards the central sector. We suggest that even during the early Holocene, relatively brief northward excursions of the SWW from their modern core at 52°S could have interrupted the overall warm conditions that characterized this time slice (Moreno and León 2003; Moreno et al., 2018), triggering what were likely the most extensive alpine glacier advances of the epoch.

Thus, our findings at 47°S support the hypothesis that Holocene glacier variability was modulated by shifts in intensity and location of the westerly winds throughout Patagonia. To drive glacier advances, these changes in SWW strength must have persisted over at least the decadal/centennial time scale. Moreno et al. (2018) proposed that centennial-scale climate variability, resembling that of the Southern Annular mode (SAM) (Moreno et al., 2018), the main mode of atmospheric variability in the mid- and high-latitudes of the Southern Hemisphere (Marshall 2003), could result in changes in mean SWW circulation over Patagonia. Therefore, we posit that centennial-scale paleo-SAM-like variations provide a mechanism

by which SWW circulation excursions could be sustained for long enough to drive glacier advances over the Holocene in central Patagonia.

We infer that the Río Tranquilo record captures much of the centennial/millennial Holocene glacier variability observed throughout Patagonia. It captures glacier advances coeval with those recorded by both small mountain glaciers and major outlet glaciers of the larger Southern Patagonian Icefield. The new comprehensive Holocene chronology confirms the idea that Patagonia exhibited progressively less extensive glacier advances throughout most of the Holocene (Reynhout et al., 2019). In addition, the maximum Holocene glacier extent in southern South America likely occurred sometime during the early part of the epoch. Such patterns appear robust generally south of (at least) 47°S, the location of San Lorenzo, although recently published glacier chronologies from Cordillera Darwin (55°S) suggests that the scenario may be different in the southernmost tip of the continent (e.g., Menouno et al., 2013; Hall et al., 2019; Reynhout et al., 2021).

Finally, the observed high-resolution pattern of multiple moraine building events with slightly decreasing net extent throughout the early, mid- and late Holocene, appears to be one of the most distinctive signatures of glacier behavior in the southern Hemisphere. This pattern has not only been recognized in the southern mid-latitudes including New Zealand (e.g., Putnam et al., 2012; Kaplan et al., 2013; Dowling et al., 2021), but also around the Antarctic Peninsula, at 64°S (Kaplan et al., 2020). Recently, Bakke et al. (2021) documented a trend of gradually smaller glaciers traceable back to the ACR on the island of South Georgia (54.2°S). Collectively, the pattern of generally smaller expansions in the southern latitudes contrasts with the general pattern observed in the Northern Hemisphere, where glaciers reached their maximum extent in the late Holocene (e.g., Grove, 2004; Holzhauser et al., 2005; Schimmelpfennig et al., 2014, 2021; Luckman et al., 2017; Wittmeier et al., 2020; Braumann et al., 2020, 2021). This long-term, asymmetrical Holocene glacier pattern between Hemispheres seems at odds with the global glacier response during the last decades, when anthropogenic warming has overwhelmed the natural forcing (IPCC, 2021) and appears to be driving inter-hemispherically synchronized and accelerating glacier retreat.

DATA AVAILABILITY STATEMENT

The original contributions presented in the study are included in the article; further inquiries can be directed to the corresponding author.

AUTHOR CONTRIBUTIONS

ES, SR, JA, MK, and JS contributed to conception and design of the study, and analysis of the results. ES, SR, JA, PA, MK, and BL conducted field mapping and sample collection. SR, PA, and RS conducted laboratory work. ES, MK, and SR wrote the first draft of the manuscript. All authors contributed to manuscript revision, read, and approved the submitted version.

FUNDING

This project was funded by the ANID Millennium Science Initiative/Millennium Nucleus Paleoclimate NCN17_079; FONDECYT 1180717, and NSF EAR-1804816 (MK and JS). We also acknowledge support from the Fulbright Visiting Scholar Program (MK) and the LDEO and NASA GISS Climate Center (MK). SR was a recipient of a CONICYT-PCHA Beca de Doctorado Nacional (year 2015).

ACKNOWLEDGMENTS

We thank J. Araos, I. González, F. González, J. Koch, R. Orrego, L. Soto, Rodrigo Soteres, and L. Gómez, for providing field assistance. JS also acknowledges support by the NSF (award #1853881) and the Vetlesen Foundation.

REFERENCES

Aniya, M. (1995). Holocene Glacial Chronology in Patagonia: Tyndall and Upsala Glaciers. *Arctic Alpine Res.* 27 (4), 311–322. doi:10.2307/1552024

Aniya, M. (2013). Holocene Glaciations of Hielo Patag‍oacute;nico (Patagonia Icefield), South America: A Brief Review. *Geochem. J.* 47 (2), 97–105. doi:10.2343/GEOCHEMJ.1.0171

Aravena, J. C. (2007). *Reconstructing Climate Variability Using Tree Rings and Glacier Fluctuations in the Southern Chilean Andes, PhD Thesis*. Ontario: University of Western Western Ontario, 236.

Bakke, J., Paasche, Ø., Schaefer, J. M., and Timmermann, A. (2021). Long-term Demise of Sub-antarctic Glaciers Modulated by the Southern Hemisphere Westerlies. *Sci. Rep.* 11 (1), 1–10. doi:10.1038/s41598-021-87317-5

Balco, G., Stone, J. O., Lifton, N. A., and Dunai, T. J. (2008). A Complete and Easily Accessible Means of Calculating Surface Exposure Ages or Erosion Rates from 10Be and 26Al Measurements. *Quat. Geochronol.* 3, 174–195. doi:10.1016/j.quageo.2007.12.001

Bond, G., Kromer, B., Beer, J., Muscheler, R., Evans, M. N., Showers, W., et al. (2001). Persistent Solar Influence on North Atlantic Climate during the Holocene. *Science* 294, 2130–2136. doi:10.1126/science.1065680

Braumann, S. M., Schaefer, J. M., Neuhuber, S. M., Lüthgens, C., Hidy, A. J., and Fiebig, M. (2021). Early Holocene Cold Snaps and Their Expression in the Moraine Record of the Eastern European Alps. *Clim. Past* 17, 2451–2479. doi:10.5194/cp-17-2451-2021

Braumann, S. M., Schaefer, J. M., Neuhuber, S. M., Reitner, J. M., Lüthgens, C., and Fiebig, M. (2020). Holocene Glacier Change in the Silvretta Massif (Austrian Alps) Constrained by a New 10Be Chronology, Historical Records and Modern Observations. *Quat. Sci. Rev.* 245, 106493. doi:10.1016/j.quascirev.2020.106493

Bronk Ramsey, C. (2009). Bayesian Analysis of Radiocarbon Dates. *Radiocarbon* 51 (1), 337–360. doi:10.1017/S0033822200033865

Clapperton, C., and Sugden, D. (1988). Holocene Glacier Fluctuations in South America and Antarctica. *Quat. Sci. Rev.* 7, 185–198. doi:10.1016/0277-3791(88)90005-4

Davies, B. J., Thorndycraft, V. R., Fabel, D., and Martin, J. R. V. (2018). Asynchronous Glacier Dynamics during the Antarctic Cold Reversal in central Patagonia. *Quat. Sci. Rev.* 200, 287–312. doi:10.1016/j.quascirev.2018.09.025

Denton, G. H., and Broecker, W. S. (2008). Wobbly Ocean Conveyor Circulation during the Holocene? *Quat. Sci. Rev.* 27, 1939–1950. doi:10.1016/j.quascirev.2008.08.008

Denton, G. H., and Karlén, W. (1973). Holocene Climatic Variations-Their Pattern and Possible Cause. *Quat. Res.* 3, 155–205. doi:10.1016/0033-5894(73)90040-9

Dowling, L., Eaves, S., Norton, K., Mackintosh, A., Anderson, B., Hidy, A., et al. (2021). Local Summer Insolation and Greenhouse Gas Forcing Drove Warming and Glacier Retreat in New Zealand during the Holocene. *Quat. Sci. Rev.* 266, 107068. doi:10.1016/j.quascirev.2021.107068

Falaschi, D., Bravo, C., Masiokas, M., Villalba, R., and Rivera, A. (2013). First Glacier Inventory and Recent Changes in Glacier Area in the Monte San Lorenzo Region (47°S), Southern Patagonian Andes, South America. *Arctic, Antarctic, Alpine Res.* 45 (1), 19–28. doi:10.1657/1938-4246-45.1.19

Falaschi, D., Lenzano, M. G., Villalba, R., Bolch, T., Rivera, A., and Lo Vecchio, A. (2019). Six Decades (1958-2018) of Geodetic Glacier Mass Balance in Monte San Lorenzo, Patagonian Andes. *Front. Earth Sci.* 7, 326. doi:10.3389/feart.2019.00326

García, J.-L., Hall, B. L., Kaplan, M. R., Gómez, G. A., De Pol-Holz, R., García, V. J., et al. (2020). 14C and 10Be dated Late Holocene fluctuations of Patagonian glaciers in Torres del Paine (Chile, 51°S) and connections to Antarctic climate change. *Quat. Sci. Rev.* 246, 106541. doi:10.1016/j.quascirev.2020.106541

Garibotti, I. A., and Villalba, R. (2017). Colonization of Mid- and Late-Holocene Moraines by Lichens and Trees in the Magellanic Sub-antarctic Province. *Polar Biol.* 40 (9), 1739–1753. doi:10.1007/s00300-017-2096-1

Garreaud, R., Lopez, P., Minvielle, M., and Rojas, M. (2013). Large-scale Control on the Patagonian Climate. *J. Clim.* 26 (1), 215–230. doi:10.1175/JCLI-D-12-00001.1

Glasser, N. F., Harrison, S., Schnabel, C., Fabel, D., and Jansson, K. N. (2012). Younger Dryas and Early Holocene Age Glacier Advances in Patagonia. *Quat. Sci. Rev.* 58, 7–17. doi:10.1016/j.quascirev.2012.10.011

Glasser, N. F., Jansson, K. N., Harrison, S., and Rivera, A. (2005). Geomorphological Evidence for Variations of the North Patagonian Icefield during the Holocene. *Geomorphology* 71 (3-4), 263–277. doi:10.1016/j.geomorph.2005.02.003

Grove, J. M. (1988). *Little Ice Ages: Ancient and Modern*. 2nd ed. Oxfordshire, England, UK: Routledge. doi:10.4324/9780203505205

Hall, B. L., Lowell, T. V., Bromley, G. R. M., Denton, G. H., and Putnam, A. E. (2019). Holocene Glacier Fluctuations on the Northern Flank of Cordillera Darwin, Southernmost South America. *Quat. Sci. Rev.* 222, 105904. doi:10.1016/j.quascirev.2019.105904

Hogg, A. G., Heaton, T. J., Hua, Q., Palmer, J. G., Turney, C. S., Southon, J., et al. (2020). SHCal20 Southern Hemisphere Calibration, 0-55,000 Years Cal BP. *Radiocarbon* 62 (4), 759–778. doi:10.1017/RDC.2020.59

Holzhauser, H., Magny, M., and Zumbuühl, H. J. (2005). Glacier and lake-level Variations in West-central Europe over the Last 3500 Years. *The Holocene* 15 (6), 789–801. doi:10.1191/0959683605hl853ra

Horta, L. R., Georgieff, S. M., Aschero, C. A., and Goñi, R. A. (2017). Paleolacustrine Records from Late Pleistocene - Holocene in the Perito Moreno National Park, Argentinian Patagonian Andes. *Quat. Int.* 436, 8–15. doi:10.1016/j.quaint.2017.01.001

Kaplan, M. R., Schaefer, J. M., Denton, G. H., Doughty, A. M., Barrell, D. J. A., Chinn, T. J. H., et al. (2013). The Anatomy of Long-Term Warming since 15 Ka in New Zealand Based on Net Glacier Snowline Rise. *Geology* 41 (8), 887–890. doi:10.1130/G34288.1

Kaplan, M. R., Schaefer, J. M., Strelin, J. A., Denton, G. H., Anderson, R. F., Vandergoes, M. J., et al. (2016). Patagonian and Southern South Atlantic View of Holocene Climate. *Quat. Sci. Rev.* 141, 112–125. doi:10.1016/j.quascirev.2016.03.014

Kaplan, M. R., Strelin, J. A., Schaefer, J. M., Denton, G. H., Finkel, R. C., Schwartz, R., et al. (2011). *In-situ* Cosmogenic 10Be Production Rate at Lago Argentino, Patagonia: Implications for Late-Glacial Climate Chronology. *Earth Planet. Sci. Lett.* 309, 21–32. doi:10.1016/j.epsl.2011.06.018

Kaplan, M. R., Strelin, J. A., Schaefer, J. M., Peltier, C., Martini, M. A., Flores, E., et al. (2020). Holocene Glacier Behavior Around the Northern Antarctic Peninsula and Possible Causes. *Earth Planet. Sci. Lett.* 534, 116077. doi:10.1016/j.epsl.2020.116077

Kelly, M. A. (2003).*The Late Wurmian Age in the Western Swiss Alps - Last Glacial Maximum (LGM) Ice-Surface Reconstruction and 10Be Dating of Late-Glacial Features*. Bern, Switzerland: University of Bern, 105. PhD dissertation.

Kuylenstierna, J. L., Rosqvist, G. C., and Holmlund, P. (1996). Late-Holocene glacier variations in the Cordillera Darwin, Tierra del Fuego, Chile. *The Holocene* 6 (3), 353–358. doi:10.1177/095968369600600310

Lal, D. (1991). Cosmic ray Labeling of Erosion Surfaces: *In Situ* Nuclide Production Rates and Erosion Models. *Earth Planet. Sci. Lett.* 104, 424–439. doi:10.1016/0012-821X(91)90220-C

Lifton, N., Sato, T., and Dunai, T. (2014). Scaling In Situ Cosmogenic Nuclide Production Rates Using Analytical Approximations to Atmospheric Cosmic-Ray Fluxes. *Earth Planet. Sci. Lett.* 386, 149–160. doi:10.1016/j.epsl.2013.10.052

Luckman, B. H., Masiokas, M. H., and Nicolussi, K. (2017). Neoglacial History of Robson Glacier, British Columbia. *Can. J. Earth Sci.* 54 (11), 1153–1164. doi:10.1139/cjes-2016-0187

Marshall, G. J. (2003). Trends in the Southern Annular Mode from Observations and Reanalyses. *J. Clim.* 16 (24), 4134–4143. doi:10.1175/1520-0442(2003)016<4134:titsam>2.0.co;2

Martin, J. R. V., Davies, B. J., and Thorndycraft, V. R. (2019). Glacier Dynamics during a Phase of Late Quaternary Warming in Patagonia Reconstructed from Sediment-Landform Associations. *Geomorphology* 337, 111–133. doi:10.1016/j.geomorph.2019.03.007

Mendelová, M., Hein, A. S., Rodés, Á., Smedley, R. K., and Xu, S. (2020a). Glacier Expansion in central Patagonia during the Antarctic Cold Reversal Followed by Retreat and Stabilisation during the Younger Dryas. *Quat. Sci. Rev.* 227, 106047. doi:10.1016/j.quascirev.2019.106047I

Mendelová, M., Hein, A. S., Rodés, Á., and Xu, S. (2020b). Extensive Mountain Glaciation in central Patagonia during Marine Isotope Stage 5. *Quat. Sci. Rev.* 227, 105996. doi:10.1016/j.quascirev.2019.105996

Menounos, B., Clague, J. J., Osborn, G., Davis, P. T., Ponce, F., Goehring, B., et al. (2013). Latest Pleistocene and Holocene glacier fluctuations in southernmost Tierra del Fuego, Argentina. *Quat. Sci. Rev.* 77, 70–79. doi:10.1016/j.quascirev.2013.07.008

Mercer, J. H. (1968). Variations of Some Patagonian Glaciers since the Late-Glacial. *Am. J. Sci.* 266, 91–109. doi:10.2475/ajs.266.2.91

Mercer, M. (1982). Transition Metal Chlorofluorides. *J. Fluorine Chem.* 21, 35–40. doi:10.1016/s0022-1139(00)85381-6

Moreno, P. I., and León, A. L. (2003). Abrupt Vegetation Changes during the Last Glacial to Holocene Transition in Mid-latitude South America. *J. Quat. Sci.* 18, 787–800. doi:10.1002/jqs.801

Moreno, P. I., Vilanova, I., Villa-Martínez, R., Dunbar, R. B., Mucciarone, D. A., Kaplan, M. R., et al. (2018). Onset and Evolution of Southern Annular Mode-like Changes at Centennial Timescale. *Sci. Rep.* 8 (1), 3458. doi:10.1038/s41598-018-21836-6

Nimick, D. A., McGrath, D., Mahan, S. A., Friesen, B. A., and Leidich, J. (2016). Latest Pleistocene and Holocene Glacial Events in the Colonia valley, Northern Patagonia Icefield, Southern Chile. *J. Quat. Sci.* 31 (6), 551–564. doi:10.1002/jqs.2847

Nishiizumi, K., Imamura, M., Caffee, M. W., Southon, J. R., Finkel, R. C., and McAninch, J. (2007). Absolute Calibration of 10Be AMS Standards. *Nucl. Instr. Methods Phys. Res. Section B: Beam Interactions Mater. Atoms* 258, 403–413. doi:10.1016/j.nimb.2007.01.297

Peltier, C., Kaplan, M. R., Birkel, S. D., Soteres, R. L., Sagredo, E. A., Aravena, J. C., et al. (2021). The Large MIS 4 and Long MIS 2 Glacier Maxima on the Southern Tip of South America. *Quat. Sci. Rev.* 262, 106858. doi:10.1016/j.quascirev.2021.106858

Porter, S. C., and Denton, G. H. (1967). Chronology of Neoglaciation in the North American Cordillera. *Am. J. Sci.* 265, 177–210. doi:10.2475/ajs.265.3.177

Putnam, A. E., Schaefer, J. M., Denton, G. H., Barrell, D. J. A., Finkel, R. C., Andersen, B. G., et al. (2012). Regional Climate Control of Glaciers in New Zealand and Europe during the Pre-industrial Holocene. *Nat. Geosci* 5 (9), 627–630. doi:10.1038/ngeo1548

Reynhout, S. A., Kaplan, M. R., Sagredo, E. A., Aravena, J. C., Soteres, R. L., Schwartz, R., et al. (2021). Holocene Glacier History of Northeastern Cordillera Darwin, Southernmost South America (55°S). *Quat. Res.*, 1–16. doi:10.1017/qua.2021.45

Reynhout, S. A., Sagredo, E. A., Kaplan, M. R., Aravena, J. C., Martini, M. A., Moreno, P. I., et al. (2019). Holocene Glacier Fluctuations in Patagonia Are

Modulated by Summer Insolation Intensity and Paced by Southern Annular Mode-like Variability. *Quat. Sci. Rev.* 220, 178–187. doi:10.1016/j.quascirev.2019.05.029

Sagredo, E. A., Kaplan, M. R., Araya, P. S., Lowell, T. V., Aravena, J. C., Moreno, P. I., et al. (2018). Trans-pacific Glacial Response to the Antarctic Cold Reversal in the Southern Mid-latitudes. *Quat. Sci. Rev.* 188, 160–166. doi:10.1016/j.quascirev.2018.01.011

Sagredo, E. A., Lowell, T. V., Kelly, M. A., Rupper, S., Aravena, J. C., Ward, D. J., et al. (2017). Equilibrium Line Altitudes along the Andes during the Last Millennium: Paleoclimatic Implications. *The Holocene* 27 (7), 1019–1033. doi:10.1177/0959683616678458

Schaefer, J. M., Denton, G. H., Kaplan, M., Putnam, A., Finkel, R. C., Barrell, D. J. A., et al. (2009). High-Frequency Holocene Glacier Fluctuations in New Zealand Differ from the Northern Signature. *Science* 324, 622–625. doi:10.1126/science.1169312

Schimmelpfennig, I., Schaefer, J., Lamp, J., Godard, V., Schwartz, R., Bard, E., et al. (2021). Glacier Response to Holocene Warmth Inferred from *In Situ* 10Be and 14C Bedrock Analyses in Steingletscher's Forefield (central Swiss Alps). *Clim. Past Discuss.*, 1–27. doi:10.5194/cp-2021-110

Schimmelpfennig, I., Schaefer, J. M., Akçar, N., Koffman, T., Ivy-Ochs, S., Schwartz, R., et al. (2014). A Chronology of Holocene and Little Ice Age Glacier Culminations of the Steingletscher, Central Alps, Switzerland, Based on High-Sensitivity Beryllium-10 Moraine Dating. *Earth Planet. Sci. Lett.* 393, 220–230. doi:10.1016/j.epsl.2014.02.046

Stone, J. O. (2000). Air Pressure and Cosmogenic Isotope Production. *J. Geophys. Res.* 105, 23753–23759. doi:10.1029/2000JB900181

Strelin, J. A., Denton, G. H., Vandergoes, M. J., Ninnemann, U. S., and Putnam, A. E. (2011). Radiocarbon Chronology of the Late-Glacial Puerto Bandera Moraines, Southern Patagonian Icefield, Argentina. *Quat. Sci. Rev.* 30, 2551–2569. doi:10.1016/j.quascirev.2011.05.004

Strelin, J. A., Kaplan, M. R., Vandergoes, M. J., Denton, G. H., and Schaefer, J. M. (2014). Holocene Glacier History of the Lago Argentino basin, Southern Patagonian Icefield. *Quat. Sci. Rev.* 101, 124–145. doi:10.1016/j.quascirev.2011.05.00410.1016/j.quascirev.2014.06.026

Strelin, J., Casassa, G., Rosqvist, G., and Holmlund, P. (2008). Holocene glaciations in the Ema Glacier valley, Monte Sarmiento Massif, Tierra del Fuego. *Palaeogeogr. Palaeoclimatol. Palaeoecol.* 260, 299–314. doi:10.1016/j.palaeo.2007.12.002

IPCC (2021). in *Climate Change 2021: The Physical Science Basis. Contribution of Working Group I to the Sixth Assessment Report of the Intergovernmental Panel on Climate Change*. Editors V. Masson-Delmotte, P. Zhai, A. Pirani, S. L. Connors, C. Péan, S. Berger, et al. (Cambridge UK: Cambridge University Press). In press.

Wenzens, G. (1999). Fluctuations of Outlet and Valley Glaciers in the Southern Andes (Argentina) during the Past 13,000 Years. *Quat. Res.* 51, 238–247. doi:10.1006/qres.1999.2043

Wenzens, G. (2005). *Glacier Advances East of the Southern Andes between the Last Glacial Maximum and 5,000 BP Compared with lake Terraces of the Endorrheic Lago Cardiel (49° S, Patagonia, Argentina)*. NF: Zeitschrift für Geomorphologie, 433–454. doi:10.1127/zfg/49/2005/433

Wittmeier, H. E., Schaefer, J. M., Bakke, J., Rupper, S., Paasche, Ø., Schwartz, R., et al. (2020). Late Glacial Mountain Glacier Culmination in Arctic Norway Prior to the Younger Dryas. *Quat. Sci. Rev.* 245, 106461. doi:10.1016/j.quascirev.2020.106461

Conflict of Interest: The authors declare that the research was conducted in the absence of any commercial or financial relationships that could be construed as a potential conflict of interest.

Publisher's Note: All claims expressed in this article are solely those of the authors and do not necessarily represent those of their affiliated organizations, or those of the publisher, the editors and the reviewers. Any product that may be evaluated in this article, or claim that may be made by its manufacturer, is not guaranteed or endorsed by the publisher.

frontiers in Earth Science

ORIGINAL RESEARCH
published: 23 December 2021
doi: 10.3389/feart.2021.713011

Climatic and Morphometric Explanatory Variables of Glacier Changes in the Andes (8–55°S): New Insights From Machine Learning Approaches

Alexis Caro, Thomas Condom and Antoine Rabatel*

Univ. Grenoble Alpes, CNRS, IRD, Grenoble-INP, Institut des Géosciences de l'Environnement, Grenoble, France

OPEN ACCESS

Edited by:
Juan-Luis García, Pontificia Universidad Católica de Chile, Chile

Reviewed by:
Alfonso Fernandez, University of Concepcion, Chile
Lucas Ruiz, CONICET Argentine Institute of Nivology, Glaciology and Environmental Sciences (IANIGLA), Argentina

***Correspondence:**
Alexis Caro
alexis.caro.paredes@gmail.com

Specialty section:
This article was submitted to Cryospheric Sciences, a section of the journal Frontiers in Earth Science

Received: *21 May 2021*
Accepted: *06 December 2021*
Published: *23 December 2021*

Citation:
Caro A, Condom T and Rabatel A (2021) Climatic and Morphometric Explanatory Variables of Glacier Changes in the Andes (8–55°S): New Insights From Machine Learning Approaches. Front. Earth Sci. 9:713011. doi: 10.3389/feart.2021.713011

Over the last decades, glaciers across the Andes have been strongly affected by a loss of mass and surface areas. This increases risks of water scarcity for the Andean population and ecosystems. However, the factors controlling glacier changes in terms of surface area and mass loss remain poorly documented at watershed scale across the Andes. Using machine learning methods (Least Absolute Shrinkage and Selection Operator, known as LASSO), we explored climatic and morphometric variables that explain the spatial variance of glacier surface area variations in 35 watersheds (1980–2019), and of glacier mass balances in 110 watersheds (2000–2018), with data from 2,500 to 21,000 glaciers, respectively, distributed between 8 and 55°S in the Andes. Based on these results and by applying the Partitioning Around Medoids (PAM) algorithm we identified new glacier clusters. Overall, spatial variability of climatic variables presents a higher explanatory power than morphometric variables with regards to spatial variance of glacier changes. Specifically, the spatial variability of precipitation dominates spatial variance of glacier changes from the Outer Tropics to the Dry Andes (8–37°S) explaining between 49 and 93% of variances, whereas across the Wet Andes (40–55°S) the spatial variability of temperature is the most important climatic variable and explains between 29 and 73% of glacier changes spatial variance. However, morphometric variables such as glacier surface area show a high explanatory power for spatial variance of glacier mass loss in some watersheds (e.g., Achacachi with r^2 = 0.6 in the Outer Tropics, Río del Carmen with r^2 = 0.7 in the Dry Andes). Then, we identified a new spatial framework for hydro-glaciological analysis composed of 12 glaciological zones, derived from a clustering analysis, which includes 274 watersheds containing 32,000 glaciers. These new zones better take into account different seasonal climate and morphometric characteristics of glacier diversity. Our study shows that the exploration of variables that control glacier changes, as well as the new glaciological zones calculated based on these variables, would be very useful for analyzing hydro-glaciological modelling results across the Andes (8–55°S).

Keywords: climate drivers, morpho-topographic drivers, glacier changes, machine learning, clustering, andes

1 INTRODUCTION

The Andes contain the largest concentration of ice in the southern hemisphere outside the Antarctic and its periphery (RGI Consortium, 2017). Andean glaciers have been affected by an almost continuous negative mass balance and consecutive shrinkage since the middle of the 20th century (Rabatel et al., 2013; Zemp et al., 2019). Despite considerable efforts in recent years regarding quantifications of glacier changes (e.g., Meier et al., 2018; Braun et al., 2019; Dussaillant et al., 2019; Seehaus et al., 2019, 2020), there is still much to investigate in order to analyze the controlling factors of these changes and to determine the hydrological significance of this glacier surface and mass loss on fresh water resources (e.g., Vuille et al., 2018; Masiokas et al., 2020). A better understanding of glacier changes across the Andes could contribute to anticipate and mitigate the related consequences and hazards at watershed scale, for instance in terms of water supply for roughly 45% of the population in Andean countries (Devenish and Gianella, 2012) and for ecosystems (Dangles et al., 2017; Zimmer et al., 2018; Cauvy-Fraunié & Dangles, 2019), primarily during the dry season (Mark et al., 2005; Baraer et al., 2012; Soruco et al., 2015; Guido et al., 2016; Ayala et al., 2020).

Glaciological studies carried out on a limited number of glaciers in the Outer Tropics (8–17°S) have underlined that atmospheric warming is an important control on the current glacier change mainly through the precipitation phases and consecutive albedo effect (Favier et al., 2004; Rabatel et al., 2013). The surface area and elevation of glaciers are morphometric variables that have also been identified to modulate the magnitude of glacier mass loss (e.g., Rabatel et al., 2006, 2013; Soruco et al., 2009). In the Southern Andes (17–55°S), studies focusing on long-term behavior of glaciers (i.e., since the mid-20th century) highlight a high correlation between precipitation and glacier mass balance in the Dry Andes (Rabatel et al., 2011; Masiokas et al., 2016; Kinnard et al., 2020), and with temperature in the Wet Andes (Masiokas et al., 2015; Abdel Jaber et al., 2019; Falaschi et al., 2019). These variables, primarily temperature and precipitation, have been widely used across the Andes to simulate glacier changes and related hydrological contribution through conceptual and physically-based hydro-glaciological models from a local scale to the scale of the Andes (Sicart et al., 2008; Ragettli and Pellicciotti, 2012; Huss and Hock, 2015, 2018; Soruco et al., 2015; Ayala et al., 2016, 2020; Bravo et al., 2017; Mernild et al., 2018; Burger et al., 2019; Shaw et al., 2020).

However, these studies did not quantified the relevance of morphometric variables to estimate glacier changes such as elevation and aspect, or glacier surface area and slope; these variables have already been significantly correlated to glacier changes in studies either dedicated to the Tropical and Southern Andes (e.g., Soruco et al., 2009; Rabatel et al., 2011) or in other mountain ranges (e.g., Rabatel et al., 2016; Brun et al., 2019; Bolibar et al., 2020; Davaze et al., 2020). In addition, simulations of glacier changes are traditionally conducted using geodetic mass balance products and few *in situ* glacier measurements available for calibration/validation purposes. However, glacier surface area changes are not frequently considered in hydro-glaciological simulations (e.g., Ayala et al., 2020; Baraer et al., 2012) and therefore this represents a source of uncertainty in long-term simulations of glacier changes and related impacts.

Currently, several glaciological datasets are available across the Andes thanks to local and international initiatives. Products estimating the geodetic glacier mass balance (GMB) for the whole Andes were recently published (Braun et al., 2019; Dussaillant et al., 2019), while glacier inventories have been made freely available (ANA, 2014; DGA, 2014; IANIGLA-CONICET, 2018; Seehaus et al., 2019, 2020). At the Andes scale, Dussaillant et al. (2019) estimated a negative GMB of -0.72 ± 0.22 m w.e. yr^{-1} (2000–2018), with most negative values in Patagonia (-0.86 ± 0.27 m w.e. yr^{-1}) followed by the Outer Tropics (-0.42 ± 0.23 m w.e. yr^{-1}), compared to moderate losses in the Dry Andes (-0.31 ± 0.19 m w.e. yr^{-1}). Similar results were observed by Braun et al. (2019) for the Patagonian glaciers (0.91 ± 0.08 m w.e. yr^{-1}) over a slightly shorter period (2000–2011/2015). Both works used version 6.0 of the Randolph Glacier Inventory (RGI Consortium, 2017) to map glacier outlines for GMB estimations, which includes fewer glaciers compared with national inventories (Zalazar et al., 2020). Conversely to GMB, no product is available for the whole Andes for glacier area variation (GAV). However, many studies have pointed out a negative GAV at a multidecadal time scale across all glacierized regions from the Outer Tropics to Tierra del Fuego (8–55°S). For example, Seehaus et al. (2019, 2020) observed an average GAV of -29% ($\pm 1.8\%$ a^{-1}) (2000–2016) in the Outer Tropics. In the Dry Andes, an average GAV of -29% (1955–2007) was estimated in the Desert Andes (Rabatel et al., 2011), similar to that observed by Malmros et al. (2016) in the Central Andes (average of $-30 \pm 3\%$, 1955–2014). However, a sharp contrast was observed in the Wet Andes, where the Lakes District shows a GAV between -87% (1975–2007) and -20% (1961–2007) on different volcanoes (Rivera and Bown, 2013), in the North Patagonia this reduction was -25% (1985–2011, Paul and Mölg, 2014), and from the Northern Patagonian ice-field to Tierra del Fuego, Meier et al. (2018) estimated an average GAV of $-9 \pm 5\%$ (1986–2016) including several exceptions of glacier advance, e.g., Glacier Pio XI in the Southern Patagonian ice-field (Hata and Sugiyama, 2021; Rivera and Casassa, 1999; Wilson et al., 2016).

In the present study, our goal is to identify the main climate and morphometric variables that explain the spatial variance of glacier changes across the Andes (8–55°S) using GAV over the 1980–2019 period and GMB over the 2000–2018 period. Our approach is based on machine learning tools. The main explanatory variables of GAV and GMB will be identified at watershed scale using the Least Absolute Shrinkage and Selection Operator (LASSO) linear regression algorithm (Tibshirani, 1996), which has shown good results at glacier scale in the Alps (Bolibar et al., 2020; Davaze et al., 2020). These results will be used to determine new glaciological zones (hereafter named "clusters") across the Andes, composed of glacierized watersheds with similar morphometric and climatic characteristics. This

TABLE 1 | List of different glacier inventories is used to generate the multi-temporal glacier surface areas dataset across the Andes between 8–55°S.

Country	Location, watersheds	Latitude range	Year range	Total glacier surface area [km^2]	Glacier number	Type of resource	Delineation technique	References
Perú	Across Perú	8.2–15.8°S	1955–1962	2,487	3,331	O	M	Hidrandina (1989)
	Across Perú	8.3–16.2°S	2005–2012	1,299	2,679	S	A + M	ANA (2014)
	Across Perú	8.4–18.4°S	2000–2016	4,901*	5,835*	S	A	Seehaus et al. (2019)
	Across Perú	8.4–15.9°S	2016	1,118	2,259	S	A + M	INAIGEM (2018)
Bolivia	Cordillera Real	16.1–16.3°S	2006	23	86	S	M	Soruco et al. (2009)
	Cordillera Real	15.8–17.1°S	2000–2016	730*	976*	S	A	Seehaus et al. (2020)
Chile	Maipo	33.1–34.3°S	1955–1976	626	1,466	O	M	Marangunic (1979)
	Cachapoal watershed	34.3–34.7°S	1955	323	273	O	M	Caviedes (1979)
	Tinguiririca watershed	34.6–34.9°S	1955	166	312	O	M	Valdivia (1984)
	Atacama	18.4–29.8°S	1955–1976	54	11	O	M	Garín (1987)
	Isla Riesco	53.2°S	1984	20	17	S	A + M	Casassa et al. (2002)
	Gran Campo Nevado	52.6–53.1°S	1998	254	75	O + S	A + M	Möller et al. (2007)
	Copiapó	27.7–28.6°S	2002	23	92	O + S	A + M	Vivero (2008)
	North and volcanoes	29.3, 37.9–41.2°S	1961–2011	123*	103*	O + S	A + M	DGA (2011)
	Volcanoes	35.2–41.1°S	1961–2011	83*	163*	O + S	A + M	Rivera & Bown (2013)
	Across Chile	17.6–55.4°S	1996–2009	23,641	24,109	O + S	A + M	DGA (2014) Barcaza et al. (2017)
	North of Chile	26.5–29.7°S	Until 2015	95	884	S	A + M	García et al. (2017)
	Olivares watershed	32.9–33.5°S	1955–2013	1,289*	428*	O + S	A + M	Malmros et al. (2016)
	Maipo	33.1–34.3°S	2018	366	1,232	S	A + M	AMTC (2019)
AR	Across Argentina	22.1–54.9°S	2004–2015	5,749	17,957	O + S	A + M	IANIGLA-CONICET (2018) Zalazar et al. (2020)
CL and AR	Patagonia and Tierra del Fuego	45.5–55.5°S	1984–2017	117,216*	41,062*	S	A	Meier et al. (2018)
PE, BO and CL	PE, BO and CL	8.8–55.3°S	1955–2011	107,245*	35,950*	O + S	A + M	GLIMS (Raup et al., 2007)

Country code: AR, Argentina; CL, Chile; PE, Perú; BO, Bolivia.
Type of document: O, Orthophotographs; S, Satellite images. Delineation technique: A, automatic; M, manual.
**Multitemporal glacier surface area inventory.*

clustering will be performed *via* the Partitioning Around Medoids (PAM) algorithm (Kaufman and Rousseeuw, 2008). We therefore propose an alternative to the glaciological zones used to date (hereafter named "classic zones") based mainly latitudinal ranges (Barcaza et al., 2017; Dussaillant et al., 2019; Lliboutry, 1998; Masiokas et al., 2009; Sagredo and Lowell, 2012; Troll, 1941; Zalazar et al., 2020), and we provide a hydro-glaciological analysis framework based on the explanatory variables of glacier changes spatial variance across the Andes.

Section 2 presents the material and methods used here. In **Section 3**, we describe glacier changes (GAV and GMB) and show results regarding the controlling factors of glacier change at watershed scale and cluster scale across the Andes. Finally, in **Section 4** we discuss our results and advantages associated with carrying out future glacier change simulations.

2 MATERIALS AND METHODS

2.1 Glacier Area Variation Across the Andes

2.1.1 Collected Glacier Inventories

Glacier inventories have been published since 1950-60s with several updates in Perú, Bolivia, Chile and Argentina. For this current work, we collected data from national institutions, published studies, and the international GLIMS initiative (Raup et al., 2007). All collected glaciers inventories are listed in **Table 1** (**Supplementary Figure S3**). Glacier outlines were delineated based on aerial photographs and satellite images using visual identification (manual mapping) or by applying an automatic identification for the most recent inventories based on satellite data. In the latter case, automatic delineations were adjusted by visual checks and manual correction whenever needed. In many cases, remote sensing approaches were completed by several field campaigns for *in situ* verifications. These inventories can contain either one glacier outline per glacier (mono-temporal inventories) or several outlines from different years for each glacier (multi-temporal inventories). They have different spatial scales, from specific watersheds to national and multinational extensions.

2.1.2 Glacier Inventories Merging

Based on the most recent glacier inventories made by a government initiative in Perú, Chile and Argentina (ANA, 2014; DGA, 2014; IANIGLA-CONICET, 2018), which are hereafter called the national glacier inventories (NGIs), and the Seehaus et al. (2020) glacier inventory in Bolivia. For Argentina, we do not consider some missing glaciers outlines in the inventory (without polygons), located in the Patagonian ice-field, due to this, the total glacierized area will decrease. It was possible to generate a merged product with glacier outlines from these four Andean countries, where each glacier has an identifier (ID). This ID allows to extract information from each glacier,

such as: coordinates of the centroid, glacier surface areas (and corresponding dates), elevation (maximum, minimum and mean) and aspect (Degree). The slope variable (Degree) was extracted for each glacier from the Shuttle Radar Topography Mission (SRTM) v4.1 product with a pixel size of 100 m (Farr et al., 2007). Here, the surface slope of all glaciers was estimated with the DEM in order to have values quantified in the same way, since no slope data are available for some inventories.

The following procedures and limitations were applied: 1) the glacier inventories were processed in the World Geodetic System (WGS84) and the slope data was extracted using Universal Transverse Mercator (UTM) coordinate system; 2) a glacier is considered to be a polygon found entirely within a single watershed, so that the same glacier cannot be located in two or more watersheds; and 3) rock glaciers and debris-covered glaciers were not considered.

2.1.3 Glacier Area Variation Algorithm

The multi-temporal glacier surface areas dataset (**Table 1**) is used to apply a linear regression for each glacier (surface area = f (time)), where glacier areas per each year until 2018 were used. In order to have a homogeneous dataset across the Andes, we consider the surface area changes over the 1980–2019 period from linear regression of multi-temporal glacier surface areas (glacier outlines) identified in the national glacier inventories. For each glacier, we obtained the slope of linear regression and a coefficient of determination that are both used to evaluate the regressions. After that, we only retain the glaciers that meet the following criteria:

- Glaciers are assumed to show a reduction in the surface area since 1980 up to 2019 (Malmros et al., 2016; Meier et al., 2018; Rabatel et al., 2011; Rivera and Bown, 2013; Seehaus et al., 2019, 2020; Soruco et al., 2009). Therefore, we keep the glaciers for which the linear regression slope between the glacier surface area and date (year) is negative. A positive slope can be found due to differences in the method used to identify glacier outlines, given that all inventories did not use the same criteria to define accumulation zone limits. An example of a positive slope is observed in the Patagonian ice-fields from Meier et al. (2018) in comparison with the Chilean glacier national inventory (Barcaza et al., 2017; DGA, 2014). Another reason for the positive slope is the source date of certain inventories, since discrepancies were observed between the Chilean and Argentine national glacier inventories *versus* the GLIMS inventory data.
- Taking the above information into account, glaciers that show a positive linear regression slope or a negative slope with $r^2 < 0.7$ are removed.
- Subsequently, when looking at the values of the linear regression slope (GAV rates by year), we identified high GAV rates for some glaciers. For example, if a glacier with a surface area of 3 km^2 shrinks to 0.01 km^2 within a 1-year interval (i.e., a reduction of 99.7%, which is very unlikely) the slope of resulting linear regression is -2.99 km^2 yr^{-1}. Due to the above, such glaciers with a linear regression slope lower than -1 were considered as outliers and consequently discarded.
- Large glaciers associated with the Patagonian ice-fields that are calving were filtered out. This criterion was chosen because most of the contours of these glaciers show high differences in accumulation zones, where we cannot discriminate if glacier reduction is for differences in accumulation zones or for frontal retreat. In addition, for these glaciers, the water temperature is an important calving process (Sakakibara et al., 2013; Sakakibara and Sugiyama, 2014), that we have not considered in our study.

These filters allowed to obtain GAV data for 4,865 glaciers out of a total of 9,229 glaciers analyzed, where the average number of data used per glacier for estimate GAV was four outlines (polygons). The mean statistical significance (*p-value*) of GAV was < 0.001.

2.2 Glacier Mass Balance

The average annual glacier-wide mass balance for each glacier was recalculated for the 2000–2018 period from the glacier change elevation produced by Dussaillant et al. (2019) using ASTER stereo images and applying the ASTERiX methodology. In contrast with Dussaillant et al. (2019), who used the Randoph Glacier Inventory (RGI Consortium, 2017) to calculate the glacier-wide mass balance, we used glacier outlines from the national glacier inventories compiled for Perú, Bolivia, Chile and Argentina (8–55°S). The specific glacier mass balance (mb) was estimated using the glacier surface elevation change by cell (~30 × 30 m) and a glacier ice density of 900 kg/m^3 (Cuffey and Paterson, 2010). Finally, in order to obtain a comparative indicator of mass change we calculated the glacier mass balance per glacier (GMB_n) as the addition of mb (**Eq. 1**).

$$GMB_n = \sum_{i=1}^{n} mb_i \quad (1)$$

In addition, we did not extrapolate the glacier change elevation for data gaps which occur in some glaciers of the Patagonian ice-fields. The mass balance uncertainty per glacier was estimated using the random error methodology that considers uncertainties on surface elevation change, glacierized area and the volume to mass conversion factor (Brun et al., 2017). In the supplementary material, the GMB derived by Dussaillant et al. (2019) and the ones from the present study are compared considering 1° latitudinal ranges.

2.3 Terra Climate Dataset

The TerraClimate dataset comprises a global dataset based on reanalysis data since 1958, with a 4 km grid size at a monthly time scale. This dataset was validated with the Global Historical Climatology Network using 3,230 stations for temperature (r = 0.95; mean absolute error 0.32°C) and 6,102 stations for precipitation (r = 0.90; mean absolute error 9.1%) (Abatzoglou et al., 2018). Here, variables such as the mean temperature, maximum temperature, minimum temperature and precipitation were processed. Based on these four variables, we calculated monthly averages for the periods 1980–2019 and 2000–2018, resulting in 36 (except mean temperature) and 48

climate variables, respectively. These variables were extracted for each grid cell where a glacier was found.

A monthly scale was necessary in order to be able to consider the seasonal differences across the Andes. Most of the glaciers are contained in a single TerraClimate cell, however, for the large glaciers of the Patagonian ice-fields, we only consider cells that encompass the centroid of those glaciers. Mean temperature was estimated from the maximum and minimum monthly temperatures. The mean temperature was not considered for the GAV analysis because the LASSO method should not have more variables than glaciers as samples in linear regression. Below, we show that smallest number of samples by watershed are 35 glaciers for the GAV analysis. For precipitation, we consider snowfall and rainfall together, i.e., we do not perform a phase discrimination using a temperature threshold.

2.4 Explanatory Variables of GAV and GMB

2.4.1 Data Pre-processing and Watershed Delineation

Morphometric and climate variables extracted from the national glacier inventories and TerraClimate dataset allowed to create two matrices for GAV (1980–2019) and GMB (2000–2018), respectively. The spatial domain at which the GAV and GMB analyses are carried out is the watershed. The watersheds were estimated using the ArcGis v10.6 software. The SRTM v4.1 product with a 100 m resolution (Farr et al., 2007) allowed estimating watershed contours by means of the flow direction and accumulation modules. For the Chilean Patagonian islands, we used the watershed classification provided by the *Dirección General de Aguas* of Chile (Benítez, 1978). Overall, we identified 274 watersheds with a surface area ranging from 260 to 8,095 km^2 (mean 2,058 ± 1,271 km^2), with a glacierized surface area > 0.01% and hosting at least 10 glaciers. Each watershed has an identification (ID) associated with the glacier central coordinates (centroid).

2.4.2 Explanatory Variables Estimation Using the LASSO Method

Correlations between variables with respect to GAV and GMB for each glacier at watershed scale were estimated through LASSO (Tibshirani, 1996) on at least 35 and 50 glaciers by watersheds for GAV and GMB, respectively. This consideration is associated with the existence of glacier change data inside of each watershed, and because LASSO needs a sample minimum greater than a number of predictive variables of GAV and GMB. Recently, Bolibar et al. (2020) and Davaze et al. (2020) have shown satisfactory results using this algorithm in the Alps but at glacier scale and using temporal series. Classical linear regression methods calculate a coefficient values that maximize the r^2 value and minimize the error using all available explanatory variables, which results in a high variance and low bias model. The LASSO algorithm trades some of variance with bias to reduce the predictive error and to discard variables that do not explain a sufficient amount of variance in data. To reduce the prediction error, the cross-validation (CV) method is applied, which allows to select an optimal value of lambda penalty parameter. It consists of choosing a set of values for lambda where the error is calculated for each value and lambda value that gives least error is chosen. Afterward, the model is used with a chosen lambda value. We used the package "glmnet" in R to implement the LASSO algorithm (Friedman et al., 2010; Simon et al., 2011), considering 80% of data for training and remaining 20% to evaluate the error at watershed scale. Because no test method exists yet to evaluate the LASSO algorithm performance (Lockhart et al., 2015), we used the root mean square error (RMSE) derived from the LASSO algorithm to evaluate the results and we implemented the *p-value* test from the multiple linear regression method (MLR) to evaluate statistical significance of variables selected by the LASSO algorithm.

Additionally, to analyze the explanatory variables contribution of GAV and GMB at cluster and classic zone scales, we group the monthly climate variables selected by the LASSO algorithm to a single one, where the percentage of variance explained by each monthly variable will be combined. For example, OT3 (with data from seven watersheds for GMB) groups 25 values of morphometric and monthly climate variables, repeating some variables between watersheds, but identifying 15 unique variables for the whole cluster. In each watershed, the sum of each variable's value contributes 100% to the explained variance (r^2). Subsequently, the percentages of repeated climatic variables are added where, for example, monthly values of P_{Jul} present in three watersheds (three values) will be added and called P_{Jul}. As a result, the 25 variables' value become 15 and when added together contribute 100% of the explained variance. In summary, precipitation variables (composed of 9 monthly values) contribute 82% to the GMB variance in OT3, followed by slope (13%), surface area (2%), and other variables (3%).

2.5 Clustering Analysis to Define New Glaciological Zones Derived From the Explanatory Variables of GAV and GMB

A clustering analysis is used to group together glacierized watersheds with similarities by taking the relevant morphometric and climate variables of the GAV and GMB analysis into account. In order to do this, we use the Partitioning Around Medoids (PAM) algorithm (Kaufman and Rousseeuw, 2008), and the Hopkins and Gap statistical methods were used to estimate clustering tendency and optimal number of clusters, respectively (Lawson and Jurs, 1990; Tibshirani et al., 2001). We used the package "cluster" in R to implement the PAM algorithm (Maechler et al., 2021), organizing variables in columns and watersheds in rows to run the PAM algorithm and all subsequent tests. The Hopkins method shows a value of 0 when a dataset is optimal for performing a clustering analysis, whereas a value of 1 shows that data is already clustered. We used this test to show the high diversity between glacierized watersheds across the Andes. In hydrology, homogeneous hydro-meteorological regions are commonly identified using a clustering analysis to transfer information toward ungauged watersheds, assuming a similarity approach. For example, the fuzzy clustering algorithm uses climate variables to determine homogeneous regions (Hall and Minns, 1999; Dikbas et al., 2012; Sahin and Kerem, 2012; Bharath and Srinivas, 2015; Matiu et al., 2020). Sometimes, geomorphological variables are also

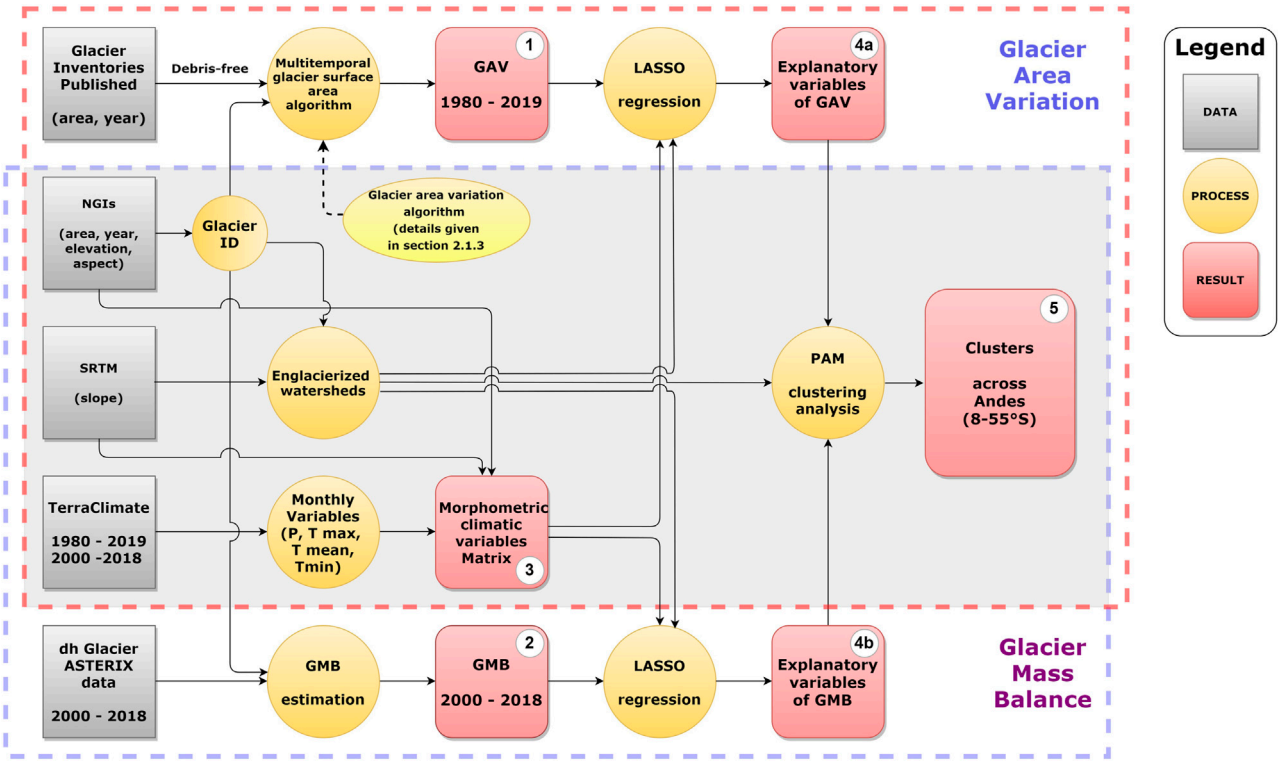

FIGURE 1 | The workflow to obtain the explanatory variables of the glacier area variation (GAV) and glacier mass balance (GMB) spatial variances is presented. The final results are used to estimate clusters between 8–55°S using the explanatory variables of glacier changes. The numbers from 1 to 5 refer to the 5 steps described in the text.

considered (e.g., Pagliero et al., 2019). Inside the fuzzy clustering algorithm, the PAM algorithm divides a dataset into groups where each one is represented by one of data points in the group. These points are called a medoids cluster, which is an object within a cluster for which average difference between it and all other clustering members is minimal (Kaufman and Rousseeuw, 2008; Lee et al., 2020). This method, using k-medoids, represents an improvement on the k-means algorithm; it is less sensitive to outliers because it does not use an average as central object (Arora et al., 2016; Lee et al., 2020). Finally, explanatory capacity of each variable in the GAV and GMB represented variances is given for each watershed and then at cluster scale.

Considering the sensitivity of the watersheds to cluster assignment by the PAM algorithm, we performed a sensitivity analysis associated with the removal of variables or group of variables and also by changing the variable values. Considering 1,000 iterations of the PAM algorithm, in each iteration, different variables were removed from the dataset. For example, monthly Tmax, then monthly Tmin and after monthly precipitation were excluded, then morphometric variables were also excluded one by one. On the other hand, in each new iteration the variable values were increased or decreased considering factors between 0.9 and 1.1. Factor values were random for each variable associated with a watershed and were updated for each new iteration. The evaluation was conducted using 274 watersheds and considering comparisons between the PAM runs (the most frequent assignment of a cluster to a watershed) using: 1) only climatic variables, 2) only morphometric variables, and 3) morphometric and climatic variables (removing one variable or a group of variables at each PAM iteration), in relation to each single PAM run removing one morphometric variable or a group of climatic variables. This means that each single PAM run removing one morphometric variable or a group of climatic variables were evaluated with regards to (i), (ii), and (iii) through the coefficient of determination.

2.6 Methodological Workflow

This section considered the next overall steps: In step 1) "Glacier area variations 1980–2019", the glacier inventories used to identify each glacier and how its surface area has changed are used. The morphometric variables (surface area, elevation and aspect) are extracted from these inventories and from SRTM data (slope). In step 2) "Glacier mass balance 2000–2018," the procedure used to obtain glacier mass change data based on the ASTERIX product (e.g., Dussaillant et al., 2019) is applied. In step 3) "Morphometric-climatic variables matrix", the monthly climate values (precipitation and temperature) are extracted and implemented in a matrix with the morphometric variables. In step 4) "Explanatory variables of GAV (4a) and GMB (4b)", the matrix of variables is used to derive relationships to explain GAV and GMB through the LASSO algorithm. In step 5) "Clusters", a

clustering analysis is carried out based on the explanatory variables of GAV and GMB.

Figure 1 illustrates the methodological workflow used in this study. It is composed of five steps that are first used to identify the explanatory variables for GAV over the 1980–2019 period and GMB over the 2000–2018 period. Then, the workflow allows to cluster watersheds based on the explanatory variables of recent glacier changes from the Outer Tropics to Tierra del Fuego (8–55°S).

3 RESULTS

3.1 Morphometric and Climate Settings

From the national glacier inventories, we considered and identified 44,853 glaciers with a total glacierized area of 29,387 km^2 between 8 and 55°S. Of this glacierized surface area, 95% (33,000 glaciers, 27,793 km^2) corresponds to free-of-debris glaciers, while 3% (10,881 glaciers, 1,041 km^2) are rock glaciers (not considered in this study) and 2% (972 glaciers, 552 km^2) are debris-covered glaciers (not considered in this study). Within the studied countries, Chile has the largest glacierized area comprising 78% of the total, followed by Argentina (16%), Peru (5%) and Bolivia (1%). Due to data lacks on glacier outlines of the Southern Patagonian Icefield (on the Argentinean side mainly), these were not considered in this analysis. Therefore, our final sample contains 85% (31,963) of glaciers covering 71% (24,888 km^2) of the glacierized surface area across the Andes identified here.

Following the classic zones defined based on former studies (Troll, 1941; Lliboutry, 1998; Masiokas et al., 2009; Sagredo and Lowell, 2012; Barcaza et al., 2017; Dussaillant et al., 2019; Zalazar et al., 2020), 72% of the glacierized area are concentrated in South Patagonia and North Patagonia between 42 and 53°S, where glaciers have a mean elevation of 1,560 m a.s.l. The Tierra del Fuego zone (53–55°S) concentrates 14% of the glacierized area with a mean elevation of 830 m a.s.l. The longest latitudinal extent north of the North Patagonia include zones from the Outer Tropics to the Lakes District (8–42°S) which only contains 14% of the glacierized area. Along this extent (8–42°S), the Outer Tropics (8–17°S) and the Central Andes (30–37°S) zones contain 6% of the glacierized area each. The highest mean elevations of glaciers are found in the Desert Andes (5,575 m a.s.l.) followed by the Outer Tropics (5,177 m a.s.l.).

From a climatic point of view, the mean annual temperature over the 1980–2019 period at glacier elevation tend to decrease from the Outer Tropics (3.2°C) to the Central Andes (-2.7°C). Southward of the Lakes District, the mean annual temperature increases (5.4°C) above the values found in the north and then decreases toward Tierra del Fuego (3.8°S). With regards to precipitation, the mean annual amount decreases from the Outer Tropics (912 mm yr^{-1}) to the Dry Andes (151 mm yr^{-1}), from where it increases to Southern Patagonia (1,770 mm yr^{-1}). Southward, Tierra del Fuego shows a lower amount of precipitation, even less than the Lakes District (1,105 mm yr^{-1}). In addition to observed morphometric and climatic differences between the classic zones, it is also possible to identify major differences inside these zones at grid scale (1 × 1°) as shown in the supplementary material (**Supplementary Figure S1** and **Supplementary Figure S2**).

3.2 Glacier Surface and Mass Loss

Across the Andes between 8 and 55°S, the mean GAV was estimated to be -31.2 ± 0.6%. This was quantified from data available on 21% (5,160 km^2) of the glacierized area across the Andes (**Figure 2A**). The Outer Tropics showed a reduction of −41 ± 0.01% whereas a reduction of −30 ± 0.6% was found for the Southern Andes. For these two regions, these estimates are based on 50 and 19% of the glacierized area, respectively. In the Southern Andes, the Desert Andes (17–30°S) shows the largest shrinkage (−53 ± 0.002%), followed by the Central Andes (30–37°S) with a GAV of −39 ± 0.01%. In the Wet Andes (37–55°S), the Lakes District shows a GAV of −52 ± 0.1%, followed by North Patagonia (−32 ± 1.3%), South Patagonia (−28 ± 1.4%) and Tierra del Fuego (−24 ± 0.4%). For these GAV estimates, the proportion of glacierized area considered varies from one zone to another, comprising 23% of the glacierized area in the Central Andes, 20 and 13% in North and South Patagonia, respectively, and 33% in Tierra del Fuego. In smaller glacierized zones of the Andes (representing 2% of the total), GAV estimates for the Desert Andes and the Lakes District is based on 13% of the glacierized area. Regarding GAV statistical significance, the mean *p-value* was < 0.001. However, 11 of 48 latitudinal ranges from 8 to 55°S showed *p-values* > 0.05. These are located at 12–14°S, 15–16°S, 18°S, 36°S, 38°S, 40°S, and 46–47°S.

Additionally, the GMB is estimated to be -0.82 ± 0.12 m w.e. yr^{-1} when considering 96% (23,978 km^2) of the glacierized area of the Andes between 8 and 55°S (**Figure 2B**). The Outer Tropics show a lower mass loss (−0.47 ± 0.03 m w.e. yr^{-1}) compared to the southern Andes (−0.84 ± 0.13 m w.e. yr^{-1}). In the Dry Andes, the Central Andes show a greater loss (−0.43 ± 0.05 m w.e. yr^{-1}) compared to the Desert Andes (−0.22 ± 0.03 m w.e. yr^{-1}). In the Wet Andes, North Patagonia presents the greatest loss with −0.96 ± 0.18 m w.e. yr^{-1}, followed by South Patagonia (−0.9 ± 0.27 m w.e. yr^{-1}), the Lakes District (−0.72 ± 0.08 m w.e. yr^{-1}), and Tierra del Fuego (−0.56 ± 0.24 m w.e. yr^{-1}). The proportion of glacierized area considered to estimate that GMB is greater than 94% in most of the zones, except in the Central and Desert Andes where these percentages are 72 and 47%, respectively. **Table 2** summarizes GAV and GMB for the classic zones, while differences observed in the GMB estimation by this work, Dussaillant et al. (2019), Braun et al. (2019) and Seehaus et al. (2019, 2020) are shown in the supplementary material (**Supplementary Figure S4** and **Supplementary Table S1**).

Regarding the relationship between GAV and GMB at watershed scale (n = 107; for 3,978 glaciers with a minimum of 10 and maximum of 176 per watershed), **Figure 3** shows that even if the two variables are statistically correlated for several watersheds (mostly located in the Southern Andes between 45 and 50°S), no correlation is found across the Andes. This result justifies identifying separately the morphometric and climate controls for GAV and on the other hand for GMB,

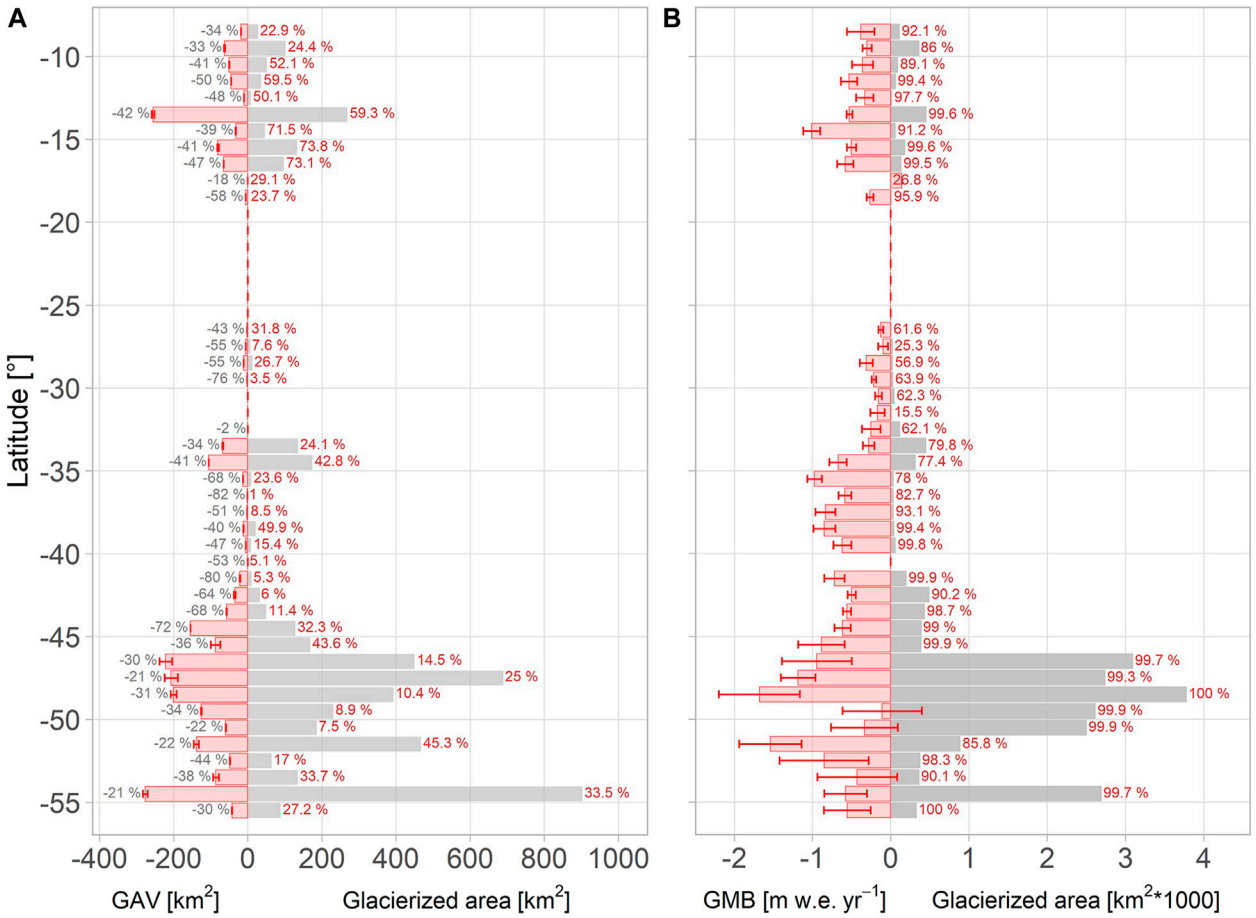

FIGURE 2 | The latitudinal GAV (1980–2019) and GMB (2000–2018) across the Andes (8–55°S) are presented in this figure. **(A)** For each 1° latitudinal bar of GAV (red bars) the GAV error (red lines), and percentage of the mean GAV (gray texts) are presented, while the glacierized area used in GAV estimation (gray bars), as well as the percentage of this glacierized area with regards to the total estimated by the national inventories (red text) are shown. **(B)** The GMB (red bars), the GMB error (red lines), and the related glacierized area (gray bars) are presented, indicating the percentage of the glacierized area used in the GMB estimation with regard to the total estimated in the national inventories (gray text). The GMB estimation contains 96% (23,978 km^2) of the glacierized area distributed between 26,856 glaciers considered in this study.

considering that the GAV and GMB data include different time ranges with different response times and glacier dynamics.

3.3 Explanatory Variables of Glacier Changes Across the Andes

The explanatory capacity of variables on the spatial variance of GAV (1980–2019) and GMB (2000–2018) in Perú, Bolivia, Argentina, and Chile were obtained from 35 watersheds for GAV and from 110 watersheds for GMB (**Figure 4A**) through the LASSO method. The watersheds where the GAV variance was predicted show a mean coefficient of determination of 0.49 (RMSE = 0.85 km^2; *p-value* from MLR < 0.05; number of glaciers = 2,484). The lower number of glaciers considered here with regard to the total GAV data (4,865 glaciers) is due to removal of watersheds that do not have a glacierized area > 0.01% of watershed area and a minimum of 35 glaciers. For the remaining 35 watersheds, the LASSO algorithm identified 39 explanatory variables for the GAV dataset. However, this number of explanatory variables differs between watersheds, with a maximum of 21 variables identified by LASSO in some watersheds. Similarly, the GMB analysis considered a minimum of 50 glaciers per watershed, resulting in a mean coefficient of determination of 0.35 for the 110 watersheds (RMSE = 0.35 m w.e. yr^{-1}; *p-value* from MLR < 0.05; number of glaciers = 20,740) (**Figure 4B**). The reduction in the number of glaciers (from 31,963 to 20,740) used in the LASSO analysis was due to the smallest number of glaciers considered by watershed. For these 110 watersheds, the LASSO algorithm identified 54 explanatory variables (43 explanatory variables in certain watersheds). These results are presented for the classic zones in the supplementary material (**Supplementary Table S2**), while the coefficient of determination for LASSO and MLR (*p-value*) results are shown in **Supplementary Figure S5**.

Based on the 39 variables that explain the GAV variance, on average for the entire study region (8–55°S), the morphometric

TABLE 2 | GAV (1980–2019) and GMB (2000–2018) for the classic zones of the Andes.

Zones	Latitude (°S)	Glacierized area [%]	Glacierized area [km^2]	GAV used area [%]	Mean GAV [%]	GAV st. Dev. [%]	GMB* used area [%]	Mean GMB [m w.e. yr^{-1}]	GMB st. Dev. [m w.e. yr^{-1}]
Outer Tropics	8–17	6	1,555	50	−41.0 ± 0.01	25	94	−0.47 ± 0.03	0.49
Desert Andes	17–30	1	217	13	−53.3 ± 0.002	27	47	−0.22 ± 0.03	0.17
Central Andes	30–37	6	1,398	23	−39.0 ± 0.01	27	72	−0.43 ± 0.05	0.31
Lakes District	37–42	1	351	13	−51.7 ± 0.1	30	98	−0.72 ± 0.08	0.40
North Patagonia	42–48	31	7,638	20	−32.2 ± 1.3	27	99	−0.96 ± 0.18	0.34
South Patagonia	48–53	41	10,303	13	−27.6 ± 1.4	25	98	−0.90 ± 0.27	0.82
Tierra del Fuego	53–55	14	3,426	33	−23.9 ± 0.4	24	98	−0.56 ± 0.24	0.81
Southern Andes	17–55	94	23,333	19	−29.5 ± 0.6	26	96	−0.84 ± 0.13	0.56
Andes	8–55	100	24,888	21	−31.2 ± 0.6	27	96	−0.82 ± 0.12	0.56

**This "GMB, used area" comprises glacier surface area of each glacier where GMB, data is available.*

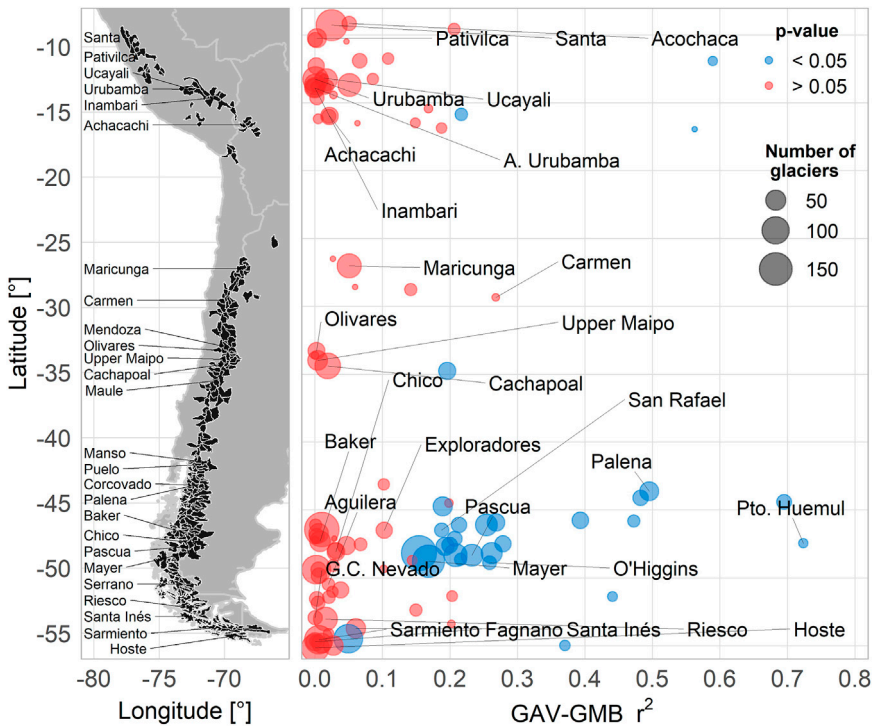

FIGURE 3 | The distribution of the 274 glacierized watersheds (glacier cover > 0.01%) across the Andes (8–55°S) and the GAV (1980–2019) and GMB (2000–2018) correlation at watershed scale for 107 watersheds are presented, with its statistical significance and number of glaciers considered in each watershed.

variables such as surface area (16%) and elevation (7%) are those that contribute most, whereas highest contribution of a climate variable is only 5% ($Tmax_{Jan}$). However, if we combine the contribution of monthly climate variables to the GAV variance, the order of explanatory variables changes (e.g., the contribution of monthly climate variables are combined in a single percentage for precipitation, Tmax and Tmin). As such, the climate variables explain 65% of the GAV variance (with temperature and precipitation contributing 35 and 30%, respectively), whereas surface area and elevation explain 16 and 15% of variance, respectively, followed by slope (4%) and aspect (1%). Looking at the GMB variance, on average across the Andes, surface area of glaciers (26%) is the variable that contributes highest percentage, followed by $Tmax_{Nov}$ (5%)

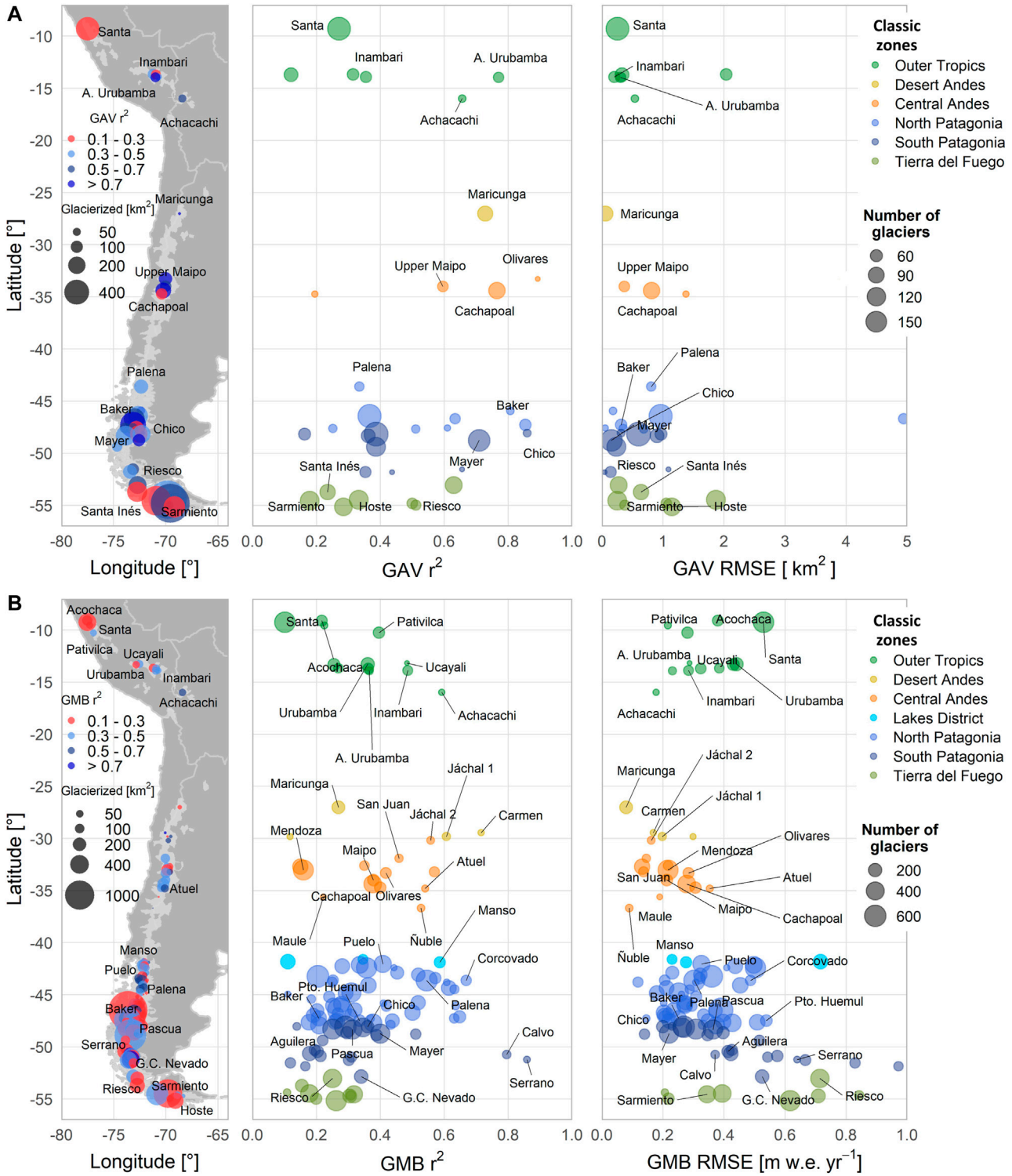

FIGURE 4 | The coefficient of determination and RMSE values are presented for 35 watersheds using the GAV 1980–2019 data **(A)** and for 110 watersheds using the GMB 2000–2018 data **(B)**. The values for each watershed were obtained through the LASSO algorithm, which identified the explanatory variables of the GAV and GMB spatial variances. All 274 glacierized watersheds (> 0.01%, number of glaciers >10) identified here are presented (clear gray).

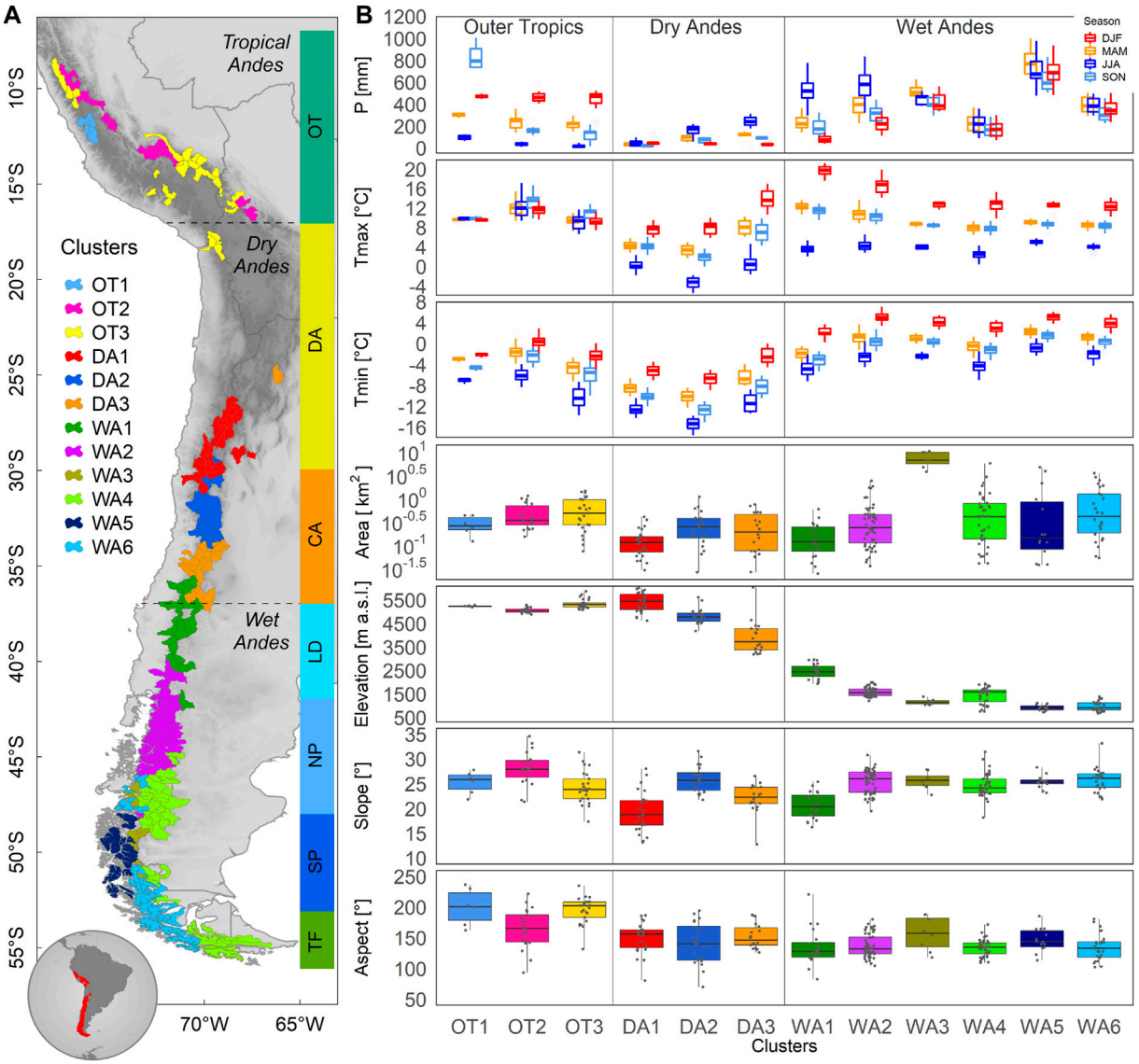

FIGURE 5 | The 12 clusters of the glacierized watersheds across the Andes (8–55°S) and the behavior of climatic and morphometric variables. The average values of variables (for 274 watersheds and using 31,963 glaciers) are presented for the 12 clusters identified (PAM algorithm) using the GAV and GMB explanatory variables (LASSO algorithm). These clusters are found in three regions: Outer Tropics (OT; 8–17°S), Dry Andes (DA; 17–37°S) and Wet Andes (WA; 37–55°S). **(A)** shows the cluster distribution across the Andes and the classic zones, from north to south are: Outer Tropics (OT; 8–17°S), Desert Andes (DA; 17–30°S), Central Andes (CA; 30–37°S), Lakes District (LD; 37–42°S), North Patagonia (NP; 42–48°S), South Patagonia (SP; 48–53°S) and Tierra del Fuego (TF; 53–55°S). **(B)** presents the climatic variables (1980–2019) which are grouped into the summer (DJF), autumn (MAM), winter (JJA), and spring (SON) seasons for the Southern Hemisphere. The sum of the precipitation and the extreme temperatures averages are shown here. Additionally, morphometric variables associate with the glacierized area (*i.e.*, surface area, elevation, slope, and aspect) are shown.

and slope (3.5%), with P_{Apr} contributing only 3.3%. As observed for GAV, when monthly explanatory variables are combined, the order of explanatory variables with regards to the GMB variance changes. Therefore, the climate variables explain most of the GMB represented variance with 66% compared to the morphometric variables, with temperature contributing 37% and precipitation contributing 29% of the represented variance. Surface area is the morphometric variable that contributes highest percentage to the GMB variance (26%), followed by elevation (4%), slope (4%) and aspect (0.2%).

3.3.1 New Classification Zones of Andean Glaciers

We performed a cluster analysis based on 274 watersheds (31,963 glaciers) using the explanatory variables selected by the LASSO algorithm. Considering the assumption that variables that explain the glacier change spatial variance in 35 watersheds for GAV and in 110 watersheds for GMB can explain glacier change in rest of

Andean watersheds, we use 42 relevant variables selected by LASSO for the GAV and GMB datasets. These 42 variables are 12 monthly values for three climate variables (precipitation, Tmax and Tmin) and six values for morphometric variables (area, slope, aspect, max. elevation, min elevation and mean elevation). Tmean variable was not considered because it showed lowest explanatory capacity of the glacier changes spatial variance. According to the Hopkins method, our dataset shows a high potential to form clusters (the Hopkins test result is equal to 0.1), while the GAP statistic method allowed to quantify the cluster optimal number as 12. Concerning to the PAM algorithm sensitivity, PAM runs using climatic variables and morphometric-climatic variables showed a lower explained variance by the predictors if precipitation or Tmax variables are removed (see **Supplementary Figure S6** in the supplementary material). This means that the cluster assignment of each watershed changes more if these two variables are not present in the cluster analysis. In comparison, the removal of morphometric variables and Tmin showed PAM runs with greater explained variances, meaning that the cluster assignment of each watershed is less sensitive to the removal of these variables. In contrast, PAM runs using only morphometric variables showed a lower explanatory capacity of the variance, associated with an increase of the change to the cluster assignment of each watershed. About increase and decrease of the variable values between 0 and 10%, a way to add uncertainty to variable values, it was not observed any change in the cluster assignment of each watershed.

One cluster in the Outer Tropics (OT1) does not have data of GAV and GMB in some watersheds for estimating the explanatory variables of glacier changes. However, this zone is different from the two others in the Outer Tropics (i.e., OT2 and OT3) due to lower extreme temperature and mean glacier size values, for example. These numeric results are presented in the supplementary material (**Supplementary Table S3**).

Figure 5A shows the map that results from the clustering. A clear latitudinal distribution can be seen between 25°S and 40°S, with some overlaps resulting from similar morphometric and climatic configurations between watersheds located on eastern and western sides of the Andes. Here, one interesting latitudinal overlap example can be observed in Dry Andes. A watershed located in DA3 (id = 25,001; p = 185 mm yr^{-1}; elevation = 6,039 m a.s.l.) close to DA1 watersheds (id = 26,426; p = 79 mm yr^{-1}; elevation = 5,753 m a.s.l.) shows higher precipitation and elevation. However, in the Outer Tropics and the Wet Andes the clusters in general are not delimited with respect to latitude. An exception is the WA2 cluster, which covers watersheds west and east of the mountain range. Watersheds that show similar morphometric and climatic configurations are clustered even if they are not contiguous to one another. An example of this can be seen from watersheds inside W5 and W6 clusters, where they present close values of aspect, slope, and elevation, even the temperature values are close, but the precipitation presents high differences within the clusters even higher than between the two clusters. In addition, Tierra del Fuego is longitudinally split into two clusters (WA4 and WA6).

Figure 5B provide more details about the 12 clusters and their relevant morphometric and climatic characteristics. Considering the glacierized surface area in this work, which comprises 71% of the total surface area of the inventoried glaciers in the Andes, the Outer Tropics (8–17°S) comprise three clusters (OT1, OT2, OT3) concentrating 5.7% of the total glacierized area. OT3 contributes to 67% of the glacierized area in the Outer Tropics (3.8% in the Andes; 921 km^2). OT3 includes glaciers in Peru, Bolivia and volcanoes in northern Chile and western Bolivia. Within the Outer Tropics, the three clusters show an annual precipitation range between 782 mm yr^{-1} (OT3) and 1,654 mm yr^{-1} (OT1), concentrated during the DJF season (up to 500 mm) in all of the clusters and with a marked dry season in JJA (less than 100 mm). Tmax shows similar values throughout the year for all three clusters, and is slightly higher in OT2 (13.1°C), whereas Tmin shows a seasonal variation with higher values in DJF (OT2; 0.3°C) than in JJA (OT3; -10.3°C). With regards to the morphometric variables, cluster OT3 shows the largest mean glacier surface area (0.6 km^2), an average glacier elevation (5,335 m a.s.l.), and the lowest slope (24°). The Dry Andes (17–37°S) gather three clusters (DA1, DA2, DA3) which represent 6.7% of the total glacierized area. In this region, many glaciers (19–26°S) inside watersheds with a lower glacierized areas (glacierized watershed < 0.01%) were excluded. DA2 contains the most extensive glacier coverage with 52% (3.4% of the total for the Andes; 807 km^2). Within these three clusters, the annual amount of precipitation increases southward, with 150 mm yr^{-1} in DA1 and 483 m yr^{-1} in DA3. Precipitation is mainly concentrated during JJA in DA2-DA3 and is more evenly distributed in DA1. The extreme temperatures show the highest values in the DJF season (both for Tmax which reaches a maximum of 14°C and Tmin which reaches a minimum of -2.3°C) and lowest values in JJA (Tmax < 0.5°C; Tmin < -11°C). The largest average glacier surface area is found in DA2 (0.3 km^2) and the smallest is in DA1 (0.1 km^2) where glaciers are also found at the highest elevation (5,389 m a.s.l.) and have the lowest slope (19°) of all the Andes.

The Wet Andes (37–55°S) comprise 87.7% of the total glacierized area of the Andes, distributed in six clusters (WA1 to WA6), where WA3 contains 34% (30.1% in the Andes; 7,205 km^2) and WA4 29% (25.9% in the Andes; 6,194 km^2) of the glacierized area in the Wet Andes. The annual amount of precipitation differs considerably between the clusters ranging from 2,858 mm yr^{-1} (WA5) to 784 mm yr^{-1} (WA4). Precipitation is concentrated in JJA in WA1 and WA2 (approximately 580 mm) and MAM-JJA in WA3 to WA6 (approximately 800 mm). Extreme temperatures in the Wet Andes present maximum values in DJF (Tmax of roughly 20°C and Tmin of roughly 5°C) and minimum values during JJA (Tmax of roughly 5°C and Tmin of roughly -0.8°C). With regards to morphometric variables, the largest mean glaciers size is found in WA3 (8 km^2), and a decrease in the glacier mean elevation is observed from WA1 to WA6, with an average difference of 1,500 m. The slope is similar in all of the Wet Andes (25–26°) clusters although it is slightly lower in WA1 (21°).

3.3.2 Explanatory Variables at Cluster and Watershed Scale

The explanatory variables of the GAV and GMB represented variances at watershed scale are presented in detail for GAV (**Figure 6**) and GMB (**Figure 7**), using the 12 clusters. In the

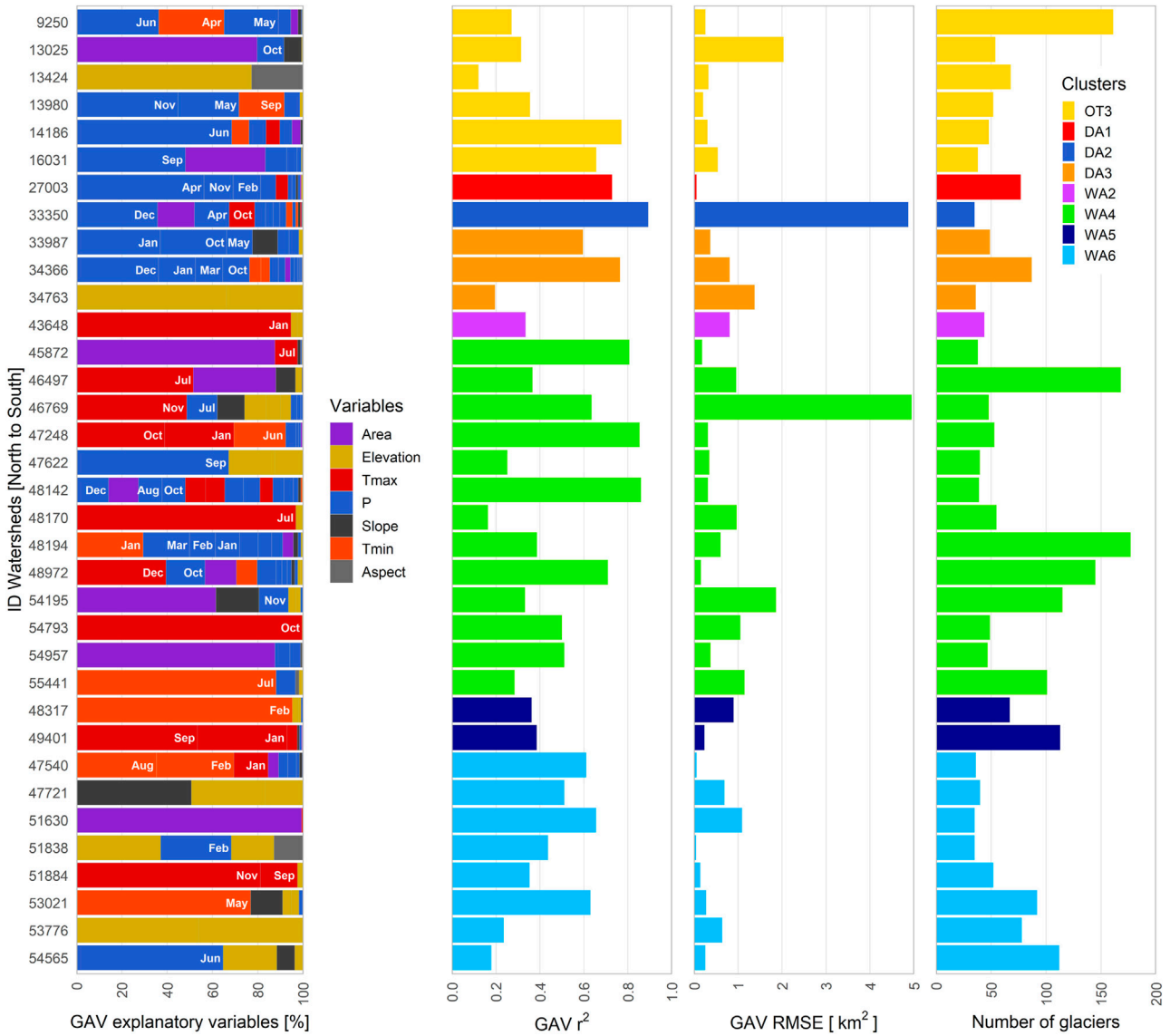

FIGURE 6 | Relevance of the morphometric and climatic variables identified by LASSO algorithm to the spatial variance of GAV (1980–2019) across the Andes (8–55°S). The GAV explanatory variables, at watershed scale, is added to represent the 100% associate to each GAV r^2 (variance by watershed). Other relevant data as RMSE and the number of glaciers used in estimations are showed. Due to data limitation, the results are available for 8 of the 12 clusters.

Outer Tropics, the explanatory variables of the GMB variance in cluster OT2 are precipitation (71%, P_{Aug} and P_{Dec} mainly) and temperature (19%). In cluster OT3, on average, the GAV variance is explained by precipitation (50%) and temperature (10%), with an increased explanatory power for precipitation (82%, mainly P_{Sep} and P_{Oct}) in the GMB variance. In OT3, for the Achacachi watershed (id = 16,031; GAV $r^2 = 0.7$; GMB $r^2 = 0.6$) P_{Oct} and P_{Sep} are most relevant for the GMB and GAV variances, followed by the surface area and slope.

In the Dry Andes, the explanatory variables in cluster DA1 are precipitation (93%) and temperature (5%) for GAV. The variance of GMB is mainly explained by precipitation (49%) and surface area (49%). In DA1, the Río del Carmen watershed (id = 29,516; GMB $r^2 = 0.7$) shows that precipitation and surface area have a similar contribution to the GMB variance. In cluster DA2, the explanatory variables of the GAV and GMB variances are precipitation (> 67%) followed by temperature (> 16%). One of the most glacierized watersheds of the Dry Andes is the Olivares watershed (id = 33,350; GAV $r^2 = 0.9$; GMB $r^2 = 0.4$) for which P_{Dec} and P_{Apr} and surface area explain most of the GAV variance, and P_{Oct}, P_{Aug} and P_{Jun} explain most of the GMB variance. In cluster DA3, the explanatory variables of the GAV and GMB variances are precipitation (> 57%), followed by elevation (34%) for GAV and temperature (37%) for GMB. In this cluster, for the Upper Maipo (id = 33,987; GAV $r^2 = 0.6$; GMB $r^2 = 0.4$) and Cachapoal (id = 34,366; GAV $r^2 = 0.8$; GMB $r^2 = 0.4$)

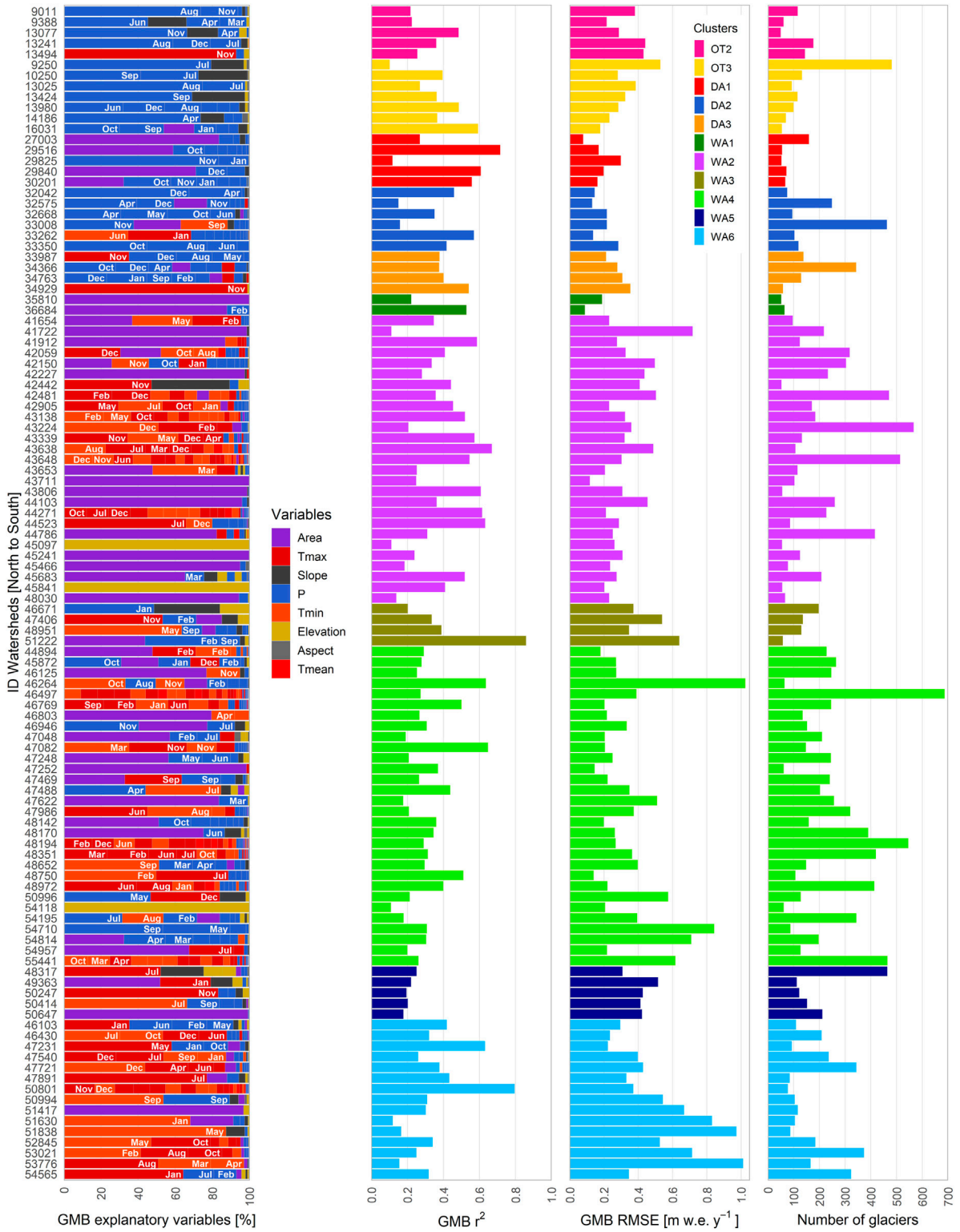

FIGURE 7 | Relevance of the morphometric and climatic variables identified by LASSO algorithm to the spatial variance of GMB (2000–2018) across the Andes (8–55°S). The GMB explanatory variables, at watershed scale, is added to represent the 100% associate to each GMB r^2 (variance by watershed). Other relevant data as RMSE and the number of glaciers used in estimations are showed. Due to data limitation, the results at watershed scale are available for 11 of the 12 clusters.

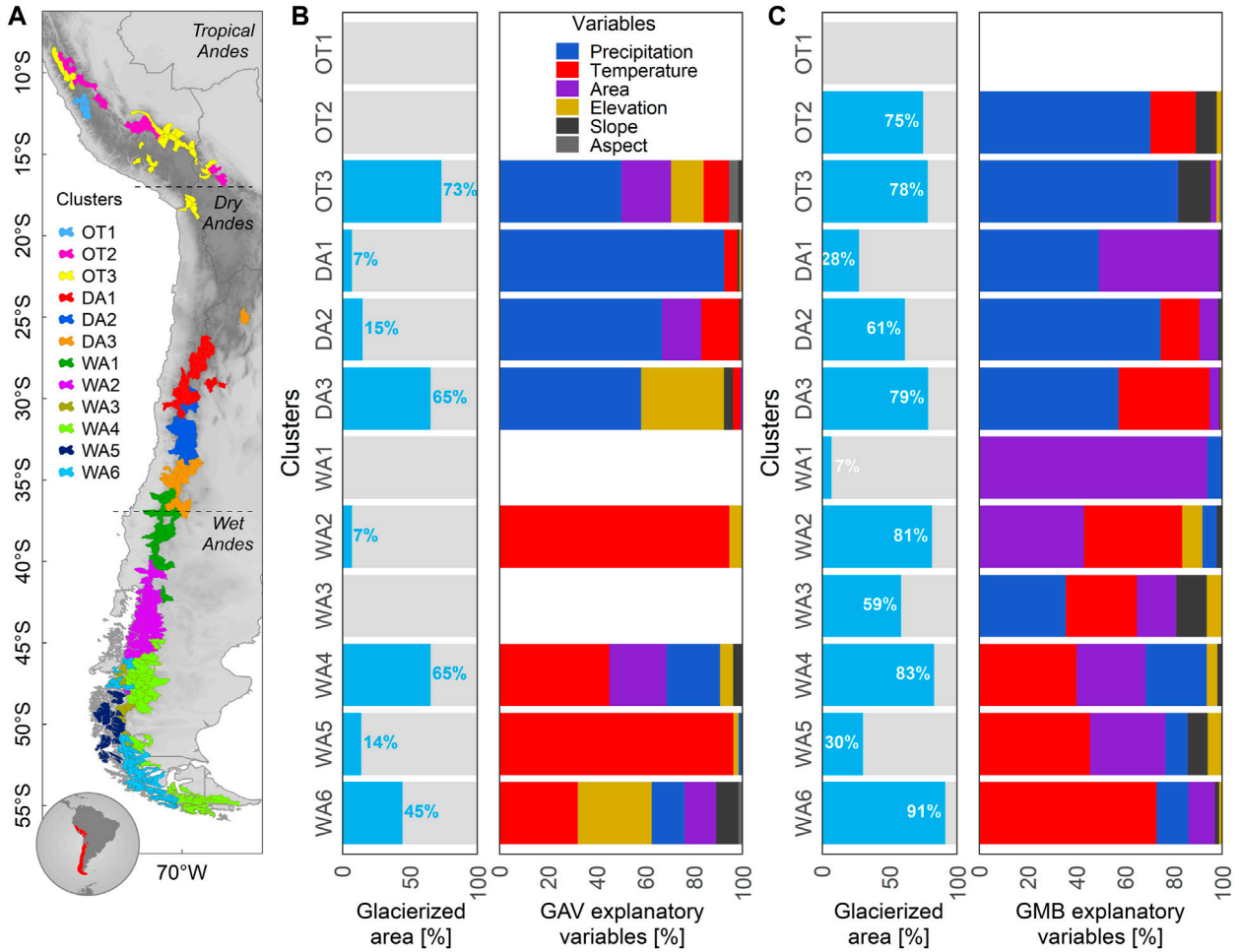

FIGURE 8 | Explanatory variables of glacier changes across the Andes (8–55°S) since 1980 at watershed scale. **(A)** The 274 glacierized watersheds inside 12 clusters are shown on the map of South America. The glacierized area considered in estimates of the **(B)** GAV (1980–2019) and **(C)** GMB (2000–2018) explanatory variables (light blue bars) are shown with regard to the percentage of explanatory variables for the GAV and GMB spatial variances (blank spaces are due to a lack of data in that cluster).

watersheds, P_{Dec} (GMB) and P_{Oct} (GAV) are the most relevant. Whereas in the Atuel watershed (id = 34,929; GMB r^2 = 0.5), $Tmax_{Nov}$ explains most of the GMB variance.

In the Wet Andes, the WA1 and WA2 clusters are located to the north of the Patagonian ice-fields. In WA1, the GMB variance is mainly explained by the surface area (94%) followed by precipitation (6%). Meanwhile, in WA2, the variable that mainly explains the GAV variance is temperature (95%), whereas the GMB variance is mainly explained by area (43%) and temperature (40%). The GMB variance in the Río Ñuble watershed (id = 26,684; GMB r^2 = 0.5), in WA1, is explained by surface area followed by P_{Feb}. In cluster WA2, the glacier surface area explains most of the GMB variance in the Río Manso watershed (id = 41,912; GMB r^2 = 0.6), and $Tmax_{Dec}$ and surface area are the dominant variables in the Río Puelo watershed (id = 42,059; GMB r^2 = 0.4).

Clusters WA3 to WA6 are found between the Northern Patagonian ice-field and the Cordillera Darwin. Cluster WA3 comprises the largest glacierized area in the Andes (30%). Precipitation and temperature (36 and 29%) explained most of the GMB variance, followed by surface area and slope (16–13%). Close to the Southern Patagonian ice-field, in the Río Serrano watershed (id = 51,222; GMB r^2 = 0.9), the glacier surface area, P_{Feb} and P_{Sep} are the most statistically significant explanatory variables. In WA4, the variables that explain most of the GAV and GMB variances are temperature (40–45%), followed by surface area (24–38%) and precipitation (22–25%). This cluster contains watersheds that are primarily located to the east of the Patagonian ice-fields, and in the Cordillera Darwin to the east of Monte Sarmiento. To the east of the Southern Patagonian ice-field, the Lago O'Higgins watershed (id = 48,652; GMB r^2 = 0.3) shows the statistical importance of $Tmin_{sep}$ and P_{Mar} and P_{Apr}. On the southern side of Cordillera Darwin (id = 54,793; GAV r^2 = 0.5) the main explanatory variable is $Tmax_{Oct}$, whereas on the northern side, it was found that morphometric and

climatic variables had a very limited explanatory capacity (id = 54,195; GAV r^2 = 0.3; GMB r^2 = 0.2).

The WA5 and WA6 clusters are located on the western side of the Patagonian Andes. Watersheds in WA5 are mainly found to the west of the Southern Patagonian ice-field, in the coastal region where the highest amount of precipitation in the Andes was identified. For these watersheds, temperature is the most relevant variable. For example, in Río Pascua watershed (id = 48,317; GAV r^2 = 0.4; GMB r^2 = 0.3) $Tmax_{Jul}$ and $Tmin_{Feb}$ are important in the spatial variance of the glacier changes and in Isla Wellington (id = 50,401; GAV r^2 = 0.4) are $Tmax_{Sep}$ and $Tmax_{Jan}$. Whereas in WA6, the explanatory variables strongly differ between GAV and GMB. The morphometric variables (30% elevation) explain 54% of the GAV variance and climate variables (73% temperature) explain 86% of the GMB variance. This cluster comprises watersheds that are primarily distributed around the Northern Patagonian ice-field and the south of the Southern Patagonian ice-field down to Monte Sarmiento, where the largest ice concentration outside the Patagonian ice-fields and Cordillera Darwin is found.

3.3.3 Explanatory Variables at the Regional Scale

Figure 8 shows the explanatory variables of GAV and GMB spatial variances at cluster scale. At first glance, it can be observed that precipitation explains the highest percentage of GAV and GMB variances for clusters located within the Outer Tropics (OT1, OT2, OT3) and the Dry Andes (D1, D2, D3), whereas temperature is most relevant variable in the Wet Andes (WA1 to WA6). Within the Outer Tropics and the Dry Andes clusters, precipitation explains between 49–93% of the GAV and GMB variances, whereas temperature only explains between 3 and 37%. In the Wet Andes, the explanatory variables of GAV and GMB variances are inverted, with temperature contributing between 29 and 73% of variation and precipitation between 1 and 36%.

In further detail, this explanatory power of precipitation in the Outer Tropics and the Dry Andes clusters and of temperature in the Wet Andes clusters is clear for seven clusters that concentrate 77% of the Andean glacierized area (OT2, OT3, DA2, DA3, WA9, WA10 and WA11). Other clusters show differences in the main explanatory variables for the GAV and GMB variances.

For instance, the DA1 cluster shows that climate variables (98%) predominantly explain the GAV variance, manly for precipitation (93%). On the other hand, GMB is explained in similar proportion by climate (49%) and morphometric (51%) variables, where the most important variables are precipitation and surface area with 49% each. For cluster WA1, without GAV variables identified, morphometric (94%) variables explain the GMB variance through surface area (93.9%). In WA2, temperature (95%) explain the GAV variance while the GMB variance is dominated by morphometric variables (54%) being more relevant surface area (43%) followed by temperature (40%). In WA6, 54% of the GAV variance is explained by morphometric variables (elevation alone explains 30%), and 86% of the GMB variance is explained by climate variables, where temperature explains 73%.

Finally, differences in explanatory power of morphometric and climate variables for the GAV and GMB spatial variances when considering the classic zones or the clusters can be observed in the supplementary material (**Supplementary Table S4** and **Supplementary Table S5**).

4 SUMMARY AND CONCLUDING REMARKS

This study is the first to explore climatic and morphometric variables of the spatial variance of glacier changes through a machine learning method across the Andes (8–55°S), in terms of surface area variations since 1980 and mass balance changes since 2000. Overall, we found that the spatial variability of glacier changes is primarily controlled by spatial variability of precipitation from the Outer Tropics to the Dry Andes (8–37°S) and of temperature in the Wet Andes (40–55°S). These results, obtained at watershed scale, allowed to identify 12 new glaciological zones via a clustering analysis that depicts more details compared with the classic zones based on latitude ranges.

4.1 Overall Glacier Area and Mass Balance Variations

At the scale of the entire study region, the mean GAV and GMB were calculated at −31.2 ± 2% (1980–2019) and −0.82 ± 0.12 m w.e. yr^{-1} (2000–2018), respectively. Our GMB estimation is close to the one obtained by Dussaillant et al. (2019) of -0.72 ± 0.22 m w.e. yr^{-1} (2000–2018), and more negative in comparison with Braun et al. (2019) estimate (-0.61 ± 0.07 m w.e. yr^{-1}; 2000–2015), in both cases at the scale of the entire Andes. Differences between the estimates are related to the use of different glacier inventories to quantify the mass balance from glacier surface elevation differencing data and mass balance calculations. In fact, some glaciers found in the Patagonian ice-fields do not have elevation difference information in the accumulation zone, therefore our results may overestimate the negative mass balance here as we did not extrapolate the glacier change elevation data to fill the gaps, as done by Dussaillant et al. (2019). Our error estimations are lower in comparison with Dussaillant et al. (2019), possibly due to the outlines precision of glaciers identified from the national glacier inventories compared to RGI v6.0. Despite the above, and as shown in **Supplementary Figure S4**, considering ranges of 1° latitude between 8–55°S, we did not observe relevant differences in terms of average mass balance (< 0.3 m w.e.) in comparison with the mass balance estimated in Dussaillant et al. (2019), except between 48–49°S where we estimated a less negative mass balance.

Regarding GAV, the Desert Andes (-53 ± 0.002%) and the Lakes District (-52 ± 0.1%), which include the smallest glacierized surface areas, showed highest glacier shrinkage. The glacier shrinkage estimated here is higher than the one estimated by Rabatel et al. (2011) at -29% over the 1955–2007 period in the Desert Andes and that the one reported by Paul and Mölg (2014) at -25% over the 1985–2011 period in the Lake District, but it is

worth noting that the study period are different and that we consider in the overall study period used here the decade 2010–2020 during which glacier loss in these regions has strongly increased (Dussaillant et al., 2019). Southward of 42°S, the mean GAV estimated here (-24 ± 0.4% to -32 ± 1.3%) was higher than that observed by Meier et al. (2018) (-9 ± 5%, 1986–2016): this is likely related to differences in the study periods and also because we did not consider the large calving glaciers of the Patagonian ice-fields, where we found glacier outlines inconsistences, particularly in accumulation zones; these glaciers covering an area up to 13% of the total in South Patagonia and 20% in North Patagonia. Overall, we discarded the glacier growth due to methodological limitations, but this should have a limited impact because many studies have described a general glacier shrinking across the Andes (e.g., Malmros et al., 2016; Meier et al., 2018; Paul and Mölg, 2014; Rabatel et al., 2011; Rivera and Bown, 2013; Seehaus et al., 2019, 2020), with few exceptions that have been reported (Rivera and Casassa, 1999; Wilson et al., 2016; Hata and Sugiyama, 2021).

Although our GAV estimates show $r^2 > 0.7$, we identified 11 latitudinal ranges in which there are low statistical significance in the relationship between GAV and morphometric or climatic variables (*p-value* > 0.05), concentrated mainly in the Lakes District (between 38 to 39°S and 40 to 41°S) and North Patagonia (between 42 to 43°S and 46 to 48°S).

We found that the statistical relationship between GAV and GMB is mostly non-significant across the Andes. This is not really surprising as the considered time scales for GAV and GMB are not the same and they are of different length. In addition, GAV is related to glacier response times which depends on glacier dynamics, and is therefore related to its morphometric characteristic and thus specific to each glacier. This response time may largely exceed the study period length, particularly for outlet glaciers of the Patagonian ice-fields where it can be on a secular time scale. One consequence of this absence of a relationship between GAV and GMB is that their explanatory variables were identified separately.

4.2 Main Controls of Glacier Changes

In relation to the relevant variables at watershed scale for GAV (r^2 = 0.5, n = 35) and GMB (r^2 = 0.4, n = 110), we found that, on average for the entire study region (8–55°S), climate variables explain an highest percentage of the GAV and GMB spatial variances with more than 65% (> 35% for temperature), whereas the surface area is the most relevant (> 16%) for morphometric variables. We observe a latitudinal limit from 37.5°S (DA3 in Argentina) to 39.9°S (WA2 in Chile) between the explanatory capacity of precipitation and temperature in GAV and GMB spatial variances across the Andes. Precipitation explains highest percentage of GAV and GMB spatial variances (ranging from 49 to 93% depending on the clusters) for the Outer Tropics and the Dry Andes (8–37°S), whereas temperature is the most relevant climate variable (between 29 and 73% of explained spatial variance depending on the cluster) for the Wet Andes (40–55°S). The importance of precipitation in the GMB variability had already been observed in several studies based on *in situ* glacier monitoring by Favier et al. (2004) and Wagnon et al. (2001) in the Outer Tropics. More specifically, Sicart et al. (2003, 2011) showed that during the transition season (Sep-Dec) when ice melt increases, precipitation frequency and intensity are key to modulating ablation because of the impact on glacier surface albedo. In the Dry Andes, no link was found between GAV or GMB which is in agreement with Rabatel et al. (2011). In addition, Rabatel et al. (2011), Masiokas et al. (2016) and Kinnard et al. (2020) pointed out the sensitivity of GMB to precipitation. For this region, we also found that glacier surface area has significant explanatory power for the GMB variance (49% in DA1), which is in agreement with Rabatel et al. (2011) who showed that small glaciers in the Desert Andes have a very negative GMB in comparison with a moderate mass loss for larger glaciers. With regards to the Wet Andes, in the Patagonian ice-fields, spatial variances of glacier changes are mainly controlled by the temperature (WA3 to WA6). This is in agreement with Abdel Jaber et al. (2019) who found that the mass loss in the Northern Patagonia ice-field is likely due to higher temperatures. Outside the Patagonian ice-fields in east (WA4), the glacier shrinkage could be explained by a temperature increase as no change in precipitation was observed (1979–2002) (Masiokas et al., 2015). In addition, Falaschi et al. (2019) found a high correlation between GMB and temperature in Monte San Lorenzo since 1958 to 2018 (temperature Oct to Mar, r = -0.86, *p-value* = 0.1).

4.3 Clusters Without a Latitudinal Distribution Across the Andes

In the present work, we used morphometric and climatic variables associated with GMB data for 20,740 glaciers and GAV data for 2,484 glaciers to propose a new classification that comprises 12 clusters encompassing a total of 274 watersheds and 31,963 glaciers between 8 and 55°S. This regional identification was based on the main explanatory variables of glacier changes (GAV and GMB). Up to now, only one type of classification of the glacier environments based on latitudinal ranges has been used, first by Troll (1941) and Lliboutry (1998), followed by recent studies (e.g., Barcaza et al., 2017; Dussaillant et al., 2019; Masiokas et al., 2009, 2020; Zalazar et al., 2020). Sagredo and Lowell (2012) proposed another glaciological classification with nine zones between 8–55°S; this was based on climate variables only, and with a small number of glaciers (n < 234). Here, the clusters provide a classification with greater detail allowing to better take the regional-scale diversity in the glacier characteristics and evolution into account. For instance, glaciers on volcanoes in northern Chile and western Bolivia are no longer linked to the Dry Andes but clustered with those of the Outer Tropics (OT3). In addition, watersheds located at the same latitude sometimes belong to different clusters. These results are in line with Ayala et al. (2020) who identified significant differences (GMB, runoff contribution and glacier elevation) between the southern (DA2) and northern (DA3) watersheds inside the Río Maipo watershed. With regards to the Outer Tropics and the Wet Andes, our results show that a

latitudinal classification is not possible, which is in agreement with previous studies (e.g., Caro et al., 2020; Sagredo & Lowell, 2012). Southward of 46°S, we found different clusters, from west to east, related to the high contrast in precipitation and temperature amounts (WA3 to WA6) related to the wet western air masses originating from the Pacific Ocean (Langhamer et al., 2018). Studies on the Patagonian ice-fields have demonstrated this large difference in precipitation between the western and eastern sides of the cordillera (Warren, 1993; Barcaza et al., 2017; Bravo et al., 2019).

Despite these results, the sensitivity analysis showed that the absence of the variables Tmax and precipitation causes a rearrangement of the cluster assignment to each watershed, while the absence of the morphometric variables and Tmin does not show a major change in this assignment.

4.4 Implications in the Glacier Changes Simulations at the Andes Scale

Results obtained through linear machine learning method provide a new framework for glacier changes simulations across the Andes. The increase in temperature-driven and decrease in precipitation-driven glacier changes from the Outer Tropics to the Wet Andes highlights that:

a) A reduction in annual precipitation and changes in their monthly distribution will have a greater impact on glacier mass loss in the Outer Tropics and the Dry Andes in comparison with the Wet Andes. Conversely, changes in monthly temperature will be more relevant to simulate glacier mass loss in the Wet Andes.
b) The newly defined clusters will allow to orient the glacier change simulations, based on the main variables that control GAV and GMB across the Andes. For example, for regional studies across the Dry Andes to the Wet Andes, precipitation and temperature relevancies presented here can be efficiently used to estimate the mass balance, through the precipitation and ice melt factors that can be derived from numerous studies (e.g., Ayala et al., 2020; Bravo et al., 2017; Caro, 2014; Farías-Barahona et al., 2020; Huss and Hock, 2018; Masiokas et al., 2016). In this context, our results will be able to guide future regional hydro-glaciological simulations at watershed and cluster scales across the Andes.

DATA AVAILABILITY STATEMENT

The original contributions presented in the study are included in the article/**Supplementary Material**, further inquiries can be directed to the corresponding author.

AUTHOR CONTRIBUTIONS

AC: data processing, analysis, interpretation, and writing. TC and AR: supervision, interpretation and writing.

FUNDING

This study was conducted as part of the International Joint Laboratory GREAT-ICE, a joint initiative of the IRD and universities and institutions in Bolivia, Peru, Ecuador and Colombia. This research was funded by the National Agency for Research and Development (ANID)/Scholarship Program/ DOCTORADO BECAS CHILE/2019—72200174.

ACKNOWLEDGMENTS

We acknowledge the LabEx OSUG@2020 (Investissement d'Avenir,—ANR10 LABX56). The first author would like to thank Francisca Bown (Tambo Austral), Edwin Loarte Cadenas (INAIGEM), Katy Medina Marcos (INAIGEM), Justiniano Alejo Cochacin Rapre (ANA), James McPhee (U. of Chile), Diego Cusicanqui, Jeppe Malmros, David Farías-Barahona and Thorsten Seehaus for providing the glacier inventories between the Outer Tropics and Tierra del Fuego (8–55°S), and Fernando Gimeno, Jean Carlos Ruiz Hernández, Inés Dussaillant and Vanesa Carreño for fruitful discussions on this article. Finally, we acknowledge the numerous and constructive comments and suggestions provided by the two reviewers and the Editor.

SUPPLEMENTARY MATERIAL

The Supplementary Material for this article can be found online at: https://www.frontiersin.org/articles/10.3389/feart.2021.713011/full#supplementary-material

REFERENCES

Abatzoglou, J. T., Dobrowski, S. Z., Parks, S. A., and Hegewisch, K. C. (2018). TerraClimate, a High-Resolution Global Dataset of Monthly Climate and Climatic Water Balance from 1958-2015. *Sci. Data* 5, 1–12. doi:10.1038/sdata.2017.191

Abdel Jaber, W., Rott, H., Floricioiu, D., Wuite, J., and Miranda, N. (2019). Heterogeneous Spatial and Temporal Pattern of Surface Elevation Change and Mass Balance of the Patagonian Ice fields between 2000 and 2016. *The Cryosphere* 13 (9), 2511–2535. doi:10.5194/tc-13-2511-2019

AMTC (2019). *Inventario de glaciares de la cuenca río Maipo año 2018*. Santiago: CSIRO.

ANA (2014). *Data from: Inventario de Glaciares en el Perú. 2da Actualización*. Huaraz: Ministerio de Agricultura y Riego. Available at: http://geo2.ana.gob.pe:8080/geonetwork/srv/spa/catalog.search;jsessionid=6E35D3AA343E29DA1447AC04F968932B#/metadata/1099ce9e-bd97-49c1-a32a-2eccb35fcf79.

Arora, P., Deepali and Varshney, S. (2016). Analysis of K-Means and K-Medoids Algorithm for Big Data. *Proced. Comp. Sci.* 78 (12), 507–512. doi:10.1016/j.procs.2016.02.095

Ayala, Á., Farías-Barahona, D., Huss, M., Pellicciotti, F., McPhee, J., and Farinotti, D. (2020). Glacier Runoff Variations since 1955 in the Maipo River Basin, Semiarid Andes of central Chile. *Cryosphere Discuss.* 14, 1–39. doi:10.5194/tc-2019-233

Ayala, A., Pellicciotti, F., MacDonell, S., McPhee, J., Vivero, S., Campos, C., et al. (2016). Modelling the Hydrological Response of Debris-free and

Debris-Covered Glaciers to Present Climatic Conditions in the Semiarid Andes of central Chile. *Hydrol. Process.* 30 (22), 4036–4058. doi:10.1002/hyp.10971

Baraer, M., Mark, B. G., Mckenzie, J. M., Condom, T., Bury, J., Huh, K.-I., et al. (2012). Glacier Recession and Water Resources in Peru's Cordillera Blanca. *J. Glaciol.* 58 (207), 134–150. doi:10.3189/2012JoG11J186

Barcaza, G., Nussbaumer, S. U., Tapia, G., Valdés, J., García, J.-L., Videla, Y., et al. (2017). Glacier Inventory and Recent Glacier Variations in the Andes of Chile, South America. *Ann. Glaciol.* 58 (75), 166–180. doi:10.1017/aog.2017.28

Benítez, A. (1978). *Clasificación de Cuencas Hidrográficas de Chile*. Santiago: Unirioja.

Bharath, R., and Srinivas, V. V. (2015). Delineation of Homogeneous Hydrometeorological Regions Using Wavelet-Based Global Fuzzy Cluster Analysis. *Int. J. Climatol.* 35 (15), 4707–4727. doi:10.1002/joc.4318

Bolibar, J., Rabatel, A., Gouttevin, I., Galiez, C., Condom, T., and Sauquet, E. (2020). Deep Learning Applied to Glacier Evolution Modelling. *The Cryosphere* 14 (2), 565–584. doi:10.5194/tc-14-565-2020

Braun, M. H., Malz, P., Sommer, C., Farías-Barahona, D., Sauter, T., Casassa, G., et al. (2019). Constraining Glacier Elevation and Mass Changes in South America. *Nat. Clim Change* 9 (2), 130–136. doi:10.1038/s41558-018-0375-7

Bravo, C., Bozkurt, D., Gonzalez-Reyes, Á., Quincey, D. J., Ross, A. N., Farías-Barahona, D., et al. (2019). Assessing Snow Accumulation Patterns and Changes on the Patagonian Icefields. *Front. Environ. Sci.* 7 (3), 1–18. doi:10.3389/fenvs.2019.00030

Bravo, C., Loriaux, T., Rivera, A., and Brock, B. W. (2017). Assessing Glacier Melt Contribution to Streamflow at Universidad Glacier, central Andes of Chile. *Hydrol. Earth Syst. Sci.* 21 (7), 3249–3266. doi:10.5194/hess-21-3249-2017

Brun, F., Berthier, E., Wagnon, P., Kääb, A., and Treichler, D. (2017). A Spatially Resolved Estimate of High Mountain Asia Glacier Mass Balances from 2000 to 2016. *Nat. Geosci* 10 (9), 668–673. doi:10.1038/ngeo2999

Brun, F., Wagnon, P., Berthier, E., Jomelli, V., Maharjan, S. B., Shrestha, F., et al. (2019). Heterogeneous Influence of Glacier Morphology on the Mass Balance Variability in High Mountain Asia. *J. Geophys. Res. Earth Surf.* 124 (6), 1331–1345. doi:10.1029/2018JF004838

Burger, F., Ayala, A., Farias, D., Shaw, T. E., MacDonell, S., Brock, B., et al. (2019). Interannual Variability in Glacier Contribution to Runoff from a High-elevation Andean Catchment: Understanding the Role of Debris Cover in Glacier Hydrology. *Hydrological Process.* 33 (2), 214–229. doi:10.1002/hyp.13354

Caro, A. (2014). *Estudios glaciológicos en los nevados de Chillán*. Santiago: University of Chile. [thesis].

Caro, A., Gimeno, F., Rabatel, A., Condom, T., and Ruiz, J. C. (2020). Identificación de clústeres glaciares a lo largo de los Andes chilenos usando variables topoclimáticas. *Investig. Geogr.* 60, 119–133. doi:10.5354/0719-5370.2020.59009

Casassa, G., Smith, K., Rivera, A., Araos, J., Schnirch, M., and Schneider, C. (2002). Inventory of Glaciers in Isla Riesco, Patagonia, Chile, Based on Aerial Photography and Satellite Imagery. *Ann. Glaciol.* 34 (1), 373–378. doi:10.3189/172756402781817671

Cauvy-Fraunié, S., and Dangles, O. (2019). A Global Synthesis of Biodiversity Responses to Glacier Retreat. *Nat. Ecol. Evol.* 3 (12), 1675–1685. doi:10.1038/s41559-019-1042-8

Caviedes, J. (1979). *Inventario de glaciares en la hoya del río Cachapoal y predicción de la escorrentía del deshielo, Andes centrales*. Santiago: Universidad de Chile.

Cuffey, K. M., and Paterson, W. S. B. (2011). *The Physics of Glaciers*. Fourth edi. Academic Press. doi:10.3189/002214311796405906

Dangles, O., Rabatel, A., Kraemer, M., Zeballos, G., Soruco, A., Jacobsen, D., et al. (2017). Ecosystem Sentinels for Climate Change? Evidence of Wetland Cover Changes over the Last 30 Years in the Tropical Andes. *PLoS ONE* 12 (5), e0175814–22. doi:10.1371/journal.pone.0175814

Davaze, L., Rabatel, A., Dufour, A., Hugonnet, R., and Arnaud, Y. (2020). Region-Wide Annual Glacier Surface Mass Balance for the European Alps from 2000 to 2016. *Front. Earth Sci.* 8 (May), 1–14. doi:10.3389/feart.2020.00149

Devenish, C., and Gianella, C. (2012). *Sustainable Mountain Development in the Andes. 20 Years of Sustainable Mountain Development in the Andes - from Rio 1992 to 2012 and beyond*. Lima, Peru: CONDESAN.

DGA (2014). *Data from: Inventario Nacional de Glaciares de Chile*. Dirección General de Aguas. Available at: http://www.geoportal.cl/geoportal/catalog/search/resource/resumen.page?uuid=%7B9C5CBF38-72D5-4489-A745-30AEAF1CDFC2%7D.

DGA (2011). Variaciones recientes de glaciares en Chile según principales zonas glaciológicas. Santiago: Available at: http://bibliotecadigital.ciren.cl/handle/123456789/32678.

Dikbas, F., Firat, M., Koc, A. C., and Gungor, M. (2012). Classification of Precipitation Series Using Fuzzy Cluster Method. *Int. J. Climatol.* 32 (10), 1596–1603. doi:10.1002/joc.2350

Dussaillant, I., Berthier, E., Brun, F., Masiokas, M., Hugonnet, R., Favier, V., et al. (2019). Two Decades of Glacier Mass Loss along the Andes. *Nat. Geosci.* 12 (10), 802–808. doi:10.1038/s41561-019-0432-5

Falaschi, D., Lenzano, M. G., Villalba, R., Bolch, T., Rivera, A., and Lo Vecchio, A. (2019). Six Decades (1958-2018) of Geodetic Glacier Mass Balance in Monte San Lorenzo, Patagonian Andes. *Front. Earth Sci.* 7 (12), 1. doi:10.3389/feart.2019.00326

Farías-Barahona, D., Wilson, R., Bravo, C., Vivero, S., Caro, A., Shaw, T. E., et al. (2020). A Near 90-year Record of the Evolution of El Morado Glacier and its Proglacial lake, Central Chilean Andes. *J. Glaciol.* 66, 846–860. doi:10.1017/jog.2020.52

Farr, T. G., Rosen, P. A., Caro, E., Crippen, R., Duren, R., Hensley, S., et al. (2007). The Shuttle Radar Topography mission. *Rev. Geophys.* 45, 1. doi:10.1029/2005RG000183

Favier, V., Wagnon, P., and Ribstein, P. (2004). Glaciers of the Outer and Inner Tropics: A Different Behaviour but a Common Response to Climatic Forcing. *Geophys. Res. Lett.* 31 (16), 1. doi:10.1029/2004GL020654

Friedman, J., Hastie, T., and Tibshirani, R. (2010). Regularization Paths for Generalized Linear Models via Coordinate Descent. *J. Stat. Soft.* 33 (1), 1–22. doi:10.18637/jss.v033.i01

García, A., Ulloa, C., Amigo, G., Milana, J. P., and Medina, C. (2017). An Inventory of Cryospheric Landforms in the Arid diagonal of South America (High Central Andes, Atacama Region, Chile). *Quat. Int.* 438 (11), 4–19. doi:10.1016/j.quaint.2017.04.033

Garín, C. (1987). Inventario de glaciares de los Andes chilenos desde los 18° a los 23° de latitud sur. *Resvista de Geografía Norte Grande* 14, 15.

Guido, Z., McIntosh, J. C., Papuga, S. A., and Meixner, T. (2016). Seasonal Glacial Meltwater Contributions to Surface Water in the Bolivian Andes: A Case Study Using Environmental Tracers. *J. Hydrol. Reg. Stud.* 8, 260–273. doi:10.1016/j.ejrh.2016.10.002

Hall, M. J., and Minns, A. W. (1999). The Classification of Hydrologically Homogeneous Regions. *Hydrological Sci. J.* 44 (5), 693–704. doi:10.1080/02626669909492268

Hata, S., and Sugiyama, S. (2021). Changes in the Ice-Front Position and Surface Elevation of Glaciar Pío XI, an Advancing Calving Glacier in the Southern Patagonia Icefield, from 2000-2018. *Front. Earth Sci.* 8 (1), 1–12. doi:10.3389/feart.2020.576044

Hidrandina, S. A. (1989). *Inventario de glaciares del Perú*. . Huaraz: CONCYTEC.

Huss, M., and Hock, R. (2015). A New Model for Global Glacier Change and Sea-Level Rise. *Front. Earth Sci.* 3 (9), 1–22. doi:10.3389/feart.2015.00054

Huss, M., and Hock, R. (2018). Global-scale Hydrological Response to Future Glacier Mass Loss. *Nat. Clim Change* 8 (2), 135–140. doi:10.1038/s41558-017-0049-x

IANIGLA-CONICET (2018). Data from: Resultados del Inventario Nacional de Glaciares. Available at: https://www.argentina.gob.ar/ambiente/agua/glaciares/inventario-nacional.

INAIGEM (2018). Data from: Inventario de lagunas y glaciares del Perú. Available at: https://inaigem.maps.arcgis.com/apps/opsdashboard/index.html#/f37b51cf963642c0aca30056b445ef63.

Kaufman, L., and Rousseeuw, P. (2008). "Partitioning Around Medoids (Program PAM)," in *In Finding Groups in Data*. Editors P. J. Kaufman and L. Rousseeuw (John Wiley & Sons), 68–125. doi:10.1002/9780470316801.ch2

Kinnard, C., Ginot, P., Surazakov, A., MacDonell, S., Nicholson, L., Patris, N., et al. (2020). Mass Balance and Climate History of a High-Altitude Glacier, Desert Andes of Chile. *Front. Earth Sci.* 8 (2), 1–20. doi:10.3389/feart.2020.00040

Langhamer, L., Sauter, T., and Mayr, G. J. (2018). Lagrangian Detection of Moisture Sources for the Southern Patagonia Icefield (1979-2017). *Front. Earth Sci.* 6 (11), 1–17. doi:10.3389/feart.2018.00219

Lawson, R. G., and Jurs, P. C. (1990). New Index for Clustering Tendency and its Application to Chemical Problems. *J. Chem. Inf. Comput. Sci.* 30 (1), 36–41. doi:10.1021/ci00065a010

Lee, S., Kim, J., Hwang, J., Lee, E., Lee, K.-J., Oh, J., et al. (2020). Clustering of Time Series Water Quality Data Using Dynamic Time Warping: A Case Study from the Bukhan River Water Quality Monitoring Network. *Water* 12 (9), 2411. doi:10.3390/w12092411

Lliboutry, L. (1998). "Glaciers of Chile and Argentina," in *Satellite Image Atlas of Glaciers of the World* (South America: U.S. Geological Survey), I1–I206.

Lockhart, R., Taylor, J., and Tibshirani, R. (2015). A Significance Test for the Lasso. *Ann. Stat.* 42 (2), 413–468. doi:10.1214/13-AOS1175.A

Maechler, M., Rousseeuw, P., Struyf, A., Hubert, M., and Hornik, K. (2021). *Cluster: Cluster Analysis Basics and Extensions*. version 2.1.2. R package.

Malmros, J. K., Mernild, S. H., Wilson, R., Yde, J. C., and Fensholt, R. (2016). Glacier Area Changes in the central Chilean and Argentinean Andes 1955-2013/14. *J. Glaciol.* 62, 391–401. doi:10.1017/jog.2016.43

Marangunic, C. (1979). *Inventario de glaciares hoya del río Maipo*. Santiago: Snia.

Mark, B. G., McKenzie, J. M., and Gómez, J. (2005). Hydrochemical evaluation of changing glacier meltwater contribution to stream discharge: Callejon de Huaylas, Peru/Evaluation hydrochimique de la contribution évolutive de la fonte glaciaire à l'écoulement fluvial: Callejon de Huaylas, Pérou. *Hydrological Sci. J.* 50 (6), 1. doi:10.1623/hysj.2005.50.6.975

Masiokas, M. H., Christie, D. A., Le Quesne, C., Pitte, P., Ruiz, L., Villalba, R., et al. (2016). Reconstructing the Annual Mass Balance of the Echaurren Norte Glacier (Central Andes, 33.5° S) Using Local and Regional Hydroclimatic Data. *The Cryosphere* 10 (2), 927–940. doi:10.5194/tc-10-927-2016

Masiokas, M. H., Delgado, S., Pitte, P., Berthier, E., Villalba, R., Skvarca, P., et al. (2015). Inventory and Recent Changes of Small Glaciers on the Northeast Margin of the Southern Patagonia Icefield, Argentina. *J. Glaciol.* 61 (227), 511–523. doi:10.3189/2015JoG14J094

Masiokas, M. H., Rabatel, A., Rivera, A., Ruiz, L., Pitte, P., Ceballos, J. L., et al. (2020). A Review of the Current State and Recent Changes of the Andean Cryosphere. *Front. Earth Sci.* 8 (6), 1–27. doi:10.3389/feart.2020.00099

Masiokas, M. H., Rivera, A., Espizua, L. E., Villalba, R., Delgado, S., and Aravena, J. C. (2009). Glacier Fluctuations in Extratropical South America during the Past 1000years. *Palaeogeogr. Palaeoclimatol. Palaeoecol.* 281 (3–4), 242–268. doi:10.1016/j.palaeo.2009.08.006

Matiu, M., Crespi, A., Bertoldi, G., Carmagnola, C. M., Marty, C., Morin, S., et al. (2020). Observed Snow Depth Trends in the European Alps 1971 to 2019. *Cryosphere Discuss.* 10, 1–50. doi:10.5194/tc-2020-289

Meier, W. J.-H., Grießinger, J., Hochreuther, P., and Braun, M. H. (2018). An Updated Multi-Temporal Glacier Inventory for the Patagonian andes with Changes between the Little Ice Age and 2016. *Front. Earth Sci.* 6 (5), 1. doi:10.3389/feart.2018.00062

Mernild, S. H., Liston, G. E., Hiemstra, C. A., Yde, J. C., and Casassa, G. (2018). Annual River Runoff Variations and Trends for the Andes Cordillera. *J. Hydrometeorology* 19, 1167–1189. doi:10.1175/JHM-D-17-0094.1

Möller, M., Schneider, C., and Kilian, R. (2007). Glacier Change and Climate Forcing in Recent Decades at Gran Campo Nevado, Southernmost Patagonia. *Ann. Glaciol.* 46, 136–144. doi:10.3189/172756407782871530

Pagliero, L., Bouraoui, F., Diels, J., Willems, P., and McIntyre, N. (2019). Investigating Regionalization Techniques for Large-Scale Hydrological Modelling. *J. Hydrol.* 570 (9), 220–235. doi:10.1016/j.jhydrol.2018.12.071

Paul, F., and Mölg, N. (2014). Hasty Retreat of Glaciers in Northern Patagonia from 1985 to 2011. *J. Glaciol.* 60 (224), 1033–1043. doi:10.3189/2014JoG14J104

Rabatel, A., Castebrunet, H., Favier, V., Nicholson, L., and Kinnard, C. (2011). Glacier Changes in the Pascua-Lama Region, Chilean Andes (29° S): Recent Mass Balance and 50 Yr Surface Area Variations. *The Cryosphere* 5 (4), 1029–1041. doi:10.5194/tc-5-1029-2011

Rabatel, A., Dedieu, J. P., and Vincent, C. (2016). Spatio-temporal Changes in Glacier-wide Mass Balance Quantified by Optical Remote Sensing on 30 Glaciers in the French Alps for the Period 1983-2014. *J. Glaciol.* 62 (236), 1153–1166. doi:10.1017/jog.2016.113

Rabatel, A., Francou, B., Soruco, A., Gomez, J., Cáceres, B., Ceballos, J. L., et al. (2013). Current State of Glaciers in the Tropical Andes: A Multi-century Perspective on Glacier Evolution and Climate Change. *The Cryosphere* 7, 81–102. doi:10.5194/tc-7-81-2013

Rabatel, A., Machaca, A., Francou, B., and Jomelli, V. (2006). Glacier Recession on Cerro Charquini (16° S), Bolivia, since the Maximum of the Little Ice Age (17th century). *J. Glaciol.* 52 (176), 110–118. doi:10.3189/172756506781828917

Ragettli, S., and Pellicciotti, F. (2012). Calibration of a Physically Based, Spatially Distributed Hydrological Model in a Glacierized basin: On the Use of Knowledge from Glaciometeorological Processes to Constrain Model Parameters. *Water Resour. Res.* 48 (3), 1–20. doi:10.1029/2011WR010559

Raup, B., Racoviteanu, A., Khalsa, S. J. S., Helm, C., Armstrong, R., and Arnaud, Y. (2007). The GLIMS Geospatial Glacier Database: A New Tool for Studying Glacier Change. *Glob. Planet. Change* 56 (1–2), 101–110. doi:10.1016/j.gloplacha.2006.07.018

RGI Consortium (2017). "Randolph Glacier Inventory – A Dataset of Global Glacier Outlines: Version 6.0," in *GLIMS Technical Report* (Collardo: Glaciers contribution to sea level rise). doi:10.7265/N5-RGI-60

Rivera, A., and Bown, F. (2013). Recent Glacier Variations on Active Ice Capped Volcanoes in the Southern Volcanic Zone (37°-46°S), Chilean Andes. *J. South Am. Earth Sci.* 45, 345–356. doi:10.1016/j.jsames.2013.02.004

Rivera, A., and Casassa, G. (1999). Volume Changes on Pio XI Glacier, Patagonia: 1975-1995. *Glob. Planet. Change* 22 (1–4), 233–244. doi:10.1016/S0921-8181(99)00040-5

Sagredo, E. A., and Lowell, T. V. (2012). Climatology of Andean Glaciers: A Framework to Understand Glacier Response to Climate Change. *Glob. Planet. Change* 86-87 (4), 101–109. doi:10.1016/j.gloplacha.2012.02.010

Sahin, S., and Kerem Cigizoglu, H. (2012). The Sub-climate Regions and the Sub-precipitation Regime Regions in Turkey. *J. Hydrol.* 450-451, 180–189. doi:10.1016/j.jhydrol.2012.04.062

Sakakibara, D., and Sugiyama, S. (2014). Ice-front Variations and Speed Changes of Calving Glaciers in the Southern Patagonia Icefield from 1984 to 2011. *J. Geophys. Res. Earth Surf.* 119, 2541–2554. doi:10.1002/2014JF003148

Sakakibara, D., Sugiyama, S., Sawagaki, T., Marinsek, S., and Skvarca, P. (2013). Rapid Retreat, Acceleration and Thinning of Glaciar Upsala, Southern Patagonia Icefield, Initiated in 2008. *Ann. Glaciol.* 54 (63), 131–138. doi:10.3189/2013AoG63A236

Seehaus, T., Malz, P., Sommer, C., Lippl, S., Cochachin, A., and Braun, M. (2019). Changes of the Tropical Glaciers throughout Peru between 2000 and 2016 - Mass Balance and Area Fluctuations. *The Cryosphere* 13 (10), 2537–2556. doi:10.5194/tc-13-2537-2019

Seehaus, T., Malz, P., Sommer, C., Soruco, A., Rabatel, A., and Braun, M. (2020). Mass Balance and Area Changes of Glaciers in the Cordillera Real and Tres Cruces, Bolivia, between 2000 and 2016. *J. Glaciol.* 66 (255), 124–136. doi:10.1017/jog.2019.94

Shaw, T. E., Caro, A., Mendoza, P., Ayala, Á., Pellicciotti, F., Gascoin, S., et al. (2020). The Utility of Optical Satellite Winter Snow Depths for Initializing a Glacio-Hydrological Model of a High-Elevation, Andean Catchment. *Water Resour. Res.* 56 (8), 1–19. doi:10.1029/2020WR027188

Sicart, J. E., Hock, R., Ribstein, P., Litt, M., and Ramirez, E. (2011). Analysis of Seasonal Variations in Mass Balance and Meltwater Discharge of the Tropical Zongo Glacier by Application of a Distributed Energy Balance Model. *J. Geophys. Res.* 116 (13), 1–18. doi:10.1029/2010JD015105

Sicart, J. E., Hock, R., and Six, D. (2008). Glacier Melt, Air Temperature, and Energy Balance in Different Climates: The Bolivian Tropics, the French Alps, and Northern Sweden. *J. Geophys. Res.* 113 (24), 1–11. doi:10.1029/2008JD010406

Sicart, J. E., Ribstein, P., Francou, B., and Gallaire, R. (2003). Etude des précipitations et de la fonte sur un glacier tropical: le glacier du Zongo, Bolivie, 16°S. *Hydrological Sci. J.* 48 (5), 799–808. doi:10.1623/hysj.48.5.799.51453

Simon, N., Friedman, J., Hastie, T., and Tibshirani, R. (2011). Regularization Paths for Cox's Proportional Hazards Model via Coordinate Descent. *J. Stat. Soft.* 39 (5), 1–13. doi:10.18637/jss.v039.i05

Soruco, A., Vincent, C., Francou, B., and Gonzalez, J. F. (2009). Glacier Decline between 1963 and 2006 in the Cordillera Real, Bolivia. *Geophys. Res. Lett.* 36 (3), a–n. doi:10.1029/2008GL036238

Soruco, A., Vincent, C., Rabatel, A., Francou, B., Thibert, E., Sicart, J. E., et al. (2015). Contribution of Glacier Runoff to Water Resources of La Paz City, Bolivia (16° S). *Ann. Glaciol.* 56 (70), 147–154. doi:10.3189/2015AoG70A001

Tibshirani, R. (1996). Regression Shrinkage and Selection via the Lasso. *J. R. Stat. Soc. Ser. B (Methodological)* 58 (1), 267–288. doi:10.1111/j.2517-6161.1996.tb02080.x

Tibshirani, R., Walther, G., and Hastie, T. (2001). Estimating the Number of Clusters in a Data Set via the gap Statistic. *J. R. Stat. Soc.* 63, 1. doi:10.1111/1467-9868.00293

Troll, C. (1941). *Studien zur Vergleichenden Geographie der Hochgebirge der Erde*. Bonner Mit.

Valdivia, P. (1984). *Inventario de glaciares. Andes de Chile central.* . Santiago: Hoyas de los ríos Aconcagua, Maipo, Cachapoal y Tinguiririca.

Vivero, S. (2008). *Inventario de glaciares descubiertos de la cuenca del río Copiapó y variaciones recientes en sus frentes Informe final de práctica profesional.* . Santiago: CSIRO.

Vuille, M., Carey, M., Huggel, C., Buytaert, W., Rabatel, A., and Jacobsen, D. (2018). Rapid decline of snow and ice in the tropical Andes: Impacts, uncertainties and challenges ahead. *Earth Science Reviews* 176, 195–213.

Wagnon, P., Ribstein, P., Francou, B., and Sicart, J. E. (2001). Anomalous Heat and Mass Budget of Glaciar Zongo, Bolivia, during the 1997/98 El Niño Year. *J. Glaciol.* 47 (156), 21–28. doi:10.3189/172756501781832593

Warren, C. R. (1993). Rapid Recent Fluctuations of the Calving San Rafael Glacier, Chilean Patagonia: Climatic or Non-climatic? *Geografiska Annaler: Ser. A, Phys. Geogr.* 75 (3), 111–125. doi:10.1080/04353676.1993.11880389

Wilson, R., Carrión, D., and Rivera, A. (2016). Detailed Dynamic, Geometric and Supraglacial Moraine Data for Glaciar Pio XI, the Only Surge-type Glacier of the Southern Patagonia Icefield. *Ann. Glaciol.* 57 (73), 119–130. doi:10.1017/aog.2016.32

Zalazar, L., Ferri, L., Castro, M., Gargantini, H., Gimenez, M., Pitte, P., et al. (2020). Spatial Distribution and Characteristics of Andean Ice Masses in Argentina: Results from the First National Glacier Inventory. *J. Glaciol.* 66, 938–949. doi:10.1017/jog.2020.55

Zemp, M., Huss, M., Thibert, E., Eckert, N., McNabb, R., Huber, J., et al. (2019). Global Glacier Mass Changes and Their Contributions to Sea-Level Rise from 1961 to 2016. *Nature* 568 (7752), 382–386. doi:10.1038/s41586-019-1071-0

Zimmer, A., Meneses, R. I., Rabatel, A., Soruco, A., Dangles, O., and Anthelme, F. (2018). Time Lag between Glacial Retreat and Upward Migration Alters Tropical alpine Communities. *Perspect. Plant Ecol. Evol. Syst.* 30, 89–102. doi:10.1016/j.ppees.2017.05.003

Conflict of Interest: The authors declare that the research was conducted in the absence of any commercial or financial relationships that could be construed as a potential conflict of interest.

Publisher's Note: All claims expressed in this article are solely those of the authors and do not necessarily represent those of their affiliated organizations, or those of the publisher, the editors and the reviewers. Any product that may be evaluated in this article, or claim that may be made by its manufacturer, is not guaranteed or endorsed by the publisher.

frontiers in Earth Science

ORIGINAL RESEARCH
published: 25 January 2022
doi: 10.3389/feart.2022.817775

Evolution of Glacial Lake Cochrane During the Last Glacial Termination, Central Chilean Patagonia (~47°S)

Alicia Vásquez[1,2], Valentina Flores-Aqueveque[1,2], Esteban Sagredo[2,3,4], Rodrigo Hevia[2,3], Rodrigo Villa-Martínez[2,5], Patricio I. Moreno[2,6] and Jose L. Antinao[7]*

[1]Departamento de Geología, FCFM, Universidad de Chile, Santiago, Chile, [2]Millennium Nucleus Paleoclimate, ANID Millennium Science Initiative, Santiago, Chile, [3]Instituto de Geografía, Pontificia Universidad Católica de Chile, Santiago, Chile, [4]Estación Patagonia de Investigaciones Interdisciplinarias UC, Pontificia Universidad Católica de Chile, Santiago, Chile, [5]Centro de Investigación Gaia-Antártica, Universidad de Magallanes, Punta Arenas, Chile, [6]Instituto de Ecología y Biodiversidad, Centro de Estudios del Clima y la Resiliencia, Departamento de Ciencias Ecológicas, Universidad de Chile, Santiago, Chile, [7]Indiana Geological and Water Survey, Indiana University, Bloomington, IN, United States

Large ice-dammed lakes developed along the eastern margin of the Patagonian Ice Sheet (PIS) during the Last Glacial Termination (T1). Their spatial/temporal evolution, however, remains poorly constrained despite their importance for deciphering fluctuations of the shrinking PIS, isostatic adjustments, and climate forcing. Here we examine the distribution and age of shoreline features deposited or sculpted by Glacial Lake Cochrane (GLC) in the Lago Cochrane/Pueyrredón (LCP) basin, Central Patagonia, following recession of the LCP glacier lobe from its final Last Glacial Maximum (LGM) moraines. GLC drained initially toward the Atlantic Ocean and continuing ice shrinking opened new drainage routes allowing the discharge toward the Pacific Ocean. We identify five clusters of lake terraces, shorelines, and deltas between elevations ~600–500 (N5), ~470–400 (N4), ~360–300 (N3), ~230–220 (N2), and ~180–170 masl (N1) throughout the LCP basin. The distribution of these clusters and associated glaciolacustrine deposits provide constraints for the evolving position of the damming glacier bodies. Elevation gradients within the landform clusters reveal glacio-isostatic adjustments that enable us to quantify the magnitude of deglacial rebound and construct isostatically corrected surfaces for the different phases in the evolution of GLC. Our chronology, based principally on radiocarbon dates from lake sediment cores and new OSL dating, suggests that these phases developed between ~20.7–19.3 ka (N5), ~19.3–14.8 ka (N4), ~14.8–11.3 ka (N3), and shortly thereafter (N2 and N1). The N3 landforms are the most ubiquitous, well-preserved, and voluminous, attributes that resulted from a ~3,500-year long period of glacial stability, enhanced sediment supply by peak precipitation regime, and profuse snow and ice melting during the most recent half of T1. This scenario differs from the cold and dry conditions that prevailed during the brief N5 phase and the moderate amount of precipitation during the N4 phase. We interpret the limited development of the N2 and N1 landforms as ephemeral stabilization events following the final and irreversible disappearance of GLC after N3. This event commenced shortly after the onset of an early Holocene westerly minimum at pan-Patagonian scale at ~11.7 ka, contemporaneous with peak atmospheric and oceanic temperatures in the middle and high latitudes of the Southern Hemisphere.

OPEN ACCESS

Edited by:
Jacob M. Bendle, University of Northern British Columbia, Canada

Reviewed by:
Andrew S. Hein, University of Edinburgh, United Kingdom
Adrian Palmer, Royal Holloway, University of London, United Kingdom

***Correspondence:**
Alicia Vásquez
alicia.vasquez@ug.uchile.cl

Specialty section:
This article was submitted to Quaternary Science, Geomorphology and Paleoenvironment, a section of the journal Frontiers in Earth Science

Received: *18 November 2021*
Accepted: *05 January 2022*
Published: *25 January 2022*

Citation:
Vásquez A, Flores-Aqueveque V, Sagredo E, Hevia R, Villa-Martínez R, Moreno PI and Antinao JL (2022) Evolution of Glacial Lake Cochrane During the Last Glacial Termination, Central Chilean Patagonia (~47°S). Front. Earth Sci. 10:817775. doi: 10.3389/feart.2022.817775

Keywords: glacial lake cochrane, last glacial termination, isostatic rebound, central patagonia, patagonian ice sheet

1 INTRODUCTION

The Last Glacial Termination (T1: ~18–11 ka, ka = 10^3 calibrated years before present) is the most recent transition from glacial maximum to interglacial conditions and constitutes a key target for understanding the functioning of the global climate system through Quaternary ice ages. T1 featured a general trend of increase in atmospheric CO_2, along with abrupt temperature and atmospheric circulation swings at millennial timescales that led to the abrupt collapse of continental ice sheets from their LGM (~26.5–19 ka, Clark et al., 2009) positions, and subsequent rapid sea-level rise (Denton et al., 2010). Recent studies have emphasized the importance of changes in the Southern Westerly Winds (SWW) as a key factor in the climatic transformations that terminated the last glaciation at regional, hemispheric, and global scale (Toggweiler et al., 2006; Lamy et al., 2007; Anderson et al., 2009; Moreno et al., 2018). The western portion of Patagonia (40°–55°S), in southern South America, is a key region to monitor T1 and associated SWW swings because it is the sole continuous landmass that extends south into the subantarctic realm, intersecting a large portion of the SWW belt. Furthermore, it harbored the largest ice mass in the Southern Hemisphere outside Antarctica during the LGM, the PIS, which allows the study of past changes in the

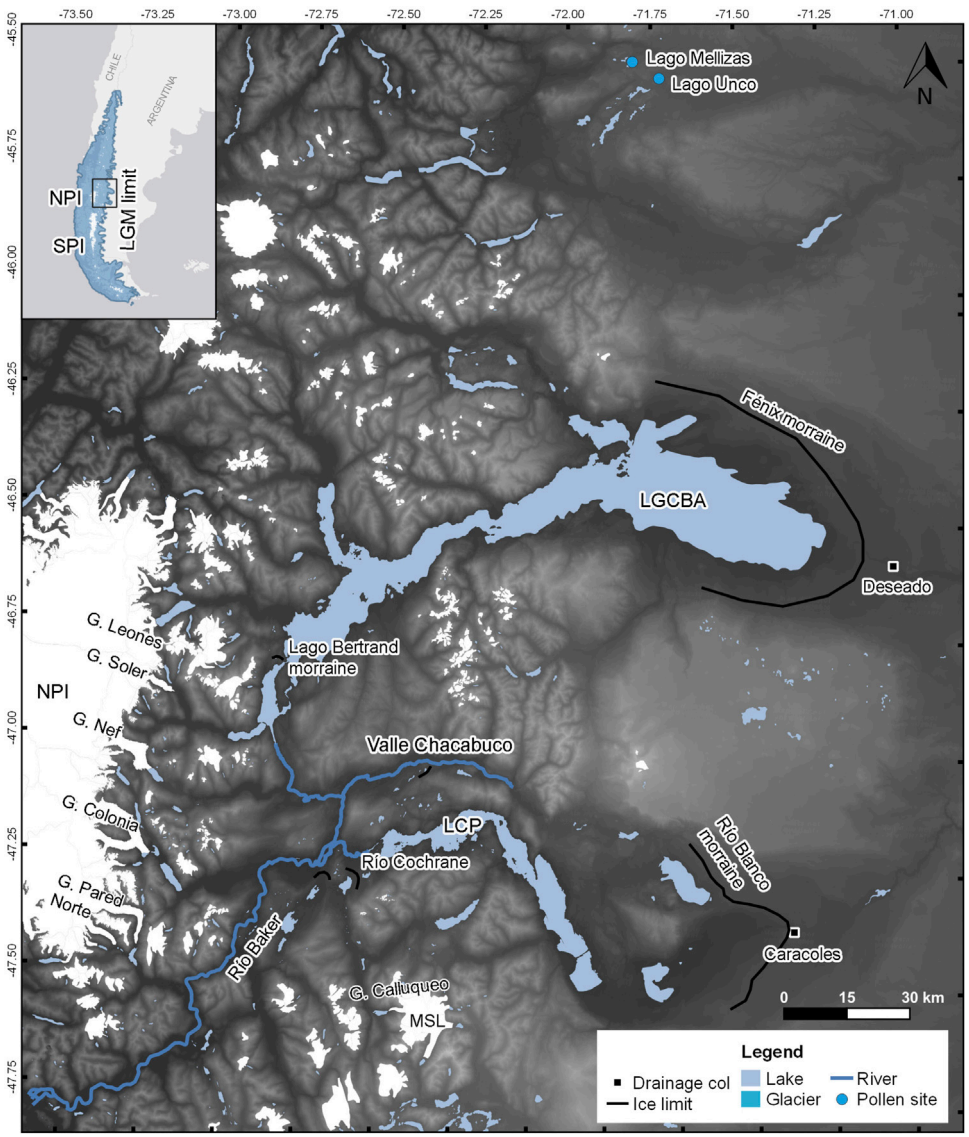

FIGURE 1 | Overview of the study region. Lake, river, glacier, and LGM limit shapes were obtained from Davies et al. (2020) for reference only. NPI, North Patagonian Icefield; SPI, South Patagonian Icefield; MSL, Monte San Lorenzo Ice Cap. LCP, Lago Cochrane/Pueyrredon; LGCBA, Lago General Carrera/Buenos Aires.

cryosphere, atmosphere, hydrosphere, and biosphere, and their reciprocal relationships.

The PIS covered the Patagonian Andes and adjacent regions multiple times during Quaternary ice ages (Rabassa and Clapperton, 1990; Glasser et al., 2008). Large eastward-flowing outlet glacier lobes filled the basins of Lago General Carrera/Buenos Aires (LGCBA) and LCP in Central Patagonia (44°–48°S) during the LGM (**Figure 1**) (Turner et al., 2005; Bell, 2008; Hein et al., 2010). The Fénix and Río Blanco moraines define the LGM positions of these lobes, respectively (Douglass et al., 2006; Hein et al., 2010; Kaplan et al., 2011), and constrain the initial formation of ice-dammed proglacial lakes in both basins. These glacial lakes drained eastward to the Atlantic Ocean during the earliest stages of T1. Continuing ice retreat allowed the opening of new drainage routes and, eventually, both lakes merged through the upper Valle Río Baker (Turner et al., 2005; Hein et al., 2010; Glasser et al., 2016; Davies et al., 2018; Thorndycraft et al., 2019). The subsequent separation of the North and South Patagonian Icefields (NPI and SPI, respectively) and associated outlet glacier lobes, during the later stages of T1, allowed the drainage of this merged glacial lake via the lower Valle Río Baker towards the Pacific Ocean, establishing the drainage pattern that persists until the present (Turner et al., 2005). Deciphering the sequence of events through this process spurred a flurry of research over the last 17 years, leading to multiple interpretations (Turner et al., 2005; Hein et al., 2010; Bourgois et al., 2016; Glasser et al., 2016; Davies et al., 2018; Thorndycraft et al., 2019). We identify three main sources of divergence among these alternative models. First, although they agree on the identification of the principal steps that took place in the lake evolution, the timing of events varies considerably, owing mainly to differences in geomorphic/stratigraphic interpretations and the precision and accuracy of the available geochronological data. Second, most of the data come from the LGCBA basin and the upper Valle Río Baker, with relatively few field-based measurements and stratigraphic data from the LCP basin. And third, the majority of models do not consider the glacio-isostasy effects, which caused an important uplift on the western sector. The latter factor was discussed by Thorndycraft et al. (2019), who produced isostatically corrected lake surfaces. Their approach is based on digital elevation models (DEM) with coarse vertical (~20 m) and horizontal (~30 m) resolution along with selected geomorphologic, stratigraphic, and chronologic constraints.

Here we report new data on shoreline-related landforms (raised deltas and paleoshorelines) in the LCP area, which is located ~70 km east of the NPI (**Figure 1**), along with sediment cores from small closed-basin threshold lakes to decipher the evolution of GLC through T1. We provide Global Navigation Satellite System (GNSS) measurements with high precision for constraining the elevation at the brink points of the landforms, and the age for the transition from glaciolacustrine to organic-rich mud deposition in sediment cores from threshold lakes distributed at different elevations. We assess these results in the context of previously published geochronologies and interpretations, which we collated from the literature, recalculated, and recalibrated. We aim to 1) identify ancient lake levels in the LCP basin, 2) constrain their chronology, and 3) examine their response to glacial isostatic and climatic influences. These data allow assessment of the following questions: 1) When did the LCP glacier lobe abandon the LCP basin? 2) did recession of the LCP glacier lobe proceed steadily, or was it punctuated by stabilizations or reversals? 3) did variations in the extent and elevation of GLC represent responses to climate forcing through T1? and 4) what are the regional implications of the GLC evolution?

2 PREVIOUS WORK

The first study of glacial landforms in the area was carried out by Caldenius (1932), who identified, named, and assigned tentative ages for several moraines east of LCP. A long hiatus in geomorphic studies followed until the publication of the Turner et al. (2005), Bell (2008), Glasser et al. (2008), and Hein et al. (2010) papers early during the 21st century. The latter study mapped multiple glacial limits around LCP and reported ^{10}Be measurements from the Río Blanco moraines (**Figure 2**). These dates yielded a mean age of 20.7 ± 1.3 ka (recalculated) for the innermost crests (Hein et al.'s (2010) third limit). Subsequently, Boex et al. (2013) reported cosmogenic exposure ages from erratics at Cerro Oportus, with ages ranging between ~19 and 17 ka (elevation range: 1,900–1,300 masl), Cerro Tamango, with ages ranging between ~17–16 ka (elevation range: 1,500–500 masl), in the highlands that separate the LCP basin from Valle Chacabuco, and the María Elena moraines on the Valle Chacabuco floor (**Figure 3**), with a recalculated mean age of 16.2 ± 0.5 ka (elevation range: 600–450 masl). Davies et al. (2018) reported a recalculated mean age of 13.0 ± 0.4 ka for the Esmeralda lateral moraines and one sample from the Salto moraine (359 masl) (**Figure 3**) with an age of 12.5 ± 0.4 ka, both located in Valle Río Baker, southwest to LCP. They also dated two boulders below 350 masl on the Salto moraine with a recalculated mean age of 12.1 ± 0.4 ka, which they interpreted as anomalously young ages as a result of water shielding by the merged lake. Upstream in Valle Río Baker, the same authors reported a recalculated mean age of 14.0 ± 0.5 ka for the inner Lago Bertrand moraine (**Figure 1**), which they considered as a maximum limiting age for the merged lake phase, referred to in the literature as the "Lower United Lake" (Turner et al., 2005) and "Lago Chalenko" (Davies et al., 2018; Thorndycraft et al., 2019).

Henríquez et al. (2017) studied sediment cores from Lago Edita (570 masl, GNSS), a small closed-basin lake located on the highlands that separate Valle Chacabuco from the LCP basin (**Figure 3**). They reported two identical radiocarbon dates from the basal organic sediments that yielded a median probability age of ~19.4 ka. This constitutes a minimum limiting age estimate for local ice-free conditions and cessation of glaciolacustrine sedimentation at the Puesto Tejuela col (580 masl) (**Figure 3**). An identical age and interpretation apply to the Lago Augusta (440 masl, GNSS) (Villa-Martínez et al., 2012) record, a small closed-basin lake located ~7 km northeast from Lago Edita in Valle Chacabuco (**Figure 3**). Turner et al. (2005) reported minimum limiting ages of

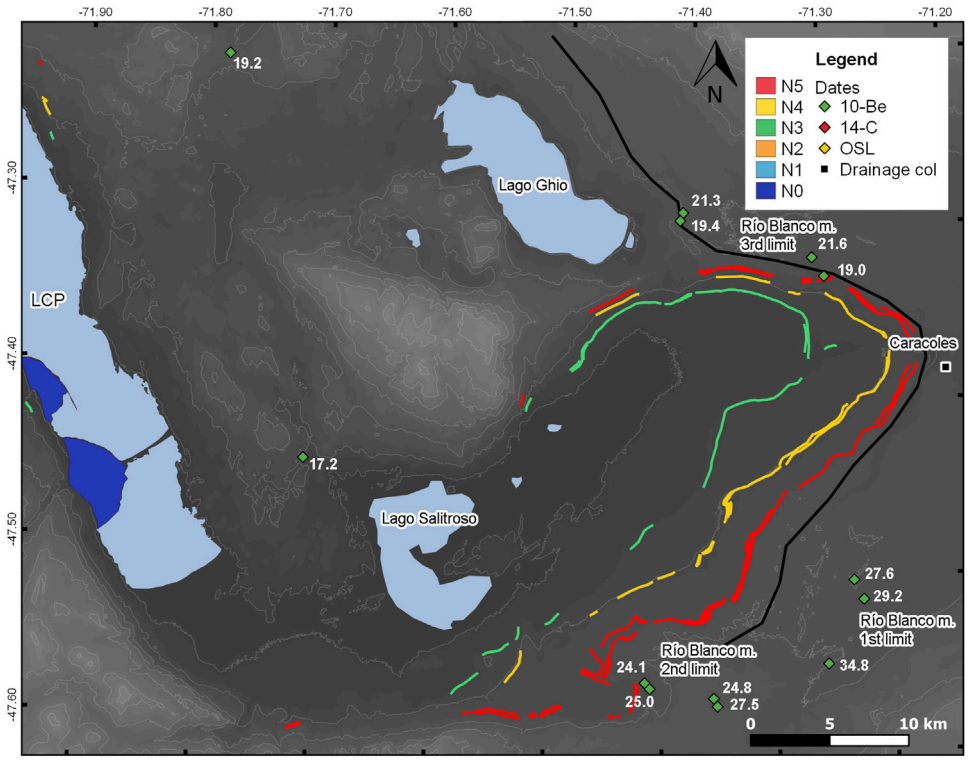

FIGURE 2 | Distribution of shoreline-related landforms in the eastern sector of LCP, grouped according to their elevation in N5 (~600–500 m), N4 (~470–400 m), N3 (~360–300 m), N2 (~230–220 m), N1 (~180–170 m), and N0, which correspond to active deltas. Lines represent paleo-shorelines (beaches, wave-cut scarps and benches, and delta brink-points) and polygons deltas. Geochronological data are shown in ka, without uncertainty (see details in **Supplementary Tables S1–S3**). Black lines represent ice limits.

kettle holes and shoreline features and concluded that the final drainage of the Lower United Lake occurred at ~12.8 ka. Thorndycraft et al. (2019) combined radiocarbon dates reported by Turner et al. (2005) and cosmogenic ages reported by Glasser et al. (2012) to propose that the end of the Lower United Lake drainage occurred between ~12.4–11.8 ka, using a Bayesian age model.

3 MATERIALS AND METHODS

This study combines analyses of satellite data, field-based descriptions, and GNSS measurements of key sediment-landform assemblages, along with collection of sedimentary samples for documenting changes in depositional environments and obtaining absolute dates. We used high-resolution satellite imagery from Google Earth Pro and Esri™ World Imagery, ALOS PALSAR DEM (12.5 m horizontal resolution), and field data to construct a geomorphological map of selected sectors of the LCP basin (**Figures 2**, **3**). We mapped shoreline-related landforms, including active deltas, raised deltas and their brink points, paleo-beaches, and wave-cut scarps and benches, using QGIS v3.10. We also described the sedimentology and stratigraphy of natural and artificial outcrops according to the depositional setting.

We acquired geodetic GNSS data (vertical datum WGS 84 ellipsoid; horizontal datum WGS 84) from the brink points of the landforms using a Trimble R1 GNSS receiver paired to a Juno 5 collector with Terrasync v5.85. The measurements were post-processed with the software Trimble Business Center, yielding an average vertical accuracy of ~0.7 m. We extracted the elevation of geomorphic features that we were unable to visit on the field from ALOS PALSAR DEMs (vertical datum WGS 84 ellipsoid). Ten measurements were obtained from each linear shape. The DEM data accuracy was validated statistically by comparing it with our GNSS data and calculating their correlation coefficient, Root Mean Square Error (RMSE), and bias. The same process was applied to ASTER G-DEM to evaluate its vertical accuracy as well. We considered the NPI vertical elevation model proposed by Hubbard et al. (2005) and defined a simplified ice flow direction of 97° azimuth. We defined isobase zero orthogonally, passing through the Caracoles col (**Figure 1**). Finally, we plotted the elevation dataset in a scatter diagram against their distance to the isobase zero measured along the flowline of the LCP glacier lobe (we discarded landforms with strong evidence of erosion because of the difficulties in identifying their original brink point elevation). Using this plot together with field observations, we clustered landforms in six distinct groups according to their elevation (N5-N0, with N0 the lowest). We applied second-order polynomial regressions to N5, N4, and N3 using R

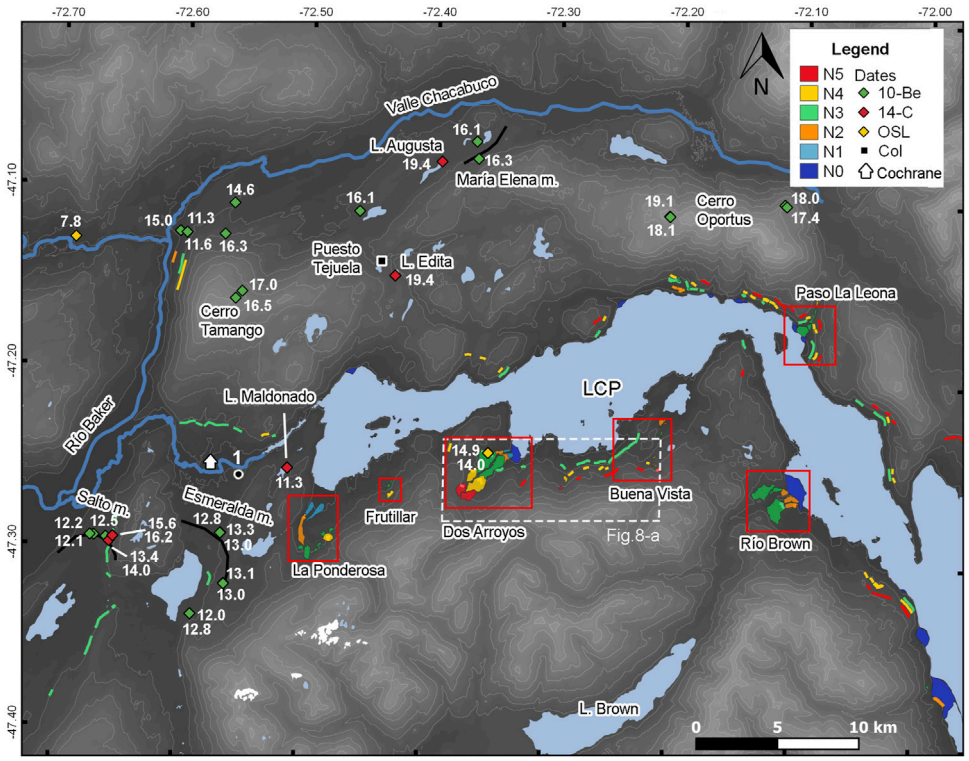

FIGURE 3 | Distribution of shoreline-related landforms in the western sector of LCP, grouped according to their elevation in N5 (~600–500 m), N4 (~470–400 m), N3 (~360–300 m), N2 (~230–220 m), N1 (~180–170 m), and N0, which correspond to active deltas. Lines represent paleo-shorelines (beaches, wave-cut scarps and benches, and delta brink-points) and polygons deltas. Geochronological data are shown in ka, without uncertainty (see details in **Supplementary Tables S1–S3**). Black lines represent ice limits. Site 1 (**Table 1**) is shown as black circle. Red panels show sectors with field recognition (see **Supplementary Figure S7** for more details).

(R Core Team, 2020) to obtain the glacio-isostatic gradients and paleolevels. Based on these results we adjusted the ALOS PALSAR DEMs in QGIS v3.10 to produce an isostatically corrected landscape reconstruction of the LCP area. We used these paleolake reconstructions, together with the inferred ice position, to estimate the water volume drained in each stage using raster analysis tools from QGIS. Some of the morphologies did not belong to the main levels and are therefore cataloged as sub-levels and not considered in the glacio-isostatic calculations. It is important to mention that although the aforementioned data processing was done using ellipsoidal elevations, all elevation data reported in the text are orthometric (EGM96).

We obtained multiple overlapping sediment cores from Lago Maldonado (−47.255, −72.512; 325 masl, GNSS) (**Figure 3**), a small closed-basin lake located on an ice-molded bedrock promontory ~2 km west of LCP. Coring was carried out from an anchored raft equipped with a 7.5 cm diameter aluminum casing tube using a square-rod Livingstone corer. All cores were wrapped in plastic foil and stored at 4°C in a walk-in cooler. We obtained digital X radiographs to detect potential stratigraphic structures on the sediment cores, carried out loss-on-ignition analyses using the protocol described by Heiri et al. (2001) and obtained seven radiocarbon dates on bulk sediments, upon which we developed a Bayesian age model using the Bacon package of R (Blaauw and Christeny, 2011; R Core Team, 2020). We recalibrated the radiocarbon dates from Lago Augusta and Lago Edita (**Figure 3**) (Villa-Martínez et al., 2012; Henríquez et al., 2017) and updated the age models incorporating, in the case of Lago Augusta, the following modifications: 1) we excluded the radiocarbon date CAMS-144599 from the new age model considering it is anomalously young in the context of the over and underlying dates, and 2) we included the basal dates from Lago Edita (UCIAMS-133418, CAMS-144454) in the new Lago Augusta age model based on the Henríquez et al. (2017) discussion of the Lago Augusta record reported by Villa-Martínez et al. (2012), and their congruence with the basal date from Lago Edita (CAMS-144600).

We obtained two OSL dates from a raised delta front in Dos Arroyos (site 5) (**Figure 3**; **Table 1**). Measurements were performed on quartz following the single-aliquot regenerative-dose (SAR) protocols (Murray and Wintle, 2000, Murray and Wintle, 2003) at the Luminescence Laboratory, Indiana Geological and Water Survey, Indiana University. The SAR protocol was applied on 39 and 11 multi-grain aliquots (25–40 grains each). Equivalent dose and age distributions were estimated using the Minimum Age Model (Galbraith et al., 1999). The dose rate and age for each sample was calculated using the online DRAC v1.2 calculator tool (Durcan et al., 2015).

We compiled 122 dates from previously published articles in the LGCBA and LCP basins, including cosmogenic, radiocarbon,

TABLE 1 | Summary of stratigraphic sections. See locations in **Supplementary Figure S7**.

Site	Lat (°)	Lon (°)	Elev (masl)	Sector	Level	Deposit	Description method
1	−47.2578	−72.5492	173	Río Cochrane	N3 or N2	glaciolacustrine rhythmites	*In situ*
2	−47.2598	−72.4278	343	Frutillar	N3	Delta topset and foreset	*In situ*
3	−47.2677	−72.4290	457	Frutillar	N4	Delta topset and foreset	*In situ*
4	−47.2428	−72.3316	148	Dos Arroyos	N1	Delta topset	*In situ*
5	−47.2427	−72.3410	222	Dos Arroyos	N2	Delta topset	*In situ*
6	−47.2430	−72.3498	330	Dos Arroyos	N3	Delta topset and foreset	*In situ*
7	−47.2627	−72.3653	489	Dos Arroyos	N4	Delta topset and foreset	Through field photograph
8	−47.2652	−72.3719	632	Dos Arroyos	N5	Delta topset and foreset	Through field photograph
9	−47.2641	−72.1140	330	Río Brown	N3	Aeolian and delta topset	Through field photograph
10	−47.1683	−72.0964	331	Paso La Leona	N3	Delta topset	Through field photograph

and OSL dates (**Supplementary Tables S1–S3**). ^{10}Be ages were recalculated with the CRONUS-Earth exposure age calculator v3, with version 2.2.1 of the constants files (Balco et al., 2008), and the high-resolution version of the geomagnetic framework (Lifton et al., 2008). All ages are presented using the time-dependent Lal/Stone scaling model (Lal, 1991; Stone, 2000) and the regional Patagonian production rate assuming zero erosion (Kaplan et al., 2011). We report cosmogenic dates with ±1σ analytical uncertainty. We decided not to use external uncertainties because we consider their use unnecessary given that all the ages presented here were calculated using a local production rate, which was empirically derived against radiocarbon dates. In this sense, for moraines, the arithmetic mean was calculated including the propagation of the analytical uncertainty and the local production rate uncertainties (3%) (Kaplan et al., 2011). All radiocarbon ages were recalibrated and converted to calendar years BP using the CALIB 8.2 (Stuiver et al., 2021) and the SHCal20 calibration dataset (Hogg et al., 2020) and are presented with ±2σ ranges. We report the calculated ages from OSL dates as reported in their original publications.

4 RESULTS

4.1 Geomorphic Features and Sedimentology

Field mapping and satellite imagery revealed lake marginal features in LCP that include raised deltas, paleo-beaches, wave-cut scarps, and benches (**Figures 2**, **3**). Raised deltas are distinguishable in the study area as flat surfaces composed of sedimentary materials, usually located upstream from active modern deltas (**Figure 4**). Their delta-top area range from 0.01 to 1 km^2, and their top slope varies between 1° and 10°. In general, they show well-defined brink points and steep fronts, and show well-developed topset and steeply inclined foreset beds (**Figures 5**, **6**), which are the main features of Gilbert-type deltas, similar to those described in LGCBA by Bell (2008). Paleo-beaches show parallel lineations of gravel bars, gently concave towards the lake. Other paleo-shorelines are identified as narrow erosive or depositional terraces or scarps throughout the margins of LCP.

We mapped a total of 568 landforms (**Figures 2**, **3**), which fall into six clusters of lake-marginal features with elevations between ~600–500 (N5), ~470–400 (N4), ~360–300 (N3), ~230–220 (N2), ~180–170 masl (N1), and the currently active morphologies (N0), with their elevations close to the present-day water level (~150 masl). The Río Blanco LGM moraines, located in the easternmost sector, feature shorelines at ~500 (N5), 400 (N4), and 300 (N3) masl. They exhibit a steady rise in elevation toward the west, which explains the broad range of elevation within the clusters. In the following paragraphs we describe key sectors we visited during fieldwork or monitored from satellite imagery (Valle Río Baker).

Most of the landforms located in the Valle Río Baker (**Figure 3**) range between ~360 and 350 masl, falling in the elevation range of the N3 cluster. The most conspicuous shoreline extends for ~4 km, north of Cochrane township. The western side of Cerro Tamango contains shorelines with elevations of ~460, ~350, and ~200 masl, associated to the N4, N3, and N2 clusters, respectively. We found glaciolacustrine rhythmites close to Río Cochrane at 173 masl (site 1 in **Figure 3** and **Table 1**), composed of alternating millimetric clay and silt layers of dark and lighter sediments (**Supplementary Figures S8A,B**). Considering its elevation and the inferred ice position (discussed in **Section 5.1**), this deposit is most likely related to paleolevel N3 or N2.

We detect four raised deltas at La Ponderosa (**Figure 3**) which belong to clusters N4 to N1 (**Figure 4A**). N4 delta has a gently sloping upper surface and a steep delta-front slope, with a sharp and well-defined brink point at ~470 masl. N3 presents a sharp brink point at 365 masl (GNSS) and erosional notches incised along its sloping front. The N2 delta extends over a larger area and has a diffuse brink point at 222 masl (GNSS). The N1 delta does not show a distinguishable brink point.

In the Frutillar sector (**Figure 3**) we detect two raised deltas (**Figures 4B,C**) which occupy small areas and have a moderately steep delta top slope (5–10°). The N4 delta has a somewhat diffuse and convex brink point at 455 masl (GNSS). The delta located within the N3 level does not show a clear brink point but its delta top has an elevation of 350 masl (GNSS). Outcrops in both deltas reveal the topset/foreset contacts for N3 and N4 landforms (sites 2 and 3, respectively) (**Table 1**). Topset beds at site 2 (**Figures 5A–C**) have a thickness of ~3 m and correspond to alternating centimetric layers of darker matrix-supported pebbles in a matrix of coarse sand and layers of clast-supported sub-rounded well-sorted granules to pebbles, with normal gradation. We find scour

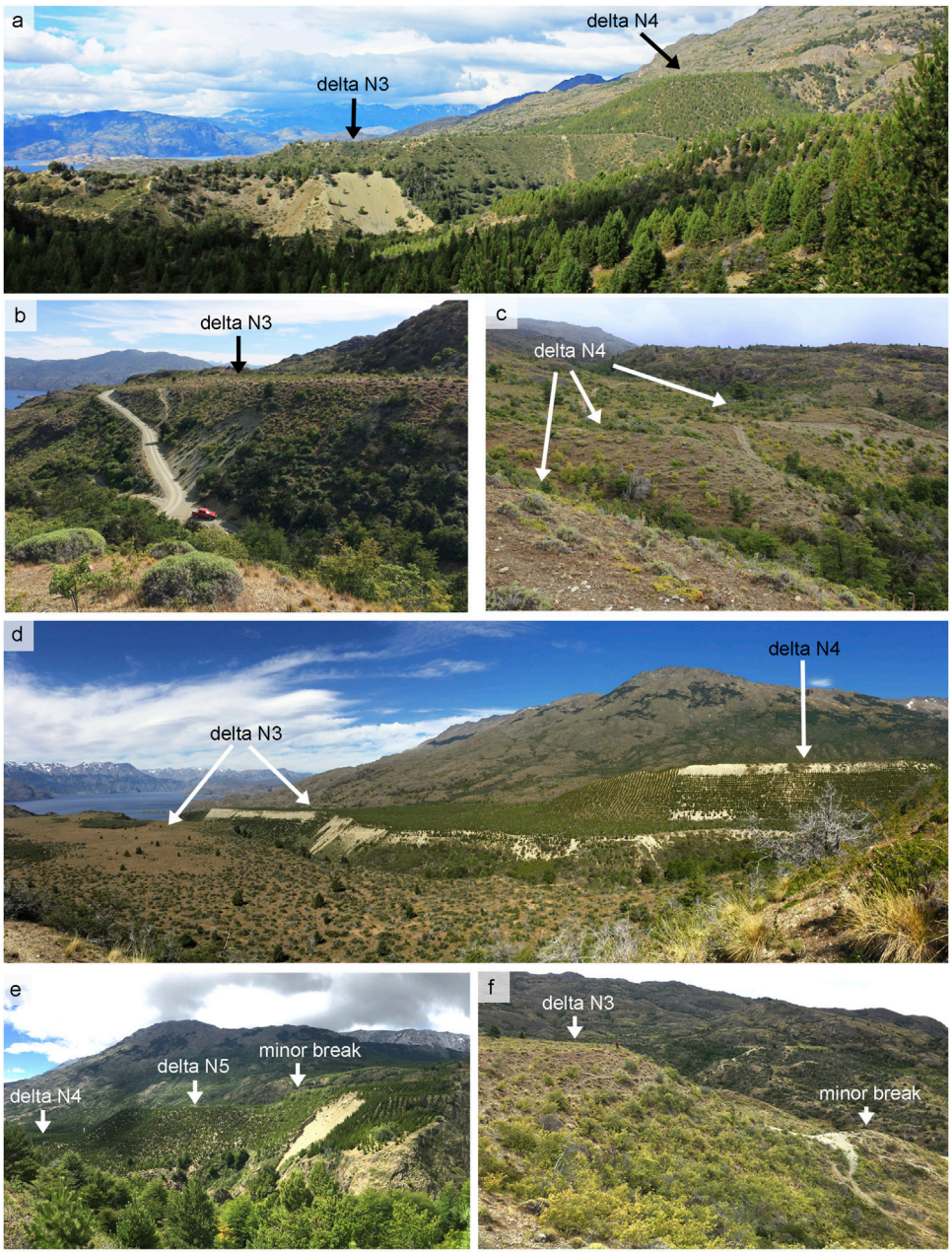

FIGURE 4 | Field photographs from La Ponderosa **(A)**, Frutillar **(B,C)**, and Dos Arroyos **(D–F)** deltas. The location of these sites is expressed in **Supplementary Figure S7**.

and fill structures, planar and trough cross-bedding, and conglomerate lenses. The foreset beds are ~2 m thick and exhibit steeply dipping (~30°) decimetric layers of sub-rounded fine-grained to medium-grained massive sand with some isolated pebbles, intercalated with centimetric layers of coarse-grained sand to pebbles showing normal gradation (**Figure 5D**) and planar lamination. At site 3 (**Figure 5E**), the topset beds are ~50 cm thick, and the contact between the topset and foreset is diffuse. Topset beds are composed mainly of subangular matrix-supported pebbles in a granule to sandy matrix, with a slight imbrication of clasts. Foreset beds have a thickness of ~3 m and present a well-defined parallel lamination with an orientation of 25° NE. They correspond to alternating layers of massive matrix-supported granule clasts in a sandy matrix and massive matrix-supported pebbles in a granule sandy matrix.

The Dos Arroyos sector (**Figure 3**) contains the most extensive and well-preserved perched deltas in LCP (**Figures 4D–F**), which encompass elevations that correspond with the N5 to N1 clusters. The N5 delta top has a gentle slope and irregular surface, possibly due to fluvial erosion. The front is

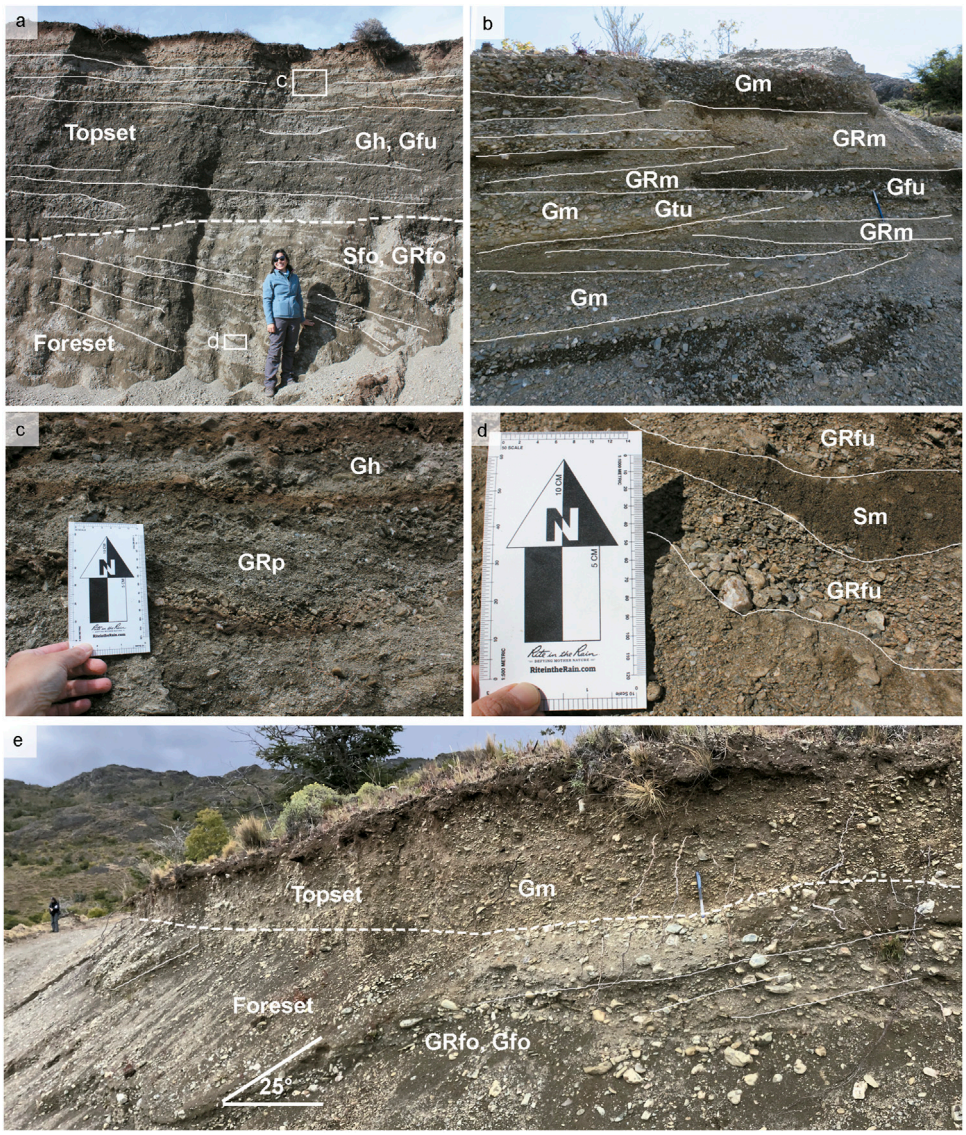

FIGURE 5 | Main stratigraphic and sedimentological features of deltas in Frutillar sector. **(A)** Outcrop showing the topset/foreset contact on site 2. **(B)** Trough cross-bedded gravel in topset. **(C)** Planar cross-bedding in topset. **(D)** Upward fining granules in foreset. **(E)** Topset/Foreset contact on site 3. Gm, clast-supported massive gravel; Gfo, deltaic foreset gravel; Gh, horizontally bedded gravel; Gt, Trough cross-bedded gravel; Gfu, Upward-finning gravel; GRm, massive granule; GRfu, upward-finning granule; GRp, Cross-bedded granule; GRfo, deltaic foreset granule; Sfo, deltaic foreset sand; Sm, massive sand.

very eroded as well, but the brink point is distinguishable at 600 masl (GNSS). Deltas at N4 and N3 are extensive (~0.8 and 1 km^2, respectively) and have sharp and well-defined brink points at 458 and 345 masl (GNSS), respectively. There are also minor breaks at 584 and 333 masl (GNSS). N2 and N1 deltas are considerably smaller in size and have no distinguishable brink points. In the following sentences we describe outcrops from the N1 (site 4), N2 (site 5), and N3 (site 6) levels. Site 4 features a ~5 m high and ~30 m wide outcrop that reveals alternating decimetric layers of sand-pebble and granule-boulder (**Figures 6A,B**). Sand-pebble layers correspond to matrix-supported pebbles in a matrix of angular medium-grained to coarse-grained metamorphic sand, showing horizontal stratification. Granule-boulder layers are composed of clast-supported subrounded pebbles to boulders (up to ~30 cm diameter) in a granule matrix. Imbrication is occasionally observed in the deposit. Site 5 consists of a 2.3-m high section composed of clast to matrix-supported pebbles to cobbles of metamorphic origin in a medium-grained sandy matrix (**Figure 6C**). Clasts are sub-angular to sub-rounded. Well-developed imbrication and parallel lamination are evident in the finer sediments. At site 6 we find a ~2 m high outcrop of tabular morphology composed of 2 conformable units recognized as topset and foreset beds (**Figure 6D**). Foreset beds consist of 1.5 m of alternating steeply dipping (~30°NW) layers of clast-supported pebbles (~1 cm)

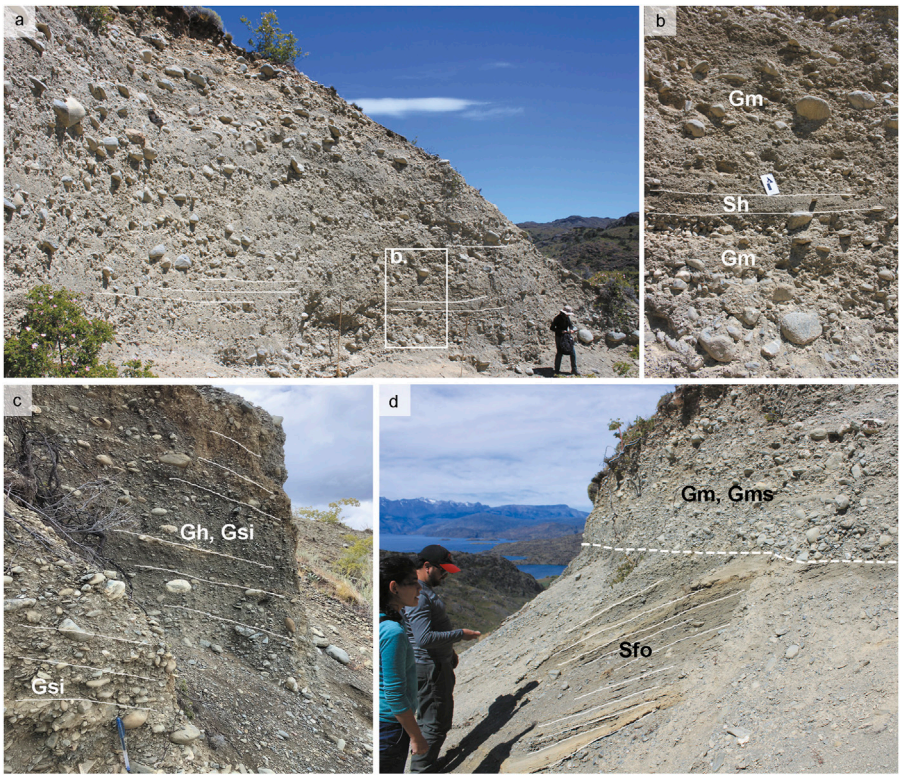

FIGURE 6 | Deltas from the Dos Arroyos sector. **(A)** Main stratigraphic features of site 4. **(B)** Detail showing main sedimentary facies of site 4. **(C)** Delta topset on site 5. **(D)** Topset and foreset on site 6. Sh, horizontally bedded sand; Gsi, matrix-supported imbricated gravel; Gms, matrix-supported massive gravel.

TABLE 2 | OSL dates of delta-front deposits from Dos Arroyos site.

Field sample ID	Aliquots used	Lat (°)	Lon (°)	Elevation (masl)	Sample depth (m)	Dose rate (Gy/ka)	Equivalent dose	Water (%)	Age (ka)
D3.1	11	−47.2430	− 72.3498	335	2.00	2.78 ± 0.21	39 ± 7	7 ± 4	14.0 ± 2.7
D3.2	39	−47.2430	− 72.3498	335	2.05	2.82 ± 0.11	42 ± 3	7 ± 4	14.9 ± 1.2
Weighted mean age									14.8 ± 1.1

and layers of 3–20 cm of fine-grained sand with parallel lamination. We collected two samples for OSL dating from this unit ~1 m below its upper limit (**Table 2**; **Supplementary Figures S1, S.2**), yielding an weighted mean age of 14.8 ± 1.1 ka. The topset is composed of ~1 m of massive matrix to clast-supported pebbles-to-cobbles in a coarse sand matrix. The topset/foreset contact was also recognizable at N4 (site 7, **Supplementary Figure S8C**) and N5 (site 8, **Supplementary Figure S8D**) delta outcrops in the Dos Arroyos sector, but not accessible *in situ*.

We found two small raised deltas in the Buena Vista sector (**Figure 3**) falling in the elevation range of the N5 and N4 clusters (**Figures 7A,B**). These exhibit smooth and inconspicuous brink points at 576 and 443 masl (GNSS) and minor slope breaks at 542 and 431 masl (GNSS). A very distinctive paleo-beach within N3 shows parallel and slightly concave gravel lineations, with its lowest shoreline at 331 masl (GNSS) (**Figure 7C**). Small deltas within the N3 and N2 elevation ranges are preserved in this sector but their brink points are not well-defined.

We detect several small terraces within the elevations of the N5-N3 clusters between Dos Arroyos and Buena Vista (**Figure 7D**). The continuity of the N3 shoreline is remarkable, extending almost uninterrupted for ~5 km with an average elevation of ~330 masl.

We identify an extensive delta within the N3 range and smaller deltas at N2 elevations in the Río Brown sector (**Figures 3**, **8A**). The brink point in the N3 delta is well defined at 324 masl (GNSS). There is a lateral section in its delta-top that shows alternating layers of clast-supported subrounded pebbles and clast-supported granules (site 9, **Supplementary Figure S8E**).

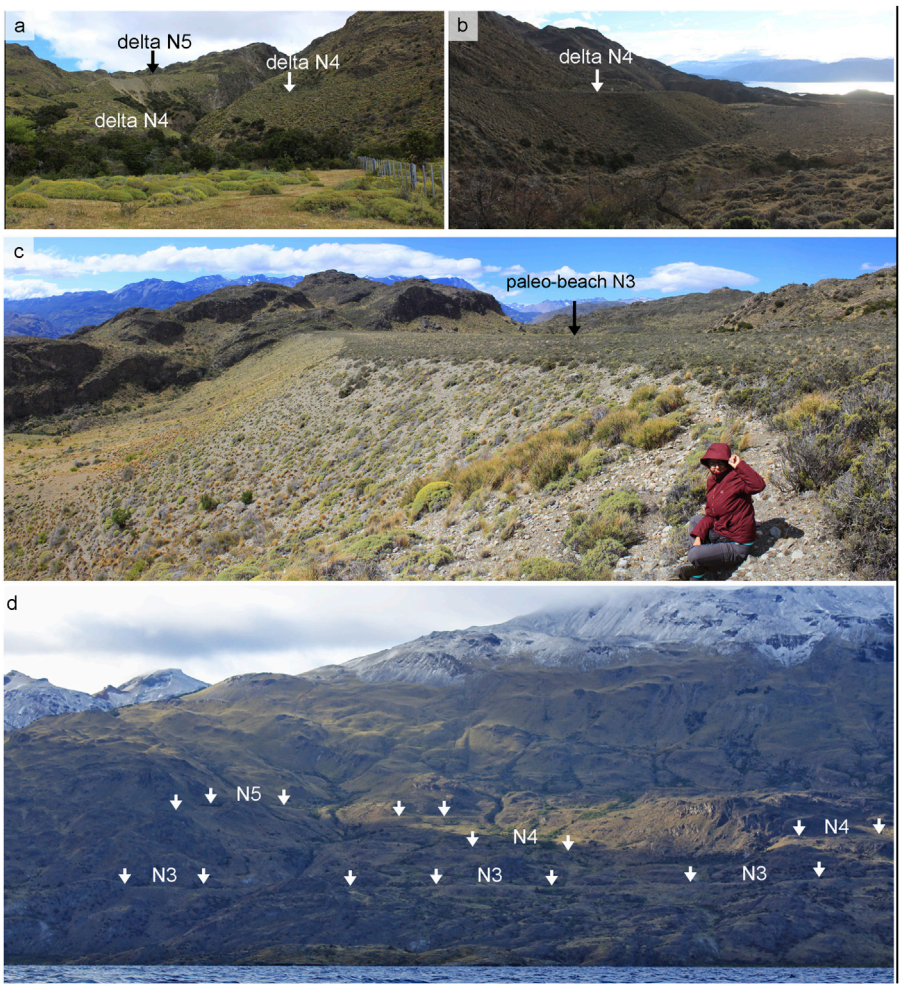

FIGURE 7 | (A–C) Field photographs from the Buena Vista sector. **(D)** Shorelines between the Dos Arroyos and Buena Vista sectors. Note the remarkable preservation and continuity of N3. See location in **Supplementary Figure S7**.

The N2 deltas are considerably smaller with restricted, underdeveloped delta fronts, and a major slope break at 217 masl (GNSS), and minor breaks at 289 and 278 masl.

At Paso La Leona sector (**Figure 3**) we found geomorphic features that fall in the elevation ranges of clusters N5 to N3 (**Figures 8B–E**). The N5 landforms are preserved as isolated terraces and paleo-beaches. The lowest break of slope measured in the field has an elevation of ~530 masl (GNSS). N4 landforms comprise some sharp isolated terraces as well, one of them with an altitude of 414 masl (GNSS), and a small delta with no distinguishable brink point. A large delta with a gentle sloping top surface shows a well-defined brink point at 319 masl (GNSS), and some associated terraces fall in the N3 elevation range. Topset beds were observed at the N3 delta (site 10, **Supplementary Figure S8F**). They consist of centimetric sub-horizontal layers with alternations between pebble-rich layers and finer sediments. West of Paso La Leona we observe several small terraces belonging to clusters N5 to N2 (**Figure 3**), whose elevations were extracted from ALOS PALSAR DEMs.

4.2 Isostasy and Paleolake Levels

The elevation dataset used to calculate the glacio-isostasy includes GNSS (sites with *in situ* field measurements) and ALOS PALSAR DEMs (sites lacking *in situ* field measurements) data. We first evaluated the accuracy of DEMs by comparing them with our GNSS data. They show a very strong correlation ($r = 0.999$) with a RMSE of 7.94 m. Although these are good results, we note that ALOS PALSAR systematically underestimates elevations, with a bias of −6.49 m (**Supplementary Figure S3**; **Supplementary Tables S4, S5**). Likewise, ASTER G-DEM shows a very strong correlation ($r = 0.997$) with a RMSE of 10.18 m and a bias of −6.38 m (**Supplementary Figure S4**; **Supplementary Tables S4, S5**). The elevation differences between the DEM and our GNSS data range between −18 and 2 m for ALOS PALSAR, and between −22 and 19 m for ASTER G-DEM, resulting in a higher terrain ruggedness (**Supplementary Figure S5**). Based on these results we favor the ALOS PALSAR dataset.

We plotted the elevation data obtained at the slope breaks of shoreline-related landforms against distance to the Caracoles col

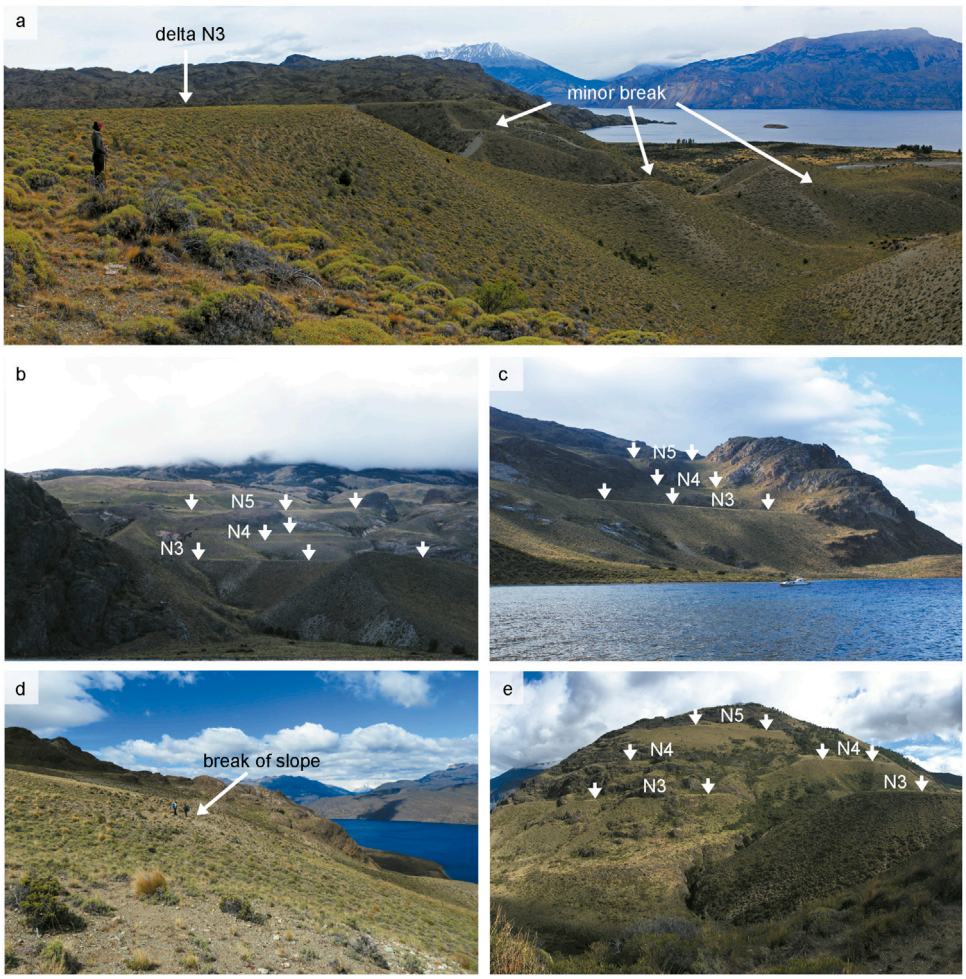

FIGURE 8 | Field photographs from the Río Brown **(A)** and Paso La Leona sectors **(B–E)**. See location in **Supplementary Figure S7**.

to explore trends along the former glacier flowline (**Figure 9**). Second-order polynomial regressions applied to each cluster (N5, N4, and N3) show very strong correlations ($r \geq 0.89$). We observe successively decreasing slopes from the highest to the lowest clusters, which implies that glacio-isostasy has been stronger at higher (and older) than at lower (and younger) levels. Average gradients, between 0 and 100 km (i.e., between the Río Blanco moraines and the western end of the lake) are 1.16, 0.81, and 0.51 m km^{-1} for N5, N4, and N3, respectively. The *y*-intercept of each regression represents the lake level during each phase, i.e, the paleolevel (see equations in **Figure 9**). The orthometric elevations of these are ~485, ~385, and ~295 masl for N5, N4, and N3, respectively. Gradients for N2 and N1 were not calculated owing to the scarcity of morphologies classified within these clusters and the difficulty to identify their brink points. The reconstructions of these phases, therefore, are based on current elevations.

Considering the paleolake reconstructions of phases N5, N4, and N3, together with the inferred ice position, which will be discussed in **Section 5.1**, we estimate water discharges of ~150–200 km^3 for the N5-N4 transition, 100–150 km^3 for the N4-N3, and ~300 km^3 during the N3 drainage.

4.3 Lake Sediment Cores

We retrieved overlapping sediment cores from Lago Maldonado (core series PC0904A, B, and C) from a water depth of 680 cm. Core series PC0904A (**Supplementary Figure S6**) is 13-m long and features a blueish/grey inorganic mud (organic matter <5%) unit between 1,300 and 760 cm depth, with occasional laminations and matrix-supported clasts in the granule and pebble-sized range. This shifts to an organic-rich silty unit at 760 cm through a gradual transition between 760 and 742 cm depth. The organic unit persists with variations in the amount of organic material until the modern water-sediment interface. Seven radiocarbon dates obtained from the lowermost 80 cm of organic sediments yielded a sequence of ages between ~12.2 and ~9 ka (**Table 3**). Four out of five radiocarbon dates obtained in the narrow interval between 759 and 755 cm depth yielded statistically identical ages that produce an error weighted mean age of 9,828 ± 21 ^{14}C yr BP with a median calibrated age of ~11.2 ka. One of them (CAMS-144603) yielded an age of ~12.2 ka that is inconsistent in the context of the stratigraphic sequence, being >3σ older than the enveloping radiocarbon dates UCIAMS-146440 and UCIAMS-146441. Therefore, we consider the age of

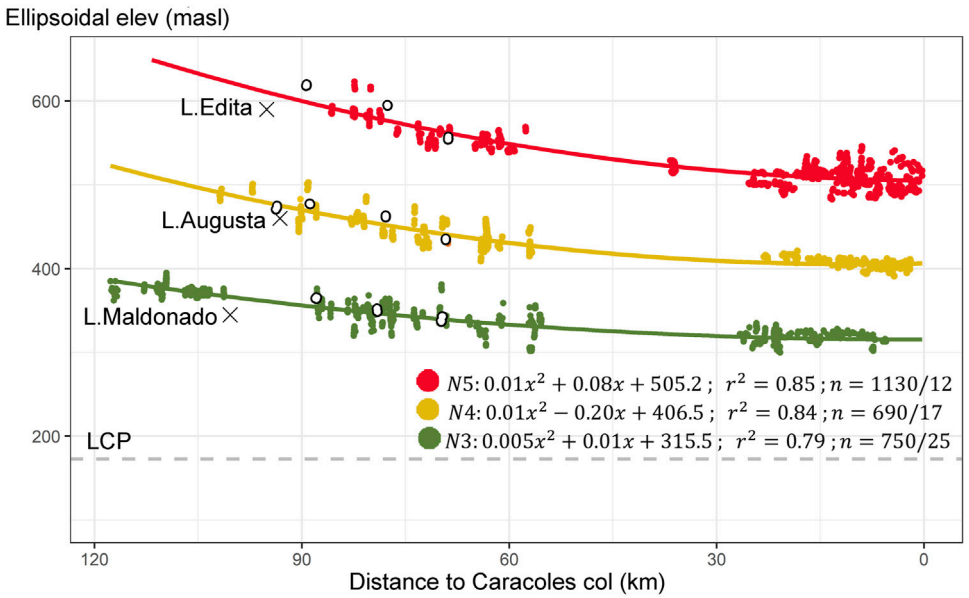

FIGURE 9 | Glacio-isostatic gradients along the flowline of the former LCP glacier lobe. Polynomial regressions are shown with their equations, coefficients of determination, and the total number of points used (*n* = DEM/GNSS). Differential GNSS data are shown as white circles. Elevations in this figure are ellipsoidal and in the text are referred in their orthometric conversion (~20 m lower). Current elevation of LCP shown as dashed line for reference.

TABLE 3 | AMS radiocarbon dates from sediment cores and calibrated ages.

Lake	Lab Code	Material	Depth	$\delta^{13}C$ (‰)	^{14}C yr BP ± 1σ error	2σ range cal BP	Median probability (years)
L. Maldonado	CAMS-144601	Bulk	679	−27	8,100 ± 35	8,772–9,123	8,986
L. Maldonado	CAMS-144602	Bulk	727	−27	9,315 ± 35	10,293–10,577	10,457
L. Maldonado	UCIAMS-146438	Bulk	755	−27	9,840 ± 35	11,176–11,260	11,219
L. Maldonado	UCIAMS-146439	Bulk	756	−27	9,760 ± 45	10,815–11,242	11,155
L. Maldonado	UCIAMS-146440	Bulk	757	−27	9,800 ± 50	10,885–11,262	11,193
L. Maldonado	CAMS-144603[a]	Bulk	758	−27	10,415 ± 40	12,018–12,473	12,260
L. Maldonado	UCIAMS-146441	Bulk	759	−27	9,885 ± 40	11,191–11,315	11,239
L. Edita	UCIAMS-133501	Bulk	660	−27	8,935 ± 25	9,901–10,180	10,033
L. Edita	UCIAMS-133416	Bulk	705	−27	11,350 ± 60	13,108–13,313	13,219
L. Edita	UCIAMS-133417	Bulk	757	−27	13,740 ± 70	16,335–16,883	16,583
L. Edita	UCIAMS-133418	Bulk	795	−27	16,250 ± 90	19,336–19,866	19,566
L. Edita	CAMS-144454	Bulk	795	−27	16,020 ± 50	19,135–19,465	19,298
L. Augusta	CAMS-144596	Bulk	269	−27	8,890 ± 35	9,747–10,168	9,972
L. Augusta	CAMS-144597	Bulk	301	−27	10,225 ± 35	11,722–11,945	11,852
L. Augusta	CAMS-144598	Bulk	325	−27	12,725 ± 35	14,988–15,267	15,132
L. Augusta	CAMS-146711	Bulk	343	−27	12,850 ± 45	15,131–15,513	15,294
L. Augusta	CAMS-144599[a]	Bulk	351	−27	12,785 ± 35	15,061–15,344	15,205
L. Augusta	CAMS-144600	Bulk	359	−27	16,445 ± 45	19,587–19,932	19,764

[a]*We consider this date as an outlier because it is older/younger than contiguous over and underlying dates.*

sample CAMS-144603 as an outlier. A Bayesian age model applied to all the radiocarbon dates in the Lago Maldonado core pinpoints the onset of organic-rich sediments in Lago Maldonado at a median age of ~11.3 ka (2σ range: 11.226–11.345 ka) (**Figure 10**).

Lake sediment cores from Lago Augusta and Lago Edita (Villa-Martínez et al., 2012; Henríquez et al., 2017) show abrupt transitions from high-density blueish/grey inorganic mud (organic matter <5%) to lower-density organic silts similar to that observed in Lago Maldonado. The exact onset of organic sedimentation in Lago Edita is constrained by two accelerator mass spectrometry (AMS) dates (UCIAMS-133418, CAMS-144454) succeeded by progressively younger dates further up in the stratigraphy. The age model estimate for this irreversible transition is ~19.3 ka (2σ range: 19.5–19 ka) (**Figure 10**). In the case of Lago Augusta the shift from glaciolacustrine mud is constrained by one AMS date (CAMS-144600), overlain by one anomalously young date (CAMS-144599) located 8 cm

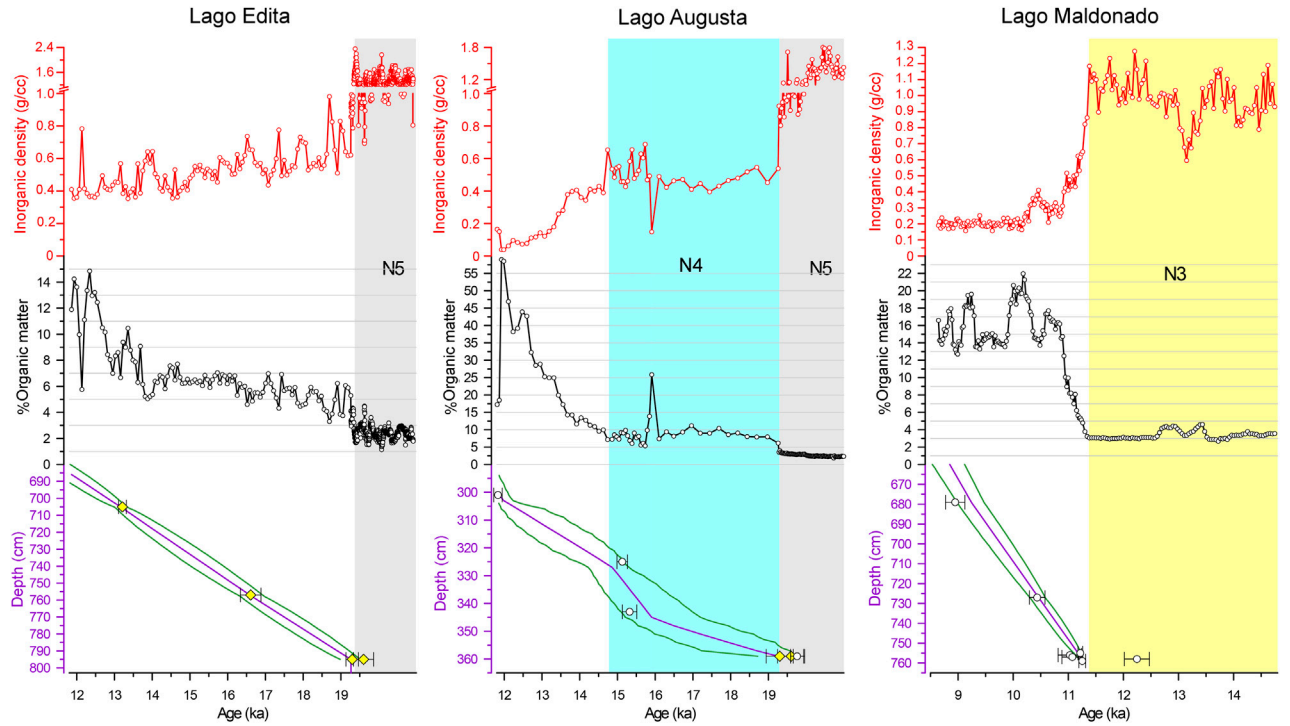

FIGURE 10 | Inorganic density, organic percentage, and age model from the Lago Edita, Lago Augusta, and Lago Maldonado records. The magenta line (lower panel) represents the median probability of the interpolated age, the green lines indicate the 95% confidence interval. The white circles in the lower panels indicate the median probability of the calibrated age for each radiocarbon date, the black horizontal bars represent the 95% confidence interval for each calibrated date. The yellow-filled diamonds represent the calibrated radiocarbon dates from Lago Edita. Notice that the age model from Lago Augusta includes an *in-situ* obtained radiocarbon date and the correlated basal radiocarbon dates from Lago Edita. The time intervals N5, N4, and N3 are shown as shaded rectangles.

above, and several AMS dates in stratigraphic order further up in the section. A Bayesian age model that excludes CAMS-144599 and incorporates CAMS-144600 along with the basal Lago Edita AMS dates mentioned above, yielded an interpolated age of ~19.3 ka (2σ range: 19.6–18.7 ka) for the end of the basal inorganic mud. Light brown/yellowish low-density organic silts with plant macrofossils persist in the Lago Augusta record until 343 cm (mean organic content: 10.3%), followed by a shift to higher-density grey organic silts without plant macrofossils until 325 cm (mean organic content: 7.7%). From that point onward the inorganic density of the sediments declines and their organic content increases steadily to a maximum of 60% at ~11.9 ka. The reversal to grey inorganic mud is bracketed by radiocarbon dates CAMS-144598 and CAMS-146711, and age model-based interpolations of ~15.8 ka (2σ range: 16.9–15.1 ka) and ~14.8 ka (2σ range: 15.2–13.9 ka) for its onset and termination, respectively (**Figure 10**).

5 DISCUSSION

5.1 Evaluation of Paleo-Shorelines and Paleolake Reconstructions

We clustered the landforms in six groups according to their elevation, numbered N5 to N0 from highest to lowest, with N0 corresponding to the modern active deltas (**Section 4.1**). These clusters attest to at least five ancient phases of stabilization of GLC, which occupied the LCP basin following glacier withdrawal from the Río Blanco moraines.

Landforms grouped in N5 are present on the northern and southern valley walls surrounding the LCP basin (**Figures 2**, **3**), with its westernmost position found at the Dos Arroyos sector. This distribution suggests that the LCP glacier lobe receded ~95 km from the Río Blanco moraines, stabilized and established an effective dam for the development of GLC west of Dos Arroyos (**Figure 11A**). The reconstruction of paleolevel N5 shows that LCP and Valle Chacabuco were connected through the Puesto Tejuela col (580 masl), as stated originally by Glasser et al. (2016). This is in agreement with the findings reported by Henriquez et al. (2017), who observed exposed glaciolacustrine beds and lake terrace fragments (590 masl) around Lago Edita, documenting the highest-elevation proglacial lake phase in this area. Drainage of GLC during this phase must have occurred through the easternmost spillway of the basin, the Caracoles col (480 masl), toward the Atlantic Ocean.

N4 landforms are widespread from the Río Blanco moraines to the western end of LCP, with its westernmost position at La Ponderosa (**Figures 2**, **3**), which suggests that the LCP Glacier Lobe retreated and stood just west of this sector by this time (**Figure 11B**). This phase began with a water level drop of ~100 m

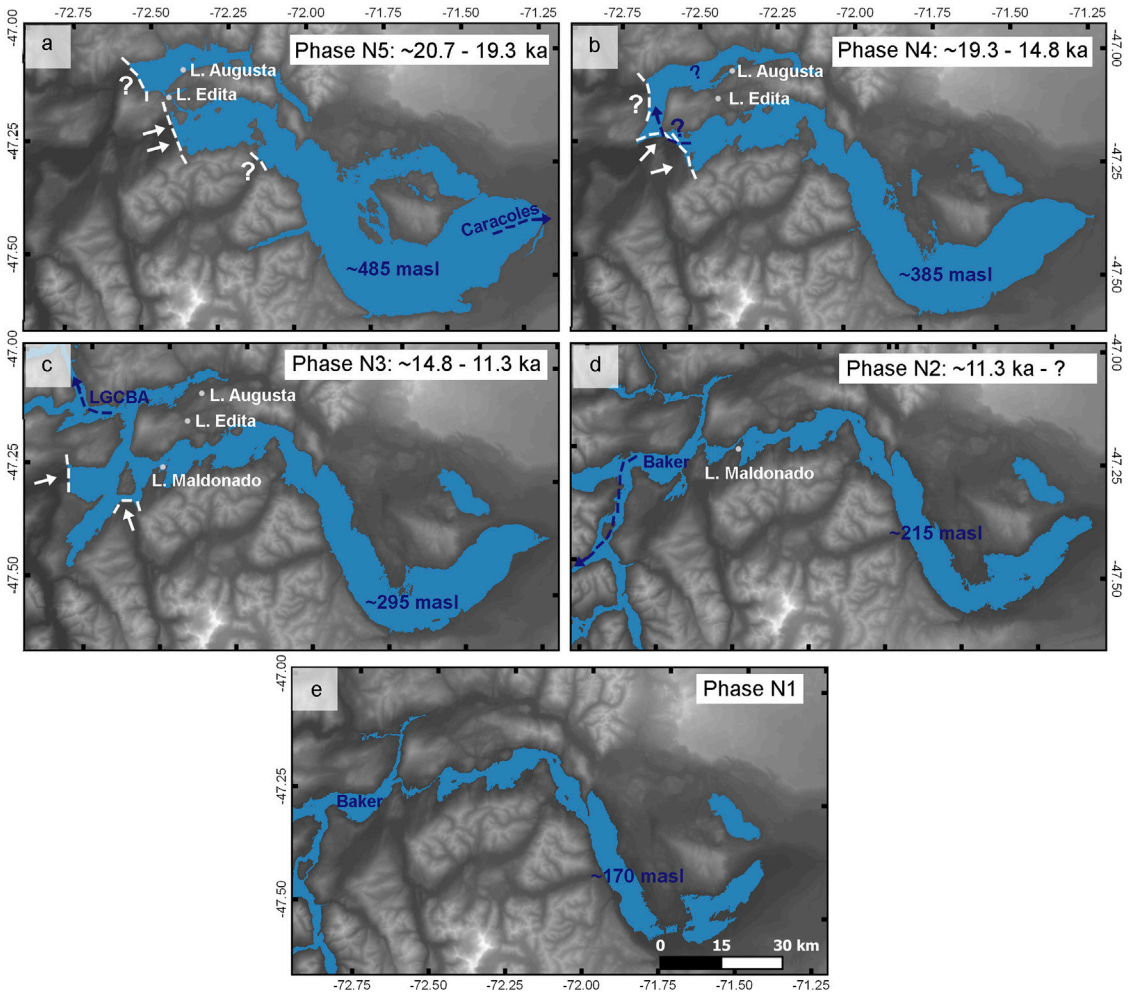

FIGURE 11 | Summary of the main phases proposed for the evolution of GLC. White dashed lines show inferred ice positions. Blue dashed lines show possible drainage routes. Paleolevels are shown in blue text. N5 to N3 phases **(A–C)** show glacio-isostatically corrected landscapes. N2 and N1 reconstructions **(D,E)** are based on current elevations.

from N5 to N4, which may represent an ice dam rupture or, alternatively, thinning and recession of the damming ice front. The N4 paleolevel reconstruction (**Figure 11B**) shows that GLC ceased to inundate Valle Chacabuco through the Puesto Tejuela col after the N5 phase and, likewise, ceased to drain through Caracoles col. We also note a ~1.7 km long shoreline on the western side of Cerro Tamango within the elevation range of the N4 cluster (**Figure 3**), indicating continuity of GLC between Valle Chacabuco and the LCP basin through this short portion of Valle Río Baker.

N3 landforms are the most ubiquitous and extensive around LCP, suggesting that they formed during an extended period of lake stability, and/or the fluvial discharge and sediment load was higher during this phase. Landforms associated with this level are abundant along the adjacent portion of Valle Río Baker, suggesting local ice-free conditions during this interval (**Figure 11C**). Considering the distribution of N3 landforms, we infer that the damming glacier bodies must have lain downstream from LCP along the modern drainage system, potentially by the expanded Colonia and Calluqueo glaciers (**Figure 1**).

Geomorphic features clustered in N2 and N1 are very sparse and small, suggesting that these represent minor events during the late phases of GLC. The relatively small difference in their current elevations (N2: 230–220, N1: 180–170 masl) suggests ephemeral stabilizations in lake level during the regressive phase following N3. Considering the slight difference in elevation with the modern lake, it is likely that the current drainage configuration was achieved during these phases (**Figures 11D,E**).

5.2 Isostatic Adjustments

Glacio-isostatic uplift results are presented in **Figure 9**, and yield average gradients of 1.16, 0.81, and 0.51 m km^{-1}, for N5, N4, and N3 levels, respectively. The variability of elevations within each level is probably associated with the effects of glacio-isostatic

rebound, the erosion over the brink points, the imprecision of ALOS PALSAR DEMs, and the difficulties involved in recognizing brink points in areas not visited during fieldwork. In the Dos Arroyos sector (where morphologies are best preserved), we find that the uplift due to glacio-isostasy reaches ~115 m for the N5 delta, ~70 m for the N4 delta, and ~50 m for the N3 delta (this is considering the paleolevel of each phase vs. their current elevation).

5.3 Timing of Events

In this section we assess the age of the lake marginal features associated to GLC through comparisons with radiocarbon and exposure-age dated lacustrine and glacial features in and around the study area. The innermost Río Blanco moraines (Hein et al., 2010) have a recalculated mean age of 20.7 ± 1.3 ka ($n = 3$), which constitutes a maximum limiting constraint for the N5 level. A minimum limiting age for this level is afforded by the radiocarbon-dated transition from glaciolacustrine mud to organic lake sediments at ~19.3 ka in Lago Edita (570 masl, GNSS) (Henríquez et al., 2017), which was flooded by GLC during the N5 phase. Lago Edita became isolated from GLC during the regressive glaciolacustrine phase that led to the N4 phase of GLC, attesting to the end of flooding of the Puesto Tejuela col.

The age for the cessation of glaciolacustrine influence in Lago Augusta at ~19.3 ka (Villa-Martínez et al., 2012; Henríquez et al., 2017) is statistically identical to the age from Lago Edita. Unlike Lago Edita, however, Lago Augusta is located in Valle Chacabuco at 440 masl (GNSS). These findings imply a synchronous cessation of glaciolacustrine flooding in the highest section of Valle Chacabuco and Puesto Tejuela col by the end of the N5 phase. The stratigraphy from Lago Augusta indicates a subsequent transgressive glaciolacustrine phase in Valle Chacabuco between ~15.8–14.8 ka. Together these results imply that: 1) the glaciolacustrine regressive phase following N5 must have reached elevations below 440 masl in Valle Chacabuco after ~19.3 ka, and 2) the subsequent transgressive phase of Valle Chacabuco must have started from elevations below ~440 masl before ~15.8 ka.

Considering our N4 reconstruction, it is possible that GLC remained separated from and slightly higher than the Chacabuco glacial lake at the beginning of the N4 phase, probably by an ice dam west to Cerro Tamango (**Figure 11B**). Glaciolacustrine transgression of Valle Chacabuco during N4 might have occurred through hydraulic continuity with GLC through the damming ice body (englacially) and/or by slight recession and thinning of the ice dam. Rising Chacabuco glacial lake levels reached and surpassed the elevation of closed-basin Lago Augusta, depositing the grey organic silts without plant macrofossils. This persisted until ~14.8 ka followed by a reversal back to organic-rich lake sediments in the Lago Augusta sediment cores, thus affording a minimum limiting age for the culmination of the N4 phase.

The N3 phase in the evolution of GLC is constrained by two OSL dates that yielded a weighted mean age of 14.8 ± 1.1 ka for the construction of the thickest and most extensive delta in the Dos Arroyos sector. The OSL dates inform us of the timing of construction of the delta front, which does not necessarily imply a close limiting age estimate for the beginning or end of this geomorphic feature. We note, however, that our chronology for the end of the N4 flooding of Lago Augusta is indistinguishable from the weighted mean age of the Dos Arroyos N3 delta. Our radiocarbon dates from Lago Maldonado, located at a current elevation of 325 masl (GNSS) and ~12 km west of the N3 delta front in Dos Arroyos, afford a minimum limiting age of ~11.3 ka for a regressive phase of GLC after the deposition of the N3 landforms. This independent minimum age constraint is coherent and compatible with the young confidence age limit of the OSL age. Combining these dates, we interpret that the N3 phase must have taken place between ~14.8–11.3 ka (**Figure 11C**). Drainage of GLC after ~11.3 ka was punctuated by brief stabilizations marked by the N2 and N1 deltas in the Dos Arroyos sector, for which chronologic data is currently unavailable.

5.4 Regional Implications

In this section we compare our reconstruction of the evolution of GLC with previous studies in the LGCBA, Valle Río Baker, and sectors adjacent to LCP.

(1) Our reconstruction of paleolevels in the LCP basin distinguishes three main stages between ~20.7–11.3 ka, named N5, N4, and N3 phases. These reconstructions consider the elevation of more than 500 landforms and glaciolacustrine deposits along the flowline of the former LCP ice lobe. Although we followed a similar procedure to that reported by Thorndycraft et al. (2019), our results indicate larger-magnitude uplift estimates in the western sector, with average gradients of 1.16, 0.81, and 0.51 m km^{-1} for N5, N4, and N3, respectively. Thorndycraft et al. (2019), in contrast, reported average gradients of 0.78, 0.65, and 0.51 m km^{-1} for the equivalent paleolevels. We note an important difference for N5 and N4 which, according to our observations, emerges from the selection of landforms made by the different authors and the distinct elevation datasets used. Our study uses a combination of GNSS data with ALOS PALSAR DEM, which yielded higher precision results than ASTER G-DEM (used by Thorndycraft et al. (2019)), and a more accurate basis for the correct delineation of geomorphic features and extraction of their elevation data.

(2) Glacial withdrawal and rapid recession of the LCP ice lobe from the Río Blanco moraines occurred between ~20.7–19.3 ka (N5 phase), which differs from the ~18 ka age estimate for the LGCBA lobe (Bendle et al., 2017). This implies that the LCP glacier lobe abandoned the LGM moraines ~2,700 years earlier and retreated much faster than the LGCBA lobe, most likely driven by intense calving. The LCP glacier lobe then stabilized in a position ~50% from its final LGM extent and featured a much slower, step-wise recession through the remainder of T1.

(3) We consider the onset of organic sedimentation in small closed-basin lakes Lago Edita and Lago Augusta at ~19.3 ka

as the decisive marker for the termination of the N5 phase. In addition, this transition constitutes a maximum age for the emplacement of the N4 landforms and deposits. This implies that the 16.2 ± 0.5 ka age from the María Elena moraine (450–600 masl) (Boex et al., 2013), located adjacent to Lago Augusta on the Valle Chacabuco floor, should be considered as a minimum age estimate for local ice-free conditions. Shielding by the proglacial lake, shown in the paleolevel reconstructions, and potential exhumation may account for these anomalously young cosmogenic ages. Thorndycraft et al.'s (2019) model for the lake evolution did not take into account these constraints and interpretations, diverging from our reconstruction.

(4) The elevation, extent, and age of the GLC N3 phase are equivalent to Turner et al.'s (2005) Lower United Lake phase and "Lago Chalenko" in Thorndycraft et al.'s (2019) terminology. Our results suggest that N3 landforms developed between ~14.8–11.3 ka, an interval within which Soler glacier abandoned the Lago Bertrand moraine LBM3 (14.0 ± 0.5 ka) (Davies et al., 2018), permitting the connection between LCP and LGCBA through the upper Valle Río Baker. We note that the ~95% confidence interval for LBM3 (15–13 ka) overlaps with the confidence interval for our maximum limiting age estimate for the beginning of N3 (15.2–13.9 ka) and thus, are statistically indistinguishable. This supports that the connection between LGCBA and LCP basins started with the shrinking of the Soler glacier, as proposed by Thorndycraft et al. (2019).

(5) Turner et al. (2005) reported eleven radiocarbon dates aimed at constraining the chronology of the Lower United Lake phase. They deduced a minimum limiting age constraint of ~12.8 ka, considering radiocarbon dates from shoreline sediments and minimum limiting ages from kettle holes. This estimate is ~1,500 years older than the transition from glaciolacustrine to organic mud in Lago Maldonado. Unlike the results reported by Turner et al. (2005), the elevation and age estimates from Lago Maldonado are robust and precise, based on geodetic GNSS measurements with a vertical error of ±70 cm, and dating of autochthonous organic matter produced within a small closed-basin lake environment, in the context of a complete stratigraphic record from the onset of ice-free conditions until the present that shows a gradual and comformably lain transition from glaciolacustrine to organic mud. Moreover, our age estimate is constrained by multiple, statistically indistinguishable AMS radiocarbon dates sampled from contiguous and narrow stratigraphic interval immediately above the cessation of glaciolacustrine deposition, as Lago Maldonado detached from a lowering GLC during the abandonment of the N3 level. We attribute the divergence with Turner et al.'s (2005) estimate to imprecisions related to single radiocarbon dating measurements from each site, intersite variability, and differences in the elevation and diagnostic value of kettle holes to constrain lake-level fluctuations which, by definition are located on morainal topography which do not necessarily constitute prime locations for monitoring lake-level changes.

(6) The N3 glaciolacustrine phase provides the timing and context for the subaqueous deposition of the Salto and Esmeralda moraines (**Figure 3**). Davies et al. (2018) reported a date of 12.5 ± 0.4 ka (recalculated) for the Salto moraine at 359 masl, and a mean age of 13.0 ± 0.4 ka (n = 5, recalculated) (**Supplementary Table S1**) for the Esmeralda moraines (360–520 masl). These authors also reported paleoshorelines carved on their proximal and distal slopes at ~350 masl. The depositional setting and ages for these moraines are coherent with our findings from LCP.

(7) According to Thorndycraft et al. (2019) the end of the Lower United Lake/Chalenko phase occurred between ~12.4–11.8 ka, an inference based on one radiocarbon date reported by Turner et al. (2005) from a kettle hole in El Maitén (geographical location poorly constrained) and six cosmogenic exposure ages, originally reported by Glasser et al. (2012), that they reinterpreted as boulders that were shielded by the water column of the Lower United Lake. This minimum limiting age estimate is significantly older than our interpretation from Lago Maldonado which, as discussed in previous paragraphs, we consider robust and precise.

(8) We estimate water discharges of ~150–200 km^3 for the N5-N4 transition, 100–150 km^3 for the N4-N3, and ~300 km^3 during the N3 drainage. The latter estimate assumes that LCP and LGCBA were connected during the Lower United phase. Our estimate is in broad agreement with Thorndycraft et al.'s (2019) Stage 7, with an estimated water volume of 312 km^3 during the drainage of their Lago Chalenko stage.

(9) Benito and Thorndycraft (2020) interpreted catastrophic floods from the geomorphological and sedimentological evidence presented in the middle Valle Baker, such as gravel and sand bars, antidune landforms, and erosional evidence. Some of these sites are located downstream from Río Cochrane, at elevations ranging from ~170–100 masl. We speculate that these floods might be related to transitions between the ephemeral N2 and N1 phases of GLC.

(10) Glasser et al.'s (2016) timing and structure of changes in glacial lake development in this area is incompatible with our findings in terms of chronology. Their stage A, potentially equivalent to our N5 phase, is dated at ~13.8–11.5 ka on the basis of cosmogenic ages from Lago Tranquilo, Lago Negro, and the valley mouths from Valle Leones and Valle Chacabuco, originally published by Glasser et al. (2006) and Glasser et al. (2012). For reference, our N5 phase is constrained between ~20.7–19.3 ka. Moreover, Glasser et al. (2016) place the termination of the Lower United Lake at 8.5 ± 0.9 ka, based on OSL samples from sites located around LGCBA. Our estimate for the end of N3, equivalent to Turner et al.'s (2005) Lower United Lake phase, is ~11.3 ka (2σ range: 11.3–11.2 ka). We observe that their modeled effect of

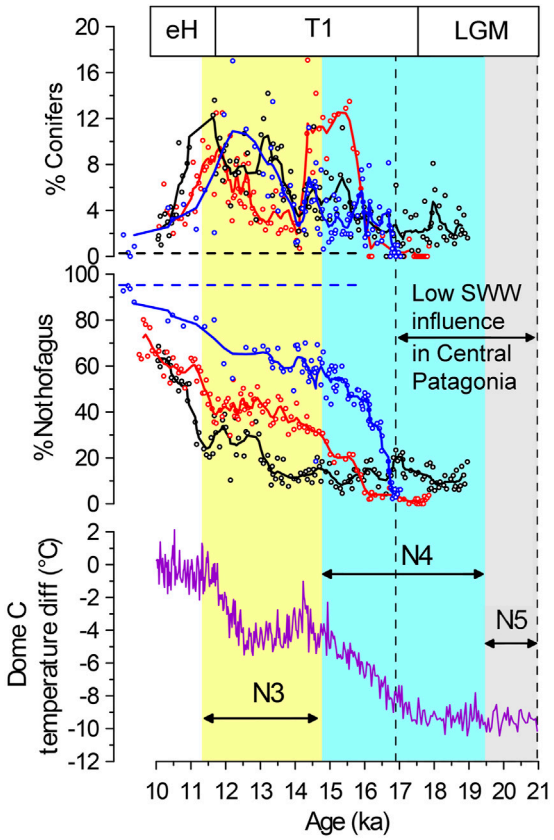

FIGURE 12 | Palynological record from Lago Mellizas (blue line), Lago Edita (black line), and Lago Unco (red line). Curves represent weighted moving averages. Black and blue dashed lines represent the Conifers and *Nothofagus* average during the last 10,000 years, respectively. The bottom panel shows the temperature variations recorded in the Dome C ice core, Antarctica. The time intervals N5, N4, and N3 are shown as shaded rectangles.

freshwater hosing from the PIS into the SE Pacific Ocean between ~13.8–8.5 ka must be reassessed in the context of the new evidence reported in this study (timing, duration, and volume).

5.5 Climatic Implications

The pollen record from Lago Edita (Henríquez et al., 2017), along with the L. Unco and L. Mellizas sites (Vilanova et al., 2019; Villa-Martínez and Moreno, 2021) from the Coyhaique area, located ~200 km north of LCP (**Figure 1**), afford valuable information for examining the climatic context in which the LCP deltas were built (**Figure 12**). These pollen sites indicate warming at ~17.9 ka and an increase in precipitation brought by stronger SWW influence in pulses centered at ~16.6 and ~14.8 ka. Cool-temperate and hyper humid conditions persisted between ~14.8–11.7 ka, spanning the Antarctic Cold Reversal (ACR) and Younger Dryas (YD) chonozones, followed by warming and decline in SWW influence during the early Holocene (~11.7–9.4 ka). Based on these findings, we interpret that the large volume of the N3 deltas in LCP represents a combination of factors including a ~3,500-year long period of GLC stability brought by cool-temperate conditions, enhanced sediment supply by increased precipitation, and profuse snow and ice melting driven by air temperatures higher than during the LGM and early T1. This climatic scenario differs from the cold and dry conditions that prevailed during the formation of the N5 deltas in LCP, constrained between ~20.7–19.3 ka, and the relatively temperate, and intermediate-precipitation N4 phase constrained between ~19.3–14.8 ka. We note that the end of the N3 phase at ~11.3 ka occurred shortly after the warm pulse and decline in SWW influence that initiated the Holocene at pan Patagonian scale (~11.7 ka) (Moreno et al., 2021).

6 CONCLUSION

(1) GLC stabilized multiple times above the modern elevation of Lago Cochrane (~150 masl) during the T1. We recognize five clusters of shoreline features at ~600–500 (N5), ~470–400 (N4), ~360–300 (N3), ~230–220 (N2), and ~180–170 masl (N1). We estimate new glacio-isostatic gradients and generated isostatically corrected surfaces of the distinct phases of GLC. From these results we estimate uplifts of ~150, ~70, and ~50 m for the N5, N4, and N3 deltas, respectively, in the Dos Arroyos sector.

(2) During the N5 phase GLC was connected to Valle Chacabuco through the Puesto Tejuela col and drained towards the Atlantic Ocean through the Caracoles col. Cosmogenic dates of 20.7 ± 1.3 ka from the innermost Río Blanco moraines afford a maximum limiting age constraint for the N5 phase. A minimum limiting age constraint comes from basal radiocarbon dates from Lago Edita and Lago Augusta, which afford an age of ~19.3 ka.

(3) The surface elevation of GLC dropped ~100 m after ~19.3 ka, below the elevation of Caracoles and Puesto Tejuela cols. This event could represent an ice dam rupture or a lake level decline driven by thinning and recession of the damming ice front. The distribution of N4 landforms suggests that the ice dam was positioned at the westernmost end of LCP against Cerro Tamango. The Lago Augusta stratigraphic record suggests that the Chacabuco and Cochrane glacial lakes could have remained independent of each other at the beginning of the N4 phase and were eventually reconnected by drainage from the LCP basin, causing a transgressive glaciolacustrine phase in Valle Chacabuco. A subsequent regressive glaciolacustrine phase in Lago Augusta affords a minimum limiting age of ~14.8 ka for the end of the N4 phase.

(4) The N3 landforms are widely distributed in the LCP basin and Valle Río Baker attesting to a major glacier retreat phase. We constrain its chronology with a maximum limiting age of ~14.8 ka from Lago Augusta, two OSL dates that yielded a weighted mean age of 14.8 ± 1.1 ka for the construction of the N3 delta at Dos Arroyos, and a minimum limiting age of ~11.3 ka from Lago Maldonado. Our N3 phase in the LCP basin represents the local expression of the Lower United

Lake or Chalenko phase, made possible by recession of the Soler glacier from the Lago Bertrand moraines.

(5) We infer the opening of the lower Valle Río Baker and the irreversible establishment of the current drainage setting shortly before ~11.3 ka. The subsequent N2 and N1 phases represent ephemeral stabilization events related probably to moraine collapses.

(6) We observe that the N3 landforms are the most ubiquitous, well-preserved, and largest morphologies in the study area, aspects that may represent an extended period of glacial lake stability, enhanced sediment supply by increased precipitation, and profuse snow and ice melting driven by temperate conditions between ~14.8–11.3 a. This climatic scenario differs from the colder and drier conditions that prevailed during the N4 and N5 phases between ~20.7–14.8 ka. The end of the N3 phase occurred shortly after a warm pulse and decline in precipitation at ~11.7 ka that initiated the Holocene at western Patagonian scale.

DATA AVAILABILITY STATEMENT

The raw data supporting the conclusion of this article will be made available by the authors, without undue reservation.

AUTHOR CONTRIBUTIONS

AV: Conceptualization, methodology, investigation, visualization, writing—original draft preparation. VF-A: Conceptualization, methodology, writing—review and editing. ES: Conceptualization, writing—review and editing. RH: Methodology. RV-M: writing—review and editing. PM: Conceptualization, methodology, formal analysis, visualization, writing—review and editing. JL: Methodology.

FUNDING

This work was funded by Iniciativa Científica Milenio NC120066, FONDECYT 1180815 (RV-M), and FONDECYT 1191942 (VF-A).

ACKNOWLEDGMENTS

We thank D. Briones, M. Martini, L. Guerra, E. Fercovic, and V. Rivillo for providing field assistance, and A. Arancibia for GNSS data processing. Our appreciation goes to O. Pesce, W. Henríquez, and I. Jara for providing coring assistance. We thank T. Guilderson, R. De Pol, and J. Southon for their contributions to the development of radiocarbon dates from Lago Maldonado.

SUPPLEMENTARY MATERIAL

The Supplementary Material for this article can be found online at: https://www.frontiersin.org/articles/10.3389/feart.2022.817775/full#supplementary-material

REFERENCES

Anderson, R. F., Ali, S., Bradtmiller, L. I., Nielsen, S. H. H., Fleisher, M. Q., Anderson, B. E., et al. (2009). Wind-Driven Upwelling in the Southern Ocean and the Deglacial Rise in Atmospheric CO 2. *Science* 323 (5920), 1443–1448. doi:10.1126/science.1167441

Balco, G., Stone, J. O., Lifton, N. A., and Dunai, T. J. (2008). A Complete and Easily Accessible Means of Calculating Surface Exposure Ages or Erosion Rates from 10Be and 26Al Measurements. *Quat. Geochronol.* 3 (3), 174–195. doi:10.1016/j.quageo.2007.12.001

Bell, C. M. (2008). Punctuated Drainage of an Ice-dammed Quaternary lake in Southern South america. *Geografiska Annaler: Ser. A, Phys. Geogr.* 90 (1), 1–17. doi:10.1111/j.1468-0459.2008.00330.x

Bendle, J. M., Palmer, A. P., Thorndycraft, V. R., and Matthews, I. P. (2017). High-resolution Chronology for Deglaciation of the Patagonian Ice Sheet at Lago Buenos Aires (46.5°S) Revealed through Varve Chronology and Bayesian Age Modelling. *Quat. Sci. Rev.* 177, 314–339. doi:10.1016/j.quascirev.2017.10.013

Benito, G., and Thorndycraft, V. R. (2020). Catastrophic Glacial-lake Outburst Flooding of the Patagonian Ice Sheet. *Earth-Science Rev.* 200, 102996. doi:10.1016/j.earscirev.2019.102996

Blaauw, M., and Christen, J. A. (2011). Flexible Paleoclimate Age-Depth Models Using an Autoregressive Gamma Process. *Bayesian Anal.* 6 (3), 457–474. doi:10.1214/11-BA618

Boex, J., Fogwill, C., Harrison, S., Glasser, N. F., Hein, A., Schnabel, C., et al. (2013). Rapid Thinning of the Late Pleistocene Patagonian Ice Sheet Followed Migration of the Southern Westerlies. *Sci. Rep.* 3 (1), 1–6. doi:10.1038/srep02118

Bourgois, J., Cisternas, M. E., Braucher, R., Bourlès, D., and Frutos, J. (2016). Geomorphic Records along the General Carrera (Chile)-Buenos Aires (Argentina) Glacial Lake (46°-48°S), Climate Inferences, and Glacial Rebound for the Past 7-9 Ka. *J. Geology.* 124 (1), 27–53. doi:10.1086/684252

Caldenius, C. C. z. (1932). Las Glaciaciones Cuaternarias en la Patagonia y Tierra del Fuego. *Geografiska Annaler* 14 (1-2), 1–164. doi:10.2307/519583

Clark, P. U., Dyke, A. S., Shakun, J. D., Carlson, A. E., Clark, J., Wohlfarth, B., et al. (2009). The Last Glacial Maximum. *Science* 325 (59411), 710–714. doi:10.1126/science.1172873

Davies, B. J., Darvill, C. M., Lovell, H., Bendle, J. M., Dowdeswell, J. A., Fabel, D., et al. (2020). The Evolution of the Patagonian Ice Sheet from 35 Ka to the Present Day (PATICE). *Earth-Science Rev.* 204, 103152. doi:10.1016/j.earscirev.2020.103152

Davies, B. J., Thorndycraft, V. R., Fabel, D., and Martin, J. R. V. (2018). Asynchronous Glacier Dynamics during the Antarctic Cold Reversal in central Patagonia. *Quat. Sci. Rev.* 200, 287–312. doi:10.1016/j.quascirev.2018.09.025

Denton, G. H., Anderson, R. F., Toggweiler, J. R., Edwards, R. L., Schaefer, J. M., and Putnam, A. E. (2010). The Last Glacial Termination. *Science* 328 (5986), 1652–1656. doi:10.1126/science.1184119

Douglass, D., Singer, B., Kaplan, M., Mickelson, D., and Caffee, M. (2006). Cosmogenic Nuclide Surface Exposure Dating of Boulders on Last-Glacial and Late-Glacial Moraines, Lago Buenos Aires, Argentina: Interpretive Strategies and Paleoclimate Implications. *Quat. Geochronol.* 1 (1), 43–58. doi:10.1016/j.quageo.2006.06.001

Durcan, J. A., King, G. E., and Duller, G. A. T. (2015). DRAC: Dose Rate and Age Calculator for Trapped Charge Dating. *Quat. Geochronol.* 28, 54–61. doi:10.1016/j.quageo.2015.03.012

Galbraith, R. F., Roberts, R. G., Laslett, G. M., Yoshida, H., and Olley, J. M. (1999). Optical Dating of Single and Multiple Grains of Quartz from Jinmium Rock Shelter, Northern Australia: Part I, Experimental Design and Statistical Models. *Archaeometry* 41 (2), 339–364. doi:10.1111/j.1475-4754.1999.tb00987.x

Glasser, N. F., Harrison, S., Ivy-Ochs, S., Duller, G. A. T., and Kubik, P. W. (2006). Evidence from the Rio Bayo valley on the Extent of the North Patagonian Icefield during the Late Pleistocene-Holocene Transition. *Quat. Res.* 65 (1), 70–77. doi:10.1016/j.yqres.2005.09.002

Glasser, N. F., Harrison, S., Schnabel, C., Fabel, D., and Jansson, K. N. (2012). Younger Dryas and Early Holocene Age Glacier Advances in Patagonia. *Quat. Sci. Rev.* 58, 7–17. doi:10.1016/j.quascirev.2012.10.011

Glasser, N. F., Jansson, K. N., Duller, G. A. T., Singarayer, J., Holloway, M., and Harrison, S. (2016). Glacial lake Drainage in Patagonia (13-8 Kyr) and Response of the Adjacent Pacific Ocean. *Sci. Rep.* 6 (1), 1–7. doi:10.1038/srep21064

Glasser, N. F., Jansson, K. N., Harrison, S., and Kleman, J. (2008). The Glacial Geomorphology and Pleistocene History of South America between 38°S and 56°S. *Quat. Sci. Rev.* 27 (3–4), 365–390. doi:10.1016/j.quascirev.2007.11.011

Hein, A. S., Hulton, N. R. J., Dunai, T. J., Sugden, D. E., Kaplan, M. R., and Xu, S. (2010). The Chronology of the Last Glacial Maximum and Deglacial Events in central Argentine Patagonia. *Quat. Sci. Rev.* 29 (9–10), 1212–1227. doi:10.1016/j.quascirev.2010.01.020

Heiri, O., Lotter, A. F., and Lemcke, G. (2001). Loss on Ignition as a Method for Estimating Organic and Carbonate Content in Sediments: Reproducibility and Comparability of Results. *J. Paleolimnology* 25, 101–110. doi:10.1023/A:1008119611481

Henríquez, W. I., Villa-Martínez, R., Vilanova, I., de Pol-Holz, R., and Moreno, P. I. (2017). The Last Glacial Termination on the Eastern Flank of the central Patagonian Andes (47 ° S). *Clim. Past* 13 (7), 879–895. doi:10.5194/cp-13-879-2017

Hogg, A. G., Heaton, T. J., Hua, Q., Palmer, J. G., Turney, C. S., Southon, J., et al. (2020). SHCal20 Southern Hemisphere Calibration, 0-55,000 Years Cal BP. *Radiocarbon* 62 (4), 759–778. doi:10.1017/RDC.2020.59

Hubbard, A., Hein, A. S., Kaplan, M. R., Hulton, N. R. J., and Glasser, N. (2005). A Modelling Reconstruction of the Last Glacial Maximum Ice Sheet and its Deglaciation in the Vicinity of the Northern Patagonian Icefield, South America. *Geografiska Annaler: Ser. A, Phys. Geogr.* 87 (2), 375–391. doi:10.1111/j.0435-3676.2005.00264.x

Kaplan, M. R., Strelin, J. A., Schaefer, J. M., Denton, G. H., Finkel, R. C., Schwartz, R., et al. (2011). *In-situ* Cosmogenic 10Be Production Rate at Lago Argentino, Patagonia: Implications for Late-Glacial Climate Chronology. *Earth Planet. Sci. Lett.* 309 (1–2), 21–32. doi:10.1016/j.epsl.2011.06.018

Lal, D. (1991). Cosmic ray Labeling of Erosion Surfaces: *In Situ* Nuclide Production Rates and Erosion Models. *Earth Planet. Sci. Lett.* 104 (2–4), 424–439. doi:10.1016/0012-821X(91)90220-C

Lamy, F., Kaiser, J., Arz, H. W., Hebbeln, D., Ninnemann, U., Timm, O., et al. (2007). Modulation of the Bipolar Seesaw in the Southeast Pacific during Termination 1. *Earth Planet. Sci. Lett.* 259 (3–4), 400–413. doi:10.1016/j.epsl.2007.04.040

Lifton, N., Smart, D. F., and Shea, M. A. (2008). Scaling Time-Integrated *In Situ* Cosmogenic Nuclide Production Rates Using a Continuous Geomagnetic Model. *Earth Planet. Sci. Lett.* 268 (1–2), 190–201. doi:10.1016/j.epsl.2008.01.021

Moreno, P. I., Henríquez, W. I., Pesce, O. H., Henríquez, C. A., Fletcher, M. S., Garreaud, R. D., et al. (2021). An Early Holocene westerly Minimum in the Southern Mid-latitudes. *Quat. Sci. Rev.* 251, 106730. doi:10.1016/j.quascirev.2020.106730

Moreno, P. I., Videla, J., Valero-Garcés, B., Alloway, B. v., and Heusser, L. E. (2018). A Continuous Record of Vegetation, Fire-Regime and Climatic Changes in Northwestern Patagonia Spanning the Last 25,000 Years. *Quat. Sci. Rev.* 198, 15–36. doi:10.1016/j.quascirev.2018.08.013

Murray, A. S., and Wintle, A. G. (2000). Luminescence Dating of Quartz Using an Improved Single-Aliquot Regenerative-Dose Protocol. *Radiat. Measurements* 32 (1), 57–73. doi:10.1016/S1350-4487(99)00253-X

Murray, A. S., and Wintle, A. G. (2003). The Single Aliquot Regenerative Dose Protocol: Potential for Improvements in Reliability. *Radiat. Measurements* 37 (4–5), 377–381. doi:10.1016/S1350-4487(03)00053-2

R Core Team (2020). *R: A Language and Environment for Statistical Computing*. Vienna, Austria: R Foundation for Statistical Computing. Available at: https://www.R-project.org/.

Rabassa, J., and Clapperton, C. M. (1990). Quaternary Glaciations of the Southern Andes. *Quat. Sci. Rev.* 9 (2-3), 153–174. doi:10.1016/0277-3791(90)90016-4

Stone, J. O. (2000). Air Pressure and Cosmogenic Isotope Production. *J. Geophys. Res.* 105 (B10), 23753–23759. doi:10.1029/2000JB900181

Stuiver, M., Reimer, P. J., and Reimer, R. W. (2021). CALIB 8.2. [WWW program]. Available at: http://calib.org (Accessed 7 30, 2021).

Thorndycraft, V. R., Bendle, J. M., Benito, G., Davies, B. J., Sancho, C., Palmer, A. P., et al. (2019). Glacial lake Evolution and Atlantic-Pacific Drainage Reversals during Deglaciation of the Patagonian Ice Sheet. *Quat. Sci. Rev.* 203, 102–127. doi:10.1016/j.quascirev.2018.10.036

Toggweiler, J. R., Russell, J. L., and Carson, S. R. (2006). Midlatitude Westerlies, Atmospheric CO2, and Climate Change during the Ice Ages. *Paleoceanography* 21 (2). doi:10.1029/2005PA001154

Turner, K. J., Fogwill, C. J., Mcculloch, R. D., and Sugden, D. E. (2005). Deglaciation of the Eastern Flank of the north Patagonian Icefield and Associated continental-scale lake Diversions. *Geografiska Annaler: Ser. A, Phys. Geogr.* 87 (2), 363–374. doi:10.1111/j.0435-3676.2005.00263.x

Vilanova, I., Moreno, P. I., Miranda, C. G., and Villa-Martínez, R. P. (2019). The Last Glacial Termination in the Coyhaique Sector of central Patagonia. *Quat. Sci. Rev.* 224, 105976. doi:10.1016/j.quascirev.2019.105976

Villa-Martínez, R., and Moreno, P. I. (2021). Development and Resilience of Deciduous Nothofagus Forests since the Last Glacial Termination and Deglaciation of the central Patagonian Andes. *Palaeogeogr. Palaeoclimatol. Palaeoecol.* 574, 110459. doi:10.1016/j.palaeo.2021.110459

Villa-Martínez, R., Moreno, P. I., and Valenzuela, M. A. (2012). Deglacial and Postglacial Vegetation Changes on the Eastern Slopes of the central Patagonian Andes (47°S). *Quat. Sci. Rev.* 32, 86–99. doi:10.1016/j.quascirev.2011.11.008

Conflict of Interest: The authors declare that the research was conducted in the absence of any commercial or financial relationships that could be construed as a potential conflict of interest.

The handling Editor declared a past co-authorship with one of the authors ES.

Publisher's Note: All claims expressed in this article are solely those of the authors and do not necessarily represent those of their affiliated organizations, or those of the publisher, the editors and the reviewers. Any product that may be evaluated in this article, or claim that may be made by its manufacturer, is not guaranteed or endorsed by the publisher.

frontiers in Earth Science

ORIGINAL RESEARCH
published: 04 March 2022
doi: 10.3389/feart.2022.833219

Climatic and Ecological Changes in the Subtropical High Andes During the Last 4,500 Years

Cesar Mayta[1] *and Antonio Maldonado*[1,2,3]*

[1]Centro de Estudios Avanzados en Zonas Áridas (CEAZA), La Serena, Chile, [2]Departamento de Biología, Universidad de La Serena, La Serena, Chile, [3]Departamento de Biología Marina, Universidad Católica del Norte, Coquimbo, Chile

The effects of climate change may be more evident in mountainous areas. In these areas, an increase in temperature and a decrease in precipitation can reduce the amount of snow, which represents a source of water for human consumption and vegetation. To analyze the effects of climate change on vegetation, it is possible to examine the climate–vegetation relationship in the past and observe the influence of variation in temperature and precipitation on the dynamics of plant communities. The aim of the present work was to describe the climate–vegetation dynamics of the last 4,500 years in the high subtropical Andes of Chile (30°S). The paleoclimatic reconstruction was carried out through the analysis of fossil pollen and macroscopic carbon obtained from sediment cores from two high Andean lakes. The dynamics of the vegetation was analyzed taking into account the alpha and beta diversity. The pollen and carbon records showed three contrasting periods during the last 4,500 years. From the beginning of the sequences until ~1900 cal. yr BP, relatively dry climatic conditions are suggested, with a slight trend toward more humid conditions after 2,700 cal. yr BP. Pollen records from ~1900 to ~600 cal. yr BP suggest wetter conditions than today. Finally, relatively arid conditions have reappeared in the last ~600 years. The diversity analysis showed that the climate mainly influences the composition of taxa in the communities (beta diversity) and not the richness (alpha diversity). In periods of dry/wet transition and vice versa, beta diversity changes. On the other hand, richness remains relatively constant throughout the record.

Keywords: subtropical Andes, pollen records, late Holocene (~4 ka), southern westerly wind belt, alpine vegetation, alpha diversity, beta diversity

OPEN ACCESS

Edited by:
Neil Franklin Glasser, Aberystwyth University, United Kingdom

Reviewed by:
Maarten Blaauw, Queen's University Belfast, United Kingdom
Alberto Saez, University of Barcelona, Spain

***Correspondence:**
Antonio Maldonado
antonio.maldonado@ceaza.cl

Specialty section:
This article was submitted to Cryospheric Sciences, a section of the journal Frontiers in Earth Science

Received: *10 December 2021*
Accepted: *08 February 2022*
Published: *04 March 2022*

Citation:
Mayta C and Maldonado A (2022) Climatic and Ecological Changes in the Subtropical High Andes During the Last 4,500 Years. Front. Earth Sci. 10:833219. doi: 10.3389/feart.2022.833219

1 INTRODUCTION

Although climate change is a global phenomenon, arid and semiarid areas may be more vulnerable (World Water Council, 2009); one of these areas is located from 27 to 32°S in Chile (Sarricolea et al., 2016). This area is a transition between arid regions such as the Atacama Desert (~18–27°S) and semiarid Mediterranean areas (~31–37°S) (Kaiser et al., 2008). At this latitude, precipitation occurs in winter and is generated by the interaction of two systems: the southern westerlies and the South Pacific anticyclone (Montecinos and Aceituno, 2003). In summer, the anticyclone blocks the storms associated with the westerly winds; in winter, the anticyclone is less intense, moves north, and allows the generation of rainfall associated with the system of westerly winds (Quintana, 2012). The area includes high-mountain ecosystems, which are important for the water balance of the watersheds, since they store it in the form of snow and glaciers. Their melting is important for human

consumption and the functioning of these ecosystems (Pellicciotti et al., 2014). The effects of climate change may be more evident in mountainous areas, due to temperature increases and increases in drought which diminish the amount of snow, impacting the plant communities and ecosystem functioning (Schickhoff et al., 2016). To understand better the relationship between climate change and ecosystem impact, studies may be performed to analyze the effects of variation in precipitation and temperature patterns on past plant communities (Birks et al., 2010).

Plant community dynamics may be affected by changes in precipitation and temperature, influencing the composition and abundance of species (Woodward and Williams, 1987); additionally, glacier retreats leave ice-free areas that may be colonized (Losapio et al., 2021). The region located between ~30 and ~36° is a transition zone and presents different types of vegetation. The region is dominated by deciduous shrubs and succulents, but there are evergreen sclerophyllous trees (Armesto et al., 2007). Pollen studies have been performed in the Andean region of northern Chile, estimating the composition of plant communities and climate by pollen analysis (Martel-Cea et al., 2016; de Porras and Maldonado, 2018). As well as by providing information on climate conditions, pollen records may also be used to study aspects related to plant ecology at a scale of thousands of years; pollen analysis may be used to relate changes in diversity to the environment (Blarquez et al., 2014). Many concepts and theories generated in areas such as community ecology, such as alpha, beta, and gamma diversity, may be applied in paleoecological studies (Jackson and Blois, 2015). However, it must be taken into account that the taxonomic resolution obtained through pollen is low, and this could influence the results of diversity analysis (Mander and Punyasena, 2014). Some studies in the mountain zone of north–central Chile show that there is lower alpha and beta diversity at higher altitudes, related to climate conditions less favorable for plant development (López-Angulo et al., 2018).

Paleoclimate studies in north–central Chile indicate that during the Late Holocene there were variations in the climate conditions (Martel-Cea et al., 2016; Tiner et al., 2018). For example, in the last ~700 years, a relatively dry period began, which continues until now (Martel-Cea et al., 2016). However, how this variation may influence the diversity of plant communities has not been analyzed. This study presents the results of pollen records obtained in lakes formed by glacial retreat in the high mountains of subtropical Chile (30°S) for the last 4,500 years, complemented with macroscopic carbon analysis and the changes in alpha and beta diversity in the plant communities during this period.

2 Study Area

The study area is located on the western side of the subtropical Andes, in the north–central region of Chile, specifically in lakes Corralito (30° 22′ S; 70° 28′ W; 3,800 m above sea level (a.s.l.)) and Quebrada Parada (30° 24′ S; 70° 25′ W; 3,889 m a.s.l.). Both are contained in the Área Protegida Privada y Santuario de la Naturaleza Estero Derecho (APPSNED). The altitude of the area ranges from 2,000 m to above 4,000 m a.s.l.; the local climate varies with the altitude. There is a cold desert climate between 2,000 and 3,000 m a.s.l., with an annual mean temperature of 11°C and mean precipitation of 30 mm, which occurs mainly in winter (CAEED, 2017). From 3,000 to 4,000 m a.s.l., there is a cold mountain steppe climate with high solar radiation, mean annual temperature of 8°C, and mean annual precipitation of 300 mm, which falls mainly as snow in winter. Above 4,000 m a.s.l., there are areas covered with ice all year round; the temperature fluctuates around 0°C and usually does not exceed 10°C (Cepeda and Novoa, 2006). Rock glaciers are present in this zone (Valois et al., 2020). Precipitation is controlled by the interaction between the system of westerly winds and the Southeast Pacific subtropical anticyclone (Montecinos and Aceituno, 2003). The anticyclone is less intense during winter; it moves northward and allows storms associated with westerly winds to arrive, generating precipitation (Quintana, 2012). The study area is sensitive to interannual variations associated with the El Niño Southern Oscillation (ENSO). The negative phase of ENSO (El Niño) produces abnormally warm and rainy winters, while the opposite occurs in the positive phase (La Niña) (Aceituno, 1988). There are small lakes of glacial origin above 3,800 m a.s.l. in the area, including Laguna Corralito with an area of 0.02 Km^2 and Laguna Quebrada Parada, which covers 0.01 km^2 (**Figure 1**; **Supplementary Material S1**). The sediment cores were obtained from these small lakes.

The vegetation in this area is Andean steppe, which covers xerophytic herbs, shrubs, and subshrubs. There are four vegetation belts in the area: below 2,700 m a.s.l. is the pre-Andean belt, with desert shrubs (e.g., *Atriplex desertícola*) and trees (e.g., *Prosopis chilensis*); the sub-Andean belt from 2,700 to 3,500 m a.s.l., with shrubby vegetation and grasslands dominated by *Stipa chrysophylla*, *Viviana marifolia*, and *Cristaria andicola*; the lower Andean zone from 3,500 to 4,250 m a.s.l., with cushion plants of *Adesmia subterranea*, *Calceolaria pinifolia*, and *Azorella cryptantha*; and the upper Andean belt from 4,250 to 4,450 m a.s.l., with species such as *Menonvillea cuneata* (Squeo et al., 2009). The study area has patchy vegetation, and there are many places prone to landslides that make the vegetation scarce in some places (Squeo et al., 2009). The lakes from which sediment cores were obtained are in the lower Andean belt.

3 METHODS

3.1 Sampling, Lithology, and Dating

During the summer of 2018, two sediment cores were extracted from Laguna Corralito (LCO) and two from Quebrada Parada (LQP) using a UWITEC gravity corer. The LCO core was 83 cm and that of LQ Parada was 183 cm. The sediment description of the cores includes texture, color, photographs, X-ray images, and loss on ignition. The chronology of the cores was obtained using eight dates obtained by AMS ^{14}C analysis for each lake. The dates were corrected for the reservoir effect considering the age obtained at the surface sediments of lake LCO (244 calendar years before present "cal. yr BP" (BP = ad 1950)); this correction was applied to both lakes given that the deposition environment and the geology of the lakes are equivalent (Velásquez et al.,

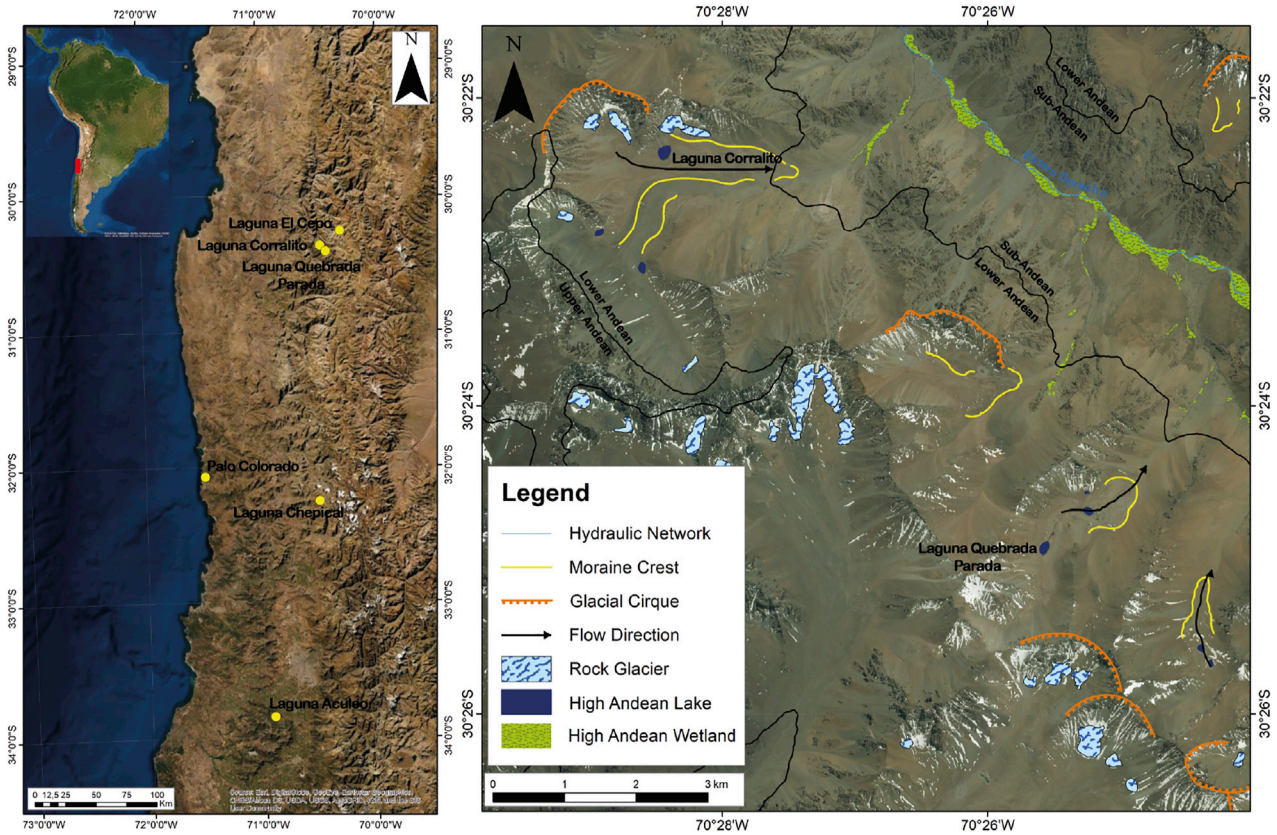

FIGURE 1 | Map of the study area showing the location of lakes analyzed, the main geomorphological characteristics of the area, and sites discussed in the text.

2021). Temporal variations of the reservoir effect during the last 4,000 years do not seem to have importance according to studies close to the study area (Tiner et al., 2018).

The ages were calibrated with the SHCal20 curve (Hogg et al., 2020); the age–depth model was generated using the Bacon package version 2.5.7 (Blaauw and Christen, 2011). Two cores from LCO were used, namely LCO-shc1 (73 cm) and LCO-shc2 (66 cm); the former covers a time scale of ~3,000 years and the latter of ~4,500 years. We analyzed the lithological characteristics, loss on ignition, and dates of both cores to obtain a composite sequence that covered the last ~4,500 years. Centimeter 73 of core LCO-shc1 was assembled with centimeter 48–58 of core LCO-shc2. The cores have different sediment accumulation, and thus the union of these cores generated an artificial inflection in the age–depth curve of the sediments. The possibility of a hiatus in the bottom part of core LCO-shc2 (with a lower sedimentation rate) is unlikely, considering the sedimentary structures seen in the X-ray images and the sedimentation rate of the complete core.

3.2 Analysis of Pollen and Macroscopic Carbon Particles

The sediment samples were taken every 2 cm of the cores for the pollen study. Pollen extraction was performed using routine protocols (Faegri and Iversen, 1989), including deflocculation and elimination of humic acids (KOH 10%), removal of carbonates (HCL 10%), removal of silicates (HF 40%), and acetolysis to eliminate the organic material. *Lycopodium* tablets were included in the extraction to calculate the concentration (Stockmarr, 1971) and later pollen accumulation rate. At least 300 pollen grains of terrestrial taxa were counted in each level, using an optical microscope under 400x and 1,000x. Pollen grains were identified using bibliography (Heusser, 1971; Markgraf and D'Antoni, 1978) and reference samples from the Laboratorio de Paleoecología y Paleoclimatología of the Centro de Estudios Avanzados en Zonas Áridas (CEAZA). Pollen diagrams, cluster analysis using restricted incremental sums of squares, (CONISS) and calculation of the rate of pollen accumulation were performed in the TILIA 1.7.16 program (Grimm, 2011). Pollen diagrams and cluster analysis were performed using the pollen types with more than two percent. The number of zones was determined using the "broken stick" test implemented in the Rioja package of R version 3.4.4 (O'Reilly et al., 2014). Only the main terrestrial taxa described for the study area (Squeo et al., 2009; Villagrán et al., 1983) were graphed in the pollen diagrams.

Carbon macroparticles from both lakes were analyzed, using sediment samples of 2 cm^3 from each centimeter of the cores. KOH 10% was added to each sample for 6 h, after which they

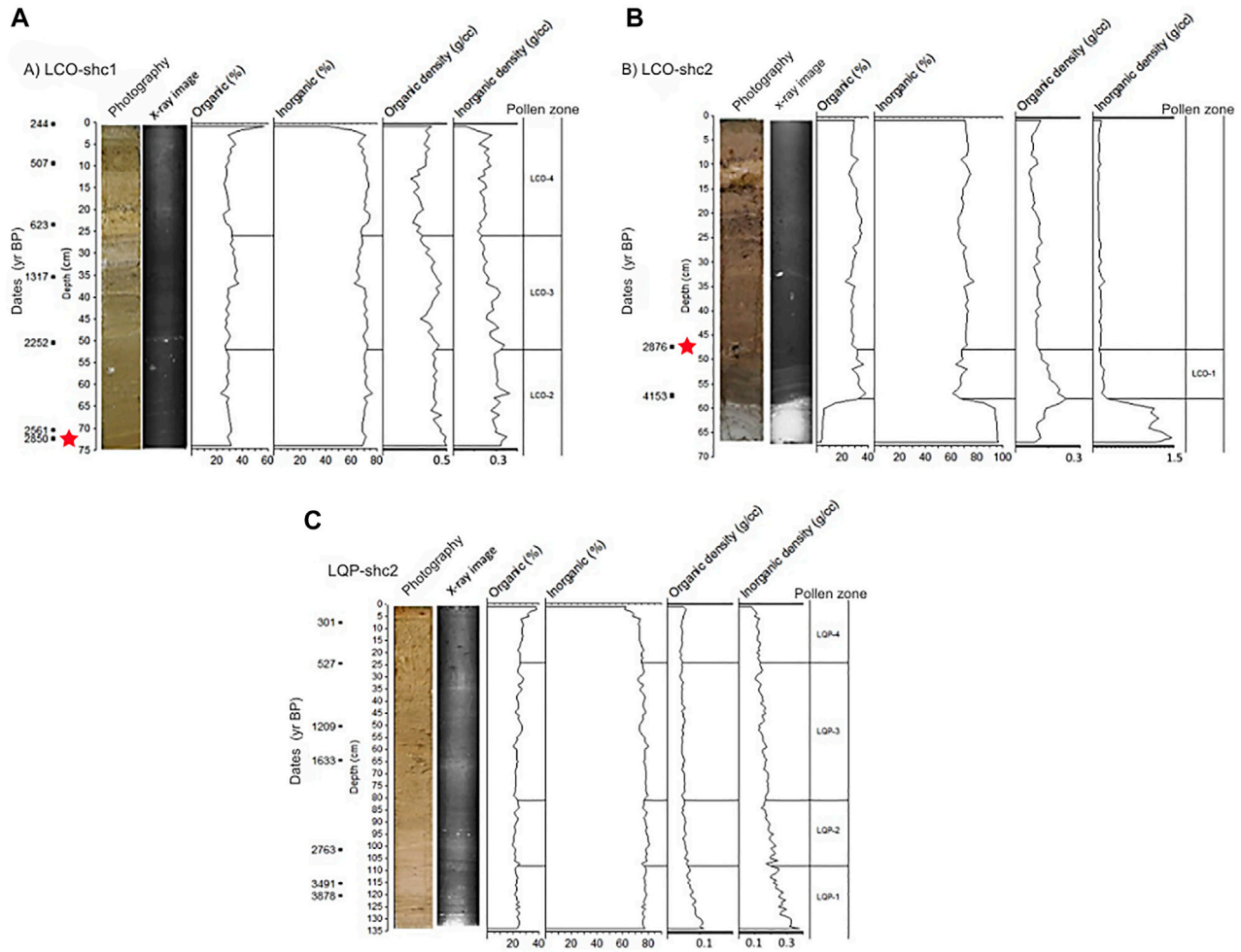

FIGURE 2 | Photographs, X-ray images, percentage and density of organic and inorganic matter, and radiocarbon ages of the cores from **(A)** Laguna Corralito LCO-shc1, and **(B)** Laguna Corralito LCO-shc2 (The LCO-shc2 is attached to the LCO-shc1 base from 48 cm). **(C)** Laguna Quebrada Parada LQP-shc2. The red star denotes the tie point between LCO-shc1 and LCO-shc2.

were sifted using 250- and 125-μm sieves. Carbon particles were counted on a stereoscopic microscope and were quantified as the number of particles per cm^3 of sediment (Whitlock and Larsen, 2002). Carbon data were analyzed with the program CharAnalysis, which uses the accumulation of macroscopic carbon particles in sediment cores to estimate a number of parameters such as local fire episodes, magnitude and frequency of the events, recurrence time, and others (Higuera et al., 2009).

3.3 Analysis of Alpha and Beta Diversity

Alpha diversity was calculated as the number of pollen types found in each sample in the sediment core (Gosling et al., 2018). Detrended correspondence analysis (DCA) was performed on the square root-transformed pollen abundance, obtaining values of changes in the vegetation composition (beta diversity) over time from the fossil pollen (Correa-Metrio et al., 2014). Euclidean distances between ordination scores in the first axis (DCA 1) were measured for each sample to estimate the dissimilarity in the composition of the communities among the samples and to be used as a value of "ecological change," which is also a proxy of beta diversity (Correa-Metrio et al., 2014). The comparison of alpha and beta diversity values over time was performed for the two lakes, thus allowing us to estimate whether or not the behavior of the two nearby lakes changed synchronically with the climate changes in the last 4,500 years. DCA was calculated in the vegan package of R (Oksanen et al., 2015).

4 RESULTS

4.1 Laguna Corralito

4.1.1 Lithological Description, Loss due to Ignition, and Chronology

The composite sequence of LCO had 83 cm; the first 73 cm was from the first core and 10 cm from the second. The first 6 cm of LCO-shc2 from the base was composed of gray clay with 95% inorganic material; from 58 to 51 cm, the core had a yellowish

TABLE 1 | Radiocarbon-dated from cores of Laguna Corralito (LCO) and Laguna Quebrada Parada (LQP). All dates were obtained from bulk sediments, and all dates were adjusted by 244 ± 26 ^{14}C years.

Lab. Id	Core sample ID	Depth (cm)	Age (^{14}C yr BP)
D-AMS 030099	LCO shc-1 (0–1)	0	244 ± 26
D-AMS 034535	LCO shc-1 (9–10)	9	507 ± 22
D-AMS 032839	LCO shc-1 (23–24)	23	623 ± 27
D-AMS 032840	LCO shc-1 (35–36)	35	1,317 ± 28
D-AMS 034537	LCO shc-1 (50–51)	50	2,252 ± 26
D-AMS 032841	LCO shc-1 (70–71)	70	2,761 ± 28
D-AMS 034538	LCO shc-1 (72–73)	72	2,850 ± 25
D-AMS 034539	LCO shc-2 (48–49)	74	2,876 ± 26
D-AMS 030100	LCO shc-2 (58–59)	82	4,163 ± 31
D-AMS 034540	LQP shc-2 (7–8)	7	351 ± 23
D-AMS 034541	LQP shc-2 (24–25)	24	523 ± 23
D-AMS 032842	LQP shc-2 (50–51)	50	1,318 ± 31
D-AMS 034542	LQP shc-2 (64–65)	64	1766 ± 30
D-AMS 032843	LQP shc-2 (101–102)	101	2,667 ± 27
D-AMS 034543	LQP shc-2 (115–116)	115	3,311 ± 34
D-AMS 034544	LQP shc-2 (120–121)	120	3,745 ± 29
D-AMS 030098	LQP shc-2 (133–134)	133	4,384 ± 31

color with a silty texture, with 33.19% organic matter and 0.09 g/cc organic density, while 50–48 cm had a brown color with a clayey texture, with 31.48% organic matter and 0.06 g/cc organic density (**Figure 2B**). The LCO-shc1 between 73 and 68 centimeters has a dark brown color and a silty texture, with 30.33% of organic matter and 0.07 g/cc of organic density. The sequence from 68 to 23 cm was dark brown with a silty texture, with 29.97% organic matter and 0.06 g/cc organic density. The sequence from 23 to 18 cm had a yellowish brown color with a silty/clayey texture, with 27.71% organic matter and 0.04 g/cc density. The sequence from 18 to 3 cm had a brown color with a clayey texture, with 28.98% organic matter and 0.05 g/cc density. The sequence from 3 to 2 cm had light brown color and silty texture, with 30.33% organic matter and 0.05 g/cc density. The upper 2 cm was dark brown with a silty/clayey texture, with 47.17% organic matter and 0.06 g/cc density (**Figure 2A**). The percentage of inorganic matter was relatively constant in both cores.

A total of eight ^{14}C dates were obtained, from the later sediments to the gray inorganic clays, which were corrected for the reservoir effect, considering the surface age as reservoir (**Table 1**). Thus, the sequence includes a range from ~4,300 cal. yr BP to the present. The change of slope in the age–depth curve is due to the change of core because of the difference in sedimentation rates of the cores. From 83 to 73 cm, the mean sedimentation rate was 0.003 cm/year, after which it increased to a mean of 0.03 cm/year (**Figure 3A**).

4.1.2 Analysis of Pollen and Macroscopic Carbon Particles

The pollen diagram was divided into four pollen zones (LCO-1, LCO-2, LCO-3, and LCO-4). The most abundant pollen type was *Ephedra*, which reached up to ~30%. Other types of pollen were generally less than 10% (**Figure 4**).

LCO-1: From ~4,300 to ~2,760 cal. yr BP, *Ephedra* dominates (around 50%). Companion taxa are Asteraceae *Mutisia*-type (around 4%), Apiaceae *Mulinum*-type (around 2%), Chenopodiaceae (around 5%), and Poaceae (around 2%). The greatest abundance of pollen in this area is from taxa of the sub-Andean belt, reaching up to 70%. The rate of pollen accumulation was the lowest of all records in almost all the periods. No carbon particles were recorded in this zone.

LCO-2: From ~2,760 to ~1,980 cal. yr BP, *Ephedra* continued to be the most abundant pollen type (57%). Other pollen types, present in less than 10%, were Asteraceae *Mutisia*-type (4%), Poaceae (3%), Asteraceae *Leucheria/Nassauvia*-type (1.8%), and Apiaceae *Azorella*-type (1.7%). There was a small increase of Solanaceae *Solanum*-type (2%) pollen. Sub-Andean pollen continued to dominate in this period (up to 71%), but with fluctuations. The percentage of lower Andean taxa decreased (to 9%) but not considerably. Pre-Andean taxa maintained low percentages (7%). The content of macroscopic carbon particles increased considerably; a fire event about ~2,400 cal. yr BP is inferred.

LCO-3: From ~1,980 to ~790 cal. yr BP, there was a decrease in the percentage of *Ephedra* (33%) and an increase in Poaceae (14%), Asteraceae *Leucheria/Nassauvia*-type, and Apiaceae *Azorella*-type (3%). Apiaceae *Laretia*-type was recorded for the last time about 800 cal. yr BP. This period had a reduced sub-Andean pollen percentage (42%), reaching the lowest percentage in the entire record. There was an increase in pollen of the lower Andean belt (22%). The record of carbon particles suggests two fire events at ~1,500 and ~1,300 cal. yr BP; the second event was larger.

LCO-4: This period from ~790 cal. yr BP to the present was dominated by *Ephedra* (40%), with the presence of pollen types of sub-Andean vegetation: Asteraceae *Mutisia*-type (6%) and Apiaceae *Mulinum*-type (5%). The pollen of the higher zones (lower Andean zone) such as Poaceae decreased to 3%. The record of carbon particles from ~500 to ~200 cal. yr BP was not enough to infer fire events.

4.2 Laguna Quebrada Parada

4.2.1 Lithological Description, Loss due to Ignition, and Chronology

Core LQP-shc2 had a total of 134 cm. From 134 to 124 cm, the core was brown with a clayey texture, with 23.96% organic material and 0.07 g/cc organic density. From 124 to 107 cm, the core was brown with a silty texture, with 11.76% organic matter and 0.05 g/cc density. From 107 to 105 cm, the core was dark brown with a silty/clayey texture, with 22.96% organic matter and 0.04 g/cc density. From 105 to 4 cm, the core was olive brown with a silty texture, with 23.68% organic matter and 0.04 g/cc. From 4 to 2 cm, the core was yellowish brown with a silty texture, with 31.98% organic matter and density of 0.04 g/cc. The first 2 cm of the core was brown with a silty texture, with 37.81% organic matter and 0.04 g/cc density. The X-ray images show greater presence of inorganic material from 134 to 129 cm and clasts in 100–95 cm. The percentage of inorganic matter was relatively constant from 134 to 5 cm, with a mean of 76%. The percentage of inorganic matter decreased to 65% in the last 5 cm (**Figure 2C**).

A total of eight ^{14}C dates were obtained, which were corrected for the reservoir effect and calibrated in cal. yr BP the same way as

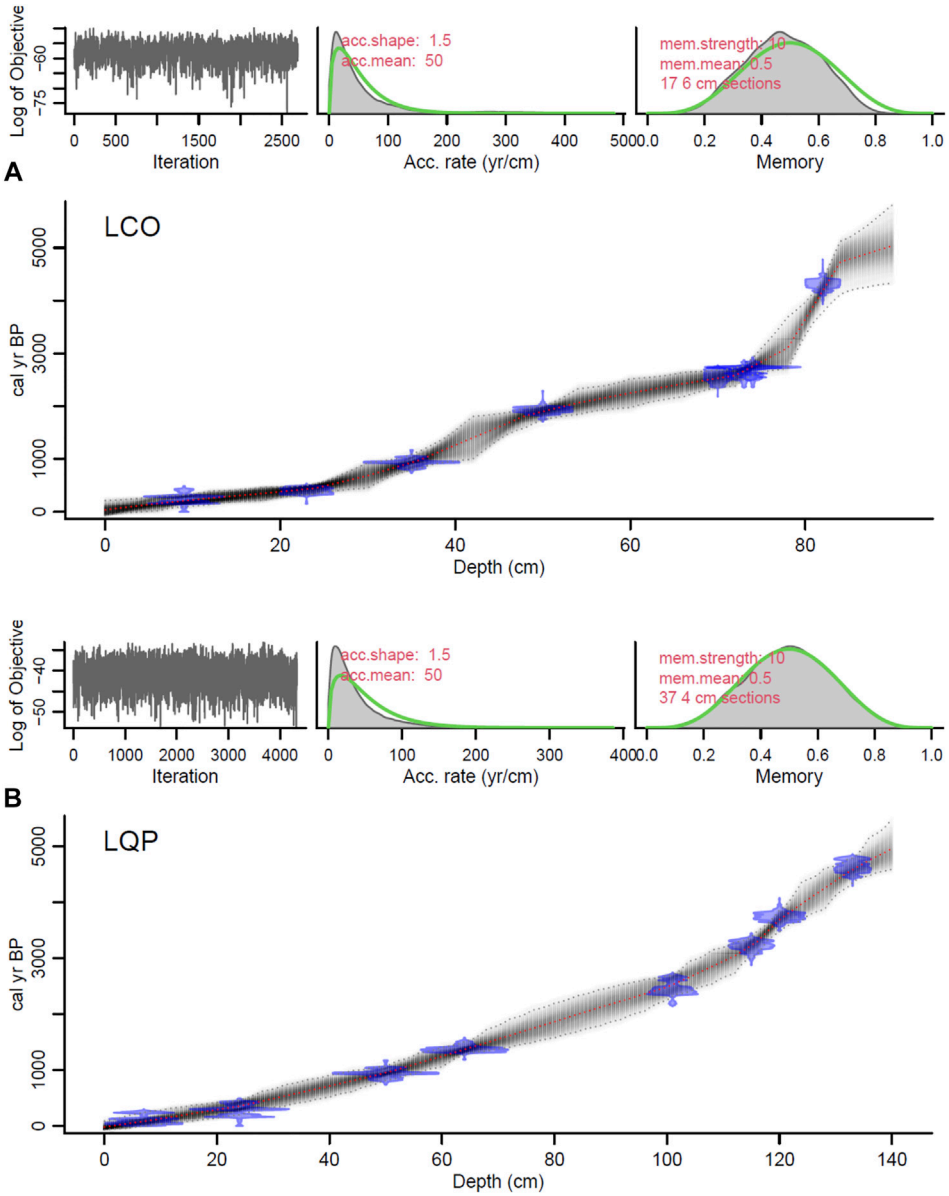

FIGURE 3 | Age–depth model of the core of **(A)** Laguna Corralito (LCO) and **(B)** Laguna Quebrada Parada (LQP). The top panels show, from left to right, Markov chain Monte Carlo iteration, prior (green curves)/posterior (gray histograms) distributions of the accumulation rate and memory of LCO and LQP. In the main panel, calibrated radiocarbon ages are shown in blue, and the age–depth model is represented by the gray dots, with a darker gray indicating more probable calendar ages. The gray dotted lines show 95% confidence intervals, and the red curve indicates the best model that was used for the study of both lakes.

in LCO (**Table 1**). Thus, the period that the core includes is from ~4,500 cal. yr BP. Between 134 and 102 cm, the sedimentation rate was 0.02 cm/year; from 102 to 26 cm, the rate was 0.03 cm/year, and from cm 26 to 0 the sedimentation rate increased to 0.07 cm/year (**Figure 3B**).

4.2.2 Analysis of Pollen and Macroscopic Carbon Particles

A total of four pollen zones (LQP-1, LQP-2, LQP-3, and LQP-4) were identified from the analysis of the conglomerate. The most abundant type of pollen was *Ephedra*, which reached 53%, followed by Asteraceae *Mutisia*-type with 16%, Poaceae and Asteraceae *Leucheria/Nassauvia*-type with 12%, and Apiaceae *Azorella*-type with 6% (**Figure 5**).

LQP-1: The period from ~4,500 to ~2,660 cal. yr BP was dominated by *Ephedra*, which reached 53%. Lesser amounts of Apiaceae *Mulinum*-type (3%), Asteraceae *Mutisia*-type (7%), Poaceae (1%), Asteraceae *Leucheria/Nassauvia*-type (5%), and Apiaceae -*Azorella*-type (1%) were found. The pollen types of the pre-Andean belt were 2% or less. Species of the sub-Andean belt

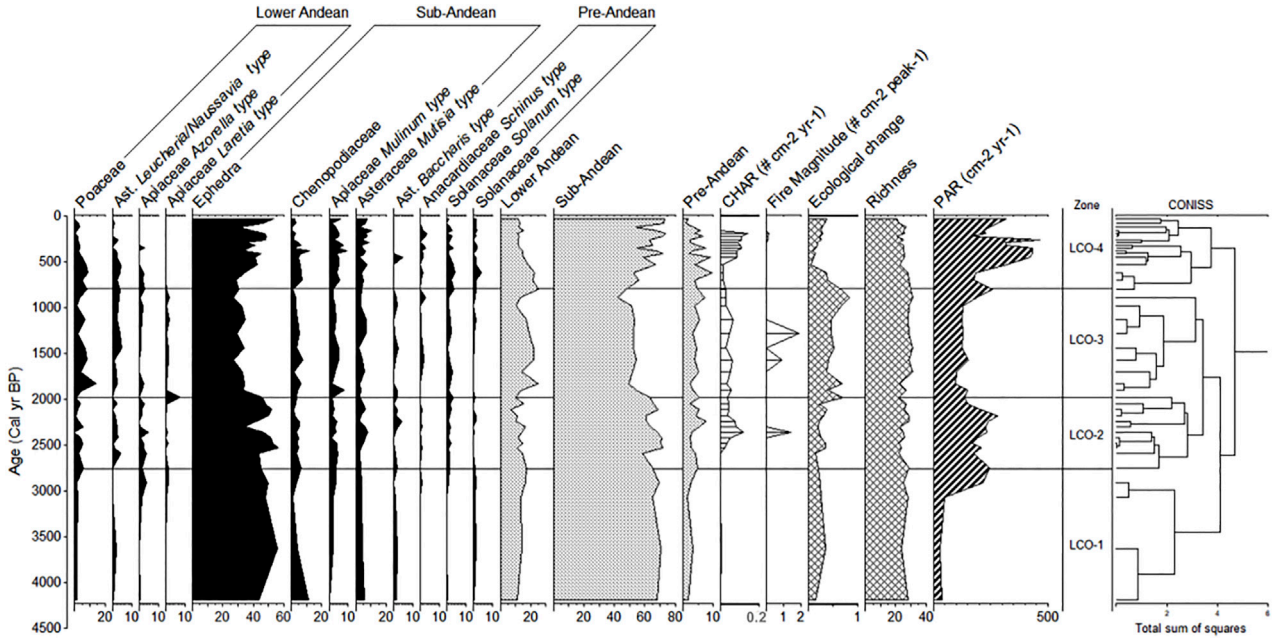

FIGURE 4 | Pollen diagram of the percentage of the main taxa of Laguna Corralito. The carbon accumulation rate "CHAR" (# particles cm-2 years-1), the magnitude of the fire (# particles cm-2 peak-1), and the pollen accumulation rate "PAR" (# pollen grains cm-2 years-1) are shown. The values of the ecological change and the pollen richness recorded throughout the record are also shown.

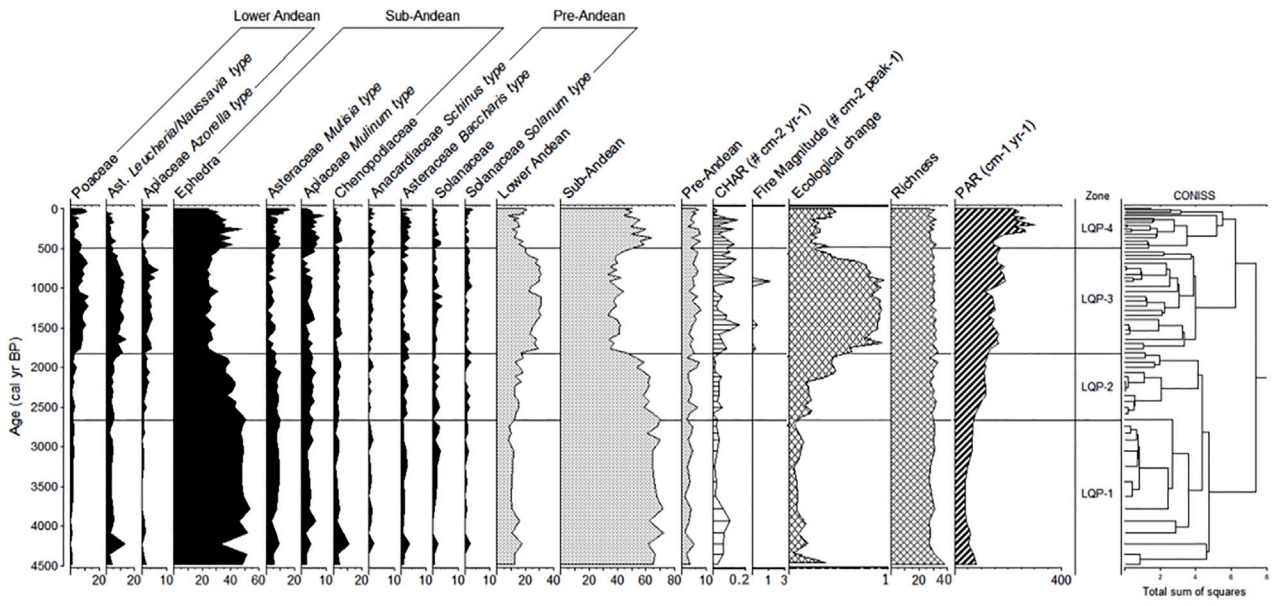

FIGURE 5 | Pollen diagram of the percentage of the main taxa of Laguna Quebrada Parada. The carbon accumulation rate "CHAR" (# particles cm-2 years-1), the magnitude of the fire (# particles cm-2 peak-1), and the pollen accumulation rate "PAR" (# pollen grains cm-2 years-1) are shown. The values of the ecological change and the pollen richness recorded throughout the record are also shown.

were dominant in this period (up to 72%); the carbon accumulation rate was low (mean 0.03 particles cm^{-2} $year^{-1}$), and no fire events were inferred.

LQP-2: This period from ~2,660 to ~1,820 cal. yr BP showed dominance of *Ephedra* (around 42%). The other pollen types were Asteraceae *Mutisia*-type (8%), Apiaceae *Mulinum*-type

TABLE 2 | DCA results of the abundance of fossil pollen from Laguna Corralito (LCO) and Laguna Quebrada Parada (LQP).

	Axis 1	Axis 2
Eigenvalue LCO	0.11	0.05
Length of gradient LCO	1.17	1.04
Variance percentage LCO	17.74	8.06
Eigenvalue LQP	0.13	0.03
Length of gradient LQP	1.01	1.18
Variance percentage LQP	14.13	3.26

(4%), Poaceae (2%), Apiaceae *Azorella*-type (2%), and Asteraceae *Leucheria/Nassauvia*-type (5%). This period is dominated by pollen of sub-Andean species (up to 70%). The carbon accumulation rate was low, and no fire events were inferred.

LQP-3: Between ~1,820 and ~490 cal. yr BP, *Ephedra* (26%), Asteraceae *Mutisia*-type (4%), and Apiaceae *Mulinum*-type (3%) all reduced their percentages. Poaceae pollen increased (8%), as did Asteraceae *Leucheria/Nassauvia*-type (10%) and Apiaceae *Azorella*-type (3%). Although *Ephedra* continued to be the dominant taxon, the percentage of pollen of the sub-Andean belt decreased (34%), which was the lowest value of the entire record. Pollen of species of the lower Andean belt increased up to 31%, which is the highest value of the record. The carbon accumulation rate reached its highest value (0.14 particles cm^{-2} $year^{-1}$) but was not constant; it oscillated during the period. Three fire events were inferred in this zone, and the largest around ~1,000 cal. yr BP.

LQP-4: Between ~490 cal. yr BP and the present, there was an increase in the percentages of *Ephedra* (34%), Asteraceae *Mutisia*-type (8%), and Apiaceae *Mulinum*-type (5%). Poaceae decreased (5%), as did Asteraceae *Leucheria/Nassauvia*-type (3%), which disappeared after 190 cal. yr BP. The lowest rate of carbon accumulation of the last ~4,500 years was recorded, and no fire events were detected.

4.2.3 Alpha and Beta Diversity

The results of the DCA analysis in LCO showed 17.74% of the variation explained by the first component (**Table 2**). LCO-4, LCO-2, and LCO-1 showed mostly negative values, while values were positive in the LCO-3 zone (**Figure 6**). The first component explained 39.59% of the variation in LQP. Again, LQP-4, LQP-2, and LQP-1 showed mostly negative values. LQP-4 showed positive values beginning with ~1970 years AD. The values were positive in the LQP-3 zone on this axis.

The pollen types related to species of the sub-Andean belt, associated with drier and/or less cold conditions, are at the left of the graphs (e.g., j. Asteraceae *Chuquiraga*-type, Solanaceae *Fabiana*-type, and *Ephedra*). The values for beta diversity (ecological change) had standard deviations less than one for both lakes; the most important changes coincide with the periods of transition between the different periods (**Figures 6**, **7**). The values remained relatively constant in LCO-1 up to the transition to LCO-2 around ~2,600 cal. yr BP, when the ecological change increased. LCO-2 showed oscillations during the entire period, one of which coincided with the transition to LCO-3. LCO-3 had the highest values of change, with the most important maximum around ~850 cal. yr BP (**Figure 4**).

The Laguna Quebrada Parada, as in the LCO, showed relatively constant values of ecological change in the LQP-1 period, which deceased during the transition to LQP-2 with minimum values around ~2,600 cal. yr BP. The LQP-3 period had the highest values of ecological change; however, there were oscillations. The LQP-4 period showed relatively low values of beta diversity, which increased starting about ~200 cal. yr BP (**Figure 5**).

The alpha diversity did not show large oscillations of pollen richness. LCO had a mean of 26 pollen types during the whole record (**Figure 4**), varying from 25 to 28 in the four zones, while LQP had a mean of 29 pollen types, varying from 28 to 30 in the four zones (**Figure 5**).

5 DISCUSSION

5.1 Interpretation of the Paleoclimate

The pollen ensembles of LCO and LQP were interpreted according to the altitudinal gradient of vegetation and climate conditions. Thus, for example, the sub-Andean belt is associated with lower precipitation and higher temperature than the lower Andean belt, which has more precipitation and temperatures below 0°C (Cepeda and Novoa, 2006). The main pollen types associated with the sub-Andean zone are *Ephedra*, Asteraceae *Mutisia*-type, and Apiaceae *Mulinum*-type. The genus *Ephedra* is anemophilous; thus, it produces and disperses a large amount of pollen, which explains its high presence in both records; it is also a genus vulnerable to freezing temperatures (Cavieres et al., 2000). Thus, the presence and abundance of *Ephedra* in the record is an indicator of less humid and cold conditions. The pollen types Poaceae, Apiaceae *Azorella*-type, and Asteraceae *Leucheria/Nassauvia*-type are associated with the lower Andean belt. The presence of grasses in the arid and semiarid Andes is related to soil humidity; more humid soils have a greater diversity of Poaceae. The species of this family tolerate freezing temperatures (Cavieres et al., 2000). Thus, the presence and abundance of Poaceae pollen in the sediments are a good indicator of humid and cold conditions, which are characteristics of the lower Andean zone.

The first axis of the DCA may be related to the gradient of precipitation and temperature (**Figures 6**, **7**). In this axis, the pollen types and dry and less cold periods have negative values and are on the left of the axis, while the pollen types and more humid and cold periods have positive values and are on the right of the axis. Thus, pollen of shrubs such as *Fabiana*, *Ephedra,* and *Chuquiraga* are associated with relatively dry periods, while Poaceae and *Leucheria/Nassauvia* are related to relatively humid periods.

The carbon analysis showed the greatest activity between ~1,900 and ~600 cal. yr BP. The presence of macroscopic carbon particles in the sediment cores is associated with fire events (Whitlock et al., 2010). In the north–central region of Chile, there is a relation between fires, climate, and ENSO (Altamirano et al., 2013). Rainy years favor vegetation growth;

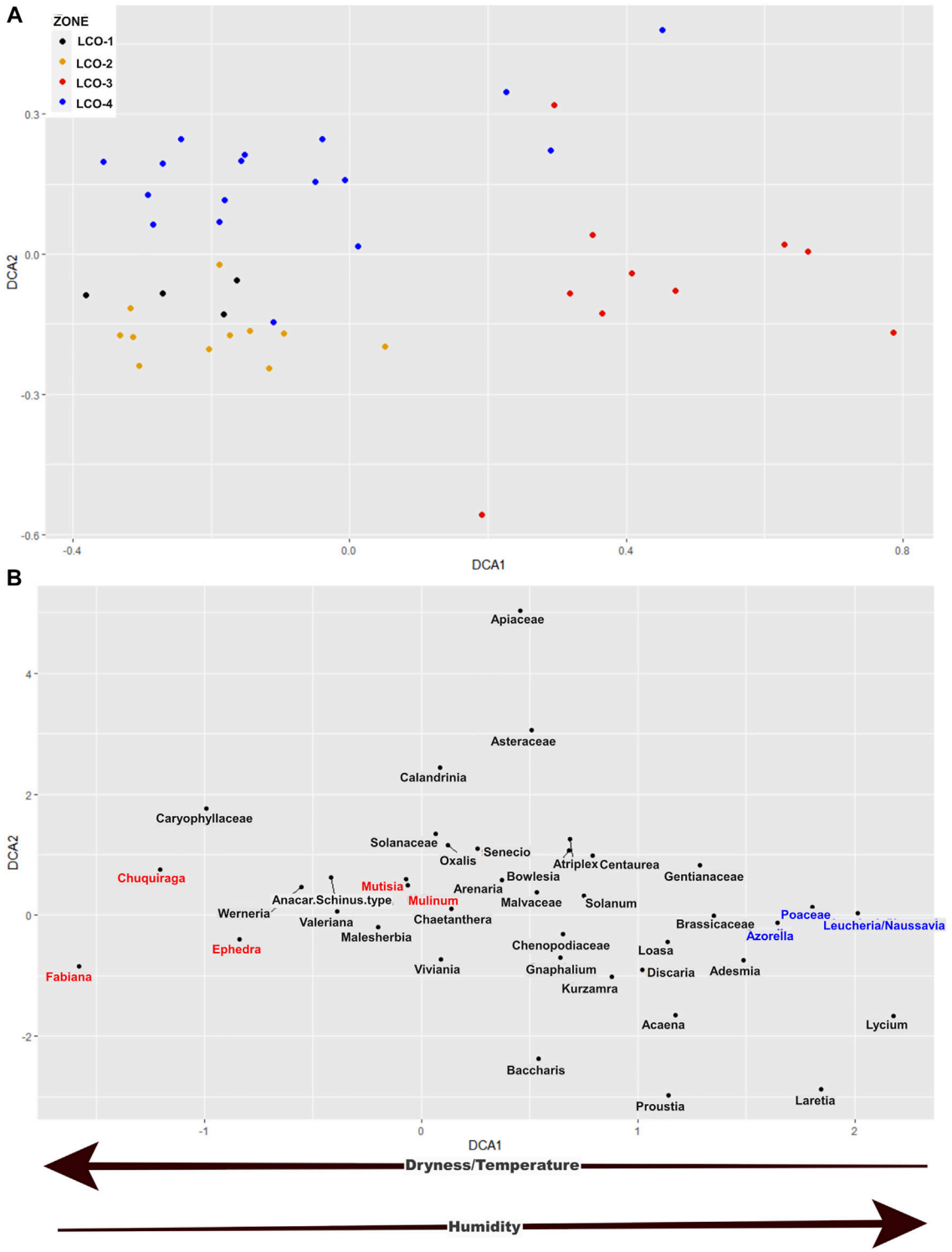

FIGURE 6 | DCA results from the pollen abundance of Laguna Corralito. **(A)** Ordering of the levels (colored points) grouped in the zones, obtained by the cluster analysis; on the left, are the levels with environmental conditions of lower humidity and on the right, the levels with higher humidity. **(B)** Ordering of pollen types with a similar arrangement in the multivariate space as the levels. Pollen types related to warmer and less humid conditions are highlighted in red. Pollen types related to cool and humid conditions are highlighted in blue. The arrows below indicate how the humidity and temperature conditions vary along the DCA 1 axis.

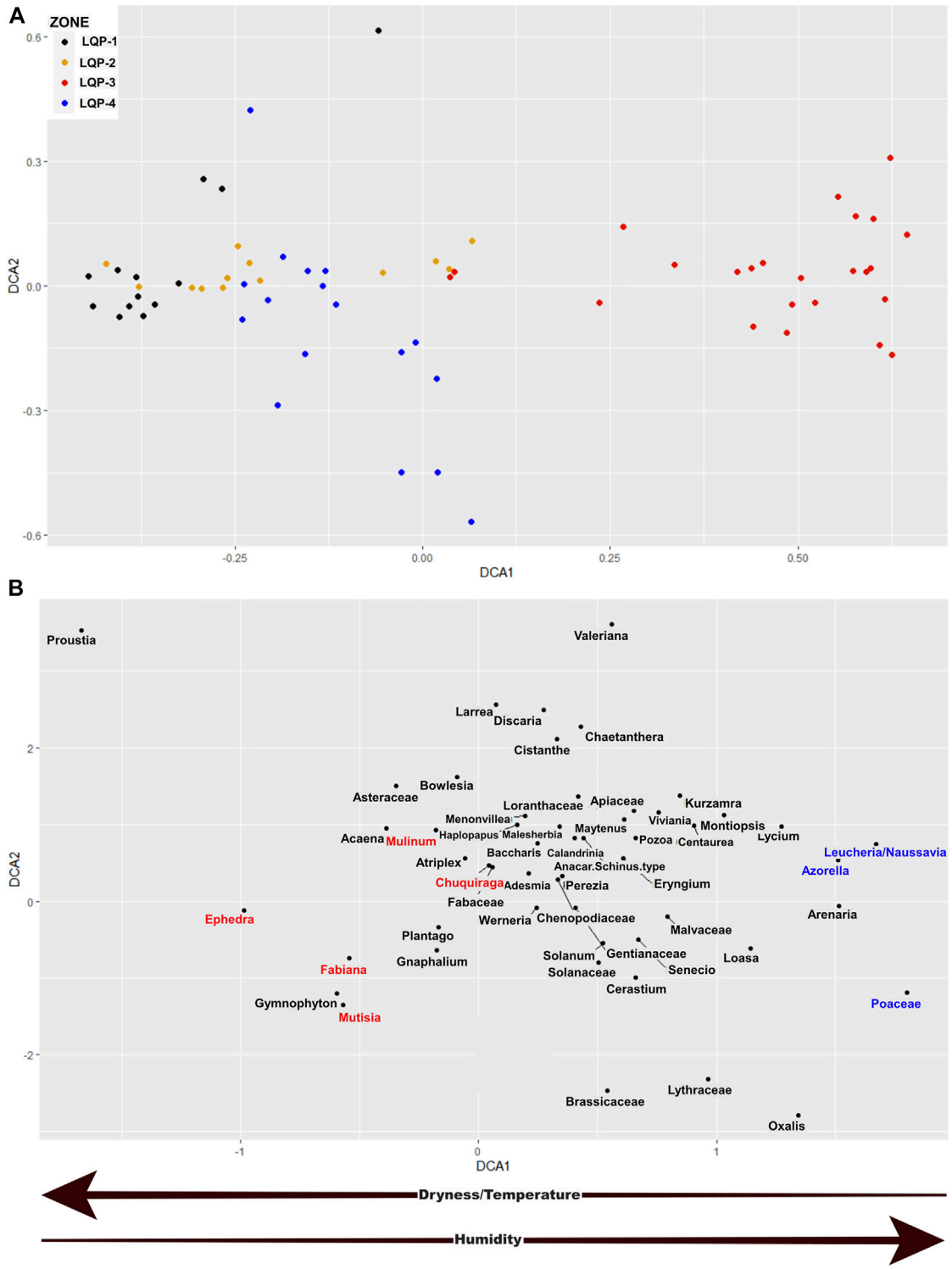

FIGURE 7 | DCA results from the pollen abundance of Laguna Quebrada Parada. **(A)** Ordering of the levels (colored points) grouped in the zones, obtained by the cluster analysis; on the left, are the levels with environmental conditions of lower humidity and on the right, the levels with higher humidity. **(B)** Ordering of pollen types, with a similar arrangement in the multivariate space as the levels. Pollen types related to warmer and less humid conditions are highlighted in red. Pollen types related to cool and humid conditions are highlighted in blue. The arrows below indicate how the humidity and temperature conditions vary along the DCA 1 axis.

in dry periods, this is converted into biomass that may burn (Gonzáles et al., 2011), and thus humid periods with marked seasonality may favor the propagation of fires (Gonzáles et al., 2011). The record of macroscopic carbon particles may thus serve to help identify periods with humid conditions but marked seasonality (rainy winters and very dry and/or hot summers) or strong interannual variation in precipitation and temperature which are mainly associated with the dynamics of the ENSO (Montecinos and Aceituno, 2003).

At the beginning of the records, there was a higher proportion of inorganic sediments in both lakes, especially LCO. The sediment record began with gray clay, barren of pollen, of glacial origin, which suggests that the beginning of organic deposits at ~4,000 cal. yr BP is associated with a small glacial retreat at 3,800–3,900 m a.s.l., which may have liberated the area for the formation of the current lakes. Later, both lakes showed alternation of dry and humid periods in the last ~4,500 years. From ~4,500 to ~2,700 cal. yr BP, the domination of *Ephedra*, Asteraceae *Mutisia*-type, and Apiaceae *Mulinum*-type in LQP suggests a relatively dry period. The low fire activity period and negative values in the DCA 1 axis reinforce the idea of dry conditions that did not favor plant growth and thus little accumulation of biomass that could generate fires. From ~2,700 to ~1,900 cal. yr BP, the same taxa continued to dominate; however, the decrease of elements of the sub-Andean belt and the gradual increase of elements of the lower Andean belt and the first record of fire in the LCO suggest a period of transition toward more humid conditions.

Between ~1,900 and ~600 cal. yr BP, there was an increase in pollen associated with the lower Andean belt, represented by Poaceae, Asteraceae *Leucheria/Nassauvia*-type, and Apiaceae *Azorella*-type and a concomitant decrease in pollen of species of the sub-Andean belt. This suggests a wetter and colder period than the anterior. This period also had the greatest carbon accumulation and the most fire events. This suggests a period with greater seasonality and/or greater interannual variability, which concurs with reports that this period had the greatest frequency of ENSO events in the entire Holocene (Moy et al., 2002; Rein et al., 2005).

The last ~600 years again showed an increase in pollen associated with the sub-Andean belt and the accumulation of carbon decreased, suggesting a new dry period. The tendency of an increase in temperature and a reduction in precipitation in recent years in the study area is registered not only in paleoclimatic studies. For example, Souvignet et al. (2012) observed that in the last 30 years in the study area there is an increase in temperature and an annual reduction in precipitation; this could be related to climate change caused by human activities.

5.2 Regional Correlations

The beginning of the records in LCO and LQP lakes has been associated with a glacial retreat in the high mountains, which may be related with the global event at 4,200 cal. yr BP that in some records of the Northern Hemisphere has been indicated as a cold event (Orme et al., 2018) and that marks the beginning of the late Holocene (Wanner et al., 2015). There is not much evidence of new glacial advances in the sub-tropical Andes; however, there is a report of an advance at 35°S in the Andes of Argentina at 4,700–4,300 cal. yr BP (Espizua, 2005), which could be related to the beginning of more organic deposition in our study area. The cores of both LCO and LQP showed the alternation of relatively dry and humid periods from the beginning of the records. The first period, from ~4,500 to ~1,900 cal. yr BP, had relatively dry conditions, with a transition phase from ~2,700 to ~1,900 cal. yr BP. This result is coherent with the geochemical and physical indicators of the Laguna El Cepo and Cerritos Blancos near the study area (30°S), which suggest relatively dry conditions in this period (Tiner et al., 2018).

These results are somewhat different than those obtained by Martel-Cea et al. (2016), who analyzed the record of the Laguna Chepical in the high Andean zone of central Chile (32°S); they found that the period 3,100–2,000 cal. yr BP was relatively humid and cold, followed by the maximum values of humidity indicators from 2,000 to 1,200 cal. yr BP, possibly associated with higher summer temperatures. The record of the Laguna Aculeo (34°S) in the lowlands showed an important increase in the humidity indicators beginning 3,000 cal. yr BP and an important increase in torrential rains associated with El Niño starting 1,800 cal. yr BP (Jenny et al., 2002; Villa-Martínez et al., 2003). Considering the beginning of the decrease of indicators of the low vegetation belt (sub-Andean) in LCO and LQP, there is some correspondence in the chronology of this humid phase, although at different times and intensity or maximum values from those found in the Laguna Chepical and Laguna Aculeo. Relatively humid conditions at ~4,000 cal. yr BP were observed in the coast of central Chile (32°S), which became more arid from 3,000 to 2,200 cal. yr BP (Maldonado and Villagrán, 2006; Méndez et al., 2015). In spite of the differences in the dates of change, most of the records suggest relatively dry conditions at least until ~2,700 or ~2,000 cal. yr BP (**Figure 8**). On the other hand, it is possible that the differences found are related to the different latitudes of the studies mentioned.

From ~1,900 to ~600 cal. yr BP, the records of LCO and LQP suggest relatively humid conditions, with an increase in the indicators of the lower Andean belt. This result concurs with the records of Laguna Chepical, Cerritos Blancos and El Cepo (Martel-Cea et al., 2016; Tiner et al., 2018), and the coastal area of the same region (Maldonado and Villagrán, 2006). The greatest influx of carbon was found in this period, and thus it is the period in which the largest number of fire events is inferred. The greatest activity of ENSO was found from 2,000 to 600 cal. yr BP (Jenny et al., 2002; Moy et al., 2002; Rein et al., 2005) and thus high interannual variability in the study area, which would favor the generation of fires. The differences in the times of the most humid period of the last 3,000 years between the records at 30°S and those further south may be related to a greater impact of the precipitations associated with ENSO in the north. Although the ENSO is also important further south, the dynamics of the westerly winds independent of the ENSO years may also explain the humid period beginning at 3,000 cal. yr BP.

Our records of the last ~600 years again show an increase in the indicators of the sub-Andean belt, associated with a relatively dry condition. This result coincides with studies performed in

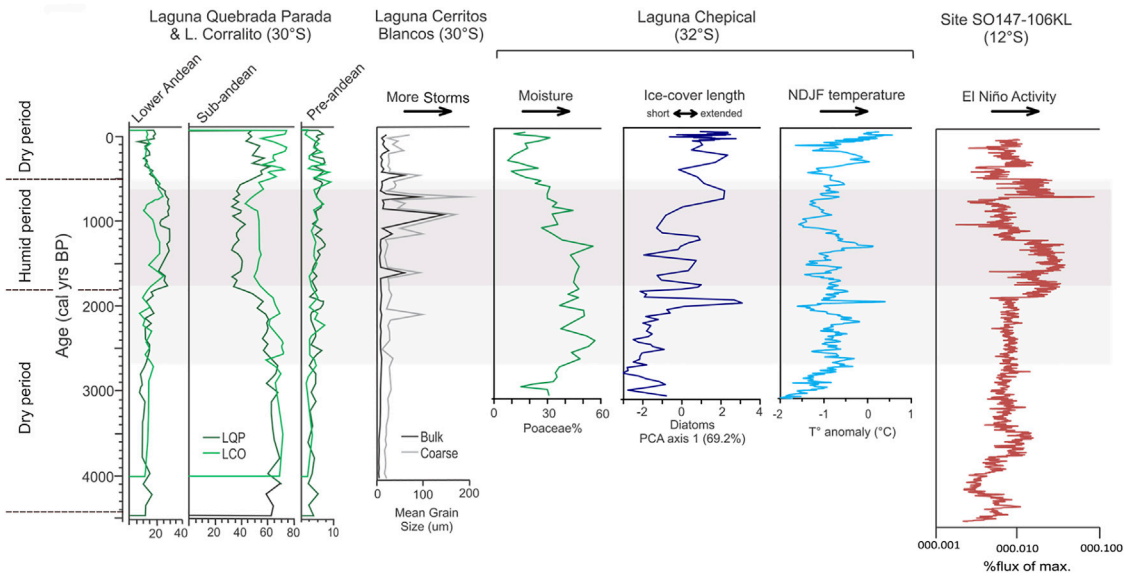

FIGURE 8 | Comparison of the pollen record summary from Laguna Corralito and Laguna Quebrada Parada, with Laguna Cerritos Blancos (Tiner et al., 2018), Poaceae pollen % (Martel-Cea et al., 2016), diatom record axis 1 PCA scores (Martel-Cea et al., 2016), NDJF temperature anomalies (de Jong et al., 2013) from Laguna Chepical and lithic content in the marine record, site SO 147-106KL, and offshore Peru (Rein et al., 2005). Wetter periods are highlighted in gray.

high Andean lakes in north–central Chile (Martel-Cea et al., 2016; Tiner et al., 2018) and in the coastal area of central Chile (Maldonado and Villagrán, 2006). The record of fossil pollen, in addition to detecting changes in the climate, is capable of giving clues about the origin of these changes (Li et al., 2008). Several studies show that changes in vegetation can be due to natural factors or related to human activities (Zhao et al., 2010; Paus, 2013). Thus, current climate change can be addressed through pollen analysis, and this information can be used to better analyze the consequences of climate change for biodiversity.

5.3 Alpha and Beta Diversity

The changes in the composition of the communities (ecological changes), used as a proxy of beta diversity (Correa-Metrio et al., 2014), were not constant during the last ~4,500 years. Ecological changes were related to environmental conditions in both lakes. The dry/humid/dry transition which occurred at ~1,900 and ~600 cal. yr BP is related to the decrease or increase in ecological change values. This variation in the composition of taxa may be because the new conditions generated by environmental changes generate ecological filters, which only allow some taxa to establish (Püttker et al., 2014). The coincidences between transition periods (niche changes) and increases or decreases in ecological change may indicate that when there are environmental changes, communities assemble due to deterministic processes related to the niche more than due to random processes (Püttker et al., 2014). The humid period showed greater values of ecological changes than the dry periods in both lakes.

Our study is the first to analyze changes in plant communities in terms of alpha and beta diversity in northern Chile, which makes it hard to compare with patterns found in other studies. However, studies of community ecology may be considered to analyze paleoecological patterns, since both disciplines study community dynamics with respect to spatial or environmental changes (Jackson and Blois, 2015). For example, studies in grasslands in semiarid areas of Africa (Anderson, 2008), California (Eskelinen and Harrison, 2015), and Asia (Zhang et al., 2014) show that sites with higher humidity have greater change in the community composition. One of the patterns observed in beta diversity is that it increases with productivity (Chase and Leibold, 2002; Chase, 2010). Productivity in our study area is mainly related to water availability; more precipitation yields more productivity (Jaksic, 2001; Rudloff et al., 2021). The relation between productivity and beta diversity may be one of the reasons that the humid period from ~1,900 to ~600 cal. yr BP had the highest values of ecological changes in the two lakes studied, since higher humidity would have produced greater productivity.

Species richness (alpha diversity) in both lakes oscillated slightly during the last 4,000 years but did not undergo abrupt changes. This stability of richness over time was described in pollen records (Haskell, 2001; Giesecke et al., 2012) and in rodents (Brown et al., 2001; Sax, 2002), amphibians, birds, and invertebrates (Sax, 2002). The stability of alpha diversity in many organisms was found at scales from tens to thousands of years. This may be related to the carrying capacity of ecosystems, which is related to resource availability; as long as the latter does not undergo large changes, richness is expected to be stable (Brown et al., 2001). Although the records of both lakes showed changes in environmental conditions, they were not sufficiently great to change stability in richness. The period of our study (~4,500 years) did not have extreme changes in environmental conditions compared to other periods such as the end of the Pleistocene (Kull and Grosjean, 2000) or the middle Holocene

(Maldonado et al., 2010). The stability of richness may also be influenced by problems of taxonomic resolution of pollen grains. In our study, this would have reduced the number of taxa, especially of the Poaceae, in which there were probably various species, which would not allow us to distinguish the true richness of plant species in the study area, and thus its variation in time. The problem of taxonomic resolution may be overcome using molecular techniques, for example, the use of sedimentary DNA, which improves the detection of species in paleoecological studies (Liu et al., 2020).

6 CONCLUSION

The sedimentary composition of the cores showed glacial activity before ~4,000 cal. yr BP, suggesting glacial retreat around this time above 3,800 m a.s.l.. Although we cannot use these records to decide when the last period of glacial advance began, we can indicate that it ended around 4,000 years ago, which may be related to the global event around ~4,200 cal. yr BP.

The records of pollen and carbon analyzed differentiated three contrasting periods during the last ~4,500 years. From the beginning of the sequences until ~1,900 cal. yr BP, the pollen ensembles suggest relatively dry climate conditions, with a slight tendency to more humid conditions after 2,700 cal. yr BP. From ~1,900 to ~600 cal. yr BP, the pollen records suggest more humid conditions than the present day, with more winter rains, which would be associated with greater influence of westerly winds and/or a decrease in the south Pacific subtropical anticyclone, which also coincides with greater ENSO activity and greater fire events in the study area, associated with high climatic interannual and/or intra-annual variability. Finally, in the last ~600 years, relatively arid conditions have appeared again. This chronology and direction of changes concurs with other records available for the region, showing that climate oscillations had a regional influence in the last ~4,500 years. Differences with the records from south of 32°S may be explained by a more important influence of ENSO activity in the study area than further south.

The analysis of diversity shows that the climate influences mainly the composition of taxa in the communities (beta diversity) but not in richness (alpha diversity). Beta diversity increases in dry–humid transition periods and decreases in humid–dry transition periods. Richness in transition periods remained relatively constant, suggesting equilibrium between extinction and local migration, which marks changes in species composition but not large oscillations in richness.

The results obtained in this study show how the Andean flora has behaved from a glacial retreat, passing to relatively dry and/or warm, humid and/or cold conditions, and again to relatively dry and/or warm conditions, associated with fluctuations in the intensity of the westerly wind belt in the area, suggesting increases in the vegetation belts in the warm and/or dry periods and decreases in the cold and/or humid periods, maintaining the alpha diversity but changing the beta diversity. These changes, mainly those associated with increased dry and/or warm conditions, may show how the vegetation is expected to behave in the future considering the current climate change scenarios for the area, which suggest an increase in the zero isotherm, temperatures in general, and decreases in precipitation.

DATA AVAILABILITY STATEMENT

The original contributions presented in the study are included in the article/**Supplementary Material**, further inquiries can be directed to the corresponding author.

AUTHOR CONTRIBUTIONS

CM and AM contributed to the conception and design of the study. CM wrote the first draft of the manuscript. CM and AM contributed to manuscript revision and approved the submitted version.

FUNDING

The funding for this work was provided by the ANID-FONDECYT #1180413, CONICYT-R16A10003, ANID-Millennium Science Initiative Program—NCN19_153, and ANID-"Concurso de Fortalecimiento al Desarrollo Científico de Centros Regionales 2020-R20F0008-CEAZA."

ACKNOWLEDGMENTS

We thank Marigen Heise and Jeremy Acevedo for their assistance during the coring collection campaign.

SUPPLEMENTARY MATERIAL

The Supplementary Material for this article can be found online at: https://www.frontiersin.org/articles/10.3389/feart.2022.833219/full#supplementary-material

REFERENCES

Aceituno, P. (1988). On the Functioning of the Southern Oscillation in the South American Sector. Part I: Surface Climate. *Mon. Wea. Rev.* 116, 505–524. doi:10.1175/1520-0493(1988)116<0505:OTFOTS>2.0.CO;2

Altamirano, A., Salas, C., Yaitul, V., Smith-Ramirez, C., and Ávila, A. (2013). Influencia de la heterogeneidad del paisaje en la ocurrencia de incendios forestales en Chile Central. *Rev. Geogr. Norte Gd.* 55, 157–170. doi:10.4067/s0718-34022013000200011

Birks, H. J. B., Heiri, O., Seppä, H., and Bjune, A. (2011). Strengths and Weaknesses of Quantitative Climate Reconstructions Based on Late-Quaternary Biological Proxies. *Toecolj* 3, 68–110. doi:10.2174/1874213001003020068

Blaauw, M., and Christen, J. A. (2011). Flexible Paleoclimate Age-Depth Models Using an Autoregressive Gamma Process. *Bayesian Anal.* 6 (3), 457–474. doi:10.1214/11-BA61810.1214/ba/1339616472

Blarquez, O., Carcaillet, C., Frejaville, T., and Bergeron, Y. (2014). Disentangling the Trajectories of Alpha, Beta and Gamma Plant Diversity of North American Boreal Ecoregions since 15,500 Years. *Front. Ecol. Evol.* 2, 1–8. doi:10.3389/fevo.2014.00006

Brown, J. H., Ernest, S. K. M., Parody, J. M., and Haskell, J. P. (2001). Regulation of Diversity: Maintenance of Species Richness in Changing Environments. *Oecologia* 126 (3), 321–332. doi:10.1007/s004420000536

Cavieres, L. A., Peñaloza, A., and Kalin Arroyo, M. (2000). Altitudinal Vegetation Belts in the High-Andes of central Chile (33°S). *Rev. Chil. Hist. Nat.* 73, 331–344. doi:10.4067/S0716-078X2000000200008

Cepeda, J., and Novoa, J. (2006). "La cordillera altoandina de la cuenca del Río Elqui," in *Los Sistemas Naturales de la Cuenca del Río Elqui*. Editor J. Cepeda (La Serena: Ediciones Universidad de La Serena), 551.

Chase, J. M., and Leibold, M. A. (2002). Spatial Scale Dictates the Productivity-Biodiversity Relationship. *Nature* 416, 427–430. doi:10.1038/416427a

Chase, J. M. (2010). Stochastic Community Assembly Causes Higher Biodiversity in More Productive Environments. *Science* 328, 1388–1391. doi:10.1126/science.1187820

Comunidad Agrícola Estancia Estero Derecho (CAEED) (2017). *Plan de Manejo para la Conservación del Área Protegida Privada y Santuario de la Naturaleza Estero Derecho*. La Serena, Chile: DocPlayer, 77.

Correa Metrio, A., Dechnik, Y., Lozano García, S., and Caballero, M. (2014). Detrended Correspondence Analysis: A Useful Tool to Quantify Ecological Changes from Fossil Data Sets. *Bsgm* 66 (1), 135–143. doi:10.18268/bsgm2014v66n1a10

de Jong, R., von Gunten, L., and Maldonado, A. (2013). Late Holocene Summer Temperatures in the Central Andes Reconstructed From the Sediments of High-Elevation Laguna Chepical, Chile (32° S). *Clim.Past.* 9, 1921–1932. doi:10.5194/cp-9-1921-2013

de Porras, M., and Maldonado, A. (2018). Metodologías Y Avances De La Palinología Del Cuaternario Tardío a Lo Largo De La Diagonal Árida Sudamericana. *Peapa* 18 (2), 18–38. doi:10.5710/PEAPA.08.07.2018.255

Eskelinen, A., and Harrison, S. P. (2015). Resource Colimitation Governs Plant Community Responses to Altered Precipitation. *Proc. Natl. Acad. Sci. USA* 112 (42), 13009–13014. doi:10.1073/pnas.1508170112

Espizua, L. E. (2005). Holocene Glacier Chronology of Valenzuela Valley, Mendoza Andes, Argentina. *The Holocene* 15 (7), 1079–1085. doi:10.1191/0959683605hl866rr

Faegri, K., and Iversen, J. (1989). *Textbook of Pollen Analysis (Fourth)*. New York: John Wiley & Sons.

Giesecke, T., Wolters, S., Jahns, S., and Brande, A. (2012). Exploring Holocene Changes in Palynological Richness in Northern Europe-Ddid Postglacial Immigration Matter? *PLOS ONE* 7 (12), e51624–11. doi:10.1594/PANGAEA.73842910.1371/journal.pone.0051624

González, M. E., Lara, A., Urrutia, R., and Bosnich, J. (2011). Cambio climático y su impacto potencial en la ocurrencia de incendios forestales en la zona centro-sur de Chile (33° - 42° S). *Bosque (Valdivia)* 32 (3), 215–219. doi:10.4067/S0717-92002011000300002

Gosling, W. D., Julier, A. C. M., Adu-Bredu, S., Djagbletey, G. D., Fraser, W. T., Jardine, P. E., et al. (2018). Pollen-vegetation Richness and Diversity Relationships in the Tropics. *Veget Hist. Archaeobot* 27, 411–418. doi:10.1007/s00334-017-0642-y

Grimm, E. C. (2011). *TILIA software version 1.7.16*. Illinois State Museum: Springfield, Illinois.

Haskell, J. (2001). The Latitudinal Gradient of Diversity through the Holocene as Recorded by Fossil Pollen in Europe. *Evol. Ecol. Res.* 3, 345–360.

Heusser, C. J., and Moar, N. T. (1973). Pollen and Spores of Chile: Modern Types of the Pteridophyta, Gymnospermae, and Angiospermae. *New Zealand J. Bot.* 11. 389–391. doi:10.1080/0028825X.1973.10430287

Higuera, P. E., Brubaker, L. B., Anderson, P. M., Hu, F. S., and Brown, T. A. (2009). Vegetation Mediated the Impacts of Postglacial Climate Change on Fire Regimes in the South-central Brooks Range, Alaska. *Ecol. Monogr.* 79 (2), 201–219. doi:10.1890/07-2019.1

Hogg, A. G., Heaton, T. J., Hua, Q., Palmer, J. G., Turney, C. S., Southon, J., et al. (2020). SHCal20 Southern Hemisphere Calibration, 0-55,000 Years Cal BP. *Radiocarbon* 62, 759–778. doi:10.1017/RDC.2020.59

Jackson, S. T., and Blois, J. L. (2015). Community Ecology in a Changing Environment: Perspectives from the Quaternary. *Proc. Natl. Acad. Sci. USA* 112 (16), 4915–4921. doi:10.1073/pnas.1403664111

Jaksic, F. M. (2001). Ecological Effects of El Niño in Terrestrial Ecosystems of Western South America. *Ecography* 24, 241–250. doi:10.1111/j.1600-0587.2001.tb00196.x

Jenny, B., Valero-Garcés, B. L., Villa-Martínez, R., Urrutia, R., Geyh, M., and Veit, H. (2002). Early to Mid-holocene Aridity in Central Chile and the Southern Westerlies: The Laguna Aculeo Record (34°S). *Quat. Res.* 58, 160–170. doi:10.1006/qres.2002.2370

Kaiser, J., Schefuß, E., Lamy, F., Mohtadi, M., and Hebbeln, D. (2008). Glacial to Holocene Changes in Sea Surface Temperature and Coastal Vegetation in north central Chile: High versus Low Latitude Forcing. *Quat. Sci. Rev.* 27, 2064–2075. doi:10.1016/j.quascirev.2008.08.025

Kull, C., and Grosjean, M. (2000). Late Pleistocene Climate Conditions in the north Chilean Andes Drawn from a Climate-Glacier Model. *J. Glaciol.* 46 (155), 622–632. doi:10.3189/172756500781832611

Li, Y., Zhou, L., and Cui, H. (2008). Pollen Indicators of Human Activity. *Sci. Bull.* 53, 1281–1293. doi:10.1007/s11434-008-0181-0

Liu, S., Stoof-leichsenring, K. R., Kruse, S., Pestryakova, L. A., and Herzschuh, U. (2020). Holocene Vegetation and Plant Diversity Changes in the North-Eastern Siberian Treeline Region from Pollen and Sedimentary Ancient DNA. *Front. Ecol. Evol.* 8, 1–17. doi:10.3389/fevo.2020.560243

López-Angulo, J., Pescador, D. S., Sánchez, A. M., Mihoč, M. A. K., Cavieres, L. A., and Escudero, A. (2018). Determinants of High Mountain Plant Diversity in the Chilean Andes: From Regional to Local Spatial Scales. *PLOS ONE* 13 (7), e0200216–16. doi:10.1371/journal.pone.0200216

Losapio, G., Cerabolini, B. E. L., Maffioletti, C., Tampucci, D., Gobbi, M., and Caccianiga, M. (2021). The Consequences of Glacier Retreat Are Uneven between Plant Species. *Front. Ecol. Evol.* 8, 1–11. doi:10.3389/fevo.2020.616562

Maldonado, A., Méndez, C., Ugalde, P., Jackson, D., Seguel, R., and Latorre, C. (2010). Early Holocene Climate Change and Human Occupation along the Semiarid Coast of north-central Chile. *J. Quat. Sci.* 25, 985–988. doi:10.1002/jqs.1385

Maldonado, A., and Villagrán, C. (2006). Climate Variability over the Last 9900 Cal Yr BP from a Swamp forest Pollen Record along the Semiarid Coast of Chile. *Quat. Res.* 66, 246–258. doi:10.1016/j.yqres.2006.04.003

Mander, L., and Punyasena, S. W. (2014). On the Taxonomic Resolution of Pollen and Spore Records of Earth's Vegetation. *Int. J. Plant Sci.* 175, 931–945. doi:10.1086/677680

Markgraf, V., and D'Antoni, H. (1978). *Pollen flora of Argentina*. Tucson: The University of Arizona Press.

Martel-Cea, A., Maldonado, A., Grosjean, M., Alvial, I., de Jong, R., Fritz, S. C., et al. (2016). Late Holocene Environmental Changes as Recorded in the Sediments of High Andean Laguna Chepical, Central Chile (32°S; 3050 M a.s.l.). *Palaeogeogr. Palaeoclimatol. Palaeoecol.* 461, 44–54. doi:10.1016/j.palaeo.2016.08.003

Méndez, C., Gil, A., Neme, G., Nuevo Delaunay, A., Cortegoso, V., Huidobro, C., et al. (2015). Mid Holocene Radiocarbon Ages in the Subtropical Andes (~29°-35° S), Climatic Change and Implications for Human Space Organization. *Quat. Int.* 356, 15–26. doi:10.1016/j.quaint.2014.06.059

Michael Anderson, T. (2008). Plant Compositional Change over Time Increases with Rainfall in Serengeti Grasslands. *Oikos* 117, 675–682. doi:10.1111/j.0030-1299.2008.16516.x

Montecinos, A., and Aceituno, P. (2003). Seasonality of the ENSO-Related Rainfall Variability in Central Chile and Associated Circulation Anomalies. *J. Clim.* 16 (2), 281–296. doi:10.1175/1520-0442(2003)016<0281:SOTERR>2.0.CO;2

Moy, C. M., Seltzer, G. O., Rodbell, D. T., and Anderson, D. M. (2002). Variability of El Niño/Southern Oscillation Activity at Millennial Timescales during the Holocene Epoch. *Nature* 420, 162–165. doi:10.1038/nature01163.110.1038/nature01194

Oksanen, J., Blanchet, F. G., Friendly, M., Kindt, R., Legendre, P., Mcglinn, D., et al. (2015). *Vegan*. Community Ecology Package (Version 2.2-1). Available at: https://cran.r-project.org/web/packages/vegan/index.html.

O'Reilly, B. C., Finkelstein, S. A., and Bunbury, J. (2014). Pollen-Derived Paleovegetation Reconstruction and Long-Term Carbon Accumulation at a Fen Site in the Attawapiskat River Watershed, Hudson Bay Lowlands, Canada. *Arctic, Antarctic, Alpine Res.* 46 (1), 6–18. doi:10.1657/1938-4246-46.1.6

Orme, L. C., Miettinen, A., Divine, D., Husum, K., Pearce, C., Van Nieuwenhove, N., et al. (2018). Subpolar North Atlantic Sea Surface Temperature since 6 Ka BP: Indications of Anomalous Ocean-Atmosphere Interactions at 4-2 Ka BP. *Quat. Sci. Rev.* 194, 128–142. doi:10.1016/j.quascirev.2018.07.007

Paus, A. (2013). Human Impact, Soil Erosion, and Vegetation Response Lags to Climate Change: Challenges for the Mid-scandinavian Pollen-Based Transfer-Function Temperature Reconstructions. *Veget Hist. Archaeobot* 22 (3), 269–284. doi:10.1007/s00334-012-0360-4

Pellicciotti, F., Ragettli, S., Carenzo, M., and McPhee, J. (2014). Changes of Glaciers in the Andes of Chile and Priorities for Future Work. *Sci. Total Environ.* 493, 1197–1210. doi:10.1016/j.scitotenv.2013.10.055

Püttker, T., de Arruda Bueno, A., Prado, P. I., and Pardini, R. (2014). Ecological Filtering or Random Extinction? Beta-Diversity Patterns and the Importance of Niche-Based and Neutral Processes Following Habitat Loss. *Oikos* 124 (2), 206–215. doi:10.1111/oik.01018

Quintana, J. (2012). Changes in the Rainfall Regime along the Extratropical West Coast of South America (Chile): 30-43° S. *Atmósfera* 25 (1), 1–22.

Rein, B., Lückge, A., Reinhardt, L., Sirocko, F., Wolf, A., and Dullo, W.-C. (2005). El Niño Variability off Peru during the Last 20,000 Years. *Paleoceanography* 20, a–n. doi:10.1029/2004PA001099

Rudloff, V. M., Rutllant, J. A., Martel-Cea, A., and Maldonado, A. (2021). Hydrothermal Modulation of NDVI in the High-Altitude Semiarid Andes of Chile (30-34°S). *J. Arid Environments* 186, 104397. doi:10.1016/j.jaridenv.2020.104397

Sarricolea, P., Herrera-ossandon, M., and Meseguer-ruiz, Ó. (2016). Climatic Regionalisation of continental Chile. *J. Maps* 13 (2), 66–73. doi:10.1080/17445647.2016.1259592

Sax, D. F. (2002). Equal Diversity in Disparate Species Assemblages: a Comparison of Native and Exotic Woodlands in California. *Glob. Ecol. Biogeogr.* 11, 49–57. doi:10.1046/j.1466-822x.2001.00262.x

Schickhoff, U., Singh, R. B., and Mal, S. (2016). "Climate Change and Dynamics of Glaciers and Vegetation in the Himalaya: An Overview," in *Climate Change, Glacier Response, and Vegetation Dynamics in the Himalaya*. Editors R. Singh, U. Schickhoff, and S. Mal (Cham: Springer), 1–26. doi:10.1007/978-3-319-28977-910.1007/978-3-319-28977-9_1

Souvignet, M., Oyarzún, R., Verbist, K. M. J., Gaese, H., and Heinrich, J. (2012). Hydro-meteorological Trends in Semi-arid north-central Chile (29-32°S): Water Resources Implications for a Fragile Andean Region. *Hydrological Sci. J.* 57 (3), 479–495. doi:10.1080/02626667.2012.665607

Squeo, F., Tracol, Y., López, D., León, M., and Gutiérrez, J. (2009). "Vegetación nativa y variación temporal de la productividad en la Provincia del Elqui," in *Los Sistemas Naturales de la Cuenca del Río Elqui*. Editor J. Cepeda (La Serena, Chile: Ediciones Universidad de La Serena).

Stockmarr, J. (1971). Tablets with Spores Used in Absolute Pollen Analysis. *Pollen Spores* 13, 614–621. doi:10.1046/j.1466-822x.2001.00262.x

Tiner, R. J., Negrini, R. M., Antinao, J. L., McDonald, E., and Maldonado, A. (2018). Geophysical and Geochemical Constraints on the Age and Paleoclimate Implications of Holocene Lacustrine Cores from the Andes of central Chile. *J. Quat. Sci.* 33 (2), 150–165. doi:10.1002/jqs.3012

Valois, R., Schaffer, N., Figueroa, R., Maldonado, A., Yáñez, E., Hevia, A., et al. (2020). Characterizing the Water Storage Capacity and Hydrological Role of Mountain Peatlands in the Arid Andes of North-Central Chile. *Water* 12, 1071. doi:10.3390/w12041071

Veblen, T., Young, K., Orme, A., and Hinojosa, L. F. (2007). "The Physical Geography of South America," in *The Physical Geography of South America*. Editors T. T. Velben, K. R. Young, and A. R. Orme (New York: Oxford University Press), 184–199. doi:10.1093/oso/9780195313413.001.0001

Velásquez, R., Coloma, F., Murillo, I., Merino, R. N., and Ortiz, M. (2021). Geología de las áreas Pisco Elqui y Paso del Agua Negra, región de Coquimbo. Servicio Nacional de Geología y Minería, Carta Geológica de Chile. *Serie Geología Básica* 211-212, 201.

Villagrán, C., Arroyo, M., and Marticorena, C. (1983). Efectos de la desertización en la distribución de la flora andina de Chile. *Revista Chilena de Historia Natural* 56, 137–157.

Villa-Martínez, R., Villagrán, C., and Jenny, B. (2003). The Last 7500 Cal Yr B.P. Of westerly Rainfall in Central Chile Inferred from a High-Resolution Pollen Record from Laguna Aculeo (34°S). *Quat. Res.* 60, 284–293. doi:10.1016/j.yqres.2003.07.007

Wanner, H., Mercolli, L., Grosjean, M., and Ritz, S. P. (2015). Holocene Climate Variability and Change; a Data-Based Review. *J. Geol. Soc.* 172, 254–263. doi:10.1144/jgs2013-101

Whitlock, C., Higuera, P. E., Mcwethy, D. B., and Briles, C. E. (2010). Paleoecological Perspectives on Fire Ecology: Revisiting the Fire-Regime Concept~!2009-09-02~!2009-11-09~!2010-03-05~!. *Toecolj* 3, 6–23. doi:10.2174/1874213001003020006

Whitlock, C., and Larsen, C. (2002). "Charcoal as a Fire Proxy," in *Tracking Environmental Change Using Lake Sediments*. Editors J. P. Smol, H. J. B. Birks, and W. M. Last (Dordrecht: Springer), 75–97. doi:10.1007/0-306-47668-1_5

Woodward, F. I., and Williams, B. G. (1987). Climate and Plant Distribution at Global and Local Scales. *Vegetatio* 69, 189–197. doi:10.1007/BF00038700

World Water Council (2009). *Vulnerability of Arid and Semi-arid Regions to Climate Change*. Cairo, Egypt: Perspectives on Water and Climate Change Adaptation.

Zhang, Q., Hou, X., Li, F. Y., Niu, J., Zhou, Y., Ding, Y., et al. (2014). Alpha, Beta and Gamma Diversity Differ in Response to Precipitation in the Inner Mongolia Grassland. *PLOS ONE* 9 (3), e93518–9. doi:10.1371/journal.pone.0093518

Zhao, Y., Chen, F., Zhou, A., Yu, Z., and Zhang, K. (2010). Vegetation History, Climate Change and Human Activities over the Last 6200years on the Liupan Mountains in the Southwestern Loess Plateau in central China. *Palaeogeogr. Palaeoclimatol. Palaeoecol.* 293, 197–205. doi:10.1016/j.palaeo.2010.05.020

Conflict of Interest: The authors declare that the research was conducted in the absence of any commercial or financial relationships that could be construed as a potential conflict of interest.

Publisher's Note: All claims expressed in this article are solely those of the authors and do not necessarily represent those of their affiliated organizations, or those of the publisher, the editors, and the reviewers. Any product that may be evaluated in this article, or claim that may be made by its manufacturer, is not guaranteed or endorsed by the publisher.

frontiers in Earth Science

ORIGINAL RESEARCH
published: 22 March 2022
doi: 10.3389/feart.2022.863933

Multi-Decadal Glacier Area and Mass Balance Change in the Southern Peruvian Andes

Liam S. Taylor[1,2]*, *Duncan J. Quincey*[1], *Mark W. Smith*[1], *Emily R. Potter*[1], *Joshua Castro*[3] *and Catriona L. Fyffe*[4]

[1]School of Geography and Water@leeds, University of Leeds, Leeds, United Kingdom, [2]Centre for Polar Observation and Modelling, University of Leeds, Leeds, United Kingdom, [3]Instituto de Investigación, Universidad y Región, Universidad Nacional de San Antonio Abad del Cusco, Cusco, Peru, [4]Department of Geography and Environmental Sciences, Northumbria University, Newcastle Upon Tyne, United Kingdom

Around 70% of the world's tropical glaciers are located in Peru, and they are melting rapidly in response to climate change. The glaciers of the data-sparse Southern Peruvian Andes, comprising the Cordilleras Vilcanota, Vilcabamba, and Urubamba, are a primary water source for thousands of people living in the rural foothills, and support people throughout the wider Cusco region. Here, we calculate geodetic mass balance for the Cordillera Vilcanota (–0.48 ± 0.07 m w.e. yr^{-1}) using the ASTER satellite archive and derive a total loss of 3.18 ± 0.44 Gt ice between 2000 and 2020. Glacierised area has shrunk rapidly since the 1970s (losses of 54, 56, and 64% for the Cordilleras Vilcanota, Vilcabamba, and Urubamba respectively) as a consequence of changing climatic patterns, with low-lying glaciers receding the most across all regions. We calculate a rise in the median elevation of glaciers ranging from 15.9 m per decade over the Quelccaya ice cap in the Cordillera Vilcanota, to 32.8 m per decade in the Cordillera Vilcabamba, over the period 1975 to 2020. This change implies an increased hazard potential as the mountain regions become destabilised, and will lead to increasing pressure on fresh water supply as meltwater streamflow decreases and river discharge becomes increasingly, and irreversibly, variable.

Keywords: Cordillera Vilcanota, Cordillera Urubamba, Cordillera Vilcabamba, ASTER, tropical glacier, mountain cryosphere

OPEN ACCESS

Edited by:
Neil Franklin Glasser, Aberystwyth University, United Kingdom

Reviewed by:
Fabian Drenkhan, Pontifical Catholic University of Peru, Peru
Bethan Joan Davies, University of London, United Kingdom

***Correspondence:**
Liam S. Taylor
gylst@leeds.ac.uk

Specialty section:
This article was submitted to Cryospheric Sciences, a section of the journal Frontiers in Earth Science

Received: *27 January 2022*
Accepted: *07 March 2022*
Published: *22 March 2022*

Citation:
Taylor LS, Quincey DJ, Smith MW, Potter ER, Castro J and Fyffe CL (2022) Multi-Decadal Glacier Area and Mass Balance Change in the Southern Peruvian Andes. Front. Earth Sci. 10:863933. doi: 10.3389/feart.2022.863933

INTRODUCTION

Tropical glaciers are highly sensitive to climatic changes and those in Peru, where the vast majority (~70%) are located, have been rapidly receding for several decades (Chevallier et al., 2011; Salzmann et al., 2013; Schauwecker et al., 2014; Zemp et al., 2019). Consequently, as mountain slopes become destabilised, there has been increased threat from natural hazards, an observed growth in the number and area of glacial lakes, and changes to primary water supply (Drenkhan et al., 2019; Brügger et al., 2021; Thompson et al., 2021; Veettil and Kamp, 2021). Glacier recession is unlikely to be reversed as reductions in precipitation and increases in temperature are projected until at least 2100 (Kronenberg et al., 2016). Studies of future river discharge are unanimous in predicting a reduction in longer-term water supply, particularly during the dry season when glacier melt provides a critical buffer against drought (Vuille et al., 2008).

Compared to other mountain glacier regions around the world, there is a notable dearth of region-wide estimates of mass balance change for those located in Peru (Vuille et al., 2018).

Previous studies have focussed on quantifying rates of glacier recession using satellite-based measurements of both area and volume change. At a continental-scale, Dussaillant et al. (2019) assessed mass balance across the Andes, noting that the glaciers of the tropical Andes (-0.42 ± 0.24 m w.e. yr^{-1}) were losing mass at a steady rate between 2000 and 2018. At a national scale, Seehaus et al. (2019) presented areal losses of 28.6% from 2000 to 2016 and a Peru-wide mass balance of -0.457 ± 0.064 m w.e. yr^{-1}. In contrast to Dussaillant et al. (2019), Seehaus et al. (2019) found a recent (2013–2016) increase in the rate of mass loss. The National Inventory of Glaciers in Peru quantified a 48% decline of glacial area from 2,041.85 km^2 in 1962 to 1,058.37 km^2 as of 2021 (ANA, 2021).

Regional studies of glacier recession in Peru disproportionately focus on the largest region; the Cordillera Blanca. Here, glacier loss has accelerated since the 1970s with consequent increases in their terminus elevations (Racoviteanu et al., 2008), following 20th century retreat from their Little Ice Age maximum extent (Georges, 2004) with a brief glacial advance interruption in the 1920s (Kaser, 1999). Glaciers in the Cordillera Blanca extend to lower elevations than the second-largest region, the Cordillera Vilcanota, owing to a lower annual freezing line altitude (Sagredo and Lowell, 2012; Schauwecker et al., 2017). Nevertheless, the Cordillera Vilcanota follows similar trends to the Cordillera Blanca, having lost 30% of its glacierised area and 45% of its volume from 1985 to 2006 (Salzmann et al., 2013). The National Inventory of Glaciers shows a decline of 48% of glacierised area in the Cordillera Vilcanota from 1962 to 2017 (INAIGEM, 2017; ANA, 2021). Measurements of mass balance on individual glaciers show that topography is a key control on ice loss; glaciers with a maximum elevation below 5400 m above sea level (m a.s.l.) are estimated to be losing mass at a rate (-1.2 m w.e. yr^{-1}) double that of glaciers with an elevation above 5400 m a.s.l. (-0.6 m w.e. yr^{-1}) (Rabatel et al., 2013a).

The controls of glacier recession in the Peruvian Andes appear to be numerous, and are often interlinked. Overall, lower lying and smaller glaciers have been observed to be in rapid retreat (Rabatel et al., 2013a), although there is variability related to aspect, and therefore radiation receipt (Veettil et al., 2018). The surface energy balance of Peruvian glaciers is primarily controlled by precipitation, which impacts albedo and therefore radiation receipt over low-lying glacial termini (Vuille et al., 2008; Fyffe et al., 2021), particularly in the outer tropics (Kaser, 2001). Air temperature controls this precipitation phase, such that warming temperatures increase the proportion of a glacier receiving rainfall rather than snowfall, which subsequently also impacts their albedo and radiation receipt. The pattern is more complex when looking at specific regions of Peruvian glaciers. Some studies have made different links between discrete climatic variables and rates of glacier recession—for example, changes in temperature appear to be most important for glaciers in the Cordillera Huaytapallana (López-Moreno et al., 2014), while precipitation is a more important driver in the Cordillera Blanca (Fyffe et al., 2021). Over longer timescales, specific humidity may also play a key role in mass loss in other areas (Vuille et al., 2008; Salzmann et al., 2013). For tropical glaciers more broadly, Kaser (1999) suggests both air temperature and humidity play a role in causing recent (post-1980s) retreat. There is also some indication that the interannual variability of the El Niño Southern Oscillation (ENSO) impacts glacier mass change in the Peruvian Andes, with heavy snowfall during La Niña phases and stronger ablation during El Niño, though these linkages are weaker (Vuille et al., 2008; Drenkhan et al., 2018).

Given contemporary rates of recession, there is growing concern that many glacierised areas across Peru could be ice-free by the end of the century (Drenkhan et al., 2018). However, robust measurements of glacier change are still sparse, and future projections are highly uncertain owing to the complexity of climatic and topographic factors driving change between regions (Schauwecker et al., 2017; Hock et al., 2019). The small size of tropical glaciers, and the fact that they are located in steep terrain, presents challenges for satellite-based observations as well as *in-situ* monitoring, meaning gaps in mass balance and ice area loss data persist for some regions, such as the Southern Peruvian Andes (Berthier et al., 2006; Prinz et al., 2018; Taylor et al., 2021). There remains a need for accurate, detailed and comprehensive studies that combine multiple datasets together to fully assess the dynamics of glaciers at high spatial and temporal resolution, the outputs from which can be invaluable for stakeholders and planners working to mitigate ongoing changes in runoff in these locations and guide climate change adaptation (Bury et al., 2011; Carey et al., 2012). A growing archive of satellite observations, along with the increasing availability of cloud-based and high-performance computing, provides an opportunity to fill some of those gaps.

Here, we use the 20-year ASTER (Advanced Spaceborne Thermal Emission and Reflection radiometer) satellite image archive as the basis for our analysis of glacier change in the Peruvian Andes. Previous studies have already defined a framework for producing regional (Dussaillant et al., 2018), continental (Brun et al., 2017; Dussaillant et al., 2019), and global (Hugonnet et al., 2021) measurements of glacier change using these data. Such datasets provide valuable insight into mountain glacier dynamics, their contribution to sea-level rise, and acceleration of melt, but they inevitably focus on the big picture of broad area changes. However, the usefulness of these large-scale datasets has seldom been examined in monitoring small mountain glaciers, particularly at their relatively coarse (100 m+) resolution. The overall aim of this research is, therefore, to provide detailed measurements of glacier area and volume change for the Cordilleras Vilcanota, Vilcabamba, and Urubamba, using the ASTER and Landsat satellite image archives, dating back to the 1970s. We generate high-resolution (30 m) products of elevation change using the ASTER archive to assess the quality of the global Hugonnet et al. (2021) dataset in measuring mass balance over small mountain glaciers. We explore the key processes driving ice loss across these regions, and discuss likely future changes to these glaciers under various climate scenarios, all of which result in a rise in equilibrium line altitude (ELA) and thus continued, unabated mass loss.

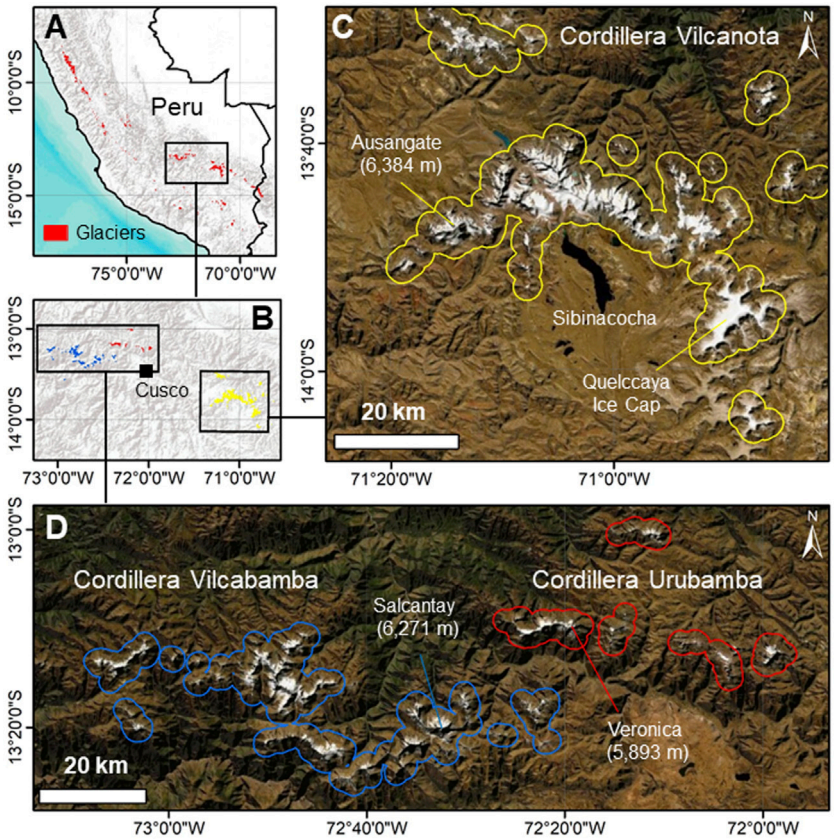

FIGURE 1 | Location of the Southern Peruvian Cordilleras within **(A)** Peru and **(B)** the Cusco region. **(C)** The Cordillera Vilcanota outlined in yellow (with a 2 km buffer around glacierised areas), and **(D)** The Cordilleras Vilcabamba (blue) and Urubamba (red). Satellite imagery from DigitalGlobe. Glacier outlines from RGI Consortium (2017) **(A)** and this study **(B–D)**.

STUDY AREA

The Cordilleras Vilcanota (246.8 km^2 glacierised area in 2020; from this study), Vilcabamba (100.4 km^2), and Urubamba (24.2 km^2) represent a combined glacierised area of 371.4 km^2. These regions are relatively understudied in comparison to the Cordillera Blanca (which is larger than all three together); yet, they represent a water source for hundreds of thousands of people in the wider Cusco region, many of which are located in the city of Cusco (population 470,000) (Drenkhan et al., 2018; Martínez et al., 2020). Recent glacial lake outburst floods at Salkantaycocha in 2020 (Vilca et al., 2021) and Riticocha in 2010 (Drenkhan et al., 2019) provide stark reminders of the threat that climatic changes pose in this region.

The Cordillera Vilcanota comprises a central mountain range (ranging from ~4,600 m a.s.l. to the peak of 6,384 m a.s.l at Ausangate) arcing above Sibinacocha (**Figure 1**)—a large (~28 km^2) lake, which began being used for hydroelectricity generation in 1996. The Quelccaya ice cap (ranging from ~5,200 to 5,743 m a.s.l) dominates the east of the Cordillera Vilcanota with a maximum ice thickness of 150–170 m (Salzmann et al., 2013). Until recently, Quelccaya was the largest tropical ice cap on Earth, replaced by the Coropuna Ice Cap in the South of Peru (not analysed in this study) (Kochtitzky et al., 2018). In the immediate vicinity of the glaciers of the Cordillera Vilcanota are small indigenous farming communities made up of a few thousand individuals. The largest, the Phinaya community, has witnessed glacier fluctuations for centuries, and is therefore well aware of the causes and consequences of glacier recession and the likely impact it will have on their futures (Orlove, 2009). Recession of glaciers in the Cordillera Vilcanota has previously been documented by Salzmann et al. (2013), but extending only as far back as 2009 for ice area and 2006 for ice volume change, and not benefiting from the availability of more recent and more robust methods of calculating mass balance. The National Inventory of Glaciers provides ice area change from the Cordillera Vilcanota to 2017 (246 km^2) and Cordilleras Vilcabamba and Urubamba to 2016 (96 and 18 km^2 respectively) (INAIGEM, 2017; ANA, 2021). Detailed assessments of mass balance have been limited to individual glaciers based on field monitoring campaigns (Molina et al., 2015).

The Cordilleras Vilcabamba and Urubamba are smaller in size, and together comprise around half the glacierised area of the Cordillera Vilcanota. They are located to the west and north-west of Cusco and stretch for around 100 km east-west, ranging from

~4,600 m a.s.l to peaks of 6,271 m a.s.l at Salcantay in the Vilcabamba and 5,893 m a.s.l at Veronica in the Urubamba. Glaciers in this region have deep spiritual connotations as mountain deities to indigenous communities (Drenkhan et al., 2018). In addition, their demise impacts directly on the agriculture-based economy, which relies on glacial meltwater as a source of irrigation. Measurements of glacier change in this region are extremely limited, restricted to individual watersheds (Drenkhan et al., 2018) or specific glaciers (Veettil et al., 2018).

DATA AND METHODS

Available Datasets

Satellite image archives are increasingly vast, as well as open-access, and computational advances have led to methodological frameworks that allow for robust analyses of glacier change that we employ here in the Cordilleras Vilcanota, Vilcabamba and Urubamba. The Landsat archive provides a record of ice area change almost continuously from 1972 to the present day, interrupted only by periods of heavy cloud and snow and short discontinuities in satellite operation. The small size of some glaciers in this region presents a challenge to delineating ice areas, but for decadal rates of change the measured rates of recession frequently exceed any uncertainties in the data.

Deriving volumetric changes from these stereoscopic sensors relies on there being sufficient contrast over snow and ice-covered surfaces for feature matching to be successful. Reconnaissance images (e.g. Corona KH-4; Bolch et al., 2008) acquired over the high-elevation accumulation areas of the Cordilleras Vilcanota, Vilcabamba, and Urubamba are largely featureless however, meaning surface elevations cannot be extracted. For this reason, we focussed our mass balance estimations on the ASTER archive, which provides a continuous record from 2000 to the present day of stereoscopic scenes across the world. ASTER acquires images every 16 days through a 14-band nadir sensor and a single band backward looking sensor to acquire stereo images. These data are collected at 15 and 30 m resolution to produce 30 m-resolution digital elevation models (DEMs). Cloud and snow also interfere with the production of digital elevation models, but the huge data redundancy afforded by the archive means this issue is relatively easy to overcome.

Area Change Between 1975 and 2020

Orthorectified Landsat-2 scenes (Level L1TP, 60 m spatial resolution; **Supplementary Table S1**) were used to manually delineate glacier outlines for the 1970s, conducted in ArcMap. All Landsat-2 scenes were acquired between the 25th June—31st July 1975 to minimise the influence of snow cover. All other glacier outlines were produced from 30 m imagery from the full-archive Landsat-5 Tier 1 Top of Atmosphere (1984–2012) and Landsat-8 Tier 1 Top of Atmosphere (2013–2020) datasets using a Normalised Difference Snow/Water Index (NDSI, NDWI) in Google Earth Engine. A cloud-free composite was produced for each year by extracting the median pixel value from the driest months (July 1st to September 30th) to minimise snow and cloud cover. Due to heavy cloud in these regions, there are some years within the time series with no usable imagery. The resulting images were split into their respective boundaries from the Randolph Glacier Inventory 6.0 (RGI) dataset (RGI Consortium, 2017) and manually extended outwards using the ASTER GDEM. On inspection, a small number of RGI outlines in these regions seemed highly improbable, and so we manually delineated flowlines where it was clear the RGI database was merging multiple glaciers together. All shapefiles were clipped to remove polygons smaller than 0.01 km^2 in area and manually inspected to ensure no ice-free area was being incorrectly classified.

When determining glacier area, we calculated a conservative estimate of uncertainty for Landsat-2 scenes by assuming all glacier periphery pixels were misclassified, and calculated the total area of these periphery pixels, representing an error of 11%. Studies which have calculated uncertainty in a similar way produce comparable estimates of uncertainty (e.g. 11% for Kochtitzky et al., 2018). Rocky outcrops between glaciers and nunataks were particularly problematic to determine whether they were glacierised or snow-covered. Glacier boundaries from 1984 onwards were calculated *via* an automated method. Where this method is applied over predominantly clean-ice, associated error is 2–5% (Paul et al., 2013), and so we use a conservative estimate of 5% as the uncertainty value for glacier area delineated in this way, as the Southern Peruvian Andes are mostly clean-ice. We acknowledge that this method excludes any small debris cover patches that exist, but this is consistent with other studies who also exclude these areas due to their scarcity in this region (Salzmann et al., 2013).

Volume Change Between 2000 and 2020

To calculate glacier volume change, we extracted all L1A ASTER tiles collected over these regions in the 20-year timespan from 1st January 2000 to 31st December 2020. We derived 631 DEMs using the AMES Stereo Pipeline with a 7 pixel correlation kernel, using a 12 m TanDEM-X tile seed. To ensure accurate co-registration, they were corrected for planimetric and altimetric shifts against the TanDEM-X tile with a third-order polynomial transformation in stable, off-ice areas using the method of Nuth and Kääb (2011). Using a higher resolution DEM (12 m) compared to Hugonnet et al. (2021) (90 m) for co-registration should result in more accurate elevation models. DEMs that passed this correction phase were uploaded to Google Earth Engine using *geeup* (Roy, 2021), and clipped to elevations between 2000 and 6500 m a.s.l. (the approximate range of elevation within these Cordilleras) to exclude grossly erroneous pixels. A single value per pixel per year was extracted from all DEM tiles by collecting the median value (excluding values above and below the median ±100 m). Using these single values per year, a linear fit through the surface elevation was then calculated over three time periods: 2000–2010; 2010–2020; and 2000–2020 to represent elevation change per year during these intervals. Hugonnet et al. (2021) produce elevation change at 5-year intervals, but the associated error is often far larger than in the decadal intervals, and so we consider only the 10-year products to be usable. More detailed

methodology including the parameters used at each stage is given in **Supplementary Datasheet S2**.

For the conversion of elevation change to mass change, there are three key sources of uncertainty:

1) Error in glacier area (σ_A)
2) Error in the calculated elevation change ($\sigma_{\Delta z}$)
3) Error in ice density calculations ($\sigma_{f\Delta V}$)

We followed the method presented by Brun et al. (2017) to calculate overall uncertainty for mass balance calculations. We calculate uncertainty for the region-wide mass loss and use this fraction to attribute uncertainty in mass balance. Uncertainty in volume change is calculated using the standard deviation of elevation change on stable ground ($\sigma_{\Delta h}$). We cast a 2 km buffer outwards from the glacier margin into stable ground and used the standard deviation of all pixels in this buffer area as $\sigma_{\Delta h}$. We follow Brun et al. (2017) in using a decorrelation length of 500 m, but use a glacier area uncertainty (σ_A) of 5% as we have greater confidence that this region is predominantly clean-ice. Finally, we use an ice density uncertainty ($\sigma_{f\Delta V}$) of 60 kg m^{-3} following Huss (2013).

Calculation of Geodetic Mass Balance and Median Glacier Elevation

Geodetic mass balance was calculated by taking into account the elevation change per pixel, pixel size (30 m), and ice density of 850 ± 60 kg m^3 (Huss, 2013). Calculation of surface mass balance, which would include estimates of glacier flow from modelled ice thickness and velocity (Miles et al., 2021), was not possible in this region owing to lack of available flow data. This precluded a robust estimate of the glacier ELA using our surface elevation data alone. Therefore, in the absence of any *in-situ* data, we investigated previously published methods to quantify ELA change through time. These included quantifying changes to the freezing-line altitude (e.g. Schauwecker et al., 2017; Yarleque et al., 2018), the end of summer snowline altitude (Condom et al., 2007; Rabatel et al., 2013b), and the use of the median glacier elevation as an ELA proxy (e.g. Braithwaite and Raper, 2009; King et al., 2017). We adopted this final approach in the absence of higher spatial resolution climate data or reliable cloud-free satellite data to quantify snowlines, though we acknowledge this is likely to underestimate actual ELAs as the glaciers are out of balance with the climate. We calculated median glacier elevation for every glacier, and herein summarise an area-weighted average region-wide median glacier elevation for the Cordilleras Vilcabamba and Urubamba, and separate the Cordillera Vilcanota into five sub-regions reflecting the differing altitudes and topographies of each (**Supplementary Figure S3**).

Topography and Climate Data

To identify the most significant controls on ice loss in each region, we correlated the variables of change (volume and area loss) against topographic and climate data. Topographic data (aspect, elevation, slope) were derived from the ASTER GDEM and averaged over the shapefiles of each glacier. Climate data were created using the Weather Research and Forecasting (WRF) model and bias-corrected against daily precipitation and maximum and minimum daily temperature data in the region, from 1980 to 2018. Frost days were calculated as the number of days in the year where the minimum daily temperature fell below 0°C. For full details of the WRF model setup and bias-correction, see (Fyffe et al., 2021).

Climate data were correlated to glacier area change from 1984 (the first year of overlap between the Landsat record and climate dataset) to 2018 (the end of the climate dataset) for every glacier individually. These coefficients were then transformed to z-values using Fisher's Z to ensure a normal distribution of data. A mean was taken of these Fisher's Z values, which was subsequently back-transformed to achieve an overall region-wide correlation coefficient between ice area and climatic variables. Significance for these values was calculated using the Harmonic mean *p*-value, weighted to the size of the glacier, as a robust measure of significance in large datasets (Wilson, 2019). These steps ensure each glacier is statistically analysed against only the climate data that are of most relevance to that particular glacier.

RESULTS AND DISCUSSION

Ice Area Change (1975–2020)

Overall, glacierised area of the Southern Peruvian Andes shrunk from 833.6 ± 91.7 km^2 in 1975 to 312.6 ± 15.6 km^2 in 2020 (**Figure 2**). This loss has predominantly occurred at low elevations (**Figure 3**). The Cordillera Vilcanota shrunk from a regional total of 540.6 ± 59.4 km^2 in 1975 to 246.8 ± 12.3 km^2 in 2020. This represents a loss of 54.3% of the glacier ice that was present in 1975 over a 45-year time period. 82 of the 257 glaciers present in 1975 had been lost by 2020 (or shrunk smaller than 0.01 km^2 in size). There has been consistent and steady recession of ice across the region in this time. The Quelccaya ice cap, which is included within the area for the Cordillera Vilcanota, shrunk from 57.4 ± 5.4 km^2 in 1975 to 41.6 ± 2.1 km^2 in 2020, representing a loss (27.5%) that is below the regional average (**Figure 2**). There has, in contrast to the region-wide Cordillera Vilcanota, been an observable slowdown of ice area loss in recent years.

The Cordillera Vilcabamba shrunk from 226.1 ± 24.9 km^2 in 1975 to 98.9 ± 4.9 km^2 in 2020, a loss of 56% of glacierised area. 25 of the 169 glaciers present in 1975 had been lost by 2020. The Cordillera Urubamba shrunk from a glacierised area of 66.9 ± 7.4 km^2 in 1975 to 24.2 ± 1.2 km^2 in 2020; a loss of 64%. This represents the largest relative decline in glacierised area of the regions as this is the lowest-lying of the three Cordilleras. Of the 39 glaciers in the Cordillera Urubamba in 1975, seven had been lost by 2020.

These area changes, which predominantly affect lower-lying zones, have driven the glaciers to higher elevations over the 45-year study period (**Figure 3**). It is notable that in all three Cordilleras, glacier ice has all but disappeared from elevations below 4,700 m a.s.l. but is largely preserved above elevations of

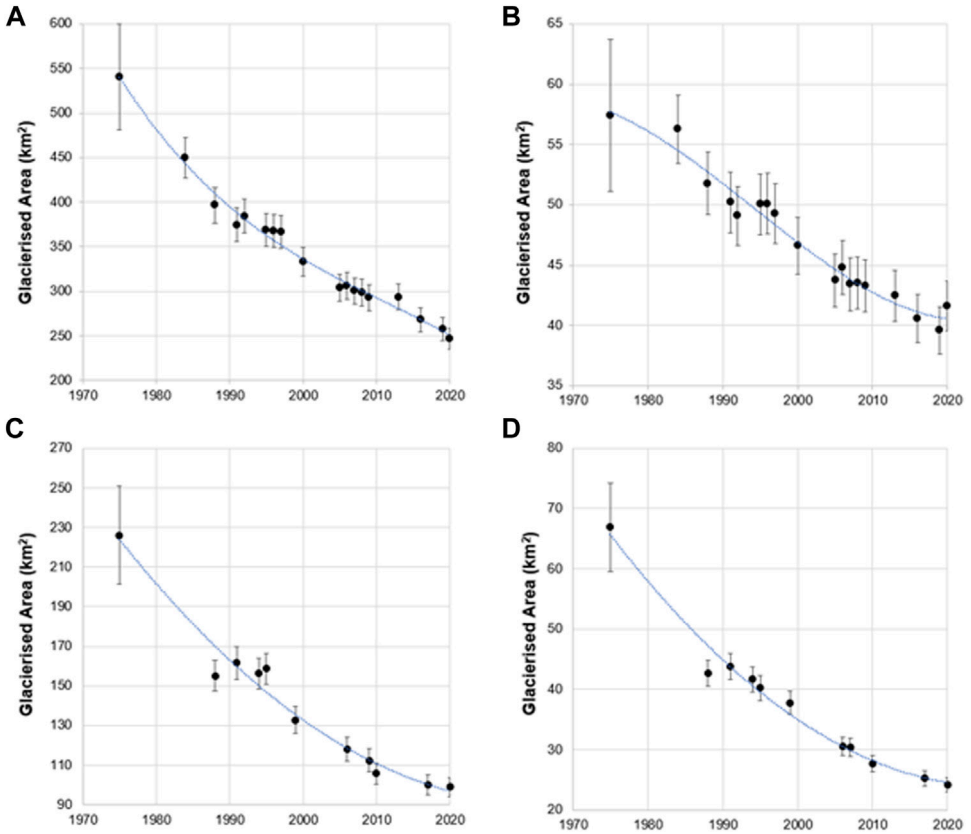

FIGURE 2 | Glacierised Area of **(A)** Cordillera Vilcanota, **(B)** Quelccaya ice cap, **(C)** Cordillera Vilcabamba, and **(D)** Cordillera Urubamba. Note the varying *y*-axis scales. Blue line represents second-order polynomial fit.

5,500 m a.s.l. In each case, the hypsometry is skewed towards lower elevations. In contrast, the hypsometry of Quelccaya is skewed towards higher elevations, and consequently the bins with greatest area have been largely preserved. For Quelccaya, there is no observed change in glacier area above 5,550 m a.s.l. from 1975 to 2020.

Across the Cordillera Vilcanota, there is a moderate correlation between mean annual air temperature (which has risen by ~0.2°C per decade from 1980 to 2020) and rate of ice area change (R = -0.514, $p < 0.01$), and maximum annual temperature and ice area loss (R = -0.576, $p < 0.01$) (**Figure 3**; **Table 1**). There is no statistically significant link (at $p < 0.01$) between ice area change and precipitation, but there is a corresponding correlation between the number of frost days in the year and ice area loss. The key topographic control on rate of ice area change is maximum elevation ($R = -0.394$, $p < 0.01$), with a second-order control of slope ($R = -0.269$, $p < 0.01$). There is no significant ($p < 0.01$) co-linearity between maximum elevation and slope. The prevalence of cloud or snow-covered scenes in our record limits our ability to analyse the role that ENSO plays in affecting glacier area change (shown in **Figure 2**).

Over the Cordilleras Vilcabamba and Urubamba, there is also a moderate correlation between maximum annual temperature and rate of ice area change ($R = -0.338$, $p < 0.01$ and $R = -0.576$, $p < 0.01$ respectively). There is no statistically significant link between ice area change and precipitation. Similar to the Cordillera Vilcanota, the primary topographic control on ice area change in the Cordilleras Vilcabamba and Urubamba is maximum elevation ($R = -0.241$, $p < 0.01$; $R = -0.677$, $p < 0.01$ respectively) though this driver is much weaker in the Cordillera Vilcabamba. Slope is not a statistically significant control in the Cordillera Vilcabamba, but is in the Cordillera Urubamba ($R = -0.301$, $p < 0.01$), though there is co-linearity between elevation and slope in the Urubamba (R = 0.515, $p < 0.01$).

Ice Volume and Mass Balance (2000–2020)

Between 2000 and 2020, the Cordillera Vilcanota shrunk at a rate of -0.159 ± 0.022 Gt yr^{-1} (-0.48 ± 0.07 m w.e. yr^{-1}). There was no significant change in the mass balance between the two sub-decadal periods; from -0.49 ± 0.17 m w.e. yr^{-1} between 2000–2010 to -0.44 ± 0.16 m w.e. yr^{-1} between 2010–2020 (**Figure 4**). Owing to the cloudiness of ASTER data, smaller glaciers, and steeper slopes over the Cordilleras Vilcabamba and Urubamba, the uncertainty in our mass balance calculation was much larger than it was for the Vilcanota. Between 2000 and 2020, the Cordillera Vilcabamba shrunk at a rate of $-0.405 \pm$

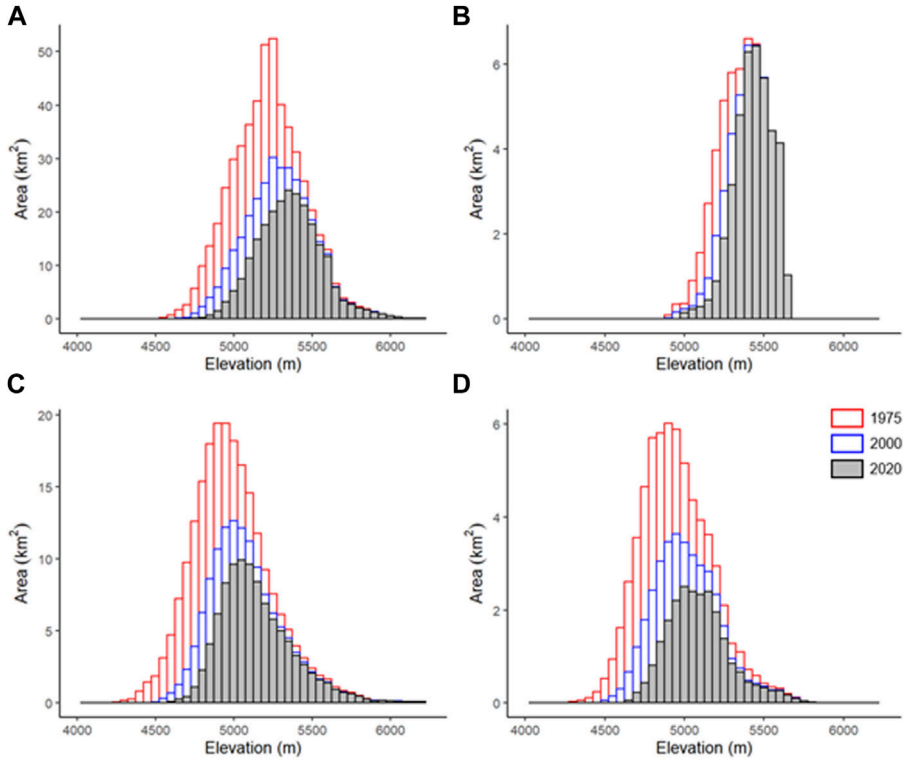

FIGURE 3 | Evolving glacier hypsometry (1975, 2000, and 2020) in 50 m elevation bins for the **(A)** Cordillera Vilcanota, **(B)** Quelccaya ice cap, **(C)** Cordillera Vilcabamba, **(D)** Cordillera Urubamba. Note varying *y*-axis in each graph.

TABLE 1 | Correlation coefficients for drivers of ice area change. Full table and graphs are given in the **Supplementary Table S7** and **Supplementary Figure S8**. Significance (*p*) denoted as * = $p < 0.1$, ** = $p < 0.05$, *** = $p < 0.01$.

	Vilcanota *R*	Vilcabamba *R*	Urubamba *R*
Max. annual air temperature	−0.576***	−0.338***	−0.576***
Mean annual air temperature	−0.514***	−0.277**	−0.446***
Annual precipitation	0.193**	−0.163	−0.156*
Number of frost days	0.361***	0.305**	0.370***
Mean elevation	−0.233***	−0.161**	−0.578***
Max elevation	−0.394***	−0.241***	−0.677***
Min elevation	−0.169***	0.0803	0.368**
Aspect	0.174***	−0.0482	0.0125
Slope	−0.269***	−0.107	−0.301*

0.451 m w.e. yr^{-1}, while the Cordillera Urubamba shrunk at a rate of −0.559 ± 1.575 m w.e. yr^{-1}. We present these figures here for completeness, but do not analyse them further given the extent to which the uncertainty exceeds any signal in the data. Thinning of debris-covered ice, which is not included in the glacier area polygons but only makes up a minimal percentage of ice in the region, can be observed in the surface elevation change (e.g. **Figures 4B,C**).

There is a moderate correlation between volume change over the full 20-year period and elevation ($R = 0.38$, $p < 0.001$), suggesting that low-lying areas are thinning, as well as receding, the most. There is a slight, but significant, correlation between volume change and slope ($R = 0.16$, $p < 0.001$) and aspect ($R = -0.04$, $p < 0.001$). This is particularly noticeable over the Nevado Ausangate cluster of glaciers, where South-facing glaciers are largely shadowed from solar radiation, while North-facing glaciers are experiencing large thinning (**Figure 4B**).

The median elevation (which we use as a proxy for ELA) of the Cordilleras Vilcabamba and Urubamba rose at the fastest rates across the full 1975–2020 time series (3.28 m yr^{-1} and 3.27 m yr^{-1} respectively), from 4,966 m a.s.l. to 5,110 m a.s.l. for the Cordillera Vilcabamba and 4,930 m a.s.l. to 5,077 m a.s.l. for the Cordillera Urubamba (**Figure 5**). However, the rate of change between the regions through time varies. The median elevation of the Cordillera Urubamba is accelerating upwards (from 2.88 m yr^{-1} for 2000–2010 to 4.59 m yr^{-1} for 2010–2020), while the rate of change in the Cordillera Vilcabamba is decelerating (from 3.69 m yr^{-1} for 2000–2010 to 3.06 m yr^{-1} for 2010–2020) (**Supplementary Figure S5**).

The rate of median elevation change over the Cordillera Vilcanota is lower in all sub-regions than the Cordilleras Vilcabamba and Urubamba. The northernmost region of the Cordillera Vilcanota (Nevado Qolquepunco) has the lowest median elevation of the region (at 5,163 m a.s.l. in 2020; compared to 5,451 m a.s.l. at Quelccaya), but the rate of change has remained steady in recent decades. Quelccaya

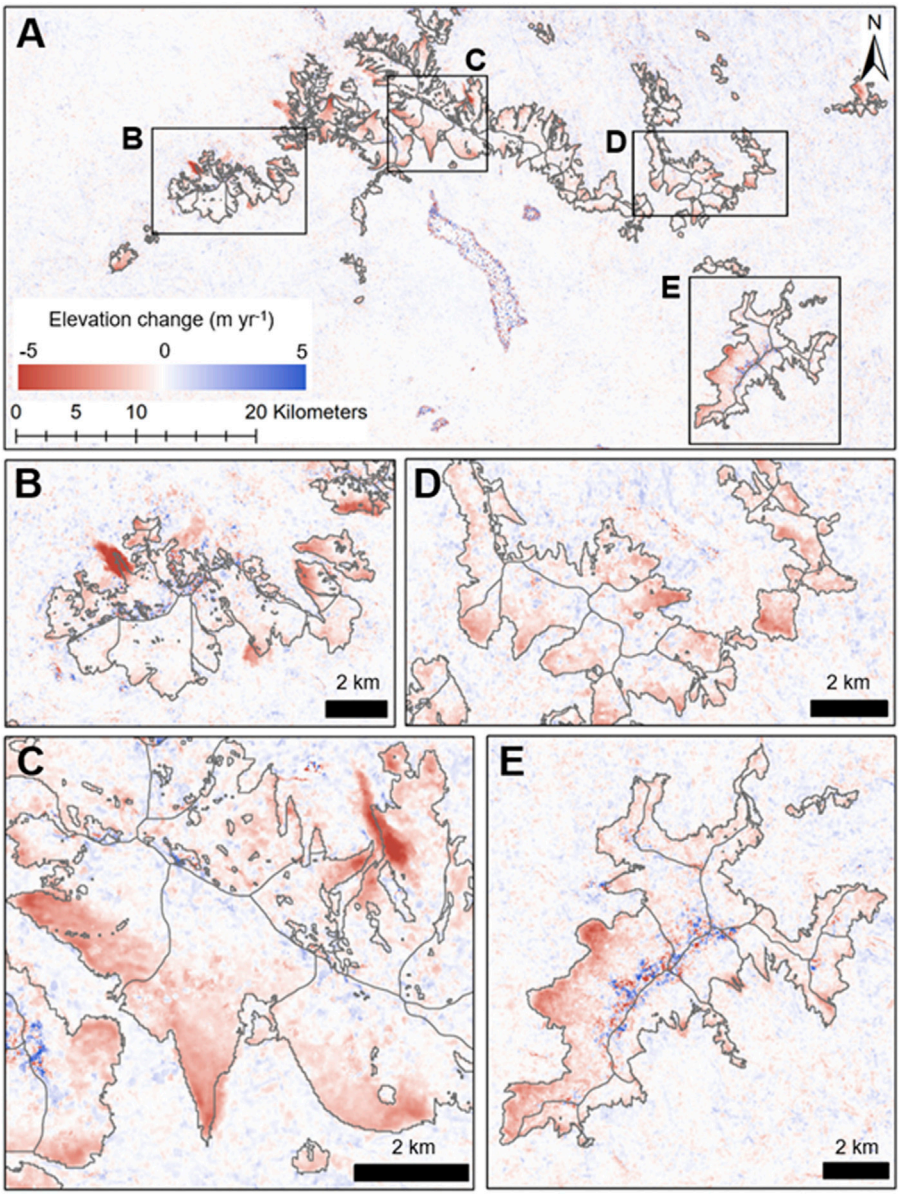

FIGURE 4 | Elevation change from 2000 to 2020 over the central range of the Cordillera Vilcanota. **(A)** Overview of elevation change in the Cordillera Vilcanota. The large pixelated body in the centre of the figure is Laguna Sibinacocha. **(B)** Nevado Ausangate. **(C)** Chumpe Glacier. **(D)** Cluster of lower-lying Eastern glaciers. **(E)** Quelccaya ice cap. Glacier outlines from the year 2000 are in light grey. Large surface elevation changes in off-ice areas most notably in **(B,C)** are from debris-covered ice.

exhibits the lowest rate of median elevation change of all the regions at 1.59 m yr^{-1} from 1975 to 2020, likely due to its high elevation and flat topography. This rate of change has decelerated to 1.06 m yr^{-1} between 2010 and 2020. The key driver for the rate of median elevation change across the Cordillera Vilcanota is temperature; there is a significant correlation between maximum annual temperature and median elevation (R = 0.603, p < 0.001). The role of precipitation and frost in driving median elevation was not significant at p < 0.01.

DISCUSSION

Comparison to Previous Works

Published estimates of glacier area in these regions are scarce, and many studies limit their efforts to studying specific watersheds within the wider region (e.g. Veettil and de Souza, 2017; Drenkhan et al., 2018). Furthermore, definitions of the boundaries of the Cordilleras are not fixed, with differing assessments of how many smaller periphery glaciers are included in calculations of the glacierised area of the region

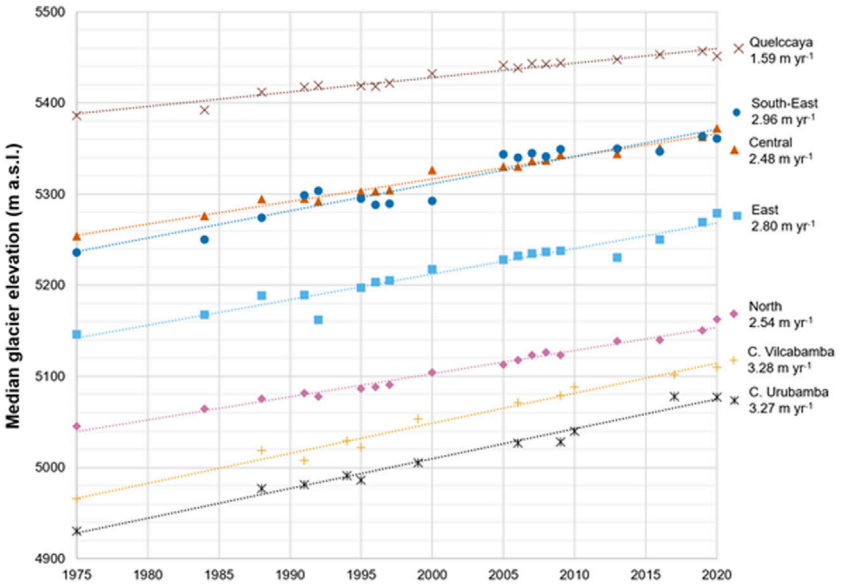

FIGURE 5 | Change in median glacier elevation between 1975 and 2020 over the Southern Peruvian Andes. The North, East, Central, South-East, and Quelccaya categories are sub-regions of the Cordillera Vilcanota (**Supplementary Figure S3**). Dotted lines represent linear regressions.

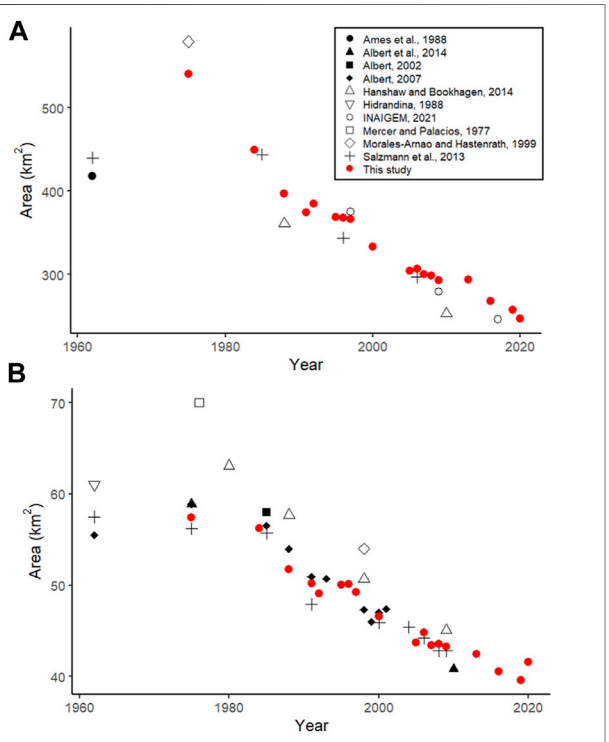

FIGURE 6 | Ice area change comparison to published studies over **(A)** The Cordillera Vilcanota and **(B)** The Quelccaya ice cap.

(Hanshaw and Bookhagen, 2014). Nevertheless, being cognisant of the slight variability in study areas, our estimations of ice recession fit well with the trend presented by other publications (**Figure 6**). To our knowledge, only the National Inventory of Glaciers presents information on glacier area change in the Cordilleras Vilcabamba and Urubamba. Our results for the area of the Cordillera Vilcabamba in 2017 (100.07 ± 5.00 km^2) are comparable to the INAIGEM data (95.54 km^2), but are slightly higher for the Cordillera Urubamba (25.27 ± 1.26 km^2 to the INAIGEM's 24.92 km^2). Note there is a discrepancy between the INAIGEM published estimate for the Cordillera Urubamba of 17.89 km^2 and their dataset of 24.92 km^2, likely due to the way boundaries are drawn between Cordilleras (INAIGEM, 2017; ANA, 2021).

There have been no comparable estimates of mass balance over the Cordillera Vilcanota specifically; however, the global ASTER dataset of glacier change (Hugonnet et al., 2021) provides reasonable context for our findings. The primary difference between the two datasets is their spatial resolution: the current study reports data at 30 m spatial resolution, while Hugonnet et al. (2021) is downsampled to 100 m resolution. Our mass balance estimate over the 20-year time period (−0.477 ± 0.067 m w.e. yr^{-1}) is nearly identical to using their dataset (−0.479 ± 0.048 m w.e. yr^{-1}). We attribute our slightly higher level of uncertainty to our finer spatial resolution which introduces some small artefacts into our dataset. However, the trade-off is that we are able to observe much more closely the changes of individual glaciers (an example comparison is shown over Chumpe glacier, in the Cordillera Vilcanota in **Figure 7**). The problem of very large uncertainty of mass balance change over the Cordilleras Vilcabamba and Urubamba was not unique to our dataset as Hugonnet et al. (2021) had large data gaps over this region, rendering their data unusable. Our high errors were due to cloud rather than steep terrain. Over the Cordilleras Vilcabamba and Urubamba, we produced far fewer DEMs per pixel (~20 DEMs over the 20-year time period) in comparison to the Cordillera Vilcanota (~75 DEMs per pixel).

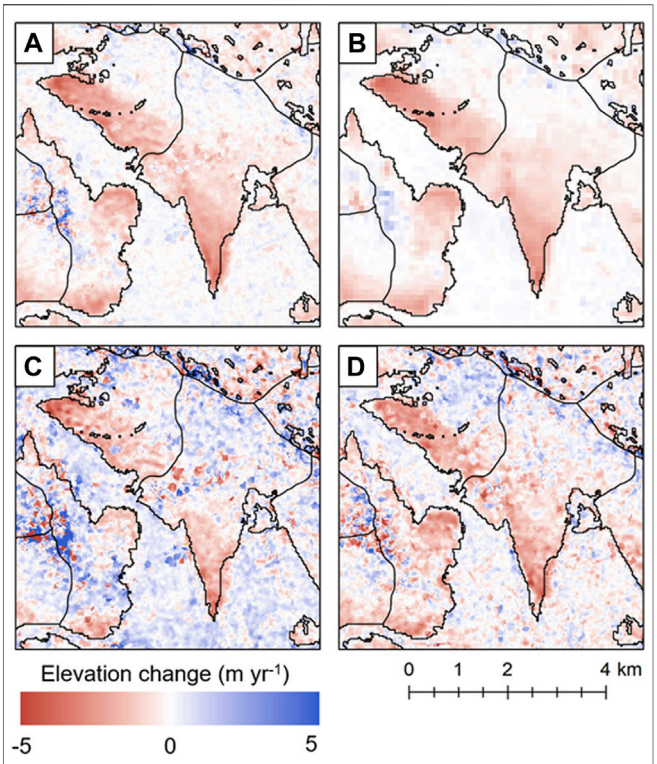

FIGURE 7 | Comparison of datasets over Chumpe Glacier, Cordillera Vilcanota. **(A)** 2000 to 2020 change in elevation generated by this study, **(B)** Comparison to Hugonnet et al. (2021) and their 100 m resolution product over the same 20-year time period, **(C)** 2000–2010 change in elevation generated by this study, **(D)** 2010–2020 change in elevation. Black outlines represent the glacier area in 2000 produced by this study.

Our 2020 median glacier elevation estimate of 5,357 m a.s.l. for the central sub-region of the Cordillera Vilcanota is comparable to the 5,399 m a.s.l. (2016 figure) calculated by Drenkhan et al. (2018), with the difference attributed to different spatial areas covered (their study includes only glaciers in the Vilcanota-Urubamba-Vilcabamba basin). Our 1975–2020 rate of median elevation increase over the Quelccaya ice cap (15.9 m per decade) is comparable to the 1980–2017 estimate of 16.3 m per decade over the Quelccaya ice cap estimated by Yarleque et al. (2018). Our 1975–2020 rate of median elevation increase over the Central region of the Cordillera Vilcanota (24.8 m per decade) is slightly higher than the 22.8 m per decade between 1988 and 2010 estimated by Hanshaw and Bookhagen (2014). Our changes in the rate of median glacier elevation change show high variability across regions and decadal intervals (**Supplementary Figure S6**). This is not inconsistent with the interannual variability of measured ELA change over glaciers in the Cordillera Blanca (Kaser and Georges, 1997; Condom et al., 2007) and Cordillera Ampato (Veettil et al., 2016) which have been attributed to fluctuations in air humidity and the role of ENSO respectively. The interannual variation we exhibit in the Cordillera Vilcanota correlated to maximum air temperature, though this warrants further investigation given the high variability between sub-regions.

Ice area retreat is prolific across all areas of the Southern Peruvian Cordilleras. In the Cordillera Vilcanota, 82 of 257 glaciers (which represented 11.2% of the 1975 glacierised area) disappeared completely over the study period–most notably a cluster of glaciers to the south-east of the Quelccaya ice cap (**Figure 8**). However, deglaciation is occurring at differing rates between regions. Between 1988 and 2020, the Cordillera Vilcabamba lost 34% of its glacial area, compared to 45% for the Cordillera Vilcanota between 1984 and 2020. This is likely due to the differing morphology of glaciers between the regions–glaciers in the Vilcabamba are generally smaller and at lower elevations (Drenkhan et al., 2018) in comparison to the Vilcanota, which means less relative area is exposed to rapid melt. A differing climate setting between the regions is also likely to affect area change: the Cordilleras Vilcabamba and Urubamba are generally wetter than the Vilcanota (Kaser, 2001; Fyffe et al., 2021) though, unlike Fyffe et al. (2021), we did not observe precipitation to be a statistically significant driver of ice area change. This is likely due to the temporal resolution of our dataset; we examined annual precipitation and often with gaps between years in the dataset. Fyffe et al. (2021) studied the influence of precipitation at daily to weekly timescales, and found high variability in melt due to these precipitation dynamics. Further work is needed at a higher temporal resolution to better understand the role precipitation plays in regulating ice area change over long time scales.

Glacier thinning has been consistent throughout the two decadal intervals studied. It is difficult to make an authentic comparison of our mass balance rate (-0.477 ± 0.067 m w.e. yr^{-1}) to other estimates as differing proportions of the regions are studied. Using thickness-volume scaling, Salzmann et al. (2013) calculated an approximate thinning of -0.39 m a^{-1} from 1985–2006 (Seehaus et al., 2019), which would suggest that thinning has accelerated in recent decades when compared to our estimate of -0.563 m a^{-1} from 2000–2020. Limited field-based point measurements of mass balance over individual glaciers of the Cordillera Vilcanota have largely focussed on understanding the role micro-topography plays on the spatial differentiation of mass balance; ranging from -4 to 1.4 m w.e. yr^{-1} across the surface of Suyuparina glacier in the Cordillera Vilcanota in 2013 (Molina et al., 2015). While we do not have exact location information on their stakes, our results for the 2010–2020 time interval show ranges of -4.79 to 2.28 m w.e. yr^{-1} over the same glacier. Our estimates of mass balance are slightly larger than the -0.42 ± 0.24 m w.e. yr^{-1} calculated by Dussaillant et al. (2019), which suggests this region is also thinning faster than their Andes-wide average. A Peru-wide calculation of glacier thinning from 2000–2016 was estimated to be -0.359 ± 0.068 m a^{-1} (Seehaus et al., 2019), which suggests that thinning in the Cordillera Vilcanota is generally faster than the Peru-wide average.

Future Perspectives

In this study, we did not explicitly consider the change in glacial lakes across these regions and how this affects glacier loss. Previous studies (e.g. Drenkhan et al., 2018; Wood et al., 2021), have shown glacial lake expansion across each of these

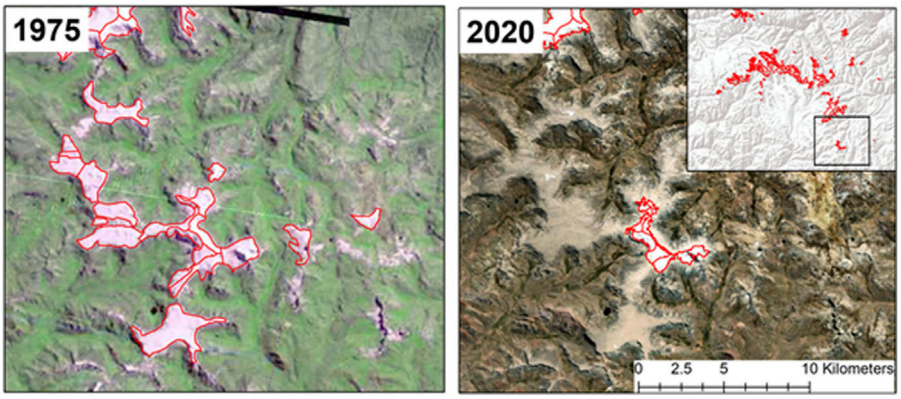

FIGURE 8 | A small cluster of glaciers in the Cordillera Vilcanota to the south-east of the Quelccaya ice cap almost completely melting in the 45-year time span of this series. 1975 background image is from Landsat-2, 2020 image is from DigitalGlobe.

Cordilleras in line with climatic changes. The role of glacial lakes may be important in evaluating future change for tropical mountain glaciers, as lakes have been shown to accelerate ice recession when in direct contact (King et al., 2019). As more lakes develop in overdeepenings left by glacial recession (Colonia et al., 2017), this opens up the opportunity for accelerated ice loss. Similarly, in areas where glacial lakes do currently exist and ice is currently in contact with these lakes (such as the Western face of the Quelccaya ice cap), there may be a slow-down in areal recession in future decades as ice retreats up-slope and out of these lakes. This is particularly important in the Cordillera Vilcanota where 117 new large (>10,000 m^2) lakes are projected to develop by 2050; the greatest of any Peruvian Cordillera (Guardamino et al., 2019), which is likely to accelerate glacier recession.

Future projections of glacier change in the Andes are stark. Even under a low emissions pathway, Schauwecker et al. (2017) suggest a rise in the freezing line of the Cordillera Vilcanota of 230 ± 190 m by 2100, which would lead to greater committed ice loss. The close relationship between temperature and ELA, projected 2.5–4.5°C warming over these glaciers by 2100 (Yarleque et al., 2018; Fyffe et al., 2021; Veettil and de Souza, 2017), and presence of low-lying glacier tongues across the regions suggest there will be significant melt of the Southern Peruvian Andes this century. Studies projecting future increase in ELA over the Vilcanota and Quelccaya (Schauwecker et al., 2017; Yarleque et al., 2018) also suggest this rate is likely to rise sharply in the coming decades. Low-lying regions within the Cordillera Vilcanota (South-East and North; **Supplementary Figure S3**) will likely experience the most glacier loss in the near future. Predictions of remaining glacial ice in 2100 for the Cordillera Vilcanota range from a pessimistic 13 km^2 to an optimistic 155 km^2 (5.4–63.0% of 2020 ice extent) (Schauwecker et al., 2017).

For people living in close proximity to this glacial ice, this represents a major loss of a freshwater resource. Following the approach of Drenkhan et al. (2018), we can contextualise this by noting that in our 2000–2020 study of volume change, the loss of 3.44 km^3 of water from the Cordillera Vilcanota represents ~84 years of water supply for the city of Cusco. Up to 33% of the population of Cusco rely on glacial meltwater during dry seasons (3% annually) (Martínez et al., 2020). Future ice melt is also unlikely to be even. Key glaciers supplying the Laguna Sibinacocha would lose over 90% of their glacierised area by 2100 (Drenkhan et al., 2018), while the Quelccaya ice cap would likely be below the ELA by mid-century (Yarleque et al., 2018). The low-lying Cordillera Urubamba is particularly at threat of severe ablation over the coming decades owing to the high rate of ELA change, posing an imminent risk of loss of water for irrigation, hydropower, and a drinking source in dry seasons (Chevallier et al., 2011). Ice melt is also unlikely to be even in time. While few studies have examined these specific Cordilleras for the timing of "peak water" (a maximum river discharge from the glacial melt contribution), indications from other Cordilleras of Peru show that peak water is likely to pass in the near-future (Drenkhan et al., 2014; Mark et al., 2017; Huss and Hock, 2018; Drenkhan et al., 2019).

An immediate concern is also the increased risk of outburst flood events and hazards to communities downstream of these destabilising glaciers (Vilca et al., 2021). Urgent adaptation measures, such as alternative agricultural practices (e.g. sustainable irrigation systems) and glacial lake outburst flood monitoring systems, are needed across the Southern Peruvian Andes to minimise the impact of this loss on communities (Veettil and Kamp, 2019). This must be integrated with a social perspective to recognise the cultural and spiritual loss marked by the recession of these glaciers, and connection of indigenous communities to the ice (Motschmann et al., 2020).

The drivers of ice loss across all three regions are largely due to warming maximum air temperatures (which correlated with ice area loss and ELA changes in all regions) and topographic controls, most notably, elevation. This is as expected; freezing levels are rising in line with temperature rises and low-lying glacier tongues, many of which are low-gradient and thus susceptible to even minor temperature shifts, are now exposed to melt processes (Thompson et al., 2011). However, we did not have the data available to explore all the predicted key climatic drivers of ice loss, such as atmospheric humidity and radiation

(Kaser, 1999; Vuille et al., 2008). Furthermore, the role of ENSO as a driver of tropical glacier mass loss is becoming realised over individual glaciers across the Andes (Maussion et al., 2015; Veettil et al., 2016), but we could not explore this phenomenon within the available datasets. This signal is thought to be lesser over the Cordilleras Vilcanota, Vilcabamba, and Urubamba as they receive moisture from the Amazon during La Niña; thereby dampening the ENSO signal (Perry et al., 2014). This highlights the need to complement remote sensing observations with *in-situ* data to bridge such gaps.

The optical imagery from Landsat and ASTER used in this study provides useful insights into the dynamics of changes to mountain glaciers, and the long archives of both have been particularly beneficial to generate these results. However, their limitation is highlighted by the lower numbers of usable images we were able to acquire over the Cordilleras Vilcabamba and Urubamba and steep terrain. Mass balance estimates over the Peruvian Andes are few and can be improved using satellite data (Vuille et al., 2018), but the level of uncertainty driven by lack of usable DEM data from ASTER images remains too high. We have demonstrated in this study that the 100 m resolution Hugonnet et al. (2021) dataset provides comparable estimates of mass balance over small mountain glaciers as a higher resolution 30 m product. Radar satellites are able to penetrate cloud, which overcomes the primary limitation, but are challenged by steep topography, which often limits their usefulness to glaciers far larger than those in the Southern Peruvian Andes (Lee et al., 2013). Furthermore, with the steady decay of ASTER as the Terra satellite drifts further out of orbit, and with no current plans for an alternative non-commercially operated stereo satellite, there is an urgent need to find alternative sources to derive regional-level and multi-temporal digital elevation data.

CONCLUSION

In this study, we used the Landsat and ASTER archives to quantify glacier area and mass balance change across the Peruvian Cordilleras Vilcanota, Vilcabamba, and Urubamba–three regions typically understudied in the Andes. We identify a decline in both ice area and mass balance across the Southern Peruvian Andes which is most closely linked to the elevation of the individual Cordilleras; low-lying glaciers are most at risk of immediate melt, and those are most prevalent in the Cordillera Vilcanota. Over the period from 1975 to 2020, glaciers in the Southern Peruvian Andes have receded by ~512 km^2 and are now at less than half their original size. These glaciers are also rapidly thinning; losing 3.18 ± 0.44 Gt ice from 2000–2020. As the climate continues to warm though, the ELA will shift further upwards, which will consequently expose large flat glaciers (including the Quelccaya ice cap) to net ablation. Optical imagery, and stereo imagery, can provide useful insights into the dynamics of small mountain glaciers, but the heavy presence of cloud and snow in long archives still limit the usability of these data and future research needs to validate and extend these data with *in-situ* measurements. These data provide a closer insight into interdecadal patterns of glacier change in these data sparse regions, and can be used to help inform policymaking to manage the future threat of glacial hazards and ensure water security across the Cusco region.

DATA AVAILABILITY STATEMENT

The original contributions presented in the study are publicly available. This data can be found here: https://doi.org/10.5285/d4dedc2d-1f7f-45c8-8b04-41b8b099cef9.

AUTHOR CONTRIBUTIONS

LT co-designed the study, conducted data analysis, and wrote the manuscript. DQ and MS co-designed the study, supervised the data analysis, and contributed to writing the manuscript. EP conducted climate data analysis, and contributed to writing the manuscript. JC and CF contributed expertise on Peruvian glacier dynamics for data analysis and wrote the manuscript.

FUNDING

This research was funded by a NERC Doctoral Training Partnership studentship to LST (NE/L002574/1) and a NERC Newton Fund grant led by DJQ (PEGASUS; NE/S013318/1).

ACKNOWLEDGMENTS

The authors are also grateful to support in the form of data grants from the European Space Agency (ESA) (ID: 49613) and TanDEM-X (ID: DEM_GLAC2721). We are also grateful to Fabian Drenkhan and Bethan Davies for their reviews which substantially improved this manuscript.

SUPPLEMENTARY MATERIAL

The Supplementary Material for this article can be found online at: https://www.frontiersin.org/articles/10.3389/feart.2022.863933/full#supplementary-material

REFERENCES

Ana (2021). *Reserva hídrica en los glaciares del Perú*. Lima: Repositorio Institucional - ANA.

Berthier, E., Arnaud, Y., Vincent, C., and Rémy, F. (2006). Biases of SRTM in High-Mountain Areas: Implications for the Monitoring of Glacier Volume Changes. *Geophys. Res. Lett.* 33 (8), L08502. doi:10.1029/2006gl025862

Bolch, T., Buchroithner, M., Pieczonka, T., and Kunert, A. (2008). Planimetric and Volumetric Glacier Changes in the Khumbu Himal, Nepal, since 1962 Using

Corona, Landsat TM and ASTER Data. *J. Glaciol.* 54 (187), 592–600. doi:10.3189/002214308786570782

Braithwaite, R. J., and Raper, S. C. B. (2009). Estimating Equilibrium-Line Altitude (ELA) from Glacier Inventory Data. *Ann. Glaciol.* 50 (53), 127–132. doi:10.3189/172756410790595930

Brügger, A., Tobias, R., and Monge-Rodríguez, F. S. (2021). Public Perceptions of Climate Change in the Peruvian Andes. *Sustainability* 13 (5), 2677.

Brun, F., Berthier, E., Wagnon, P., Kääb, A., and Treichler, D. (2017). A Spatially Resolved Estimate of High Mountain Asia Glacier Mass Balances from 2000 to 2016. *Nat. Geosci* 10 (9), 668–673. doi:10.1038/ngeo2999

Bury, J. T., Mark, B. G., McKenzie, J. M., French, A., Baraer, M., Huh, K. I., et al. (2011). Glacier Recession and Human Vulnerability in the Yanamarey Watershed of the Cordillera Blanca, Peru. *Climatic Change* 105 (1), 179–206. doi:10.1007/s10584-010-9870-1

Carey, M., Huggel, C., Bury, J., Portocarrero, C., and Haeberli, W. (2012). An Integrated Socio-Environmental Framework for Glacier hazard Management and Climate Change Adaptation: Lessons from Lake 513, Cordillera Blanca, Peru. *Climatic Change* 112 (3), 733–767. doi:10.1007/s10584-011-0249-8

Chevallier, P., Pouyaud, B., Suarez, W., and Condom, T. (2011). Climate Change Threats to Environment in the Tropical Andes: Glaciers and Water Resources. *Reg. Environ. Change* 11 (1), 179–187. doi:10.1007/s10113-010-0177-6

Colonia, D., Torres, J., Haeberli, W., Schauwecker, S., Braendle, E., Giraldez, C., et al. (2017). Compiling an Inventory of Glacier-Bed Overdeepenings and Potential New Lakes in De-glaciating Areas of the Peruvian Andes: Approach, First Results, and Perspectives for Adaptation to Climate Change. *Water* 9 (5), 336. doi:10.3390/w9050336

Condom, T., Coudrain, A., Sicart, J. E., and Théry, S. (2007). Computation of the Space and Time Evolution of Equilibrium-Line Altitudes on Andean Glaciers (10°N–55°S). *Glob. Planet. Change* 59 (1), 189–202. doi:10.1016/j.gloplacha.2006.11.021

Drenkhan, F., Guardamino, L., Huggel, C., and Frey, H. (2018). Current and Future Glacier and lake Assessment in the Deglaciating Vilcanota-Urubamba basin, Peruvian Andes. *Glob. Planet. Change* 169, 105–118. doi:10.1016/j.gloplacha.2018.07.005

Drenkhan, F., Huggel, C., Guardamino, L., and Haeberli, W. (2019). Managing Risks and Future Options from New Lakes in the Deglaciating Andes of Peru: The Example of the Vilcanota-Urubamba basin. *Sci. Total Environ.* 665, 465–483. doi:10.1016/j.scitotenv.2019.02.070

Drenkhan, F., Huggel, C., Salzmann, N., Giráldez, C., Suarez, W., Rohrer, M., et al. (2014). *Present and Future Water Resources Supply and Demand in the Central Andes of Peru: A Comprehensive Review with Focus on the Cordillera Vilcanota*. Austria: EGU General Assembly, 13194.

Dussaillant, I., Berthier, E., and Brun, F. (2018). Geodetic Mass Balance of the Northern Patagonian Icefield from 2000 to 2012 Using Two Independent Methods. *Front. Earth Sci.* 6, 8. doi:10.3389/feart.2018.00008

Dussaillant, I., Berthier, E., Brun, F., Masiokas, M., Hugonnet, R., Favier, V., et al. (2019). Two Decades of Glacier Mass Loss along the Andes. *Nat. Geosci.* 12 (10), 802–808. doi:10.1038/s41561-019-0432-5

Fyffe, C. L., Potter, E., Fugger, S., Orr, A., Fatichi, S., Loarte, E., et al. (2021). The Energy and Mass Balance of Peruvian Glaciers. *J. Geophys. Res. Atmospheres* 126 (23), e2021JD034911. doi:10.1029/2021jd034911

Georges, C. (2004). 20th-Century Glacier Fluctuations in the Tropical Cordillera Blanca, Perú. *Arctic, Antarctic, Alpine Res.* 36 (1), 100–107. doi:10.1657/1523-0430(2004)036[0100:tgfitt]2.0.co;2

Guardamino, L., Haeberli, W., Muñoz, R., Drenkhan, F., Tacsi, A., and Cochachin, A. (2019). Proyección de Lagunas Futuras en las Cordilleras Glaciares del Perú [Online]. Lima. Available from https://repositorio.ana.gob.pe/handle/20.500.12543/3597.

Hanshaw, M. N., and Bookhagen, B. (2014). Glacial Areas, lake Areas, and Snow Lines from 1975 to 2012: Status of the Cordillera Vilcanota, Including the Quelccaya Ice Cap, Northern central Andes, Peru. *The Cryosphere* 8 (2), 359–376. doi:10.5194/tc-8-359-2014

Hock, R., Bliss, A., Marzeion, B., Giesen, R. H., Hirabayashi, Y., Huss, M., et al. (2019). GlacierMIP - A Model Intercomparison of Global-Scale Glacier Mass-Balance Models and Projections. *J. Glaciol.* 65 (251), 453–467. doi:10.1017/jog.2019.22

Hugonnet, R., McNabb, R., Berthier, E., Menounos, B., Nuth, C., Girod, L., et al. (2021). Accelerated Global Glacier Mass Loss in the Early Twenty-First century. *Nature* 592 (7856), 726–731. doi:10.1038/s41586-021-03436-z

Huss, M. (2013). Density Assumptions for Converting Geodetic Glacier Volume Change to Mass Change. *The Cryosphere* 7 (3), 877–887. doi:10.5194/tc-7-877-2013

Huss, M., and Hock, R. (2018). Global-scale Hydrological Response to Future Glacier Mass Loss. *Nat. Clim Change* 8 (2), 135–140. doi:10.1038/s41558-017-0049-x

INAIGEM (2017). *Informe de la Situación de los Glaciares y Ecosistemas de Montaña en el Perú [Online]*. Lima: Instituto Nacional de Investigación en Glaciares y Ecosistemas de Montaña. Available from: https://www.inaigem.gob.pe/wp-content/uploads/2019/04/Interiores-Informe-anual-2017.pdf (Accessed March 3, 2022).

Kaser, G. (1999). A Review of the Modern Fluctuations of Tropical Glaciers. *Glob. Planet. Change* 22 (1), 93–103. doi:10.1016/s0921-8181(99)00028-4

Kaser, G., and Georges, C. (1997). Changes of the Equilibrium-Line Altitude in the Tropical Cordillera Blanca, Peru, 1930-50, and Their Spatial Variations. *A. Glaciology.* 24, 344–349. doi:10.1017/s0260305500012428

Kaser, G. (2001). Glacier-climate Interaction at Low Latitudes. *J. Glaciol.* 47 (157), 195–204. doi:10.3189/172756501781832296

King, O., Bhattacharya, A., Bhambri, R., and Bolch, T. (2019). Glacial Lakes Exacerbate Himalayan Glacier Mass Loss. *Sci. Rep.* 9 (1), 18145. doi:10.1038/s41598-019-53733-x

King, O., Quincey, D. J., Carrivick, J. L., and Rowan, A. V. (2017). Spatial Variability in Mass Loss of Glaciers in the Everest Region, central Himalayas, between 2000 and 2015. *The Cryosphere* 11 (1), 407–426. doi:10.5194/tc-11-407-2017

Kochtitzky, W. H., Edwards, B. R., Enderlin, E. M., Marino, J., and Marinque, N. (2018). Improved Estimates of Glacier Change Rates at Nevado Coropuna Ice Cap, Peru. *J. Glaciol.* 64 (244), 175–184. doi:10.1017/jog.2018.2

Kozhikkodan Veettil, B., Bremer, U. F., de Souza, S. F., Maier, É. L. B., and Simões, J. C. (2016). Variations in Annual Snowline and Area of an Ice-Covered Stratovolcano in the Cordillera Ampato, Peru, Using Remote Sensing Data (1986-2014). *Geocarto Int.* 31 (5), 544–556. doi:10.1080/10106049.2015.1059902

@@@Veettil, B., and de Souza, S. F. (2017). Study of 40-year Glacier Retreat in the Northern Region of the Cordillera Vilcanota, Peru, Using Satellite Images: Preliminary Results. *Remote Sensing Lett.* 8 (1), 78–85. doi:10.1080/2150704x.2016.1235811

Kronenberg, M., Schauwecker, S., Huggel, C., Salzmann, N., Drenkhan, F., Frey, H., et al. (2016). The Projected Precipitation Reduction over the Central Andes May Severely Affect Peruvian Glaciers and Hydropower Production. *Energ. Proced.* 97, 270–277. doi:10.1016/j.egypro.2016.10.072

Lee, H., Shum, C. K., Tseng, K.-H., Huang, Z., and Sohn, H.-G. (2013). Elevation Changes of Bering Glacier System, Alaska, from 1992 to 2010, Observed by Satellite Radar Altimetry. *Remote Sensing Environ.* 132, 40–48. doi:10.1016/j.rse.2013.01.007

López-Moreno, J. I., Fontaneda, S., Bazo, J., Revuelto, J., Azorin-Molina, C., Valero-Garcés, B., et al. (2014). Recent Glacier Retreat and Climate Trends in Cordillera Huaytapallana, Peru. *Glob. Planet. Change* 112, 1–11.

Mark, B. G., French, A., Baraer, M., Carey, M., Bury, J., Young, K. R., et al. (2017). Glacier Loss and Hydro-Social Risks in the Peruvian Andes. *Glob. Planet. Change* 159, 61–76. doi:10.1016/j.gloplacha.2017.10.003

Martínez, E., Drenkhan, F., Zogheib, C., Ochoa-Tocachi, B., and Buytaert, W. (2020). Emerging Water Scarcity Risks In Peruvian Glacier-Fed River Basins *[Online]*. Rochester, NY: Social Science Research Network. Available from: https://papers.ssrn.com/abstract=3696758 (Accessed March 1, 2022).

Maussion, F., Gurgiser, W., Großhauser, M., Kaser, G., and Marzeion, B. (2015). ENSO Influence on Surface Energy and Mass Balance at Shallap Glacier, Cordillera Blanca, Peru. *The Cryosphere* 9 (4), 1663–1683. doi:10.5194/tc-9-1663-2015

Miles, E., McCarthy, M., Dehecq, A., Kneib, M., Fugger, S., and Pellicciotti, F. (2021). Health and Sustainability of Glaciers in High Mountain Asia. *Nat. Commun.* 12 (1), 2868. doi:10.1038/s41467-021-23073-4

Molina, E., Schauwecker, S., Huggel, C., Haeberli, W., Cochachin, A., and Condom, T. (2015). Iniciación de un monitoreo del balance de masa en el glaciar Suyuparina, Cordillera Vilcanota. *Perú. Clim. Chang. Trop. Andes.* 2 (2), 1–14.

Motschmann, A., Huggel, C., Carey, M., Moulton, H., Walker-Crawford, N., and Muñoz, R. (2020). Losses and Damages Connected to Glacier Retreat in the Cordillera Blanca, Peru. *Climatic Change* 162 (2), 837–858. doi:10.1007/s10584-020-02770-x

Nuth, C., and Kääb, A. (2011). Co-registration and Bias Corrections of Satellite Elevation Data Sets for Quantifying Glacier Thickness Change. *The Cryosphere* 5 (1), 271–290. doi:10.5194/tc-5-271-2011

Orlove, B. (2009). The Past, the Present And Some Possible Futures Of Adaptation *[Online]*. Rochester, NY: Social Science Research Network. Available from: https://papers.ssrn.com/abstract=2240439 (Accessed September 27, 2021).

Paul, F., Barrand, N. E., Baumann, S., Berthier, E., Bolch, T., Casey, K., et al. (2013). On the Accuracy of Glacier Outlines Derived from Remote-Sensing Data. *Ann. Glaciol.* 54 (63), 171–182. doi:10.3189/2013aog63a296

Perry, L. B., Seimon, A., and Kelly, G. M. (2014). Precipitation Delivery in the Tropical High Andes of Southern Peru: New Findings and Paleoclimatic Implications. *Int. J. Climatol.* 34 (1), 197–215. doi:10.1002/joc.3679

Prinz, R., Heller, A., Ladner, M., Nicholson, L., and Kaser, G. (2018). Mapping the Loss of Mt. Kenya's Glaciers: An Example of the Challenges of Satellite Monitoring of Very Small Glaciers. *Geosciences* 8 (5), 174. doi:10.3390/geosciences8050174

Rabatel, A., Francou, B., Soruco, A., Gomez, J., Cáceres, B., Ceballos, J. L., et al. (2013a). Current State of Glaciers in the Tropical Andes: a Multi-century Perspective on Glacier Evolution and Climate Change. *The Cryosphere* 7 (1), 81–102. doi:10.5194/tc-7-81-2013

Rabatel, A., Letréguilly, A., Dedieu, J.-P., and Eckert, N. (2013b). Changes in Glacier Equilibrium-Line Altitude in the Western Alps from 1984 to 2010: Evaluation by Remote Sensing and Modeling of the Morpho-Topographic and Climate Controls. *The Cryosphere* 7 (5), 1455–1471. doi:10.5194/tc-7-1455-2013

Racoviteanu, A. E., Arnaud, Y., Williams, M. W., and Ordoñez, J. (2008). Decadal Changes in Glacier Parameters in the Cordillera Blanca, Peru, Derived from Remote Sensing. *J. Glaciol.* 54 (186), 499–510. doi:10.3189/002214308785836922

RGI Consortium (2017). Randolph Glacier Inventory 6.0. Available from: http://www.glims.org/RGI/randolph60.html (Accessed November 24, 2021).

Roy, S. (2021). Samapriya/Geeup: Geeup: Simple CLI for Earth Engine Uploads [Online]. Zenodo. Available from: https://zenodo.org/record/4852799 (Accessed July 12, 2021).

Sagredo, E. A., and Lowell, T. V. (2012). Climatology of Andean Glaciers: A Framework to Understand Glacier Response to Climate Change. *Glob. Planet. Change* 86-87 (87), 101–109. doi:10.1016/j.gloplacha.2012.02.010

Salzmann, N., Huggel, C., Rohrer, M., Silverio, W., Mark, B. G., Burns, P., et al. (2013). Glacier Changes and Climate Trends Derived from Multiple Sources in the Data Scarce Cordillera Vilcanota Region, Southern Peruvian Andes. *The Cryosphere* 7 (1), 103–118. doi:10.5194/tc-7-103-2013

Schauwecker, S., Rohrer, M., Acuña, D., Cochachin, A., Dávila, L., Frey, H., et al. (2014). Climate Trends and Glacier Retreat in the Cordillera Blanca, Peru, Revisited. *Glob. Planet. Change* 119, 85–97. doi:10.1016/j.gloplacha.2014.05.005

Schauwecker, S., Rohrer, M., Huggel, C., Endries, J., Montoya, N., Neukom, R., et al. (2017). The Freezing Level in the Tropical Andes, Peru: An Indicator for Present and Future Glacier Extents. *J. Geophys. Res. Atmos.* 122 (10), 5172–5189. doi:10.1002/2016jd025943

Seehaus, T., Malz, P., Sommer, C., Lippl, S., Cochachin, A., and Braun, M. (2019). Changes of the Tropical Glaciers throughout Peru between 2000 and 2016 - Mass Balance and Area Fluctuations. *The Cryosphere* 13 (10), 2537–2556. doi:10.5194/tc-13-2537-2019

Taylor, L. S., Quincey, D. J., Smith, M. W., Baumhoer, C. A., McMillan, M., and Mansell, D. T. (2021). Remote Sensing of the Mountain Cryosphere: Current Capabilities and Future Opportunities for Research. *Prog. Phys. Geogr. Earth Environ.* 45 (6), 931–964. doi:10.1177/03091333211023690

Thompson, L. G., Davis, M. E., Mosley-Thompson, E., Porter, S. E., Corrales, G. V., Shuman, C. A., et al. (2021). The Impacts of Warming on Rapidly Retreating High-Altitude, Low-Latitude Glaciers and Ice Core-Derived Climate Records. *Glob. Planet. Change* 203, 103538. doi:10.1016/j.gloplacha.2021.103538

Thompson, L. G., Mosley-Thompson, E., Davis, M. E., and Brecher, H. H. (2011). Tropical Glaciers, Recorders and Indicators of Climate Change, Are Disappearing Globally. *Ann. Glaciol.* 52 (59), 23–34. doi:10.3189/172756411799096231

Veettil, B. K., Bremer, U. F., de Souza, S. F., Maier, É. L. B., and Simões, J. C. (2016). Influence of ENSO and PDO on Mountain Glaciers in the Outer Tropics: Case Studies in Bolivia. *Theor. Appl. Climatology* 125 (3), 757–768. doi:10.1007/s00704-015-1545-4

Veettil, B. K., and Kamp, U. (2021). Glacial Lakes in the Andes under a Changing Climate: A Review. *J. Earth Sci.* 32 (6), 1575–1593. doi:10.1007/s12583-020-1118-z

Veettil, B. K., and Kamp, U. (2019). Global Disappearance of Tropical Mountain Glaciers: Observations, Causes, and Challenges. *Geosciences* 9 (5), 196. doi:10.3390/geosciences9050196

Veettil, B. K., Wang, S., Simões, J. C., Ruiz Pereira, S. F., and de Souza, S. F. (2018). Regional Climate Forcing and Topographic Influence on Glacier Shrinkage: Eastern Cordilleras of Peru. *Int. J. Climatol* 38 (2), 979–995. doi:10.1002/joc.5226

Vilca, O., Mergili, M., Emmer, A., Frey, H., and Huggel, C. (2021). The 2020 Glacial lake Outburst Flood Process Chain at Lake Salkantaycocha (Cordillera Vilcabamba, Peru). *Landslides* 18 (6), 2211–2223. doi:10.1007/s10346-021-01670-0

Vuille, M., Carey, M., Huggel, C., Buytaert, W., Rabatel, A., Jacobsen, D., et al. (2018). Rapid Decline of Snow and Ice in the Tropical Andes - Impacts, Uncertainties and Challenges Ahead. *Earth-Science Rev.* 176, 195–213. doi:10.1016/j.earscirev.2017.09.019

Vuille, M., Kaser, G., and Juen, I. (2008). Glacier Mass Balance Variability in the Cordillera Blanca, Peru and its Relationship with Climate and the Large-Scale Circulation. *Glob. Planet. Change* 62 (1), 14–28. doi:10.1016/j.gloplacha.2007.11.003

Wilson, D. J. (2019). The Harmonic Mean P -value for Combining Dependent Tests. *Proc. Natl. Acad. Sci. U.S.A.* 116 (4), 1195–1200. doi:10.1073/pnas.1814092116

Wood, J. L., Harrison, S., Wilson, R., Emmer, A., Yarleque, C., Glasser, N. F., et al. (2021). Contemporary Glacial Lakes in the Peruvian Andes. *Glob. Planet. Change* 204, 103574. doi:10.1016/j.gloplacha.2021.103574

Yarleque, C., Vuille, M., Hardy, D. R., Timm, O. E., De la Cruz, J., Ramos, H., et al. (2018). Projections of the Future Disappearance of the Quelccaya Ice Cap in the Central Andes. *Sci. Rep.* 8 (1), 15564. doi:10.1038/s41598-018-33698-z

Zemp, M., Huss, M., Thibert, E., Eckert, N., McNabb, R., Huber, J., et al. (2019). Global Glacier Mass Changes and Their Contributions to Sea-Level Rise from 1961 to 2016. *Nature* 568 (7752), 382–386. doi:10.1038/s41586-019-1071-0

Conflict of Interest: The authors declare that the research was conducted in the absence of any commercial or financial relationships that could be construed as a potential conflict of interest.

frontiers in Earth Science

ORIGINAL RESEARCH
published: 29 March 2022
doi: 10.3389/feart.2022.813396

Late Glacial and Holocene Palaeolake History of the Última Esperanza Region of Southern Patagonia

Stephen J. Roberts[1], Robert D. McCulloch[2], Joseph F. Emmings[3], Sarah J. Davies[4], Wim Van Nieuwenhuyze[5], Mieke Sterken[5], Katrien Heirman[6], Jeroen Van Wichelen[5,7], Carolina Diaz[8], Evelien Van de Vyver[5,9], Alex Whittle[1], Wim Vyverman[5], Dominic A. Hodgson[1] and Elie Verleyen[5]*

[1]British Antarctic Survey, Natural Environment Research Council, Cambridge, United Kingdom, [2]Centro de Investigación en Ecosistemas de la Patagonia (CIEP), Coyhaique, Chile, [3]British Geological Survey, Nottingham, United Kingdom, [4]Department of Geography and Earth Sciences, Aberystwyth University, Aberystwyth, United Kingdom, [5]Protistology and Aquatic Ecology, Ghent University, Gent, Belgium, [6]TNO—Geological Survey of the Netherlands, Utrecht, Netherlands, [7]Research Institute for Nature and Forest, Herman Teirlinckgebouw, Brussels, Belgium, [8]Institute of Ecology and Biodiversity (IEB), Universidad de Chile, Santiago, Chile, [9]Flanders Environment Agency, Aalst, Belgium

OPEN ACCESS

Edited by:
Bethan Joan Davies, Royal Holloway, University of London, United Kingdom

Reviewed by:
Patricio Iván Moreno, University of Chile, Chile
Olga Solomina, Institute of Geography (RAS), Russia

***Correspondence:**
Stephen J. Roberts
sjro@bas.ac.uk

Specialty section:
This article was submitted to Quaternary Science, Geomorphology and Paleoenvironment, a section of the journal Frontiers in Earth Science

Received: *11 November 2021*
Accepted: *10 February 2022*
Published: *29 March 2022*

Citation:
Roberts SJ, McCulloch RD, Emmings JF, Davies SJ, Van Nieuwenhuyze W, Sterken M, Heirman K, Van Wichelen J, Diaz C, Van de Vyver E, Whittle A, Vyverman W, Hodgson DA and Verleyen E (2022) Late Glacial and Holocene Palaeolake History of the Última Esperanza Region of Southern Patagonia. Front. Earth Sci. 10:813396. doi: 10.3389/feart.2022.813396

We undertook multi-proxy analyses on two sediment cores from Lago Pato, a small lake basin at 51°S topographically separated from Lago del Toro in Torres del Paine (TdP), to provide insights into glacier dynamics and lake-level change in the TdP and Última Esperanza region over the last ~30,000 cal a BP (30 ka). Lago Pato is situated in a region overridden by the Southern Patagonian Ice Field during the Last Glacial and in a transitional climatic zone of Southern Patagonia sensitive to seasonal- to millennial-scale changes in the Southern Hemisphere Westerly Winds (SWW). Results show that a deep ice-dammed and enlarged palaeolake encompassed Lago del Toro and Lago Pato c. 30–20 ka after the ice had retreated from local-Last Glacial Maximum (l-LGM) limits at c. 48–34 ka and during the build-up to the global-Last Glacial Maximum (g-LGM), c. 26–19 ka. Gaps in both sediment records between c. 20–13.4 ka and c. 20–10 ka suggest hiatuses in sediment accumulation during the g-LGM and Antarctic Cold Reversal (ACR) readvances and/or removal by lake lowering or flushing during the Late Glacial–early Holocene. The palaeolake level dropped from >100 m a.s.l. to ~40–50 m a.s.l. towards the end of the ACR c. 13.4–13.0 ka, creating a shallower glaciolacustrine environment dammed by an ice tongue in the Estancia Puerto Consuelo–Última Esperanza fjord. Further lowering of the enlarged palaeolake level occurred when the ice thinned to <40 m a.s.l., eventually isolating Lago Pato from Lago del Toro and glaciogenic sediment input at c. 11.7 ka. After isolation, the ecology and water levels in Lago Pato became sensitive to regional climate shifts. The shallow, stable, and highly anoxic environment that developed after c. 11.7 ka is associated with weaker (or poleward shifted) SWW at 51°S and was replaced at c. 10 ka by an increasingly productive shallow-littoral lake with a variable lake-level and periodic shifts in anoxic-oxic bottom water conditions and ratios of benthic-planktonic diatoms. A more open *Nothofagus* forest, established at c. 8.6–7.5 ka, and more arid conditions c. 7.5–5.7 cal ka BP are linked to another phase of weaker (or poleward shifted) SWW at 51°S. More persistently wet conditions from c. 5.7 ka, with extensive closed *Nothofagus* forests and planktonic diatoms dominant, are associated

with stronger (or equatorward shifted) SWW over 51°S. The abrupt return of benthic-to-tychoplanktonic diatoms after c. 3 ka reflects enhanced SWW at 51°S. Increasingly stable lacustrine and littoral wetland conditions established in the last ~500 years reflect weaker SWW and lasted until recent decades.

Keywords: Last Glacial Maximum (LGM), palaeoclimate, palaeolimnology, glaciation, lake-level changes, Patagonia, Southern Hemisphere westerly winds (SWW)

1 INTRODUCTION

The Southern Patagonian Ice Sheet reached its local-Last Glacial Maximum (l-LGM) at c. 48 ka [48,000 calibrated (cal) years before present (BP), where the present is 1950 CE], during Marine Isotope Stage 3 (MIS 3) (**Figure 1**), with secondary readvances at c. 39 ka and 34 ka (García et al., 2018). Outlet glaciers extended offshore to the west onto the continental shelf of the Pacific and crossed eastwards into Argentina and eastern valleys and fjords of the Última Esperanza province. Ice-lobes from the Cordillera Paine extended out beyond the eastern end of Lago del Toro forming complex terminal moraine systems, scouring deep lake basins such as Lago del Toro, while reaching their maximum advance limits at the l-LGM (limit A_1 in **Figure 2A**) (Sagredo et al., 2011; García et al., 2012; García et al., 2014; García et al., 2018; Davies et al., 2020). At the global-Last Glacial Maximum (g-LGM), c. 26.5–19 ka, the Southern Patagonian Ice Sheet was more than 200 km wide and over 1800 km long, yet it reached only half its maximum Marine Isotope Stage 3 extent due to milder winters and drier conditions associated with a weaker, broader, and equatorward shifted Southern Westerly wind belt that extended into the mid-latitudes (McCulloch and Davies, 2001; Kaplan et al., 2007; Kaplan et al., 2008; García et al., 2014; Darvill et al., 2015; Glasser et al., 2017; García et al., 2018; Davies et al., 2020; McCulloch et al., 2020).

The Southern Hemisphere Westerly Winds (SWW) are one of the main drivers of the global climate system, regulating the capacity of the Southern Ocean to absorb or release CO_2 through diffusion and biological uptake at the surface (Hodgson and Sime, 2010; Marshall and Speer, 2012) (**Figure 1A**). Recent global warming is thought to have led to an intensification and/or poleward shift in the mean annual position of the core SWW belt, and this is either reducing (Le Quere et al., 2007) or increasing (Landschützer et al., 2016) the capacity of surface waters in the Southern Ocean to absorb atmospheric CO_2. The "reducing hypothesis" is supported by recent observational and palaeo data, which shows a substantial rise in CO_2 during the transition into the Holocene coincident with an increased ventilation of carbon from the deep Southern Ocean (Moreno et al., 2010; Fletcher and Moreno, 2012; Saunders et al., 2018), rising global sea levels (Spratt and Lisiecki, 2016), and rapid deglaciation of the South Patagonian Ice Field (Davies et al., 2020; Palacios et al., 2020).

Dating of moraines and shorelines; changes in basin topography (García et al., 2012; García et al., 2014; García et al., 2018); multi-proxy, isotopic, and pollen analysis of lake and marine sediment records (Huber et al., 2004; Fletcher and Moreno, 2012; Mayr et al., 2013; Zolitschka et al., 2013; Moreno et al., 2018; McCulloch et al., 2020; Moreno et al., 2021); and larger-scale regional data compilations (Glasser et al., 2008; Davies et al., 2020; Palacios et al., 2020) have been used to reconstruct past glacier extent and deglaciation in Patagonia (**Figure 3**), with many studies linking glacier advance and retreat to past changes in precipitation and SWW intensity and/or latitudinal position over Southern South America (**Figure 1**).

The Seno Última Esperanza province and the Parque Nacional Torres del Paine have a wide variety of outstanding glacial geomorphological features. Many palaeoenvironmental studies have also been undertaken in the region (**Figures 1**, **3**), but the timing, impact, and drivers of Late Glacial and Holocene deglaciation remain debated (Moreno et al., 2018; Davies et al., 2020). The lake level history of Lago del Toro and the Holocene vegetational history of the surrounding area are detailed and well-studied (**Figure 3**, reference nos. 7–15 for summary) (García et al., 2012; Solari et al., 2012; García et al., 2014; García et al., 2018; Moreno et al., 2018; Moreno et al., 2021). A large ice-dammed proglacial lake, palaeo-Lago Tehuelche, once covered Lago del Toro and Lago Sarmiento sometime after c. 38 ka but before c. 17.6–16.8 ka; that is, between the l-LGM and g-LGM (Sagredo et al., 2011; Moreno et al., 2012; García et al., 2014). After the g-LGM, another large ice-dammed palaeolake encompassed Lago del Toro as far south as the southern end of the Puerto Consuelo–Última Esperanza fjord between c. 18 and 10.2 ka (but possibly as late as c. 7.1 ka) (locations B_1, B_2 in **Figures 2A**, **3** reference nos. 7–10). This palaeolake has been associated with local glacier readvance stages B–D (Stages TDP-I–IV), phases of ice retreat associated with Meltwater Pulse 1A c. 14.7 ka, and following readvances during the Antarctic Cold Reversal (ACR: 14.5–12.9 ka) (Blunier et al., 1997; García et al., 2012; Solari et al., 2012; García et al., 2014; Davies et al., 2020).

Moraines along the northern shoreline of Lago del Toro, with maximum cosmogenic isotope ages of c. 24 ka, have been linked to the g-LGM advance, while ages of c. 14.5–12.5 ka from the innermost moraines to the north of Lago Sarmiento imply ice could have also readvanced to the eastern end of Lago del Toro during the ACR (García et al., 2014; Fogwill and Kubik, 2016; García et al., 2018). No post-LGM chronology has been established for these moraines or those along the southern margin of Lago del Toro, adjacent to Lago Pato (**Figures 2A,B**). Glacier advances were driven by the alignment of the SWW over 51–52°S, which persisted between c. 13.4 and 11.3 ka as ACR glaciers retreated, but then became weaker, more diffuse, or poleward shifted during the "Early Holocene Westerlies

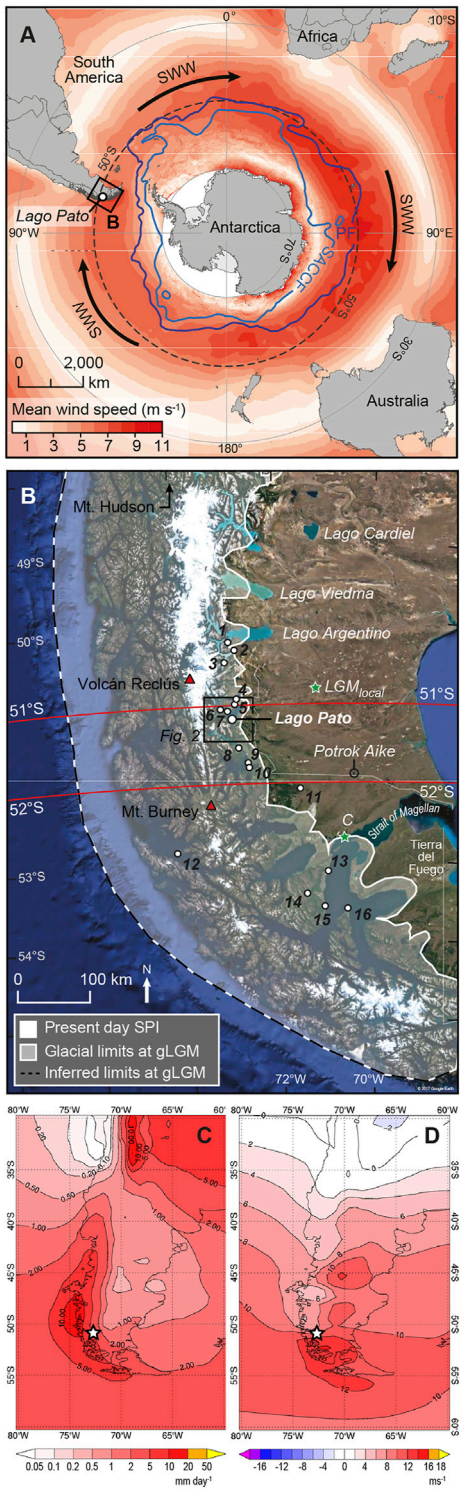

FIGURE 1 | (A) Location of Lago Pato in relation to the Southern Hemisphere Westerly Winds (SWW), the Southern Antarctic Circumpolar Current Front (SACCF), and the Polar Front (PF). **(B)** Location of Lago Pato, the extent of the global-Last Glacial Maximum (g-LGM) South Patagonian Ice Field, c. 20–25 ka (McCulloch et al., 2005; Davies et al., 2020). The green star marked LGM_{local} is the local-Last Glacial Maximum (l-LGM) (*Continued*)

FIGURE 1 | extent c. 48–34 ka (Glasser et al., 2008; García et al., 2014); the green star marked C is the ice-extent of Stage C advance in the Strait of Magellan (McCulloch et al., 2005). Red triangles are major volcanoes active during the Holocene. Key locations mentioned in the text and the sites of previous studies are as follows: 1, Peninsula Avellaneda; 2, Cerro Frías peat sequence; 3, Brazo Sur; 4, Vega Ñandú; 5, Pantano Margarita; 6, Lago Guanaco; 7, Meteorological Station; 8, Eberhard Site; 9, Pantano Dumestre; 10, Puerto Natales; 11, Río Rubens; 12, Lake Tamar; 13, Punta Arenas; 14, Puerto del Hambre; 15, Estancia Esmeralda II; 16, Isla Dawson. The background LANDSAT imagery in **(B)** courtesy of the U.S. Geological Survey (https://www.usgs.gov/centers/eros) generated in Google Earth, © Google. **(C,D)** ERA-INTERIM reanalysis (Dee et al., 2011) for **(C)** mean annual surface precipitation (mm per day; 1/6/1979–1/6/2017) and **(D)** zonal wind velocity (U on P at 850 hPa over the Andes; ms^{-1}; 1/6/1979–1/6/2017) over southern South America (30–60°S), covering the period up to when cores were taken from LP16. Lago Pato is located at the white star.

Minimum" (Mayr et al., 2013; Quade and Kaplan, 2017; Moreno et al., 2018; Zolitschka et al., 2018; McCulloch et al., 2020; Moreno et al., 2021).

To better understand changes in regional glacier dynamics and the nature and timing of climate changes, including the impact of changing SWW intensity over 51°S during the Late Glacial and Holocene, we present new data from two sediment records extracted from Lago Pato (S51°18.020′, W72°40.716′).

Lago Pato is a small, low altitude basin at 30–35 m a.s.l. located outside, but immediately adjacent to, moraines that run along the southern shoreline of Lago del Toro. It is located approximately mid-way between l-LGM and g-LGM maxima and present-day ice limits and in a transitional climatic zone east of the Andes (**Figures 1**, **2**). Previous studies and new geomorphological mapping of the area (**Figure 2**) show that Lago Pato would have been joined to Lago del Toro when lake levels were >40–50 m a.s.l. Using new geomorphological information collected in the field and high-resolution multi-proxy sedimentology and geochemistry (supported by fossil pollen and diatom evidence) from sediment records extracted from the present-day depocentre and a former littoral part of the basin within the catchment area of Lago Pato, we examine how regional deglaciation of the Última Esperanza region drove (palaeo) lake-level change within TdP. More specifically, we test the hypothesis that Lago Pato became isolated from Lago del Toro and glaciogenic sediment input when lake levels fell below the retaining sill following deglaciation and sometime after the Antarctic Cold Reversal (ACR: c. 14.6–12.8 ka). As Lago Pato is located within a transitional climatic zone east of the Andes, we also examine how deglaciation and isolation relate to broader climate changes during the Late Glacial and Holocene, particularly the variability of the SWW over ~51°S (as well as southern South America). Our key findings are summarised in **Figure 3** (reference no. 15) within the context of the existing glacial and climatic history of Southern Patagonia (reference nos. 1–14).

2 SITE DESCRIPTION AND BACKGROUND

Lago Pato is a relatively shallow (~4 m deep), well-mixed ellipsoidal freshwater lake, covering an area of approximately

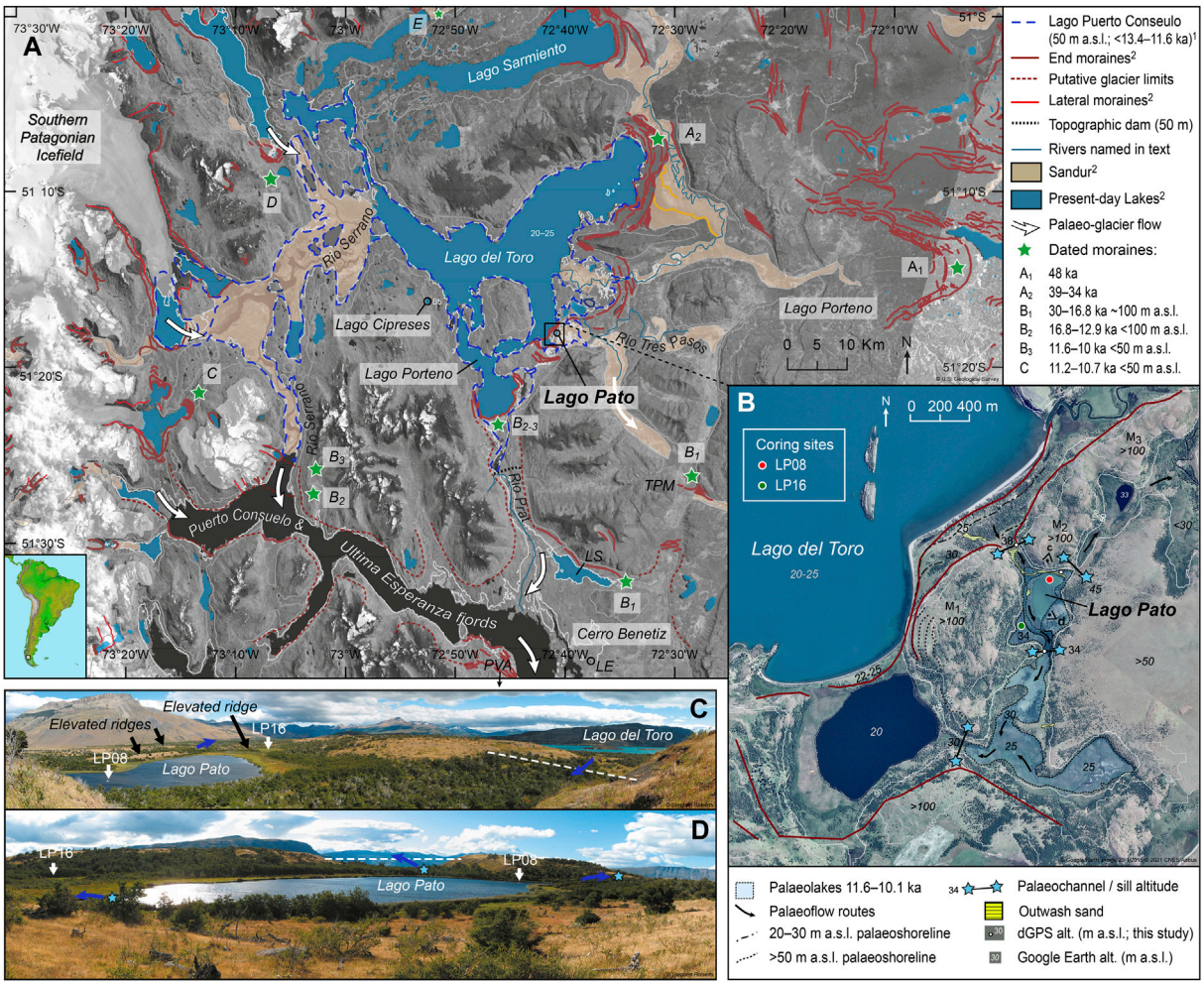

FIGURE 2 | (A) Location map highlighting key geomorphological features in the Torres Del Paine region [based on data in Glasser et al. (2008)]. The 50 m a.s.l. contour is shown as a dotted blue line. Green stars summarise the extent and age of former regional glaciations. 1, Garcia et al. (2014); 2, Glasser et al. (2008). Attribution: LANDSAT-8 satellite image was superimposed on the GEOTOP30 DEM in ARC-Map (www.esri.com), courtesy of the U.S. Geological Survey (https://www.usgs.gov/centers/eros). **(B)** Summary geomorphological sketch showing the ~40 m a.s.l. palaeoshoreline of Lago Pato and flow pathways and retaining ridges that would isolate Lago Pato from Lago del Toro (blue stars) as follows: 1) in the wetland to the south, separated by a sill elevation of 33.4 ± 0.1 m a.s.l.; 2) at 38.0 ± 0.1 m a.s.l., through a gap filled with outwash sand deposits between the prominent moraine complex that runs parallel with the southern shore of Lago del Toro to the northwest; 3) outflow breaching the northeastern sill at ~40–45 m a.s.l., requiring more substantial lake level rise of >10 m. Once the lake level in Lago del Toro dropped below ~40–38 m a.s.l., the only drainage route from Lago Pato was to the south, over the southern sill at ~32 m a.s.l. into the adjacent lake and Lago del Toro (~20–25 m a.s.l.). Areas to the south and southeast of Lago Pato, mapped as sandurs by Glasser et al. (2008), were visited during coring and interpreted as temporary wetlands that dry up during summer. LS is Lago Sofia, LE is Lago Eberhard, TPM is Tres Pasos Moraine, and PVA is Pantano Antonio Varas. Attribution: Google Earth, © Google.com, image 23/1/2015 © 2021 CNES/Airbus. **(C)** View from the northern side of Lago Pato showing the coring sites LP08 and LP16 and meltwater channels cut through the elevated moraine ridges on the NW and SE shores. **(D)** View looking towards the NE ridge and meltwater channel from the southern side of Lago Pato.

35,000 m^2 (~250 m × 130 m). It is located just outside the Parque Nacional Torres del Paine and on the eastern slopes of the Andes, on the southern shore of Lago del Toro (**Figure 2**). Both lakes are located to the east of the southern margin of the Southern Patagonian Ice Field and have been overridden and influenced by past glacial advances from the Cordillera Paine massif (**Figure 2A**).

Several outlet glaciers feed rivers that flow into Lago del Toro. However, Lago Pato, at ~33 m a.s.l., is currently an isolated and closed basin system with no direct glacial meltwater input. It is separated from the glaciolacustrine-influenced Lago del Toro, at 25 m a.s.l., by low-lying ridges at ~25–34 m a.s.l. to the south and east and elevated moraines, at ~ 38 m a.s.l., immediately to the north, northeast, and northwest (**Figures 2B–D**; **Table 1**). Former shorelines are clearly visible on the adjacent moraines and in the surrounding area on satellite imagery and are marked in the field by notable changes in catchment vegetation cover from grassland to dwarf shrubs (**Figures 2B–D**). Presently, the lake level in Lago del Toro is between 10 and 15 m below Lago Pato, depending on seasonal meltwater inputs into Lago del Toro (**Figure 2B**).

Lago Pato is located ~4–5° south of the region offshore in the Pacific Ocean where the present-day Antarctic Circumpolar

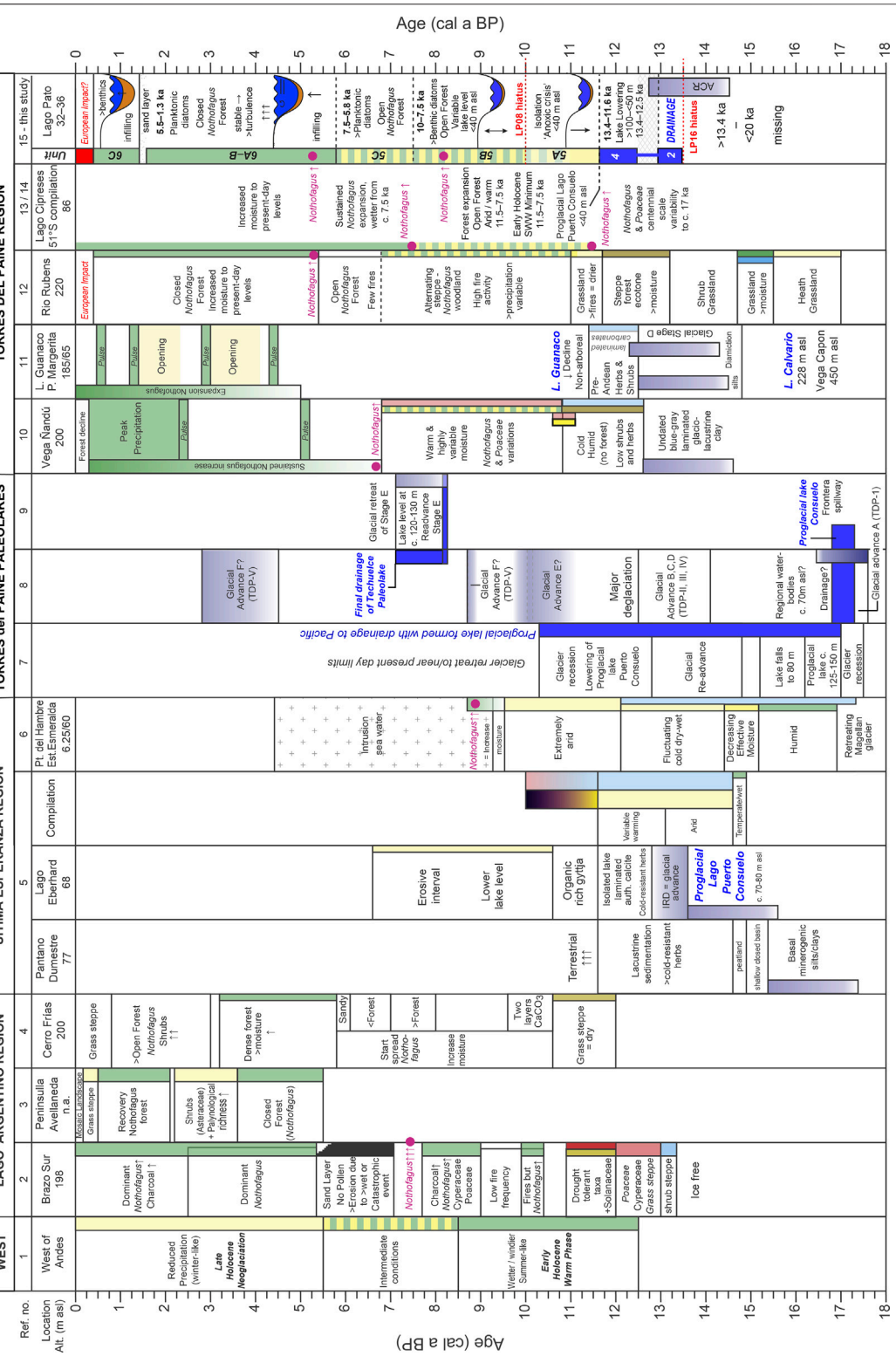

FIGURE 3 | Summary palaeoenvironmental interpretations for key studies from in Chilean Patagonia mentioned in the text (1–14). Summary findings from Lago Pato from this study are included in 15 for comparison. References: 1, Lamy et al. (2010); 2, Wille and Schäbitz (2008); 3, Echeverria et al. (2014); 4, Mancini (2009); 5, Moreno et al. (2012); 6, McCulloch and Davies (2001); 7, Sagredo et al. (2011); 8, García et al. (2014); 9, Solari et al. (2012); 10, Villa-Martínez and Moreno (2017); 11, Moreno et al. (2009a) and Moreno et al. (2009b); 12, Markgraf and Huber (2010); 13/14, Moreno et al. (2018) and Moreno et al. (2021); 15, this study.

TABLE 1 | Geomorphological data collected from Lago Pato. Data marked with an asterisk were calculated by subtracting the mean Google Earth offset (6.70 ± 5.95 m) from GPS measured data. Field measurements were undertaken using a Trimble 5700 GPS in December 2015, with a tripod height correction of 0.523 m using WGS84 as the reference ellipsoid, corrected using the EGM96 geoid model. Calculated elevations are shown to three decimal places, but the actual precision is, at best, one decimal place.

ID	Location description	Latitude (°S)	±2σ (m)	Longitude (°W)	±2σ (m)	WGS84 ellipsoidal height (m)	±2σ (m)	Geoid height (m)	Uncorrected elevation (m a.s.l.)	Corrected elevation (m a.s.l.)	Google Earth alt. (m a.s.l.)	Google Earth offset (m)
LP1	NW Sill to Lago del Toro 1	51°17′ 53.4218″	0.215	72°40′ 55.1173″	0.288	51.397	0.398	13.02	38.377	37.854	41	3.15
LP2	NW sill to Lago del Toro 2	51°17′ 53.4196″	0.044	72°40′ 55.1224″	0.097	51.508	0.145	13.02	38.488	37.965	41	3.04
LP3	LP16 coring site	51°18′ 11.3293″	0.059	72°40′ 53.6633″	0.107	46.682	0.112	13.01	33.672	33.149	40	6.85
LP4	S sill towards wetland	51°18′ 16.7246″	0.067	72°40′ 45.9815″	0.113	46.914	0.126	13.00	33.914	33.391	40	6.61
LP5	NE edge of Lago Pato	51°17′ 59.4762″	0.044	72°40′ 39.4845″	0.136	49.497	0.210	13.01	36.487	32.686	43	10.31
LP6	LP08 coring site	51°18′ 01.2000″	-	72°40′ 42.9600″	—	—	—	—	—	32.297*	39	—

Current (ACC) splits into equator- and pole-ward flows (Lamy et al., 2010; Caniupán et al., 2017), making it particularly sensitive to regional and spatial variations in the SWW-driven precipitation-evaporation balance over the Andes (**Figure 4**). Following post-glacial isolation, Lago Pato would have been a small, responsive lake located at the boundary with the eastern forest-steppe ecotone and in a transitional climatic zone between "wet" western and 'dry' eastern Patagonia. Our working hypothesis was that even relatively small changes in wind-driven precipitation in the past led to significant changes in lake level, lake ecology, and catchment vegetation cover.

2.1 Climate

Climate data from the Administración PN Torres del Paine Meteorological Station ~25 km from Lago Pato is characterised by a mean annual air temperature of 7.3°C (1964–2011 CE, 3 years after the LP08 core was taken), with minimum and maximum monthly averages of 3.6°C (in 1976 CE) and 9.1°C (in 1983 CE), mean annual precipitation of 817 mm a^{-1}, and mean annual wind speed (at ground level) of 24 km h^{-1}, predominantly from the W and NW (data from http://www.meteochile.gob.cl). In comparison, the mean annual precipitation along the west coast of Chilean Patagonia and western Andes is up to 7,000 mm a^{-1} but declines to 400 mm a^{-1} on the eastern steppe (Schneider et al., 2013). Temperature and precipitation anomaly profiles for TdP between 1979 and 2021 CE (compared to the 30-year mean between 1980 and 2010 CE) are shown in **Figure 4A**.

The Andean Cordillera creates an orographic barrier to the SWW (currently focussed at ~50–52°S) and a complex spatial (latitudinal) and temporal relationship between wind strength and precipitation (**Figures 1C**,D, **4B–I**). Analysis of weather station data has shown annual precipitation immediately east of the Andes, around Lago del Toro and Lago Pato, to have been neutral to slightly positively correlated to zonal wind flow over the high Andes (U on P at 850 mbar) over the last ~40 years (Garreaud et al., 2013; Schneider et al., 2013; Moreno et al., 2018). Studies combining weather station data and mesoscale modelling of the eastern Andean slopes have shown a more consistently positive correlation (Moreno et al., 2014; Moreno et al., 2018). Seasonally, there is only marginally more precipitation in the Última Esperanza region compared to winter (June–July–August, JJA) (**Figures 4B,D**), but the core SWW are stronger and more poleward shifted (south of 50–52°S) over Southern Patagonia during the Austral summer (December–January–February, DJF; **Figures 4C,E**). Consequently, zonal winds over the Andes have had a consistently neutral to negative correlation with precipitation at Lago Pato between 1979 and 2017 CE during the Austral summer. This relationship has become more negative over the last decade (2007–2017 CE; **Figures 4F,G**). In contrast, during winter, zonal winds over the Andes and precipitation over Lago Pato have been positively correlated over the last decade (**Figure 4H**), leading to a net neutral to negative annual correlation between precipitation and wind velocity (**Figure 4I**). At Lago Potrok Aike, ~175 km ESE of Lago Pato at 51°S, where the orographic effect of the Andes is reduced, easterly frontal system incursions are more prevalent, and winter precipitation can also increase when the SWW become weaker and/or when its core belt widens latitudinally (Garreaud et al., 2009; Fletcher and Moreno, 2012; Zolitschka et al., 2013).

Regionally, longer-term climate changes are controlled by the interplay between the changing strength and influence of interannual–millennial-scale climate drivers, such as the El Niño Southern Oscillation (ENSO) and the Southern Annular Mode (SAM), defined as the atmospheric pressure difference between the mid and high latitudes in the Southern Hemisphere (Garreaud et al., 2013). Decadal-scale variability in precipitation and temperature is evident in the TdP reanalysis data (**Figure 4A**). Positive phases of the SAM reflect warmer and drier conditions and higher pressure in the

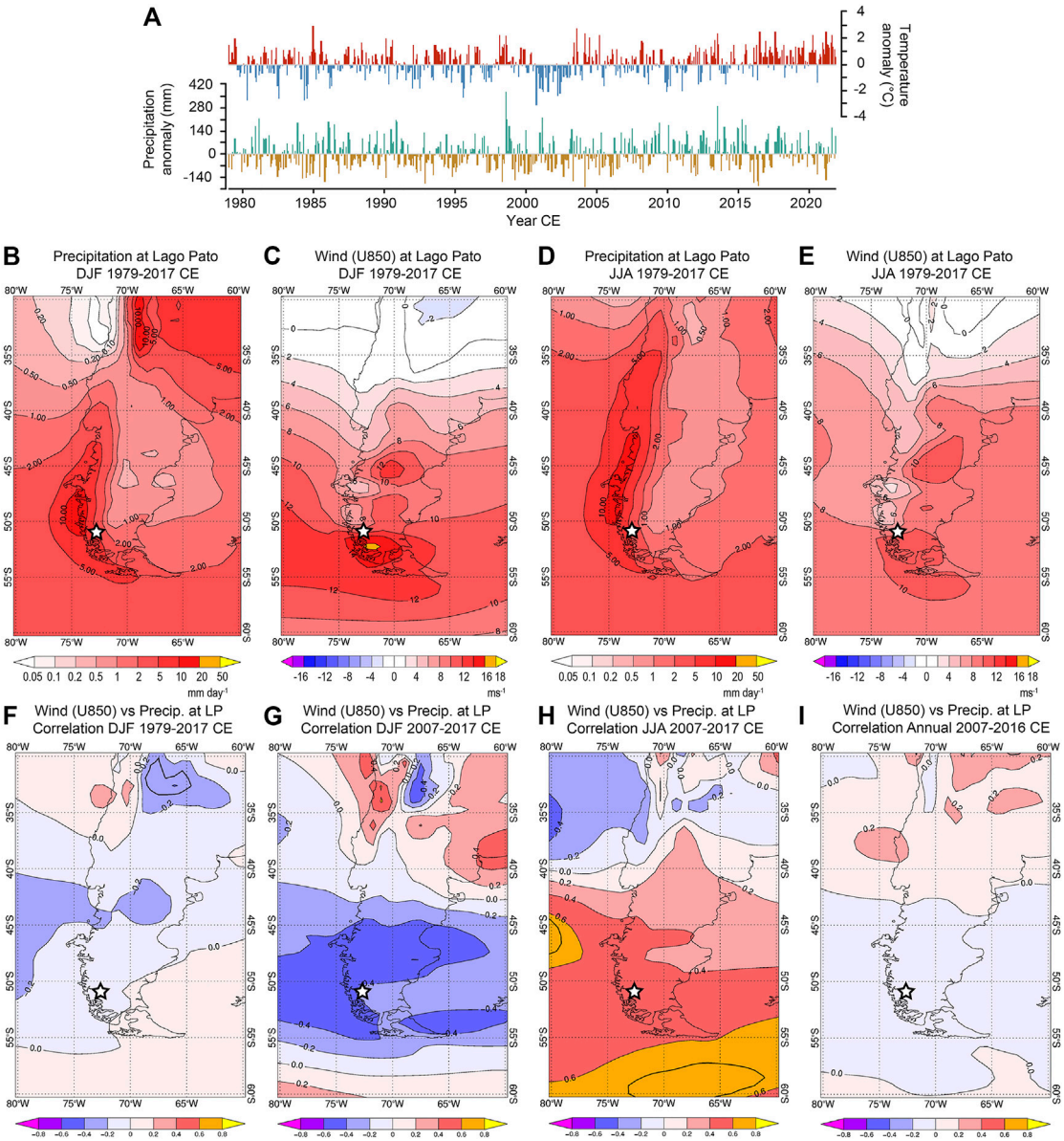

FIGURE 4 | (A) Temperature and precipitation anomaly data from Parque Nacional Torres del Paine meteorological station between 1979 and 2021. Data generated from and copyright of https://www.meteoblue.com, used here with permission. **(B–E)** ERA-INTERIM reanalysis (Dee et al., 2011) for mean Austral summer (December–January–February; DJF) and winter (June–July–August; JJA) mean surface precipitation (mm per day; 1/12/1979–1/3/2017) and zonal wind speed (U on P at 850-hPa over the Andes in ms^{-1}; 1/12/1979–1/3/2016) over southern South America (30–60°S) between 1979 and 2017 CE. The white star is the location of Lago Pato. **(F)** ERA-INTERIM reanalysis data showing neutral to marginally negative correlation coefficients between mean zonal wind velocity over southern South America and mean surface precipitation at Lago Pato for the austral summer (DJF) from 1/12 to 1/3 between 1979 and 2017 CE compared to **(G)** increasingly negative time mean correlation coefficients over Lago Pato for the austral summer (DJF) from 1/12 to 1/3 between 2007 and 2017 CE and **(H)** positive time mean correlation coefficients at Lago Pato for the austral winter (JJA) from 1/6 to 1/9 between 2007 and 2017 CE. **(I)** Time mean correlation coefficient map of annual mean wind velocity over southern South America (30–60°S) and annual mean precipitation at Lago Pato (white circle) between 1/12/1979 and 1/12/2016 CE. ERA-INTERIM data and maps were generated using a BAS internal portal to the Dee et al. (2011) dataset with the final layout made in Adobe Illustrator.

mid-latitudes (e.g., Patagonia) with lower pressures and stronger and more poleward shifted SWW (Marshall, 2003; 2007). In essence, the situation is analogous to the seasonal Westerlies (summer/winter) cycle in that the SWW are more intense and focused during positive (warmer) phases of the SAM (the current situation) and weaker, latitudinally broader, and less focussed during negative (colder) phases of the SAM (Perren et al., 2020).

Warming in recent decades has led to an increasingly positive Southern Annular Mode and a greater influence of the El Nino

Southern Oscillation (Marshall, 2003; Abram et al., 2014), with reduced precipitation and weaker Southern Westerlies in the high-to-mid-latitudes of southern South America (Garreaud et al., 2009). Similar processes are thought to occur over decadal–centennial and longer timescales, with an equatorward core SWW belt maintaining high lake levels in northern and eastern Patagonia between c. 51 ka and 9 ka (Zolitschka et al., 2013; Van Daele et al., 2016; Henríquez et al., 2021). Millennial-scale periodicities recorded in various proxy records are thought to be driven by changes in insolation and solar activity [e.g., the ~2.4–2.5 kyr Hallstatt cycle (Viaggi, 2021)], the planetary radiative imbalance (i.e., the amount of insolation absorbed versus the energy radiated back into space at the top of the atmosphere), internal ice sheet dynamics, and CO_2 outgassing, driven largely by changes in the SWW (Emile-Geay et al., 2007; Steinhilber et al., 2009; Baggenstos et al., 2019; Dickens et al., 2019; Henríquez et al., 2021; Shin et al., 2021; Evans et al., 2022).

2.2 Vegetation and Geology

Vegetation patterns in Southern Patagonia closely follow the sharp west-to-east precipitation gradient across the Andes, superimposed on latitudinal variations (Tuhkanen, 1992). As moisture-laden air masses cross the Andes, the hyper-humid region in the west transitions into a more arid steppe in the east. The western side of the Andes is dominated by Magellanic moorland communities and evergreen *Nothofagus* forests (southern beech), while the eastern slopes and those close to the Patagonian Ice Field are characterised by winter deciduous *Nothofagus* forests. The wider Provincia de Última Esperanza is a diverse eco-climatic region from hyper-humid in the west and arid in the east. Southern beech forests in western regions, with annual precipitation between ~450 and 1,000 mm a^{-1}, gradually merge into a transition zone of dry scrub and fescue grassland in regions with precipitation regimes below ~450 mm a^{-1} and finally become Patagonian steppe in drier eastern areas (Tuhkanen, 1992). Lago Pato is located just outside the Parque Nacional Torres del Paine, in the Comuna de Torres del Paine. As part of the Región de Magallanes, it is in an ecological transition zone between the *Nothofagus* dominated and steppe biomes, although the natural vegetation has been altered by agricultural and land management activity in and around Parque Nacional Torres del Paine and Lago Pato. The local geology is dominated by shales, intercalated by marls, sandstones, and conglomerates (Altenberger et al., 2003). The glaciated landscape of the Southern Patagonian Ice Sheet dominates the southern Andes and the Cordillera Paine massif to the west and northwest of Lago Pato.

3 METHODS

3.1 Geomorphology and Limnology

We measured the geoid-corrected elevation above sea level (m a.s.l.) of former lake shorelines and retaining moraine ridges around Lago Pato using a Trimble differential GPS (dGPS) accurate to down to 0.1 m with values quoted as ±two-sigma errors (**Table 1**). Other elevations were determined from "Google Earth" and are on average 6.7 ± 5.9 m (two-sigma) higher than the geoid-corrected dGPS field measurements; hence, we assigned ±10 m errors. Standard limnological properties (pH, conductivity, temperature, and dissolved oxygen) were measured in and around Lago Pato and other Southern Patagonian lakes with a YSI600 Sonde. Light penetration was measured with a Secchi disc and water samples for diatom and chemical analysis were taken at 1 m intervals in the water column.

3.2 Sedimentology, Geochemistry, and Chronology

Using a combination of a UWITEC-gravity corer, a Livingston piston corer, and a Russian corer, two sediment records were extracted from the deepest point (~3.5 m of water depth) in the lake—the 600 cm long LP08 record (S51° 18′01.2″, W72° 40′43.0″, 32 m a.s.l.)—and from a littoral wetland area—the 295 cm long LP16 record (S51°18′11.3″, W72° 40′53.7″, 33–34 m a.s.l.) (**Figure 2A**; **Table 1**). A surface gravity core from the LP08 site was sliced at 0.5 cm (0–20 cm) and 1 cm (20–41 cm) intervals in the field. Livingston piston cores (LP08) and Russian cores (LP16) were retained intact.

Intact cores were split in the laboratory and analysed for physical properties with a Geotek® multi-sensor core logger (MSCL) (Gunn and Best, 1998) to obtain gamma-ray wet density (ɣ-density or GRD), resistivity, and magnetic susceptibility (MSκ; SIx10^{-5}) data (Bartington Instruments; LP08: MS2C loop sensor, 2 mm intervals, 10 s; LP16: MS2E point sensor, 0.5 mm intervals; 10 s) and density-corrected MSχ (κ/ρ; kg m^{-3}). Digital X-radiographs were obtained from split cores using a rotating anode mobile digital Celtic SMR CR computerised X radiography unit at Cambridge University Vet School (48 kV; 4 mAs; no grid) and as ITRAX™ digital X-radiographs (45 kV, 50 mA.ms, 200 ms, 60 μm interval) at Aberystwyth University. Contiguous downcore wet-sediment Energy Dispersive Spectrometry (EDS) X-ray fluorescence core scanning (XRF-CS) geochemistry data were obtained using the ITRAX™ XRF core scanner fitted with a Molybdenum (Mo) anode X-ray tube (settings: 30 kV, 50 mA, count time 10 s). Machine and sample calibration was undertaken using a synthetic glass standard and XRF fused glass discs from the Ardley Lake and Yanou Lake sediment cores (Roberts et al., 2017) with similar compositional variability at the start and end of each core-site run. Measurements were made at 2 mm contiguous intervals for LP08 (equivalent to mean ± two-sigma: 4.5 ± 7 years), with duplicate scans undertaken at 200 μm intervals for LP08 Unit 1 (1.3 ± 4.2 years) and at 100 μm for the basal LP08 Unit 1 core section. LP16 Units 3–6 were scanned at 500 μm (9.6 ± 17.4 years) and LP16 Units 1-2 at 200 μm (1.1 ± 1.6 years). Data from finely laminated glaciolacustrine sediments in Units 1-2 were measured at, or smoothed to, 200 μm (from 100 μm interval data).

Raw count per second (cps) XRF-CS data were analysed using the Q-spec software v8.6.0 (Cox Analytical), with MSE values minimised to optimise the fit of the "as-measured" spectra to

TABLE 2 | Summary descriptions and interpretations of the lithofacies units in the Lago Pato LP08 and LP16 records.

Record	Unit subunit	Depth (cm)	Modelled age range (cal a BP ± 95% CI)	Summary lithological description	Summary interpretation	Lake history and palaeoclimate SWW position and movement
LP08	1	600–470	29,800 ± 1,020 to 21,230 ± 520	Light grey, finely laminated glaciolacustrine silty clay with pale greyish-orange layers enriched in Ti and Ca. The lowermost laminated sub-unit (1A) grades into a paler green-grey massive sub-unit (1B). In LP08, a sharp erosional upper boundary separates Unit 1 and Unit 5B at 470 cm. Units 2–5A are missing from LP08. In LP16, step changes to lower MS values separate sub-units 1A and 1B at 187 cm (25.5 cal ka BP) and Units 1 and 2 at ~110 cm (20.4 cal ka BP)	Unit 1 represents the 'background' glaciogenic detrital composition, with well-developed fine scale internal structure, most notably within Unit 1A, and dominated by glaciogenic physical weathering products associated with allochthonous catchment erosion. Fine grey (glaciogenic) laminations are enriched in Fe and Mn, reflecting reduced conditions and/or the decomposition of organic matter at the sediment-water interface	Lago del Toro and Lago Pato were part of a larger proglacial Palaeo-Lago Tehuelche after the l-LGM and before the g-LGM Lago Pato was overridden at the g-LGM SWW: N of 51°S, limited latitudinal movement in run-up to g-LGM
LP16		295–112 (112–110 hiatus)	27,530 ± 270 to 20,490 ± 350			
LP16	2	110–83	13,390 ± 640 to 13,060 ± 390	Unit 2 has similar sedimentological characteristics to the upper parts of Unit 1 but is distinguished by the lack of well-defined orange-brown banding and the presence of embedded fine subaquatic *Myriophyllum* sp. fragments	Glaciogenic physical weathering products associated with allochthonous catchment erosion. Embedded sub-aquatic macrofossils imply a shallower environment than Unit 1	First substantial lake level reduction at c. 13.4 ka: shallow, >productive lake (lake level: >100 m asl → <50 m asl) SWW: At 51°S, moving S from ACR SWW peak north of 51°S at c. 13.5 ka
LP16	3	83–74	13,070 ± 390 to 12,500 ± 220	Unit 3 is composed entirely of subaquatic *Myriophyllum* sp.	Shallower and more productive glaciogenic environment	A further reduction in lake level between c. 13.0 and 12.5 cal ka BP following glacier retreat after the ACR. SWW: S of 51°S, moving S
LP16	4	74–67	12,500 ± 220 to 11,720 ± 280	Unit 4 has a similar composition to Unit 2 but has increasingly elevated Ca and Sr and a reduced density of subaquatic *Myriophyllum* sp.	Shallower and more productive glaciogenic environment with authigenic precipitation (or redeposition) of Ca-, Sr-rich deposits. Still connected to Lago del Toro	Gradual refilling of Lago Pato while still connected to Lago del Toro SWW: S 51°S, moving N
LP16	5A	67–47	11,720 ± 280 to 10,120 ± 190	Unit 5 is structureless organic lake mud characterised by fluctuating Fe/Mn and Mn/Ti, with Ca and S peaks. Subunits 5A–C in LP16 characterised by exceptionally elevated (>+2-sigma) Fe/Mn and Mn/Ti between c. 11.7–10 cal ka BP (Unit 5A) and c. 8.4–7 cal ka BP. Subunits 5B and C are characterised by lower but still elevated Fe/Mn and Mn/Ti ratios and higher C/N values than Unit 1. Elevated Fe/Mn ratios reflecting minerogenic input are correlated with Mn/Ti ratios	Shallow-littoral environment isolated from glaciogenic inputs from Lago del Toro at 11.7 ka. Unit 5A represents an 'Anoxic Crisis' with the eventual loss of benthic diatoms within the lake. Units 5B and C represent a more restricted shallow and productive basin, with increased input of terrestrial vegetation ad periodic oxic phases consisting of Mn-oxides and co-precipitated hydroxides	Second major lake level reduction at c. 11.7 cal ka BP, continuing until complete isolation from Lago del Toro at c. 11.3 cal ka BP (lake level: <50 m asl → <40 m asl). Erosional and overspill/flushing events (or, less likely, palaeolake reformation and emptying) at c. 10 ka and c. 8.9–8.6 ka? SWW: S 51°S, moving N back over 51°S by 8 ka
	5B/C	47–35	10,120 ± 190 to 5,720 ± 130			
LP08	5B	470–378	10,160 ± 480 to 7,370 ± 290			
	5C	378–324	7,370 ± 290 to 5,600 ± 250			
LP08	6A	324–175	5,600 ± 250 to 3,310 ± 330	Highly organic, structureless, and increasingly fibrous macrophytic lake mud with low Mn/Ti ratios divided into subunits at 175 cm by a reduction in Mn (6B) and at 45 cm by a ~15 cm thick Sr-rich inwash sand layer (6c)	Significant Mn enrichment, with sporadic Mn and Ca peaks implying that Lago Pato was occasionally shallow and highly anoxic well into the mid Holocene. Increasing Fe/Mn ratios reflect a general increase in anoxia linked to greater stability and lake infilling	Shift to more persistently wet conditions with increased turbulence in the last 2 ka. LP16 became a subaerial environment in the last 200 years. SWW: marginally north of 51°S and generally stable; increased ENSO influence
	6B	175–45	3,310 ± 330 to 1,380 ± 130			
LP16	6A–C	45–0	1,380 ± 130 to −60 ± 3			
	6A–C	35–0	5,720 ± 130 to −10 ± 1			

modelled spectra. Element and scatter cps were normalised by total scatter cps (incoherent (Compton) scatter + coherent (Rayleigh) scatter; inc.+coh.) as element/inc.+coh. (Kylander et al., 2011). Data are presented as percentages of the total scatter normalised ratio sum [%∑TSN or, more simply, %TSN (Roberts et al., 2017)], equivalent to percentages of the cps sum (or %cps), to account for downcore variations in count rate, density, water, and organic content and to investigate covariance, closed-sum effects between elements and scatter parameters, and the non-stationarity and equifinality of geochemical responses through time (Tjallingii et al., 2007). Data less than mean minus two-sigma kcps (mainly due to gaps in the core) and greater than MSE plus two-sigma (representing a poor fit between measured to modelled spectra) were filtered before analysis. 'Noisy' and poorly measured elements were eliminated by comparing cps and using %TSN thresholds of >0.1% mean and >0.5% maximum and examining autocorrelation profiles for each element (Bishop, 2021). This left 12 'well-measured' elements for the LP08 record (Si, S, K, Ca, Ti, Mn, Fe, Zn, Br, Rb, Sr, Zr, and inc., coh. scatter) and 17 'well-measured' elements for the LP16 record (Si, S, K, Ca, Ti, V, Cr, Mn, Fe, Ni, Zn, As, Br, Rb, Sr, Zr, Ba, and inc., coh. scatter) (see the Supplementary Material for details).

Centred element log ratios (clr) and log element ratios of XRF-CS can produce similar downcore profiles to quantitative (Wavelength Dispersive Spectroscopy, WDS-XRF) analysis of dry and organic free samples (Weltje and Tjallingii, 2008; Davies et al., 2015; Roberts et al., 2017; Dunlea et al., 2020). Therefore, the key elements used in interpretations (S, Ca, Ti, Mn, Fe, Br, and Sr) are presented as natural log (i.e., log-n or Ln) ratios of cps data or their Z-scores (i.e., centred around the mean and standardised by subtracting the mean from observed values and dividing by the 1σ). As Al is not well-measured using an ITRAX^{TM} XRF core scanner with a Mo-tube (Löwemark et al., 2011), Ti-normalised log-n ratios were used to estimate elemental variations relative to the background bedrock input (Weltje and Tjallingii, 2008; Kylander et al., 2011; Davies et al., 2015; Roberts et al., 2017; Saunders et al., 2018).

Core sections were aligned into composite records from field depth measurements from visual stratigraphy, bulk density, MS, XRF-CS data, and, for LP08, subsample data (loss-on-ignition (LOI), and total organic carbon (TOC)), and using AnalySeries (Paillard et al., 1996).

A chronology for each record was established using Accelerator Mass Spectrometry (AMS) radiocarbon dating of 21 samples from the LP08 record and 15 samples from the LP16 record. Identifiable macrofossils were dated preferentially, but where bulk samples were the only option, we avoided intervals likely to contain significant authigenic carbonate, characterised by exceptionally elevated Ca, Sr, and/or Mn in XRF-CS profiles. Calibration of radiocarbon ages was undertaken in OXCAL v.4.4 (Bronk Ramsey, 2016) using the SHCal20.14C Southern Hemisphere atmosphere calibration dataset (Hogg et al., 2016; Hogg et al., 2020). Radiocarbon ages are reported as conventional radiocarbon years BP (^{14}C years BP) ±1σ and calibrated ages as 2σ (95.4%) ranges, median and mean calendar years BP (cal a BP and cal ka BP, relative to 1950 CE), rounded to the nearest 10 years. Age-depth models for both records were developed using Bayesian age-depth modelling software (BACON v.2.5) (Blaauw and Christen, 2011), incorporating a hiatus of 10,000 years at 470 cm in LP08 and 7,000 years at 110 cm in LP16 between Unit 1 and its overlying deposits (**Supplementary Figure S1**). Ages are rounded to the nearest 10 calendar years (cal a BP) in **Section 4** and to the nearest 100 years (0.1 cal ka BP) in the **Section 5** to reflect dating and age-depth modelling uncertainties.

Units with common characteristics were identified using constrained CONISS cluster analysis with broken stick on square root transformed 2 mm and 1 cm interval smoothed % TSN XRF-CS geochemical data and as-measured 1 cm interval diatom and pollen datasets. To establish provenance relationships, the Pearson product-moment correlation coefficient (PPMCC), multivariate principal components analysis (PCA), which reduces correlations between elements to the smallest set of linear combinations possible plotted on dimensionless axes, and discriminant hierarchical (k-means) cluster analysis, which uses a measure of statistical distance (dissimilarity) between multiple elements to generate groups, were applied to 12 'measurable' elements common to LP08 and LP16 (Si, S, K, Ca, Ti, Mn, Fe, Zn, Br, Rb, Sr, and Zr) and incoherent, coherent scatter parameters. Measured %TSN data were log-transformed, centred, and standardised as Z-scores prior to PCA.

Log-n element/Ti ratio XRF-CS Z-scores were used for time series analysis (Fast Fourier Transform, FFT, periodograms, Lomb–Scargle Power Spectrum, wavelet power spectrum, peak identification in MATLAB; **Figure 6**; **Supplementary Figure S6**) (Grinsted et al., 2004; Trauth, 2015). Equally spaced (10-year and 100-year) time intervals were generated for time series analysis using Piecewise Cubic Hermite Interpolated Polynomial (PCHIP) datasets, which avoids spline artefacts and preserves the shape of the original XRF-CS data series. Time series data were detrended (polynomial linear best fit) to remove the long-term linear trend. Second-order polynomial Locally Weighted Scatterplot Smoothing (LOESS) 100-year smoothing (0.1 sampling interval with outliers removed) was also used to compare datasets to published data.

3.3 Carbon, Diatom, and Pollen Analysis

Geochemical and sedimentological interpretations of the lake-level change in Lago Pato were inferred from multi-proxy analysis of the <10 cal ka BP organic deposits of Unit 6 in the LP08 record. This part of the LP08 was more highly resolved than the LP16 Holocene record and contained sufficient diatoms and pollen for quantitative analysis. Loss-on-ignition (LOI) (12 h drying at 110°C, 4 h at 550°C (LOI_{550}), and 2 h at 950°C for carbonate-proxy ($LOI_{950} \times 1.36$) (Heiri et al., 2001)), total organic carbon (TOC, $\%C_{org}$) and total nitrogen (%N) were determined at 1 and 4 cm intervals in the LP08 core. Bulk organic carbon isotopic ratios ($\delta^{13}C_{org}$), determined by combustion on a Costech EA interfaced with the VG Triple Trap and Optima IRMS at NIGL (NERC Isotope Geosciences Laboratory), were calculated to the V_{PDB} scale using a within-run laboratory standard calibrated against NBS-19 and NBS-22. Replicate analyses of sample material gave a precision of ±0.1 (per mil) for $\delta^{13}C_{org}$ and

10% for C/N. Flux data (g cm^{-2} a^{-1}) were calculated from the product of dry mass accumulation rates (g cm^{-2} a^{-1}) (as dry bulk density (g cm^{-3}) x sedimentation rate (cm a^{-1})) and proxy concentration measurements (Street-Perrott et al., 2007).

Subsamples for diatom and stomatocyst analysis were taken at 4 and 8 cm intervals from the LP08 core following standard preparation techniques (Renberg, 1990; Sterken et al., 2012). At least 400 valves were counted per slide, and species were identified to at least genus level using taxonomic studies from the region (Rumrich et al., 2000; Guerrero and Echenique, 2002). Where feasible, distinctions were made between different morphotypes of the small benthic fragilariod species (e.g., *Staurosirella* aff. *pinnata*; *Staurosira* aff. *venter*) because this can reflect different environmental conditions (Stevenson et al., 2008). No distinction was made between stomatocyst morphotypes.

Microscopic pollen, charcoal, and cryptotephra shards were counted at 8 cm intervals in the LP08 core (Moore et al., 1991) with *Lycopodium* spores of known concentration added for quantification (Stockmarr, 1971). The total pollen sum from each subsample is at least 300 land pollen grains (total land pollen, TLP) above 470 cm in the LP08 record (i.e., above the hiatus between Unit 1 and 5B). Local site indicators (e.g., obligate aquatic plants, moss spores, and algae) were calculated as TLP + taxon. Charcoal was classified into five different size classes, <25, 25–50, 50–75, 75–100, and >100 μm, to distinguish between proximal and distal fires, assuming hydrodynamic fractionation at the regional scale. Diatom and pollen data were obtained from the more highly resolved Holocene-age Unit 5 and 6 sediments of the LP08 record. Both proxies were largely absent from the basal glaciolacustrine deposits in Unit 1 of both records.

Data were analysed and figures constructed in R v. 4.1.0/ Rstudio v. 1.4.1717, using the R packages Vegan, Rioja, Tidyverse (ggplot2), Ggally v. 2.1.2 (Juggins, 2012; Oksanen, 2014; Barret, 2021; Galili, 2021) (and other packages listed in the figure captions and Supplementary Material); SigmaPlot v. 14.0, C2 v.1.7.7 (Juggins, 2007); MATLAB v. R2021a; and ESRI ArcGIS v. 10.4. The final layout of all figures was achieved in Adobe Illustrator CC v. 2021.

4 RESULTS

4.1 Geomorphology and Limnology

The NE shoreline of Lago Pato has a differential GPS (dGPS) ellipsoid corrected elevation of 32.7 ± 1 m a.s.l. (**Table 1**). Former lake shorelines immediately surrounding the lake are visible on satellite images between ~35 and 40 m a.s.l., and there are two further prominent shorelines at ~40–45 m a.s.l. and ~45–50 m a.s.l. that delineate the visible break from grassy wetlands to more densely vegetated bushland around the lake and the transition to more barren grassland cover on the surrounding moraine complexes. The LP08 site is the deepest point of the current lake, with a water level at ~32 m a.s.l. (**Table 1**), while the LP16 core site is located on a slightly elevated (~33–34 m a.s.l.) infilled littoral area of the basin, which is currently a seasonal (ephemeral) wetland, approximately 200 m SW of the LP08 core site (**Figure 2B**). Lago del Toro, immediately north, has a seasonally dependent water level of ~24 ± 5 m a.s.l.

Retaining shoreline ridges separating Lago Pato from Lago del Toro are ~4–10 m above the present water level in Lago Pato, suggesting that moderately higher lake levels in Lago del Toro could plausibly overspill into Lago Pato (**Figure 2B**). Our geomorphological data show that Lago Pato would have become an isolated and closed basin once the water level in Lago del Toro was <32–37 m a.s.l. Water column chemistry measured at the Lago Pato depocentre (LP08 coring site) in February 2007 had a pH of 8.87 ± 0.01 (n = 3; mean ± 1σ), a specific conductance of 331 ± 2 μS cm^{-1}, and a temperature of 11.81 ± 0.04°C and dissolved O_2 of 11.92 ± 0.05 mg L^{-1} (equivalent to 372.5 ± 1.7 μM). Visibility was limited to less than 1 m water depth due to relatively high phytoplankton primary production.

4.2 Sedimentology, Geochemistry, and Chronology

The LP08 and LP16 records were divided into six lithofacies units shown in **Figure 5**. These are summarised and interpreted in **Table 2**, the Supplementary Material, and **Section 5.1**. In summary, the littoral record (LP16) contains all six units, but glaciolacustrine Units 2–4 and the more organic subunit 5A were missing from the depocentre (LP08) record (**Figure 5**; **Supplementary Figure S1**). Units 5B–C and 6 (c. 10–5.8 cal ka BP) were preserved at a much higher resolution in the LP08 record, 0–470 cm (**Figure 5A**) compared to 0–50 cm in LP16 (**Figure 5B**). **Figure 6A** shows the transition from glaciolacustrine to full organic sedimentation at the start of the Holocene between Units 2–4 and 6 in LP16 when Lago Pato was isolated from Lago del Toro and a short-lived return to glaciolacustrine sedimentation between c. 8.9 and 8.6 ka in Units 5B and 6 in LP08 (**Figure 6A**). **Figures 6B–F–F** and **Supplementary Figures S3D, S6** show the decadal-to-centennial-scale variability of erosional inputs into the deep glaciolacustrine basin of Unit 1 in the LP08 and LP16 records between c. 20 and 30 cal ka BP. In LP08, elevated C/N ratios in Units 5 and 6 reflect increased terrestrial organic matter input, with a notable increase in all productivity proxies from c. 5.6 cal ka BP onwards (**Figure 5A**). Principal components analysis (PCA) summarised in **Figure 7** shows that the variance in both LP08 and LP16 XRF-CS datasets is driven by erosional inputs (characterised most strongly by Ti, Rb, and K along the first PC axis in a positive direction) versus negative PC axis 1 values (inc. and coh. scatter, Br, which reflect organic productivity but not Zr as a matrix effect) (**Supplementary Figures S2, S3, S5**).

A complex relationship between Ca, S, Mn, Sr, and, to some degree, Fe exists, driven by a mixture of detrital and/or authigenic processes, but mainly redox changes, represented by the second PC axis. This relationship varies between the two records and between units within each record. For example, in the LP08 record, an inverse correlation between K, Fe, Rb, Zn, and, to some

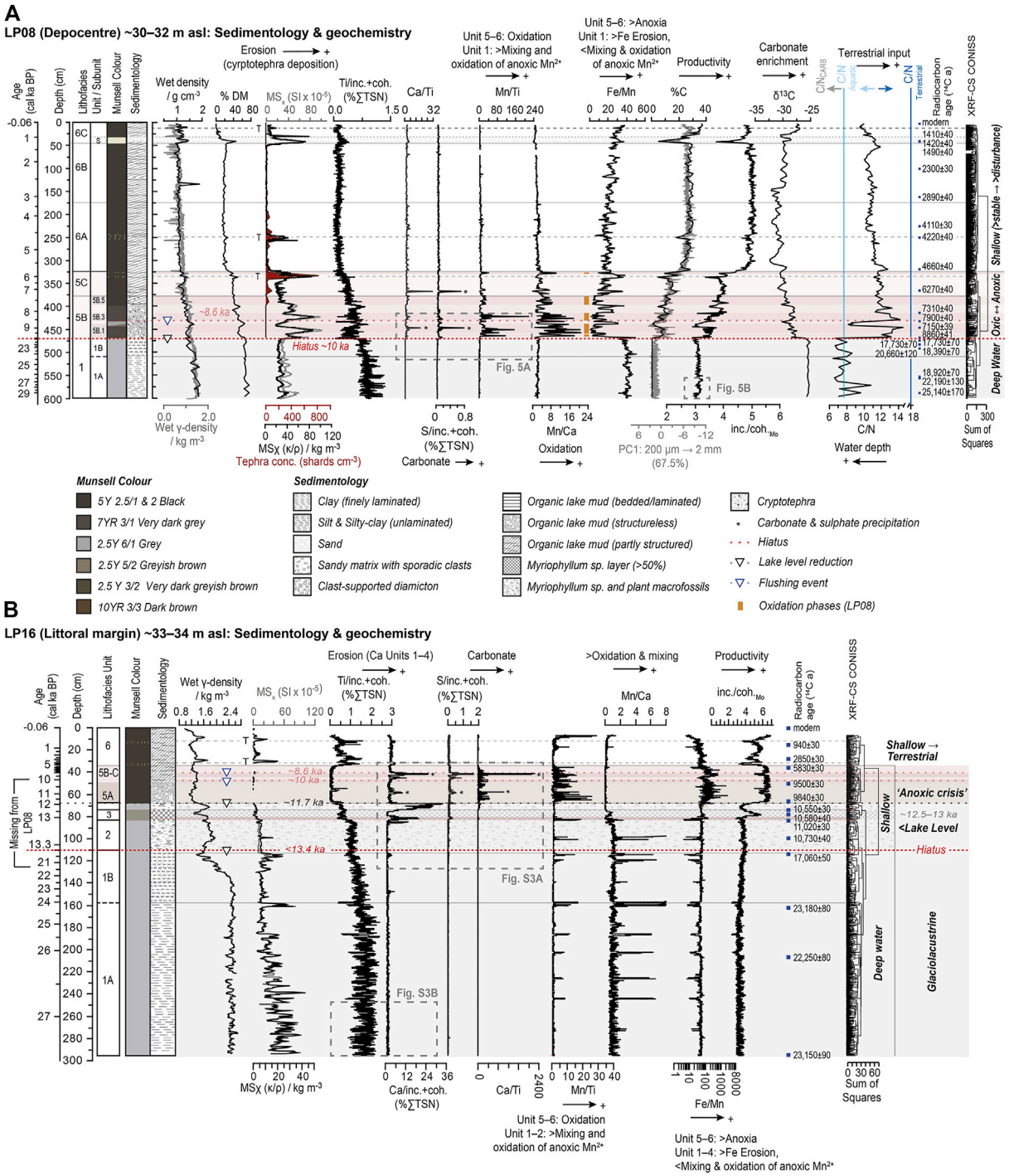

FIGURE 5 | Summary sedimentology and geochemistry data for Lago Pato sediment records. **(A)** LP08 (depocentre site). **(B)** LP16 (littoral-catchment site). This figure integrates sedimentological observations, key core scanning parameters, ratios, and subsample data and shows the main changes in key elements (Ti, Mn, Ca, Fe) and their ratios in both records. Data points between 68 and 62 cm in the LP08 record were not plotted or included in the analysis due to low counts from an extrusion-related surface gap. Data were plotted in C2 (Juggins, 2007) and R, with the final layout achieved in Adobe Illustrator.

degree, Mn versus incoherent and coherent scatter and Br broadly aligns with PC1, while S is strongly correlated with Ca, Mn, and Sr, to a lesser degree, between PC1 and PC2 (**Figures 7A**; **Supplementary Figure S2A**). The PC3 axis reflects an inverse correlation between Mn and Ca, S (**Figure 7B**, **Supplementary Figures S2E–H**). In contrast, the LP16 record has increased variance along the PC2 axis, with Sr and Ca positively correlated with each other yet negatively correlated with all

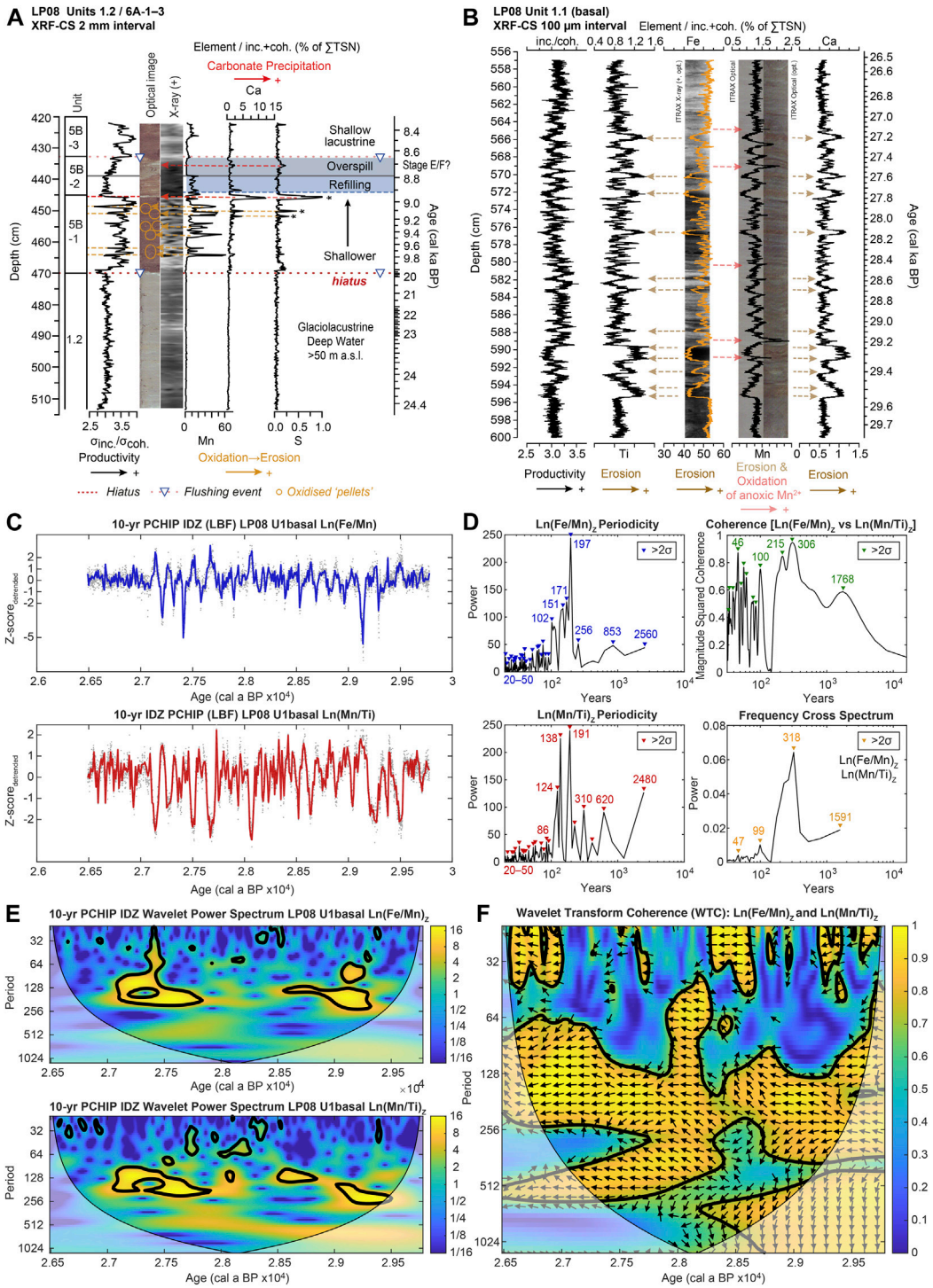

FIGURE 6 | Key geochemical features of the LP08 XRF-CS record. **(A)** Close-up of the Unit 1/Unit 6 boundary showing the sharp boundary (hiatus) at ~470 cm depth (c. 10 cal ka BP) and Mn-rich nodules, and Ca- and S-rich layers associated with carbonate precipitation in a shallow water (arid) sedimentary environment. A short-lived phase of glacier readvance and reformation of palaeo Lago Tehuelche–Puerto Consuelo to >40–<50 m a.s.l. might have occurred between 8.9 and 8.6 ka (Units 5B-2). **(B)** Ultra-high-resolution (100 µm; 44 cm core length) XRF-CS data from the LP08 basal core section plotted against depth and weighted mean modelled age (SH20-M1H model). Variations in organic (inc./coh.), erosional (Ti/inc.+coh. and Ca/inc.+coh. as %TSN), and redox (Mn/inc.+coh. as %TSN) geochemical ratios are shown. **(C)** Time series analysis of the 10-year PCHIP (Piecewise Cubic Hermite Interpolating Polynomial) interpolated $Ln(Fe/Mn)_{Z\text{-scores}}$ (blue line) and $Ln(Mn/Ti)_{Z\text{-scores}}$ (red line) and from the LP08 basal core section (B). The mean sample interval for the dataset (grey dots) is 0.75 ± 0.31 years. **(D)** Power spectrum periodicity, cross-coherence, and cross-spectrum bi-plots for $Ln(Fe/Mn)_{Z\text{-scores}}$ and $Ln(Mn/Ti)_{Z\text{-scores}}$ data from **(C)** with prominent (i.e., >2-sigma) decadal-to-millennial-scale

(*Continued*)

FIGURE 6 | periodicities highlighted. MSC is Magnitude Squared Coherence. **(E)** Wavelet power spectrum and **(F)** wavelet transform coherence (WTC) plots (Grinsted et al., 2004) for $Ln(Fe/Mn)_{Z\text{-scores}}$ $Ln(Mn/Ti)_{Z\text{-scores}}$ from **(C)** showing decadal-to-centennial-scale periodicity [period, in years in **(E,F)**] and time-dependent changes in correlation [0–1 in **(F)**]. WTC uses Monte Carlo methods to assess the statistical significance of cross-coherence against red noise in both time series. Significant (>95% confidence) decadal-to-centennial-scale periodicities and correlations are outlined in black, with a strong and significant correlation for $Ln(Fe/Mn)_{Z\text{-scores}}$ $Ln(Mn/Ti)_{Z\text{-scores}}$. Periodicities of 128–512 years between 30 and 26 ka. Directional arrows in **(F)** show that Ln(Fe/Mn) and Ln(Mn/Ti) are always anti-correlated. Data were plotted and analysed in C2 (Juggins, 2007) and MATLAB, with the final layout achieved in Adobe Illustrator.

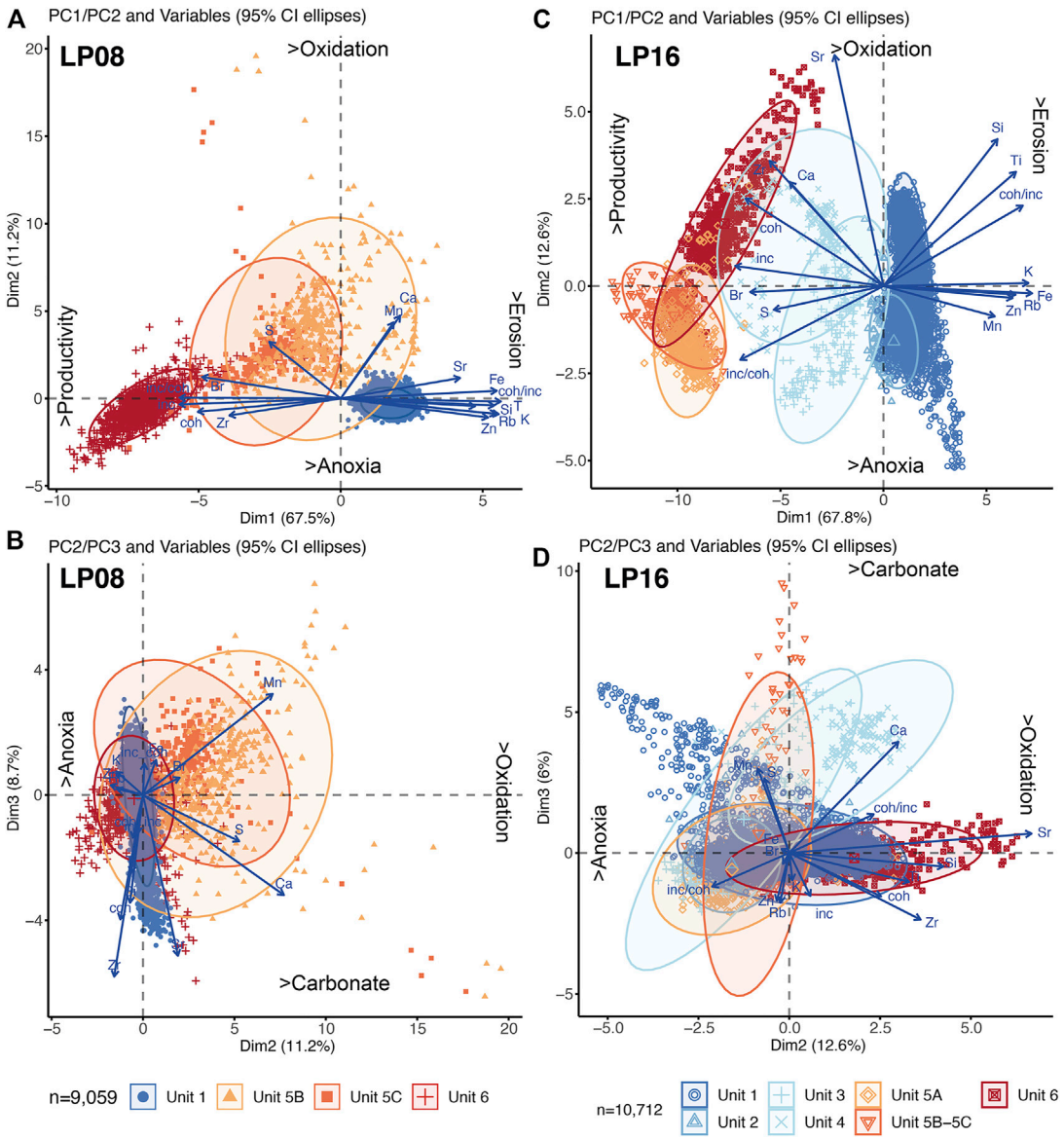

FIGURE 7 | Principal component analysis (PCA) biplots and summary interpretation for **(A)** LP08: PC1/PC2, **(B)** LP08: PC1/PC3, **(C)** LP16: PC1/PC2, and **(D)** LP16: PC1/PC3. Further analysis and PCA biplots are shown in **Supplementary Figures S2, S3**). 'As-measured' 200 μm→2 mm element/total scatter XRF-CS datasets (expressed as a percentage of total scatter normalised sum) were used. Data were $\log_n$ transformed, centred, standardised, and then grouped by lithofacies units as defined by CONISS cluster analysis shown in **Figure 5**. Data were plotted and analysed in R, with the final layout achieved in Adobe Illustrator.

other elements (**Supplementary Figure S3D**). In LP16, S is strongly aligned along PC1, reflecting increased productivity and anoxia within Unit 5A (rather than carbonate), while the PC3 axis describes a positive correlation between Mn and S within Unit 1 (**Supplementary Figure S3**) and is most likely related to deep water anoxia and the Mn and S peaks present in **Figure 5B**.

TABLE 3 | Radiocarbon dating data for the LP08 and LP16 records. Aw, acid wash; a/a/a, acid-alkali-acid pre-treatment; M, macrofossil age; P, paired bulk-macrofossil ages; R, age reversal and length of reversal in years in brackets. Reasons for rejection: X-a, organic sediments emplaced on extraction; X-b, drag down of younger roots during coring.

No.	Lab ID	Core ID and section depth (cm)	Strat. depth (cm)	Carbon source: pre-treatment	$\delta^{13}C_{IRMS}$ (‰)	^{14}C (ab. pMC) (% mod.±1σ)	C-14 age (^{14}C a±1σ)	SH20 calibrated ages (cal a BP) (2σ, 95.4% probability) max.–min.	Mean ± 1σ	Median	Notes
1	SUERC-20903	LP08-SC 1.5–2.0	1.5–2	Macrophytic lake mud: aw	−27.8	104.09 ± 0.45	—	−6 to −70	−15 ± 19	−7	—
2	BETA-281397	LP08-1A: 26.5–27	39.5–40	Macrophytic lake mud: aw	−26.9	83.9 ± 0.42	1,410 ± 40	1,360–1,170	1,270 ± 50	1,280	—
3	BETA-283772	LP08-SC:40 M	40–41	Plant material: a/a/a	−28.5	83.8 ± 0.42	1,420 ± 40	1,360–1,170	1,280 ± 50	1,290	P
4	BETA-281396	LP08-SC:40 B	40–41	Macrophytic lake mud: aw	−29.2	83.07 ± 0.41	1,490 ± 40	1,410–1,280	1,340 ± 30	1,340	P
5	BETA-476098	LP08-1A: 81–82	100.2–101.3	Macrophytic lake mud: aw	−30.0	75.1 ± 0.28	2,300 ± 30	2,350–2,140	2,240 ± 60	2,220	—
6	BETA-281398	LP08-1B: 48–48.5	162–162.5	Macrophytic lake mud: aw	−31.1	69.78 ± 0.35	2,890 ± 40	3,150–2,850	2,980 ± 70	2,970	—
7	BETA-476104	LP08-1C: 53–54	225.2–226.2	Macrophytic lake mud: aw	−31.5	59.95 ± 0.22	4,110 ± 30	4,810–4,420	4,590 ± 100	4,570	—
8	BETA-281399	LP08-1C: 78–78.5	250–250.5	Plant material: a/a/a	−29.5	59.14 ± 0.29	4,220 ± 40	4,850–4,570	4,710 ± 80	4,720	M
9	BETA-281400	LP08-1D: 69–69.5	319.6–320.1	Macrophytic lake mud: aw	−29.2	55.98 ± 0.28	4,660 ± 40	5,480–5,060	5,370 ± 90	5,390	—
10	BETA-281402	LP08-1E: 30–31	365.4–366.4	Plant material: a/a/a	−30.8	45.82 ± 0.23	6,270 ± 40	7,260–6,990	7,130 ± 80	7,120	M
11	BETA-288873	LP08-1E 79–80	414.4–415.4	Organic-rich sediment: aw	−27.8	40.25 ± 0.20	7,310 ± 40	8,180–7,980	8,090 ± 50	8,100	—
12	SUERC-20906	LP08-1F: 10–11	432–433	Organic-rich sediment: aw	−28.3	37.38 ± 0.19	7,900 ± 40	8,980–8,540	8,690 ± 100	8,670	R (-720)
13	SUERC-20907	LP08-1F: 25–26	447–448	Organic-rich sediment: aw	−27.7	41.05 ± 0.20	7,150 ± 39	8,020–7,840	7,930 ± 50	7,940	—
14	SUERC-20909	LP08-1F: 46–47	468–469	Organic-rich sediment: aw	−28.7	33.20 ± 0.17	8,860 ± 41	10,160–9,680	9,900 ± 130	9,880	—
15	BETA-281403	LP08-1F: 52.5–53	474.5–475.5	Glaciogenic clay-rich sediment: aw	−25.2	11.00 ± 0.10	17,730 ± 70	21,790–21,090	21,450 ± 180	21,430	—
16	BETA-281405	LP08-1G: 17.5–18	483.5–484	Glaciogenic clay-rich sediment: aw	−25.2	11.03 ± 0.10	17,710 ± 70	21,760–21,050	21,400 ± 180	21,390	—
17	BETA-281404	LP08-1F: 61.5–62	483.5–484.5	Glaciogenic clay-rich sediment: aw	−24.9	10.13 ± 0.09	18,390 ± 70	22,440–22,130	22,290 ± 70	22,300	—
18	BETA-271299	LP08-1G 26–27	492–493	Glaciogenic clay-rich sediment: aw	−25.6	7.64 ± 0.11	20,660 ± 120	25,200–24,370	24,830 ± 190	24,850	—
19	BETA-281406	LP08-1H: 46–46.5	554.2–554.7	Glaciogenic clay-rich sediment: aw	−24.8	9.49 ± 0.08	18,920 ± 70	22,990–22,550	22,790 ± 120	22,800	R (-3,600)
20	BETA-271298	LP08-1H 48–49	556.2–557.2	Glaciogenic clay-rich sediment: aw	−25.5	6.31 ± 0.10	22,190 ± 130	26,910–25,990	26,420 ± 250	26,380	—
21	BETA-271297	LP08-1I 33–34	589.4–590.4	Glaciogenic clay-rich sediment: aw	−25.3	4.37 ± 0.09	25,140 ± 170	29,910–29,050	29,440 ± 230	29,420	—
22	BETA-480157	LP16-1C(SUR)_0–2	0–2	Plant material: a/a/a	−27.8	103.2 ± 0.40	—	−6 to −7	−6 ± 1	−6	M
23	BETA-480156	LP16-1C(SUR)_15–16	15–16	Organic-rich sediment: aw	−27.8	88.96 ± 0.33	940 ± 30	910–730	820 ± 50	800	—
24	BETA-476093	LP16-1A: 0–1	28–29	Organic-rich sediment: aw	−28.2	70.13 ± 0.26	2,850 ± 30	3,060–2,780	2,920 ± 60	2,920	—
25	BETA-476099	LP16-1A: 8–9	36–37	Organic-rich sediment: aw	−29.7	48.4 ± 0.18	5,830 ± 30	6,730–6,480	6,590 ± 50	6,590	—
26	BETA-476094	LP16-1A: 22–23	50–51	Organic-rich sediment: aw	−28.7	30.65 ± 0.11	9,500 ± 30	11,070–10,570	10,720 ± 110	10,700	—
27	BETA-476095	LP16-1A: 38–39	66–67	Glaciogenic clay-rich sediment: aw	−31.4	29.38 ± 0.11	9,840 ± 30	11,260–11,170	11,220 ± 20	11,220	—
28	BETA-476100	LP16-2A: 20–21 M	74–74.5	*Myriophyllum* sp. aq. moss; a/a/a	−33.0	26.89 ± 0.10	10,550 ± 30	12,620–12,470	12,550 ± 60	12,550	P

(Continued on following page)

TABLE 3 | (*Continued*) Radiocarbon dating data for the LP08 and LP16 records. Aw, acid wash; a/a/a, acid-alkali-acid pre-treatment; M, macrofossil age; P, paired bulk-macrofossil ages; R, age reversal and length of reversal in years in brackets. Reasons for rejection: X-a, organic sediments emplaced on extraction; X-b, drag down of younger roots during coring.

No.	Lab ID	Core ID and section depth (cm)	Strat. depth (cm)	Carbon source: pre-treatment	$\delta^{13}C_{IRMS}$ (‰)	^{14}C (ab. pMC) (% mod.±1σ)	C-14 age (^{14}C a±1σ)	SH20 calibrated ages (cal a BP) (2σ, 95.4% probability) max.–min.	Mean ± 1σ	Median	Notes
29	BETA-476101	LP16-2A: 20–21 B	74–74.5	Glaciogenic grey clay-rich sediment: aw	–27.1	26.79 ± 0.13	10,580 ± 40	12,690–12,470	12,560 ± 70	12,550	P
30	BETA-476096	LP16-2A: 24–24.5_M	78–78.5	*Myriophyllum* sp. aq. moss layer; a/a/a	–36.3	25.36 ± 0.09	11,020 ± 30	13,070–12,780	12,900 ± 60	12,900	M
32	BETA-480158	LP16-2A_46-M	100–100.5	*Myriophyllum* sp. aq. moss; a/a/a	–30.5	26.3 ± 0.13	10,730 ± 40	12,750–12,620	12,700 ± 30	12,710	M
33	BETA-476102	LP16-2B: 22–23	114–115	Glaciogenic clay-rich sediment: aw	–25.0	11.96 ± 0.07	17,060 ± 50	20,780–20,430	20,580 ± 90	20,560	—
34	BETA-480160	LP16-3A_33	162–163	Glaciogenic clay-rich sediment: aw	–25.2	5.58 ± 0.06	23,180 ± 80	27,650–27,250	27,420 ± 110	27,400	—
35	BETA-476103	LP16-3B: 38–39	206.8–207.8	Glaciogenic clay-rich sediment: aw	–25.1	6.27 ± 0.06	22,250 ± 80	26,920–26,120	26,540 ± 200	26,480	—
36	BETA-476097	LP16-4B: 47–48	294.52–295.5	Glaciogenic clay-rich sediment: aw	–25.5	5.6 ± 0.06	23,150 ± 90	27,640–27,230	27,400 ± 110	27,370	—
-	SUERC-20910	LP08-LP08-1I: 51–52	607.4–608.4	Organic sediment: acid washes	–29.3	39.52 ± 0.20	7,460 ± 40	8,370–8,050	8,250 ± 60	8,260	X-a
-	SUERC-20911	LP08-1I: 55–56	611.4–612.4	Organic sediment: acid washes	–29.1	40.34 ± 0.18	7,290 ± 40	8,180–7,970	8,080 ± 60	8,080	X-a
31	BETA-480159	LP16-2A: 30–30.5_M	84–84.5	Plant root material (terrestrial); a/a/a	–27.5	37.68 ± 0.14	7,840 ± 30	8,690–8,450	8,570 ± 50	8,570	X-b

In both records, all calibrated Unit 1 ages from glaciolacustrine sediments were older than 20 cal ka BP, with basal ages of ~30–27 cal ka BP (**Table 3**). In LP08, a significant age gap exists between radiocarbon ages from the top of Unit 1 (471 cm: 21,230 ± 510 cal a BP modelled age ± mean 95% confidence interval) and the base of Unit 6 (470 cm: 10,160 ± 2,120 cal a BP), where a sharp (erosional) boundary exists. Units 2–5 appear to be missing and are present in LP16 only. Units 1 and 2 in the LP16 record are separated by a large age gap, defined by a large downshift in MS values at 110 cm and embedded *Myriophyllum* sp. macrofossils into Unit 2, but without a visually obvious sedimentary discontinuity between 115 and 111 cm (20,660 ± 250–20,440 ± 410 cal a BP) and ~110 cm (13,390 ± 440 cal a BP) (**Table 3**; **Supplementary Figure S1**).

Late Glacial transition ages in LP16 and Holocene ages from both cores (i.e., Units 2–6) were in broadly stratigraphic order, except for a minor age-reversal at 433 cm in LP08 (**Table 2**), where sediment reworking within the shallow basin is evident (**Figures 5A**; **Supplementary Figure S3**; **Table 3**). Ages from Units 2–6 had lower mean ± 2σ 95% confidence ranges (LP08: 300 ± 500 cal years; LP16: 320 ± 280 cal years) than the glaciolacustrine Unit 1 ages (LP08: 890 ± 560 cal years; LP16: 720 ± 440 cal years). Post-bomb calibration ages from an unconsolidated, macrophytic lake mud sample at 1.5–2 cm in the LP08 record, core-top terrestrial vegetation at 0–0.5 cm in the LP16 record, and overlapping ages from paired lake-mud and plant macrofossil remaining at ~40 cm depth imply that exchange between atmospheric and lacustrine carbon reservoirs have been in equilibrium during the late Holocene.

4.3 Diatom and Pollen Analysis

Diatom and pollen were largely absent from Unit 1 of the LP08 record, meaning only samples from 470 cm (10,160 ± 2,120 cal a BP) upwards (Unit 5B) in the LP08 record had sufficient valves and concentrations of palynomorphs for reliable counting statistics. Although single valves of *Staurosirella* aff. *pinnata* (532.7 cm), *Achnanthes* spp. (530.3 cm), and *Fragilaria capucina* s.l., (486.3 cm) diatoms were found, the minerogenic sediments of Unit 1 and Unit 5 sediments up to 454 cm (>9,280 ± 680 cal a BP) were characterised by a near absence of diatoms. Based on cluster analysis, the LP08 core was subdivided into six diatom zones (DZ1–6) between 454 and 0 cm depth (**Figure 8**; **Supplementary Figure S7**). Diatom concentrations remained low (<50 × 10^6 valves g^{-1} dry mass) in DZ1 (454–339 cm; 9,280 ± 680–6,180 ± 560 cal a BP). A diverse benthic diatom community, dominated by *Pseudostaurosira* spp., *Staurosira* aff. *venter*, *Staurosirella* aff. *lapponica*, *Staurosirella* aff. *pinnata*, and *Mastogloia* spp., was already established, supporting geochemical evidence that the first phase of isolation from Lago del Toro (Unit 5A) is missing from the LP08 record. At 416 cm (8,150 ± 160 cal a BP), the initially turbulent, shallow-brackish, and nutrient-enriched lacustrine regime of DZ1a was replaced briefly by more stable and possibly deeper water, indicated by the dominance (~80%) of planktonic species, *Discostella stelligera* species l

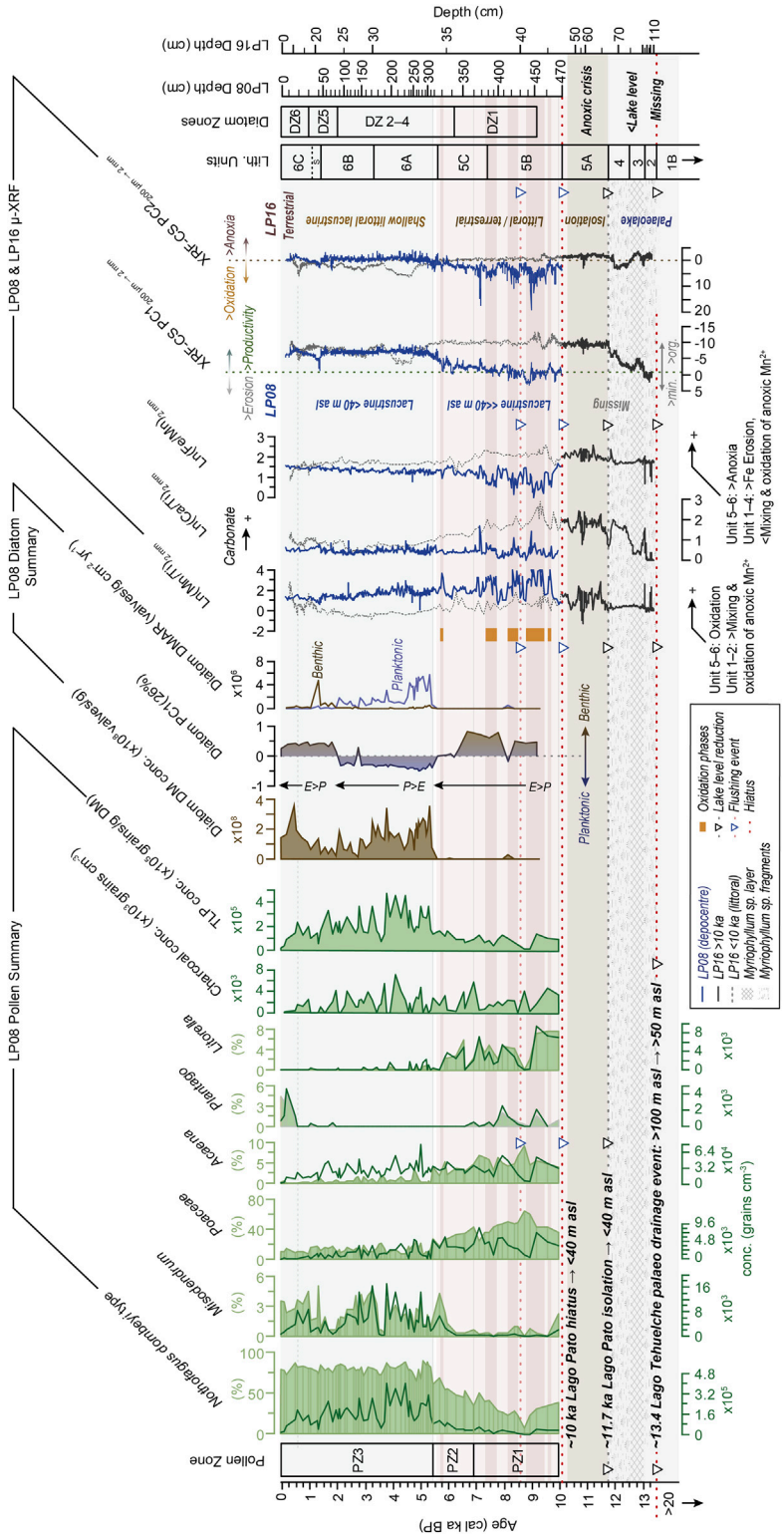

FIGURE 8 | Summary key pollen and diatom compositional diagram for Holocene-age sediments in the LP08 record compared to key geochemical $\log_n$ ratios and principal component (PC1) profiles from the LP08 and LP16 records shown in **Figures 5**–**7**. DM, dry mass concentration, DMAR, dry mass accumulation rate. Data were plotted and analysed in C2 (Juggins, 2007), with the final layout achieved in Adobe Illustrator.

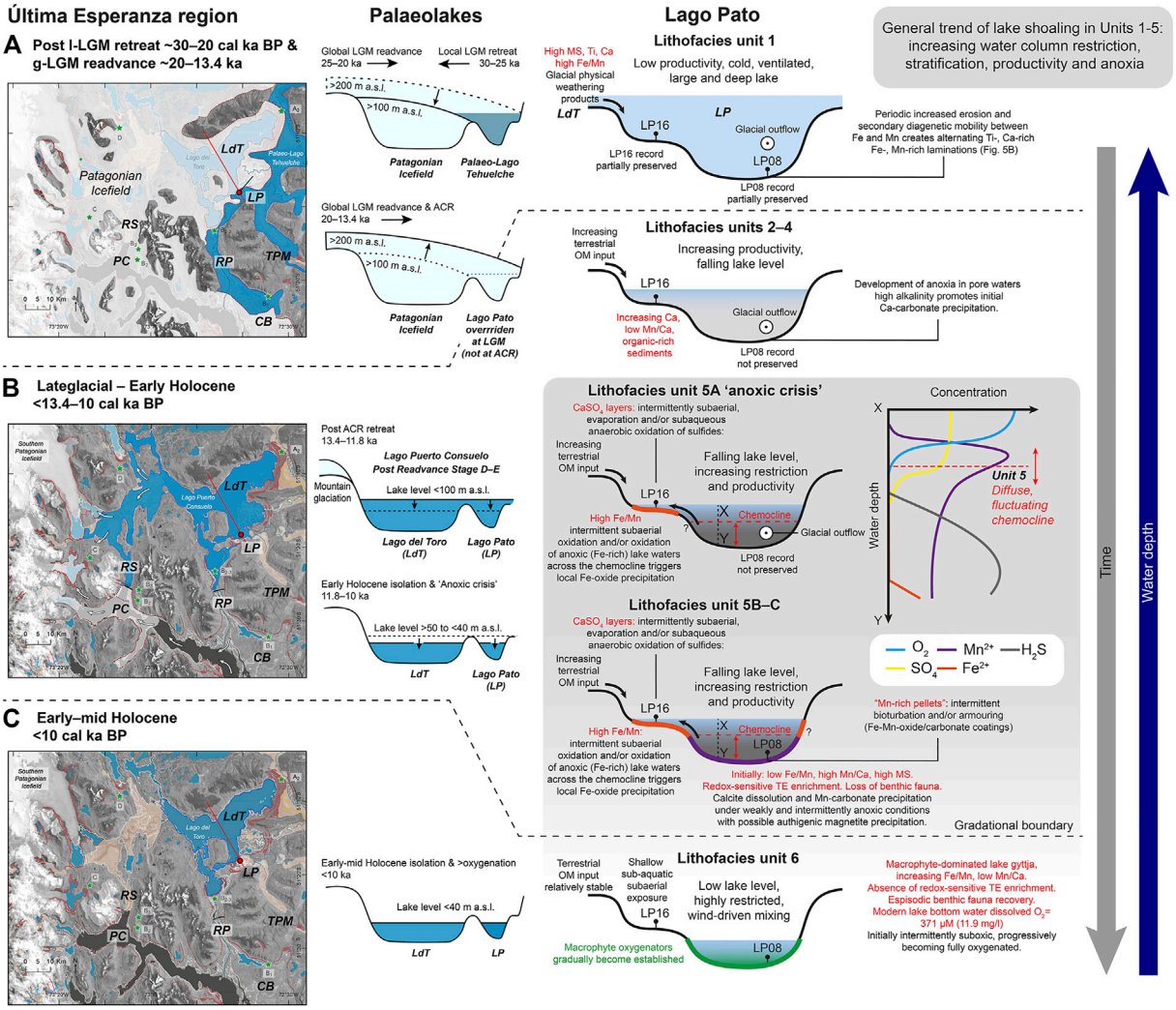

FIGURE 9 | Schematic cartoon and lake ontogeny model illustrating changes in glacial activity and its impact on the Lago del Toro lake level and development of Lago Pato and in the last ~30 ka. **(A)** Cross section across Lago del Toro (LdT) and Lago Pato (LP) during the retreat from local-LGM (l-LGM) glacial limits and during readvance to global-LGM (g-LGM) limit. The outline of Palaeo-Lago Tehuelche (blue) formed after the l-LGM and the extent of the Southern Patagonia Icefield are adapted from Garcia et al. (2014). PC is Puerto Consuelo, TPM is Tres Paso Moraine, CB is Cerro Benetiz, and RS is Rio Serrano. **(B)** Palaeo-Lago Puerto Consuelo at c. 13.4–11.7 ka after the first major lake lowering event and during the early Holocene isolation of Lago del Toro and Lago Pato, between c. 11.7 and 10 ka. Isolation occurred when the palaeolake level fell below ~40 m a.s.l. after glaciers retreated from the Puerto Consuelo area, removing the ice-dam at ~50 m a.s.l. that retained the enlarged palaeolake over Lago del Toro and Lago Pato. Glacier limits shown in **(B)** are minima at c. 11.3 ka following the retreat from advanced ACR positions along the Río Serrano (RS) and from the Cerro Benetiz (CB) area (adapted from García et al. (2014) and the references therein). **(C)** Development of Lago Pato as an isolated basin <10 ka. Chemocline changes in the lithofacies model are based on the Brownie Lake profiles (Wittkop et al., 2020), with observations in black text and interpretations in red text. This figure was made in ARC-GIS and Adobe Illustrator.

(sp.1). More turbulent and shallow-brackish conditions, with benthic *Pseudostaurosira* spp., *Staurosira* aff. *venter*, and *Mastogloia* spp. dominating, returned in DZ1b (**Supplementary Figure S7**).

DZ2 and DZ3 (339–228 cm; 6,180 ± 380–4,520 ± 170 cal a BP) are characterised by the increasing dominance of large and heavily silicified (tycho-) planktonic *Aulacoseira* species and smaller planktonic *Discostella stelligera* s.l., both indicating an increasingly stable, stratified lake with a shallow epilimnion. There is a dramatic increase in diatom concentration at c. 307 cm (*c.* 5,320 ± 210 cal a BP) to >300 × 10^6 valves g^{-1}, followed shortly after by a significant increase in chrysophyte cyst concentration to >250 cysts g^{-1} (**Supplementary Figure S7**). *Aulacoseira ambigua* became increasingly abundant (>~50–60%) at this time, implying that a less well-stratified water column existed.

While *Aulacoseira ambigua* is absent further up-core, the dominance of planktonic species such as *Discostella stelligera* s.l. and *Aulacoseira granulata* s.l. implies more stable conditions (perhaps deeper water) persisted in DZ4 and DZ3 (229–83 cm; 4,530 ± 180–1960 ± 260 cal a BP). Benthic species such as *Staurosirella* aff. *pinnata* briefly became dominant at ~140 cm

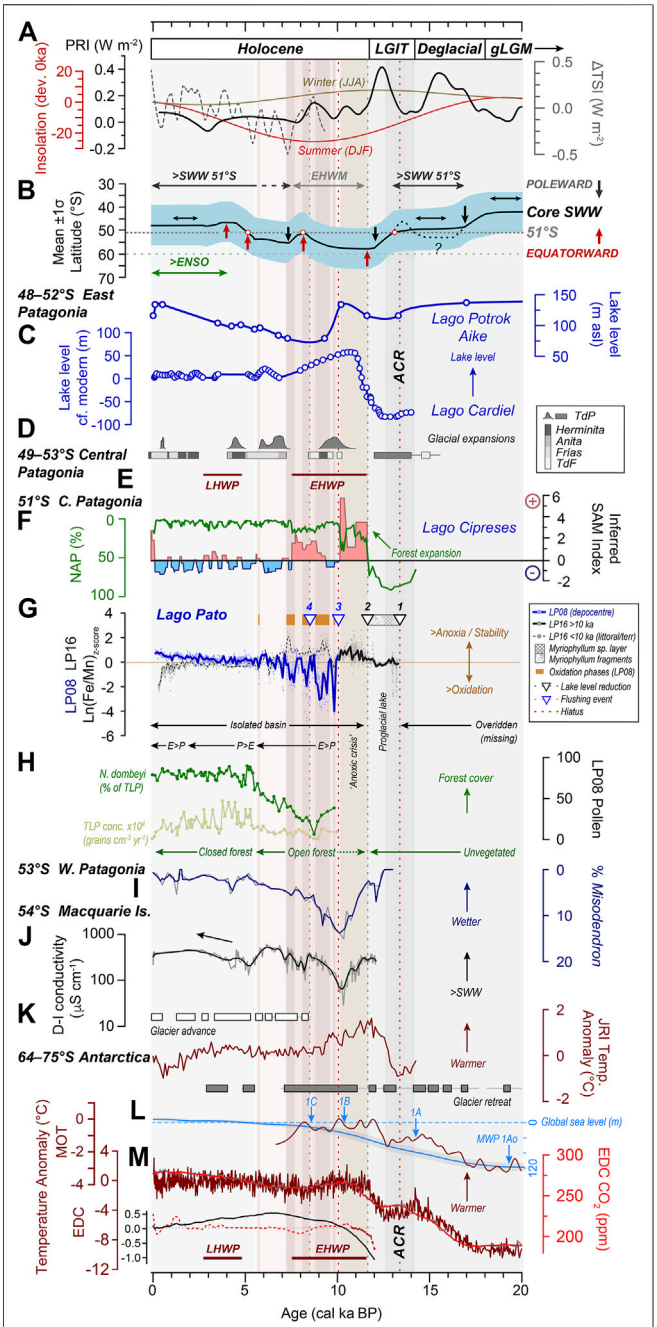

FIGURE 10 | Regional-global driving mechanisms of glacier dynamics and palaeoclimatic change compared with lake-level change in Patagonia and the Fe/Mn (redox) record from Lago Pato over the last 20 cal ka BP. **(A)** Total Solar Irradiance deviation (ΔTSI, dashed grey line) from present-day value (a solar forcing parameter based on variations in ^{10}Be isotope data from ice cores) (Steinhilber et al., 2009), austral winter insolation (June–July–August, JJA; brown line), and summer insolation (December–January–February, DJF; red line) at 51°S (Laskar et al., 2004); the planetary radiative imbalance at the top of the atmosphere (PRI, solid black line). This is the principal driver of global climate change, defined as the difference between the total insolation absorbed at the top of the atmosphere and the amount of energy radiated back into space (Baggenstos et al., 2019). **(B)** Hypothetical representation of the mean annual latitudinal position of the

(*Continued*)

FIGURE 10 | core SWW intensity belt and an approximate 1σ latitudinal range of enhanced precipitation associated with it (Ariztegui et al., 2010; Quade and Kaplan, 2017). Figure adapted from Quade and Kaplan (2017) to include a northward shift in the SWW, driving glacier readvance in the TdP region and between 50 and 55°S during the ACR. The grey dotted line is 51°S; dark grey horizontal arrows represent phases of increased SWW; light grey horizontal arrows represent the Early Holocene Westerlies Minimum (EHWM) ~11.5–7.5 ka (Moreno et al., 2021), which drove the reduction in atmospheric CO_2 between 10 and 8 ka shown in (M). Black arrows represent poleward (or less diffuse) or stable SWW, dark red arrows represent equatorward (or more diffuse) SWW. Selected regional records between ~49 and 53°S that follow are shown in order from east to west across Patagonia and from north to south. **(C)** Lake-level changes at Potrok Aike, a closed basin ~150 km southeast of Lago Pato (Zolitschka et al., 2013), and Lago Cardiel, ~280 km north of Lago Pato in central (Argentinean) Patagonia. Increased lake levels at the latter during the Late Glacial have been linked to stronger SWW and increased precipitation between 48 and 52°S. For Potrok Aike, increased precipitation and higher lake levels during the EHWM were associated with the incursion of the Easterlies (Ariztegui et al., 2010; Zolitschka et al., 2013). **(D)** Compilation of cosmogenic surface exposure dating constraints on glacier expansion for Southern Patagonia and Tierra del Fuego (adapted from Darvill et al. (2015), Kaplan et al. (2020). **(E)** Summary timing of the Early Holocene Warm Period (EHWP) and the Late Holocene Warm Period (LHWP) (Marcott et al., 2013; Kaufman et al., 2020). **(F)** Inferred Holocene SAM-index from positive (red) to negative (blue) SAM-like states overlain by the Northern Arboreal Pollen (NAP) percentage plot from Lago Cipreses, ~11 km WNW of Lago Pato (Moreno et al., 2018; Kaplan et al., 2020). **(G)** LP08 and LP16 Ln(Fe/Mn) ratios as Z-scores representing anoxia/stability ↔ oxidation/instability in Lago Pato. The solid blue (LP08) and solid/dashed black (LP16) lines are a 100-year interval Piecewise Cubic Hermite Interpolating Polynomial (PCHIP) smoothing of measured interval data (light blue, LP08, and grey, LP16, circles). Downward black triangles denote lake level reductions at 1) c. 13.4, 2) 11.7 ka in LP16. Downward blue triangles represent flushing events at c. 10 ka (3, erosional hiatus) and c. 8.6 ka (4, refilling/emptying event) in the LP08 depocentre record. **(H)** Percentage count data for *Nothofagus dombeyi type* and total land pollen (TLP) concentrations as proxies for changes in vegetational cover in the Lago Pato catchment over the last c. 10 cal ka BP and a summary of the inferred precipitation: evaporation (P:E) balance, based on the LP08 PC1 axis diatom data (**Figure 8**). **(I)** Relative percentage changes in *Misodendrum* (mistletoes commonly found on deciduous *Nothofagus* species) in sediment records from the western Andes (Lamy et al., 2010; Fletcher and Moreno (2012) interpretation). **(J)** Changes in diatom-inferred **(D–I)** conductivity from Macquarie Island (Saunders et al., 2018) as an indicator of increasing SWW at ~54°S. The black line is a 100-year LOESS smoothing of as-measured D-I data (grey line). **(K)** A compilation of the timing of glacier advance and retreat on the northern Antarctic Peninsula (Kaplan et al., 2020) and temperature anomaly data from the James Ross Island ice core record (Mulvaney et al., 2012). **(L)** Global Mean Ocean Temperature (MOT) 20–6.5 cal ka BP (Bereiter et al., 2018) and a stacked global mean sea level curve 20–0 ka (Spratt and Lisiecki, 2016). **(M)** Atmospheric CO_2 concentrations (100-year LOESS smoothing (red line) of raw data (grey line) and temperature anomaly data from the EPICA Dome C ice core record in Antarctica (dark red line) (Monnin et al., 2001; Jouzel et al., 2007), Holocene palaeotemperature compilation of median temperature anomalies (relative to 1800–1900 CE) for 60–90°S (dashed red line), and globally (black line) (Kaufman et al., 2020) and a summary of the main Holocene warm periods at 30–90°S (Marcott et al., 2013) (dark red bars). The grey dotted line is the median 12 kyr temperature value for 60–90°S (0.02); fifth (–2.21) and 95th (1.51) error percentiles are out of the plotting range. The background shading in this figure summarises the timing of the key features in the Lago Pato record as follows: green shading represents a late Holocene phase of enhanced ENSO (El Niño Southern Oscillation); light red shading represents more arid conditions; dark red shading with orange bars represents enhanced oxidation phases; light brown shading represents the "Anoxic Crisis"; light grey shading represents glaciogenic deposits; dark grey shading indicating the time period covered by the Antarctic Cold Reversal (ACR: 14.6–12.8 ka). Data in this figure were analysed and plotted in SigmaPlot and R, with the final layout achieved in Adobe Illustrator.

(2,740 ± 260 cal a BP) within DZ4 when a dramatic reduction in the planktonic *Discostella stelligera* species to <20% abundance occurred. This brief excursion to more unstable conditions coincided with a shift to lower S/Ti ratios, indicative of slightly shallower, less anoxic conditions, a shift to less depleted $\delta^{13}C$ values (~ −30%), and a short-lived erosional phase in the LP16 record at c. 2,700 cal a BP. The return of *Discostella stelligera* s.l. to 60%–80% abundance suggests that a more stable deeper lake persisted until c. 2000 cal a BP when an abrupt increase in benthic species (e.g., *Staurosirella* aff. *pinnata*) reoccurred. Low chrysophyte cyst concentrations between 78 and 30 cm within DZ5 (DZ5: 83–30 cm; 1,960 ± 260–1,020 ± 310 cal a BP) also indicate more turbulent conditions. These conditions persisted during the last c. 1,000 cal a BP (DZ6: 0–30 cm; 1,020 ± 310 to −60 ± 10), but with *Staurosira* aff. *venter* (>75%) dominating. In contrast, the most recent surface sample (0.25 cm) is dominated by planktonic *Cyclotella meneghiniana* (75%) species.

Above 470 cm (10,160 ± 2,120 cal a BP), we identified 13 pollen taxa with a relative abundance of more than 2% and three significant local pollen assemblage zones (PZ 1–3 in **Figure 8**, **Supplementary Figure S8**). Pollen zones 1 and 2 (470–359 and 359–315 cm; 10,160 ± 2,120–6,890 ± 300 and 6,890 ± 300–5,400 ± 180 cal a BP), which map broadly onto Units 5B and 5C, are characterised by low total pollen (and diatom) concentrations and relatively high values of Poaceae that reach a maximum (>60%) at 436 cm depth (8,730 ± 270 cal a BP) and decline towards the top of the zone. Poaceae are commonly used as an aridity indicator species in Patagonia (Moreno et al., 2018; Moreno et al., 2021) and are more elevated in Unit 5B of LP08 where Fe/Mn and Mn/Ti are more variable, and elevated Ca/Ti and Sr/Ti (carbonate) ratios and S peaks exist. Together, these proxies indicate that a very restricted lake system existed in the early Holocene between c. 10,000 and 7,500 cal a BP (**Figures 5A**, **8**). Most notably, *Nothofagus dombeyi* type pollen starts to increase from ~420 cm (c. 8,270 ± 240 cal a BP) onwards, and there are low percentages of dwarf shrubs and herbs such as *Empetrum rubrum*, Asteraceae, *Acaena,* and *Litorella* (**Figure 8**, **Supplementary Figure S8**). *Nothofagus dombeyi* type, inversely related to Poaceae, increases towards the top of this zone, while the abundance of Cyperaceae (as well as Polypodiaceae and *Pediastrum*, not shown in the summary of **Figure 8**, **Supplementary Figure S8**) remains high throughout.

In local pollen assemblage zone 3 (PZ 3 in **Figure 8**, **Supplementary Figure S8**; 315–0 cm; 5,400 ± 180 to −60 ± 10 cal a BP), *Nothofagus dombeyi* type continues to dominate (60%–80%), with the total pollen concentration higher than in PZ 1 and 2, indicating a generally more productive (wetter) environment. The hemiparasite *Misodendrum* requires *Nothofagus* as a host for germination and establishment; hence, *Misodendrum* and *Nothofagus dombeyi* are well-correlated (**Figure 8**). Poaceae abundances were lower (<30%) and oscillated at (sub)millennial timescales, while other dwarf shrubs and herbs almost disappeared from the record until the last 500 years. The decline in Cyperaceae at the start of pollen zone 1 continued until the present. The relative abundance of *Pediastrum* is lower than PZ 1 but oscillates, reaching peak values between ~200 and 100 cm (3,920–2,220 cal a BP). Small amounts of introduced European taxa (e.g., *Plantago* and *Rumex acetosella*, not shown in **Figure 8**) were present near the top of the core.

5 DISCUSSION

5.1 Lake Geochemistry and Ontogeny

In the following section, we interpret the main geochemical changes in the LP08 and LP16 records (**Table 2** for a summary).

Unit 1 (30–20 ka): the elevated sediment density, magnetic susceptibility, and minerogenic input (e.g., K, Ti, Fe, Rb, and Sr) and the near-complete absence of pollen in Unit 1 are consistent with a high input of fine glacial clay eroded from an enlarged, glaciated, and sparsely vegetated catchment (**Figure 9**). Fine glacial sediment in suspension would have created 'turbid' conditions even within a relatively deep lake, preventing the establishment of photoautotrophic diatom communities (Karst-Riddoch et al., 2009). Prolonged phases of perennial lake-ice cover and increased turbidity are consistent with the low primary production and production proxy values (e.g., $\%C_{org}$, C/N, inc./coh.), the absence of diatoms (Hodgson et al., 2009), and stratification within perennially ice-covered and deep glaciolacustrine lakes (Wennrich et al., 2014).

Fine grey glaciolacustrine sediments are enriched in Fe and Mn but have broadly stable Fe/Mn ratios throughout Unit 1, suggesting an erosional source of glaciogenic sediment into Lago del Toro that did not change substantially until the start of the Holocene. As Fe^{2+} is less stable in anoxic lake sediments and precipitates before Mn^{2+}, elevated Fe/Mn ratios have been used as a proxy for increased stability (and anoxia) in deep, well-ventilated lakes (Kylander et al., 2011). Decadal-scale elevation of Mn and Fe coincides with phases of reduced erosional input (shown by <Ti in **Figure 6B**) and is associated with manganese carbonate formation, rhodochrosite ($MnCO_3$), commonly found in areas of shale bedrock and anoxic conditions (Melles et al., 2012), but has also been used as an indicator of increased oxidation where wind-driven mixing of the water column exists in deep lakes (Moreno et al., 2007; Kylander et al., 2011). In shallow(er) lakes, >Mn can reflect complete overturning (as well as oxygenation) of stratification, reducing Mn solubility and causing manganese oxides and hydroxides to co-precipitate with iron oxy-hydroxides (Wennrich et al., 2014; Davies et al., 2015).

Comparatively minor increases in Fe/Mn and decreased Mn/Ti in Unit 1 (relative to Unit 5) most likely reflect short-lived bottom water anoxia interspersed with oxidation events linked to minor increases in Mn^{2+} precipitation and/or secondary mobility between Fe and Mn phases within laminations (**Figures 5**, **6**, **8A**). High MS and exceptionally elevated Mn/Ti peaks in LP16 Unit 1 (as well as 2) reflect increased mixing and oxidation of anoxic Mn^{2+} during lake overturning (**Figures 6B–D–D**, **8**). A minor component of biogenic magnetite formed under anoxic conditions (Kirschvink and Chang, 1984) could exist, but this is more likely in Unit 5, where strong anti-correlation between

these ratios also exists during an early to mid Holocene arid phase c. 11.8–7.5 ka, extending until c. 5.6 ka (**Figures 6A**, **8B**).

Periodic orangey-brown Ti- and Ca-rich bands within Unit 1 imply decadal-centennial-scale phases of increased erosion or erosion from a different local source, perhaps with a degree of secondary diagenetic mobility between Fe and Mn, between 29.8 and 20.5 ka (i.e., the period covered by Unit 1 in Lago Pato) (**Figures 6B–F–F**, **9A**, **Supplementary Figures S3B, S6**). Fe/Mn and Mn/Ti profiles within the basal deposits of Unit 1 and across the whole of Unit in LP08 have several significant (>two-sigma) periodicities (**Figure 6D**, **Supplementary Figures S6E,F**). Decadal-scale variability is apparent within Unit 1 of both records, notwithstanding its average age model 95% CI of >700 years. The mean prominent peak-peak interval for Ln(Fe/Mn) and Ln(Mn/Ti) in LP08 Unit 1 is 35 ± 19 and 37 ± 22 years (**Supplementary Figures S6C,D**) and 34 ± 16 and 37 ± 16 years for LP16 Unit 1 (**Supplementary Figures S6N,O**). Decadal-scale variations are also apparent in the wavelet analysis shown in **Figures 6D–F**. Because the data shown have been interpolated to evenly spaced 10-year intervals, a combination of multiple 8–16-year SAM cycles (Yuan and Yonekura, 2011) could plausibly be responsible for the low frequency 20–40-year periodicities observed in Unit 1 (**Figures 6D–F**, **Supplementary Figures S6E–K**). At the centennial scale, the 197-year periodicity in Fe/Mn and the 191-year periodicity in Mn/Ti for the LP08 Unit 1 basal deposits (**Figure 6D**) and the 197/233-year periodicity in Fe/Mn and the 248-year periodicity in Mn/Ti for the whole of LP08 Unit 1 (**Supplementary Figure S6E,F**) are broadly similar to the ~200–250-year solar cycle that is thought to modulate SWW airflow detected in high-resolution pollen records from Patagonia and the Falkland Islands (Turney et al., 2016; Moreno et al., 2018). Longer (centennial–millennial) periodicities in Unit 1 deposits of both LP08 and LP16 might reflect 'grand solar cycles' driven by changes in the Sun's magnetic field (Ineson et al., 2015). Although we failed to find convincing evidence for the ~2.4–2.5 kyr Hallstatt solar activity cycle (Viaggi, 2021), it seems likely that millennial-to-centennial-scale variations in solar activity (shown in **Figure 10A**), SWW, and SAM (**Figures 10B,F**), coupled with changes in internal glacier dynamics, drove fluctuations in glacier accumulation, meltwater input, and seasonal lake-ice cover between the l-LGM and g-LGM, which account for variations in deep water (in)stability, redox conditions, and lake stratification processes between 29.8 and 20.5 ka.

Several lines of evidence support Units 2–5A being missing from the LP08 record: 1) the lack of pollen from a cold-steppe scrubland environment and the existence of an already established open landscape with a *Nothofagus* forest (comprising ~30% of TLP) around Lago Pato; 2) the existence of a benthic diatom community in organic sediments of Unit 5B that were deposited unconformably on top of Unit 1 glacial sediments; 3) the presence of shallow-water sub-aquatic angiosperm *Myriophyllum* sp., an early coloniser in organic deposits <10 ka (Unit 5 in LP08); and 4) the absence of two substantial Volcan Reclus tephras dated to 9,320 ± 15 ^{14}C yr BP (10,570–10,300 cal a BP) in the basal glaciolacustrine unit in a record from nearby Lago Eberhard (Moreno et al., 2012) and other lake records in the Última Esperanza region (Sagredo et al., 2011) and the R1 tephra dated to 12,627 ± 48 ^{14}C a BP (15,190–14,610 cal a BP) (Sagredo et al., 2011). The latter is >20 cm thick in the Cerro Benitez area ~31 km S of Lago Pato (McCulloch et al., 2021), and the presence in lacustrine deposits indicates that ice had thinned to at least ~215 m a.s.l. by 17.5 ka (Sagredo et al., 2011).

Units 2–4 (13.4–11.8 ka): the presence of *Myriophyllum* sp. fragments embedded in the glaciogenic deposits of Unit 2, and a ~10 cm thick *Myriophyllum* sp. layer is evidence of a substantial increase in lake productivity following a dramatic drop in lake level c. 13.4–13.0 ka. Increasing Ca and Sr (but not S) towards the top of Unit 3 and into Unit 4 relates to precipitation of authigenic calcite, likely triggered by increased alkalinity linked to anaerobic degradation of organic matter (Torres et al., 2020) (**Supplementary Figure S3A**). The lack of Mn enrichment in Units 3 and 4 (characterised by low Mn/Ca, **Figure 5B**, **Supplementary Figure S3**) suggests Mn was not available for fixation during authigenic (early diagenetic) carbonate precipitation (**Figure 9B**).

Unit 5 (11.6–5.6 ka): exceptionally elevated and concomitant Ca/Ti and S/Ti and low Mn/Ca in Unit 5 represent localised authigenic carbonate and/or sulphate precipitation, possibly gypsum ($CaSO_4{\cdot}2H_2O$; asterisks in **Figure 5**) or anhydrite. The presence of large S peaks indicates relatively S-rich lake bottom waters (SO_4 or H_2S, depending on local redox conditions) despite freshwater conditions. Gypsum precipitation implies subaerial exposure (drying) or potentially subaqueous anaerobic oxidation of solid sulphides by Fe^{3+} or Mn^{4+} (Aller and Rude, 1988; Pirlet et al., 2010). This seems plausible because Unit 5 exhibits phases of authigenic enrichment in Mn (exceptionally high Mn/Ti; **Figures 5**, **8**).

Unit 5 of LP16 has two phases of exceptionally elevated Fe/Mn ratios: an initial 'Anoxic Crisis' following isolation from Lago del Toro at the start of the Holocene and a secondary phase between c. 9 and 7.5 ka. High Fe/Mn and high Fe/Ti in Unit 5 (**Figures 5**, **8**, **Supplementary Figure S6**), above the 'background' glaciogenic detrital signal, implies a preference for authigenic enrichment of Fe compared to Mn. Assuming redox conditions analogous to Brownie Lake (Wittkop et al., 2020), fixation of Fe^{2+} was most likely triggered by oxidation of anoxic (Fe-rich) lake waters across the chemocline (**Figure 9C**). Alternatively, the very high Fe content of Unit 5A might be attributed to a very shallow, possibly even terrestrial, environment at the littoral LP16 site as peat can become highly enriched in Fe^{3+} during more oxic (drier) conditions (Schittek et al., 2015). Fe enrichment also occurs in anaerobic (very shallow) organic lake and peat deposits when organic material breaks down under stable conditions (Damman, 1978). Mn is then reduced from tetravalent MnO_2 to its divalent Mn^{2+} state and removed from organic matter, elevating Mn values and ratios. The near absence of Mn and low Mn/Ti when Fe/Mn is elevated in Units 5B/C implies that the LP08 depocentre remained submerged throughout the Holocene.

More stable conditions associated with reduced SWW between c. 11.6 and 5.5 ka were interrupted by short-lived

phases of instability, most notably at c. 10.5–10.0 ka in LP16, which coincides with the timing of the erosional hiatus in the LP08 record at c. 10.1–10.0 ka. The concomitant reversal in the Fe/Mn profiles of LP08 and LP16 following the 'Early Holocene Anoxic Crisis' (c. 11.7–10.1 ka) in Unit 5A of LP16 (**Figures 7**, **10G**) suggests local redox processes and water depth, rather than regional (climatic) processes, were the main control on the distribution of these metals during the Holocene.

A simple 'oxide model' attributing Mn enrichment to the onset of more oxygenated bottom water conditions (Force and Cannon, 1988; Calvert and Pedersen, 1996) is not considered plausible because bottom waters were least ventilated at LP08, the lake depocentre, compared to LP16. A more credible explanation invokes Mn-carbonate (most likely rhodochrosite, $MnCO_3$) precipitation immediately beneath the chemocline at LP08, with trapping of Fe-oxides above the chemocline at LP16 (**Figure 9B**), consistent with redox systematics in analogous lakes (e.g., Brownie Lake; Wittkop et al., 2020). Fixation of Mn in carbonate is supported by increased Mn/Ca in Units 5B-C at LP08. A fluctuating and complex redox relationship between Fe and Mn in LP08 is evident in orange 'pelletised' deposits with exceptionally elevated MS, Mn, and Mn/Ti ratios in Unit 5B (**Figure 6A**). These are most likely due to co-precipitation of Mn under anoxic conditions (or possibly the formation of rhodochrosite or kutnahorite minerals, particularly where Fe enrichment occurs). The presence of benthic diatoms in Unit 5B implies bottom water conditions at LP08 during the early to mid Holocene were only intermittently (rather than persistently) anoxic (**Figures 7**–**9**), while the disappearance of benthic diatoms at the base of Unit 5C and through most of Unit 6, until c. 1.5 ka, suggests the development of more permanent anoxia in a deeper and more stable lake between c. 7.3 and 5.6 ka onwards.

Unit 6 (5.6 to–0.06 ka): increasing Ti content and Mn/Ca implies Unit 6 at LP16 was deposited under progressively shallow water (above the chemocline), culminating in a sharp decline in the Fe/Mn profile at LP16 profile c. 500–200 years ago, which mirrors the increasingly anoxic >Fe/Mn trend in the submerged LP08 site (**Figure 10G**) and implies a shift to terrestrial subaerial conditions at the littoral margins of Lago Pato. At LP08, the continued accumulation of macrophytic organic matter suggests lacustrine conditions were more favourable for colonisation. Progressively increasing Fe/Mn, a sharp decrease in Mn/Ca and Mn/Ti (**Figures 5A**, **8**), a lack of authigenic enrichment in redox-sensitive metals (e.g., V), and a return of benthic diatoms (**Figure 8**, **Supplementary Figure S7**) all suggest bottom waters became progressively more ventilated at the depocentre in the late Holocene, consistent with the well-oxygenated modern lake conditions (371 μM O_2 (11.9 mg/L)).

To summarise, we have identified five key phases in the history of Lago Pato. In the following sections, we relate these five phases to glacier retreat and readvance and lake-level change in the Torres del Paine and Última Esperanza region since ~39 ka and, more widely, to hemispheric-global driving mechanisms of paleoclimatic change, in particular, the changing strength and position of the SWW relative to 51°S.

5.2 Local to Regional Implications

5.2.1 Local-LGM—Global-LGM and Deglaciation (<39–>14 ka)

The LP08 and LP16 records provide evidence of glaciolacustrine deposition into Lago Pato until c. 11.7 ka (**Figure 10G**; **Table 2** for a summary). High volumes of minerogenic erosional inputs and low productivity fluxes throughout lithofacies Unit 1 and in Units 2–4 reflect the proximity of an ice tongue from an expanded Southern Patagonian Ice Field following the retreat from the l-LGM (c. 37–30 ka) and after the g-LGM (c. 26–19 ka) (Hughes and Gibbard, 2015). The large ice-dammed proglacial lake, palaeo-Lago Tehuelche, covered Lago del Toro and Lago Sarmiento <c. 38 ka and >c. 17.6–16.8 ka, between local- and global-LGM advances (c. 32–27 ka) and as glaciers withdrew after the g-LGM (García et al., 2012; García et al., 2014; Davies et al., 2020) (locations B_1, B_2 in **Figures 2A**, **9**). Unit 1 in LP08 and LP16 is a preserved fragment of this former palaeolake sedimentary record, with a 'floating chronology' reflecting deposition in a deep palaeo-proglacial lake that existed at Lago Pato between 30 and 20 ka, prior to g-LGM, and ACR readvances over Lago del Toro and Lago Pato between 14.6 and 12.9 ka. (**Figures 8**–**10**).

A glaciolacustrine environment existed at Lago Pato between c. 28 and 20 ka after glaciers had receded from their most advanced (MIS 3) positions along the Río Tres Pasos valley to the south-east, where a terminal moraine has been dated to c. 39–37 ka (location A_2 in **Figure 2A**). From c. 30 ka onwards, as the Antarctic Ice Sheet and sea-ice grew during the g-LGM, the core belt of SWW became weaker at 51°S as it shifted equatorward to ~40–45°S, north of Lago Pato and its current alignment with the Antarctic Circumpolar Current off the coast of Chile at ~50–52°S (Toggweiler and Russell, 2008; Van Daele et al., 2016; Quade and Kaplan, 2017) (**Figure 10B**). Reduced precipitation supply in the Última Esperanza region led to glacier retreat and large palaeolakes formed as the main SPI outlet glacier covering Lago del Toro thinned and withdrew eastwards and from its maximum extent along the Río Prat and Río Tres Paso valleys to the south and south-east (**Figure 9A**) (Sagredo et al., 2011; Solari et al., 2012; García et al., 2014). Palaeolakes in the Puerto Consuelo and Última Esperanza fjords merged, forming a much larger palaeo-Lago Tehuelche–Puerto Consuelo up to 280 m a.s.l. deep along the Río Prat valley (García et al., 2014; Davies et al., 2020) (location B_1, **Figures 2A**, **9A**). Ice-dammed deposits and terraces in the Río Prat, Río Tres Paso, and Puerto Consuelo valleys between 125 and 155 m a.s.l. have been dated to c. 18–17 ka (García et al., 2014), suggesting that an ice dam up to 150–200 m a.s.l. existed along the Puerto Consuelo-Última Esperanza fjord at the gLGM.

The absence of deglacial age sediments <20 ka, at both coring sites in Lago Pato, implies that it was overridden by readvancing LGM and ACR glaciers or sediments were removed when palaeo-Lago Tehuelche emptied across the Lago Pato spillway sometime between c. 20 and 13.4 ka, in line with García et al. (2014) (**Figures 2B**, **9B**,C). The latter interpretation is more probable as geomorphological evidence and glacial debris associated with

glacier advances over Lago Pato are absent. After glaciers had retreated in the early Holocene, the removal of Units 2–4 from LP08 and the exceptionally sharp erosional boundary between the glaciogenic sediments of Unit 1 and organic deposits of Unit 6 were created by meltwater emptying across the Lago Pato depocentre at c. 10 ka (**Figures 8**, **9**).

Successive palaeolake lowering after the g-LGM occurred sometime before c. 17 ka during Stage I of the Cordillera Paine glaciation scheme (García et al., 2014; García et al., 2018) and after glacial advance stages C and D in the Strait of Magellan that ended between c. 21.7–20.4 ka and c. 17 ka (McCulloch et al., 2005). The oldest minimum radiocarbon ages for ice retreat and the formation of ice-dammed lake deposits in the Lago Sofia-Puerto Consuelo valley area are c. 18–17 cal ka BP (Sagredo et al., 2011; McCulloch et al., 2021) (**Figure 2**).

Garcia et al. (2014) associated a small moraine-arc to a former ice-lobe that extended east and southwards into the Río Prat Valley (B_1 in **Figure 2A**) and the now-abandoned outwash sandur plains formed along to the south and east of Lago del Toro with ice-dammed palaeo-Lago Tehuelche. This finally emptied, sometime after c. 16.8 ka but before the start of the ACR at c. 14.6 ka when a northward latitudinal shift in the SWW drove glacier readvance across this part of Patagonia (**Figure 2A**) (Pesce and Moreno, 2014; Moreno et al., 2018; Moreno, 2020; Fletcher et al., 2021). The absence of sediments dated between c. 20 and 13.5 ka from both Lago Pato records is consistent with basal ages of c. 14.6 ka from the Lago Cipreses record (~11 km west WNW of Lago Pato at 51°17′16.43″S, 72°50′12.18″W; **Figure 10F**) that constrain the initiation of local ice-free and the end ice-marginal glaciolacustrine conditions at ~110 m a.s.l. along the southern shore of Lago del Toro (i.e., ~85 m above Lago del Toro at 25 m a.s.l.) (Moreno et al., 2018).

Organic sedimentation in the higher altitude closed basin Lago Cipreses record at 110 m a.s.l. suggests that ice covering Lago del Toro had receded by, more than 12 km, from the end of the lake (and, inward by more than 50%), by 14.6 ka (Moreno et al., 2018). A similar transition is recorded in lake records from the Puerto Consuelo area at ~15.4 ka (80 m a.s.l.) (Pantano Dumestre), implying that a stepwise regression of Lago Puerto Consuelo began before the start of the ACR at c. 14.6 ka (Moreno et al., 2012).

5.2.2 Late Glacial–Holocene (13.4–11.7 ka)

The lower-altitude Lago Pato records provide evidence of two further stepwise lowering events during the Late Glacial: 1) at c. 13.4–13.0 ka, towards the end of the ACR, when lake levels dropped from >100 m a.s.l. to between 40 and 50 m a.s.l. (**Figures 5B**, **8**, **9B**), which is consistent with the c. 12.8 ka cessation of glaciolacustrine deposition at Lago Eberhard ~70 m a.sl. (cf. Moreno et al., 2012); 2) at c. 11.7 ka, when water levels dropped below 40 m a.s.l., Lago Pato became isolated from Lago del Toro (**Figure 9C**).

The most dramatic reduction in lake level at c. 13.4–13.0 ka is represented in LP16 by the presence of the shallow-water *Myriophyllum* sp. layer Unit 3 within glaciogenic sediments and exceptionally elevated Ca (as well as S and Sr) due to increased deposition of shallow-water carbonates (Units 3 and 4) (**Figure 8**). This post ACR drainage event occurred after Meltwater Pulse 1A at c.14 ka during a phase of rapidly rising global sea level and oceanic warming (**Figure 10L**) and before unprecedented 700-year warming of the Southern Ocean at c. 12 ka (Bereiter et al., 2018). During the Late Glacial, an enlarged proglacial lake encompassed Lago Pato, Lago del Toro, Lago Porteño, and all the smaller basins and sandur along the Río Serrano (Garcia et al., 2014). This palaeolake was topographically dammed at ~50 m a.sl. in the Río Prat valley and at a similar elevation by the glacier that still occupied the Puerto Consuelo fjord (**Figure 9B**). A lower-altitude ice tongue in Río Serrano Valley (B_3 in **Figures 2A**, **9A**), at least 25 m a.s.l. along the western outflow of Lago del Toro, would have also been necessary to create an ice-dammed palaeolake in contact with the SPI (Marden and Clapperton, 1995; Garcia et al., 2014).

Lago Pato is bounded topographically at ~40–50 m a.s.l. to the south and east and by a broad, undated (probably ACR) moraine complex that runs parallel with the present-day southern shoreline of the Bahía del Bote section of Lago del Toro to the northeast and west (**Figure 2A**). As Lago Pato was topographically constrained to the north and east (>~45 m a.s.l.) and the wetlands and the retaining sill to the south are at a much lower elevation (32–33 m a.s.l.; **Table 1**), the c. 13.4–13.0 ka lake drainage event, near the end of the ACR, would have passed through the Lago Porteño-Río Prat valley, rather than directly over Lago Pato (**Figure 9B**). A lower altitude palaeolake implied by the presence of shallow subaquatic macrofossils in the Lago Pato LP16 record is supported by a lack of glaciolacustrine deposits above 100 m a.s.l. younger than 16.8 cal ka BP in the Última Esperanza–Puerto Consuelo fjords.

As the core SWW belt migrated equatorward past 51°S during the ACR, outlet glaciers were maintained in relatively advanced positions in TdP (Bertrand et al., 2017; Quade and Kaplan, 2017; Fletcher et al., 2021) (**Figures 10B,D**). The southward movement of the SWW back past 51°S after the ACR continued poleward until c. 12 ka (Quade and Kaplan, 2017; McCulloch et al., 2020) and likely drove down precipitation levels, leading to the removal of high-altitude ice dams that had maintained palaeolake Tehuelche-Puerto Consuelo >100 m a.s.l. (**Figures 10B,D**)

The second reduction in lake level to between ~30 and 40 m a.s.l. at c. 11.7 cal ka BP isolated Lago Pato from Lago del Toro, cutting off the glaciolacustrine sediment supply from erosion of the TdP massif. An enlarged Lago del Toro had remained topographically dammed up to ~50 m a.s.l. along the Río Prat valley until low-level ice dams <~40–50 m a.s.l. in the Puerto-Consuelo fjord area most likely failed. This phase of lake regression is consistent with the minimum age for organic sedimentation of 10.3 ka from the Pantano Antonio Varas lake record at ~25 m a.s.l. and a ~30 m terrace constraining ice-dammed lake regression on the southern peninsula of Puerto Consuelo Fjord (Sagredo et al., 2011) (**Figure 2A**).

5.2.3 Early-Mid Holocene (11.7–5.6 ka)

The isolation of Lago Pato from Lago del Toro at the start of Unit 5A, c. 11.7 cal ka BP, is marked by a shift to a shallower lake system dominated by organic-rich lake muds and littoral vegetation. The time period covered by the zonally coherent

Early Holocene Westerlies Minimum (EHWM: 11.5–7.5 ka; Moreno et al., 2021) is initially characterised by greater stability in the littoral environment of Lago Pato between c. 11.7 and 10.1 ka, with exceptionally elevated Fe/Mn during the 'Anoxic Crisis' phase (**Figure 10G**) and possible peat formation over the LP16 site. Two early Holocene erosional contacts, between Units 1 and 6 at c. 10 ka and at the boundary between Units 5B-2 and 5B-3 at c. 8.9–8.6 ka in LP08 (**Figures 5A**, **6A**), coincide with increased oxidation in LP16 sediments (downward arrows 3 and 4 in **Figure 10F**), suggesting a highly variable lake level, fluctuating at or near the height of the retaining sill during the early Holocene, with occasional flushing through the depocentre (**Figures 5**, **6**, **8**, **9B**, **10F**).

At the start of the Holocene, glaciers along the SPI retreated rapidly to close to their present-day, land-locked, limits, as evidenced by moraines preserved in Río Serrano area ~30 km west of Lago Pato with cosmogenic surface exposure isotope ages of 11.3–10.7 cal ka BP (location C in **Figure 2B**) (Marden and Clapperton, 1995; Solari et al., 2012; Aniya, 2013). Similar to nearby lake studies (e.g., Lago Cipreses; **Figure 10F**) (Moreno et al., 2018), we found no evidence of further glacier readvances over Lago Pato during the Holocene.

New data from Lago Pato are consistent with the timing of 1) forest expansion in and around Última Esperanza from c. 11.9 cal ka BP onwards (Moreno et al., 2012; Moreno and Videla, 2016; Moreno et al., 2018; McCulloch et al., 2021; Moreno et al., 2021); 2) regional fjord deglaciation (Bertrand et al., 2017); and 3) regional pollen and lacustrine records from 52 to 55°S (Zolitschka et al., 2018; McCulloch et al., 2020; Moreno et al., 2021). Increasingly arid conditions (linked to falling lake levels) have been found in several early Holocene terrestrial records from Southern Patagonia (Moreno et al., 2012; Zolitschka et al., 2013; Moreno et al., 2018; Zolitschka et al., 2018; Reynhout et al., 2019; McCulloch et al., 2020; Moreno et al., 2021) and in the wider sub-Antarctic region, for example, Macquarie Island at 54°S in the Southern Ocean (Saunders et al., 2018) (**Figures 10C,F,G,I,J**).

During the transition into the Holocene, the core SWW belt remained strong and possibly more poleward-shifted but weaker at its northern margins (Toggweiler et al., 2006; Toggweiler and Russell, 2008; Quade and Kaplan, 2017; Moreno et al., 2021). This drove down moisture leading to deglaciation in Patagonia (Quade and Kaplan, 2017; Moreno et al., 2018; Kaplan et al., 2020). A phase of exceptionally positive planetary radiative imbalance following the ACR between c. 12 and 9 ka (Baggenstos et al., 2019) (**Figure 10A**) and the shift to an increasing trend in summer insolation at 51°S from c. 10 ka (**Figure 10A**) likely resulted in the contraction of the polar vortex, leading to a poleward shift in the SWW and the prolonged period of positive SAM-like conditions between c. 11.5 and 10 ka (**Figure 10F**).

Continued lake regression at this time reflects the poleward limit of the SWW (~55°S) and/or a zonally coherent EHWM (11.5–7.5 ka) between 50 and 54°S (Saunders et al., 2018; Moreno et al., 2021) and is coupled with a prolonged phase of increasingly positive SAM-like conditions (**Figures 10B–G**) (Quade and Kaplan, 2017). Elevated conductivity in a lake record from Macquarie Island at the start of the Holocene, followed by a reduction in conductivity to a minimum between c. 11 and 10 ka, implies that a hemispheric poleward shift of the core SWW to the south of ~54°S could have occurred during the EHWM (Saunders et al., 2018). The removal of sediments at c. 10 ka from the Lago Pato depocentre (LP08) occurred as the SWW were starting to move equatorward once more from their most poleward position of the early Holocene (**Figure 10B**).

A return to glaciolacustrine sedimentation in Lago Pato at c. 8.9 ka implies an isolation breach, most likely due to a precipitation-driven refilling/flushing event during a regionally wetter phase (**Figure 6A**) (Moreno et al., 2018; Zolitschka et al., 2018), or a short-lived enlargement of Lago del Toro between c. 8.9 and 8.6 ka, possibly linked to glacier readvance, re-damming, and subsequent dam failure at the Río Serrano/Puerto Consuelo Fjord outlet (**Figure 2**, location B3). Both scenarios are consistent with the core SWW returning northward from ~55 to 60°S to ~51°S between c. 10 and 8 ka, bringing increased precipitation (**Figure 10B**) (Quade and Kaplan, 2017; Moreno et al., 2021). The increasing conductivity trend between c. 10 and 6 cal ka BP in a lake record from Macquarie Island (Saunders et al., 2018) suggests a potential hemispheric equatorward shift in the SWW back over ~54°S at this time.

All proxy evidence from Lago Pato points to more arid conditions with decadal-to-centennial-scale fluctuations in water column stability (redox) until c. 7.5 ka (**Figures 8**, **10G**). Lower lake levels in Lago Pato (below the overspill ridge limit of ~30–35 m a.s.l. into Lago del Toro) between 9.7 and 7 cal ka BP are broadly consistent with: 1) an extended period of 'extreme dryness' in the Laguna Potrok Aike, a closed basin ~175 km southeast of Lago Pato, which is not influenced by SPI glacial activity in an area where the local correlation between the present-day annual wind speed and precipitation is negative (Zolitschka et al., 2013) (**Figure 10C**); 2) pollen records from Isla Navarino, further south (54–55°S) (McCulloch et al., 2020); and 3) an the early Holocene dry period in Laguna Azul, south-eastern Patagonia (52°S), between c. 10.1 and 8.3 cal ka BP (Zolitschka et al., 2018). While higher lake levels at Potrok Aike during the EHWM time period have been associated with phases of an incursion of precipitation bearing Easterlies (Ariztegui et al., 2010), consistently drier conditions across all these records likely reflect the increasing trend in summer insolation over 50°S–55°S, the poleward migration of the core SWW belt south of 52°S, and/or phases of reduced Easterlies incursion into eastern Patagonia (Fletcher and Moreno, 2012; Saunders et al., 2018; Moreno et al., 2021) (**Figures 10A,B**). These interpretations have not yet been reconciled with generally wetter and windier conditions inferred from some records from the west coast of Patagonia (Lamy et al., 2010) and further north in Chile (Van Daele et al., 2016) during the early Holocene.

The Lago Pato pollen record is overwhelmingly dominated by forest taxa (mainly *Nothofagus* pollen) (**Figures 8**, **10G**, **Supplementary Figure S8**). Unlike nearby Lago Cipreses (Moreno et al., 2018) and similarly high-resolution pollen records further east (Mayr et al., 2007) and south (McCulloch et al., 2020), we found limited evidence of high frequency or rapid (climate-driven) variability in our pollen data during the

Holocene. The more highly resolved lacustrine redox proxies (e.g., Fe/Mn (anoxia) and Mn/Ti (oxidation)) display sub-millennial/centennial-scale variability. This is less well-defined than the centennial–millennial-scale periodicities in the Fe/Mn in the pre-Holocene LP08 record, but broadly similar to the variability found in pollen data produced by Moreno et al. (2018) from Lago Cipreses (~11 km WNW of Lago Pato), and some other SE Patagonian lakes (Zolitschka et al., 2018).

Several palaeorecords suggest that a highly variable precipitation regime existed in Patagonia well into the mid-Holocene (Mayr et al., 2007; Lamy et al., 2010; Moreno et al., 2018; Zolitschka et al., 2018). These include, for example, the occurrence of a grass steppe biome in a pollen record from Cerro Frías (Mancini, 2002; Mancini, 2009) and increased fire activity in the Río Rubens region (Huber et al., 2004). These two records were later re-evaluated, with periods of relatively high but extremely variable precipitation with extended periods of summer drought between c. 11 and 5.5 ka (Markgraf and Huber, 2010). Variable redox conditions in Lago Pato during the early–mid Holocene reflect changes in lake stability and are consistent with the variable precipitation and SAM regimes identified between c. 10.8 and 6.8 ka in the nearby Vega Ñandú (Villa-Martínez and Moreno, 2017) and Lago Cipreses lake records (Moreno et al., 2018) (**Figures 10C,F,G**). A period of increased early–mid Holocene variability is also consistent with an "erosive" interval found between c. 10.6 and 6.6 ka in the Lago Eberhard sediment core (Moreno et al., 2012), attributed to a lake low-stand, warmer/drier conditions, and a reduction in SWW influence over the TdP region and Patagonia more generally, between c. 10.4 and 7.5 ka either as the SWW migrated poleward again (after 8 ka) or when SWW zonal intensity declined (**Figure 10B**) (Quade and Kaplan, 2017; Moreno et al., 2021).

From c. 7.4 ka onwards, Lago Pato maintained an organic-rich depositional environment. Even in wetter periods, the maximum water level remained below the retaining sill at ~33 m a.s.l., forming an enlarged and more stable (increasingly more anoxic) palaeo-Lago Pato that most likely encompassed both the LP08 and LP16 core sites. This is evident in **Figure 8** and **Figure 10G** from increasing similarity between the PC1 and Fe/Mn profiles for both records from c. 7.4 ka onwards and supported by the greater prevalence of pollen and diatom species associated with wetter conditions and forest density from c. 7.7 ka (**Figures 8**, **9**, **10G**,H).

Wetter conditions after c. 7.4 ka are consistent with the expansion of humid-temperate closed forests dominated by mainly *Nothofagus* from c. 7.5 ka in lake records in the Última Esperanza Province and further south after c. 7 ka (McCulloch et al., 2020; Moreno et al., 2021). Progression to wetter and more stable conditions during the mid to late Holocene is also mirrored at localities of similar distances from the eastern flank of the Andes and in palaeo records across a W-E transect at ~51°S (**Figures 3**, **10**). A co-eval readvance of the Cordillera Darwin Ice Field occurred between c. 7.3 and 5.7 ka (Bertrand et al., 2017), with refilling of Laguna Potrok Aike accelerating after c. 7 ka (Zolitschka et al., 2013) (**Figure 10C**). The shift to a more closed forest, indicative of generally wetter conditions, also began at c. 7.7 ka in records from the eastern shore of Brazo Sur (Wille and Schäbitz, 2008; Markgraf and Huber, 2010), but it was delayed until c. 5.1 ka in the Vega Ñandú area (Villa-Martínez and Moreno, 2017). The establishment of a dense *Nothofagus* forest in the Vega Ñandú area also coincided with an abrupt decrease in fire frequency and a shift from minerotrophic to ombrotrophic bog taxa at Río Rubens after c. 5.5 ka (Huber et al., 2004). Increasingly wetter conditions in these records reflects generally wetter conditions in southern Patagonia and the more stable and equatorward expansion of the core SWW belt and more negative SAM-like conditions after c. 5.7 ka (**Figures 10B,F**) (Markgraf and Huber, 2010; Moreno et al., 2021). The transition from open to closed forests at Lago Pato coincided with rising temperatures between 60 and 90°S from 7.5 ka (Marcott et al., 2013) and the global 'Holocene thermal maximum' centred on 6.5–6.0 ka cal BP, which was 0.7°C warmer than the pre-industrial 19th Century (Kaufman et al., 2020) (**Figures 10H,M**).

5.2.4 Mid–Late Holocene (5.7–1.9 ka)

Greater hydrological stability with a more stable lake water column and increasing stratification in Lago Pato between c. 5.6 and 1.9 ka is shown by consistent C/N ratio values (**Figure 5A**), the increasing dominance of planktonic diatoms, which reflect progressively deeper water levels and a reduced littoral zone, and an increasingly anoxic trend (**Figures 5A**, **8**, **10G**, **Supplementary Figure S7**). For example, between c. 6.5 and 3.0 ka, heavily silicified planktonic diatom species (e.g., *Aulacoseira ambigua*, *Aulacoseira granulata* s.l., and *Cyclostephanos* cf. *patagonicus*) were relatively abundant, indicating more stable water levels (**Supplementary Figure S7**), yet turbulent mixing likely prevented these relatively heavy taxa from sinking out of the photic zone (Kilham and Kilham, 1975; Rioual et al., 2007). A concomitant gradual increase in *Discostella stelligera* s.l., a smaller euplanktonic diatom with an efficient nutrient uptake strategy, implies periodic stratification of the water column (**Supplementary Figure S7A**) (Rühland et al., 2003; Tolotti et al., 2007; Rühland et al., 2008; Winder et al., 2009). In TdP, Patagonian steppe pollen (mainly Poaceae), indicating drier conditions, was replaced by increasingly dominant *Nothofagus* pollen suggesting a more closed and dense forest.

The mid–late Holocene stabilisation of Lago Pato is consistent with cooler and wetter conditions at ~51°S that have been attributed to a relatively minor reduction and/or continued equatorward shift in the SWW north of ~51°S into the lower latitudes (**Figure 10B**) (Lamy et al., 2010; McCulloch et al., 2020; Moreno et al., 2021). The intensification of the SWW over southern Patagonia at this time is thought to have been modulated by an increasing trend in summer insolation and initiated at c. 7.5 ka (**Figure 10A**) by steepening the pole-to-equator temperature gradient (Lamy et al., 2010). This led to a cooling trend in the South Pacific Ocean (Lamy et al., 2010; Whitlock et al., 2017; Moreno et al., 2018), as well as increased sea-ice and reduced ocean productivity around Antarctica (Mayr et al., 2007; Peck et al., 2015).

Decadal (ENSO-like) to millennial–centennial-scale (SAM-like) variability in the SWW during the mid–late Holocene has been detected in several small and sensitive lake systems in Patagonia (Moreno et al., 2018; Reynhout et al., 2019). West of the Andes, wetter conditions are also thought to reflect the increased regional-seasonal variability in SWW intensity (Moreno et al., 2009a; Kilian and Lamy, 2012; Villa-Martínez and Moreno, 2017). Meanwhile, in the east, the equatorward shift in the SWW from c. 5.5 ka led to increasing lake levels as precipitation-laden frontal systems from the Atlantic became more dominant (Lamy et al., 2010; Zolitschka et al., 2013). The increased influence of the ENSO in the last four thousand years is thought to have contributed to minor readvances of glaciers across Southern Patagonia (Moreno et al., 2010; Fletcher and Moreno, 2012; Villa-Martínez and Moreno, 2017; Kaplan et al., 2020; McCulloch et al., 2020).

Between c. 5.6 and 1.9 ka, the proxy data from Lago Pato indicate that net annual precipitation-evaporation was broadly balanced (**Figure 8**, **Supplementary Figure S7**). Since 2010 CE, the wind strength in Patagonia has increased during summer, when the core SWW are more focussed and poleward shifted. As austral summer winds have strengthened over the last decade, the correlation between wind strength and precipitation over Lago Pato during the austral summer has become increasingly negative (r = 0, 1979–2010 CE; r = −0.2 to −0.4, 2007–2017 CE) (**Figures 4F,G**). In the austral winter, the SWW are more diffuse, with the core SWW belt driven slightly northwards as the jet stream moves into subtropical latitudes of about 30°S. This equatorward shift broadens and weakens, the core wind belt, particularly north of ~50°S (Garreaud et al., 2013; Bertrand et al., 2014; Fiers et al., 2019). As a result, winter precipitation is more intense further north of ~35°S (**Figure 4D**). At Lago Pato, the SWW have become marginally weaker and the correlation between wind and rainfall in the winter consistently positive (r = +0.4–0.6 in 2017) (**Figure 4H**). A similar scenario in autumn or winter during the mid–late Holocene would have resulted in higher amounts of precipitation and a well-mixed water column in Lago Pato. Less intense SWW and reduced precipitation during the austral summer would have led to smaller phytoplankton taxa blooms as more stable but nutrient-depleted conditions. For small lake systems such as Lago Pato in transitional locations between the Andes and eastern Patagonia, even a comparatively small net reduction in SWW and/or warmer temperatures in summer would result in a relatively more stable water column. Additionally, increased precipitation in winter (**Figure 4D**) would have maintained glaciers and a denser, more closed *Nothofagus* forest ecosystem. This kind of seasonal response has been inferred from pollen records elsewhere in Torres del Paine (Moreno et al., 2018) and from Isla Navarino at ~54–55°S (McCulloch et al., 2020).

5.2.5 Late Holocene–Recent (1.9–0 ka)

Shallower and more turbulent conditions in Lago Pato between c. 1.9 and 0.5 ka are marked by an increase in benthic diatoms in Diatom Zone 6, Mn/Ti ratios, indicating increased mixing and oxidation, and higher C/N values (**Figures 5A**, **8**, **Supplementary Figure S7**), reflecting a greater input of terrestrial material or a higher contribution of macrophytes to lake primary production (Duff and Smol, 1995). In sub-Arctic lakes, planktonic diatoms are rare or absent if the water level is less than 5 m deep (Karst-Riddoch et al., 2009). In Lago Pato, previously dominant planktonic taxa were replaced by c. 1.9 ka by assemblages composed of small chain-forming benthic/tychoplanktonic *Fragilariod* species. The latter are common during pioneering turbid and lower nutrient conditions (Bigler et al., 2003) and also occur in lakes with increased alkalinity (Wilson et al., 2012), longer winter lake ice-cover (Smol, 1983), and increased availability of aerophilic habitats (Van Dam et al., 1994).

While further studies are needed to understand the ecological preferences of *Fragilariod* species (Bennion et al., 2010), their abrupt development after c. 1.9 ka coincides with a decline in the total amount of stomatocysts mainly formed by euplanktonic chrysophytes (**Supplementary Figures S7A,B**). Increased wind-induced detachment from the littoral zone likely brought more benthic diatoms into suspension. Enlargement of the wetland area surrounding Lago Pato and its shallow benthic zone explains the continuous deposition of organic matter at the shallower/littoral LP16 core site throughout the Holocene. The presence of an extensive shallow wetland basin (LP16) with a deeper water zone (LP08) also explains the co-existence of planktonic and benthic diatom communities in the LP08 sediments. This culminated in the (re)deposition of a Sr-rich outwash sand layer (S) in LP08 at c. 1.4 ka and a dramatic increase in oxidation at the LP16 site in the last ~200 years, indicative of recent subaerial exposure of the littoral zone (**Figures 5A**, **8**, **10G**).

Declining biological productivity and total land pollen between c. 1.4 ka and the present day (**Figure 8**) were driven by predominantly negative SAM-like conditions at ~51°S between c. 2 and 0.5 ka in South America (**Figure 10F**) (Abram et al., 2014). The SAM was modulated by increasing SWW at ~51°S and an enhanced ENSO in this interval and, in particular, during the Medieval Climate Anomaly (MCA: c. 1–0.7 ka, 1,250–950 CE) (Mann et al., 2009; Abram et al., 2014). Changes linked to a warmer MCA in South America have been inferred from some (Moreno and Videla, 2016), but not all, records in the Última Esperanza region (Moreno et al., 2010; Villa-Martínez and Moreno, 2017; Moreno et al., 2018). The influence of the MCA is not well-represented in the Lago Pato data (**Figures 8**, **10G**).

In the last ~500 years, the *Nothofagus* forest cover remained relatively constant, while carbon and nitrogen content rose. The declining benthic diatom community suggests reduced levels of turbulence and catchment instability, consistent with 1) an equatorward shifted SWW during a 'post-MCA' phase of negative SAM-like conditions; 2) extreme cold 'events' in most Southern Hemisphere palaeorecords (Neukom et al., 2014); 3) minor glacier advances across the Patagonian Ice Field and the Northern Antarctic Peninsula (Reynhout et al., 2019; Kaplan et al., 2020; Simms et al., 2021); and 4) the Northern Hemisphere 'Little Ice Age' (0.55–0.25 ka, 1,400–1,700 CE) (Mann et al., 2009; Kaufman et al., 2020; Perren et al., 2020). European weed species,

such as *Plantago* and *Rumex acetosella*, became established in the Lago Pato catchment (**Figure 8**). These species are commonly found in other pollen records from Patagonia and relate to increased human activity, principally pastoral farming, which has converted much of the natural *Nothofagus* forest to a grass-steppe biome. Natural lake infilling processes combined with increased human activity in the TdP area could have led to increased macrophyte development and elevated lake sediment carbon and nitrogen levels observed in Lago Pato (>30% C and ~4% N, approximately double the mid-late Holocene mean N value). Recent increases in *Cyclotella meneghiniana* are also likely related to human-induced changes in the lake catchment (Van Dam et al., 1994), rather than (natural) lake ontogeny or warmer conditions.

6 CONCLUSION

We analysed two sediment core records from Lago Pato, a small lake basin located in a climatically transitional location east of the Andes and topographically separated from Lago del Toro in the Torres del Paine National Park, Southern Chile, to provide insights into changing glacier configurations, lake-level change, and climate-driven regional vegetation changes in the Última Esperanza region over the last ~30,000 years. Focussing on the last glacial-interglacial transition and Holocene parts of the well-preserved records, we undertook detailed geochemical, pollen, and diatom analysis to examine the relationship between changes in the lake level, water column stability, bottom water redox conditions, and precipitation-evaporation balance at the site.

We identified the following five evolutionary phases in the history of Lago Pato, which we link to deglaciation and palaeoenvironmental change in the Torres del Paine and Última Esperanza region and wider regional to global climate changes during the Late Glacial and Holocene:

1) <39 ka–13.4 ka: a deep proglacial lake encompassing Lago del Toro and Lago Pato, with evidence of decadal-centennial-scale redox variations, developed between the l-LGM ~38–30 cal ka BP and the g-LGM ~26–19 cal ka BP. This palaeolake was dammed by glacier ice >100 m thick along the Puerto Consuelo–Última Esperanza fjord to the south. Sediments dated between 20 and 13.4 ka were removed from the Lago Pato littoral record following a large lake drainage event near the end of the ACR.
2) <13.4–11.7 ka: lake levels over Lago Pato were lowered from >~100 m a.s.l. to ~40–50 m by two drainage events. The enlarged palaeolake became shallower as regional glaciers retreated and low altitude ice-dams in the Última-Esperanza fjord failed at c. 13.4 ka and c. 11.7 cal ka BP as the SWW shifted poleward south of 51°S after the ACR. Lago Pato was isolated from Lago del Toro at 11.7 ka by the second lake lowering event.
3) 11.7–5.6 ka: a stable, anoxic early Holocene shallow-littoral–terrestrial environment was replaced by an increasingly productive shallow-littoral and periodically oxidising lacustrine environment with a variable lake level. The presence of open *Nothofagus* forests and benthic diatom assemblages are consistent with regional aridity associated with more positive SAM-like conditions and poleward SWW south of ~51°S. Two refilling and flushing (erosional) events create a hiatus at c. 10 ka and a brief return to glaciolacustrine sedimentation at c. 8.6–8.4 ka in the LP08 depocentre record due to the enlargement of Lago del Toro as the SWW moved equatorward towards ~51°S between c. 10 and 8 ka. Lago Pato returned to an isolated and productive regime between 8.4 and 5.6 ka as the SWW shifted poleward, south of ~51°S again.
4) 5.6–1.9 ka: increasing stability and anoxia between c. 4.5 and 4 cal ka BP in Lago Pato is associated with an equatorward shift in the SWW back past ~51°S as negative SAM-like conditions prevailed during the mid–late Holocene.
5) 1.9–0 ka: a shallower subaqueous lacustrine phase in the depocentre with increased turbulence reflecting generally increased SWW in the second half of the late Holocene. In the last 500 years, reduced levels of turbulence and catchment instability reflect reduced or equatorward shifted SWW during the 'Little Ice Age' advance in TdP. Vegetational changes in recent centuries and decades most likely relate to increased pastoral farming and human activity in the Torres del Paine area.

DATA AVAILABILITY STATEMENT

The original contributions presented in the study are included in the article/**Supplementary Material**, further inquiries can be directed to the corresponding author. Data has been deposited in the NERC EDS UK Polar Data Centre (PDC) as follows: Bathymetric and lake chemistry data: https://doi.org/10.5285/D55D7619-3E07-41B0-929E-C9DA0A4B61AF; LP08 lake sediment record data: https://doi.org/10.5285/C75EA98B-080E-455E-A54F-A9E8CF07AA73; LP16 lake sediment record data: https://doi.org/10.5285/F85EE4EB-8918-4AA4-8E51-6C46F4C812CB; Time series data: https://doi.org/10.5285/6BD95602-F2E3-4968-8622-C4AEB71C214C. Code and data can be found at: https://github.com/stever60/Lago_Pato.

AUTHOR CONTRIBUTIONS

SR, RM, JE, SD, WN, and EV conceived the research questions, obtained funding, wrote the manuscript, constructed figures and tables, undertook XRF-CS, pollen, diatom analysis, analysed the data, and wrote code. MS and EvdeV identified diatoms and collected diatom samples. SR, MS, KH, JV, CD, EV, DH, and WV undertook fieldwork. SD, JE, and AW undertook laboratory and data analysis and helped construct figures. All authors edited and commented on the final manuscript.

FUNDING

This project was funded by the Natural Environment Research Council (NERC) through the British Antarctic Survey (BAS) and

an UGent BOF bilateral collaboration project. RMcC was supported by Programa Regional R17A10002 and R20F0002 (PATSER) ANID.

ACKNOWLEDGMENTS

We gratefully acknowledge the University of Magallanes (UMAG) and the University of Santiago (Carolina Diaz) for assistance with fieldwork; the NERC/SUERC AMS Radiocarbon Facility for providing initial range-finder radiocarbon dates; the NERC Isotope Geosciences Laboratory (NIGL, now National Environmental Isotope Facility, NEIF, at the British Geological Survey) and Melanie Lang for stable carbon isotope analysis; Aberystwyth University (David Kelly), Durham University (Neil Tunstall and Christopher Longley), and Edinburgh University (Chris Hayward) for the use of their core scanning and microprobe facilities and technical support. We also thank John Turner and Tony Phillips for assistance with ERA-INTERIM analysis; Chris Darvill, Neil Glasser, Mike Kaplan, and Patricio Moreno for access to their published datasets; and Mike Kaplan for permission to use and adapt the SAM-index diagram used in **Figure 10F**. We are grateful to the two reviewers for their constructive and insightful comments, which helped improve the manuscript.

SUPPLEMENTARY MATERIAL

The Supplementary Material for this article can be found online at: https://www.frontiersin.org/articles/10.3389/feart.2022.813396/full#supplementary-material

REFERENCES

Abram, N. J., Mulvaney, R., Vimeux, F., Phipps, S. J., Turner, J., and England, M. H. (2014). Evolution of the Southern Annular Mode during the Past Millennium. *Nat. Clim Change* 4, 564–569. doi:10.1038/nclimate2235

Aller, R. C., and Rude, P. D. (1988). Complete Oxidation of Solid Phase Sulfides by Manganese and Bacteria in Anoxic marine Sediments. *Geochimica et Cosmochimica Acta* 52, 751–765. doi:10.1016/0016-7037(88)90335-3

Altenberger, U., Oberhansli, R., Putlitz, B., and Wemmer, K. (2003). Tectonic controls and Cenozoic magmatism at the Torres del Paine, southern Andes (Chile, 51 degrees 10'S). *Revista Geologica De Chile* 30, 65–81. doi:10.4067/s0716-02082003000100005

Aniya, M. (2013). Holocene Glaciations of Hielo Patag¯oacute;nico (Patagonia Icefield), South America: A Brief Review. *Geochem. J.* 47, 97–105. doi:10.2343/geochemj.1.0171

Ariztegui, D., Gilli, A., Anselmetti, F. S., Goñi, R. A., Belardi, J. B., and Espinosa, S. (2010). Lake-level Changes in central Patagonia (Argentina): Crossing Environmental Thresholds for Lateglacial and Holocene Human Occupation. *J. Quat. Sci.* 25, 1092–1099. doi:10.1002/jqs.1352

Baggenstos, D., Häberli, M., Schmitt, J., Shackleton, S. A., Birner, B., Severinghaus, J. P., et al. (2019). Earth's Radiative Imbalance from the Last Glacial Maximum to the Present. *Proc. Natl. Acad. Sci. USA* 116, 14881–14886. doi:10.1073/pnas.1905447116

Barret, S. (2021). *Ggobi/Ggally*. v2.1.2. doi:10.5281/zenodo.5009047

Bennion, H., Sayer, C. D., and Tibby, J. (2010). "Diatoms as Indicators of Environmental Change in Shallow Lakes," in *The Diatoms: Applications for the Environmental and Earth Sciences*. Editors J. P. Smol and E. F. Stoermer. 2nd ed (Cambridge University Press), 152–173.

Bereiter, B., Shackleton, S., Baggenstos, D., Kawamura, K., and Severinghaus, J. (2018). Mean Global Ocean Temperatures during the Last Glacial Transition. *Nature* 553, 39–44. doi:10.1038/nature25152

Bertrand, S., Hughen, K., Sepúlveda, J., and Pantoja, S. (2014). Late Holocene Covariability of the Southern Westerlies and Sea Surface Temperature in Northern Chilean Patagonia. *Quat. Sci. Rev.* 105, 195–208. doi:10.1016/j.quascirev.2014.09.021

Bertrand, S., Lange, C. B., Pantoja, S., Hughen, K., Van Tornhout, E., and Wellner, J. S. (2017). Postglacial Fluctuations of Cordillera Darwin Glaciers (Southernmost Patagonia) Reconstructed from Almirantazgo Fjord Sediments. *Quat. Sci. Rev.* 177, 265–275. doi:10.1016/j.quascirev.2017.10.029

Bigler, C., Grahn, E., Larocque, I., Jeziorski, A., and Hall, R. (2003). Holocene Environmental Change at Lake Njulla (999 M Asl), Northern Sweden: a Comparison with Four Small Nearby Lakes along an Altitudinal Gradient. *J. Paleolimnology* 29, 13–29. doi:10.1023/a:1022850925937

Bishop, T. (2021). *itraxR: Itrax Data Analysis Tools*. Available at: https://CRAN.R-project.org/package=itraxR.

Blaauw, M., and Christen, J. A. (2011). Flexible Paleoclimate Age-Depth Models Using an Autoregressive Gamma Process. *Bayesian Anal.* 6, 457–474. doi:10.1214/ba/1339616472

Blunier, T., Schwander, J., Stauffer, B., Stocker, T., Dällenbach, A., Indermühle, A., et al. (1997). Timing of the Antarctic Cold Reversal and the Atmospheric CO2increase with Respect to the Younger Dryas Event. *Geophys. Res. Lett.* 24, 2683–2686. doi:10.1029/97gl02658

Bronk Ramsey, C. (2016). Development of the Radiocarbon Calibration Program. *Radiocarbon* 43, 355–363. doi:10.1017/s0033822200038212

Calvert, S. E., and Pedersen, T. F. (1996). Sedimentary Geochemistry of Manganese; Implications for the Environment of Formation of Manganiferous Black Shales. *Econ. Geology.* 91, 36–47. doi:10.2113/gsecongeo.91.1.36

Caniupán, M., Lamy, F., Lange, C. B., Kaiser, J., Kilian, R., Arz, H. W., et al. (2017). Holocene Sea-Surface Temperature Variability in the Chilean Fjord Region. *Quat. Res.* 82, 342–353.

Dam, H., Mertens, A., and Sinkeldam, J. (1994). A Coded Checklist and Ecological Indicator Values of Freshwater Diatoms from The Netherlands. *Neth. J. Aquat. Ecol.* 28, 117–133. doi:10.1007/bf02334251

Damman, A. W. H. (1978). Distribution and Movement of Elements in Ombrotrophic Peat Bogs. *Oikos* 30, 480–495. doi:10.2307/3543344

Darvill, C. M., Bentley, M. J., Stokes, C. R., Hein, A. S., and Rodés, Á. (2015). Extensive MIS 3 Glaciation in Southernmost Patagonia Revealed by Cosmogenic Nuclide Dating of Outwash Sediments. *Earth Planet. Sci. Lett.* 429, 157–169. doi:10.1016/j.epsl.2015.07.030

Davies, B. J., Darvill, C. M., Lovell, H., Bendle, J. M., Dowdeswell, J. A., Fabel, D., et al. (2020). The Evolution of the Patagonian Ice Sheet from 35 Ka to the Present Day (PATICE). *Earth-Science Rev.* 204, 103152. doi:10.1016/j.earscirev.2020.103152

Davies, S. J., Lamb, H. F., and Roberts, S. J. (2015). "Micro-XRF Core Scanning in Palaeolimnology: Recent Developments," in *Micro-XRF Studies of Sediment Cores*. Editors I. W. Croudace and R. G. Rothwell (Dordrecht: Springer Netherlands), 189–226. doi:10.1007/978-94-017-9849-5_7

Dee, D. P., Uppala, S. M., Simmons, A. J., Berrisford, P., Poli, P., Kobayashi, S., et al. (2011). The ERA-Interim Reanalysis: Configuration and Performance of the Data Assimilation System. *Q.J.R. Meteorol. Soc.* 137, 553–597. doi:10.1002/qj.828

Dickens, W. A., Kuhn, G., Leng, M. J., Graham, A. G. C., Dowdeswell, J. A., Meredith, M. P., et al. (2019). Enhanced Glacial Discharge from the Eastern Antarctic Peninsula since the 1700s Associated with a Positive Southern Annular Mode. *Sci. Rep.* 9, 14606. doi:10.1038/s41598-019-50897-4

Duff, K. E., and Smol, J. P. (1995). The Relationship of Chrysophycean Stomatocysts to Environmental Variables in Freshwater Lakes in British Columbia. *Can. J. Bot.* 73, 1097–1111. doi:10.1139/b95-119

Dunlea, A. G., Murray, R. W., Tada, R., Alvarez-Zarikian, C. A., Anderson, C. H., Gilli, A., et al. (2020). Intercomparison of XRF Core Scanning Results from Seven Labs and Approaches to Practical Calibration. *Geochem. Geophys. Geosystems* 21, e2020GC009248. doi:10.1029/2020gc009248

Echeverria, M. E., Sottile, G. D., Mancini, M. V., and Fontana, S. L. (2014). Nothofagus forest Dynamics and Palaeoenvironmental Variations during the Mid and Late Holocene, in Southwest Patagonia. *The Holocene* 24, 957–969. doi:10.1177/0959683614534742

Emile-Geay, J., Cane, M., Seager, R., Kaplan, A., and Almasi, P. (2007). El Niño as a Mediator of the Solar Influence on Climate. *Paleoceanography* 22, PA3210. doi:10.1029/2006pa001304

Evans, G., Augustinus, P., Gadd, P., Zawadzki, A., Ditchfield, A., and Hopkins, J. (2022). Millennial-scale Periodicities Associated with Changes in Wind Ansd Precipitation over the Last Glacial Cycle (Ca. 117 ± 8.5 Ka BP) Recorded in Sediments from Lake Kai Iwi, Northland, New Zealand. *Glob. Planet. Change* 208, 103688. doi:10.1016/j.gloplacha.2021.103688

Fiers, G., Bertrand, S., Van Daele, M., Granon, E., Reid, B., Vandoorne, W., et al. (2019). Hydroclimate Variability of Northern Chilean Patagonia during the Last 20 Kyr Inferred from the Bulk Organic Geochemistry of Lago Castor Sediments (45°S). *Quat. Sci. Rev.* 204, 105–118. doi:10.1016/j.quascirev.2018.11.015

Fletcher, M.-S., and Moreno, P. I. (2012). Have the Southern Westerlies Changed in a Zonally Symmetric Manner over the Last 14,000 Years? A Hemisphere-wide Take on a Controversial Problem. *Quat. Int.* 253, 32–46. doi:10.1016/j.quaint.2011.04.042

Fletcher, M.-S., Pedro, J., Hall, T., Mariani, M., Alexander, J. A., Beck, K., et al. (2021). Northward Shift of the Southern Westerlies during the Antarctic Cold Reversal. *Quat. Sci. Rev.* 271, 107189. doi:10.1016/j.quascirev.2021.107189

Fogwill, C. J., and Kubik, P. W. (2016). A glacial stage spanning the antarctic cold reversal in torres del paine (51°s), chile, based on preliminary cosmogenic exposure ages. *Geografiska Annaler: Ser. A, Phys. Geogr.* 87, 403–408. doi:10.1111/j.0435-3676.2005.00266.x

Force, E. R., and Cannon, W. F. (1988). Depositional Model for Shallow-marine Manganese Deposits Around Black Shale Basins. *Econ. Geology.* 83, 93–117. doi:10.2113/gsecongeo.83.1.93

Galili, T. (2021). *Dendextend: Extending 'dendrogram' Functionality in R*. Available at: https://cran.r-project.org/package=dendextend.

García, J.-L., Hall, B. L., Kaplan, M. R., Vega, R. M., and Strelin, J. A. (2014). Glacial geomorphology of the Torres del Paine region (southern Patagonia): Implications for glaciation, deglaciation and paleolake history. *Geomorphology* 204, 599–616.

García, J.-L., Hein, A. S., Binnie, S. A., Gómez, G. A., González, M. A., and Dunai, T. J. (2018). The MIS 3 maximum of the Torres del Paine and Última Esperanza ice lobes in Patagonia and the pacing of southern mountain glaciation. *Quat. Sci. Rev.* 185, 9–26.

García, J. L., Kaplan, M. R., Hall, B. L., Schaefer, J. M., Vega, R. M., Schwartz, R., et al. (2012). Glacier Expansion in Southern Patagonia throughout the Antarctic Cold Reversal. *Geology* 40, 859–862.

Garreaud, R. D., Vuille, M., Compagnucci, R., and Marengo, J. (2009). Present-day South American Climate. *Palaeogeogr. Palaeoclimatol. Palaeoecol.* 281, 180–195. doi:10.1016/j.palaeo.2007.10.032

Garreaud, R., Lopez, P., Minvielle, M., and Rojas, M. (2013). Large-Scale Control on the Patagonian Climate. *J. Clim.* 26, 215–230. doi:10.1175/jcli-d-12-00001.1

Glasser, N. F., Jansson, K. N., Goodfellow, B. W., De Angelis, H., Rodnight, H., and Rood, D. H. (2017). Cosmogenic Nuclide Exposure Ages for Moraines in the Lago San Martin Valley, Argentina. *Quat. Res.* 75, 636–646. doi:10.1016/j.yqres.2010.11.005

Glasser, N. F., Jansson, K. N., Harrison, S., and Kleman, J. (2008). The Glacial Geomorphology and Pleistocene History of South America between 38°S and 56°S. *Quat. Sci. Rev.* 27, 365–390. doi:10.1016/j.quascirev.2007.11.011

Grinsted, A., Moore, J. C., and Jevrejeva, S. (2004). Application of the Cross Wavelet Transform and Wavelet Coherence to Geophysical Time Series. *Nonlin. Process. Geophys.* 11, 561–566. doi:10.5194/npg-11-561-2004

Guerrero, J. M., and Echenique, R. O. (2002). Cyclostephanos Patagonicussp. Nov., a New Freshwater Diatom from Western Patagonia (Argentina). *Diatom Res.* 17, 141–151. doi:10.1080/0269249x.2002.9705535

Gunn, D. E., and Best, A. I. (1998). A New Automated Nondestructive System for High Resolution Multi-Sensor Core Logging of Open Sediment Cores. *Geo-Marine Lett.* 18, 70–77. doi:10.1007/s003670050054

Heiri, O., Lotter, A. F., and Lemcke, G. (2001). Loss on Ignition as a Method for Estimating Organic and Carbonate Content in Sediments: Reproducibility and Comparability of Results. *J. Paleolimnology* 25, 101–110. doi:10.1023/a:1008119611481

Henríquez, C. A., Moreno, P. I., Dunbar, R. B., and Mucciarone, D. A. (2021). The Last Glacial Termination in Northwestern Patagonia Viewed from the Lago Fonk (~40°S) Record. *Quat. Sci. Rev.* 271, 107197.

Hodgson, D. A., Roberts, S. J., Bentley, M. J., Carmichael, E. L., Smith, J. A., Verleyen, E., et al. (2009). Exploring Former Subglacial Hodgson Lake, Antarctica. Paper II: Palaeolimnology. *Quat. Sci. Rev.* 28, 2310–2325. doi:10.1016/j.quascirev.2009.04.014

Hodgson, D. A., and Sime, L. C. (2010). Southern Westerlies and CO2. *Nat. Geosci* 3, 666–667. doi:10.1038/ngeo970

Hogg, A. G., Heaton, T. J., Hua, Q., Palmer, J. G., Turney, C. S., Southon, J., et al. (2020). SHCal20 Southern Hemisphere Calibration, 0-55,000 Years Cal BP. *Radiocarbon* 62, 759–778. doi:10.1017/rdc.2020.59

Hogg, A. G., Hua, Q., Blackwell, P. G., Niu, M., Buck, C. E., Guilderson, T. P., et al. (2016). SHCal13 Southern Hemisphere Calibration, 0-50,000 Years Cal BP. *Radiocarbon* 55, 1889–1903. doi:10.2458/azu_js_rc.55.16783

Huber, U. M., Markgraf, V., and Schäbitz, F. (2004). Geographical and Temporal Trends in Late Quaternary Fire Histories of Fuego-Patagonia, South America. *Quat. Sci. Rev.* 23, 1079–1097. doi:10.1016/j.quascirev.2003.11.002

Hughes, P. D., and Gibbard, P. L. (2015). A Stratigraphical Basis for the Last Glacial Maximum (LGM). *Quat. Int.* 383, 174–185. doi:10.1016/j.quaint.2014.06.006

Ineson, S., Maycock, A. C., Gray, L. J., Scaife, A. A., Dunstone, N. J., Harder, J. W., et al. (2015). Regional Climate Impacts of a Possible Future Grand Solar Minimum. *Nat. Commun.* 6, 7535. doi:10.1038/ncomms8535

Jouzel, J., Masson-Delmotte, V., Cattani, O., Dreyfus, G., Falourd, S., Hoffmann, G., et al. (2007). Orbital and Millennial Antarctic Climate Variability over the Past 800,000 Years. *Science* 317, 793–796. doi:10.1126/science.1141038

Juggins, S. (2007). *C2 Version 1.5 User Guide. Software for Ecological and Palaeoecological Data Analysis and Visualisation*. Newcastle: Newcastle University.

Juggins, S. (2012). *Rioja: Analysis of Quaternary Science Data, R Package Version*. 0.8-5.

Kaplan, M. R., Coronato, A., Hulton, N. R. J., Rabassa, J. O., Kubik, P. W., and Freeman, S. P. H. T. (2007). Cosmogenic Nuclide Measurements in Southernmost South America and Implications for Landscape Change. *Geomorphology* 87, 284–301. doi:10.1016/j.geomorph.2006.10.005

Kaplan, M. R., Fogwill, C. J., Sugden, D. E., Hulton, N. R. J., Kubik, P. W., and Freeman, S. P. H. T. (2008). Southern Patagonian Glacial Chronology for the Last Glacial Period and Implications for Southern Ocean Climate. *Quat. Sci. Rev.* 27, 284–294. doi:10.1016/j.quascirev.2007.09.013

Kaplan, M. R., Strelin, J. A., Schaefer, J. M., Peltier, C., Martini, M. A., Flores, E., et al. (2020). Holocene Glacier Behavior Around the Northern Antarctic Peninsula and Possible Causes. *Earth Planet. Sci. Lett.* 534, 116077. doi:10.1016/j.epsl.2020.116077

Karst-Riddoch, T. L., Malmquist, H. J., and Smol, J. P. (2009). Relationships between Freshwater Sedimentary Diatoms and Environmental Variables in Subarctic Icelandic Lakes. *fal* 175, 1–28. doi:10.1127/1863-9135/2009/0175-0001

Kaufman, D., Mckay, N., Routson, C., Erb, M., Davis, B., Heiri, O., et al. (2020). A Global Database of Holocene Paleotemperature Records. *Sci. Data* 7, 115. doi:10.1038/s41597-020-0445-3

Kilham, S. S., and Kilham, P. (1975). Melosira Granulata (Ehr.) RALFS: Morphology and Ecology of a Cosmopolitan Freshwater Diatom. *SIL Proc. 1922-2010* 19, 2716–2721. doi:10.1080/03680770.1974.11896368

Kilian, R., and Lamy, F. (2012). A Review of Glacial and Holocene Paleoclimate Records from Southernmost Patagonia (49-55°S). *Quat. Sci. Rev.* 53, 1–23. doi:10.1016/j.quascirev.2012.07.017

Kirschvink, J. L., and Chang, S.-B. R. (1984). Ultrafine-grained Magnetite in Deep-Sea Sediments: Possible Bacterial Magnetofossils. *Geol* 12, 559–562. doi:10.1130/0091-7613(1984)12<559:umidsp>2.0.co;2

Kylander, M. E., Ampel, L., Wohlfarth, B., and Veres, D. (2011). High-resolution X-ray Fluorescence Core Scanning Analysis of Les Echets (France) Sedimentary Sequence: New Insights from Chemical Proxies. *J. Quat. Sci.* 26, 109–117. doi:10.1002/jqs.1438

Lamy, F., Kilian, R., Arz, H. W., Francois, J.-P., Kaiser, J., Prange, M., et al. (2010). Holocene Changes in the Position and Intensity of the Southern westerly Wind belt. *Nat. Geosci* 3, 695–699. doi:10.1038/ngeo959

Landschützer, P., Gruber, N., and Bakker, D. C. E. (2016). Decadal Variations and Trends of the Global Ocean Carbon Sink. *Glob. Biogeochem. Cycles* 30, 1396–1417.

Laskar, J., Robutel, P., Joutel, F., Gastineau, M., Correia, A. C. M., and Levrard, B. (2004). A Long-Term Numerical Solution for the Insolation Quantities of the Earth. *A&A* 428, 261–285. doi:10.1051/0004-6361:20041335

Le Quéré, C., Rödenbeck, C., Buitenhuis, E. T., Conway, T. J., Langenfelds, R., Gomez, A., et al. (2007). Saturation of the Southern Ocean CO2 Sink Due to Recent Climate Change. *Science* 316, 1735–1738. doi:10.1126/science.1136188

Löwemark, L., Chen, H. F., Yang, T. N., Kylander, M., Yu, E. F., Hsu, Y. W., et al. (2011). Normalizing XRF-Scanner Data: A Cautionary Note on the Interpretation of High-Resolution Records from Organic-Rich Lakes. *J. Asian Earth Sci.* 40, 1250–1256.

Mancini, M. V. (2009). Holocene Vegetation and Climate Changes from a Peat Pollen Record of the forest - Steppe Ecotone, Southwest of Patagonia (Argentina). *Quat. Sci. Rev.* 28, 1490–1497. doi:10.1016/j.quascirev.2009.01.017

Mancini, M. V. (2002). Vegetation and Climate during the Holocene in Southwest Patagonia, Argentina. *Rev. Palaeobotany Palynology* 122, 101–115. doi:10.1016/s0034-6667(02)00105-7

Mann, M. E., Zhang, Z., Rutherford, S., Bradley, R. S., Hughes, M. K., Shindell, D., et al. (2009). Global Signatures and Dynamical Origins of the Little Ice Age and Medieval Climate Anomaly. *Science* 326, 1256–1260. doi:10.1126/science.1177303

Marcott, S. A., Shakun, J. D., Clark, P. U., and Mix, A. C. (2013). A Reconstruction of Regional and Global Temperature for the Past 11,300 Years. *Science* 339, 1198–1201. doi:10.1126/science.1228026

Marden, C. J., and Clapperton, C. M. (1995). Fluctuations of the South Patagonian Ice-Field during the Last Glaciation and the Holocene. *J. Quat. Sci.* 10, 197–209. doi:10.1002/jqs.3390100302

Markgraf, V., and Huber, U. M. (2010). Late and postglacial vegetation and fire history in Southern Patagonia and Tierra del Fuego. *Palaeogeogr. Palaeoclimatol. Palaeoecol.* 297, 351–366. doi:10.1016/j.palaeo.2010.08.013

Marshall, G. J. (2007). Half-century Seasonal Relationships between the Southern Annular Mode and Antarctic Temperatures. *Int. J. Climatol.* 27, 373–383. doi:10.1002/joc.1407

Marshall, G. J. (2003). Trends in the Southern Annular Mode from Observations and Reanalyses. *J. Clim.* 16, 4134–4143. doi:10.1175/1520-0442(2003)016<4134:titsam>2.0.co;2

Marshall, J., and Speer, K. (2012). Closure of the Meridional Overturning Circulation through Southern Ocean Upwelling. *Nat. Geosci* 5, 171–180. doi:10.1038/ngeo1391

Mayr, C., Lücke, A., Wagner, S., Wissel, H., Ohlendorf, C., Haberzettl, T., et al. (2013). Intensified Southern Hemisphere Westerlies Regulated Atmospheric CO2 during the Last Deglaciation. *Geology* 41, 831–834. doi:10.1130/g34335.1

Mayr, C., Wille, M., Haberzettl, T., Fey, M., Janssen, S., Lucke, A., et al. (2007). Holocene Variability of the Southern Hemisphere Westerlies in Argentinean Patagonia (52°S). *Quat. Sci. Rev.* 26, 579–584. doi:10.1016/j.quascirev.2006.11.013

Mcculloch, R. D., Bentley, M. J., Tipping, R. M., and Clapperton, C. M. (2005). Evidence for Late-Glacial Ice Dammed Lakes in the central Strait of Magellan and Bahía Inútil, Southernmost South america. *Geografiska Annaler: Ser. A, Phys. Geogr.* 87, 335–362. doi:10.1111/j.0435-3676.2005.00262.x

Mcculloch, R. D., Blaikie, J., Jacob, B., Mansilla, C. A., Morello, F., De Pol-Holz, R., et al. (2020). Late Glacial and Holocene Climate Variability, Southernmost Patagonia. *Quat. Sci. Rev.* 229, 106131. doi:10.1016/j.quascirev.2019.106131

Mcculloch, R. D., and Davies, S. J. (2001). Late-glacial and Holocene Palaeoenvironmental Change in the central Strait of Magellan, Southern Patagonia. *Palaeogeogr. Palaeoclimatol. Palaeoecol.* 173, 143–173. doi:10.1016/s0031-0182(01)00316-9

Mcculloch, R. D., Mansilla, C. A., Martin, F., Borrero, L., Staff, R. A., and Tisdall, E. W. (2021). The Nature and Timing of Landscape Change at Cerro Benítez, Última Esperanza, Southern Patagonia (52°S): New Insights into the History of Megafaunal Extinctions and Human Occupation. *Quat. Int.* 601, 116–129. doi:10.1016/j.quaint.2021.07.018

Melles, M., Brigham-Grette, J., Minyuk, P. S., Nowaczyk, N. R., Wennrich, V., Deconto, R. M., et al. (2012). 2.8 Million Years of Arctic Climate Change from Lake El'gygytgyn, NE Russia. *Science* 337, 315–320. doi:10.1126/science.1222135

Monnin, E., Indermühle, A., Dällenbach, A., Flückiger, J., Stauffer, B., Stocker, T. F., et al. (2001). Atmospheric CO 2 Concentrations over the Last Glacial Termination. *Science* 291, 112–114. doi:10.1126/science.291.5501.112

Moore, P. D., Webb, J. A., and Collinson, M. E. (1991). *Pollen Analysis*. Blackwell Scientific Publications.

Moreno, A., Giralt, S., Valero-Garcés, B., Sáez, A., Bao, R., Prego, R., et al. (2007). A 14kyr Record of the Tropical Andes: The Lago Chungará Sequence (18°S, Northern Chilean Altiplano). *Quat. Int.* 161, 4–21. doi:10.1016/j.quaint.2006.10.020

Moreno, P. I., Francois, J. P., Moy, C. M., and Villa-Martínez, R. (2010). Covariability of the Southern Westerlies and Atmospheric CO2 during the Holocene. *Geology* 38, 727–730. doi:10.1130/g30962.1

Moreno, P. I., François, J. P., Villa-Martínez, R. P., and Moy, C. M. (2009a). Millennial-scale Variability in Southern Hemisphere westerly Wind Activity over the Last 5000 Years in SW Patagonia. *Quat. Sci. Rev.* 28, 25–38. doi:10.1016/j.quascirev.2008.10.009

Moreno, P. I., Henríquez, W. I., Pesce, O. H., Henríquez, C. A., Fletcher, M. S., Garreaud, R. D., et al. (2021). An Early Holocene westerly Minimum in the Southern Mid-latitudes. *Quat. Sci. Rev.* 251, 106730. doi:10.1016/j.quascirev.2020.106730

Moreno, P. I., Kaplan, M. R., François, J. P., Villa-Martínez, R., Moy, C. M., Stern, C. R., et al. (2009b). Renewed Glacial Activity during the Antarctic Cold Reversal and Persistence of Cold Conditions until 11.5 Ka in Southwestern Patagonia. *Geology* 37, 375–378. doi:10.1130/g25399a.1

Moreno, P. I. (2020). Timing and Structure of Vegetation, Fire, and Climate Changes on the Pacific Slope of Northwestern Patagonia since the Last Glacial Termination. *Quat. Sci. Rev.* 238, 106328. doi:10.1016/j.quascirev.2020.106328

Moreno, P. I., and Videla, J. (2016). Centennial and Millennial-Scale Hydroclimate Changes in Northwestern Patagonia since 16,000 Yr BP. *Quat. Sci. Rev.* 149, 326–337. doi:10.1016/j.quascirev.2016.08.008

Moreno, P. I., Vilanova, I., Villa-Martínez, R., Dunbar, R. B., Mucciarone, D. A., Kaplan, M. R., et al. (2018). Onset and Evolution of Southern Annular Mode-like Changes at Centennial Timescale. *Sci. Rep.* 8, 3458. doi:10.1038/s41598-018-21836-6

Moreno, P. I., Vilanova, I., Villa-Martínez, R., Garreaud, R. D., Rojas, M., and De Pol-Holz, R. (2014). Southern Annular Mode-like Changes in Southwestern Patagonia at Centennial Timescales over the Last Three Millennia. *Nat. Commun.* 5, 4375. doi:10.1038/ncomms5375

Moreno, P. I., Villa-Martínez, R., Cárdenas, M. L., and Sagredo, E. A. (2012). Deglacial Changes of the Southern Margin of the Southern westerly Winds Revealed by Terrestrial Records from SW Patagonia (52°S). *Quat. Sci. Rev.* 41, 1–21. doi:10.1016/j.quascirev.2012.02.002

Mulvaney, R., Abram, N. J., Hindmarsh, R. C. A., Arrowsmith, C., Fleet, L., Triest, J., et al. (2012). Recent Antarctic Peninsula Warming Relative to Holocene Climate and Ice-Shelf History. *Nature* 489, 141–144. doi:10.1038/nature11391

Neukom, R., Gergis, J., Karoly, D. J., Wanner, H., Curran, M., Elbert, J., et al. (2014). Inter-hemispheric Temperature Variability over the Past Millennium. *Nat. Clim. Change* 4, 362–367. doi:10.1038/nclimate2174

Oksanen, J. (2014). *Vegan: Community Ecology Package*. R package version 2.3-0Available at: http://cran.r-project.org/web/packages/vegan/index.html.

Paillard, D., Labeyrie, L., and Yiou, P. (1996). Macintosh Program Performs Time-Series Analysis. *Eos Trans. AGU* 77, 379. doi:10.1029/96eo00259

Palacios, D., Stokes, C. R., Phillips, F. M., Clague, J. J., Alcalá-Reygosa, J., Andrés, N., et al. (2020). The Deglaciation of the Americas during the Last Glacial Termination. *Earth-Science Rev.* 203, 103113. doi:10.1016/j.earscirev.2020.103113

Peck, V. L., Allen, C. S., Kender, S., Mcclymont, E. L., and Hodgson, D. A. (2015). Oceanographic Variability on the West Antarctic Peninsula during the Holocene and the Influence of Upper Circumpolar Deep Water. *Quat. Sci. Rev.* 119, 54–65. doi:10.1016/j.quascirev.2015.04.002

Perren, B. B., Hodgson, D. A., Roberts, S. J., Sime, L., Van Nieuwenhuyze, W., Verleyen, E., et al. (2020). Southward Migration of the Southern Hemisphere westerly Winds Corresponds with Warming Climate over Centennial Timescales. *Commun. Earth Environ.* 1, 58. doi:10.1038/s43247-020-00059-6

Pesce, O. H., and Moreno, P. I. (2014). Vegetation, fire and climate change in central-east Isla Grande de Chiloé (43°S) since the Last Glacial Maximum, northwestern Patagonia. *Quat. Sci. Rev.* 90, 143–157. doi:10.1016/j.quascirev.2014.02.021

Pirlet, H., Wehrmann, L. M., Brunner, B., Frank, N., Dewanckele, J., Van Rooij, D., et al. (2010). Diagenetic Formation of gypsum and Dolomite in a Cold-Water Coral mound in the Porcupine Seabight, off Ireland. *Sedimentology* 57, 786–805. doi:10.1111/j.1365-3091.2009.01119.x

Quade, J., and Kaplan, M. R. (2017). Lake-level Stratigraphy and Geochronology Revisited at Lago (Lake) Cardiel, Argentina, and Changes in the Southern Hemispheric Westerlies over the Last 25 Ka. *Quat. Sci. Rev.* 177, 173–188. doi:10.1016/j.quascirev.2017.10.006

Renberg, I. (1990). A Procedure for Preparing Large Sets of Diatom Slide from Sediment Cores. *J. Paleolimnology* 4, 87–90. doi:10.1007/bf00208301

Reynhout, S. A., Sagredo, E. A., Kaplan, M. R., Aravena, J. C., Martini, M. A., Moreno, P. I., et al. (2019). Holocene Glacier Fluctuations in Patagonia Are Modulated by Summer Insolation Intensity and Paced by Southern Annular Mode-like Variability. *Quat. Sci. Rev.* 220, 178–187. doi:10.1016/j.quascirev.2019.05.029

Rioual, P., Andrieu-Ponel, V., De Beaulieu, J.-L., Reille, M., Svobodova, H., and Battarbee, R. W. (2007). Diatom Responses to Limnological and Climatic Changes at Ribains Maar (French Massif Central) during the Eemian and Early Würm. *Quat. Sci. Rev.* 26, 1557–1609. doi:10.1016/j.quascirev.2007.03.009

Roberts, S. J., Monien, P., Foster, L. C., Loftfield, J., Hocking, E. P., Schnetger, B., et al. (2017). Past Penguin colony Responses to Explosive Volcanism on the Antarctic Peninsula. *Nat. Commun.* 8, 14914. doi:10.1038/ncomms14914

Rühland, K. M., Smol, J. P., and Pienitz, R. (2003). Ecology and Spatial Distributions of Surface-Sediment Diatoms from 77 Lakes in the Subarctic Canadian Treeline Region. *Can. J. Bot.* 81, 57–73.

Rühland, K., Paterson, A. M., and Smol, J. P. (2008). Hemispheric-scale Patterns of Climate-Related Shifts in Planktonic Diatoms from North American and European Lakes. *Glob. Change Biol.* 14, 2740–2754.

Rumrich, U., Lange-Bertalot, H., and Rumrich, M. (2000). *Diatoms of the Andes*. Königstein, Germany: Koeltz Scientific Books.

Sagredo, E. A., Moreno, P. I., Villa-Martínez, R., Kaplan, M. R., Kubik, P. W., and Stern, C. R. (2011). Fluctuations of the Última Esperanza Ice Lobe (52°S), Chilean Patagonia, during the Last Glacial Maximum and Termination 1. *Geomorphology* 125, 92–108. doi:10.1016/j.geomorph.2010.09.007

Saunders, K. M., Roberts, S. J., Perren, B., Butz, C., Sime, L., Davies, S., et al. (2018). Holocene Dynamics of the Southern Hemisphere westerly Winds and Possible Links to CO2 Outgassing. *Nat. Geosci* 11, 650–655. doi:10.1038/s41561-018-0186-5

Schittek, K., Forbriger, M., Mächtle, B., Schäbitz, F., Wennrich, V., Reindel, M., et al. (2015). Holocene Environmental Changes in the highlands of the Southern Peruvian Andes (14° S) and Their Impact on Pre-columbian Cultures. *Clim. Past* 11, 27–44. doi:10.5194/cp-11-27-2015

Schneider, C., Glaser, M., Kilian, R., Santana, A., Butorovic, N., and Casassa, G. (2013). Weather Observations across the Southern Andes at 53°S. *Phys. Geogr.* 24, 97–119. doi:10.2747/0272-3646.24.2.97

Shin, J., Ahn, J., Chowdhry Beeman, J., Lee, H. G., and Brook, E. J. (2021). Millennial Variations of Atmospheric CO2 during the Early Holocene (11.7–7.4 Ka). *Clim. Past Discuss.* 2021, 1–22.

Simms, A. R., Bentley, M. J., Simkins, L. M., Zurbuchen, J., Reynolds, L. C., Dewitt, R., et al. (2021). Evidence for a "Little Ice Age" Glacial advance within the Antarctic Peninsula - Examples from Glacially-Overrun Raised Beaches. *Quat. Sci. Rev.* 271, 107195. doi:10.1016/j.quascirev.2021.107195

Smol, J. P. (1983). Paleophycology of a High Arctic lake Near Cape Herschel, Ellesmere Island. *Can. J. Bot.* 61, 2195–2204. doi:10.1139/b83-238

Solari, M. A., Le Roux, J. P., Herve, F., Airo, A., and Calderon, M. (2012). Evolution of the Great Tehuelche Paleolake in the Torres del Paine National Park of Chilean Patagonia during the Last Glacial Maximum and Holocene. *Andean Geology.* 39, 1–21. doi:10.5027/andgeov39n1-a01

Spratt, R. M., and Lisiecki, L. E. (2016). A Late Pleistocene Sea Level Stack. *Clim. Past* 12, 1079–1092. doi:10.5194/cp-12-1079-2016

Steinhilber, F., Beer, J., and Fröhlich, C. (2009). Total Solar Irradiance during the Holocene. *Geophys. Res. Lett.* 36. doi:10.1029/2009gl040142

Sterken, M., Roberts, S. J., Hodgson, D. A., Vyverman, W., Balbo, A. L., Sabbe, K., et al. (2012). Holocene Glacial and Climate History of Prince Gustav Channel, Northeastern Antarctic Peninsula. *Quat. Sci. Rev.* 31, 93–111. doi:10.1016/j.quascirev.2011.10.017

Stevenson, R. J., Hill, B. H., Herlihy, A. T., Yuan, L. L., and Norton, S. B. (2008). Algae-P Relationships, Thresholds, and Frequency Distributions Guide Nutrient Criterion Development. *J. North Am. Benthological Soc.* 27, 783–799. doi:10.1899/07-077.1

Stockmarr, J. (1971). Tablets with Spores Used in Absolute Pollen Analysis. *Pollen et Spores* 13, 615–621.

Street-Perrott, F. A., Barker, P. A., Swain, D. L., Ficken, K. J., Wooller, M. J., Olago, D. O., et al. (2007). Late Quaternary Changes in Ecosystems and Carbon Cycling on Mt. Kenya, East Africa: a Landscape-Ecological Perspective Based on Multi-Proxy lake-sediment Influxes. *Quat. Sci. Rev.* 26, 1838–1860. doi:10.1016/j.quascirev.2007.02.014

Tjallingii, R., Röhl, U., Kölling, M., and Bickert, T. (2007). Influence of the Water Content on X-ray Fluorescence Core-Scanning Measurements in Soft marine Sediments. *Geochem. Geophys. Geosystems* 8. doi:10.1029/2006gc001393

Toggweiler, J. R., Russell, J. L., and Carson, S. R. (2006). Midlatitude Westerlies, Atmospheric CO2, and Climate Change during the Ice Ages. *Paleoceanography* 21, n/a. doi:10.1029/2005pa001154

Toggweiler, J. R., and Russell, J. (2008). Ocean Circulation in a Warming Climate. *Nature* 451, 286–288. doi:10.1038/nature06590

Tolotti, M., Corradini, F., Boscaini, A., and Calliari, D. (2007). Weather-driven Ecology of Planktonic Diatoms in Lake Tovel (Trentino, Italy). *Hydrobiologia* 578, 147–156. doi:10.1007/s10750-006-0441-4

Torres, M. E., Hong, W.-L., Solomon, E. A., Milliken, K., Kim, J.-H., Sample, J. C., et al. (2020). Silicate Weathering in Anoxic marine Sediment as a Requirement for Authigenic Carbonate Burial. *Earth-Science Rev.* 200, 102960. doi:10.1016/j.earscirev.2019.102960

Trauth, M. H. (2015). "Time-Series Analysis," in *MATLAB® Recipes for Earth Sciences*. Editor M. H. Trauth (Berlin, Heidelberg: Springer Berlin Heidelberg), 151–213. doi:10.1007/978-3-662-46244-7_5

Tuhkanen, S. (1992). The climate of Tierra del Fuego from a vegetation geographical point of view and its ecoclimatic counterparts elsewhere. *Acta Botanica Fennica* 145, 1–64.

Turney, C. S. M., Jones, R. T., Fogwill, C., Hatton, J., Williams, A. N., Hogg, A., et al. (2016). A 250-year Periodicity in Southern Hemisphere westerly Winds over the Last 2600 Years. *Clim. Past* 12, 189–200. doi:10.5194/cp-12-189-2016

Van Daele, M., Bertrand, S., Meyer, I., Moernaut, J., Vandoorne, W., Siani, G., et al. (2016). Late Quaternary Evolution of Lago Castor (Chile, 45.6°S): Timing of the Deglaciation in Northern Patagonia and Evolution of the Southern Westerlies during the Last 17 Kyr. *Quat. Sci. Rev.* 133, 130–146. doi:10.1016/j.quascirev.2015.12.021

Viaggi, P. (2021). Quantitative Impact of Astronomical and Sun-Related Cycles on the Pleistocene Climate System from Antarctica Records. *Quat. Sci. Adv.* 4, 100037. doi:10.1016/j.qsa.2021.100037

Villa-Martínez, R., and Moreno, P. I. (2017). Pollen Evidence for Variations in the Southern Margin of the westerly Winds in SW Patagonia over the Last 12,600 Years. *Quat. Res.* 68, 400–409.

Weltje, G. J., and Tjallingii, R. (2008). Calibration of XRF Core Scanners for Quantitative Geochemical Logging of Sediment Cores: Theory and Application. *Earth Planet. Sci. Lett.* 274, 423–438. doi:10.1016/j.epsl.2008.07.054

Wennrich, V., Minyuk, P. S., Borkhodoev, V., Francke, A., Ritter, B., Nowaczyk, N. R., et al. (2014). Pliocene to Pleistocene Climate and Environmental History of Lake El'gygytgyn, Far East Russian Arctic, Based on High-Resolution Inorganic Geochemistry Data. *Clim. Past* 10, 1381–1399. doi:10.5194/cp-10-1381-2014

Whitlock, C., Moreno, P. I., and Bartlein, P. (2017). Climatic Controls of Holocene Fire Patterns in Southern South America. *Quat. Res.* 68, 28–36. doi:10.1016/j.yqres.2007.01.012

Wille, M., and Schäbitz, F. (2008). Late-glacial and Holocene Climate Dynamics at the Steppe/forest Ecotone in Southernmost Patagonia, Argentina: the Pollen

Record from a Fen Near Brazo Sur, Lago Argentino. *Veget Hist. Archaeobot* 18, 225–234. doi:10.1007/s00334-008-0194-2

Wilson, C. R., Michelutti, N., Cooke, C. A., Briner, J. P., Wolfe, A. P., and Smol, J. P. (2012). Arctic lake Ontogeny across Multiple Interglaciations. *Quat. Sci. Rev.* 31, 112–126. doi:10.1016/j.quascirev.2011.10.018

Winder, M., Reuter, J. E., and Schladow, S. G. (2009). Lake Warming Favours Small-Sized Planktonic Diatom Species. *Proc. R. Soc. B.* 276, 427–435. doi:10.1098/rspb.2008.1200

Wittkop, C., Swanner, E. D., Grengs, A., Lambrecht, N., Fakhraee, M., Myrbo, A., et al. (2020). Evaluating a Primary Carbonate Pathway for Manganese Enrichments in Reducing Environments. *Earth Planet. Sci. Lett.* 538, 116201. doi:10.1016/j.epsl.2020.116201

Yuan, X., and Yonekura, E. (2011). Decadal Variability in the Southern Hemisphere. *J. Geophys. Res. Atmospheres* 116. doi:10.1029/2011jd015673

Zolitschka, B., Anselmetti, F., Ariztegui, D., Corbella, H., Francus, P., Lücke, A., Maidana, N. I., Ohlendorf, C., Schäbitz, F., and Wastegård, S. (2013). Environment and climate of the last 51,000 years - new insights from the Potrok Aike maar lake Sediment Archive Drilling prOject (PASADO). *Quaternary Science Reviews* 71, 1–12. doi:10.1016/j.quascirev.2012.11.024

Zolitschka, B., Fey, M., Janssen, S., Maidana, N. I., Mayr, C., Wulf, S., Haberzettl, T., Corbella, H., Lücke, A., Ohlendorf, C., and Schäbitz, F. (2018). Southern Hemispheric Westerlies control sedimentary processes of Laguna Azul (south-eastern Patagonia, Argentina). *The Holocene* 29, 403–420. doi:10.1177/0959683618816446

Conflict of Interest: The authors declare that the research was conducted in the absence of any commercial or financial relationships that could be construed as a potential conflict of interest.

Publisher's Note: All claims expressed in this article are solely those of the authors and do not necessarily represent those of their affiliated organizations or those of the publisher, the editors, and the reviewers. Any product that may be evaluated in this article, or claim that may be made by its manufacturer, is not guaranteed or endorsed by the publisher.

frontiers | Frontiers in Earth Science

ORIGINAL RESEARCH
published: 04 April 2022
doi: 10.3389/feart.2022.813574

Quantifying Geodetic Mass Balance of the Northern and Southern Patagonian Icefields Since 1976

Morgan McDonnell, Summer Rupper and Richard Forster*

Department of Geography, University of Utah, Salt Lake City, UT, United States

Southern Andean glaciers contribute substantially to global sea-level rise. Unfortunately, mass balance estimates prior to 2000 are limited, hindering our understanding of the evolution of glacier mass changes over time. Elevation changes over 1976/1979 to 2000 derived from historical KH-9 Hexagon imagery and NASADEM provide the basis for geodetic mass balance estimates for subsets of the Northern Patagonian Icefield (NPI) and the Southern Patagonian Icefield (SPI), extending current mass balance observations by ~20 years. Geodetic mass balances were –0.63 ± 0.03 m w.e. yr^{-1} for 63% of the NPI and –0.33 ± 0.05 m w.e. yr^{-1} for 52% of the SPI glacierized areas for this historical period. We also extend previous estimates temporally by 25% using NASADEM and ASTER elevation trends for the period 2000 to 2020, and find geodetic mass balances of –0.86 ± 0.03 m w.e. yr^{-1} for 100% of the NPI and –1.23 ± 0.04 m w.e. yr^{-1} for 97% of the SPI glacierized areas. 2000–2020 aggregations for the same areas represented in the 1976/1979 to 2000 estimates are –0.78 ± 0.03 m w.e. yr^{-1} in the NPI and –0.80 ± 0.04 m w.e. yr^{-1} on the SPI. The significant difference in SPI geodetic mass balance in the modern period for 100% vs. 52% of the glacierized area suggests subsampling leads to significant biases in regional mass balance estimates. When we compare the same areas in each time period, the results highlight an acceleration of ice loss by a factor of 1.2 on the NPI and 2.4 on the SPI in the 21st century as compared to the 1976/1979 to 2000 period. While lake-terminating glaciers show the most significant increase in mass loss rate from 1976/1979–2000 to 2000–2020, mass balance trends are highly variable within glaciers of all terminus environments, which suggests that individual glacier sensitivity to climate change is dependent on a multitude of morphological and climatological factors.

Keywords: glaciers, geodetic mass balance, KH-9 Hexagon, cryosphere, sea-level rise (SLR)

OPEN ACCESS

Edited by:
Neil Franklin Glasser, Aberystwyth University, United Kingdom

Reviewed by:
Eric Rignot, University of California, Irvine, United States
Mauri Pelto, Nichols College, United States

****Correspondence:***
Morgan McDonnell
morgancmcdonnell@gmail.com

Specialty section:
This article was submitted to Cryospheric Sciences, a section of the journal Frontiers in Earth Science

Received: *12 November 2021*
Accepted: *07 March 2022*
Published: *04 April 2022*

Citation:
McDonnell M, Rupper S and Forster R (2022) Quantifying Geodetic Mass Balance of the Northern and Southern Patagonian Icefields Since 1976. Front. Earth Sci. 10:813574. doi: 10.3389/feart.2022.813574

1 INTRODUCTION

In this study, we concentrate on the Northern and Southern Patagonian Icefields (NPI and SPI) and surrounding mountain glaciers (**Figure 1**). The NPI and SPI of South America are the largest ice masses on the continent and in the Southern Hemisphere outside of Antarctica (Schaefer et al., 2015). Glaciers of the Southern Andes, a region dominated by Patagonian Icefields, are the second-largest mountain-glacier contributors to sea-level rise after Alaskan glaciers; however, uncertainties surrounding their mass budgets remain large (Hock et al., 2019). In addition, the NPI and SPI host several intriguing characteristics and phenomena of interest to the scientific community, which

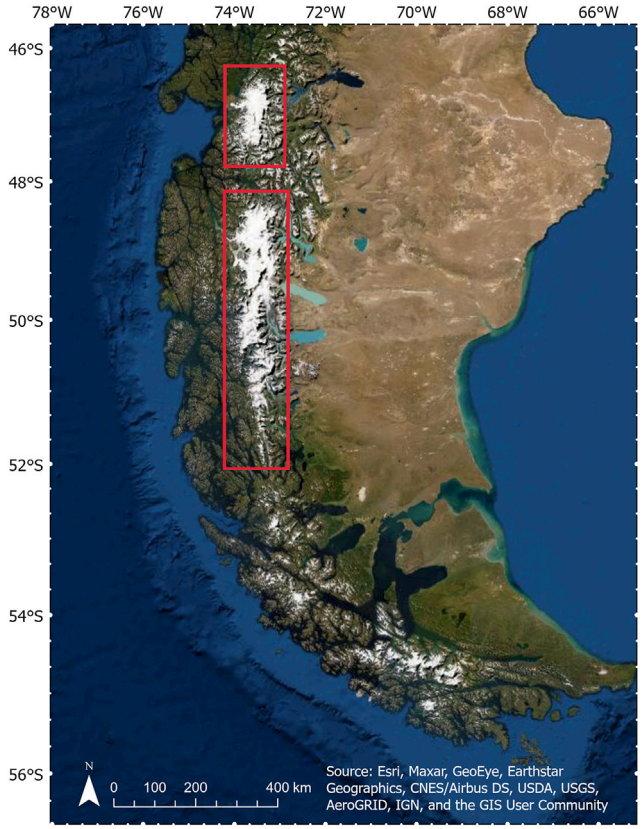

FIGURE 1 | Study area. Red boxes indicate the Northern Patagonian Icefield (NPI) and the Southern Patagonian Icefield (SPI).

previous studies highlight well: many glaciers interact with lakes and fjords at their termini; the San Rafael Glacier in the NPI is the closest marine-terminating glacier to the equator on Earth (Willis et al., 2012a); HPS-12, a small tidewater glacier of the SPI, has alarmingly high thinning rates ($-44\ m\ yr^{-1}$ in the 21st century (Dussaillant et al., 2019); Pio XI, a large tidewater glacier on the SPI, has anomalously positive mass balance (Rivera et al., 1997; Wilson et al., 2016); glaciers also span from sea level to several thousand meters above sea level (Dussaillant et al., 2019). These myriad factors contribute to the NPI and SPI being ideal targets for assessing spatial and temporal variability in glacier mass changes over time.

Observations and model-based studies highlight important changes in the ice fields over the past 40 years. For example, Glasser et al. (2016) found that eastern NPI glaciers experienced a high increase in debris-covered area from 1987–2015. Changes in debris cover often indicate shifts in glacier mass balance and ice flux dynamics. Koppes et al. (2011) used various climatological data in addition to observations of thickness and positional changes over 1950–2005 to quantify fluctuations in the mass balance of San Rafael Glacier. The results show that marine-terminating glaciers are influenced by both morphological and climatological drivers of mass change. Observations over a larger number of marine-terminating glaciers and over longer periods could provide critical information on these complex relationships. Minowa et al. (2021) focus on filling in some of these gaps by estimating frontal ablation from a combination of observations and models for the two icefields. They found that the frontal ablation for lake- and marine-terminating glaciers was $-24.1 \pm 1.7\ Gt\ yr^{-1}$ for the two icefields over 2000–2019, accounting for nearly one half of the total ablation in the SPI, but only 20% of the ablation in the NPI. These results again highlight the importance of mass loss processes of glaciers of differing terminus conditions. Modeling studies also illustrate the spatial heterogeneity in surface mass balance across the ice fields. For example, Schaefer et al. (2013) model surface mass balance for the NPI from 1970–2080. They find increasing accumulation later in the historical period, but an increase in ablation by 2050. Schaefer et al. (2015) model the surface mass balance for the SPI from 1975–2011 and find positive mass balance over the SPI. Bravo et al. (2019) also modeled surface mass balance, as well as equilibrium-line altitudes, and compared results over 1976–2050 for the icefields under different climate scenarios. The model results show significant differences in mass balance between the two ice fields, with the NPI showing a negative mass balance and, similar to the Schaefer et al. (2015) study, a positive mass balance over the SPI in response to climate forcing. Together, these results all point to the significant changes in glaciers occurring across the icefields. Spatially complete data is critical to better identifying the magnitude and variance in these changes.

Geodetic mass balance observations are often used to help fill spatial gaps in mass balance data, and provide opportunities to assess model results and statistical evaluations of spatial patterns in glacier mass changes. Many recent studies (Willis et al., 2012a; Willis et al., 2012b; Dussaillant et al., 2018; Malz et al., 2018; Abdel Jaber et al., 2019; Braun et al., 2019; Dussaillant et al., 2019; Cirací et al., 2020; Hugonnet et al., 2021) have quantified geodetic mass balance for the Patagonia region for the 21st century and explored the spatial heterogeneity across the icefields. The global studies (Cirací et al., 2020; Hugonnet et al., 2021) found the Southern Andes to have the highest rate of mass loss after the Canadian Arctic, Alaska, and High-Mountain Asia. These observations generally show regional mass losses, including for land-terminating glaciers over both the NPI and SPI regions, which contrasts with some modeling studies showing increasing surface mass balance over the SPI (e.g., Schaefer et al., 2015; Bravo et al., 2019). However, since these studies are limited to the past 20 years, it is difficult to attribute the negative geodetic mass balance to changes in climate occurring at longer timescales or assess how persistent these mass loss trends are regionally and for differing glacier types.

Historical imagery and photogrammetric techniques have been utilized by many recent studies to extend the record of glacier geodetic mass balance before 2000 (Pieczonka et al., 2013; Holzer et al., 2015; Pellicciotti et al., 2015; Pieczonka and Bolch, 2015; Maurer et al., 2016; Lamsal et al., 2017; Zhou et al., 2018; Belart et al., 2019; King et al., 2019; Maurer et al., 2019; Dehecq et al., 2020; King et al., 2020; Bhattacharya et al., 2021). One study has generated historical photogrammetric DEMs over three Patagonian glaciers from archived imagery (Falaschi et al., 2019). The authors found negative geodetic mass balance since 1958 for these three glaciers in the Monte San Lorenzo region,

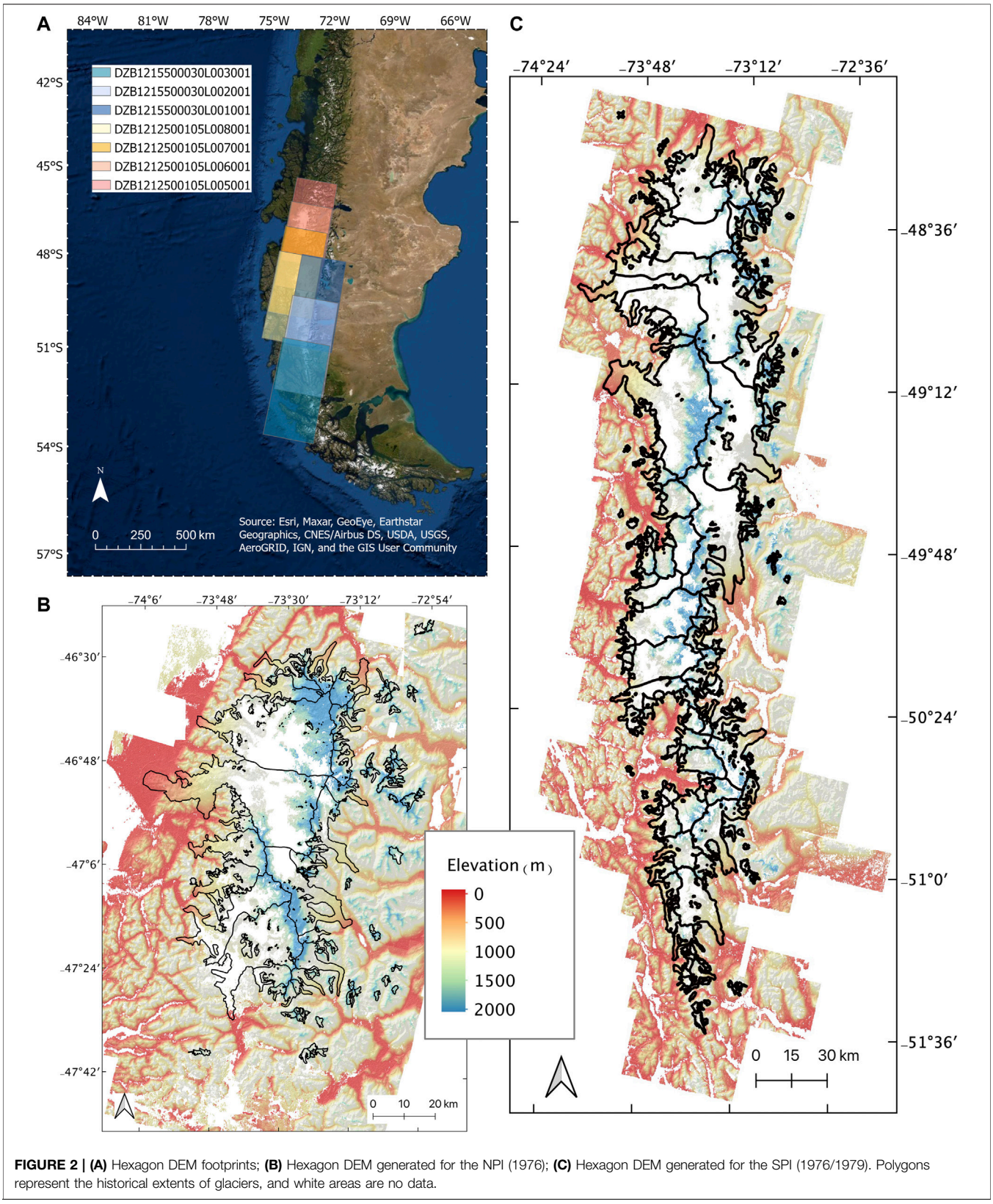

FIGURE 2 | (A) Hexagon DEM footprints; **(B)** Hexagon DEM generated for the NPI (1976); **(C)** Hexagon DEM generated for the SPI (1976/1979). Polygons represent the historical extents of glaciers, and white areas are no data.

TABLE 1 | Entity IDs of downloaded hexagon imagery.

Region	Hexagon entity ID	Acquisition date
NPI	DZB1212-500105L005001	1976-07-29
NPI	DZB1212-500105L006001	1976-07-29
SPI	DZB1212-500105L007001	1976-07-29
SPI	DZB1212-500105L008001	1976-07-29
SPI	DZB1215-500030L001001	1979-03-20
SPI	DZB1215-500030L002001	1979-03-20
SPI	DZB1215-500030L003001	1979-03-20

near the icefields. This study covers a small spatial extent but provides regional context for the historical geodetic mass balance of the icefields. The authors found that while the mass balance of these glaciers has remained negative, one has become less negative since 1958, one has become consistently more negative, and one has alternated between relative rates of mass loss. Another study quantified 1968/1975–2000 volume change for 63 of the largest glaciers in the icefields using differences in historical cartography and SRTM and found that they contributed 0.042 ± 0.002 mm yr^{-1} to sea-level rise during this period (Rignot et al., 2003). This study highlights the importance of quantifying ice loss before 2000; however, it lacks geodetic mass balance measurements for individual glaciers and has large uncertainties in elevation estimates (Falaschi et al., 2019).

We focus on reconstructing a longer and spatially distinct record of mass balance observations to further assess spatial and temporal variability in mass balance trends on timescales more relevant to climate trends and glacier dynamics. Herein, we build on previous work by calculating the geodetic mass balance of 275 Patagonian glaciers for 1976/1979–2000 utilizing historical DEMs generated with the Hexagon Imagery Automated Imagery Pipeline (HEXIMAP) (Maurer and Rupper, 2015). This extends the use of HEXIMAP, originally developed for Himalayan mountain glaciers, to large ice-covered areas. We analyze only glaciers with an area of 3 km^2 or greater, as glaciers smaller than this do not typically have enough data coverage for successful geodetic mass balance calculation (Maurer et al., 2019). In addition, we calculate the geodetic mass balance for 2000–2020 to extend previous estimates to the present and to validate the methodology used for the historical time period.

2 MATERIALS AND METHODS

2.1 Data Acquisition and Image Processing

Declassified KH-9 Hexagon imagery is utilized for historical DEM generation since global DEMs are not readily available before 2000 (U.S. Geological Survey, 2002). KH-9, or Keyhole Hexagon imagery, was part of a military intelligence satellite mission in operation from 1971–1980 (U.S. Geological Survey, 2008). The United States government declassified these images in 2002 without their corresponding metadata, and therefore the raw images are not georeferenced. Hexagon DEMs are extracted, georeferenced, and co-registered to a reference Copernicus DEM (CopDEM) using HEXIMAP (Maurer and Rupper, 2015).

This historical DEM extraction method is described in detail in Maurer and Rupper (2015) and updated in Maurer et al. (2019). Briefly here, HEXIMAP utilizes traditional photogrammetry and structure-from-motion (SfM), removing the need for the manual selection of ground control points. It utilizes the OpenCV library FLANN (Fast Library for Approximate Nearest Neighbors) for stereo rectification and the SGBM (semi-global block-matching) algorithm for disparity map generation. We download raw Hexagon imagery from USGS Earth Explorer at approximately 6–9 m spatial resolution (**Figure 2A**; **Table 1**) and the CopDEM from ESA's Planetary Data Access tool (PANDA) at 30 m resolution (European Space Agency, 2020). The HEXIMAP pipeline resamples the Hexagon DEM to the CopDEM resolution with linear interpolation to allow for elevation change analysis at the pixel scale. The final extracted Hexagon DEMs are in **Figures 2B,C**.

We utilize Advanced Spaceborne Thermal Emission and Reflection Radiometer (ASTER) DEMs, launched on NASA's Terra satellite in 1999, for the modern DEMs (NASA JPL, 2004; NASA, METI, AIST, 2019). We download all ASTER DEMs (data1.l3a.demzs product) with acquisition dates 2000–2020 *via* METI AIST Data Archive System (MADAS) at 30 m spatial resolution. Maurer et al. (2019) provide detailed methods for processing the ASTER DEMs. To summarize here, ASTER DEMs are cleaned and co-registered to the CopDEM which includes the removal of pixels saturated in ASTER's nadir band 3 (0.76–0.86 μm). The NASADEM is also used in the 2000–2020 elevation trend and is the modern (year 2000) timestamp for differencing with the Hexagon DEM. We download the NASADEM from NASA EarthData at 30 m resolution (NASA JPL, 2020). To co-register the NASADEM to the Copernicus DEM, we utilize an automated software that is based on the algorithm by Nuth and Kääb (2011) and Shean et al. (2016).

During co-registration to the CopDEM, a maximum elevation outlier threshold (E_t) is specified since outliers may still be present in the Hexagon, NASADEM, and ASTER DEMs, in part due to clouds (**Eq. 1**). We determined the elevation outlier threshold according to the estimated maximum elevation change (ΔE) expected over the glaciers (15 m yr^{-1} for the NPI and 30 m yr^{-1} for the SPI) (Dussaillant et al., 2018; Dussaillant et al., 2019) and the time difference between the specific DEM or DEM set and the CopDEM (Δt). As the CopDEM has a temporal range of 2010–2015, the maximum difference in temporal acquisition time is 15 years for the ASTER and NASADEM, and 39 years for the Hexagon DEM. For one glacier in the SPI, HPS-12, thinning rates of 44 m yr^{-1} have been observed in the 21st century (Dussaillant et al., 2019); therefore, ASTER and NASADEM DEMs were co-registered to the CopDEM again according to this maximum expected elevation change. These DEMs were used in the elevation trend acquisition and geodetic mass balance estimate for 2000–2020 for HPS-12. We conservatively add an additional 5 m to this maximum elevation outlier threshold to account for the maximum expected CopDEM X-band penetration into snow/firn. Maximum penetration depth (δ_p) of X-band (10 GHz) into firn was measured as 4.7 m by Davis and Poznyak (1993) in

TABLE 2 | Geodetic mass balance sensitivity to maximum standard deviation allowed in 2000–2020 elevation trend. For HPS-12, DEMs were co-registered to the CopDEM using higher elevation outlier threshold than other glaciers (see **Section 2.1**).

Glacier	Geodetic mass balance (m w.e. yr^{-1}) with varying standard deviation				Percent data coverage improvement (%)
	50 m	100 m	150 m	200 m	
HPN-1 (RGI60-17.15899)	−1.76 ± 0.18	−1.87 ± 0.19	—	—	4
Acodado (RGI60-17.15898)	−0.95 ± 0.10	−0.88 ± 0.10	—	—	1
Steffen (RGI60-17.15897)	−1.44 ± 0.15	−1.38 ± 0.14	—	—	0
Fiero (RGI60-17.1583)	−0.90 ± 0.11	−0.76 ± 0.13	—	—	1
Upsala (RGI60-17.00172)	−2.91 ± 0.29	−3.14 ± 0.31	—	—	4
Jorge Montt (RGI60-17.06074)	−2.33 ± 0.24	—	−3.94 ± 0.39	—	23
HPS-12 (RGI60-17.5031)	−1.11 ± 0.15	—	—	−3.23 ± 0.35	5

Antarctica, where drier and colder conditions likely lead to higher penetration than we would see in Patagonia (Gardelle et al., 2012). NASADEM C-band penetration into snow/firn has been found negligible in the Patagonian Icefields (Dussaillant et al., 2018), however, we incorporate a conservative error term in the elevation change uncertainty, which is discussed in the **Supplementary Material**.

$$E_t = (\Delta E * \Delta t) + \delta p \quad (1)$$

2.2 Elevation Change Maps

Subtracting the Hexagon DEM from the NASADEM provides an elevation difference over the glaciers in the historical time period. For the 2000–2020 time period, multitemporal ASTER DEM stacks, plus the NASADEM for the year 2000, provide an average elevation trend for the 20 years over each glacier. We use the Random Sample Consensus (RANSAC) trend fitting algorithm to determine the average elevation trend at the pixel-scale (Martinez-Camara et al., 2014; Maurer et al., 2019). RANSAC randomly selects two DEMs within the ASTER stack and fits a trend to the elevation, repeating for 250 iterations. The elevation trend with the least outliers and a standard deviation of less than 50 m was selected for each pixel. In the case where no trend with less than 50 m standard deviation was found for a given pixel, no elevation trend was calculated. We allowed a higher maximum standard deviation between 100 and 200 m for select glaciers due to calving fronts causing nonlinear behavior on their termini (**Table 2**; **Supplementary Figure S2**).

In the SPI, many DEMs contained few valid pixels, typically due to persistent cloud cover. A filtering step selects only ASTER DEMs containing at least 10% valid pixels to increase the chances for RANSAC to select DEMs with valid pixels. For data coverage, see **Supplementary Figure S3**. To fill data gaps, elevation trend/change data is grouped into 50-m elevation bins. Bins with at least 100 pixels within a 2–98% quantile range are used to linearly interpolate gaps within glacier polygons (see the **Supplementary Material** for information on the error term associated with interpolating data gaps). If the highest and lowest elevation bins did not have at least 100 pixels, zero change was assumed. A 5 × 5-pixel median filter smooths the final elevation trend results and removes unrealistic slopes greater than 45° (Maurer et al., 2019).

2.3 Volume Change and Mass Change

For an individual glacier, multiplying all elevation change pixels by their pixel area converts them to pixel volume change. The sum of these volume change pixels represents the ice volume change for the glacier, which is divided by the average glacier area (the methods used to define the glacier area at each timestamp are provided in **Section 2.5**). We then multiply the glacier thickness change by 850 km m^{-3}, the average ice-firn density (Huss, 2013). The resulting value is geodetic mass balance in meters of water equivalent per year (Maurer et al., 2019). Uncertainty associated with the chosen density value and error propagation for the geodetic mass balance calculation are discussed in **Supplementary Section S1.3**.

2.4 Regional Aggregations

The volume change rate for an entire region is the summation of individual glacier volume change rates. The volume change rate is converted to Gt yr^{-1} by multiplying the volume change rate by the density conversion factor of 0.850 Gt/km^3. This mass rate (Gt yr^{-1}) is then divided by 362.5 Mm^2, which is representative of the amount of water needed to raise the eustatic sea level by 1 mm (Cogley, 2012). In each geodetic mass balance aggregation (GMB_{region}, m w.e. yr^{-1}), the geodetic mass balance of each glacier in the region (GMB_i, m w.e. yr^{-1}) is multiplied by its area (A_i, km^2), and all area-weighted mass balance values are summed together and divided by the total area of the aggregation (A_{region}, km^2) (**Eq. 2**).

$$GMB_{region} = \frac{\Sigma_{i=1}^{n} (GMB_i * A_i)}{A_{region}} \quad (2)$$

2.5 Glacier Inventories

Integrating elevation changes over the glacier area requires the average glacier area during each time interval. Thus, we require glacier polygons for the years 1976, 2000, and 2020. Polygons from the Randolph Glacier Inventory 6.0 (RGI 6.0) provide a glacier inventory baseline for each timestamp (Pfeffer et al., 2014; Randolph Glacier Inventory Consortium, 2017). RGI 6.0 can have significant uncertainties associated with them and they are not temporally distinct. Thus, we use the glacier inventories produced by Meier et al. (2018), Google Earth, and the following imagery to aid in the manual delineation of glacier extents. For the 1976 timestamp, we utilize Global Land Survey 1975 (GLS 1975)

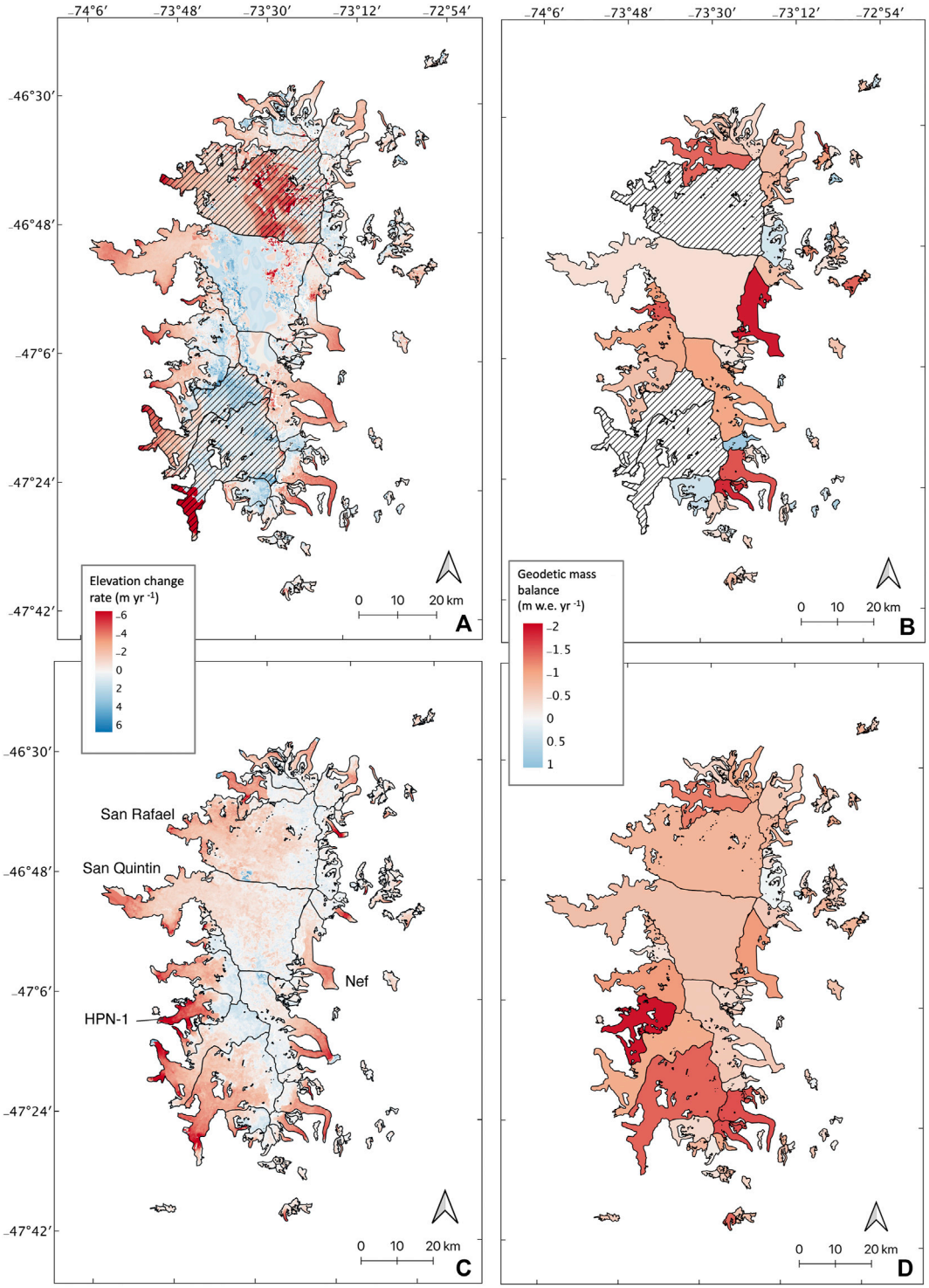

FIGURE 3 | Elevation change observed on the NPI in **(A)** 1976–2000 and **(C)** 2000–2020. Hatched glaciers are those with less than 50% data coverage. This elevation change integrated over the glacier surfaces results in geodetic mass balance for **(B)** the historical period and **(D)** the modern period.

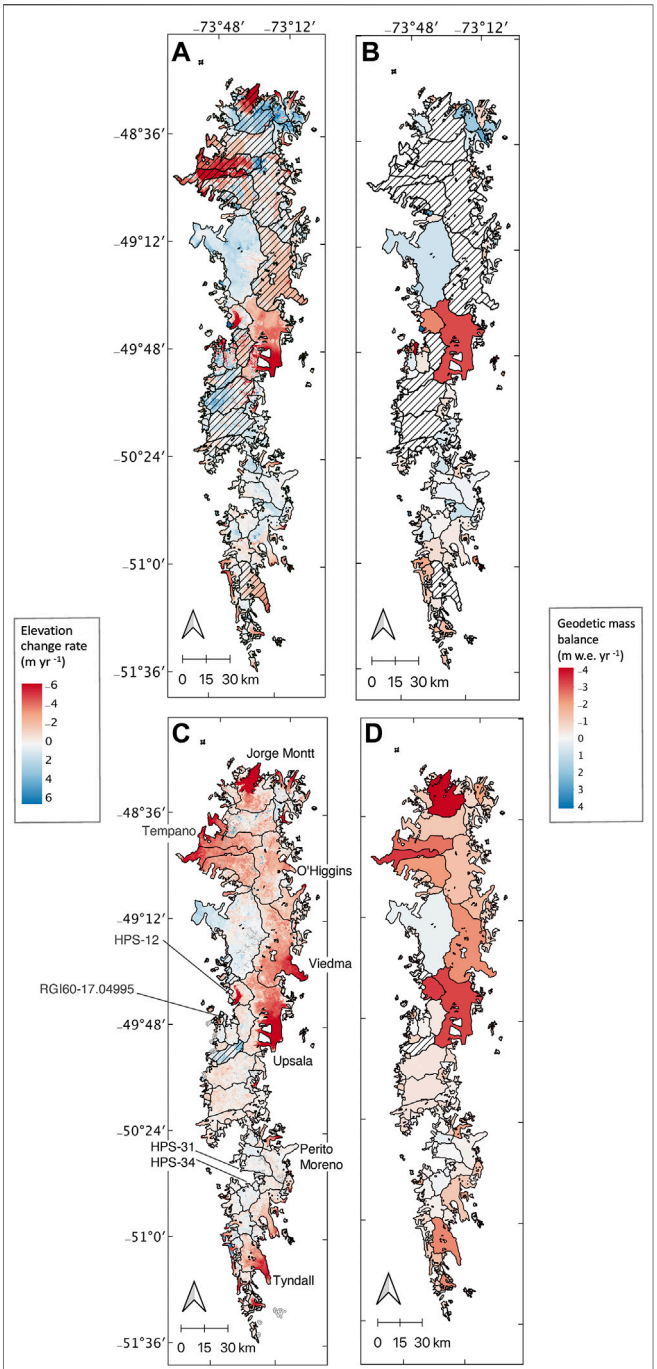

FIGURE 4 | Elevation change observed on the SPI in **(A)** 1976/1979–2000 and **(C)** 2000–2020. Hatched glaciers are those with less than 50% data coverage. Glacier outlines are representative of their 2000 extent. Glaciers shaded gray in **(C)** have no geodetic mass balance estimate. This elevation change integrated over the glacier surfaces results in geodetic mass balance for **(B)** the historical period and **(D)** the modern period. The geodetic mass balance color range presented does not represent the full range of data. To see all data points for the icefields, see **Supplementary Figures S4, S5**.

imagery and a preliminary elevation change map for the historical period. Several glaciers in the southeast SPI are not covered by GLS 1975, and therefore their 2000 outlines were utilized for the 1976 timestamp. We use cloud-free GLS 2000 imagery and summer 2018–2020 Landsat 8 imagery for 2000 and 2020 delineations, respectively.

2.6 Uncertainty

The uncertainty associated with glacier elevation and volume changes, regional geodetic mass balance, and subsequent conversions to Gigatons and millimeters of sea-level rise equivalent are provided in the **Supplementary Equations S1–S5**. Generally, the errors associated with individual glaciers follow the methodology presented in Maurer et al. (2019). For regional aggregations, the errors are propagated using summation in quadrature.

3 RESULTS

3.1 Elevation Change

Figures 3A, **4A** present elevation change over 1976–2000 for the NPI and 1976/1979–2000 for the SPI, respectively. Hatched glaciers have less than 50% valid data coverage. These data gaps tend to occur where elevation data could not be extracted due to low contrast and oversaturation in accumulation zones of the satellite photos (Maurer et al., 2019). Thinning rates increase during 2000–2020 for both the NPI and SPI (**Figures 3C**, **4C**), although spatial patterns in thinning remain similar. For example, higher rates of elevation change generally occur on the glacier termini. For some glaciers, rapid thinning extends to higher elevations in the second time period (e.g., HPN-1, labeled in **Figure 3C**).

3.2 Geodetic Mass Balance

Choropleth maps (**Figures 3B,D**, **4B,D**) show how elevation change is translated to geodetic mass balance for individual glaciers. The NPI and SPI area-weighted geodetic mass balance averages for the icefields are provided in **Table 3**. The area-weighted average only includes glaciers with at least 50% data coverage. Both NPI and SPI show negative mass balance trends for the modern period, albeit the SPI is significantly more negative (-1.23 ± 0.04 m w.e. yr^{-1}) as compared to the NPI (-0.86 ± 0.03 m w.e. yr^{-1}). **Section 4.6** discusses a comparison to previous studies.

There is less coverage for the historical period, but we can compare trends across both time periods for 33 NPI glaciers and 142 SPI glaciers. 33 glaciers on the NPI are equivalent to 63% of the NPI glacierized area and 142 glaciers on the SPI are equivalent to 52% of the SPI glacierized area (**Table 3**). For the NPI, the 2000–2020 geodetic mass balance of 100% of the area (-0.86 ± 0.03 m w.e. yr^{-1}, 2000–2020 all in **Table 3**) is similar to that of 63% of the ice field (-0.78 ± 0.03 m w.e. yr^{-1}, 2000–2020 overlap). Conversely, for the SPI, the estimated mass balance for the 2000–2020 period is reduced significantly (-1.23 ± 0.04 m w.e. yr^{-1} versus -0.80 ± 0.04 m w.e. yr^{-1}) when only utilizing the region of overlapping data (97% vs. 52% areal coverage). This suggests that having data for 63% of the glacierized area is sufficient to capture the regional trend for the NPI, and 52% is not sufficient enough to capture the regional trend for the

TABLE 3 | Area-weighted geodetic mass balance of the icefields. Total glacierized area is calculated from year 2000 glacier outlines. "Area with valid elevation data in region" corresponds to percent of the total glacierized region which has valid elevation data (includes all glaciers, not only those that have more than 50% valid data). "Valid elevation data used" corresponds to the valid data (of the entire region) that is utilized in the aggregation (i.e., the data that was within glaciers with at least 50% data coverage). "Area included in the estimate" is the total area (data plus interpolated area) included in the aggregation for the geodetic mass balance estimate with respect to the total glacierized area, including only glaciers that had at least 50% valid elevation data. For example, 63% in the first column represents the unhatched glaciers on the icefield (which all include some interpolation) in **Figure 3A**. "Number of glaciers included in the estimate" are those that had at least 50% valid elevation data before interpolation.

Time period and dataset	Area with valid elevation data in region (%)	Valid elevation data in region used (%)	Area included in estimate		n glaciers	Average timespan (years)	Volume change ($km^3\ yr^{-1}$)	Geodetic mass balance		Contribution to SLR ($mm\ yr^{-1}$)
			km^2	%				m w.e. yr^{-1}	Gt yr^{-1}	
NPI sensu stricto (total glacierized region 3,849 km^2)										
1976–2000 overlap and all	62	45	2,435	63	33	23.5	−1.37 ± 0.05	−0.63 ± 0.03	−1.17 ± 0.13	0.0032 ± 0.0003
2000–2020 overlap	94	59	2,435	63	33	20.8	−2.15 ± 0.03	−0.78 ± 0.03	−1.82 ± 0.15	0.0050 ± 0.0004
2000–2020 all	94	94	3,849	100	36	20.8	−3.73 ± 0.04	−0.86 ± 0.03	−3.17 ± 0.26	0.0088 ± 0.0007
SPI sensu stricto (total glacierized region 12,403 km^2)										
1976/1979–2000 overlap	52	34	6,392	52	142	20.9–23.5	−2.49 ± 0.09	−0.33 ± 0.05	−2.11 ± 0.23	0.0058 ± 0.0006
2000–2020 overlap	80	42	6,392	52	142	19.9	−5.66 ± 0.06	−0.80 ± 0.04	−4.81 ± 0.39	0.0133 ± 0.0011
1976/1979–2000 all	52	35	6,548	53	156	20.9–23.5	−2.49 ± 0.09	−0.32 ± 0.05	−2.11 ± 0.23	0.0058 ± 0.0006
2000–2020 all	80	79	12,082	97	161	19.9	−16.87 ± 0.08	−1.23 ± 0.04	−14.34 ± 1.08	0.0396 ± 0.0030
NPI and SPI sensu stricto										
1976/1979–2000 all	See corresponding columns above for each icefield								−3.28 ± 0.32	0.0091 ± 0.0009
2000–2020 all									−17.51 ± 1.32	0.0484 ± 0.0036

SPI. Only including glaciers in the icefields with coverage in both periods, geodetic mass balance decreased by 0.15 m w.e. yr^{-1} from 1976–2000 to 2000–2020 in the NPI, equivalent to a mass loss rate increasing by a factor of 1.2. In the SPI, the geodetic mass balance decreased by 0.47 m w.e. yr^{-1} and by a factor of 2.4.

3.3 Spatial Variability

While geodetic mass balance on average is negative for the icefields, geodetic mass balances are spatially heterogeneous across the region. In the SPI, Pio XI experiences a positive change while highly negative change is observed on HPS-12, and Perito Moreno experiences little mass change over time.

TABLE 4 | Geodetic mass balance averages (not area-weighted) for NPI and SPI glacier aggregations described by terminus type and location relative to the ice divide.

Time period and dataset	Average geodetic mass balance (m w.e. yr^{-1})				
	Whole dataset (NPI + SPI)	West		East	
		NPI	SPI	NPI	SPI
Land					
1976/1979–2000 overlap	−0.20 ± 0.04 (n = 77)	−0.17 ± 0.12 (n = 5)	−0.12 ± 0.09 (n = 33)	−0.47 ± 0.05 (n = 11)	−0.20 ± 0.06 (n = 28)
2000–2020 overlap	−0.52 ± 0.03 (n = 76)	−0.65 ± 0.05 (n = 4)	−0.51 ± 0.04 (n = 34)	−0.73 ± 0.04 (n = 10)	−0.43 ± 0.05 (n = 28)
Lake					
1976/1979–2000 overlap	−0.22 ± 0.02 (n = 78)	−0.68 ± 0.09 (n = 8)	−0.47 ± 0.05 (n = 20)	−0.58 ± 0.06 (n = 9)	0.07 ± 0.03 (n = 41)
2000–2020 overlap	−0.71 ± 0.02 (n = 79)	−0.79 ± 0.05 (n = 9)	−0.62 ± 0.04 (n = 19)	−0.54 ± 0.04 (n = 10)	−0.78 ± 0.03 (n = 41)
Marine					
1976/1979–2000 overlap	−0.38 ± 0.06 (n = 20)	—	−0.38 ± 0.06 (n = 20)	—	—
2000–2020 overlap	−0.20 ± 0.04 (n = 20)	—	−0.20 ± 0.04 (n = 20)	—	—

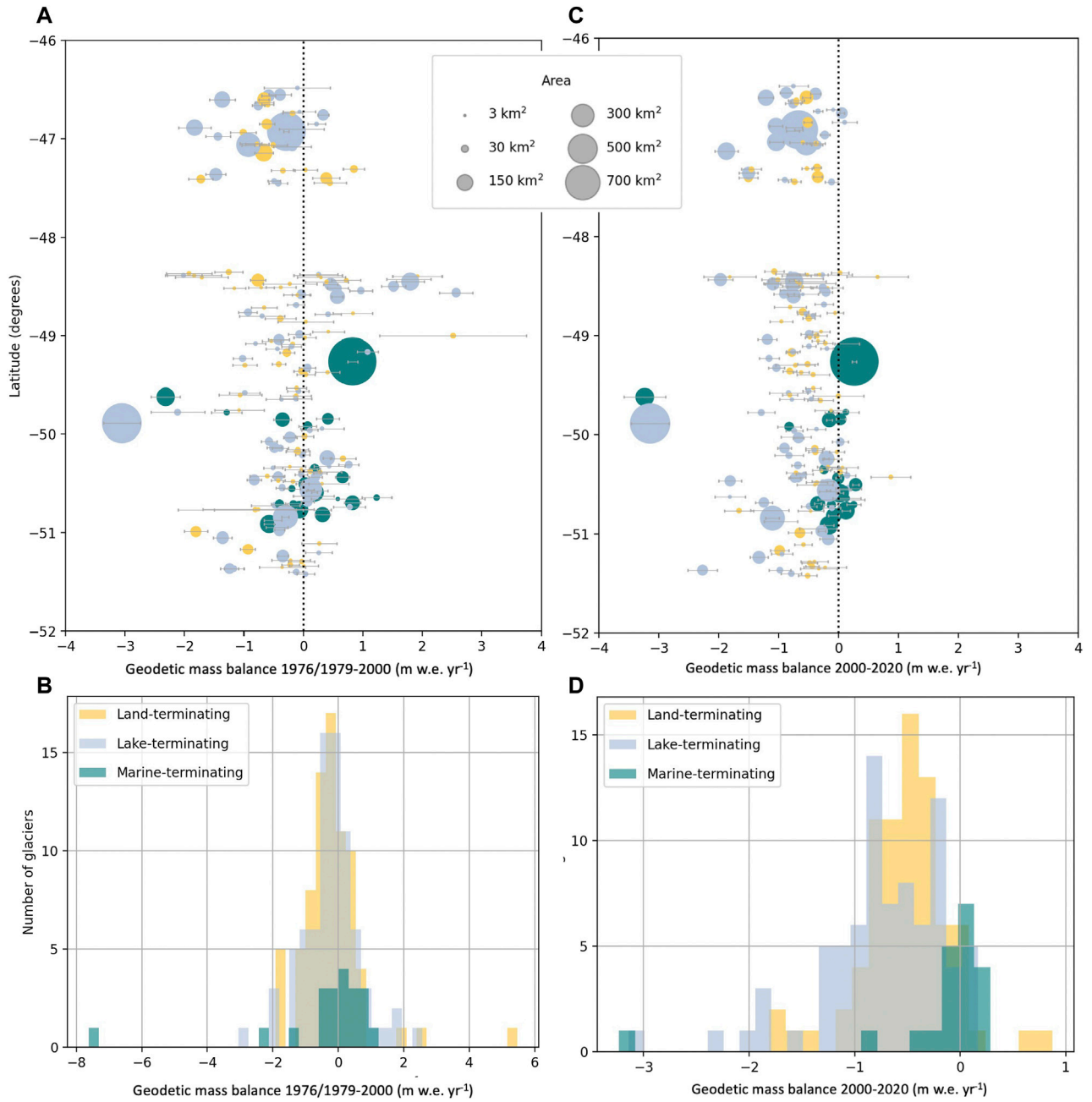

FIGURE 5 | Geodetic mass balance plotted with latitude for **(A)** the historical time period (1976–2000 overlap and 1976/1979–2000 overlap in **Table 3**), clipped to −4 to +4 m w.e. yr^{-1} to show the spread around 0 m w.e. yr^{-1}; and **(C)** the modern time period (2000–2020 overlap in **Table 3**). Histograms for **(B)** 1976/1979–2000 and **(D)** 2000–2020 show the distribution of geodetic mass balance according to glacier terminus type. Panel **(B)** extends the 1976/1979–2000 results to show all glaciers with data in both time periods.

Table 4 presents the average geodetic mass balance for glaciers of each terminus type (including only the icefields). In the overlap aggregations for each terminus type, land-, lake-, and marine-terminating glaciers have similar average geodetic mass balances in the historical time period. In the modern period, lake-terminating glaciers have the most negative geodetic mass balance, while land-terminating glaciers also become more negative. Averages for marine-terminating glaciers are misleading, as they are skewed by a few highly-negative glaciers (**Figure 5**; **Supplementary Figure S4**). In **Figures 5A,C**, geodetic mass balance is plotted against latitude for glaciers that have estimates in each time period. For these

175 glaciers, 64% had a negative geodetic mass balance in the historical period. This percentage increased to 87% in the modern period.

Histograms (**Figures 5B,D**) display the mass balance distributions for each terminus type. The histogram for the historical time period (**Figure 5B**) shows the distribution is centered near 0 m w.e. yr^{-1} for marine-terminating glaciers, while it is negative for the lake- and land-terminating glaciers. The histogram for the modern time period (**Figure 5D**) shows marine-terminating glaciers remained centered around 0 m w.e. yr^{-1} while both land- and lake-terminating glaciers become more negative on average (lake-terminating slightly more so than land-terminating). The distributions are unique for the modern time period (**Figure 5D**), but are not statistically different for the historical period (**Figure 5B**), based on a Kruskal–Wallis One-Way ANOVA. A Mann-Whitney U Test on each of the contributions further reveals that all three distributions are statistically different at the 95% confidence interval in the modern time period. We do not repeat statistical tests for "all data" distributions shown in **Supplementary Figure S4** (all rows in **Table 3**), but the overall patterns are the same when all glaciers with data are considered for each time period, rather than only those with data in both periods.

Figure 6A presents the geodetic mass balance of the historical time period subtracted from the modern measurement to visualize how mass change rates have evolved over time. Similar to the results of Falaschi et al. (2019), variation exists for individual glaciers. For the glaciers we can compare between the time periods, all (regardless of terminus type) have shifted more negatively in the 21st century (**Figure 6B**). A secondary histogram (**Figure 6C**) shows a handful of glaciers that have changed terminus type between the time periods. Although the sample size is small, those that formed proglacial lakes in the modern time period (blue bars) have become more negative, and those that receded from lakes (orange bars) become less negative.

To explore the potential effects of the orographic barrier on geodetic mass balance, we plotted glacier mass balance against longitude for both time periods (**Figures 7A,D**). Histograms for the historical period (**Figures 7B,C**) and modern period (**Figures 7E,F**) show distributions of western and eastern glaciers for each icefield. In the supplement we provide the same plots for all icefield glaciers that have an estimate in either time period

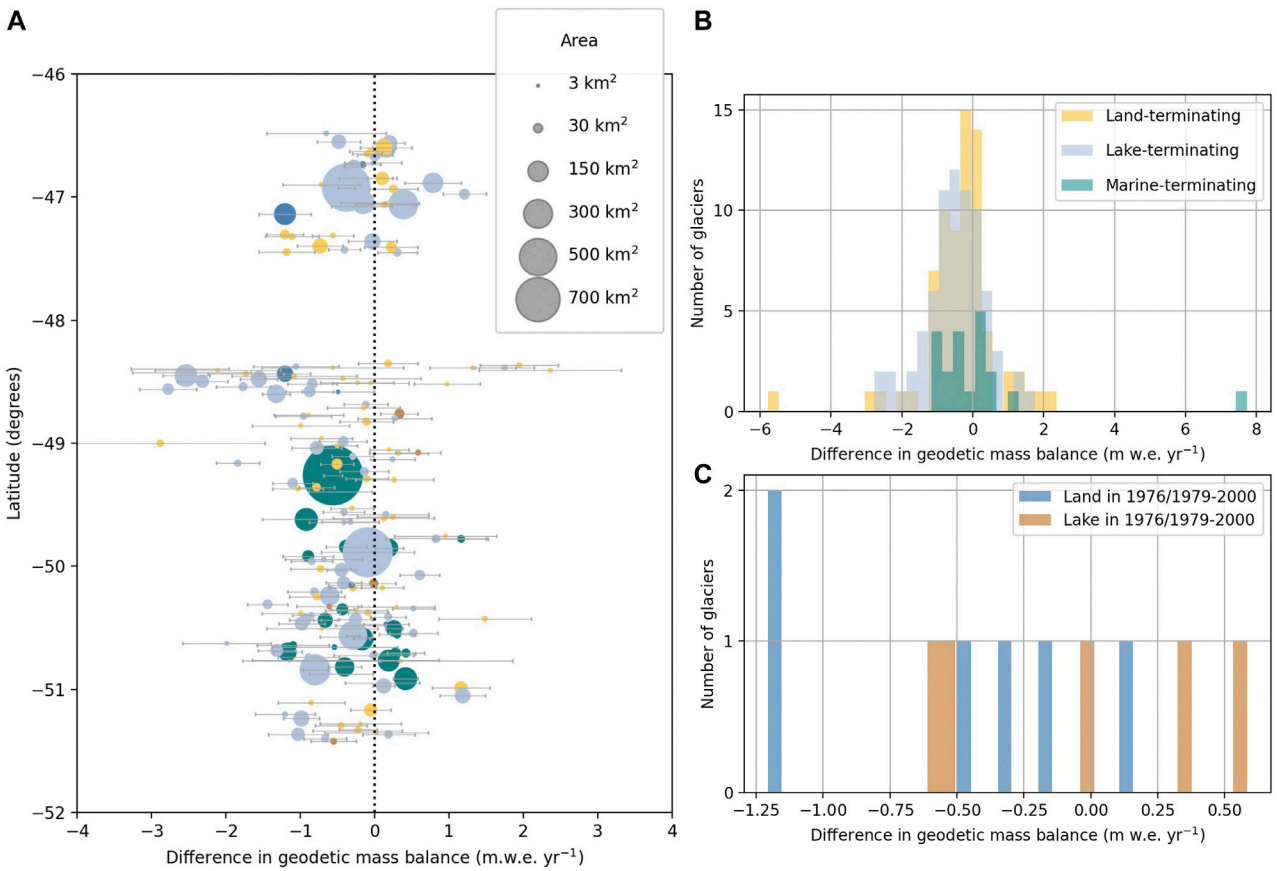

FIGURE 6 | (A) Historical geodetic mass balance subtracted from the modern geodetic mass balance plotted with latitude, which is clipped to show the distribution around zero. Dotted line indicates where no change in geodetic mass balance occurs. **(B,C)** display the full range of geodetic mass balance change for different glacier terminus types.

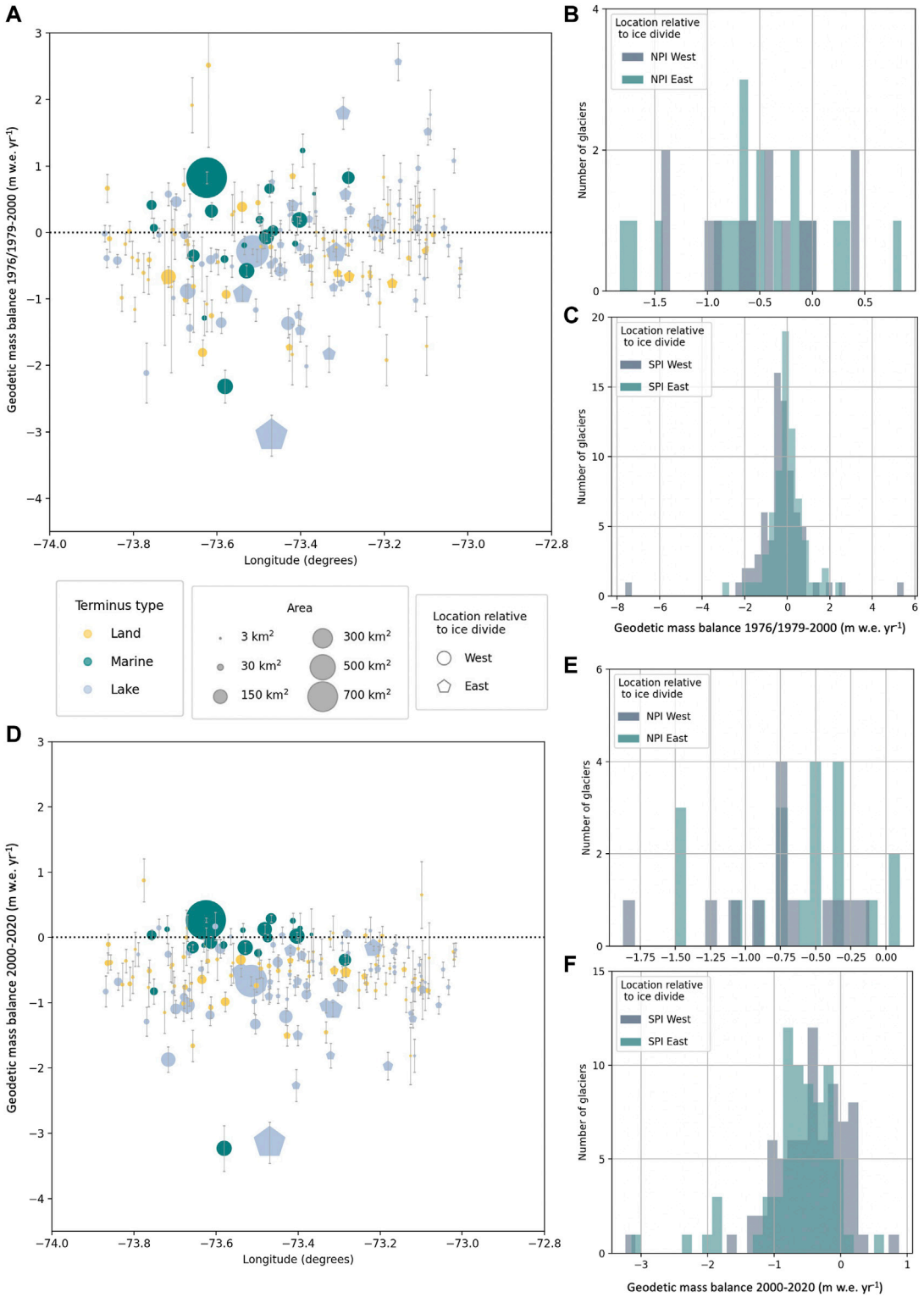

FIGURE 7 | Geodetic mass balance plotted with longitude for **(A)** the historical time period (1976–2000 overlap and 1976/1979–2000 overlap in **Table 3**), clipped to −4 to +3 m w.e. yr^{-1} to show the spread around 0 m w.e. yr^{-1}; and **(D)** the modern time period (2000–2020 overlap in **Table 3**). Histograms for 1976/1979–2000 **(B,C)** and 2000–2020 **(E,F)** show the distribution of geodetic mass balance according to glacier location east or west of the ice divide.

(**Supplementary Figure S5**). We separate the icefields in the histograms in order to better evaluate the SPI mass balance trends. We focus on the SPI here as the NPI sample size is extremely small and previous work (e.g., Foresta et al., 2018; Abdel Jaber et al., 2019) has stated that spatial heterogeneity in elevation change is particularly apparent in the SPI. Indeed, we observe that SPI eastern, lake-terminating glaciers have undergone the most rapid thinning between 1976/1979–2000 and 2000–2020. In the SPI, east and west distributions appear similar in the historical period, but eastern SPI glaciers appear more negative than western SPI glaciers in the modern time period. We perform a Mann-Whitney U-Test for both time periods and find that the distributions of east versus west for the SPI are statistically different in the modern time period at the 95% confidence interval. **Figure 8** displays the difference in geodetic mass balance between the time periods plotted with longitude, and reiterates this observed trend of divergence in the SPI. We do not draw conclusions from the NPI histograms or averages in **Table 4** since the sample size is small; however, from the elevation change maps, we can see that western glaciers of the NPI have been retreating very rapidly (i.e., HPN-1 and nearby glaciers in **Figure 3C**).

3.4 Sea-Level Rise Contributions

While we do not fill in missing glaciers with any regional average, we can estimate the amount of volume the measured glaciers have contributed to eustatic sea-level rise in each time period. Together, 100% of the NPI and 97% of the SPI have a mass change value of -17.51 ± 1.32 Gt yr^{-1} and contribute 0.0484 ± 0.0036 mm yr^{-1} to sea-level rise in 2000–2020 (**Table 3**). Dussaillant et al. (2019) estimate that the entire Andes contributed 0.06 ± 0.02 mm yr^{-1} from 2000–2018, and cite this value as just over 10% of the glacier contributions across the globe 2002–2016 (Bamber et al., 2018). For 63% of the NPI in 1976–2000 and 53% of the SPI in 1976/1979–2000, the mass change rate was −3.28 ± 0.32 Gt yr^{-1}. These glaciers contributed 0.0091 ± 0.0009 mm yr^{-1} from 1976/1979–2000. Although we cannot make a direct comparison to their study, Rignot et al. (2003) found the 63 largest glaciers contributed 0.042 ± 0.002 mm yr^{-1} over 1968/1975–2000. Our estimate includes only those glaciers that are unhatched in **Figures 3A**, **4A**, which are disproportionately smaller glaciers, and we do not extrapolate to the full region due to extreme heterogeneity observed in glaciers across the icefields for 2000–2020. This may contribute to the significant difference in our historical SLR estimates as compared to Rignot et al. (2003).

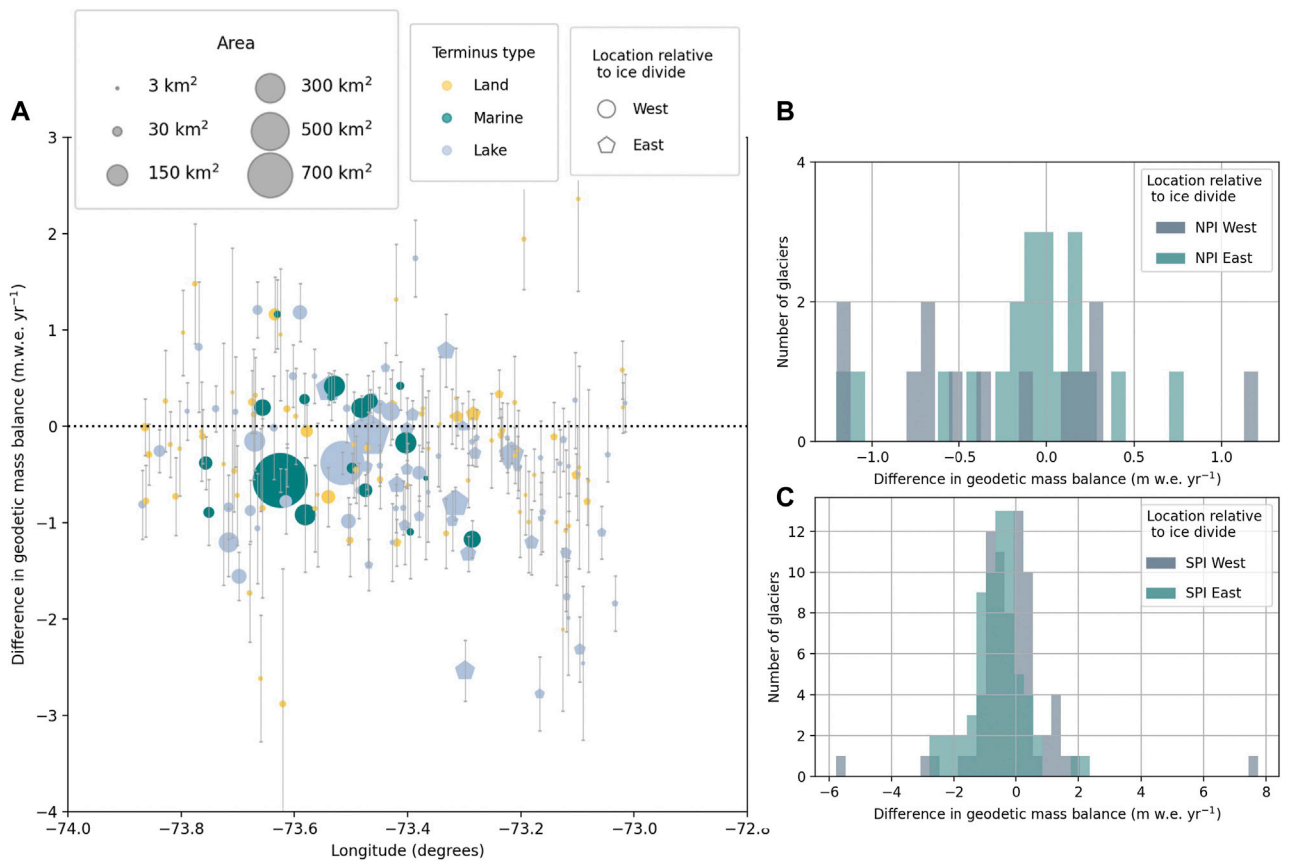

FIGURE 8 | (A) Historical geodetic mass balance subtracted from the modern geodetic mass balance plotted with longitude, which is clipped to show the distribution around zero. Dotted line indicates where no change in geodetic mass balance occurs. **(B)** displays the full range distribution of geodetic mass balance change for NPI glaciers west and east of the ice divide. **(C)** is the same as **(B)**, but for the SPI glaciers.

4 DISCUSSION

4.1 Regional Trends in Geodetic Mass Balance and Climate Drivers

Mass loss rates increased by a factor of 1.2 for 63% of the NPI and 2.4 for 52% of the SPI over 1976/1979–2000 to 2000–2020, which likely indicates an acceleration of warming, a change in precipitation, or a change in glacier sensitivity to climate in the 21st century. Braun et al. (2019) show surface temperatures of South Patagonia have increased significantly over the period 1979–2017, according to climate reanalysis data and suggest warming as a mechanism for increased ablation. In their 2020 Global Climate Report, NOAA (2021) reported that in 2015–2020, South America had experienced the five warmest years on record. Additionally, some studies suggest that snow-covered mountainous regions are experiencing accelerated warming near the zero-degree isotherm due to the snow/ice-albedo feedback (Pepin and Lundquist, 2008; Rangwala and Miller, 2012; Pepin et al., 2015). Factors like this may enhance glacier melt as temperatures increase.

Due to sparse climatological observations, precipitation data is largely modeled for the region and the trend is less clear. Reanalysis data shows that no significant change in precipitation has occurred from 1960–1999 (Rasmussen et al., 2007) or 1979–2017 (Braun et al., 2019), which suggests changes in the amount of precipitation are not likely the dominant driver of mass loss in the region. However, reanalysis data is poorly informed at high elevations due to very sparse observations and coarse spatial resolutions (Lanaerts et al., 2014; Condom et al., 2020). For example, ERA-interim, used in the analysis by Braun et al. (2019), has a horizontal resolution of 80 km (Condom et al., 2020). The width of the NPI and SPI is more narrow than this horizontal resolution in some areas, and the icefields also experience an enormous precipitation gradient from west-east (exceeds 10 m w.e. yr^{-1} on the west side and is near 1 m w.e. yr^{-1} to the east) (Lanaerts et al., 2014). Lanaerts et al. (2014) addressed the coarseness of reanalysis products by downscaling ERA-interim to 5.5 km 1979–2012 and observed upward trending, yet insignificant, precipitation with large interannual variability. Downscaling of reanalysis products over the NPI by Schaefer et al. (2013) also found a slight increasing precipitation trend over the NPI from 1975–1990 to 1990–2011. Although the overall precipitation trend is unclear, increased temperatures may cause a change in the state of precipitation that does fall. In the 1960–1999 period, Rasmussen et al. (2007) quantified warming of 0.5°C over the icefields, which translates to 5% of solid precipitation changing to rain. This estimate is also derived from reanalysis data and may vary significantly according to longitude and altitude, but it provides an example of how warming temperatures may affect precipitation in the region.

Although the NPI and SPI are adjacent to each other, they have slightly differing climates. According to a cluster analysis done by Sagredo and Lowell (2012), the NPI receives most precipitation during the winter months, and the SPI receives constant precipitation throughout the year, including more summer precipitation. This difference in climate could result in the SPI having different sensitivity to changes in temperature and precipitation than the NPI. In particular, glaciers that receive significant summer accumulation are much more sensitive to changes in temperature through surface albedo feedbacks (e.g., Johnson and Rupper, 2020). While somewhat speculative, the precipitation seasonality difference between NPI and SPI may point to one mechanism giving rise to SPI losing mass faster than NPI.

While there are large-scale shifts in mass balance across the region that are likely explained by shifts in climate (e.g., differences in average mass balance between SPI and NPI, differences in average mass balance over time), mass balance changes are spatially heterogeneous within these regions. This spatial heterogeneity is likely driven by variable topographic settings, glacier morphology, and terminus conditions that modulate the individual glacier response to regional-scale climate perturbations.

4.2 Spatial Patterns in Geodetic Mass Balance

4.2.1 Terminus Environment

Geodetic mass balance does not distinguish between mass balance processes. For example, we do not distinguish mass loss due to increased surface melt, calving, or subaqueous melt. However, these processes vary significantly between lake, marine, and land-terminating glaciers. We find lake-terminating glaciers to have the most negative geodetic mass balance in the modern time period. This group of glaciers also has the greatest magnitude of change in their average geodetic mass balance between the two time periods (**Table 4**). Increased retreat for lake-terminating glaciers in the NPI has been attributed to glacial lake development and expansion in other studies (Loriaux and Casassa, 2013; Glasser, 2016). This result also agrees with Falaschi et al. (2019), who found the highest thinning rates among lake-terminating glaciers from 2000–2012 on the eastern flanks of the SPI and in mountain ranges directly east of the icefields. Additionally, our results compare favorably with studies from other regions in the world: Maurer et al. (2019), Sutherland et al. (2020), and Larsen et al. (2007) highlight the phenomenon that lake-terminating glaciers in the Himalayas, New Zealand, and Alaska lose mass faster than land-terminating glaciers due to proglacial lake-enhanced frontal ablation. In our "overlap" aggregations, about half of NPI glaciers are calving. For the SPI, more than half of the glaciers measured are calving, which may be a driver for more negative regional mass balance in the SPI. Modeling studies in the region also support the idea that frontal ablation accounts for a disproportionate amount of mass loss in the icefields. Schaefer et al. (2013) modeled surface mass balance for the NPI and quantified a doubling of calving activity from 1975–2000 to 2000–2009, indicating an acceleration of mass loss from frontal ablation mechanisms over time. Schaefer et al. (2015) used similar methodology for the SPI and found that calving losses also increased for the SPI from 1975–2000 to 2000–2011, and that calving influences more mass loss than melt. Both Bravo et al. (2019) and Schaefer et al. (2015) modeled positive surface

mass balance over the SPI (1975–2040 and 1975–2011, respectively), and suggested that mass losses from frontal ablation dominate the observed highly negative geodetic mass balance signal. While these modeling studies do not distinguish between lake- and marine-terminating glaciers, they do illustrate the importance of ablation mechanisms that occur at the ice-water interface.

A notable observation from the geodetic mass balance results is that marine-terminating glaciers have the most variability in mass changes. While several marine-terminating glaciers experience the highest rates of mass loss, many have small magnitudes of mass change or are slightly positive (**Figure 5**). Subaqueous melt, frontal calving, and sedimentation, as well as surface processes, influence tidewater glaciers. Because of this, they can act anomalously when compared to their land-terminating and freshwater-calving counterparts and appear out of sync with regional climatic forces (Truffer and Motyka, 2016; Brinkerhoff et al., 2017). Long periods of advancement and rapid retreat characterize a tidewater glacier cycle (TGC) (McNabb and Hock, 2014). The period of advancement occurs when the glacier deposits eroded sediments in a proglacial shoal, limiting the glacier's interaction with the ocean water (Motyka et al., 2006). Where the glacier becomes ungrounded from the shoal, it becomes exposed to deep water and associated calving and thermal undercutting processes, resulting in rapid retreat uninfluenced by climate (although climate perturbations may exacerbate the retreat) (Meier and Post, 1987; Motyka et al., 2006; Brinkerhoff et al., 2017). Taku glacier in Alaska is a well-documented glacier currently undergoing advancements as part of the TGC (Motyka et al., 2006; McNeil et al., 2020). Over 1946–2018, McNeil et al. (2020) found that while Taku was steadily advancing, nearby land-terminating Lemon Creek has been retreating amidst the same regional climate. In our dataset, it is likely Pio XI is in the advancing stage of the TGC (its geodetic mass balance estimates are 0.82 ± 0.09 m w.e. yr^{-1} in 1976–2000 and 0.26 ± 0.04 m w.e. yr^{-1} in 2000–2020). Observations of rapid retreat at marine-terminating Columbia glacier in Alaska (Meier and Post, 1987; Pfeffer, 2007) provide insight as to the future of Pio XI. Enderlin et al. (2013) describe how the outlet valley geometry primarily influences the quality of retreat. Recent studies highlight the importance of studying the glacier dynamics and fjord bathymetry of Pio XI (Wilson et al., 2016; Hata and Sugiyama, 2021).

An unnamed tidewater glacier (RGI60-17.04995) displays extremely high mass loss rates in the historical period (-7.62 ± 0.83 m w.e. yr^{-1}) and is close to zero in the modern time period (0.12 ± 0.21 m w.e. yr^{-1}). Upon further inspection, this is a confluence of several glaciers defined as one glacier by RGI 6.0 (**Supplementary Figure S6**). Our estimate is therefore an average of several individual glaciers here. Nonetheless, this highly negative estimate is likely due to rapid retreat in the historical period when the glacier system became disconnected from the fjord and the associated dynamics. Across the fjord from this glacier, HPS-12 (-2.32 ± 0.25 m w.e. yr^{-1} in 1976–2000 and -3.23 ± 0.35 m w.e. yr^{-1} in 2000–2020) is likely affected by the same mechanisms that caused rapid retreat for the RGI60-17.04995 confluence.

An additional factor to consider for marine-terminating glaciers is their connection with the ocean. Although Jorge Montt does not have a geodetic mass balance estimate for the historical time period, we can infer from the elevation change map that it was thinning rapidly (**Figure 4A**). The 2000–2020 estimate for Jorge Montt is -3.94 ± 0.39 m w.e. yr^{-1}. This glacier is well-connected to the ocean, whereas RGI60-17.04995 and HPS-12 are deeper in the fjords. Tempano glacier is also highly negative but is close to the ocean, like Jorge Montt. Farther south, HPS-31 and HPS-34 are similarly deep into the fjords but undergo small magnitudes of mass change. These results suggest that depth into the fjords and connection with the ocean may not be the most important determinants of geodetic mass balance.

It is important to note that not only tidewater glaciers display contrasting behavior. Perito Moreno, a lake-terminating glacier on the eastern side of the SPI, has a geodetic mass balance notably close to zero in both time periods. This is in contrast to nearby Tyndall glacier, which is highly negative. In the NPI, Nef and HPN-1 are both lake-terminating in 2000–2020, yet HPN-1 is thinning faster (**Figures 3B,C**). At the northern tip of the SPI (around 48.5°S in **Figure 6A**), some small, land-terminating glaciers in close proximity to each other exhibit contrasting behavior. Some have become more positive in the 21st century, while others have become more negative. Nearly all larger, lake-terminating glaciers of this area appear to have become more negative in the 21st century.

4.2.2 Position Relative to Ice Divide

Because the distribution of these glacier types is not balanced between the east and west sides of the icefields, this can lead to regionally different mass balances. In particular, there are more lake-terminating glaciers east of the divide, while only the west side of the divide has marine-terminating glaciers. Histograms of eastern versus western glaciers (**Figure 7**) reveal that eastern, lake-terminating glaciers of the SPI have experienced the most rapid thinning over the observed timespan leading to greater regional mass loss east of the divide. West of the ice divide, lake-terminating glaciers account for one third of the glaciers, as compared to half for east of the divide (**Table 4**). Eastern SPI glaciers also have larger ablation zones than their western counterparts, which would also lead to greater mass loss as compared to glaciers in the western SPI (**Figure 4**). These results are broadly consistent with previous work. Willis et al. (2012a) and Willis et al. (2012b) use SRTM and ASTER to calculate elevation and volume changes of the icefields and show that from 2000–2012, 40% of the SPI volume loss is derived from eastern lake-terminating glaciers retreat. Willis et al. (2012a) find that NPI western glaciers are thinning rapidly from 2000–2011 and hypothesize that this is due to their lower elevation. While we do not claim that western NPI glaciers are thinning more rapidly than eastern, we do observe rapid

thinning in elevation change maps for this group over 2000–2020 (**Figure 3C**).

4.3 Spatial Patterns in Elevation Change

While we linearly interpolate elevation bins, assume zero change at the highest and lowest elevation bins, and only use glaciers that had 50% valid data coverage in their areas to calculate geodetic mass balance, many glaciers are lacking most elevation data in their accumulation zones, especially for the historical period. This is a well-documented problem with DEMs in snow-covered areas: the inability to extract elevation data well over low-contrast, featureless accumulation zones (Dussaillant et al., 2019; Maurer et al., 2019). These data voids in accumulation zones introduce additional uncertainty in geodetic mass balance. For glaciers where the Hexagon DEM is successfully extracted at high elevations, notably glaciers in the northern SPI, it is possible that the values are not accurate (blue-colored accumulation zones in **Figure 4A**). In order for the elevations in the accumulation zones to increase over the time period, while the ablation zones are rapidly thinning, accumulation must be large enough to more than offset any increase in ice flux down-glacier. Since there is no strong evidence of precipitation increasing 1976–2000, this DEM extraction method is likely overestimating thickening in accumulation zones, and we are likely underestimating geodetic mass balance in the historical time period. For the modern time period, the observed thickening in accumulation zones is more plausible. Although there are still issues with extracting elevation data in the accumulation zones using modern imagery, we calculate the elevation trend using multiple DEMs, which decreases uncertainty. Additionally, some evidence does point to an increase in precipitation over the icefields, as discussed above. However, in order for thickening to occur in the accumulation zones, it would have to exceed dynamic thinning in response to mass loss in the lower elevations. Lack of climatological observations is a pervasive issue in this region and makes it particularly difficult to objectively assess the elevation change reconstructions over the accumulation zones. However, we do note that there is a distinct probability that geodetic mass balance estimates in this region may be underestimated due to potential positive elevation-change biases in the accumulation zones in some regions of the icefields.

4.4 Spatial Coverage

While the spatial coverage of the overlapping data (2000–2020 overlap in **Table 3**) was 63% for the NPI, the geodetic mass balance did not differ much from the 2000–2020 geodetic mass balance representing 100% of the area (2000–2020 all in **Table 3**). The spatial coverage is 52% of the total area in the SPI for the overlapping data. For this smaller area, the 2000–2020 geodetic mass balance was much less negative than the 2000–2020 geodetic mass balance for 97% of the area. Thus, a subset of glaciers can represent the entire region in some cases (NPI) but not in all (SPI). The historical geodetic mass balance estimate for 63% of the NPI glacierized area likely represents the average geodetic mass balance for the full NPI region. In contrast, with this sample set, the historical estimate for 52% of the SPI is probably biased less negative than the historical mass balance for the full SPI, as the small glaciers do not appear to be representative of the region. Even at a more local scale, our results show that geodetic mass balance can be extremely spatially heterogeneous (e.g., northern tip of SPI). These results strongly suggest it is not always appropriate to use the regional average mass balance to fill in missing glaciers in order to estimate mass balance or sea-level rise contributions for the full glacierized region, as is done by comparable studies (e.g., Dussaillant et al., 2019).

4.5 Regional Versus Glacier-Specific Thresholds

Manipulating processing thresholds, such as maximum allowed standard deviation in an elevation trend, can greatly affect results. While tailoring these parameters for individual glaciers is not feasible at a regional scale, we do additional processing for select glaciers. For several marine- and lake-terminating glaciers, the standard deviation of the elevation trend was allowed to exceed 50 m, to account for non-linear behavior at their termini (**Table 2**). Although we set the limit to 50 m for the majority of the icefields, several large, calving glaciers are subject to real, irregular behavior on their termini, which would be excluded with a threshold of 50 m. The new thresholds for these glaciers were determined by inspecting the greatest realistic standard deviation values of the elevation trends, before any cleanup of the trend maps (these figures are provided in **Supplementary Figure S2**). While this does introduce extra noise in the data, we find this has minimal impact on the geodetic mass balance uncertainties. Importantly, the increased threshold captures substantial nonlinear termini behavior, which should be included in the elevation trends. Increasing the maximum allowed standard deviation in the elevation trend from 50 m to 150 m for the Jorge Montt glacier increases the data coverage by 23%, and the resulting geodetic mass balance measurement becomes significantly more negative. Three glaciers of the NPI (Acodado, Steffen, and Fiero), only have their data coverage increase by 0%–1% with the increased standard deviation from 50–100 m, and their resulting geodetic mass balance measurements become less negative. This result could be due to a decrease in interpolation occurring at the termini. In contrast, a medium-sized marine-terminating glacier of the SPI, HPS-12, which is currently losing mass at significantly fast rates, gains only 5% more data coverage by including elevation trends up to a standard deviation of 200 m, but its geodetic mass balance estimate becomes more negative by nearly three-fold. Thresholds have a variable impact on the resulting geodetic mass balance, but for glaciers with known nonlinear terminus mass loss behavior, imposing regional thresholds is likely inappropriate and can significantly impact the geodetic mass balance calculations.

4.6 Comparison With Other Observations

Our geodetic mass balance estimates for the NPI and SPI sensu stricto agree with those provided by Dussaillant et al. (2019) for post-2000 (**Figures 9A,B**; **Supplementary Table S2**). Our estimate for the NPI is slightly less negative than Jaber et al.

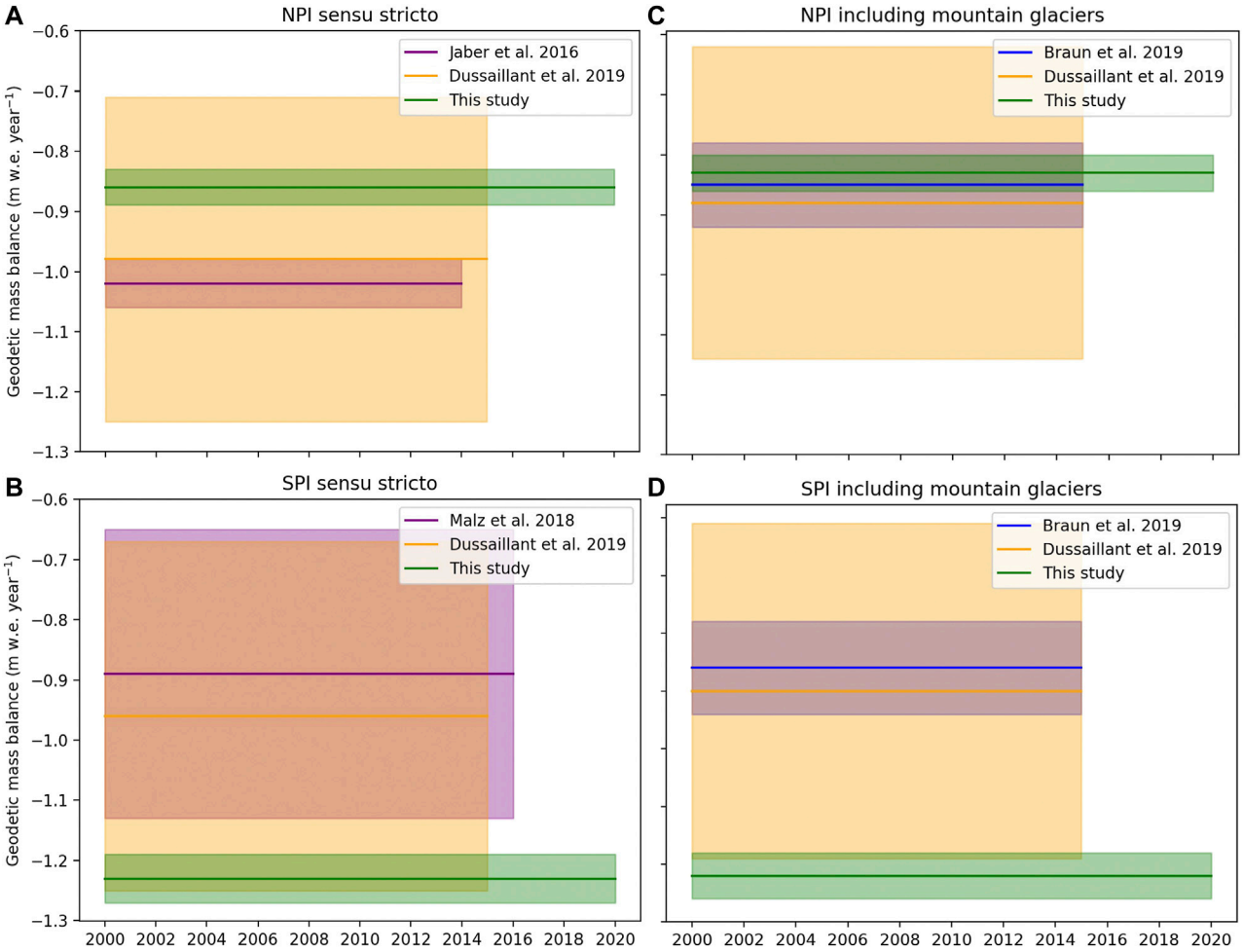

FIGURE 9 | Our regional area-weighted geodetic mass balance estimates for the icefields sensu stricto **(A,B)** and the icefields plus surrounding mountain glaciers **(C,D)** compared to other recent studies.

(2016) for the NPI, and our estimate for the SPI is more negative than the value provided by Malz et al. (2018). When mountain glaciers are included (**Figures 9C,D**; **Supplementary Tables S1, S2**), our estimates agree with both Braun et al. (2019) and Dussaillant et al. (2019) for the NPI. For the SPI, our estimate is more negative than those studies. Several factors may influence these differences. First, our estimate extends that of other studies by 5–6 years, representing ~25% increase in temporal coverage. Given the relatively short observation period, these additional years could significantly impact the results. In addition, our methodology and data are different from Jaber et al. (2016) and Malz et al. (2018), who both utilize SRTM and TanDEM-X to find an elevation change over the icefields. We utilize the NASADEM (which is based on SRTM) and ASTER stack to fit an elevation trend. This is similar to the approach utilized by Dussaillant et al. (2019), who fit a linear regression to a stack of ASTER DEMs, plus SRTM for glaciers south of 48°S. However, we use RANSAC to fit an elevation trend rather than a linear regression. The total areas used also differ slightly between ours and other studies. Additionally, Dussaillant et al. (2019) and Jaber et al. (2016) do not consider areal changes in their geodetic mass balance calculation, whereas in our method we use the average glacier area over the timespan from the manual delineation of time-specific glacier inventories. Glaciers included in our estimate also required more stringent data coverage thresholds, using only glaciers with greater than 50% valid elevation data in the geodetic mass balance estimate. Dussaillant et al. (2019) include all glaciers except for those with mass balance uncertainty of greater than 1 m w.e. yr^{-1} and less than 20% data coverage. They also replace those excluded glaciers with the regional mean, which our work demonstrates may not be appropriate in some regions of the Patagonian Icefields, as proximal glaciers may exhibit quite different mass balance trends.

The following studies did not publish mass balance estimates in m w.e. yr^{-1}, which precludes including them in the direct comparisons above and in **Figure 9**. However, we convert our mass balance values to Gt yr^{-1} in order to provide another set of comparisons. A recent study by Hugonnet et al. (2021) estimated a mass loss rate of −18.7 Gt yr^{-1} for the southern region of the

Southern Andes, containing the icefields. Our work focuses on a subset of that same region and shows the combined icefields mass loss was -17.51 ± 1.32 Gt yr^{-1} for 2000–2020. Together, these results imply that the icefields make up the bulk of this region's ice loss. Willis et al. (2012b) provide a combined NPI and SPI mass loss from 2000–2012 of -24.4 ± 1.4 Gt yr^{-1}. This is a significantly larger mass loss estimate than ours. Willis et al. (2012b) use a density assumption of 900 kg m^{-3}, which could account for part of the discrepancy between our results and theirs. However, their results are over a much shorter time span, which may be prone to greater influence of interannual variability. Cirací et al. (2020) also estimate a greater mass loss than our results. They estimate 28 ± 6 Gt yr^{-1} mass loss for both icefields 2002–2019, derived from Gravity Recovery and Climate Experiment (GRACE) measurements. According to Dussaillant et al. (2019), glacial isostatic adjustment in the region likely leads to overestimation of ice loss from GRACE and Velicogna and Wahr (2013) discuss the poor horizontal resolution of GRACE as a limitation of the methodology. Thus, GRACE may be overestimating the magnitude of geodetic mass balance in the region. However, our results may also be underestimating mass loss due to issues extracting accurate elevations in the accumulations zones, as discussed in **Section 4.1**. The comparisons between the differing studies highlights both the utility of geodetic mass balance estimates as well as remaining issues. Comparisons across different regions and time spans make it difficult to directly assess why differences emerge but also points to the importance of potentially combining different methods in order to circumvent the limitations of any single approach.

5 CONCLUSION

Geodetic mass balance measurements of −0.86 ± 0.03 m w.e. yr^{-1} for the NPI and −1.23 ± 0.04 m w.e. yr^{-1} for the SPI agree with recently published estimates for the 2000–2020 observation period. While the results for the historical period over the NPI are likely representative of the full NPI region, the historical mass balance estimates for the SPI are biased towards the behavior of smaller glaciers for the SPI due to poor data coverage over significant portions of the largest glaciers in the region, which precludes extrapolating the results to the full region. We therefore focus comparisons between the historical and modern periods on glaciers with overlapping data for both periods, which includes 63% of the area of the NPI and 52% of the are for the SPI. For these reduced regions, the negative geodetic mass balance increased by a factor of 1.2 for the NPI and 2.4 for the SPI from 1976/1979–2000 to 2000–2020. Increased warming in the region is likely the dominant driver of increased mass loss over the historical and modern periods. In our dataset, more glaciers are lake-terminating in the SPI than the NPI which likely results in the more negative SPI estimates. Greater intensification of mass loss in the SPI could also be related to a slightly differing mean climate farther south, where glaciers receive year-round precipitation, in contrast to the NPI where winter precipitation dominates. These differences in mean climate can result in different mass balance sensitivity and feedback processes in response to climate change.

There is significant spatial heterogeneity in geodetic mass balance across both NPI and SPI and across both time periods. Capturing that spatial heterogeneity accurately may require glacier-specific processing techniques, especially for calving glaciers. This study looks in detail at the effect of glacier terminus type on geodetic mass balance and finds that lake-terminating glaciers exhibit the highest acceleration of mass loss rate since the 1970s, and on average have the most negative 2000–2020 values. In the modern time period, distributions of geodetic mass balance for glaciers with different terminus environments, and eastern versus western glaciers in the SPI, are statistically unique. Extreme heterogeneity in geodetic mass balance, especially among calving glaciers complicates projections of sea-level rise from this region of the world.

DATA AVAILABILITY STATEMENT

The datasets presented in this study can be found in online repositories. The names of the repository/repositories and accession number(s) can be found below: https://github.com/morgan-mcdonnell/patagonia-gmb.

AUTHOR CONTRIBUTIONS

MM processed and analyzed the data, produced all figures, and wrote the manuscript. SR conceived of the study. SR and RF provided feedback on data analysis, results and writing. All authors provided feedback and edits on the manuscript.

FUNDING

This project was funded by NSF Award Number 1853881 awarded to SR and RF.

ACKNOWLEDGMENTS

We thank Simon Brewer for feedback on statistical analyses and Josh Maurer for help accessing and running HEXIMAP. We also acknowledge CHPC at the University of Utah for their installation and maintenance of software required for this research.

SUPPLEMENTARY MATERIAL

The Supplementary Material for this article can be found online at: https://www.frontiersin.org/articles/10.3389/feart.2022.813574/full#supplementary-material

REFERENCES

Abdel Jaber, W., Rott, H., Floricioiu, D., Wuite, J., and Miranda, N. (2019). Heterogeneous Spatial and Temporal Pattern of Surface Elevation Change and Mass Balance of the Patagonian Ice fields between 2000 and 2016. *The Cryosphere.* 13 (9), 2511–2535. doi:10.5194/tc-13-2511-2019

Bamber, J. L., Westaway, R. M., Marzeion, B., and Wouters, B. (2018). The Land Ice Contribution to Sea Level during the Satellite Era. *Environ. Res. Lett.* 13, 063008. doi:10.1088/1748-9326/aac2f0

Belart, J. M. C., Magnússon, E., Berthier, E., Pálsson, F., Aðalgeirsdóttir, G., and Jóhannesson, T. (2019). The Geodetic Mass Balance of Eyjafjallajökull Ice Cap for 1945-2014: Processing Guidelines and Relation to Climate. *J. Glaciol.* 65, 395–409. doi:10.1017/jog.2019.16

Bhattacharya, A., Bolch, T., Mukherjee, K., King, O., Menounos, B., Kapitsa, V., et al. (2021). High Mountain Asian Glacier Response to Climate Revealed by Multi-Temporal Satellite Observations since the 1960s. *Nat. Commun.* 12 (1), 1–13. doi:10.1038/s41467-021-24180-y

Braun, M. H., Malz, P., Sommer, C., Farías-Barahona, D., Sauter, T., Casassa, G., et al. (2019). Constraining Glacier Elevation and Mass Changes in South America. *Nat. Clim Change* 9 (2), 130–136. doi:10.1038/s41558-018-0375-7

Bravo, C., Bozkurt, D., Ross, A. N., and Quincey, D. J. (2019). Projected Increases in Surface Melt and Ice Loss for the Northern and Southern Patagonian Icefields. *Scientific Rep.* 11 (1), 1–13. doi:10.1038/s41598-021-95725-w2

Brinkerhoff, D., Truffer, M., and Aschwanden, A. (2017). Sediment Transport Drives Tidewater Glacier Periodicity. *Nat. Commun.* 8, 90. doi:10.1038/s41467-017-00095-5

Ciracì, E., Velicogna, I., and Swenson, S. (2020). Continuity of the Mass Loss of the World's Glaciers and Ice Caps From the GRACE and GRACE Follow-On Missions. *Geophys. Res. Lett.* 47 (9), 1–11. doi:10.1029/2019GL086926

Cogley, J. G. (2012). Area of the Ocean. *Mar. Geodesy* 35, 379–388. doi:10.1080/01490419.2012.709476

Condom, T., Martínez, R., Pabón, J. D., Costa, F., Pineda, L., Nieto, J. J., et al. (2020). Climatological and Hydrological Observations for the South American Andes: *In Situ* Stations, Satellite, and Reanalysis Data Sets. *Front. Earth Sci.* 8, 92. doi:10.3389/feart.2020.00092

Davis, C. H., and Poznyak, V. I. (1993). The Depth of Penetration in Antarctic Firn at 10 GHz. *IEEE Trans. Geosci. Remote Sensing.* 31 (5), 1107–1111. doi:10.1109/36.263784

Dehecq, A., Gardner, A. S., Alexandrov, O., McMichael, S., Hugonnet, R., Shean, D., et al. (2020). Automated Processing of Declassified KH-9 Hexagon Satellite Images for Global Elevation Change Analysis since the 1970s. *Front. Earth Sci.* 8, 566802. doi:10.3389/feart.2020.566802

Dussaillant, I., Berthier, E., and Brun, F. (2018). Geodetic Mass Balance of the Northern Patagonian Icefield from 2000 to 2012 Using Two Independent Methods. *Front. Earth Sci.* 6, 8. doi:10.3389/feart.2018.00008

Dussaillant, I., Berthier, E., Brun, F., Masiokas, M., Hugonnet, R., Favier, V., et al. (2019). Two Decades of Glacier Mass Loss along the Andes. *Nat. Geosci.* 12 (10), 802–808. doi:10.1038/s41561-019-0432-5

Enderlin, E. M., Howat, I. M., and Vieli, A. (2013). High Sensitivity of Tidewater Outlet Glacier Dynamics to Shape. *The Cryosphere.* 7 (3), 1007–1015. doi:10.5194/tc-7-1007-2013

European Space Agency (2020). Copernicus DEM (GLO-30) [Data Set]. Available at: https://panda.copernicus.eu/web/cds-catalogue/panda.

Falaschi, D., Lenzano, M. G., Villalba, R., Bolch, T., Rivera, A., and Lo Vecchio, A. (2019). Six Decades (1958-2018) of Geodetic Glacier Mass Balance in Monte San Lorenzo, Patagonian Andes. *Front. Earth Sci.* 7, 326. doi:10.3389/feart.2019.00326

Foresta, L., Gourmelen, N., Weissgerber, F., Nienow, P., Williams, J. J., Shepherd, A., et al. (2018). Heterogeneous and Rapid Ice Loss over the Patagonian Ice Fields Revealed by CryoSat-2 Swath Radar Altimetry. *Remote Sensing Environ.* 211, 441–455. doi:10.1016/j.rse.2018.03.041

Gardelle, J., Berthier, E., and Arnaud, Y. (2012). Impact of Resolution and Radar Penetration on Glacier Elevation Changes Computed from DEM Differencing. *J. Glaciol.* 58 (208), 419–422. doi:10.3189/2012JoG11J175

Glasser, N. F., Holt, T. O., Evans, Z. D., Davies, B. J., Pelto, M., and Harrison, S. (2016). Recent Spatial and Temporal Variations in Debris Cover on Patagonian Glaciers. *Geomorphology* 273, 202–216. doi:10.1016/j.geomorph.2016.07.036

Hata, S., and Sugiyama, S. (2021). Changes in the Ice-Front Position and Surface Elevation of Glaciar Pío XI, an Advancing Calving Glacier in the Southern Patagonia Icefield, From 2000-2018. *Front. Earth Sci.* 8, 576044. doi:10.3389/feart.2020.576044

Hock, R., Rasul, J., Adler, C., Cáceres, B., Gruber, S., Hirabayashi, Y., et al. (2019). "High Mountain Areas," in *IPCC Special Report on the Ocean and Cryosphere in a Changing Climate*. Editor H. O. Pörtner. In press.

Holzer, N., Vijay, S., Yao, T., Xu, B., Buchroithner, M., and Bolch, T. (2015). Four Decades of Glacier Variations at Muztagh Ata (Eastern Pamir): a Multi-Sensor Study Including Hexagon KH-9 and Pléiades Data. *The Cryosphere.* 9, 2071. doi:10.5194/tc-9-2071-2015

Hugonnet, R., McNabb, R., Berthier, E., Menounos, B., Nuth, C., Girod, L., et al. (2021). Accelerated Global Glacier Mass Loss in the Early Twenty-First century. *Nature.* 592 (7856), 726–731. doi:10.1038/s41586-021-03436-z

Huss, M. (2013). Density Assumptions for Converting Geodetic Glacier Volume Change to Mass Change. *The Cryosphere.* 7 (3), 877–887. doi:10.5194/tc-7-877-2013

Jaber, W. A., Floricioiu, D., and Helmut, R. (2016). "Geodetic Mass Balance of the Patagonian Icefields Derived from SRTM and TanDEM-X Data," in Paper presented at 2016 IEEE International Geoscience and Remote Sensing Symposium (Beijing, China: IGARSS). doi:10.1109/igarss.2016.7729082

Johnson, E., and Rupper, S. (2020). An Examination of Physical Processes that Trigger the Albedo-Feedback on Glacier Surfaces and Implications for Regional Glacier Mass Balance across High Mountain Asia. *Front. Earth Sci.* 8, 129. doi:10.3389/feart.2020.00129

King, O., Bhattacharya, A., Bhambri, R., Bolch, T., Meier, W., Casassa, G., et al. (2019). Glacial Lakes Exacerbate Himalayan Glacier Mass lossElevation and Mass Changes of the Southern Patagonia Icefield Derived from TanDEM-X and SRTM Data. *Sci. Rep.Remote Sensing.* 910 (2), 18145188. doi:10.1038/s41598-019-53733-x

King, O., Bhattacharya, A., Ghuffar, S., Tait, A., Guilford, S., Elmore, A. C., et al. (2020). Six Decades of Glacier Mass Changes Around Mt. Everest Are Revealed by Historical and Contemporary Images. *One Earth.* 3 (5), 608–620. doi:10.1016/j.oneear.2020.10.019

Koppes, M., Conway, H., Rasmussen, L. A., and Chernos, M. (2011). Deriving Mass Balance and Calving Variations from Reanalysis Data and Sparse Observations, Glaciar San Rafael, Northern Patagonia, 1950-2005. *The Cryosphere.* 5 (3), 791–808. doi:10.5194/tc-5-791-2011

Lamsal, D., Fujita, K., and Sakai, A. (2017). Surface Lowering of the Debris-Covered Area of Kanchenjunga Glacier in the Eastern Nepal Himalaya since 1975, as Revealed by Hexagon KH-9 and ALOS Satellite Observations. *The Cryosphere.* 11, 2815–2827. doi:10.5194/tc-11-2815-2017

Larsen, C. F., Motyka, R. J., Arendt, A. A., Echelmeyer, K. A., and Geissler, P. E. (2007). Glacier Changes in Southeast Alaska and Northwest British Columbia and Contribution to Sea Level Rise. *J. Geophys. Res.* 112 (F1), F01007. doi:10.1029/2006JF000586

Lenaerts, J. T. M., van den Broeke, M. R., van Wessem, J. M., van de Berg, W. J., van Meijgaard, E., van Ulft, L. H., et al. (2014). Extreme Precipitation and Climate Gradients in Patagonia Revealed by High-Resolution Regional Atmospheric Climate Modeling. *J. Clim.* 27 (12), 4607–4621. doi:10.1175/JCLI-D-13-00579.1

Loriaux, T., and Casassa, G. (2013). Evolution of Glacial Lakes from the Northern Patagonia Icefield and Terrestrial Water Storage in a Sea-Level Rise Context. *Glob. Planet. Change.* 102, 33–40. doi:10.1016/j.gloplacha.2012.12.012

Malz, P., Meier, W., Casassa, G., Jaña, R., Skvarca, P., and Braun, M. (2018). Elevation and Mass Changes of the Southern Patagonia Icefield Derived from TanDEM-X and SRTM Data. *Remote Sensing.* 10 (2), 188–217. doi:10.3390/rs10020188

Martinez-Camara, M., Béjar Haro, B., Stohl, A., and Vetterli, M. (2014). A Robust Method for Inverse Transport Modeling of Atmospheric Emissions Using Blind Outlier Detection. *Geosci. Model. Dev.* 7 (3), 2303–2311. doi:10.5194/gmd-7-2303-2014

Maurer, J. M., Rupper, S. B., and Schaefer, J. M. (2016). Quantifying Ice Loss in the Eastern Himalayas since 1974 Using Declassified Spy Satellite Imagery. *The Cryosphere.* 10 (5), 2203–2215. doi:10.5194/tc-10-2203-2016

Maurer, J. M., Schaefer, J. M., Rupper, S., and Corley, A. (2019). Acceleration of Ice Loss across the Himalayas over the Past 40 Years. *Sci. Adv.* 5 (6), eaav7266. doi:10.1126/sciadv.aav7266

Maurer, J., and Rupper, S. (2015). Tapping into the Hexagon Spy Imagery Database: A New Automated Pipeline for Geomorphic Change Detection. *ISPRS J. Photogrammetry Remote Sensing.* 108, 113–127. doi:10.1016/j.isprsjprs.2015.06.008

McNabb, R. W., and Hock, R. (2014). Alaska Tidewater Glacier Terminus Positions, 1948-2012. *J. Geophys. Res. Earth Surf.* 119 (2), 153–167. doi:10.1002/2013JF002915

McNeil, C., O'Neel, S., Loso, M., Pelto, M., Sass, L., Baker, E. H., et al. (2020). Explaining Mass Balance and Retreat Dichotomies at Taku and Lemon Creek Glaciers, Alaska. *J. Glaciol.* 66 (258), 530–542. doi:10.1017/jog.2020.22

Meier, M. F., and Post, A. (1987). Fast Tidewater Glaciers. *J. Geophys. Res.* 92 (B9), 9051–9058. doi:10.1029/JB092iB09p09051

Meier, W. J.-H., Grießinger, J., Hochreuther, P., Braun, M. H., and Braun, M. H. (2018). An Updated Multi-Temporal Glacier Inventory for the Patagonian Andes with Changes between the Little Ice Age and 2016. *Front. Earth Sci.* 6, 62. doi:10.3389/feart.2018.00062

Minowa, M., Schaefer, M., Sugiyama, S., Sakakibara, D., and Skvarca, P. (2021). Frontal Ablation and Mass Loss of the Patagonian Icefields. *Earth Planet. Sci. Lett.* 561, 116811. doi:10.1016/j.epsl.2021.116811

Motyka, R. J., Truffer, M., Kuriger, E. M., and Bucki, A. K. (2006). Rapid Erosion of Soft Sediments by Tidewater Glacier advance: Taku Glacier, Alaska, USA. *Geophys. Res. Lett.* 33 (24), L24504. doi:10.1029/2006GL028467

NASA JPL (2004). ASTER: Advanced Spaceborne thermal Emission and Reflection Radiometer. Available at: https://asterweb.jpl.nasa.gov/.

NASA JPL (2020). NASADEM Merged DEM Global 1 Arc-Second (001) [Data Set]. Available at: https://search.earthdata.nasa.gov/search.

NASA, METI, AIST (2019). Japan Spacesystems, and U.S./Japan ASTER Science Team. ASTER GDEM product [Data set]Available at: https://gbank.gsj.jp/madas/map/.

NOAA (2021). Global Climate Report - Annual 2020. Available at: https://www.ncdc.noaa.gov/sotc/global/202013.

Nuth, C., and Kääb, A. (2011). Co-registration and Bias Corrections of Satellite Elevation Data Sets for Quantifying Glacier Thickness Change. *The Cryosphere.* 5, 271–290. doi:10.5194/tc-5-271-2011

Pellicciotti, F., Stephan, C., Miles, E., Herreid, S., Immerzeel, W. W., and Bolch, T. (2015). Mass-balance Changes of the Debris-Covered Glaciers in the Langtang Himal, Nepal, from 1974 to 1999. *J. Glaciol.* 61 (226), 373–386. doi:10.3189/2015jog13j237

Pepin, N., Bradley, R. S., Diaz, H. F., Baraer, M., Caceres, E. B., Forsythe, N., et al. (2015). Elevation-dependent Warming in Mountain Regions of the World. *Nat. Clim Change.* 5 (5), 424–430. doi:10.1038/NCLIMATE2563

Pepin, N. C., and Lundquist, J. D. (2008). Temperature Trends at High Elevations: Patterns across the globe. *Geophys. Res. Lett.* 35 (14), L14701. doi:10.1029/2008GL034026

Pfeffer, W. T. (2007). A Simple Mechanism for Irreversible Tidewater Glacier Retreat. *J. Geophys. Res.* 112, F03S25. doi:10.1029/2006JF000590

Pfeffer, W. T., Arendt, A. A., Bliss, A., Bolch, T., Cogley, J. G., Gardner, A. S., et al. (2014). The Randolph Glacier Inventory: a Globally Complete Inventory of Glaciers. *J. Glaciol.* 60, 537–552. doi:10.3189/2014JoG13J176

Pieczonka, T., Bolch, T., Junfeng, W., and Shiyin, L. (2013). Heterogeneous Mass Loss of Glaciers in the Aksu-Tarim Catchment (Central Tien Shan) Revealed by 1976 KH-9 Hexagon and 2009 SPOT-5 Stereo Imagery. *Remote Sensing Environ.* 130, 233–244. doi:10.1016/j.rse.2012.11.020

Pieczonka, T., and Bolch, T. (2015). Region-wide Glacier Mass Budgets and Area Changes for the Central Tien Shan between ~1975 and 1999 Using Hexagon KH-9 Imagery. *Glob. Planet. Change.* 128, 1–13. doi:10.1016/j.gloplacha.2014.11.014

Randolph Glacier Inventory Consortium (2017). *Global Land Ice Measurements from Space* Dataset of Global Glacier Outlines: Version 6.0: Technical Report. Colorado, United States: Digital Media. doi:10.7265/N5-RGI-60

Rangwala, I., and Miller, J. R. (2012). Climate Change in Mountains: a Review of Elevation-dependent Warming and its Possible Causes. *Climatic Change.* 114 (3-4), 527–547. doi:10.1007/s10584-012-0419-3

Rasmussen, L. A., Conway, H., and Raymond, C. F. (2007). Influence of Upper Air Conditions on the Patagonia Icefields. *Glob. Planet. Change.* 59 (1-4), 203–216. doi:10.1016/j.gloplacha.2006.11.025

Rignot, E., Rivera, A., and Casassa, G. (2003). Contribution of the Patagonia Icefields of South America to Sea Level Rise. *Science.* 302 (5644), 434–437. doi:10.1126/science.1087393

Rivera, A., Lange, H., Carlos Aravena, J., and Casassa, G. (1997). The 20th-century advance of Glaciar Pio XI, Chilean Patagonia. *Ann. Glaciol.* 24, 66–71. doi:10.1017/s0260305500011952

Sagredo, E. A., and Lowell, T. V. (2012). Climatology of Andean Glaciers: A Framework to Understand Glacier Response to Climate Change. *Glob. Planet. Change.* 86-87, 101–109. doi:10.1016/j.gloplacha.2012.02.010

Schaefer, M., Machguth, H., Falvey, M., and Casassa, G. (2013). Modeling Past and Future Surface Mass Balance of the Northern Patagonia Icefield. *J. Geophys. Res. Earth Surf.* 118 (2), 571–588. doi:10.1002/jgrf.20038

Schaefer, M., Machguth, H., Falvey, M., Casassa, G., and Rignot, E. (2015). Quantifying Mass Balance Processes on the Southern Patagonia Icefield. *The Cryosphere.* 9 (1), 25–35. doi:10.5194/tc-9-25-2015

Shean, D. E., Alexandrov, O., Moratto, Z. M., Smith, B. E., Joughin, I. R., Porter, C., et al. (2016). An Automated, Open-Source Pipeline for Mass Production of Digital Elevation Models (DEMs) from Very-High-Resolution Commercial Stereo Satellite Imagery. *ISPRS J. Photogrammetry Remote Sensing.* 116, 101–117. doi:10.1016/j.isprsjprs.2016.03.012

Sutherland, J. L., Carrivick, J. L., Gandy, N., Shulmeister, J., Quincey, D. J., and Cornford, S. L. (2020). Proglacial Lakes Control Glacier Geometry and Behavior during Recession. *Geophys. Res. Lett.* 47 (19), e2020GL088865. doi:10.1029/2020GL088865

Truffer, M., and Motyka, R. J. (2016). Where Glaciers Meet Water: Subaqueous Melt and its Relevance to Glaciers in Various Settings. *Rev. Geophys.* 54 (1), 220–239. doi:10.1002/2015RG000494

U.S. Geological Survey (2002). KH-9 Hexagon Imagery [Data Set]. Available at: https://earthexplorer.usgs.gov/.

U.S. Geological Survey (2008). Declassified Intelligence Satellite Photographs. *Fact Sheet*, 2008–3054. doi:10.3133/fs20083054

Velicogna, I., and Wahr, J. (2013). Time-variable Gravity Observations of Ice Sheet Mass Balance: Precision and Limitations of the GRACE Satellite Data. *Geophys. Res. Lett.* 40, 3055–3063. doi:10.1002/grl.50527

Willis, M. J., Melkonian, A. K., Pritchard, M. E., and Ramage, J. M. (2012a). Ice Loss Rates at the Northern Patagonian Icefield Derived Using a Decade of Satellite Remote Sensing. *Remote Sensing Environ.* 117, 184–198. doi:10.1016/j.rse.2011.09.017

Willis, M. J., Melkonian, A. K., Pritchard, M. E., and Rivera, A. (2012b). Ice Loss from the Southern Patagonian Ice Field, South America, between 2000 and 2012. *Geophys. Res. Lett.* 39, a–n. doi:10.1029/2012GL053136

Wilson, R., Carrión, D., and Rivera, A. (2016). Detailed Dynamic, Geometric and Supraglacial Moraine Data for Glaciar Pio XI, the Only Surge-type Glacier of the Southern Patagonia Icefield. *Ann. Glaciol.* 57 (73), 119–130. doi:10.1017/aog.2016.32

Zhou, Y., Li, Z., Li, J., Zhao, R., and Ding, X. (2018). Glacier Mass Balance in the Qinghai-Tibet Plateau and its Surroundings from the Mid-1970s to 2000 Based on Hexagon KH-9 and SRTM DEMs. *Remote Sensing Environ.* 210, 96–112. doi:10.1016/j.rse.2018.03.020

Conflict of Interest: The authors declare that the research was conducted in the absence of any commercial or financial relationships that could be construed as a potential conflict of interest.

frontiers | Frontiers in Environmental Science

ORIGINAL RESEARCH
published: 05 April 2022
doi: 10.3389/fenvs.2022.840884

The Recent Relationships Between Andean Ice-Core Dust Record and Madeira River Suspended Sediments on the Wet Season

Rafael S. dos Reis[1], Rafael da Rocha Ribeiro[1], Barbara Delmonte[2], Edson Ramirez[3], Norberto Dani[1], Paul A. Mayewski[4] and Jefferson C. Simões[1,4]**

[1]Centro Polar e Climático, Universidade Federal Do Rio Grande do Sul, Porto Alegre, Brazil, [2]Environmental and Earth Sciences Department, University Milano-Bicocca, Milan, Italy, [3]Instituto de Hidráulica e Hidrología, Universidad Mayor de San Andrés, La Paz, Bolivia, [4]Climate Change Institute, University of Maine, Orono, ME, United States

OPEN ACCESS

Edited by:
Juan-Luis García, Pontificia Universidad Católica de Chile, Chile

Reviewed by:
Ana María Durán-Quesada, University of Costa Rica, Costa Rica
Jan Kavan, Masaryk University, Czechia

***Correspondence:**
Rafael S. dos Reis
sdosreis.rafael@gmail.com
Jefferson C. Simões
jefferson.simoes@ufrgs.br

Specialty section:
This article was submitted to Interdisciplinary Climate Studies, a section of the journal Frontiers in Environmental Science

Received: *21 December 2021*
Accepted: *16 March 2022*
Published: *05 April 2022*

Citation:
Reis RS, da Rocha Ribeiro R, Delmonte B, Ramirez E, Dani N, Mayewski PA and Simões JC (2022) The Recent Relationships Between Andean Ice-Core Dust Record and Madeira River Suspended Sediments on the Wet Season. Front. Environ. Sci. 10:840884. doi: 10.3389/fenvs.2022.840884

Dust particle studies in ice cores from the tropical Andes provide important information about climate dynamics. We investigated dust concentrations from a 22.7 m ice-core recovered from the Quelccaya Ice Cap (QIC) in 2018, representing 14 years of snow accumulation. The dust seasonality signal was still preserved with homogenization of the record due to surface melting and percolation. Using a microparticle counter, we measured the dust concentration from 2 to 60 µm and divided the annual dust concentration into three distinct groups: fine particle percentage (FPP, 2–10 µm), coarse particle percentage (CPP, 10–20 µm), and giant particle percentage (GPP, 20–60 µm). Increased dust was associated with the warm stage of the Pacific Decadal Oscillation index (PDO) after 2013 with significant increases in FPP and a relative decrease in CPP and GPP. There was a positive correlation between PDO and FPP ($r = 0.70$, p-value < 0.005). CPP and GPP were dominant during the mainly PDO cold phase (2003–2012). The FPP increase record occurs during the positive phase of PDO and snow accumulation decrease. We also revealed a potential link between QIC record and Madeira River during the wet season through two relationships: between QIC snow accumulation and runoff during transitional season, QIC dust, and suspended sediments during high-water discharge. The snow accumulation (during September-November) and runoff (during November-January) relationship present similar variability using a time-lag (60 days) while total dust and FPP group are associated with average suspended sediments concentration during February-April. Assessing dust record variability by distinct size groups can help to improve our knowledge of how the Pacific ocean influence dust record in the QIC. In addition, the association of snow accumulation and dust variability with dynamic changes in suspended sediments load and runoff in the Madeira River system demonstrates the potential for future investigation of linkages between QIC record and Amazon basin rivers.

Keywords: ice-core, quelccaya, dust, andes, Amazon

INTRODUCTION

Dust particles, the most abundant aerosol type in the atmosphere, significantly influence climate. This can occur both directly, through scattering and absorption of solar radiation (Kok et al., 2017; Di Biagio et al., 2020), and indirectly, as cloud condensation nuclei and ice nuclei along with biogeochemical cycling of nutrients to marine phytoplankton (Ansmann, 2005; Jickells, 2005; Stevens and Feingold, 2009; Carslaw et al., 2010).

Particles archived in Peruvian ice cores preserve the region's climate history, but insufficient knowledge of their size distribution hinders a better understanding of climate dynamics, which can be retrieved by measuring the absolute levels (*i.e.,* total number), size distribution, and composition. Variability in the particle concentration and size distributions is usually directly correlated with changes in climate dynamics along the ice-core record (Delmonte et al., 2002; Ruth, 2002; Wegner et al., 2015; Delmonte et al., 2017; Li et al., 2019). While absolute concentration depends on many factors (e.g., snow accumulation rate, dust source, and transport processes), the size distribution and relative proportion of particles within a given grain size depends primarily on transport conditions (Delmonte et al., 2004; Delmonte et al., 2017). Atmospheric dust transport occurs through advection, convection, and turbulent diffusion, while removal occurs through dry and wet deposition (Tegen and Fung, 1994; Li et al., 2008).

South American mountain glaciers function as a buffer for freshwater resources, especially during low-precipitation seasons in countries such as Bolivia and Peru (Vuille et al., 2008). The Andes host >99% of all tropical glaciers on Earth (Kaser, 1999), providing dust archives that reveal seasonality, allow dry/wet season differentiation, and enable annual layer counting (Ramirez et al., 2003; Kutuzov et al., 2019). South America encompasses many temperature and precipitation zones, with the central Andes being affected by both Atlantic and Pacific atmospheric circulation patterns in the north and south, respectively (Sagredo and Lowell, 2012).

Over the last 50 years, the tropical glacier retreat is slightly faster than the global scale (Rabatel et al., 2013). Model projections of future climate change in the tropical Andes indicate a continued warming of the tropical troposphere throughout the 21st century, with a temperature increase that is enhanced at higher elevations. As consequence, the tropical Andes may experience a massive warming scenario on the order of 4.5–5°C by the end of the 21st century (Vuille et al., 2008). Recent warming in the latter half of the 20th century has impacted the preservation of $\delta^{18}O$-derived seasonality data in Quelccaya Ice Cap (QIC, 13o56′ S, 70o50' W, 5,670 m above sea level) ice cores, while dust records remain well preserved (Vuille et al., 2015; Yarleque et al., 2018) and offer more reliable data on climate dynamics.

Recent changes have also been observed over the Madeira River basin in the Amazon-Andean region (Espinoza Villar et al., 2009; Molina-Carpio et al., 2017), which is the largest contributor of suspended sediments to the Amazon River (Vauchel et al., 2017; Ayes Rivera et al., 2019). Erosion of the Andean Cordillera (Ayes Rivera et al., 2019) means that suspended sediment transport from the Amazon basin to the Atlantic Ocean is mainly driven by rivers (Filizola and Guyot, 2011). The junction of the Beni and Mamoré rivers forms the Madeira River (**Figure 1**) and connects it to the main suspended sediment source in the Andes (Vauchel et al., 2017). As the Madeira River has a significant impact on Amazonian suspended sediment balance (Ayes Rivera et al., 2019), understanding potential connections between QIC variability and Amazon rivers could help improve our understanding of this complex climate region.

In this study, we present total dust and density data derived from recent expedition QIC and use this to investigate 1) the large-scale influence of Pacific Decadal Oscillation (PDO) and Niño 3.4 index in the QIC dust groupings, and 2) the dynamic relationship between QIC dust, snow accumulation and the Amazon region using suspended sediment and precipitation data from the Madeira River at the Porto Velho gauge station, which has a complete data series during 2003–2017 period. Considering the importance of both dynamic for the Amazon system, the relationships between the QIC and Madeira river can improve the contemporaneous knowledge about the dynamic involving the Andean ice cores and Amazon rivers.

THE STUDY AREA

Tropical Andean glaciers belong to two distinct continental climate zones (Kaser, 2001) with clear differences in temperature, precipitation, and humidity (Sagredo and Lowell, 2012; Veettil et al., 2016; Kozhikkodan Veettil and de Souza, 2017). The outer tropics (Peru, Bolivia, and northern Chile) are characterized by a tropical climate during the austral summer (high precipitation) and subtropical conditions during the austral winter (little to no precipitation).

The QIC is located at the northern edge of the Altiplano in the Cordillera Vilcanota (CV) of southern Peru (**Figure 1**). This is the world's largest tropical ice cap (median area of 50.2 km^2 (Hanshaw and Bookhagen, 2014), from which a previous deep core campaign recovered 1800 years of climate information (Thompson et al., 2013). Located between the Pacific Ocean and the Amazon Basin, during the wet season (austral summer) it is influenced by the South American summer monsoon (SASM), when most precipitation occurs (Garreaud, 2009). The Bolivian High and the northward extension of the low-level jet are associated with precipitation over the Andes between 20° S and 8° S from December-March. Extreme wet monthly events on interannual time scales are related to convection over the western Amazon during this period (Segura et al., 2019). Extratropical cold air incursions influence the wet season initiation (Li and Fu, 2006) which are responsible for trigger the most snowfall at QIC (Hurley et al., 2015). Observations using micro rain radar characterize the afternoon precipitation maxima as primarily convective, whereas the nighttime precipitation was largely stratiform at Cordillera Vilcanota (Perry et al., 2017). In the dry season (austral winter), westerly flow predominates (Vuille et al., 2000; Garreaud and Aceituno, 2001) and higher dust concentrations

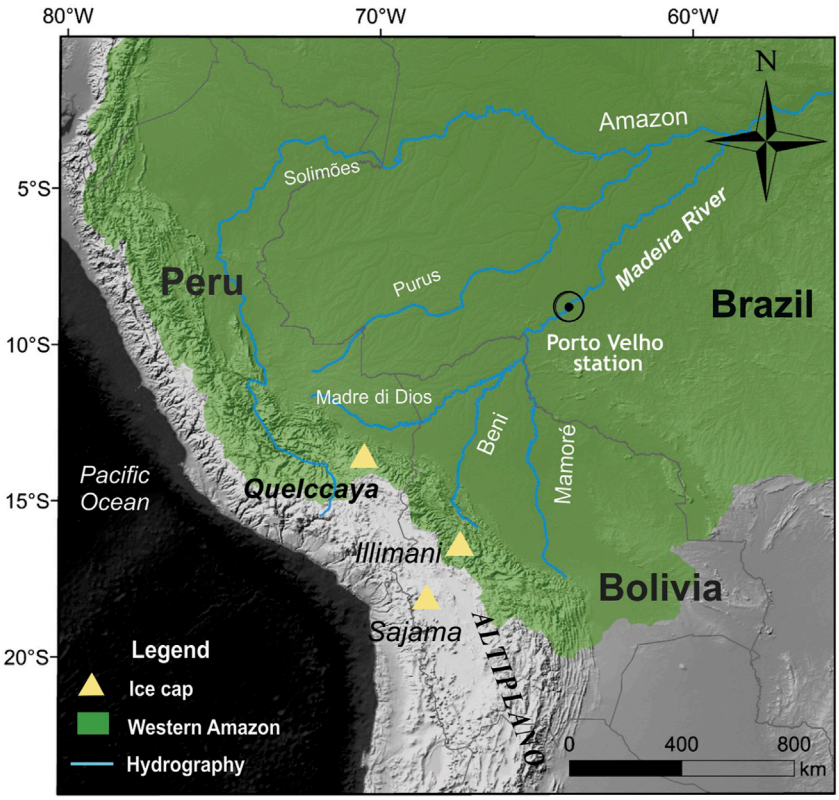

FIGURE 1 | Ice-core sites and main rivers from Upper Madeira Basin in the western Amazon region; map layers were extracted from www.naturalearthdata.com and http://terrabrasilis.dpi.inpe.br.

are attributed to dominant higher wind speeds from the west and northwest, which facilitate entrainment and transport of dust from the high, dry Altiplano. Still, during this season intense radiation receipt accompanied by little accumulation (with minor sublimation), which leaves the insoluble particles concentrated at the surface (Thompson et al., 1986). Dust peaks events (920 and 600 CE) analyzed by microscopy indicate as source particles derived by wind-blown dust with minor amounts of diatoms and volcanic particles. Between these peaks was observed bimodal volume with fine fraction dominant (0.63–1.6 μm) suggesting a lake sediment source, while coarser particles (8–16 μm) fraction is dominant during other sections (Thompson et al., 1988). The diatoms species indicates origin from dilute freshwater lake or wetland with excellent valve preservation suggesting a local source rather than long-transport distance of dust, such Altiplano (Fritz et al., 2015). At Illimani (Bolivia), giant dust particles (∅>20 μm) increase was associated with oscillations of stable isotope records. In addition, the geochemical and mineralogy study indicates dust attributed to the regional sources (Lindau et al., 2021).

The net annual increase during a hydrologic year is about 1.8 m on average (~0.85 m water equivalent per year 2003–2014) is positively correlated with snow accumulation season (wet season). Recently, during the 2013–2014 hydrologic year the snow increased by more than 2.6 m (Hurley et al., 2015). The backward air trajectories for precipitation events in Quelccaya suggest that Amazon air parcels originating to the northwest and north of the Cordillera Vilcanota is associated with the majority of the precipitation events during the 2014–2015 wet season, nonetheless, the trajectories ending at 6,000 m and 8,000 m (at the Cusco precipitation) were more varied, with several originating over the Pacific Ocean (Perry et al., 2017). For the QIC, the most important terms able to significantly influence the surface energy balance of a tropical glacier are: net solar radiation and net longwave radiation. On tropical high-elevation glaciers, there are different factors that can modify albedo, including changes in precipitation in relation with air temperature (rain or snow) and factors like debris cover, dust, and soot (Salzmann et al., 2013).

The PDO, a pattern of climatic variability over the North Pacific, has warm and cold phases. During the former, the eastern Pacific exhibits above average temperatures that coincide with wet periods in south-central South America. Two types of pressure anomalies occur during this phase: low pressure over the North Pacific causes wind to flow counterclockwise, and high pressure in the northern subtropical Pacific causes winds to flow clockwise (Mantua and Hare, 2002; Guevara-Guillén et al., 2015).

Atmospheric circulation over the Amazon basin is influenced by the tropical Atlantic Ocean and is the main source of precipitation (snow) for tropical Andean glaciers. Tropical

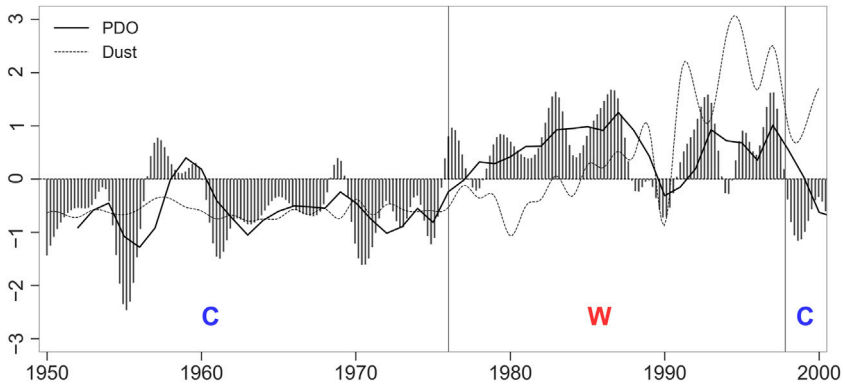

FIGURE 2 | Dust record and Pacific Multidecadal Oscillations since 1950. Annual dust concentration profile of QIC (1950–2000 period) derived from past study (Thompson et al., 2013) for particles between 0.63 and 20 μm. The data were extracted from https://www.ncdc.noaa.gov/. Annual PDO index (solid line) extracted from https://psl.noaa.gov/. C marks periods dominantly cold observed between 1950 and 2003, whereas W marks the warm periods. The dust concentrations values are normalized.

North Atlantic (TNA) is an indicator of surface temperatures in the eastern tropical North Atlantic Ocean (Enfield et al., 1999). Rainfall increases in the Amazon basin are related to increased water vapor transport from the Atlantic. In addition, droughts in this basin are associated with El Niño or northern tropical Atlantic warming (da Rocha Ribeiro et al., 2018). Severe droughts in 2005 and 2010 over the Amazon basin were associated with warmer TNA conditions, under which an anomalously northward displacement of the Intertropical Convergence Zone leads to weaker northeasterly Atlantic trade winds and rainfall reduction over the Amazon basin (Marengo and Espinoza, 2016).

The El Niño Southern Oscillation (ENSO) has environmental and economic impacts on a global scale (McPhaden et al., 2006). Very strong El Niño events (Oceanic Niño Index > +2.0) occurred in 1982–1983, 1997–1998, and 2015–2016, during which QIC margin retreat was greatly enhanced (Thompson et al., 2017). Nonetheless, there is no clear relation to ENSO events visible for the glacier ice reduction in the CV area. But, an increase of specific humidity for the area of CV is very likely, which may explain part of the observed substantial ice loss. In addition, with the increased humidity the longwave energy loss would generally be small (Salzmann et al., 2013). The QIC experiences an increase in westerly wind strength under El Niño conditions and easterly enhancement during La-Niña (Vuille et al., 2000; Garreaud and Aceituno, 2001). Tropical Pacific sea-surface temperatures and the associated ENSO provide a strong influence on the interannual variability of precipitation in the outer tropical Andes (Perry et al., 2017). In general, tropical Andes experiences below-normal precipitation and higher temperatures during El-Niño (Vuille et al., 2003). During this phase, there is a less snow accumulation at QIC and austral summer precipitation has an earlier onset than it does during La Niña with less middle to late summer snowfall. Also, the warmer sea surface temperature in the eastern tropical Pacific correspond with higher δ18O ratios at QIC, while anomalous convective activity over the Amazon Basin corresponds with lower δ18O ratios (Hurley et al., 2019).

The PDO and TNA influence precipitation in the Amazon region and the accumulation rate of tropical Andean glaciers during warm and cold phases (da Rocha Ribeiro et al., 2018). In Peru, ENSO and PDO influence precipitation. The country has at least three climatic regions: the west coast, the Andes Cordillera, and the east, with the Cordillera acting as a natural barrier that greatly affects precipitation patterns (Tapley and Waylen, 1990; Mohammadi et al., 2020). When ENSO occurs in phase with PDO, the influence on glacial snowline is stronger and more visible than ENSO events during neutral periods or opposite PDO phases. Due to geography, the Pacific influence primarily determines most of the climate in the Cordillera Blanca (western Peru), which influences the surface energy balance and surface mass balance. However, during El Niño, these events do not significantly affect air temperature trends in the eastern cordilleras, which include glaciers in the Cordillera Vilcanota (Salzmann et al., 2013; Veettil et al., 2016).

In the second half of the 20th century, annual QIC dust grew during the warm PDO phases (**Figure 2**), but did not change significantly otherwise. The warm and cold TNA phases did not appear to have a significant effect on overall dust concentration. During 1950-2000 period PDO and annual QIC dust presents a moderate correlation ($r = 0.42$, p-value < 0.01). High total dust concentration level was observed during period El-Niño event (1997/1998),

The Madeira River is the second-largest tributary of the Amazon Basin, with a mean annual discharge at the Porto Velho station of 18,500 m^3/s from 1967 to 2013 (Molina-Carpio et al., 2017). The Upper Madeira River drainage basin extends over three countries, with 11% in Peru, 73% in Bolivia, and 16% in Brazil (Molina-Carpio et al., 2017). The Madeira River basin at Porto Velho station consists of four main tributaries: Madre de Dios arriving from the Peruvian Andes, Beni and Mamoré from the central Bolivian Andes, and the Guaporé River from the southeastern part of the basin (Brazilian Shield). In the upper Madeira Basins, the wet season coincides with the mature phase of the SASM from December to March (Vera et al., 2006; Marengo et al., 2012) with mean rainfall

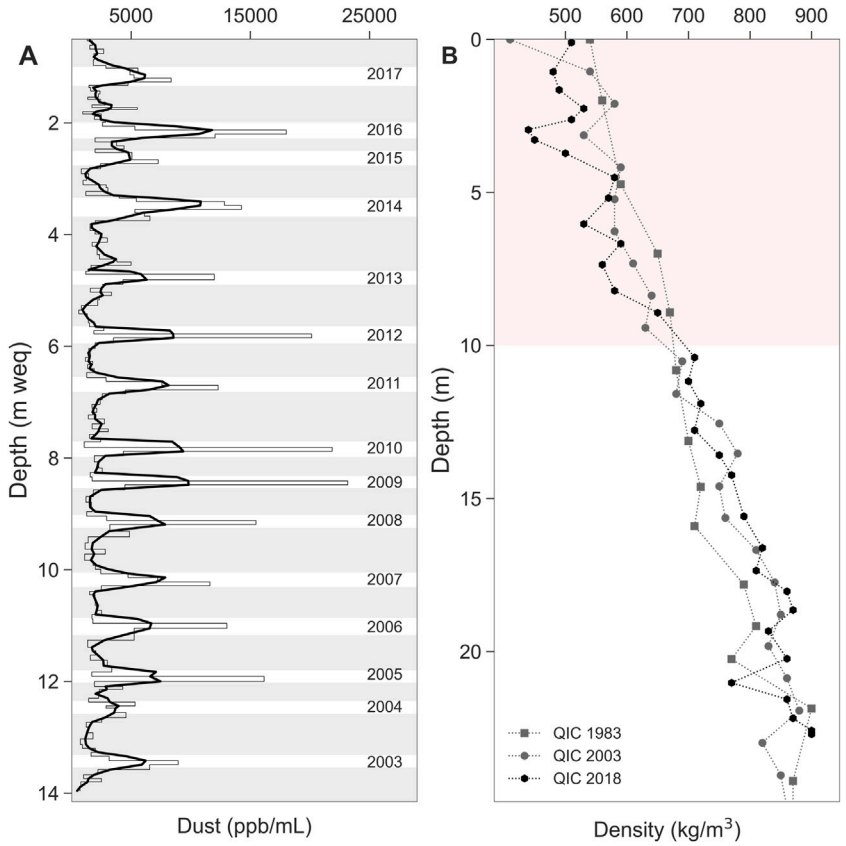

FIGURE 3 | 22.7 m ice-core profile recovered in September 2018 from the Quelccaya Ice Cap, Peru. **(A)** 13.96 m ice-core dust profile (in water equivalent); grey and white shading marking wet and dry seasonality, respectively. The calibration was based on snow accumulation data available from Hurley et al., 2019. **(B)** 2018 density profile compared with 1983 and 2003 ice cores (Thompson et al., 2017); red shading marks the first 10 m with observable density alterations between the three cores.

values higher than 6 mm/day over the 1982–2017 period (Espinoza et al., 2019a). ~50% of its annual precipitation occurs during the wet season from December to February (DJF) (Espinoza Villar et al., 2009). Over the upper part of the Madre de Dios, Beni and Mamoré basins, during January and February occurs the maximum daily rainfall (more than 16 mm/day) characterized by the presence of rainfall "hotspot" regions. In absence of the SASM, a marked dry season predominates during the austral winter from June until August (Espinoza et al., 2019b).

At annual scale, the rainfall over the middle Madre de Dios, Beni and Mamoré basins (northern part) has stronger influence on runoff variability at annual scale and is mostly related to the wet season pattern, while rainfall over the southern part of the basin (south of 14°) shows low or no significant correlation with runoff at Porto Velho and more influent to runoff variability during low-water discharge (dry season) (Espinoza Villar et al., 2009; Molina-Carpio et al., 2017; Espinoza et al., 2019b). In overall scenario, the runoff decrease in recent decades is associated with an increase in the frequency of dry days and decreased rainfall south of 14° S, compared to a rainfall increase north of 14° S (Espinoza et al., 2019b).

MATERIALS AND METHODS

In September 2018, an expedition led by researchers from the Climate and Polar Center at the Federal University of Rio Grande do Sul (CPC-UFRGS) and the Climate Change Institute at the University of Maine (CCI-Maine) recovered a 22.7 m ice-core from the QIC (**Figure 1**) using an electro-mechanical Stampfli drill. Frozen ice-core sections were transported to CCI for ICP-MS and ion chromatographic analysis as well as to the Eurocold laboratory (Milan, Italy) for dust concentration analysis.

We selected 183 samples, representing 13.96 m water equivalent, for dust particle analysis. Measurements were performed in random order using a microparticle counter (Coulter Counter Multisizer IV, 400-channels) set up in a class 100 clean room at the Eurocold laboratory (Milan, Italy). The instrument was calibrated with 2.07 μm latex and set to detect particles with equivalent spherical diameters from 2 to 60 μm. Each concentration and size distribution value represented the average of at least three independent measurements in the same sample. The total mass of insoluble dust was calculated from the volume size distribution, assuming an average density of 2.5 g/cm^3. A standard was set using ultrapure water and checked after five sample analyses with an average value of ~1 ppb.

Annual dating was defined from the start of the dry season until the end of the wet season for each year (**Figure 3A**) and seasons were calibrated using QAnalysis software based on snow accumulation data during period. We smoothed the dust concentration profile with a moving average calculated using three samples for the total dust concentration to characterize seasonality. For statistical correlations, we used the mean dust concentration for each year. All correlations given here were significant at the 95% level. We defined three groups with distinct ranges: fine particle percentage (FPP, 2–10 μm), coarse particle percentage (CPP, 10–20 μm), and giant particle percentage (GPP, 20–60 μm). We defined a year as the period from June to the following May for PDO and ENSO indexes oscillations, following the recent studies observations from Hurley et al., 2019.

The study of hydrosedimentological processes involves the determination of suspended load (Qss), bed load and total solid discharge, which depends on many variables. In general, suspended sediment represents, for most cases, most of total sediment discharge (Carvalho et al., 2000). Among the several methods and approaches for this specific theme, we selected **Eq. 1** that synthetizes the suspended solid discharges calculation due to variables available at station. The Qss values (tons/months) in the Madeira River are based on the simplified method presented by (Carvalho et al., 2000), which represent the suspended solid discharge measured. We considered the month water discharge (Q, m^3/s) and suspended sediment concentration (C, mg/L) data, which were extract of Porto Velho station from website (hybam.obs-mip.fr).

$$Qss = 0.0864 * Q * C \quad (1)$$

We applied the average for the February, March and April month's data during each hydrological year. The runoff during November, December and January months (NDJ) values were extracted from Espinoza et al., 2019b during 2003–2016 hydrological year. The precipitation during December, January and February were extracted from recent study from Ayes Rivera et al., 2021 using the Porto Velho station values.

RESULTS

We assessed 14 years of dust accumulation concentrations in the QIC. The profile clearly delineated dry and wet seasons, represented by high and low concentrations, respectively (**Figure 3A**). The dust concentration measured in the samples ranged from 617 to 23,176 ppb/ml. The mean seasonal value of dust concentrations during dry and wet seasons was 6,807 (±1786) ppb/ml and 2,181 (±456) ppb/ml, respectively. From 2015 to 2016, there was a 55% increase above average during the wet season. The short snow accumulation during 2015–2016 years occurs due to very strong El-Niño when a snow accumulation decrease was observed. The thinner annual layer, as reported during 2015–2016 El-Niño year, might be a product of enhanced ablation resulting from increased insolation and higher temperatures (Perry et al., 2014). The high accumulation during 2013–2014 is compatible with above average snow-height at QIC during this wet season year observed by Hurley et al., 2015.

Recent atmospheric warming in the QIC has resulted in changing depth of the firn/ice transition (Thompson et al., 2017). Comparing with two previous ice cores recovered from QIC, we observed a density alteration in the first 10 m between ice cores over time (**Figure 3B**). For the 1983 and 2003 cores, the firn/ice transition occurred at ~21–22 and ~18–19 m depth, respectively, compared with our core at ~17–18 m.

In ice core recovered in 2018, the annual total dust concentration increase coincided with the recent inversion from the PDO cold phase (2005–2013) to the PDO warm phase (2014–2017). Different group dominates the highest concentrations over the years (**Figure 4**). CPP and GPP dominated from 2003 to 2012 (PDO cold phase dominant) with a significant increase in FPP starting in 2013, concomitantly with the PDO warm phase began (Jan-2014). Up to 2012, the annual mean dust of the FPP group was 952 (±171) ppb/ml, while CPP and GPP had average concentrations of 1,231 ± 301 and 1,436 ± 266 ppb/ml, respectively. From 2013, FPP became the dominant group with a concentration increase of 54.7%, while CPP and GPP showed decreases of 5.62 and 21.8%, respectively. The dominance inversion occurs during the highest snow accumulation year, already observed in the profile.

The direct relationship between fine particles and PDO index is supported by a positive correlation, at the 95% level, between the annual mean dust concentration of FPP and this annual index ($r = 0.70$, $p < 0.005$) in 2018. Exploring the relationship between FPP dust and snow accumulation (**Figure 5**) we observed inverse relationship between them. During the high accumulation period we observed lower concentration and negative PDO values, whereas during lower snow accumulation was noted high FPP concentration and positive values for PDO. This hypothesis needs to be explored during a long-record using this specific dust group. For the QIC, El Niño often results in arid conditions and low accumulation on the ice cap, as recorded in the ice stratigraphy (Thompson et al., 1985; Thompson, 2000; Thompson et al., 2013). However, there is no correlation significance between FPP and Niño 3.4, but is observed high FPP concentrations during El-Niño events (2009–2010 and 2015–2016, red arrows). Also, in opposite, is noted lower FPP concentration during La-Niña events (2007–2008 and 2010–2011, blue arrows). The relative CPP group and GPP group, apparently, did not show direct relationship during ENSO oscillations. However, it is observed a relative content increase (**Figure 4**) during El-Niño event (2009–2010).

TNA did not show significant phase alterations, remaining largely in the positive phase from 2003 to 2017. Potentially, drought conditions are associated to the TNA warm phase (Marengo and Espinoza, 2016) and may have led to dry deposition of large dust groups (i.e., by gravitational settling (Tegen and Fung, 1994)) from the source area during PDO cold phase dominant.

We investigated the relationship of QIC data and Madeira river during the period observed. Assessing the snow accumulation data and dust grouping content we compared with Madeira river dynamic using the precipitation, runoff and suspended sediments data. The connection between snow accumulation and precipitation during wet seasons is more

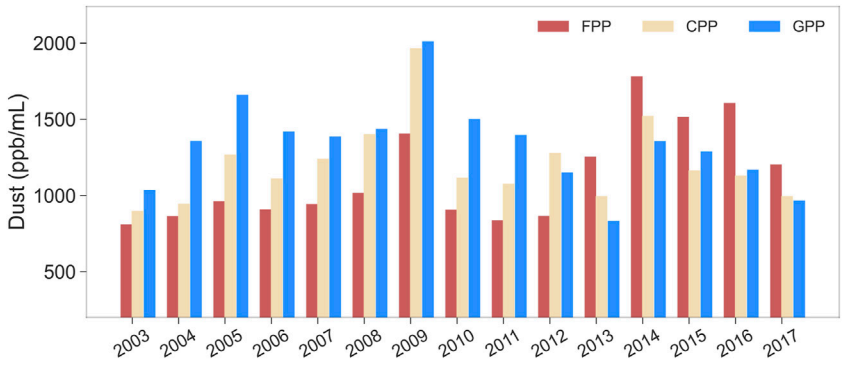

FIGURE 4 | Annual mean concentration of ice-core dust-size groups from 2003 to 2017 period for FPP (fine, 2–10 μm), CPP (coarse, 10–20 μm), and GPP (giant, 20–60 μm).

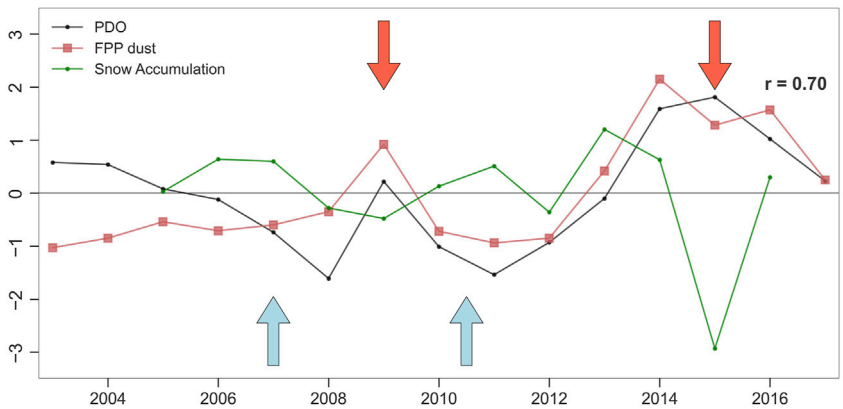

FIGURE 5 | The annual PDO index (June-May) and QIC FPP dust during 2003–2017 period. Annual snow accumulation data from AWS station (Hurley et al., 2019). Index is derived from https://psl.noaa.gov/data/climateindices. Correlation in the figure is related to PDO and FPP dust concentration. PDO index, FPP dust and Snow accumulation values are normalized. The arrows represent moderate or strong ENSO events (red = El-Niño, blue = La-Niña).

evidential during January month (**Figure 6A**). In addition, the dynamic relationship is observed during the transitional period by snow accumulation during September–November months (SON) at QIC and runoff at Porto Velho station with 60 days time-lag (**Figure 6B**). Furthermore, the link between them is noted for the dust content and suspended sediments using the similar delay mentioned. The higher correlation observed between dust groupings and riverine suspended sediments occur with FPP group (**Figure 6C**).

DISCUSSION

Large-Scale Atmospheric Circulation Patterns Over the Central Andes

During recent decades, the snowline altitude of Bolivian glaciers has fluctuated between the warm and cold PDO phases when combined with the ENSO warm and cold phases, respectively (Veettil et al., 2016). In Ecuador, the strong connection between PDO and ENSO is evident mainly in the warm phase, when rainfall is above average. This influence is also observable during drought periods, with ~70% of droughts developing in the negative PDO phase (Oñate-Valdivieso et al., 2020). The similar influence of PDO also occurs for the Niño 1 + 2 index. When Warm PDO and index are in phase, high rainfall is produced in the coast of Ecuador, meanwhile drought are expected during opposite conditions (Campozano et al., 2020).

The QIC's moisture source is mainly the tropical Atlantic via the Amazon basin (Thompson et al., 2013), but during the positive PDO phase, westerly flow is enhanced (Vuille et al., 2003) over central South America. As dry seasons, this westerly flow can facilitate dust transport from the Altiplano to the QIC region, promoting an increase in the amount of dust recorded during warm PDO periods. In addition, recent studies have documented abnormal precipitation over Peruvian regions caused by Pacific Ocean oscillations when PDO and ENSO are in their positive phases (Kayano and Andreoli, 2007; Rodríguez-Morata et al., 2019; Mohammadi et al., 2020; Vaheddoost, 2020) which could favor increases in FPP relative to other groups due to turbulent mixing or wet deposition. This direct association of the

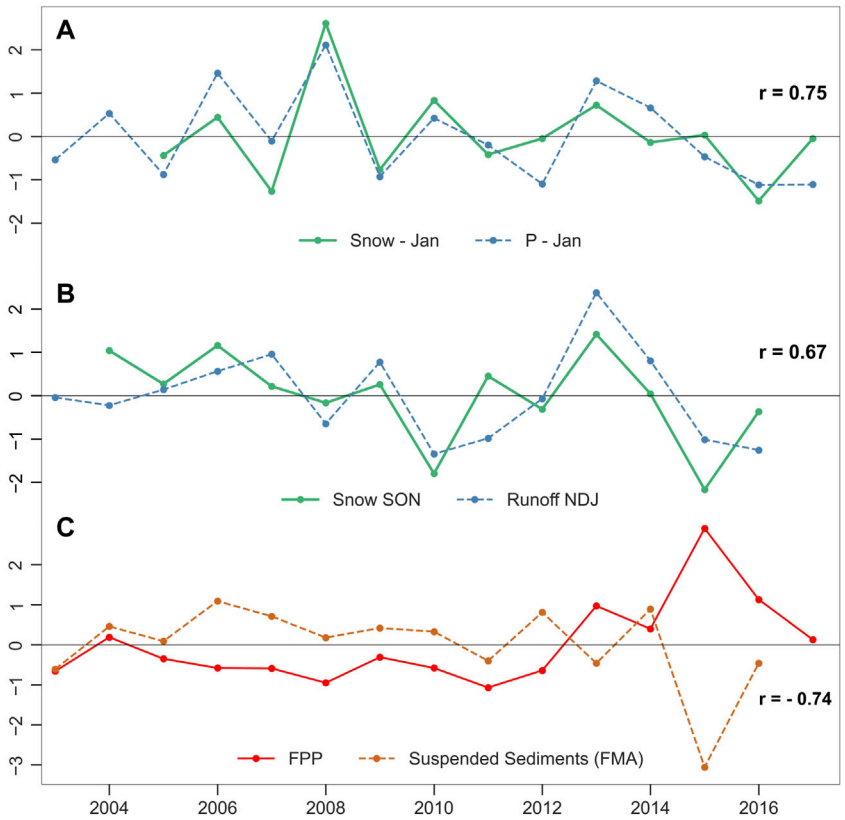

FIGURE 6 | Comparison of wet season records from the Madeira River data at the Porto Velho station (hybam.obs-mip.fr) and recent QIC data during 2003–2016 wet seasons period. All values are normalized. **(A)** Rainfall precipitation (Ayes Rivera et al., 2021) and snow accumulation (AWS station at QIC) during January. **(B)** Snow accumulation during Setember-November from AWS station (Hurley et al., 2019) and Runoff (NDJ) values (Espinoza et al., 2019b) from 2003 to 2016; **(C)** The FPP group concentration during 2003–2017 wet seasons and average suspended sediments load (tons/month) during high water discharge months (FMA) during the wet season hydrological period.

PDO index (**Figure 5**) with dust concentration was corroborated by significant correlations at the 95% level, such as %FPP (r = 0.66, *p*-value < 0.01) and %CPP (r = −0.57, *p*-value < 0.05) from 2003 to 2017. The relative higher FPP concentration observed during moderate El-Niño in 2009 (**Figure 5**) is not representative for an effective increase of fine particles in size distribution as observed (**Figure 4**). In addition, it is not observed an importance decrease in FPP during La-Niña during the period. This implies that FPP increase or decrease is more related to the PDO influence than ENSO occurrences for the period studied but such influence is not discard in long record for this group.

Madeira River Dynamic and Connections to QIC

The precipitation (snow) occurrences in the Andes primarily originate over the Atlantic Ocean and undergoes recycling due to convective precipitation and evapotranspiration over the Amazon (Grootes et al., 1989). Previous study showed that coherent isotopic profiles from four Andean glaciers (including Quelccaya) appear to relate to precipitation variability over the Amazon basin (Hoffmann et al., 2003). Exploring the relationships during the wet season, we clearly notes a highly connection during mainly January month (**Figure 6A**). The high correlation between precipitation and snow accumulation at QIC during January (r = 0.75, *p*-value < 0.01) depicts a potential link of the hotspots occurrences in the Upper part of tributaries rivers (Espinoza et al., 2019b) and snow. However, a low correlation occurs during February months over the period analyzed.

Glaciers in the tropical Andes are the headwaters for the Amazon rivers and examinate changes in their record can be helpful to understand environmental process changes in the Amazon context. In order to explore the connection between Madeira basin and QIC, we investigated the relationship snow accumulation during transition season September-November (SON) at QIC and runoff at Porto Velho station during November-January (NDJ, **Figure 6B**) over 2003-2016 period. A time-lag of 60 days between precipitation and runoff is estimed as more appropriate to general dynamic in this part of the Amazon context by (Espinoza et al., 2019b). The results indicate that the runoff dynamic coincides with the high and low snow accumulation values at QIC (r = 0.67, *p*-value < 0.05), when the precipitation (northern part) majority contributes to

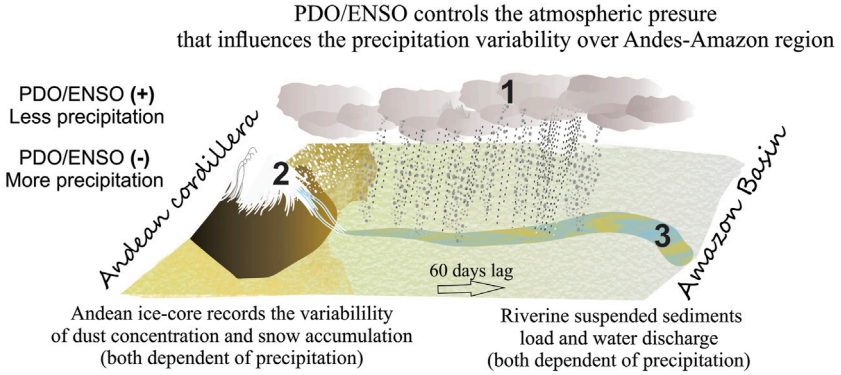

FIGURE 7 | A representative model showing the relationships in the three stages between QIC and Madeira river. The stage one indicates precipitation (rainfall/snow), the stage two the ice core record, stage three the gauge station. The 60 days time-lag represents the delay between QIC record and Madeira River suspended sediments load.

water discharge dynamic at Porto Velho station. These results provide information about similar dynamic variability of snow accumulation and runoff during the transitional period. Also indicates that the similar time-lag estimated between the precipitation of northern part basin and runoff during initial wet season is also validated for this relationship.

The average sediment production of the Andean stretch of the Upper Madeira was estimated at 640 Mtyear−1 (2002–2011 (Vauchel et al., 2017)). In the Amazon context, the recent observations point out that temporal rainfall variability is well related to the fine suspended sediment (Armijos et al., 2020). The Beni River provides nearly 80% of suspended sediment at Porto Velho, primarily originated from the Beni River itself (47%), secondly from its main tributary (32%) the Madre de Dios River (Vauchel et al., 2017). In the Upper Madeira Basin, the suspended sediment concentration in recent years revealed a concentration decrease attributed to the depletion of suspended sediments from the Beni River (Ayes Rivera et al., 2019). The sediment yield in Bolivia (the main source of Beni and Madeira river suspended sediments) is directly controlled by climate variability with precipitation seasonality (present in the outer tropics) as the principal factor in high denudation rates (Pepin et al., 2013). In addition, suspended sediments depletions during December wet season recently was attributed to the reduction of rainfall in the Madre de Dios sub-basin since October, whereas during subsequent months were associated to a rainfall magnitude increase in the Andean region after 2008. These results indicates the importance of the processes upstream in the Andean part of the basin (Ayes Rivera et al., 2021).

We investigated the relationship during 2003–2016 between FPP dust concentration during wet seasons period and the suspended sediments concentrations (**Figure 6C**). Our findings present that the dust at QIC and Madeira river suspended sediments load is well related during the high-water discharge months (February-April, FMA) when northern part is more influent in the Madeira River than low-water discharge (dry and transitional seasons). In spite of the inverse tendency, our results show that the relationship dust wet seasons and suspended sediments load (tons/months) present similarity in dynamic variability during the wet season. Due to direct association of suspended sediments and precipitation (Armijos et al., 2020), clearly, the suspended sediment concentration decreases over the years is influenced by the precipitation decrease in the southern part of Madeira basin. The fine dust and suspended sediments present strong correlation ($r = -0.74$, p-value < 0.005), while total dust and CPP dust group present a moderate correlation ($r = -0.60$, p-value < 0.05) and ($r = -0.70$, p-value < 0.01), respectively. The GPP group did not show relations with suspended sediment concentrations during November-January, December-February and February-April periods. Although dry-days increases (in the south 14°) can affect directly the runoff and suspended sediments concentration, the influence of hotspot rainfalls in the northern part also contributes to record at Porto Velho station, which shows the complexity of record variability and link of the Andes-Amazon connection.

Our findings presents that dust concentration (fine group mainly) present sensible differences during PDO phase alteration, which involves drier conditions during positive phase. The PDO/ENSO controls the atmospheric pressure over the Andes-Amazon, which tends to block the precipitation from east over the eastern Andes during warm periods (Hoffmann et al., 2003; Hurley et al., 2015). During this phase, our hypothesis suggests that westerly wind intensifies the regional transport of dust based on fine particles content increase, since drier conditions over the Altiplano leads to higher dust availability (Lindau et al., 2021). Indirectly, the Amazon precipitation and riverine suspended sediments load are under control by these atmospheric oscillations.

We developed a model of these connections (**Figure 7**) indicating three phases relationships. First, the PDO/ENSO controls the atmospheric conditions over Andes–Amazon region. This controls the precipitation (snow) influencing the snow accumulation and dust content over the Andes. In addition, the precipitation variability influences indirectly the suspended sediment load and discharge over the river. Second, the tropical glacier accumulation (ice-core) where is the headwater for the tributaries rivers. Three, the gauge station where it is possible evaluate the discharge and suspended sediment concentrations.

From the second to the third phase, a time-lag considered is the suggested for the Amazon context (Espinoza et al., 2019b). The physical mechanism that controls the variability of precipitation presented in the model depends on the atmospheric pressure conditions over the Andes- Amazon region.

We suggest that fine particles is more reliable group to represent the dynamic variability related to suspended sediment riverine due to dynamic observed with snow accumulation in recent record at QIC. Still, further investigations using a long-period record are necessary to improve knowledge about these relationships between snow accumulation and runoff during high-water discharge and QIC dust grouping and suspended sediments load over the year.

CONCLUSION

We investigated a shallow ice-core (22.7 m) recovered from the QIC in 2018 and found that seasonal signals were preserved even after seasonal surface melting. There was an increase in total dust content during the 21st century, coinciding with a warm PDO phase and the dominance of FPP from 2013 to 2017. The PDO index is well related with FPP ($r = 0.70$, $p < 0.005$) at the 95% level from 2003 to 2017. The dominance inversion occurs during the highest snow accumulation year and during the subsequent years of positive phase of Pacific index. In the positive phase, previous studies indicate that PDO and eastern pacific index induces strong westerly winds, inhibiting easterly air flow and facilitating dust transport from the high Altiplano. This condition could facilitate the fine dust content increase during less accumulation year. The CPP and GPP dust groups were dominant during the mainly cold PDO phase (2003–2012) and TNA warm phase. Potentially, under these two phases (TNA-positive and PDO-negative), the dominant groups are dust particles >10 μm. These observations need to be explored using a dust grouping record in long period.

This study provides a potential link between dynamic of QIC records via snow accumulation and dust content with the Madeira River via precipitation, suspended sediment concentration and runoff data. The precipitation in the Madeira basin and snow accumulation at QIC relationship, we verify a highly connection during January month (wet season). The snow accumulation and runoff we note a better relationship considering 60 days time–lag (similar to northern part of upper Madeira basin). Our findings observed that the snow accumulation during SON season presents similar dynamic with runoff NDJ at Porto Velho station during the transitional season. The similar behavior implies SON snow accumulation is indicative of tributaries discharge variability for the Madeira basin during this period of year. This relationship is helpful to examinate about dynamic of melt water variability and effects in the drainage in the headwater basin during the rest of year.

We observed inverse tendency of the dust content during wet season at QIC and decreasing suspended sediment concentration at the Porto Velho station during high-water discharge (February-April). Our findings present the negative correlation between FPP and suspended sediment ($r = -0.74$, p-value <0.005) at the 95% level from 2003 to 2016. We understand that this group is more reliable for this connection due to wetter condition mechanism for the record along suspended sediments load and precipitation association in the Amazon context.

In conclusion, examining distinct particle-size groups in the QIC dust record can improve our understanding of how the Pacific ocean influence dust particle variability in this region. We determined the dynamic similarities between dust content variability, snow accumulation, suspended sediment concentration, precipitation and runoff for the Madeira River, demonstrating the potential for future investigations of the relationship between QIC dust content and Amazon Basin Rivers in a long period record.

DATA AVAILABILITY STATEMENT

The original contributions presented in the study are included in the article/**Supplementary Material**, further inquiries can be directed to the corresponding author.

AUTHOR CONTRIBUTIONS

RR, RdaR, ND and JS wrote the original manuscript. RR, RdaR, JS and BD designed the research. JS and PM designed and led the drilling campaign. RR and BD conducted dust analyses. ER, PM, and BD advice on data collection and interpretation and provided comments to the original manuscript.

FUNDING

The 2018 international fieldwork in the Quellcaya Ice Cap was a joint operation organized by the Centro Polar e Climático (UFRGS/Brazil) and Climate Change Institute (UMaine/ME, United States), supported by the US National Science Foundation P2C2 1600018 and Appalachian State University (Boone, NC, United States) in collaboration with the Instituto Nacional de Investigación en Glaciares y Ecosistemas de Montaña (INAIGEM, Peru), and the Universidad Nacional de San Antonio Abad del Cusco (Peru). This research was supported by the Brazilian National Council for Scientific and Technological Development—CNPq (Process 465680/2014-3—INCT da Criosfera).

ACKNOWLEDGMENTS

RR thanks CNPq for his scholarship (Process 141081/2018-0).

SUPPLEMENTARY MATERIAL

The Supplementary Material for this article can be found online at: https://www.frontiersin.org/articles/10.3389/fenvs.2022.840884/full#supplementary-material

REFERENCES

Ansmann, A. (2005). Ice Formation in Saharan Dust over central Europe Observed with Temperature/humidity/aerosol Raman Lidar. *J. Geophys. Res.* 110, D18S12. doi:10.1029/2004JD005000

Armijos, E., Crave, A., Espinoza, J. C., Filizola, N., Espinoza-Villar, R., Ayes, I., et al. (2020). Rainfall Control on Amazon Sediment Flux: Synthesis from 20 Years of Monitoring. *Environ. Res. Commun.* 2, 051008. doi:10.1088/2515-7620/ab9003

Ayes Rivera, I., Armijos Cardenas, E., Espinoza-Villar, R., Espinoza, J., Molina-Carpio, J., Ayala, J., et al. (2019). Decline of Fine Suspended Sediments in the Madeira River Basin (2003-2017). *Water* 11, 514. doi:10.3390/w11030514

Ayes Rivera, I. E., Molina-Carpio, J., Espinoza, J. C., Gutierrez-Cori, O., Cerón, W. L., Frappart, F., et al. (2021). The Role of the Rainfall Variability in the Decline of the Surface Suspended Sediment in the Upper Madeira Basin (2003-2017). *Front. Water*, 116. doi:10.3389/frwa.2021.738527

Campozano, L., Robaina, L., and Samaniego, E. (2020). The Pacific Decadal Oscillation Modulates the Relation of ENSO with the Rainfall Variability in Coast of Ecuador. *Int. J. Climatol.* 40, 5801–5812. doi:10.1002/joc.6525

Carslaw, K. S., Boucher, O., Spracklen, D. V., Mann, G. W., Rae, J. G. L., Woodward, S., et al. (2010). A Review of Natural Aerosol Interactions and Feedbacks within the Earth System. *Atmos. Chem. Phys.* 10, 1701–1737. doi:10.5194/acp-10-1701-2010

Carvalho, N. de. O., Filizola, N., Santos, P. M. C., and Lima, J. (2000). *Sedimentometric Pratices Guide*. Brasilia, Brazil.

da Rocha Ribeiro, R., Simões, J. C., Ramirez, E., Taupin, J.-D., Assayag, E., and Dani, N. (2018). Accumulation Rate in a Tropical Andean Glacier as a Proxy for Northern Amazon Precipitation. *Theor. Appl. Climatol.* 132, 569–578. doi:10.1007/s00704-017-2108-7

Delmonte, B., Paleari, C. I., Andò, S., Garzanti, E., Andersson, P. S., Petit, J. R., et al. (2017). Causes of Dust Size Variability in central East Antarctica (Dome B): Atmospheric Transport from Expanded South American Sources during Marine Isotope Stage 2. *Quat. Sci. Rev.* 168, 55–68. doi:10.1016/j.quascirev.2017.05.009

Delmonte, B., Petit, J. R., Andersen, K. K., Basile-Doelsch, I., Maggi, V., and Ya Lipenkov, V. (2004). Dust Size Evidence for Opposite Regional Atmospheric Circulation Changes over East Antarctica during the Last Climatic Transition. *Clim. Dyn.* 23, 427–438. doi:10.1007/s00382-004-0450-9

Delmonte, B., Petit, J. R., and Maggi, V. (2002). LGM-holocene Changes and Holocene Millennial-Scale Oscillations of Dust Particles in the EPICA Dome C Ice Core, East Antarctica. *Ann. Glaciol.* 35, 306–312. doi:10.3189/172756402781816843

Di Biagio, C., Balkanski, Y., Albani, S., Boucher, O., and Formenti, P. (2020). Direct Radiative Effect by Mineral Dust Aerosols Constrained by New Microphysical and Spectral Optical Data. *Geophys. Res. Lett.* 47, 1–12. doi:10.1029/2019GL086186

Enfield, D. B., Mestas-Nuñez, A. M., Mayer, D. A., and Cid-Serrano, L. (1999). How Ubiquitous Is the Dipole Relationship in Tropical Atlantic Sea Surface Temperatures? *J. Geophys. Res.* 104, 7841–7848. doi:10.1029/1998JC900109

Espinoza, J. C., Ronchail, J., Marengo, J. A., and Segura, H. (2019a). Contrasting North-South Changes in Amazon Wet-Day and Dry-Day Frequency and Related Atmospheric Features (1981-2017). *Clim. Dyn.* 52, 5413–5430. doi:10.1007/s00382-018-4462-2

Espinoza, J. C., Sörensson, A. A., Ronchail, J., Molina-Carpio, J., Segura, H., Gutierrez-Cori, O., et al. (2019b). Regional Hydro-Climatic Changes in the Southern Amazon Basin (Upper Madeira Basin) during the 1982-2017 Period. *J. Hydrol. Reg. Stud.* 26, 100637. doi:10.1016/j.ejrh.2019.100637

Espinoza Villar, J. C., Ronchail, J., Guyot, J. L., Cochonneau, G., Naziano, F., Lavado, W., et al. (2009). Spatio-temporal Rainfall Variability in the Amazon basin Countries (Brazil, Peru, Bolivia, Colombia, and Ecuador). *Int. J. Climatol.* 29, 1574–1594. doi:10.1002/joc.1791

Filizola, N., and Guyot, J. L. (2011). Fluxo de sedimentos em suspensão nos rios da Amazônia. *Rbg* 41, 566–576. doi:10.25249/0375-7536.2011414566576

Fritz, S. C., Brinson, B. E., Billups, W. E., and Thompson, L. G. (2015). Diatoms at >5000 Meters in the Quelccaya Summit Dome Glacier, Peru. *Arctic, Antarctic, Alpine Res.* 47, 369–374. doi:10.1657/AAAR0014-075

Garreaud, R., and Aceituno, P. (2001). Interannual Rainfall Variability over the South American Altiplano. *J. Clim.* 14, 2779–2789. doi:10.1175/1520-0442(2001)014<2779:irvots>2.0.co;2

Garreaud, R. D. (2009). The Andes Climate and Weather. *Adv. Geosci.* 22, 3–11. doi:10.5194/adgeo-22-3-2009

Grootes, P. M., Stuiver, M., Thompson, L. G., and Mosley-Thompson, E. (1989). Oxygen Isotope Changes in Tropical Ice, Quelccaya, Peru. *J. Geophys. Res.* 94, 1187. doi:10.1029/JD094iD01p01187

Guevara-Guillén, C., Shirasago-Germán, B., and Pérez-Lezama, E. L. (2015). The Influence of Large-Scale Phenomena on La Paz Bay Hydrographic Variability. *Ojms* 05, 146–157. doi:10.4236/ojms.2015.51012

Hanshaw, M. N., and Bookhagen, B. (2014). Glacial Areas, lake Areas, and Snow Lines from 1975 to 2012: Status of the Cordillera Vilcanota, Including the Quelccaya Ice Cap, Northern central Andes, Peru. *The Cryosphere* 8, 359–376. doi:10.5194/tc-8-359-2014

Hoffmann, G., Ramirez, E., Taupin, J. D., Francou, B., Ribstein, P., Delmas, R., et al. (2003). Coherent Isotope History of Andean Ice Cores over the Last century. *Geophys. Res. Lett.* 30, 1–4. doi:10.1029/2002GL014870

Hurley, J. V., Vuille, M., Hardy, D. R., Burns, S. J., and Thompson, L. G. (2015). Cold Air Incursions, δ 18 O Variability, and Monsoon Dynamics Associated with Snow Days at Quelccaya Ice Cap, Peru. *J. Geophys. Res. Atmos.* 120, 7467–7487. doi:10.1002/2015JD023323

Hurley, J. V., Vuille, M., and Hardy, D. R. (2019). On the Interpretation of the ENSO Signal Embedded in the Stable Isotopic Composition of Quelccaya Ice Cap, Peru. *J. Geophys. Res. Atmos.* 124, 131–145. doi:10.1029/2018JD029064

Jickells, T. D., An, Z. S., Andersen, K. K., Baker, A. R., Bergametti, G., Brooks, N., et al. (2005). Global Iron Connections between Desert Dust, Ocean Biogeochemistry, and Climate. *Science* 308, 67–71. doi:10.1126/science.1105959

Kaser, G. (1999). A Review of the Modern Fluctuations of Tropical Glaciers. *Glob. Planet. Change* 22, 93–103. doi:10.1016/S0921-8181(99)00028-4

Kaser, G. (2001). Glacier-climate Interaction at Low Latitudes. *J. Glaciol.* 47, 195–204. doi:10.3189/172756501781832296

Kayano, M. T., and Andreoli, R. V. (2007). Relations of South American Summer Rainfall Interannual Variations with the Pacific Decadal Oscillation. *Int. J. Climatol.* 27, 531–540. doi:10.1002/joc.1417

Kok, J. F., Ridley, D. A., Zhou, Q., Miller, R. L., Zhao, C., Heald, C. L., et al. (2017). Smaller Desert Dust Cooling Effect Estimated from Analysis of Dust Size and Abundance. *Nat. Geosci* 10, 274–278. doi:10.1038/ngeo2912

Kozhikkodan Veettil, B., and de Souza, S. F. (2017). Study of 40-year Glacier Retreat in the Northern Region of the Cordillera Vilcanota, Peru, Using Satellite Images: Preliminary Results. *Remote Sensing Lett.* 8, 78–85. doi:10.1080/2150704X.2016.1235811

Kutuzov, S., Legrand, M., Preunkert, S., Ginot, P., Mikhalenko, V., Shukurov, K., et al. (2019). The Elbrus (Caucasus, Russia) Ice Core Record - Part 2: History of Desert Dust Deposition. *Atmos. Chem. Phys.* 19, 14133–14148. doi:10.5194/acp-19-14133-2019

Li, F., Ginoux, P., and Ramaswamy, V. (2008). Distribution, Transport, and Deposition of mineral Dust in the Southern Ocean and Antarctica: Contribution of Major Sources. *J. Geophys. Res.* 113, 1–15. doi:10.1029/2007JD009190

Li, P., Wu, G., Zhang, X., Yan, N., and Zhang, X. (2019). Variation in Atmospheric Dust since 1950 from an Ice Core in the Central Tibetan Plateau and its Relationship to Atmospheric Circulation. *Atmos. Res.* 220, 10–19. doi:10.1016/j.atmosres.2018.12.030

Li, W., and Fu, R. (2006). Influence of Cold Air Intrusions on the Wet Season Onset over Amazonia. *J. Clim.* 19, 257–275. doi:10.1175/JCLI3614.1

Lindau, F. G. L., Simões, J. C., Delmonte, B., Ginot, P., Baccolo, G., Paleari, C. I., et al. (2021). Giant Dust Particles at Nevado Illimani: a Proxy of Summertime Deep Convection over the Bolivian Altiplano. *The Cryosphere* 15, 1383–1397. doi:10.5194/tc-15-1383-2021

Mantua, N. J., and Hare, S. R. (2002). The Pacific Decadal Oscillation. *J. Oceanogr.* 58, 35–44. doi:10.1023/A:1015820616384

Marengo, J. A., and Espinoza, J. C. (2016). Extreme Seasonal Droughts and Floods in Amazonia: Causes, Trends and Impacts. *Int. J. Climatol.* 36, 1033–1050. doi:10.1002/joc.4420

Marengo, J. A., Liebmann, B., Grimm, A. M., Misra, V., Silva Dias, P. L., Cavalcanti, I. F. A., et al. (2012). Recent Developments on the South American Monsoon System. *Int. J. Climatol.* 32, 1–21. doi:10.1002/joc.2254

McPhaden, M. J., Zebiak, S. E., and Glantz, M. H. (2006). ENSO as an Integrating Concept in Earth Science. *Science* 314, 1740–1745. doi:10.1126/science.1132588

Mohammadi, B., Vaheddoost, B., and Danandeh Mehr, A. (2020). A Spatiotemporal Teleconnection Study between Peruvian Precipitation and Oceanic Oscillations. *Quat. Int.* 565, 1–11. doi:10.1016/j.quaint.2020.09.042

Molina-Carpio, J., Espinoza, J. C., Vauchel, P., Ronchail, J., Gutierrez Caloir, B., Guyot, J.-L., et al. (2017). Hydroclimatology of the Upper Madeira River basin: Spatio-Temporal Variability and Trends. *Hydrological Sci. J.* 62, 911–927. doi:10.1080/02626667.2016.1267861

Oñate-Valdivieso, F., Uchuari, V., and Oñate-Paladines, A. (2020). Large-Scale Climate Variability Patterns and Drought: A Case of Study in South - America. *Water Resour. Manage.* 34, 2061–2079. doi:10.1007/s11269-020-02549-w

Pepin, E., Guyot, J. L., Armijos, E., Bazan, H., Fraizy, P., Moquet, J. S., et al. (2013). Climatic Control on Eastern Andean Denudation Rates (Central Cordillera from Ecuador to Bolivia). *J. South Am. Earth Sci.* 44, 85–93. doi:10.1016/j.jsames.2012.12.010

Perry, L. B., Seimon, A., Andrade-Flores, M. F., Endries, J. L., Yuter, S. E., Velarde, F., et al. (2017). Characteristics of Precipitating Storms in Glacierized Tropical Andean Cordilleras of Peru and Bolivia. *Ann. Am. Assoc. Geogr.* 107, 309–322. doi:10.1080/24694452.2016.1260439

Perry, L. B., Seimon, A., and Kelly, G. M. (2014). Precipitation Delivery in the Tropical High Andes of Southern Peru: New Findings and Paleoclimatic Implications. *Int. J. Climatol.* 34, 197–215. doi:10.1002/joc.3679

Rabatel, A., Francou, B., Soruco, A., Gomez, J., Cáceres, B., Ceballos, J. L., et al. (2013). Current State of Glaciers in the Tropical Andes: A Multi-century Perspective on Glacier Evolution and Climate Change. *The Cryosphere* 7, 81–102. doi:10.5194/tc-7-81-2013

Ramirez, E., Hoffmann, G., Taupin, J. D., Francou, B., Ribstein, P., Caillon, N., et al. (2003). A New Andean Deep Ice Core from Nevado Illimani (6350 M), Bolivia. *Earth Planet. Sci. Lett.* 212, 337–350. doi:10.1016/S0012-821X(03)00240-1

Rodríguez-Morata, C., Díaz, H. F., Ballesteros-Canovas, J. A., Rohrer, M., and Stoffel, M. (2019). The Anomalous 2017 Coastal El Niño Event in Peru. *Clim. Dyn.* 52, 5605–5622. doi:10.1007/s00382-018-4466-y

Ruth, U. (2002). Concentration and Size Distribution of Microparticles in the NGRIP Ice Core (Central Greenland) during the Last Glacial Period. Reports; Berichte zur Polar-und Meeresforsch. Available at: http://epic.awi.de/26607/1/BerPolarforsch2002428.pdf (Accessed June, 2021).

Sagredo, E. A., and Lowell, T. V. (2012). Climatology of Andean Glaciers: A Framework to Understand Glacier Response to Climate Change. *Glob. Planet. Change* 86-87, 101–109. doi:10.1016/j.gloplacha.2012.02.010

Salzmann, N., Huggel, C., Rohrer, M., Silverio, W., Mark, B. G., Burns, P., et al. (2013). Glacier Changes and Climate Trends Derived from Multiple Sources in the Data Scarce Cordillera Vilcanota Region, Southern Peruvian Andes. *The Cryosphere* 7, 103–118. doi:10.5194/tc-7-103-2013

Segura, H., Junquas, C., Espinoza, J. C., Vuille, M., Jauregui, Y. R., Rabatel, A., et al. (2019). New Insights into the Rainfall Variability in the Tropical Andes on Seasonal and Interannual Time Scales. *Clim. Dyn.* 53, 405–426. doi:10.1007/s00382-018-4590-8

Stevens, B., and Feingold, G. (2009). Untangling Aerosol Effects on Clouds and Precipitation in a Buffered System. *Nature* 461, 607–613. doi:10.1038/nature08281

Tapley, T. D., and Waylen, P. R. (1990). Spatial Variability of Annual Precipitation and ENSO Events in Western Peru. *Hydrological Sci. J.* 35, 429–446. doi:10.1080/02626669009492444

Tegen, I., and Fung, I. (1994). Modeling of mineral Dust in the Atmosphere: Sources, Transport, and Optical Thickness. *J. Geophys. Res.* 99, 22897. doi:10.1029/94jd01928

Thompson, L. G., Davis, M. E., Mosley-Thompson, E., Beaudon, E., Porter, S. E., Kutuzov, S., et al. (2017). Impacts of Recent Warming and the 2015/2016 El Niño on Tropical Peruvian Ice Fields. *J. Geophys. Res. Atmos.* 122 (12), 688. doi:10.1002/2017JD026592

Thompson, L. G., Davis, M. E., Mosley-Thompson, E., and Liu, K.-b. (1988). Pre-Incan Agricultural Activity Recorded in Dust Layers in Two Tropical Ice Cores. *Nature* 336, 763–765. doi:10.1038/336763a0

Thompson, L. G. (2000). Ice Core Evidence for Climate Change in the Tropics: Implications for Our Future. *Quat. Sci. Rev.* 19, 19–35. doi:10.1016/S0277-3791(99)00052-9

Thompson, L. G., Mosley-Thompson, E., Bolzan, J. F., and Koci, B. R. (1985). A 1500-Year Record of Tropical Precipitation in Ice Cores from the Quelccaya Ice Cap, Peru. *Science* 229, 971–973. doi:10.1126/science.229.4717.971

Thompson, L. G., Mosley-Thompson, E., Dansgaard, W., and Grootes, P. M. (1986). The Little Ice Age as Recorded in the Stratigraphy of the Tropical Quelccaya Ice Cap. *Science* 234, 361–364. doi:10.1126/science.234.4774.361

Thompson, L. G., Mosley-Thompson, E., Davis, M. E., Zagorodnov, V. S., Howat, I. M., Mikhalenko, V. N., et al. (2013). Annually Resolved Ice Core Records of Tropical Climate Variability over the Past ~1800 Years. *Science* 340, 945–950. doi:10.1126/science.1234210

Vaheddoost, B. (2020). A Spatiotemporal Classification of the Peruvian Precipitations between 1990 and 2015. *Pure Appl. Geophys.* 177, 4509–4520. doi:10.1007/s00024-020-02454-8

Vauchel, P., Santini, W., Guyot, J. L., Moquet, J. S., Martinez, J. M., Espinoza, J. C., et al. (2017). A Reassessment of the Suspended Sediment Load in the Madeira River basin from the Andes of Peru and Bolivia to the Amazon River in Brazil, Based on 10 Years of Data from the HYBAM Monitoring Programme. *J. Hydrol.* 553, 35–48. doi:10.1016/j.jhydrol.2017.07.018

Veettil, B. K., Bremer, U. F., de Souza, S. F., Maier, É. L. B., and Simões, J. C. (2016). Influence of ENSO and PDO on Mountain Glaciers in the Outer Tropics: Case Studies in Bolivia. *Theor. Appl. Climatol.* 125, 757–768. doi:10.1007/s00704-015-1545-4

Vera, C., Higgins, W., Amador, J., Ambrizzi, T., Garreaud, R., Gochis, D., et al. (2006). Toward a Unified View of the American Monsoon Systems. *J. Clim.* 19, 4977–5000. doi:10.1175/JCLI3896.1

Vuille, M., Bradley, R. S., Werner, M., Healy, R., and Keimig, F. (2003). Modeling δ18O in Precipitation Over the Tropical Americas: 1. Interannual Variability and Climatic Controls. *J. Geophys. Res.* 108 (D6). doi:10.1029/2001jd002039

Vuille, M., Bradley, R. S., and Keimig, F. (2000). Climate Variability in the Andes of Ecuador and its Relation to Tropical Pacific and Atlantic Sea Surface Temperature Anomalies. *J. Clim.* 13, 2520–2535. doi:10.1175/1520-0442(2000)013<2520:cvitao>2.0.co;2

Vuille, M., Francou, B., Wagnon, P., Juen, I., Kaser, G., Mark, B. G., et al. (2008). Climate Change and Tropical Andean Glaciers: Past, Present and Future. *Earth-Science Rev.* 89, 79–96. doi:10.1016/j.earscirev.2008.04.002

Vuille, M., Franquist, E., Garreaud, R., Lavado Casimiro, W. S., and Cáceres, B. (2015). Impact of the Global Warming Hiatus on Andean Temperature. *J. Geophys. Res. Atmos.* 120, 3745–3757. doi:10.1002/2015JD023126

Wegner, A., Fischer, H., Delmonte, B., Petit, J. R., Erhardt, T., Ruth, U., et al. (2015). The Role of Seasonality of mineral Dust Concentration and Size on Glacial/interglacial Dust Changes in the EPICA Dronning Maud Land Ice Core. *J. Geophys. Res. Atmos.* 120, 9916–9931. doi:10.1002/2015JD023608

Yarleque, C., Vuille, M., Hardy, D. R., Timm, O. E., De la Cruz, J., Ramos, H., et al. (2018). Projections of the Future Disappearance of the Quelccaya Ice Cap in the Central Andes. *Sci. Rep.* 8, 1–11. doi:10.1038/s41598-018-33698-z

Conflict of Interest: The authors declare that the research was conducted in the absence of any commercial or financial relationships that could be construed as a potential conflict of interest.

Publisher's Note: All claims expressed in this article are solely those of the authors and do not necessarily represent those of their affiliated organizations, or those of the publisher, the editors and the reviewers. Any product that may be evaluated in this article, or claim that may be made by its manufacturer, is not guaranteed or endorsed by the publisher.

frontiers | Frontiers in Earth Science

ORIGINAL RESEARCH
published: 05 April 2022
doi: 10.3389/feart.2022.833637

Holocene Environmental Dynamics of the Lago Cochrane/Pueyrredón Valley, Central West Patagonia (47°S)

Antonio Maldonado[1,2]*, *María Eugenia de Porras*[3], *Alejandra Martel-Cea*[1,4], *Omar Reyes*[5,6], *Amalia Nuevo-Delaunay*[5] and *César Méndez*[5]

[1]Centro de Estudios Avanzados en Zonas Áridas (CEAZA), La Serena, Chile, [2]Departamento de Biología Marina, Universidad Católica del Norte, Coquimbo, Chile, [3]Instituto Argentino de Nivología, Glaciología y Ciencias Ambientales (IANIGLA), CCT CONICET Mendoza, Mendoza, Argentina, [4]Instituto de Ciencias de La Tierra, Facultad de Ciencias, Universidad Austral de Chile, Valdivia, Chile, [5]Centro de Investigación en Ecosistemas de la Patagonia (CIEP), Coyhaique, Chile, [6]Centro de Estudios del Hombre Austral, Instituto de la Patagonia, Universidad de Magallanes, Punta, Arenas

Deglaciation modeling of the Patagonian Ice Field since the Last Glacial Maximum has been a topic of intensive research in Central West Patagonia (44°–49°S). However, the chronology of deglaciation onset, acceleration, and the subsequent thinning and recession of the different ice lobes as well as the timing and extension of large proglacial systems are still a matter of discussion. The maximum eastward extension the Lago Cochrane/Pueyrredón ice lobe was around ~20,000–27,000 cal yrs BP; its associated proglacial lake drained toward the Pacific between 12,600 and 8,000 cal yrs BP. This study presents the first two pollen and charcoal records from the Lago Cochrane/Pueyrredón valley, spanning the last 11,650 cal yrs BP. The Laguna Maldonado record spans between 11,650 and 8,500 cal yrs BP, while the Laguna Anónima record the last 8,500 cal yrs BP, thereby overlapping chronologically. The lithological record of Laguna Maldonado shows that organic sedimentation began at the onset of the Holocene (11,650 cal yrs BP), once the site was free of glacio-lacustrine influence. Between 11,650 and 10,500 cal yrs BP, an open *Nothofagus* forest developed associated with high fire occurrence/frequency, followed by a transitional phase to a closer forest associated with a shift from low to high fire activity up to 9,400 cal yrs BP. Between 9,400 and 8,500 cal yrs BP, the Laguna Maldonado record suggests the development of an open forest or probably scattered patches of forest of variable size in a steppe matrix, probably related to geomorphological and paraglacial dynamics as well as climatic forcings, while the Laguna Anónima record indicates the development of a closed *Nothofagus* forest and high to low fire occurrence/frequency from 8,200 to 3,800 cal yrs BP. Since 3,800 cal yrs BP, a highly dynamic open forest or forest patches scattered in a grass/shrub–grass steppe matrix occurred around Laguna Anónima associated with high fire occurrence/frequency synchronous with an important increase in the presence of hunter-gatherers during the last 3,000 years. The results from the Lago Cochrane/Pueyrredón valley are integrated and discussed at the regional scale alongside other records from Central West Patagonia.

Keywords: Holocene, pollen records, human–environment interaction, environmental dynamics, Central West Patagonia

OPEN ACCESS

Edited by:
Michael R. Kaplan, Columbia University, United States

Reviewed by:
Claudia Mansilla, University of Magallanes, Chile
Bethan Joan Davies, University of London, United Kingdom

***Correspondence:**
Antonio Maldonado
antonio.maldonado@ceaza.cl

Specialty section:
This article was submitted to Cryospheric Sciences, a section of the journal Frontiers in Earth Science

Received: *11 December 2021*
Accepted: *07 March 2022*
Published: *05 April 2022*

Citation:
Maldonado A, de Porras ME, Martel-Cea A, Reyes O, Nuevo-Delaunay A and Méndez C (2022) Holocene Environmental Dynamics of the Lago Cochrane/Pueyrredón Valley, Central West Patagonia (47°S). Front. Earth Sci. 10:833637. doi: 10.3389/feart.2022.833637

INTRODUCTION

During the Last Glacial Maximum (LGM), Central West Patagonia (44–49°S; CWP, **Figure 1A**) was completely covered by the Patagonian Ice Sheet (PIS) which consisted of terrestrial lobes that retreated into large paleolakes on the east and is inferred to have reached the continental shelf on the west coast (e.g., Caldenius, 1932; Coronato and Rabassa, 2011; Harrison and Glasser, 2011; Davies et al., 2020). The PIS retreated into the Andes after the LGM, but the chronology of the onset of deglaciation, its acceleration, the subsequent thinning and recession of the different ice lobes, and the timing and age of large proglacial systems are still a matter of discussion, even though intensive research has been undertaken recently (e.g., Bendle et al., 2017; García et al., 2019; Thorndycraft et al., 2019; Davies et al., 2020; Leger et al., 2021).

The Lago Cochrane–Pueyrredón lobe (47°S) occupied the homonymous and the Chacabuco valleys and reached its eastward maximum extension in the Patagonian steppe around ~20,000–27,000 yrs BP (**Figure 1B**; Turner et al., 2005; Hein et al., 2009; Hein et al., 2010; Hein et al., 2011; Boex et al., 2013; Bendle et al., 2017; Thorndycraft et al., 2019; Davies et al., 2020). Large proglacial lakes developed in these valleys after the onset of deglaciation ca. 18,000 cal yrs BP, until they drained toward the Pacific between 12,600 and 8,000 cal yrs BP (Thorndycraft et al. (2019) and references therein). Large areas were exposed due to these major landscape transformations, offering a wide range of environments to be colonized by biota. Only three paleoenvironmental records, two located in the Chacabuco valley and one in the low Baker River valley, provide insights into the environmental dynamics of CWP (**Figures 1B,C**; Villa-Martínez et al., 2012; Henríquez et al., 2017; Iglesias et al., 2018). On one hand, Lago Edita and Lago Augusta records date back to Termination 1 (19,400 and 15,600 cal yrs BP, respectively) when a mosaic of cold-resistant hygrophilous conifers and rainforest trees along with alpine herbs developed in the Chacabuco valley (Villa-Martínez et al., 2012; Henríquez et al., 2017), followed by the development of a *Nothofagus* forest up to the present (Villa-Martínez et al., 2012). On the other hand, the Mallín Casanova record spans the last 9,950 cal yrs BP and revealed the development of *Nothofagus/Pilgerodendron* rainforests until the Late Holocene, when a major vegetation change led to the development of a more open forest in a grass steppe matrix (Iglesias et al., 2018). As recorded in several records from CWP, the Late Holocene presented vegetation changes of moderate magnitude related to an increased fire event frequency (Markgraf et al., 2007; de Porras et al., 2012; de Porras et al., 2014; Nanavati et al., 2019). This is synchronous with an increase in the human presence of hunter-gatherer groups who occupied the Chacabuco valley at least since 8,600 cal yrs BP, as indicated by a colonization process rooted in the extra-Andean steppes (Mena and Blanco, 2017; Borrero et al., 2019; Nuevo-Delaunay et al., 2022). CWP and supraregional archeological records show marked increases in the number of radiocarbon ages dating to the Late Holocene, which are indicative of human demographic growth and are supported by other archeological evidence (e.g.,

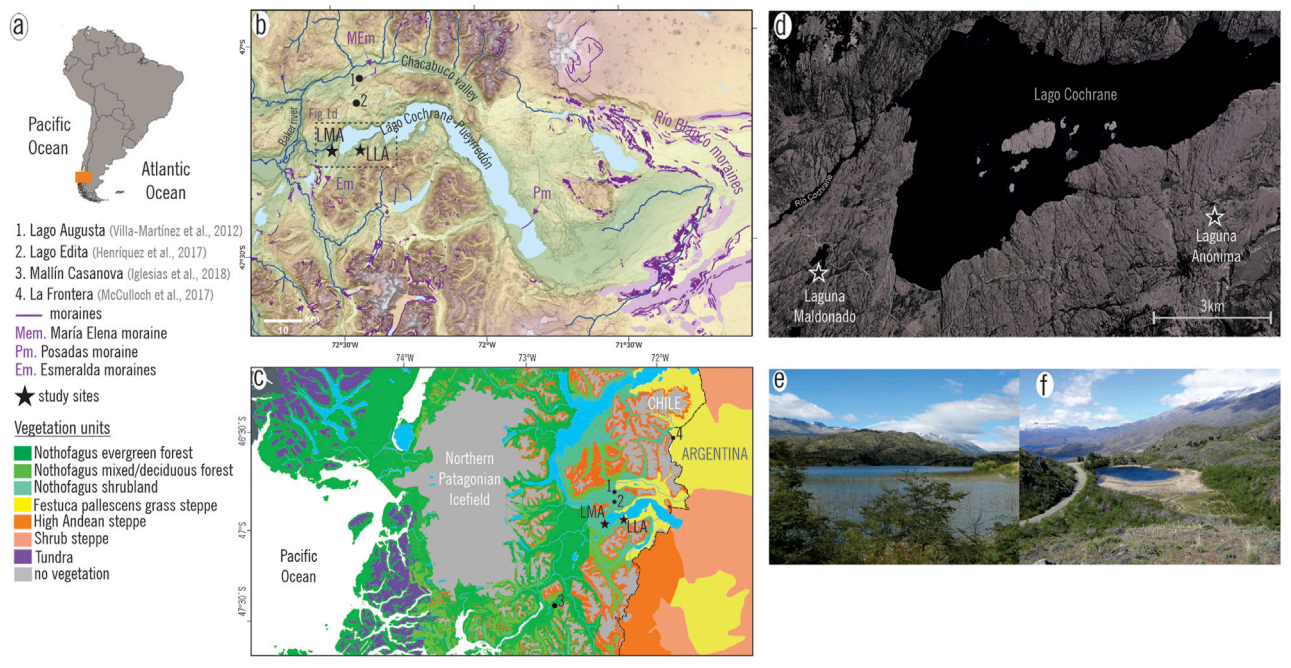

FIGURE 1 | (A) Map of South America showing the study area location; **(B)** digital elevation model (DEM) showing the location of Laguna Maldonado (LMA) and Laguna Anónima (LLA), main glacial geomorphological features (moraines; modified from Bendle et al., 2017; Thorndycraft et al., 2019; Davies et al., 2018, 2020), and sites mentioned in the text; **(C)** vegetation map (taken from Luebert and Pliscoff, 2017) showing the steep west–east gradient and the locations of the paleoenvironmental records reported in this paper and previously published; **(D)** satellite image of the western and southern coasts of Lago Cochrane showing the location of LMA and LLA; photographs of **(E)** LMA and **(F)** LLA.

artifact deposition rates, changes in landscape use), suggesting greater anthropogenic pressure on the ecosystems (García Guraieb et al., 2015; Pérez et al., 2016).

As the geomorphological data indicate, the different glacial lobes in CWP may have undergone independent dynamics during Termination 1 and even well into the Holocene (e.g., Kaplan et al., 2004; Douglass et al., 2006; García et al., 2019; Thorndycraft et al., 2019; Davies et al., 2020; Leger et al., 2021). At the time that cold-resistant hygrophilous conifers and rainforest trees occurred in the Chacabuco valley up to 11,800 cal yrs BP, the Lago Cochrane–Pueyrredón valley was still occupied by a moraine-dammed lake. Hence, the environmental evidence could not be extrapolated to large spatial scales (e.g., other valleys) in CWP, since it may just provide a local and biased picture of past environments. Although landscapes in CWP (47°S) were still under configuration (e.g., proglacial lake drainage, Neoglacial advances) well into the Holocene, most paleoecological records fail to show changes, probably due to their location and sensitivity to track moderate vegetation changes. Thus, the present study aims to 1) reconstruct the environmental dynamics of the Lago Cochrane/Pueyrredón valley since 11,650 cal yrs BP by analyzing the first pollen and charcoal records in this valley, Laguna Maldonado and Laguna Anónima, two small, closed-basin lakes located in the forest-steppe ecotone (**Figure 1C**); 2) relate those environmental changes to the associated drivers (e.g., glacial/postglacial dynamics, climate, humans); and 3) discuss the results in a broader context in order to shed light on the Holocene environmental and climate dynamics of CWP (47°S). The location of Laguna Maldonado and Laguna Anónima at the forest-steppe ecotone in the Lago Cochrane/Pueyrredón valley implies that both pollen records are highly sensitive to track vegetation changes of moderate/slight magnitude associated with Holocene geomorphological, climatic, and/or potentially human-induced changes. The Laguna Maldonado record spans between 11,650 and 8,500 cal yrs BP, while the Laguna Anónima record encompasses the last 8,500 cal yrs BP; the records are correlated stratigraphically by the presence of the conspicuous Hudson volcano (H1) tephra layer (Stern et al., 2016).

MODERN SETTING

The landscape of Central West Patagonia has been modified by glacial action during the whole Quaternary and particularly since the LGM, when the PIS covered the whole region. At present, the Northern Patagonian Ice Field (**Figure 1C**) and other important but smaller glaciers remain after the PIS recession and the accelerated glacial retreat due to the ongoing global warming. The Lago Cochrane/Pueyrredón valley (47°S, **Figure 1B**) is a west–east oriented basin, once occupied by the Lago Cochrane/Pueyrredón ice lobe during the LGM, which reached its maximum eastward extension between 20,000 and 27,000 cal yrs BP (Río Blanco moraine; Hein et al., 2010). The onset of deglaciation of the Lago Cochrane/Pueyrredón ice lobe, as well as most ice lobes in the southern CWP (Glasser et al., 2012; Boex et al., 2013), is dated around 18,000 cal yrs BP (Hein et al., 2010); it was followed by an acceleration of ice thinning and recession that enabled the formation and growth of a large proglacial lake system called Lago Chalenko (e.g., Turner et al., 2005; Bell, 2008; Thorndycraft et al., 2019). Altitudinal, geochronological and isostatic shoreline data indicate that Lago Chalenko drained (at the Bayo level, 350 m a.s.l.) to the Pacific Ocean through the Baker valley between 12,000 and 10,000 cal yrs BP (Thorndycraft et al., 2019) when the Lago Cochrane/Pueyrredón valley was completely free of glacial influence. However, the Lago Cochrane/Pueyrredón valley landscape was similar to that at present ca. 8,000 cal yrs BP, given that a moraine-dammed lake (>120 m a.s.l.) prevailed in the valley until then, as suggested by glacial lake outburst flood (GLOF) records (e.g., flood bars) and stepped deltas (e.g., Turner et al., 2005; Thorndycraft et al., 2019).

The Lago Cochrane/Pueyrredón valley is under the yearlong influence of cold fronts associated with the Southern Westerlies system (SWs) that bring precipitation to southernmost western South America (Garreaud, 2009; Garreaud et al., 2013; Viale et al., 2019). As the cold fronts migrate from the Pacific coast to the east and are intercepted by the Andes, a rain shadow effect is produced by the forced subsidence of surface air masses, producing a steep west–east decreasing precipitation gradient (Garreaud et al., 2013; Viale et al., 2019). Vegetation distribution is conditioned by the W–E precipitation gradient from the *Donatia fascicularis*–dominated tundra and evergreen *Nothofagus betuloides* forests to the *Nothofagus antarctica* and *Berberis ilicifolia* shrubland and the *Festuca pallescens* and *Mulinum spinosum* steppe (**Figure 1C**) (Luebert and Pliscoff, 2017). Evergreen forests are dominated by *Nothofagus betuloides* and the deciduous *Nothofagus pumilio* along with *Berberis ilicifolia*, *Gaultheria mucronata*, and herbs in the understory strata. The *Nothofagus antarctica* and *Berberis ilicifolia* shrubland is a transitional vegetation unit between the forests and the grass steppes (forest-steppe ecotone), which has small (<2 m) *Nothofagus* trees along with shrubs such as *Berberis microphylla*, *Ovidia andina*, and *Ribes magellanicum*, herbs (e.g., *Geranium berteroanum*, *Osmorhiza chilensis*), and ferns (*Blechnum penna-marina*). The easternmost vegetation unit in this steep gradient is the grass steppe dominated by *Festuca pallescens* associated with *Mulinum spinosum*, *Acaena splendens*, and *Baccharis patagonica*.

Laguna Maldonado (LMA; 47,26°S; 72,51°W; 324 m a.s.l.; 207 ha; **Figures 1D,E**) and Laguna Anónima (LLA; 47,25°S; 72,37°W; 484 m a.s.l.; 7 ha; **Figures 1D,F**) are small closed lakes located at the western and southern margins of Lago Cochrane, respectively, and 10 km away from each other (**Figures 1B–D**). Both are located in the "ecotonal" *N. antarctica* shrublands, an ideal and extremely sensitive location to trace past precipitation changes based on vegetation (pollen record) changes. Given the proximity of the lakes along with their location in the same vegetation unit, their pollen records might be similar in vegetation and climatic terms.

MATERIALS AND METHODS

Two independent series of overlapped cores were retrieved from the wetland areas located on the present shores of Laguna

TABLE 1 | AMS radiocarbon ages from cores LMA0608B and LLA 0607A from Laguna Maldonado and Laguna Anónima, respectively. The data marked with * were not included in the age–depth model (see *Materials and Methods*).

Lake	Lab code	Depth (cm)	Adjusted depth (cm)	Material	Age (^{14}C yrs BP)	Age (cal yrs BP)
Laguna Maldonado	*UGAMS 3013	10	0	Bulk sediment	6,880 ± 40	7,674
	*UGAMS 3014	27	16	Charcoal	7,410 ± 40	8,185
	BETA 239612	62	50	Bulk sediment	8,470 ± 40	9,466
	BETA 235377	75	63	Seeds	8,590 ± 50	9,527
	UGAMS 3015	101	85	Bulk sediment	9,380 ± 40	10,554
	BETA 239613	169	153	Bulk sediment	10,080 ± 40	11,528
	*BETA 235378	176	159	Plant material	8,770 ± 50	9,709
Laguna Anónima	D-AMS 038624	55	56	Bulk sediment	650 ± 22	607
	D-AMS 038625	185	184	Bulk sediment	1,629 ± 22	1,477
	UGAMS 16784	307	306	Seeds	1,910 ± 20	1796
	UGAMS 16782	426	425	Charcoal	4,010 ± 30	4,443
	UGAMS 16783	521	520	Charcoal	5,000 ± 25	5,680
	D-AMS 038626	630	629	Bulk sediment	6,448 ± 30	7,340
	BETA 235379	735–738	732–735	Charcoal	7,410 ± 50	8,185

Maldonado (LMA0608B; 193 cm) and Laguna Anónima (LLA 0607A; 745 cm) using a modified Livingstone piston corer. The uppermost part of the Laguna Maldonado core was the present surface of the coastal wetland, underlied by the uppermost reported tephra layer in this paper that dates back to the middle Holocene (see *Results*; Stern et al., 2016). Laguna Anónima yielded a thick volcanic ash layer at 745 cm depth, which impeded coring deeper to a base (potentially glacial clays or an organic sedimentation contact) in this lake.

The sedimentary sequences of both cores were characterized by naked-eye lithological description and X-ray analysis. Loss-on-ignition analysis at 1–2 cm intervals was used to determine organic and inorganic (carbonate and clastic fraction) content (Bengtsson and Enell, 1986; Heiri et al., 2001). The main volcanic ash layers from both records were analyzed and published by Stern et al. (2016). Their origin and eruption were based on age, tephra glass color, morphology, mineralogy, and both bulk and glass chemical analysis (petrology, geochemical composition, and chronology; Stern et al., 2016).

The chronology of cores LMA0608B and LLA0607A was based on seven radiocarbon dates each (**Table 1**), which were calibrated with the Southern Hemisphere calibration curve (SHCal20; Hogg et al., 2020) using the CALIB 8.0.1 program (Stuiver et al., 2020). A Bayesian age–depth model was produced for each composite core with the "rbacon" package (Blaauw et al., 2021) in R platform (R core team, 2021). The basal age and the two uppermost ages of the LMA0608B core from Laguna Maldonado were excluded from the age–depth model. The basal age showed to be an outlier, considering the other ages. The two uppermost ages were excluded since they were younger than the basal H1 tephra layer age ~7,663 ± 35 ^{14}C years, according to Stern et al. (2016). This is probably related to the coring site location and the fact that this is the uppermost part of the core, so it might have been contaminated by younger material from the modern surface of the shore of the lake. We included the average maximum (lake core) basal age of the H1 tephra layer (Stern et al., 2016) to build the Laguna Maldonado age–depth model. Adjusted depths were used to construct an age model assuming instantaneous deposition of tephra layers.

Pollen analysis was performed from 1 cm^3 of sediment samples which were obtained at 4–5 cm intervals and treated with standard laboratory techniques for pollen extraction from the sediments (Faegri and Iversen, 1989). Tablets of the exotic spore *Lycopodium clavatum* were added to each sample to calculate pollen concentration (grains cm^{-3}) (Stockmarr, 1971) and pollen accumulation rates (PARs; grains cm^{-2} yr^{-1}). Pollen grains were identified at 400–1,000 × magnification under a light microscope. The basic pollen sum included at least 300 terrestrial pollen grains per sample. Pollen percentages of terrestrial taxa were based on the sum of trees, shrubs, herbs, and grasses. Aquatic/paludal and fern taxa were calculated based on a sum that included the basic pollen sum and the sum of aquatic and paludal taxa or the sum of ferns, respectively. The pollen diagram was divided into zones using unconstrained CONISS cluster analysis (Grimm, 1987), considering all local terrestrial pollen taxa >2%. The interpretation of LMA and LLA records was aided by comparison with the uppermost pollen samples of both records. The LMA superficial pollen assemblages have ~45% of *Nothofagus dombeyi* type and ~25–12% Poaceae along with Podocarpaceae, *Fitzroya*/*Pilgerodendron*, *Saxegothaea conspicua*, and *Weinmannia trichosperma* (forest); *Escallonia* and *Ribes* (understory); and Asteraceae subf. Asteroideae, Fabaceae, Chenopodiaceae, and *Rumex* (steppe) with percentages under 5% (data not shown).

Macroscopic charcoal particles (>125 um) were counted in both records to infer local fire history in the LLA and LMA sediment cores. 2 cm^3 of the sediment was sampled at contiguous 1 cm intervals, deflocculated in 10% KOH, and sieved through a 125 μm screen (Whitlock and Larsen, 2001). The residual particles were counted in gridded Petri dishes using a stereomicroscope at 10–40 × magnification. The charcoal series of each core was interpolated at its median sample resolution (10 yrs sample^{-1} in LLA and 18 yrs sample^{-1} in LMA) using CHARanalysis software (Higuera et al., 2009).

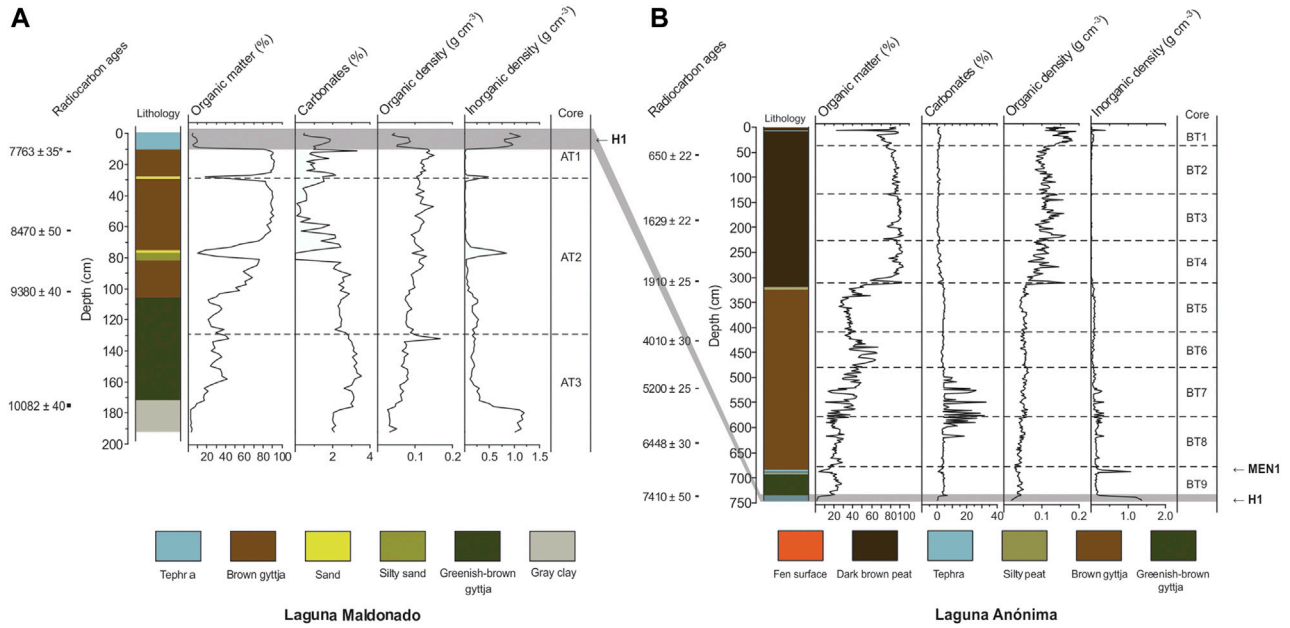

FIGURE 2 | Radiocarbon ages, lithology, and loss-on-ignition results of **(A)** LMA0608B and **(B)** LLA 0607A cores. Letters represent tephra layers described by Stern et al. (2016), and dashed horizontal lines indicate the core boundaries.

The interpolated charcoal accumulation rates ($CHAR_{interpol}$; $cm^{-2}\ yr^{-1}$) were separated into their background ($CHAR_{back}$) and peak accumulations ($CHAR_{peak}$) (Long et al., 1998), which detects significant charcoal peaks interpreted as local fire events.

The series of $CHAR_{back}$ of LLA and LMA were determined using a locally weighted regression (LOWESS) robust to outliers, using a window width of 1,000 years. This window selection allows maximizing the signal-to-noise index and the goodness-of-fit between the empirical and modeled noise distributions (Kelly et al., 2011). The $CHAR_{peak}$ values were calculated by subtracting $CHAR_{back}$ from $CHAR_{interpol}$, and their noise distributions were determined by a Gaussian mixture model using the 99th percentile threshold. The charcoal peaks that exceeded this threshold were considered fire events. Later, the fire peak magnitude (charcoal particles cm^{-2} $peak^{-1}$) and fire event frequency (peaks 1,000 $years^{-1}$) were estimated. Finally, the raw charcoal series of both sites (and their respective age–depth models) were homogenized using bootstrap resampling (min–max rescaling, Box–Cox, and Z-score transformation) to compute one composite curve (binned per 100 years) that was calculated with the "paleofire" R package (Blarquez et al., 2014) as an approach to biomass burning and to summarize the main fire trends through time in the study area.

RESULTS

Lithology and Chronology

The Laguna Maldonado sequence of 193 cm depth is composed of laminated gray clays (193–172 cm) with low organic (2–9%) and carbonate (~2%) content and high values of inorganic density (>1 g cm^{-3}) (**Figure 2A**). Between 172 and 105 cm, the sequence presents a greenish-brown gyttja with variable values of organic matter up to 42% and a concomitant decline of inorganic density (0.15–0.3 g cm^{-3}). From 105 to 10 cm, the occurrence of a brown organic gyttja is associated with the rise of organic matter (up to 90%) at the expense of inorganic density, which had its lowest values (<0.1 g cm^{-3}), except for abrupt increments ranging from 0.5 to 1.1 g cm^{-3} related to volcanic ash layer deposition at the top 10 cm and a silty sand/sand layer observed at 76–81 and 28 cm. Carbonate percentages remained below 4% throughout the sequence, with minimum values from 80 cm to the top of the record.

The Laguna Anónima record is a 747 cm long core including a basal volcanic ash layer of 9 cm at the bottom with high inorganic density values (>1 g cm^{-3}; **Figure 2B**). Between 738 and 689 cm, a layer of greenish-brown gyttja is present, with organic matter values that fluctuate between 21 and 25%. This is overlaid by a 2 cm tephra layer (689–687 cm). Between 687 and 325 cm, the sediment is brown gyttja with highly variable values of organic content (20–60%), particularly between 600 and 510 cm where peaks of carbonates reach up to 31%. A silty peat layer occurs between 325 and 319 cm, overlaid by a dark brown peat associated with a major increase of organic matter (from 30 to 90%) and density (0.5 to >1 g cm^{-3}) from 319 cm to the top. Between 319 and 0 cm, dark brown peat shows low inorganic density (below 0.1 g cm^{-3}), except for a volcanoclastic deposit at 5–6 cm.

Based on previous tephrochronological studies by Stern et al. (2016), the volcanic ash layers were attributed to different Holocene eruptions of the Hudson or Mentolat volcanos. Thus, the tephra layer at 687–689 cm in LLA corresponds to the MEN1 eruption (Mentolat volcano) dated at ca. 7,689 cal yrs BP. The

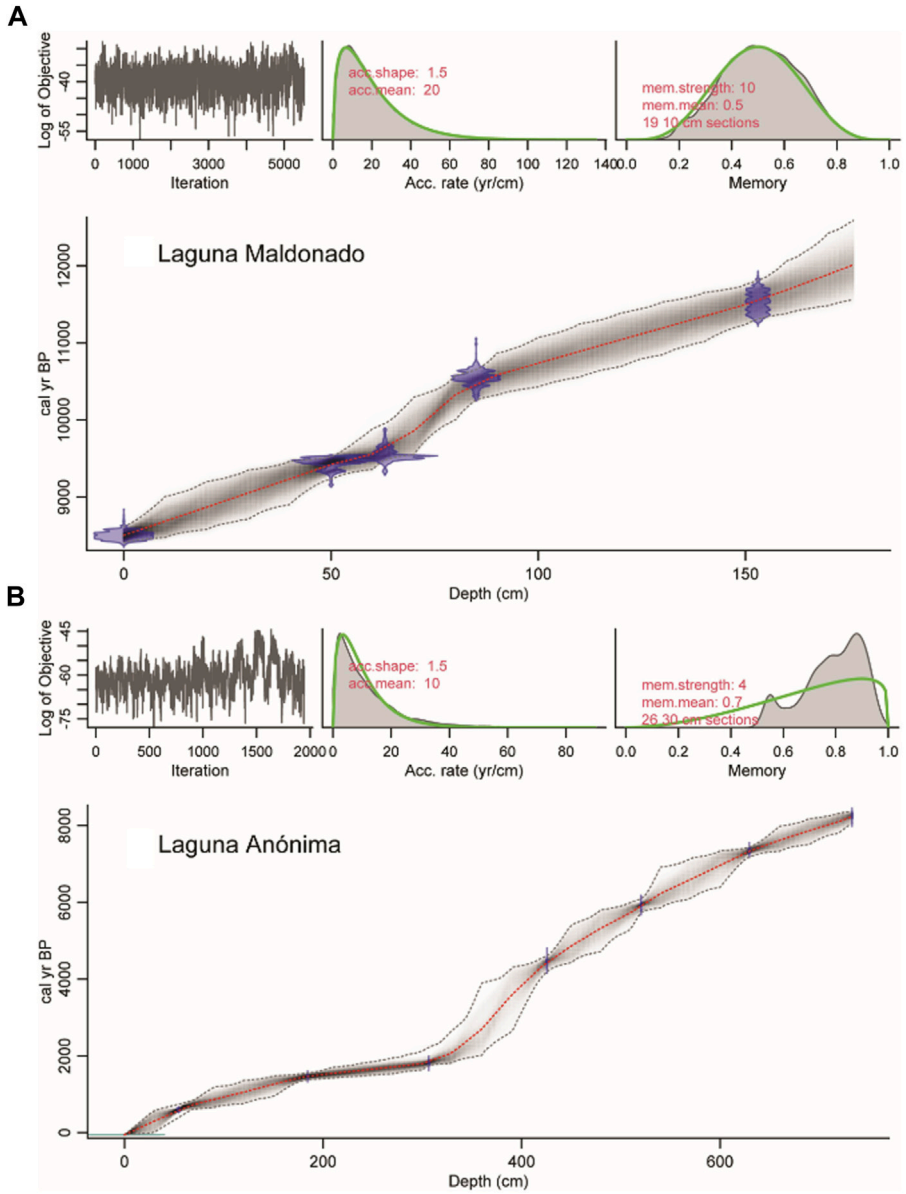

FIGURE 3 | Age–depth models of **(A)** Laguna Maldonado and **(B)** Laguna Anónima records.

tephra layers located in the top 10 cm of the LMA sedimentary sequences and at 736–747 cm of the LLA sedimentary sequences belong to the large explosive H1 eruption (Hudson volcano) dated ca. 8,440 cal yrs BP (median probability).

The record of LMA ranges from 11,650 to 8,500 cal yrs BP (**Figure 3A**; **Table 1**). The sediment deposition time is about 19 years cm^{-1} between 11,650 and 10,500 cal yrs BP and increases up to 25–40 yrs cm^{-1} between 10,500 and 9,700 cal yrs BP (**Figure 4A**). After 9,700 and up to 8,500 cal yrs BP, it dropped to 20 yrs cm^{-1}. The sedimentary record of LLA covers the last 8500 cal yrs BP (**Figure 3B**; **Table 1**). The sediment deposition time overlying the H1 tephra layer gradually increased from 10 to 25 yrs cm^{-1} between 8,200 and 4,200 yrs cm^{-1} and remained relatively constant until 2,100 cal yrs BP (**Figure 4B**). During the last two millennia, the sedimentation rates declined and fluctuated around 5–14 yrs cm^{-1}. This drop in deposition time is associated with a lithological shift from gyttja to peat that indicates the transition of the deposition environment from a lake to a wetland, given the core location at the current position of the lake's shoreline.

Pollen Records of Laguna Maldonado and Laguna Anónima

The pollen record of LMA (ca. 11,650–8,500 cal yrs BP, **Figure 4A**) is dominated mainly by *Nothofagus dombeyi* type and Poaceae. The cluster analysis divided the pollen assemblages into three major zones.

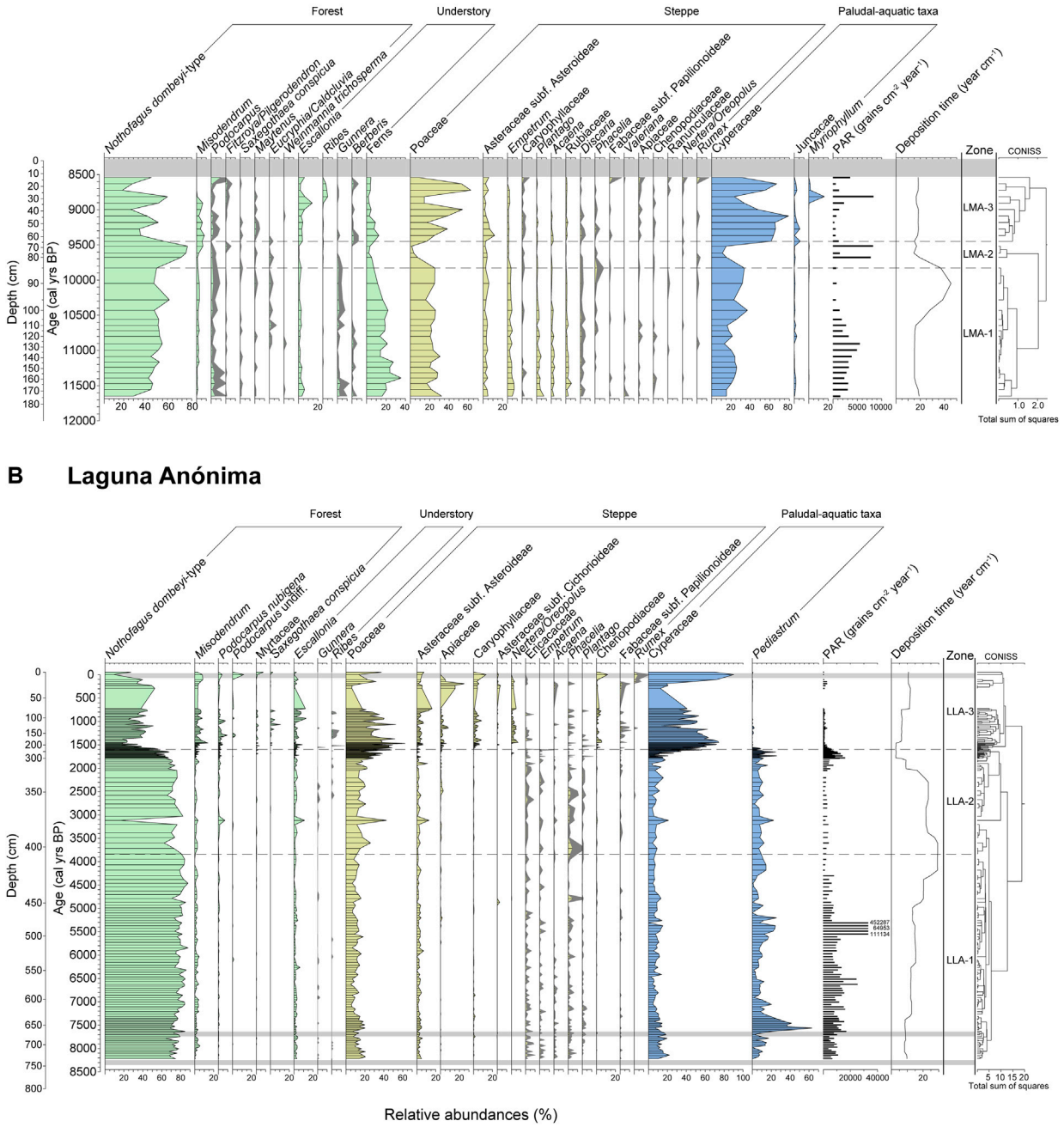

FIGURE 4 | Pollen diagrams of **(A)** Laguna Maldonado and **(B)** Laguna Anónima in percentages including the total pollen accumulation rate (PAR; grains cm^{-3} $year^{-1}$), the deposition time (year cm^{-1}), and the CONISS analysis. Dashed lines denote the pollen zones, and gray horizontal lines denote the position of tephra layers. Gray shadows in some curves of pollen types indicate an exaggeration factor of 4x.

LMA-1 (174–85 cm; 11,650–9,830 cal yrs AP): It is dominated by *Nothofagus dombeyi* type which rapidly increases from 30 to 50% in the first 200 years of the record. Poaceae as secondary taxa fluctuates around 25%. Other forest taxa occur in traces, such as *Podocarpus*, *Escallonia*, and *Gunnera*. Poaceae and other steppe taxa represented by Asteraceae subf. Asteroideae, Rubiaceae, *Acaena*, *Plantago*, and *Empetrum* show percentages below 10%. Fern spores display the highest values (20–30%), whereas the paludal Cyperaceae remains around 30%.

LMA-2 (85–64 cm; 9,830–9,450 cal yrs BP): *Nothofagus dombeyi* type has the highest values (80–85%) in the record, while *Misodendrum* increases after 9,600 cal yrs BP. Poaceae

declines to its lowest values, and the steppe taxa are only recorded in low abundance. Ferns and Cyperaceae also show their lowest values.

LMA-3 (64–11 cm; 9,450–8,500 cal yrs BP): It is characterized by a decline of *Nothofagus dombeyi* type (20–50%) and an increase of Poaceae, which fluctuates between 62 and 8%. Among the forest and understory taxa, *Misodendrum* remains stable, while *Escallonia*, *Ribes*, and ferns increase. Asteraceae subf. Asteroideae shows a slight increase (5–10%) similar to Juncaceae and *Myriophyllum*, whereas Cyperaceae reaches its highest values (up to 80%).

The total pollen accumulation rate (PAR) ranges from ~1,500 to 5,500 grains cm^3 yr^{-1} from 11,650 to 10,400 cal yrs BP (**Figure 4A**) with the highest rates for the whole record of pioneer and cold steppe taxa (**Supplementary Figure S1**). Around 9,700–9,500 cal yrs BP, peaks in PAR (up to 8,100 grains cm^3 yr^{-1}; **Figure 4A**) are mainly associated with a significant increase of *Nothofagus dombeyi*–type PAR (**Supplementary Figure S1**), resembling the percentage diagram. Between 9,400 and 7,700 cal yrs BP, the PAR is the lowest (<1,100 grains cm^3 yr^{-1}; **Figure 4A**) for the whole record except for two minor peaks at 8,800 and 8,500 cal yrs BP which are related to a generalized decrease in the PAR of most taxa (**Supplementary Figure S1**).

The record pollen of LLA encompassed the last 8,200 years and was divided into three zones, where the dominant taxon is *Nothofagus dombeyi* type, accompanied by Poaceae (**Figure 4B**).

LLA-1 (731–404 cm; 8,200–3,830 cal yrs BP): *Nothofagus dombeyi* type dominates the pollen assemblages (~80%, with maxima around 7,200–3,830 cal yrs BP), whereas other forest and understory taxa values such as *Misodendrum* and *Escallonia*, respectively, are present under 5%. Poaceae (~15%) followed by Asteraceae subf. Asteroideae (<10%) is the main representative of the steppe, while Ericaceae, *Empetrum*, *Acaena*, and *Phacelia* only occur in very low percentages (>3%) or have intermittent presence. Among the aquatic and paludal taxa, Cyperaceae and the non-pollen palynomorph *Pediastrum* show values below 20%. Nevertheless, *Pediastrum* displays two increments, around 7,600–7,100 cal yrs BP (up to 60%) and 5,600–5,100 cal yrs BP (up to 25%).

LLA-2 (404–236 cm; 3,830–1,600 cal yrs BP): It is characterized by a slight decrease of *Nothofagus dombeyi* type (~70%) and the concomitant increase of Poaceae (20–40%). The other taxa remain with abundances similar to the previous zone. *Nothofagus dombeyi* type shows an abrupt decrease around 3,200 cal yrs BP, while *Escallonia*, Poaceae, and Asteraceae subf. Asteroideae increase.

LLA-3 (236–0 cm; last 1,600 cal yrs BP): *Nothofagus dombeyi* type shows an important and rapid decline (from 70% to 30%) followed by a slight increase up to 50% after 1,400 cal yrs BP but with highly fluctuating values. Poaceae pollen varies in an opposite way to *Nothofagus dombeyi* type, reaching maximum values above 60%. *Misodendrum*, *Podocarpus nubigenus*, and *Saxegothaea conspicua* increase their percentages, similar to steppe taxa such as Asteraceae subf. Asteroideae, Apiaceae, Caryophyllaceae, Asteraceae subf. Cichioroideae, and *Nertera*/*Oreopolus*. Exotic taxa such as *Rumex* (<10%) occur in the last ~150 cal yrs BP of the record. Cyperaceae values rise close to 90%, while *Pediastrum* decreases almost to zero.

PAR values are highly variable, ranging between 3,700 and 450,000 grains cm^3 yr^{-1} (**Figure 4B**), but are much higher than those in the LMA record. *Nothofagus dombeyi* type and Poaceae are the two most abundant pollen types in the total PAR throughout the record (**Supplementary Figure S2**). The PAR remains under 20,000 grains cm^3 yr^{-1} from 8,200 to 4,500 cal yrs BP, interrupted by a major PAR peak between 5,600 and 5,200 cal yrs BP which is associated with a generalized PAR increase of most of the pollen types (**Figure 4B**; **Supplementary Figure S2**). Between 4,500 and 1900 cal yrs BP, the PAR remains stable around 5,000 grains cm^3 yr^{-1}, mostly associated with a steady PAR of *Nothofagus dombeyi* type (~1,000–5,000 grains cm^3 yr^{-1}). Around 1900 cal yrs BP, a second minor peak in PAR is recorded, probably associated with a change in the deposition time as a consequence of the clogging of the shore of LLA (wetland). *Nothofagus dombeyi* type, ferns, Poaceae, and Asteraceae subf. Asteroideae show this peak in PAR individually (**Supplementary Figure S2**). A dramatic reduction in total PAR, as well as in the individual pollen type PAR, occurs around 1,600 cal yrs BP associated with the development of the wetland, implying a higher (lower) sedimentation rate (deposition time) (**Figure 4B**).

The Macro-Charcoal Particle Records of Laguna Maldonado and Laguna Anónima

The charcoal records of LMA and LLA show high variability on millennial and multi-centennial scales (**Figure 5**). The LMA record displays the highest CHAR around 11,650–10,500, 9,700–9,500, and 8,800–8,500 cal yrs BP (**Figure 5A**), while the highest CHAR values in LLA occur around 8,200–7,500 cal yrs BP, 6,600 cal yrs BP, and 1,100–700 cal yrs BP (**Figure 5B**). The global signal-to-noise index of LMA and LLA records reaches 5.8 and 6.6, respectively, indicating that both records are suitable for peak detection (Kelly et al., 2011).

Eighteen significant fire events were inferred in the LMA record (11,700–8,500 cal yrs BP). Periods with high fire event frequency are around 11,700–10–500 cal yrs BP and after 9,700 cal yrs BP (4–9.5 fire events 1,000 $years^{-1}$), whereas low incidence occurs between 10,500 and 9,700 cal yrs BP. The largest fires may have occurred around 9,700 cal yrs BP, where a fire event magnitude reached up to 8,000 particles cm^{-2} $peak^{-1}$.

In the LLA record (8,500 cal yrs BP), 47 significant fire events were inferred, reaching the highest frequency prior to 7,500 cal yrs BP, and between 2000 and 1,000 cal yrs BP (up to 12 fire events 1,000 $years^{-1}$). In the last millennia, the decline of CHAR values and the fire frequency suggest that fire activity decreases. The maximum fire peak magnitudes occur around ~8,200–7,600, ~6,600, 5,500–4,800, and ~1,100 cal yrs BP, reaching up to 18,400 particles cm^{-2} $peak^{-1}$ in the last one.

The composite charcoal curve summarizes the main patterns of the charcoal deposition of the LMA and LLA records that can be interpreted as biomass burning over time (**Figure 5C**). Positive trends of biomass burning are noted at ~11,650–10,500, ~9,500, ~8,700–5,100, and 1800–600 cal yrs BP, intercalated with periods with negative values at ~10,500, ~9,300–8,700, and 5,100–1900 cal yrs BP and during the last 600 years.

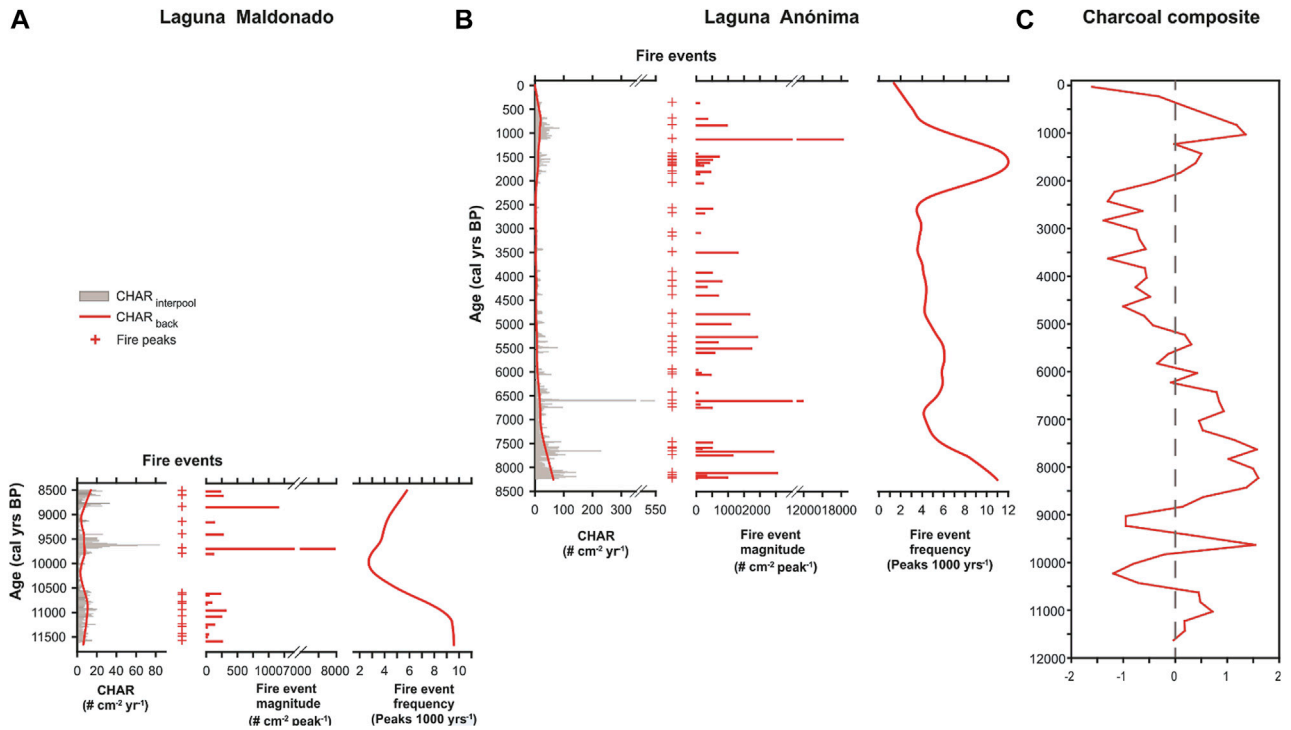

FIGURE 5 | Charcoal accumulation rates ($CHAR_{interpol}$ and $CHAR_{back}$), inferred fire events, fire peak magnitudes, and fire event frequency of **(A)** Laguna Maldonado and **(B)** Laguna Anónima. **(C)** Composite curve of the charcoal series of Laguna Maldonado and Laguna Anónima records summarizing biomass burning over time. The gray shadow indicates the 95% confidence interval.

DISCUSSION

Paleoenvironmental Interpretation

The pollen and charcoal records of Laguna Maldonado and Laguna Anónima (**Figures 4A,B**, **5A–C**) provide a quite complete picture of the paleoenvironmental dynamics of the Lago Cochrane/Pueyrredón valley during the Holocene, once the westernmost area of Lago Cochrane was free of ice influence. Once the Chalenko lake was drained through the Baker River valley (<350 m a.s.l.), organic sedimentation began in Laguna Maldonado (~324 m a.s.l.) around 11,650 cal yrs BP, as reflected by the transition between lacustrine gray clays and greenish-brown gyttja (**Figure 2A**). Between 11,650 and 10,500 cal yrs BP, an open *Nothofagus* forest developed, as suggested by the percentages of *Nothofagus dombeyi* type reaching up to 50% associated with *Escallonia*, *Berberis*, and ferns in the understory (**Figure 4A**). This forest was intermingled with a cold steppe dominated by Poaceae along with *Empetrum*, *Acaena*, *Plantago*, and Rubiaceae, most pioneer and/or shade-intolerant species, indicating primary colonization stages of new ecological niches in the postglacial landscapes (de Porras et al., 2012; Markgraf et al., 2007; Moreno, 2020, Heusser, 2003). This vegetation assemblage suggests colder conditions than present, although under similar precipitation. The high CHAR values, frequency fire events, and positive anomaly of the CHAR composite curve (**Figure 5A**) are synchronous with relatively high PAR values between 11,650 and 10,400 cal yrs BP (**Supplementary Figure S1**), which suggests an increment of burnable fuel but also a marked dry season (precipitation seasonality), hence ideal conditions for fire to occur in ecotone areas (Holz and Veblen, 2012). From 10,500 to 9,800 cal yrs BP, *Nothofagus dombeyi*–type percentages increase slightly, while *Escallonia*, *Gunnera*, and fern values decrease along with cold steppe taxon percentages (**Figure 4A**), thus suggesting a transitional phase to a more closed forest associated with a shift to low fire activity (**Figure 5A**). Thus, the pollen record suggests the onset of an increasing precipitation trend synchronous with a temperature increase up to those similar to the present values, while the charcoal record points to a reduction in seasonality.

By 9,800 cal yrs BP and up to 9,400 cal yrs BP, an increase in *Nothofagus dombeyi*–type percentages at the expense of understory pollen types (*Escallonia*, *Gunnera*, fern spores), Poaceae, and *Empetrum* indicates the development of a closed *Nothofagus* forest which is followed by an increment of fire activity at 9,600–9,400 cal yrs BP. This may suggest a rise in precipitation (even over modern values) with a completely reduced seasonal and/or interannual (wet winters and dry summers) variability that may have promoted the colonization of *Nothofagus* species after fire disturbances (e.g., Mallín El Embudo, de Porras et al., 2014). Locally, the decrease in Cyperaceae values (<20%) supports the latter, since a yearlong high lake level would have reduced coastal areas to be colonized

by species of this family (**Figure 4A**; Heusser, 2003; de Porras et al., 2012).

Between 9,400 and 8,500 cal yrs BP, a decrease of *Nothofagus dombeyi*–type percentages (even under the present ones) along with highly variable values associated with an increase of understory taxon percentages such as *Escallonia* and *Ribes* and the rise of the values of the exclusive *Nothofagus* parasite *Misodendrum* (more frequent in periodically disturbed forests; Haberle et al., 2000) as well as steppe pollen types such as Poaceae and Asteraceae subf. Asteroideae (**Figure 4A**) suggest not just an open forest but probably scattered patches of forest of variable size developed in a steppe matrix. This may indicate a reduction in precipitation except for a short period between ~8,900 and 8,800 cal yrs BP when *Nothofagus dombeyi*–type percentages increased. The latter might be indicating a reversal in moisture availability (precipitation), similar to the period between 9,800 and 9,400 cal yrs BP associated with high charcoal accumulation rate and the deposition of clastic layers. Cyperaceae percentages support both inferences (**Figure 4A**): first, the reduction in precipitation as paludal vegetation is favored by larger coastal areas, and second, the 200-year precipitation increase is reflected as a Cyperaceae percentage decrease due to a reduction of areas around the lake to be colonized. However, it is key to highlight that the western Lago Cochrane/Pueyrredón valley was still undergoing large landscape transformations related to the postglacial and Neoglacial processes. On the one hand, three moraine-dammed lakes that occupied the Lago Cochrane/Pueyrredón valley collapsed, as shown by the GLOFs and their associated geoforms as flood bars, between ~11,700 and 8,000 cal yr BP (Thorndycraft et al., 2019), while Neoglacial advances were recorded ~10,900 ± 1,300 and ~7,900 ± 1,100 years BP in the Lago General Carrera/Buenos Aires basin (Bourgois et al., 2016). On the other hand, the Lago Cochrane/Pueyrredón valley and most CWP experienced the fall of volcanic ash of two explosive eruptions from the Mentolat (MEN1) and Hudson (H1) volcanos (Stern et al., 2016). Since the opening of the forest predates either glacial or volcanic processes, it is likely that this change responds to a climatic forcing (precipitation decrease), though it cannot be excluded that the high variability of pollen assemblages (and therefore vegetation) during this time is associated with a combination of forcings. The high fire activity between 9,400 and 8,500 cal yrs BP is just based on the fire frequency but not on biomass burning due to the low magnitude of fire events.

Unlike the record of Laguna Maldonado (LMA), Laguna Anónima (LLA) reflects the development of a closed *Nothofagus* forest at least from 8,200 until 3,800 cal yrs BP, as suggested by steady percentages of *Nothofagus dombeyi* type around 70–80% (**Figure 4B**). It is likely that the location of LLA 10 km eastward and 150 m higher in altitude than LMA (**Figure 1B**) provided more stable environmental conditions and lesser magnitude geomorphological changes than those occurring further west in the Lago Cochrane/Pueyrredón valley; hence, vegetation was less disturbed. Besides, ash fall of both explosive eruptions (MEN1 and H1) did not affect vegetation in any significant manner around LLA (**Figure 4B**). Thus, the presence of a closed *Nothofagus* forest around LLA associated with low fire occurrence frequency, particularly between 7,100 and 3,800 cal yrs BP, suggests higher than present precipitation and reduced seasonality.

Since 3,800 cal yrs BP, a slight decrease in *Nothofagus dombeyi*–type percentages (65–50%) and the concomitant increase of Poaceae indicate a gradual opening of the forest up to 1,600 cal yrs BP, when a major change is recorded at both the local (basin) and regional scales (**Figure 4B**). The coastal areas of Laguna Anónima became a wetland, as revealed by the changes in lithology (shift to peat sediment), organic matter percentages (80%; **Figure 2B**), and the Cyperaceae (*Pediastrum*) percentages increasing (decrease) up to 70% (almost 0%) (**Figure 4B**). A dramatic increase of Poaceae and other steppe taxa (Asteraceae subf. Asteroideae, Apiaceae, and Caryophyllaceae) at the expense of *Nothofagus dombeyi* type from 1,600 up to 150 cal yrs BP (**Figure 4B**) occurred later, associated with the highest fire occurrence frequency for the whole record. Even though there is synchronicity of local and regional vegetation changes, we think it has no relationship to the changes in the deposition environment, as it is supported by the PAR results (**Supplementary Figure S2**), as well as similar and synchronous changes recorded in other sites of CWP (Iglesias et al., 2018; de Porras et al., 2014; see *Regional Discussion*). This implies the development of a highly dynamic open forest or forest patches scattered in a grass/shrub–grass steppe matrix, suggesting a decrease in precipitation but under strong seasonality, as revealed by the high fire occurrence frequency.

The last 150 cal yrs BP reflects a decrease in *Nothofagus dombeyi* type, interpreted as Euro-Chilean settlement–related changes as a consequence of logging and/or opening areas for cattle breeding as well as the appearance of *Rumex*, an exotic and invasive herb, related to the introduction of livestock (**Figure 4B**; Cárdenas et al., 1993; Martinic, 2005).

Regional Discussion

After the Lago Cochrane/Pueyrredón ice lobe reached its LGM extension into the steppe around 20,000–27,000 cal yrs BP, as indicated by the Río Blanco moraines, the deglaciation of this ice lobe began at around 20,000–18,000 cal yrs BP (**Figure 6A**; Hein et al., 2009; Hein et al., 2010; Hein et al., 2011, Thorndycraft et al., 2019). Consequently, the Chacabuco and Lago Cochrane/Pueyrredón valleys experienced ice thinning and recession and the development of large proglacial lakes that drained to the Atlantic above 500–600 m a.s.l. (Stage 1; **Figure 6A**; Thorndycraft et al., 2019). Once proglacial lakes ceased to inundate deglaciated areas, a mosaic of cold-resistant hygrophilous conifers and rainforest trees and a scrubland dominated by Poaceae and accompanied by cold steppe taxa developed above the modern tree line in the Chacabuco valley (570 m a.s.l.) between 19,000 and 16,800 cal yrs BP (**Figure 6B**; Henríquez et al., 2017). Similar vegetation was recorded around Lago Augusta by 16,000–15,000 cal yrs BP (**Figure 6C**; Villa-Martínez et al., 2012) when the Atlantic drainage of the proglacial lakes in the Chacabuco and Lago Cochrane/Pueyrredón valleys (~460 m a.s.l.) was abandoned and the ice front was westward of the easternmost part of both valleys (Stages 2 and 3; **Figure 6A**; Thorndycraft et al., 2019). By 15,000 cal yrs BP, the Barrancos

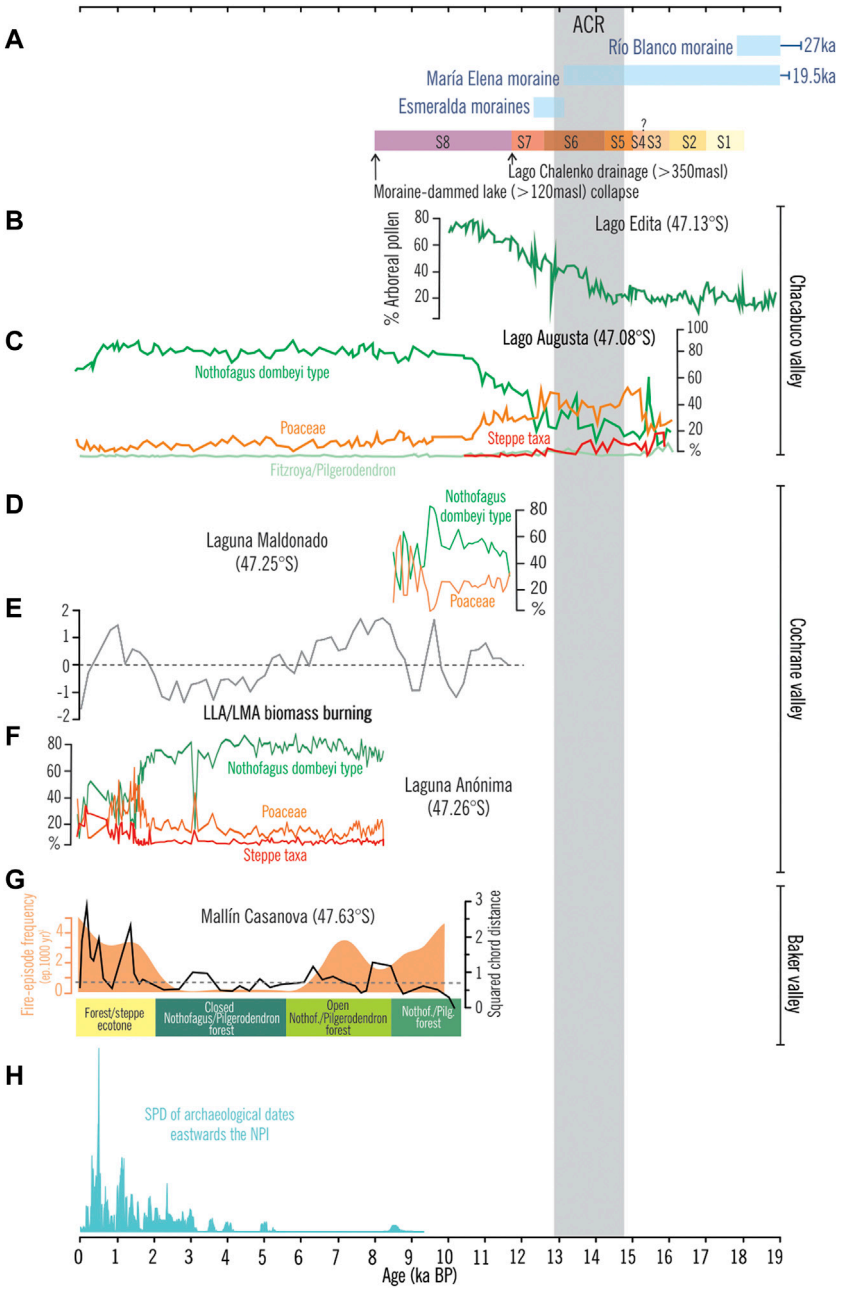

FIGURE 6 | Integration of selected paleoenvironmental data from CWP since the LGM showing **(A)** the chronology of the Chacabuco and Lago Cochrane/Pueyrredón main moraines and the deglaciation stages of Lago Buenos Aires/General Carrera and Lago Cochrane/Pueyrredón proposed by Hein et al., 2009, 2010; Villa-Martínez et al., 2012; Boex et al., 2013; Turner et al., 2005; Glasser et al., 2012; Davies et al., 2018, 2020; Thorndycraft et al., 2019; **(B)** Lago Edita arboreal pollen percentages (Henríquez et al., 2017); **(C)** Lago Augusta summarized pollen diagram (Villa-Martínez et al., 2012); **(D)** a summarized pollen diagram (%) of Laguna Maldonado; **(E)** raw composite charcoal series as a proxy of biomass burning from LMA and LLA; **(F)** a summarized pollen diagram (%) of Laguna Anónima; **(G)** Mallín Casanova vegetation changes, fire-episode frequency, and square chord distance as a proxy of vegetation change magnitude (Iglesias et al., 2018); **(H)** summed probability distribution curve of archeological ^{14}C ages from the eastern side of the NPI (Nuevo Delaunay et al., 2022).

spillway opened (440 m a.s.l.) and the proglacial lakes drained to the Pacific Ocean through the Baker River valley (Stage 4; **Figure 6A**; Thorndycraft et al., 2019). After glaciers re-advanced during the Antarctic Cold Reversal (ACR; Stage 5; **Figure 6A**), a large proglacial lake called Lago Chalenko formed, inundating the Lago General Carrera/Buenos Aires, Chacabuco, and Lago Cochrane/Pueyrredón basins below 350 m a.s.l. between 14,200 and 12,600 cal yrs BP (Stage 6; **Figure 6A**; Davies et al., 2018; Thorndycraft et al., 2019). The mosaic of hygrophilous *Fitzroya/Pilgerodendron* conifers and scrubland prevailed in the Chacabuco valley under millennial-scale fluctuations until 11,800 cal yrs BP (**Figures 6B,C**; Villa-

Martínez et al., 2012; Henríquez et al., 2017) even though no vegetation changes occurred synchronous to the ACR and/or the Lago Chalenko formation.

The drainage of Lago Chalenko (at the Bayo level, 350 m a.s.l.) to the Pacific Ocean through the Baker valley occurred around 12,000–10,000 cal yrs BP (Stage 7; **Figure 6A**; Thorndycraft et al., 2019). After 11,800 and up to 9,800 cal yrs BP, a dense *Nothofagus* forest established at the expense of the decline in hygrophilous and cold-resistant trees, herbs, and shrubs associated with high fire frequency in the Chacabuco valley (**Figures 6B,C**; Villa-Martínez et al., 2012; Henríquez et al., 2017). In the Lago Cochrane/Pueyrredón valley, organic sedimentation began in Laguna Maldonado at 11,650 cal yrs BP when an open *Nothofagus* forest intermingled with a cold steppe (**Figure 6D**) developed up to 10,400 cal yrs BP, suggesting colder conditions but similar precipitation to the present. These colder conditions could be related to a glacial re-advance recorded in CWP (Bourgois et al., 2016; Davies et al., 2020; Glasser et al., 2012; Harrison et al., 2012). The pollen record of Laguna Maldonado also shows low percentages (<5%) of hygrophilous and cold-resistant trees (e.g., *Podocarpus*, *Fitzroya*/*Pilgerodendron*) similar to that recorded in the Chacabuco valley during Termination 1 (18,000–11,000 cal yrs BP). However, based on the comparison of the LMA pollen assemblages and modern pollen assemblages from westernmost CWP rainforests (Haberle and Bennett, 2001), we interpret the low percentages of hygrophilous and cold-resistant trees as indicating azonal conditions restricted to the border of the lake rather than reflecting zonal vegetation, and/or long-distance dispersal of pollen grains from rainforests located westward (Haberle and Bennett, 2004). The occurrence of positive anomalies of CHAR in the Lago Cochrane/Pueyrredón (**Figure 6E**) and Chacabuco valleys between ca. 11,700–10,500 and 11,800–9,800 cal yrs BP, respectively, is synchronous with a shift in the fire regime of CWP (de Porras et al., 2012, 2014; Nanavati et al., 2019) and most Patagonian records south of 40°S (e.g., Markgraf et al., 2007; Whitlock et al., 2007; Abarzúa and Moreno, 2008; Power et al., 2008; Nanavati et al., 2019; Villa-Martínez and Moreno, 2021). This may have been related to the increase in *Nothofagus* abundance, as well as to warmer winters which extended the growing season and effectively drier summers which increased fire activity (Renssen et al., 2005; Whitlock et al., 2007). This environmental setting occurs broadly in southern most South America, linked to a decline of the SWs wind strength between ~11,300 and 7,500 cal yrs BP (Moreno et al., 2021).

It was not until 8,000 cal yrs BP that the landscape of the Lago Cochrane/Pueyrredón valley became similar to the present, given that a moraine-dammed lake (>120 m a.s.l.) developed and collapsed sometime between 11,000 and 8,000 cal yrs BP (Stage 8; **Figure 6A**; Thorndycraft et al., 2019). A transitional phase to a closed forest and the associated fire regime shift to low fire activity that occurred from 10,500 to 9,800 cal yrs BP in the Lago Cochrane/Pueyrredón valley (**Figures 6D,E**), while closed *Nothofagus* forests were established in the Chacabuco and Coyhaique valleys showing little variation from 9,800 and 9,400 cal yrs BP to recent, respectively (**Figures 6B,C**; Villa-Martínez et al., 2012) (Villa-Martínez and Moreno, 2021). Unlike the Chacabuco and Coyhaique valleys, the Laguna Maldonado record suggests the development of an open forest or probably scattered patches of forest of variable size in a steppe matrix between 9,400 and 8,500 cal yrs BP, probably related to climatic forcings and alternatively geomorphological and paraglacial dynamics. The Laguna Anónima record, located at a more distal position regarding the periglacial influence, indicates the development of a closed-canopy *Nothofagus* forest (peaking ~7,100 cal yrs BP) and low fire occurrence frequency from ~8,250 to 3,800 cal yrs BP. Further south and west, alternating open-to-closed evergreen *Nothofagus* and *Pilgerodendron* forests developed around Mallín Casanova since the Early Holocene to 2000 cal yrs BP without major changes (**Figure 6G**; Iglesias et al., 2018). This sustained forest development since the Early Holocene to the Late Holocene associated with a low fire occurrence/frequency was recorded regionally in CWP and was related to increased precipitation but under reduced seasonality (Markgraf et al., 2007; de Porras et al., 2012; de Porras et al., 2014; Nanavati et al., 2019; Villa-Martínez and Moreno, 2021). Neoglacial advances do not seem to have strongly affected the dynamics of vegetation, except for a strong increase of PAR in Laguna Anónima between ~5,500 and 5,000 yrs BP, which may be an expression of a more dense forest, consistent with glacial advances recorded in CWP and South West Patagonia (Davies et al., 2020; Harrison et al., 2012; Kaplan et al., 2016; Sagredo et al., 2018). These Neoglacial advances were associated with a strengthening of the Southern Westerlies winds and a negative phase of SAM-like to millennial–submillenial time scale (Kaplan et al., 2016; Kaplan et al., 2020). A mild decreasing trend in *Nothofagus* percentages began at 3,800 cal yrs BP around Laguna Anónima, followed by a major change from a closed to an open *Nothofagus* forest peaking at 1900–1,600 cal yrs BP (**Figure 6F**) associated with an increased fire occurrence/frequency and magnitude since 2000 cal yrs BP (**Figure 6E**). A synchronous vegetation and fire regime change occurred around Mallín Casanova, where a closed *Nothofagus*/*Pilgerodendron* forest changed to a forest/steppe ecotone, also associated with a rise in the fire occurrence frequency (**Figure 6G**; Iglesias et al., 2018), which suggests regional (rather than local) forcing as a driver of such important vegetation changes. Late Holocene changes were also recorded in other sites of CWP at 44°S, with retraction of *Nothofagus* forest and steppe expansion. Forest around Lago Shaman began retraction at 3,000 cal yrs BP, peaking between 2000 and 1,500 cal yrs BP, while the Mallín El Embudo record shows forest retraction between 4,200 and 2000 cal yrs BP (de Porras et al., 2012, 2014). At 47°S, La Frontera shows a *Nothofagus* forest retraction between 4,000 and 2,100 cal yrs BP (McCulloch et al., 2017). Other records, such as Lago Augusta (47°S) (**Figure 6C**; Villa-Martínez et al., 2012), Lago Mellizas and Lago Churrasco at 45°S (Moreno et al., 2019; Villa-Martinez and Moreno, 2021), do not show any vegetation changes until recent times (last 150 cal yrs BP) when the European settlement started in this part of Patagonia (Nuevo-Delaunay, 2015).

The fact that some records show Late Holocene vegetation changes while some others fail to do so could be related to their location and/or the sensitivity of the surrounding vegetation to

respond to moderate magnitude and/or sudden climatic changes. Late Holocene vegetation and fire regime changes could be the result of a summer insolation anomaly increase regarding the present levels during the Late Holocene (Alder and Hostetler, 2015; Nanavati et al., 2019), superimposed on an intensified seasonal and/or interannual precipitation variability, and therefore highly variable Southern Westerlies winds, in response to the increased frequency at annual to secular timescale of the Southern Annular Mode-like (SAM-like) conditions as reported at the regional scale for Sudamerica (Dätwyler et al., 2018), James Ross Island (58°S; Abram et al., 2014), and at the local scale for Lago Cipreses (49°S; Moreno et al., 2014; Moreno et al., 2018).

The pollen record of Laguna Anónima does not show conclusive evidence related to glacial advances in the Late Holocene which have been recorded along Patagonia, especially between ~2000–1,000 cal yrs BP and ~500–200 cal yrs BP (e.g., Davies et al., 2020 and references therein). Those advances were of a lesser magnitude and extension than those that occurred during the Early Holocene and Mid-Holocene. Thus, pollen records within the forest such as Lago Augusta (Villa-Martínez et al., 2012) and Lago Mellizas (Villa-Martinez and Moreno, 2021) or near the modern forest-steppe ecotone such as Lago Shaman (de Porras et al., 2012), Mallín El Embudo (de Porras et al., 2014) and Laguna Anónima are not sensitive to variations of this magnitude. However, records such as La Frontera (McCulloch et al., 2017), in the forest-steppe ecotone but very close to mountains up to 2000 m high, and Mallín Casanova (Iglesias et al., 2018) in the Baker River watershed very close to NPI show changes in concordance with the main Neoglacial advances occurred during the Late Holocene.

Similar to the glacial advances/retreats, changes in vegetation have been associated with greater or lesser influence of the SWs (e.g., de Porras et al., 2012; Glasser et al., 2012; Kaplan et al., 2016; Davies et al., 2020; Villa-Martinez and Moreno, 2021). However, the changes recorded are very dissimilar throughout the latitudinal range of Southern Westerlies' influence, from subtropical to Antarctic zones (e.g., Villa-Martínez et al., 2003; Maldonado and Villagrán, 2006; Moreno et al., 2018; Nanavati et al., 2019; Davies et al., 2020; Kaplan et al., 2020). Particularly in Patagonia, the differences between records have been associated with latitudinal expansions or retractions of the SWs, greater or lesser strength of the SWs, and/or latitudinal displacement of this climatic belt (e.g., Villa-Martínez et al., 2012; de Porras et al., 2014; Quade and Kaplan, 2017; Moreno et al., 2019). Our records, like most CWP pollen records, show changes in pollen assemblages associated with greater or lesser influence of SWs, with greater influence of SWs during times of expansion of the forests. In this sense, the differences with other records of this nature in CWP (e.g., Markgraf et al., 2007; de Porras et al., 2012; Villa-Martínez et al., 2012; Henríquez et al., 2017; McCulloch et al., 2017; Nanavati et al., 2019; Villa-Martínez and Moreno, 2021) are related with a different sensitivity of the records. Thus, a more complete view of the behavior of SWs, particularly during the Holocene, where the magnitude of change is smaller than during the last glacial termination, requires the integration of information from different records at the regional scale.

Besides to the climatic forcing, the archeological record eastward the Northern Patagonian Ice Field reveals a marked increase in dated occupational events, indicating a change from a discontinuous human presence from 8,600 to 3,000 cal yrs BP to a continuous one from 3,000 cal yrs BP onward (**Figure 6H**; Nuevo-Delaunay et al., 2022). This trend has been acknowledged for Late Holocene archeological records of the wider west central Santa Cruz area (Argentina), encompassing several neighboring basins to the east of the study area (Sacchi et al., 2016; Goñi et al., 2019; Mengoni Goñalons et al., 2019). Groups residing more permanently in the eastern steppes have been interpreted as part of the same mobile populations occupying western valleys less intensely, for instance, as indicated by the use of geochemically traced toolstones procured in eastern sources (Borrero, 2004; Méndez et al., 2018). Thus, humans occupying the broader area cannot be discarded as potential ignition agents forcing vegetation change, as has been suggested for other valleys in CWP (Méndez et al., 2016).

CONCLUSION

The Laguna Maldonado and Laguna Anónima lake sediment cores are the first paleoenvironmental records from the Lago Pueyrredón/Cochrane valley. They provide key evidence to constrain the deglaciation dynamics of CWP. The contact of glacio-lacustrine clays and organic sediments in the Laguna Maldonado record indicates a minimum age for the drainage of Lago Chalenko (below 324 m a.s.l.) through the Baker River valley at the onset of the Holocene.

The establishment of open *Nothofagus* forests associated with cold steppes between 11,650 and 10,400 cal yrs BP followed by a transitional phase to closed *Nothofagus* forests by 10,400–9,400 cal yrs BP suggests increasing trends in temperature and precipitation up to 10,400 and 9,400 cal yrs BP, respectively. Centennial-scale fluctuating scattered patches of *Nothofagus* forest of variable size in a steppe matrix from 9,400 to 8,500 cal yrs BP were related to geomorphological and paraglacial dynamics as well as climatic forcing. The Laguna Anónima record, located in an upper/eastward and therefore more stable position, indicates the development of a closed *Nothofagus* forest and low fire occurrence frequency from 8,200 to 3,800 cal yrs BP, thus suggesting higher than present precipitation and reduced seasonality. Since 3,800 cal yrs BP, a decreasing trend in *Nothofagus* percentages is recorded, followed by a major change from a closed to an open *Nothofagus* forest that peaked between 1900 and 1,600 cal yrs BP, associated with increased fire occurrence frequency and magnitude since 2000 cal yrs BP. The synchronicity and direction of Late Holocene vegetation changes in the Lago Cochrane/Pueyrredón valley with other records from CWP reveal a regional climatic driver, probably associated with a summer insolation anomaly increase superimposed on SAM-like short-scale climatic variability. However, the synchronous sudden increase of local/regional hunter-gatherer presence since 3,000 cal yrs BP led us to hypothesize that humans could have also played a key role in the fire regime and vegetation changes.

To conclude, our results indicate that far from being stable, the western Lago Cochrane/Pueyrredón valley was still undergoing large landscape transformations during the Early-to-Middle Holocene and that these were related to the last stages of deglaciation associated with the dynamics of the SWs. It is key therefore to continue pursuing the search for sensitive sites, for instance, sites revealing changes of lesser intensity than those of the Holocene-Pleistocene transition, to show a robust and complete picture of landscape and environmental and climate change, and to shed light on the past scenarios of CWP since the Last Glacial Maximum.

DATA AVAILABILITY STATEMENT

The original contributions presented in the study are included in the article/**Supplementary Material**, and further inquiries can be directed to the corresponding author.

AUTHOR CONTRIBUTIONS

AM designed the study, performed fieldwork, obtain the funding and wrote the manuscript with contributions from all coauthors. MEdP and AM-C analyzed the data and participated in writing and editing the manuscript. OR designed the study, performed fieldwork and contributed with archaeological data and ideas. CM and AN-D obtained funding and participated in writing and editing the manuscript.

FUNDING

Funded by ANID FONDECYT 1180306; ANID FONDECYT 1210042; ANID FONDECYT 1210045; ANID Regional R20F0002; National Geographic Grant HJ-150R-17.

ACKNOWLEDGMENTS

To Varyl Thorndycraft for **Figure 1A**, Dra. Ana M. Abarzúa for fieldwork assistance, Francisco Mena and Víctor Lucero.

SUPPLEMENTARY MATERIAL

The Supplementary Material for this article can be found online at: https://www.frontiersin.org/articles/10.3389/feart.2022.833637/full#supplementary-material

REFERENCES

Abarzúa, A. M., and Moreno, P. I. (2008). Changing Fire Regimes in the Temperate Rainforest Region of Southern Chile over the Last 16,000 Yr. *Quat. Res.* 69, 62–71. doi:10.1016/j.yqres.2007.09.004

Abram, N. J., Mulvaney, R., Vimeux, F., Phipps, S. J., Turner, J., and England, M. H. (2014). Evolution of the Southern Annular Mode during the Past Millennium. *Nat. Clim Change* 4, 564–569. NATURE. doi:10.1038/NCLIMATE2235

Alder, J. R., and Hostetler, S. W. (2015). Global Climate Simulations at 3000-year Intervals for the Last 21 000 Years with the GENMOM Coupled Atmosphere-Ocean Model. *Clim. Past* 11, 449–471. doi:10.5194/cp-11-449-2015

Bell, C. M. (2008). Punctuated Drainage of an Ice-dammed Quaternary lake in Southern South america. *Geografiska Annaler: Ser. A, Phys. Geogr.* 90, 1–17. doi:10.1111/j.1468-0459.2008.00330.x

Bendle, J. M., Thorndycraft, V. R., and Palmer, A. P. (2017). The Glacial Geomorphology of the Lago Buenos Aires and Lago Pueyrredón Ice Lobes of central Patagonia. *J. Maps* 13, 654–673. doi:10.1080/17445647.2017.1351908

Bengtsson, L., and Enell, M. (1986). "Chemical Analysis," in *Handbook of Holocene Palaeoecology and Palaeohydrology*. Editor B. E. Berglund (Chichester: Wiley), 423–445.

Blaauw, M., Christen, J. A., and Aquino-López, M. A. (2021). *Rbacon: Age-Depth Modelling Using Bayesian Statistics*. R package version 2.5.7. https://CRAN.R-project.org/package=rbacon.

Blarquez, O., Vannière, B., Marlon, J. R., Daniau, A.-L., Power, M. J., Brewer, S., et al. (2014). Paleofire: An R Package to Analyse Sedimentary Charcoal Records from the Global Charcoal Database to Reconstruct Past Biomass Burning. *Comput. Geosciences* 72, 255–261. doi:10.1016/j.cageo.2014.07.020

Boex, J., Fogwill, C., Harrison, S., Glasser, N. F., Hein, A., Schnabel, C., et al. (2013). Rapid Thinning of the Late Pleistocene Patagonian Ice Sheet Followed Migration of the Southern Westerlies. *Sci. Rep.* 3, 2118. doi:10.1038/srep02118

Borrero, L. A., Nuevo Delaunay, A., and Méndez, C. (2019). Ethnographical and Historical Accounts for Understanding the Exploration of New Lands: The Case of Central Western Patagonia, Southernmost South America. *J. Anthropological Archaeology* 54, 1–16. doi:10.1016/j.jaa.2019.02.001

Borrero, L. A. (2004). "The Archaeozoology of the Andean 'Dead Ends' in Patagonia: Living Near the continental Ice Cap," in *Colonisation, Migration, and Marginal Areas: A Zooarchaeological Approach*. Editors M. Mondini, S. Muñoz, and S. Wickler (Havertown: Oxbow Books), 55–61.

Bourgois, J., Cisternas, M. E., Braucher, R., Bourlès, D., and Frutos, J. (2016). Geomorphic Records along the General Carrera (Chile)-Buenos Aires (Argentina) Glacial Lake (46°-48°S), Climate Inferences, and Glacial Rebound for the Past 7-9 Ka. *J. Geology*. 124, 27–53. doi:10.1086/684252

Caldenius, C. (1932). Las Glaciaciones Cuaternarias en Patagonia y Tierra del Fuego, *Dirección Genera de Minas y Geología*, 95. Ministerio de Agricultura de la Nación, 148.

Cárdenas, R., Vera, D., and Hall, C. G. (1993). *Los Chono y Los Veliche de Chiloé*. Santiago: Olimph.

Coronato, A., and Rabassa, J. (2011). "Pleistocene Glaciations in Southern Patagonia and Tierra del Fuego," in *Developments in Quaternary Sciences*. Editors J. Ehlers, P. L. Gibbard, and P. D. Hughes (Elsevier), 715–727. Chapter. doi:10.1016/b978-0-444-53447-7.00051-9

Dätwyler, C., Neukom, R., Abram, N. J., Gallant, A. J. E., Grosjean, M., Jacques-Coper, M., et al. (2018). Teleconnection Stationarity, Variability and Trends of the Southern Annular Mode (SAM) during the Last Millennium. *Clim. Dyn.* 51 (5), 2321–2339. doi:10.1007/s00382-017-4015-0

Davies, B. J., Darvill, C. M., Lovell, H., Bendle, J. M., Dowdeswell, J. A., Fabel, D., et al. (2020). The Evolution of the Patagonian Ice Sheet from 35 Ka to the Present Day (PATICE). *Earth-Science Rev.* 204, 103152. doi:10.1016/j.earscirev.2020.103152

Davies, B. J., Thorndycraft, V. R., Fabel, D., and Martin, J. R. V. (2018). Asynchronous Glacier Dynamics during the Antarctic Cold Reversal in central Patagonia. *Quat. Sci. Rev.* 200, 287–312. doi:10.1016/j.quascirev.2018.09.025

de Porras, M. E., Maldonado, A., Abarzúa, A. M., Cárdenas, M. L., Francois, J. P., Martel-Cea, A., et al. (2012). Postglacial Vegetation, Fire and Climate Dynamics at Central Chilean Patagonia (Lake Shaman, 44°S). *Quat. Sci. Rev.* 50, 71–85. doi:10.1016/j.quascirev.2012.06.015

de Porras, M. E., Maldonado, A., Quintana, F. A., Martel-Cea, A., Reyes, O., and Méndez, C. (2014). Environmental and Climatic Changes in central Chilean Patagonia since the Late Glacial (Mallín El Embudo, 44° S). *Clim. Past* 10, 1063–1078. doi:10.5194/cp-10-1063-2014

Douglass, D., Singer, B., Kaplan, M., Mickelson, D., and Caffee, M. (2006). Cosmogenic Nuclide Surface Exposure Dating of Boulders on Last-Glacial and Late-Glacial Moraines, Lago Buenos Aires, Argentina: Interpretive Strategies and Paleoclimate Implications. *Quat. Geochronol.* 1, 43–58. doi:10.1016/j.quageo.2006.06.001

Faegri, K., and Iversen, J. (1989). *Textbook of Pollen Analysis*. Londres: John Wiley & Sons Ld.

García Guraieb, S., Goñi, R., and Tessone, A. (2015). Paleodemography of Late Holocene hunter-gatherers from Patagonia (Santa Cruz, Argentina): An Approach Using Multiple Archaeological and Bioarchaeological Indicators. *Quat. Int.* 356, 147–158.

García, J.-L., Maldonado, A., de Porras, M. E., Nuevo Delaunay, A., Reyes, O., Ebensperger, C. A., et al. (2019). Early Deglaciation and Paleolake History of Río Cisnes Glacier, Patagonian Ice Sheet (44°S). *Quat. Res.* 91, 194–217. doi:10.1017/qua.2018.93

Garreaud, R. D. (2009). The Andes Climate and Weather. *Adv. Geosci.* 22, 3–11. doi:10.5194/adgeo-22-3-2009

Garreaud, R., Lopez, P., Minvielle, M., and Rojas, M. (2013). Large-scale Control on the Patagonian Climate. *J. Clim.* 26, 215–230. doi:10.1175/JCLI-D-12-00001.1

Glasser, N. F., Harrison, S., Schnabel, C., Fabel, D., and Jansson, K. N. (2012). Younger Dryas and Early Holocene Age Glacier Advances in Patagonia. *Quat. Sci. Rev.* 58, 7–17. doi:10.1016/j.quascirev.2012.10.011

Goñi, R., Re, A., García Guraieb., S., Cassiodoro, G., Tessone, A., Rindel, D., et al. (2019). Climate Changes, Human Peopling and Regional Differentiation during Late Holocene in Patagonia. *Quat. Int.* 505, 4–20.

Grimm, E. C. (1987). CONISS: a FORTRAN 77 Program for Stratigraphically Constrained Cluster Analysis by the Method of Incremental Sum of Squares. *Comput. Geosciences* 13, 13–35. doi:10.1016/0098-3004(87)90022-7

Haberle, S., and Bennett, K. D. (2004). Postglacial Formation and Dynamics of North Patagonian Rainforest in the Chonos Archipelago, Southern Chile. *Quat. Sci. Rev.* 23, 2433–2452. doi:10.1016/j.quascirev.2004.03.001

Haberle, S. G., and Bennett, K. D. (2001). Modern Pollen Rain and lake Mud-Water Interface Geochemistry along Environmental Gradients in Southern Chile. *Rev. Palaeobotany Palynology* 117, 93–107. doi:10.1016/S0034-6667(01)00079-3

Haberle, S. G., Szeicz, J. M., and Bennett, K. D. (2000). Late Holocene Vegetation Dynamics and lake Geochemistry at Laguna Miranda, XI Region, Chile. *Revista Chilena de Historia Nat.* 73, 655–669. doi:10.4067/s0716-078x2000000400010

Harrison, S., Glasser, N. F., Duller, G. A. T., and Jansson, K. N. (2012). Early and Mid-holocene Age for the Tempanos Moraines, Laguna San Rafael, Patagonian Chile. *Quat. Sci. Rev.* 31, 82–92. doi:10.1016/j.quascirev.2011.10.015

Harrison, S., and Glasser, N. F. (2011). "The Pleistocene Glaciations of Chile," in *Developments in Quaternary Sciences*. Editors J. Ehlers, P. L. Gibbard, and P. D. Hughes (Elsevier), 739–756. doi:10.1016/b978-0-444-53447-7.00054-4

Hein, A. S., Dunai, T. J., Hulton, N. R. J., and Xu, S. (2011). Exposure Dating Outwash Gravels to Determine the Age of the Greatest Patagonian Glaciations. *Geology* 39, 103–106. doi:10.1130/g31215.1

Hein, A. S., Hulton, N. R. J., Dunai, T. J., Schnabel, C., Kaplan, M. R., Naylor, M., et al. (2009). Middle Pleistocene Glaciation in Patagonia Dated by Cosmogenic-Nuclide Measurements on Outwash Gravels. *Earth Planet. Sci. Lett.* 286, 184–197. doi:10.1016/j.epsl.2009.06.026

Hein, A. S., Hulton, N. R. J., Dunai, T. J., Sugden, D. E., Kaplan, M. R., and Xu, S. (2010). The Chronology of the Last Glacial Maximum and Deglacial Events in central Argentine Patagonia. *Quat. Sci. Rev.* 29, 1212–1227. doi:10.1016/j.quascirev.2010.01.020

Heiri, O., Lotter, A. F., and Lemcke, G. (2001). Loss on Ignition as a Method for Estimating Organic and Carbonate Content in Sediments: Reproducibility and Comparability of Results. *J. Paleolimnology* 25, 101–110. doi:10.1023/A:1008119611481

Henríquez, W. I., Villa-Martínez, R., Vilanova, I., De Pol-Holz, R., and Moreno, P. I. (2017). The Last Glacial Termination on the Eastern Flank of the central Patagonian Andes (47 ° S). *Clim. Past* 13, 879–895. doi:10.5194/cp-13-879-2017

Heusser, C. J. (2003). *Ice Age Southern Andes: A Chronicle of Paleoecological Events*. Amsterdam: Elsevier.

Higuera, P. E., Brubaker, L. B., Anderson, P. M., Hu, F. S., and Brown, T. A. (2009). Vegetation Mediated the Impacts of Postglacial Climate Change on Fire Regimes in the South-central Brooks Range, Alaska. *Ecol. Monogr.* 79, 201–219. doi:10.1890/07-2019.1

Hogg, A. G., Heaton, T. J., Hua, Q., Palmer, J. G., Turney, C. S., Southon, J., et al. (2020). SHCal20 Southern Hemisphere Calibration, 0-55,000 Years Cal BP. *Radiocarbon* 62, 759–778. doi:10.1017/RDC.2020.59

Holz, A., and Veblen, T. T. (2012). Wildfire Activity in Rainforests in Western Patagonia Linked to the Southern Annular Mode. *Int. J. Wildland Fire* 21, 114–126. doi:10.1071/WF10121

Iglesias, V., Haberle, S. G., Holz, A., and Whitlock, C. (2018). Holocene Dynamics of Temperate Rainforests in West-Central Patagonia. *Front. Ecol. Evol.* 5 (177). doi:10.3389/fevo.2017.00177

Kaplan, M. R., Ackert, R. P., Jr., Singer, B. S., Douglass, D. C., and Kurz, M. D. (2004). Cosmogenic Nuclide Chronology of Millennial-Scale Glacial Advances during O-Isotope Stage 2 in Patagonia. *Geo. Soc. Am. Bull.* 116, 308–321. doi:10.1130/b25178.1

Kaplan, M. R., Schaefer, J. M., Strelin, J. A., Denton, G. H., Anderson, R. F., Vandergoes, M. J., et al. (2016). Patagonian and Southern South Atlantic View of Holocene Climate. *Quat. Sci. Rev.* 141, 112–125. doi:10.1016/j.quascirev.2016.03.014

Kaplan, M. R., Strelin, J. A., Schaefer, J. M., Peltier, C., Martini, M. A., FloresWinckler, E. G., et al. (2020). Holocene Glacier Behavior Around the Northern Antarctic Peninsula and Possible Causes. *Earth Planet. Sci. Lett.* 534, 116077. doi:10.1016/j.epsl.2020.116077

Kelly, R. F., Higuera, P. E., Barrett, C. M., and Hu, F. S. (2011). Short Paper: A Signal-To-Noise index to Quantify the Potential for Peak Detection in Sediment-Charcoal Records. *Quat. Res.* 75, 11–17. doi:10.1016/j.yqres.2010.07.011

Leger, T. P. M., Hein, A. S., Bingham, R. G., Rodés, Á., Fabel, D., and Smedley, R. K. (2021). Geomorphology and 10Be Chronology of the Last Glacial Maximum and Deglaciation in Northeastern Patagonia, 43°S-71°W. *Quat. Sci. Rev.* 272, 107194. doi:10.1016/j.quascirev.2021.107194

Luebert, F., and Pliscoff, P. (2017). *Sinopsis bioclimática y vegetacional de Chile*. Santiago, Chile: Editorial Universitaria.

Maldonado, A., and Villagrán, C. (2006). Climate Variability over the Last 9900 Cal Yr BP from a Swamp forest Pollen Record along the Semiarid Coast of Chile. *Quat. Res.* 66, 246–258. doi:10.1016/j.yqres.2006.04.003

Markgraf, V., Whitlock, C., and Haberle, S. (2007). Vegetation and Fire History during the Last 18,000 Cal Yr B.P. In Southern Patagonia: Mallín Pollux, Coyhaique, Province Aisén (45°41′30″ S, 71°50′30″ W, 640 M Elevation). *Palaeogeogr. Palaeoclimatol. Palaeoecol.* 254, 492–507. doi:10.1016/j.palaeo.2007.07.008

Martinic, M. (2005). *De La Trapanada Al Aysén*. Santiago: Pehuén Editores.

McCulloch, R. D., Figuerero Torres, M. J., Mengoni Goñalons, G. L., Barclay, R., and Mansilla, C. (2017). A Holocene Record of Environmental Change from Río Zeballos, central Patagonia. *The Holocene* 27, 941–950. doi:10.1177/0959683616678460

Mena L., F., and Blanco J., J. F. (2017). Estado De La Investigación Arqueológica Del Valle Del Chacabuco. Andes Centro Patagónicos. Xi Region De Aisén, Chile. *Magallania* 45, 199–217. doi:10.4067/s0718-22442017000200199

Méndez, C., de Porras, M. E., Maldonado, A., Reyes, O., Nuevo Delaunay, A., and García, J.-L. (2016). Human Effects in Holocene Fire Dynamics of Central Western Patagonia (~44° S, Chile). *Front. Ecol. Evol.* 4 (100). doi:10.3389/fevo.2016.00100

Méndez, C., Stern, C. R., Nuevo Delaunay, A., Reyes, O., Gutiérrez, F., and Mena, F. (2018). Spatial and Temporal Distributions of Exotic and Local Obsidians in Central Western Patagonia, Southernmost South America. *Quat. Int.* 468, 155–168. doi:10.1016/j.quaint.2017.08.062

Mengoni Goñalons, G. L., Figuerero Torres, M. J., Fernández, M. V., Rocco, M., and Dekmak, W. (2019). "Persistencia y hiatos en el área de Los Antiguos, Monte Zeballos y Paso Roballos, NO de Santa Cruz, Patagonia: nuevas dataciones para la cronología regional," in *Arqueología de la Patagonia: el Pasado en las Arenas*. Editors J. Gómez Otero, S. Ariadna, and A. Banegas (Puerto Madryn: Instituto de Diversidad y Evolución Austral), 327–338.

Moreno, P. I., Henríquez, W. I., Pesce, O. H., Henríquez, C. A., Fletcher, M. S., Garreaud, R. D., et al. (2021). An Early Holocene westerly Minimum in the Southern Mid-latitudes. *Quat. Sci. Rev.* 251, 106730. doi:10.1016/j.quascirev.2020.106730

Moreno, P. I., Simi, E., Villa-Martínez, R. P., and Vilanova, I. (2019). Early Arboreal Colonization, Postglacial Resilience of Deciduous Nothofagus Forests, and the

Southern Westerly Wind Influence in central-east Andean Patagonia. *Quat. Sci. Rev.* 218, 61–74. doi:10.1016/j.quascirev.2019.06.004

Moreno, P. I. (2020). Timing and Structure of Vegetation, Fire, and Climate Changes on the Pacific Slope of Northwestern Patagonia since the Last Glacial Termination. *Quat. Sci. Rev.* 238, 106328. doi:10.1016/j.quascirev.2020.106328

Moreno, P. I., Vilanova, I., Villa-Martínez, R., Dunbar, R. B., Mucciarone, D. A., Kaplan, M. R., et al. (2018). Onset and Evolution of Southern Annular Mode-like Changes at Centennial Timescale. *Sci. Rep.* 8 (1), 3458. doi:10.1038/s41598-018-21836-6

Moreno, P. I., Vilanova, I., Villa-Martínez, R., Garreaud, R. D., Rojas, M., and De Pol-Holz, R. (2014). Southern Annular Mode-like Changes in Southwestern Patagonia at Centennial Timescales over the Last Three Millennia. *Nat. Commun.* 5, 4375. doi:10.1038/ncomms5375

Nanavati, W. P., Whitlock, C., Iglesias, V., and de Porras, M. E. (2019). Postglacial Vegetation, Fire, and Climate History along the Eastern Andes, Argentina and Chile (Lat. 41-55°S). *Quat. Sci. Rev.* 207, 145–160. doi:10.1016/j.quascirev.2019.01.014

Nuevo Delaunay, A. (2015). *Transformación del paisaje arqueológico rural en el centro-oeste de la provincia de Santa Cruz, siglo XX*. Unpublished PhD dissertation, Universidad de Buenos Aires.

Nuevo-Delaunay, A., Méndez, C., Reyes, O., Seelenfreund, A., and Belmar, C. (2022). *La ocupación humana antigua de los callejones sin salida de los Andes de Patagonia: midiendo la intensidad de uso del espacio en los márgenes del Campo de Hielo Norte (Aisén, Chile)*. Chungara Revista de Antropología Chilena In press. doi:10.4067/S0717-73562022005000203

Pérez, S. I., Postillone, M. B., Rindel, D., Gobbo, D., Gonzalez, P. N., and Bernal, V. (2016). Peopling Time, Spatial Occupation and Demography of Late Pleistocene–Holocene Human Population from Patagonia. *Quat. Int.* 425, 214–223.

Power, M. J., Marlon, J., Ortiz, N., Bartlein, P. J., Harrison, S. P., Mayle, F. E., et al. (2008). Changes in Fire Regimes since the Last Glacial Maximum: an Assessment Based on a Global Synthesis and Analysis of Charcoal Data. *Clim. Dyn.* 30, 887–907. doi:10.1007/s00382-007-0334-x

Quade, J., and Kaplan, M. R. (2017). Lake-level Stratigraphy and Geochronology Revisited at Lago (Lake) Cardiel, Argentina, and Changes in the Southern Hemispheric Westerlies over the Last 25 Ka. *Quat. Sci. Rev.* 177, 173–188. doi:10.1016/j.quascirev.2017.10.006

R Core Team (2021). *R: A Language and Environment for Statistical Computing*. Vienna, Austria: R Foundation for Statistical Computing. URL https://www.R-project.org/.". (Viena).

Renssen, H., Goosse, H., Fichefet, T., Masson-Delmotte, V., and Koç, N. (2005). Holocene Climate Evolution in the High-Latitude Southern Hemisphere Simulated by a Coupled Atmosphere-Sea Ice-Ocean-Vegetation Model. *The Holocene* 15, 951–964. doi:10.1191/0959683605hl869ra

Sacchi, M., Bozzuto, D., Horta, L., Fernández, N., De Nigris, M., Civalero, T., et al. (2016). Dataciones y circulación humana: influencia de las fluctuaciones del sistema lacustre Pueyrredón-Posadas durante el Holoceno. *Andes* 27, 1–17.

Sagredo, E. A., Kaplan, M. R., Araya, P. S., Lowell, T. V., Aravena, J. C., and Moreno, P. I. (2018). Trans-pacific Glacial Response to the Antarctic Cold Reversal in the Southern Mid-latitudes. *Quat. Sci. Rev.* 188, 160–166. doi:10.1016/j.quascirev.2018.01.011

Stern, C., Henríquez, W., Villa-Martínez, R., Sagredo, E., Aravena, J., and De Pol-Holz, R. (2016). Holocene Tephrochronology Around Cochrane (~47° S), Southern Chile. *Andean Geology*. 43, 1–19. doi:10.5027/andgeoV43n1-a01

Stockmarr, J. (1971). Tablets with Spores Used in Absolute Pollen Analysis. *Pollen spores* 13, 615–621.

Stuiver, M., Reimer, P. J., and reimer, R. W. (2020). *CALIB*. 8.0.1 (http://calib.org).

Thorndycraft, V. R., Bendle, J. M., Benito, G., Davies, B. J., Sancho, C., Palmer, A. P., et al. (2019). Glacial lake Evolution and Atlantic-Pacific Drainage Reversals during Deglaciation of the Patagonian Ice Sheet. *Quat. Sci. Rev.* 203, 102–127. doi:10.1016/j.quascirev.2018.10.036

Turner, K. J., Fogwill, C. J., McCulloch, R. D., and Sugden, D. E. (2005). Deglaciation of the Eastern Flank of the north Patagonian Icefield and Associated continental-scale lake Diversions. *Geografiska Annaler: Ser. A, Phys. Geogr.* 87, 363–374. doi:10.1111/j.0435-3676.2005.00263.x

Viale, M., Bianchi, E., Cara, L., Ruiz, L. E., Villalba, R., Pitte, P., et al. (2019). Contrasting Climates at Both Sides of the Andes in Argentina and Chile. *Front. Environ. Sci.* 7. doi:10.3389/fenvs.2019.00069

Villa-Martínez, R., and Moreno, P. I. (2021). Development and Resilience of Deciduous Nothofagus Forests since the Last Glacial Termination and Deglaciation of the central Patagonian Andes. *Palaeogeogr. Palaeoclimatol. Palaeoecol.* 574, 110459. doi:10.1016/j.palaeo.2021.110459

Villa-Martínez, R., Moreno, P. I., and Valenzuela, M. A. (2012). Deglacial and Postglacial Vegetation Changes on the Eastern Slopes of the central Patagonian Andes (47°S). *Quat. Sci. Rev.* 32, 86–99. doi:10.1016/j.quascirev.2011.11.008

Villa-Martínez, R., Villagrán, C., and Jenny, B. (2003). The Last 7500 Cal Yr B.P. Of westerly Rainfall in Central Chile Inferred from a High-Resolution Pollen Record from Laguna Aculeo (34 °S). *Quat. Res.* 60, 284–293. doi:10.1016/j.yqres.2003.07.007

Whitlock, C., and Larsen, C. (2001). "Charcoal as a Proxy Fire," in *Tracking Environmental Change Using Lake Sediments: Terrestrial, Algal, and Siliceous Indicators*. Editors J. P. Smol, H. J. B. Birks, and W. M. Last (Dordrecht, Netherlands: Kluwer Academic Publishers), 75–97.

Whitlock, C., Moreno, P. I., and Bartlein, P. (2007). Climatic Controls of Holocene Fire Patterns in Southern South America. *Quat. Res.* 68, 28–36. doi:10.1016/j.yqres.2007.01.012

Conflict of Interest: The authors declare that the research was conducted in the absence of any commercial or financial relationships that could be construed as a potential conflict of interest.

Publisher's Note: All claims expressed in this article are solely those of the authors and do not necessarily represent those of their affiliated organizations, or those of the publisher, the editors, and the reviewers. Any product that may be evaluated in this article, or claim that may be made by its manufacturer, is not guaranteed or endorsed by the publisher.

frontiers | Frontiers in Earth Science

ORIGINAL RESEARCH
published: 11 April 2022
doi: 10.3389/feart.2022.838826

Palaeoglaciation in the Low Latitude, Low Elevation Tropical Andes, Northern Peru

Ethan Lee[1]*, *Neil Ross*[1], *Andrew C. G. Henderson*[1], *Andrew J. Russell*[1], *Stewart S. R. Jamieson*[2] and *Derek Fabel*[3]

[1]School of Geography, Politics and Sociology, Newcastle University, Newcastle-upon-Tyne, United Kingdom, [2]Department of Geography, Durham University, Durham, United Kingdom, [3]Scottish Universities Environmental Research Centre, AMS Laboratory, Scotland, United Kingdom

Characterising glaciological change within the tropical Andes is important because tropical glaciers are sensitive to climate change. Our understanding of glacier dynamics and how tropical glaciers respond to global climate perturbations is poorly constrained. Studies of past glaciation in the tropical Andes have focused on locations where glaciers are still present or recently vacated cirques at high elevations. Few studies focused on lower elevation localities because it was assumed glaciers did not exist or were not as extensive. We present the first geomorphological evidence for past glaciations of the Lagunas de Las Huaringas, northern Peru, at elevations of 3,900–2,600 m a.s.l. Mapping was conducted using remotely-sensed optical imagery and a newly created high-resolution (~2.5 m) digital elevation model (DEM). The area has abundant evidence for glaciation, including moraines, glacial cirques, hummocky terrain, glacial lineations and ice-sculpted bedrock. Two potential models for glaciation are hypothesised: 1) plateau-fed ice cap, or 2) valley glaciation. Assuming glaciers reached their maximum extent during the Local Last Glacial Maximum (LLGM), between 23.5 ± 0.5 and 21.2 ± 0.8 ka, the maximum reconstructed glacial area was 75.6 km^2. A mean equilibrium line altitude (ELA) of 3,422 ± 30 m was calculated, indicating an ELA change of −1,178 ± 10 m compared to modern snowline elevation. There is an east to west ELA elevation gradient, lower in the east and higher in the west, in-line with modern day transfer of moisture. Applying lapse rates between 5.5 and 7.5°C/km provides a LLGM temperature cooling of between 6.5–8.8°C compared to present. These values are comparable to upper estimates from other studies within the northern tropical Andes and from ice-core reconstructions. The mapping of glacial geomorphology within the Lagunas de las Huaringas, evidences, for the first time, extensive glaciation in a low elevation region of northern Peru, with implications for our understanding of past climate in the sub-tropics. Observations and reconstructions support a valley, rather than ice cap glaciation. Further work is required to constrain the timing of glaciations, with evidence of moraines younger than the LLGM up-valley of maximum glacier extents. Numerical modelling will also enable an understanding of the controls of glaciation within the region.

Keywords: Peru, tropical Andes, glacial geomorphology, tropical glaciers, ELA, LGM, glacier reconstruction

OPEN ACCESS

Edited by:
Bethan Joan Davies,
Royal Holloway, University of London, United Kingdom

Reviewed by:
Naki Akçar,
University of Bern, Switzerland
José Araos,
Alberto Hurtado University, Chile

***Correspondence:**
Ethan Lee
e.lee5@newcastle.ac.uk

Specialty section:
This article was submitted to Quaternary Science, Geomorphology and Paleoenvironment, a section of the journal Frontiers in Earth Science

Received: *18 December 2021*
Accepted: *08 March 2022*
Published: *11 April 2022*

Citation:
Lee E, Ross N, Henderson ACG, Russell AJ, Jamieson SSR and Fabel D (2022) Palaeoglaciation in the Low Latitude, Low Elevation Tropical Andes, Northern Peru. Front. Earth Sci. 10:838826. doi: 10.3389/feart.2022.838826

1 INTRODUCTION

Tropical glaciers are important indicators of current climate change, and many are thinning and retreating rapidly as a result of a warming climate (Ramírez et al., 2001; Thompson et al., 2021). The tropical Andes are influenced by the tropical Pacific and Atlantic ocean-atmospheric dynamics and are a key location in the movement of air masses to adjacent regions, with a subsequent global climate impact (Lea et al., 2003; Visser et al., 2003). They are also an important region for understanding how past climate change impacted glacier change. Palaeoglaciological evidence (e.g., geomorphological landforms such as moraines) can provide fundamental information to reconstruct climate variability over glacial-interglacial timescales and to provide insights into former glacier dynamics, behaviours and extent at specific locations (Evans, 2003). Ice mass reconstructions such as these can provide insight into how the present-day tropics, specifically tropical glaciers, will respond to predicted future global warming (Bromley et al., 2009).

A number of palaeoglaciological studies have been conducted across the tropical Andes, within the Venezuelan Mérida Andes (e.g., Mahaney et al., 2010; Stansell et al., 2010; Carcaillet et al., 2013; Angel, 2016), Colombian Andes (e.g., van't Veer et al., 2000; Helmens, 2004), Ecuadorian Andes (e.g., Clapperton, 1990; Clapperton et al., 1997b; Rodbell et al., 2002), Peruvian Andes (e.g., Smith et al., 2005; Jomelli et al., 2008; Shakun et al., 2015; Bromley et al., 2016; Stansell et al., 2017) and the Bolivian Andes (e.g., Zech et al., 2007; Smith et al., 2011; Blard et al., 2014). A number of reviews have been conducted collating and analysing the results within: 1) Venezuela, Colombia and Ecuador (Angel et al., 2017); 2) Peru and Bolivia (Mark et al., 2017); and 3) for the whole of South America (Palacios et al., 2020). As a result we do not repeat this exercise here. Instead we use these papers to determine the general timing of the Last Glacial Maximum (LGM; between 23.5 ± 0.5 and 21.2 ± 0.8 ka) within the northern tropical Andes. This provides a likely period when LGM ice masses were present within our study area.

While there are numerous palaeoglaciological studies from the South American tropical region, these typically focus on locations where ice masses still exist (e.g., Cordillera Blanca, Peru) (Farber et al., 2005; Glasser et al., 2009), or high elevation locations that glaciers have recently vacated their cirques (Smith and Rodbell, 2010; Blard et al., 2014; Shakun et al., 2015). Further, there has been relatively little modern mapping concerned with the identification of the glacial geomorphology and reconstruction of potential glacial dynamics. The exceptions are investigations of individual glacial valleys (e.g., Małecki et al., 2018) and the mapping of glacial lakes (e.g., Vilímek et al., 2016). Systematic geomorphological mapping of previously unstudied regions and the identification of glacial landforms permits a first order understanding for how these landforms formed, providing insights into the extent, thickness, and ice dynamics of past ice masses. Geomorphological mapping can also be used to target sampling for the dating of glacial landforms (e.g., for terrestrial cosmogenic nuclide analysis) thereby enabling the development of glacial advance-retreat chronologies for testing mechanisms of glacier-climate interactions (Sutherland et al., 2019).

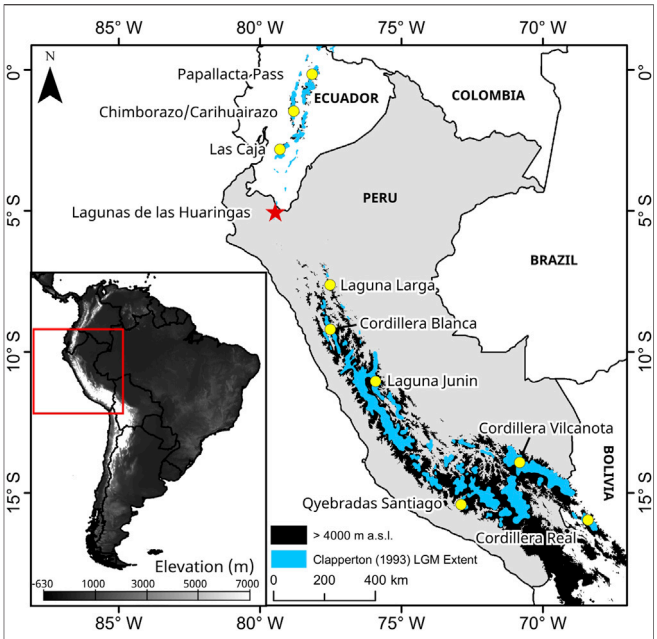

FIGURE 1 | Map of Peru showing the study site location in northern Peru (red star; Lagunas de las Huaringas) within a data gap between former palaeoglaciological studies mentioned within the text (yellow circles). The majority of these locations are located above 4,000 m above sea level (a.s.l.) shown by the black outline. The hypothesised LGM extent is from Clapperton (1993) shown by the blue outline.

Palaeoglacial evidence in lower elevation tropical Andean regions (i.e., with summit peaks <4,000 m a.s.l.) has rarely been identified and investigated. As a result, there is relatively limited understanding of their glacial dynamics and whether they were able to persist in these regions after their LGM extents compared to higher elevation or higher latitude locations. This has left a latitudinal data-gap within the tropical Andes, particularly in the northern Peruvian and southern Ecuadorian highlands (4°–8°S), an area generally below 4,000 m a.s.l., between existing studies in southern Ecuador and southern Peru (e.g., Clapperton et al., 1997b; Mark et al., 1999; Hastenrath, 2009). Our study area, the Lagunas de las Huaringas, is located within this latitudinal data gap (**Figure 1**).

We aim to reconstruct the palaeoglacial dynamics of the Lagunas de las Huaringas, an area that had not previously received detailed investigation in the literature, except preliminary ice extent estimations from Clapperton (1993). We provide: 1) a detailed glacial geomorphological map of the region; 2) a reconstruction of the likely maximum glacial extent, along with a reconstructed equilibrium line altitude (ELA) for the reconstructed ice masses; and 3) ELA-derived palaeotemperature estimates for the Local Last Glacial Maximum (LLGM), used to discuss the palaeoclimate implications of our findings. These outputs aid in allowing us to determine if glacial ice was present at this location, to understand the glacial dynamics, to assess whether the region incurred valley glaciation or an icecap with outlet glaciers, and to determine the potential climate glaciers would have formed under.

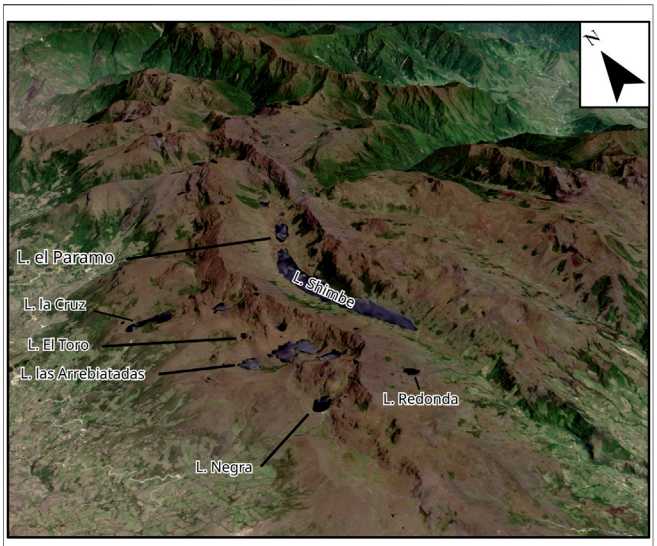

FIGURE 2 | A Sentinel-2 optical imagery of Lagunas de las Huaringas (red star in **Figure 1**), draped over a 30 m ALOS DEM. This show the main central valley (Shimbe Valley) with the largest lake, Laguna Shimbe running almost along its entire length. Arcuate moraines and lake-filled depressions are seen on its western edge with their lake names detailed.

2 STUDY AREA

2.1 Lagunas de las Huaringas

Lagunas de las Huaringas (here after referred to as Las Huaringas; ~3,900 m a.s.l.; 5°00′S, 79°27′W) is located in the northern highlands of Peru (**Figure 1**) within the Huancabamba river catchment (Lila et al., 2016). The underlying geology comprises Paleogene to Neogene age volcanic-sedimentary rocks (Gómez et al., 2019), and the region is not currently glaciated. The main valley, the Shimbe valley (**Figure 2**), stretches north to south for ~22 km and is characterised by two major depressions; a smaller up valley section occupied by Laguna el Paramo and a larger section occupied by Laguna Shimbe, the latter having an estimated maximum water depth of ~30 m. Within the Shimbe valley and throughout the study area, there are a number of smaller arcuate valleys with lakes dammed by ridges or bedrock indicative of past glaciation, the most striking of which are situated on the western side of the Las Huaringas Massif (**Figure 2**). An area that we assume to be Las Huaringas was suggested as likely to have been glaciated during the LGM by Clapperton (1993). Clapperton mapped areas of potential glacial ice cover within the tropical Andes based on his extensive field experience in the region, and an assumption that most topography above 3,400 m would have been covered by ice during the LGM (blue outlines in **Figure 1**). As far as we are aware, this mapping was not based on any specific fieldwork, especially within the Las Huaringas area, nor via the use of any remotely sensed analysis (e.g., satellite or aerial imagery). Las Huaringas was only one of several such locations where past glaciation was suggested as likely in the northern Peru and southern Ecuador region (Clapperton, 1993). Many of these potential formerly glaciated areas in the region surrounding Las Huaringas have, as far as can be found in the literature, received no investigation since. Analysis of modern-day satellite datasets, and reconnaissance fieldwork by the authors of this study, indicate that palaeoglacial landforms (e.g., moraines and eroded bedrock surfaces) are abundant and well preserved within Las Huaringas, supporting Clapperton's hypothesis for glaciation at this locality.

The climate of the Las Huaringas is subtropical and modulated by tropical Pacific Sea surface temperatures (SSTs) and ocean temperature at depths. These drive variations in the El Niño Southern Oscillation (ENSO) that itself influences interannual precipitation and air temperature variability (Garreaud, 2009; Kiefer and Karamperidou, 2019). Other influences include the transfer of moisture via the easterlies, which originate from the Atlantic Ocean, and track over the Amazon Basin incurring evapotranspiration. The easterlies flow over the eastern Andes brings enhanced precipitation, predominantly during the summer months, in response to the migration of the Inter-Tropical Convergence Zone (ITZC) southwards (Garreaud, 2009; Álvarez-Villa et al., 2011; Staal et al., 2018). On average, the Las Huaringas region receives ~400 mm of precipitation per year, with the majority of precipitation falling between October and April (tropical summer season) with very little between June and August (tropical winter season). The intra-annual temperature variation of ~0.5°C is exceeded by the diurnal temperature variation of ~4°C.

2.2 Palaeoclimate of Northern Peru and Surrounding Areas During the LGM

Palaeotemperature and palaeoprecipitation can be reconstructed using a range of proxy records: palaeo-Equilibrium Line Altitudes (ELAs) from reconstructed glaciers (e.g., Porter, 2001), ice-cores ($\delta^{18}O$ and ^{2}H) (e.g., Thompson et al., 1998), lake sediment cores (e.g., pollen and diatoms) (e.g., Stansell et al., 2014), and palaeoecological techniques (e.g., Chevalier et al., 2020). Temperature reconstructions from palaeo-ELA reconstructions have estimated the LLGM temperature of Peru to range between 6.4 and 2°C cooler than present (Rodbell, 1992; Mark and Helmens, 2005; Ramage et al., 2005; Smith et al., 2005; Bromley et al., 2011a; Úbeda et al., 2018). The wide range in the estimated values is due to local controlling factors such as local topography, aspect, and relief. Some of the lowest estimates of temperature depression are yielded from glaciers constrained by topography sourced from predominantly westward facing cirques (−2.5°C; Ramage et al., 2005; −2 to −4°C; Smith et al., 2005), while higher estimates of cooling have been either from topographically unconstrained localities (e.g., volcanos) (−6.4°C; Úbeda et al., 2018) or glaciers that were predominantly eastward facing (−5 to −6°C; Rodbell, 1992). These suggest an east to west gradient yielding differing temperature reconstructions (Klein et al., 1999). $\delta^{18}O$ analysis of ice-cores from the Sajama and Huascarán ice-caps suggests a potential LGM cooling of 8–12°C (Thompson et al., 1995; Thompson et al., 1998), consistent with a substantially cooler LGM climate. Sea surface temperatures also support a cooler LGM, with reconstructed tropical Pacific sea surface temperatures 2.8°C cooler than present (Lea et al., 2000), similar to the 2.3°C cooler global average (CLIMAP, 1976).

Palaeohydration studies from lake cores and other palaeoecological studies in the outer tropics demonstrate latitudinal and regional variability in precipitation patterns. Lake cores and palaeo-shorelines from more northern locations within the northern tropical Andes indicate a wetter LGM (Rodbell, 1993; Clapperton et al., 1997a; Chepstow-Lusty et al., 2005) linked to an intensified South American Summer Monsoon (SASM) in response to orbital variations (Baker et al., 2001). Other studies within the Bolivian Altiplano (straddling southern Peru and northern Bolivia) indicate little to no increase in precipitation during the LGM (Placzek et al., 2013; Nunnery et al., 2019), although there was an effective amount of moisture to maintain lake levels. Palaeoecological studies from the Amazon basin, an important location for moisture transfer to Peru and Bolivia, suggest it was drier during the LGM (Mourguiart and Ledru, 2003; Häggi et al., 2017; Novello et al., 2019). It has been hypothesised that increased LGM precipitation identified from lake sediment records in the Peruvian and northern Bolivian Andes was possible even with a drier Amazon basin (Vizy and Cook, 2007). This would be because zonal low-level flow would be able to move over the Andean mountains directly, convecting upwards rather than paralleling the Andes to the north (seen in the modern day), thereby creating an east-west precipitation gradient during the LGM.

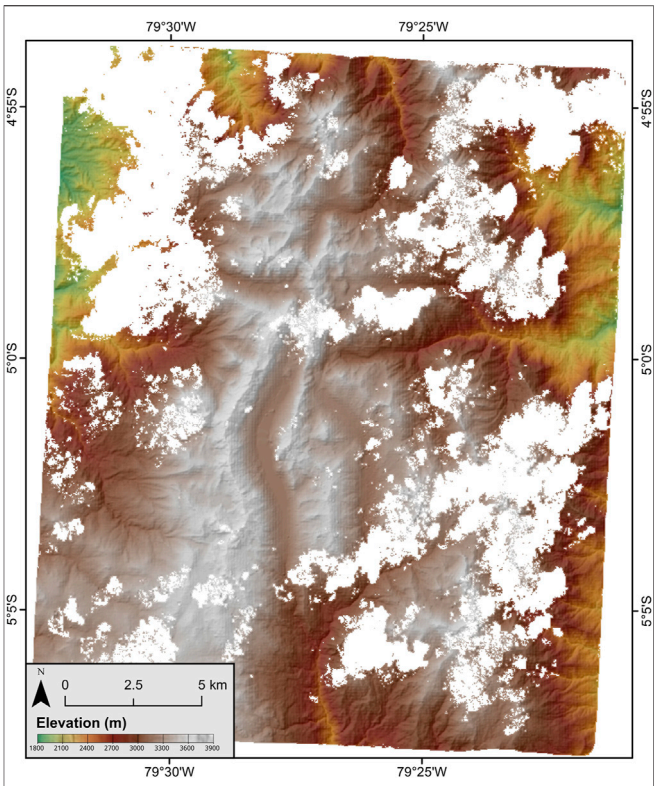

FIGURE 3 | 2.5 m horizontal resolution SPOT 7 derived DEM of the Lagunas de las Huaringas area as a hillshaded image (azimuth: 315°, z-factor: 1) overlain by elevation. White "fuzzy" areas are no data generation errors removed due to cloud cover precluding data capture.

3 METHODS

3.1 Datasets

A geomorphological map and glacial reconstruction were based on analysis of multiple remotely sensed high-resolution images and digital elevation models (DEMs) (**Supplementary Table 1**). Newly-acquired high resolution tri-stereo SPOT 7 (1.5 m) and archived Pléiades (0.5 m) imagery was obtained through the European Space Agency (ESA) from Airbus Defence and Space and the National Centre for Space Studies (CNES). Large portions of Las Huaringas were cloud covered in the Pléiades imagery, leading to the eastern side of Las Huaringas and the Laguna Shimbe valley not being mapped at the highest resolution. As a result, these areas were mapped using the most recent cloud free image which could be obtained from Landsat 8 (30 m, pansharpened to 15 m), Sentinel-2A (10 m), RapidEye (5 m) or PlanetScope (4 m). Openly available imagery from Google Earth™ and Bing Maps, with a mixture of resolutions, were used to complement the other optical datasets.

DEMs used included: 1) the 30-m resolution Advanced Land Observing Satellite (ALOS) DEM from the Japan Aerospace Exploration Agency (JAXA; https://global.jaxa.jp). This DEM was generated from images acquired between 2006 and 2011 from the Panchromatic Remote-sensing Instrument for Stereo Mapping (PRISM) sensor onboard the ALOS (Tadono et al. (2014); 2) a new high-resolution DEM of the study area generated from the tri-stereo SPOT 7 imagery. The process for generation of this DEM, along with an evaluation of its uncertainty, is outlined below. The 30 m ALOS DEM was initially used for macro scale geomorphological mapping, with the higher resolution DEM needed to permit identification of smaller scale landforms (e.g., recessional moraines) (Pearce et al., 2014; Chandler et al., 2018) and to confirm the interpretation of any landforms identified and mapped using the lower-resolution datasets.

3.2 Digital Elevation Model Generation

Satellite Pour l'Observation de la Terre (SPOT) 7 tri-stereo imagery acquired on 11th May 2020 was used to create the high-resolution DEM (**Figure 3**). The SPOT 7 images were processed to the primary product level by Airbus Defence and Space. The three SPOT 7 images were used to generate point clouds within ERDAS Imagine 2018's Photogrammetry Suite. Using the LAS Dataset to Raster tool in ArcGIS 10.6.1 the generated point cloud was processed into a DEM. To generate the DEM the rational polynomial coefficients (RPCs) provided with each image were used to provide georeferencing and satellite characteristics. The tri-stereo imagery was tied together using ~100 tie-points, although those with the highest RMSE were removed to minimise the RMSE for the triangulation. This generated a RMSE of 0.07 pixels for the tied-together images. A point cloud with over 28.4 million points was generated, producing a DEM with a spatial resolution of ~2.5 m.

To interpolate across the point cloud and generate a DEM, Guo et al. (2010) suggests that the use of simple interpolation techniques (such as Natural Neighbor, Inverse Distance Weighting and

TABLE 1 | Criteria for landform identification on remotely sensed imagery loosely modified from the landform identification criteria from Glasser et al. (2008).

Landform	Identification Criteria	Identification Limitations	Reconstruction Significance
Moraines	Are linear, curved or sometimes sinuous ridges. Prominent features of singular or multiple ridges. Lateral moraines found along the sides of valleys; terminal moraines cut across a valley. Moraines can also be rocky in appearance or subdued	Shadows can preclude moraine identification. Could be misidentified as trimlines if low in height. Moraines may not be prominent enough to be identified within the remote imagery. Other linear features could be misidentified as morainic features	Denotes the maximum extent of a glacier at a certain point in time before retreat (after an advance phase) or a standstill during deglaciation. Multiple moraines in close proximity denote a fluctuating glacial margin or recessional moraines
Glacial deposits	Complex moraine systems with multiple moraines nested together, while glacial deposits have a clear colour difference, being lighter in colour along with the aforementioned moraines on top	Shadowing from the surrounding terrain, while vegetation can cover the glacial deposits making it hard to discern from the surrounding terrain	Maximum extents of glaciers, and a location of glacial activity. Deposition of former supraglacial material providing indication of potential sedimentation transportation pathways
Smoothed bedrock/ steep sloped bedrock	Rock which is bare or lightly vegetated. Visible joints can be seen. Seen near cirque headwalls. Can be stepped features with small bodies of water in between rock outcrops or within larger joints. Steep sloped bedrock are steeply inclined bedrock, usually location on the top of valley walls	Vegetation cover and any shadowing can preclude identification	Areas of glacial activity. Evidence of basal ice at pressure melting point allowing erosion to occur. Could be used to see areas of erosion compared to area of deposition
Cirque headwalls	"Bowl" or amphitheatre-shaped depressions in the side of valleys or high relief ground. Either shallow and vegetated, or steep and bare bedrock with or without an overdeepening infilled with a lake. The edges of the cirque can be sharp or rounded	Could be confused with large landslip features	Indicates the origin location of glacial ice. Also indicates restricted glaciation. Cirques on valley walls, could have coalesced with the main valley glacier if one was present
Glacial lineations	Linear landforms running parallel with the direction the glacier was flowing. Identified in between moraines	Vegetation may cover over glacial linear features	Indicates area of glacial activity. Shows the direction of ice flow
Boulders	Large generally circular features which can be found on or near moraines, or along the valley side or floor. Can also occur in boulder moraines, where boulders are deposited in a linear line along the side of valleys	Could be covered in vegetation. Size of boulder could be smaller than image resolution precluding their mapping	Indicates the erosion of a glacier and where it has been deposited either during advance, or glacial retreat. Can be used to determine where to take sample for dating techniques
(Palaeo) Hill slope failures	On the side of valley walls, or large pronounced moraines, where there is a change in colour compared to the surrounding ground. If fresh they are light in colour, while if they are palaeo, they are either darker in colour or be lightly vegetated over with clear scarp/source area scar	If vegetated could be obscured from mapping. Unlikely, but could cover or bulldoze other geomorphological features	Unstable ground potentially due to glacial material
Waterbodies	Freshwater bodies found within overdeepenings and depressions. Usually found within a glacier cirque. Some small lakes are found independent of a glacial overdeepening but can form in a depression in the ground, for example within joints in bedrock	Reflectance of remotely sensed image can make the colours of lakes change from the expected colour. If smaller lakes are covered by shadow, they will not be easily indefinable. Smaller water bodies may be smaller than the image resolution and may preclude their mapping	They indicate presence of glacial overdeepenings if occupied by one water body. Multiple smaller water bodies may indicate glacial erosion of the bed rock
Rivers/streams	Linear when flowing down steep slopes, but sinuous features when on the valley floor. Occupy the lowest elevation in a valley, that conjoin with other streams down valley	Hard to determine where they start near the headwaters due to being small streams. When reaching further down valley, may become obscured by vegetation which prevent accurate delineation	Indicate the lowest elevation within a valley. Provide inferences on the influence of fluvial processes

Triangulated Irregular Network methods) are more efficient for high density data, such as that used within this study. To determine the best technique to interpolate between no data points within the DEM we compared "linear", and "natural neighbour" approaches ("simple" interpolation was discounted as is can only interpolate over no data areas which are the size of a few pixels), that are present within the LAS Dataset to Raster tool. Using previously collected and processed dGPS points, acquired from the study area in 2017 as a control on absolute elevation, we determined the most accurate interpolation technique to be "Natural Neighbour". Acquired dGPS points have a conservative estimate of uncertainty of ~5 m due to the long baseline between rover and the local base station. The "Natural neighbour" method produced

an elevation RMSE of 2.10 m compared to 2.14 m for the "linear" interpolation method, and there was no difference in the computational time between the two methods.

Large-scale landforms identified throughout the 30 m ALOS DEM and satellite imagery, demonstrated that the 2.5 m SPOT DEM was well aligned and thus the generated DEM required no further georeferencing. Many locations covered by the SPOT DEM were affected by cloud cover in the original imagery, while its resolution is not fine enough to allow adequate mapping of more subdued moraines (<2 m relief).

3.3 Geomorphological Mapping

Geomorphological mapping was conducted following well-established remotely sensed techniques (Chandler et al., 2018). We mapped geomorphological landforms determined to be of glacial origin using the criteria in **Table 1**, which follows a similar criteria to Glasser et al. (2008). Some landform criteria were not used due to landforms not being present or impossible to identify within our study region (e.g., shorelines). Small adjustments were made to the identification criteria for some features due to Glasser et al. (2008) mapping features in currently glaciated locations where landforms had a "fresher" appearance than those in our study area. Images were used in the "true colour" band combinations for their respective sensors, which allow a good assessment of landforms. To further enhance landform detection, where landforms were ambiguous by two-dimensional mapping, Google Earth™ was used for three-dimensional projection of remotely sensed imagery over topographic data, albeit sometimes at a lower resolution or lower quality imagery (Chandler et al., 2018). The mapping of glacial geomorphology includes moraines, trimlines, glacial lineations, cirques headwalls, glacial headwalls, boulders, and glacially smoothed bedrock. Non-glacial geomorphic features (e.g., streams and lakes) were also mapped to add context to the mapping. Due to datasets from multiple sensors being used to map features, and the errors and uncertainties associated with each of them, we conservatively estimate that mapped features might be horizontally offset from their true position by ±30 m (**Supplementary Figure 1**). Three of the authors visited the field area prior to this study, providing some limited ground truthing to mapped features within the Laguna Shimbe valley, though systematic and extensive fieldwork has not yet been undertaken.

3.4 Palaeoglaciological Reconstruction

We reconstructed the extent of all glaciers hypothesized to have occupied Las Huaringas to their most prominent and extensive mapped moraine. In the absence of any dating control on these moraines and any significant moraines between the cirque and these lower moraines, we assume that they represent the LLGM extents. This is consistent with the approach of other studies where dating controls are unavailable (e.g., Emmer et al., 2021). However, there is potential for some of the most downvalley glacial evidence in our study area to pre-date the LLGM. A number of studies have identified pre-LGM moraines down valley of glacial cirques within the northern tropical Andes (e.g., Goodman et al., 2001; Dirszowsky et al., 2005), although these would likely have much less relief and be less distinct compared to LLGM moraines. Without dating of moraines to create a chronology of glacial advances, it is currently not possible to constrain the age of the moraines at Las Huaringas.

We extracted basic metrics from these reconstructed glaciers, such as their mean, minimum and maximum elevations, glacier aspect and length. Where glaciers split into multiple outlets, we took the longest length. The cirque floor elevation was also extracted from the cirques from which glaciers were hypothesised to have originated from. Glacier ice surface contours were generated with contour intervals of 100 m to create ice surface profiles during their maximum extents. Contours were generated, in accordance with well established procedures detailed by earlier studies of glacier reconstructions (e.g., Sissons, 1974; Bendle and Glasser, 2012), across the glacier profiles. These contours were adjusted to be in-line with observed modern day glacial dynamics (Ng et al., 2010), with ice thickness reduced below the ELA (generation discussed below) closest to the terminus (convex contours), and with greater ice thickness above the ELA in areas closest to the headwall (concave contours).

The subjective nature of palaeo ice extent reconstruction is the main source of uncertainty for reconstructing palaeo glacier extent and thickness. Whilst lateral-terminal moraines provide elevation constraint and delimit potential glacier margins, they are not always present or easily identifiable. In such cases, a best estimate of the ice margin was determined using the elevation from the DEM using the terminus elevation of surrounding glaciers as a reference. The most common area where a best estimate was used was the terminus of the palaeo glaciers, where no well-defined (or mapped) terminal moraine could be delineated, or where lateral moraines are mapped on one side of the valley but were not apparent on the other. Uncertainty can also be seen in the glacier ice surface contours. Where ice split into two or more outlets from one accumulation source (e.g., Huancabamba 1), there may be some uncertainty as to how well they may represent the LGM ice surfaces. However, these were produced to provide a visual representation and were not used for any analysis.

3.5 Palaeo Equilibrium Line Altitude Reconstruction

The ELA is the theoretical line where accumulation and ablation are equal (Benn et al., 2005) and has been frequently used as a proxy of the surrounding climate conditions of temperature and precipitation for the reconstruction of tropical Andean glaciers and climate (Porter, 2001; Mark and Helmens, 2005; Bromley et al., 2011a; Martin et al., 2020). Although the ELA would not have been static for long periods of time due to the varying climate conditions, the reconstructed palaeo-ELA inferred in this study is assumed to be at its lowest potential elevation and thus represents the time the glaciers were at their most extensive (i.e., LLGM).

To reconstruct palaeo-ELAs we used the ArcGIS Toolbox created by Pellitero et al. (2015) which reconstructs palaeo-ELAs using a generated glacier DEM and using a number of different methods (MGE, AAR and AABR). We generated the

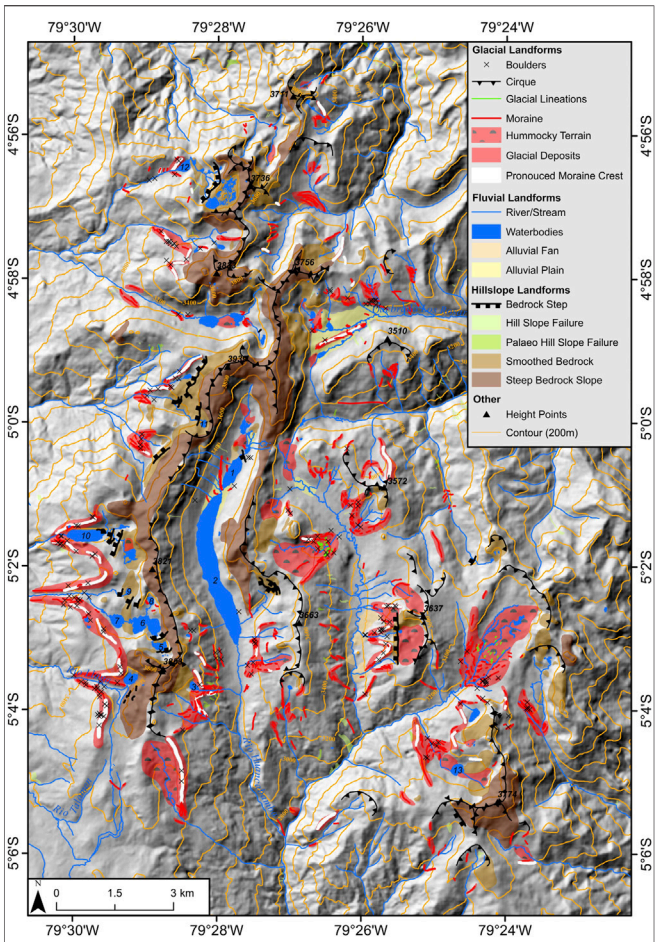

FIGURE 4 | Geomorphological map of the Lagunas de las Huaringas. Basemap is a hillshade of the 30 m ALOS DEM (Azimuth: 315°, Z-factor: 1). A full resolution A0 version of the map can be found within the supplementary information. Lake names are: 1 – L. el Paramo; 2 – L. Shimbe; 3 – L. Redonda; 4 – L. Negra; 5 – L. las Arrebiatadas 1; 6 – L. las Arrebiatadas 2; 7 – L. las Arrebiatadas 3; 8 – L. las Arrebiatadas4; 9 – L. el Toro; 10 – L. la Cruz; 11 – L. el Rey Inca; 12 – L. Negra de San Pablo; and 13 – L. Redondo de Zapalche.

glacier DEM using vertices of the glacier extent polygon to act as elevation and used the Natural neighbor interpolation method to reconstruct a flat glacier surface, as used in other studies for ELA reconstructions (e.g., Lee et al., 2021). This was then inputted into the Pellitero et al. (2015) tool using the Accumulation-Area Balance Ratio (AABR) method to generate the ELAs, as it has been shown to be the most accurate in reconstructing ELAs (Santos-González et al., 2013; Pearce et al., 2017; Quesada-Román et al., 2020). One of the main sources of uncertainty for the reconstruction of palaeo-ELAs using the AABR method is the choice of the balance ratio. There is however a lack of data on balance ratios across the tropical Andes, thus making the choice of balance ratio difficult to determine. Tropical glaciers generally have high ablation rates throughout the year, and also have small ablation areas (Rea, 2009). As such, some studies have assigned high balance ratios. For example, Quesada-Román et al. (2020) used a value of 2. To account for the uncertainty in constraining the balance ratio for tropical glaciers, several balance ratios were tested; 1.00, 1.25, 1.50, 1.75, 2.00, 2.25 and 2.50, with 1.75 being the global average (Rea, 2009). The use of multiple balance ratios results in variations in reconstructed ELAs by only a few tens of meters, or a ~0.87% difference (if any difference is seen). The balance ratio of 1.75 was therefore used within this study as a median between the two extremes. It is acknowledged that the balance ratio could be higher, however.

3.6 Palaeotemperature Reconstruction

The reconstructed palaeo-ELAs and subsequent ELA change (ΔELA) were used to reconstruct palaeo-temperature. Given the uncertainty about past climate in the region, three potential atmospheric temperature lapse rates (ATLR) were used to calculate temperature change (ΔT): −5.5, −6.5 and −7.5°C/km (Quesada-Román et al., 2020). Although the ELA is controlled by a range of climate conditions including precipitation (e.g., Stansell et al., 2007), temperature has an overarching influence. The palaeo-ELA was compared to the modern ELA in order to calculate ΔELA. In this region the snowline lies above the highest local summit and therefore the nearest identifiable snowline that intercepted with topography was used to infer the modern ELA. The elevation of 4,600 m from a location ~8°S was used (Hammond et al., 2018).

4 RESULTS AND DISCUSSION

4.1 Geomorphological Interpretation and Reconstructed Glacier Extents

Within **Section 4.1** we describe the results of both the geomorphological mapping (**Figure 4**) and reconstructed glacial ice extents (**Figure 5**) and metrics (**Table 2**). We provide a localised description and interpretation of our results for five geographical areas (**Figure 5**). These areas are: 1) Laguna Shimbe valley (LS); 2) eastern glacier valley (EG); 3) western glacier cirques (WG); 4) northern glacier valleys (NG); and 5) south-eastern glacier cirques (SEG). Reconstructed glacial ELAs and the estimated palaeotemperatures are reported study area wide and discussed.

Across the study area we identified a number of moraines, while mapping over 830 moranic fragments or singular prominent moraine features, 44 individual glacial cirques with floor elevations ranging from between ~3,150 and 3,600 m, 38 mapped glacial lineations with lengths between ~23 and 103 m, 32 bedrock steps, a number of individual boulders mapped within or on a moraine that may be used for dating purposes, hill slope failures, smoothed bedrock surfaces, and hummocky terrain. All these features are used to evidence glacial activity and their extent within the Las Huaringas region.

4.1.1 Laguna Shimbe Valley

The mapped geomorphology (**Figure 6A**) suggests a large valley glacier formed in the central Laguna Shimbe valley (LS) during the LLGM (**Figure 6B**). This glacier ("Shimbe Glacier") likely extended to a minimum elevation of 2,652 m, 12.7 km down

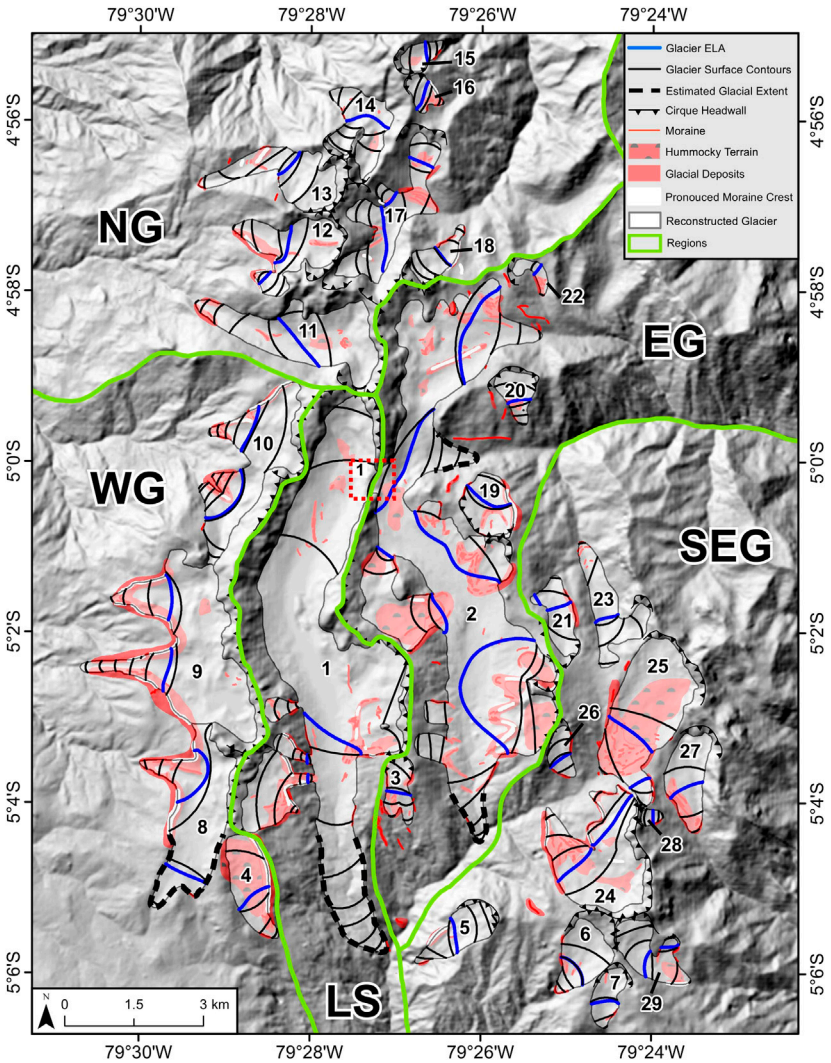

FIGURE 5 | Reconstructed glacial extents within the Lagunas de las Huaringas along with reconstructed ELAs, glacier surface contours (100 m interval) and geomorphic evidence (i.e., moraines) used to delineate the glaciers. Glaciers 1, 2 and 8 have estimated glacier extents shown by the dashed lines. Extents overlie a hillshade of the 30 m ALOS DEM (azimuth: 315°, z-factor 1). The five areas defined for interpretations are delineated by thick green lines. These also define the extents in subsequent figures. Names and reconstructed ELA elevations of glaciers relate to those shown in **Table 2** within the ELA reconstruction section. Acronyms are: LS–Laguna Shimbe valley (**Figure 6**); EG–Eastern Glacier valley (**Figure 8**); SEG–South-Eastern Glacial cirques (**Figure 9**); WG–Western Glacier cirques (**Figure 10**); and NG–Northern Glacier valleys (**Figure 11**). Subset 1 shown by the dashed lines corresponds to the col shown in detail within **Figure 7**.

valley, with a reconstructed area of 18.46 km^2. Lateral moraines are located along the western wall of the Shimbe valley, at ~3,420 and ~3,340 m, respectively, and constrain the lateral and vertical extent of the glacier. However, the greatest extent of the Shimbe Glacier cannot be established confidently due to downvalley evidence being difficult to discern. This may be due to postglacial erosion and fluvial reworking. As a result, we provide a hypothesised maximum LLGM limit for the Shimbe Glacier.

Between the hypothesised maximum glacial extent, and moraines further up valley (~9 km), little geomorphic evidence is apparent (**Figure 6**). This may be due to rapid retreat from its maximum extent during deglaciation, burial of evidence (e.g., by peat accumulation) or fluvial reworking of evidence. Some moraines are observed, though they are likely due to ice flow from glacial cirques on either side of the main valley. Closely spaced (~20 m) moraines between Laguna el Paramo (lake #1) and the larger Laguna Shimbe (lake #2) (**Figure 6**) could indicate glacial advances that postdate the LLGM, either during the late-glacial or early-Holocene. Glacial advances of these ages have been documented in a number of studies in Peru (e.g., Bromley et al., 2011b) and northern Bolivia (e.g., Zech et al., 2007).

Glacial cirques are located along the LS valley walls with cirque floor elevations between ~3,370 and 3,550 m a.s.l. (**Figure 6**). These cirques contain geomorphic evidence with moraines both within and just outside their cirque confines, indicating that

TABLE 2 | Metrics of area, length, glacier elevation, aspect, cirque floor elevation for reconstructed glaciers. Glacier # corresponds to the numbers in **Figure 5**. Glacier names are derived from either a named lake that occupies a depression within the valley, the cirque the glacier occupied (e.g., Shimbe), or the nearest named river the valley flows into (e.g., Huancabamba). Aspect visualised in **Supplementary Figure 2**.

Glacier name	#	Area (km^2)	Length (km)	Elevation (m)				Aspect (°)
				Min	Max	Mean	Cirque floor	
Shimbe Glacier[a]	1	18.46	12.67	2,652	3,761	3,346	3,415	177
Huancabamba 1[a]	2	21.00	8.64	2,953	3,624	3,322	3,364	126
Huancabamba 2	3	0.69	1.56	3,259	3,668	3,471	3,532	178
Huancabamba 3	4	1.51	2.46	3,356	3,750	3,581	3,465	160
Huancabamba 4	5	1.11	2.03	2,930	3,521	3,223	2,191	232
Huancabamba 5	6	1.27	1.84	3,112	3,525	3,376	3,217	197
Huancabamba 6	7	0.64	1.42	3,193	3,527	3,365	3,277	197
Negra Glacier[a]	8	3.88	3.89	3,345	3,775	3,626	3,547	239
Arrebiatadas Glacier	9	6.39	4.42	3,045	3,694	3,512	3,506	287
el Rey Inca Glacier	10	3.65	2.27	3,066	3,710	3,443	3,492	290
Palo Blanco 1	11	3.68	4.79	2,988	3,726	3,328	3,293	300
Palo Blanco 2	12	2.08	2.43	3,177	3,764	3,481	3,442	296
Palo Blanco 3	13	2.00	3.35	3,124	3,620	3,414	3,567	275
Aranza 1	14	1.54	2.68	3,071	3,632	3,348	3,361	240
Aranza 2	15	0.40	1.02	3,258	3,631	3,482	3,396	56
Aranza 3	16	0.38	0.94	3,350	3,649	3,518	3,532	132
Aranza 4	17	2.52	3.01	3,116	3,577	3,326	3,309	58
Aranza 5	18	0.68	1.57	3,148	3,618	3,408	3,354	47
Quebrada Los Rosarios 1	19	1.15	1.52	3,254	3,522	3,370	3,227	351
Quebrada Los Rosarios 2	20	0.66	1.25	3,062	3,432	3,321	3,178	163
Quebrada Los Rosarios 3	21	0.93	1.77	3,168	3,442	3,305	3,246	354
Quebrada Los Rosarios 4	22	0.26	1.21	3,194	3,382	3,299	3,331	127
Quebrada Los Rosarios 5	23	1.56	2.98	2,980	3,460	3,192	3,301	315
Redondo de Zapalache 1	24	3.64	2.81	3,109	3,563	3,382	3,319	324
Redondo de Zapalache 2	25	4.15	3.26	3,182	3,516	3,326	3,264	205
Redondo de Zapalache 3	26	0.47	1.20	3,217	3,569	3,401	3,268	169
Samaniego 1	27	1.42	2.16	3,086	3,343	3,237	3,291	190
Samaniego 2	28	0.13	0.50	3,341	3,543	3,448	3,341	77
Samaniego 3	29	1.26	2.07	3,203	3,686	3,418	3,339	131

[a]*Maximum glacial extent was estimated by surrounding glacier terminus elevations.*

during their maximum extent these would have coalesced with the main trunk of the Shimbe glacier. Closely spaced moraines just beyond, or within, the glacial cirques suggests that glaciers that occupied these cirques became decoupled from the Shimbe glacier during post-LLGM deglaciation and did not reconnect during any subsequent glacial advances. The geomorphic evidence suggests that the Shimbe glacier did not advance back to, or close to, its former extent after deglaciation from its LLGM maximum.

Near the head of the Shimbe Valley there is a topographic low ("col") at ~3,460 m a.s.l. on the eastern valley wall (**Figure 7**). This dip features smoothed bedrock, compared to the rougher surrounding valley walls, indicating it has been smoothed by glacial ice. Either a localised glacier was present at this location adjacent to the Shimbe glacier, or the Shimbe glacier was thick enough to overcome the valley topography and flow into the adjacent valley. To allow ice to overcome the col, it would have required a minimum ice thickness of ~200 m thicker than any other LLGM reconstructed ice masses across the study area.

4.1.2 Eastern Glacial Valley

The valley to the east of LS exhibits extensive evidence of glaciation with a number of mapped moraines along the valley walls and floor, eight distinct glacial cirques, and nineteen mapped glacial lineations (**Figure 8A**). The evidence suggests one of the largest glaciers within the Las Huaringas region, with a reconstructed estimate of the Huancabamba 1 glacier area of 21 km^2 (**Figure 8B**). The extents and area metrics of the reconstructed glacier are an estimate, due to the absence of any discernible cross valley terminal moraines downvalley. The geomorphic evidence within the EG suggests an interconnected glacial valley system with three terminus locations, that can be split into two distinct "zones"; 1) the valley running south paralleling the Shimbe valley with a singular glacier terminus, and 2) the two valleys, with a glacier terminus each, to the north which run eastward–all hypothesised to have terminated at ~3,000 m a.s.l. due to the absence of obvious terminal moraines (**Supplementary Figure 5**). All valleys within the EG area contain valley wall cirques with cirque floor elevations ranging from 3,178–3,420 m a.s.l. At their largest extent, glaciers flowing from these cirques would have connected with the main valley glacier during the LLGM. Similar to the cirque glaciers reconstructed in the LS area, mapped moraines beyond and within their cirque extents suggests that after deglaciation from the LLGM any subsequent readvances would not have seen their reconnection with any main valley glacier, otherwise such evidence beyond their cirque confines would likely have been removed by glacial erosion.

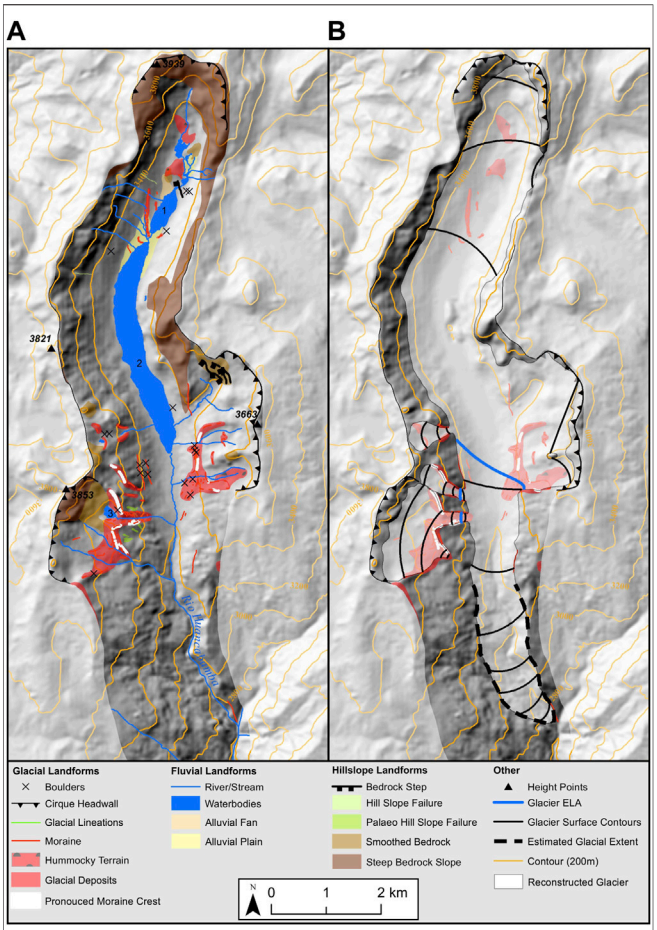

FIGURE 6 | The Laguna Shimbe valley (LS) with **(A)** mapped glacial geomorphology, and **(B)** reconstructed glacier to its estimated LLGM extent. Base map is a hillshade of the 30 m ALOS DEM (azimuth: 315°, z-factor 1). Lake names: 1 – L. el Paramo, 2 – L. Shimbe.

These two zones are split by the col (**Figures 7**, **8**), through which the Shimbe and Huancabamba 1 glaciers could have potentially been connected at the height of their LLGM glacial extents. Evidence for this is smoothed bedrock exposed in the col between LS and EG suggesting that at some point the Shimbe glacier was thick enough (>200 m thickness) to overcome the topography and make a direct connection between these two glacial masses. Without further infield investigations however, we cannot determine whether this occurred at the LLGM or during an earlier glaciation.

Evidence for the potential "spill over" of ice from the LS to the EG area can be seen within the northern zone of EG (**Figure 8** section labelled N). This zone has two eastward flowing valleys, with the most southerly valley exhibiting little evidence for glaciation apart from a singular glacial cirque on either side of the valley. The southernmost cirque (**Figure 8B** subset 1; **Supplementary Figure 3**) has a well-developed set of moraines perhaps indicating multiple glacial events. The northernmost valley hosts the most striking evidence with a prominent medial moraine (**Figure 8B** subset 2; **Supplementary Figure 4**) running down the centre of the valley going eastward. This demonstrates that glacial ice flowed both from the glacial cirques in the northern valley and from the south, potentially from ice flowing over from SG area. This southern input is hypothesised due to the absence of a clear glacial cirque above the valley. The medial moraine is located to the southern side of the east-west trending valley, suggesting that ice flow was dominated by flow originating from the northern cirques.

Within the southern zone of the EG area (**Figure 8** section labelled "S"), are a number of predominantly westward facing glacial cirques, the majority of which exhibit classic evidence of cirque glaciation. These would have likely contained ice, feeding into the main Huancabamba glacier flowing southward, during their most extensive LLGM extent. Two cirques are of particular

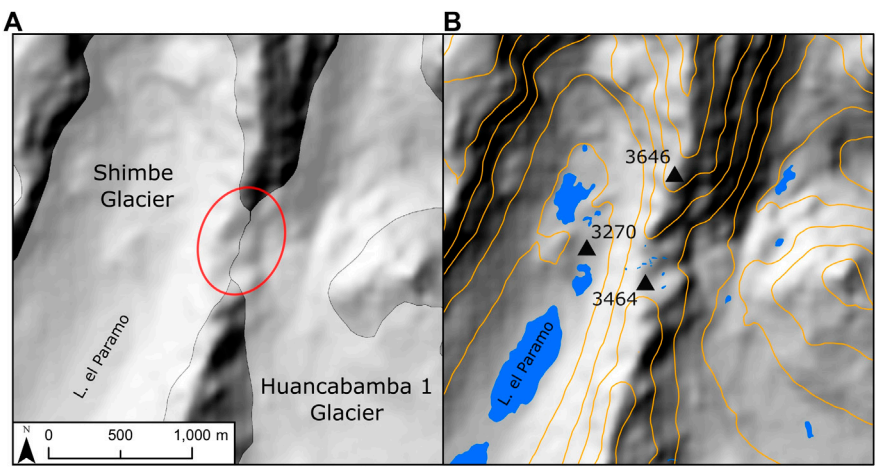

FIGURE 7 | Confluence of glacier ice at the col with the location can be seen in **Figure 5** 1), that shows the connection (red circle) between the Shimbe glacier and Huancabamba 1 glacier during their LLGM maximum extent in a col with a maximum elevation of 3,464 m a.s.l. that is lower than the surrounding valley wall ridges (3,646 m a.s.l.). Yellow contours are at 100 m intervals.

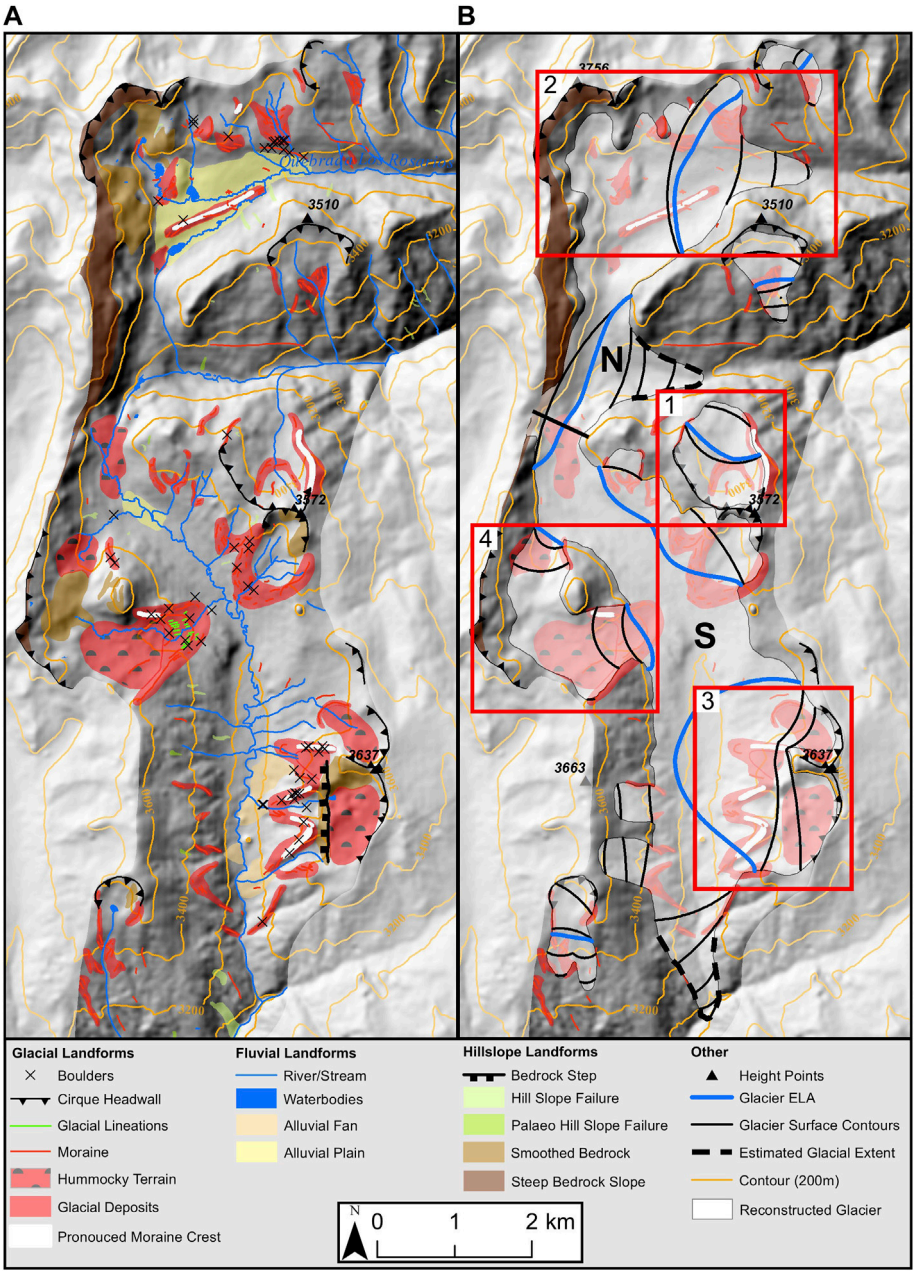

FIGURE 8 | The Eastern Glacial valley (EG) with **(A)** mapped glacial geomorphology, and **(B)** the reconstructed glaciers to their estimated LLGM extent. The Huancabamba 1 glacier is split into two zones: the northern (N) and southern (S) zones. The separation is the split at the col that connected the two valleys, shown in **Figure 7**. Subsets **(B)** 1, 2, 3 and 4 correspond to **Supplementary Figures 3, 4, 5 and 6**, respectively. Base map is a hillshade of the 30 m ALOS DEM (azimuth: 315°, z-factor 1).

interest within the southern zone of the EG: 1) one near the southern end on the east side of the valley (**Figure 8** subset 3; **Supplementary Figure 5**), and 2) the other on to western flanks (**Figure 8** subset 4; **Supplementary Figure 6**). The first location contains three reconstructed glacier outlets connecting to an individual cirque. Prominent moraines connect through all three outlets and appear to have once contained lakes within each outlet depression. Moraines may delineate individual advances after the LLGM when they become disconnected from the main valley glacier during deglaciation. These lakes were moraine dammed and drained at some point after deglaciation. This was probably the result of moraine dam failures, evidenced by the lack of an enclosing terminal moraine and deposits of alluvial material in front of the glacial moraines. Within the second location, the glacial cirque splits into two outlets, with the southern outlet being one of only two

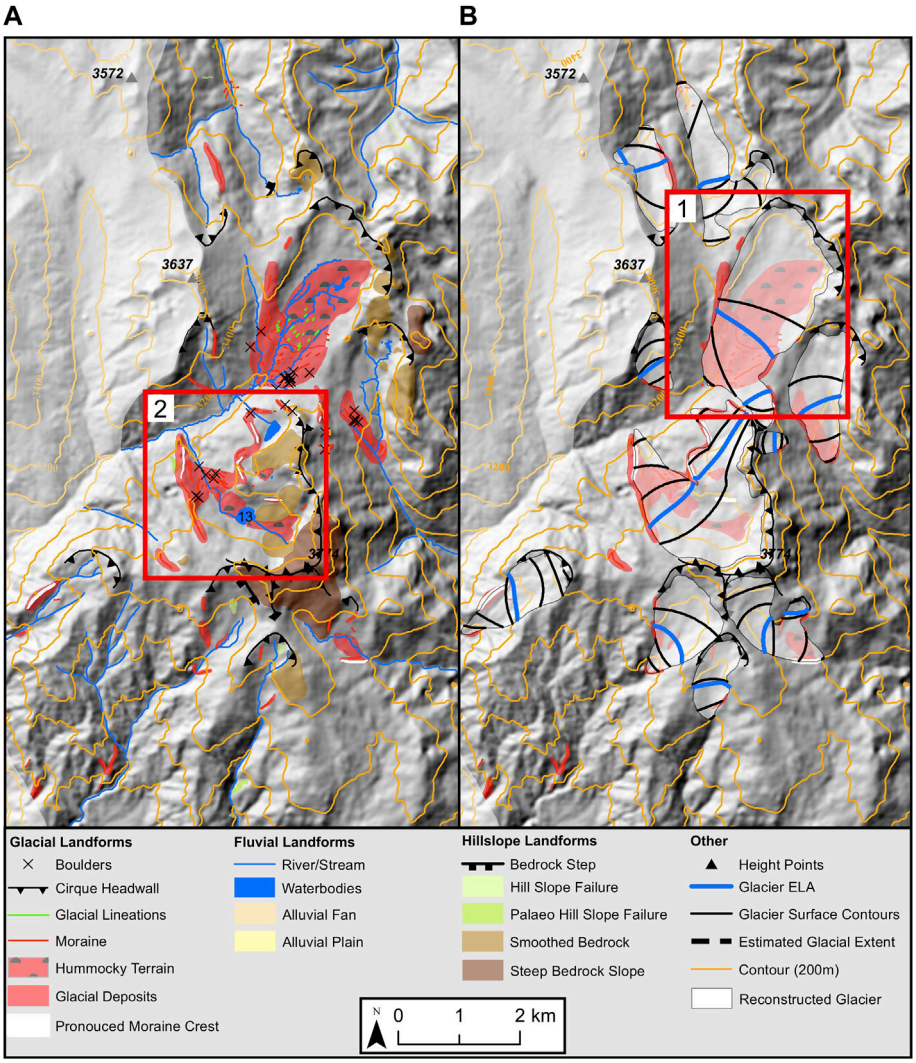

FIGURE 9 | The southeastern glacial cirques (SEG) with **(A)** mapped glacial geomorphology, and **(B)** the reconstructed glaciers to their LLGM extents. Subsets **(B)** 1 and **(A)** 2 correspond to **Supplementary Figure 7 and Supplementary Figure 8**, respectively. Base map is a hillshade of the 30 m ALOS DEM (azimuth: 315°, z-factor 1). Lake name: 13 – L. Redondo de Zapalache.

locations that exhibit possible glacial lineations. There is a potential for these features to be glacial flutes, however because of their small-scale further investigation with a finer resolution DEM along with infield techniques is required.

4.1.3 South-Eastern Glacial Cirques

Geomorphological evidence within the south-eastern zone (SEG) of the study area (**Figure 9A**), suggests a cirque to valley glacier configuration (**Figure 9B**). There are twelve identified cirques that would likely have contained reconstructed glaciers in this zone. The reconstructed glacial area during the LLGM was 17.7 km^2. Multiple moraines are nested within many of the cirques, but glacial geomorphic evidence is more discontinuous further south. The absence of this evidence is likely due to decreasing topographic elevation, which may not have permitted glacier ice to persist even during the LLGM. Many cirques exhibit extensive erosion with glacially smoothed bedrock indicative of warm-based basal conditions, in line with evidence across the study region. Many of the cirques would have contained a separate and confined glacier, with no evidence for ice masses coalescing. The dominant orientation for cirques in this zone is south and south-westward facing, which could be due to the predominant direction of incoming solar radiation in the southern hemisphere.

Similar to the EG, the SEG zone is the only other location within the study area to contain mapped lineation features (**Figure 9A** subset 1; **Supplementary Figure 7**). nineteen features were mapped with lengths between 23 m and 100 m. These lineations are located within the extent of the Redondo de Zapalache 2 glacier valley (#25) behind discontinuous closely spaced moraines, with the orientation of the lineations indicating a northeast to southwest direction of glacier flow, similar to that

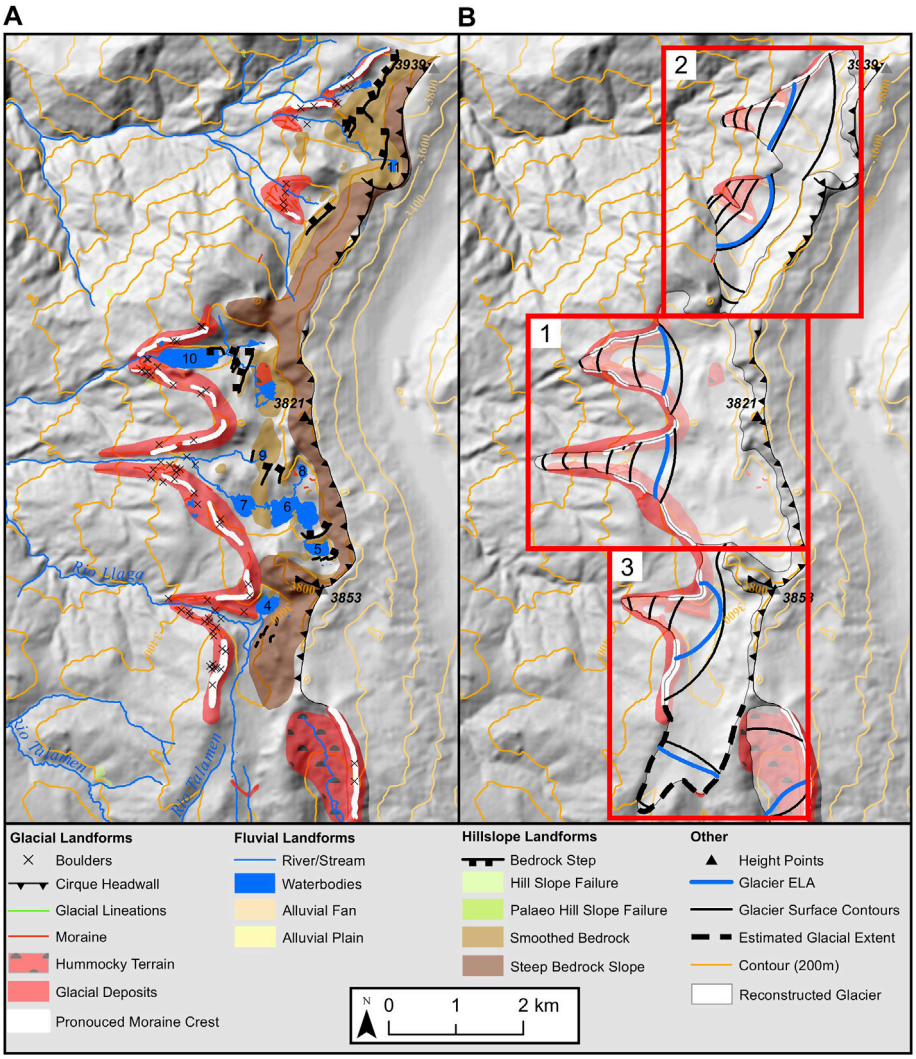

FIGURE 10 | The western glacial cirques (WG) with **(A)** mapped glacial geomorphology, and **(B)** the reconstructed glaciers to their estimated LLGM extents. Subsets **(B)** 1, 2 and 3 correspond to **Supplementary Figures 9, 10 and 11**. Base map is a hillshade of the 30 m ALOS DEM (azimuth: 315°, z-factor 1). Lake names: 4 – L. Negra, 5 – L. las Arrebiatadas 1, 6 – L. las Arrebiatadas 2, 7 – L. las Arrebiatadas 3, 8 – L. las Arrebiatadas 4, 9 – L. el Toro, 10 – L. la Cruz, 11 – L. el Ray Inca.

suggested by the lineations in the EG valley. We hypothesise that these lineations are only found in these two locations due to their relatively unusual location on flat terrain. The remainder of the study area either lacks wide areas of sufficiently flat terrain where such lineations may develop, or lineations may have existed previously but have been eroded by post-depositional geomorphic action.

The Redondo de Zapalache 1 glacier area (#24) (**Figure 9B** subset 2; **Supplementary Figure 8**) is unique compared to the surrounding glacier cirques in the SEG zone, being similar to the two cirque glaciers discussed within the EG. The geomorphological evidence here suggests two glacier outlets that flowed from a shared accumulation zone. The total reconstructed glacier area was 3.6 km^2. Prominent moraines indicate maximum lateral extents of these ice masses. Further lateral moraines up-valley from these lateral-terminal moraines indicate that the two glacier outlets separated during deglaciation, dividing into two glaciers each occupying their own cirque, and potentially producing moraines suggesting post-LLGM readvance. The westernmost outlet of this glacier contains multiple closely spaced moraines (20–100 m apart) at its terminus potentially indicating a fluctuating ice front.

4.1.4 Western Glacial Cirques

The western zone of the Las Huaringas region (WG) contains some of the largest and most extensive moraines in the study region (**Figure 10A**). These moraines extend down to a minimum elevation of ~3,100 m a.s.l. We reconstructed three glaciers, the Arrebiatadas Glacier, the el Rey Inca glacier and the Negra Glacier (**Figure 10B**), which occupy five large west-facing cirques. These cirques have steep headwalls and are well developed, indicating significant backward erosion while also having wide open

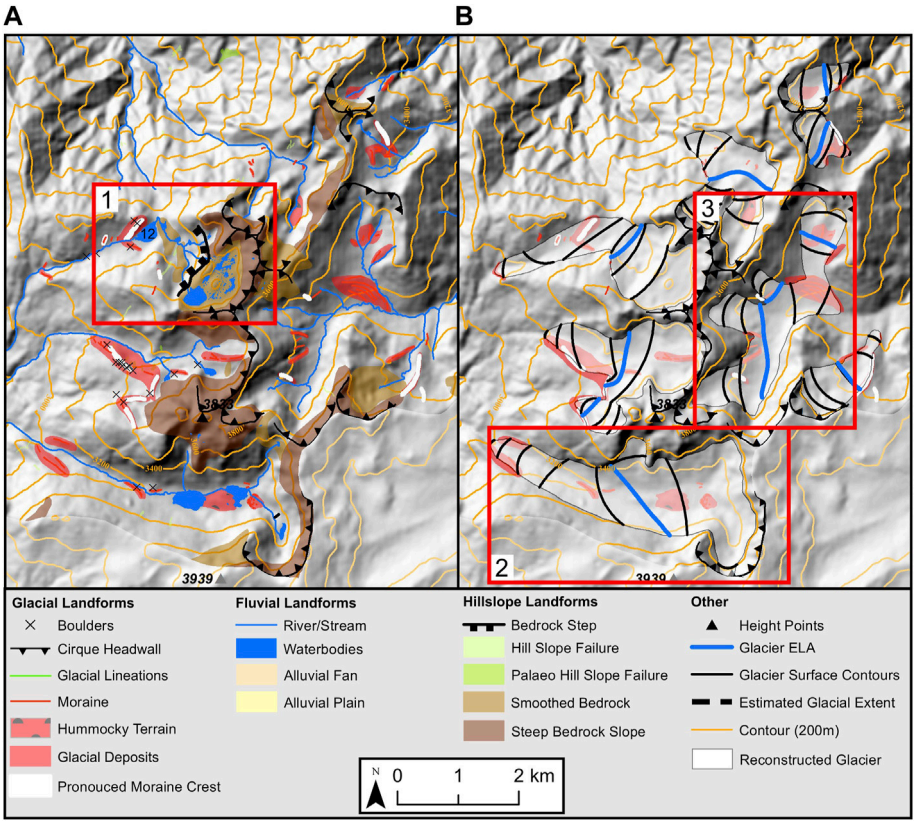

FIGURE 11 | The northern glacial valleys (NG) with **(A)** mapped glacial geomorphology, and **(B)** the reconstructed glaciers to their estimated LLGM extents. Subsets **(A)** 1 and **(B)** 2 and 3, correspond to **Supplementary Figures 12, 13 and 14**, respectively. Base map is a hillshade of the 30 m ALOS DEM (azimuth: 315°, z-factor 1). Lake name: 12 – L. Negra de San Pablo.

backwalls that do not follow an amphitheatre-like shape that is seen across the study area; this makes it hard to determine an individual "source" cirque. Depressions containing water bodies are common across the WG. These twenty-six bodies of water are either dammed by bedrock (e.g., Lagunas las Arrebiatadas) or a moraine (e.g., Lagunas la Cruz), often coinciding with bedrock steps and smoothed bedrock indicating warmed based glaciers that produced significant glacial erosion with a high discharge of ice and a high mass turnover (MacGregor et al., 2000; Cook and Swift, 2012; Evans, 2021).

The form of the Arrebiatadas Glacier (**Figurer 10B** subset 1; **Supplementary Figure 9**), and the el Ray Inca Glacier (**Figure 10B** subset 2; **Supplementary Figure 10**) suggest they both potentially had two source areas which coalesced to create an individual ice mass, from which two separate glacial outlets extended from. The Arrebiatadas Glacier area, covering 6.4 km^2, has well defined and interconnected moraines up-valley. These run down into, and demarcate, the individual outlets providing further evidence that ice came from a single source area. Moraines within the confines of the most extensive terminal moraine of the Arrebiatadas Glacier are closely spaced (20–50 m), which may indicate oscillating climate condition during formation. Similar dynamics are possible for the el Ray Inca Glacier. The el Ray Inca Glacier covered 3.6 km^2, had prominent lateral moraines on its northern most glacial outlet, and more closely spaced moraines near its terminus. Within the southern outline, it lacks many prominent moranic features, but hosts smaller closely-spaced moraines.

The Negra Glacier (**Figure 10B** subset 3; **Supplementary Figure 11**), the most southern of the glaciers in the WG area covered an area of 3.9 km^2. This glacier may have connected with the Arrebiatadas system at the LLGM as indicated by lateral moraines which appear to connect. Like other glaciers within WG, geomorphological evidence indicates that glacial ice flowed from a single source zone into two outlets, westward and southward. Although the moraines to the west clearly indicate the former glacier ice extent, little geomorphic evidence for the southern outlet is observed. Although a single moraine is mapped, no further evidence is seen to demark its most southerly advance, potentially indicating reworking from post-glacial fluvial action. Although glacial ice is reconstructed to the only mapped moraine in the outlet, due to the flatter profile of the topography when compared to its western counterparts, ice could have flowed further south than this position, but would require further infield investigation to determine this.

TABLE 3 | Results of the palaeo-ELA calculations (m) using the AABR method with different ratios.

Glacier name	#	AABR ELA Elevation (m)						
		1.0	1.25	1.5	1.75[a]	2.0	2.25	2.5
Shimbe Glacier[b]	1	3,450	3,450	3,420	3,420	3,420	3,390	3,390
Huancabamba 1[b]	2	3,376	3,376	3,376	3,376	3,376	3,346	3,346
Huancabamba 2	3	3,470	3,470	3,470	3,470	3,440	3,440	3,440
Huancabamba 3	4	3,630	3,600	3,600	3,600	3,600	3,600	3,600
Huancabamba 4	5	3,241	3,241	3,241	3,211	3,211	3,211	3,211
Huancabamba 5	6	3,421	3,421	3,421	3,391	3,391	3,391	3,391
Huancabamba 6	7	3,404	3,374	3,374	3,374	3,374	3,374	3,374
Negra Glacier[b]	8	3,680	3,680	3,680	3,680	3,650	3,650	3,650
Arrebiatadas Glacier	9	3,586	3,586	3,556	3,556	3,556	3,556	3,556
el Rey Inca Glacier	10	3,586	3,586	3,556	3,556	3,556	3,556	3,556
Palo Blanco 1	11	3,416	3,416	3,416	3,416	3,386	3,386	3,386
Palo Blanco 2	12	3,540	3,510	3,510	3,510	3,510	3,510	3,480
Palo Blanco 3	13	3,450	3,420	3,420	3,420	3,390	3,390	3,390
Aranza 1	14	3,374	3,374	3,374	3,344	3,344	3,344	3,344
Aranza 2	15	3,521	3,491	3,491	3,491	3,491	3,491	3,491
Aranza 3	16	3,531	3,531	3,531	3,531	3,531	3,501	3,501
Aranza 4	17	3,348	3,348	3,348	3,318	3,318	3,318	3,318
Aranza 5	18	3,421	3,421	3,421	3,391	3,391	3,391	3,391
Quebrada Los Rosarios 1	19	3,396	3,396	3,396	3,396	3,396	3,396	3,366
Quebrada Los Rosarios 2	20	3,347	3,347	3,317	3,317	3,317	3,317	3,317
Quebrada Los Rosarios 3	21	3,342	3,342	3,312	3,312	3,312	3,312	3,312
Quebrada Los Rosarios 4	22	3,309	3,279	3,279	3,279	3,279	3,279	3,279
Quebrada Los Rosarios 5	23	3,214	3,214	3,184	3,184	3,184	3,184	3,184
Redondo de Zapalache 1	24	3,439	3,439	3,439	3,439	3,439	3,409	3,409
Redondo de Zapalache 2	25	3,384	3,384	3,384	3,354	3,354	3,354	3,354
Redondo de Zapalache 3	26	3,417	3,417	3,417	3,387	3,387	3,387	3,387
Samaniego 1	27	3,259	3,259	3,259	3,259	3,259	3,259	3,259
Samaniego 2	28	3,467	3,437	3,437	3,437	3,437	3,437	3,437
Samaniego 3	29	3,439	3,439	3,439	3,409	3,409	3,409	3,409
Mean		3,430	3,422	3,420	3,422	3,418	3,400	3,398

[a]*Global average determined by Rea (2009) used for temperature change calculations.*
[b]*Maximum glacial extent was estimated by surrounding glacier terminus elevations.*

4.1.5 Northern Glacial Valleys

Glaciers reconstructed in the northern glacial valleys (NG) north study region generally exhibit a cirque- to valley-glacier configuration like the glaciers of the SEG area. Geomorphological evidence (**Figure 11A**) suggests the most extensive glaciers developed (**Figure 11B**) on the westward side of the region (mean ice mass area of 2.3 km^2), while smaller glaciers developed to the east (mean ice mass area of 1 km^2). These reconstructed glaciers cover a total area of 9.6 km^2 originating from twelve cirques with cirque floor elevations between 3,257 and 3,567 m a.s.l. One of the most striking features within this zone is the large bowl-like depression eroded down to bedrock with lakes filling the depression and bedrock joints (**Figure 11** subset 1; **Supplementary Figure 12**). The significant erosion down to the bedrock, along with headward erosion of the cirque provides further evidence these glaciers had a high mass turnover during the LLGM.

Glaciers located on the western side of the NG zone have multiple moraines downvalley. These reach elevations as low as ~3,100–3,200 m a.s.l. while each have multiple lakes either occupying a cirque depression or a depression behind a moraine dam further down valley (e.g., Laguna de San Pablo). This is in stark contrast to the eastern glaciers that have either no lake, or relatively small bodies of water. Glaciers in the northwest (Palo Blanco 1, 2 and 3) have reconstructed lengths of 4.79, 2.43, 2.00 km, respectively, with the longest seen in **Figure 11** subset 2 (**Supplementary Figure 13**), the longest of any glaciers within the study area, but extend down to similar elevations to that of the Arrebiatadas and La Cruz glaciers. This could be due to the topography having a shallower incline (~−11.4%) compared to those to the immediate west of the Shimbe valley (~−18.5%), thereby allowing ice to flow further down valley while remaining at an elevation high enough to minimise mass loss.

Reconstructed glaciers located on the east side of the NG were generally limited to, or extended just beyond, their glacial cirques. The Aranza 4 glacier (**Figure 11B** subset 3; **Supplementary Figure 14**) is the only glacier to have evidence of any extensive advance, connecting with several cirque glaciers downvalley. Geomorphic evidence downvalley shows five lateral moraines towards it's downvalley bend. These moraines are found at a range of elevations between 3,250 and 3,180 m, respectively. These could indicate a thinning glacier front during deglaciation from the LLGM. Glacier ice in the valley just above these lateral moraines (to its north) could have flowed down and connected with the main valley glacier during the LLGM (we have mapped this here), but it may have been limited to or just to the

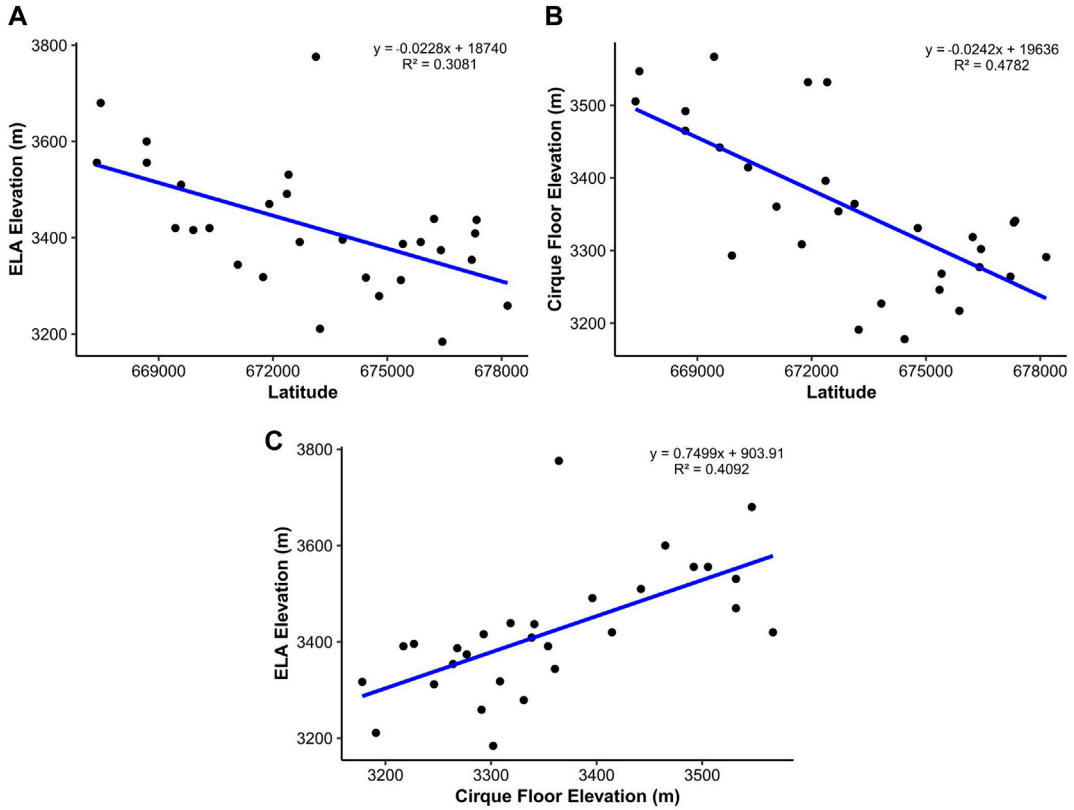

FIGURE 12 | Elevations for **(A)** reconstructed glacier ELAs and **(B)** cirque floors against their locations latitudinally, and **(C)** the ELA elevation and cirque floor elevation plotted against each other.

edge of the main valley glacier contributing little ice to the general flow of the main glacier.

4.2 ELA Reconstructions and Their Spatial Distribution

The reconstructed ELAs were derived from the reconstructed glacial ice extents using the AABR technique with a balance ratio of 1.75 ± 0.71 (Rea, 2009), ranged from 3,184 ± 27 m to 3,776 ± 33 m with a mean of 3,422 ± 30 m (**Table 3**). The reconstructed ELAs of glaciers without a confident determination of their terminal extent (e.g., Shimbe and Huancabamba 4 glaciers), may be lower or higher in elevation than that reported here. As expected, using higher and lower balance ratios give lower and higher ELAs, respectively. Rea (2009) and Quesada-Román et al. (2020) suggest a higher balance ratio may be more accurate for conditions within the tropical Andes. As shown by the comparison of lower and higher balance ratios, in this case, the balance ratios have little effect on the reconstructed ELA elevations with variations of up to only ~20 m. This minimal difference does not affect temperature estimations significantly (~± 0.2°C). We therefore recommend that similar studies should have confidence in using the global scenario (balance ratio of 1.75) for locations which do not have detailed studies on their accumulation-ablation balance ratios determined for ELA reconstructions. Although the global balance ratio produces little variance in results, the largest variance stems from accurate delineation of the past glacial extent. If ice limits are not accurate, they could have significant influence on local and regional climate interpretations.

Within our ELA reconstruction estimates there is an east-to-west gradient in the spatial distribution within Las Huaringas (**Figure 12A**). On average, the ELAs from glaciers situated on the eastern side of the study region had a lower reconstructed ELA while glaciers to the west had a higher ELA. This may suggest that the glaciers on the east side of Las Huaringas received more precipitation than those on the west side during the LLGM, resulting in a lower ELA. Similar east-to-west gradients have been identified by Porter (2001) and Martini et al. (2017) in their ELA reconstruction studies across the tropical Andes and Cordillera Oriental. This gradient is similar to the present day subtropical climate patterns and the movement of moisture via the easterly trade winds and trans-Andean flow, from the Amazon basin to the eastern flanks of the Andean mountains (Espinoza et al., 2020). This brings an asymmetric precipitation pattern with increased rates in the east compared to the west (Kumar et al., 2019). A similar east-to-west gradient is seen for cirque floor elevations (**Figure 12B**). When compared with ELA elevations (**Figure 12C**) it could suggest that ELAs were lower in the east because the overall elevation is situated lower, but this could

simply be because of increased maximum erosion at or below the ELA due to increased accumulation compared to the west, therefore lowering cirque floor elevations.

4.3 Palaeotemperature Estimate and its Comparison to Surrounding Studies

The reconstructed LLGM ELAs for the Las Huaringas region were used to estimate palaeotemperature. It is simplistic to assume that temperature alone would have changed since the LGM to present, as precipitation would also have changed in response to temperature changes and atmospheric-circulatory system changes. Whilst we acknowledge the likely impact of precipitation changes on palaeo-glacier mass balance, being a key driver of tropical glaciations (Fyffe et al., 2021), a simple palaeotemperature reconstruction can aid in understanding the potential climate the glaciers would have been present under.

The mean ΔELA change across Las Huaringas, from LLGM to present is 1,178 ± 10 m. This represents an average ΔT of −7.6 ± 0.2°C using a ATLR of 6.5°C/km. Higher and lower ATLR predictably result in lower and higher average ΔT, with 6.5 and 8.9°C using ATLRs of 5.5 and 7.5°C/km, respectively.

Our lowest estimate of temperature cooling (i.e., 8.9°C) is consistent with other palaeo-ELA temperature reconstructions within the tropical Andes (see **Supplementary Table 2**) (Rodbell, 1992; Mark et al., 2005; Mark and Helmens, 2005; Ramage et al., 2005; Smith et al., 2005; Bromley et al., 2011a; Úbeda et al., 2018). Temperature cooling estimates from valley glaciation locations that are considerably lower than those reported by our study, with Ramage et al. (2005) reporting a cooling of 2.5°C in Lake Junin, and Smith et al. (2005) estimating a cooling between 2°C and 4°C for the Lake Junin and Milluni and Zongo valleys. This difference in results may be due to the higher elevation of those study areas, with the maximum elevation in Lake Junin and the Milluni and Zongo valleys being ~4,600 m a.s.l. and ~5,600 m a.s.l., respectively. This would require less cooling to initiate glaciation compared to lower elevation locations, such as ours. Thus, greater cooling would be needed, if it is assumed only temperature changed, for extensive glaciation within Las Huaringas, due to the massif being below 4,000 m in elevation. However, if precipitation and temperature changed in tandem, then a smaller temperature change may be required (e.g., if the rate of precipitation was higher during the LLGM).

There are very few studies that produce LLGM temperature estimates from low elevation locations, especially in or near our study area. This makes comparisons difficult, as study sites that are distant from Las Huaringas are likely to be affected by different climate influences. Our higher temperature cooling estimate is closer to estimates from the Merida Andes with a lowest estimated cooling of 6.4°C (Stansell et al., 2007), the High Plain of Bogotá with a cooling of 7.6°C (Mark and Helmens, 2005), and modelled temperature changes across the Bolivian and Peruvian Andes from the Junín Valley, Cordillera Vilcanota and Laguna Kollpa Kkota, where a cooling of 5–9°C has been reported (Klein et al., 1999). The two former studies, though higher in latitude (i.e., Venezuela and Colombia), did reconstruct similar temperature cooling from locations with a similar elevation (4,500 m a.s.l.) to Las Huaringas. Klein et al. (1999) estimates are from across the Bolivian and Peruvian Andes, but are from higher elevation locations above 5,000 m. Though this is significantly higher in elevation than our area, the temperature cooling estimates are similar. Estimates from other methods are also consistent with our results of a substantial cooling during the LLGM. Analysis of ice-cores from the Huascarán and Samaja ice-caps (Thompson et al., 1995; Thompson et al., 1998; Thompson et al., 2006), suggests potential cooling of between 5 and 8°C at the LLGM. Our two higher estimates from the ALTR (5.5 and 6.5°C/km) fall within their temperature range.

4.4 Uncertainties

The reconstructions presented here are based on their most extensively mapped moraine, which are assumed to be the LLGM extent of the reconstructed ice mass. However, these moraines could be later or earlier in age and that could affect the climate reconstruction derived from this study. The reconstructed glaciers have also been assumed to have advanced synchronously across the region. Whilst this would not impact maximum extent calculations (i.e., area and ELAs), without any dating of these features there are implications for LLGM timing and glacial-climate interactions. Because we are unable to attribute the advances and climate cooling to any specific time period or event we do not infer any regional or hemispheric scale palaeoclimatic significance from our analysis. We also inferred the glacier terminus position where no palaeoglacial evidence existed due to inferred postglacial processes, thus there will likely be uncertainties in glacier extent and ELA reconstructions. Without detailed fieldwork these uncertainties cannot be addressed.

Other uncertainties arise from the datasets used. Although the newly generated 2.5 m resolution DEM is the highest resolution DEM of the area available, clouds precluded mapping of certain areas of the region, whilst the general image quality limited its use for mapping small-scale geomorphic landforms or performing more detailed analysis. The collection of a cloud-free set of SPOT-7 images would allow more areas to be studied, whilst the generation of higher resolution DEMs (<10 m) or the collection of LiDAR data would allow finer resolutions DEMs (<1 m) with better data quality. If these data were generated, or openly released, for the tropical Andes, it would allow more detailed geomorphic mapping of hard to access locations and allow more efficient field sampling campaigns (e.g., for dating purposes).

Lastly, the geomorphic mapping shown within this study is not constrained by any substantive field ground truthing which is typically standard in geomorphological studies (Chandler et al., 2018). Due to this, we cannot extract finer details in the geomorphic record, nor make any major inferences in the connectivity of the features to one another. Instead, our approach has been to report our "discovery" of the palaeoglaciation of Las Huaringas, to define the macro-scale geomorphology, reconstruct the maximum extent and glacial dynamics of the study area and to showcase the substantial potential of the study area for further investigation.

4.5 Future Work

This study demonstrates that there is an abundance of geomorphic evidence for former glaciation within the Las Huaringas region. This confirms that the area was glaciated, which we hypothesise to have occurred at and since the LLGM (Clapperton, 1993). While this work does not quantitatively confirm the timing of glaciations, dating of glacial landforms would enable a more complete understanding of the timing and nature of the glaciation. Multiple moraines point to several periods of glacial advances, potentially Younger Dryas or later, with multiple moraine crests up-valley from the most extensive moraines identified and mapped here. Each of these systems could be specifically targeted for terrestrial cosmogenic nuclide dating, which would reveal the timing of glaciation. Lakes and peat-filled depressions exist within the limits of the glacial extent we reconstruct here, and these could be cored and dated to determine minimum and maximum limiting carbon dates of when they were uncovered (Lowe and Walker, 2014). This would fill a significant gap spatially between studies that date glacial advances in mid-Peru (Stansell et al., 2013), and those in more southerly Ecuador (Clapperton, 1990; Heine and Heine, 1996). It would also provide an understanding of glaciation in low elevation locations, which have not previously been studied, and independent assessment of any cosmogenic dating.

Limited numerical modelling has been conducted of tropical Andean valley glaciation, with the focus in South America primarily on the icefields of Patagonia (e.g., Hubbard et al., 2005; Collao-Barrios et al., 2018). Numerical modelling of the Las Huaringas valley system, and potentially other valley systems in the wider region, would enable a better understanding of the climatic requirements for glaciation in these low-elevation low-latitude locations. Detailed geomorphic mapping can be used to test and constrain any modelled ice extents. This is important within the Las Huaringas region as it is located in a transition zone between the inner and outer tropical climates, which are under different patterns of precipitation which enable glacial formation and development (Kaser, 2001). A potential understanding of the climate that permitted ice mass development, particularly during the LGM, can aid in furthering our overall comprehension of the LGM climate in the northern tropical Andes.

Clapperton (1993) inferred several areas that may have incurred LGM glaciation within the northern tropical Andes and beyond. Many of these have never been tested with detailed investigations such as those demonstrated by this study. There are still several locations (e.g., in southern Ecuador) that have yet to receive any study which confirms or refutes Clapperton's inferred glaciation extent. With advancements in remote sensing technology, including access to high-resolution satellite imagery and the generation of high resolution DEMs (<30 m) being easily generated, or becoming more freely available, these locations can now be explored with relative ease. This would enable a better understanding of glacial dynamics within the tropical Andes, along with glacial-climatic interactions (e.g., testing hypotheses of east-west ELA and precipitation gradients). Further, with this plethora of high-resolution data, previously studied areas in Ecuador (e.g., Hastenrath, 1981) should warrant an updated investigation using new techniques and datasets to confirm their existence and the timing and glaciology of their glaciation.

5 CONCLUSION

The detailed mapping and glacial reconstruction presented here provides the first evidence for glaciation within the Las Huaringas region of northern Peru. It shows that extensive highly-erosive warm-based ice masses were present, likely at the LLGM. The dominant type of glaciation is valley type, with valley glaciers extending from cirques, with some potentially interconnected glacial systems over cols. The present evidence is not consistent with ice cap glaciation. This work supports the hypothesis of Clapperton (1993) that glacial ice was likely present at relatively low elevation sites in northern Peru during the LGM.

The geomorphic mapping was used to reconstruct glacier extents and to calculate palaeo-ELA estimates. Palaeotemperatures of between 6.5°C and 8.8°C cooler than present were determined. These are within the upper limits of other valley palaeoglaciological reconstruction based palaeotemperature estimates. Evidence for an ELA asymmetry of east-to-west (lowest to east, highest in the west), is in agreement with the present-day flow of moisture and climate patterns, suggesting that the broader climate circulatory systems in the region may not have been very different at the LLGM.

The exact timing of this glaciation is unknown. The absence of dated moraines means that best estimates for the age of glaciation are determined by assuming an LLGM-age for the most extensive sets of mapped moraines. Within Las Huaringas, moraines behind the most extensive extents mapped are hypothesized to be younger than the LLGM and are likely late-glacial or early-Holocene in nature. Testing of these hypotheses would require further investigation using terrestrial cosmogenic nuclide dating, analysis and dating of sediment and peat cores, in conjunction with field and remote mapping.

The evidence found within the Las Huaringas region strongly suggests that other relatively low elevation areas of northern Peru, and the surrounding areas of the tropical Andes, were potentially glaciated during the LGM and warrant further investigation.

DATA AVAILABILITY STATEMENT

The datasets presented in this study can be found in online repositories. The names of the repository/repositories and accession number(s) can be found in the article/ **Supplementary Material**.

AUTHOR CONTRIBUTIONS

EL designed the study and led the work; NR, AH, AR, SJ and DF provided guidance on the conceptualisation, research analysis and content, manuscript structure and suggested figures. AH, AR and NR conducted field reconnaissance of the study area prior to this research. EL conducted the data collection and analysis, led the writing of the manuscript and creation of the figures. NR, AH, AR, SJ and DF contributed to the interpretation and discussion of the results and aided in reviewing and editing the manuscript.

FUNDING

This study was supported and funded by the IAPETUS2, Natural Environment Research Council (NERC) Doctoral Training Partnership (DTP) grant NE/S007431/1, a NERC Urgency Grant (NE/R004528/1 to ACGH and NR) and a Royal Society Research Grant (RG120575 to ACGH). The Pléiades high resolution imagery and SPOT 7 tri-stereo satellite imagery were provided by CNES and Airbus DS, respectively, through ESA's "data available for research and application development" project ID: 59560.

ACKNOWLEDGMENTS

The Pléiades imagery (© CNES 2020) and SPOT 7 (© Airbus DS 2020), stereo satellite images were provided through ESA by CNES and Airbus DS. Landsat and Sentinel-2 satellite images were provided by USGS and ESA, respectively, and the ALOS DEM was provided by the JAXA. We would like to thank Rodolfo Rodriguez of the Universidad de Piura for the modern climate data and support with field logistics during the initial preliminary field work. We would also like to thank Rachel Carr and Stuart Dunning from Newcastle University, Arminel Lovell from the Carbon Disclosure Project (CDP), and Liam Taylor from the University of Leeds for aiding in the generation of the SPOT 7 DEM. All mapping of geomorphology was conducted in QGIS, while figure making was conducted in ArcMap 10.8.1.

SUPPLEMENTARY MATERIAL

The Supplementary Material for this article can be found online at: https://www.frontiersin.org/articles/10.3389/feart.2022.838826/full#supplementary-material

REFERENCES

Álvarez-Villa, O. D., Vélez, J. I., and Poveda, G. (2011). Improved Long-Term Mean Annual Rainfall fields for Colombia. *Int. J. Climatol.* 31 (14), 2194–2212. doi:10.1002/joc.2232

Angel, I., Guzman, O., and Carcaillet, J. (2017). Pleistocene Glaciations in the Northern Tropical Andes, South America (Venezuela, Colombia and Ecuador). *Cuadernos de Investigacion Geografica* 43 (2), 571. doi:10.18172/cig.3202

Angel, I. (2016). *Late Pleistocene Deglaciation Histories in the central Mérida Andes (Venezuela)*. Ph. D. Grenoble, France: Université de Grenoble Alpes-Universidad Central de Venezuela.

Baker, P. A., Rigsby, C. A., Seltzer, G. O., Fritz, S. C., Lowenstein, T. K., Bacher, N. P., et al. (2001). Tropical Climate Changes at Millennial and Orbital Timescales on the Bolivian Altiplano. *Nature* 409 (6821), 698–701. doi:10.1038/35055524

Bendle, J. M., and Glasser, N. F. (2012). Palaeoclimatic Reconstruction from Lateglacial (Younger Dryas Chronozone) Cirque Glaciers in Snowdonia, North Wales. *Proc. Geologists' Assoc.* 123 (1), 130–145. doi:10.1016/j.pgeola.2011.09.006

Benn, D. I., Owen, L. A., Osmaston, H. A., Seltzer, G. O., Porter, S. C., and Mark, B. (2005). Reconstruction of Equilibrium-Line Altitudes for Tropical and Sub-tropical Glaciers. *Quat. Int.* 138-139, 8–21. doi:10.1016/j.quaint.2005.02.003

Blard, P.-H., Lave, J., Farley, K. A., Ramirez, V., Jimenez, N., Martin, L. C. P., et al. (2014). Progressive Glacial Retreat in the Southern Altiplano (Uturuncu Volcano, 22°S) between 65 and 14 Ka Constrained by Cosmogenic 3He Dating. *Quat. Res.* 82 (1), 209–221. doi:10.1016/j.yqres.2014.02.002

Bromley, G. R. M., Hall, B. L., Rademaker, K. M., Todd, C. E., and Racovteanu, A. E. (2011a). Late Pleistocene Snowline Fluctuations at Nevado Coropuna (15°S), Southern Peruvian Andes. *J. Quat. Sci.* 26 (3), 305–317. doi:10.1002/jqs.1455

Bromley, G. R. M., Hall, B. L., Schaefer, J. M., Winckler, G., Todd, C. E., and Rademaker, K. M. (2011b). Glacier Fluctuations in the Southern Peruvian Andes during the Late-Glacial Period, Constrained with Cosmogenic 3 He. *J. Quat. Sci.* 26 (1), 37–43. doi:10.1002/jqs.1424

Bromley, G. R. M., Schaefer, J. M., Hall, B. L., Rademaker, K. M., Putnam, A. E., Todd, C. E., et al. (2016). A Cosmogenic 10Be Chronology for the Local Last Glacial Maximum and Termination in the Cordillera Oriental, Southern Peruvian Andes: Implications for the Tropical Role in Global Climate. *Quat. Sci. Rev.* 148, 54–67. doi:10.1016/J.QUASCIREV.2016.07.010

Bromley, G. R. M., Schaefer, J. M., Winckler, G., Hall, B. L., Todd, C. E., and Rademaker, K. M. (2009). Relative Timing of Last Glacial Maximum and Late-Glacial Events in the central Tropical Andes. *Quat. Sci. Rev.* 28 (23), 2514–2526. doi:10.1016/j.quascirev.2009.05.012

Carcaillet, J., Angel, I., Carrillo, E., Audemard, F. A., and Beck, C. (2013). Timing of the Last Deglaciation in the Sierra Nevada of the Mérida Andes, Venezuela. *Quat. Res.* 80 (3), 482–494. doi:10.1016/j.yqres.2013.08.001

Chandler, B. M. P., Lovell, H., Boston, C. M., Lukas, S., Barr, I. D., Benediktsson, Í. Ö., et al. (2018). Glacial Geomorphological Mapping: A Review of Approaches and Frameworks for Best Practice. *Earth-Science Rev.* 185, 806–846. doi:10.1016/j.earscirev.2018.07.015

Chepstow-Lusty, A., Bush, M. B., Frogley, M. R., Baker, P. A., Fritz, S. C., and Aronson, J. (2005). Vegetation and Climate Change on the Bolivian Altiplano between 108,000 and 18,000 Yr Ago. *Quat. Res.* 63 (1), 90–98. doi:10.1016/j.yqres.2004.09.008

Chevalier, M., Davis, B. A. S., Heiri, O., Seppä, H., Chase, B. M., Gajewski, K., et al. (2020). Pollen-based Climate Reconstruction Techniques for Late Quaternary Studies. *Earth-Science Rev.* 210, 103384. doi:10.1016/j.earscirev.2020.103384

Clapperton, C. M., Clayton, J. D., Benn, D. I., Marden, C. J., and Argollo, J. (1997a). Late Quaternary Glacier Advances and Palaeolake Highstands in the Bolivian Altiplano. *Quat. Int.* 38-39, 49–59. doi:10.1016/s1040-6182(96)00020-1

Clapperton, C. M., Hall, M., Mothes, P., Hole, M. J., Still, J. W., Helmens, K. F., et al. (1997b). A Younger Dryas Icecap in the Equatorial Andes. *Quat. Res.* 47 (1), 13–28. doi:10.1006/QRES.1996.1861

Clapperton, C. M. (1990). Glacial and Volcanic Geomorphology of the Chimborazo-Carihuairazo Massif, Ecuadorian Andes. *Trans. R. Soc. Edinb. Earth Sci.* 81 (2), 91–116. doi:10.1017/S0263593300005174

Clapperton, C. M. (1993). "Late Cenozic Glacial History of the Andes Part III: The Last Glacial Maximum (Isotope Stage 2)," in *Quaternary Geology and Geomorphology of South America* (Oxford, UK: Elsevier), 395–424.

CLIMAP (1976). The Surface of the Ice-Age Earth. *Science* 191 (4232), 1131–1137. doi:10.1126/science.191.4232.1131

Collao-Barrios, G., Gillet-Chaulet, F., Favier, V., Casassa, G., Berthier, E., Dussaillant, I., et al. (2018). Ice Flow Modelling to Constrain the Surface Mass Balance and Ice Discharge of San Rafael Glacier, Northern Patagonia Icefield. *J. Glaciol.* 64 (246), 568–582. doi:10.1017/jog.2018.46

Cook, S. J., and Swift, D. A. (2012). Subglacial Basins: Their Origin and Importance in Glacial Systems and Landscapes. *Earth-Science Rev.* 115 (4), 332–372. doi:10.1016/j.earscirev.2012.09.009

Dirszowsky, R. W., Mahaney, W. C., Hodder, K. R., Milner, M. W., Kalm, V., Bezada, M., et al. (2005). Lithostratigraphy of the Mérida (Wisconsinan) Glaciation and Pedregal Interstade, Mérida Andes, Northwestern Venezuela. *J. South Am. Earth Sci.* 19 (4), 525–536. doi:10.1016/j.jsames.2005.07.001

Emmer, A., Le Roy, M., Sattar, A., Veettil, B. K., Alcalá-Reygosa, J., Campos, N., et al. (2021). Glacier Retreat and Associated Processes since the Last Glacial Maximum in the Lejiamayu valley, Peruvian Andes. *J. South Am. Earth Sci.* 109, 103254. doi:10.1016/j.jsames.2021.103254

Espinoza, J. C., Garreaud, R., Poveda, G., Arias, P. A., Molina-Carpio, J., Masiokas, M., et al. (2020). Hydroclimate of the Andes Part I: Main Climatic Features. *Front. Earth Sci.* 8, 64. doi:10.3389/feart.2020.00064

Evans, D. (2003). *Glacial Landsystems*. London: Routledge.

Evans, I. S. (2021). Glaciers, Rock Avalanches and the 'buzzsaw' in Cirque Development: Why Mountain Cirques Are of Mainly Glacial Origin. *Earth Surf. Process. Landforms* 46 (1), 24–46. doi:10.1002/esp.4810

Farber, D. L., Hancock, G. S., Finkel, R. C., and Rodbell, D. T. (2005). The Age and Extent of Tropical alpine Glaciation in the Cordillera Blanca, Peru. *J. Quat. Sci.* 20 (7-8), 759–776. doi:10.1002/jqs.994

Fyffe, C. L., Potter, E., Fugger, S., Orr, A., Fatichi, S., Loarte, E., et al. (2021). The Energy and Mass Balance of Peruvian Glaciers. *JGR Atmospheres* 126 (23), e2021JD034911. doi:10.1029/2021JD034911

Garreaud, R. D. (2009). The Andes Climate and Weather. *Adv. Geosci.* 22, 3–11. doi:10.5194/adgeo-22-3-2009

Glasser, N. F., Clemmens, S., Schnabel, C., Fenton, C. R., and McHargue, L. (2009). Tropical Glacier Fluctuations in the Cordillera Blanca, Peru between 12.5 and 7.6ka from Cosmogenic 10Be Dating. *Quat. Sci. Rev.* 28 (27), 3448–3458. doi:10.1016/j.quascirev.2009.10.006

Glasser, N. F., Jansson, K. N., Harrison, S., and Kleman, J. (2008). The Glacial Geomorphology and Pleistocene History of South America between 38°S and 56°S. *Quat. Sci. Rev.* 27 (3-4), 365–390. doi:10.1016/j.quascirev.2007.11.011

Gómez, J., Schobbenhaus, C., and Montes, N. E. (2019). *Geological Map of South America 2019, Scale 1:5,000,000*. Paris: (Commission for the Geological Map of the World (CGMW), Colombian Geological Survey, and Geological Survey of Brazil). https://doi.org/10.32685/10.143.2019.929

Goodman, A. Y., Rodbell, D. T., Seltzer, G. O., and Mark, B. G. (2001). Subdivision of Glacial Deposits in Southeastern Peru Based on Pedogenic Development and Radiometric Ages. *Quat. Res.* 56 (1), 31–50. doi:10.1006/qres.2001.2221

Guo, Q., Li, W., Yu, H., and Alvarez, O. (2010). Effects of Topographic Variability and Lidar Sampling Density on Several DEM Interpolation Methods. *Photogramm Eng. Remote Sensing* 76, 701–712. doi:10.14358/PERS.76.6.701

Häggi, C., Chiessi, C. M., Merkel, U., Mulitza, S., Prange, M., Schulz, M., et al. (2017). Response of the Amazon Rainforest to Late Pleistocene Climate Variability. *Earth Planet. Sci. Lett.* 479, 50–59. doi:10.1016/j.epsl.2017.09.013

Hammond, J. C., Saavedra, F. A., and Kampf, S. K. (2018). Global Snow Zone Maps and Trends in Snow Persistence 2001-2016. *Int. J. Climatol* 38 (12), 4369–4383. doi:10.1002/joc.5674

Hastenrath, S. (1981). *The Glaciation of the Ecuadorian Andes*. Rotterdam: Balkema Publishers.

Hastenrath, S. (2009). Past Glaciation in the Tropics. *Quat. Sci. Rev.* 28, 790–798. doi:10.1016/j.quascirev.2008.12.004

Heine, K., and Heine, J. T. (1996). Late Glacial Climatic Fluctuations in Ecuador: Glacier Retreat during Younger Dryas Time. *Arctic Alpine Res.* 28 (4), 496–501. doi:10.2307/1551860

Helmens, K. F. (2004). "The Quaternary Glacial Record of the Colombian Andes," in *Developments in Quaternary Sciences*. Editors J. Ehlers and P. L. Gibbard (Elsevier), 115–134. doi:10.1016/s1571-0866(04)80117-9

Hubbard, A., Hein, A. S., Kaplan, M. R., Hulton, N. R. j., and Glasser, N. (2005). A Modelling Reconstruction of the Last Glacial Maximum Ice Sheet and its Deglaciation in the Vicinity of the Northern Patagonian Icefield, South America. *Geografiska Annaler: Ser. A, Phys. Geogr.* 87 (2), 375–391. doi:10.1111/j.0435-3676.2005.00264.x

Jomelli, V., Grancher, D., Brunstein, D., and Solomina, O. (2008). Recalibration of the Yellow Rhizocarpon Growth Curve in the Cordillera Blanca (Peru) and Implications for LIA Chronology. *Geomorphology* 93 (3-4), 201–212. doi:10.1016/j.geomorph.2007.02.021

Kaser, G. (2001). Glacier-climate Interaction at Low Latitudes. *J. Glaciol.* 47 (157), 195–204. doi:10.3189/172756501781832296

Kiefer, J., and Karamperidou, C. (2019). High-Resolution Modeling of ENSO-Induced Precipitation in the Tropical Andes: Implications for Proxy Interpretation. *Paleoceanography and Paleoclimatology* 34 (2), 217–236. doi:10.1029/2018pa003423

Klein, A. G., Seltzer, G. O., and Isacks, B. L. (1999). Modern and Last Local Glacial Maximum Snowlines in the Central Andes of Peru, Bolivia, and Northern Chile. *Quat. Sci. Rev.* 18 (1), 63–84. doi:10.1016/S0277-3791(98)00095-X

Kumar, S., Vidal, Y.-S., Moya-Álvarez, A. S., and Martínez-Castro, D. (2019). Effect of the Surface Wind Flow and Topography on Precipitating Cloud Systems over the Andes and Associated Amazon basin: GPM Observations. *Atmos. Res.* 225, 193–208. doi:10.1016/j.atmosres.2019.03.027

Lea, D. W., Pak, D. K., Peterson, L. C., and Hughen, K. A. (2003). Synchroneity of Tropical and High-Latitude Atlantic Temperatures over the Last Glacial Termination. *Science* 301 (5638), 1361–1364. doi:10.1126/science.1088470

Lea, D. W., Pak, D. K., and Spero, H. J. (2000). Climate Impact of Late Quaternary Equatorial Pacific Sea Surface Temperature Variations. *Science* 289 (5485), 1719–1724. doi:10.1126/science.289.5485.1719

Lee, E., Carrivick, J. L., Quincey, D. J., Cook, S. J., James, W. H. M., and Brown, L. E. (2021). Accelerated Mass Loss of Himalayan Glaciers since the Little Ice Age. *Sci. Rep.* 11 (1), 24284. doi:10.1038/s41598-021-03805-8

Lila, F. D. H. P., Joshua, T. M. G. V., Solorzano, A. C. C., and Mott, G. M. G. C. (2016). *Paisaje Cultural "Complejo de Lagunas las Huaringas*. Editor M. D. Cultura. First ed. (Peru: Ministro de Cultura).

Lowe, J. J., and Walker, M. (2014). *Reconstructing Quaternary Environments*. New York, USA: Routledge.

MacGregor, K. R., Anderson, R. S., Anderson, S. P., and Waddington, E. D. (2000). Numerical Simulations of Glacial-valley Longitudinal Profile Evolution. *Geology* 28 (11), 1031–1034. doi:10.1130/0091-7613(2000)028<1031:nsogvl>2.3.co;2

Mahaney, W. C., Kalm, V., Menzies, J., Hancock, R. G. V., and Milner, M. W. (2010). Reconstruction of the Pre-merida Glaciation, Northwestern Venezuelan Andes. *Sediment. Geology*. 230 (1), 10–20. doi:10.1016/j.sedgeo.2010.06.016

Małecki, J., Lovell, H., Ewertowski, W., Górski, Ł., Kurczaba, T., Latos, B., et al. (2018). The Glacial Landsystem of a Tropical Glacier: Charquini Sur, Bolivian Andes. *Earth Surf. Process. Landforms* 43 (12), 2584–2602. doi:10.1002/esp.4417

Mark, B. G., Harrison, S. P., Spessa, A., New, M., Evans, D. J. A., and Helmens, K. F. (2005). Tropical Snowline Changes at the Last Glacial Maximum: A Global Assessment. *Quat. Int.* 138-139, 168–201. doi:10.1016/j.quaint.2005.02.012

Mark, B. G., and Helmens, K. F. (2005). Reconstruction of Glacier Equilibrium-Line Altitudes for the Last Glacial Maximum on the High Plain of Bogotá, Eastern Cordillera, Colombia: Climatic and Topographic Implications. *J. Quat. Sci.* 20 (7-8), 789–800. doi:10.1002/jqs.974

Mark, B. G., Rodbell, D. T., Seltzer, G. O., Goodman, A. Y., Castiglia, P. J., Moy, C. M., et al. (1999). "Late-Glacial Fluctuations of Ice Volume Inferred from Lakesediment Mineralogy and Terrain Modeling in the Cordillera Blanca, Peru," in Spring AGU Conference. Boston, MA.

Mark, B., Stansell, N., and Zeballos, G. (2017). The Last Deglaciation of Peru and Bolivia. *Cig* 43 (2), 591–628. doi:10.18172/cig.3265

Martin, L. C. P., Blard, P.-H., Lavé, J., Jomelli, V., Charreau, J., Condom, T., et al. (2020). Antarctic-like Temperature Variations in the Tropical Andes Recorded by Glaciers and Lakes during the Last Deglaciation. *Quat. Sci. Rev.* 247, 106542. doi:10.1016/j.quascirev.2020.106542

Martini, M. A., Kaplan, M. R., Strelin, J. A., Astini, R. A., Schaefer, J. M., Caffee, M. W., et al. (2017). Late Pleistocene Glacial Fluctuations in Cordillera Oriental, Subtropical Andes. *Quat. Sci. Rev.* 171, 245–259. doi:10.1016/j.quascirev.2017.06.033

Mourguiart, P., and Ledru, M.-P. (2003). Last Glacial Maximum in an Andean Cloud forest Environment (Eastern Cordillera, Bolivia). *Geol* 31 (3), 195–198. doi:10.1130/0091-7613(2003)031<0195:lgmiaa>2.0.co;2

Ng, F. S. L., Barr, I. D., and Clark, C. D. (2010). Using the Surface Profiles of Modern Ice Masses to Inform Palaeo-Glacier Reconstructions. *Quat. Sci. Rev.* 29 (23), 3240–3255. doi:10.1016/j.quascirev.2010.06.045

Novello, V. F., Cruz, F. W., McGlue, M. M., Wong, C. I., Ward, B. M., Vuille, M., et al. (2019). Vegetation and Environmental Changes in Tropical South America from the Last Glacial to the Holocene Documented by Multiple Cave Sediment Proxies. *Earth Planet. Sci. Lett.* 524, 115717. doi:10.1016/j.epsl.2019.115717

Nunnery, J. A., Fritz, S. C., Baker, P. A., and Salenbien, W. (2019). Lake-level variability in Salar de Coipasa, Bolivia during the past ~40,000 yr. *Quat. Res.* 91 (2), 881–891. doi:10.1017/qua.2018.108

Palacios, D., Stokes, C. R., Phillips, F. M., Clague, J. J., Alcalá-Reygosa, J., Andrés, N., et al. (2020). The Deglaciation of the Americas during the Last Glacial Termination. *Earth-Science Rev.* 203, 103113. doi:10.1016/j.earscirev.2020.103113

Pearce, D. M., Ely, J. C., Barr, I. D., and Boston, C. M. (2017). "3.2.9 Glacier Reconstruction," in *Geomorphological Techniques*. Editors S. J. Cook, L. E. Clarke, and J. M. Nield (London, UK: British Society for Geomorphology).

Pearce, D., Rea, B. R., Bradwell, T., and McDougall, D. (2014). Glacial Geomorphology of the Tweedsmuir Hills, Central Southern Uplands, Scotland. *J. Maps* 10 (3), 457–465. doi:10.1080/17445647.2014.886492

Pellitero, R., Rea, B. R., Spagnolo, M., Bakke, J., Hughes, P., Ivy-Ochs, S., et al. (2015). A GIS Tool for Automatic Calculation of Glacier Equilibrium-Line Altitudes. *Comput. Geosciences* 82, 55–62. doi:10.1016/j.cageo.2015.05.005

Placzek, C. J., Quade, J., and Patchett, P. J. (2013). A 130ka Reconstruction of Rainfall on the Bolivian Altiplano. *Earth Planet. Sci. Lett.* 363, 97–108. doi:10.1016/j.epsl.2012.12.017

Porter, S. C. (2001). Snowline Depression in the Tropics during the Last Glaciation. *Quat. Sci. Rev.* 20 (10), 1067–1091. doi:10.1016/S0277-3791(00)00178-5

Quesada-Román, A., Campos, N., Alcalá-Reygosa, J., and Granados-Bolaños, S. (2020). Equilibrium-line Altitude and Temperature Reconstructions during the Last Glacial Maximum in Chirripó National Park, Costa Rica. *J. South Am. Earth Sci.* 100, 102576. doi:10.1016/j.jsames.2020.102576

Ramage, J. M., Smith, J. A., Rodbell, D. T., and Seltzer, G. O. (2005). Comparing Reconstructed Pleistocene Equilibrium-Line Altitudes in the Tropical Andes of central Peru. *J. Quat. Sci.* 20 (7-8), 777–788. doi:10.1002/jqs.982

Ramírez, E., Francou, B., Ribstein, P., Descloitres, M., Guérin, R., Mendoza, J., et al. (2001). Small Glaciers Disappearing in the Tropical Andes: a Case-Study in Bolivia: Glaciar Chacaltaya (16o S). *J. Glaciol.* 47 (157), 187–194. doi:10.3189/172756501781832214

Rea, B. R. (2009). Defining Modern Day Area-Altitude Balance Ratios (AABRs) and Their Use in Glacier-Climate Reconstructions. *Quat. Sci. Rev.* 28 (3), 237–248. doi:10.1016/j.quascirev.2008.10.011

Rodbell, D. T., Bagnato, S., Nebolini, J. C., Seltzer, G. O., and Abbott, M. B. (2002). A Late Glacial-Holocene Tephrochronology for Glacial Lakes in Southern Ecuador. *Quat. Res.* 57 (3), 343–354. doi:10.1006/QRES.2002.2324

Rodbell, D. T. (1992). Late Pleistocene Equilibrium-Line Reconstructions in the Northern Peruvian Andes. *Boreas* 21 (1), 43–52. doi:10.1111/j.1502-3885.1992.tb00012.x

Rodbell, D. T. (1993). The Timing of the Last Deglaciation in Cordillera Oriental, Northern Peru, Based on Glacial Geology and lake Sedimentology. *Geol. Soc. America Bull.* 105 (7), 923–934. doi:10.1130/0016-7606(1993)105<0923:ttotld>2.3.co;2

Santos-González, J., Redondo-Vega, J. M., González-Gutiérrez, R. B., and Gómez-Villar, A. (2013). Applying the AABR Method to Reconstruct Equilibrium-Line Altitudes from the Last Glacial Maximum in the Cantabrian Mountains (SW Europe). *Palaeogeogr. Palaeoclimatol. Palaeoecol.* 387, 185–199. doi:10.1016/j.palaeo.2013.07.025

Shakun, J. D., Clark, P. U., Marcott, S. A., Brook, E. J., Lifton, N. A., Caffee, M., et al. (2015). Cosmogenic Dating of Late Pleistocene Glaciation, Southern Tropical Andes, Peru. *J. Quat. Sci.* 30 (8), 841–847. doi:10.1002/jqs.2822

Sissons, J. B. (1974). A Late-Glacial Ice Cap in the Central Grampians, Scotland. *Trans. Inst. Br. Geogr.* (62), 95–114. doi:10.2307/621517

Smith, C. A., Lowell, T. V., Owen, L. A., and Caffee, M. W. (2011). Late Quaternary Glacial Chronology on Nevado Illimani, Bolivia, and the Implications for Paleoclimatic Reconstructions across the Andes. *Quat. Res.* 75 (1), 1–10. doi:10.1016/j.yqres.2010.07.001

Smith, J. A., and Rodbell, D. T. (2010). Cross-cutting Moraines Reveal Evidence for North Atlantic Influence on Glaciers in the Tropical Andes. *J. Quat. Sci.* 25 (3), 243–248. doi:10.1002/jqs.1393

Smith, J. A., Seltzer, G. O., Farber, D. L., Rodbell, D. T., and Finkel, R. C. (2005). Early Local Last Glacial Maximum in the Tropical Andes. *Science* 308 (5722), 678–681. doi:10.1126/science.1107075

Staal, A., Tuinenburg, O. A., Bosmans, J. H. C., Holmgren, M., van Nes, E. H., Scheffer, M., et al. (2018). Forest-rainfall Cascades Buffer against Drought across the Amazon. *Nat. Clim Change* 8 (6), 539–543. doi:10.1038/s41558-018-0177-y

Stansell, N. D., Abbott, M. B., Rull, V., Rodbell, D. T., Bezada, M., and Montoya, E. (2010). Abrupt Younger Dryas Cooling in the Northern Tropics Recorded in lake Sediments from the Venezuelan Andes. *Earth Planet. Sci. Lett.* 293 (1), 154–163. doi:10.1016/j.epsl.2010.02.040

Stansell, N. D., Licciardi, J. M., Rodbell, D. T., and Mark, B. G. (2017). Tropical Ocean-atmospheric Forcing of Late Glacial and Holocene Glacier Fluctuations in the Cordillera Blanca, Peru. *Geophys. Res. Lett.* 44 (9), 4176–4185. doi:10.1002/2016gl072408

Stansell, N. D., Polissar, P. J., Abbott, M. B., Bezada, M., Steinman, B. A., and Braun, C. (2014). Proglacial lake Sediment Records Reveal Holocene Climate Changes in the Venezuelan Andes. *Quat. Sci. Rev.* 89, 44–55. doi:10.1016/j.quascirev.2014.01.021

Stansell, N. D., Polissar, P. J., and Abbott, M. B. (2007). Last glacial maximum equilibrium-line altitude and paleo-temperature reconstructions for the Cordillera de Mérida, Venezuelan Andes. *Quat. Res.* 67 (1), 115–127. doi:10.1016/j.yqres.2006.07.005

Stansell, N. D., Rodbell, D. T., Abbott, M. B., and Mark, B. G. (2013). Proglacial lake Sediment Records of Holocene Climate Change in the Western Cordillera of Peru. *Quat. Sci. Rev.* 70, 1–14. doi:10.1016/j.quascirev.2013.03.003

Sutherland, J. L., Carrivick, J. L., Evans, D. J. A., Shulmeister, J., and Quincey, D. J. (2019). The Tekapo Glacier, New Zealand, during the Last Glacial Maximum: An Active Temperate Glacier Influenced by Intermittent Surge Activity. *Geomorphology* 343, 183–210. doi:10.1016/j.geomorph.2019.07.008

Tadono, T., Ishida, H., Oda, F., Naito, S., Minakawa, K., and Iwamoto, H. (2014). "Precise Global DEM Generation by ALOS PRISM," in ISPRS Annals of the Photogrammetry, Remote Sensing and Spatial Information Sciences Volume II-4, 71–76. doi:10.5194/isprsannals-II-4-71-2014

Thompson, L. G., Davis, M. E., Mosley-Thompson, E., Porter, S. E., Corrales, G. V., Shuman, C. A., et al. (2021). The Impacts of Warming on Rapidly Retreating High-Altitude, Low-Latitude Glaciers and Ice Core-Derived Climate Records. *Glob. Planet. Change* 203, 103538. doi:10.1016/j.gloplacha.2021.103538

Thompson, L. G., Davis, M. E., Mosley-Thompson, E., Sowers, T. A., Henderson, K. A., Zagorodnov, V. S., et al. (1998). A 25,000-Year Tropical Climate History from Bolivian Ice Cores. *Science* 282 (5395), 1858–1864. doi:10.1126/science.282.5395.1858

Thompson, L. G., Mosley-Thompson, E., Brecher, H., Davis, M., León, B., Les, D., et al. (2006). Abrupt Tropical Climate Change: Past and Present. *Proc. Natl. Acad. Sci. U.S.A.* 103 (28), 10536–10543. doi:10.1073/pnas.0603900103

Thompson, L. G., Mosley-Thompson, E., Davis, M. E., Lin, P.-N., Henderson, K. A., Cole-Dai, J., et al. (1995). Late Glacial Stage and Holocene Tropical Ice Core Records from Huascarán, Peru. *Science* 269 (5220), 46–50. doi:10.1126/science.269.5220.46

Úbeda, J., Bonshoms, M., Iparraguirre, J., Sáez, L., De la Fuente, R., Janssen, L., et al. (2018). Prospecting Glacial Ages and Paleoclimatic Reconstructions Northeastward of Nevado Coropuna (16° S, 73° W, 6377 M), Arid Tropical Andes. *Geosciences* 8 (8), 307. doi:10.3390/geosciences8080307

van't Veer, R., Islebe, G. A., and Hooghiemstra, H. (2000). Climatic Change during the Younger Dryas Chron in Northern South America: a Test of the Evidence. *Quat. Sci. Rev.* 19 (17), 1821–1835. doi:10.1016/S0277-3791(00)00093-7

Vilímek, V., Klimeš, J., and Červená, L. (2016). Glacier-related Landforms and Glacial Lakes in Huascarán National Park, Peru. *J. Maps* 12 (1), 193–202. doi:10.1080/17445647.2014.1000985

Visser, K., Thunell, R., and Stott, L. (2003). Magnitude and Timing of Temperature Change in the Indo-Pacific Warm Pool during Deglaciation. *Nature* 421 (6919), 152–155. doi:10.1038/nature01297

Vizy, E. K., and Cook, K. H. (2007). Relationship between Amazon and High Andes Rainfall. *J. Geophys. Res.* 112 (D7), D07107. doi:10.1029/2006JD007980

Zech, R., Kull, C., Kubik, P. W., and Veit, H. (2007). LGM and Late Glacial Glacier Advances in the Cordillera Real and Cochabamba (Bolivia) Deduced from 10Be Surface Exposure Dating. *Clim. Past* 3 (4), 623–635. doi:10.5194/cp-3-623-2007

Conflict of Interest: The authors declare that the research was conducted in the absence of any commercial or financial relationships that could be construed as a potential conflict of interest.

Publisher's Note: All claims expressed in this article are solely those of the authors and do not necessarily represent those of their affiliated organizations, or those of the publisher, the editors and the reviewers. Any product that may be evaluated in this article, or claim that may be made by its manufacturer, is not guaranteed or endorsed by the publisher.

frontiers | Frontiers in Earth Science

ORIGINAL RESEARCH
published: 12 April 2022
doi: 10.3389/feart.2022.791487

Ice Dynamics and Morphological Changes During Proglacial Lake Development at Exploradores Glacier, Patagonia

Inigo Irarrazaval[1,2,3]*, *Alejandro Dussaillant*[3,4], *Sebastián Vivero*[1], *Pablo Iribarren-Anacona*[5] *and Gregoire Mariethoz*[1]

[1]Institute of Earth Surface Dynamics, Faculty of Geosciences, University of Lausanne, Lausanne, Switzerland, [2]Centro de Investigación en Ecosistemas de la Patagonia, Coyhaique, Chile, [3]Departamento de Ciencias Naturales y Tecnología, Universidad de Aysén, Coyhaique, Chile, [4]Department of Natural Sciences, Middlesex University, London, United Kingdom, [5]Institute of Earth Science, University Austral Chile, Valdivia, Chile

OPEN ACCESS

Edited by:
Juan-Luis García, Pontificia Universidad Católica de Chile, Chile

Reviewed by:
Koji Fujita, Nagoya University, Japan
Adina Elena Racoviteanu, UMR5001 Institut des Géosciences de l'Environnement (IGE), France

***Correspondence:**
Inigo Irarrazaval
inigo.irarrazaval@ciep.cl

Specialty section:
This article was submitted to Cryospheric Sciences, a section of the journal Frontiers in Earth Science

Received: *08 October 2021*
Accepted: *16 March 2022*
Published: *12 April 2022*

Citation:
Irarrazaval I, Dussaillant A, Vivero S, Iribarren-Anacona P and Mariethoz G (2022) Ice Dynamics and Morphological Changes During Proglacial Lake Development at Exploradores Glacier, Patagonia. Front. Earth Sci. 10:791487. doi: 10.3389/feart.2022.791487

Proglacial lakes are ubiquitous features formed during deglaciarization and are currently increasing in number in Patagonia and elsewhere. Proglacial lakes can affect glacier dynamics, catchment hydrology and have the potential to cause glacial lake outburst floods. Therefore, monitoring the onset and development of proglacial lake formation is relevant to understand glacial processes and anticipate glacier response to climate change. In this study, we integrate geomorphological and ice-dynamic information to assess proglacial lake development in Exploradores Glacier, Chilean Patagonia. We monitor recent spatial and temporal changes in the lower trunk of Exploradores Glacier (10 km^2) to provide a 20-year observation record by combining eight uncrewed aerial vehicles (UAV) surveys between 2019 and 2020, with high-medium resolution satellite imagery (Rapid Eye and Landsat) between 2000 and 2018. We use feature tracking techniques, digital surface elevation model analysis and field data to create a multi-temporal scale (inter-annual and seasonal) and a multi-spatial (cm to km) data set. Our analysis shows that surface velocity overall trend has not changed over the last 20 years and that surface velocity near the terminus is significant (>10 m a^{-1}). Moreover, an exceptional advance over moraine deposits was detected. We also found low downwasting rates (<0.5 m a^{-1}) close to the glacier terminus which are attributed to sufficient ice flux and the insulation effect of the debris-covered surface. However, hundreds of supraglacial ponds were observed and are currently coalescing and expanding by ice-cliff backwasting favoring glacier disintegration. Lastly, it was found that calving losses at the east marginal lake equaled ice-flux input into the lake for the UAV monitored period. This study contributes to a better understanding of glacial lake dynamics during proglacial lake development, and our results may help ice modelling efforts to predict glacier response to future climate scenarios.

Keywords: Patagonia, proglacial lakes, supraglacial ponds, ice-cliff backwasting, aerial vehicle, Exploradores Glacier

1 INTRODUCTION

Proglacial lakes have reportedly grown in number and size across different mountain regions such as the Southern Alps of New Zealand, the Himalayas and Patagonian Andes (e.g., Kirkbride, 1993; Sakai and Fujita, 2010; Carrivick and Tweed, 2013; Loriaux and Casassa, 2013; Iribarren Anacona et al., 2014; Nie et al., 2017; Shukla et al., 2018; Shugar et al., 2020; Zhang et al., 2021). Proglacial lake development can alter ice dynamics by several mechanisms such as flotation of the glacier's terminus, formation of a calving front, and increased ice flow (e.g., Robertson et al., 2012; Tsutaki et al., 2013; Tsutaki et al., 2019). In addition, proglacial lake development can enhance mass loss by adding frontal ablation components such as calving and subaerial melting (e.g., Benn et al., 2007; Sakai et al., 2009; Minowa et al., 2017). In the Himalayas, studies have found that the rate of loss of area of lake terminating glaciers is five to six times greater than land terminating glaciers (e.g., King et al., 2018; King et al., 2019; Maurer et al., 2019; Watson et al., 2020). Moreover, glacial lakes represent a potential risk for glacial lake outburst floods (GLOFs), which can damage infrastructure and incur considerable socioeconomic impact (Tweed and Russell, 1999; Iribarren Anacona et al., 2015; Carrivick and Tweed, 2016). Glacial lake outburst floods in Patagonia have occurred through the actual deglacierization period (e.g., Davies et al., 2020; Benito et al., 2021), and they are currently a major concern in Patagonia as they are likely to increase in frequency in the future (Dussaillant et al., 2010). With predictions of climate change, glaciers will continue to retreat (e.g., Vaughan et al., 2013). Therefore, the study of the onset and development of proglacial lakes is relevant to improve the understanding and prediction of glacier response to climate change in future environmental systems (e.g., Carrivick and Tweed, 2016).

The development of ice-contact proglacial lakes have demonstrated complex system interdependencies and feedback mechanisms, which can be partially decoupled from climate (e.g., Kirkbride, 1993). Glacier-lake interaction can often present tipping points or switching behavior: the formation of a proglacial lake and a calving front can shift the glacier from slow to fast retreat (Kirkbride and Warren, 1999). Examples of studies on proglacial lake formation include: the Southern Alps of New Zealand (e.g., Kirkbride, 1993; Kirkbride and Warren, 1999; Purdie and Fitzharris, 1999; Quincey and Glasser, 2009; Dykes et al., 2011), the European Alps (e.g., Tsutaki et al., 2013), Iceland (e.g., Baurley et al., 2020), and the Himalayas (e.g., Haritashya et al., 2018; King et al., 2018; Tsutaki et al., 2019; Sato et al., 2021a). In particular, proglacial lake formation associated with the disintegration of debris-covered glaciers has been generalized in a three-phase sequence of retreat (e.g., Kirkbride, 1993; Purdie and Fitzharris, 1999; Quincey and Glasser, 2009; Sakai et al., 2009; Benn et al., 2012). First, there is a phase of slow downwasting, under a thickening supraglacial debris-cover. Debris-thickness and melt rate relationships are describe by the Østrem curve (Østrem, 1959), where the formation of a few centimeters debris layer can isolate ice and reduce ablation (e.g., Pellicciotti et al., 2015). Second, the glacier transits to a phase where the debris-covered area is disrupted by the development of supraglacial ponds, streams and ice cliffs, leading to the characteristic hummocky texture (e.g., Mölg et al., 2020). Moreover, ice cliffs and supraglacial ponds can act as melt hotspots (e.g., Buri et al., 2021). Supraglacial ponds can contribute to ablation forming thermo-erosional notches or melt water undercutting which increases calving (e.g., Röhl, 2006; Sakai et al., 2009). In addition, ice cliffs expose clean ice walls enhancing ablation by ice-cliff backwasting (e.g., Miles et al., 2017; Brun et al., 2018; Steiner et al., 2019; Buri et al., 2021). It has been noted that supraglacial pond coalescence is favorable when glacier surface has a low gradient (<2°) and surface velocity is lower than 10 m a^{-1} (Reynolds, 2000; Quincey et al., 2007). Lastly, the debris-covered area disintegration can lead to the development of a calving front and a phase of rapid calving retreat through an overdeepened glacially-excavated depression (e.g., Kirkbride, 1993; Warren and Aniya, 1999; King et al., 2018; Tsutaki et al., 2019).

However, processes associated with proglacial lake development and the disintegration of debris-covered glaciers need to be better characterized to improve estimates of ablation and feedback mechanisms. Understanding small-scale process as well as a detailed relief and surface characterization is required for accurately modelling energy balances and ice dynamics (e.g., Mölg et al., 2020). Ice-contact proglacial lakes and their influence on ice dynamics remain poorly quantified and their incorporation into glacier evolution numerical models remain challenging (e.g., Carrivick et al., 2020; Sutherland et al., 2020). Yet, recent advances in uncrewed aerial vehicles (UAVs) and Structure-from-Motion Multi-View Stereo (SfM-MVS) photogrammetric methods have allowed monitoring and quantifying changes in glacial features. Examples of surface characteristics studies by UAV include: surface velocity (e.g., Kraaijenbrink P. et al., 2016; Bhardwaj et al., 2016; Rossini et al., 2018; Benoit et al., 2019), glacier downwasting (Immerzeel et al., 2014), ice-cliff backwasting (e.g., Steiner et al., 2019; Mölg et al., 2020; Sato et al., 2021b), and supraglacial pond development (e.g., Kraaijenbrink P. et al., 2016; Miles et al., 2017). The UAVs derived products have provided insights into mechanisms that are only possible to observe by high resolution images and high-density point clouds (e.g., Rossini et al., 2018; Watson et al., 2018). Moreover, UAVs have become useful tools to reduce the gap between different spatial scales from satellite images to field observations.

This work investigates glacier-lake interaction processes at Exploradores Glacier, Patagonia, located at the north of the Northern Patagonian Ice Field (NPI). The objective of this study is to characterize and monitor the spatial and temporal changes on the glacier surface over the last 20 years. We integrate geomorphological and ice-dynamics analysis to characterize main controls (i.e., surface downwasting, surface velocity and pond coalescence) of the proglacial lake development.

The study incorporates recent UAV and archival satellite imagery to observe ice and lake changes in multi-temporal scales (inter-annual, seasonal) and multi-spatial (cm to whole ablation area). The UAV images are analyzed by feature tracking to determine surface velocity, digital surface models (DSMs) comparison and by mapping surface features (e.g., crevasses and supraglacial ponds). Due to challenging terrain access, the

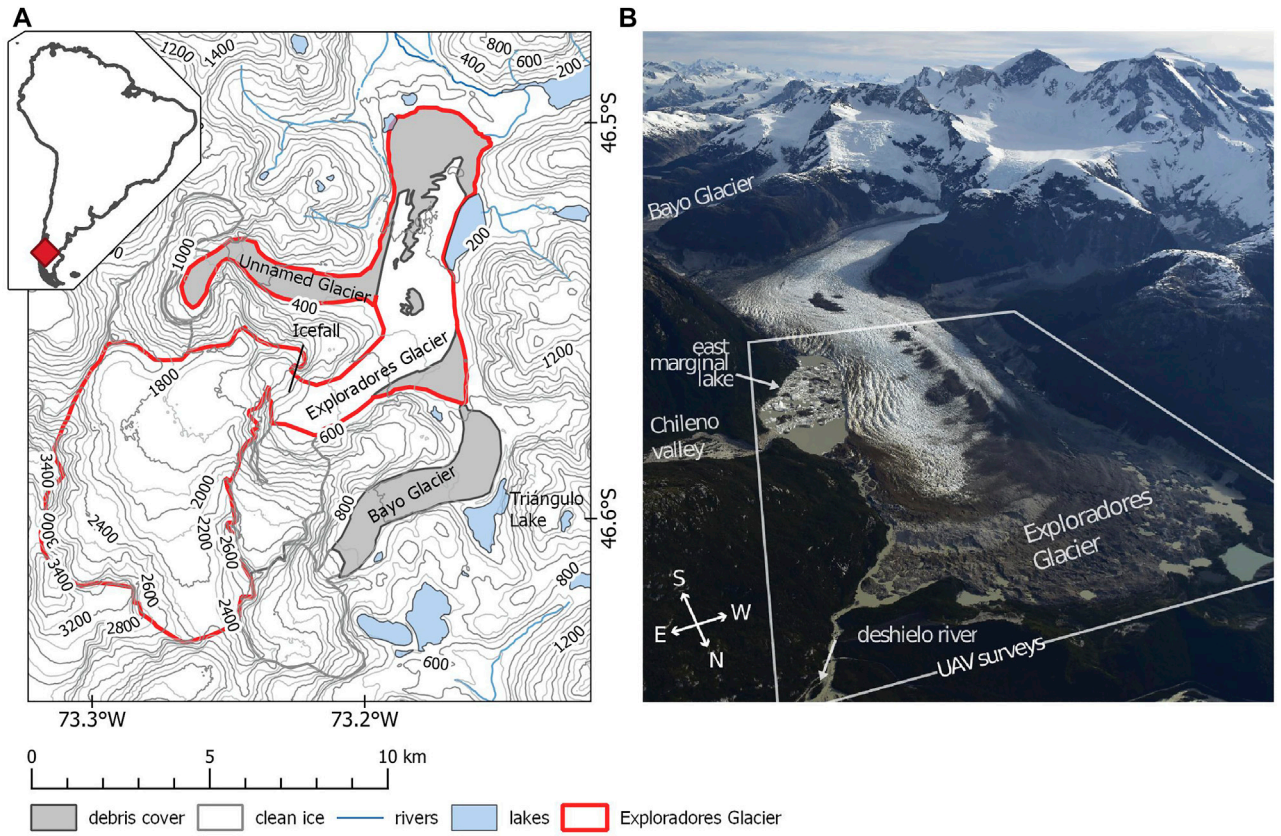

FIGURE 1 | (A) Exploradores Glacier (WGS84). **(B)** Aerial photo of Exploradores Glacier (credit to Guy Wenborne). Highest peak corresponds to Mount St. Valentín (4,032 m a.s.l.).

UAV-SfM products are not well registered with robust tie points off-glacier terrain. However, the degree of detected displacement and morphological changes are greater than the uncertainty so that it would not affect the findings. The data set is complemented with water level monitoring in supraglacial ponds and lakes as well as meteorological data.

It is worth noting that most studies in Patagonian glaciers have focused on one aspect of ice dynamics, such as mass balance or ice thickness estimations. More research is needed towards integrating ice dynamic responses to climate change at the individual glacier scale (e.g., Bown et al., 2019; Falaschi et al., 2019). Lastly, Exploradores Glacier is a recognized tourist destination for glacier walking tours, where up to one hundred visitors hike each day during summer. A transition to a fast retreating phase and development of a proglacial lake could not only impact ice dynamics but tourist guiding services which supports local economy (Bañales-Seguel et al., 2020).

2 STUDY SITE

Exploradores Glacier (46.5714°S, 73.2463°W) is located at the north of the North Patagonian Ice Field (NPI). The NPI is comprised of 38 main glaciers, including 18 lacustrine calving glaciers (covering 64% of the surface area), 19 land terminating glaciers (covering 18% surface area) and one tidewater glacier covering 18% of the surface area (RGI, 2017; Collao-Barrios et al., 2018). Overall the NPI mass balances are negative (e.g., Jaber et al., 2016; Dussaillant et al., 2018; Dussaillant et al., 2019b; Minowa et al., 2021) and predicted mass-loss rates are likely to continue increasing towards the end of the century (e.g., Schaefer et al., 2013). Exploradores Glacier has a surface area of 85.9 km^2 (RGI, 2017), an elevation range from ~180 to 3,900 m. asl (**Figure 1**). Geodetic mass balance measurements for the period 2000–2014 indicate that the glacier is losing mass at a rate of −1.01 ± 0.12 m w.e. a^{-1} (Dussaillant et al., 2018). The glacier is influenced by westerly airflows that deliver large year-round quantities of precipitation (e.g., Carrasco et al., 2002).

The main trunk of Exploradores glacier receives inputs from two tributaries, Bayo Glacier and an unnamed glacier from the west (**Figure 1**; RGI, 2017). The accumulation area lies below the north face of Mount San Valentin (4,032 m asl). The equilibrium line altitude (ELA) is located at ca. 1,200 m asl (Rivera et al., 2007) and the glacier has an accumulation area ratio of 0.62 (Willis et al., 2012). Also, there is a prominent icefall located in between the accumulation and ablation areas that extends from ~500 to 1,500 m asl (**Figure 1A**). At this icefall, surface velocities are in

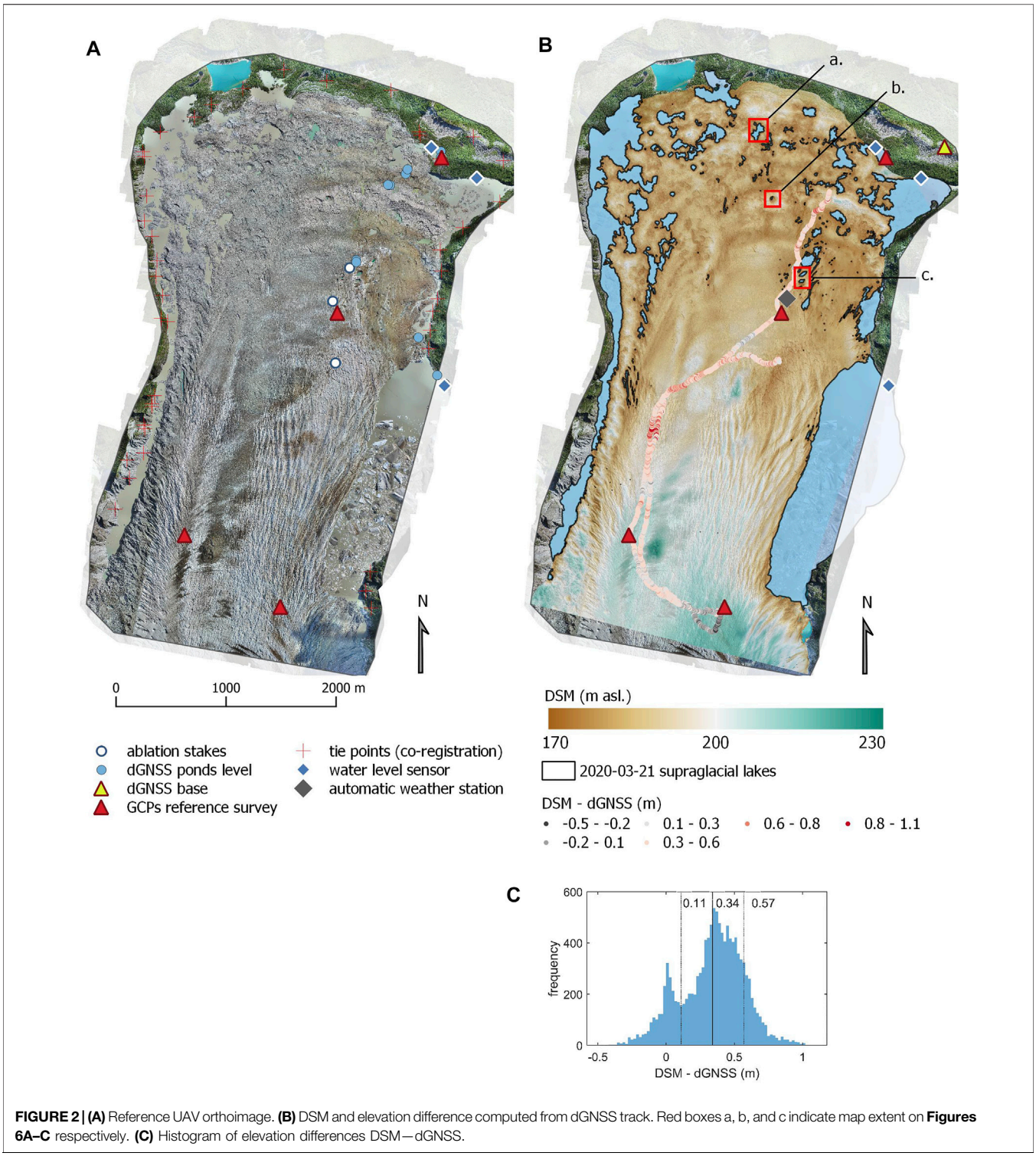

FIGURE 2 | (A) Reference UAV orthoimage. **(B)** DSM and elevation difference computed from dGNSS track. Red boxes a, b, and c indicate map extent on **Figures 6A–C** respectively. **(C)** Histogram of elevation differences DSM−dGNSS.

the order of ~300–600 m a^{-1} (Mouginot and Rignot, 2015; Gardner et al., 2019). The ablation area has a low gradient (<1°), covering an area of 20 km^2 and ranging in elevation from 170 to 500 m asl. Recent ice-thickness model estimations in the ablation area indicate a prominent bed overdeepening with a maximum ice thickness of 570 m (Farinotti et al., 2019).

The debris-covered area spreads up to 2 km from the terminus and extends further up in medial moraines. Near the glacier terminus, the debris-covered area is disrupted by several supraglacial ponds (**Figure 1**). A marginal lake is currently expanding by calving at the confluence of Chileno Valley and the main trunk of Exploradores Glacier (e.g., Loriaux and

Casassa, 2013). We refer to this lake as the east marginal lake (**Figure 1**). Lastly, the proglacial stream (Deshielo River, **Figure 1**) originates from a moraine-dammed lake, hereafter referred to as the terminal lake.

The study area (10 km^2) is located in the lower section of the ablation area of the main trunk of Exploradores Glacier (**Figure 1**). In this area, precipitation models estimate nearly 2000 mm of annual precipitation for the last 35 years (Funk et al., 2015). However, precipitation up to 3,000 mm annually has been measured for the 2003–2005 period close to the terminus (Aniya et al., 2007). During the year 2019, a mean annual air temperature of 7°C has been measured in a meteorological station located on the glacier (**Figure 1**), with only 4 days reaching minimum temperatures below 0°C. In addition, ablation stakes installed in the lower trunk of the glacier (**Figure 2**) by the Chilean Water Directorate were monitored. Summer ablation rates for the surveyed period (2019–2020), assuming an ice density of 900 kg m^3, ranged from 30 to 100 mm d^{-1} w.e. (**Figure 2**; **Supplementary Table S3**). The observed meteorological conditions and ablation rates for years 2019–2020 are comparable to those found in previous studies in 2003–2005 (Aniya et al., 2007; Konya and Matsumoto, 2010). Water levels from the east marginal lake, terminal lake, and one supraglacial pond (**Figure 2**) were monitored by installing HOBO U20L temperature and pressure transducers for the period (20-January-2019 to 29-May-2020). Pressure transducer measurements were corrected by atmospheric pressure variations, and georeferenced using dGNSS to obtain water levels. In addition, on 28-May-2020 water elevation levels of several supraglacial ponds located near the terminus were measured using a differential GNSS (**Figure 2**). The survey, conducted in a time span of 3 hours (to minimize diurnal oscillations), indicated that all surveyed pods shared similar water elevation ±50 cm.

In addition, two recent GLOFs have been reported on Exploradores Glacier. In 2015 a debris flow entered Chileno Lake, located in Chileno Valley (**Figure 1A**), triggering a GLOF that drained an estimated volume of 105 × 10^6 m^3 of water over 7 days (Wilson et al., 2019). In April 2018, the failure of a lateral moraine located in Bayo Glacier, drained Triángulo Lake (0.95 km^2) (Loriaux and Casassa, 2013). During the GLOF event, water discharge entered the main trunk of Exploradores Glacier and drained supra- and sub-glacially, damaging a gauging station located downstream. Rough estimates of peak discharge at Exploradores Glacier proglacial stream indicate 350 m^3 s^{-1} (Bañales-Seguel et al., 2020) and an approximate drained volume of ~20 × 10^6 m^3 (Chilean-Water-Directorate, 2018). Up to date, the event has not been studied in detail (Bañales-Seguel et al., 2020).

3 DATA AND METHODS

3.1 Uncrewed Aerial Vehicle Surveys

3.1.1 Data Acquisition

The UAV survey area extends 4 km from the glacier front with a width up to 3 km and an elevation range from 170 to 220 m asl, covering the lower trunk of Exploradores Glacier and its margins (**Figure 1**). We conducted eight UAVs surveys between March 2019 and May 2020. A fixed wing autonomous eBee Classic from SenseFly UAV equipped with a 20 Mpx SenseFly S.O.D.A 10.5 mm focal length camera (global shutter system) was employed. The camera is static within the UAV, and images are nearly nadir. Flight plans were designed in Emotion 3 with 60% lateral and 80% longitudinal overlaps, and a target image resolution of 8.5 cm px^{-1}. Most UAV flights were deployed from the glacier surface near the AWS (**Figure 1**). Four to seven flights were needed to complete each survey, and approximately 1,100 images were obtained on each survey (**Table 1**).

We measured five ground control points (GCPs) to georeference the UAV survey from 9 March 2020 (see **Section 3.1.2**). The GCPs marks were laid in the frontal moraine and on the glacier surface as the lateral moraines are inaccessible (**Figures 1**, **2**). The GCPs measurements were done employing a single frequency (L1) Emlid Reach RS + differential GNSS (dGNSS) setup (base and rover receivers). The base station was located on a stable boulder off glacier, where a screw was fixed in place to facilitate the same occupation during all surveys (**Figure 2B**). Before each survey, the base station was initialized for at least 30 min before the first measurement. The rover receiver was configured in kinematic mode with a logging interval of 1 s. Maximum baseline lengths were up to 5 km, and occupation time for each GCP was 1 min. A post-processing kinematic (PPK) treatment of the raw receiver data (RINEX) was done by RTKlib version 2.4.3 Emlid b28 (Takasu and Yasuda, 2009), following settings suggested by Emlid Reach RS + manufacturer. We only consider points that are resolved on a fixed precision for analysis. The PPK solution reached horizontal and vertical precisions in the order of 5 cm horizontally and 10 cm, respectively. For the reference UAV survey (09 March 2020), the GCP measurements during the dGNSS survey were acquired with less than 4 hours difference from the UAV survey.

3.1.2 Data Processing

The UAV images were processed using a SfM-MVS workflow in Pix4Dmapper Pro version 4.4.12 (Vallet et al., 2011). The first step consists of a bundle adjustment comprising key point extraction/matching, a self-calibration of camera parameters and the reconstruction of the external camera parameters (position and orientation). As recommended by the manufacturer, the process is done considering geometrically verified matching and re-match options. The second step consisted of a densifying of the point clouds using the key points derived from the first step and then applying clustering and patch-based MVS algorithms (e.g., Smith et al., 2015; Rodriguez et al., 2020). Lastly, seamless DSMs and orthomosaics were derived from the points clouds and original images, respectively.

Ground control points are commonly used to georeference the resulting models (i.e., orthomosaics and DSMs) and to improve the interior and external orientation parameters (Immerzeel et al., 2014; James and Robson, 2014; Kraaijenbrink P. et al., 2016; Rossini et al., 2018; James et al., 2019). However, the study site

TABLE 1 | UAVs image acquisition and co-registration data.

Date	Interval (days)	No. flights	No. images	Area km^2	Mean reproj. error [px]	No. co-registration tie points	X standard deviation [m]	Y standard deviation [m]	Z standard deviation [m]
07.03.2019	—	7	1,181	15.24	0.25	23	0.58	0.635	0.510
21.03.2019	14	7	1,669	17.7	0.25	34	0.533	0.467	0.562
24.11.2019	248	4	1,043	14.32	0.24	34	0.235	0.381	0.578
16.12.2019	22	4	1,148	15.19	0.25	33	0.247	0.309	0.506
22.01.2020	37	5	949	13.5	0.25	21	0.356	0.463	0.547
20.02.2020	29	4	1,103	16.13	0.24	40	0.296	0.309	0.695
09.03.2020[a]	18	5	1,222	17.45	0.25	5b	0.045	0.021	0.07
28.05.2020	80	6	1,231	17.82	0.25	32	0.304	0.352	0.580

[a]*Reference UAV survey.*
[b]*dGNSS measured ground control points.*
No.: number of.

accessibility is challenging as lateral moraines are virtually inaccessible, and the glacier presents crevasses that limit our reach. Therefore, we employed the following processing strategy following Benoit et al. (2019): 1) We selected a reference UAV survey (March 2020) that was georeferenced by five GCPs (**Figure 2**). 2) Based on this reference UAV survey, we manually selected between 20 and 40 tie points that were used as GCPs to process the remaining seven UAV surveys (see **Table 1**). The tie points (used as GCPs) are included in the bundle adjustment to generate a stackable co-registrated products among the UAV-derived orthomosaics and DSMs (e.g., Benoit et al., 2019). The tie points were preferentially chosen close to the glacier margin in stable bedrock outcrops. In areas without bedrock outcrops, tie points were selected in boulders that remained stable (visual inspection).

Previous studies have found that UAV-derived DSMs processed by SfM-MVS approaches are susceptible to certain systematic errors such as doming or dishing, and these error are more likely to occur if only nadir image acquisitions are used (e.g., James and Robson, 2014; Sanz-Ablanedo et al., 2020). Note that the maximum reported systematic errors were smaller than 2 m elevation difference (Sanz-Ablanedo et al., 2020). The inaccessibility and extent of the study area limited our ability to deploy checkpoints to robustly validate our results and correct for systematic errors. To estimate the magnitude of the vertical accuracy of the reference survey, we use the rover dGNSS positions to obtain a 12 km track containing ~1 m spaced points on the glacier (more than 12,000 points). The track elevation and reference DSM are compared to evaluate vertical mismatch independently. Note that we do not consider correcting the reference survey with the track points, neither use the data as a comprehensive accuracy assessment, as the track orientation does not necessarily match the location of systematic errors. As our GCPs are limited, we aim to provide a rough evaluation of possible systematic errors.

Lastly, DSMs of 21-March-2019 and 9-March-2020 were post-processed using point cloud analysis using CloudCompare V2.11.0 (CloudCompare, 2020) to remove artifacts inside supraglacial ponds. The artifacts are produced as the plain water texture impedes to accurate locate tie points on image pairs to allow correct SfM-MVS matching. Considering the water level at the perimeter of the pond well resolved, the artifacts correspond to points inside the pond perimeter which are above or under the water level. In addition, artifacts produced by fast moving objects (e.g., icebergs) are removed as well.

3.1.3 Quality Assessment

First, we inspected the quality of the reference UAV survey (March 2020). The bundle adjustment re-projection error, which correspond to the distance in the raw images and modelled position after the optimization of the camera position and orientation. The reference survey reached subpixel mean re-projection error and camera calibration parameters reached sub pixel uncertainties as well. In addition, we inspected the correlation matrix between camera calibration parameters. Moreover, the calibrated internal parameters from the S.O.D.A. camera converged to comparable values across all surveys (**Supplementary Table S1**). Lastly, the reference survey using 5 GCPs reached subcentimeter mean errors in x, y, and z, and a maximum standard deviation of 0.07 m in the z axis.

To independently gauge the quality of the reference UAV survey, we subtracted the dGNSS elevation values at the dGNSS x and y track-point locations from the DSM. The elevation mismatch is presented along the dGNSS track and in a histogram (**Figures 2B,C**). The errors are not randomly distributed across the dGNSS. Near the GCPs uncertainty and bias decrease, whereas in between GCPs the elevation difference ranges between 1 and −0.5 m revealing a vertical doming or convex artifact (**Figure 2C**). The mismatch is visible in the histogram showing two modes. The first mode located at 0.36 m shows that the DSM is on average higher than the dGNSS elevation data. The second mode shows a non-biased distribution, which is consistent with the dGNSS track points near the GCPs. Note that systematic errors cannot be attributed to the dGNSS rover measurements as similar bias is found in back-and-forth directions. As mentioned earlier, the trajectory of the dGNSS track and its spatial distribution does not allow for a full systematic error assessment.

Next, co-registration accuracy was assessed by inspecting the root mean square error (RMSE) for co-registration tie points

(used as GCPs). Results show that root mean square error for all surveys is less than 0.57 m. In addition, for all surveys bias is less than 1 cm and maximum standard deviation errors are 0.53 m in x, 0.6 m in y and 0.69 m in z (**Table 1**). The errors are attributed to difficulties in identifying tie points on changing sunlight exposure to sub-pixel precision level. However, tie points errors are not correlated in space and tend to compensate each other. As an independent assessment, 3 and 4 checkpoint marks were placed on the glacier surface in January and February respectively. The dGNSS resulted in a ±0.4 m horizontal and 0.7 m vertical maximum displacement error.

Given the challenging assessment of our UAV-derived datasets, and our limitation in obtaining several GCPs for the SfM-MVS workflow, conservatively we consider an empirically accuracy of ±0.5 m horizontally and ±1 m vertically for the derived orthomosaics and DSMs. Consequently, the following analysis is restricted to the aforementioned spatial resolution.

3.2 Surface Displacements

Horizontal displacements were computed from consecutive UAVs orthoimages resampled at 1 m resolution by the feature tracking algorithm ImGRAFT (Messerli and Grinsted, 2015). Results were post-processed to remove outliers by thresholding the signal-to-noise ratio as defined in ImGRAFT and by removing unrealistic large displacements. In addition, we limited the feature tracking to bare terrain, excluding points from vegetated areas and water bodies. We inspected the results through manual mapping of distinct features in the glacier surface (e.g., boulders), and compared velocities with ablation stakes horizontal displacement measured by dGNSS. UAVs surveys were complemented by annual surface velocity available from 1998 to 2018 by the NASA MEaSUREs ITS_LIVE project (Gardner et al., 2019).

3.3 Feature Mapping

Selected supraglacial ponds were mapped from the UAV-derived orthoimages and DSMs resampled at 0.5 m resolution. The vast majority of supraglacial pond water levels correspond to the hydrological base level. Therefore, to identify the margins of supraglacial ponds we extracted the 170.5 m a.s.l contour line, which represents the maximum observed water level. Pond margins are manually compared with the orthoimages and corrected. Lastly, satellite images from Landsat and Rapid Eye (**Supplementary Table S2**) were used to manually map the perimeter of the east marginal lake from 2000 to 2019.

4 RESULTS

4.1 Surface Elevation Changes

First, we present the surface elevation changes between between 9 March, 2020 and and 21 March, 2019 (**Figures 3A,B**). Overall, we found a mean surface difference of $-0.7\ m\ a^{-1}$ for the lower trunk of Exploradores Glacier. Considering biases and uncertainties from the quality assessment, downwasting rates lay within the uncertainties of the method (±1 m vertically). Results are coherent with previous studies indicating average rates of $-0.5\ m\ a^{-1}$ using digital elevation models derived from ASTER stereo images (Dussaillant et al., 2019b). Locally, most elevation changes are attributed to the advection of the hummocky topography composed by ice cliffs, peaks and troughs that can reach a relief up to 10–20 m (**Figure 3A**). The first kilometer from the glacier terminus, which corresponds to the debris-covered area, shows positive and negative elevation changes of ±15 m amplitude. Areas of sharp negative changes are attributed to ice-cliff backwasting (**Figure 3A**; **Figures 6A,B**). One of the most noticeable ice dynamics, is the west-east advection of crevasses (running parallel to the glacier centerline) near the east marginal lake, that can reach more than 20 m of relief (see (2.) in **Figure 3A**). The advection of the surface can be seen as semi-parallel red and blue bands, most noticeable near profile C (**Figure 3C**).

Second, we analyze the interannual elevation changes during 2019–2020 through elevation profiles (**Figures 3C–E**). Profile C (**Figure 3C**) comprises the first 300 m from the glacier terminus and runs parallel to the centerline. We note the advection (south-north direction) of a topographical peak or crest located 300 m from the terminus (horizontal arrow in **Figure 3C**). In addition, 50 m from the glacier terminus the surface raises almost ~5 m between the first and last survey (vertical arrow in **Figure 3C**). Profile D, runs perpendicular to the centerline and near to the east margin. The DSM profiles reveal horizontal displacement towards the calving front (horizontal arrow in **Figure 3D**). Here, peaks and troughs run parallel to the centerline reaching an elevation difference of 15–20 m (amplitude) and are separated by 50 m (wavelength). Lastly, profile E (**Figure 3E**) located approximately 2 km from the glacier terminus along the glacier centerline shows the advection of peaks and troughs (**Figure 3E**), where at 150 m the surface raises. In addition, the arrow located at 700 m displays the advection and elevation changes of the surface. Note that described local surface elevation changes are larger than DSMs uncertainties previously discussed (±1 m).

4.2 Surface Velocity

The surface velocity from two periods: 2019–2020 derived from the UAV high-resolution images and from period 1998–2018 obtained from ITS_live project (Gardner et al., 2019) are presented in **Figure 4**. First, note that the ITS_live project velocities are in agreement with the UAV derived velocities of this study. Moreover, surface velocities match boulder displacements velocity measured during years 2003/2005 by (Aniya et al., 2007).

The surface velocity spatial pattern shows that velocity decreases long the glacier centerline towards the terminus (**Figures 4A,C,G**). UAV derived velocities show velocities of $\sim 150\ m\ a^{-1}$ at the glacier's most upstream section (southern section of the study area). Note that ~300 m from the glacier terminus surface velocity is $10\ m\ a^{-1}$. Exceptionally in one location the glacier advanced 3.5 m over older moraine deposits (white square in **Figure 4A**). Surface velocity vectors were decomposed into orthogonal components oriented parallel to the centerline i.e. x- and y-axis rotated 15 degrees with respect

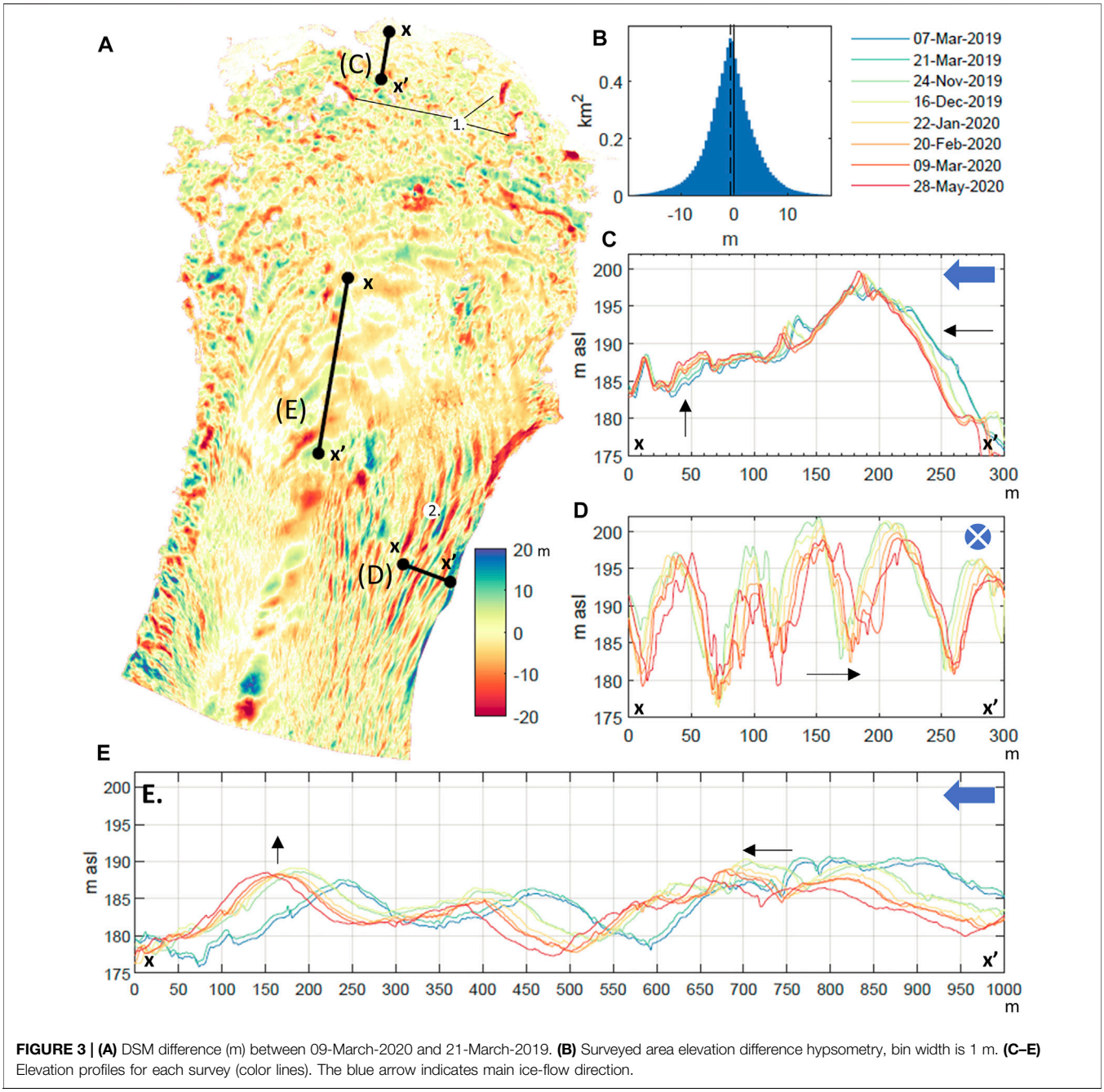

FIGURE 3 | (A) DSM difference (m) between 09-March-2020 and 21-March-2019. **(B)** Surveyed area elevation difference hypsometry, bin width is 1 m. **(C–E)** Elevation profiles for each survey (color lines). The blue arrow indicates main ice-flow direction.

to the North (**Figures 4B,C**). Note that the arrows size is relatively scaled for each plot. The *x-axis* component (perpendicular to glacier centerline) shows that surface velocity increases from the centerline towards the east marginal lake reaching 50 m a^{-1} (**Figure 4B**). The *y-axis* velocity magnitudes indicate that most of the ice flux occurs parallel to the centerline (**Figure 4C**).

The temporal trend of surface velocity is inspected at different points of the glacier in **Figures 4D,E**. Note that the date corresponds to the midpoint between image acquisition dates and uncertainties are denoted with a vertical black line. From **Figure 4D** it is observed that the first 2 km from the glacier terminus surface velocity remained stable between 2000 and 2009. However, 2–4 km from the terminus the glacier experienced an acceleration of 10% between 2009–2014 and deceleration between 2014 and 2019 (**Figure 4D**). Lastly, from the interannual velocities of the UAVs surveys, it is found that mid-summer velocities (January–February 2020) are ~10% higher than velocities computed in early spring and end of summer (**Figure 4E**).

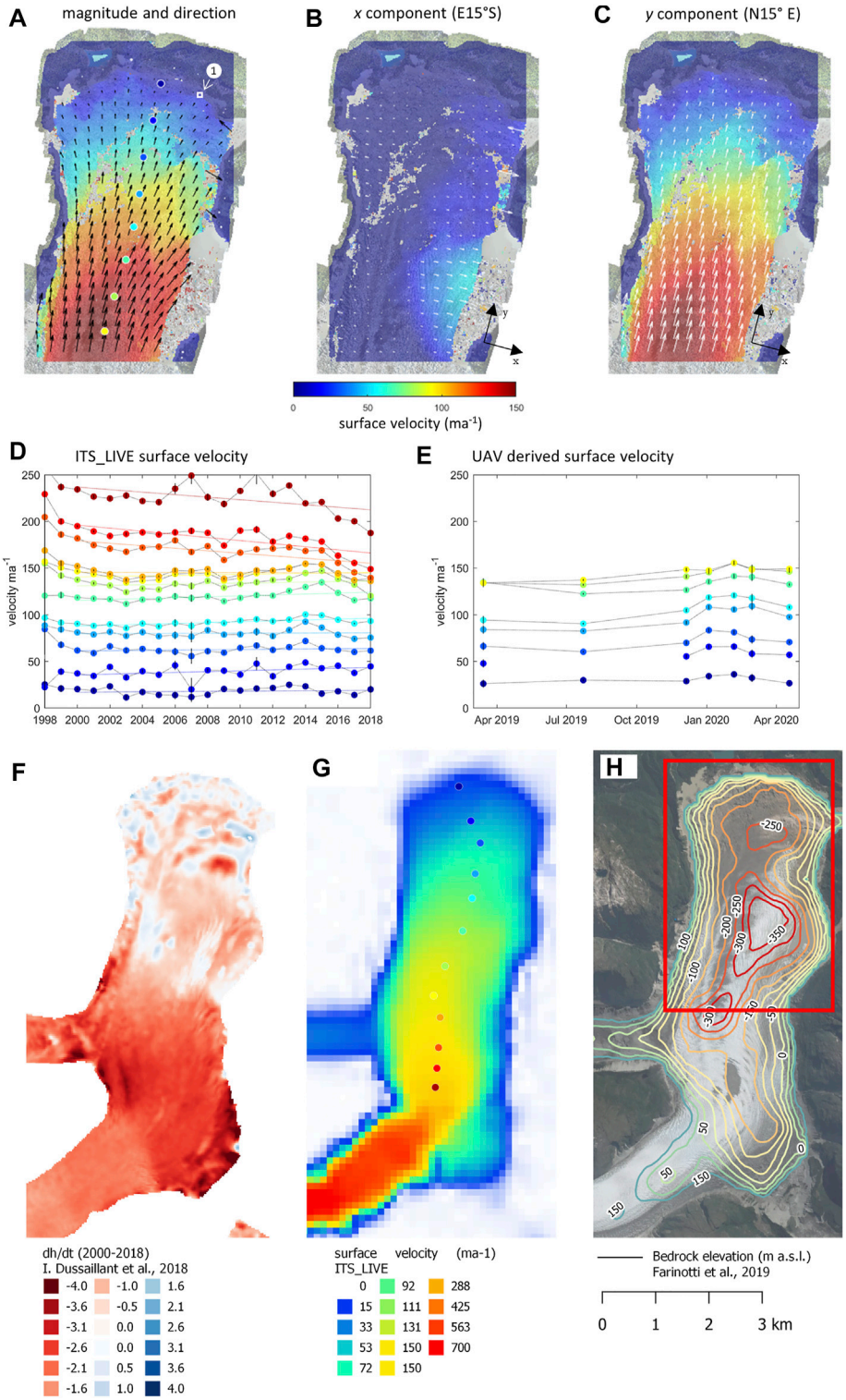

FIGURE 4 | (A–C) UAV derived surface velocity from surveys from March 2020 to May 2020. Note that the arrows size is relatively scaled for each plot. **(A)** Surface velocity magnitude and direction. The color dots correspond to locations points in plots **(D–E)** and white square indicated with (1) show area of glacier advance. **(B)** Surface velocity *x* component. **(C)** Surface velocity *y* component. **(D,E)** Surface velocity (ordinates) at different locations and date (abscises). **(F)** Thinning rates dh/dt (m a^{-1}) from dates 2000–2018 (Dussaillant et al., 2019b). **(G)** Ice surface velocity (m a^{-1}) ITS_LIVE (Gardner et al., 2019). **(H)** Bedrock elevation model (Farinotti et al., 2019). Red square corresponds to the extent of plots **(A–C)**.

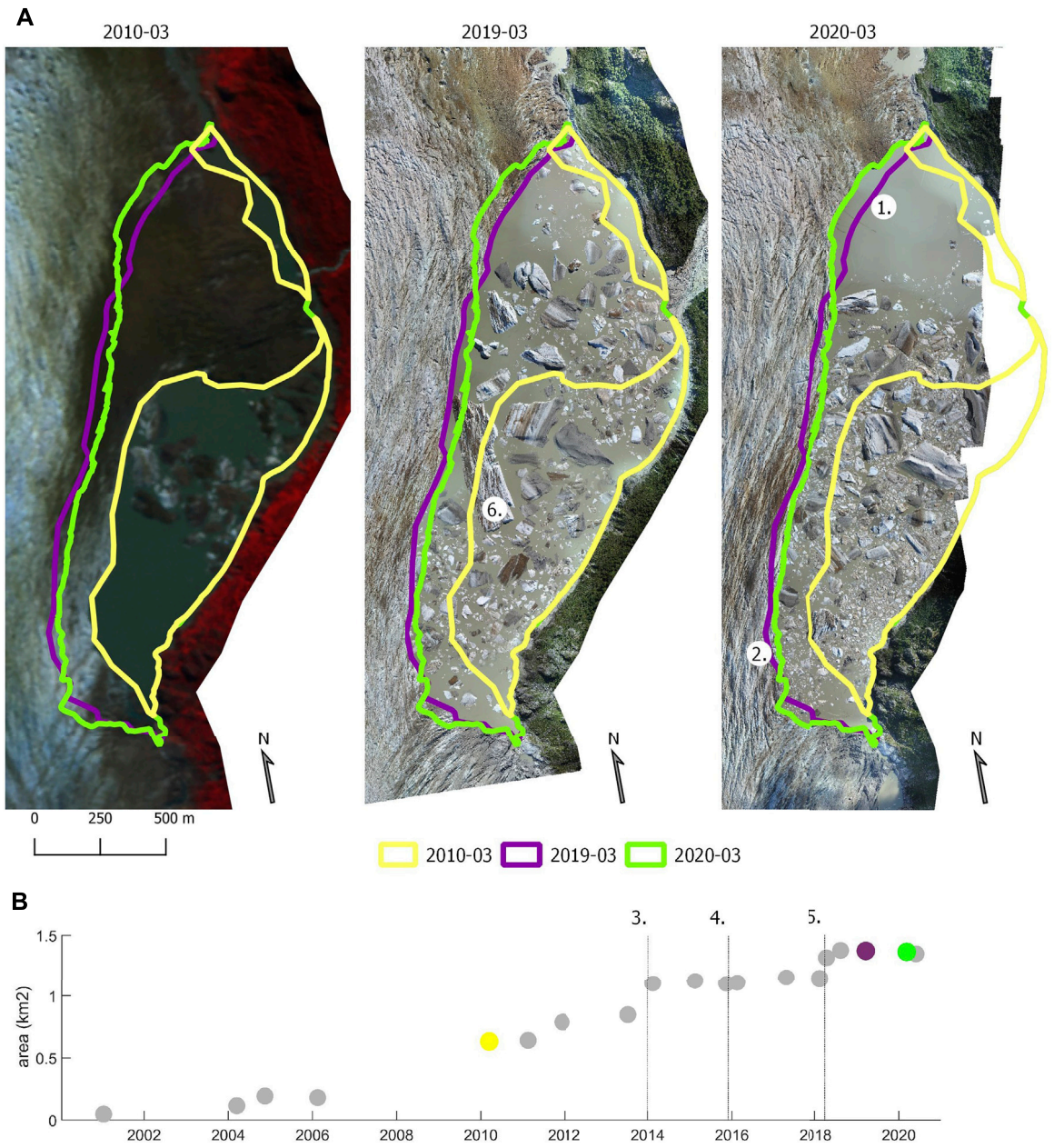

FIGURE 5 | (A) Landsat March-2010, UAV March-2019 and UAV March-2020 images. **(B)** East marginal lake area over 20 years.

4.3 Development of Lakes and Ponds

The lower trunk of Exploradores Glacier is surrounded by ice-contact lakes at the east and west margins. Moreover, multiple supraglacial ponds are observed on the surface (**Figure 2**). The larger lake development is observed at the east margin (**Figure 5A**). The first evidence of the east marginal lake development can be observed in the 2002 Landsat images. However, before 2010 the east marginal lake corresponded to small ponds near the glacier margin. Moreover, due to the coarse image resolution of the Landsat satellite image (30 m) the surface of the ponds is not well detected. Since 2010, the lake reached an area larger than 0.5 km^2 and expanded steadily until 2014, reaching an area of 1.1 km^2 (see (3.) in **Figure 5B**). Note that the date of GLOF from Chileno Valley is marked with (4.) in **Figure 5B**. Since 2014, the east marginal lake maintained this extent until April 2018 where it expanded ~0.3 km^2 (see (5.) in **Figure 5B**). The sudden expansion of the lake in 2018 matches with GLOF date from Triángulo Lake located at tributary Bayo Glacier (Bañales-Seguel et al., 2020). Lastly, UAVs images show that in March 2019 the area corresponded to 1.405 km^2 and in March 2020 the area decreased to 1.397 km^2. The UAV images show that the lake expanded by calving to the north (see (1.) in

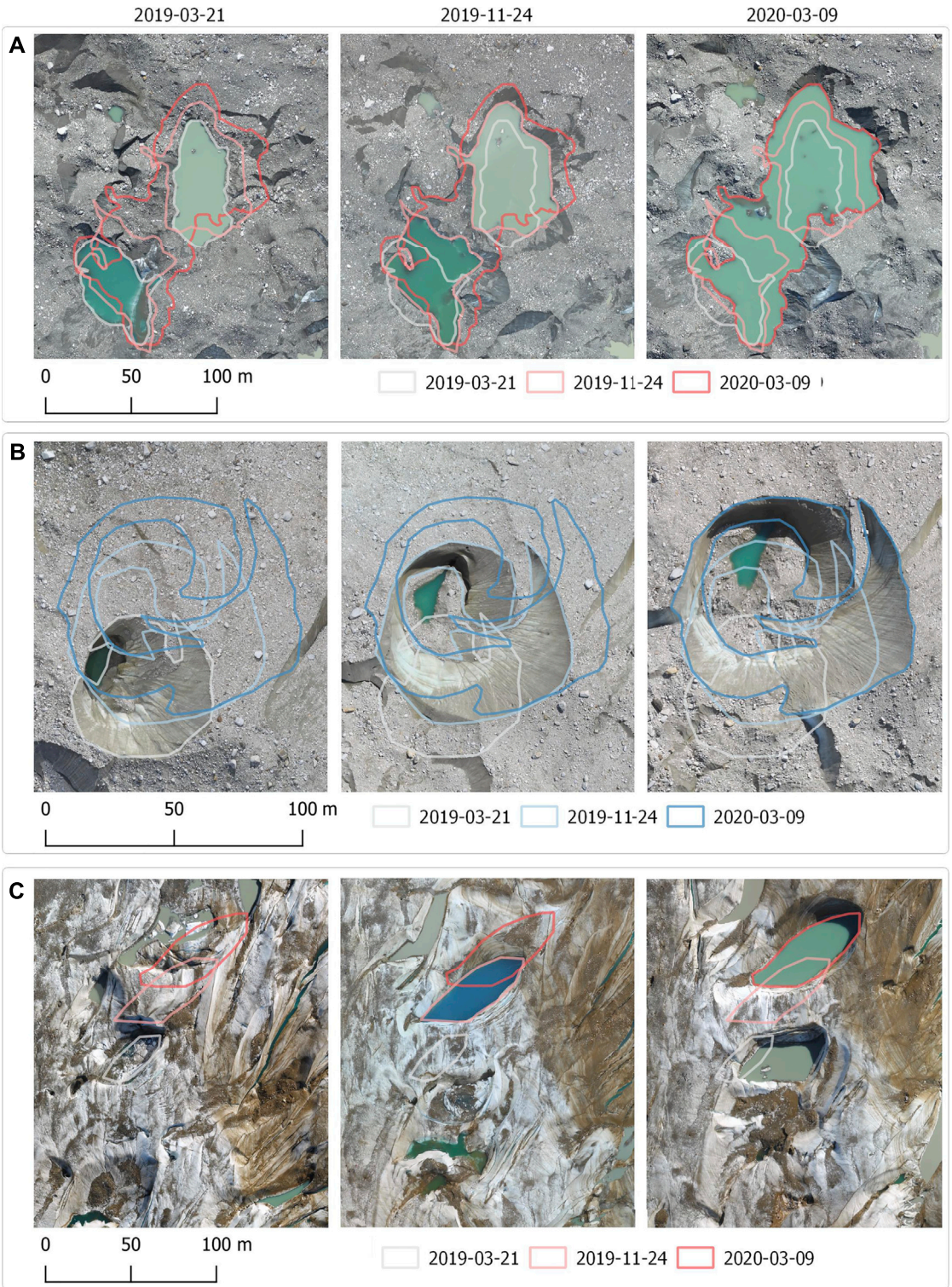

FIGURE 6 | (A) Supraglacial pond coalescence by ice-cliff backwasting. **(B)** Thermo-karst sink hole and ice-cliff backwasting. **(C)** En-echelon crevasses and supraglacial pond formation. Location of the ponds is provided in **Figure 2B**.

Figure 4A) and shrunk to the south by the advance of the glacier (see (2.) in **Figure 4A**). In addition, note the large iceberg ~450 by 130 m (55,000 m^2) in March 2019 image (see (6.) in **Figure 5A**).

In the western part of the glacier, a marginal lake extends 4 km from the frontal moraine covering an area of 0.5 km^2 (**Figure 2**). Near the terminus, the lake perimeter consists of debris-covered ice and ice cliffs. On the upper section of the study area, the west marginal lake perimeter consists in a steep lateral moraine, a partially debris-covered ice and marked splaying crevasses.

The first 200 m from the terminus present a hummocky topography commonly found in debris-covered glaciers (e.g., Mölg et al., 2020). Supraglacial ponds present ice cliffs up to 20 m high. It is observed that supraglacial ponds expand by ice-cliff backwasting and pond coalescence (**Figure 6A**). Moreover, field observations identified that supraglacial ponds formed thermo-erosional notches on ice cliffs near the terminus (**Figure 6A**). Up to 400 m from the terminus thermo-karst lakes are observed surrounded by funnel shape ice cliffs (**Figure 6B**). Approximately 1.5 km from the terminus, the UAV-derived orthoimages show the development of supraglacial ponds initiated by compressional crevasses (parallel to the main ice-flow direction), as well as strike-slip structures (en-echelon structures) (e.g., **Figure 6C**).

Results from DSMs and dGNSS surveys indicate that supraglacial pond water level is near 170 m asl reaching a 170.5 m asl maximum at the end of March 2020. The supraglacial ponds water level are in agreement with the terminal and east marginal lake levels, showing few centimeters (<10 cm) of diurnal fluctuations. No evident supraglacial pond surface drainage system has been observed near the glacier terminus. Note that on a larger scale (>200 m) there is near zero surface gradient on the debris-covered area. Lake level monitoring from pressure transducers indicates that the east marginal lake and the terminal lake (lake located at the glacier snout) have a synchronous in-phase water level (no lag) (**Supplementary Figure S1**). Lastly, temperature from the east marginal lake ranged between 0.3–0.5 ± 0.5°C from February to May 2020.

5 DISCUSSION

In this section we discuss Exploradores Glacier ice dynamics, morphological changes and indicators of the possible onset of proglacial lake development. The terminus of Exploradores Glacier has remained in a relatively stable position and only retreated approximately 100–200 m from its Neoglacial position, attested by the LIA moraines (Aniya et al., 2007). This is a distinct feature of a glacier in this location, given that most NPI glaciers have experienced a net retreat of the termini from their LIA moraines dated 12th–17th century (Aniya et al., 2007). Recent geomorphological changes in Exploradores Glacier include the development of an ice-dammed lake at the eastern margin (Loriaux and Casassa, 2013; Wilson et al., 2018), an increase in debris cover thickness (Glasser et al., 2016) and supraglacial pond enlargement (Aniya et al., 2007). Moreover, current debris cover disruption by formation of supraglacial ponds and lakes have led previous researchers to hypothesize that the first kilometers (from the glacier front) are disintegrating (Aniya et al., 2007). Following similar cases found in the literature (e.g., Kirkbride, 1993; Kirkbride and Warren, 1999), it can be expected that a calving front would develop implying an increase in ablation rates and extension of proglacial lake into overdeepening areas in the coming years. King et al. (2018) argues, with examples from the Himalayas, that there are common criteria that allow to predict proglacial lake development. These criteria include terminus stagnation (displacements <5 m a^{-1}), glacier thinning, low gradient ablation area (<2 degrees), supraglacial ponds coalescence and terminus flotation (e.g., Kirkbride, 1993; Reynolds, 2000; Benn et al., 2001; Quincey et al., 2007; Quincey and Glasser, 2009; Sakai and Fujita, 2010; Tsutaki et al., 2013).

5.1 Terminus Disintegration

There are multiple evidences that the terminus of Exploradores Glacier is disintegrating and this process will continue forming a proglacial lake. The first 2 km of Exploradores Glacier terminus are covered by debris and this zone has a low surface gradient (<1 degree) which is common in glaciers which front disintegrated by the formation of glacial lakes. According to Aniya et al. (2007), between 2000–2004 supraglacial ponds and ice cliffs started to develop a hummocky texture near the glacier front. Furthermore, within the UAV monitored period (2019–2020), it was observed that supraglacial ponds expand via ice-cliff backwasting and subaqueous melt, without evident surface drainage (**Figure 6A,B**). The high-resolution of the acquired UAV images (less than 20 cm) allowed to observe pond initiation by crevasses opening. Interestingly, the analysis of the UAV images (2019–2020) showed that longitudinal crevasses (parallel to the main ice flow direction), marginal shear crevasses as well as strike-slip structures (en-echelon structures) provide fractures for pond initiation (**Figure 6C**). These ponds present a low turbidity at an initial stage and are later expanded by ice-cliff backwasting and subaqueous melt (e.g., **Figure 6C**). In addition, measured water levels indicate that most supraglacial ponds and marginal lakes have the same water level (170.5 m a.s.l ± 0.5), indicating hydrological connection which could favor lakes coalescence. The analysis of summer ablation stakes from December 2019 to March 2020 showed ice-loss ranging from 3.6 to 12 meters (30–100 w.e. mm d^{-1}). However, the downwasting of the terminus ranged between −0.5 and −1 m a^{-1} based on UAV-derived DSMs from 2019–2020 (**Figure 2A**). Note that those rates are similar to elevation changes during 2000–2014 of ~−0.5 m a^{-1} at the first 4 km from Exploradores Glacier terminus (**Figure 4F**) (Jaber et al., 2016; Dussaillant et al., 2019a; Dussaillant et al., 2019b).

The observed crevasse opening, ponds formation as well as ice downwasting contribute to the disintegration of the debris-covered glacier terminus (e.g., King et al., 2018). However, previous studies have noted that disintegration of the terminus is favorable when the terminus is stagnant (<5 m a^{-1}) (King et al., 2018). Here, the analysis of high-resolution UAV images (March 2019 to May 2020) show that velocity around 300 m from the terminus reaches 10 m a^{-1}. Moreover, velocity show a stable trend over the last 20 years. In addition, in 2020 we observed at one

location the advance of 3 m of the glacier over moraine deposits (**Figure 4**). The actual surface velocity patterns show that predominant ice flux occurs parallel to the centerline (**Figures 4A,C,G**) decreasing in velocity towards the terminus. In addition, longitudinal crevasses (oriented parallel to the glacier centerline) are observed as well as splaying crevasses near the margin (**Figure 2**). This regime and the observed surface uplift found in profiles (**Figures 3C,E**), are indicators of glacier deceleration and a compressional regime (e.g., Sato et al., 2021a). Therefore, surface velocity and surface elevation changes observations indicate that within the study area the high ablation rates are partially compensated by the upstream glacier.

5.2 Terminus Flotation

The modelled ice thickness based on Farinotti et al., 2019, indicates a prominent bed overdeepening extending 4 km from the terminus (**Figure 4H**). Interestingly, considering a point at the center of the ablation area, the bedrock elevation reaches a minimum of −350 m asl, surface elevation is near 200 m asl and lake level is near 170 m asl. Therefore, at this point water level is above 94% of the ice thickness. Consequently, we suggest that at least a portion of the lower trunk of Exploradores Glacier has reached flotation (e.g., Boyce et al., 2007). However, the analysis is not conclusive as ice thickness estimation, for Exploradores Glacier, is based on numerical modelling without geophysical measurements or direct borehole drilling for validation. Therefore, uncertainties are significant (Farinotti et al., 2019). Moreover, glacier flotation is associated with extensive regimes where surface velocity increases towards the terminus (e.g., Tsutaki et al., 2013; Tsutaki et al., 2019). In the case of Exploradores Glacier, glacier surface velocity decreases towards the terminus showing similar behavior to land terminating glaciers (e.g., Tsutaki et al., 2019; Sato et al., 2021a). This can be interpreted as the glacier has not reached flotation yet, or a coherent section of the lower trunk is well grounded. For comparison, the onset of proglacial lake development at the debris-free Rhone Glacier (European Alps) showed an increase in surface velocity by a factor of 2.7 during 2006–2008 (Tsutaki et al., 2013). Moreover, lake development at Rhone Glacier showed surface uplift and extensive strain rates. This is attributed to the glacier reaching flotation and consequently decrease on basal drag (e.g., Iken, 1981; Boyce et al., 2007).

5.3 East Marginal Lake Expansion

Another relevant component of mass loss is the development of a calving front at the east marginal lake. Previous studies have described the east marginal lake as an ice-dammed lake that started developing in 2011 (Loriaux and Casassa, 2013; Wilson et al., 2019). We found evidence of the lake in archival satellite images as early as 2002. However, many images present shadows and clouds inhibiting accurate mapping. Note that before 2014, the east marginal lake was drained by a meandering supraglacial stream (Aniya, 2017). Nowadays, the east marginal lake is drained via englacial/subglacial hydraulic pathways as the glacier is in contact with the lateral moraine in two 200 m sections before the glacier terminus. From 2010, the east marginal lake expanded until 2014 and after the 2018 GLOF event in a stepwise manner. Previous studies have found that GLOFs can accelerate and hydraulically lift glaciers during drainage (Sugiyama et al., 2008). However, from our data, it is not clear the role played by the 2018 GLOF and if may have triggered a large calving event (see (6.) in **Figure 5A**). Note that within the UAV monitored period 2019–2020, the ice flux towards the east marginal lake was higher than calving flux, reducing the lake area. Note that the surface velocity component towards the calving front was near 50 m a^{-1} (**Figure 4B**), which is coherent with DSM profiles (**Figure 3E**) which show extensional characteristics.

5.4 Ice Dynamics of the Ablation Area

On a larger spatiotemporal scale, considering the whole of the ablation area of the glacier and the last 20 years, it is possible to identify two areas of the glacier whose dynamics differ: the first 4 km from the terminus and between 4 km and the icefall at approximately 6 km from the terminus. This is most noticeable by inspecting the thinning rates derived from geodetic mass balance (**Figure 4F**). Geodetic mass balance studies found that the first 4 km from the glacier terminus have thinning rates ranging −0.5–0 m a^{-1} and from 4 km up to the icefall thinning rates of 2 m a^{-1} (Jaber et al., 2016; Dussaillant et al., 2019b). Note that the first 4 km of the glacier include areas with and without debris-cover which show similar thinning rates. In addition, the velocity of the first 4 km of the glacier has remained stable over the last 20 years, and between 4 and 6 km the velocity magnitude has decreased by 15% (**Figure 4D**). The decrease in velocity implies a lower ice flux towards the glacier front from 2014–2018. Therefore, we interpret that thinning rates differences between the first 4 km, and in between 4–6 km are more likely dependent on the ice flux. One explanation is that dynamic thinning is taking place in between 4–6 km (from the UAV surveyed area up to the icefall, **Figure 4H**). Interestingly, according to ice-thickness maps the over-deepened area decreases at 4–6 km from the terminus. Lastly, it is worth noting that geodetic mass balance studies (2000–2014 and 2000–2018) have shown that the thinning rate in the accumulation area is near 0 m a^{-1} (Jaber et al., 2016; Dussaillant et al., 2019b).

5.5 Outlook

Further work should prioritize establishing an ice-flow dynamic model to test hypothesis/predictions regarding Exploradores Glacier response to climate drivers and calving fluxes (e.g., Tsutaki et al., 2019; Sato et al., 2021a). Efforts should focus on modelling the complete ablation area to explore downwasting rates below the icefall which could be attributed to dynamic thinning (e.g., Tsutaki et al., 2013). It is crucial to gather ice thickness data to improve bedrock elevation models. Furthermore, efforts might be directed to model ice melt at the debris-cover area to further study the disintegration of the glacier terminus. In this line, the acquired UAVs images can be used to improve quantification on ice-cliff backwasting and pond coalescence (e.g., Steiner et al., 2019) which is not explored in this study.

Lastly, it is worth noting that previous literature has pointed out that east marginal lake is an ice-dammed lake (e.g., Loriaux and Casassa, 2013; Wilson et al., 2019).

Unravelling this is critical, as ice-dammed lakes are more susceptible to glacial lake outburst floods (e.g., Tweed and Russell, 1999; Carrivick and Tweed, 2016). Moreover, as the glacier reaches flotation, subglacial conduits are not likely to close solely due to viscous ice creep from the ice overburden pressure (e.g., Iken, 1981).

6 CONCLUSION

The formation of proglacial lakes at Exploradores Glacier has been ongoing for decades as a result of the relatively slow disintegration process of the debris-covered tongue. In this work, we monitored the ablation area of Exploradores Glacier by repeated UAV surveys and satellite images over the last 20 years. We observed that the debris-covered area of Exploradores is disintegrating by pond coalescence favored by low gradient slope and glacier thinning. However, surface velocities near the terminus are significant ($>10\ m\ a^{-1}$), implying a substantial ice flux towards the terminus which partially compensates surface ablation. We observed that the east marginal lake area has remained unchanged over the last 6 years, with the exception of a surface increase after a glacial lake outburst flood in 2018. Moreover, high-resolution UAV images from 2019–2020 show that the east marginal lake calving losses equaled upcoming ice flux. This is coherent with observed surface velocities towards the calving front of $\sim 50\ m\ a^{-1}$.

We found that the east marginal lake, previously described in the literature as an ice-dammed lake is hydraulically efficiently connected to the terminal lake at the glacier outlet, showing the same synchronous water level across the study period. However, the monitoring period is less than a year and further monitoring is needed to evaluate GLOFs risk from the east marginal lake.

The study identified main controls on Exploradores Glacier ongoing lake development and provide information to assessing further glacier evolution. The observed geomorphological and ice dynamics characteristics imply that Exploradores Glacier is disintegrating at a slow rate given the steady ice flux from upstream. However, proglacial lake formation often implies nonlinear responses and tipping points which are difficult to predict. Future scientific effort in the region should be drawn to improve/collect ice-thickness data, as is a key to assessing further proglacial lake development as well as setting up ice-dynamic models to predict glacier evolution.

DATA AVAILABILITY STATEMENT

The raw data supporting the conclusion of this article will be made available by the authors, without undue reservation. The UAV derived orthomosaics and DSMs can be found at https://doi.org/10.5281/zenodo.5483840 under license CC 4.0. In addition, ice thickness model for Exploradores Glacier was obtained from Farinotti et al. (2019) available at https://www.researchcollection.ethz.ch/handle/20.500.11850/315707 under license CC 4.0. Surface velocities from Gardner et al. (2019) ITS_LIVE available https://its-live.jpl.nasa.gov/ under MIT license. Glacier elevation changes available from Dussaillant et al. (2019a) in repository https://doi.org/10.1594/PANGAEA.903618 under license CC-BY-4.0.

AUTHOR CONTRIBUTIONS

The study was designed by II with the inputs from GM, AD, SV, and PI-A. Field work was done by II and AD. Drone images were processed by II and SV. Analysis were performed by II and discussed among all co-authors. II prepared the paper, which was edited and proofread by all co-authors.

FUNDING

II was funded by the Swiss National Foundation through SNF-Doc Mobility fellowship 2019 (187738). In addition, II received funding from the National Agency for Research and Development (ANID) through BECAS CHILE/2015–72160092 and PATSER R-20F0002. The Doc.Mobility 2018 fellowship from Centro Latinoamericano–Suizo of St. Gallen University financed March 2019 field work. PI-A was funded by the Fondecyt de Iniciación project No 11190389. AD received field funding from SNF-SEED 2018. CONAF authorized and supported the project inside the National Park Laguna San Rafael, as well as providing fieldwork safety backups. The Water Cadastre of Chile (DGA) provided data from meteorological station as well as field work support in May 2020.

ACKNOWLEDGMENTS

We are grateful to C. Rodríguez-Morata, A. Muñoz-Torrero-Manchado, who provide helpful field support and to Guy Wenborne who provided the photo from **Figure 1**. Lastly, we are grateful to Francisco Croxatto and the park rangers from Parque Exploradores (www.parquexploradores.cl) who provided crucial support for logistics and field work across all the study period.

SUPPLEMENTARY MATERIAL

The Supplementary Material for this article can be found online at: https://www.frontiersin.org/articles/10.3389/feart.2022.791487/full#supplementary-material

REFERENCES

Aniya, M., Barcaza, G., and Iwasaki, S. (2007). Recent Glacier Advances at Glaciar Exploradores, Hielo Patagónico Norte, Chile. *Bull. Glaciological Res.* 24, 49–57.

Aniya, M. (2017). Glacier Variations of Hielo Patagónico Norte, Chile, over 70 Years from 1945 to 2015. *Bull. Glacier Res.* 35, 19–38. doi:10.5331/bgr.17R01

Bañales-Seguel, C., Salazar, A., and Mao, L. (2020). Hydro-morphological Characteristics and Recent Changes of a Nearly Pristine River System in Chilean Patagonia: The Exploradores River Network. *J. South Am. Earth Sci.* 98, 102444. doi:10.1016/j.jsames.2019.102444

Baurley, N. R., Robson, B. A., and Hart, J. K. (2020). Long-term Impact of the Proglacial lake Jökulsárlón on the Flow Velocity and Stability of Breiðamerkurjökull Glacier, Iceland. *Earth Surf. Process. Landforms* 45 (11), 2647–2663. doi:10.1002/esp.4920

Benito, G., Thorndycraft, V. R., Medialdea, A., Machado, M. J., Sancho, C., and Dussaillant, A. (2021). Declining Discharge of Glacier Outburst Floods through the Holocene in central Patagonia. *Quat. Sci. Rev.* 256, 106810. doi:10.1016/j.quascirev.2021.106810

Benn, D. I., Bolch, T., Hands, K., Gulley, J., Luckman, A., Nicholson, L. I., et al. (2012). Response of Debris-Covered Glaciers in the Mount Everest Region to Recent Warming, and Implications for Outburst Flood Hazards. *Earth-Science Rev.* 114 (1), 156–174. doi:10.1016/j.earscirev.2012.03.008

Benn, D. I., Warren, C. R., and Mottram, R. H. (2007). Calving Processes and the Dynamics of Calving Glaciers. *Earth-Science Rev.* 82 (3), 143–179. doi:10.1016/j.earscirev.2007.02.002

Benn, D. I., Wiseman, S., and Hands, K. A. (2001). Growth and Drainage of Supraglacial Lakes on Debris-Mantled Ngozumpa Glacier, Khumbu Himal, Nepal. *J. Glaciol.* 47 (159), 626–638. doi:10.3189/172756501781831729

Benoit, L., Gourdon, A., Vallat, R., Irarrazaval, I., Gravey, M., Lehmann, B., et al. (2019). A High-Resolution Image Time Series of the Gorner Glacier - Swiss Alps - Derived from Repeated Unmanned Aerial Vehicle Surveys. *Earth Syst. Sci. Data* 11 (2), 579–588. doi:10.5194/essd-11-579-2019

Bhardwaj, A., Sam, L., AkankshaMartín-Torres, F. J., Martín-Torres, F. J., and Kumar, R. (2016). UAVs as Remote Sensing Platform in Glaciology: Present Applications and Future Prospects. *Remote Sensing Environ.* 175, 196–204. doi:10.1016/j.rse.2015.12.029

Bown, F., Rivera, A., Pętlicki, M., Bravo, C., Oberreuter, J., and Moffat, C. (2019). Recent Ice Dynamics and Mass Balance of Jorge Montt Glacier, Southern Patagonia Icefield. *J. Glaciol.* 65 (253), 732–744. doi:10.1017/jog.2019.47

Boyce, E. S., Motyka, R. J., and Truffer, M. (2007). Flotation and Retreat of a lake-calving Terminus, Mendenhall Glacier, Southeast Alaska, USA. *J. Glaciol.* 53 (181), 211–224. doi:10.3189/172756507782202928

Brun, F., Wagnon, P., Berthier, E., Shea, J. M., Immerzeel, W. W., Kraaijenbrink, P. D. A., et al. (2018). Ice Cliff Contribution to the Tongue-wide Ablation of Changri Nup Glacier, Nepal, central Himalaya. *The Cryosphere* 12 (11), 3439–3457. doi:10.5194/tc-12-3439-2018

Buri, P., Miles, E. S., Steiner, J. F., Ragettli, S., and Pellicciotti, F. (2021). Supraglacial Ice Cliffs Can Substantially Increase the Mass Loss of Debris-Covered Glaciers. *Geophys. Res. Lett.* 48 (6), e2020GL092150. doi:10.1029/2020GL092150

Carrasco, J. F., Casassa, G., and Rivera, A. (2002). "Meteorological and Climatological Aspects of the Southern Patagonia Icefield," in *The Patagonian Icefields: A Unique Natural Laboratory for Environmental and Climate Change Studies*. Editors G. Casassa, F. V. Sepúlveda, and R. M. Sinclair (Boston, MA: Springer US), 29–41. doi:10.1007/978-1-4615-0645-4_4

Carrivick, J. L., and Tweed, F. S. (2016). A Global Assessment of the Societal Impacts of Glacier Outburst Floods. *Glob. Planet. Change* 144, 1–16. doi:10.1016/j.gloplacha.2016.07.001

Carrivick, J. L., and Tweed, F. S. (2013). Proglacial Lakes: Character, Behaviour and Geological Importance. *Quat. Sci. Rev.* 78, 34–52. doi:10.1016/j.quascirev.2013.07.028

Carrivick, J. L., Tweed, F. S., Sutherland, J. L., and Mallalieu, J. (2020). Toward Numerical Modeling of Interactions between Ice-Marginal Proglacial Lakes and Glaciers. *Front. Earth Sci.* 8 (500), 68. doi:10.3389/feart.2020.577068

Chilean-Water-Directorate (2018). *Minuta Técnica: Incremento de caudal en Río Exploradores*. Región de Aysén, Chile: Dirección General de Aguas - Ministerio de Obras Públicas.

CloudCompare (2020). CloudCompare. version 2.11.0. GPL software. Available at: http://www.cloudcompare.org/.

Davies, B. J., Darvill, C. M., Lovell, H., Bendle, J. M., Dowdeswell, J. A., Fabel, D., et al. (2020). The Evolution of the Patagonian Ice Sheet from 35 Ka to the Present Day (PATICE). *Earth-Science Rev.* 204, 103152. doi:10.1016/j.earscirev.2020.103152

Dussaillant, A., Benito, G., Buytaert, W., Carling, P., Meier, C., and Espinoza, F. (2010). Repeated Glacial-lake Outburst Floods in Patagonia: an Increasing hazard? *Nat. Hazards* 54 (2), 469–481. doi:10.1007/s11069-009-9479-8

Dussaillant, I., Berthier, E., and Brun, F. (2018). Geodetic Mass Balance of the Northern Patagonian Icefield from 2000 to 2012 Using Two Independent Methods. *Front. Earth Sci.* 6, 8. doi:10.3389/feart.2018.00008

Dussaillant, I., Berthier, E., Brun, F., Masiokas, M., Hugonnet, R., Favier, V., et al. (2019a). South American Andes Elevation Changes from 2000 to 2018, Links to GeoTIFFs. *PANGAEA* 12 (10). 3618. doi:10.1594/PANGAEA.903618

Dussaillant, I., Berthier, E., Brun, F., Masiokas, M., Hugonnet, R., Favier, V., et al. (2019b). Two Decades of Glacier Mass Loss along the Andes. *Nat. Geosci.* 12 (10), 802–808. doi:10.1038/s41561-019-0432-5

Dykes, R. C., Brook, M. S., Robertson, C. M., and Fuller, I. C. (2011). Twenty-First Century Calving Retreat of Tasman Glacier, Southern Alps, New Zealand. *Arctic, Antarctic, Alpine Res.* 43 (1), 1–10. doi:10.1657/1938-4246-43.1.1

Falaschi, D., Lenzano, M. G., Villalba, R., Bolch, T., Rivera, A., and Lo Vecchio, A. (2019). Six Decades (1958-2018) of Geodetic Glacier Mass Balance in Monte San Lorenzo, Patagonian Andes. *Front. Earth Sci.* 7, 326. doi:10.3389/feart.2019.00326

Farinotti, D., Huss, M., Fürst, J. J., Landmann, J., Machguth, H., Maussion, F., et al. (2019). A Consensus Estimate for the Ice Thickness Distribution of All Glaciers on Earth. *Nat. Geosci.* 12 (3), 168–173. doi:10.1038/s41561-019-0300-3

Funk, C., Peterson, P., Landsfeld, M., Pedreros, D., Verdin, J., Shukla, S., et al. (2015). The Climate Hazards Infrared Precipitation with Stations-A New Environmental Record for Monitoring Extremes. *Sci. Data* 2 (1), 150066. doi:10.1038/sdata.2015.66

Gardner, A. S., Fahnestock, M. A., and Scambos, T. A. (2019). *ITS_LIVE Regional Glacier and Ice Sheet Surface Velocities*. Boulder, CO: Data archived at National Snow and Ice Data Center. [accessed March 2021]:. doi:10.5067/6II6VW8LLWJ7

Glasser, N. F., Holt, T. O., Evans, Z. D., Davies, B. J., Pelto, M., and Harrison, S. (2016). Recent Spatial and Temporal Variations in Debris Cover on Patagonian Glaciers. *Geomorphology* 273, 202–216. doi:10.1016/j.geomorph.2016.07.036

Haritashya, U., Kargel, J., Shugar, D., Leonard, G., Strattman, K., Watson, C., et al. (2018). Evolution and Controls of Large Glacial Lakes in the Nepal Himalaya. *Remote Sensing* 10 (5), 798. doi:10.3390/rs10050798

Iken, A. (1981). The Effect of the Subglacial Water Pressure on the Sliding Velocity of a Glacier in an Idealized Numerical Model. *J. Glaciol.* 27 (97), 407–421. doi:10.3198/1981JoG27-97-407-42110.1017/s0022143000011448

Immerzeel, W. W., Kraaijenbrink, P. D. A., Shea, J. M., Shrestha, A. B., Pellicciotti, F., Bierkens, M. F. P., et al. (2014). High-resolution Monitoring of Himalayan Glacier Dynamics Using Unmanned Aerial Vehicles. *Remote Sensing Environ.* 150, 93–103. doi:10.1016/j.rse.2014.04.025

Iribarren Anacona, P., Mackintosh, A., and Norton, K. P. (2015). Hazardous Processes and Events from Glacier and Permafrost Areas: Lessons from the Chilean and Argentinean Andes. *Earth Surf. Process. Landforms* 40 (1), 2–21. doi:10.1002/esp.3524

Iribarren Anacona, P., Norton, K. P., and Mackintosh, A. (2014). Moraine-dammed lake Failures in Patagonia and Assessment of Outburst Susceptibility in the Baker Basin. *Nat. Hazards Earth Syst. Sci.* 14 (12), 3243–3259. doi:10.5194/nhess-14-3243-2014

Jaber, W. A., Floricioiu, D., and Rott, H. (2016). "Geodetic Mass Balance of the Patagonian Icefields Derived from SRTM and TanDEM-X Data." in Proceeding of the 2016 IEEE International Geoscience and Remote Sensing Symposium (IGARSS), Beijing, China, July 2016, 342–345.doi:10.1109/igarss.2016.7729082

James, M. R., Chandler, J. H., Eltner, A., Fraser, C., Miller, P. E., Mills, J. P., et al. (2019). Guidelines on the Use of Structure-from-motion Photogrammetry in

Geomorphic Research. *Earth Surf. Process. Landforms* 44 (10), 2081–2084. doi:10.1002/esp.4637

James, M. R., and Robson, S. (2014). Mitigating Systematic Error in Topographic Models Derived from UAV and Ground-Based Image Networks. *Earth Surf. Process. Landforms* 39 (10), 1413–1420. doi:10.1002/esp.3609

King, O., Bhattacharya, A., Bhambri, R., and Bolch, T. (2019). Glacial Lakes Exacerbate Himalayan Glacier Mass Loss. *Sci. Rep.* 9 (1), 18145. doi:10.1038/s41598-019-53733-x

King, O., Dehecq, A., Quincey, D., and Carrivick, J. (2018). Contrasting Geometric and Dynamic Evolution of lake and Land-Terminating Glaciers in the central Himalaya. *Glob. Planet. Change* 167, 46–60. doi:10.1016/j.gloplacha.2018.05.006

Kirkbride, M. P. (1993). The Temporal Significance of Transitions from Melting to Calving Termini at Glaciers in the central Southern Alps of New Zealand. *The Holocene* 3 (3), 232–240. doi:10.1177/095968369300300305

Kirkbride, M. P., and Warren, C. R. (1999). Tasman Glacier, New Zealand: 20th-century Thinning and Predicted Calving Retreat. *Glob. Planet. Change* 22 (1), 11–28. doi:10.1016/S0921-8181(99)00021-1

Konya, K., and Matsumoto, T. (2010). Influence of Weather Conditions and Spatial Variability on Glacier Surface Melt in Chilean Patagonia. *Theor. Appl. Climatol* 102 (1), 139–149. doi:10.1007/s00704-009-0248-0

Kraaijenbrink, P., Shea, J. M., Pellicciotti, F., Jong, S. M. d., and Immerzeel, W. W. (2016b). Object-based Analysis of Unmanned Aerial Vehicle Imagery to Map and Characterise Surface Features on a Debris-Covered Glacier. *Remote Sensing Environ.* 186, 581–595. doi:10.1016/j.rse.2016.09.013

Kraaijenbrink, P., Meijer, S. W., Shea, J. M., Pellicciotti, F., De Jong, S. M., and Immerzeel, W. W. (2016a). Seasonal Surface Velocities of a Himalayan Glacier Derived by Automated Correlation of Unmanned Aerial Vehicle Imagery. *Ann. Glaciol.* 57 (71), 103–113. doi:10.3189/2016AoG71A072

Loriaux, T., and Casassa, G. (2013). Evolution of Glacial Lakes from the Northern Patagonia Icefield and Terrestrial Water Storage in a Sea-Level Rise Context. *Glob. Planet. Change* 102, 33–40. doi:10.1016/j.gloplacha.2012.12.012

Maurer, J. M., Schaefer, J. M., Rupper, S., and Corley, A. (2019). Acceleration of Ice Loss across the Himalayas over the Past 40 Years. *Sci. Adv.* 5 (6), eaav7266. doi:10.1126/sciadv.aav7266

Messerli, A., and Grinsted, A. (2015). Image Georectification and Feature Tracking Toolbox: ImGRAFT. *Geosci. Instrum. Method. Data Syst.* 4 (1), 23–34. doi:10.5194/gi-4-23-2015

Miles, E. S., Steiner, J., Willis, I., Buri, P., Immerzeel, W. W., Chesnokova, A., et al. (2017). Pond Dynamics and Supraglacial-Englacial Connectivity on Debris-Covered Lirung Glacier, Nepal. *Front. Earth Sci.* 5, 69. doi:10.3389/feart.2017.00069

Minowa, M., Schaefer, M., Sugiyama, S., Sakakibara, D., and Skvarca, P. (2021). Frontal Ablation and Mass Loss of the Patagonian Icefields. *Earth Planet. Sci. Lett.* 561, 116811. doi:10.1016/j.epsl.2021.116811

Minowa, M., Sugiyama, S., Sakakibara, D., and Skvarca, P. (2017). Seasonal Variations in Ice-Front Position Controlled by Frontal Ablation at Glaciar Perito Moreno, the Southern Patagonia Icefield. *Front. Earth Sci.* 5, 1. doi:10.3389/feart.2017.00001

Mölg, N., Ferguson, J., Bolch, T., and Vieli, A. (2020). On the Influence of Debris Cover on Glacier Morphology: How High-Relief Structures Evolve from Smooth Surfaces. *Geomorphology* 357, 107092. doi:10.1016/j.geomorph.2020.107092

Mouginot, J., and Rignot, E. (2015). Ice Motion of the Patagonian Icefields of South America: 1984-2014. *Geophys. Res. Lett.* 42 (5), 1441–1449. doi:10.1002/2014GL062661

Nie, Y., Sheng, Y., Liu, Q., Liu, L., Liu, S., Zhang, Y., et al. (2017). A Regional-Scale Assessment of Himalayan Glacial lake Changes Using Satellite Observations from 1990 to 2015. *Remote Sensing Environ.* 189, 1–13. doi:10.1016/j.rse.2016.11.008

Østrem, G. (1959). Ice Melting under a Thin Layer of Moraine, and the Existence of Ice Cores in Moraine Ridges. *Geografiska Annaler* 41 (4), 228–230. doi:10.1080/20014422.1959.11907953

Pellicciotti, F., Stephan, C., Miles, E., Herreid, S., Immerzeel, W. W., and Bolch, T. (2015). Mass-balance Changes of the Debris-Covered Glaciers in the Langtang Himal, Nepal, from 1974 to 1999. *J. Glaciol.* 61 (226), 373–386. doi:10.3189/2015JoG13J237

Purdie, J., and Fitzharris, B. (1999). Processes and Rates of Ice Loss at the Terminus of Tasman Glacier, New Zealand. *Glob. Planet. Change* 22 (1), 79–91. doi:10.1016/S0921-8181(99)00027-2

Quincey, D. J., and Glasser, N. F. (2009). Morphological and Ice-Dynamical Changes on the Tasman Glacier, New Zealand, 1990-2007. *Glob. Planet. Change* 68 (3), 185–197. doi:10.1016/j.gloplacha.2009.05.003

Quincey, D. J., Richardson, S. D., Luckman, A., Lucas, R. M., Reynolds, J. M., Hambrey, M. J., et al. (2007). Early Recognition of Glacial lake Hazards in the Himalaya Using Remote Sensing Datasets. *Glob. Planet. Change* 56 (1), 137–152. doi:10.1016/j.gloplacha.2006.07.013

Reynolds, J. M. (2000). *On the Formation of Supraglacial Lakes on Debris-Covered Glaciers*, 264. Wallingford, Oxfordshire, UK: IAHS Publ., 153–161. Symposium at Seattle 2000 - Debris-Covered Glaciers.

RGI, C. (2017). *Randolph Glacier Inventory – A Dataset of Global Glacier Outlines: Version 6.0: Technical Report, Global Land Ice Measurements from Space*. Colorado, USA: Digital Media. doi:10.7265/N5-RGI-60

Rivera, A., Benham, T., Casassa, G., Bamber, J., and Dowdeswell, J. A. (2007). Ice Elevation and Areal Changes of Glaciers from the Northern Patagonia Icefield, Chile. *Glob. Planet. Change* 59 (1), 126–137. doi:10.1016/j.gloplacha.2006.11.037

Robertson, C. M., Benn, D. I., Brook, M. S., Fuller, l. C., and Holt, K. A. (2012). Subaqueous Calving Margin Morphology at Mueller, Hooker and Tasman Glaciers in Aoraki/Mount Cook National Park, New Zealand. *J. Glaciol.* 58 (212), 1037–1046. doi:10.3189/2012JoG12J048

Rodriguez, J., Macciotta, R., Hendry, M. T., Roustaei, M., Gräpel, C., and Skirrow, R. (2020). UAVs for Monitoring, Investigation, and Mitigation Design of a Rock Slope with Multiple Failure Mechanism" a Case Study. *Landslides* 17 (9), 1–14. doi:10.1007/s10346-020-01416-4

Röhl, K. (2006). Thermo-erosional Notch Development at Fresh-Water-Calving Tasman Glacier, New Zealand. *J. Glaciol.* 52 (177), 203–213. doi:10.3189/172756506781828773

Rossini, M., Di Mauro, B., Garzonio, R., Baccolo, G., Cavallini, G., Mattavelli, M., et al. (2018). Rapid Melting Dynamics of an alpine Glacier with Repeated UAV Photogrammetry. *Geomorphology* 304, 159–172. doi:10.1016/j.geomorph.2017.12.039

Sakai, A., and Fujita, K. (2010). Formation Conditions of Supraglacial Lakes on Debris-Covered Glaciers in the Himalaya. *J. Glaciol.* 56 (195), 177–181. doi:10.3189/002214310791190785

Sakai, A., Nishimura, K., Kadota, T., and Takeuchi, N. (2009). Onset of Calving at Supraglacial Lakes on Debris-Covered Glaciers of the Nepal Himalaya. *J. Glaciol.* 55 (193), 909–917. doi:10.3189/002214309790152555

Sanz-Ablanedo, E., Chandler, J. H., Ballesteros-Pérez, P., and Rodríguez-Pérez, J. R. (2020). Reducing Systematic Dome Errors in Digital Elevation Models through Better UAV Flight Design. *Earth Surf. Process. Landforms* 45 (9), 2134–2147. doi:10.1002/esp.4871

Sato, Y., Fujita, K., Inoue, H., Sakai, A., and Karma (2021a). Land- to lake-terminating Transition Triggers Dynamic Thinning of a Bhutanese Glacier. *Cryosphere Discuss.* 2021, 1–21. doi:10.5194/tc-2021-286

Sato, Y., Fujita, K., Inoue, H., Sunako, S., Sakai, A., Tsushima, A., et al. (2021b). Ice Cliff Dynamics of Debris-Covered Trakarding Glacier in the Rolwaling Region, Nepal Himalaya. *Front. Earth Sci.* 9 (398), 623623. doi:10.3389/feart.2021.623623

Schaefer, M., Machguth, H., Falvey, M., and Casassa, G. (2013). Modeling Past and Future Surface Mass Balance of the Northern Patagonia Icefield. *J. Geophys. Res. Earth Surf.* 118 (2), 571–588. doi:10.1002/jgrf.20038

Shugar, D. H., Burr, A., Haritashya, U. K., Kargel, J. S., Watson, C. S., Kennedy, M. C., et al. (2020). Rapid Worldwide Growth of Glacial Lakes since 1990. *Nat. Clim. Chang.* 10, 939–945. doi:10.1038/s41558-020-0855-4

Shukla, A., Garg, P. K., and Srivastava, S. (2018). Evolution of Glacial and High-Altitude Lakes in the Sikkim, Eastern Himalaya over the Past Four Decades (1975-2017). *Front. Environ. Sci.* 6, 81. doi:10.3389/fenvs.2018.00081

Smith, M. W., Carrivick, J. L., and Quincey, D. J. (2015). Structure from Motion Photogrammetry in Physical Geography. *Prog. Phys. Geogr. Earth Environ.* 40 (2), 247–275. doi:10.1177/0309133315615805

Steiner, J. F., Buri, P., Miles, E. S., Ragettli, S., and Pellicciotti, F. (2019). Supraglacial Ice Cliffs and Ponds on Debris-Covered Glaciers: Spatio-

Temporal Distribution and Characteristics. *J. Glaciol.* 65 (252), 617–632. doi:10.1017/jog.2019.40

Sugiyama, S., Bauder, A., Huss, M., Riesen, P., and Funk, M. (2008). Triggering and Drainage Mechanisms of the 2004 Glacier-Dammed lake Outburst in Gornergletscher, Switzerland. *J. Geophys. Res.* 113 (F4), 920. doi:10.1029/2007JF000920

Sutherland, J. L., Carrivick, J. L., Gandy, N., Shulmeister, J., Quincey, D. J., and Cornford, S. L. (2020). Proglacial Lakes Control Glacier Geometry and Behavior during Recession. *Geophys. Res. Lett.* 47 (19), e2020GL088865. doi:10.1029/2020gl088865

Takasu, T., and Yasuda, A. (2009). "Development of the Low-Cost RTK-GPS Receiver with an Open Source Program Package RTKLIB." in Proceedings of the International Symposium on GPS/GNSS, Jeju, Korea, 4–6 November 2009, Available at: http://www.rtklib.com/.

Tsutaki, S., Fujita, K., Nuimura, T., Sakai, A., Sugiyama, S., Komori, J., et al. (2019). Contrasting Thinning Patterns between lake- and Land-Terminating Glaciers in the Bhutanese Himalaya. *The Cryosphere* 13 (10), 2733–2750. doi:10.5194/tc-13-2733-2019

Tsutaki, S., Sugiyama, S., Nishimura, D., and Funk, M. (2013). Acceleration and Flotation of a Glacier Terminus during Formation of a Proglacial lake in Rhonegletscher, Switzerland. *J. Glaciol.* 59 (215), 559–570. doi:10.3189/2013JoG12J107

Tweed, F. S., and Russell, A. J. (1999). Controls on the Formation and Sudden Drainage of Glacier-Impounded Lakes: Implications for Jökulhlaup Characteristics. *Prog. Phys. Geogr. Earth Environ.* 23 (1), 79–110. doi:10.1177/030913339902300104

Vallet, J., Panissod, F., Strecha, C., and Tracol, M. (2011). Photogrammetric Performance of an Ultra Light Weight Swinglet "UAV. *ISPRS - Int. Arch. Photogrammetry, Remote Sensing Spat. Inf. Sci.* 3822, 253.

Vaughan, D. G., Comiso, J. C., Allison, I., Carrasco, J., Kaser, G., Kwok, R., et al. (2013). "Observations: Cryosphere," in *Climate Change 2013: The Physical Science Basis. Contribution of Working Group I to the Fifth Assessment Report of the Intergovernmental Panel on Climate Change*. Editors T. F. Stocker, D. Qin, G.-K. Plattner, M. Tignor, S. K. Allen, J. Boschung, et al. (Cambridge, United Kingdom and New York, NY, USA: Cambridge University Press), 317–382.

Warren, C., and Aniya, M. (1999). The Calving Glaciers of Southern South America. *Glob. Planet. Change* 22 (1), 59–77. doi:10.1016/S0921-8181(99)00026-0

Watson, C. S., Kargel, J. S., Shugar, D. H., Haritashya, U. K., Schiassi, E., and Furfaro, R. (2020). Mass Loss from Calving in Himalayan Proglacial Lakes. *Front. Earth Sci.* 7 342. doi:10.3389/feart.2019.00342

Watson, C. S., King, O., Miles, E. S., and Quincey, D. J. (2018). Optimising NDWI Supraglacial Pond Classification on Himalayan Debris-Covered Glaciers. *Remote Sensing Environ.* 217, 414–425. doi:10.1016/j.rse.2018.08.020

Willis, M. J., Melkonian, A. K., Pritchard, M. E., and Ramage, J. M. (2012). Ice Loss Rates at the Northern Patagonian Icefield Derived Using a Decade of Satellite Remote Sensing. *Remote Sensing Environ.* 117, 184–198. doi:10.1016/j.rse.2011.09.017

Wilson, R., Glasser, N. F., Reynolds, J. M., Harrison, S., Anacona, P. I., Schaefer, M., et al. (2018). Glacial Lakes of the Central and Patagonian Andes. *Glob. Planet. Change* 162, 275–291. doi:10.1016/j.gloplacha.2018.01.004

Wilson, R., Harrison, S., Reynolds, J., Hubbard, A., Glasser, N. F., Wündrich, O., et al. (2019). The 2015 Chileno Valley Glacial lake Outburst Flood, Patagonia. *Geomorphology* 332, 51–65. doi:10.1016/j.geomorph.2019.01.015

Zhang, B., Liu, G., Zhang, R., Fu, Y., Liu, Q., Cai, J., et al. (2021). Monitoring Dynamic Evolution of the Glacial Lakes by Using Time Series of Sentinel-1A SAR Images. *Remote Sensing* 13 (7), 1313. doi:10.3390/rs13071313

Conflict of Interest: The authors declare that the research was conducted in the absence of any commercial or financial relationships that could be construed as a potential conflict of interest.

Publisher's Note: All claims expressed in this article are solely those of the authors and do not necessarily represent those of their affiliated organizations, or those of the publisher, the editors and the reviewers. Any product that may be evaluated in this article, or claim that may be made by its manufacturer, is not guaranteed or endorsed by the publisher.

frontiers | Frontiers in Earth Science

ORIGINAL RESEARCH
published: 05 July 2022
doi: 10.3389/feart.2022.848652

Chlorine-36 Surface Exposure Dating of Late Holocene Moraines and Glacial Mass Balance Modeling, Monte Sierra Nevada, South-Central Chilean Andes (38°S)

Brittany N. Price[1], Nathan D. Stansell[1], Alfonso Fernández[2], Joseph M. Licciardi[3], Alia J. Lesnek[3,4], Ariel Muñoz[5,6,7], Mary K. Sorensen[1], Edilia Jaque Castillo[8], Tal Shutkin[9,10], Isabella Ciocca[2] and Ianire Galilea[8]*

[1]Department of Earth, Atmosphere and Environment, Northern Illinois University, Dekalb, IL, United States, [2]Department of Geography, Mountain GeoScience Group, Universidad de Concepción, Concepción, Chile, [3]Department of Earth Sciences, University of New Hampshire, Durham, NH, United States, [4]School of Earth and Environmental Sciences, Queens College, City University of New York, Queens, NY, United States, [5]Institute of Geography, Pontificia Universidad Católica de Valparaíso, Valparaíso, Chile, [6]Center for Climate and Resilience Research CR2, Santiago, Chile, [7]Center for Climate Action, Pontificia Universidad Católica de Valparaíso, Valparaíso, Chile, [8]Department of Geography, Universidad de Concepción, Concepción, Chile, [9]The Ohio State University, Byrd Polar and Climate Research Center and Department of Geography, Columbus, OH, United States, [10]The Ohio State University, Department of Geography, Columbus, OH, United States

OPEN ACCESS

Edited by:
Jacob M. Bendle,
University of Northern British Columbia, Canada

Reviewed by:
Joanna Charton,
Aix-Marseille Université, France
Lucas O. Bianchi,
Consejo Nacional de Investigaciones Científicas y Técnicas (CONICET), Argentina

***Correspondence:**
Brittany N. Price
bprice@niu.edu

Specialty section:
This article was submitted to Quaternary Science, Geomorphology and Paleoenvironment, a section of the journal Frontiers in Earth Science

Received: 04 January 2022
Accepted: 06 June 2022
Published: 05 July 2022

Citation:
Price BN, Stansell ND, Fernández A, Licciardi JM, Lesnek AJ, Muñoz A, Sorensen MK, Jaque Castillo E, Shutkin T, Ciocca I and Galilea I (2022) Chlorine-36 Surface Exposure Dating of Late Holocene Moraines and Glacial Mass Balance Modeling, Monte Sierra Nevada, South-Central Chilean Andes (38°S). Front. Earth Sci. 10:848652. doi: 10.3389/feart.2022.848652

The development of robust chronologies of Neoglaciation from individual glaciers throughout the high-altitude Andes can provide fundamental knowledge of influences such as regional temperature and precipitation variability, and aid in predicting future changes in the Andean climate system. However, records of Late Holocene glaciation from the Central Chilean Andes are sparse, and often poorly constrained. Here, we present ^{36}Cl surface exposure ages, dendrochronologic constraints, and glacial mass balance modeling simulations of Late Holocene glacier fluctuations in the Central-South Chilean Andes. A series of concentric moraine ridges were identified on Monte Sierra Nevada (38°S), where exposure dating of basaltic boulders was used to establish a chronology of ice recession. We infer that moraine abandonment of the most distal ridge in the valley commenced by ~4.2 ka, and was followed by glacier margin retreat to an up-valley position. Exposure ages of the oldest Late Holocene boulders (~2.5–0.8 ka) along the marginal extents of the moraine complex indicate fluctuations of the glacier terminus prior to ~0.65 ka. A final expansion of the ice margin reoccupied the position of the 4.2 ka moraine, with abatement from the outermost composite moraine occurring by ~0.70 ka, as constrained by tree-ring data from live *Araucaria araucana* trees. Finally, a series of nested moraines dating to ~0.45–0.30 ka, formed from a pulsed ice recession during the latest Holocene when the lower reaches of the glacial snout was most likely debris mantled. A distributed temperature index model combined with a glacier flow model was used to quantify an envelope of possible climatic conditions of Late Holocene glaciation. The glacial modeling results suggest conditions were ~1.5°C colder and 20% wetter during peak Neoglaciation relative to modern conditions. These records also suggest a near-coeval record of Late Holocene climate variability between the middle and high southern latitudes. Furthermore, this study presents some of the youngest ^{36}Cl exposure ages reported for moraines in the

Andes, further supporting this method as a valuable geochronologic tool for assessing Late Holocene landscape development.

Keywords: cosmogenic nuclides, alpine glaciers, paleoclimate, little ice age, temperature index model, moraine chronology, dendrochronology, glacial geomorphology

INTRODUCTION

The Central-South Chilean (CSCh, **Table 1**) Andes (~37.5°S) marks a critical climatic and geographic boundary between the low and high latitudes (Muñoz et al., 2016), thus studying glacial fluctuations in this region can provide information about past inter-hemispheric oceanic and atmospheric dynamics (Liu and Yang, 2003). To the south, glacial mass balances in the Northern Patagonian Andes are largely dominated by the strength of Pacific Ocean westerlies, El Niño Southern Oscillation (ENSO), and the South Pacific Subtropical High (SPSH) (Aravena and Luckman, 2009; Garreaud et al., 2009; Garreaud et al., 2013). Likewise, the Southern Annular Mode (SAM) affects the position and intensity of the westerlies, summer temperatures, and rainfall distribution (Gillett et al., 2006; Reynhout et al., 2019). Disentangling these complex systems is critical for our ability to predict future changes in the Andean environment and global climate system in response to natural and anthropogenic forcings. Our research aims to evaluate the climatic conditions driving glacial growth and decay in the CSCh Andes over the Late Holocene, and assess whether discreet leads and lags in the Andean cryosphere system are discernable regionally over the Neoglacial period.

Glacial melt is an important source of water in CSCh, so properly understanding the conditions and locations of glacier survival under future warming scenarios is pivotal to mitigating current water usages for sustainability (Huss and Fischer, 2016; Barcaza et al., 2017; Racoviteanu et al., 2021). In this context, it is unclear how individual glaciers might respond to localized climatic effects vs. more regional or synoptic-scale processes (Rupper and Roe, 2008), as future climate change scenarios will not impact all regions of the Andes synchronously, or at the same rate or magnitude. Furthermore, other landscape-specific questions have yet to be addressed, such as the extent of debris coverage on regional glaciers in the recent past, an important factor for understanding mountain water storage.

Our ability to link Chilean glacial variability and specific environmental forcings will be improved with a robust chronology of past events. At present, individual records are often broadly bracketed by both minimum and maximum ages, resulting in chronologies that lack the resolution necessary to fully decern the local stratigraphy. By integrating surface exposure dating and dendrochronology (Harrison et al., 2008; Nimick et al., 2016), we aim to better constrain the timing of Late Holocene glacial fluctuations from CSCh.

Various chronologies of glacial advances have been proposed to reflect the datasets gathered from southernmost South America. For example, Mercer (1976) originally proposed three distinct Neoglacial events in the Chilean Andes, while Aniya (2013) posited five Neoglacial events over the same interval, with subtle differences in the timing of glacial advances and retreat. Nevertheless, glacier fluctuations in the CSCh Andes and northern Patagonia still lack detailed regional records to constrain large scale recessional timing during Neoglaciation, and particularly the Late Holocene. A more recent examination of glacial records from northern Patagonia dates the greatest ice readvances from the Late Holocene to between 2–1 ka and 0.5–0.2 ka, with the largest overall advances since the mid-Holocene occurring at ~5 ka (Davies et al., 2020).

Recent developments in cosmogenic dating now allow direct age determination on Neoglacial moraine boulders, including the Southern Hemisphere expression of the LIA, defined as 0.67–0.17 ka (García-Ruiz et al., 2014; Solomina et al., 2015; Jomelli et al., 2016). Exposure ages this young have more commonly been derived from ^{10}Be measurements on silica-rich rocks (Licciardi et al., 2009; Schürch et al., 2016; Dong et al., 2017; Biette et al., 2021), and until recently dating the basalt-rich rocks in the CSCh Andes has been seldomly attempted. These basalts often lack well-developed phenocrysts (e.g., feldspars) necessary for analyzing ^{36}Cl in mineral separates, which can minimize complexities and uncertainties in ^{36}Cl production and exposure age interpretations (Wirsig et al., 2016). Currently, only a few studies have applied similar methods to date moraine boulders in volcanic landscapes (e.g., Alcalá-Reygosa et al., 2018), largely because of ^{36}Cl production systematics that yield high uncertainties in Cl-rich rocks (e.g., Palacios et al., 2017). Despite challenges associated with ^{36}Cl surface exposure dating, this cosmogenic nuclide is well-suited for lithologies lacking quartz, and allows for exposure dating of moraine boulders that in some cases were emplaced only hundreds of years ago (Jomelli et al., 2016; Jomelli et al., 2017; Charton et al., 2021a; Verfaillie et al., 2021).

TABLE 1 | Abbreviations used in manuscript.

Term	Abbreviation
Central-South Chile	CSCh
El Niño Southern Oscillation	ENSO
South Pacific Subtropical High	SPSH
Southern Annular Mode	SAM
above sea level	a.s.l
accelerator mass spectroscopy	AMS
Little Ice Age	LIA
Southern Westerly Wind Belt	SWWB
Antarctic Circumpolar Current	ACC
Global Historical Climate Network	GHCN
Area Altitude Balance-Ratio	AABR
equilibrium line altitude	ELA
distributed temperature index model	DETIM
sea surface temperatures	SSTs
degree day factor	DDF

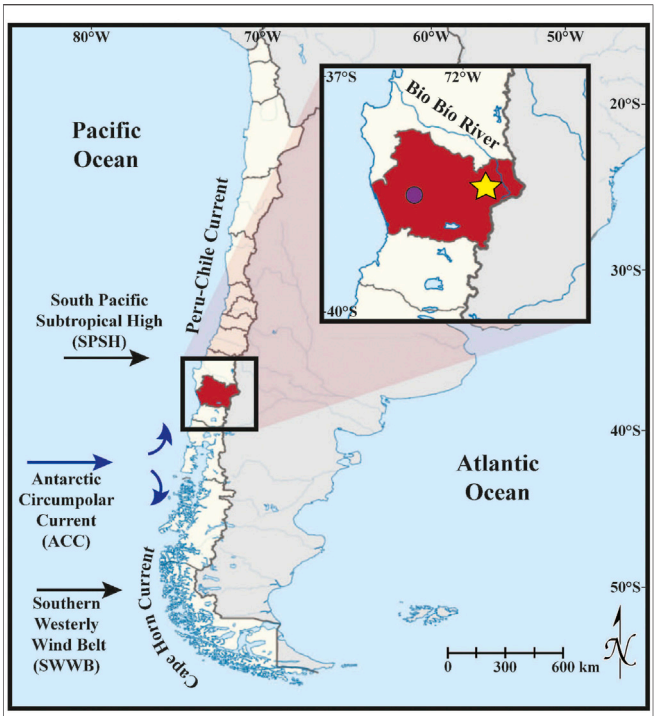

FIGURE 1 | Map of South America with Chile (beige with brown outline). Relative positions of the winds associated with the dominant precipitation bearing South Pacific Subtropical High (SPSH), and Southern Westerly Wind Belt (SWWB) during the Austral summer months are indicated with black arrows. Major oceanic currents near the study site (Antarctic Circumpolar Current, Peru-Chile Current and Cape Horn Current) are indicated with blue arrows. Inset box shows the proximity of the identified modern climatic transition zone of ~37.5°S (Muñoz et al., 2016) to the nearby Araucanía region of Chile (filled in red). A yellow star identifies the location of Monte Sierra Nevada (~38°S), and the location of the Temuco weather station used for the modeling analysis is represented by a purple circle.

Glacial studies in the Chilean Andes have also been hindered by a lack of physically-based models that test a range of climate drivers (Pellicciotti et al., 2014). As such, our knowledge of fundamental influences like temperature and precipitation changes on individual glaciers and ice caps throughout the Andes remain minimally constrained. Moreover, different modeling approaches produce a diverse range of outputs at varying resolutions, making it difficult to converge on a standardized approach for interpreting past glacial variability (Fernández and Mark, 2016). Nevertheless, coupling local station data with temperature index models produces first-order estimates of glacial sensitivity to climate change (Hock and Holmgren, 2005), including paleo-climate scenarios (Kull and Grosjean, 2000). Testing and deploying a physically-based glacier mass balance model provides a tool for addressing outstanding questions relating to the timing and causes of Late Holocene climate change. Climatic conditions during Late Holocene glacial advances are assessed to have been cold and wet, corresponding to a negative SAM phase (Moreno et al., 2018), but the magnitude of these temperature and precipitation changes have yet to be quantified for specific regions of the Andes.

Here we present a new glacial chronology using independently derived tree-ring data combined with ^{36}Cl ages on glacial boulders from a cirque valley atop Monte Sierra Nevada, Chile (38°34′56″ S, 71°34′47″ W) (**Figure 1**). Located at the southernmost expression of an area (31–38°S) categorized as hosting warm- and wet-based glaciers, the glacial mass balance here should be sensitive to both temperature and precipitation changes (Sagredo and Lowell, 2012). This chronology is coupled with the Hock (1999) distributed temperature index model (DETIM), establishing a range of possible precipitation and temperature values at the time of moraine abandonment using proxy and modeled data.

BACKGROUND

Geologic Setting and Geomorphology

Monte Sierra Nevada stands at 2,527 m above sea level (a.s.l.), with ice capping the highest peaks and extending partially down several east-facing cirque valleys (**Figure 2**). The site is located to the west of the Cordillera Principal, which is made up of the granitoid North Patagonia Batholith (The Cura-Mallin Formation) of Cretaceous and Miocene age (Glodny et al., 2006). Pleistocene and Holocene volcanoes (e.g., Llaima, Lonquimay, Sierra Nevada, and Tolhuaca) make up the active volcanic arc of the Cordillera Principal that formed on the eroded, and relatively flat-lying Miocene-aged rocks (Muñoz et al., 2011). Regionally, this southern volcanic zone is predominantly composed of basalts and basaltic andesites (Hickey et al., 1986; Ferguson et al., 1992; Muñoz et al., 2011). Additionally, these active Holocene volcanos might have deposited volcanic ash on glaciated terrain, potentially affecting glaciers' response to climate changes by two competing effects associated with debris thickness and temperature: insulation from incoming energy or enhancement of ablation (Davies and Glasser, 2012).

In our study area, there are a total of five morainal loops along the valley floor over a distance of ~350 m (**Figure 3**). Mapped moraines exhibit variable effects of weathering and erosion suggesting relative age differences. We number each moraine, starting with the oldest and most distal from the current glacier front (M1), progressing westward to the youngest, most ice-proximal moraine (M5) (**Figure 3**). Visually, moraine M2 is the largest and most intact of the moraine complex, while moraine M1 is the sole moraine in the valley with observed soil development, and exhibits a subtle dual-crest to the south of the field site. On the ice-proximal side of moraine M5 chaotic hummocks are observed, with glacial scree deposits further up valley (**Figure 4**). Additionally, several striated boulders and roches moutonnées are observed, both within and outside of the moraine complex.

The geomorphology of Monte Sierra Nevada yields information on the relative timing of glacial landform development due to the stratigraphy observed in the valley. For example, the distal end of the valley is truncated by a steep cliff at the contact between the relatively flat-lying Pleistocene volcanic layers and the underlying Miocene plutonic rocks (**Figure 4**). The steep topography below this

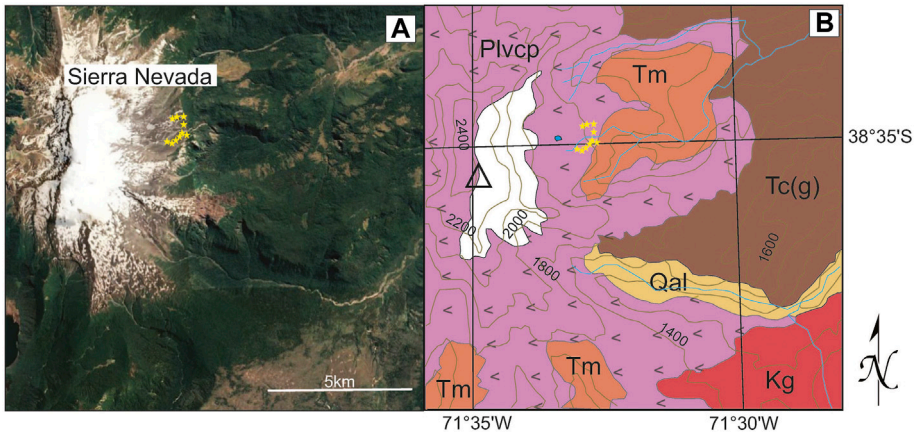

FIGURE 2 | Panel **(A)** Google Earth map of Monte Sierra Nevada and surrounding area with sample locations marked by yellow stars. Panel **(B)** Geologic map, modified from Muñoz et al. (2011). Qal—Quaternary alluvium, Plvcp—Upper Pleistocene-Holocene volcanic rocks, Tc—Miocene Cura-Mallin Formation, Tm—Miocene Melipeuco Plutonic Group, Kg—Cretaceous Galletué Plutonic Group.

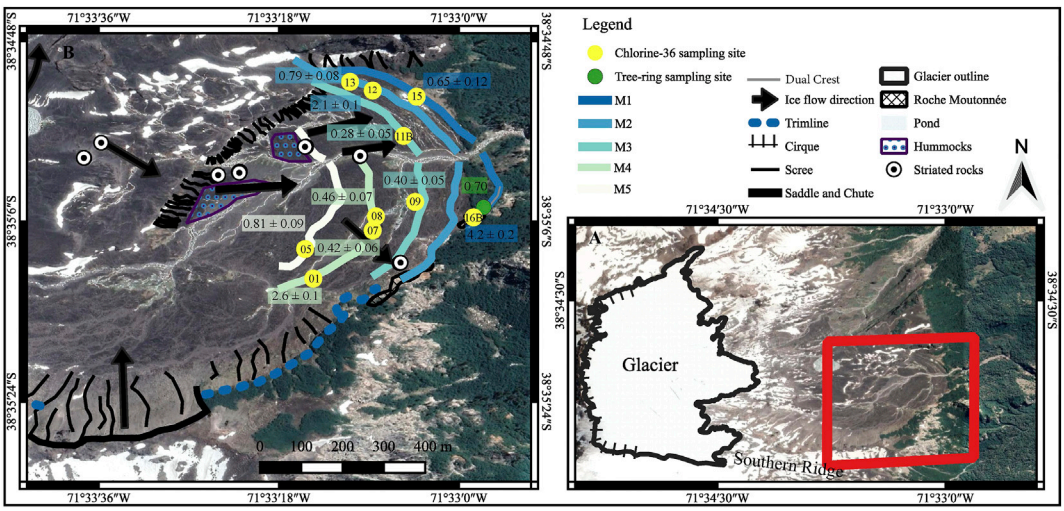

FIGURE 3 | Panel **(A)** Google Earth image of the Monte Sierra Nevada field site, with the modern glacier outlined in black and the moraine complex outlined in red. Panel **(B)** Ariel photograph of the field site as delineated by red box in panel A. Map identifies glacial moraines (M1-M5), locations of samples taken for ^{36}Cl (yellow circles with abbreviated sample number) and tree ring (green circle) dating. ^{36}Cl ages are reported in thousand years before present with internal uncertainty. Probable ice flow directions are represented by black arrows based on observed striated rock surfaces (white circles). Trimline along the southern ridge of the valley is marked (blue dashed line), as well as the saddle and chute (black line).

contact likely precludes the establishment of moraines from glacial advances that were more extensive than the presumed Late Holocene moraines that end just before a steep drop in topography to the valley below. On Monte Sierra Nevada, moraines are generally limited to elevations between ~1,703 and 1,722 m a.s.l (**Table 2**) and the moraines have since been bifurcated by Holocene stream development.

Directly south of the valley with the mapped moraine complex is a ridge separating it from the adjacent, topographically higher valley (**Figure 3**). On the ridge separating the two valleys is a well-defined saddle and chute, both of which are currently ice free. Along this same ridge is a trimline indicating the most recent highest extent of ice thickness in the valley. This trimline extends down valley intersecting moraine M1, as well as up valley past the saddle and chute towards the mountain's peak. The chute exhibits a cross-cutting relationship with the trimline, having eroded any recognizable lateral features. Notable talus deposits are identifiable along the northern and southern valley walls, particularly below the trimline and along the chute. The modern glacial ice cap on Monte Sierra Nevada extends into the uppermost reaches of both valleys.

Climate and the Westerlies

Central Chile has a Mediterranean-type climate with mild, wet winters and dry, hot summers. The modern climate is largely

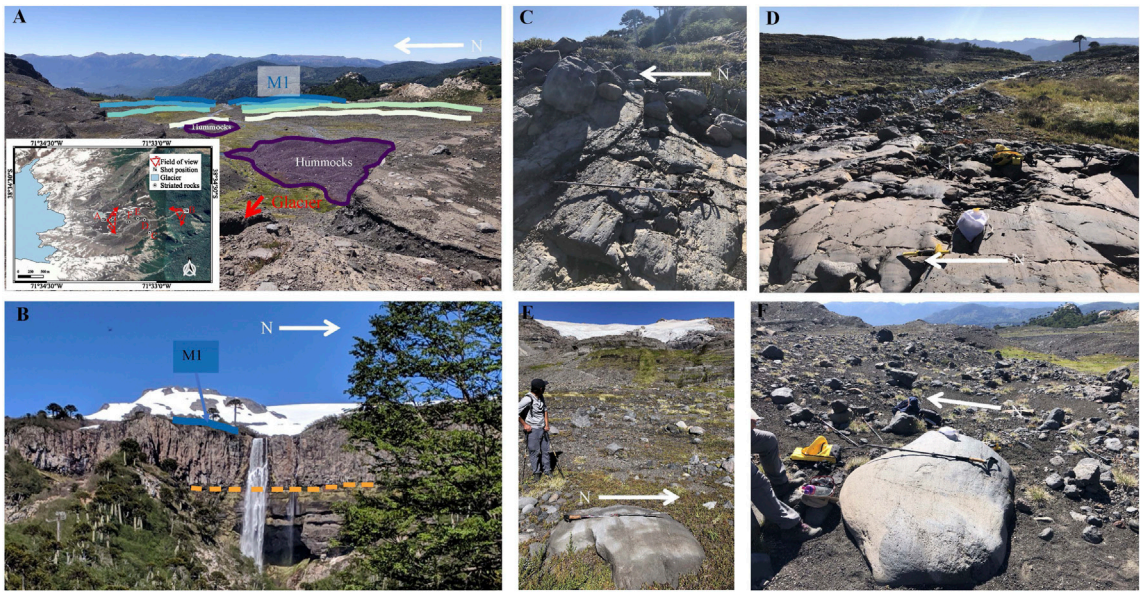

FIGURE 4 | Photographs of the Monte Sierra Nevada field site. Panel **(A)** Facing east the hummocky areas of the field site are outlined on the glacier proximal side of moraine M5 (purple). Panel **(B)** Facing west with the modern glacier in the background and contact between Pleistocene and Miocene volcanic rocks (orange dashed line) in the foreground behind waterfall. The cliff marks the limit of preserved Neoglacial moraine boulders, with moraine M1 (blue line) denoted to the south of the waterfall. The combined effects of topoclimatic constrains (i.e., lower elevations, seasonally constrained snow accumulation) make the existence of large glaciers in CSCh unlikely, as Neoglacial landforms are generally indistinguishable below this abrupt change in elevation. A grove of *A. araucana* trees is pictured to the south of the waterfall in the foreground. Panel **(C–F)** Striated boulders and roches moutonnées used for directional data to infer paleo-flowlines of the glacier. Inset map in panel A shows the location of each field picture, with letters corresponding to each panel.

TABLE 2 | Sample information used in the calculation of the ^{36}Cl boulder age expressed with internal uncertainty, calculated with a rock formation age of 130 ka using a developmental version of the CRONUS-Earth ^{36}Cl calculator (Balco et al., 2008; http://stoneage.ice-d.org/math/Cl36/v3/v3_Cl36_age_in.html) and LSDn scaling. The ICE-D calibration datasets used can be found at http://calibration.ice-d.org/allcds.

Sample ID	Moraine ID	Sample thickness (cm)	Latitude (°N)	Longitude (°S)	Elevation (m asl)	Topographic Shielding correction	^{36}Cl concentration	^{36}Cl Boulder age (ka)
AFCL18-05	M5	1.25	−38.58572	−71.55426	1721	0.9618	26,455 ± 2,525	0.81 ± 0.09
AFCL18-01	M4	0.4	−38.58654	−71.55409	1722	0.9414	64,419 ± 2,819	2.6 ± 0.1
AFCL18-07	M4	0.75	−38.58526	−71.55244	1712	0.9678	6,087 ± 783	0.42 ± 0.06
AFCL18-08	M4	1	−38.58487	−71.55235	1711	0.9734	19,023 ± 2,354	0.46 ± 0.07
AFCL18- 09	M3	1	−38.58441	−71.55126	1704	0.9726	5,490 ± 631	0.40 ± 0.05
AFCL18-11B	M3	1.25	−38.58258	−71.55158	1704	0.9689	13,408 ± 1850	0.28 ± 0.05
AFCL18-12	M2	0.75	−38.58132	−71.55244	1720	0.8741	58,565 ± 3,247	2.1 ± 0.1
AFCL18-13	M2	1.25	−38.58108	−71.55307	1717	0.743	23,502 ± 2,816	0.79 ± 0.08
AFCL18-15	M1	1.5	−38.58149	−71.55122	1711	0.9293	14,619 ± 2,392	0.65 ± 0.12
AFCL18-16B	M1	2	−38.58484	−71.54964	1703	0.9677	111,396 ± 5,503	4.2 ± 0.2

modulated by Pacific and Southern Ocean processes, resulting in a strong seasonality of precipitation south of ~35°. winter storms dominate here, bringing ~2,000 mm of annual rainfall to the region (Sinclair, 1996; Garreaud et al., 2009). However, Monte Sierra Nevada (38°S) is located near what is considered to be a transition zone between Mediterranean-subtropical and temperate-humid climatic zones, identified at ~37.5°S (**Figure 1**; Muñoz et al., 2016). Precipitation at this location is therefore impacted by shifts in the subtropical South Pacific Subtropical High (SPSH) and extratropical Southern Westerly Wind Belt (SWWB) year-round (Miller, 1976; Espinoza et al., 2020).

Glaciers in CSCh predominantly receive precipitation sourced from the Pacific Ocean due to the moisture barrier produced by the Andes mountains (Montecinos and Aceituno, 2003). Isotopic analyses of precipitation suggest that Atlantic-derived moisture rarely penetrates through to the western flanks of the Andes (Hoke et al., 2013). While regionally both the height and width of

the CSCh Andes are smaller in comparison to the Northern Cordillera, orographic precipitation leads to continental precipitation values that are up to three times larger than corresponding oceanic amounts (Garreaud et al., 2009).

In Central Chile the SPSH typically fluctuates between ~25 and 35°S and delivers moist air masses to the western slope of the Andes (Ancapichún and Garcés-Vargas, 2015). Active year-round, the position of the SPSH is modulated by the Bolivian High, which migrates northward during the austral winter (May-August) as the jet stream moves equatorward. This increase in winter storm tracks drives midlatitude precipitation along the central Chilean coast (Sinclair, 1996; Lamy et al., 2001; Garreaud et al., 2009; Espinoza, et al., 2020). From February-April the SPSH shifts south, resulting in increased precipitation off the coast of CSCh (~37°S) (Ancapichún and Garcés-Vargas, 2015). This hydrologic regime results in an enhanced probability of aridity in CSCh, as streamflow peaks in winter due to rainfall and again in late spring as seasonal snow melts in the mountains.

The regional climate in the CSCh Andes is also affected by the Antarctic Circumpolar Current (ACC). The ACC splits as it approaches the western coast of South America between ~40 and 45°S (Boltovskoy, 1976; Villalba et al., 2012), with the Peru-Chile Current flowing north and the Cape Horn Current flowing south (Lamy et al., 2007). The Peru-Chile Current transports cold, low-saline waters equatorward (Strub, 1998), with seasonal changes in upwelling driven by the position and intensity of the SPSH (Garreaud et al., 2009; Ancapichún and Garcés-Vargas, 2015). The SPSH is thus one of the dominant controls on sea surface temperatures (SSTs) associated with the Peru-Chile Current, with the ability to increase upwelling and offshore Ekman transport. The position of the ACC also results in strong winds directed at the coast, in the form of the SWWB. Situated between the subtropical anticyclone and subpolar cyclonic air masses, these westerlies bring strong winds and abundant precipitation to CSCh and the adjacent northern Patagonian Andes, intersecting the western coast of South America between 40°S-55°S (Bertrand et al., 2014). During Austral summer the SWWB strengthens, contracts, and shifts to the southern extent of its range in response to southern-ocean processes, while during the winter months the SWWB weakens and expands both poleward and towards the equator (Bentley et al., 2009). Comparatively, the SWWB is stronger than the storm tracks associated with the SPSH at the study location, as it is confined to a smaller latitudinal range and more directly affects regional precipitation.

El Niño Southern Oscillation and Southern Annular Mode

Located in the transition zone between Mediterranean and temperate climates, both ENSO and SAM play important roles in driving changes in temperature and moisture availability to Monte Sierra Nevada. ENSO is characterized by shifting oceanic-atmospheric conditions in the tropical Pacific, the effects of which are superimposed on the climate system of CSCh. El Niño (La Niña) years are associated with a weakening (strengthening) of the Peru-Chile Current, due to a reduction in the east-west pressure gradient (Montecinos and Aceituno, 2003), forcing a weaker SPSH into more northerly position (Villalba, 1994). This northward displacement of the SPSH reduces moisture availability in CSCh. When SSTs are lower the high-pressure system strengthens, and westerly trade winds intensify in response (Bertrand et al., 2014). In the northern portion of the transition zone (35–40°S), ENSO is characterized as having a stronger influence on the SPSH (Rutllant and Fuenzalida, 1991), whereas south of ~40°S interannual precipitation driven by the SWWB is heavily modulated by the strength/phase of the SAM (Aravena and Luckman, 2009; Garreaud et al., 2009; Villalba et al., 2012).

The SAM is measured by changes in sea-surface pressure between the mid- and high-latitudes (Villalba et al., 2012; Ancapichún and Garcés-Vargas, 2015). Both the strength and position of the SWWB is dictated by SSTs, and sea surface pressure gradients associated with the ACC and the Southern Ocean, specifically the SAM (Gillett et al., 2006; Reynhout et al., 2019). Enhancement of precipitation in Patagonia south of ~55°S is predominantly driven by a southern displacement of the SWWB, subsequently resulting in decreased precipitation around 38–43°S. During negative (positive) phases of the SAM the SWWB shifts equatorward (poleward), resulting in more humid (arid) conditions in CSCh (Garreaud et al., 2009; Bertrand et al., 2014; Muñoz et al., 2016).

Regional Records of Late Holocene Climate Change

Proxy paleo-climate evidence suggests that Late Holocene glacial variability in the northern Patagonia Ice Field was driven by both precipitation and temperature (Bertrand et al., 2012). A tree-ring reconstruction of summer temperatures from northern Patagonia suggests there was a cold interval from ~1.1 to 0.95 ka, followed by warming until ~0.77 ka and another phase of cool and wet conditions peaking between ~0.68 and 0.38 ka (Villalba, 1994). Proxy paleoclimate records also suggest that from ~0.65 ka until the last century was the wettest interval of the last ~5,000 years in the southern Chilean Andes (Moreno et al., 2009). Moreno et al. (2018) strengthened this analysis, and documented that regional glacial advances in the southern Patagonia Ice Field were forced from negative SAM phases (cold and wet), that were modulated on regional scales by the position and intensity of the SWWB. Recently, Davies et al. (2020) compiled geomorphic evidence and recalibrated chronological data from dozens of studies assessing fluctuations of the Patagonian Ice Sheet from 35 ka to the present. Records detailing the Late Holocene from 41°S to 52°S noted climatic conditions alternated between cold/wet and warm/dry on centennial time scales (Elbert et al., 2013; Álvarez et al., 2015; Moreno and Videla, 2016; Moreno et al., 2018; Davies et al., 2020). Well-defined Late Holocene moraines are apparent regionally (Glasser et al., 2008; Glasser and Jansson, 2008; Davies and Glasser, 2012; Davies et al., 2020), but these advances overall do not seem to surpass moraines emplaced at ~5 ka. While these Late Holocene landforms exhibit clear evidence of later formation, such as vegetation differences and degradation (Davies and Glasser, 2012; Davies et al., 2020), it is

possible that positions of earlier advances were reoccupied (Sagredo et al., 2016; Davies et al., 2020).

Additional records of Neoglaciation in CSCh and to the north are also coarsely resolved. For example, glacier advances have been dated in the nearby Rio Grande basin (35°S) on the eastern (Argentinian) slope of the Andes: radiocarbon dating from peat bogs in contact with terminal moraines, which are located at elevations around 2,500 m, yielded ages between ~0.5 and 0.2 ka (Espizua and Pitte, 2009). On Monte Tronador (41°S), located to the south, tree-ring dating of frontal and lateral moraines (elevations around 1,000 m) of glaciers flowing toward the eastern side of the Andes indicated ages between ~1 and 0.4 ka, with some smaller ridges suggesting advances between the late 19th and early 20th centuries (Masiokas et al., 2009). On the Chilean slope, ^{10}Be exposure dating of boulders located atop moraines ridges (elevations between 1,700 and 2,000 m) in the foreground of the Cipreses glacier (34°S) yielded older ages compared to the other sites, clustered between ~1 and 0.6 ka, but with some samples older than 8.0 ka (Sagredo et al., 2016). Thus, while regionally distributed records suggest ice advanced at or around the time of the LIA, comprehensive studies that combine multiple independent dating methods, such as tree-ring records, with direct moraine ages in the same valley are lacking (Fernández et al., 2022).

METHODS

Mapping and Sampling

Moraines were initially mapped and targeted for sampling using Google Earth Pro imagery. The location and extent of these moraines was documented in greater detail in the field utilizing handheld GPS methods during our field campaign of November 2018, with additional geomorphic observations and mapping of the valley conducted in January 2022, when directional measurements were taken from striated rock surfaces to assess paleo ice-flow directions. Sample locations were measured with a single-frequency GPS receiver (Emlid reach). The receiver was placed on a rod and positioned on top of or to the side of each boulder, and recorded continuously for 10–15 min in RINEX format. Subsequently, these data were post-processed using the closest GPS base station available, located in Temuco, about 100 km from Monte Sierra Nevada (**Figure 1**). This differential correction delivered uncertainties in the order of ±0.8 m.

Basaltic boulders located atop moraine ridges were sampled for surface exposure dating, with a total of 10 processed for ^{36}Cl measurement. These boulders heights ranged from ~0.42 to ~2.3 m, and included basaltic conglomerates and fine-grained crystalline basalts (**Figure 5**). We preferentially selected the largest boulders perched on or near moraine crests, which increases the likelihood that the boulders have been stable and experienced minimal snow cover since deposition (**Supplementary Figure S1**.; Ivy-Ochs and Kober, 2008; Balco, 2011). Additionally, boulders were assessed for weathering characteristics to distinguish moraine boulders from rock fall (Zreda and Phillips, 2000; Briner et al., 2001). No suitable sample material for exposure dating was found on the expression of the proximal (M5) or near proximal (M4) moraines to the north of the stream, as an immature drainage network had eroded large sections of these moraines (**Figure 3**). Samples (~1 kg) were chiseled from the upper few centimeters of these basaltic boulders. Topographic shielding was measured by collecting azimuth and zenith angles every 15° at each sample location using a Suunto tandem compass/clinometer.

^{36}Cl Processing

Whole rock samples were sawed to a measured thickness of between 0.4 and 2.0 cm before crushing and sieving to collect grains between 250 and 125 μm. Chemical preparation of samples was conducted at the University of New Hampshire Cosmogenic Isotope Lab using a modified version of the protocols presented in Stone et al. (1996) and Licciardi et al. (2008). A key component of the modified procedures includes measuring ^{35}Cl/^{37}Cl on a ~1 g aliquot of rock prior to ^{36}Cl extraction and measurement on the full sample. The ~1 g aliquot was spiked with a ^{37}Cl-enriched solution ("LLNL Spike A"; ^{35}Cl/^{37}Cl = 0.93) and ~4,000 μg of Br, which served to increase the size of the final precipitate. Total sample Cl was determined through isotope dilution methods. ^{36}Cl was extracted as Ag(Cl,Br) from full rock samples in two analytical batches following standard procedures. All samples received a carrier solution containing ~4,000 μg of Br and a natural ratio Cl carrier (^{35}Cl/^{37}Cl = 3.127). This technique was used to better control the total Cl within the analytical batch and reduce potential AMS memory effects (Arnold et al., 2010; Finkel et al., 2013).

^{36}Cl Measurements and Calculations

Measurements of ^{35}Cl/^{37}Cl and ^{36}Cl/^{37}Cl were conducted using the 10 MV tandem accelerator at the Lawrence Livermore National Laboratory Center for Accelerator Mass Spectrometry (LLNL-CAMS). Analytical uncertainty on ^{35}Cl/^{37}Cl measurements ranged from 0.42 to 0.45%. Analytical uncertainty on ^{36}Cl/^{37}Cl AMS measurements was between 4.3 and 13%. Sample ^{36}Cl concentrations are corrected for lab background using an average blank value for the two analytical batches (4.12×10^4 atoms ^{36}Cl, n=2). Major and trace element concentrations in the samples were determined using x-ray fluorescence and inductively coupled plasma mass spectrometry at SGS Mineral Services in Burnaby, British Columbia, Canada. Analytical data used to determine surface exposure ages are provided in **Table 3**.

Moraine boulder exposure ages were calculated using a developmental version of the CRONUS-Earth ^{36}Cl calculator (Balco et al., 2008; http://stoneage.ice-d.org/math/Cl36/v3/v3_Cl36_age_in.html) and LSDn scaling (**Table 2**; Lifton et al., 2014). The ^{36}Cl calibration datasets applied by the calculator can be found in the ICE-D database at http://calibration.ice-d.org/allcds. Based on field observations, no corrections were made for rock surface erosion, vegetation cover, or snow coverage. A bulk density value of 2.7 was used for all samples. All cosmogenic ages here are presented as years prior to sampling (AD 2018).

We made corrections for nucleogenic ^{36}Cl production using a rock formation age of 130 ka (Muñoz et al., 2011). Nucleogenic

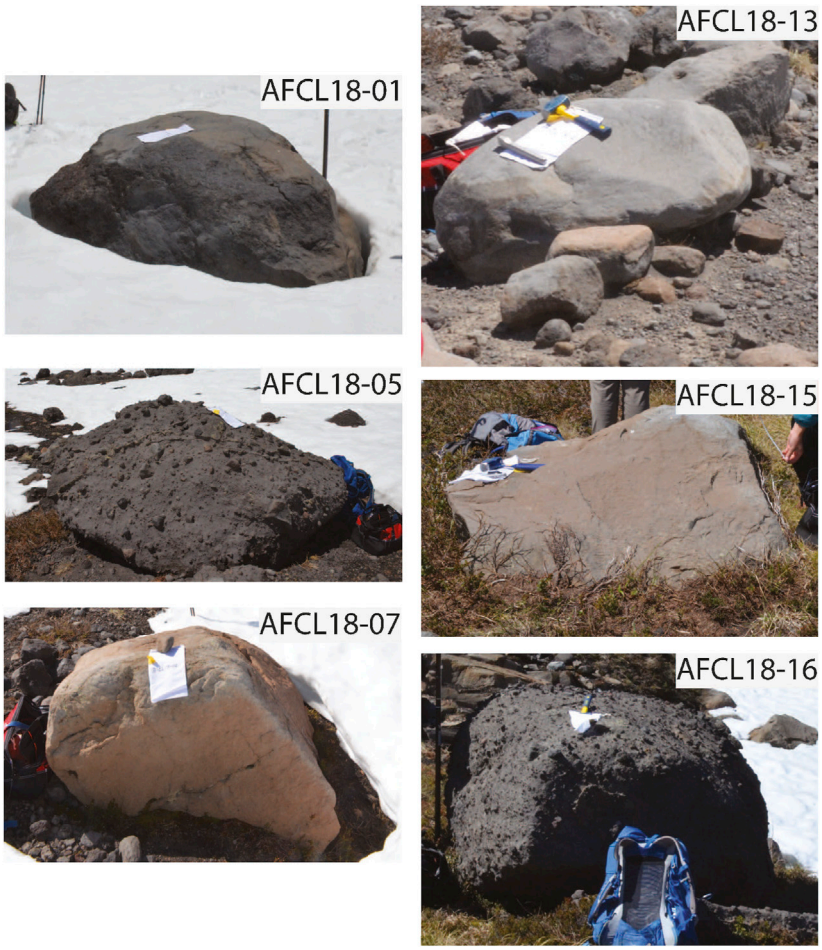

FIGURE 5 | Representative basaltic boulders (conglomerates and fine-grained crystalline) sampled for ^{36}Cl surface exposure dating.

^{36}Cl is produced in moderate amounts when ^{35}Cl absorbs neutrons released by the decay of U and Th isotopes (Gosse and Phillips, 2001). In rocks with high Cl, U, or Th concentrations, nucleogenic ^{36}Cl can thus constitute a substantial proportion of the total ^{36}Cl. In typical exposure age calculations, the amount of nucleogenic ^{36}Cl in a sample is calculated assuming steady state production, and that value is subtracted from the total ^{36}Cl to obtain the cosmogenic component (Marrero et al., 2016b). However, in young rocks (<1 Ma formation age), production and decay of nucleogenic ^{36}Cl may not be in equilibrium, and erroneously assuming steady state could lead to uncertain and/or inaccurate surface exposure age determinations (e.g., Sarikaya et al., 2019; Anjar et al., 2021). To assess the sensitivity of our ^{36}Cl ages to the time of rock formation, we also calculated ^{36}Cl ages assuming a rock formation age of 30 ka. Calculated surface exposure ages presented in the results and discussion of this study use a rock formation age of 130 ka to represent the last stage of volcanism on Monte Sierra Nevada based on lack of visual evidence of younger vents or deposits to support a formation age of 30 ka (Muñoz et al., 2011). Surface exposure ages representative of a younger date of rock formation of 30 ka are presented in **Supplementary Table S1**, as a possible late Pleistocene formation age has not been dismissed by available evidence.

Dendrochronology

Dendrochronology was used to obtain an approximate date of establishment for *Araucaria araucana* (Pewén) trees growing on the most distal moraine in the valley, to provide an independent minimum age of moraine formation and deglacial processes. To assess the minimum age of the moraine, increment borers were used to collect samples from mature *A. araucana* trees atop the outermost moraine (M1) of the proglacial area of the study site (**Figure 3**). These trees were selected with consideration to morphological attributes such as bark, height, diameter, as well as size and form of branches, all visual characteristics associated with old *A. araucana* trees. Two cores per tree from *A. araucana* (n=35) were extracted from living trees growing on the site using the aforementioned criteria, forming the "NEV" chronology. Samples were taken at 1.3 m from the soil, to assess a minimum age of the trees. Tree cores were then sanded for visual identification of growth rings (Stokes and Smiley, 1996), in

TABLE 3 | Elemental composition measured on whole rock samples after leaching. Major elements are in wt%, and trace elements in ppm unless noted otherwise.

	Major elements										Trace elements					
Sample ID	Al_2O_3 (wt%)	CaO (wt%)	Fe_2O_3 (wt%)	K_2O (wt%)	MgO (wt%)	MnO (wt%)	Na_2O (wt%)	P_2O_5 (wt%)	SiO_2 (wt%)	TiO_2 (wt%)	Cl (ppm)	B (mg/kg)	Sm (ppm)	Gd (ppm)	U (ppm)	Th (ppm)
AFCL18-01	17.84	7.17	9.46	1.15	2.98	0.14	4.11	0.03	55.51	1.1	93.85	15	1.8	2.23	0.81	2
AFCL18-05	18.6	8.68	9.71	0.61	5.05	0.15	3.18	0.14	51.8	0.92	163.39	13	3.1	3.59	0.52	1.6
AFCL18-07	21.37	9.18	7.06	0.8	2.22	0.11	3.92	0.02	53.52	0.88	22.49	14	3.2	3.55	0.67	1.8
AFCL18-08	17.41	7.99	10.31	0.8	5.38	0.16	3.26	0.18	51.95	1	205.26	14	3.7	3.6	0.7	2.3
AFCL18-09	20.94	9.04	7.34	0.81	2.39	0.12	3.84	0.02	53.3	0.9	20.02	29	3.1	3.27	0.76	1.6
AFCL18-11B	19.79	8.83	9.09	0.84	3.32	0.14	3.65	0.15	52.04	1.03	219.01	15	3.6	4.13	0.75	1.6
AFCL18-12	19.7	8.88	9.63	0.59	4.55	0.15	3.45	0.02	51.73	0.87	128.51	15	2.8	3.2	0.38	1.1
AFCL18-13	19.66	8.84	8.66	0.88	3.6	0.14	3.49	0.08	52.68	0.88	172.85	16	3.3	3.68	0.6	1.6
AFCL18-15	17.21	5.96	9.57	1.24	2.4	0.16	4.61	0.02	56.36	1.34	122.71	19	5.1	5.34	0.9	2.4
AFCL18-16B	17.94	8.37	10.24	0.71	5.49	0.16	3.39	0.15	52.03	1.03	159.74	17	3.6	4.15	0.5	1.3

order to be counted and measured in the Laboratory of Dendrochonology and Environmental Studies at Pontificia Universidad Católica de Valparaíso, Chile (https://www.pucv.cl/uuaa/site/edic/base/port/dendrolab.html). Ring width was measured to ±1 μm resolution using a Velmex system (https://www.velmex.com/), after which the COFECHA software (Holmes, 1983) was used to assess and corroborate the dating of each tree using the ring width measurement patterns across the suite of tree cores. Of the 35 sampled trees, 30 were able to be properly cross-dated. From these 30 trees, 20 exhibited curvatures close to the pith. We selected the five oldest trees that exhibited this curvature, suggesting a minimal age close to the total age of the tree, and using the Duncan method (Duncan, 1989) estimated the number of missing rings. The age of the oldest tree was used to provide an independent and cross-dated minimum age of the glacial landform from which the trees had colonized.

Glacial Modeling

We applied a modified version of DETIM by Hock (1999), which is available at http://regine.github.io/meltmodel/. As inputs, we used a climate file from the Global Historical Climatology Network (GHCN) (https://www.ncei.noaa.gov/products/land-based-station/global-historical-climatology-network-daily) with daily data from AD 2004–2013 (Temuco station, **Figure 1**), as well as the gridded NASADEM surface. The model also requires gridded surfaces for aspect and slope values that were calculated using the spatial analyst tools in ArcGIS 10.4.1. The model ran on the Cygwin64 C compiler following the approach of Stansell et al. (2022). The model ran with degree-day factors (DDFs) for ice and snow of 7 and 3.5 mmw. e. $K^{-1}\,d^{-1}$, values typically used for Chilean glaciers (Möller and Schneider, 2010).

The climate input file requires some pre-processing of climate data, including the calculation of a precipitation gradient and temperature lapse rate. The precipitation amount was set at a value of ×1.5 the values recorded from the Temuco station, which is similar to what is observed at other GHCN stations of similar elevation offsets in the region. No lapse rate was applied to the precipitation amounts along the glacier profile.

The model also requires an estimated temperature offset (Tdiff) corresponding to the location of the oldest mapped moraine (M1), which we independently determined by finding the difference between present (pr) and past (pa) Equilibrium Line Altitudes (ELAs) and applying a simple linear relationship using a lapse rate of 6.5°C/100 m:

$$T_{diff} = \left(ELA_{pr} - ELA_{pa}\right) \times 0.0065$$

We used the Area Altitude Balance-Ratio (AABR) method (Osmaston, 2005) to determine ELAs. The AABR method estimates the ELA using the hypsometry of the glacier or the proglacial area within the limits of former ice extents, usually demarked by moraines. We used the 12.5 pixel size DEM available from ALOS PALSAR imagery as a source of topographical information to build the hypsometric curve (ASF DAAC, 2015), and a 3-m resolution true-color composite from the Planet Constellation to interpret the glacier margin in 2013 and to derive ELA_{pr}. For the past hypsometry, we trimmed the ALOS DEM extending the current margin by following the pattern of the trimline to the moraine crest closest to the cliff (M1). For the calculation, the method iteratively searches the elevation of the zero-balance, assuming that the mass balance gradient is linear, with a steeper slope in the ablation zone (Kaser and Osmaston, 2002). A key component of this approach is to select a suitable ratio between mass balance gradients, which can be computed from mass balance observations and assumed to hold in the past. In our case we face the challenge that almost no mass balance data exists for the region. The few direct measurements available from the Mocho Glacier (Rivera et al., 2005; Schaefer et al., 2017), situated about 115 km to the south, suggest a balance ratio of 3.2, larger than figures commonly used, such as 1.75 or 2 (Osmaston, 2005). A recent study found that a value of 1.56 represents glaciers at a global scale, although with important spread (Oien et al., 2021). Guided by these studies, we tested several ratios, opting for 2.38 as a best approximation to represent this region. We notice, however, that the difference in ELAs between ratios of 1.56 and 3.2 is 47 and 77 m for the present and the past, respectively, which translates to an uncertainty of 0.2°C. Using the median AABR value of 2.38 results in an ELA_{pr} and an ELA_{pa} of ~2,267 m a.s.l. and ~2029 m a.s.l. This change in ELA (ΔELA) of -238 m translates to T_{diff} of ~−1.5°C.

We then ran the DETIM with multiple climate scenarios. First, the model was run over the interval from A.D. 2004 to 2013 with no change in temperature and precipitation relative to today. Next, we ran the model with 1.5°C cooling and a 20% increase in precipitation as a first approximation to simulate Neoglacial conditions that are represented by the AABR method. We assumed wetter conditions were associated with ice advances because proxy and modeling studies suggest that this region had increased precipitation amounts at times when it was colder during the Late Holocene (Bertrand et al., 2014). In order to test glacier sensitivity, we also ran the model with temperature changes of +1°C with a doubling of precipitation amounts. A series of other tests were run by changing only one variable at a time using ±1°C change in temperature, ±20% change in precipitation, and lapse rates ranging from 0.55°C/100 to 0.75°C/100. Additionally, to test the influence of DDFs, we adjusted the ice and snow values by ±1, following the approach of Möller et al. (2007).

Finally, we applied the flow model of Plummer and Phillips (2003) to simulate glacial thickness using the input of the mass balance grid. While the mass balance model identifies areas of ablation and accumulation, the flow model predicts the shape, size, and extent that a glacier stabilizes at for those conditions at steady-state. The model applies the standard flow law for ice using the shallow ice approximation, and using multiple interpolation methods. The results of the combined energy mass balance and flow models are shown in **Figure 6**. For all model runs, we present the lowest altitude of ice limit, maximum and average ice thickness values (**Table 4**).

RESULTS

Boulder ^{36}Cl Ages

The surface exposure ages of moraines on Monte Sierra Nevada range from 4.2 ± 0.2 ka to 0.28 ± 0.05 ka, and represent multiple phases of glacial growth and decay (**Figure 7**; **Table 2**). Sample AFCL18-16B, located on the most distal moraine in the valley, M1, is dated to 4.2 ± 0.2 ka. A second boulder sampled from M1, AFCL18-15, yielded a younger age of 0.65 ± 0.12 ka. Two samples dating to 2.1 ± 0.1 and 0.79 ± 0.08 ka are located on moraine M2, near the cliff on the north end of the valley. On the center moraine of the complex, M3, samples dated to 0.39 ± 0.05 and 0.28 ± 0.05 ka. Three samples from M4 yielded exposure ages of 2.6 ± 0.1, 0.46 ± 0.07, and 0.42 ± 0.06 ka. On M5, the innermost moraine in the valley, a single sample dated to 0.82 ± 0.09 ka. No apparent age biases (e.g., too young or too old) were detected between the fine-grained crystalline vs the basaltic conglomerate source rocks.

Dendrochronology

The cross-dating process resulted in an inter-correlation value of 0.55, a high correlation for *A. araucana* ring width chronologies (Muñoz et al., 2014). The five oldest trees comprising the NEV chronology, which showed a complete curvature close to the pith, were established between five and six hundred years ago. The first rings in samples from this group of trees were developed around the years AD 1407, 1462, 1511, 1559, and 1609. With the addition of missing rings due to the exhibited curvature (Duncan, 1989), the first ring for each of these five trees results in an approximate year of AD 1318, 1378, 1482, 1535, and 1580, respectively. The oldest tree of the NEV chronology yielded a date of AD 1318, providing a minimum limiting age of moraine M1 at 0.70 ka. This tree cross-dated to 0.54 with the complete set of trees measured, a value close to the mean inter-correlation value at this site, corroborating the age of this tree. Finally, due to the height of the extraction (1.3 m from the ground), a number of rings were missing with respect to the complete age of the trees, leading to an underestimation of the age of each tree. As such, a number of years, not determinate, should be added on to the determined age after ring counting, necessary to obtain the growth height observed. Following Lusk and Le Quesne (2000), the mean height growth rates of *A. araucana* were 169 mm/year in sun-grown trees, and 111 mm/year in shade-grown individuals. Considering these estimations, a minimum period of around 10 years should be added to the age of each tree. However, depending on competition and site requirements, this period could be longer than 10 years.

Glacial Modeling

The combined glacier mass balance and flow models produced simulated ice extents that mimic the modern and paleo-conditions. Using the GHCN temperature and precipitation values produced an ice margin at an elevation (~1905 m) that is similar to today. Using a cooling of 1.5°C and a 20% increase in precipitation produced a modeled ice extent that is similar to the outer-most mapped and dated moraines on Monte Sierra Nevada (**Figure 6**). As the moraine complex represents an elevation change of only ~19 m over a distance of ~350 m, distinguishing between moraines on the gridded volume proves difficult. In general, the model produces the thinnest ice near moraine positions and thicker ice elsewhere. Glacial coverage on Monte Sierra Nevada also tends to be thicker on the eastern slopes that are less steep than the western slopes. For modeling purposes, we assumed that periods of colder temperatures were associated with wetter conditions over the last several millennia (see Discussion). Nevertheless, the sensitivity analysis indicates that varying temperature alone by ±0.5°C shifted the elevation of the lowest ice position by ~±130 m, while adjusting precipitation by ±20% shifted the ice margin by ~−40 and +125 m (**Table 4**). Shifting the lapse rate by ±1.0°C/100 m offset the lowest ice position by −230 and +330 m. Lastly, shifting the DDF values by ±1 offset the lowest ice limit by +120 and −110 m.

DISCUSSION

^{36}Cl Dating of Late Holocene Moraine Boulders

The exposure ages presented here are some of the youngest to be developed using ^{36}Cl methods on glacial boulders in the Andes. While our dataset includes only a modest number of ages, these results demonstrate the feasibility of using ^{36}Cl to date young

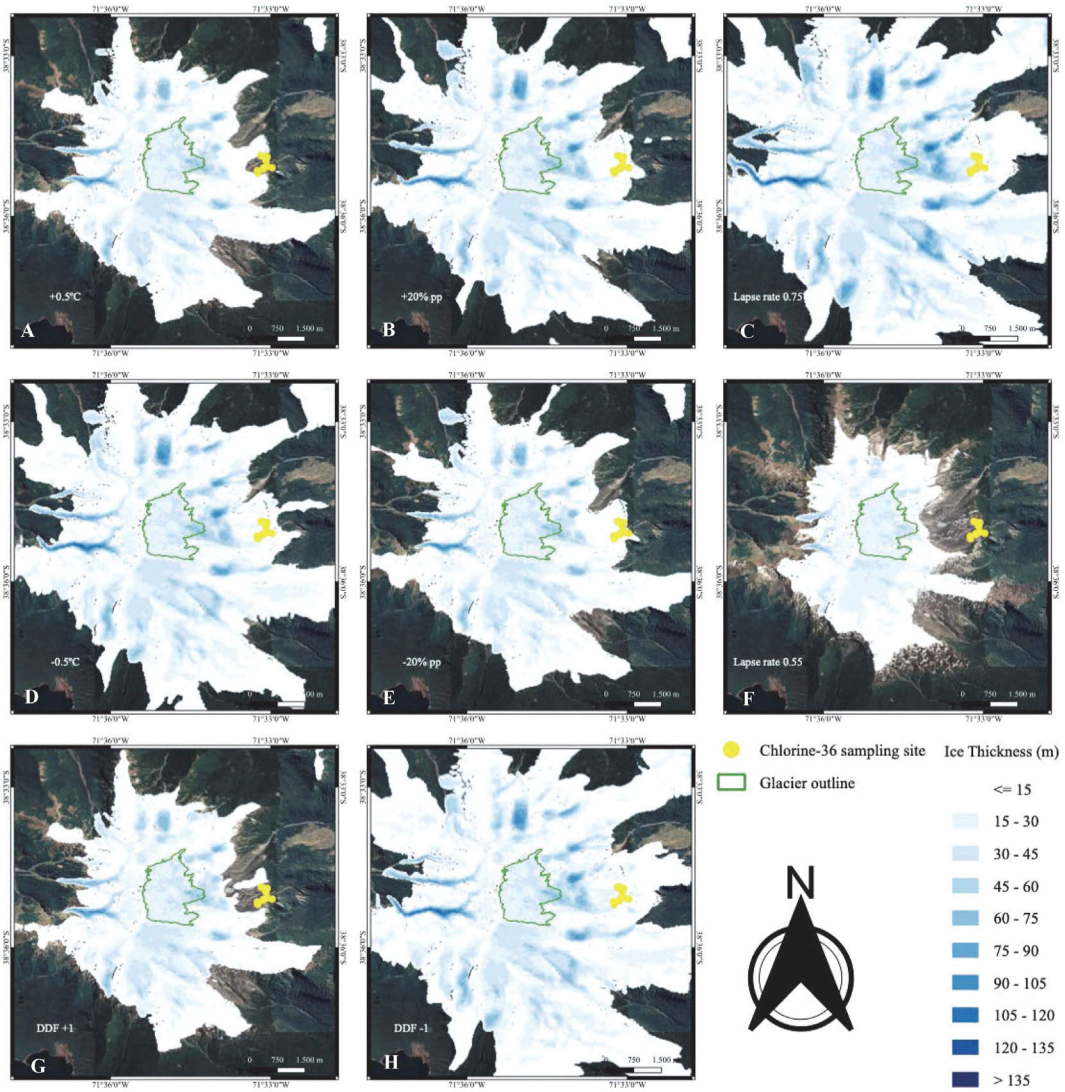

FIGURE 6 | Google Earth image of Monte Sierra Nevada with ice thickness results from the combined mass balance and flow models superimposed. The yellow circles mark the locations of dated moraine positions from this study, the modern glacial outline is represented in green. From top left to bottom middle. **(A)** Temperature increase of 0.5°C. **(B)** Precipitation increase of 20%. **(C)** Lapse rate of 0.75°C/100 m. **(D)** Temperature decrease of 0.5°C. **(E)** Precipitation decrease of 20%. **(F)** Lapse rate of 0.55°C/100 m. **(G)** DDF of +1. **(H)** DDF of -1.

TABLE 4 | Parameters used for modeling of the glacial mass energy balance sensitivity analysis.

Variable	Lowest ice limit (m asl)	Max. thick (m)	Avg. thick (m)
baseline conditions −1.5°C, +20% precip, Lapse rate: 0.65°C/100 m	1,600	115	6
+0.5°C	1,725	100	5
−0.5°C	1,530	125	8
+20% precip	1,560	120	8
−20% precip	1,725	110	5
Lapse rate: 0.75°C/100 m	1,370	130	13
Lapse rate: 0.55°C/100 m	1,930	75	2
Degree-day factor +1	1,720	100	7
Degree-day factor −1	1,490	120	10

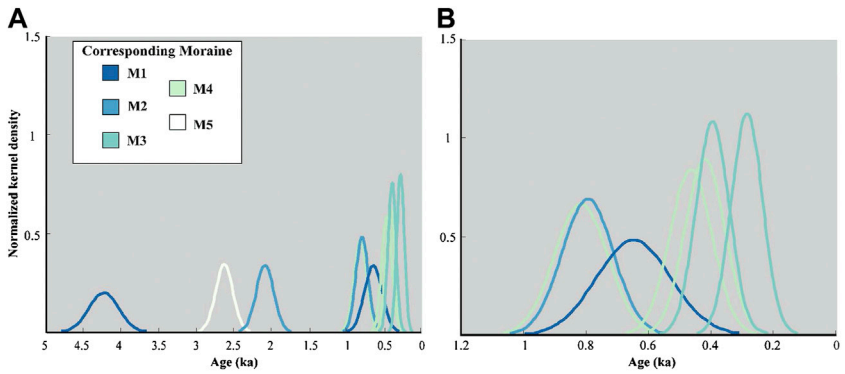

FIGURE 7 | Panel **(A)** Normalized kernel density estimates for all samples. Panel **(B)** Normalized kernel density estimates for samples that fall within the Southern Hemisphere expression of the Little Ice Age. Sample ages in both panels are plotted with internal analytical uncertainties.

glacial deposits of similar compositions elsewhere in the Chilean Andes. Due in part to the small number of boulders, definitive and discreet ages cannot be confidently assigned to each moraine position. However, the chronology established for this moraine complex provides clear documentation for multiple phases of retreat and readvance of Monte Sierra Nevada glacier during the Late Holocene.

Multiple sources of uncertainty must be considered when using ^{36}Cl to date Late Holocene moraine boulders. Processes such as post depositional erosion and boulder rotation can contribute to uncertainties in surface exposure dating (e.g., Balco, 2020). In addition, the presence of nucleogenic (i.e., non-cosmogenic) ^{36}Cl in rock surfaces can introduce considerable uncertainty to exposure age calculations. In a setting such as Monte Sierra Nevada, where the target landforms for dating and the lithologic units are likely relatively young, low-energy neutron capture can also produce non-negligible amounts of ^{36}Cl. In exposure age calculations, the nucleogenic ^{36}Cl must be subtracted from the total ^{36}Cl to obtain the concentration of cosmogenic ^{36}Cl. At this time, ^{36}Cl production rates from low-energy neutron capture are the least well-characterized production pathway (Marrero et al., 2016a), partially because low-energy neutron flux depends on difficult-to-constrain paleoenvironmental factors such as snow cover and presence of water (Zreda et al., 1993; Phillips et al., 2001; Schimmelpfennig et al., 2009; Zweck et al., 2013; Dunai and Lifton., 2014). Improved constraints on the timing of volcanic episodes of Monte Sierra Nevada will help to fully evaluate the nucleogenic production of ^{36}Cl in the Monte Sierra Nevada moraines, as these Pleistocene deposits have likely not reached steady-state production for nucleogenic ^{36}Cl (Sarikaya et al., 2019; Anjar et al., 2021). With these considerations in mind, we applied recent advances in ^{36}Cl methods to produce robust ages for the last several millennia.

Mid and Early Late Holocene Moraine Chronology

The cosmogenic ^{36}Cl ages from Monte Sierra Nevada suggest glaciers in the CSCh Andes fluctuated throughout the latest Middle and Late Holocene. Ice margin retreat from the oldest and most distal moraine, M1, likely commenced by ~4.2 ± 0.2 ka based on sample AFCL18-16B (**Figure 3**). A second boulder sampled from M1 to the north of the stream yielded a much younger age (AFCL18-15; 0.65 ± 0.12 ka), which aligns with the establishment of *A. araucana* trees on this glacial landform by 0.70 ka. Additional exposure samples are needed from moraine M1 to further assess the potential of nuclide inheritance due to unknown timing of boulder stabilization over melting debris covered ice, as well as to produce a statistically robust age determination of this landform. However, the morphology of the M1 moraine might aid in deciphering this complex glacial setting. The subtle duel-crested nature of the southern extent of M1 and observed pedogenesis on the moraine surface (Jenny, 1944; Mason and Jacobs, 2018) may suggest that M1 demarcates an expansion of the ice front prior to 4.2 ± 0.2 ka, and again before 0.65 ± 0.12 ka. Prior to 0.65 ± 0.12 ka the glacier likely expanded to the position of moraine M1, resulting in reoccupation of this landform, abutted the ice-proximal expression of M1 formed in the mid-Holocene, and shaped the dual-crest observed on the southernmost extent. The glacier then commenced its final retreat from the M1 position by ~0.65 ± 0.12 ka.

The composite nature of moraine M1, with a potential formation in the mid-Holocene followed by a latest Holocene glacial advance reoccupying this landform, would allow for a period of several thousands of years for soil development to occur. While soil may develop rapidly on deglaciated terrain, this process is largely dependent on environmental factors such as humidity and precipitation, as well as weathering rates of the original parent material (Mason and Jacobs, 2018). The lack of soil development on moraines M2-M5, along with an initial colonization age of moraine M1 by *A. araucana* trees of 0.70 ka, suggests that attributing a younger moraine formation age of ~0.65 ± 0.12 ka would preclude sufficient time for pedogenesis to support the colonization of *A. araucana* on that landform. When combined, these independent datasets suggest glaciers were at more advanced positions in the region just prior to ~4.2 ka, and supports assigning M1 an initial mid-Holocene formation age.

The trimline abutting M1 along the southern ridge of the valley suggests these features formed concurrently, and while no samples were dated from up-valley of the moraine complex, we suggest the trimline formed contemporaneously with M1. The continuation of the trimline along the southern ridge up-valley of the chute suggests that ice from the cirque directly up-valley from the dated moraines contributed to the formation of M1 in the mid-Holocene. However, this up-valley source of ice was likely minimal during the Late Holocene, with ice predominantly flowing over the southern ridge from the adjacent valley, as interpreted from the cross-cutting stratigraphy of the chute eroding a portion of the trimline (dashed blue, and black lines respectively, **Figure 3**). The modeling results suggest that greatest ice thicknesses in the valley were obtained when the ice margin expanded past the mapped extent of the moraine complex, which based on both the exposure ages and dendrochronology, has not occurred in the Late Holocene. Thus, this expression of high ice thickness in the valley likely formed during a period of glacial expansion during the mid-Holocene, predating glacial retreat from the M1 position at ~4.2 ± 0.2 ka. The glacier then retreated to an up-valley position before retreat halted. During this interval of glacial recession, ice from the cirque likely retreated up valley, separating from the glacial tongue flowing over the saddle on the southern ridge.

Four samples (AFCL18-01; 2.6 ± 0.1 ka, AFCL18-05: 0.81 ± 0.09 ka, AFCL18-12; 2.1 ± 0.1 ka, and AFCL18-13; 0.79 ± 0.08 ka) date from 2.6 ± 0.1 ka to 0.79 ± 0.08 ka, and are located at the northern and southernmost extents of the moraine complex (**Figure 3**). The exposure ages obtained from these samples support a fluctuating ice margin, and initial exposure from the subglacial environment predating a final glacial advance in the valley during the latest Holocene. The mapped locations of these samples at the outermost extents of the moraines on which they are perched suggests reworking and transport to their present locations by one or more readvances of the glacier. Additionally, the older exposure ages of these marginal samples compared to samples closer to the center of the moraine complex supports the likelihood of multiple stages of ice marginal expansion. Ice flow directions assessed from striated surfaces (**Figure 3**) indicate a radial advance of glacial ice in the valley, which would have obliterated previously formed moraines, and redeposited these boulders in more lateral positions of the moraine complex. These samples may have originally been deposited on the valley floor during recession of the ice margin, or were potentially exposed from subglacial conditions on the southern ridge. Additionally, these samples may have variable amounts of ^{36}Cl inheritance, which could explain some of the scatter seen in the available ages. Finally, these boulders may have experienced destabilization and subsequent rotation as underlying ice melted, an inherent pitfall to interpreting surface exposure ages on ice-cored moraines.

Latest Holocene Moraine Chronology

The youngest surface exposure ages (AFCL18-07, 0.42 ± 0.12 ka; AFCL18-08, 0.46 ± 0.07 ka; AFCL18-09, 0.40 ± 0.05 ka; AFCL18-11B, 0.28 ± 0.05 ka; and AFCL18-15, 0.65 ± 0.12 ka), and the development of moraines M2-M5 provide evidence for multiple phases of ice expansion in the valley over the latest Holocene. Two scenarios are plausible to explain the formation of moraines M2-M5 between this final glacial advance and the modern. The first would entail a glacier with minimal to no debris coverage commencing a continuous pulsed retreat of the ice marginal environment from 0.65 ± 0.12 ka through the modern, emplacing moraines M2-M5. However, it is more likely that during this interval, and perhaps the entirety of the Holocene, that the lower portion of the glacier was debris-mantled, as debris coverage on many regional glaciers has been increasing in modern times (Glasser et al., 2016). If the glacial snout was indeed debris-mantled, the response of the ice marginal environment to climate-driven changes could be more muted (Kirkbride and Warren, 1999; Naito et al., 2000; Davies and Glasser, 2012).

Critically thin ice margins along the frontal edge of the glacier likely resulted in instability of slope angles on moraine M1, and potentially along the northern and southernmost lateral positions of the other moraines in the complex, leading to partial or full collapse and deposition of supraglacial debris. Several exposure ages towards the center of moraines M3 (0.40 ± 0.05 ka) and M4 (0.42 ± 0.12 ka and 0.46 ± 0.07 ka) are in close agreement. The location of these samples may have been better insulated from more rapid fluctuations of the ice margins at the time collapse was initiated, as surface melt rates often vary spatially depending on the thickness of debris coverage (Östrem, 1959; Moore, 2018). The timing between the final abandonment of moraine M1 at 0.65 ± 0.12 ka and the exposure of boulders on the central portions of moraines M3 and M4 at ~0.4 ka may represent an interval when climatic conditions were cooler and wetter, resulting in temporary stabilization of the ice margin at moraine M3. Furthermore, the cluster of ages on moraines M3 and M4 between 0.46 ± 0.07 ka and 0.40 ± 0.05 ka might suggest that latest Holocene warming and/or drying resulted in ice surface lowering, the melt out of supra- and englacial debris, and the continued recession of the ice margin up valley. However, as debris can either increase insulation or enhance ablation of the glacial ice depending on both the thickness and extent of coverage (Davies and Glasser, 2012; Bartlett et al., 2021), further data and modeling are needed to substantiate these tentative interpretations.

On the ice-proximal side of moraine M5 to the north of the stream, hummocks were surveyed (**Figure 3**, **Figure 4**). The area over which hummocks are observed has been substantially dissected by an immature drainage network that has also eroded large sections of moraines M4 and M5. Development of this chaotic terrain suggests a rapid retreat from the location of moraine M5 (Owen and England, 1998; **Figure 3**). The development of hummocks also supports the idea of a debris-covered glacier in the lower reaches of the valley, particularly along the glacial snout (Anderson, 2000; Bartlett et al., 2021). An abundance of observed glacial scree and talus deposits in the valley, particularly along the southern ridge of the valley, would provide sufficient source material to generate debris coverage of the snout of the paleo-glacier (Shakesby et al., 1987; Giardino and Vitek, 1988; Moran et al., 2016; Charton et al., 2021b). As the talus is most extensive beneath the trimline and covering the chute

along the southern ridge of the valley, debris coverage of the lowest extents of the glacier most likely increased following the initial abatement from the M1 location and thinning of the glacial surface.

Moraines M4 and M5 to the north of the stream are also weakly preserved, potentially indicating that these moraines were ice-cored, where dead ice would possibly be entrained along with glacial debris (Evans, 2009). Deflation of these glacial landforms would occur as the ice core melted, resulting in the poor preservation observed, and the destabilization of perched boulders (Putkonen and Swanson, 2003; Briner et al., 2005). A debris-mantled glacier would present a possible explanation in the scatter of the cosmogenic ages from this study site, such as the younger exposure age of sample AFCL18-11B (0.28 ± 0.05 ka) on M3, as it may have experienced some rotation due to debris coverage limiting ablation and the enhanced likelihood of boulder rotation upon destabilization.

The glacier modeling results and geomorphic evidence provides additional support that the present-day ice cap system was more extensive at times during the Late Holocene. Our model indicates that as the ice cap expanded, it likely covered more ridges and had additional source-ice regions with more complex ice-flow dynamics down-valley than what is seen in present-day (**Figure 6**). These complex ice patterns likely explain part of the scatter of available ages as the glacier did not follow a standard down-valley glacier pathway in the latest Holocene. Additionally, an eroded trimline indicates ice was flowing from south-to-north in the valley from a ridge that is currently ice-free (**Figure 3**). Combined, this evidence supports the initial formation of moraine M1 *via* a combination of glacial ice flow from the cirque of the modern glacier, merged with ice sourced from the valley directly to the south *via* the saddle along the southern ridge, and possibly the north side of the valley as well (**Figure 3**). The eroded trimline feature also suggests that following the abandonment of the M1 position at ~4.2 ± 0.2 ka, glacial ice was likely sourced solely from the southern ridge of the valley with little to no contribution directly down-valley from the glacial cirque. That ice then flowed outward in a radial piedmont-style pattern across the table-top-like valley floor to reoccupy M1, and to the positions of moraines M2-M5 as supported by the striated surfaces throughout the lower extents of the valley.

Dendrochronology

Our chronology of Late Holocene glacial fluctuations from Monte Sierra Nevada is further augmented with independent tree-ring data collected near the margins of the apparent trim-line (**Figure 3**). The ^{36}Cl ages suggest that a Late Holocene retreat of the frontal/lateral margin occurred at ~0.65 ± 0.12 ka. While the chronology of the oldest tree provided by the NEV record only extends to 0.70 ka, it provides a minimum-limiting age of glacial retreat from M1. It is possible that this landform has been colonialized by successive generations of *A. araucana* trees, as very few specimens have been dated to older than 500 years (Aguilera-Betti et al., 2017). Additionally, the period necessary between moraine stabilization and seedling establishment depends in part on the soil evolution of the landform to provide conditions for germination and growth, as well as individual species capacities to grow under limited conditions. This period could take several decades in most cases. However, *A. araucana* is a recognized species that can grow on low developed soils (Veblen, 1982). This, combined with the time required for the tree to grow to the height at which cores were extracted, results in a likely formation age of moraine M1 at minimum a few decades prior to 0.70 ka, further suggesting the true age of the moraine is older than 0.70 ka.

Glacial Mass Balance and Flow Modeling

The modeling results presented here provide a physical and quantitative basis for interpreting glacial variability at Monte Sierra Nevada, and despite not being fully capable of handling the complex dynamics of a debris-mantled glacier, the Temperature-Index approach provides an important first-order estimate at quantifying paleo-environmental conditions on Monte Sierra Nevada. Additionally, the interpretation of a debris-covered glacier for this valley concerns only the snout, not the entire ablation area, and even less of the whole glacier surface. On modern decadal timescales, the dynamics of debris-covered glaciers are observed to operate differently than clean glaciers, but very little research exists to determine whether debris cover exerts a significant effect on the temperature sensitivity at centennial to millennia scales. Furthermore, when climate trends are strong, debris-cover does not cause a significant insulation effect (Burger et al., 2019), suggesting that under certain scenarios, in particular considering relatively persistent climate changes, debris-coverage does not alter glacier sensitivity significantly.

This model was parameterized with a range of representative temperature and precipitation values from the AABR calculations, suggesting temperatures were ~1.5°C colder and precipitation was ~20% higher during peak Neoglacial ice advances over the last several millennia. It is presently unclear, based on the available chronology, whether the peak Neoglacial ice advance at Monte Sierra Nevada was associated with the LIA or an earlier advance. However, the modeling outcome is generally the same regardless of the chronology when recognizing that it was wetter when it was colder at multiple times during the Neoglacial (Bertrand et al., 2014). Following this assumption, we were able to achieve ice margin reconstructions that match the mapped moraine positions on the landscape (**Figure 6**). The sensitivity analysis also highlights that a 20% increase in precipitation offsets a temperature shift by ~0.5°C, which is less than other modeling studies that suggest a doubling of precipitation is needed to offset a ~1°C temperature change (**Figure 6**; Sagredo et al., 2014). The results also highlight that multiple combinations of climate parameters are capable of explaining glacial variability in this region, and these modeling scenarios will improve as independent proxy evidence of Late Holocene environmental conditions, such as tree-ring records, continue to be developed.

Regional and Southern South America Proxy Record Comparison

The results presented here are not of sufficient resolution to attribute confident alignment of this record of glacial fluctuations

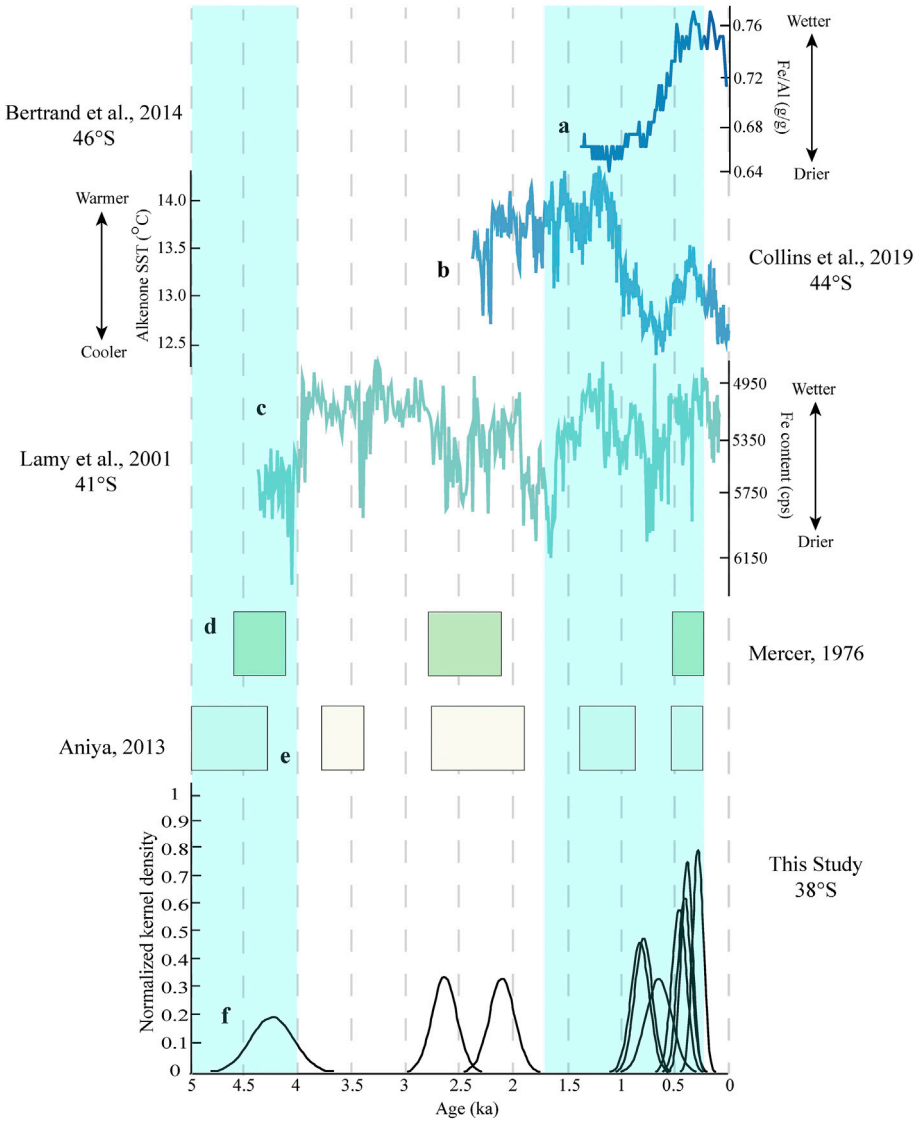

FIGURE 8 | From top to bottom: **(A)** Ratio of Iron (Fe) to Aluminum (Al) (g/g) from sediment core PC29A retrieved from Quitralco fjord (46°S), as a proxy for precipitation seasonality. An increase in Fe/Al is interpreted as increased precipitation regionally due to latitudinal variations in the position of the SWWB (Bertrand et al., 2014). **(B)** An alkenone based proxy record for SST (°C) from oceanic sediment core MD07-3093 (44°S) (Collins et al., 2019). **(C)** Iron (Fe) intensity (cps) from oceanic sediment core GeoB 3313-1 (41°S), as a proxy for position of the SWWB. Decreased Fe intensity is interpreted as the SWWB located in a more northerly position compared to the study location, resulting in wetter conditions regionally (Lamy et al., 2001). **(D)** Timing of "Mercer-type" glaciations in Southern Chile (Mercer, 1976). **(E)** Timing of "Aniya-type" glaciations in Southern Chile (Aniya, 2013). **(F)** Chlorine-36 surface exposure ages from this study. Blue vertical bars indicate assessed intervals of SAM negative phases (cold and wet), inferred from the Lago Cipreses sediment core record (51°S) (Moreno et al., 2018).

to either the "Aniya-type" or "Mercer-type" chronology of Neoglacial events (**Figure 8**), however, certain similarities exist. Event I of Aniya (2013) is proposed to have occurred at ~5.0 to 4.3 ka, while Mercer (1976) designates a first Neoglacial advance between 4.6 and 4.1 ka. Thus, the timing from both chronologies is similar to the oldest, outermost moraine age of 4.2 ± 0.2 ka. No samples dated in this study fall within the event II range of the "Aniya-type" chronology (3.7–3.4 ka), suggesting that either the climatic conditions in CSCh did not support a glacial advance during this interval, or that evidence of this event locally was destroyed by subsequent Neoglacial ice fluctuations. As the two exposure ages from this study (2.6 ± 0.2 ka and 2.1 ± 0.1 ka) that overlap with Mercer's second event and Aniya's III event are from proposed reworked boulders, we cannot assess any overlap in glacial advances from these samples. Similarly, while two exposure ages developed from our study (0.81 ± 0.09 ka and 0.79 ± 0.08 ka) fit into the event IV range (1.4–0.7 ka) of the Aniya chronology, we are unsure if these samples were recycled from a previous exposure due in part to sample placements at the far northern and southern lateral extents of the moraine complex. The latest Holocene glacial readvance is assigned an approximate range of 0.57 to 0.27 ka in the Mercer (1976) chronology and 0.52

to 0.3 ka (event IV) in the Aniya (2013) chronology. Four of the developed exposure ages from this study fit into this interval (0.46 ± 0.07 ka, 0.42 ± 0.12 ka, 0.40 ± 0.05 ka, and 0.28 ± 0.05 ka) of the Southern Hemisphere expression of the LIA. However as previously discussed, these ages are distributed across two moraines, M3 and M4 (**Figure 3**), precluding a definitive assessment as to which moraine represents the LIA with the current data set.

Slightly different regions were assessed to build the afore mentioned chronologies. The Mercer-type chronology evaluated a latitudinally longer corridor of glacial records from 39°S to 53°S, while the Aniya-type chronology was slightly more restricted and was compiled from records sourced from between ~46°S and 52°S. Additionally, the inclusion of records from tide-water glaciers as opposed to a restriction of the analysis to fully terrestrial based glacial systems could potentially result in more variability in age control in these records. As highlighted by Glasser et al. (2004), the differences between the Aniya-type and Mercer-type chronologies are also likely more related to dating uncertainties and the lack of bracketing age control rather than actual differences in interhemispheric glacier behavior. The "Aniya-type" chronology though widely recognized, was developed largely from ^{14}C dating of organic material combined with tree-ring data and lichenometry (Aniya, 1995; Aniya, 1996). Since the establishment of these chronologies numerous advancements have been made in various dating methods (i.e., cosmogenic nuclide exposure age dating, optically stimulated luminescence, tephrochronology, etc.) providing researchers a lens through which age constraints on regional records can be reexamined. Nevertheless, additional multi-proxy approaches similar to what we present here for Monte Sierra Nevada are needed as researchers work to develop comprehensive chronologies of past glacial variability in the high-latitude Andes.

The data reanalysis on the Patagonian Ice Sheet published by Davies et al. (2020) includes recalibrated chronologies of glacial fluctuations, but notes that the Late Holocene is not yet well understood over large regions of southernmost South America. However, three intervals of Neoglacial advances were well supported from the studies reviewed within: in the mid-Holocene at 5 ka, a smaller Late Holocene advance between 2.0–1.0 ka, and a LIA advance between 0.5–0.2 ka (Davies et al., 2020). Our proposed advance prior to 4.2 ± 0.2 ka, and the cluster of ages that fall within the LIA (0.46 ± 0.07 ka, 0.42 ± 0.12 ka, 0.40 ± 0.05 ka, and 0.28 ± 0.05 ka), are supported by this large-scale assessment from the Patagonia Ice Sheet. Nevertheless, our ability to disentangle how much past glacial variability in the Chilean Andes was driven by climate-related processes versus hypsometric controls will improve as we continue to apply more comprehensive dating methods, including additional direct ages on moraine boulders.

Climate Forcings and Regional Dynamics

Andean glaciers have varying sensitivities to temperature and hydrologic changes depending on location, geometry and other local and regional factors (e.g., Sagredo et al., 2014). CSCh glaciers are typical of mid-latitude glaciers, with mass balance sensitivities that are seasonal and seemingly most sensitive to summer temperatures and winter precipitation (Masiokas et al., 2008). These temperature and precipitation anomalies are tightly coupled, with cold intervals corresponding to wetter periods and *vice versa* (Masiokas et al., 2009). Modern ice fields and outlet glaciers in Chile have historical mass balances that are sensitive to both atmospheric temperature and precipitation changes (Bown and Rivera, 2007; Casassa et al., 2007). Since 1975, the regional freezing level (0°C isotherm) has risen by ~120 m in winter and 200 m in summer (Carrasco et al., 2005), with an overall increase of 0.25°C/decade in mean annual temperature since 1979 (Falvey and Garreaud, 2007). There has also been a strong negative trend in winter precipitation amounts over the last century (Masiokas et al., 2008).

Even though the annual cycles of temperature and precipitation vary across the Andes, it is possible that Pacific oceanic-atmospheric forcing synchronized climate variability across the low and high southern latitudes during much of the Late Holocene. For example, it has been proposed that SAM and ENSO are teleconnected and possibly related on centennial time-scales, providing one possible explanation for Southern Andean glacial variability (Moreno et al., 2018). It is also possible that changes in the position of the SWWB drove much of the observed pattern of Neoglaciation as these winds deliver critical precipitation to Patagonian glaciers (Glasser et al., 2004; Kaplan et al., 2016). Millennial-scale SAM variability began after ~5.8 ka (Moreno et al., 2018), and it is suggested that insolation combined with SAM drives millennial and centennial-scale glacier variability in southern South America through the Holocene (Reynhout et al., 2019). An increase in Southern Hemisphere summer insolation (assessed at 37°S) from the start of the Holocene through the modern (Berger and Loutre, 1991; van den Bos et al., 2018), would support the largest glacial expanse recorded in the valley, predating a retreat as early as ~4.2 ± 0.2 ka. A warm and dry period during the Late Holocene (~4.1–2.8 ka) has been associated with prolonged SAM-positive phases, resulting in less extensive glaciers (Reynhout et al., 2019), while after 2.8 ka conditions appear to reflect more SAM-negative conditions, becoming colder and wetter, similar to the proposed intervals of SAM phases by Moreno et al. (2018). These SAM negative phases roughly correspond to intervals of assessed glacial expansion on Monte Sierra Nevada (**Figure 8**). Additionally, ENSO variability might make SAM stronger due to the effect of atmospheric Rossby waves across the Pacific. These SST anomalies in the tropics drive pressure anomalies in the high latitudes, as positive phases of ENSO lead to negative SAM, and *vice versa* (Moreno et al., 2018).

There are multiple proxy records of wetter conditions and evidence of a northward shift of the SWWB from ~0.82 to 0.22 ka (**Figure 8**; Lamy et al., 2001; Jenny et al., 2002; Bertrand et al., 2005; Fletcher and Moreno, 2012; Bertrand et al., 2014). Perren et al. (2020) suggests that the extratropical westerlies migrate northward during cold Neoglacial periods, and therefore, it seems likely that periods of increased precipitation were associated with colder temperatures. The tree-ring and glacier modeling results presented here further suggest that both increased precipitation and colder conditions drove the pattern of latest Holocene glacier variability.

Regardless of the degree to which temperature vs. hydroclimate were the dominant factors, Late Holocene glacial variability in the Chilean Andes was likely influenced by complex oceanic and atmospheric processes. For example, there appears to have been a close relationship between Pacific and Southern Ocean SSTs and atmospheric circulation during the Late Holocene. Oceanic SST records (44°S) demonstrate the connectivity between the Southern Ocean with increased ENSO variability, resulting in an ~2.5°C cooling trend between ~1.2–0.7 ka off the central Chilean coast (**Figure 8**; Collins et al., 2019). Additionally, precipitation proxy records suggest an equatorward or northward shift of the SWWB associated with colder SSTs and a southward shift associated with warmer SSTs (**Figure 8**; Bertrand et al., 2014). The SWWB delivers critical precipitation to temperate glaciers, especially on the windward side of the Andes (Bertrand et al., 2012) where a strong correlation exists between precipitation amounts and westerly wind anomalies (Garreaud, 2007; Moreno et al., 2009). Historical archives compared to meteorological data support this observation and suggest that some glaciers on the drier side of precipitation gradients in northern Patagonia have varied over the last several decades mostly in response to precipitation changes (Warren and Sugden, 1993). There is also a correlation between Pacific SSTs and freezing level height in the Andes (Bradley et al., 2009), suggesting that shifting ocean circulation and temperatures could drive both temperature and hydroclimate variability in CSCh.

Proxy and modeling results suggest that decreased radiative forcing due to reduced solar activity causes an equatorward shift in the mean position of the SWWB (Varma et al., 2011). During the LIA, reduced solar forcing combined with increased volcanic activity led to net global cooling (Mann et al., 2009; Miller et al., 2012). This cooling would likely have produced a similar equatorward shift in the SWWB and wetter conditions in CSCh Andes, driving the observed pattern of ice advances. The higher temperatures that followed the LIA likely led to a poleward shift in the SWWB, and drier conditions that combined, would have caused ice to retreat.

CONCLUSION

Our ^{36}Cl-based chronology of latest-Holocene glacial fluctuations from the South-Central Chilean Andes includes some of the youngest developed surface exposure ages from this nuclide system in South America. Exposure ages and observed landforms in the valley suggest that the glacier was likely debris-mantled to some extent along the lower reaches of the valley, over the area of the mapped moraine complex. This scenario would suggest that moraine formation occurred only under periods of more enhanced climatic change regionally during the Late Holocene. In combining our moraine exposure age chronology with dendrochronology, and a geomorphic analysis of the valley we estimated the past glacial hypsometry in the valley, so as to numerically model the paleo glaciers response to regional climatic forcings. This model suggests that Monte Sierra Nevada glaciers most likely experienced phases of growth and decay under a range of temperature and precipitation conditions, predominantly exhibiting glacial expansion during periods of lower temperatures and increased precipitation over the last several millennia. These conditions were possibly driven by decreased SSTs associated with enhanced offshore upwelling, and increased regional humidity from a more northernly positioned SWWB. A more thorough understanding of South American climatic processes in the recent past, coupled with more precise chronologies, will shed light on regional climate trends and better identify the timing of apparently near global climate events such as the LIA. While we produced only a limited dataset for this study, we demonstrate the ability to date relatively young glacial landforms with multiple dating methods, which should help to improve our understanding of how complex mid-latitude oceanic-atmospheric dynamics are linked to low and high latitude climate changes, especially in the context of recent warming events. This study also highlights the need to better constrain the timing of Quaternary volcanic episodes in CSCh, which will improve the accuracy of ^{36}Cl surface exposure dating in this young basalt-rich terrain and allow for a more precise characterization of regional glacial events. The record of glaciation produced here from Monte Sierra Nevada, along with additional records from other sites, will aid in assessing the sensitivity of glaciers in CSCh to Pacific Ocean-atmospheric processes throughout the Holocene, which is crucial as these glaciers are significant contributors to water availability regionally. Furthermore, in better constraining estimates of Andean alpine ice coverage throughout the Neoglacial period, global climate models will be better informed regarding complex cryosphere changes in albedo, continental temperatures of glaciated and recently deglaciated surfaces, and their associated drainage basins.

DATA AVAILABILITY STATEMENT

The original contributions presented in the study are included in the article/**Supplementary Material**, further inquiries can be directed to the corresponding author.

AUTHOR CONTRIBUTIONS

BP and NS led the writing of the manuscript with advisement from AF, JL, AL, and AM. AF, NS, AM, and EJC conceptualized the project, and wrote the National Geographic grant for initial funding. BP, AF, NS, EJC, and IC carried out the field investigation and sampling. BP, JL, and AL prepared and analyzed rock samples for ^{36}Cl. NS, MS, AF, and TS modeled the glacial system. AM, EJC, and IG measured and calibrated the dendrochronology data. All authors have read, provided edits and agreed to the published version of this manuscript.

FUNDING

Funding for this work was provided by National Geographic (CP-119R-17), The Chilean Science Bureau (ANID) ANILLO ACT210080, The Center for Climate Action (PUCV ESR UCV 2095), The Center for Climate and Resilience Research (ANID, FONDAP N°15110009), and the Northern Illinois University Department of Geology and Environmental Geosciences Goldich Fund. Funding for publication of this manuscript was provided by the Northern Illinois University and University of New Hampshire Open Access Publication funds.

ACKNOWLEDGMENTS

The Araucanía region is part of the ancestral homeland of the Mapuche people. Monte Sierra Nevada is located on these occupied lands, and we recognize the Mapuche as the original and sustained stewards of this territory. We would like to recognize the provision of PlanetScope imagery under the research and education initiative, granted to AF and IC. We would also like to thank Bradley Singer for his expert assessment in estimating the age of volcanism at Monte Sierra Nevada. Additionally, we would like to thank both reviewers of our manuscript, who provided kind, constructive feedback, which led to the improvement of this publication.

SUPPLEMENTARY MATERIAL

The Supplementary Material for this article can be found online at: https://www.frontiersin.org/articles/10.3389/feart.2022.848652/full#supplementary-material

REFERENCES

Aguilera-Betti, I., Muñoz, A. A., Stahle, D., Figueroa, G., Duarte, F., González-Reyes, Á., et al. (2017). The First Millennium-Age Araucaria Araucanain Patagonia. *Tree-Ring Res.* 73, 53–56. doi:10.3959/1536-1098-73.1.53

Alcalá-Reygosa, J., Palacios, D., Schimmelpfennig, I., Vázquez-Selem, L., García-Sancho, L., Franco-Ramos, O., et al. (2018). Dating Late Holocene Lava Flows in Pico de Orizaba (Mexico) by Means of In Situ-Produced Cosmogenic ^{36}Cl, Lichenometry and Dendrochronology. *Quat. Geochronol.* 47, 93–106. doi:10.1016/j.quageo.2018.05.011

Álvarez, D., Fagel, N., Araneda, A., Jana-Pinninghoff, P., Keppens, E., and Urrutia, R. (2015). Late Holocene Climate Variability on the Eastern Flank of the Patagonian Andes (Chile): A δ^{18}O Record from Mollusks in Lago Cisnes (47°S). *Holocene* 25, 1220–1230. doi:10.1177/0959683615580859

Ancapichún, S., and Garcés-Vargas, J. (2015). Variability of the Southeast Pacific Subtropical Anticyclone and its Impact on Sea Surface Temperature off North-Central Chile. *Cienc. Mar.* 41, 1–20. doi:10.7773/cm.v41i1.2338

Anderson, R. S. (2000). A Model of Ablation-Dominated Medial Moraines and the Generation of Debris-Mantled Glacier Snouts. *J. Glaciol.* 46, 459–469. doi:10.3189/172756500781833025

Aniya, M. (1995). Holocene Glacial Chronology in Patagonia: Tyndall and Upsala Glaciers. *Arct. Alp. Res.* 27, 311–322. doi:10.1080/00040851.1995.1200312810.2307/1552024

Aniya, M. (2013). Holocene Glaciations of Hielo Patagónico (Patagonia Icefield), South America: A Brief Review. *Geochem. J.* 47, 97–105. doi:10.2343/geochemj.1.0171

Aniya, M. (1996). Holocene Variations of Ameghino Glacier, Southern Patagonia. *Holocene* 6, 247–252. doi:10.1177/095968369600600211

Anjar, J., Akçar, N., Larsen, E. A., Lyså, A., Marrero, S., Mozafari, N., et al. (2021). Cosmogenic Exposure Dating (^{36}Cl) of Landforms on Jan Mayen, North Atlantic, and the Effects of Bedrock Formation Age Assumptions on ^{36}Cl Ages. *Geosciences* 11, 390. doi:10.3390/geosciences11090390

Aravena, J.-C., and Luckman, B. H. (2009). Spatio-Temporal Rainfall Patterns in Southern South America. *Int. J. Climatol.* 29, 2106–2120. doi:10.1002/joc.1761

Arnold, M., Merchel, S., Bourlès, D. L., Braucher, R., Benedetti, L., Finkel, R. C., et al. (2010). The French Accelerator Mass Spectrometry Facility ASTER: Improved Performance and Developments. *Nucl. Instrum. Methods Phys. Res. Sect. B Beam Interact. Mater. Atoms* 268 (11–12), 1954–1959. doi:10.1016/j.nimb.2010.02.107

ASF DAAC (2015). PALSAR_Radiometric_Terrain_Corrected_high_res. Available at: https://asf.alaska.edu/data-sets/derived-data-sets/alos-palsar-rtc/alos-palsar-radiometric-terrain-correction/.doi:10.5067/Z97HFCNKR6VA

Balco, G. (2011). Contributions and Unrealized Potential Contributions of Cosmogenic-Nuclide Exposure Dating to Glacier Chronology, 1990-2010. *Quat. Sci. Rev.* 30, 3–27. doi:10.1016/j.quascirev.2010.11.003

Balco, G. (2020). Glacier Change and Paleoclimate Applications of Cosmogenic-Nuclide Exposure Dating. *Annu. Rev. Earth Planet. Sci.* 48, 21–48. doi:10.1146/annurev-earth-081619-052609

Balco, G., Stone, J. O., Lifton, N. A., and Dunai, T. J. (2008). A Complete and Easily Accessible Means of Calculating Surface Exposure Ages or Erosion Rates from ^{10}Be and ^{26}Al Measurements. *Quat. Geochronol.* 3, 174–195. doi:10.1016/j.quageo.2007.12.001

Barcaza, G., Nussbaumer, S. U., Tapia, G., Valdés, J., García, J.-L., Videla, Y., et al. (2017). Glacier Inventory and Recent Glacier Variations in the Andes of Chile, South America. *Ann. Glaciol.* 58, 166–180. doi:10.1017/aog.2017.28

Bartlett, O. T., Ng, F. S. L., and Rowan, A. V. (2021). Morphology and Evolution of Supraglacial Hummocks on Debris-Covered Himalayan Glaciers. *Earth Surf. Process. Landforms* 46, 525–539. doi:10.1002/esp.5043

Bentley, M. J., Hodgson, D. A., Smith, J. A., Cofaigh, C. Ó., Domack, E. W., Larter, R. D., et al. (2009). Mechanisms of Holocene Palaeoenvironmental Change in the Antarctic Peninsula Region. *Holocene* 19, 51–69. doi:10.1177/0959683608096603

Berger, A., and Loutre, M. F. (1991). Insolation Values for the Climate of the Last 10 Million Years. *Quat. Sci. Rev.* 10, 297–317. doi:10.1016/0277-3791(91)90033-q

Bertrand, S., Boës, X., Castiaux, J., Charlet, F., Urrutia, R., Espinoza, C., et al. (2005). Temporal Evolution of Sediment Supply in Lago Puyehue (Southern Chile) During the Last 600 Yr and its Climatic Significance. *Quat. Res.* 64, 163–175. doi:10.1016/j.yqres.2005.06.005

Bertrand, S., Hughen, K. A., Lamy, F., Stuut, J.-B. W., Torrejón, F., and Lange, C. B. (2012). Precipitation as the Main Driver of Neoglacial Fluctuations of Gualas Glacier, Northern Patagonian Icefield. *Clim. Past.* 8, 519–534. doi:10.5194/cp-8-519-2012

Bertrand, S., Hughen, K., Sepúlveda, J., and Pantoja, S. (2014). Late Holocene Covariability of the Southern Westerlies and Sea Surface Temperature in Northern Chilean Patagonia. *Quat. Sci. Rev.* 105, 195–208. doi:10.1016/j.quascirev.2014.09.021

Biette, M., Jomelli, V., Chenet, M., Braucher, R., Menviel, L., Swingedouw, D., et al. (2021). Evidence of the Largest Late Holocene Mountain Glacier Extent in Southern and Southeastern Greenland During the Middle Neoglacial from ^{10}Be Moraine Dating. *Boreas* 51, 61–77. doi:10.1111/bor.12555

Boltovskoy, E. (1976). Distribution of Recent Foraminifera of the South American Region. *Foraminifera* 2, 171–236.

Bown, F., and Rivera, A. (2007). Climate Changes and Recent Glacier Behaviour in the Chilean Lake District. *Glob. Planet. Change* 59. doi:10.1016/j.gloplacha.2006.11.015

Bradley, R. S., Keimig, F. T., Diaz, H. F., and Hardy, D. R. (2009). Recent Changes in Freezing Level Heights in the Tropics with Implications for the Deglacierization of High Mountain Regions. *Geophys. Res. Lett.* 36. doi:10.1029/2009GL037712

Briner, J. P., Kaufman, D. S., Manley, W. F., Finkel, R. C., and Caffee, M. W. (2005). Cosmogenic Exposure Dating of Late Pleistocene Moraine Stabilization in Alaska. *Geol. Soc. Am. Bull.* 117, 1108. doi:10.1130/B25649.1

Briner, J. P., Swanson, T. W., and Caffee, M. (2001). Late Pleistocene Cosmogenic ^{36}Cl Glacial Chronology of the Southwestern Ahklun Mountains, Alaska. *Quat. Res.* 56, 148–154. doi:10.1006/qres.2001.2255

Burger, F., Ayala, A., Farias, D., Shaw, T. E., MacDonell, S., Brock, B., et al. (2019). Interannual Variability in Glacier Contribution to Runoff from a High-Elevation Andean Catchment: Understanding the Role of Debris Cover in Glacier Hydrology. *Hydrol. Process.* 33, 214–229. doi:10.1002/hyp.13354

Carrasco, J. F., Casassa, G., and Quintana, J. (2005). Changes of the 0°C Isotherm and the Equilibrium Line Altitude in Central Chile During the Last Quarter of the 20th Century/Changements de l'isotherme 0°C et de la ligne d'équilibre des neiges dans le Chili Central Durant le dernier quart du 20ème siècle. *Hydrological Sci. J.* 50. doi:10.1623/hysj.2005.50.6.933

Casassa, G., Haeberli, W., Jones, G., Kaser, G., Ribstein, P., Rivera, A., et al. (2007). Current Status of Andean Glaciers. *Glob. Planet. Change* 59, 1–9. doi:10.1016/j.gloplacha.2006.11.013

Charton, J., Jomelli, V., Schimmelpfennig, I., Verfaillie, D., Favier, V., Mokadem, F., et al. (2021a). A Debris-Covered Glacier at Kerguelen (49°S, 69°E) Over the Past 15 000 Years. *Antarct. Sci.* 33, 103–115. doi:10.1017/S0954102020000541

Charton, J., Verfaillie, D., Jomelli, V., and Francou, B. (2021b). Early Holocene Rock Glacier Stabilisation at col du Lautaret (French Alps): Palaeoclimatic Implications. *Geomorphology* 394, 107962. doi:10.1016/j.geomorph.2021.107962

Collins, J. A., Lamy, F., Kaiser, J., Ruggieri, N., Henkel, S., De Pol-Holz, R., et al. (2019). Centennial-Scale SE Pacific Sea Surface Temperature Variability Over the Past 2,300 Years. *Paleoceanogr. Paleoclimatology* 34, 336–352. doi:10.1029/2018PA003465

Davies, B. J., Darvill, C. M., Lovell, H., Bendle, J. M., Dowdeswell, J. A., Fabel, D., et al. (2020). The Evolution of the Patagonian Ice Sheet from 35 Ka to the Present Day (PATICE). *Earth-Science Rev.* 204, 103152. doi:10.1016/j.earscirev.2020.103152

Davies, B. J., and Glasser, N. F. (2012). Accelerating Shrinkage of Patagonian Glaciers from the Little Ice Age (~AD 1870) to 2011. *J. Glaciol.* 58, 1063–1084. doi:10.3189/2012JoG12J026

Dong, G., Zhou, W., Yi, C., Zhang, L., Li, M., Fu, Y., et al. (2017). Cosmogenic ^{10}Be Surface Exposure Dating of 'Little Ice Age' Glacial Events in the Mount Jaggang Area, Central Tibet. *Holocene* 27 (10), 1516–1525. doi:10.1177/0959683617693895

Dunai, T. J., and Lifton, N. A. (2014). The Nuts and Bolts of Cosmogenic Nuclide Production. *Elements* 10, 347–350. doi:10.2113/gselements.10.5.347

Duncan, R. (1989). An Evaluation of Errors in Tree Age Estimates Based on Increment Cores in Kahikatea (Dacrycarpus Dacrydioides). *N. Z. Nat. Sci.* 16.

Elbert, J., Wartenburger, R., von Gunten, L., Urrutia, R., Fischer, D., Fujak, M., et al. (2013). Late Holocene Air Temperature Variability Reconstructed from the Sediments of Laguna Escondida, Patagonia, Chile (45°30′S). *Palaeogeogr. Palaeoclimatol. Palaeoecol.* 369, 482–492. doi:10.1016/j.palaeo.2012.11.013

Espinoza, J. C., Garreaud, R., Poveda, G., Arias, P. A., Molina-Carpio, J., Masiokas, M., et al. (2020). Hydroclimate of the Andes Part I: Main Climatic Features. *Front. Earth Sci.* 8. doi:10.3389/feart.2020.00064

Espizua, L. E., and Pitte, P. (2009). The Little Ice Age Glacier Advance in the Central Andes (35°S), Argentina. *Palaeogeogr. Palaeoclimatol. Palaeoecol.* 281, 345–350. doi:10.1016/j.palaeo.2008.10.032

Evans, D. J. A. (2009). Controlled Moraines: Origins, Characteristics and Palaeoglaciological Implications. *Quat. Sci. Rev.* 28, 183–208. doi:10.1016/j.quascirev.2008.10.024

Falvey, M., and Garreaud, R. (2007). Wintertime Precipitation Episodes in Central Chile: Associated Meteorological Conditions and Orographic Influences. *J. Hydrometeorol.* 8, 171–193. doi:10.1175/JHM562.1

Ferguson, K. M., Dungan, M. A., Davidson, J. P., and Colucci, M. T. (1992). The Tatara-San Pedro Volcano, 36 S, Chile: A Chemically Variable, Dominantly Mafic Magmatic System. *J. Petrology* 33, 1–43. doi:10.1093/petrology/33.1.1

Fernández, A., and Mark, B. G. (2016). Modeling Modern Glacier Response to Climate Changes Along the A Ndes C Ordillera: A Multiscale Review. *J. Adv. Model. Earth Syst.* 8, 467–495. doi:10.1002/2015MS000482

Fernández, H., García, J.-L., Nussbaumer, S. U., Geiger, A. J., Gärtner-Roer, I., Pérez, F., et al. (2022). De-Icing Landsystem Model for the Universidad Glacier (34° S) in the Central Andes of Chile During the Past ~660 Years. *Geomorphology* 400, 108096. doi:10.1016/j.geomorph.2021.108096

Finkel, R., Arnold, M., Aumaître, G., Benedetti, L., Bourlès, D., Keddadouche, K., et al. (2013). Improved ^{36}Cl Performance at the ASTER HVE 5MV Accelerator Mass Spectrometer National Facility. *Nucl. Instrum. Methods Phys. Res. Sect. B Beam Interact. Mater. Atoms* 294, 121–125. doi:10.1016/j.nimb.2012.05.019

Fletcher, M.-S., and Moreno, P. I. (2012). Vegetation, Climate and Fire Regime Changes in the Andean Region of Southern Chile (38°S) Covaried with Centennial-Scale Climate Anomalies in the Tropical Pacific Over the Last 1500 Years. *Quat. Sci. Rev.* 46, 46–56. doi:10.1016/j.quascirev.2012.04.016

García-Ruiz, J. M., Palacios, D., de Andrés, N., Valero-Garcés, B. L., López-Moreno, J. I., and Sanjuán, Y. (2014). Holocene and 'Little Ice Age' Glacial Activity in the Marboré Cirque, Monte Perdido Massif, Central Spanish Pyrenees. *Holocene* 24 (11), 1439–1452. doi:10.1177/0959683614544053

Garreaud, R. D., Vuille, M., Compagnucci, R., and Marengo, J. (2009). Present-Day South American Climate. *Palaeogeogr. Palaeoclimatol. Palaeoecol.* 281, 180–195. doi:10.1016/j.palaeo.2007.10.032

Garreaud, R., Lopez, P., Minvielle, M., and Rojas, M. (2013). Large-Scale Control on the Patagonian Climate. *J. Clim.* 26, 215–230. doi:10.1175/JCLI-D-12-00001.1

Garreaud, R. (2007). Precipitation and Circulation Covariability in the Extratropics. *J. Clim.* 20, 4789–4797. doi:10.1175/JCLI4257.1

Giardino, J. R., and Vitek, J. D. (1988). The Significance of Rock Glaciers in the Glacial-Periglacial Landscape Continuum. *J. Quat. Sci.* 3, 97–103. doi:10.1002/jqs.3390030111

Gillett, N. P., Kell, T. D., and Jones, P. D. (2006). Regional Climate Impacts of the Southern Annular Mode. *Geophys. Res. Lett.* 33, L23704. doi:10.1029/2006GL027721

Glasser, N. F., Harrison, S., Winchester, V., and Aniya, M. (2004). Late Pleistocene and Holocene Palaeoclimate and Glacier Fluctuations in Patagonia. *Glob. Planet. Change* 43, 79–101. doi:10.1016/j.gloplacha.2004.03.002

Glasser, N. F., Holt, T. O., Evans, Z. D., Davies, B. J., Pelto, M., and Harrison, S. (2016). Recent Spatial and Temporal Variations in Debris Cover on Patagonian Glaciers. *Geomorphology* 273, 202–216. doi:10.1016/j.geomorph.2016.07.036

Glasser, N. F., Jansson, K. N., Harrison, S., and Kleman, J. (2008). The Glacial Geomorphology and Pleistocene History of South America Between 38°S and 56°S. *Quat. Sci. Rev.* 27, 365–390. doi:10.1016/j.quascirev.2007.11.011

Glasser, N., and Jansson, K. (2008). The Glacial Map of Southern South America. *J. Maps* 4, 175–196. doi:10.4113/jom.2008.1020

Glodny, J., Echtler, H., Figueroa, O., Franz, G., Gräfe, K., Kemnitz, H., et al. (2006). "Long-Term Geological Evolution and Mass-Flow Balance of the South-Central Andes," in *The Andes* (Berlin Heidelberg: Springer), 401–428. doi:10.1007/978-3-540-48684-8_19

Gosse, J. C., and Phillips, F. M. (2001). Terrestrial *In Situ* Cosmogenic Nuclides: Theory and Application. *Quat. Sci. Rev.* 20, 1475–1560. doi:10.1016/S0277-3791(00)00171-2

Harrison, S., Glasser, N., Winchester, V., Haresign, E., Warren, C., Duller, G. A. T., et al. (2008). Glaciar León, Chilean Patagonia: Late-Holocene Chronology and Geomorphology. *Holocene* 18, 643–652. doi:10.1177/0959683607086771

Hickey, R. L., Frey, F. A., Gerlach, D. C., and Lopez-Escobar, L. (1986). Multiple Sources for Basaltic Arc Rocks from the Southern Volcanic Zone of the Andes (34°-41°S): Trace Element and Isotopic Evidence for Contributions from Subducted Oceanic Crust, Mantle, and Continental Crust. *J. Geophys. Res.* 91, 5963. doi:10.1029/JB091iB06p05963

Hock, R. (1999). A Distributed Temperature-Index Ice- and Snowmelt Model Including Potential Direct Solar Radiation. *J. Glaciol.* 45, 101–111. doi:10.3189/S0022143000003087

Hock, R., and Holmgren, B. (2005). A Distributed Surface Energy-Balance Model for Complex Topography and its Application to Storglaciären, Sweden. *J. Glaciol.* 51, 25–36. doi:10.3189/172756505781829566

Hoke, G. D., Aranibar, J. N., Viale, M., Araneo, D. C., and Llano, C. (2013). Seasonal Moisture Sources and the Isotopic Composition of Precipitation, Rivers, and Carbonates across the Andes at 32.5-35.5°S. *Geochem. Geophys. Geosyst.* 14, 962–978. doi:10.1002/ggge.20045

Holmes, R. L. (1983). Computer-Assisted Quality Control in Tree-Ring Dating and Measurement. *Tree-Ring Bull.* 43, 51–67.

Huss, M., and Fischer, M. (2016). Sensitivity of Very Small Glaciers in the Swiss Alps to Future Climate Change. *Front. in Earth Sci.* 3. doi:10.3389/feart.2016.00034

Ivy-Ochs, S., and Kober, F. (2008). Surface Exposure Dating with Cosmogenic Nuclides. *E&G Quat. Sci. J.* 57, 179–209. doi:10.3285/eg.57.1-2.7

Jenny, B., Valero-Garcés, B. L., Urrutia, R., Kelts, K., Veit, H., Appleby, P. G., et al. (2002). Moisture Changes and Fluctuations of the Westerlies in Mediterranean Central Chile During the Last 2000 Years: The Laguna Aculeo Record (33°50′S). *Quat. Int.* 87. doi:10.1016/S1040-6182(01)00058-1

Jenny, H. (1944). *Factors of Soil Formation: A System of Quantitative Pedology*. New York, NY: Courier Corporation.

Jomelli, V., Lane, T., Favier, V., Masson-Delmotte, V., Swingedouw, D., Rinterknecht, V., et al. (2016). Paradoxical Cold Conditions During the Medieval Climate Anomaly in the Western Arctic. *Sci. Rep.* 6, 32984. doi:10.1038/srep32984

Jomelli, V., Mokadem, F., Schimmelpfennig, I., Chapron, E., Rinterknecht, V., Favier, V., et al. (2017). Sub-Antarctic Glacier Extensions in the Kerguelen Region (49°S, Indian Ocean) Over the Past 24,000 Years Constrained by ^{36}Cl Moraine Dating. *Quat. Sci. Rev.* 162, 128–144. doi:10.1016/j.quascirev.2017.03.010

Kaplan, M. R., Schaefer, J. M., Strelin, J. A., Denton, G. H., Anderson, R. F., Vandergoes, M. J., et al. (2016). Patagonian and Southern South Atlantic View of Holocene Climate. *Quat. Sci. Rev.* 141, 112–125. doi:10.1016/j.quascirev.2016.03.014

Kaser, G., and Osmaston, H. (2002). *Tropical Glaciers*. Cambridge, United Kingdom: Cambridge University Press.

Kirkbride, M. P., and Warren, C. R. (1999). Tasman Glacier, New Zealand: 20th-Century Thinning and Predicted Calving Retreat. *Glob. Planet. Change* 22, 11–28. doi:10.1016/S0921-8181(99)00021-1

Kull, C., and Grosjean, M. (2000). Late Pleistocene Climate Conditions in the North Chilean Andes Drawn from a Climate–Glacier Model. *J. Glaciol.* 46, 622–632. doi:10.3189/172756500781832611

Lamy, F., Hebbeln, D., Röhl, U., and Wefer, G. (2001). Holocene Rainfall Variability in Southern Chile: A Marine Record of Latitudinal Shifts of the Southern Westerlies. *Earth Planet. Sci. Lett.* 185. doi:10.1016/S0012-821X(00)00381-2

Lamy, F., Kaiser, J., Arz, H. W., Hebbeln, D., Ninnemann, U., Timm, O., et al. (2007). Modulation of the Bipolar Seesaw in the Southeast Pacific During Termination 1. *Earth Planet. Sci. Lett.* 259, 400–413. doi:10.1016/j.epsl.2007.04.040

Licciardi, J. M., Denoncourt, C. L., and Finkel, R. C. (2008). Cosmogenic ^{36}Cl Production Rates from Ca Spallation in Iceland. *Earth Planet. Sci. Lett.* 267 (1–2), 365–377. doi:10.1016/j.epsl.2007.11.036

Licciardi, J. M., Schaefer, J. M., Taggart, J. R., and Lund, D. C. (2009). Holocene Glacier Fluctuations in the Peruvian Andes Indicate Northern Climate Linkages. *Science* 325, 1677–1679. doi:10.1126/science.1175010

Lifton, N., Sato, T., and Dunai, T. J. (2014). Scaling *In Situ* Cosmogenic Nuclide Production Rates Using Analytical Approximations to Atmospheric Cosmic-Ray Fluxes. *Earth Planet. Sci. Lett.* 386, 149–160. doi:10.1016/j.epsl.2013.10.052

Liu, Z., and Yang, H. (2003). Extratropical Control of Tropical Climate, the Atmospheric Bridge and Oceanic Tunnel. *Geophys. Res. Lett.* 30, a–n. doi:10.1029/2002GL016492

Lusk, C. H., and Le-Quesne, C. (2000). Branch Whorls of Juvenile Araucaria Araucana (Molina) Koch: Are They Formed Annually? *Rev. Chil. Hist. Nat.* 73. doi:10.4067/S0716-078X2000000300013

Mann, M. E., Zhang, Z., Rutherford, S., Bradley, R. S., Hughes, M. K., Shindell, D., et al. (2009). Global Signatures and Dynamical Origins of the Little Ice Age and Medieval Climate Anomaly. *Science* 326, 1256–1260. doi:10.1126/science.1177303

Marrero, S. M., Phillips, F. M., Borchers, B., Lifton, N., Aumer, R., and Balco, G. (2016b). Cosmogenic Nuclide Systematics and the CRONUScalc Program. *Quat. Geochronol.* 31, 160–187. doi:10.1016/j.quageo.2015.09.005

Marrero, S. M., Phillips, F. M., Caffee, M. W., and Gosse, J. C. (2016a). CRONUS-Earth Cosmogenic ^{36}Cl Calibration. *Quat. Geochronol.* 31, 199–219. doi:10.1016/j.quageo.2015.10.002

Masiokas, M. H., Rivera, A., Espizua, L. E., Villalba, R., Delgado, S., and Aravena, J. C. (2009). Glacier Fluctuations in Extratropical South America During the Past 1000years. *Palaeogeogr. Palaeoclimatol. Palaeoecol.* 281, 242–268. doi:10.1016/j.palaeo.2009.08.006

Masiokas, M. H., Villalba, R., Luckman, B. H., Lascano, M. E., Delgado, S., and Stepanek, P. (2008). 20th-Century Glacier Recession and Regional Hydroclimatic Changes in Northwestern Patagonia. *Glob. Planet. Change* 60, 85–100. doi:10.1016/j.gloplacha.2006.07.031

Mason, J. A., and Jacobs, P. M. (2018). "Soils and Palaeosols in Glacial Environments," in *Past Glacial Environments* (Amsterdam, Netherlands: Elsevier), 587–605. doi:10.1016/b978-0-08-100524-8.00018-x

Mercer, J. H. (1976). Glacial History of Southernmost South America. *Quat. Res.* 6, 125–166. doi:10.1016/0033-5894(76)90047-8

Miller, G. H., Geirsdóttir, Á., Zhong, Y., Larsen, D. J., Otto-Bliesner, B. L., Holland, M. M., et al. (2012). Abrupt Onset of the Little Ice Age Triggered by Volcanism and Sustained by Sea-Ice/Ocean Feedbacks. *Geophys. Res. Lett.* 39, a–n. doi:10.1029/2011GL050168

Miller, R. F. (1976). Charging for Floor Stock Controlled Drugs. *Am. J. Hosp. Pharm.* 33 (2), 113. doi:10.1093/ajhp/33.2.113a

Möller, M., and Schneider, C. (2010). Calibration of Glacier Volume-Area Relations from Surface Extent Fluctuations and Application to Future Glacier Change. *J. Glaciol.* 56, 33–40. doi:10.3189/002214310791190866

Möller, M., Schneider, C., and Kilian, R. (2007). Glacier Change and Climate Forcing in Recent Decades at Gran Campo Nevado, Southernmost Patagonia. *Ann. Glaciol.* 46, 136–144. doi:10.3189/172756407782871530

Montecinos, A., and Aceituno, P. (2003). Seasonality of the ENSO-Related Rainfall Variability in Central Chile and Associated Circulation Anomalies. *J. Clim.* 16. doi:10.1175/1520-0442(2003)016<0281:SOTERR>2.0.CO;2

Moore, P. L. (2018). Stability of Supraglacial Debris. *Earth Surf. Process. Landforms* 43, 285–297. doi:10.1002/esp.4244

Moran, A. P., Ivy Ochs, S., Vockenhuber, C., and Kerschner, H. (2016). Rock Glacier Development in the Northern Calcareous Alps at the Pleistocene-Holocene Boundary. *Geomorphology* 273, 178–188. doi:10.1016/j.geomorph.2016.08.017

Moreno, P. I., François, J. P., Villa-Martínez, R. P., and Moy, C. M. (2009). Millennial-Scale Variability in Southern Hemisphere Westerly Wind Activity Over the Last 5000 Years in SW Patagonia. *Quat. Sci. Rev.* 28. doi:10.1016/j.quascirev.2008.10.009

Moreno, P. I., and Videla, J. (2016). Centennial and Millennial-Scale Hydroclimate Changes in Northwestern Patagonia Since 16,000 Yr BP. *Quat. Sci. Rev.* 149, 326–337. doi:10.1016/j.quascirev.2016.08.008

Moreno, P. I., Vilanova, I., Villa-Martínez, R., Dunbar, R. B., Mucciarone, D. A., Kaplan, M. R., et al. (2018). Onset and Evolution of Southern Annular Mode-Like Changes at Centennial Timescale. *Sci. Rep.* 8, 1–9. doi:10.1038/s41598-018-21836-6

Muñoz, A. A., Barichivich, J., Christie, D. A., Dorigo, W., Sauchyn, D., González-Reyes, Á., et al. (2014). Patterns and Drivers of *Araucaria Araucanaforest* Growth Along a Biophysical Gradient in the Northern Patagonian Andes: Linking Tree Rings with Satellite Observations of Soil Moisture. *Austral. Ecol.* 39, 158–169. doi:10.1111/aec.12054

Muñoz, A. A., González-Reyes, A., Lara, A., Sauchyn, D., Christie, D., Puchi, P., et al. (2016). Streamflow Variability in the Chilean Temperate-Mediterranean Climate Transition (35°S-42°S) During the Last 400 Years Inferred from Tree-Ring Records. *Clim. Dyn.* 47, 4051–4066. doi:10.1007/s00382-016-3068-9

Muñoz, M., Alam, M. A., Parada, M., and Lahsen, A. (2011). Geothermal System Associated with the Sierra Nevada Volcano, Araucanía Region, Chile. *Trans. - Geotherm. Resour. Counc.* 35, 935–941.

Naito, N., Nakawo, M., Kadota, T., and Raymond, C. F. (2000). *Numerical Simulation of Recent Shrinkage of Khumbu Glacier, Nepal Himalayas.* Editors N. Nakawo, A. Fountain, and C. Raymond. (Debris-Covered Glaciers: IAHS Publications), 264, 245–254.

Nimick, D. A., McGrath, D., Mahan, S. A., Friesen, B. A., and Leidich, J. (2016). Latest Pleistocene and Holocene Glacial Events in the Colonia Valley, Northern Patagonia Icefield, Southern Chile. *J. Quat. Sci.* 31, 551–564. doi:10.1002/jqs.2847

Oien, R. P., Rea, B. R., Spagnolo, M., Barr, I. D., and Bingham, R. G. (2021). Testing the Area-Altitude Balance Ratio (AABR) and Accumulation-Area Ratio (AAR) Methods of Calculating Glacier Equilibrium-Line Altitudes. *J. Glaciol.* 68, 357–368. doi:10.1017/jog.2021.100

Osmaston, H. (2005). Estimates of Glacier Equilibrium Line Altitudes by the Area×Altitude, the Area×Altitude Balance Ratio and the Area×Altitude Balance Index Methods and Their Validation. *Quat. Int.* 138-139, 22–31. doi:10.1016/j.quaint.2005.02.004

Östrem, G. (1959). Ice Melting Under a Thin Layer of Moraine, and the Existence of Ice Cores in Moraine Ridges. *Geogr. Ann.* 41, 228–230.

Owen, L. A., and England, J. (1998). Observations on Rock Glaciers in the Himalayas and Karakoram Mountains of Northern Pakistan and India. *Geomorphology* 26, 199–213. doi:10.1016/S0169-555X(98)00059-2

Palacios, D., García-Ruiz, J. M., Andrés, N., Schimmelpfennig, I., Campos, N., Léanni, L., et al. (2017). Deglaciation in the Central Pyrenees During the Pleistocene-Holocene Transition: Timing and Geomorphological Significance. *Quat. Sci. Rev.* 162, 111–127. doi:10.1016/j.quascirev.2017.03.007

Pellicciotti, F., Ragettli, S., Carenzo, M., and McPhee, J. (2014). Changes of Glaciers in the Andes of Chile and Priorities for Future Work. *Sci. Total Environ.* 493, 1197–1210. doi:10.1016/j.scitotenv.2013.10.055

Perren, B. B., Hodgson, D. A., Roberts, S. J., Sime, L., van Nieuwenhuyze, W., Verleyen, E., et al. (2020). Southward Migration of the Southern Hemisphere Westerly Winds Corresponds with Warming Climate Over Centennial Timescales. *Commun. Earth Environ.* 1 (1), 58. doi:10.1038/s43247-020-00059-6

Phillips, F. M., Stone, W. D., and Fabryka-Martin, J. T. (2001). An Improved Approach to Calculating Low-Energy Cosmic-Ray Neutron Fluxes Near the Land/Atmosphere Interface. *Chem. Geol.* 175, 689–701. doi:10.1016/S0009-2541(00)00329-6

Plummer, M. A., and Phillips, F. M. (2003). A 2-D Numerical Model of Snow/Ice Energy Balance and Ice Flow for Paleoclimatic Interpretation of Glacial Geomorphic Features. *Quat. Sci. Rev.* 22, 1389–1406. doi:10.1016/S0277-3791(03)00081-7

Putkonen, J., and Swanson, T. (2003). Accuracy of Cosmogenic Ages for Moraines. *Quat. Res.* 59, 255–261. doi:10.1016/S0033-5894(03)00006-1

Racoviteanu, A. E., Nicholson, L., Glasser, N. F., Miles, E., Harrison, S., and Reynolds, J. M. (2021). Debris-Covered Glacier Systems and Associated Glacial Lake Outburst Flood Hazards: Challenges and Prospects. *J. Geol. Soc.* 179, jgs2021–084. doi:10.1144/jgs2021-084

Reynhout, S. A., Sagredo, E. A., Kaplan, M. R., Aravena, J. C., Martini, M. A., Moreno, P. I., et al. (2019). Holocene Glacier Fluctuations in Patagonia Are Modulated by Summer Insolation Intensity and Paced by Southern Annular Mode-Like Variability. *Quat. Sci. Rev.* 220, 178–187. doi:10.1016/j.quascirev.2019.05.029

Rivera, A., Bown, F., Casassa, G., Acuña, C., and Clavero, J. (2005). Glacier Shrinkage and Negative Mass Balance in the Chilean Lake District (40°S). *Hydrological Sci. J.* 50, 963–974. doi:10.1623/hysj.2005.50.6.963

Rupper, S., and Roe, G. (2008). Glacier Changes and Regional Climate: A Mass and Energy Balance Approach*. *J. Clim.* 21, 5384–5401. doi:10.1175/2008JCLI2219.1

Rutllant, J., and Fuenzalida, H. (1991). Synoptic Aspects of the Central Chile Rainfall Variability Associated with the Southern Oscillation. *Int. J. Climatol.* 11, 63–76. doi:10.1002/joc.3370110105

Sagredo, E. A., and Lowell, T. V. (2012). Climatology of Andean Glaciers: A Framework to Understand Glacier Response to Climate Change. *Glob. Planet. Change* 86–87, 101–109. doi:10.1016/j.gloplacha.2012.02.010

Sagredo, E. A., Lowell, T. V., Kelly, M. A., Rupper, S., Aravena, J. C., Ward, D. J., et al. (2016). Equilibrium Line Altitudes Along the Andes During the Last Millennium: Paleoclimatic Implications. *Holocene* 27, 1019–1033. doi:10.1177/0959683616678458

Sagredo, E. A., Rupper, S., and Lowell, T. V. (2014). Sensitivities of the Equilibrium Line Altitude to Temperature and Precipitation Changes Along the Andes. *Quat. Res.* 81, 355–366. doi:10.1016/j.yqres.2014.01.008

Sarikaya, M. A., Çiner, A., Zreda, M., Şen, E., and Ersoy, O. (2019). Chlorine Degassing Constrained by Cosmogenic ^{36}Cl and Radiocarbon Dating of Early Holocene Rhyodacitic Lava Domes on Erciyes Stratovolcano, Central Turkey. *J. Volcanol. Geotherm. Res.* 369, 263–275. doi:10.1016/j.jvolgeores.2018.11.029

Schaefer, M., Rodriguez, J. L., Scheiter, M., and Casassa, G. (2017). Climate and Surface Mass Balance of Mocho Glacier, Chilean Lake District, 40°S. *J. Glaciol.* 63, 218–228. doi:10.1017/jog.2016.129

Schimmelpfennig, I., Benedetti, L., Finkel, R., Pik, R., Blard, P.-H., Bourlès, D., et al. (2009). Sources of *In-Situ* ^{36}Cl in Basaltic Rocks. Implications for Calibration of Production Rates. *Quat. Geochronol.* 4, 441–461. doi:10.1016/j.quageo.2009.06.003

Schürch, P., Densmore, A. L., Ivy-Ochs, S., Rosser, N. J., Kober, F., Schlunegger, F., et al. (2016). Quantitative Reconstruction of Late Holocene Surface Evolution on an Alpine Debris-Flow Fan. *Geomorphology* 275, 46–57. doi:10.1016/j.geomorph.2016.09.020

Shakesby, R. A., Dawson, A. G., and Matthews, J. A. (1987). Rock Glaciers, Protalus Ramparts and Related Phenomena, Rondane, Norway: A Continuum of Large-Scale Talus-Derived Landforms. *Boreas* 16, 305–317. doi:10.1111/j.1502-3885.1987.tb00099.x

Sinclair, M. R. (1996). A Climatology of Anticyclones and Blocking for the Southern Hemisphere. *Mon. Wea. Rev.* 124 (2), 245–264. doi:10.1175/1520-0493(1996)124<0245:ACOAAB>2.0.CO;2

Solomina, O. N., Bradley, R. S., Hodgson, D. A., Ivy-Ochs, S., Jomelli, V., Mackintosh, A. N., et al. (2015). Holocene Glacier Fluctuations. *Quat. Sci. Rev.* 111, 9–34. doi:10.1016/j.quascirev.2014.11.018

Stansell, N. D., Mark, B. G., Licciardi, J. M., Rodbell, D. T., Fairman, J. G., Schoessow, F. S., et al. (2022). Energy Mass Balance and Flow Modeling of Early Holocene Glaciers in the Queshque Valley, Cordillera Blanca, Peru. *Quat. Sci. Rev.* 281, 107414. doi:10.1016/j.quascirev.2022.107414

Stokes, M. A., and Smiley, T. L. (1996). *An Introduction to Tree-Ring Dating*. Tucson, AZ: University of Arizona Press.

Stone, J. O., Allan, G. L., Fifield, L. K., and Cresswell, R. G. (1996). Cosmogenic Chlorine-36 from Calcium Spallation. *Geochimica Cosmochimica Acta* 60. doi:10.1016/0016-7037(95)00429-7

Strub, P. T. (1998). "Coastal Ocean Circulation off Western South America," in *The Global Coastal Ocean* (Cambridge, MA: Regional Studies and Syntheses), 273–315.

van den Bos, V., Rees, A., Newnham, R., Vandergoes, M., Wilmshurst, J., and Augustinus, P. (2018). Holocene Temperature, Humidity and Seasonality in Northern New Zealand Linked to Southern Hemisphere Summer Insolation. *Quat. Sci. Rev.* 201, 77–88. doi:10.1016/j.quascirev.2018.10.008

Varma, V., Prange, M., Lamy, F., Merkel, U., and Schulz, M. (2011). Solar-Forced Shifts of the Southern Hemisphere Westerlies During the Holocene. *Clim. Past.* 7, 339–347. doi:10.5194/cp-7-339-2011

Veblen, T. T. (1982). Regeneration Patterns in *Araucaria Araucana* Forests in Chile. *J. Biogeogr.* 9, 11–28. doi:10.2307/2844727

Verfaillie, D., Charton, J., Schimmelpfennig, I., Stroebele, Z., Jomelli, V., Bétard, F., et al. (2021). Evolution of the Cook Ice Cap (Kerguelen Islands) Between the Last Centuries and 2100 Ce Based on Cosmogenic Dating and Glacio-Climatic Modelling. *Antarct. Sci.* 33, 301–317. doi:10.1017/S0954102021000080

Villalba, R., Lara, A., Masiokas, M. H., Urrutia, R., Luckman, B. H., Marshall, G. J., et al. (2012). Unusual Southern Hemisphere Tree Growth Patterns Induced by Changes in the Southern Annular Mode. *Nat. Geosci.* 5, 793–798. doi:10.1038/ngeo1613

Villalba, R. (1994). Tree-Ring and Glacial Evidence for the Medieval Warm Epoch and the Little Ice Age in Southern South America. *Clim. Change* 26, 183–197. doi:10.1007/BF01092413

Warren, C. R., and Sugden, D. E. (1993). The Patagonian Icefields: A Glaciological Review. *Arct. Alp. Res.* 25, 316. doi:10.2307/1551915

Wirsig, C., Ivy-Ochs, S., Akçar, N., Lupker, M., Hippe, K., Wacker, L., et al. (2016). Combined Cosmogenic ^{10}Be, *In Situ* ^{14}C and ^{36}Cl Concentrations Constrain Holocene History and Erosion Depth of Grueben Glacier (CH). *Swiss J. Geosci.* 109 (3), 379–388. doi:10.1007/s00015-016-0227-2

Zreda, M. G., and Phillips, F. M. (2000). "Cosmogenic Nuclide Buildup in Surficial Materials," in *Quaternary Geochronology: Methods and Applications*. Editors J. Stratton Noller, J. M. Sowers, and W. R. Lettis (Washington, DC: John Wiley & Sons), 61–76. doi:10.1029/RF004p0061

Zreda, M. G., Phillips, F. M., Kubik, P. W., Sharma, P., and Elmore, D. (1993). Cosmogenic ^{36}Cl Dating of a Young Basaltic Eruption Complex, Lathrop Wells, Nevada. *Geol.* 21, 57. doi:10.1130/0091-7613(1993)021<0057:CCDOAY>2.3.CO;2

Zweck, C., Zreda, M., and Desilets, D. (2013). Snow Shielding Factors for Cosmogenic Nuclide Dating Inferred from Monte Carlo Neutron Transport Simulations. *Earth Planet. Sci. Lett.* 379, 64–71. doi:10.1016/j.epsl.2013.07.023

Conflict of Interest: The authors declare that the research was conducted in the absence of any commercial or financial relationships that could be construed as a potential conflict of interest.

frontiers | Frontiers in Earth Science

ORIGINAL RESEARCH
published: 05 July 2022
doi: 10.3389/feart.2022.892316

The Last Glacial Maximum and Deglacial History of the Seno Skyring Ice Lobe (52°S), Southern Patagonia

María-Paz Lira[1], Juan-Luis García[2], Michael J. Bentley[1], Stewart S. R. Jamieson[1], Christopher M. Darvill[3], Andrew S. Hein[4], Hans Fernández[2], Ángel Rodés[5†], Derek Fabel[5], Rachel K. Smedley[6] and Steven A. Binnie[7]*

[1]Department of Geography, Durham University, Durham, United Kingdom, [2]Instituto de Geografía, Pontificia Universidad Católica de Chile, Santiago, Chile, [3]Department of Geography, The University of Manchester, Manchester, United Kingdom, [4]School of Geosciences, University of Edinburgh, Edinburgh, United Kingdom, [5]Scottish Universities Environmental Research Centre, Glasgow, United Kingdom, [6]Department of Geography and Planning, University of Liverpool, Liverpool, United Kingdom, [7]Institut für Geologie und Mineralogie, Universität zu Köln, Köln, Germany

OPEN ACCESS

Edited by:
Nadia Solovieva,
University College London,
United Kingdom

Reviewed by:
Sam Kelley,
University College Dublin, Ireland
Nathan D Stansell,
Northern Illinois University,
United States

***Correspondence:**
María-Paz Lira
maria.p.lira-bahamonde@durham.ac.uk

†Present address:
Ángel Rodés,
Departamento de Xeografía,
Universidade de Santiago de Compostela, Santiago de Compostela, Spain

Specialty section:
This article was submitted to Quaternary Science, Geomorphology and Paleoenvironment, a section of the journal Frontiers in Earth Science

Received: 08 March 2022
Accepted: 25 May 2022
Published: 05 July 2022

Citation:
Lira M-P, García J-L, Bentley MJ, Jamieson SSR, Darvill CM, Hein AS, Fernández H, Rodés Á, Fabel D, Smedley RK and Binnie SA (2022) The Last Glacial Maximum and Deglacial History of the Seno Skyring Ice Lobe (52°S), Southern Patagonia. Front. Earth Sci. 10:892316. doi: 10.3389/feart.2022.892316

There are still many uncertainties about the climatic forcing that drove the glacier fluctuations of the Patagonian Ice Sheet (PIS, 38–55°S) during the last glacial period. A key source of uncertainty is the asynchrony of ice lobe fluctuations between the northern, central, and southern PIS. To fully understand the regional trends requires careful mapping and extensive geochronological studies. This paper presents geomorphological and geochronological reconstructions of the glacial and deglacial landforms formed during the last glacial period at the Seno Skyring lobe, southernmost Patagonia (52°S, 71°W). We present a detailed geomorphological map, where we identify two moraine systems. The outer and older is named Laguna Blanca (LB) and the inner Río Verde (RV). The LB moraines were built subaerially, whereas parts of the RV were deposited subaqueously under the palaeo lake Laguna Blanca, which developed during deglaciation. We conducted surface exposure ^{10}Be dating methods on boulder samples collected from LB and RV glacial margins. The moraine LB III and LB IV formed at 26.3 ± 2.3 ka (n = 5) and 24.3 ± 0.9 ka (n = 3), respectively. For the inner RV moraine, we obtained an age of 18.7 ± 1.5 ka (n = 6). For the palaeo Laguna Blanca evolution, we performed ^{10}Be exposure ages on shoreline berms and optically stimulated luminesce dating to constrain the lake levels, and ^{10}Be depth profile dating on an outwash deposit formed by a partial lake drainage event, which occurred at 22 ± 3 ka. For the RV moraine deglaciation, we performed radiocarbon dating of basal sediments in a peat bog, which indicates that the glacier retreated from the terminal RV moraine by at least c. 16.4 cal kyr BP. Our moraine geochronology shows an asynchrony in the maximum extents and a different pattern of ice advances between neighbouring lobes in southern Patagonia. We speculate that this may be due, at least in part, to the interaction between topography and the precipitation carried by the southern westerly wind belt. However, we found broad synchrony of glacial readvances contemporaneous with the RV moraine.

Keywords: patagonian ice sheet, glacial geomorphology, cosmogenic nuclide dating, proglacial lake evolution, geochronology

1 INTRODUCTION

The location of Patagonia in the Southern Hemisphere makes it a good location to study paleoclimate of the Southern Hemisphere since it is the only continental region that straddles the core of the Southern Westerly Winds (SWWs; **Figure 1A**), which are directly linked with the precipitation and temperatures affecting the region (Garreaud, 2009). Moreover, its close position to Antarctica allows comparisons between the terrestrial and marine records from Patagonia with Antarctic climatic proxies (Sugden et al., 2009; Darvill et al., 2016; García et al., 2020). The last glacial cycle was marked by a number of cold intervals, according to Antarctic ice cores (Jouzel et al., 2007). However, these events are not consistently represented in the glacial geomorphology of the Patagonian Ice Sheet (PIS) margin (Davies et al., 2020). Terrestrial geochronologic records show that the maximum extents of the ice lobe fluctuations along the PIS occurred at different times during the last glacial period, suggesting an asynchrony between northern, central and southern Patagonia. Most moraine chronologies have recorded local ice maxima during MIS 2 and MIS 3, but also MIS 4 and MIS 5a (Kaplan et al., 2004; Douglass et al., 2006; Hein et al., 2010; Darvill et al., 2015; García et al., 2018, 2021; Mendelová et al., 2020; Leger et al., 2021; Peltier et al., 2021). This asynchrony of the glacial maximum extensions could be in response to the interaction of different factors, such as shifts of the atmospheric and oceanic frontal systems, Antarctic Sea-ice migration and Southern Ocean stratification (Darvill et al., 2016) and/or topographic controls (Sugden et al., 2002). However, the understanding of the forcing mechanisms that drove this difference in the timing of the glacial fluctuations is still incomplete. To fully understand the past climate that prevailed along the PIS during the last glacial cycle, it is necessary to perform careful mapping and extensive geochronological studies of different outlets. Here, we present glacial geomorphological observations paired with geochronology of the former Seno Skyring lobe (52°S, 71°W) to contribute to the understanding of the behaviour of the former PIS. The glacial geomorphology of this outlet has seen a range of geomorphological mapping at different scales (Caldenius, 1932; Meglioli, 1992; Lovell et al., 2012; Darvill et al., 2014) but the glacial landforms have not previously been dated. Using a combined approach of satellite images, aerial photographs stereoscopic analysis, and field mapping, we produced a more detailed geomorphological map

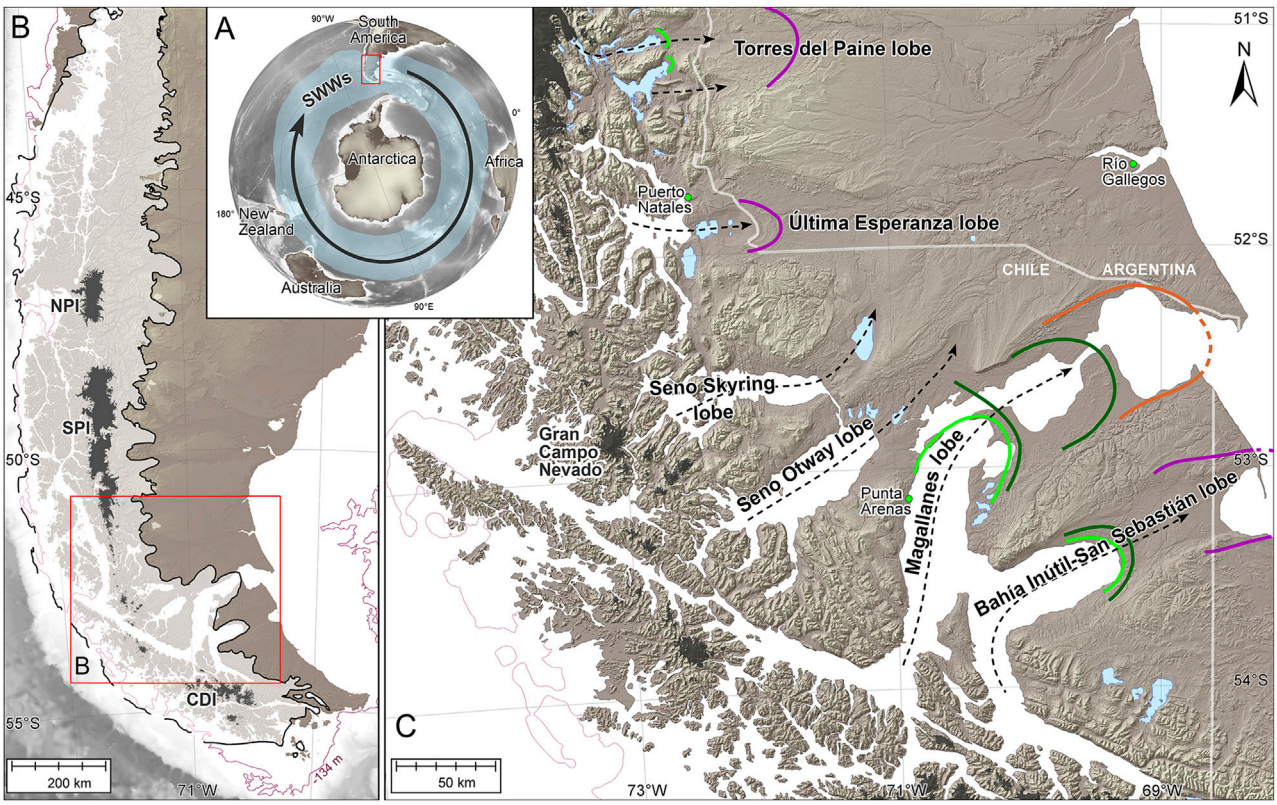

FIGURE 1 | Location Map. **(A)**. Location of Patagonia and the Southern Westerly Winds belt. **(B)**. Extension of the Patagonian Ice Sheet during the LGM at 25 ka (pale grey shading, PATICE, Davies et al., 2020). Modern ice is shown by dark grey shading; NPI: Northern Patagonian Icefield, SPI: Southern Patagonian Icefield, CDI: Cordillera de Darwin Icefield. Bathymetric contour of -134 m indicates approximate fall in eustatic sea level during the LGM (Lambeck et al., 2014). **(C)**. Location of Seno Skyring ice lobe in Southernmost Patagonia and adjacent ice lobes. Coloured arcs correspond to the age of dated moraine belts from the last glacial cycle: orange corresponds to MIS4, purple to MIS 3 and green to MIS 2 (Darvill et al., 2015; García et al., 2018; Peltier et al., 2021). Black dashed lines are hypothesised flow lines of major outlet lobes. Background image is a Copernicus DEM (30 m resolution).

of the study area than previous work and provide a detailed chronological framework using ^{10}Be exposure ages from boulders resting on moraine ridges, cobbles on beach berms and outwash plains, a ^{10}Be depth profile through outwash sediment, optically stimulated luminescence dating of lacustrine deposits, and radiocarbon dating of basal peat sediments. Our aim is to understand the behaviour of the Seno Skyring lobe during the last glacial period and termination.

2 GENERAL SETTING AND STUDY AREA

2.1 Southern Patagonian Ice Sheet Setting

During the last glacial cycle in Patagonia, the PIS developed continuously along the Andean Cordillera from 38° to 55°S (**Figure 1B**), extending for about 2000 km (Glasser and Jansson, 2008; Rabassa, 2008; Davies et al., 2020). In southernmost Patagonia, the PIS extended to the west through tidewater-terminating outlets, calving into the Pacific Ocean. To the east, the outlets extended for 10–100 s of km across the Patagonian steppe (**Figure 1C**). The bed topography in this area is slightly unusual in the way the ice occupied reverse-bed slopes whose gradient varied between lobes (Kaplan et al., 2009; Anderson et al., 2012). The eastern area contains the best-preserved records of glacial geomorphology in the region as a result of its dry conditions and relatively stable tectonic context with no major uplift (Clapperton, 1993).

The climate in Patagonia is strongly influenced by SWWs, which impact the position of the Sub Tropical and Sub Antarctic Fronts. The SWWs are directly linked with precipitation (Garreaud et al., 2013), and their core is today located between ~50–55°S (Lamy et al., 2010). During the winter months the SWWs' core expands northwards and during the summer it contracts southwards, in response to seasonal changes in the Antarctic sea ice extent (Garreaud et al., 2013). The precipitation in western Patagonia ranges between 5,000–10,000 mm/year, decreasing abruptly towards the east to less than 300 mm/year (Garreaud, 2009), due to the orographic effect produced by the Andean Cordillera. This rain shadow effect strongly affects the vegetation in the area. Magellanic Moorland and evergreen forest are dominant in the west, and a few tens of kilometres east from the Andes Cordillera, the vegetation sharply changes to Patagonian steppe (Tuhkanen et al., 1989-1990).

We focus here on the southernmost part of the PIS, from the former lobe in Torres del Paine–derived from the southernmost tip of the present-day Southern Patagonia Icefield–south to the former Bahía Inútil-San Sebastián lobe that extended across Tierra del Fuego (**Figure 1C**). This region incorporates a range of different topographic settings from former outlets that terminated close to the mountains (10 s of km length) with a steep slope (such as Torres del Paine, and Última Esperanza), to low-gradient outlets terminations that extended 100 s of km east across the low elevation areas of Patagonia, such as Magallanes, and Bahía Inútil-San Sebastián lobes (Benn and Clapperton, 2000b).

2.2 Study Area and Previous Work

The Seno Skyring ice lobe originated at Gran Campo Nevado ice cap (52°40′S), a remnant of the continuous extension of the PIS along the Austral Andes, which has altitudes up to ~1,500 m a.s.l. From there, the ice lobe extended to the east of the Andes (Kilian et al., 2007), sculpting deep valleys that today form the fjord of Seno Skyring (**Figure 1C**). Caldenius (1932) was the first to identify four moraine systems deposited east of Seno Skyring (**Figure 2**); we follow Caldenius' nomenclature for the moraine systems. After Caldenius' (1932) map, Meglioli (1992), Lovell et al. (2012), and Darvill et al. (2014) improved the glacial geomorphological mapping at a regional scale. Later studies suggested that the two inner moraine systems, Laguna Blanca (LB) and Río Verde (RV)—older and younger respectively—were formed during the last glacial cycle, based on the outlet glacier's relationship with neighbouring dated glacial lobes (Darvill et al., 2017; Davies et al., 2020). A proglacial lake formed during the retreat between these two moraine systems (Caldenius, 1932). It has been hypothesised that a partial proglacial drainage may have occurred in front of the receding Seno Otway and Magallanes lobes (Benn and Clapperton, 2000b; Lovell et al., 2012; Darvill et al., 2014). Dating of organic material in fjord cores, suggest that towards the end of the last glaciation the Seno Skyring ice lobe had retreated back and was confined to the proximity of the Gran Campo Nevado ice cap by 13.9 ± 0.3 cal. BP (Kilian et al., 2007; 2013). Until the study we present here, no detailed mapping and chronological control existed for the Skyring lobe.

3 METHODS

We undertook detailed geomorphological mapping and used the mapping to underpin the dating of key landforms to target glacial and deglacial events using cosmogenic ^{10}Be surface exposure dating, a ^{10}Be depth profile, optically stimulated luminescence (OSL) and radiocarbon dating methods. For ^{10}Be cosmogenic measurements, we took samples of boulders on moraines, cobbles on major outwash plains and palaeo-shoreline berms, and measured ^{10}Be concentrations to determine exposure histories. We also sampled one depth profile to determine the age of an outwash deposit using ^{10}Be. These approaches have been widely used in semi-arid regions of eastern Patagonia (e.g., Kaplan et al., 2004; Hein et al., 2010; Darvill et al., 2015; García et al., 2018; Mendelová et al., 2020). Furthermore, we collected lacustrine sediment and bog samples to date with OSL and radiocarbon, respectively.

3.1 Geomorphological Mapping

The glacial geomorphologic map was compiled from stereoscopic analysis of aerial photographs, satellite images, and digital elevation models (**Supplementary Table S1**; extended methods). The geomorphological interpretations were field-checked over the course of several weeks of fieldwork campaigns in 2018 and 2019. Mapping of former shorelines was supported by hand-held GPS measurement transects up to 35 km along the different terrace levels. The map was prepared in ArcMap 10.7.1 (**Figure 3**).

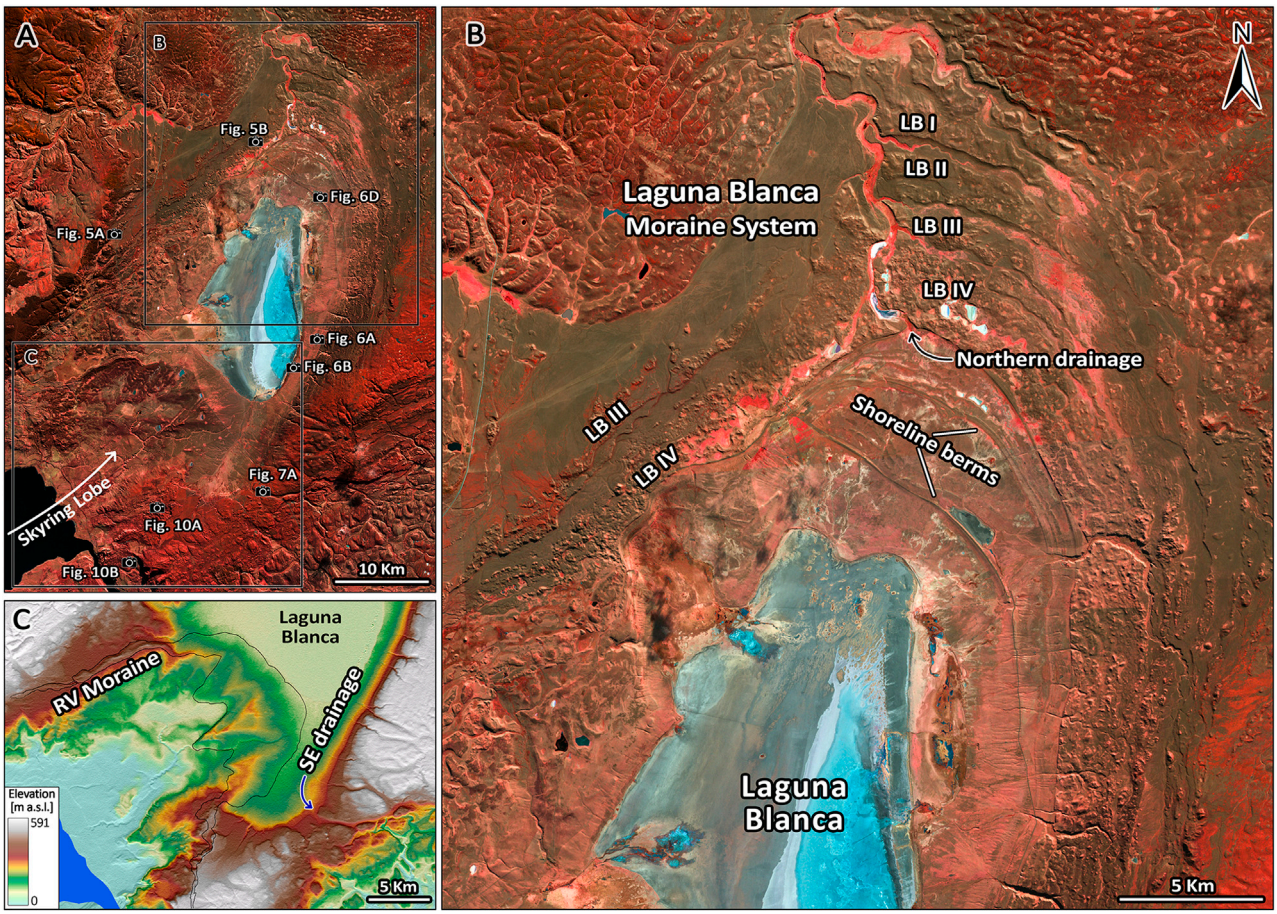

FIGURE 2 | (A) Sentinel 2 (band combination 843) image of the Seno Skyring ice lobe area. Former ice flow of the Skyring lobe was directed from Seno Skyring north-east to the Río Verde (RV) and Laguna Blanca (LB) moraine systems. **(B)** Detailed image with focus on LB moraine system, showing its four different moraine belts, from older to younger LB I, LB II, LB III and LB IV respectively. Former shoreline berms and a northern drainage spillway of the palaeo Laguna Blanca are indicated. **(C)** Hillshade and elevation colour ramp (SRTM) of the area around RV moraine system, black lines indicate the RV moraine extension. The south-eastern drainage spillway of the palaeo Laguna Blanca is marked. Note that the altitude of this drainage spillway is higher than the central (front) parts of the RV moraine, implying an ice dam must have been present.

3.2 ^{10}Be Dating

3.2.1 ^{10}Be Exposure Age Sampling

3.2.1.1 Moraines

Timing of former glacial margins were constrained through two different approaches. The first method was by the sampling of moraine boulders along the different ridges. At the Seno Skyring lobe, we sampled along LB and RV moraine systems (**Figures 2**, **3**). For LB moraines, we collected samples from multiple crests located in LB moraine III and IV. For the RV Moraine, we collected samples at the outer crest of the southeast lateral moraine. The boulder and the sampling process followed the methods of Gosse and Phillips (2001). Sampled boulders were primarily granitoid (n = 17), with some quartzites (n = 4) and one quartz arenite, all embedded in stable positions on or near moraine crests. Heyman et al. (2016) suggested that taller boulders yield more consistent results, since their tops are less likely to have suffered exhumation. We sampled boulders that were >1 m high where possible (32%), but otherwise sampled smaller boulders with ranges of 60–99 cm (45%) and 45–59 cm (23%) high (**Table 1**). For the lower relief boulders, we were careful in avoiding boulders with signs of exhumation by a visual assessment of the moraine degradation. We sampled top surfaces using nail gun cartridges and/or a hammer and chisel, avoiding erosional signs such as fresh edges, spalling or fracturing. Boulder SSK1809, had prominent quartz veins, with mean relief of 20 mm above the rest of the rock surface. We took two different samples from this boulder: SSK1809a from the boulder matrix and SSK1809b from the quartz vein (**Figures 4K,L**). We interpret the ^{10}Be on moraine boulders as minimum ages for the moraine construction and associated glacial advance.

3.2.1.2 Outwash Plains Associated to Moraine Margins

The second approach to dating glacial margins was to sample five quartz-rich cobbles embedded in the surface of an outwash plain grading from the LB Moraine III (**Figures 4C–E**). This follows the methodology of Hein et al. (2010; 2011), where outwash plain

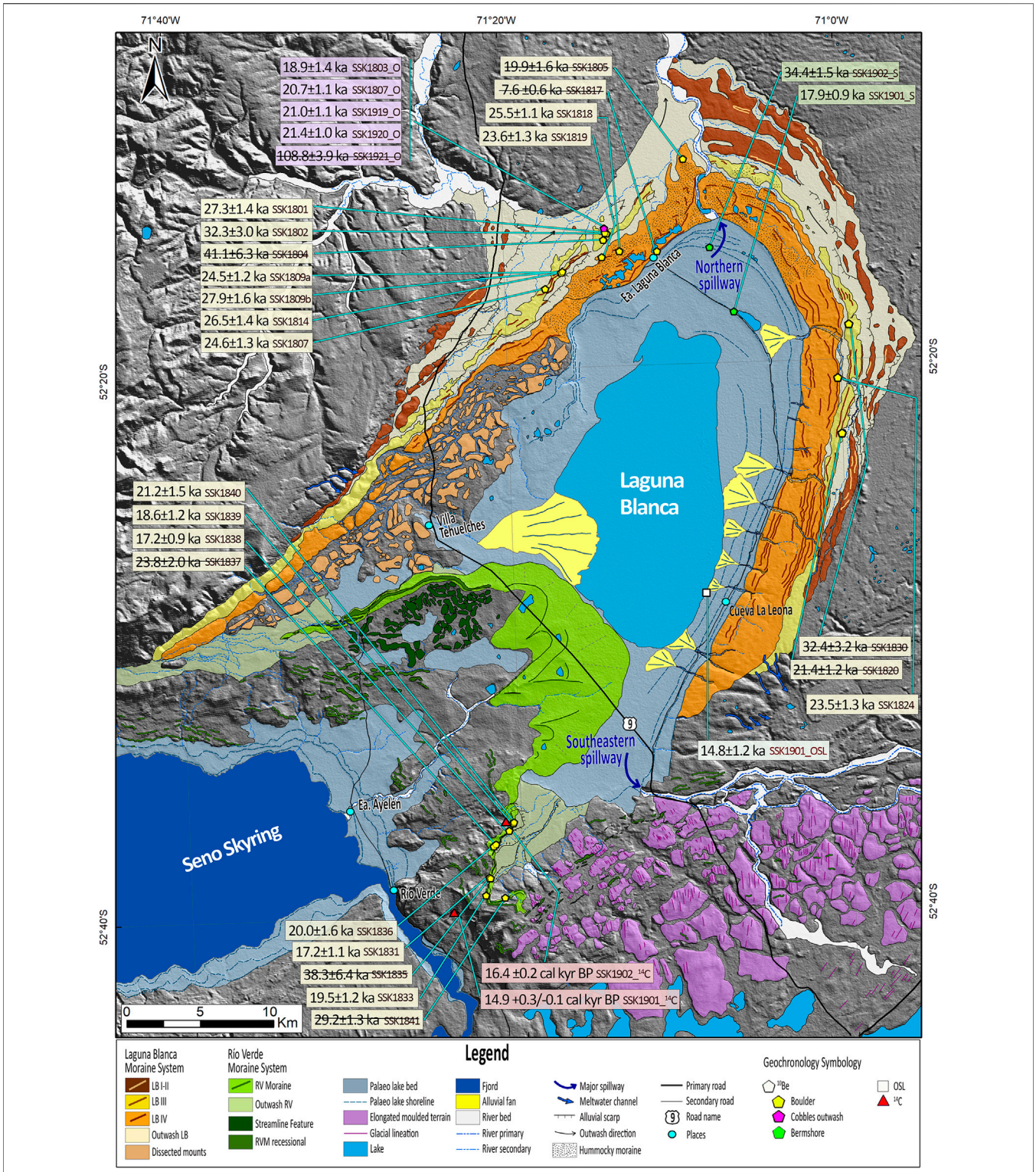

FIGURE 3 | Geomorphological map of Skyring ice lobe area. Sample locations of the cosmogenic, OSL, and radiocarbon dates are indicated. Background is a hillshade from SRTM showing the topography. Dates treated as outliers are shown crossed-out, see text for discussion.

TABLE 1 | Sample details and ^{10}Be concentrations from Skyring ice lobe and the outwash deposit located in Otway basin, associated with the southeastern Laguna Blanca spillway. The samples are grouped by landform.

Sample ID	Lat. (dd)	Lon. (dd)	Year Collected	Alt. (m asl)	Thickness (cm)	Lithology	Boulder Height (cm)	Shielding Correction	Quartz Dissolved (g)	10Be Concentration (Atoms/g)	±1σ (10Be) (Atoms/g)
Seno Skyring Ice lobe											
Laguna Blanca Moraine III											
SSK1801	−52.2558	−71.2333	2018/19	238	1.9	Quartzite	226	0.99996	23.16	147,002	7,644
SSK1802	−52.2529	−71.2313	2018	237	1.7	Granitoid	55	1.00000	21.77	174,273	16,260
SSK1804	−52.2571	−71.2333	2018/19	239	5.1	Granitoid	45	1.00000	7.00	216,115	32,612
SSK1807	−52.1496	−71.2304	2018	269	2.1	Granitoid	63	1.00000	20.72	136,186	7,150
SSK 1809a	−52.2764	−71.2761	2018/19	251	1.4	Quartzite	63	1.00000	17.91	134,406	6,505
SSK 1809b	−52.2764	−71.2761	2018	251	2.2	Quartz	63	1.00000	20.54	152,020	8,437
SSK1814	−52.2762	−71.2756	2018	247	1.5	Quartzite	45	1.00000	17.35	144,463	7,584
SSK1820	−52.3796	−71.0005	2018/19	289	3.1	Granitoid	80	1.00000	21.04	120,066	6,700
SSK1830	−52.3127	−70.9907	2018	270	2.7	Granitoid	129	0.99997	13.80	179,303	17,464
Laguna Blanca Moraine IV											
SSK1805	−52.2090	−71.1514	2018	209	1.3	Granitoid	70	0.99999	13.38	104,498	8,329
SSK1817	−52.2650	−71.1799	2018	201	1.7	Quartz arenite	84	1.00000	16.36	39,226	3,134
SSK1818	−52.2642	−71.2175	2018	209	1.6	Granitoid	127	1.00000	22.17	134,047	5,938
SSK1819	−52.2676	−71.2353	2018/19	217	2.1	Quartzite	100	1.00000	15.09	124,716	6,710
SSK1824	−52.3455	−71.0030	2018/19	246	1.9	Granitoid	104	1.00000	23.23	128,084	7,032
Río Verde Moraine											
SSK1831	−52.6455	−71.3671	2018/19	258	2.3	Granitoid	124	1.00000	17.02	94,433	5,921
SSK1833	−52.6561	−71.3713	2018	310	1.8	Granitoid	64	0.99996	16.86	113,277	7,114
SSK1835	−52.6459	−71.3670	2018	258	1.7	Granitoid	62	1.00000	11.49	212,087	35,016
SSK1836	−52.6262	−71.3618	2018	232	2.2	Granitoid	170	1.00000	17.91	107,186	8,553
SSK1837	−52.6250	−71.3596	2018	231	2.0	Granitoid	55	0.99997	20.91	128,180	10,908
SSK1838	−52.6170	−71.3459	2018	229	3.1	Granitoid	73	1.00000	21.65	91,230	4,780
SSK1839	−52.6127	−71.3413	2018/19	229	1.9	Granitoid	67	1.00000	18.47	99,761	6,594
SSK1840	−52.6123	−71.3415	2018	234	3.3	Granitoid	50	1.00000	21.40	113,220	7,869
SSK1841	−52.6580	−71.3519	2018	306	2.3	Granitoid	60	1.00000	21.70	168,115	7,616
Outwash Laguna Blanca Moraine III											
SSK1807_O	−52.2496	−71.2304	2018	230	3.8	Quartz	—	1.00000	22.13	109,191	5,525
SSK1803_O	−52.2495	−71.2296	2018	231	3.2	Quartzite	—	1.00000	13.44	99,775	7,114
SSK1919_O	−52.2520	−71.2337	2019	230	2.9	Quartz	—	1.00000	22.32	111,624	5,670
SSK1920_O	−52.2520	−71.2337	2019	230	3.1	Quartz	—	1.00000	23.49	113,129	5,408
SSK1921_O	−52.2520	−71.2337	2019	230	4.0	Quartz	—	1.00000	22.04	564,700	19,877
Shorelines											
SSK1901_S	−52.3047	−71.1030	2019	139	2.9	Quartz	-	1.00000	21.56	86,798	4,253
SSK1902_S	−52.2627	−71.1280	2019	163	3.1	Quartz	-	1.00000	21.95	170,754	7,633
Outwash deposit in Otway lobe											
Surface Samples											
SSKOH1911	−52.5996	−70.5482	2019	32	2.4	Quartz	—	0.999944	-	78,400	3,400
SSKOH1914	−52.5996	−70.5482	2019	32	2.5	Quartz	—	0.999944	-	52,100	2,200
SSKOH1915	−52.5996	-70.5482	2019	32	2.7	Quartz	—	0.999944	-	158,700	5,900
SSKOH1916	−52.5996	−70.5482	2019	32	2.4	Quartz	—	0.999944	-	88,300	3,200
CD12-OAZ-SS03	−52.5996	−70.5482	2012	32	6	Quartz	—	0.999944		73,554	2072
CD12-OAZ-SS10	−52.5996	−70.5482	2012	32	6	Quartz	—	0.999944		120,843	3,153
	−52.5996	−70.5482	2012	32	6	Quartz	—	0.999944		70,725	2,242

(Continued on following page)

TABLE 1 | (*Continued*) Sample details and ^{10}Be concentrations from Skyring ice lobe and the outwash deposit located in Otway basin, associated with the southeastern Laguna Blanca spillway. The samples are grouped by landform.

Sample ID	Lat. (dd)	Lon. (dd)	Year Collected	Alt. (m asl)	Thickness (cm)	Lithology	Boulder Height (cm)	Shielding Correction	Quartz Dissolved (g)	10Be Concentration (Atoms/g)	±1σ (10Be) (Atoms/g)
CD12-OAZ-SS11											
Depth profile samples				depth (cm)							
SSKOH1901-P020	−52.5996	−70.5482	2019	−20	4	Quartz	—	0.999944	-	77,100	2,400
SSKOH1901-P040	−52.5996	−70.5482	2019	−40	4	Quartz	—	0.999944	-	66,000	2,400
CD12-OAZ-060	−52.5996	−70.5482	2012	−60	4	Quartz	—	0.999944	—	45,811	4,476
SSKOH1901-P075	−52.5996	−70.5482	2019	−75	4	Quartz	—	0.999944	-	48,300	2,300
CD12-OAZ-090	−52.5996	−70.5482	2012	−90	4	Quartz	—	0.999944	—	28,932	3,097
CD12-OAZ-120	−52.5996	−70.5482	2012	−120	4	Quartz	—	0.999944	—	35,997	2,763
SSKOH1901-P150	−52.5996	−70.5482	2019	−150	4	Quartz	—	0.999944	-	27,100	1,500
CD12-OAZ-190	−52.5996	−70.5482	2012	-190	4	Quartz	—	0.999944	—	18,508	967

Sampled year 2018/19 is for boulders sampled in two consecutive years (2018 and 2019), this does not affect the age of the sample.
Density of 2.65 g/cm3 for all the surface samples.
Measurements of all the samples were normalized to NIST SRM4325 with nominal $^{10}Be/^{9}Be$ ratios of 2.79 10^{-11} and half-life of 1.36 Ma Nishizumi et al., 2007.
For the Skyring ice lobe, the processed blank ratio was between 2.9 and 7.4% of the sample $^{10}Be/Be$ ratios. For the outwash deposit located in Otway basin the blank ratio was between 4 and 11%. The uncertainty of these corrections is included in the stated standard uncertainties.

deposition is assumed to be broadly synchronous with associated moraine formation (Darvill et al., 2015; Mendelová et al., 2020). On imagery and in the field, the outwash plain was linked continuously to the external ridge of LB Moraine III, but the sample collection was located far enough (~100 m) from the moraine to avoid subsequent downslope deposition. The age of these cobbles provide the minimum age of the outwash deposition.

3.2.1.3 Palaeo Lake Levels

We sampled two distinctive former shorelines around Laguna Blanca for cosmogenic ^{10}Be exposure dating. These shorelines are located at the inner part of the frontal LB Moraine (**Figures 2**, **3**) and we assume the source of material corresponds to till eroded by the lake. For each shoreline, we took one sample composed of an amalgamation of ~30 cobbles and large quartz pebbles (Mendelová et al., 2020). We collected the samples on flat top surfaces of wide beach ridges; these berm ridges are large-scale features and surrounded by relatively flat relief within a 2 km radius, so we are confident no material has been deposited on the surfaces since they were deposited. The age resulting from the amalgamated samples indicates a minimum age for the shoreline berm formation.

3.2.2 ^{10}Be Depth Profile From an Outwash Located on the Otway Basin

Previous geomorphological mapping reconstructions (Lovell et al., 2011; Darvill et al., 2014), and our own work link an outwash terrace in the area formerly occupied by the Seno Otway lobe to a drainage event south-eastward from a palaeo Laguna Blanca proglacial lake associated with the Seno Skyring lobe. Dating this deposit should constrain the timing of lake drainage and provide limiting ages for glacier retreat. We adopted two approaches to dating methods on this deposit.

Firstly, we collected surface samples to obtain exposure ages. From the surface of the outwash terrace, we sampled seven mono-mineral quartz cobbles (**Table 1**).

Secondly, we samples a depth profile in the outwash and modelled nuclide concentrations using Monte Carlo simulations. This approach can be used to calculate the most likely age, erosion rate, and nuclide inheritance ranges of a deposit (Hidy et al., 2010; Rodés et al., 2011; Darvill et al., 2015). The outwash deposit is formed by unconsolidated material composed mainly of pebbles and coarse sand with matrix-supported, grading to different percentages along it. The sediments of the outwash terrace appear to have been deposited continuously, and the surface does not show clear evidence of post-depositional reworking, cryoturbation or bioturbation (e.g., surface meltwater channels are preserved), making it suitable for dating with this approach (Hein et al., 2009, 2011; Darvill et al., 2015; Cogez et al., 2018; García et al., 2021). We collected eight samples from this profile from 20 to 190 cm below soil depth through a section of a modern anthropogenic road-gravel quarry in the outwash at this location (**Table 1**). Depth profile samples were amalgams of quartz pebbles and sand from ~4 cm thick layers at each depth. Samples were collected in two stages from the same sequence, in 2012 and 2019, following the methodology of Darvill et al.

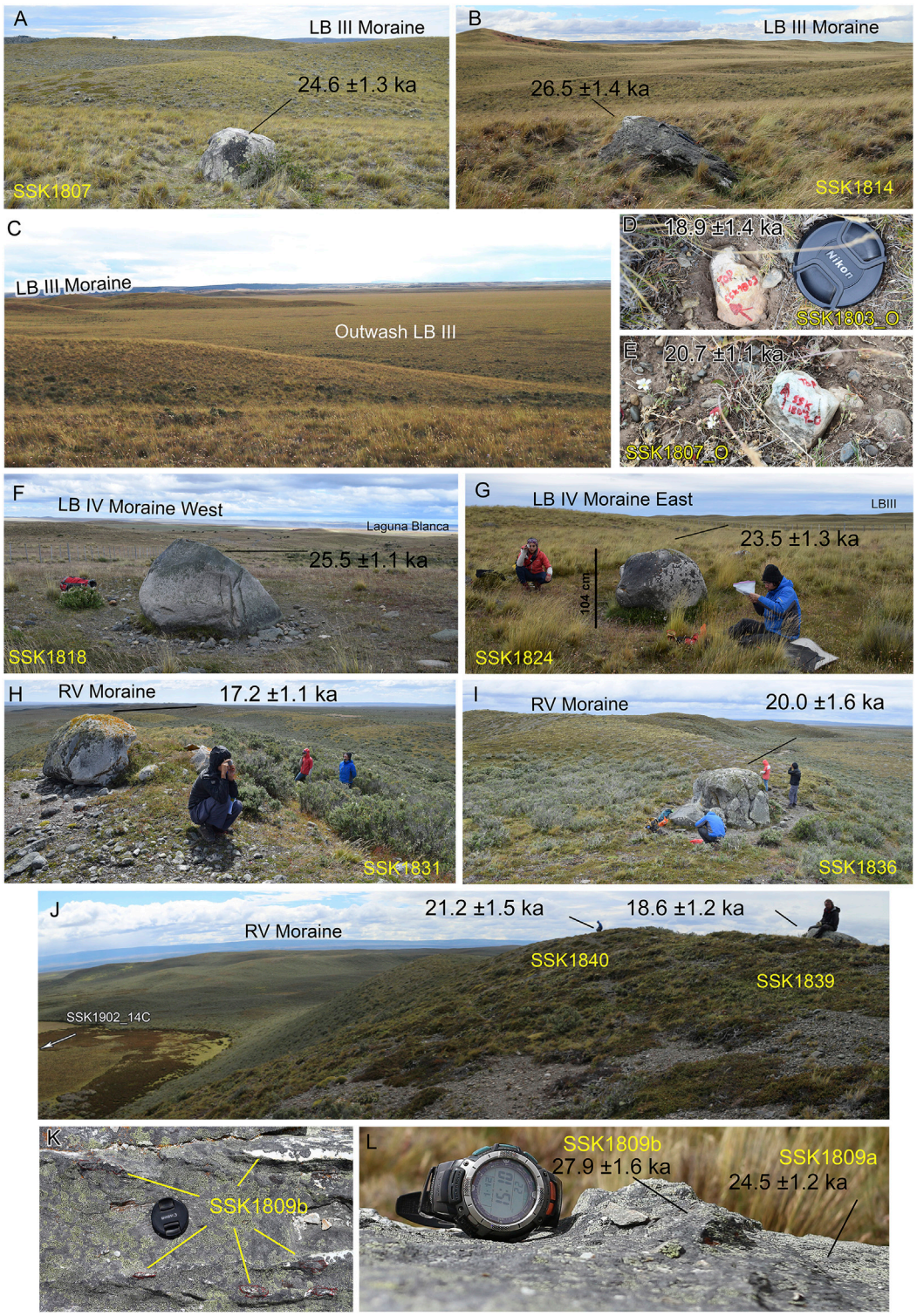

FIGURE 4 | Examples of moraine boulder samples and outwash cobbles collected. **(A,B)** Moraine boulders from LB III. **(C)** LB III outwash. **(D,E)** Cobbles collected from LB III outwash. **(F,G)** Laguna Blanca IV. **(H–J)** RV moraine. **(K,L)** Sample SSK1809 showing the sampled quartz vein and sampled boulder surface.

(2015). Soil development on the outwash surface is poor, with an average thickness of ~15 cm. Because the stratigraphy is not homogeneous, we estimated the density for each stratigraphic layer and accounted for layer thickness. We estimated the percentage of clasts bigger than sand for each layer, to which we allocated a density of 2.7 g/cm^3. For the rest of the layer, the

sand and porosity, we gave a density of 2.7 g/cm^3 and 0, respectively. The porosity values for sand and gravel were taken from the data for unconsolidated materials of Manger (1963), using the porosity range for each layer. We calculated the density proportional to the amount of each material (Hancock et al., 1999), yielding a density range of 2.1–2.3 g/cm^3.

3.2.3 ^{10}Be Laboratory Process

The boulders and surface cobble samples were prepared in a combination of the cosmogenic labs. The quartz isolation for moraine boulders and shorelines was performed at Universidad Católica in Santiago, Chile and Edinburgh University, United Kingdom. We obtained clean quartz using acid etching techniques following Hein et al. (2009) methods. The ^{10}Be/^{9}Be measurements were carried out at the Köln AMS, Germany (Dewald et al., 2013), normalized to the revised standard values reported by Nishiizumi et al. (2007). For methodological details refer to supplementary material. Final ^{10}Be concentrations and uncertainties are reported in **Table 1.**

The samples from the outwash terrace located on the Otway lobe, were entirely prepared at Scottish Universities Environmental Research Centre as part of the United Kingdom NERC National Environmental Isotope Facility. The surface samples were treated individually, while the samples from the depth profile were treated as amalgams. For the details of the sampling process from quartz isolation and purification, BeO separation, and AMS analysis, see supplementary material; extended methods. The ^{10}Be concentration, uncertainties, and samples details are given in **Table 1**.

3.2.4 ^{10}Be Exposure Age Calculation

The ages were determined with the online calculator, formerly known as the CRONUS-Earth online calculators, version 3 (Balco et al., 2008). We applied the Patagonian ^{10}Be production rate calculated from Lago Argentino (Kaplan et al., 2011). We use a general quartz density of 2.65 g/cm^3 for all the samples. The topographic shielding factor was negligible, with values between 0.999–1. We calculated the shielding by measuring the horizon geometry every 15° with a hand clinometer, then we converted these data to the shielding factors in the online calculator formerly known as CRONUS-Earth (https://hess.ess.washington.edu). For calculation and discussion of results in context with the other results in the region, we follow previous workers in assuming zero erosion and no correction for vegetation or snow cover of the boulders. However, from sample SSK1809b, we can calculate an erosion rate and we briefly discuss its implications below. For the age calculations, we used the Lm scaling scheme (Lal, 1991; Stone, 2000). Selecting a different scaling scheme would not significantly affect our conclusions. The sample characteristics and ^{10}Be data are given in **Table 1**. For the moraine ages, we present the weighted mean of the boulders with one weighted standard deviation as uncertainty. To identify outliers in each moraine group of samples, we use chi-square (χ^2_R) statistics. This method rejects samples outside the 2σ envelope, considering the number of samples (Wendt and Carl, 1991). If $\chi^2_R < \kappa$, the samples fall within the 2σ (Spencer et al., 2017). These calculations are made using the web calculator *IceTea* (Jones et al., 2019; http://ice-tea.org) when plotting a group of samples from a single moraine.

For the age comparisons with other ice lobes on the discussions, we recalculated previously published ages to Lm scaling scheme with the Patagonian production rate (Kaplan et al., 2011), with no correction for erosion, and no correction for snow or vegetation cover, to allow for direct comparisons between datasets.

3.2.5 ^{10}Be Depth Profile and Surface Ages From Outwash Deposit in Otway Basin Calculation

For the depth profile and surface samples, we applied the ^{10}Be production rate from Kaplan et al. (2011), calculated in the online calculators formerly known as the CRONUS-Earth online calculators v.3 (Balco et al., 2008) using the Lm scaling scheme (Lal, 1991; Stone, 2000). Thus, we used production rates of 4.3644, 0.01803, 0.03818 atoms/g/year and attenuation lengths of 160, 5,850, 500 g/cm^2 for spallation and fast and negative muons, respectively. For surface samples, we assumed zero erosion and densities of 2.65 g/cm^3.

To model the depth profile age we use the approach from Rodés et al. (2011) and we fitted the depth profile model to our data using the same combine surface exposure-burial MATLAB scripts as described in Rodés et al. (2014). The model requires input ranges for the deposit's possible ranges of density, age, and erosion rate. We constrained the density according to our calculations, and we used a range between 2.1 and 2.3 g/cm^3. A sensitivity test with a broader density range of 1–3 g/cm^3, showed little effect on age, erosion rate and inheritance and so use of a smaller density range is justified. For the possible age range, we are confident based on chronology of other ice lobes (Darvill et al., 2015; García et al., 2018; Peltier et al., 2021), that in the region the ice filled the Otway basin during the last glacial cycle. Nevertheless, we are ultra-cautious and use an age range of 0–1.1 Ma, where the maximum age corresponds to the greatest Patagonian Glaciation (Meglioli, 1992; Singer et al., 2004). We did not constrain the erosion rate of the deposit since we did not have independent information to do so. For each sample depth, we applied a conservative ±2 cm measurement error, which corresponds to the 4 cm sampling strip.

The Monte Carlo method utilises different solutions that best fit the given variables, that include depth profile sample ^{10}Be concentrations, density, age-range, and erosion rate of the deposit. The modelling shows all the possibilities that adjust with the given variables within a one sigma solution. We performed 50,000 models, and we obtained 3,771 possible results within one sigma of the data. Because this method is a probabilistic approach, it is possible to have different solutions that fit the given inputs. Thus, the model results are given in ranges, where different answers can be correct, especially if the input data are broad or unconstrained. Nevertheless, the model suggests the most likely data.

3.3 Optically Stimulated Luminescence

We used OSL dating to determine the age of raised lacustrine deposits around Laguna Blanca's margins. The OSL sample was taken from a 30 cm-thick sand layer, with medium sand grain size embedded within a lacustrine profile, located at the lowest palaeo lake terrace (T6). These sediments overlie glaciolacustrine sediments (with dropstones) but the context and sedimentology of the sampled layer corresponds to an alluvial fan deposit that is interfingered with lacustrine sediments and thus this age provide the timing of a higher lake levels previously to the erosion of level T6. Samples for luminescence dating were collected in opaque tubes hammered into the section and the ends sealed. These were prepared for analysis under subdued lighting conditions following the methodology of Smedley et al. (2016) Supplementary material.

3.4 Radiocarbon

We use radiocarbon dating to constrain the peat initiation of two different sites located within and inboard of the innermost RV moraines, using a Wright Piston Corer. The samples were cleaned by wet sieving to remove any potential coal present. Cleaned samples were sent to the *DirectAMS* radiocarbon dating service for final preparation and measurement. We calibrated the ages to calendar years in CALIB 8.2 program (calib.org; Stuiver et al., 2021) using the SHcal20 curve (Hogg et al., 2020). We report the calibrated ages using the 2-sigma calibrated range.

4 RESULTS

4.1 Geomorphology

The geomorphological relationships of the landscape observations are shown in the geomorphological map (**Figure 3**), and the criteria used to map them are explained in **Supplementary Table S3** (extended results).

4.1.1 Laguna Blanca Moraine System

The Laguna Blanca moraine system comprises at least four distinctive moraine belts separated by clear outwash plains; they are LB I, LB II, LB III and LB IV from oldest to youngest (**Figure 2B**). They are located in an arcuate arrangement around Laguna Blanca. In the frontal section, 10 km separates LB I from LB IV. A major meltwater spillway of a palaeo Laguna Blanca that was bigger than the present, cuts through this moraine system from the northern point of the Laguna Blanca former basin. We use this outlet to divide the glacial margins into East and West. On the eastern side of the system, the moraines are confined to the high ground that separates the basins of the former Seno Skyring and Seno Otway glacier lobes. On the west, the moraines are more widely spaced than on the eastern side. The outwash plains are narrower at the lateral parts, and they widen—up to 2 km wide in some places—as they get closer to the front of the lobe. The landform preservation decreases towards the outer moraines due to subsequent meltwater erosion, partial, overriding of the older moraines by younger glacial advances and by moraine ridge degradation through time. The outer LB moraine (LB I and LB II) relief is restricted to discontinuous ridges that we link together as a margin due to continuity of associated outwash plains along an arcuate pattern. Nevertheless, these moraines have good local preservation in the northeast area of the ice lobe, with moraine belts ranging between 1 and 2 km wide. On the other hand, the two inner moraine belts (LB III and LB IV) are preserved almost continuously enclosing Laguna Blanca. Despite the relatively poor preservation of the outer belts, all four LB belts expose similar morphostratigraphic characteristics. They have relief in general between 10–15 m high, but in some places, they can be up to 20 m, and their distal slopes are about 7° and their proximal 9° (**Figure 4A-G**). To the east, the large dimension of the inner moraine belt (LB IV) stands out, where they are up to 4 km wide in some areas and have close to 40 km of continuous lateral extension. There, the LB IV has close to 10 parallel nested ridges. The morphology is very different from the central and western area where LB III and IV are formed by a group of hills or short ridges with little structure. Hummocky relief is common in the central area, with significant intermorainic depressions. The western area is pervasively affected by meltwater erosion. Several meltwater channels cut the moraines and the outwash plains with alignments subparallel to the moraine ridges. The meltwater channels can be traced upstream to the Seno Skyring ice lobe's southwest margin. Exposed sections along the moraine belts were scarce. Nevertheless, we identified two lacustrine sediment slabs within sections from LB I and LB IV (**Figure 5**). These slabs were located in near-horizontal positions with regard to the sediment's lamination. These sediments have pervasive climbing ripple cross-lamination structure and exhibit slight brittle deformation and are overlain by till.

4.1.2 Laguna Blanca Palaeo Lake

On the inboard margins of the LB moraines, we identified six distinctive raised shorelines corresponding to formerly higher levels of the palaeo Laguna Blanca (**Figure 6**). They are located on the western and eastern sides, named T1 to T6 from older (highest) to younger (lowest), respectively and the elevations of the terraces are illustrated in **Figure 6E**. T1 and T2, were only observed to the north, and they are just represented as terraces. T3 to T6 have a good lateral continuity to the south, their frontal part is in the forms of shoreline berms while the lateral parts are terraces, interpreted as cut-wave terraces, and they are better preserved on the east side (**Figure 3**). The different levels of the upper shorelines are separated by clear scarps, with the best example being the scarp between T3 and T4 with close to 10 m of relief. In the lower terraces, these scarps are less obvious, and we simply observe a change in the slope of the terraces. Furthermore, on the east side, several alluvial fans cover the terraces with material derived from erosion of LB moraines located upslope. Our GPS surveys show that the terraces dip at low angles down towards the NNE (i.e., down-glacier direction). The greatest slopes are found on the highest shorelines, and they decrease to nearly horizontal angles towards the lowest (**Figure 6E**).

We mapped two different former spillways for deglacial palaeolake Laguna Blanca. One, located in the north, cuts the frontal area of LB moraines, has an altitude ~185 m a.s.l, and is about 150 m wide. The northern spillway was active during the lake

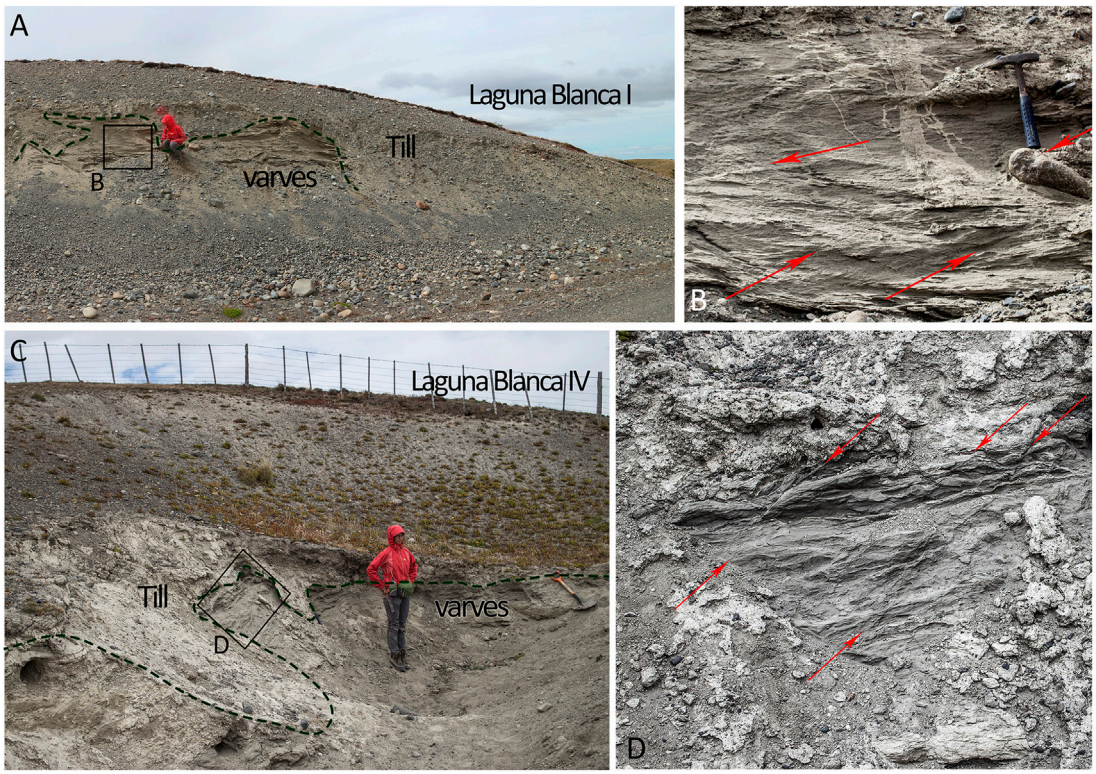

FIGURE 5 | Cut profile from LB moraines, showing lacustrine sediments overlain by till. **(A,B)**. LB I. **(C,D)**. LB IV. The sediments have climbing ripple cross-lamination structure. The sediments show evidence of brittle deformation indicated by red arrows.

levels of T1 and T2 (**Figure 6E**). Once the lake level lowered from T2, this spillway was abandoned. The second spillway is located in the southeast of the Laguna Blanca basin and cuts through soft bedrock in a series of anastomosing channels towards the Otway ice lobe (**Figure 3**; **Figure 7A**). The southeastern spillway has an altitude ~183 m a.s.l, and is about 300 m wide. This spillway drains east, where it divides into several minor channels, braiding for about 30 km before reaching the Otway basin (**Figure 7F**). Downstream of the spillway there are broad outwash terraces aligned in a west-east direction and which wrap around discontinuous older moraine ridges in the Otway basin (Lovell et al., 2012; Darvill et al., 2014; **Figure 7E,F**). The morphostratigraphic relationship between the spillway and shorelines show that this spillway was active when the lake level was at T4. We speculate that the major size of the spillway may be due to it being the route for large volumes of water during a relatively rapid partial drainage of the lake as it lowered from T3 to T4 (**Figure 6E**). After the lake level decreased from T4, this second spillway also became abandoned. T5 and T6 formed subsequently when the lake did not have any apparent spillway.

In T6, several incisions cut the distal part of the terrace, exposing large sediment sections (52.4°S; 71.1°W), at the eastern part of the Laguna Blanca (**Figure 6B**). These sections show a consistent stratigraphy composed at the bottom by at least 6 m of varves composed of clay and silt intercalation, with mm-scale horizontal lamination. Additionally, angular and rounded dropstones are embedded within the varves. On top of this unit, dropstone-free laminae are interfingered with sand and gravel with thicknesses ranging from 10 to 70 cm (**Supplementary Figure S1**, extended results). The sand and gravel layers have wedge-shaped beds becoming thinner towards Laguna Blanca and their base contact is always erosive, while in the varve layers the wedge shapes become thinner in the opposite direction. For OSL dating, we sampled a coarse sand layer located immediately on top of the 6 m of clay/silt unit (**Figure 6C**).

4.1.3 Río Verde Moraine System

The younger moraine system RV is located about 30 km inboard of the LB moraine system. It consists of one prominent terminal moraine and numerous recessional smaller moraines. The morphology of the terminal moraine has a sharp change in morphology at an elevation of 160 m a.s.l. between the lateral and frontal parts. The higher parts of this moraine system, located between 160and 310 m a.s.l., are generally higher relief and sharper-crested than the LB moraines. In the higher, lateral sections, the relief of the ridges range from 30 to 35 m, and their distal and proximal slopes are close to 16° and 20°, respectively (**Figures 4H–J**). The frontal (central) section of this terminal moraine is at a lower elevation (between 120–160 m a.s.l.) with much broader, flat and rounded ridge crests. It is composed of four coalescent ridges in an arcuate shape (**Figure 2C**). This frontal feature can be mapped on imagery but is almost imperceptible in the field; its relief of about 20 m was unnoticeable on the ground due to its width of ~10 km.

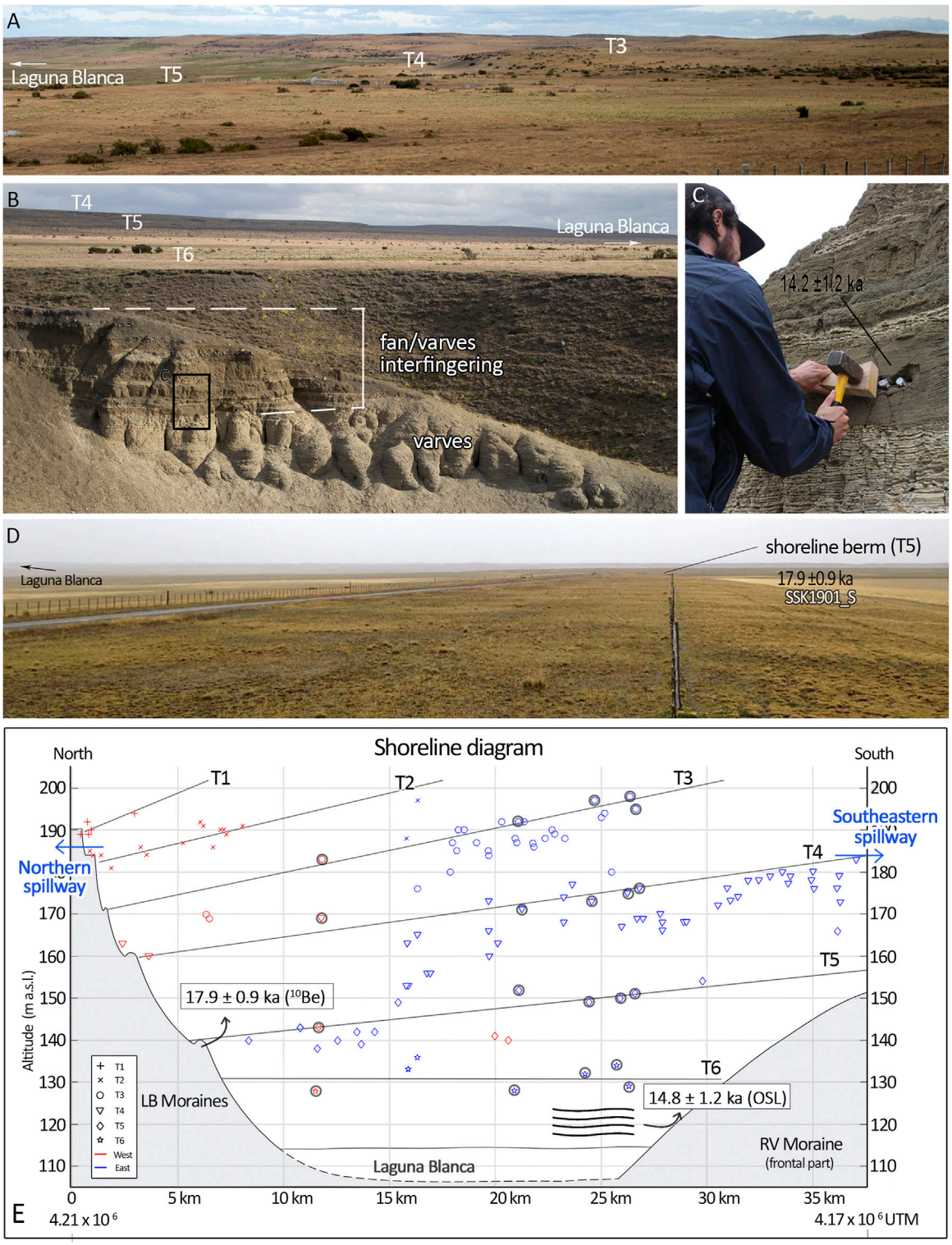

FIGURE 6 | Palaeo shorelines of Laguna Blanca. **(A)** Three terrace levels seen at the eastern side of Laguna Blanca. **(B)** Incision of the lowest terrace, T6, exposes glaciolacustrine and alluvial fan sediments. **(C)** OSL sample from a sand layer of the lacustrine profile (see panel b for location). **(D)** Palaeo shoreline berm located at the north part of Laguna Blanca, this berm is related to T5. **(E)** Shoreline Diagram of the former levels of Laguna Blanca. The symbols surrounded by a black circle correspond to the measurements done on the scarp base. The locations are marked of a ^{10}Be age of the shoreline berm on T5, and an OSL sample of a subaqueous alluvial fan taken from araised shoreline forming part of terrace T6. Data from west (red) and east (blue) are differentiated. The elevations and positions of the northern and south-eastern drainage spillways are marked. See legend for shoreline/terrace numbering.

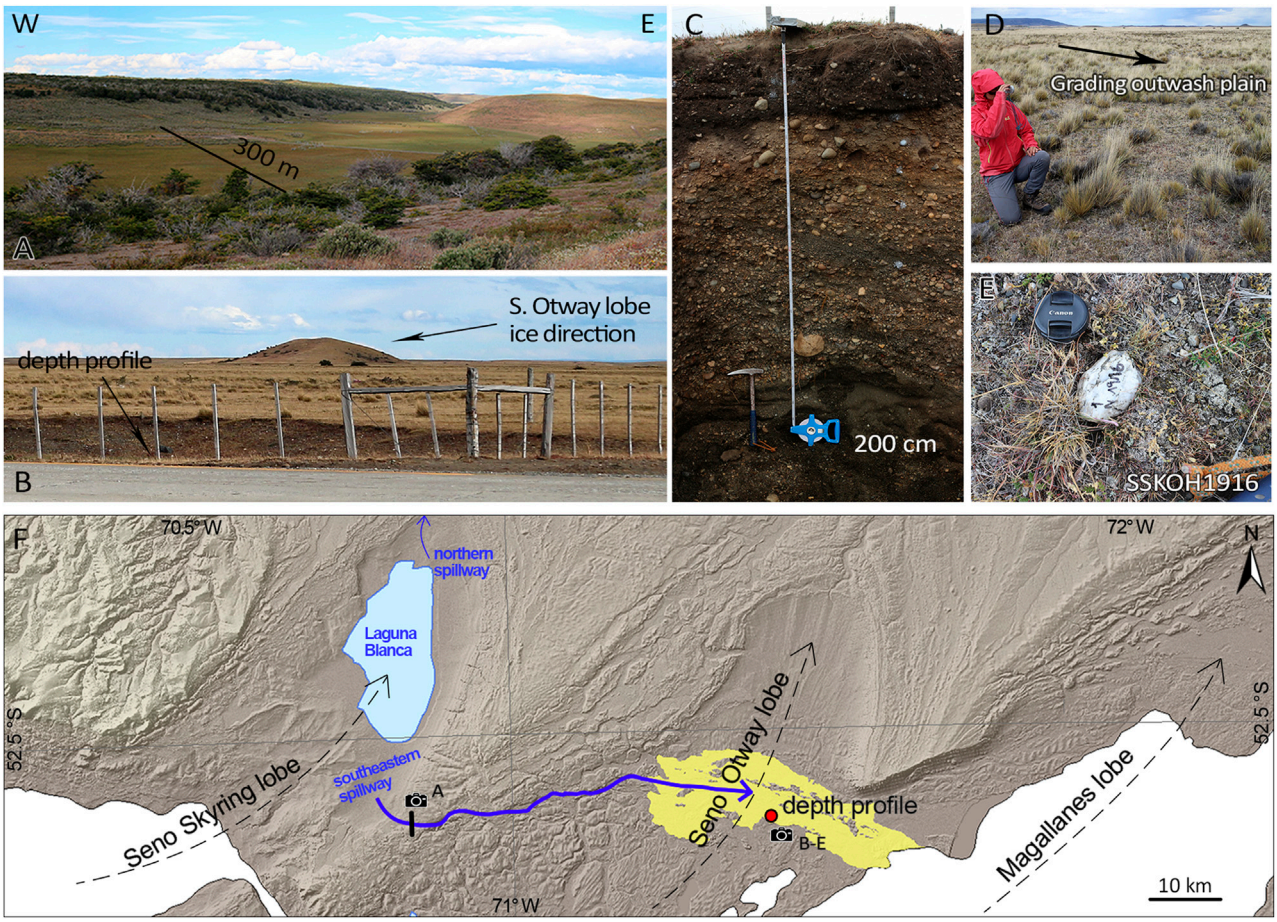

FIGURE 7 | Geomorphological record of drainage of Laguna Blanca through the southeastern spillway. **(A)** Southeastern drainage spillway viewed from the south. **(B)** Moraines of the Otway lobe surrounded and partly-buried by a later outwash deposit on both distal and proximal sides. **(C)** Depth profile of the outwash that buries the Otway moraines. **(D–E)** Cobbles sampled for cosmogenic analysis on the surface of the outwash. **(F)** Map showing the mapped drainage route from the southeastern spillway of the Seno Skyring basin towards the Otway lobe basin.

Streamlined landforms are visible on the proximal part of the northwest RV moraine. They are low flat-topped hills with rounded limits, elongated concordant with the ice direction. We mapped discontinuous moraine patches about 8 km inboard from the outer RV belt. Further inboard of these recessional moraines are at least four distinctive shorelines terraces marked by the presence of sub-vertical scarps. These terraces step down in height from 60 m a.s.l. to the present shoreline of Seno Skyring to the west.

4.2 Geochronology

4.2.1 ^{10}Be Exposure Ages

4.2.1.1 Laguna Blanca Moraine System

The presence of boulders on the LB moraines is extremely scarce. Nevertheless, we processed thirteen boulders for ^{10}Be exposure cosmogenic dating from this moraine system. We present data from the moraine LB III and LB IV in this system (**Table 2**; **Figure 4**). Additionally, we processed four surface cobbles located in the outwash plain apparently grading from LB III (**Figures 4C–E**).

On LB III, we collected eight boulder samples, six from the western lateral part and two from the eastern part. Even though these moraines do not have continuous parallel ridges, the samples SSK1801, SSK1802 and SSK1820 were collected at the outer most part. SSK1807, SSK1809a and SSK1814 were at the intermediate position, SSK1804 and SSK1830 were taken at the moraine's inner part. On LB III, three samples fall outside the 2σ envelope, therefore they would be considered outliers. Finally, for LB III, five boulders yielded ages ranging from 32.4 to 25.0 ka with a weighted mean of 26.3 ± 2.3 ka (**Figure 8A**).

On LB IV moraine, we sampled five boulders. Four of them (SSK1805, SSK1818, SKK1819, SSK1924) were located in the outer part of the moraine, and one (SSK1817) at the inner part. Two boulder ages were rejected as outliers, including the boulder located at the inner part of the moraine. The three samples yielded ages ranging from 25.5 to 23.5 ka, and a weighted mean of 24.3 ± 0.9 ka (**Figure 8B**).

We collected five cobbles from LB III outwash plain. One sample (SSK1921_O) was rejected as an outlier with an age of 108.8 ± 3.9 ka.

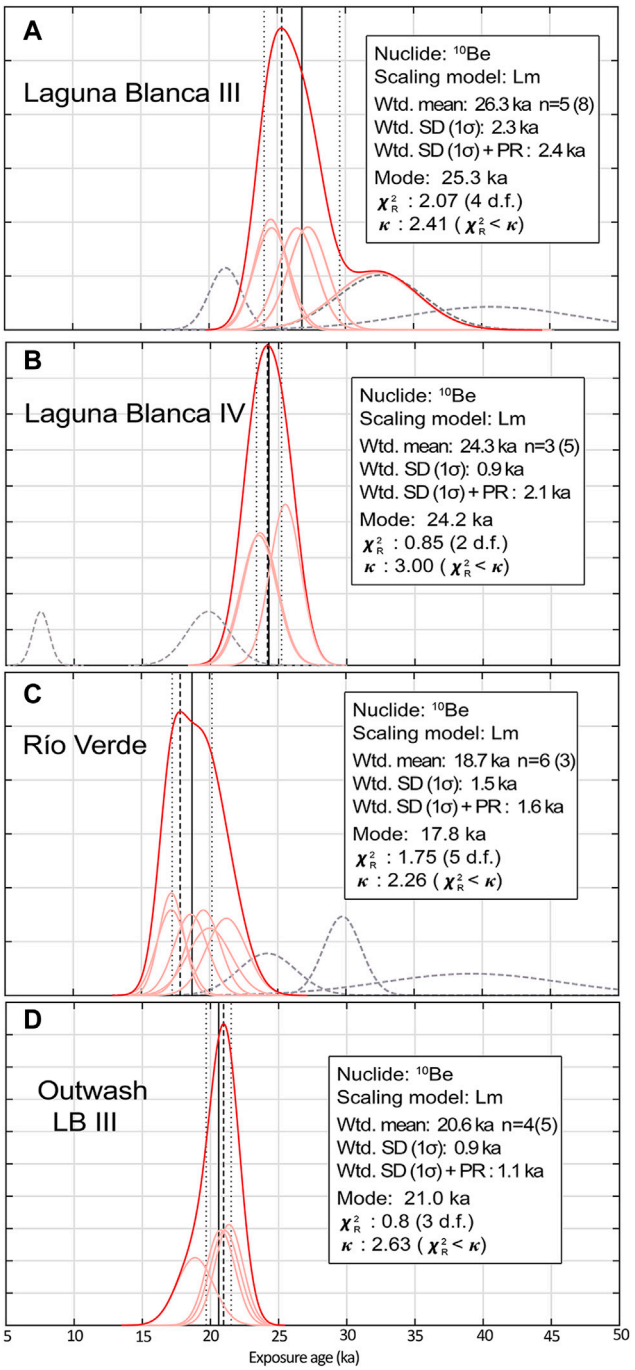

FIGURE 8 | Probability density functions ("camel plots") of the ages for moraines and outwash of the former Skyring ice lobe. All ages are calculated with the Patagonian production rate from Lago Argentino (Kaplan et al., 2011) and considering zero erosion. **(A)** Laguna Blanca III. **(B)** Laguna Blanca IV. **(C)** Río Verde moraine. **(D)** Outwash Laguna Blanca III. n corresponds to the number of samples used to calculate the weighted ages. Bracket numbers are all the samples processed, including outliers. The diagrams were plotted using IceTea (Jones et al., 2019), where the mode (black dashed line), weighted mean (solid black line) and weighted standard deviation (SD; black dotted lines) of the dataset are shown. The application also calculates the reduced chi-squared (χ^2_R) and the associated criterion (κ). The outliers are shown as grey dashed lines; they were calculated following reduced chi-squared statistics.

The remaining four cobbles yielded ages ranging from 21.4 to 18.9 ka, with a weighted mean of 20.6 ± 0.9 ka (**Figure 8D**).

4.2.1.2 Río Verde Moraine System

In the RV moraine system, there were more abundant moraine boulders than in the LB moraines. We sampled nine boulders on the outer ridge of the eastern lateral section of the RV terminal moraine between 230–310 m a.s.l., above any potential palaoelake level (**Figures 3, 4).** Three samples (SSK1835, SSK1837, SSK1841) were rejected as outliers (**Table 2**). The remaining six (SSK1831, SSK1833, SSK1836, SSK1838, SSK1839, SSK1840) samples yielded ages ranging from 21.2 to 17.2 ka with a weighted mean of 18.7 ± 1.5 ka (**Figure 8C**).

4.2.1.3 Boulder Erosion Rate

We calculated the erosion rate for one boulder (SSK1809) in the Skyring area by sampling quartz veins standing out by approximately 20 mm from the upper rock surface (**Figures 4K,L**). The vein sample, SSK1809b, has an age of 27.9 ± 1.6 ka. Assuming the quartz veins have experienced zero erosion, we calculated a linear-erosion rate of 0.72 ± 0.04 mm/kyr for this quartzite lithology. We assumed a zero erosion rate for the boulders (**Table 2**) because the erosion rate calculated was just performed on one boulder, which may not represent all the other boulder positions or lithologies. Moreover, the use of zero erosion allows us to compare to other studies in southern Patagonia, which also widely assume zero erosion. Nevertheless, to illustrate the effects of potential erosion, we additionally provide the boulder ages for only quartzite lithology, calculated using a 0.72 mm/kyr erosion rate (**Supplementary Table S4**, extended results). The age difference is minimal when applying this erosion rate for boulders with quartzite lithology. Boulders dated to about 30 ka increase in ~600 years with the erosion rate correction, and boulders dated to about 20 ka increase by ~200 years, which is within the analytical uncertainty. Note that the vein age was utilised just for the erosion rate calculation, and for the LB III moraine age calculation we used the boulder matrix sample (SSK1809a).

4.2.1.4 Laguna Blanca Palaeo Lake

We ^{10}Be dated T4 and T5 palaeo-shoreline berms from palaeo Laguna Blanca. The sample SSK1902_S (T4) yielded exposure ages of 34.4 ± 1.6 and the sample SSK1901_S (T5), 17.9 ± 0.9 ka (**Figure 3**). We rejected the sample SSK1902_S since it is anomalously old compared to the LB moraines ages. The most likely explanation for the anomalously old age is that some cobbles sampled in T4 contained inherited ^{10}Be from previous exposure histories. Moreover, the age of a cobble (SSK1921_O) on the LB III outwash plain, ~88 kyr older than the rest of its group, supports the presence of material with inheritance in the area.

4.2.2 ^{10}Be From Outwash Deposit in Otway Lobe: Surface Samples and Depth Profile

The seven surface samples from the outwash deposit yielded apparent ^{10}Be exposure ages ranging between 11.9 and 36.1 ka (**Table 2**). Four of the seven samples range between 20.1 ± 0.7 and 16.5 ± 0.5 ka, with a weighted mean of 17.7 ± 1.3 ka. Due to the scattered age range, and potential for deflation or inflation of the sediment surface and possibility of inheritance (Hein et al., 2011), we treat these data as apparent ages (**Figure 9G**).

TABLE 2 | ^{10}Be ages for the study area, assuming 0 erosion rate.

Sample Name	Lm				St				LSDn		
	Age ka	± Int ka	± Ext ka		Age ka	± Int ka	± Ext ka		Age ka	± Int ka	± Ext ka
Laguna Blanca Moraine III											
SSK1801	**27.3**	**1.4**	**2.7**	—	27.8	1.5	2.7	—	26.5	1.4	2.6
SSK1802	**32.3**	**3.0**	**4.0**	—	33.0	3.1	4.1	—	31.4	3.0	3.9
SSK1804 †	**41.1**	**6.3**	**7.1**	—	42.1	6.4	7.3	—	39.9	6.1	6.9
SSK1807	**24.6**	**1.3**	**2.4**	—	25.1	1.3	2.5	—	24.0	1.3	2.3
SSK1809a	**24.5**	**1.2**	**2.3**	—	25.0	1.2	2.4	—	23.9	1.2	2.3
SSK1809b*	**27.9**	**1.6**	**2.8**	—	28.5	1.6	2.8	—	27.2	1.5	2.7
SSK1814	**26.5**	**1.4**	**2.6**	—	27.0	1.4	2.6	—	25.8	1.4	2.5
SSK1820 †	**21.4**	**1.2**	**2.1**	—	21.8	1.2	2.2	—	20.9	1.2	2.1
SSK1830 †	**32.4**	**3.2**	**4.2**	—	33.1	3.3	4.3	—	31.5	3.1	4.0
Weighted mean (n = 5): 26.3 ka; Wtd. 1SD: 2.3 ka; Wtd. 1SD + PR (3%): 2.4 ka											
Laguna Blanca Moraine IV											
SSK1805 †	**19.9**	**1.6**	**2.3**	—	20.2	1.6	2.3	—	19.4	1.6	2.2
SSK1817 †	**7.6**	**0.6**	**0.9**	—	7.6	0.6	0.9	—	7.5	0.6	0.9
SSK1818	**25.5**	**1.1**	**2.4**	—	26.0	1.2	2.4	—	24.8	1.1	2.3
SSK1819	**23.6**	**1.3**	**2.3**	—	24.1	1.3	2.4	—	23.1	1.2	2.3
SSK1824	**23.5**	**1.3**	**2.3**	—	24.0	1.3	2.4	—	23.0	1.3	2.3
Weighted mean (n = 3): 24.3 ka; Wtd. 1SD: 0.9 ka; Wtd. 1SD + PR (3%): 1.2 ka											
Río Verde Moraine											
SSK1831	**17.2**	**1.1**	**1.8**	—	17.5	1.1	1.8	—	16.8	1.1	1.7
SSK1833	**19.5**	**1.2**	**2.0**	—	19.9	1.3	2.1	—	19.1	1.2	2.0
SSK1835 †	**38.3**	**6.4**	**7.1**	—	39.3	6.5	7.3	—	37.2	6.2	6.9
SSK1836	**20.0**	**1.6**	**2.3**	—	20.3	1.6	2.3	—	19.5	1.6	2.2
SSK1837 †	**23.8**	**2.0**	**2.8**	—	24.3	2.1	2.9	—	23.2	2.0	2.7
SSK1838	**17.2**	**0.9**	**1.7**	—	17.5	0.9	1.7	—	16.8	0.9	1.6
SSK1839	**18.6**	**1.2**	**2.0**	—	18.9	1.3	2.0	—	18.2	1.2	1.9
SSK1840	**21.2**	**1.5**	**2.3**	—	21.6	1.5	2.3	—	20.7	1.4	2.2
SSK1841 †	**29.2**	**1.3**	**2.8**	—	29.8	1.4	2.8	—	28.3	1.3	2.7
Weighted mean (n = 3): 18.7 ka; Wtd. 1SD: 1.5 ka; Wtd. 1SD + PR (3%): 1.6 ka											
Outwash Laguna Blanca III											
SSK1807_O	**20.7**	**1.1**	**2.0**	—	21.1	1.1	2.0	—	20.3	1.0	2.0
SSK1803_O	**18.9**	**1.4**	**2.1**	—	19.2	1.4	2.1	—	18.5	1.3	2.0
SSK1919_O	**21.0**	**1.1**	**2.0**	—	21.4	1.1	2.1	—	20.6	1.1	2.0
SSK1920_O	**21.4**	**1.0**	**2.0**	—	21.7	1.0	2.1	—	20.9	1.0	2.0
SSK1921_O †	**108.8**	**3.9**	**10.0**	—	111.8	4.0	10.3	—	105.3	3.8	9.6
Weighted mean (n = 3): 20.6 ka; Wtd. 1SD: 0.9 ka; Wtd. 1SD + PR (3%): 1.1 ka											
Shorelines Berm											
SSK1901_S	**17.9**	**0.9**	**1.7**	—	18.2	0.9	1.7	—	17.5	0.9	1.7
SSK1902_S †	**34.4**	**1.5**	**3.2**	—	35.1	1.6	3.3	—	33.4	1.5	3.1
Otway lobe Outwash terrace											
SSKOH1911	**17.8**	**0.8**	**1.7**	—	18.1	0.8	1.7	—	17.3	0.8	1.6
SSKOH1914	**11.9**	**0.5**	**1.1**	—	12.0	0.5	1.1	—	11.7	0.5	1.1
SSKOH1915	**36.1**	**1.4**	**3.3**	—	36.9	1.4	3.4	—	34.8	1.3	3.1
SSKOH1916	**20.1**	**0.7**	**1.8**	—	20.4	0.7	1.8	—	19.4	0.7	1.7
CD12-OAZ-SS03	**17.2**	**0.5**	**1.5**	—	17.5	0.5	1.5	—	16.7	0.5	1.4
CD12-OAZ-SS10	**28.2**	**0.7**	**2.4**	—	28.8	0.8	2.5	—	27.2	0.7	2.3
CD12-OAZ-SS11	**16.5**	**0.5**	**1.5**	—	16.8	0.5	1.5	—	16.1	0.5	1.4

SSK1809b vein sample considered for calculating the erosion rate, but not included in the moraine age calculation. For the moraine age, we used the matrix boulder sample (SSK1809a).*
† Outlier.
^{10}Be ages calculated in the online calculators formerly known as the CRONUS-Earth v.3 (Balco et al., 2008). We applied the Patagonian production rate of Kaplan et al. (2011), the calibration data set was obtained from calibration.ice-d.org. No shielding correction for snow cover or vegetation. Pressure flag: std. Summary statistics are calculated for each group of samples for a dated landform.
Ages are presented in three different scaling schemes. Lm is the time-dependant scaling scheme of Lal, 1991 and Stone, 2000, we use this for this study (highlighted in bold). St is the time independent scaling scheme of Lal (1991) and Stone (2000). LSDn, is the time-dependent scaling scheme of Lifton et al. (2014). Ages are reported with 1 standard deviation internal (int) and external (ext),. Int include analytical uncertainty, and ext includes systematic uncertainties associated with scaling scheme and production rate. Ages are rounded using three significant figures. We report them with the weighted (wtd.) mean and wtd. 1 standard deviation (sd) and the wtd. sd + the production rate uncertainty PR (3%).

The ^{10}Be concentration of the depth profile samples reduces with depth (**Figure 9A**), consistent with a post-depositional nuclide production in a stable deposit without mixing sediments (Hein et al., 2009). Two exceptions are the samples located at 60 and 90 cm depth that could have mixed sediments or material with more ^{10}Be inheritance concentration at the moment

of deposition. It is also important to note that those two samples are the ones that have the largest uncertainty.

The ^{10}Be depth profile modelling results demonstrate a modelled age range between 18–1,101 ka (**Figure 9B**) but with a most likely age between 19 and 25 ka (99.3% of solutions lie in this range; **Figure 9C**). For simplicity, we report this here as 22 ± 3 ka, whilst noting that this does not imply a normal distribution of ages and that different ages in this range may be equally likely (Rodés et al., 2011). The model yields a median inheritance estimate of between 11,422 and 14,522 ^{10}Be atoms/g (**Figure 9D**). This indicates a minimum period of prior exposure longer than ~2 kyr, if all the clasts came from the surface of the eroded deposit. Nevertheless, we know that the cosmogenic radiation decays with depth, and it is very likely that not all the clasts along the profile were located previously on the surface. Therefore, this exposure time is considered a minimum period. Moreover, as we cannot rule out that the eroded channels were active in more than one drainage event, the outwash deposition could have included material that was previously exposed, even in older glaciations. The model does not seem to be sensitive to variations in the density (**Figure 9E**), and this is also supported by the sensitivity test performed with broader parameters. For the erosion rate we obtained a range of 0–39.7 mm/ka (**Figure 9F**). The possible age solutions (0.7% of model runs) older than 22 ± 3 ka (**Figure 9H**) can be ruled out as requiring an unrealistic amount of surface lowering (40–50 m). Such high erosion rates are not likely in arid eastern Patagonia and our geomorphology observations show the outwash surface is well preserved with melt water channels with decimetre-scale scarps still visible on aerial photographs and imagery, and no signs of pervasive erosion.

We utilize the age modelled through the ^{10}Be depth profile approach (22 ± 3 ka), as the most reliable constraint for this outwash deposit formation and we regard the slightly younger date from surface cobbles as only an apparent age of the deposit.

4.2.3 Optically Stimulated Luminescence and Radiocarbon

The OSL sample SSK1901_OSL yielded a deposition age of 14.8 ± 1.2 ka. This sample was collected from a sand layer exposed along the T6 terrace (**Figures 6B,C**).

We constrained the deglaciation by ^{14}C dating of the glacial (inorganic) and peat sediment contact using two ^{14}C samples from two bog sites within and inboard of the RV moraines (**Figure 10**). One site is a peatbog occupying an intermorainic depression just inside RV terminal moraine. At this site, we cored through peat for 1,080 cm, until we reach lacustrine sediments. The sample SSK1902_14C consisted of amalgamated macro plant fossils collected right above the sharp contact between the peat and the lake sediments. The 2σ calibrated age range is 16,236–16,571 cal year BP, for convenience from here on we express the age as c.16.4 cal kyr BP (**Table 3**). Furthermore, the sample site of SSK1901_14C is a bog in an abandoned meltwater channel located inboard and at a lower elevation. There, we cored 575 cm of continuous peat until we reached coarse inorganic sand. The ^{14}C sample consisted of plant macrofossils obtained from just above the sharp contact between the inorganic sand and the overlying peat. The 2σ calibrated age range of the maximum probability is 14,781–15,143, from here on we express this age as c.14.9 cal kyr BP (**Table 3**). The cores from both sites showed sharp contact between inorganic sediments and the peat sedimentation. The type of sedimentology indicates a primary mire formation of peat initiation. This means that the peat originated on newly exposed waterlogged land (Ruppel et al., 2013; Quik et al., 2021). The abrupt nature of the contact suggests a deglaciation event (e.g., Hall et al., 2013; McCulloch et al., 2020).

5 DISCUSSION

5.1 Geomorphology and Sedimentology Interpretation

5.1.1 Laguna Blanca Moraines

We use our geomorphological mapping to compile a relative chronology of glacial advances and deglaciation, which we show in **Figure 11**, and for which we provide a geochronology in the following section.

During the LB moraine system formation, the glacier advanced several times, with at least four stable positions marked by LB I, LB II, LB III, and LB IV moraines (**Figure 11A**). From fine lacustrine sediments that we found in two places within the moraines LB I and LB IV, we suggest that the ice advanced over pre-existing glaciolacustrine deposits. In some places, the glacier detached and transported slabs of these basal sediments (**Figure 5**), emplacing them into the moraines by thrusting. Subsequently, these slabs of glaciolacustrine sediments were covered by till. Thus, the LB moraine system is at least partly glaciotectonic in origin (Benn and Clapperton, 2000a; Benn and Clapperton, 2000b; Glasser and Hambrey, 2002; García et al., 2015). Finally, we interpret an active retreat from LB IV (Bennett and Glasser, 1991; Sigfúsdóttir et al., 2018), with several stillstand positions indicated by the presence of more than ten parallel nested recessional moraines in the eastern part of the ice lobe (**Figure 3**).

5.1.2 Laguna Blanca Palaeo Lake

The glacier over deepening and the significant input of meltwater from the glacier front during the glacier retreat from LB positions allowed the formation of the Laguna Blanca proglacial lake. As the glacier retreated, this lake experienced different lake levels recorded by T1 to T6 palaeo shorelines. These shorelines dip slightly in a down-glacier direction (**Figure 6E**), which is expected as further upstream the ice thickness increases, producing a greater crustal loading, leading to larger postglacial isostatic uplift in the upstream parts of the former ice lobe (McCulloch et al., 2005a; Stern et al., 2011; Thorndycraft et al., 2019; Troch et al., 2022).

We mapped two different spillways for palaeo Laguna Blanca, located in the north and in the southeast, respectively (**Figure 3**). Today, they have similar altitudes. Nevertheless, we suggest the spillway located in the southeast, was considerably lower during its activity (~20 m), and as the terraces, it experienced isostatic uplift (**Figure 6E**). The lake initially drained to the north

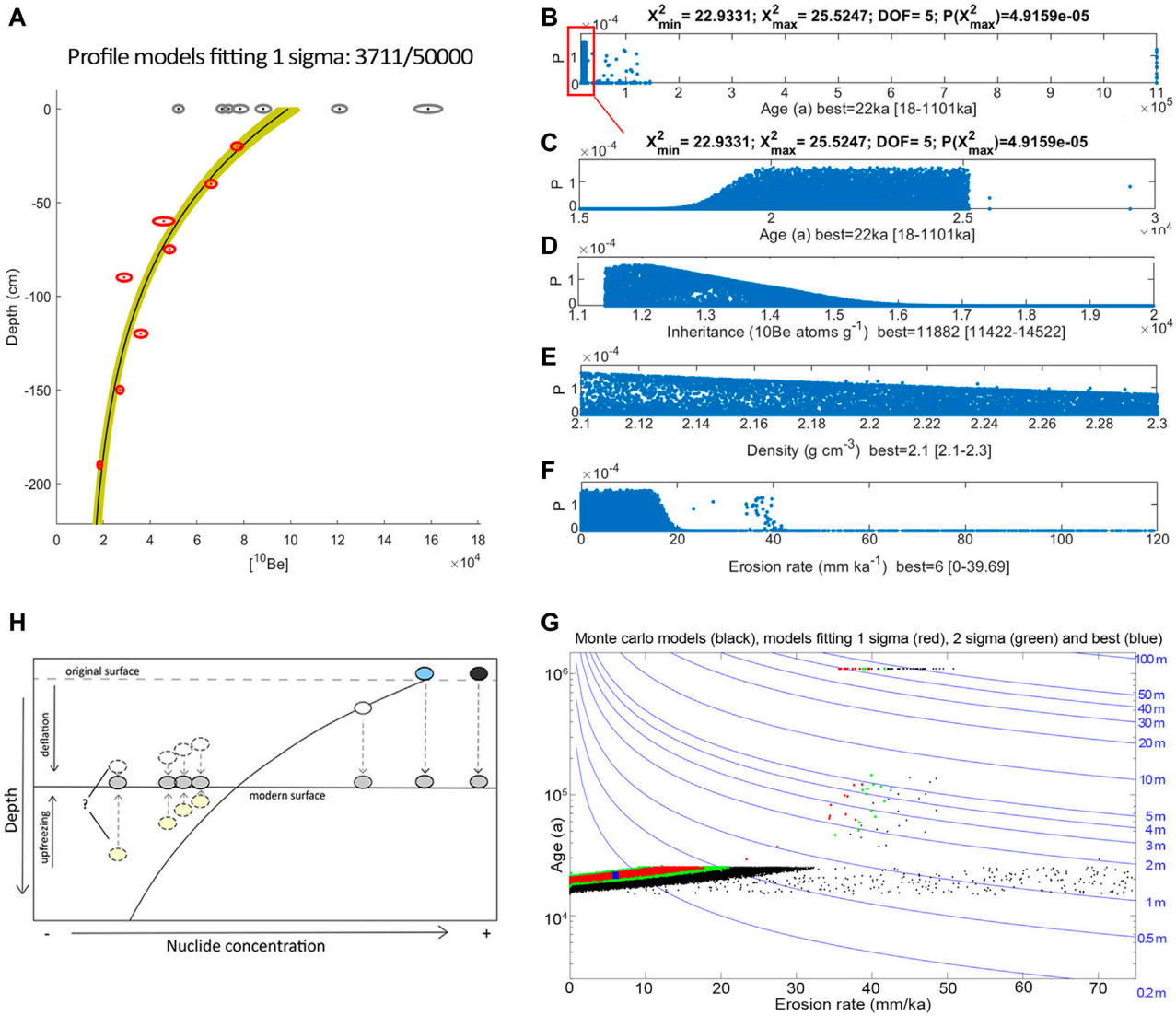

FIGURE 9 | Depth profile model results from outwash deposit located in Otway ice lobe, associated with the southeastern Laguna Blanca spillway. **(A)** Plot of ^{10}Be concentration of samples from the surface (grey circles) and depth profile (red circles), with their uncertainties as a function of depth. Green lines indicate the model results that fit within 1 sigma, the black line corresponds to the best fit model. **(B–F)** Probability density distributions of the different outputs of the model: age, inheritance, density, and erosion rate. **(B)** Shows the modelled ages plotted between 0–1,101 ka, whereas **(C)** shows the ages plotted between 15–30 ka. **(G)** Graphic showing relationship between age, erosion rate, and surface lowering. Red dots are model runs lying within 1-sigma of the data, green are those within 2-sigma, and black dots are other model runs. Model output shows 99.5% of data within 1-sigma lie within an age range of 18.6–25.1 ka, with a small component of well-fitting model runs that would require implausible (40–50 m) amounts of surface lowering. **(H)** Schematic cartoon to explain scattered age of the surface samples and reasons for their difference in age from the depth profile modelling. The older samples could have been exposed to the cosmogenic radiation from the outwash terrace formation (blue sample). If the samples have a component of inheritance from earlier exposure, then the age will be older than the terrace (black sample). A deflation of the outwash will expose samples that were initially buried, resulting in younger than the outwash age (white). Younger samples could also be raised to the surface due to inflation processes, such as upfreezing (see Hein et al. (2009), and Darvill et al. (2015) for further discussion).

(**Figure 11B**). A subsequent decrease in the lake level, possibly accompanied by some isostatic rebound, abandoned the northern spillway. As the glacier retreated back from LB moraine positions, the southeastern spillway opened causing a lake drainage towards the southeast (**Figure 11C**), eroding and transporting a high volume of material that subsequently was deposited downstream as an outwash terrace in the Otway basin (cf. Lovell et al., 2012; Darvill et al., 2014). This event probably drained the lake level of T3 down to T4 where again it stabilised (**Figure 6E**). The interpretation of an abrupt drainage is based on the large size of the southeastern spillway, with a width of 300 m, double the size of the northern spillway, thus implying the loss of higher volumes of lake waters through this channel. Nevertheless, it is possible that these channels have been formed by more than one drainage event during multiple glacial-deglacial cycles. Furthermore, the scarp between T3 and T4 is a sharp

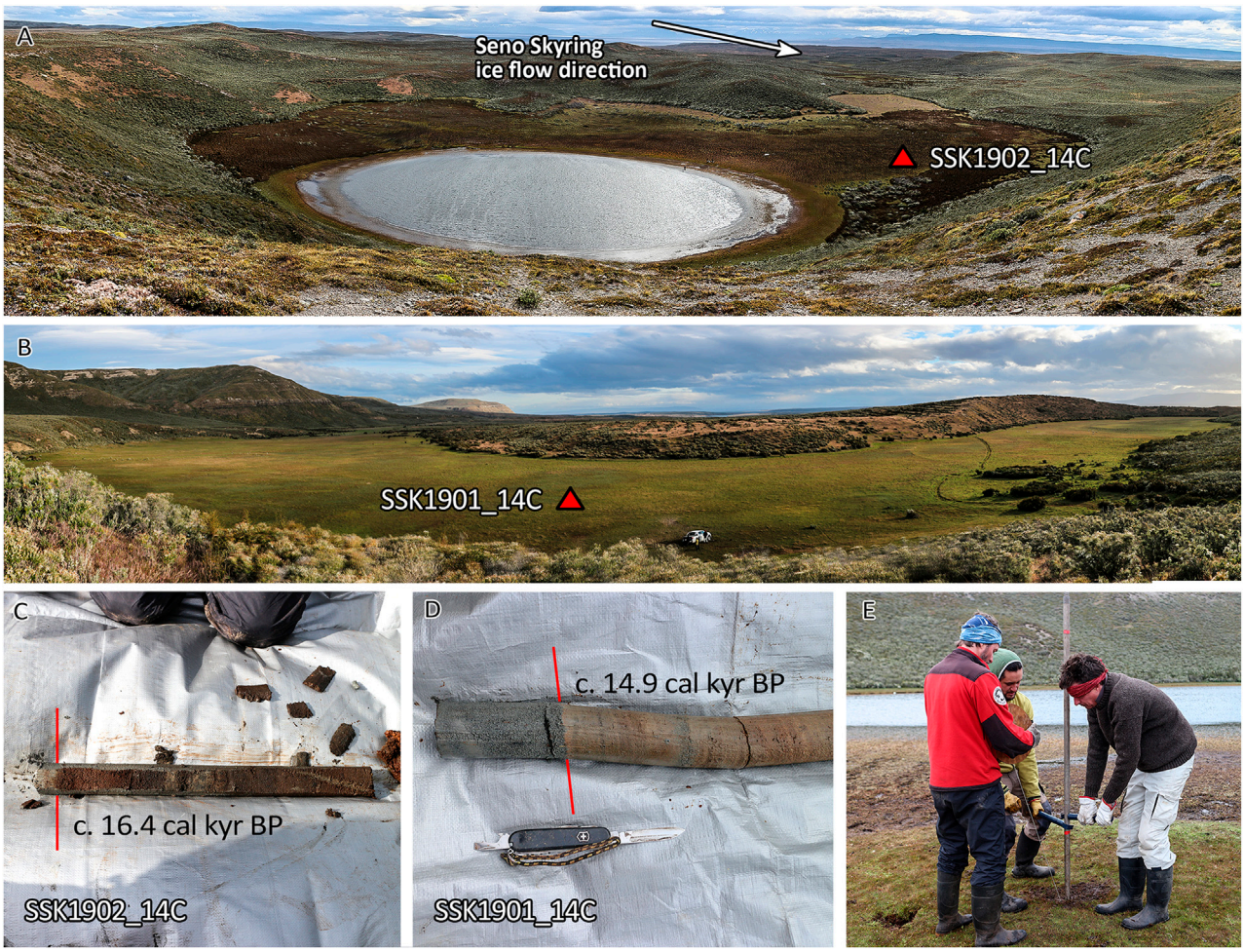

FIGURE 10 | (A–B) Sample location for radiocarbon dating in peat bogs (red triangles). In **(A)**, the core was taken close to the margin of a lake sitting on the proximal side of the terminal RV moraine. In **(B)**, the core was taken from an abandoned meltwater channel. **(C–D)** Core samples from both sites, red lines indicate the contact between organic and inorganic materials, mud and sand sediment, respectively. **(E)** Wright piston corer being used to sample SSK190214C.

prominent break (~10 m of relief) which may indicate a rapid drop in the lake level. The large outwash plains formed at the end of the channel conduits wrap around discontinuous moraine ridges. The similar altitudes between the distal and proximal part of those moraine ridges suggest a post-deposition outwash infill that partially buried pre-existing glacial landforms such as moraines. Following this stage, the lake level lowered further to stabilise at level T5, stopping the meltwater activity from Laguna Blanca to Otway Basin (**Figure 11D**).

From the stratigraphic section described in T6 from palaeo Laguna Blanca (**Figure 6**), we interpret two different depositional environments. At the base, we interpret the first 6 m as finely laminated varves composed of clay and silt intercalation including dropstones. The presence of varves and dropstones shows a direct glacier influence on sedimentation (Evans and Benn, 2021). Above this section, we interpret an interdigitation between subaqueous alluvial fan facies and varves. The clay and silt need a tranquil deposition environment, such as greater depths away from wind-related currents and from steep slopes (Zolitschka et al., 2015). We interpret that the different fan facies represent discrete pulses of tributary streams into the lake basin deposited under the lake level, deep enough and away from the direct influence of the slope to allow the subsequent deposition of varve layers. We interpret the source of the fans comes from the gullies directly east of Laguna Blanca.

5.1.3 Río Verde Moraine System

The RV moraine system marks a less extensive glaciation in Seno Skyring and has a different morphological character compared to LB with sharper slopes and higher relief. The dramatic change in morphology from the frontal part to the lateral part of RV outer moraines suggests deposition under different conditions. First, the very gentle slopes with low altitudes (120–160 m a.s.l) of the frontal portion of the RV moraine, with arcuate flat-top mounds and concave up glacier form is interpreted to be a group of subaqueous ice contact fans, where each fan was formed at the mouth of a subglacial conduit (Benn, 1996; García et al., 2015; Davies et al., 2018), discharging into the palaeo Laguna Blanca. In

TABLE 3 | Radiocarbon sample details.

Sample ID	Location			Material	Depth (cm)	Percent modern Carbon ±1σ	^{14}C age ±1σ (yr BP)	2σ Calibrated Range (cal yr BP)	Date Expressed in Text (cal kyr BP)	Probability Distribution (%)	Feature
	Lat	Lon	Altitude (m)								
SSK1902_14C	−52.6124	−71.345	185	Macro flora	1,080	18.359 ± 0.095	13,616 ± 42	16,236–16,571	c. 16.4	100	Peatbog next to intermorainic pond
	−52.6654	−71.404	62	Macro flora	575	20.89 ± 0.17	12,579 ± 65	14,781–15,143	c. 14.9	62.2	Bog in an abandoned melt water channel
SSK1901_14C											

contrast, the lateral sections of RV have higher altitudes (from 160 to 230 m a.s.l.) and relief. They show sharp-crested moraine ridges, implying formation under subaerial conditions. The transition between these two morphologies occurs at 160 m a.s.l. and this is closely similar to the palaeo Laguna Blanca level during T5 (**Figure 6E**). We therefore interpret that this altitude marks the transition between subaerial and subaqueous environment and that the RV moraine was formed at the same time as T5 and that only the lower, central portion of the glacier forming RV was in direct contact with the lake (**Figures 11D**). Following the retreat from RV, the glacier retreated into Seno Skyring. The palaeo Laguna Blanca become detached from the damming ice. Any evolution of the proglacial paleolake formed afterwards was dammed by the RV landforms (**Figures 11E,F**).

5.2 Style of Glaciation at Skyring Ice Lobe

Previous studies in Southernmost Patagonia have proposed the existence of warm-based ice lobes with periods of polythermal conditions (Glasser et al., 2008; Darvill et al., 2017). These interpretations are mainly due to the presence of substantial glaciofluvial domains, large subglacial features such as drumlin fields, and brittle deformation observed within moraine sections (Benn and Clapperton, 2000a). Moreover, at Otway and Magallanes ice lobes, located immediately south of Seno Skyring lobe, a surging type of glacier activity has also been suggested (Lovell et al., 2012).

The landform assemblage of Skyring ice lobe indicates an active temperate glacial landsystem (Evans, 2003a). These environments are characterized by three main geomorphological domains, which indicate a wet-based glacier for at least part of the year. These landform associations are push moraines, subglacial deposits, glaciofluvial and glaciolacustrine domains (Evans and Twigg, 2002; Evans, 2003b; Chandler et al., 2020). In this study area, the LB glacial margin is at least partly composed of push moraines, which are best exposed at LB IV. There, the push moraine domain is represented by up to 10 consecutive nested ridges with lengths greater than 12 km, located at the east part of LB IV moraine. Furthermore, the glaciofluvial deposits are present in close association with the moraines throughout the study area including the extensive outwash terraces in the LB system and lateral parts of RV glacial margins. Glaciolacustrine environments were common during the retreat from LB moraine system and the formation of, and retreat from RV moraine system. Finally, we also noted the streamlined mounds moulded in the direction of ice flow and located in the proximal west slope of RV moraines, which are interpreted as forming via subglacial deformation.

Hummocky relief is not common in warm-based glaciers due to the scarce presence of supraglacial debris (Evans and Twigg, 2002; Evans, 2003b). However, hummocky terrain broadly occur in the frontal moraine area of the LB system (**Figure 3**). We attribute the source of supraglacial debris to englacial thrusting of the basal and subglacial sediments, forming a series of stacked moraines (Hambrey et al., 1997; Bennett et al., 1998; Johnson and Clayton, 2003). The

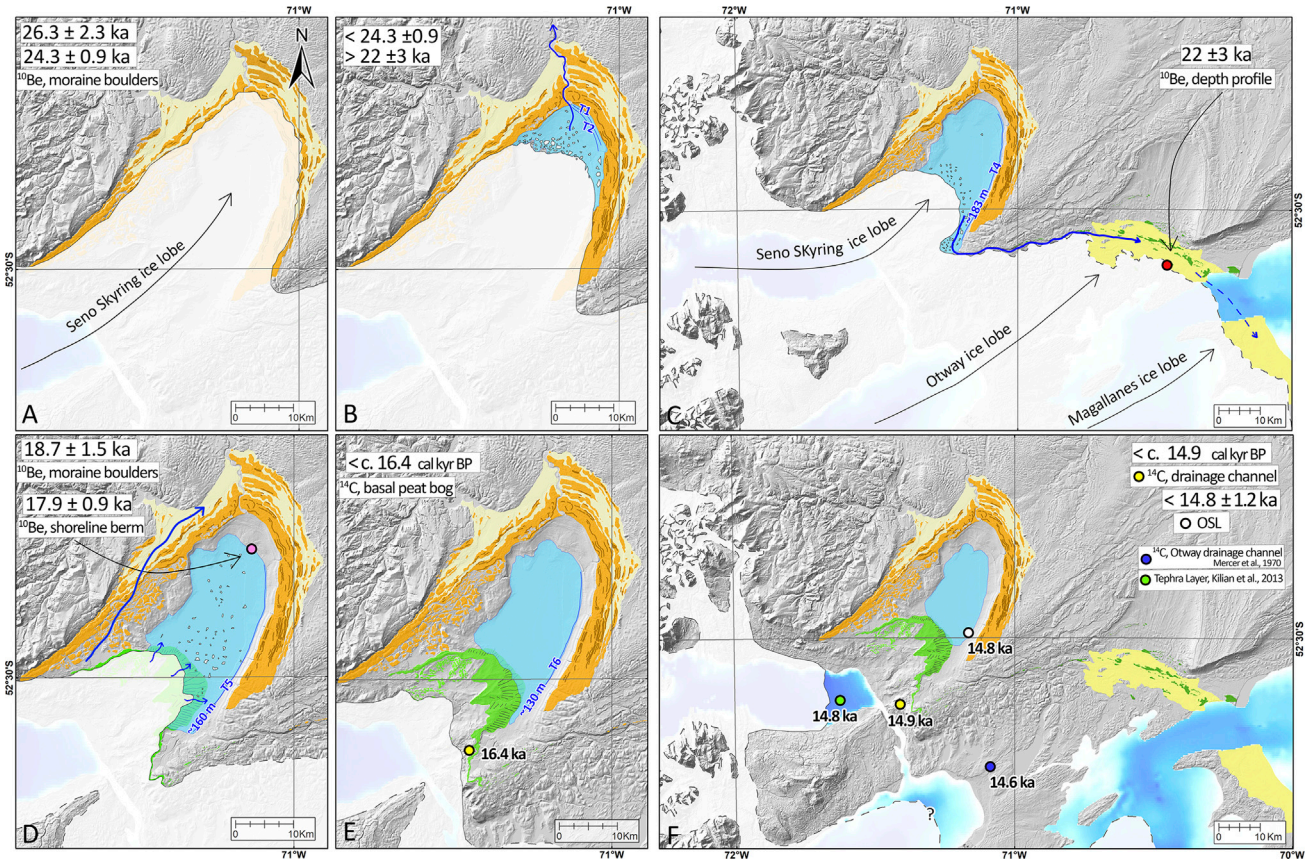

FIGURE 11 | Evolution of the former Seno Skyring ice lobe. **(A)** Glacier position during the deposition of LB III and LB IV moraines. **(B)** Formation of the Laguna Blanca proglacial lake with a northern spillway. During this period, the northern spillway served as drainage for T1 and T2 lake levels. **(C)** Abrupt (partial) drainage of Laguna Blanca to the southeast reaching the Otway lobe region, lake level decreased rapidly from T3 to T4. **(D)** Glacier position during the deposition of RV moraine; the frontal parts formed sub-aqueously under the lake level T5. During this glacial advance/stillstand, the outwash from LB moraines was reactivated at 20.6 ka. **(E)** Minimum age of the glacier abandonment from RV moraine position. **(F)** The Seno Skyring and Otway lobes retreated back to positions into the fjords, evidenced by land exposition and posterior deposition of organic material and tephra on top. At the same time, OSL dating of lacustrine sediments from the palaeo Laguna Blanca indicates a high stand of the lake level between T5 and T6. Note that the shoreline altitudes of the palaeo Laguna Blanca are from measurements taken at the southeastern area of the basin. Dashed lines around ice edges correspond to inferred limits.

glaciotectonic moraine thrusting is supported by the lacustrine sediment slabs found within moraine sections in LB moraines. In temperate environments, thrusting can occur due to ice flow compression in a reverse slope caused by a glacier over deepening (Glasser and Hambrey, 2002). Such a reverse slope is present inboard from LB moraines. On the other hand, the brittle deformation and the absence of ductile deformation in the lacustrine sediments from LB moraine sections (**Figure 5**) suggest that a rigid substrate facilitated thrusting as frozen sediments (Evans and England, 1991), likely to occur in permafrost environments or cold-based glaciers. Here, we hypothesized that the thrusting and stacking of sediment was facilitated by an ice lobe with polythermal conditions, as seasonal permafrost or cold-based margins (Glasser and Hambrey, 2003), as previously reported for the Magallanes ice lobe (Benn and Clapperton, 2000a). Therefore, the landform assemblage from Seno Skyring ice lobe suggests an active temperate glacial landsystem, with the ability to generate thrusting during the cold periods affecting a polythermal glacier.

5.3 Geochronology

Using the relative chronology derived from the geomorphological interpretations above we can place firm ages on several of the key events in the glacial history of the Seno Skyring lobe using our ^{10}Be, OSL and radiocarbon dating approach (**Figure 11**).

5.3.1 Boulder Erosion Rate

We calculated a linear erosion rate of 0.72 ± 0.04 mm/kyr for one boulder composed of quartzite lithology in LB moraines, assuming the erosion was constant since the boulder deposition. This value falls between previous calculations in Patagonia literature: Kaplan et al. (2005) estimated a maximum erosion rate of 1.4 mm/kyr in a boulder located at 46°S, while Douglass et al. (2007) constrained an erosion rate of 0.2 mm/kyr and, at 47–48°S, Mendelová et al. (2020)

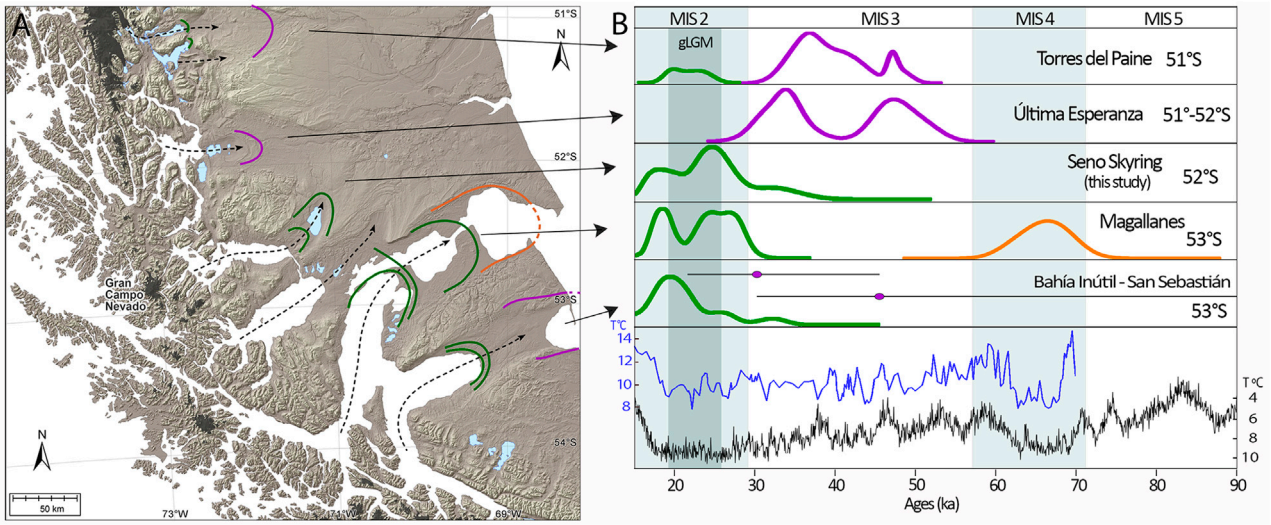

FIGURE 12 | Southern Patagonia ice lobe extents and timing of occurrence of the moraine belts during the last glacial period from 15–90 ka. **(A)** Map of major moraine belts which are coloured to match the geochronology in panel **(B)**. Orange corresponds to MIS 4, purple to MIS 3 and green to MIS 2. **(B)** Density functions (probability plots) of exposure ages of moraine boulders in Southern Patagonia moraine belts (this study; McCulloch et al., 2005b; Kaplan et al., 2008; Sagredo et al., 2011; García et al., 2018; Peltier et al., 2021). For the Bahía Inútil-San Sebastián ice lobe, the outer glacial margins were geochronological constrained through a cosmogenic nuclide depth profile approach performed on the outwash plain associated with their respective moraine (Darvill et al., 2015). These ages are indicated by a solid circle (purple) and their uncertainty by a horizontal line. The Sea Surface Temperature (SST) curve (blue) is from an off-shore core in northwestern Patagonia at 41°S (Kaiser et al., 2005) and the east Antarctic temperature record (black) from EPICA Dome C (Jouzel et al., 2007).

calculated an erosion rate of 0.035 mm/kyr from an outwash cobble.

5.3.2 Laguna Blanca Moraine System Ages

The surface exposure ages (^{10}Be) from the inner LB moraine system suggest that two Skyring ice lobe advances culminated by 26.3 ± 2.3 ka (n = 5) and 24.3 ± 0.9 ka (n = 3) when LBIII and LBIV were built, respectively (**Figure 11A**). The restricted access to LBI and LBII, the lack of preservation of these landforms on the east side and the absence of boulders mean that we are not yet able to date these outermost landforms. Our geomorphological interpretations suggest a relative contemporaneous formation of the whole LB moraine system, but we cannot yet rule out older ages for LBI and LBII. At the moment of the LB III and LB IV deposition, the glacier occupied almost the full extent of the basin, marking the near-maximum mapped ice extent. Therefore, we can establish that the Seno Skyring ice lobe reached full glacial conditions during the global Last Glacial Maximum (gLGM; MIS 2). Nevertheless, on a MIS 2 moraine, a boulder with an age of 41.1 ± 6.3 ka that we considered as an outlier is likely to contain inherited ^{10}Be from an unknown period of previous exposure. This could perhaps signify that the glacier was at or close to LB positions in an earlier advance, as expected based on neighbourhood chronologies recording middle MIS 3 (Sagredo et al., 2011; Darvill et al., 2015; García et al., 2018) or MIS 4 ice advances (Peltier et al., 2021).

The age of the outwash plain we mapped as linked to LB III yielded an age of 20.6 ± 0.9 ka. Taking the data at face value, this outwash age is 5.7 kyr younger than the LB III age (26.3 ± 2.3ka). From the assumption of an outwash formation during moraine deposition, we would expect that LB III and its associated outwash plain will have an age difference indistinguishable within uncertainties (Hein et al., 2009; Mendelová et al., 2020). The tight ages of the cobbles (**Figure 8D**) suggest this outwash plain was reactivated after the deposition of the older LB III moraine.

5.3.3 Palaeo Laguna Blanca Evolution: Partial Drainage Event and Palaeo Shorelines

The timing for a partial drainage event of the Laguna Blanca proglacial lake, when a retreating Seno Skyring ice lobe opened the southeastern spillway, and associated with the decrease of the lake level from T3 to T4, is constrained with an age of 22 ± 3 ka (Otway's outwash ^{10}Be depth profile). For the Otway lobe, this represents a minimum age for the glacial retreat from the "A" moraines (cf., Clapperton et al., 1995) that are partly buried by the outwash. Our date is consistent with recent dating of this ice margin between 23.9 ka (Peltier et al., 2021) which predates the outwash infill we have dated here at 22 ± 3 ka.

The paleolake abandoned the southeastern spillway by 17.9 ± 0.9 ka (SSK1901_S), the exposure age of the next lowest terrace, T5. The timing of RV moraine advance culmination (18.7 ± 1.5 ka) corresponds to the timing of the T5 shoreline berm within uncertainties. This agreement supports the geomorphological interpretations, where the frontal portions of RV moraine were deposited subaqueously under lake level T5 that covered the Laguna Blanca basin (**Figures 11D**). Our OSL age of subaqueous alluvial fan sands intercalated with fine lacustrine sediments suggest the palaeo lake Laguna Blanca persisted at the T6 level until at least 14.8 ± 1.2 ka (**Supplementary Figure S1**, extended results).

5.3.4 Río Verde Moraine System Age and Deglaciation

The inboard RV moraines represent a glacial readvance, during a period between 21.2 and 17.2 ka, with a peak at 18.7 ± 1.5 ka (n = 6). The timing of RV moraine advance culmination also corresponds to the timing of the T5 shoreline berm within uncertainties (17.9 ± 0.9 ka). This agreement in ages supports the geomorphology interpretations, where the frontal portions of RV moraine were deposited subaqueously under lake level T5 (**Figure 11D**). During this glacial readvance we suggest there was a reactivation of the Laguna Blanca outwash noted above in point 5.3.2., and the meltwater from the SW side of the lobe was flowing downwards along the left LB III lateral moraine, depositing younger material over the outwash plain at 20.6 ± 0.9 ka.

Final deglaciation began after the glacier retreated from RV moraine positions. Two radiocarbons dates of peat initiation indicate minimum ages for abandonment of the RV moraines. For the outer part of RV moraines, we have a minimum deglaciation age of c.16.4 cal kyr BP (SSK1901_14C). Additionally, SSK1901_14C provides a minimum age of meltwater channel abandonment at c.14.9 cal kyr BP, and a total glacier retreat from the RV moraine system (**Figures 11E,F**).

5.4 Summary of Seno Skyring Ice Lobe Evolution

Our geomorphology and geochronology reconstruction from Seno Skyring ice lobe allows us to interpret the evolution of glacial advances and subsequent deglaciation. The moraine geochronology (^{10}Be) from the inner LB moraine system shows two glacial advances culminating at 26.3 ± 2.3 ka (n = 5) and 24.3 ± 0.9 ka (n = 3) for LBIII and LBIV, respectively (**Figure 11A**). After the ice retreated from LB moraines, a proglacial lake (palaeo Laguna Blanca) formed in front of the ice lobe that first drained to the Atlantic using the northern spillway through the LB moraines. This spillway served as a drainage for T1 and T2 lake levels (**Figure 11B**). Continued ice retreat expanded the lake south-westward and opened abruptly a new spillway to the southeast, which was active by 22 ± 3 ka (**Figure 11C**). We relate the formation of this new spillway to the lake level drop from T3 to T4. A final glacial advance deposited the RV moraine by 18.7 ± 1.5 ka (n = 6; **Figure 11D**). The geomorphology suggests the frontal portions of RV moraine were deposited subaqueously under the lake level T5 (17.9 ± 0.9 ka). After RV moraine system deposition, final deglaciation started in the area. The glacier abandoned the RV terminal moraine by at least c.16.4 cal ky BP and the whole RV system by c.14.9 cal ky BP (**Figures 11E,F**). Moreover, the absence of glacial influence on the sedimentology from the palaeo Laguna Blanca section could suggest the glacier did not further influence the area by 14.8 ± 1.2 ka (OSL). The final demise of the Seno Skyring glacier is recorded by marine core data in the fjord. The presence of a 14.8 ka airfall Reclus tephra in a marine core (Stern et al., 2011; Kilian et al., 2013) showed that the ice had retreated at least 30 km from the eastern shore by this time (**Figure 11F**), and Kilian et al. (2007) suggested that by 14 ka the ice was retreating into the upper parts of the mountains, thus becoming restricted to the Gran Campo Nevado icefield by then.

5.5 Glacial Advances in Southernmost Patagonia

From published geochronological records in southernmost Patagonia, we know there were multiple glacial advances during the last glacial cycle, including during the gLGM (26.6–19 ka; Clark et al., 2009). However, the morphostratigraphic pattern of ice advances, the timing of the local LGM (lLGM), and the extent of ice at the gLGM vary between different lobes draining the southernmost portion of the PIS. For example, during the gLGM there were extensive ice advances recorded in the Seno Skyring (52°S), Magallanes (52°-53°S), Bahía Inútil-San Sebastián (53°S) and Torres del Paine lobes (51°S). But some lobes also showed prominent lLGM advances earlier in the glacial cycle: the Torres del Paine and Última Esperanza (51–52°S) ice lobes show culminations of glacial advances at 48.4 ± 1.7 ka and 48.6 ± 2.0, respectively (García et al., 2018). Similarly, in Bahía Inútil-San Sebastián lobe (53°S) in Tierra del Fuego, the ice maximum is inferred to have occurred at 45.6 ka (Darvill et al., 2015; **Figure 12**). These ice advances record the lLGM in the middle MIS 3, whereas a lLGM during MIS 4 has been recorded by the Magallanes Strait ice lobe (52°-53°S) at 67 ± 2.1 ka (Peltier et al., 2021). In contrast, our results at Seno Skyring ice lobe show full glacial conditions during gLGM at 26.3 ± 2.3 and 24.3 ± 0.9 ka during MIS 2, but no obvious indication of pre gLGM ice advances were dated, although we note that the outer LB I and II moraines remain undated. In any case, the morphostratigraphic position of the LB moraines differs from those in neighbour ice lobes exposing different ice extent through the last glacial cycle. It is notable that no single lobe in southern Patagonia appears to show all of the glacial advances recorded in the region, which in turn denote the need to for glacier records in different basins in order to obtain a complete picture of glacier/climate change during the last glacial period in Patagonia.

If we are to better understand the palaeoclimate of southernmost Patagonia two main questions need to be addressed: First, why do different lobes show different advance extension at similar times? Second, why does the timing of *maximum* extent differ between lobes?

There are a number of possible reasons for explaining the observed differences. First, there may be a sampling bias due to not all moraines being sampled. Second, there may be a preservation bias: particular moraine belts may have been eroded, overridden leading to an incomplete record of ice history. This is perhaps more likely to occur where there is a large MIS2 advance which may have eroded earlier landforms, which may be the case in Seno Skyring lobe. A third potential explanation is glaciological and topographic differences between ice lobes. For example, differences in basin geometry may control ice behaviour due to variations in the scale, shape and elevation distribution (hypsometry) of the ice drainage catchment (Furbish and Andrews, 1984; Kaplan et al., 2009; Anderson et al., 2012; Barr and Lovell, 2014), as may differences in substrate material (e.g., Benn and Clapperton, 2000b). A fourth set of explanations may lie in regional or local climatic differences. Understanding these influences could be best addressed through numerical

modelling of the PIS. Nevertheless, here we provide some initial suggestions of potential explanations.

Patagonia is marked by strong W-E contrasts in precipitation (Garreaud, 2007). This contrast is caused by a rain shadow and continentality effects where the amount of precipitation falls rapidly as air masses rise over the Andes and move progressively east. The interplay of topography and precipitation may influence the geomorphic record of past glacial cycles. For example, those areas with higher elevation can grow more extensive glaciers because they have larger accumulation areas. This is the case for Torres del Paine, Última Esperanza, Magallanes and Bahía Inútil-San Sebastián lobes. These lobes also can start advancing earlier in a glacial cycle, having the potential to record older ice advances within the last glacial cycle. It is not the case where mountains are lower in their catchments, such as Seno Skyring and Seno Otway, since it will take more time for the area to be covered by ice and thus, spread away from the mountain zone (Sugden et al., 2002). Additionally, during the PIS build-up, higher areas will progressively develop an extensive ice sheet to the west (towards the precipitation source), producing the ice divide migration to the west, and provoking snow starvation effect to the east (Sugden et al., 2002). This can imply that during one glacial cycle, subsequent (younger) glacial advances reach more restricted positions, compared to previous advances (Mendelová et al., 2020). This will not be the case where altitudes of the mountains are lower, where the precipitation influence will affect the eastern area for a longer period, and younger glacial advances could have the potential to reach further positions beyond older advances. This could be one reason that in Seno Skyring, where the altitudes of the mountains are lower, the gLGM reaches close to maximum positions, and in the rest of Southern Patagonia, pre gLGM extents are significantly greater than gLGM limits. Moreover, the areas with lower mountains in their upper catchments may have a smaller orographic effect and so may experience greater precipitation over the glaciers.

5.6 Paleoclimate in Southernmost Patagonia

A cold temperature period prevailed during MIS 2 in Patagonia, according to Antarctic and Patagonian off-shore sea surface temperatures (SSTs) proxies (Blunier and Brook, 2001; Kaiser et al., 2005; Jouzel et al., 2007). The LB III and LB IV have ages of 26.3 ± 2.3 (n = 5) and 24.3 ± 0.9 ka (n = 3). LB III coincides with the onset of the gLGM and the coldest periods from East Antarctica. Moreover, the LB moraine ages are in agreement - within uncertainties -with the A limit moraine records from Magallanes ice lobe (Clapperton et al., 1995), dating to 25.7 ± 0.8 and 23.9 ± 0.8 (Peltier et al., 2021) and the C limit in Bahía Inútil-San Sebastián dating 23.2 ± 1.3 ka (McCulloch et al., 2005b; **Figure 12**). Humidity records in Patagonia during this period (e.g., Heusser et al., 1996; Moreno et al., 2015) suggest wetter conditions for the northern part of Patagonia, and drier for the south, implying a northern migration of the SWWs (Moreno et al., 1999; Hulton et al., 2002; Rojas et al., 2009). The wetter and colder conditions for north-central Patagonia are supported by the ice maxima in central-eastern Patagonia during the gLGM (Kaplan et al., 2004; Douglass et al., 2006; Hein et al., 2010; Leger et al., 2021). Despite the apparent reduction in the precipitation in southern Patagonia for the MIS 2 period, the PIS outlets advanced between about 100–250 km from present-day ice. Therefore, the precipitation in the area should have been sufficient alongside the sharp decrease in temperatures to develop full glacial conditions in the area. Peltier et al. (2021) suggest a mean annual temperature reduction in 4.5°C temperature, when a decrease in 25% of precipitation occurred for southernmost Patagonia during MIS 2.

By the end of the LGM and shortly before the onset of the last glacial termination, a less extensive glacial readvance, inboard from the LGM positions, and culminated at 18.7 ± 1.5 ka, represented in Seno Skyring by the RV moraine system. This broad pattern occurs for several other glacier outlets: in the Magallanes lobe, there are two short periods of glacial readvance/stillstand at 18.1 ± 0.8 and 19.1 ± 0.6 ka (Peltier et al., 2021) and a similar age for the "D limit" in Bahía Inútil-San Sebastián lobe with ages 19.7 ± 2.0 ka (McCulloch et al., 2005b; Kaplan et al., 2008). At Torres del Paine the TDP I moraine dates to 21.7 ± 2.0 ka (García et al., 2018). Considering the timings of these moraines within their uncertainties, there appears to be a close concordance in the timing of a readvance or stillstand at the end of the gLGM, showing a clear regional pattern.

After the RV moraine formation in Seno Skyring lobe, our geochronology shows that by c.16.4 cal kyr BP deglaciation was underway and by 14.8 ka, the glacier was already in the fjord area (Kilian et al., 2013). A synchronous retreat is observed in the Otway ice lobe, where Mercer (1970) reports a minimum deglaciation age of 14.6 cal kyr BP, for the ice abandonment close to the eastern shore of the Otway fjord (**Figure 11F**). Similarly, in the Magallanes and Bahía Inútil-San Sebastián lobes, deglaciation records suggest the glacier retreated to the northern part of Isla Dawson before c. 16.6 cal kr BP (Mcculloch and Bentley, 1998; McCulloch et al., 2005b). Other studies suggest that the glacier was already in the Darwin Cordillera by 16.8 ka, which corresponds to the accumulation area from Magallanes and Bahía Inútil-San Sebastián lobes (e.g., Hall et al., 2013; Hall et al., 2017; Hall et al., 2019). These deglaciation events follow a sharp climatic amelioration that occurred after ~18 ka (Kaiser et al., 2005; Jouzel et al., 2007; Caniupán et al., 2011), which marks the onset of the last glacial termination in Patagonia also (Denton et al., 2010; Moreno et al., 2015). After the increase in temperature, at 18.1 ka the PIS experienced a rapid ice thinning (Boex et al., 2013) and an extraordinarily fast recession (Darvill et al., 2017; Davies et al., 2020; Moreno, 2020). By 14 ka the Seno Skyring ice lobe had retreated to the inner fjords close to Gran Campo Nevado, losing more than 80% of its length compared to its maximum of the last glacial cycle (Kilian et al., 2007).

6 CONCLUSION

Our geomorphology and geochronology reconstructions demonstrate that the Seno Skyring ice lobe reached full glacial

conditions during the gLGM, marked by the LB III and IV advances by 26.3 ± 2.3 (n = 5) ka and 24.3 ± 0.9 ka (n = 3). During the ice retreat from the LB moraine system, a proglacial lake developed, which initially drained to the north. As the ice retreated, a new spillway opened towards the southeast by 22 ± 3 ka. A glacier readvance deposited the inboard RV moraines by 18.7 ± 1.5 ka (n = 6), before the onset of the deglaciation. By at least c.16.4 cal ky BP and from the whole RV system by c.14.9 cal ky BP.

We compare our new glacier record from Seno Skyring to published records from other lobes in southernmost Patagonia. There are differences in the morphostratigraphic pattern and timing of advances between lobes, with no single lobe recording all the advances seen regionally. We speculate that some of the differences in the ice extent throughout the last glacial period may be related to the snow starvation effect in response to a northward migration of the westerlies and/or a westward migration of the ice divide during the PIS build-up throughout the last glacial period. Nevertheless, right after the gLGM and before the Termination, broadly synchronic glacial advances with relatively reduced extents are recorded along southern Patagonia.

DATA AVAILABILITY STATEMENT

The original contributions presented in the study are included in the article/**Supplementary Material**, further inquiries can be directed to the corresponding author.

AUTHOR CONTRIBUTIONS

M-PL designed this manuscript project in discussion with J-LG, MB and SJ. M-PL analysed the data and drafted the manuscript with help from MB and J-LG. M-PL, J-LG, HF, MB and AH attended to fieldwork. CD contributed with sample information and their analysis. AH, HF, AR, DF, RS and SB contributed to the laboratory sample dating process. All authors discussed the results and contributed to the final manuscript.

FUNDING

M-PL holds the PhD studentship from ANID PFCHA/Doctorado Becas Chile/2018—72190469. The fieldwork campaigns and the majority of sample analysis were funded with the Chilean Grant FONDECYT #1161110 (J-LG). The ^{10}Be depth profile sample process was funded with NERC CIAF grant 9199/1019 (MB; M-PL) and 9140/1013 (MB; CD). Gilchrist Educational Fund, Geography Department—Durham University; Norman Richardson Award—Ustinov College contributed to the fieldwork expenses of M-PL.

ACKNOWLEDGMENTS

We are grateful to Familia Vargas (Ea. Laguna Blanca), Familia Mclean (Ea. Las Charas) for the great support during fieldwork. We also thank Familia Concha (Ea. Ayelén), Ea. Cacique Mulato, Ea. La Leona, Ea. Entre Vientos, Ea. Divina Esperanza and Ea. El Ovejero for allowing us to access the field site. We thank Consuelo Antezana, Gabriel Gómez, Víctor García, Paulo Rodríguez, Tancrède Leger, Alex Mayne-Nicholls and Max Fischer for the assistance in the field. We thank Cristina Balaban and Pedro Guzmán for the useful discussions. Finally, we thank Sam Kelley and Nathan D. Stansell, two reviewers who made constructive comments on this paper.

SUPPLEMENTARY MATERIAL

The Supplementary Material for this article can be found online at: https://www.frontiersin.org/articles/10.3389/feart.2022.892316/full#supplementary-material

REFERENCES

Anderson, R. S., Dühnforth, M., Colgan, W., and Anderson, L. (2012). Far-flung Moraines: Exploring the Feedback of Glacial Erosion on the Evolution of Glacier Length. *Geomorphology* 179, 269–285. doi:10.1016/j.geomorph.2012.08.018

Balco, G., Stone, J. O., Lifton, N. A., and Dunai, T. J. (2008). A Complete and Easily Accessible Means of Calculating Surface Exposure Ages or Erosion Rates from 10Be and 26Al Measurements. *Quat. Geochronol.* 3 (3), 174–195. doi:10.1016/j.quageo.2007.12.001

Barr, I. D., and Lovell, H. (2014). A Review of Topographic Controls on Moraine Distribution. *Geomorphology* 226, 44–64. doi:10.1016/j.geomorph.2014.07.030

Benn, D. I., and Clapperton, C. M. (2000a). Glacial Sediment-Landform Associations and Paleoclimate during the Last Glaciation, Strait of Magellan, Chile. *Quat. Res.* 54 (1), 13–23. doi:10.1006/qres.2000.2140

Benn, D. I., and Clapperton, C. M. (2000b). Pleistocene Glacitectonic Landforms and Sediments Around Central Magellan Strait, Southernmost Chile: Evidence for Fast Outlet Glaciers with Cold-Based Margins. *Quat. Sci. Rev.* 19 (6), 591–612. doi:10.1016/s0277-3791(99)00012-8

Benn, D. (1996). Subglacial and Subaqueous Processes Near a Glacier Grounding Line: Sedimentological Evidence from a Former Ice-dammed Lake, Achnasheen Scotland. *Boreas* 25 (1), 23–36.

Bennett, M. R., and Glasser, N. F. (1991). The Glacial Landforms of Glen Geusachan, Cairngorms: a Reinterpretation. *Scott. Geogr. Mag.* 107 (2), 116–123. doi:10.1080/00369229118736819

Bennett, M. R., Hambrey, M. J., Huddart, D., and Glasser, N. F. (1998). Glacial Thrusting & Moraine-Mound Formation in Svalbard & Britain: The Example of Coire a'Cheud-Chnoic (Valley of Hundred Hills), Torridon Scotland. *J. Quat. Sci.* 13 (6), 17–34.

Blunier, T., and Brook, E. J. (2001). Timing of Millennial-Scale Climate Change in Antarctica and Greenland during the Last Glacial Period. *science* 291 (5501), 109–112. doi:10.1126/science.291.5501.109

Boex, J., Fogwill, C., Harrison, S., Glasser, N. F., Hein, A., Schnabel, C., et al. (2013). Rapid Thinning of the Late Pleistocene Patagonian Ice Sheet Followed Migration of the Southern Westerlies. *Sci. Rep.* 3 (1), 2118. doi:10.1038/srep02118

Caldenius, C. C. z. (1932). Las Glaciaciones Cuaternarias en la Patagonia y Tierra del Fuego. *Geogr. Ann.* 14 (1-2), 1–164. doi:10.2307/519583

Caniupán, M., Lamy, F., Lange, C., Kaiser, J., Arz, H., Kilian, R., et al. (2011). Millennial-scale Sea Surface Temperature and Patagonian Ice Sheet Changes off Southernmost Chile (53 S) over the Past~ 60 Kyr. *Paleoceanography* 26 (3), 1-10. doi:10.1029/2010pa002049

Chandler, B. M. P., Evans, D. J. A., Chandler, S. J. P., Ewertowski, M. W., Lovell, H., Roberts, D. H., et al. (2020). The Glacial Landsystem of Fjallsjökull, Iceland: Spatial and Temporal Evolution of Process-form Regimes at an Active Temperate Glacier. *Geomorphology* 361, 107192. doi:10.1016/j.geomorph.2020.107192

Clapperton, C. M., Sugden, D. E., Kaufman, D. S., and McCulloch, R. D. (1995). The Last Glaciation in Central Magellan Strait, Southernmost Chile. *Quat. Res.* 44 (2), 133–148. doi:10.1006/qres.1995.1058

Clapperton, C. (1993). *Quaternary Geology and Geomorphology of South America*. Amsterdam, Netherlands: Elsevier

Clark, P. U., Dyke, A. S., Shakun, J. D., Carlson, A. E., Clark, J., Wohlfarth, B., et al. (2009). The Last Glacial Maximum. *science* 325 (5941), 710–714. doi:10.1126/science.1172873

Cogez, A., Herman, F., Pelt, É., Reuschlé, T., Morvan, G., Darvill, C. M., et al. (2018). U-th and ¹⁰Be Constraints on Sediment Recycling in Proglacial Settings, Lago Buenos Aires, Patagonia. *Earth Surf. Dynam.* 6 (1), 121–140. doi:10.5194/esurf-6-121-2018

Darvill, C. M., Bentley, M. J., Stokes, C. R., Hein, A. S., and Rodés, Á. (2015). Extensive MIS 3 Glaciation in Southernmost Patagonia Revealed by Cosmogenic Nuclide Dating of Outwash Sediments. *Earth Planet. Sci. Lett.* 429, 157–169. doi:10.1016/j.epsl.2015.07.030

Darvill, C. M., Bentley, M. J., Stokes, C. R., and Shulmeister, J. (2016). The Timing and Cause of Glacial Advances in the Southern Mid-latitudes during the Last Glacial Cycle Based on a Synthesis of Exposure Ages from Patagonia and New Zealand. *Quat. Sci. Rev.* 149, 200–214. doi:10.1016/j.quascirev.2016.07.024

Darvill, C. M., Stokes, C. R., Bentley, M. J., Evans, D. J. A., and Lovell, H. (2017). Dynamics of Former Ice Lobes of the Southernmost Patagonian Ice Sheet Based on a Glacial Landsystems Approach. *J. Quat. Sci.* 32 (6), 857–876. doi:10.1002/jqs.2890

Darvill, C. M., Stokes, C. R., Bentley, M. J., and Lovell, H. (2014). A Glacial Geomorphological Map of the Southernmost Ice Lobes of Patagonia: the Bahía Inútil - San Sebastián, Magellan, Otway, Skyring and Río Gallegos Lobes. *J. Maps* 10 (3), 500–520. doi:10.1080/17445647.2014.890134

Davies, B. J., Darvill, C. M., Lovell, H., Bendle, J. M., Dowdeswell, J. A., Fabel, D., et al. (2020). The Evolution of the Patagonian Ice Sheet from 35 Ka to the Present Day (PATICE). *Earth-Science Rev.* 204, 103152. doi:10.1016/j.earscirev.2020.103152

Davies, B. J., Thorndycraft, V. R., Fabel, D., and Martin, J. R. V. (2018). Asynchronous Glacier Dynamics during the Antarctic Cold Reversal in Central Patagonia. *Quat. Sci. Rev.* 200, 287–312. doi:10.1016/j.quascirev.2018.09.025

Denton, G. H., Anderson, R. F., Toggweiler, J. R., Edwards, R. L., Schaefer, J. M., and Putnam, A. E. (2010). The Last Glacial Termination. *science* 328 (5986), 1652–1656. doi:10.1126/science.1184119

Dewald, A., Heinze, S., Jolie, J., Zilges, A., Dunai, T., Rethemeyer, J., et al. (2013). CologneAMS, a Dedicated Center for Accelerator Mass Spectrometry in Germany, Nuclear Instruments. *Methods in Physics Research Section B: Beam Interactions with Materials and Atoms*, 294, 18–23. doi:10.1016/j.nimb.2012.04.030

Douglass, D. C., Singer, B. S., Ackert, R. P., Stone, J., Kaplan, M. R., and Caffee, M. (2007). "Constraining Boulder Erosion Rates and Ages of Mid-pleistocene Moraines. In Lago Buenos Aires, Argentina," in *GSA Abstracts and Programs Northeastern Section, 42nd Annual Meeting*. Durham, New Hampshire

Douglass, D., Singer, B., Kaplan, M., Mickelson, D., and Caffee, M. (2006). Cosmogenic Nuclide Surface Exposure Dating of Boulders on Last-Glacial and Late-Glacial Moraines, Lago Buenos Aires, Argentina: Interpretive Strategies and Paleoclimate Implications. *Quat. Geochronol.* 1 (1), 43–58. doi:10.1016/j.quageo.2006.06.001

Evans, D. (2003a). *Glacial Landsystems*. London: Hodder Arnold.

Evans, D. (2003b). "Ice-marginal Terrestrial Landsystems: Active Temperate Glacier Margins," in *Glacial Landsystems*. London, UK: Arnold, 12–43.

Evans, D. J. A., and England, J. (1991). High Arctic Thrust Block Moraines. *Can. Geogr.* 35 (1), 93–97. doi:10.1111/j.1541-0064.1991.tb01628.x

Evans, D. J., and Benn, D. I. (2021). *A Practical Guide to the Study of Glacial Sediments*. London: QRA.

Evans, D. J., and Twigg, D. R. (2002). The Active Temperate Glacial Landsystem: a Model Based on Breiðamerkurjökull and Fjallsjökull, Iceland. *Quat. Sci. Rev.* 21 (20-22), 2143–2177. doi:10.1016/s0277-3791(02)00019-7

Furbish, D. J., and Andrews, J. T. (1984). The Use of Hypsometry to Indicate Long-Term Stability and Response of Valley Glaciers to Changes in Mass Transfer. *J. Glaciol.* 30 (105), 199–211. doi:10.3189/s0022143000005931

García, J.-L., Hall, B. L., Kaplan, M. R., Gómez, G. A., De Pol-Holz, R., García, V. J., et al. (2020). 14C and 10Be dated Late Holocene fluctuations of Patagonian glaciers in Torres del Paine (Chile, 51°S) and connections to Antarctic climate change. *Quat. Sci. Rev.* 246, 106541. doi:10.1016/j.quascirev.2020.106541

García, J.-L., Hein, A. S., Binnie, S. A., Gómez, G. A., González, M. A., and Dunai, T. J. (2018). The MIS 3 maximum of the Torres del Paine and Última Esperanza ice lobes in Patagonia and the pacing of southern mountain glaciation. *Quat. Sci. Rev.* 185, 9–26. doi:10.1016/j.quascirev.2018.01.013

García, J.-L., Lüthgens, C., Vega, R. M., Rodés, Á., Hein, A., and Binnie, S. (2021). A composite 10Be, IR-50 and 14C chronology of the pre-LGM full ice extent of the western Patagonian Ice Sheet in the Isla de Chiloé, south Chile (42°S). *E&G-Quaternary Sci. J.* 70 (1). doi:10.5194/egqsj-70-105-2021

García, J.-L., Strelin, J. A., Vega, R. M., Hall, B. L., and Stern, C. R. (2015). Deglacial ice-marginal glaciolacustrine environments and structural moraine building in Torres del Paine, Chilean southern Patagonia. *Andean Geol.* 42 (2), 190–212. doi:10.5027/andgeov42n2-a03

Garreaud, R. D. (2009). The Andes Climate and Weather. *Adv. Geosci.* 22, 3–11. doi:10.5194/adgeo-22-3-2009

Garreaud, R., Lopez, P., Minvielle, M., and Rojas, M. (2013). Large-scale Control on the Patagonian Climate. *J. Clim.* 26 (1), 215–230. doi:10.1175/jcli-d-12-00001.1

Garreaud, R. (2007). Precipitation and Circulation Covariability in the Extratropics. *J. Clim.* 20 (18), 4789–4797. doi:10.1175/jcli4257.1

Glasser, N. F., and Hambrey, M. J. (2002). Sedimentary Facies and Landform Genesis at a Temperate Outlet Glacier: Soler Glacier, North Patagonian Icefield. *Sedimentology* 49 (1), 43–64. doi:10.1046/j.1365-3091.2002.00431.x

Glasser, N. F., Jansson, K. N., Harrison, S., and Kleman, J. (2008). The Glacial Geomorphology and Pleistocene History of South America between 38 S and 56 S. *Quat. Sci. Rev.* 27 (3-4), 365–390. doi:10.1016/j.quascirev.2007.11.011

Glasser, N., and Jansson, K. (2008). The Glacial Map of Southern South America. *J. Maps* 4 (1), 175–196. doi:10.4113/jom.2008.1020

Glasser, N. S., and Hambrey, M. J. (2003). "Ice-marginal Terrestrial Landsystems: Svalbard Polythermal Glaciers," in *Glacial Landsystems* (London: Arnold), 228, 258.

Gosse, J. C., and Phillips, F. M. (2001). Terrestrial *In Situ* Cosmogenic Nuclides: Theory and Application. *Quat. Sci. Rev.* 20 (14), 1475–1560. doi:10.1016/s0277-3791(00)00171-2

Hall, B. L., Denton, G., Lowell, T., Bromley, G. R. M., and Putnam, A. E. (2017). Retreat of the Cordillera Darwin Icefield during Termination I. *Cig* 43, 751–766. doi:10.18172/cig.3158

Hall, B. L., Lowell, T. V., Bromley, G. R. M., Denton, G. H., and Putnam, A. E. (2019). Holocene Glacier Fluctuations on the Northern Flank of Cordillera Darwin, Southernmost South America. *Quat. Sci. Rev.* 222, 105904. doi:10.1016/j.quascirev.2019.105904

Hall, B. L., Porter, C. T., Denton, G. H., Lowell, T. V., and Bromley, G. R. M. (2013). Extensive Recession of Cordillera Darwin Glaciers in Southernmost South America during Heinrich Stadial 1. *Quat. Sci. Rev.* 62, 49–55. doi:10.1016/j.quascirev.2012.11.026

Hambrey, M. J., Huddart, D., Bennett, M. R., and Glasser, N. F. (1997). Genesis of 'hummocky Moraines' by Thrusting in Glacier Ice: Evidence from Svalbard and Britain. *J. Geol. Soc.* 154 (4), 623–632. doi:10.1144/gsjgs.154.4.0623

Hancock, G. S., Anderson, R. S., Chadwick, O. A., and Finkel, R. C. (1999). Dating Fluvial Terraces with 10Be and 26Al Profiles: Application to the Wind River, Wyoming. *Geomorphology* 27 (1-2), 41–60. doi:10.1016/s0169-555x(98)00089-0

Hein, A. S., Dunai, T. J., Hulton, N. R. J., and Xu, S. (2011). Exposure Dating Outwash Gravels to Determine the Age of the Greatest Patagonian Glaciations. *Geology* 39 (2), 103–106. doi:10.1130/g31215.1

Hein, A. S., Hulton, N. R., Dunai, T. J., Schnabel, C., Kaplan, M. R., Naylor, M., et al. (2009). Middle Pleistocene Glaciation in Patagonia Dated by Cosmogenic-Nuclide Measurements on Outwash Gravels. *Earth Planet. Sci. Lett.* 286 (1-2), 184–197. doi:10.1016/j.epsl.2009.06.026

Hein, A. S., Hulton, N. R., Dunai, T. J., Sugden, D. E., Kaplan, M. R., and Xu, S. (2010). The Chronology of the Last Glacial Maximum and Deglacial Events in Central Argentine Patagonia. *Quat. Sci. Rev.* 29 (9-10), 1212–1227. doi:10.1016/j.quascirev.2010.01.020

Heusser, C. J., Lowell, T. V., Heusser, L. E., Hauser, A., Andersen, B. G., and Denton, G. H. (1996). Full-glacial - Late-Glacial Palaeoclimate of the Southern Andes: Evidence from Pollen, Beetle and Glacial Records. *J. Quat. Sci.* 11 (3), 173–184. doi:10.1002/(sici)1099-1417(199605/06)11:3<173:aid-jqs237>3.0.co;2-5

Heyman, J., Applegate, P. J., Blomdin, R., Gribenski, N., Harbor, J. M., and Stroeven, A. P. (2016). Boulder Height–Exposure Age Relationships from a Global Glacial 10Be Compilation. *Quaternary Geochronol.* 34, 1–11.

Hidy, A. J., Gosse, J. C., Pederson, J. L., Mattern, J. P., and Finkel, R. C. (2010). A Geologically Constrained Monte Carlo Approach to Modeling Exposure Ages from Profiles of Cosmogenic Nuclides: An Example from Lees Ferry, Arizona. *Geochem. Geophys. Geosystems* 11 (9). doi:10.1029/2010gc003084

Hogg, A. G., Heaton, T. J., Hua, Q., Palmer, J. G., Turney, C. S., Southon, J., et al. (2020). SHCal20 Southern Hemisphere Calibration, 0-55,000 Years Cal BP. *Radiocarbon* 62 (4), 759–778. doi:10.1017/rdc.2020.59

Hulton, N. R., Purves, R., McCulloch, R., Sugden, D. E., and Bentley, M. J. (2002). The Last Glacial Maximum and Deglaciation in Southern South America. *Quat. Sci. Rev.* 21 (1-3), 233–241. doi:10.1016/s0277-3791(01)00103-2

Johnson, M., and Clayton, L. (2003). "Supraglacial Landsystems in Lowland Terrain," in *Glacial Landsystems* (London: Arnold), 228–258.

Jones, R. S., Small, D., Cahill, N., Bentley, M. J., and Whitehouse, P. L. (2019). iceTEA: Tools for Plotting and Analysing Cosmogenic-Nuclide Surface-Exposure Data from Former Ice Margins. *Quat. Geochronol.* 51, 72–86. doi:10.1016/j.quageo.2019.01.001

Jouzel, J., Masson-Delmotte, V., Cattani, O., Dreyfus, G., Falourd, S., Hoffmann, G., et al. (2007). Orbital and Millennial Antarctic Climate Variability over the Past 800,000 Years. *science* 317 (5839), 793–796. doi:10.1126/science.1141038

Kaiser, J., Lamy, F., and Hebbeln, D. (2005). A 70-kyr Sea Surface Temperature Record off Southern Chile (Ocean Drilling Program Site 1233). *Paleoceanography* 20 (4), 1-15. doi:10.1029/2005pa001146

Kaplan, M., Fogwill, C., Sugden, D., Hulton, N., Kubik, P., and Freeman, S. (2008). Southern Patagonian Glacial Chronology for the Last Glacial Period and Implications for Southern Ocean Climate. *Quat. Sci. Rev.* 27 (3-4), 284–294. doi:10.1016/j.quascirev.2007.09.013

Kaplan, M. R., Ackert, R. P., Jr, Singer, B. S., Douglass, D. C., and Kurz, M. D. (2004). Cosmogenic Nuclide Chronology of Millennial-Scale Glacial Advances during O-Isotope Stage 2 in Patagonia. *Geol. Soc. Am. Bull.* 116 (3-4), 308–321. doi:10.1130/b25178.1

Kaplan, M. R., Douglass, D. C., Singer, B. S., Ackert, R. P., and Caffee, M. W. (2005). Cosmogenic Nuclide Chronology of Pre-last Glacial Maximum Moraines at Lago Buenos Aires, 46 S, Argentina. *Quat. Res.* 63 (3), 301–315. doi:10.1016/j.yqres.2004.12.003

Kaplan, M. R., Hein, A. S., Hubbard, A., and Lax, S. M. (2009). Can Glacial Erosion Limit the Extent of Glaciation? *Geomorphology* 103 (2), 172–179. doi:10.1016/j.geomorph.2008.04.020

Kaplan, M. R., Strelin, J. A., Schaefer, J. M., Denton, G. H., Finkel, R. C., Schwartz, R., et al. (2011). *In-situ* Cosmogenic 10Be Production Rate at Lago Argentino, Patagonia: Implications for Late-Glacial Climate Chronology. *Earth Planet. Sci. Lett.* 309 (1-2), 21–32. doi:10.1016/j.epsl.2011.06.018

Kilian, R., Baeza, O., Breuer, S., Ríos, F., Arz, H., Lamy, F., et al. (2013). Late Glacial and Holocene Paleogeographical and Paleoecological Evolution of the Seno Skyring and Otway Fjord Systems in the Magellan Region. *An. Inst. Patagon. (Chile)* 41 (2), 5–26. doi:10.4067/s0718-686x2013000200001

Kilian, R., Schneider, C., Koch, J., Fesq-Martin, M., Biester, H., Casassa, G., et al. (2007). Palaeoecological Constraints on Late Glacial and Holocene Ice Retreat in the Southern Andes (53 S). *Glob. Planet. Change* 59 (1-4), 49–66. doi:10.1016/j.gloplacha.2006.11.034

Lal, D. (1991). Cosmic Ray Labeling of Erosion Surfaces: *In Situ* Nuclide Production Rates and Erosion Models. *Earth Planet. Sci. Lett.* 104 (2-4), 424–439. doi:10.1016/0012-821x(91)90220-c

Lambeck, K., Rouby, H., Purcell, A., Sun, Y., and Sambridge, M. (2014). Sea Level and Global Ice Volumes from the Last Glacial Maximum to the Holocene. *Proc. Natl. Acad. Sci. U.S.A.* 111 (43), 15296–15303. doi:10.1073/pnas.1411762111

Lamy, F., Kilian, R., Arz, H. W., Francois, J.-P., Kaiser, J., Prange, M., et al. (2010). Holocene Changes in the Position and Intensity of the Southern Westerly Wind Belt. *Nat. Geosci.* 3 (10), 695–699. doi:10.1038/ngeo959

Leger, T. P. M., Hein, A. S., Bingham, R. G., Rodés, Á., Fabel, D., and Smedley, R. K. (2021). Geomorphology and 10Be Chronology of the Last Glacial Maximum and Deglaciation in Northeastern Patagonia, 43°S-71°W. *Quat. Sci. Rev.* 272, 107194. doi:10.1016/j.quascirev.2021.107194

Lifton, N., Sato, T., and Dunai, T. J. (2014). Scaling *In Situ* Cosmogenic Nuclide Production Rates Using Analytical Approximations to Atmospheric Cosmic-Ray Fluxes. *Earth Planet. Sci. Lett.* 386, 149–160. doi:10.1016/j.epsl.2013.10.052

Lovell, H., Stokes, C. R., and Bentley, M. J. (2011). A Glacial Geomorphological Map of the Seno Skyring-Seno Otway-Strait of Magellan Region, Southernmost Patagonia. *J. Maps* 7 (1), 318–339. doi:10.4113/jom.2011.1156

Lovell, H., Stokes, C. R., Bentley, M. J., and Benn, D. I. (2012). Evidence for Rapid Ice Flow and Proglacial Lake Evolution Around the Central Strait of Magellan Region, Southernmost Patagonia. *J. Quat. Sci.* 27 (6), 625–638. doi:10.1002/jqs.2555

Manger, G. (1963). "Porosity and Bulk Density of Sedimentary Rocks," in *Geological Survey Bulletin* (Washington D.C.: US Atomic Energy Commission), 1144.

Mcculloch, R. D., and Bentley, M. J. (1998). Late Glacial Ice Advances in the Strait of Magellan, Southern Chile. *Quat. Sci. Rev.* 17 (8), 775–787. doi:10.1016/s0277-3791(97)00074-7

McCulloch, R. D., Bentley, M. J., Tipping, R. M., and Clapperton, C. M. (2005a). Evidence for Late-glacial Ice Dammed Lakes in the Central Strait of Magellan and Bahía Inútil, Southernmost South america. *Geogr. Ann. Ser. A, Phys. Geogr.* 87 (2), 335–362. doi:10.1111/j.0435-3676.2005.00262.x

McCulloch, R. D., Blaikie, J., Jacob, B., Mansilla, C. A., Morello, F., De Pol-Holz, R., et al. (2020). Late Glacial and Holocene Climate Variability, Southernmost Patagonia. *Quat. Sci. Rev.* 229, 106131. doi:10.1016/j.quascirev.2019.106131

McCulloch, R. D., Fogwill, C. J., Sugden, D. E., Bentley, M. J., and Kubik, P. W. (2005b). Chronology of the Last Glaciation in Central Strait of Magellan and Bahía Inútil, Southernmost South america. *Geogr. Ann. Ser. A, Phys. Geogr.* 87 (2), 289–312. doi:10.1111/j.0435-3676.2005.00260.x

Meglioli, A. (1992). *Glacial geology and chronology of southernmost Patagonia and Tierra del Fuego, Argentina and Chile* (Lehigh University). PhD thesis. Bethlehem, Pennsylvania.

Mendelová, M., Hein, A. S., Rodés, Á., and Xu, S. (2020). Extensive Mountain Glaciation in Central Patagonia during Marine Isotope Stage 5. *Quat. Sci. Rev.* 227, 105996. doi:10.1016/j.quascirev.2019.105996

Mercer, J. H. (1970). Variations of Some Patagonian Glaciers since the Late-Glacial; II. *Am. J. Sci.* 269 (1), 1–25. doi:10.2475/ajs.269.1.1

Moreno, P. I., Denton, G. H., Moreno, H., Lowell, T. V., Putnam, A. E., and Kaplan, M. R. (2015). Radiocarbon Chronology of the Last Glacial Maximum and its Termination in Northwestern Patagonia. *Quat. Sci. Rev.* 122, 233–249. doi:10.1016/j.quascirev.2015.05.027

Moreno, P. I., Lowell, T. V., Jacobson Jr, G. L., Jr, and Denton, G. H. (1999). Abrupt Vegetation and Climate Changes during the Last Glacial Maximumand Last Termination in the Chilean Lake District: A Case Study from Canal De La Puntilla (41oS). *Geogr. Ann. A* 81 (2), 285–311. doi:10.1111/j.0435-3676.1999.00059.x

Moreno, P. I. (2020). Timing and Structure of Vegetation, Fire, and Climate Changes on the Pacific Slope of Northwestern Patagonia since the Last Glacial Termination. *Quat. Sci. Rev.* 238, 106328. doi:10.1016/j.quascirev.2020.106328

Nishiizumi, K., Imamura, M., Caffee, M. W., Southon, J. R., Finkel, R. C., and McAninch, J. (2007). Absolute Calibration of 10Be AMS Standards. *Nucl. Instrum. Methods Phys. Res. Sect. B Beam Interact. Mater. Atoms* 258 (2), 403–413. doi:10.1016/j.nimb.2007.01.297

Peltier, C., Kaplan, M. R., Birkel, S. D., Soteres, R. L., Sagredo, E. A., Aravena, J. C., et al. (2021). The Large MIS 4 and Long MIS 2 Glacier Maxima on the Southern Tip of South America. *Quat. Sci. Rev.* 262, 106858. doi:10.1016/j.quascirev.2021.106858

Quik, C., Velde, Y., Harkema, T., Plicht, H., Quik, J., Beek, R., et al. (2021). Using Legacy Data to Reconstruct the Past? Rescue, Rigour and Reuse in Peatland Geochronology. *Earth Surf. Process. Landf.* 46 (13), 2607–2631. doi:10.1002/esp.5196

Rabassa, J. (2008). Late cenozoic glaciations in Patagonia and Tierra del Fuego. *Dev. Quat. Sci.* 11, 151–204. doi:10.1016/s1571-0866(07)10008-7

Rodés, Á., Pallàs, R., Braucher, R., Moreno, X., Masana, E., and Bourlés, D. L. (2011). Effect of Density Uncertainties in Cosmogenic 10Be Depth-Profiles: Dating a Cemented Pleistocene Alluvial Fan (Carboneras Fault, SE Iberia). *Quat. Geochronol.* 6 (2), 186–194. doi:10.1016/j.quageo.2010.10.004

Rodés, Á., Pallàs, R., Ortuño, M., García-Melendez, E., and Masana, E. (2014). Combining Surface Exposure Dating and Burial Dating from Paired Cosmogenic Depth Profiles. Example of El Límite Alluvial Fan in Huércal-Overa Basin (SE Iberia). *Quat. Geochronol.* 19, 127–134. doi:10.1016/j.quageo.2013.10.002

Rojas, M., Moreno, P., Kageyama, M., Crucifix, M., Hewitt, C., Abe-Ouchi, A., et al. (2009). The Southern Westerlies during the Last Glacial Maximum in PMIP2 Simulations. *Clim. Dyn.* 32 (4), 525–548. doi:10.1007/s00382-008-0421-7

Ruppel, M., Väliranta, M., Virtanen, T., and Korhola, A. (2013). Postglacial Spatiotemporal Peatland Initiation and Lateral Expansion Dynamics in North America and Northern Europe. *Holocene* 23 (11), 1596–1606. doi:10.1177/0959683613499053

Sagredo, E. A., Moreno, P. I., Villa-Martínez, R., Kaplan, M. R., Kubik, P. W., and Stern, C. R. (2011). Fluctuations of the Última Esperanza Ice Lobe (52°S), Chilean Patagonia, during the Last Glacial Maximum and Termination 1. *Geomorphology* 125 (1), 92–108. doi:10.1016/j.geomorph.2010.09.007

Sigfúsdóttir, T., Benediktsson, Í. Ö., and Phillips, E. (2018). Active Retreat of a Late Weichselian Marine-Terminating Glacier: an Example from Melasveit, Western Iceland. *Boreas* 47 (3), 813–836. doi:10.1111/bor.12306

Singer, B. S., Ackert, R. P., Jr, and Guillou, H. (2004). 40Ar/39Ar and K-Ar Chronology of Pleistocene Glaciations in Patagonia. *Geol. Soc. Am. Bull.* 116 (3-4), 434–450. doi:10.1130/b25177.1

Smedley, R. K., Glasser, N. F., and Duller, G. A. T. (2016). Luminescence Dating of Glacial Advances at Lago Buenos Aires (~46 °S), Patagonia. *Quat. Sci. Rev.* 134, 59–73. doi:10.1016/j.quascirev.2015.12.010

Spencer, C. J., Yakymchuk, C., and Ghaznavi, M. (2017). Visualising Data Distributions with Kernel Density Estimation and Reduced Chi-Squared Statistic. *Geosci. Front.* 8 (6), 1247–1252.

Stern, C. R., Moreno, P. I., Villa-Martínez, R., Sagredo, E. A., Prieto, A., and Labarca, R. (2011). Evolution of Ice-Dammed Proglacial Lakes in Última Esperanza, Chile: Implications from the Late-Glacial R1 Eruption of Reclús Volcano, Andean Austral Volcanic Zone. *Andean Geol.* 38 (1), 82–97. doi:10.5027/andgeov38n1-a06

Stone, J. O. (2000). Air Pressure and Cosmogenic Isotope Production. *J. Geophys. Res.* 105 (B10), 23753–23759. doi:10.1029/2000jb900181

Stuiver, M., Reimer, P., and Reimer, R. (2021). CALIB 8.2. [WWW program] at http://calib.org. Accessed 2022-04-1.

Sugden, D. E., Hulton, N. R. J., and Purves, R. S. (2002). Modelling the Inception of the Patagonian Icesheet. *Quat. Int.* 95-96, 55–64. doi:10.1016/s1040-6182(02)00027-7

Sugden, D. E., McCulloch, R. D., Bory, A. J.-M., and Hein, A. S. (2009). Influence of Patagonian Glaciers on Antarctic Dust Deposition during the Last Glacial Period. *Nat. Geosci.* 2 (4), 281–285. doi:10.1038/ngeo474

Thorndycraft, V. R., Bendle, J. M., Benito, G., Davies, B. J., Sancho, C., Palmer, A. P., et al. (2019). Glacial Lake Evolution and Atlantic-Pacific Drainage Reversals during Deglaciation of the Patagonian Ice Sheet. *Quat. Sci. Rev.* 203, 102–127. doi:10.1016/j.quascirev.2018.10.036

Troch, M., Bertrand, S., Lange, C. B., Cárdenas, P., Arz, H., Pantoja-Gutiérrez, S., et al. (2022). Glacial Isostatic Adjustment Near the Center of the Former Patagonian Ice Sheet (48°S) during the Last 16.5 Kyr. *Quat. Sci. Rev.* 277, 107346. doi:10.1016/j.quascirev.2021.107346

Tuhkanen, S., Kuokka, I., Hyvönen, J., Stenroos, S., and Niemelä, J. (1989-1990). Tierra del Fuego as a target for biogeographical research in the past and present. *Anales del Instituto de la Patagonia Serie Ciencias Naturales* 19 (2), 1–107.

Wendt, I., and Carl, C. (1991). The Statistical Distribution of the Mean Squared Weighted Deviation. *Chem. Geol. Isot. Geosci. Sect.* 86 (4), 275–285. doi:10.1016/0168-9622(91)90010-t

Zolitschka, B., Francus, P., Ojala, A. E. K., and Schimmelmann, A. (2015). Varves in Lake Sediments - a Review. *Quat. Sci. Rev.* 117, 1–41. doi:10.1016/j.quascirev.2015.03.019

Conflict of Interest: The authors declare that the research was conducted in the absence of any commercial or financial relationships that could be construed as a potential conflict of interest.

Publisher's Note: All claims expressed in this article are solely those of the authors and do not necessarily represent those of their affiliated organizations, or those of the publisher, the editors and the reviewers. Any product that may be evaluated in this article, or claim that may be made by its manufacturer, is not guaranteed or endorsed by the publisher.

frontiers | Frontiers in Earth Science

BRIEF RESEARCH REPORT
published: 08 July 2022
doi: 10.3389/feart.2022.878318

Chronology of Glacial Advances and Deglaciation in the Encierro River Valley (29° Lat. S), Southern Atacama Desert, Based on Geomorphological Mapping and Cosmogenic ^{10}Be Exposure Ages

G. Aguilar[1], R. Riquelme[2], P. Lohse[2], A. Cabré[3] and J.-L. García[4]*

[1]Advanced Mining Technology Center (AMTC), Facultad de Ciencias Físicas y Matemáticas, Universidad de Chile, Santiago, Chile, [2]Departamento de Ciencias Geológicas, Universidad Católica del Norte, Antofagasta, Chile, [3]Géosciences Environnement Toulouse (GET), CNRS/IRD/CNES/UPS, Toulouse, France, [4]Instituto de Geografía, Pontificia Universidad Católica de Chile, Santiago, Chile

OPEN ACCESS

Edited by:
Daniel Nývlt,
Masaryk University, Czechia

Reviewed by:
Henry Patton,
UiT The Arctic University of Norway, Norway
Naki Akçar,
University of Bern, Switzerland

***Correspondence:**
G. Aguilar
german.aguilar@amtc.uchile.cl

Specialty section:
This article was submitted to Quaternary Science, Geomorphology and Paleoenvironment, a section of the journal Frontiers in Earth Science

Received: *17 February 2022*
Accepted: *30 May 2022*
Published: *08 July 2022*

Citation:
Aguilar G, Riquelme R, Lohse P, Cabré A and García J-L (2022) Chronology of Glacial Advances and Deglaciation in the Encierro River Valley (29° Lat. S), Southern Atacama Desert, Based on Geomorphological Mapping and Cosmogenic ^{10}Be Exposure Ages. Front. Earth Sci. 10:878318. doi: 10.3389/feart.2022.878318

The high mountain segments of the valleys of the southernmost Atacama Desert of Chile present Late Quaternary glacial landforms that developed in already incised valleys. Glacier advances and deglaciation have left a geomorphic imprint in the southernmost Atacama Desert. In this work, the glacial landforms of the Encierro River Valley (29.1°S–69.9°W) have been revisited and new detailed geomorphological mapping is provided. This work also includes new ^{10}Be exposure ages from moraine boulders and one age from an ice-molded bedrock surface. The former glacier of the El Encierro valley extended 16 km down the valley during the last local glacial maximum recorded by a terminal moraine (ENC 1a) with an exposure age of ~40 ka. Four inboard moraine arcs were deposited upstream in telescopic patterns (ENC 1b–d), whose exposure ages range between ~25 and ~33 ka (ENC 1d). Exposure ages between ~17–24 ka on lateral moraines (ENC 1L) developed during the later ice recession of the ENC 1 drift. Thus, the ice mostly disappeared in the main valley before ~18 ka, as is also supported by the exposure age obtained from an ice-molded bedrock surface. Seven kilometers up the valley from the ENC 1, the ENC 2a–d moraine arcs correspond to a small ice advance by ~17–20 ka. The last glacial advance (ENC 2), which occurred after deglaciation of the last local glacial maximum (ENC 1), coincides with the start of the Heinrich Stadial Event 1 (HS1; 18–14.5 ka), which is thought to play a direct role in the last glacial termination in the Andes.

Keywords: Atacama desert, glacial termination, Andes cordillera, deglaciation age, ^{10}Be exposure ages

1 INTRODUCTION

The southern Atacama Desert (27–30°S) is a climatic transitional region between the tropics and the extratropic source of moisture. As such, it is not certain whether the influence of one, or the other, or both, controls glacier and climate dynamics in the region (e.g., Zech et al., 2006). There is still debate about which source of moisture was responsible for driving glacier dynamics and the associated

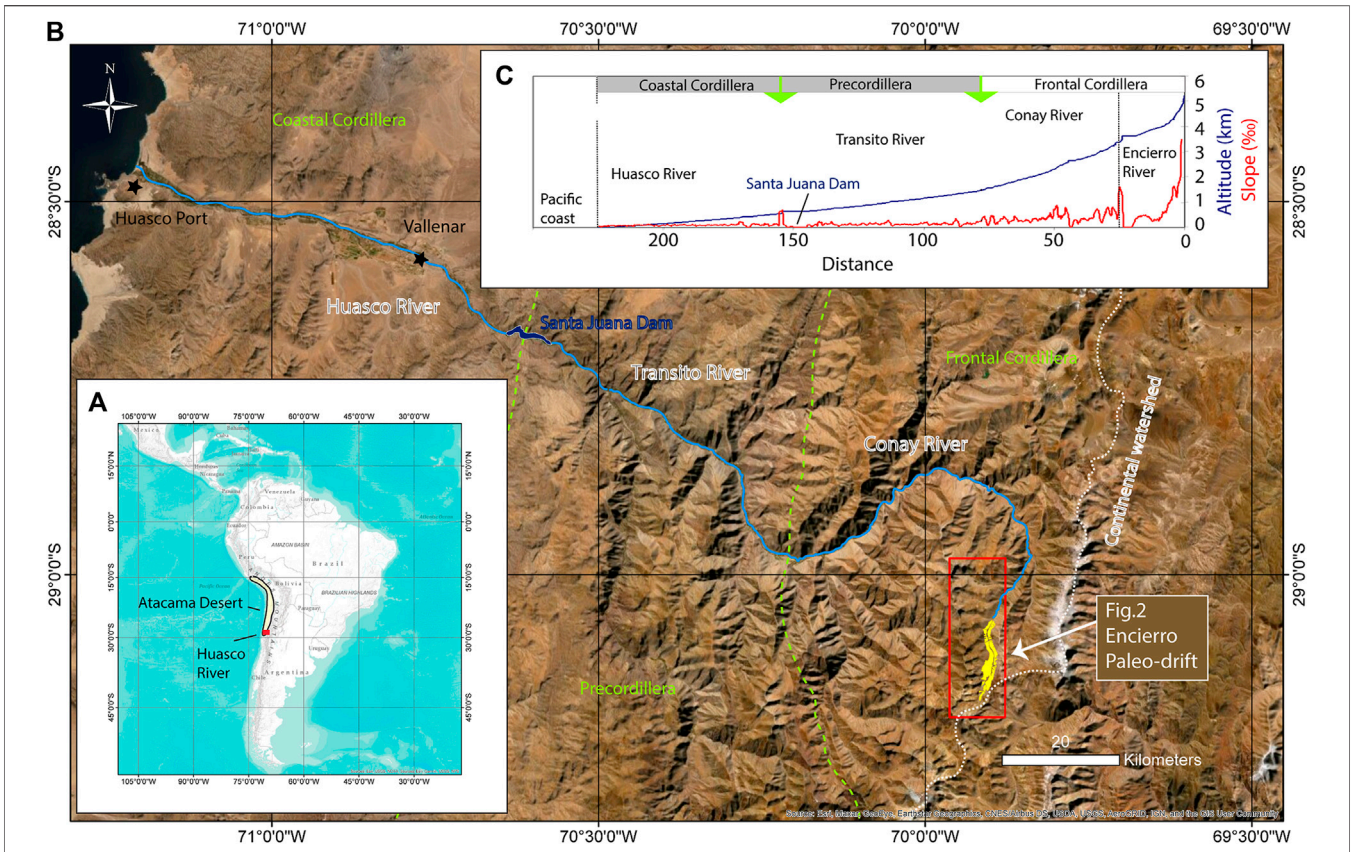

FIGURE 1 | Location map of the Encierro Valley in the Southern Atacama Desert. **(A)** Inset map with study area in South America. **(B)** DEM and morphostructural segments of the western slopes of the Andes. **(C)** Longitudinal Encierro-Huasco River topographic profile between the Encierro Valley and Pacific Coast.

hydrographic evolution during the Local Last Glacial Maximum (LLGM) and termination (e.g., Ammann et al., 2001). Therefore, determining the former geographic influence of extratropical winter westerly and/or tropical easterly wind belts in this region remains a major open question. The limited dated records in the southern Atacama region still hinder reaching firm conclusions. Veit (1993), Veit (1996), and Ammann et al. (2001) pointed to extra-tropical westerlies as responsible for driving former ice/climate fluctuations in this part of the Andes. Jenny and Kammer (1996) remark on the tropical influence through the easterlies origination in the Amazonian and the Chaco Region (e.g., D'Arcy et al., 2019), whereas Zech et al. (2017) suggest that both seasonal circulation systems were operating together. These interpretations are based on geomorphological and geochronological studies of landforms sculpted by ancient glaciers, but often lack a holistic view of the evolution of arid landscapes.

One of the valleys in the Atacama Desert where glacial landforms which originated from former glacial advances are preserved is El Encierro valley. Pioneer studies carried out by Veit (1993), Veit (1996), Jenny and Kammer (1996), and Grosjean et al. (1998) suggest that the El Encierro River Valley (ERV, 29.1°S–69.9°W, 3,750–4,150 m asl, **Figure 1**) was occupied by mountain glaciers that extended several kilometers during the LLGM. More recently, investigations by Zech et al. (2006) and Zech et al. (2017) have dated ^{10}Be the outer moraine (MII) to 20–22 ka during the LLGM inboard moraines (MIII–MV) been interpreted as recessional glacial re-advances dated between 16 and 18 ka. Zech et al. (2017) suggest this glacial re-advance was related to the humid phase recorded in the tropical Andes known as the Central Andean Pluvial Event (CAPE; Latorre et al., 2006; Quade et al., 2008). With this evidence, these authors suggest that this glacial re-advance is linked to a tropical supply of moisture reaching the southern Atacama Desert (Zech et al., 2006; Zech et al., 2017).

This research report presents a geomorphological map and reports seven new cosmogenic ^{10}Be exposure ages obtained from boulders and an ice-molded bedrock surface in the paleo-drift of the ERV. The ERV is a tributary of the El Huasco River (**Figure 1**), one of the southern Atacama Desert's main Andean catchments where the geomorphological evolution associated with Late Pleistocene and Early Holocene hydro-climatic changes is remarkably well preserved. Based on our geomorphological mapping in the field, different glacial landforms were characterized and dated with ^{10}Be to reconstruct the former glacial advances and deglaciation. We include geomorphic interpretations and recalibrated ^{10}Be data from previous works in this valley (Jenny and Kammer, 1996; Grosjean et al., 1998; Zech et al., 2006). Finally, the results are discussed to provide an updated

perspective of understanding the spatio-temporal variability of the former El Encierro Glacier during the LLGM and the Pleistocene–Holocene transition.

2 METHODS

2.1 Geomorphological Mapping and Sampling

The identification and mapping of the different landforms of the ERV were carried out based on field observations, mapping over aerial photography from the 1997 aerofotogrammetric survey carried out by SAF (www.saf.cl) and using optical satellite imagery retrieved from different sources, including Bing, ESRI, and Google Earth. Six rock samples from the largest boulders located at the crest of moraines and one sample from ice-molded bedrock surface in the valley bottom were collected for subsequent dating by ^{10}Be concentrations in quartz using the sampling protocol described by Ivy-Ochs (1996). In the field, the shielding of cosmic radiation affecting the rock surfaces was calculated considering the topography of the valley by Brunton structural compass measurement of the surface elevation angle relative to the topography for 8 azimuths. Although the blocks are not exceptionally large, it was verified in the field that they have not been rotated considering imbrications with other blocks that indicate stability.

2.2 Analytical Procedures

The measurement of the ^{10}Be concentration was performed in the year 2008. The samples were crushed and sieved to obtain the 250–710 mm size fractions for analysis. The quartz mineral was separated (see quartz mass in Supplementary Data) and dissolved in a hot ultrasonic bath and/or on a shaking table using a combination of acids (HF, HCl, and HNO_3). The extraction and preparation of BeO targets were conducted at the University of Edinburgh's Cosmogenic Isotope Laboratory following procedures adapted from the methods of Bierman et al. (2002), Kohl and Nishiizumi (1992), and Ivy-Ochs (1996). The colloid containing the ^{10}Be concentrate was precipitated from the solution, which also contains approximately 1 mg of previously added ^{9}Be (see supplementary data). Finally, the ^{10}Be/^{9}Be ratios were measured using an accelerator mass spectrometer of the Scottish Universities Environment Research Centre (SUERC; https://www.suerc-cosmo.co.uk/). All measurements are standardized relative to 07KNSD (Nishiizumi et al., 2007).

Cosmogenic ^{10}Be exposure ages were calculated using the online CREp calculator (crep.crpg.cnrs-nancy.fr; Martin et al., 2016). They were computed using the scaling scheme Lal/Stone time dependent (Lal, 1991; Stone, 2000; Balco et al., 2008), with the ERA-40 (Uppala et al., 2005), the geomagnetic record of atmospheric ^{10}Be-based VDM (Muscheler, et al., 2005; Valet et al., 2005), and the production rates (4.17 at/gr/yr) calibrated by Martin et al. (2015) at Bolivian mountains (19°S and 3,800 m asl).

Calculation of topographic shielding was included considering the fieldwork measures by Brunton Compass and using the topographic shielding calculator of CRONUS-Earth online calculators (http://stoneage.ice-d.org/math/skyline/skyline_in.html). Age calculations consider an erosion rate of 0 mm/ka, as the percentage of variation per mm of erosion is only 1%, significantly less than the error associated with the ^{10}Be measurement. Additionally, 11 ^{10}Be exposure ages previously obtained by Zech et al. (2006) were recalculated using the same parameters. The ages published by Zech et al. (2006) consider much higher ^{10}Be production rates in quartz (5.25 at/gr/yr) that are not in agreement with the rates currently used for this region of the Andes (Martin et al., 2015).

3 RESULTS

The geomorphological map allows the recognition of two moraine systems (ENCs) with a telescopic plan-view of arc morphologies. The two-terminal moraines of these systems are situated at 16 (ENC 1a) and 9 km (ENC 2a) downstream of the catchment head.

In total, three ages were obtained in moraine boulders in the outermost system (ENC 1) and two in the internal system of moraines (ENC 2). An additional ^{10}Be sample was obtained from an ice-molded bedrock surface on the valley bottom in ENC 2 and also in a lateral moraine (ENC 1L) situated between ENC 1 and ENC 2. **Table 1** summarizes the characteristics of the sample, the measured ^{10}Be concentrations, the exposure ages, and the correlation with moraine stages defined by Zech et al. (2006) in view of their recalibrated and incorporated ages in this article. ^{10}Be exposure ages range between 39.1 ± 1.7 ka and 17.2 ± 0.8 ka, without considering one outlier of 193.7 ± 7.3 ka which is not considered in the following sections of this report.

Some boulders sitting on top of moraines have a length of up to 3 m along their main axis. Some of these boulders are partially buried and emerge a few tens of centimeters above the surface, so the possibility of a prior complete burial condition of them cannot be excluded. The same post-glacial conditions of burying could be assigned to the ^{10}Be-dated ice-molded bedrock surface. So, boulders and bedrock surface ages should be considered always as minimum ones.

Rock glaciers (RGs) cover large areas of the headwaters in the tributary valleys of ERV (**Figure 2**). Some of these RGs are still actively indicated with accumulations of boulders at their front. Although they are not the focus of this brief research report, RGs are mapped to highlight that the potential preservation of moraines of tributary glaciers has been compromised. The non-consolidated Neogene Gravels Units on the hillslopes of the ERV (12 Ma, Salazar and Coloma, 2016) are included (**Figure 2**) because its distribution was not available at the time of Zech et al. (2006) and are remains of the infilling history of the valley with fluvial processes.

3.1 Moraine System ENC 1

Moraine ridges are arranged with telescoping arc morphologies in plan-view at 3,650–3,750 m asl. (**Figure 2**). The external moraine of the arc (ENC 1a) is a degraded terminal moraine while the other four inboard moraine ridges are at 100–200 m from each other (ENC 1b–d). The terminal moraine represents the outermost limit of glacial deposits in the ERV and comprises the lowermost glacial drift mapped in this valley. The ENC 1 moraine ridges correspond to the S-II system defined by Jenny and Kammer (1996) and the M-II system defined by Grosjean et al. (1998). Grosjean's nomenclature

TABLE 1 | Sample information, the measured ^{10}Be concentrations in quartz and calculated ^{10}Be exposure age of this work (HPL) and recalculated from Zech et al. (2006) in the Encierro Valley (EE). A density of 2.7 g/cm^3 was considered for quartz. Detailed analytic results in supplementary digital materials.

Sample ID	Moraine System	Landform	LAT	LONG	Altitude (m)	Topographic Shielding	Concentrations (at/gr)	1σ (at/g)	Scaling Factor	Age (ka)	1σ (ka)
EE71	ENC 1a	Outer terminal moraine arc	–29.065	–69.901	3,678	0.988	1,47E+06	6,04E+07	9.32	39.1	1.7
HPL28	ENC 1d	Inner terminal moraine arc	–29.068	–69.904	3,696	0.981	7,20E+09	1,01E+08	9.7	193.7	7.3
HPL29	ENC 1d	Inner terminal moraine arc	–29.068	–69.904	3,670	0.981	9,65E+08	1,36E+07	9.16	26.4	0.9
HPL30	ENC 1d	Inner terminal moraine arc	–29.071	–69.905	3,699	0.981	1,16E+09	1,68E+07	9.4	31.0	1.5
EE62	ENC 1d	Inner terminal moraine arc	–29.068	–69.902	3,688	0.988	7,55E+05	3,17E+07	9.16	20.5	1.0
EE63	ENC 1d	Inner terminal moraine arc	–29.068	–69.902	3,684	0.988	5,30E+05	2,17E+07	8.69	15.1	0.7
HPL26	ENC 1L	Lateral moraine, eastern slopes	–29.110	–69.891	3,970	0.978	1,38E+09	2,50E+07	10.38	33.4	1.5
EE33	ENC 1L	Lateral moraine, western slopes	–29.109	–69.901	4,055	0.997	7,92E+05	3,25E+07	10.81	18.0	0.9
EE34	ENC 1L	Lateral moraine, western slopes	–29.110	–69.901	4,029	0.997	1,00E+06	5,93E+07	11.02	22.4	1.6
EE42	ENC 1L	Lateral moraine, western slopes	–29.102	–69.901	3,955	0.997	8,38E+05	4,02E+07	10.45	19.7	1.1
EE51	ENC 1L	Lateral moraine, western slopes	–29.092	–69.907	3,900	0.984	8,98E+05	3,86E+07	10.31	21.7	1.2
EE11	ENC 2a	Outer terminal moraine arc	–29.133	–69.898	3,971	0.997	8,01E+05	3,28E+07	10.44	18.9	0.9
EE12	ENC 2a	Outer terminal moraine arc	–29.133	–69.898	3,971	0.997	7,83E+05	2,90E+07	10.41	18.5	0.9
EE22	ENC 2L	Lateral moraine on tributary	–29.125	–69.904	3,998	0.997	7,32E+05	2,71E+07	10.43	17.2	0.8
EE24	ENC 2L	Lateral moraine on tributary	–29.125	–69.905	3,994	0.997	7,64E+05	3,21E+07	10.48	17.9	0.9
HPL31	ENC 2 mb	Ice-molded bedrock	–29.155	–69.913	4,124	0.967	8,39E+08	1,27E+07	11.28	18.8	0.7
HPL07	ENC 2d	Inner recessional moraine ridge	–29.162	–69.916	4,153	0.967	8,26E+08	1,34E+07	11.39	18.4	0.7
HPL33	ENC 2d	Inner recessional moraine ridge	–29.162	–69.916	4,153	0.967	7,76E+08	1,46E+07	11.29	17.4	0.7

was the nomenclature used by Zech et al. (2006) with their ^{10}Be exposure ages.

The published exposures ^{10}Be ages of Zech et al. (2006) are recalculated here to 39.1 ± 1.7 ka (EE71) in ENC 1a and 20.5 ± 1.0 ka (EE62) and 15.1 ± 0.7 ka (EE63) in ENC 1d. There is not sufficient replicability in the ages considering the intersect of its probability (**Figure 3A**). Two new ^{10}Be exposure ages provided in this work are 26.4 ± 0.9 ka (HPL-29) and 31.0 ± 1.5 ka (HPL-30) for the well-preserved inboard moraine ENC 1d (**Figure 2**).

Only one age of 33.4 ± 1.5 (HPL-26) was obtained from the lateral moraine (ENC 1L) on the eastern hillslope that can be tracked for about 7 km upstream of the external moraine of the arc ENC 1a (**Figure 2B**, **Figure 4AB**). This lateral moraine (ENC 1L) correlates geomorphologically with the frontal moraine ENC 1d (33–25 Ka). This is an older age in relation to four ages (EE33, EE34, EE42, and EE51; **Figure 4A**) measured by Zech et al. (2006) on the lateral moraines ENC 1L of the western hillslopes with an intersect ages between 17 and 24 ka considering error in samples (**Figure 3B**).

3.2 Moraine System ENC 2

Between seven and 10 km up-valley from ENC 1a, four well-preserved moraine ridges were identified in plan-view telescoping arc morphologies between 3,900 m a.s.l. and 4,100 m a.s.l. (**Figure 2**). These moraine ridges define the glacial front of the system ENC 2. Zech et al. (2006) published exposure ^{10}Be ages recalculated here with ages of 18.9 ± 0.9 ka (EE11) and 18.5 ± 0.9 ka (EE12) in the external terminal moraine (ENC 2a). A lateral moraine (ENC 2L) in a tributary valley located downstream is dated 17.2 ± 0.8 ka (EE22) and 17.9 ± 0.9 (EE24) by Zech et al. (2006). This lateral moraine was interpreted by Zech et al. (2006) as a recessional moraine.

The two ^{10}Be exposure ages provided in this work are 17.4 ± 0.7 ka (HPL-33) and 18.4 ka ± 0.7 ka (HPL-07) for the upstream inboard recessional moraine ridge (ENC 2d), and an age of 18.8 ± 0.7 ka (HPL-31) for an ice-molded granitic bedrock surface of valley bottom 1-km downstream of ENC 2d. Moraine ridge ENC 2d and the erosional glacial landforms are not included in previous geomorphological maps of the ERV. They are mapped and dated here for the first time. Intersect ages considering the error of all samples of the ENC 2 system are between 17 and 19 ka (**Figure 3C**).

4 INTERPRETATIONS

Tills fill the valley along 16 km as low as 3,650 m a.s.l., while a preserved Neogene Gravel Units formed by non-consolidated

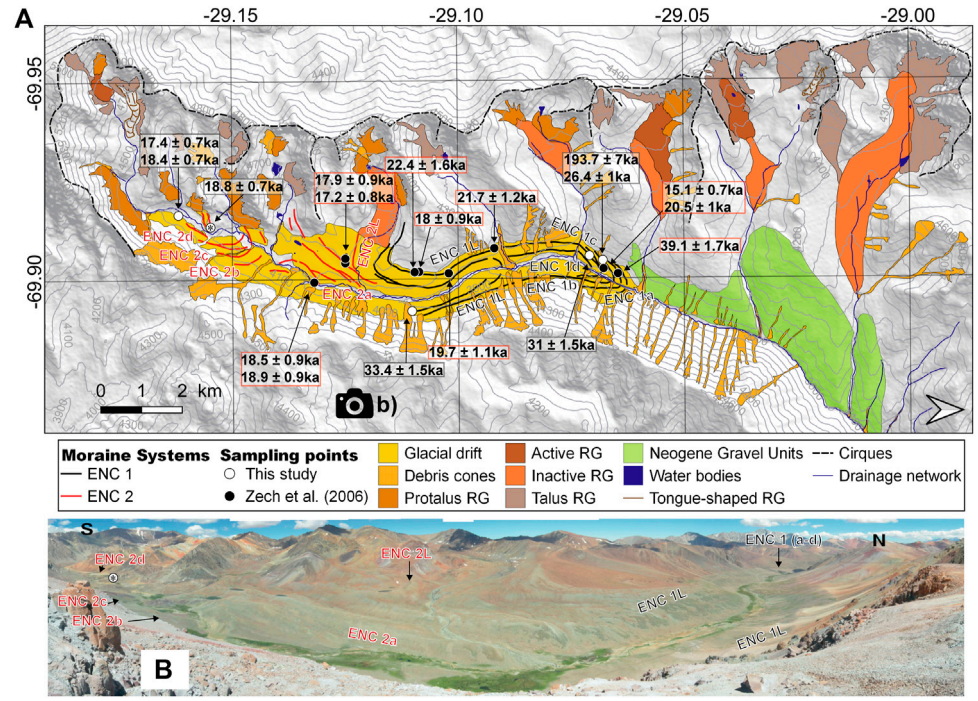

FIGURE 2 | (A) Geomorphological map showing ^{10}Be exposure ages of this study (white solid circles) and recalculated from Zech et al. (2006) (black solid circles). The sample from the ice-molded bedrock surface is highlighted within the sampling points of figure A with an *. RG: rock glacier. **(B)** Photograph toward the west taken from the east slope of the ERV showing the distribution of moraine ridges mapped in panel 2A.

polymictic alluvial deposits are identified downstream on the hillslopes of the ERV (**Figure 2**; Salazar and Coloma, 2016; Rossel et al., 2018). In the ERV, these Neogene Gravel Units hanging on valley slopes mapped in works from the Chilean Geological Survey (Salazar and Coloma, 2016) and in Miocene tectonostratigraphic Andean interpretations (Rossel et al., 2018) have been dated with interlocked tuff levels indicating a minimum age of 12 Ma. These recently published observations deny the interpretations that considered these deposits as till-forming moraines (MI) associated with a pre-LLGM glacial advance that reached 3,450 m a.s.l. and distant almost 20 km from the glacial cirque (Jenny and Kammer, 1996; Grosjean et al., 1998).

The presence of these Neogene gravels in the ERV identified by Salazar and Coloma (2016) suggests that the tills are in part composed of reworked Neogene gravels and so, the glacial forms could be in part the result of the redistribution of former non-consolidated alluvial deposits during glacial advances. The lateral moraines preserved on the hillslopes of ERV occur at a similar altitude as the non-consolidated Neogene gravels in relation to the valley floor and thus might have led to misinterpretations in the past. Thus, moraines distributions are indicators of the lateral limits of the glaciers that occupied the valley, but the supply of sediments was controlled, at least in part, by the Neogene gravels. This implies that particular attention should be paid when interpreting the spatial extent of glacial advances in arid valleys with well-preserved and thick ancient alluvial gravel successions.

In total, nine out of eleven ages of ENC 1 give a range between 40–25 ka (4 samples) and 18–22 (5 samples) (**Figure 2**, **Figure 3**), whereas one sample is younger (15 ka) and another is an outlier (193.7 ± 7.3). Thus, the oldest geomorphological evidence of glaciations in the ERV is the arc related to ENC 1, which represents the LLGM. The LLGM in the ERV was punctuated by several glacial advances (ENC 1a–d), which extended 16–14 km from the headwaters and down to 3,650–3,750 m a.s.l. In that sense, and based on the available data and supported by the preference of depositional ages assignment to the oldest-one-model (e.g., D'Arcy et al., 2019), we define that the external terminal moraine arc ENC 1a and the inner terminal moraine arc ENC 1d were deposited by full glacial conditions during ice expansions at ~40 ka and 33–25 ka respectively. Glacial advances recorded in this valley have been reported in other nearby valleys of the Atacama Desert (e.g., Zech et al., 2011; Zech et al., 2017) and on the eastern slope of the Andes at similar latitudes (e.g., D'Arcy et al., 2019, 27°S).

Overall, five ages from moraine boulders on ENC 1 system are between 17–24: Four ages on a lateral moraine ENC 1L (EE33, EE34, EE42, and EE51) in the western slope of the ERV, and one on the inner terminal moraine arc ENC 1d (EE62). We interpret that these ages constrain the glacial recession or the paraglacial readjustment of moraines after the deglaciation (**Figure 3**). In fact, the tributaries situated in the west developed several rock glaciers that filled tributary valleys and reached the trunk valley after the deglaciation. The ridges on the eastern slope that avoid the influence of rock glaciers are dated at 33.4 ± 1.5 (HPL-26) and

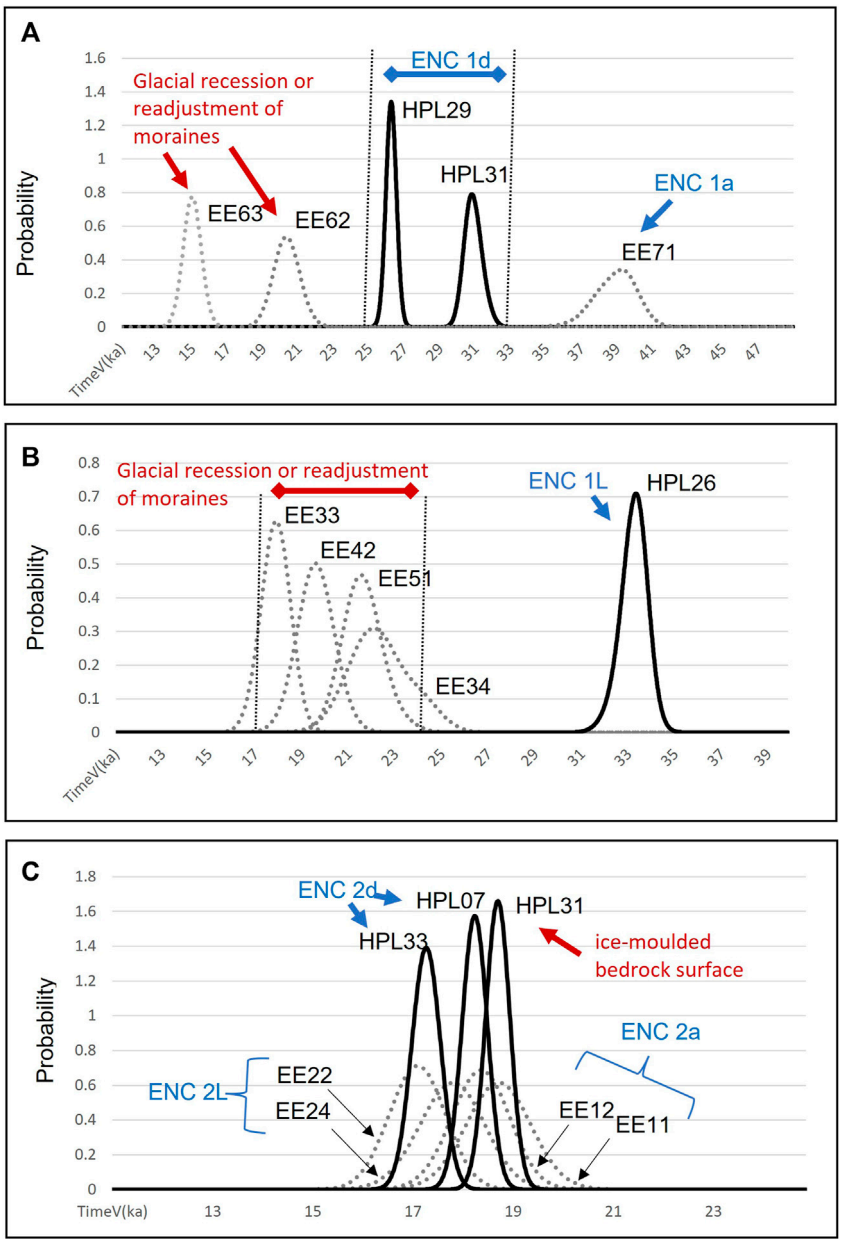

FIGURE 3 | Probability density function curves calculated from the exposure ^{10}Be ages. Age of samples obtained in this work in black solid curves and recalibrated from data of Zech et al. (2006) in gray segmented lines. **(A)** Moraines arcs of ENC 1 (25–40 ka) and glacial recession or readjustment of moraines. **(B)** Lateral moraines of ENC 1 (~33 ka) and glacial recession or readjustment of moraines (17–24 ka). **(C)** Moraine ridge and ice-molded bedrock surface of ENC2.

are much better preserved than the ones on the western side of the valley. The age of the lateral moraine agrees with the ages between 33–25 ka of inner-terminal moraine arc ENC 1d (**Figure 3**).

To recognize the age of the onset of deglaciation of glacial drift ENC 1 in the ERV, Zech et al. (2006) relied on exposure ages of lateral moraines that were developed as recessional positions of the glacier, recalibrated in this work to around 17–18 ka (EE22, EE24; **Figure 2**). This moraine ridge has been reinterpreted in this work as a lateral moraine related to the glacial advance of the tributary valley. The preservation of this ridge was only possible if the trunk valley was already deglaciated by that time. So, deglaciations of ENC 1 started at ~24 ka and finished before 18–17 ka. Indeed, this time span of deglaciation is consistent with our ice-molded bedrock age of 18.8 ± 0.7 ka (sample HPL-31) and suggests that the valley was almost completely deglaciated at that time.

Nonetheless, the time span for the deglaciation of ENC 1 coincides with the ages of boulders on moraines ENC 2a (EE11, EE12) obtained by Zech et al. (2006) a few kilometers down-valley

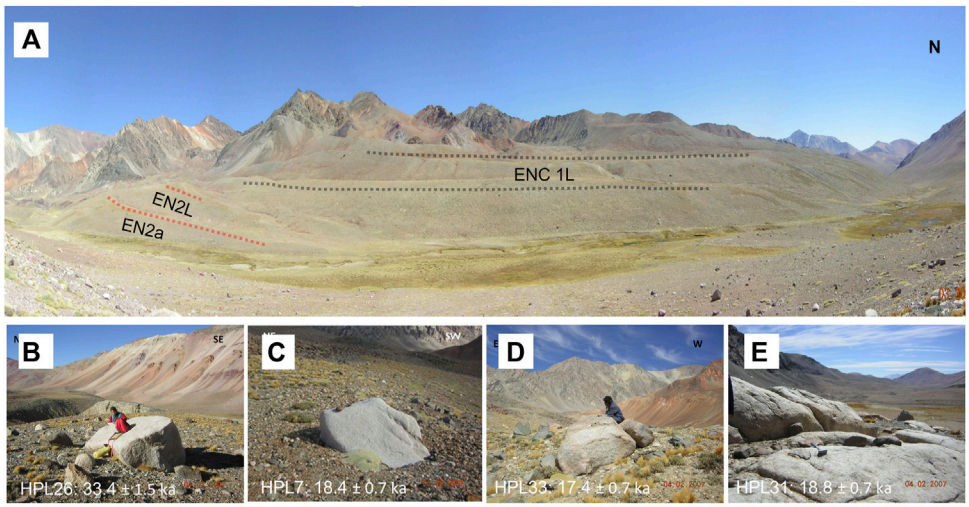

FIGURE 4 | Photographs of ^{10}Be sampling sectors. **(A)** Photograph toward the west taken from the location of sample toward the sequence of ENC 1L lateral moraines where Zech et al. (2006) dated four boulders between 17–24 ka (EE33, EE34, EE42 and EE51). **(B)** Photograph of sample HPL26 (lateral moraine of ENC 1L). **(C)** Photograph of sample HPL7 (recessional moraine ENC 2d). **(D)** Photograph of sample HPL33 (recessional moraine ENC 2d). **(E)** Photograph of ice-molded bedrock surface of valley bottom taken in the location of sample HPL31.

of the ice-molded bedrock samples (HPL-31; **Figure 2**). The ages of these two samples of moraine boulder is within 1 sigma and thus statistically the same (20–18 ka; **Figure 3B**). We interpret that the glacial advances of ENC 2a reached 9 km from the head of the valley, but the glacial erosion was not efficient to reset the nuclide concentrations of the ice-molded bedrock surface (sample HPL-31). In fact, ages of recessional moraine ridges ENC 2d (HPL07 and HPL33) suggest this glacial drift could be much thinner and retreat at 18–17 ka up the valley of the sampling site of HPL-31.

We suggest that valley deglaciation was completed by 18–17 ka. Thus, no major advances occurred in the ERV after 17 ka as proposed previously by Zech et al. (2017). Andean glaciations in the northern segment of the Atacama Desert were linked to CAPE humid events that occurred 16–10 ka (Quade et al., 2008). Any effect of this pluvial event on local glaciation was negligible in the valleys of the southern Atacama Desert, at least in the ERV (29°S), as already observed in the Cordon Doña Rosa (30°S; Zech et al., 2017). Deglaciation by 18 ka is a global warming signal at the start of the Heinrich Stadial Event 1 (HS1; 18–14.5 ka; Rasmussen et al., 2006), which is thought to play a direct role in the last glacial termination in the Andes through the high-latitude migration of the southern westerly winds and the CO_2 ventilation from the Southern Ocean (e.g., Denton et al., 2010).

DATA AVAILABILITY STATEMENT

The original contributions presented in the study are included in the article/Supplementary Material; further inquiries can be directed to the corresponding author.

AUTHOR CONTRIBUTIONS

AG: fieldwork, mapping and sampling, data interpretation, contextualization, and writing. RR: fieldwork, mapping and sampling, data interpretation, and contextualization. LP: fieldwork, mapping and sampling, and data interpretation. CA: contextualization and writing. GJ: contextualization and writing. CA: mapping and data interpretation. GJ: mapping and data interpretation.

FUNDING

This work was supported by the INNOVA-CORFO project (RR); the Basal Project of the Advanced Mining Technology Center financed by ANID Project AFB0004 (AG), and the FONDECYT grant # 1200935 (GJ).

REFERENCES

Ammann, C., Jenny, B., Kammer, K., and Messerli, B. (2001). Late Quaternary Glacier Response to Humidity Changes in the Arid Andes of Chile (18-29°S). *Palaeogeogr. Palaeoclimatol. Palaeoecol.* 172, 313–326. doi:10.1016/s0031-0182(01)00306-6

Balco, G., Stone, J. O., Lifton, N. a., and Dunai, T. J. (2008). A Complete and Easily Accessible Means of Calculating Surface Exposure Ages or Erosion Rates from 10Be and 26Al Measurements. *Quat. Geochronol.* 3, 174–195. doi:10.1016/j.quageo.2007.12.001

Bierman, P. R., Caffee, M. W., Davis, P. T., Marsella, K., Pavich, M., Colgan, P., et al. (2002). "4. Rates and Timing of Earth Surface Processes from In Situ-Produced Cosmogenic Be-10," in *Mineralogy & Geochemistry 50* (Washington: Mineralogical Society of America), 147–206. doi:10.1515/9781501508844-005

D'Arcy, M., Schildgen, T. F., Strecker, M. R., Wittmann, H., Duesing, W., Mey, J., et al. (2019). Timing of past glaciation at the Sierra de Aconquija, northwestern

Argentina, and throughout the Central Andes. *Quat. Sci. Rev.* 204, 37–57. doi:10.1016/j.quascirev.2018.11.022

Denton, G. H., Anderson, R. F., Toggweiler, J. R., Edwards, R. L., Schaefer, J. M., and Putnam, A. E. (2010). The Last Glacial Termination. *Science* 328, 1652. doi:10.1126/science.1184119

Grosjean, M., Geyh, M. A., Messerli, B., Schreier, H., and Veit, H. (1998). A Late-Holocene. *Holocene* 8 (4), 473–479. doi:10.1191/095968398677627864

Ivy-Ochs, S. (1996). *The Dating of Rock Surfaces Using* in Situ *Produced 10Be, 26Al and 36Cl, with Examples from Antarctica and the Swiss Alps*. Zürich, Switzerland: Unpublished PhD thesis.

Jenny, B., and Kammer, K. (1996). "Jungquartare Vergletscherung," in *Climate Change in Den Trockenen Anden*. Editors C. Ammann, B. Jenny, and K. Kammer (Bern, Switzerland: Geographica Bernensia), G46, 1–80.

Kohl, C. P., and Nishiizumi, K. (1992). Chemical Isolation of Quartz for Measurement of *In-Situ* -produced Cosmogenic Nuclides. *Geochimica Cosmochimica Acta* 56, 3583–3587. doi:10.1016/0016-7037(92)90401-4

Lal, D. (1991). Cosmic Ray Labeling of Erosion Surfaces: *In Situ* Nuclide Production Rates and Erosion Models. *Earth Planet. Sci. Lett.* 104, 424–439. doi:10.1016/0012-821x(91)90220-c

Latorre, C., Betancourt, J. L., and Arroyo, M. T. K. (2006). Late Quaternary Vegetation and Climate History of a Perennial River Canyon in the Río Salado Basin (22°S) of Northern Chile. *Quat. Res.* 65 (3), 450–466. doi:10.1016/j.yqres.2006.02.002

Martin, L., Blard, P.-H., Balco, G., Lave, J., Delunel, R., Lifton, N., et al. (2016). The CREp Program and the ICE-D Production Rate Calibration Database: a Fully Parameterizable and Updated Online Tool to Compute Cosmic-Ray Exposure Ages. *Quat. Geochronol.* 38, 25–49. doi:10.1016/j.quageo.2016.11.006

Martin, L. C. P., Blard, P.-H., Lavé, J., Braucher, R., Lupker, M., Condom, T., et al. (2015). *In Situ* cosmogenic 10Be Production Rate in the High Tropical Andes. *Quat. Geochronol.* 30, 54–68. doi:10.1016/j.quageo.2015.06.012

Muscheler, R., Beer, J., Kubik, P. W., and Synal, H.-A. (2005). Geomagnetic Field Intensity during the Last 60,000 Years Based on 10Be and 36Cl from the Summit Ice Cores and 14C. *Quat. Sci. Rev.* 24, 1849–1860. doi:10.1016/j.quascirev.2005.01.012

Nishiizumi, K., Imamura, M., Caffee, M. W., Southon, J. R., Finkel, R. C., and McAninch, J. (2007). Absolute Calibration of 10Be AMS Standards. *Nucl. Instrum. Methods Phys. Res. Sect. B Beam Interact. Mater. Atoms* 258, 403–413. doi:10.1016/j.nimb.2007.01.297

Quade, J., Rech, J. A., Betancourt, J. L., Latorre, C., Quade, B., Rylander, K. A., et al. (2008). Paleowetlands and Regional Climate Change in the Central Atacama Desert, Northern chile. *Quat. Res.* 69 (3), 343–360. doi:10.1016/j.yqres.2008.01.003

Rasmussen, S. O., Andersen, K. K., Svensson, A., Steffensen, J. P., Vinther, B. M., Clausen, H. B., et al. (2006). A new Greenland ice core chronology for the last glacial termination (1984e2012). *J. Geophys. Res. Atmos.* 111 (D6). doi:10.1029/2005jd006079

Rossel, K., Aguilar, G., Salazar, E., Martinod, J., Carretier, S., Pinto, L., et al. (2018). Chronology of Chilean Frontal Cordillera Building from Geochronological, Stratigraphic and Geomorphological Data Insights from Miocene Intramontane-Basin Deposits. *Basin Res.* 30, 289–310. doi:10.1111/bre.12221

Salazar, E., and Coloma, F. (2016). *Geología del Área Cerros de Cantaritos-Laguna Chica. Región de Atacama. Servicio Nacional de Geología y Minería, Carta Geológica de Chile, Serie Geología Básica*. Santiago, Chile 181, 171.

Stone, J. O. (2000). Air Pressure and Cosmogenic Isotope Production. *J. Geophys. Res.* 105, 23753–23759. doi:10.1029/2000JB900181

Uppala, S. M., KÅllberg, P. W., Simmons, A. J., Andrae, U., Bechtold, V. D. C., Fiorino, M., et al. (2005). The ERA-40 Re-analysis. *Q. J. R. Meteorological Soc.* 131, 2961–3012. doi:10.1256/qj.04.176

Valet, J.-P., Meynadier, L., and Guyodo, Y. (2005). Geomagnetic Dipole Strength and Reversal Rate over the Past Two Million Years. *Nature* 435, 802–805. doi:10.1038/nature03674

Veit, H. (1996). Southern Westerlies during the Holocene Deduced from Geomorphological and Pedological Studies in the Norte Chico, Northern Chile (27-33°S). *Palaeogeogr. Palaeoclimatol. Palaeoecol.* 123, 107–119. doi:10.1016/0031-0182(95)00118-2

Veit, H. (1993). Upper Quaternary Landscape and Clime Evolution in the Norte Chico (Northern Chile): an Review. *Mt. Res. Dev.* 13 (No. 2), 139–144. Mountain Geoecology of the Andes: Resource Management and Sustainable Development. doi:10.2307/3673631

Zech, R., Kull, C., and Veit, H. (2006). Late Quaternary Glacial History in the Encierro Valley, Northern Chile (29°S), Deduced from 10Be Surface Exposure Dating. *Palaeogeogr. Palaeoclimatol. Palaeoecol.* 234, 277–286. doi:10.1016/j.palaeo.2005.10.011

Zech, R., Zech, J., Kull, C., Kubik, P. W., and Veit, H. (2011). Early Last Glacial Maximum in the Southern Central Andes Reveals Northward Shift of the Westerlies at ~39 Ka. *Clim. Past.* 7, 41–46. doi:10.5194/cp-7-41-2011

Zech, J., Terrizzano, C., García-Morabito, E., Veit, H., and Zech, R. (2017). Timing and Extent of Late Pleistocene Glaciation in the Arid Central Andes of Argentina and Chile (22°-41°S). *Cuad. Investig. Geográfica* 43 (2), 697–718. doi:10.18172/cig.3235

Conflict of Interest: The authors declare that the research was conducted in the absence of any commercial or financial relationships that could be construed as a potential conflict of interest.

Publisher's Note: All claims expressed in this article are solely those of the authors and do not necessarily represent those of their affiliated organizations, or those of the publisher, the editors, and the reviewers. Any product that may be evaluated in this article, or claim that may be made by its manufacturer, is not guaranteed or endorsed by the publisher.

frontiers | Frontiers in Earth Science

TYPE Original Research
PUBLISHED 04 October 2022
DOI 10.3389/feart.2022.831631

OPEN ACCESS

EDITED BY
Francisco José Navarro,
Polytechnic University of Madrid, Spain

REVIEWED BY
Jan Kavan,
Masaryk University, Czechia
Andres Rivera,
University of Chile, Chile

*CORRESPONDENCE
Bethan J. Davies,
bethan.davies@ncl.ac.uk

SPECIALTY SECTION
This article was submitted to Cryospheric Sciences, a section of the journal Frontiers in Earth Science

RECEIVED 08 December 2021
ACCEPTED 20 September 2022
PUBLISHED 04 October 2022

CITATION
Martin J, Davies BJ, Jones R and Thorndycraft V (2022), Modelled sensitivity of Monte San Lorenzo ice cap, Patagonian Andes, to past and present climate.
Front. Earth Sci. 10:831631.
doi: 10.3389/feart.2022.831631

Modelled sensitivity of Monte San Lorenzo ice cap, Patagonian Andes, to past and present climate

Julian Martin[1,2], Bethan J. Davies[1,3]*, Richard Jones[4] and Varyl Thorndycraft[1]

[1]Centre for Quaternary Research, Department of Geography, Royal Holloway University of London, Egham, United Kingdom, [2]Royal Geographical Society (with IBG), London, United Kingdom, [3]School of Geography, Politics and Sociology, Newcastle University, Newcastle Upon Tyne, United Kingdom, [4]School of Earth Atmosphere and Environment, Monash University, Clayton, VIC, Australia

Sparse measurements of glacier mass balance, velocity and ice thickness in Patagonia challenge our ability to understand glacier sensitivity to climate change and relate past glacier fluctuations to palaeoclimate change. Small ice caps, such as Monte San Lorenzo, have short response times and high climate sensitivity, making well-dated moraines in their glacier foregrounds an important tool for exploring glacier response to rapid changes in palaeoclimate. Here, the Parallel Ice Sheet Model (PISM) is used to model ice flow across a domain centred on the Monte San Lorenzo ice cap. Ice-flow parameters are calibrated to match present-day ice extent, velocity and thickness. Our aim is, firstly, to quantify present-day physical glacier properties, and ice cap dynamics and sensitivities, and secondarily, to evaluate the controls on the deglaciation of the ice cap within the context of the Southern Hemisphere palaeoclimate system during the Last Glacial-Interglacial Transition (LGIT). The simulated present-day ice cap shows high surface mass flux, with ablation at outlet glacier tongues up to 18 m w. e. a^{-1}, accumulation at the highest elevations of up to 5.5 m w. e. a^{-1} and a simulated Equilibrium Line Altitude (ELA) of 1750–2000 m asl. The ice cap is more sensitive to changes in precipitation relative to changes in temperature. We provide envelopes with likely ranges of palaeotemperature and palaeoprecipitation for glacial advances to moraines formed during the Last Glacial-Interglacial Transition and Holocene. Our numerical model predicts that cooling and an increase in precipitation is required to force glacial advance to mapped moraine limits at 12.1 ka (2°C cooler, 50% more precipitation), 5.6 ka (0°C cooler, 50% more precipitation) and 0.2 ka (1°C cooler, 25% more precipitation). Our modelling results thus provide insights into the present-day mass balance, thermal regime and velocity of the ice cap, explores the sensitivities of this ice cap to various model and climatic parameters, and provide palaeoclimatic envelopes for readvances during the LGIT and Holocene in Patagonia.

KEYWORDS

Patagonia, glaciers and climate, modelling, PISM, palaeoclimate

1 Introduction

The Southern Andes currently account for 8% of the total global mass loss from glaciers (Hugonnet et al., 2021). In particular, Patagonian glaciers are among the most climatically sensitive on Earth (Mackintosh et al., 2017), with an annual specific volume loss in excess of 1 m water equivalent (w.e.), the highest observed globally (Dussaillant et al., 2019; Zemp et al., 2019). However, sparse field measurements of glacier mass balance, ice thickness, basal ice conditions and ice velocity (including that from sliding *versus* deformation) limit our understanding of the dynamics of current ice-mass change and glacier-climate interactions. This data paucity impedes our ability to relate past glacier fluctuations explicitly to changes in palaeoclimate, as mass-balance sensitivities are poorly understood. Numerical glacier modelling can be applied to reconstruct glacier mass-balance distribution, glacier physical behaviour and properties in absence of measured empirical data. These models can be used to assess the sensitivity of an ice mass to both external climatic forcings (such as past temperature and precipitation) and physical parameters that impact ice flow and glacier mass balance (*cf.* Golledge et al., 2012; Doughty et al., 2013; Ziemen et al., 2016; Nielsen et al., 2018; Yan et al., 2018).

Small temperate ice caps in Patagonia, such as Monte San Lorenzo (MSL) (Figure 1; 47.58°S, 72.35°W, 3,706 m asl), typically have short response times and high climate sensitivity (Bahr et al., 1998), making them useful for understanding rapid changes in palaeoclimate and resultant glacier response. Notably, due to the strong west-east precipitation gradient across the Patagonian Andes (Garreaud et al., 2013), and their location further inland, the smaller ice caps such as MSL east of the main Patagonian icefields (72–73°W) may be limited by precipitation, and may therefore be more sensitive to change in this than glaciers further to the west.

Geomorphological and chronological data collected from valleys around MSL show that glaciers receded rapidly through the Last Glacial-Interglacial Transition (LGIT; 15 to 11.7 ka BP; Lowe and Hoek, 2001) and Holocene (11.7 ka onwards; Rasmussen et al., 2014) (Sagredo et al., 2016, 2018; Davies et al., 2018; Martin et al., 2019, 2022; Thorndycraft et al., 2019; Mendelová et al., 2020). During this time, large-scale climatic events such as the Antarctic Cold Reversal (ACR) impacted Patagonia (Moreno et al., 2009; 2018; Tonello et al., 2009; Waldmann et al., 2010; Kilian and Lamy, 2012; Oehlerich et al., 2015; Quade and Kaplan, 2017; Kaplan et al., 2020). These climatic events resulted in changes in the Southern Westerly Winds, likely through the Southern Annular Mode (Boex et al., 2013; Moreno et al., 2018; Bendle et al., 2019; Kaplan et al., 2020; Morales et al., 2020; Moreno, 2020), driving changes in temperature and precipitation, which caused glacier fluctuations (Reynhout et al., 2019). However, the relative sensitivity of palaeo-glaciers to temperature and precipitation, and which of these forcings were the primary control on glacier mass balance at this time, remains unclear. There are few palaeoclimatic proxies available from Patagonia able to provide quantitative estimates of specific environmental conditions at particular times, especially in the study region (Kilian and Lamy, 2012; Massaferro and Larocque-Tobler, 2013). The available palaeoclimatic reconstructions often rely on qualitative comparisons (describing periods as hotter, colder, drier, wetter, for example) (Mansilla et al., 2016; Quade and Kaplan, 2017; McCulloch et al., 2020; Moreno, 2020). An improved understanding of present-day glacier dynamics and mass-balance sensitivities can inform our understanding of past glacier response to climate change.

In this study, we used the Parallel Ice Sheet Model (PISM) across a domain centred on the MSL ice cap, calibrated to match present-day ice extent, velocity and thickness. Our aim is firstly to quantify present-day physical glacier properties, ice dynamics (such as the proportion of ice deformation *versus* sliding and basal yield strength) and surface mass balance. Secondly, by comparing the LGIT landform record of outlet glaciers north of MSL (Martin et al., 2019; 2022) with results from PISM, we aim to gain insights into the palaeoclimatic controls on ice volume. We use model sensitivity experiments to assess the impact of surface air temperature, precipitation, snow and ice melt factors, bed strength and ice rheology on the simulated ice cap. These new data improve our understanding of the key controls on the behaviour of the present-day ice cap, its response to climatic perturbations, and provides climatic envelopes (the most likely mean ranges of temperature and precipitation) needed to drive glacial advances to moraines formed in the Late Glacial at the Monte San Lorenzo massif.

2 Study area and its geographic, climatic and glacial settings

2.1 Present-day glaciers of monte san lorenzo

South America is dominated on its western flank by the Andes, which extend for 68° of latitude from their northernmost point in tropical Columbia (12°N) to their southernmost extent in temperate Chile and Argentina (56°S) (Rodbell et al., 2009; Davies et al., 2020). There are three substantial icefields in the Patagonian Andes. The Northern Patagonian Icefield (NPI) covered 3,758 km^2 in the year 2000 (Barcaza et al., 2017). 90 km south of this lies the Southern Patagonian Icefield (SPI), which covered 12,485 km^2 in 2005 (Meier et al., 2018). Further south in Tierra del Fuego lies Cordillera Darwin (2,932 km^2 in 2005). Surrounding these larger icefields lie numerous glaciers, ice-capped volcanoes and small ice caps, including MSL and Sierra de Sangra (Meier et al., 2018).

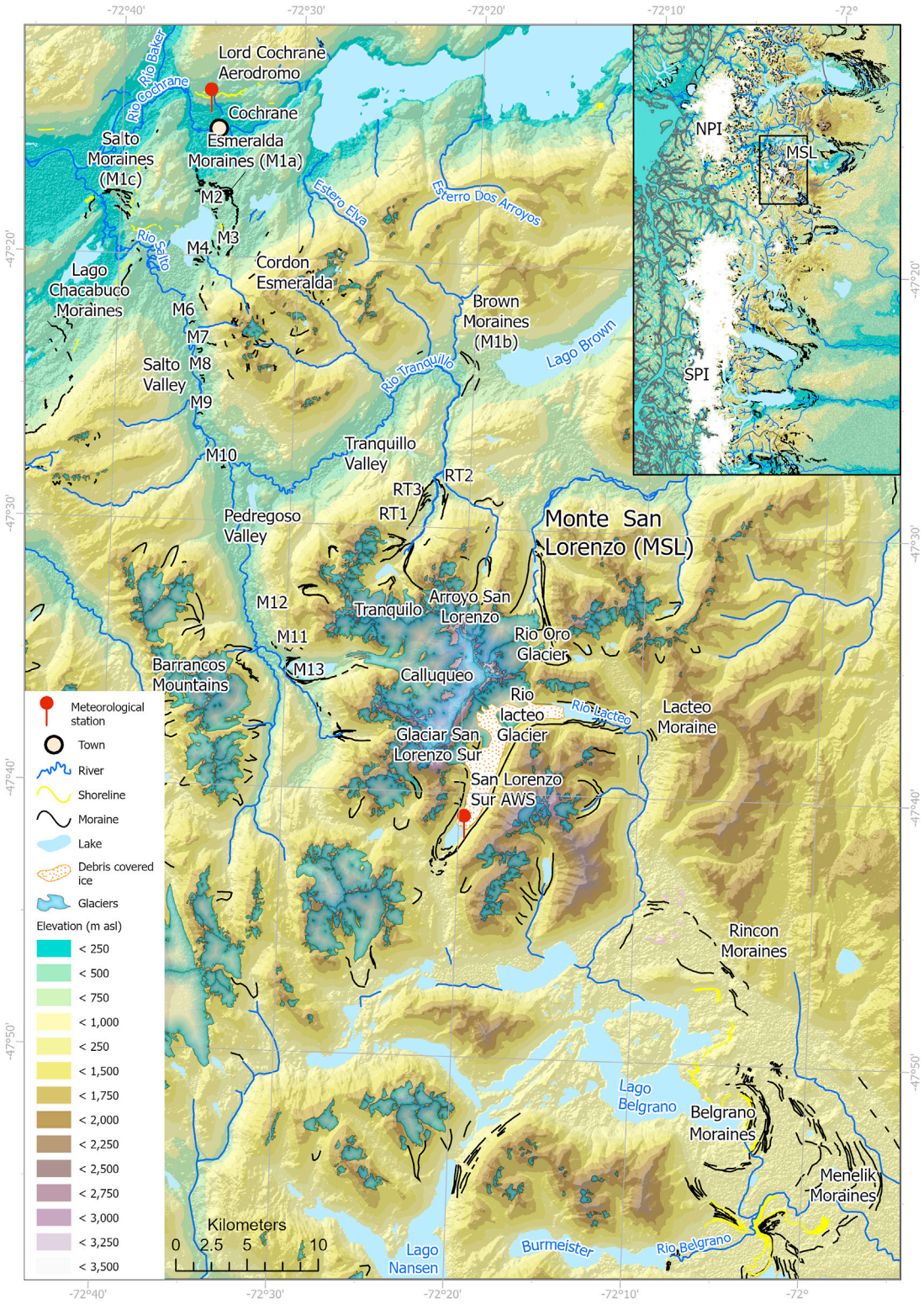

FIGURE 1
Map of the study area, with Monte San Lorenzo (MSL) and major placenames and geomorphological features mapped. Moraines, shorelines, rivers and lakes mapped in previous work (Davies and Glasser, 2012; Davies et al., 2018; 2020; Sagredo et al., 2018; Martin et al., 2019; 2022; Mendelová et al., 2020). For the inset, moraines and glaciers are from the compilation in Davies et al. (2020). Glacier outlines are derived from the Randolph Glacier Inventory v. 6.0 (Randolph Glacier Inventory Consortium et al., 2017), with a timestamp of 31.05.2003. Inset shows overview of Monte San Lorenzo (MSL), which lies to the southeast of the Northern Patagonian Icefield (NPI) and northeast of the Southern Patagonian Icefield (SPI). Moraine codes are after Martin et al. (2019), Mendelová et al. (2020), and Sagredo et al. (2018). AWS: Automatic weather station.

MSL lies southeast of the Northern Patagonian Icefield (NPI), 70 km east of the main Andean chain (Figure 1). MSL is an isolated granodiorite to granitic massif (Ramos et al., 1982), and is the third highest peak (3,706 m) in the Patagonian Andes (Masiokas et al., 2009). Up to 102 ice bodies have been mapped on MSL's flanks, covering 207 km^2 (Falaschi et al., 2013). Small glaciers also occupy the adjacent Cordon Esmeralda and Barrancos Mountains (Figure 1). The four largest glaciers at MSL are Rio Oro, Rio Lacteo, San Lorenzo Sur and Calluqueo (Martin et al., 2019). Glaciar Calluqueo is the largest, with an area of 45.3 km^2 (Falaschi et al., 2013), with its terminus reaching 600 m asl. Glaciar Calluqueo terminates on bedrock, but drains into the large, 3.5 km long proglacial Lago Calluqueo, which discharges into Rio Salto to the north. Glaciar Rio Lacteo in the east and Glaciar San Lorenzo are largely debris covered (Falaschi et al., 2021), and terminate in proglacial lakes. Glacier velocity mapping by Millan et al. (2022) indicates that the tongue of Calluqueo Glacier reaches velocities of up to 350 m a^{-1}, with slower flow of ~100 m a^{-1} in the tongue's tributaries in the accumulation area. Glacier velocities are also available in the GoLIVE dataset (Fahnestock et al., 2016), which report very similar velocities profiles. Ice thicknesses reach 330 m at the ELA, with ice under 100 m thick in the accumulation area and on the glacier tongue (Millan et al., 2022). These glaciers have a majority of glacier area at low elevations, have small accumulation area ratios, and are correspondingly sensitive to small changes in equilibrium line altitude (ELA) (Falaschi et al., 2013, 2017). They are currently undergoing surface lowering in the lower ablation areas, with rates greater than 5 m a^{-1} (Falaschi et al., 2017). Glacier area here has been decreasing at a mean rate of 0.8% a^{-1} between 1985 and 2008 (Falaschi et al., 2013). Glacier mass balance determined from geodetic data is negative, with the west flank having a mass balance of -0.31 ± 0.16 m w. e. a^{-1} (Falaschi et al., 2019).

Despite these recent observations, the glacier mass balance magnitude, distribution, and mass turnover, is poorly known for these glaciers. In the absence of field studies, ice-flow parameters and glacier flow dynamics (e.g., relative velocities from sliding and deformation) are also unclear. The glacier thermal regime, surface mass balance, distribution of temperate and cold-based ice is also unknown, as is the degree to which glaciers are sensitive to temperature and precipitation changes and the relative importance of these climate variables for driving past glacier change. To address these gaps in our understanding, we undertake a full simulation and investigation of the ice cap.

2.2 Present day temperature records

The nearest meteorological station to the MSL ice cap is located on the western lateral moraine of San Lorenzo Sur Glacier (47°42′S, 72°19′W, 1,140 m asl; Figure 1), from which Falaschi et al. (2015) report a mean annual air temperature of 3.8°C measured over the period from 2002 to 2013. The 0°C isotherm is at 1725 m asl (Falaschi et al., 2015), with a late-summer snowline between 1700–1750 m asl measured in the western sectors of the massif in February 2005 (Falaschi et al., 2013). The snowline is higher (1800 m) in the drier, eastern sectors of the massif (*ibid.*).

The nearest station recording both temperature and precipitation is at Lord Cochrane Aerodromo (47°15′S, 72°35′W, 182 m asl; Figure 1), 40 km north of MSL and 3,624 m below its summit (Direccion Meteologica de Chile, 2001). Temperature data recorded after 2000 are largely absent, however a full record from 1970 to 2000 documents a mean annual temperature of 9.4°C (ranging from 8.4°C to 10.8°C). The two mean annual temperature records from San Lorenzo Sur and Lord Cochrane Aerodromo at 1,140 m asl and 182 m asl respectively give a temperature lapse rate estimate of 0.0058°C m^{-1}. This is within the range observed across Patagonia (0.0048°C m^{-1} to 0.0072°C m^{-1}) (Table 1).

2.3 Present-day precipitation records

The meteorological station at Lord Cochrane Aerodromo provides a mean annual precipitation of 726 mm a^{-1} for 1970–2000 (range 522 mm –1,187 mm a^{-1}). There is a significant absence of precipitation measurements at higher elevations in the mountains to the east of the Patagonian icefields. Precipitation at MSL would be expected to be higher than these values obtained in the low valleys at Cochrane, due to the ice cap's significant elevation, and in particular at Glaciar Calluqueo due to the west-facing accumulation catchment and the addition of wind-blown snow.

Annual accumulation on the windward, western side of the NPI at Glaciar San Rafael has been estimated to be between 4,800 and 10,000 mm (Fujiyoshi et al., 1987; Escobar et al., 1992; Carrasco et al., 2002), with similar annual precipitation recorded west of the Southern Andes (Schneider et al., 2003), and reflected in climate modelling (Garreaud et al., 2013). Mean precipitation rates over the eastern NPI for different elevations have been recently modelled to be 7,070 ± 790 mm a^{-1} above 3,000 m, 5,480 ± 570 mm a^{-1} from 2,000 to 2,500 m, and 3,720 ± 400 mm a^{-1} below 1,000 m (Sauter 2020; Table 2). Values over the western NPI are higher, up to 7,930 ± 850 mm a^{-1} above 3,000 m and 6,840 ± 680 mm a^{-1} below 1,000 m. Such levels of precipitation are also reflected in river discharge models (Escobar et al., 1992).

On a west-east transect, mean annual precipitation and accumulation values over the Southern Patagonian Icefield (SPI) range from 2,000 to 15,000 mm w. e. a^{-1} (Inoue et al., 1987; Escobar et al., 1992; Carrasco et al., 2002; Garreaud et al., 2013; Schaefer et al., 2013), decreasing to between 7,600 mm and 2,500 mm w. e. a^{-1} on the eastern outlet glaciers (Rivera 2004; Stuefer et al., 2007) (Table 2). Precipitation at Glaciar Tyndall (SPI; 51°15′S, 73°17′W) was modelled to be 7,100 ± 1,100 mm w. e. a^{-1} for 2000–2016 (Weidemann et al., 2018).

TABLE 1 Observed temperature lapse rates from across Patagonia. Lapse rate from Cochrane to San Lorenzo Glacier calculated by the authors, using data from Falaschi et al. (2013). SPI is Southern Patagonian Icefield.

Location	Grid References	Temperature lapse rate (°C m^{-1})	Source	References
Frias Glacier	41°09′ S, 71°50′ W	0.0048	Reanalysis data	Leclercq et al. (2012)
Exploradores Glacier	46°30′ S, 73°10′ W	0.0053	Met. station	Inoue et al. (1987)
San Rafael Glacier	46°40′ S, 73°50′ W	0.0055	Reanalysis data	Koppes et al. (2011)
Cochrane–San Lorenzo Sur Glacier	47°15′ S, 72°34′ W-47°41′ S, 72°17′ W	0.0058	Met. station	Falaschi et al. (2013)
SPI transect	48°45′ S	0.0072 (east)	Met. station	Bravo et al. (2019)
		0.0055 (west)		
SPI	50°38′ S, 73°15′ W	0.0053	Assumed	Aristarain and Delmas, (1993)
Gran Campo Nevado	52°48′S, 72°56′W	0.0062	Met. station	Schneider et al. (2003)

TABLE 2 Modelled and measured precipitation and accumulation data across Patagonia. NPI: Northern Patagonian Icefield. SPI: Southern Patagonian Icefield.

Location	Latitude and longitude	Altitude (m)	Precipitation (m w.e.) (Accumulation*)	Precipitation lapse rate (mm m^{-1})	Source	References
Lago Aculeo	33°S to 34°S		0.69	0.25	Multiple met. stations	Jenny et al. (2003)
Frias Glacier	41°09′ S, 71°50′ W	2000	8.2	1.5	Mass balance model	Leclercq et al. (2012)
Chico Glacier	49°03′ S, 73°10′ W	<1,440	4.07	3	Mass balance model/Met. station	Rivera (2004)
		>1,400	4.07	3.7		
Regional	40°S to 55°S			0.00252	Regional met. station data	Bravo et al. (2015)
San Rafael Glacier (icefield plateau)	46°40′ S, 73°50′ W		4.8* to 10*		Met. station	Inoue et al. (1987); Escobar et al. (1992); Carrasco et al. (2002)
Nef Glacier	47°01′ S, 73°19′ W	1,500	2.2		Met. station	
NPI		Highest alt	15 to 24. 5 to 10. 2 to 5		Mass balance model/ reanalysis data	Schaefer et al. (2013)
		1,500–2000				
		1,000–1,500				
Eastern NPI		>3,000	7.07 ± 0.79		Linear Orographic Precipitation Model ($OPM_{0.60}$)	Sauter (2020)
		2,500–3,000	5.92 ± 0.59			
		2000–2,500	5.48 ± 0.57			
		1,000–2000	5.30 ± 0.58			
		<1,000	3.72 ± 0.40			
NPI			6.7		River discharge model	Escobar et al. (1992)
SPI			7			
Patagonia region	Western		5 to 10		Modelled climate	Garreaud et al. (2013)
	East of divide		0.5 to 0.7			
Perito Moreno Glacier	50°30′ S, 73°30′ W	2,500	7.6)		Modelled climate	Stuefer et al. (2007)
		670	0.84			
Southern Andes transect	53°S, 75°W	0	4.4		Met. station	Schneider et al. (2003)
	53°S, 73°W	383	10.9			
	53°S, 71.6°W	8	0.9			
	53°S, 70.5°W	6	0.5			

On the eastern, lee side of the SPI, annual precipitation of 4,070 mm w. e. a^{-1} was estimated based on stake measurements at Glaciar Chico (Rivera, 2004), and modelled to be 7,600 mm w. e. a^{-1} at 2,500 m asl on Glaciar Perito Moreno (Stuefer et al., 2007). Ice core data from the accumulation area (2,600 m asl) of Glaciar Pío XI (SPI) from 2001 to 2005 yield accumulation rates of 3,400 to 7,100 mm w. e. a^{-1}, with an average of 5,800 mm w. e. a^{-1} (Schwikowski et al., 2013), although these were not corrected for thinning due to glacier flow. For Glaciar Tyndall (SPI), the modelled mass balance in the accumulation area is 10,300 ± 1,800 mm w. e. a^{-1} (Weidemann et al., 2018). These glaciers are located in the southern portions of the SPI, subject to the strong effect of the Southern Westerly Winds, and higher accumulation rates are expected. Across the SPI, measured snow accumulation reaches 15,400 mm w. e. a^{-1} (Schaefer et al., 2015).

MSL's location, 90 km inland from the Andes, lies at the edge of the rain shadow where there is a sharp contrast between vegetated and arid landscapes. This location has therefore a lower annual precipitation than that observed and modelled to its west. The mean annual measured precipitation at Cochrane is 726 mm a^{-1} (1970–2000 AD). The measured precipitation at Cochrane shows a decreasing trend, and the longer annual mean from 1970–2021 is 688 mm a^{-1}. However, values after the year 2000 are not relevant to this study since we use the mean climate from 1970–2000 to initialise the model and to compare it with glacier outlines from the Randolph Glacier Inventory from 2003. Lower modelled and measured precipitation is also apparent at other low elevation sites east of the Andes range (Schneider et al., 2003; Stuefer et al., 2007; Garreaud et al., 2013). MSL sits at the northern edge of a break in the Andean range and therefore will experience less of a rain shadow effect than those regions latitudinally level with the higher-elevation NPI. However, its location 160 km inland from the coast, to the east of the mountains at the southern tip of the NPI, will still be factors contributing to lower levels of precipitation than at the NPI and SPI, which sit closer to the coast, receiving the full brunt of the precipitation-bearing Southern Westerly Winds.

Due to the scarcity of meteorological data from the Patagonian icefields and the surrounding region, in particular from ice masses at contrasting elevations, there are few measured precipitation lapse rates (those that are available are summarised in Table 2). These values are varied, ranging from 0.00252 mm m^{-1}–3.7 mm m^{-1} (Jenny et al., 2003; Rivera, 2004; Leclercq et al., 2012; Bravo et al., 2015), likely due to the complex topography creating strongly site-specific precipitation gradients.

2.4 Ice dynamics during the Last Glacial-Interglacial transition

2.4.1 Antarctic cold reversal

During the Antarctic Cold Reversal (ACR; 14.5 to 12.8 ka; Blunier et al., 1997; Pedro et al., 2016), an enlarged, northwards-flowing Glaciar Calluqueo (with accumulation areas in the Barrancos Mountains and western Monte San Lorenzo) formed the substantial Salto and Esmeralda moraines at the mouth of the Pedregoso-Salto Valley, dated to 13.4 ka (Davies et al., 2018) (Figure 1; see panel '13 ka' in Figure 2). This is the M1a moraine from Martin et al. (2019; 2022) and in Figure 1. These moraines are some 39 km from the current ice margin. Chironomid reconstructions from Lake Potrol Aike (52°S) and Antarctic ice-core records (Cuffey et al., 2016) both suggest a decrease in temperature of 3–4°C at this time (Massaferro and Larocque-Tobler, 2013). During the ACR, Glaciar Calluqueo terminated in the ice-dammed palaeolake Lago Chelenko with an outflow at 350 m asl (Figure 2) (Davies et al., 2018; 2020; Thorndycraft et al., 2019).

In the upper Tranquilo Valley, a series of inset moraines (RT1 to RT3, mean ages 13.8, 13.3 and 12.1 ka) also record stabilisation of much smaller northward-flowing MSL outlet glaciers during the ACR (Sagredo et al., 2016; 2018) (Figures 1, 2). The outermost moraines are only 14.3 km from the current ice margin. The RT1 to RT3 moraines are high above the level of any palaeolake in the study area. Below these moraines, perched deltas in the lower Tranquilo valley indicate that a palaeolake at 520 m asl existed in this valley also at this time ("Palaeolake Tranquilo"), which drained over the older Brown Moraines (M1b) into Lago Brown (Martin et al., 2019; Davies et al., 2020) (Figures 1, 2). Assuming no change in precipitation and an adiabatic lapse rate of 6.5°C/1,000 m, an estimated equilibrium line altitude (ELA) depression of 210 m would translate into temperature anomalies of just 1.6–1.8°C cooler than present during the ACR (Sagredo et al., 2016).

Outlet glaciers draining southeast from MSL also advanced during the ACR, reaching the Belgrano and Rincon moraines at 13.1 ± 0.6 ka (Mendelová et al., 2020) (Figures 1, 2). This suggests an advance of 30 km for Rio Lacteo and San Lorenzo Glacier.

2.4.2 Post-Antarctic cold reversal warming

The climate warmed across much of the Southern Hemisphere immediately following the ACR. Ice cores in Antarctica record a rapid temperature rise of 2.5°C in the century after 12.8 ka, with a bias of −2.75°C to −0.25°C compared with present day (Frieler et al., 2015; Cuffey et al., 2016). Changes in West Antarctic temperatures have been shown to be synchronous with cryospheric changes in Patagonia's mid-latitudes (Cuffey et al., 2016; Bendle et al., 2019), with upwelling of warm deep water in the Southern Ocean a potential driver of warming across the mid and high-latitudes (Pedro et al., 2016). Sea surface temperatures at 46°S also record rapid warming at this time (Haddam et al., 2018). However, while there are some palaeoclimatic records of temperature and precipitation changes post-dating the ACR (Kilian and Lamy, 2012; Villa-Martínez et al., 2012; reviewed in Davies et al., 2020), the specific palaeoclimatic envelopes describing the prevailing climate at this time and in this region of Patagonia are poorly known. The

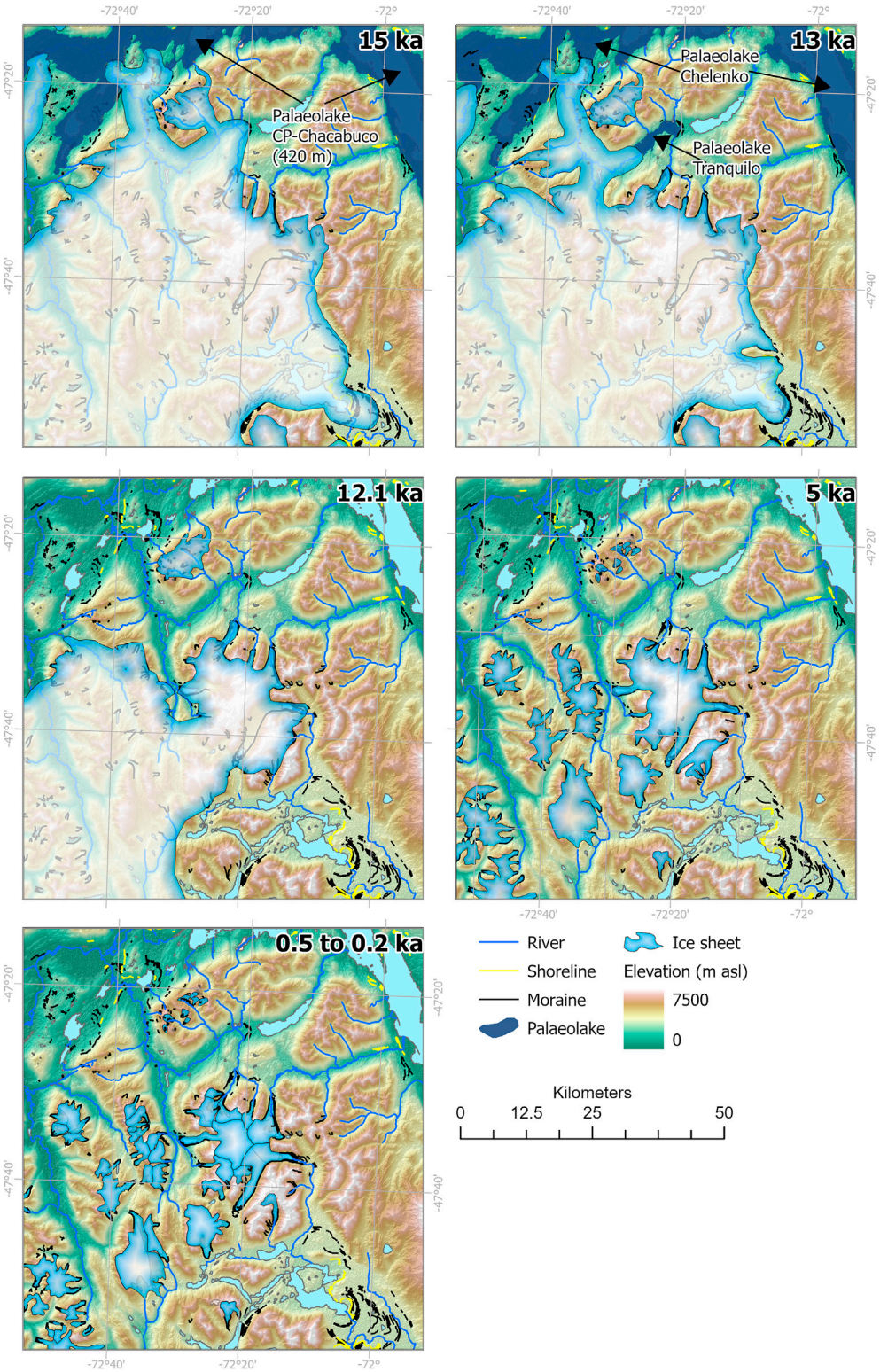

FIGURE 2
Empirical reconstruction of Monte San Lorenzo ice cap through the ACR (14.5–12.8 ka) Holocene, after numerous publications (Sagredo et al., 2016; 2018; Davies et al., 2018; 2020; Martin et al., 2019; 2022; Thorndycraft et al., 2019; Mendelová et al., 2020).

relative sensitivity of the glacier mass balance to these changes and thus drivers of change are therefore poorly understood.

There is regional evidence of glacier recession immediately following the ACR. In the Pedregoso valley, recession of Glaciar Calluqueo is denoted by a series of nested moraines (M4 to M12). The 'Moraine Mounds' (M4) are located 5.2 km behind the Esmeralda Moraines (Martin et al., 2019 and Figure 1), dated to 12.8 ka (Glasser et al., 2012), and are 37 km from the present ice margin and above 350 m asl. By 12.5 ± 0.3 ka, Glaciar Calluqueo had receded to M9 (Martin et al., 2022). Lago Chelenko drained between 12.4 and 11.8 ka (Thorndycraft et al., 2019) (Figure 1), during the rapid post-ACR warming after 12.8 ka. The M12 moraines, lateral moraines just above the Holocene-age M13 moraines, are dated to 12.1 ± 0.4 ka. Recession over 50 km therefore occurred at a mean rate of 50.3 m yr^{-1} between 12.8 (M4) and 12.1 ka (M12) (Martin et al., 2022).

Palaeolake Tranquilo drained when recession of Glaciar Calluqueo to the M12 moraine allowed a new outflow into Salto Valley (Martin et al., 2019; 2022). East of the MSL massif, the Lacteo lateral moraine, 20 km up-valley from the Rincon moraines (Figure 1), has a mean age of 12.4 ± 0.3 ka, supporting rapid recession following the ACR, followed by glacier stabilisation. Regional evidence of glacier stabilisation at this time is also supported by the formation of the RT5 Moraine in the Tranquilo valley at 12.2 ± 0.4 ka (Sagredo et al., 2018).

2.4.3 Mid-holocene and late holocene

A period of cooling during the mid-Holocene is reflected in the Antarctic ice-core record (from +0.4°C to +0.1°C from present day) (Frieler et al., 2015; Cuffey et al., 2016). During this mid-Holocene cooling, the glaciers around MSL advanced again, generally reaching the large moraines near the present-day outlet glacier termini (Davies et al., 2020), likely including the M13 moraines around Lago Calluqueo (Figures 1, 2). The moraines around the lake in the cirque in the upper Tranquilo valley date from 5.7 ka (Sagredo et al., 2016).

Across the icefield, these moraines were then re-occupied by glaciers during the Late Holocene (0.5–0.2 ka), evidenced by lichenometry (Garibotti and Villalba, 2017). Tree-ring records suggest that temperatures were 1–2°C cooler than present from 600 to 200 years ago in Patagonia (Villalba et al., 2005), driving this glacial advance (Kaplan et al., 2016). The Antarctic ice-core record shows cooler temperatures at this time, between 0.6°C and 1°C below present (Frieler et al., 2015; Cuffey et al., 2016).

2.5 Previous work modelling patagonian glaciers and icefields

Numerical modelling has previously been used to explore palaeo ice dynamics, glacier and mass-balance sensitivities in Patagonia. Model exploration of potential climates for past glacial advances so far has focused on the Last Glacial Maximum. Hulton et al. (1994) suggested that the ELA at the LGM was depressed by 160–560 m. A decade later, an updated coupled ice sheet/climate model suggested that at the LGM, the Patagonian Ice Sheet had an ice volume of 500,000 km^3, with modelled ice velocities reaching 400 m a^{-1} under a temperature decrease of 6°C and constant winds over the model domain (Hulton et al., 2002; Sugden et al., 2002).

A time-dependent model focused on the Northern Patagonian Icefield (45–48°S) suggested that an ELA lowering of 750–950 m occurred during the LGM (Hubbard et al., 2005), in order to reach the Fenix I-V moraines at Lago Buenos Aires. An ELA lowering of 900 m best matched the Fenix V moraine at 23,000 years BP. This model predicted a mean ice thickness of 1,130 m, drained by ice streams to the western and eastern margins. Forcing the model with temperature biases derived from an Antarctic ice core record suggested that the ice sheet rapidly shrank shortly after the LGM, with ice margin stabilisation during the Antarctic Cold Reversal (Hubbard et al., 2005).

More recently, a 2D ice sheet model applied over the Magallanes lobe in southern Patagonia suggested that summer temperatures were 4.5°C and 5.5°C cooler when the Magallanes lobe reached the inner and outer MIS two moraines respectively, with ~25% less precipitation than at present (Peltier et al., 2021).

There are no presently published numerical modelling studies that focus on the Late Glacial period or the Antarctic Cold Reversal, though there has been some work on using glacier models to investigate Patagonian glacier response to Holocene climate change. Bravo et al. (2015) investigated glacier behaviour in the mid-Holocene (6,000 years BP) and pre-industrial period (1750 AD) using a degree-day glacier mass balance model. They used this to explore changes in glacier ELAs between the mid-Holocene and late Holocene. They showed that the modelled ELA was 20–30 m lower in the mid-Holocene relative to the pre-industrial period (Bravo et al., 2015).

Leclercq et al. (2012) used a long and detailed record of glacier length fluctuations at Glaciar Frías (Southern Patagonian Icefield) from 1639 AD to present. They used a simplified surface energy-balance model and a flowline model to account for the response of the glaciers to climatic forcing. They found that the overall glacier retreat (1,639–2009 AD) was best explained by a mean temperature increase of 1.2°C (Leclercq et al., 2012).

Ice-flow and surface-mass balance modelling has also been applied to some present-day glaciers, mostly across the main icefields. A full-Stokes ice-flow model (Elmer/Ice) applied over Glaciar San Rafael predicted low basal shear stresses (<25 kPa) and high surface velocities (7.6 km a^{-1}) (Collao-Barrios et al., 2018). This work suggested that most of the surface velocity is due to basal sliding of the glacier tongue.

3 Materials and methods

3.1 GlaRe reconstructions of equilibrium line altitude and palaeo-precipitation

Using empirical observations of the patterns of palaeoglacier recession and landsystem change north of MSL, based on geomorphological mapping, sedimentology and cosmogenic nuclide dating (at this site, mostly Glasser et al., 2012; Davies et al., 2018; Martin et al., 2019, 2022), it is possible to reconstruct the past ice surface and ELA for palaeoglaciers (Osmaston, 2005; Braithwaite, 2008; Rea, 2009; Sagredo et al., 2014). Due to the relationship between precipitation and temperature at the ELA of land-terminating glaciers (Ohmura et al., 1992; Bendle and Glasser, 2012; Chandler and Lukas, 2017), these data, when combined with existing temperature records, can be used to estimate palaeo-precipitation at glacier ELAs. We apply this method to Glaciar Calluqueo in the post-ACR period (see Supplementary Information for more details). These ELA-based, more simple precipitation reconstructions therefore provide a hypothesis for changes in the amount of precipitation during the period of rapid warming following the ACR. These can be compared with the precipitation and temperature changes required to force the glacier model to match mapped palaeoglacier extent.

In this study, the GlaRe ice-surface reconstruction GIS tool for ArcGIS (Pellitero et al., 2016) was used to calculate palaeo three-dimensional ice-surface for the present-day glacier and when the glacier occupied the post-ACR M12 (mean age 12.1 ± 0.4 ka) and M13 moraines (both limits from Martin et al. (2022); Figures 1, 2). GlaRe reconstructs a three-dimensional ice surface based upon a given bed topography and an element of the reconstructed ice margin (e.g. lateral or frontal moraine, or a trimline). This method assumes the present-day topography is the same as that of the palaeo-glacier bedrock topography. In this case, we used the bed topography provided in Carrivick et al. (2016). Once a palaeo-ice surface has been reconstructed, this can be used as the input to an automatic calculation of the glacier ELA.

The M12 and M13 moraine limits (Figure 1) were chosen because ice had separated from other glaciers and calving into palaeolakes had ceased. The GlaRe method is not appropriate for the ACR advance to the M1 moraine due to the lacustrine calving conditions at that time. The M13 limit is hypothesised to mark the advanced position of Glaciar Calluqueo at both the latest Holocene (0.2 ka) and during a regional mid-Holocene (5–6 ka) neoglaciation, in line with regional moraine patterns (Sagredo et al., 2016; Garibotti and Villalba, 2017).

The Accumulation Area Balance Ratio (AABR) method (Osmaston, 2005; Rea, 2009; Pellitero et al., 2015) is used in combination with the GlaRe tool (Pellitero et al., 2015; 2016) to calculate ELAs for the present-day glacier and the glacier when it occupied the M12 and M13 moraines. Balance ratios from 1.5 to 2.5 were used to provide a range of possible ELAs, with a representative 'global' value of 1.75 selected for comparison to present day empirical data (*cf.* Rea, 2009) (see Supplementary Information for more detail). The standard deviation of the ELAs calculated for different balance ratios provided an estimate of uncertainty in the ELA (*cf.* Osmaston, 2005). We refer to the ELAs reconstructed in this manner as GlaRe-ELAs to differentiate them from those modelled by PISM or measured during surface mass balance campaigns.

Palaeoglacier ELAs have been widely applied in palaeoclimate studies to reconstruct former climates (Bendle and Glasser, 2012; Sagredo et al., 2014; Chandler and Lukas, 2017). Once the 3D surface of the palaeoglacier has been reconstructed, and the ELA calculated, temperature at the ELA can be computed, for example, by calculating the height above the nearest weather station and applying a temperature lapse rate (for modern day glaciers). For palaeoglaciers, the temperature at the ELA can be calculated by bias-correcting the present-day measured mean climate against palaeoclimatic records for the relevant time period.

We calculated the temperature at Lord Cochrane Aerodromo at the time of each glacier stillstand by bias-correcting the Cochrane temperature record using surface air temperature data from Antarctic ice cores (Cuffey et al., 2016) (see Supplementary Information). This leads to a temperature reduction of 0.7°C during the Late Holocene (0.5–0.2 ka), 0.3°C during the Mid Holocene (5.7 ka, when Glaciar Calluqueo reached the M13 moraine), and 1.1°C at 12.1 ka BP (when Glaciar Calluqueo reached the M12 moraine). Secondly, we apply a lapse rate (0.0058°C m^{-1}) (calculated using data from Falaschi et al., 2013) to find the temperature at the height of the GlaRe-ELA at each of these time periods. We use a temperature uncertainty of ±0.45°C, which is obtained from present day temperature records at Lord Cochrane Aerodromo meteorological station.

Finally, we use the quantitative relationship between summer temperatures and precipitation at the GlaRe-ELA (Ohmura et al., 1992) to obtain estimates of palaeo-precipitation values for phases of glacier stabilisation at the M12 and M13 moraines (following Bendle and Glasser, 2012; Chandler and Lukas, 2017; Oien et al., 2021). An uncertainty in precipitation estimates is derived from the range in mean summer temperature.

3.2 Parallel ice sheet model description

We used the Parallel Ice Sheet Model (PISM), a three-dimensional, thermomechanically-coupled ice-sheet model, which has previously been thoroughly described (e.g., Bueler and Brown, 2009; Martin et al., 2011; Winkelmann et al., 2011; Aschwanden et al., 2012, 2016; Van Pelt and Oerlemans, 2012). PISM employs an enthalpy-based energy conservation scheme, combines the Shallow Ice and Shallow Shelf

TABLE 3 Physical constants and parameter values used within the PISM model of the MSL ice cap. SIA is the Shallow Ice Approximation. SSA is the Shallow Shelf Approximation.

Name	Default	Units	Description	Source for default value and ranges
Physical constants				
A	3.8 x 10^{-24}	Pa^{-3} s^{-1}	Glenn's flow law ice-softness coefficient	Gudmundsson (1994) and Paterson (1994)
g	9.81	m s^{-1}	Acceleration due to gravity	
ρ_i	910	kg m^{-3}	Ice density	Greve and Blatter (2009)
ρ_w	1,000	kg m^{-3}	Fresh water density	Greve and Blatter (2009)
Fixed default parameters				
e_{ssa}	0.6		SSA enhancement factor	
n_{sia}	3		SIA exponent	
n_{ssa}	3		SSA exponent	
Mz	200		Number of vertical ice layers	
Mbz	50		Number of vertical bedrock layers	
Bed smoothing	50	m	Half-width of bedrock smoothing	
Tuned parameters				
Precipitation lapse rate	1.35*	mm m^{-1}	Change in precipitation with change in elevation	
Sensitivity tests				
(e_{sia})	3		SIA enhancement factor	Golledge et al. (2012); Putnam et al. (2013); Ziemen et al. (2016); Yan et al. (2018)
(τ_c)	35	kPa	Basal yield stress	Boulton and Jones (1979); Brown et al. (1987); Iverson et al. (1995); Porter et al. (1997); Golledge et al. (2012)
(F_{snow})	3	mm w.e	Positive degree day melt factor for snow	Lang (1986); Takeuchi et al. (1996); Arendt and Sharp (1999); Hock (2003); Anderson and Mackintosh (2006); Schneider et al. (2007); Golledge et al. (2012); Jouvet et al. (2017); Yan et al. (2018)
(F_{ice})	8	mm w.e	Positive degree day melt factor for ice	

approximations (a 'hybrid' approximation), and considers both vertical deformation and longitudinal stretching within the ice. PISM also adopts a 'pseudo-plastic' law that relates basal ice velocity to basal shear stress to estimate basal sliding. Neumann boundary conditions are applied in the model at the grounded lateral ice margin, while Dirichlet boundary conditions are used at the domain edge (The PISM authors, 2017). Together, this numerical implementation means that fast-flowing outlet glaciers can be adequately simulated with manageable computation time (Aschwanden et al., 2016).

Similar to previous studies that used PISM to compute the evolution and sensitivity of ice caps and ice fields (e.g., Golledge et al., 2012; Ziemen et al., 2016; Jouvet et al., 2017; Schmidt et al., 2020; Žebre et al., 2021; Köse et al., 2022), our model for the MSL ice cap used boundary distributions for the ice thickness, bed topography, climate (surface mass balance) and basal heat flux from a combination of datasets, which we described below.

PISM was initialised with bed topography from Carrivick et al. (2016). In the absence of ice-thickness surveys of MSL outlet glaciers, 'present-day' ice thickness data was taken from a dataset derived from the output of a perfect-plasticity model (Carrivick et al., 2016). An ice thickness error of ±11% is reported, introduced in the model through the assumption that the ice behaves under perfect-plasticity and through the error in thickness resulting from the spatial interpolation from the ice thickness modelled at the glacier centreline to the ice thickness across the entire glacier width (Carrivick et al., 2016). This degree of error is in line with that observed globally when modelled ice thickness is compared with radar measurements (Li et al., 2012; James and Carrivick, 2016). A comparison of the Carrivick et al. (2016) model and Millan et al. (2022) dataset shows a good agreement between them, with an offset of ±20 m at the ELA. A bedrock DEM was produced for PISM initialisation by subtracting the modelled ice thickness from an ASTER GDEM in ArcMap v10.3.

Glacier mass balance is determined in PISM by the implementation of a positive degree day (PDD) model (Sato et al., 1984; Braithwaite and Olesen, 1989; 1990; Lang and Braun, 1990; Hock, 2003). The proportion of precipitation that falls as snow and the amount of snow and ice that melts is a product of the ice surface temperature and the number of positive degree days. Accumulation is dependent on precipitation and temperature, with 100% of precipitation assumed to be solid below 0°C, and linearly reduced to zero when air temperature is above 2°C. The melt factors for snow and ice (F_{snow} and F_{ice} in Table 3), representing the thickness of snow and ice melted per degree kelvin per PDD, can be tuned within PISM. Following melting, water may become refrozen based upon a

predetermined refreeze fraction ($Ø_{refreeze}$ in Table 3). Degree-day factor values of 3 and 8 mm w. e. were used for snow and ice respectively, in line with previous modelling studies and similar to those measured in Patagonia (*cf.* Supplementary Table S1).

We applied a basal heat flux of 0.07842 W m^{-2} based upon the relationship between basal heat flux and geology over a 2° by 2° equal area grid (Davies, 2013). The granitic lithology of the MSL massif may lead to a locally higher geothermal heat flux due to higher concentration of radioactive elements. However, there are no empirical data constraining this. Glacier outlines and drainage basins used for the model were derived for 2010–2011 (Davies and Glasser, 2012). Details of model initialisation and values and constants used for key parameters are provided in Table 3.

We ran the model using parallel computation, with processors distributed across 12 computational cores. This used a 250 (x, y) by 20 m (z) resolution gridded domain over an area of 80 km by 108 km (x, y), reflecting 138,993 horizontal grid cells, 200 vertical ice layers and 50 bedrock layers. For precipitation and temperature sensitivity experiments, where simulations produce a far greater volume of ice, we used a 500 m (x, y) resolution grid to enable feasible wall-clock run times of circa 24 h.

To spin up the model, we conducted a standardised PISM multiphase procedure (Aschwanden et al., 2013). The spin-up procedure computes an approximate steady state of the model under constant boundary conditions, which is achieved in three phases. First, a short (5-year) smoothing run was performed with simplified physics, using a non-sliding Shallow Ice Approximation (SIA) (Hutter, 1983). SIA accounts for flow by shear within the ice, neglecting longitudinal and transverse stresses. SIA is a simplified version of the Stokes equations for mass continuity and stress balance which describe the flow of glacier ice. Second, a longer (5000-year) run is done, without the ice geometry evolving. Third, SIA is run in parallel with a vertically integrated, sliding shallow shelf approximation (SSA) (Weis et al., 1999) forming a 'hybrid' model (Bueler and Brown, 2009), which accounts for flow caused by sliding of the ice over a weak substrate. This phase uses constant-climate conditions, and introduces a positive degree day (PDD) model to calculate the glacier mass balance, as well as the impact of geothermal heat flux at the ice-bed interface (The PISM authors, 2017). In this final phase, the ice geometry is allowed to evolve, and the model was run until an approximate equilibrium state of constant ice area and volume was reached (~100–500 model years). The resulting spun up state was then used as the initial state for experimental runs.

An ensemble of 193 model runs was undertaken during model set up and testing. Two climate data evaluation, 11 model tuning runs and 38 sensitivity experiments were then run (Table 4). These tuning and sensitivity experiments used iterations of each variable to establish the key controls on the modelled icefield and to identify the envelope of parameter space in which the results agree most closely with the present-day observed icefield.

3.3 Climate forcing

We evaluated two climate data sets for model initialisation (Experiment A; Table 4). Two modelled climate gridded datasets, RACMO version 2.3 for Patagonia (RACMO2.3 PAT5.5) (Lenaerts et al., 2014) and WorldClim2 (Fick and Hijmans, 2017), were compared with measured meteorological station surface air temperature data from the western lateral moraine of Glaciar San Lorenzo Sur and temperature and precipitation data from Lord Cochrane Aerodromo (Figure 1). They were also compared with observed temperature lapse rates between these two meteorological stations (0.0058°C m^{-1}) (Falaschi et al., 2013) and across Patagonia (Table 1) (Inoue et al., 1987; Aristarain and Delmas, 1993; Schneider et al., 2003; Koppes et al., 2011; Leclercq et al., 2012; Bravo et al., 2019). This allowed us to evaluate the ability of both models to reproduce mean annual air temperature, temperature lapse rates, and the annual temperature cycle in the study area (Table 1; Supplementary Information). The results of this evaluation are shown in Section 4.2.

We also derived a gridded precipitation dataset using precipitation measured at Lord Cochrane Aerodromo meteorological station. The precipitation was varied with altitude, using a lapse rate, alongside the WorldClim2 surface air temperature dataset. The precipitation lapse rate was systematically varied (Experiment B) until the resulting precipitation distribution used to force the ice-flow model resulted in a steady state model simulation of an ice cap matching the present-day ice extent, thickness, velocity, and surface elevation change.

Palaeo-temperature at MSL across the LGIT was derived using relative temperature offsets from the West Antarctic Ice Sheet (WAIS) Divide surface air temperature reconstruction (Cuffey et al., 2016). Changes in West Antarctic temperatures have been shown to be synchronous with cryospheric changes in Patagonia's mid-latitudes (Bendle et al., 2019), with upwelling of warm deep water in the Southern Ocean being a potential driver of warming across the mid and high-latitudes (Pedro et al., 2016). The degree of temporal temperature change across the ACR and the early Holocene as recorded in chironomid records (Massaferro and Larocque-Tobler, 2013; Massaferro et al., 2014) indicates that fluctuations in temperature are similar in the Patagonian mid-latitudes and in the WAIS Divide surface air temperature record (Cuffey et al., 2016).

3.4 Sensitivity experiments

Sensitivity experiments were undertaken to quantify the impact of PISM parameters on model output and explore glacier sensitivities to these variables. In Experiment C, the rheology of modelled ice was adjusted using an enhancement factor to account for variables which may cause increased softening within the ice, such as anisotropy or the inclusion of

TABLE 4 Model tuning and sensitivity experiments performed in this study, documenting the number of model runs, variable(s) tested, range of parameters explored, the model resolution and model run lengths for each experiment. *references for selected parameters ranges are given under the respective variable in Table 3.

Experiment	Aim	Number of model runs	Variable(s) tested	Parameter range*	Resolution (m)	Run length (model years)
(A) Climate model evaluation	Test the suitability of modelled temperature and precipitation datasets for initialisation	2	Temperature and Precipitation datasets	RACMO2.3, WorldClim2	500	250
(B) Tuning	Tune precipitation to match model to present day ice cap	11	Precipitation lapse rate	0.01–1.5 mm m^{-1}	250	250
(C) Sensitivity	Determine sensitivity of the ice cap to changes in SIA enhancement factor in combination with basal yield stress	9	SIA enhancement factor	1, 3, 5	250	250
			Basal yield stress	25, 35, 50 kPa		
(D) Sensitivity	Determine sensitivity of the ice cap to changes in positive degree day melt factors for snow and ice in combination	9	Degree day factor for snow	1.5, 3, 8 mm w.e	250	250
			Degree day factor for ice	3, 8, 16 mm w.e		
(E) Sensitivity	Determine sensitivity of the ice cap to changes in surface air temperature, offset from present-day	5	Surface air temperature	−1, −2, −3, −4, −5	500	750
(F) Sensitivity	Determine sensitivity of the ice cap to changes in mean annual precipitation, scaled from present-day	6	Precipitation	75%–200%	500	500
(G) Sensitivity	Determine sensitivity of ice cap to changes in temperature and precipitation combinations	9	Surface air temperature	−1–-3	500	500
			Precipitation	125–200%		

impurities or dust (Ritz et al., 1996; Parizek and Alley, 2004; Golledge et al., 2012). Values of 1, 3 and 5 were chosen (Table 4) to reflect the range of values used and found to fit empirical data in other ice modelling studies in mountain environments (Golledge et al., 2012; Putnam et al., 2013; Ziemen et al., 2016; Yan et al., 2018).

In Experiment C, bed strength was varied alongside ice rheology. A uniform fixed basal yield strength is applied to represent the strength of aggregate material at the ice-bed interface (The PISM authors, 2017). Values of 25 kPa, 35 kPa and 50 kPa were tested (Table 4), reflecting a range of measured values (Boulton and Jones, 1979; Brown et al., 1987; Iverson et al., 1995; Murray, 1997; Porter et al., 1997) and those tested in modelled mountain valley glaciers (Golledge et al., 2012). Previously published sensitivity analyses of ice rheology and basal yield strength reveals a co-dependency between variables (Golledge et al., 2012) and hence they were tested in combination.

In Experiment D, a range of degree-day factors for snow and ice, and their influence on glacier mass balance and ice volume, were explored. Finally, model sensitivity to temperature and precipitation were assessed (Experiments E, F, G) (Table 4). Glacier response to cooling was investigated in −1°C increments, alongside changes in precipitation, to explore factors that may have driven past glacier advances. When one or more variables were tested, the remaining variables were fixed to default values.

4 Results

4.1 GlaRe reconstructions of equilibrium line altitude and palaeo-precipitation

Using the GlaRe GIS based ice surface reconstruction tool (Pellitero et al., 2016) in combination with the AABR method (Osmaston, 2005; Pellitero et al., 2015), and applying a balance ratio of 1.75, the present-day (2003 AD) ELA of Glaciar Calluqueo is reconstructed as 1,615 ± 20 m asl (Table 5). Using a balance ratio of 1.5 resulted in no change to the GlaRe-ELA, and balance ratios of 2–2.5 resulted in only 25–50 m differences in the GlaRe-ELA, and so therefore the choice of balance ratio had little impact on our results. Using a 0.0058°C m^{-1} temperature lapse rate appropriate for this region (calculated using data from Falaschi et al., 2013) produces a summer temperature at the present-day ELA of 6.9°C and a mean annual air temperature of 1.1°C. Using the summer air temperature-precipitation relationship at the ELA (Ohmura et al., 1992), this gives a precipitation value at the present-day GlaRe-ELA (1,615 m asl) of 2,932 ± 241 mm a^{-1} w. e.

The values for precipitation at the present-day GlaRe-ELA can be compared with that predicted at that altitude (1,615 ± 20 m asl) from various lapse rates. The precipitation at this elevation suggested by the precipitation lapse rate of Bravo et al. (2015) is far lower (730 mm a^{-1} w. e.), which suggests that this lapse rate is too low in this region (Table 5). A lapse rate

TABLE 5 [1]GlaRe-ELAs, rounded to the nearest 5 m, and the [2]temperature and [3]precipitation reconstructed at the GlaRe-ELA for the year 2010 glacier extent and for the M12 and M13 moraines. [4]The percentage difference in precipitation at the GlaRe-ELA when compared with precipitation at the present-day GlaRe-ELA. [5]The precipitation at each altitude is independently calculated using two precipitation lapse rates and precipitation data from Cochrane weather station.

	Present day	M13 moraine; late holocene (0.2 ka)	M13 moraine; mid holocene (5.6 ka)	M12 moraine (12.1 ka)
Temperature offset from present from WAIS Divide ice core record (°C) (Cuffey et al., 2016)	0	−0.7	−0.3	−1.1
[1]GlaRe-ELA (m)	1,615 ± 20	1,290 ± 50	1,290 ± 50	1,110 ± 50
[2]Summer temperature at GlaRe-ELA (°C)	6.9 ± 0.45	8.1 ± 0.45	8.5 ± 0.45	8.7 ± 0.45
[3]Precipitation at GlaRe-ELA (mm a^{-1} w.e.) (Ohmura et al., 1992 method)	2,932 ± 214	3,504 ± 224	3,706 ± 228	3,840 ± 230
[4]% of the precipitation at GlaRe-ELA compared with that at the present-day ELA (2,932 mm a^{-1})	100%	112–127%	119–134%	123–140%
[5]Precipitation (mm a^{-1} w.e.) calculated from 0.00252 mm m^{-1} (Bravo et al., 2015) lapse rate	730	729	729	728
[5]Precipitation (mm a^{-1} w.e.) calculated using the 1.35 mm m^{-1} lapse rate from model tuning experiments	2,662	2,226	2,226	1978

of 1.35 mm m^{-1} (see Section 4.3) yields a precipitation of 2,662 mm a^{-1} w. e., which is only 56 mm a^{-1} w. e. Less than the minimum value predicted at the present-day GlaRe-ELA.

The GlaRe-ELA at the M13 glacier extent is 323 m lower, at 1,290 ± 50 m asl. With a −0.7°C temperature reduction as indicated by the Antarctic ice cores at 0.2–0.5 ka BP, this predicts an annual precipitation of 3,504 ± 224 mm a^{-1} w. e., which is 12–27% higher than the precipitation that falls at the present-day GlaRe-ELA. At the M13 glacier extent in the mid-Holocene with a temperature 0.3°C lower than present, precipitation is calculated as 3,706 ± 228 mm a^{-1}. This indicates an increase in precipitation at the ELA of 19–34%. At 12.1 ka, when ice was at the M12 moraine, the GlaRe-ELA is 1,110 ± 50 m asl. At this time a −1.1°C temperature offset from present gives a precipitation value of 3,840 ± 230 mm a^{-1}. This is 23–40% more precipitation than falls at the present-day GlaRe-ELA.

4.2 Climate data evaluation (Experiment A)

Two modelled datasets, the Regional Atmospheric Climate Model (RACMO), version 2.3 for Patagonia (RACMO2.3 PAT5.5) (Lenaerts et al., 2014) and WorldClim2 (Fick and Hijmans, 2017), were investigated for their applicability to the study area and potential use to drive PISM spin-up to present-day conditions (Supplementary Figure S2). These two climate datasets were evaluated against average annual and monthly measured temperature and precipitation records from Lord Cochrane Aerodromo for the period 1970–2000 and temperature records from the metrological station at Glaciar San Lorenzo Sur (2002–2013; Falaschi et al., 2015) (Table 1; Table 6). The modelled climate data were assessed against seasonal temperature range as recorded in the meteorological station datasets, and against mean annual temperature and observed effective lapse rates at the weather stations in the local area and across Patagonia (Inoue et al., 1987; Aristarain and Delmas, 1993; Schneider et al., 2003; Koppes et al., 2011; Leclercq et al., 2012; Falaschi et al., 2013; Bravo et al., 2019) (*cf.* Table 1).

We also considered whether the spatial resolution of the two datasets allowed the temperature variations across the mountain topography to be represented (see Supplementary Information for details). WorldClim2 produces temperatures (Table 6) and temperature lapse rates (0.0051–0.0056°C m^{-1}) that are within the range of those observed in Patagonia (Table 1). WorldClim2 also produces a close fit to the measured seasonal climate cycle at Cochrane Aerodromo (Supplementary Figure S1). The WorldClim2 temperature dataset was therefore used to force PISM under 'present-day' climate conditions, using mean annual and mean July surface air temperature from 1970 to 2000, with an applied 1.25 amplitude scaling factor to account for seasonality (see Supplementary Information for details).

The RACMO2.3 and WorldClim2 datasets both model mean annual precipitation at Cochrane Aerodromo to be slightly higher than the measured value. At Glaciar Calluqueo, both datasets were considered to be unrepresentative of precipitation (Table 6; Supplementary Figure S2). WorldClim2 provides mean annual precipitation values at Glaciar Calluqueo ranging from 555 to 645 mm a^{-1}, lower than instrumentally measured values at Cochrane Aerodromo. At Glaciar Calluqueo, RACMO2.3 models mean annual precipitation up to 7,725 mm a^{-1}. This is considered to be an unrealistically high value given measured and modelled precipitation levels across Patagonia (Table 2), precipitation predicted at the GlaRe-ELA using the Ohmura et al. (1992) method (Table 5), and MSL's

TABLE 6 Point climate data and calculated lapse rates from instrumental records, RACMO2.3 and WorldClim2. Lapse rates are calculated relative to Cochrane Aerodromo. Instrumental data from Cochrane Aerodromo meteorological station and WorldClim2 modelled climate data cover the period from 1970 to 2000. Modelled climate data from RACMO2.3 covers the period 1979 to 2000. Instrumental data from the metrological station at San Lorenzo Sur covers the period 2002–2013 (Falaschi et al., 2015).

Location	Coordinates	m asl	Mean annual surface air temperature (°C)			Temperature lapse rate (°C m^{-1})		Mean annual precipitation (mm a^{-1} w.e.)			Precipitation lapse rate (mm m^{-1})	
			Instrumental data	RACMO	WorldClim2	RACMO	WorldClim2	Instrumental data	RACMO	WorldClim2	RACMO	WorldClim2
Cochrane Aerodromo	47°14′37″S, 72°35′06″W	182	9.4	9.1	8.6			726	741	740		
Calluqueo tongue	47°35′05″S, 72°27′25″W	600		1.4	6.3	−0.0184	−0.0056		3,042	555	5.5048	−0.4426
San Lorenzo Sur	47°41′46″S, 72°21′04″W	1,140	3.8	−1.0	3.8	−0.0105	−0.0058		2,175	547	1.4812	−0.2182
Calluqueo mid	47°35′32″S, 72°23′20″W	1,500		−2.4	1.9	−0.0087	−0.0051		6,640	619	4.4755	−0.0918
Calluqueo upper	47°36′07″S, 72°21′40″W	2000		−4	−1.1	−0.0072	−0.0054		7,225	645	3.5669	−0.0523

position inland of the Andes. Precipitation lapse rates calculated from RACMO2.3 point-data on Glaciar Calluqueo also give values higher than the few records from Patagonia (Table 2). Finally, initialising PISM using WorldClim2 and RACMO2.3 precipitation data (Experiment A) with WorldClim2 temperature data and 'default' parameter values (Table 3) produced models with too much and too little ice respectively in comparison with present-day ice extent (Supplementary Figure S3).

4.3 Tuning precipitation lapse rates (Experiment B)

A new gridded precipitation dataset was therefore created across the domain by applying a lapse rate to the mean precipitation value measured at Lord Cochrane Aerodromo (Supplementary Figure S2K). As lapse rates are poorly known and spatially variable in Patagonia (Table 2), an experiment with a range of simulated lapse rates was designed. In Experiment B, eleven simulations were therefore run in order to find the most appropriate lapse-rate value that forces the ice-flow model to best fit present-day observations of ice cap extent, volume and velocity (Figure 3). Due to the discrepancies around the ice cap (over-estimations in the north and south of the ice cap and underestimations of San Lorenzo and Rio Lacteo glaciers, which is likely related to debris cover), we aimed to obtain a best model fit with Glaciar Calluqueo (Figure 3B). This method allows precipitation values at MSL to be tuned while maintaining a realistic elevation dependence of precipitation across the domain. However, we note that the lapse-rate derived precipitation values do not capture spatially variable snow accumulation and ablation dynamics that are likely to be controlled by local topography and wind direction (see Supplementary Figure S2K). Further, while the prevailing wind conditions are usually a first-order control on snow accumulation, local terrain can significantly influence this (Małecki, 2015; Kavan et al., 2020).

Precipitation lapse rates from 0.1 to 1.5 mm m^{-1} (11 simulations) were applied to the 30 years mean annual measured precipitation value at the Lord Cochrane Aerodromo weather station (Table 4). Default flow enhancement factor (3), basal yield strength (35 kPa) and degree-day factor values (3 mm w. e. snow and 8 mm w. e. ice) were used (Table 3) alongside a constant 'present-day' WorldClim2 temperature dataset (*cf.* Experiment A).

The simulated extent of the ice cap is significantly different when the ice-flow model is forced with the gridded precipitation datasets derived from different precipitation lapse rates (Figure 3A). The difference in ice thickness between simulations is negligible at the highest elevations and steepest topographies at the centre of the ice cap (less than 1 m), which is where ice is also thinnest (approximately 50 m). Where simulations extend down to lower elevations of Glaciar

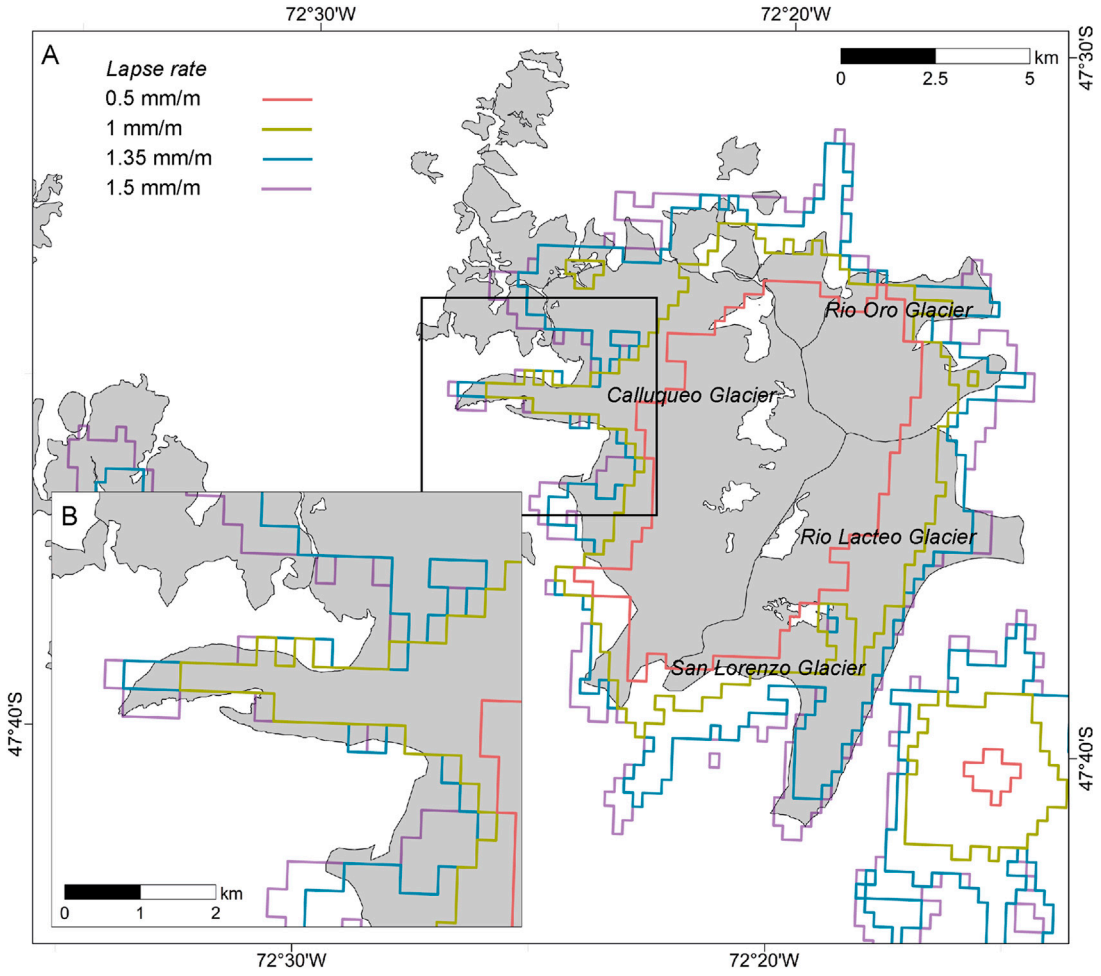

FIGURE 3
Experiment B. **(A)** Simulated ice extent produced by PISM forced using spatially variable precipitation datasets derived from different precipitation lapse rate values. The grey polygon indicates present day ice area from the RGI. **(B)** Inset map of an enlarged section of Glaciar Calluqueo.

Calluqueo, the difference in thickness varies between 5 and 10 m, with highest lapse rate simulations producing thicker ice. The thickness of Glaciar Calluqueo along this bottom 4 km section for the 1.35 mm m^{-1} lapse rate simulations is between 85 m and 100 m, similar to that modelled by Carrivick et al. (2016) (between 90 and 105 m).

The greatest difference in ice thickness between overlapping simulation outputs is at Glaciar San Lorenzo in the southeast. At its thickest point, the simulations with lapse rates of 1 mm m^{-1}, 1.35 mm m^{-1} and 1.5 mm m^{-1} have ice thickness of 334 m, 587 m and 628 m respectively. Where simulation outputs using lapse rates of 1.35 mm m^{-1} and 1.5 mm m^{-1} overlap along the lower 6 km of the glacier, the simulation forced by the higher lapse rate dataset is 40–47 m thicker along this length.

The best-fit lapse rate (1.35 mm m^{-1}) falls within the range of observed data (Table 2). This tuned dataset yields precipitation values at the ELA that are in line with those predicted by independent methods (see Section 4.1 and Table 5), providing additional confidence in the dataset. We note that it does not account for likely east-west gradients in the complex mountain topography of the study region, which are currently unquantified.

4.4 Sensitivity experiments

In Experiment C (9 simulations), the basal shear strength and ice rheology parameters were varied jointly (25 kPa, 35 kPa and 50 kPa and ice rheology of 1, 3 and 5; Table 4), whilst other parameters remained constant. This resulted in variations of ice thickness and extent (Supplementary Figure S4). A lower bed strength of 25 kPa initially leads to a longer and thinner glacier,

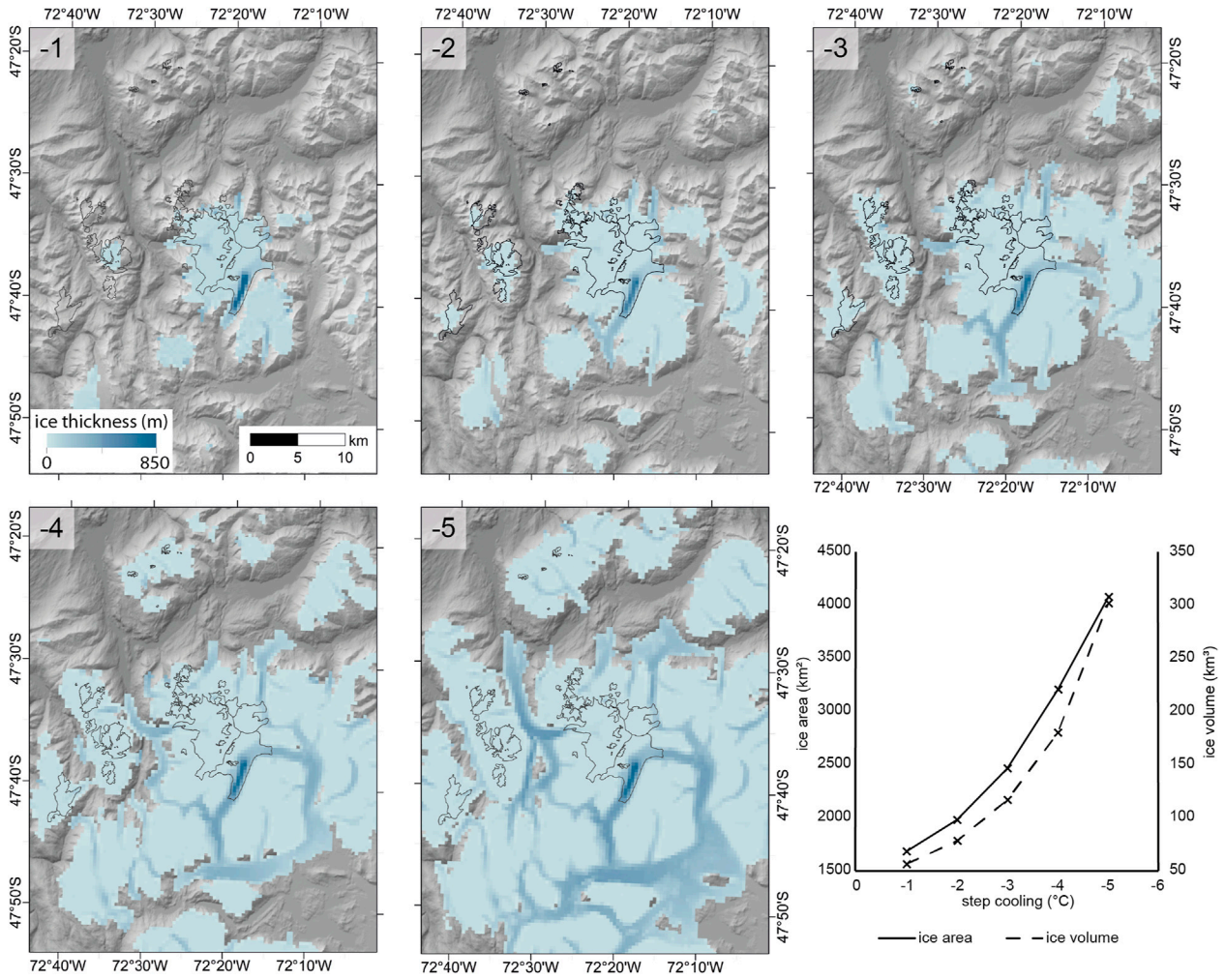

FIGURE 4
Experiment E. Model simulations of the MSL ice cap under surface air temperature step cooling of 1–5°C and present-day constant precipitation. Present-day ice extent shown as black outline. Graph shows modelled ice area and volume at equilibrium through five simulations under step cooling of −1 to −5°C.

with ice able to flow down-valley more readily. The simulations with the strongest bed strength resulted in a greater thickness of ice, which supports ablation better than the thinner glacier formed over a weaker bed (Supplementary Figure S4).

The flow enhancement factor accounts for the 'softness' of the ice and the ease with which it deforms. A flow enhancement factor of 3 produces a longer glacier profile than that produced using an enhancement factor of 1, as expected for ice that deforms more easily by internal shear (Supplementary Figure S4). A flow enhancement factor of 5 resulted in no further lengthening of the simulated glacier.

In Experiment D, the sensitivity of the modelled glaciers at MSL to changes in degree-day factors was investigated. Degree-day factors for snow of 1.5, 3 and 8 and 3, 8 and 16 for ice were chosen, to reflect the range observed globally (Lang, 1986; Takeuchi et al., 1996; Arendt and Sharp, 1999; Hock, 2003; Anderson B. et al., 2006; Möller et al., 2007; Schneider et al., 2007) and in line with previous mountain glacier modelling sensitivity studies (e.g., Golledge et al., 2012; Jouvet et al., 2017; Yan et al., 2018) (Supplementary Table S1). Setting low degree-day factors for snow and ice within PISM's positive degree day model produces a greater ice extent, as outlet glaciers flowing into low altitude valleys experience less melt for the same surface air temperature. This results in ice being maintained in the valleys (Supplementary Figure S5). Increasing ice melt (using higher degree day factor for ice) causes a greater reduction in ice extent and volume than the same change in snow melt (Supplementary Figure S5).

In Experiment E, the impact of temperature change on the simulated icefield was investigated. Running constant-climate

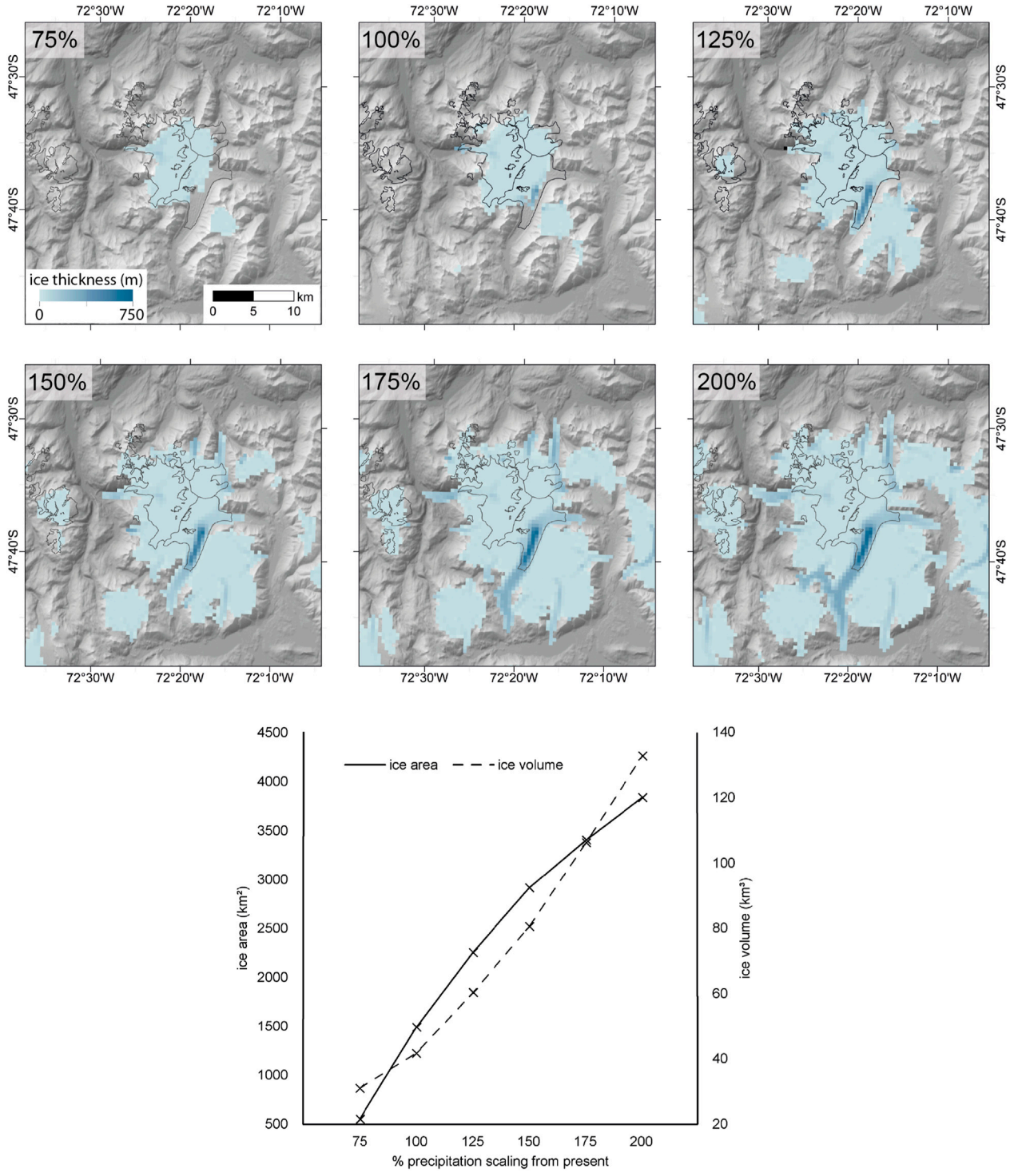

FIGURE 5
Experiment F. Model simulations of the MSL ice cap under increasingly scaled precipitation forcing from present-day. Surface air temperature is set constant to present-day. Present-day ice extent shown as black outline. Graph shows modelled ice area and volume at equilibrium through five simulations under increasingly scaled precipitation forcing.

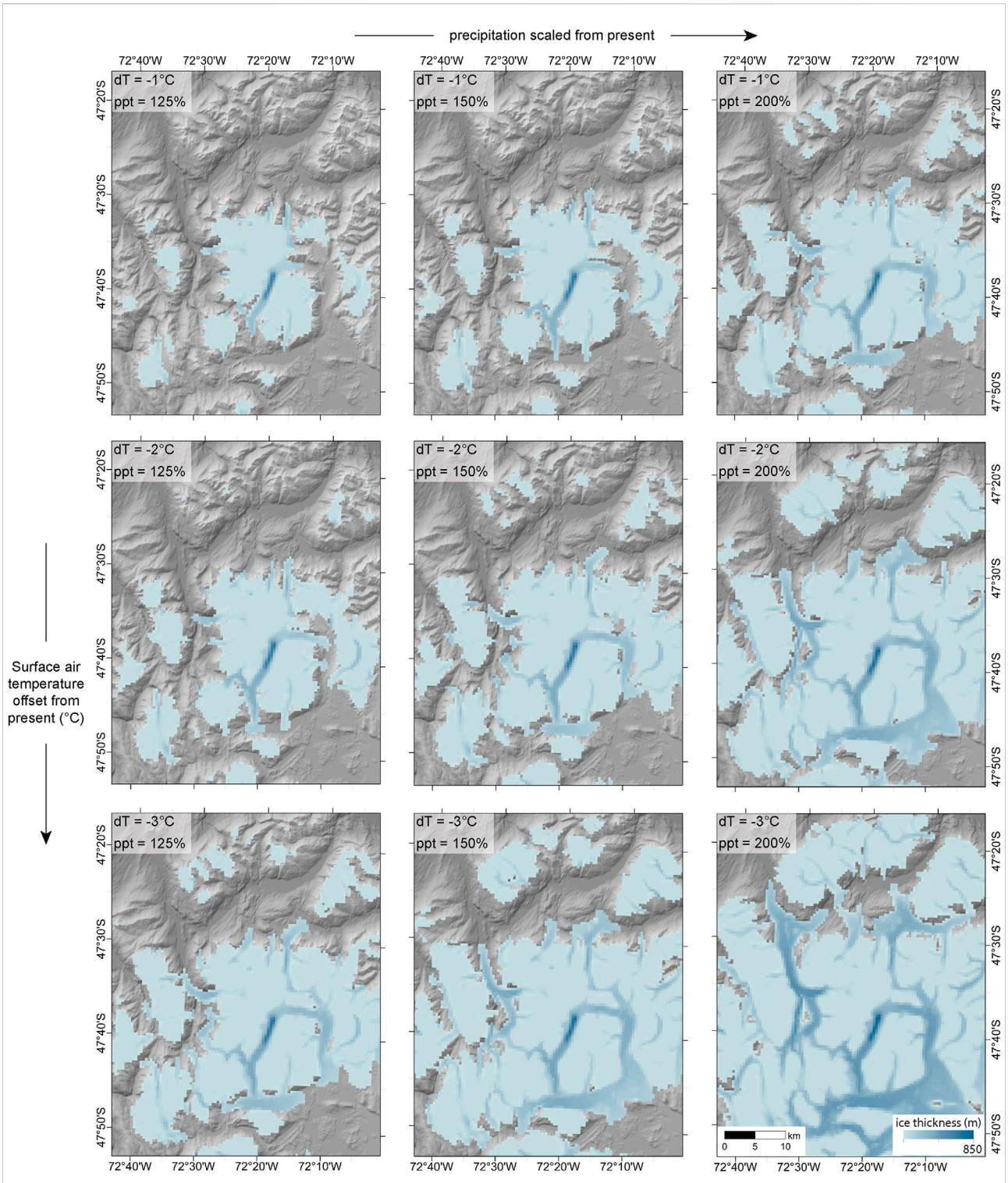

FIGURE 6
Experiment G. Model simulations of the MSL ice cap under combined surface air temperature step cooling of 1–3°C and precipitation scaling of 125%–200%.

model simulations with step cooling from −1°C to −5°C uniformly across the domain illustrates how ice area and volume expands at an increasing rate with progressively colder simulations as the ELA lowers (Figure 4). Ice cover extends over areas of highest topography, alongside the growth of outlet glaciers into lower altitude valleys. Figure 4 shows how, under a −4°C to −5°C cooling from present-day, the rate of ice area growth begins to stabilise, while the rate of ice volume growth continues to increase. This is due to the distribution of ice growth at this stage of cooling. At −5°C, the large areas of high topography are ice-covered and have stable thicknesses. Ice growth is then primarily focused in the low altitude, steep-sided valleys where ice is topographically confined and grows to large thicknesses for relatively small increases in ice area.

For Experiment F, percentage scalings of 75%, 100%, 125%, 150%, 175% and 200% modern-day precipitation were applied across the domain to the "present-day" tuned precipitation dataset; a scaling of 100% is the present-day precipitation. Model simulations forced by increasing levels of precipitation demonstrate an increase in ice area and volume across the model domain (Figure 5). Unlike with progressively colder model simulations, glacierised area does not grow at an accelerating rate as precipitation increases; the rate of ice area increase slows under the wettest scenarios. However, ice volume increases relatively linearly, as outlet glaciers begin to occupy lower altitude valleys. This provides the topographic space for increasing ice volume growth with proportionally little increase in ice area.

Precipitation and temperature were varied in combination in Experiment G. Model simulations initialised with combinations of decreasing temperature and increasing precipitation, which may have been experienced by these glaciers during previous negative phases of the Southern Annular Mode during the LGIT and Holocene (Kaplan et al., 2020), lead to significant ice growth. While separately decreasing temperature by 3°C and scaling precipitation by 200% only lead to a relatively small increase in the length of Glaciar Calluqueo (*ca* 6 km from the present-day ice front) (experiments E and F, Figures 4, 5), combining these forcings together leads to a much greater increase in glacier length of 28 km (Figure 6). This difference in ice growth at colder temperatures is due to the increased proportion of precipitation falling as snow, combined with less annual ablation. The simulation of Glaciar Calluqueo growth also shows how the glacier bifurcates at the Salto-Tranquilo valley confluence, having sufficient mass to advance up a reverse-bed gradient and dam Palaeolake Tranquilo, providing some insight into the ice-flow dynamics and accumulation areas during the ACR and LGIT. In this advanced state there is also contribution of ice from accumulation areas on the Barrancos Mountains to the west and topographic highs to the south, as well as ice growth on Cordon Esmeralda (Figure 6).

4.5 Best-fit simulation of present-day Monte San Lorenzo ice cap

4.5.1 Climatic variability across Monte San Lorenzo

The WorldClim2 temperature dataset and a mean annual precipitation value of 726 mm a^{-1} at 182 m asl, as measured at Lord Cochrane Aerodromo, with an applied lapse rate of 1.35 mm m^{-1}, produces a model output which best replicates the present-day ice cap (Figure 7A). This gives precipitation values at Glaciar Calluqueo of 1,220 mm a^{-1} at the glacier tongue (545 m asl) and 2,660 mm a^{-1} at the present-day GlaRe-ELA (1,615 ± 20 m asl). Precipitation increases to 5,480 mm a^{-1} at the summit of the massif (3,706 m asl). Precipitation between *ca* 1,200 and 5,500 mm a^{-1} at MSL, 70 km to the east of the NPI, falls within the range of the limited precipitation data available to the east of the Patagonian Icefield. The use of PISM's default positive degree day melt factor values in this present-day simulation adds further confidence that the precipitation estimate is as realistic as we are able to produce, given the absence of empirical data.

There is a good fit for the simulation at Glaciar Calluqueo, where the glacier underfits the observed geometry by only 250 m in length and width (Figure 7A). The simulation is within 75 m of the ice thicknesses predicted by Carrivick et al. (2016). The simulation overfits Glaciar Arroyo San Lorenzo to the north to a greater extent, by 2.5 km in glacier length (Figure 7A). This overfit is likely because the west-east spatial variation in precipitation across the ice cap is not well replicated by the precipitation lapse rate model dataset, making these high elevation valleys too wet. With the dominant precipitation source from the westerly winds, the north-east and south-east aspects of the valleys catchments are likely drier than the lapse rate derived precipitation dataset predicts. Reconstructing topographically controlled precipitation is especially difficult in mountain environments where topography is complex and changes dramatically over a small area.

The model underestimates the extent of the San Lorenzo and Rio Lacteo glaciers by 300 and 880 m respectively. These glaciers are covered by a thick layer of debris, which insulates the ice, reducing melting. PISM simulations do not account for this reduction in melt, and hence will simulate debris-covered glaciers to be lesser in extent than those observed.

4.5.2 Glacier mass balance

The present-day optimal-fit simulation of the MSL ice cap simulates grid cells with accumulation over the high peaks of up to 5.5 m w. e. a^{-1} (Figure 7C). At an elevation of 3,000 to 2000 m asl, accumulation is between 4.5 and 2.5 m w. e. per grid cell, decreasing to 1 to 0.5 m w. e. at the tongues of the Calluqueo and San Lorenzo Sur glaciers (1,250–500 m asl). Ablation is up to 18 m w. e. on the tongue of Glaciar Calluqueo and 12.5 m w. e. on the flat plateau of Glaciar San Lorenzo Sur (Figure 7D). Ablation decreases with elevation up

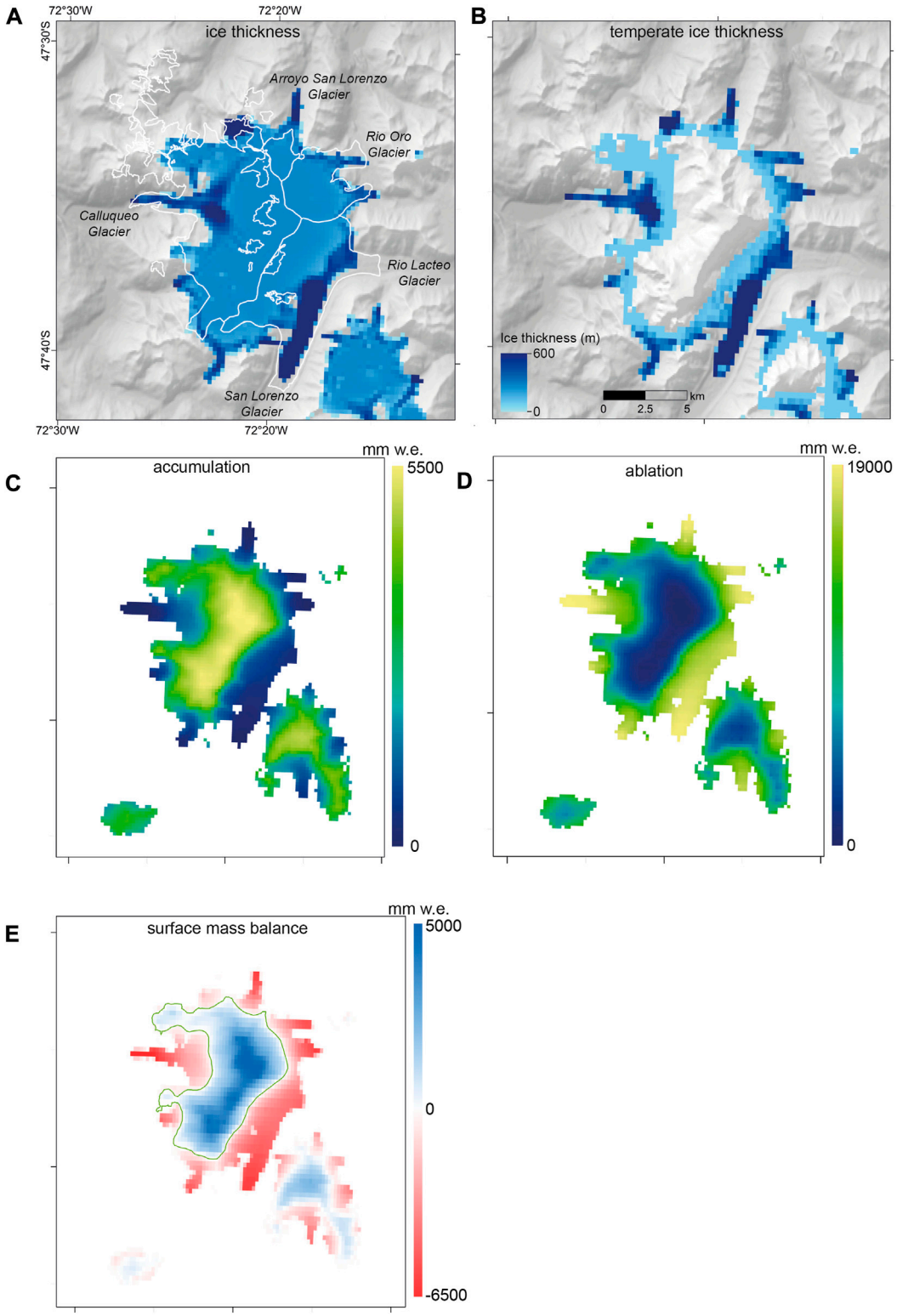

FIGURE 7
Total ice thickness **(A)** and temperate ice thickness **(B)** for the best-fit scenario of the modelled MSL ice cap. The white lines in **(A)** denotes the present-day ice extent and glacier catchment divides. Spatial distribution of annual accumulation **(C)**, ablation **(D)** and surface mass balance **(E)** across the MSL ice cap. The green line in **(E)** denotes the Equilibrium Line. Tick marks represent latitude and longitude (as shown in panel A).

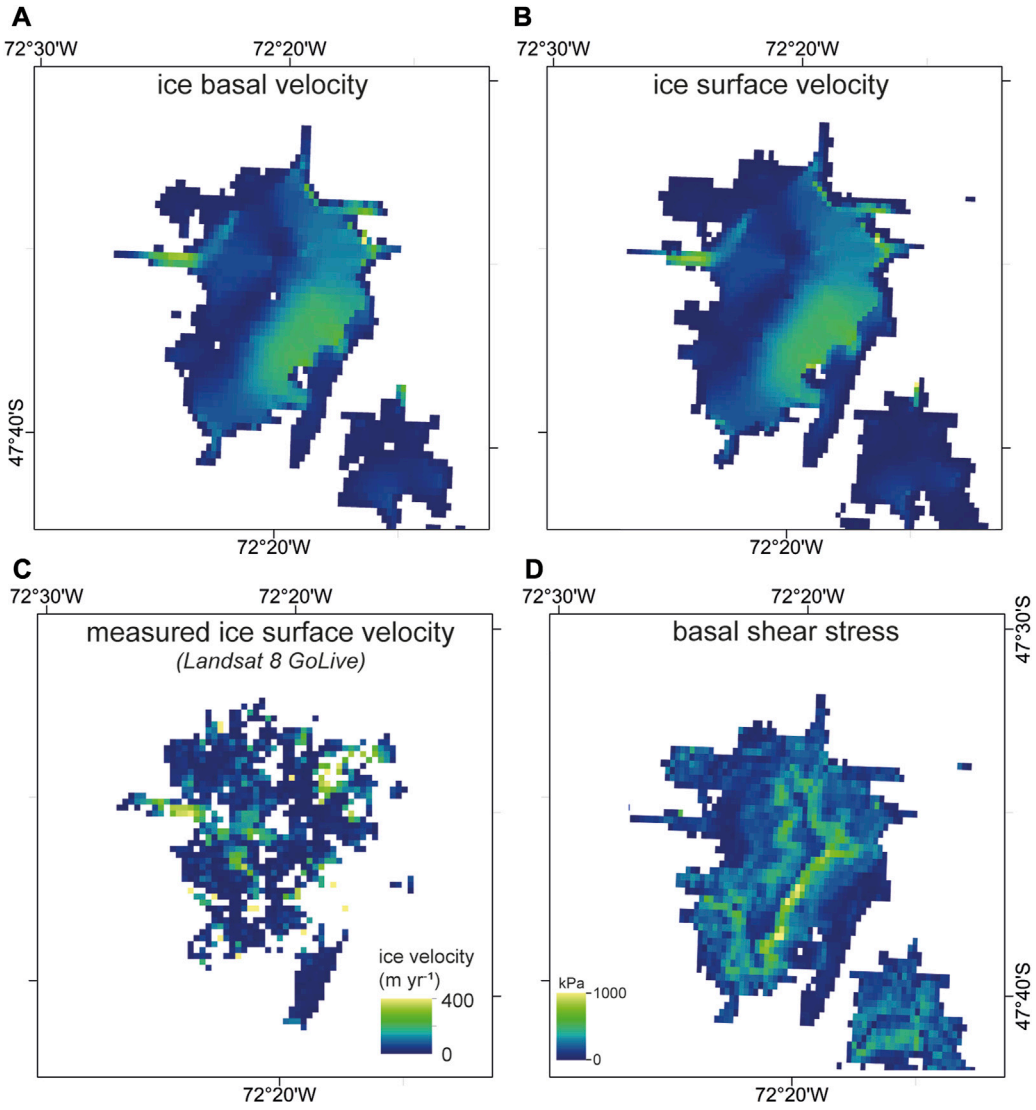

FIGURE 8
Basal ice **(A)** and surface ice **(B)** velocity of the modelled MSL ice cap. **(C)** Ice surface velocity of the MSL ice cap taken from the Global Land Ice Velocity Extraction from Landsat 8 (GoLIVE), Version 1 (image L8_231_093_032_2017_307_2017_339_RTT1, 3/11/2017 to 5/12/2017) (Fahnestock et al., 2016; Scambos et al., 2016). **(D)** Modelled basal shear stress opposing the driving stress resulting from gravity.

the ice cap, with a minimum of 0.5 mm w. e. annual ablation at the highest elevations.

Our model data provides a first indication of average mass balance conditions (1970–2000) at different locations on the icefield. The maximum measured annual surface mass balance of the MSL ice cap is a point measurement of 4.8 m w. e. at the massif's peak, decreasing to zero at the equilibrium line between 1750 m asl and 2000 m asl (Figure 7E). The lowest mass balance occurs at the glacier tongues, with values of −3 m w. e. to −6.5 m w. e. in the lower ablation area of Glaciar Calluqueo. It should be acknowledged that in these simulations the ice cap is modelled to a state of equilibrium with climate (1970–2000). In reality outlet glaciers at MSL are receding and thinning (Falaschi et al., 2013; 2019), and therefore it would be expected that the distribution of mass balance is more negative. This is observed in mass balance measurements from geodetic data at Calluqueo Glacier from Falashci et al. (2019).

4.5.3 Ice velocity, basal sliding and temperate ice

Figure 8A shows a basal ice velocity up to *ca* 330 m a^{-1}, demonstrating basal sliding at the ice cap, in particular at locations of steepest bedrock slope, at Glaciar Calluqueo in the west and in the catchment of Glaciar San Lorenzo in the

TABLE 7 Calculations of precipitation based upon GlaRe-ELA reconstructions following the method of Ohmura et al. (1992) under given temperature offsets from present (West Antarctic Ice Sheet (WAIS) Divide surface air temperature reconstruction (Cuffey et al., 2016). Temperature and precipitation forcing combinations which initialise the ice cap model to best fit empirical ice extent reconstructions are also listed.

Time period	Temperature offset from present (°C) at this time (WAIS divide ice core record)	Palaeo-precipitation difference to present (%) at GlaRe-ELA (ohmura method, Table 5)*	Independent palaeoclimate forcing required to best-fit empirical reconstructions in PISM		
			Temperature offset from present (°C)	Model precipitation from tuned dataset (mm m^{-1} w.e.) at GlaRe-ELA (*cf.* Table 5)	Model precipitation scaled from present (%)
Late-Holocene (200 years BP) (M13)	−0.7	112–127%	-1	2,783	125%
Mid-Holocene (*ca* 5.6 ka) (M13)	−0.3	119–134%	0	3,339	150%
12.1 ka (M12)	−1.1	123–140%	-2	2,967	150%
ACR (M1), 14.5–12.8 ka	−3		-3		150–200%

southeast. A marked similitude of basal and surface velocities (shown in Figures 8A,B) indicates that internal shear plays less of a role in ice flow and that the internal deformation velocity is negligible; rather, much of the ice velocity is derived through basal sliding.

The simulation shows good agreement with observed ice surface velocity (Fahnestock et al., 2016; Scambos et al., 2016) (Figure 8C). The model replicates well the ice surface velocity field at Glaciar Calluqueo, particularly in the area of fast ice flow at the lower section of the glacier. The modelled ice surface velocities of 320–340 m a^{-1} in this area shows a good agreement with the GoLIVE measured velocity of 340–390 m a^{-1}. The GoLive dataset shows two areas of faster flowing ice at higher elevations in the accumulation area of Glaciar Calluqueo, with velocities from 150 to 290 m a^{-1} (Figure 8C). These fastest ice velocities occur in areas with steeply sloping, heavily crevassed ice. Modelled velocities here are lower, at a maximum of 70 m a^{-1}, perhaps due to domain resolution not picking up these highly topographically controlled areas of rapid ice flow, or because the areas are modelled as cold-based (Figure 7B). The rest of the accumulation area has low ice velocities, with good agreement between modelled ice surface velocities and GoLive velocities.

High basal shear stresses across the ice cap greater than the constant basal shear strength of 35 kPa (Figure 8D) enable basal sliding, facilitated by temperate ice at the pressure melting point. At Glaciar Calluqueo, basal shear stresses are between 50 kPa and 200 kPa (Figure 8D). Temperate ice is found at MSL's outlet glaciers, where ice is thickest, the bed is insulated, and surface air temperature is warmer due to lower elevations (Figure 7). At highest elevations at the top of the massif, thinner ice and colder surface air temperatures thus results in cold-based ice, frozen to the bed and unable to slide.

4.6 Palaeoclimates and late glacial readvances

We examined the palaeoclimatic conditions required to explain past ice-cap extents by forcing the tuned simulation of the present-day ice cap with a suite of temperature and precipitation values, which was then assessed against ice cap extents reconstructed from empirical data (Sagredo et al., 2016; 2018; Davies et al., 2018, 2020; Martin et al., 2019; 2022; Mendelová et al., 2020) (Figure 2). Here, we evaluated the different temperature and precipitation values required to simulate mapped glacier extents through the Holocene and LGIT (Table 7). The WAIS Divide temperature (Cuffey et al., 2016) and ELA-based palaeo-precipitation reconstructions (Table 5) provide an independent indication of past climatic conditions for comparison.

4.6.1 Holocene advances

Figure 9 shows the best fit model simulations to reconstruct the ice extent for the Late-Holocene and mid-Holocene (A, B and C) (empirical reconstructions from Davies et al., 2020; 2018; Martin et al., 2019; 2022). During the mid- and Late-Holocene, periodically negative phases of the SAM brought cooler, wetter conditions to Patagonia (Abram et al., 2014; Reynhout et al., 2019; Kaplan et al., 2020), forcing glacier advances. In many cases, advances during the mid- and Late-Holocene re-occupied the same moraines, as seen at MSL.

For the Late-Holocene (*ca* 200 years BP), a combination of a temperature 1°C cooler than present and 125% of modern precipitation (Figure 9B; Table 7) most closely fits the empirical reconstruction and is in line with temperature offsets suggested by ice-core data (Cuffey et al., 2016) and our precipitation reconstructions using glacier equilibrium lines

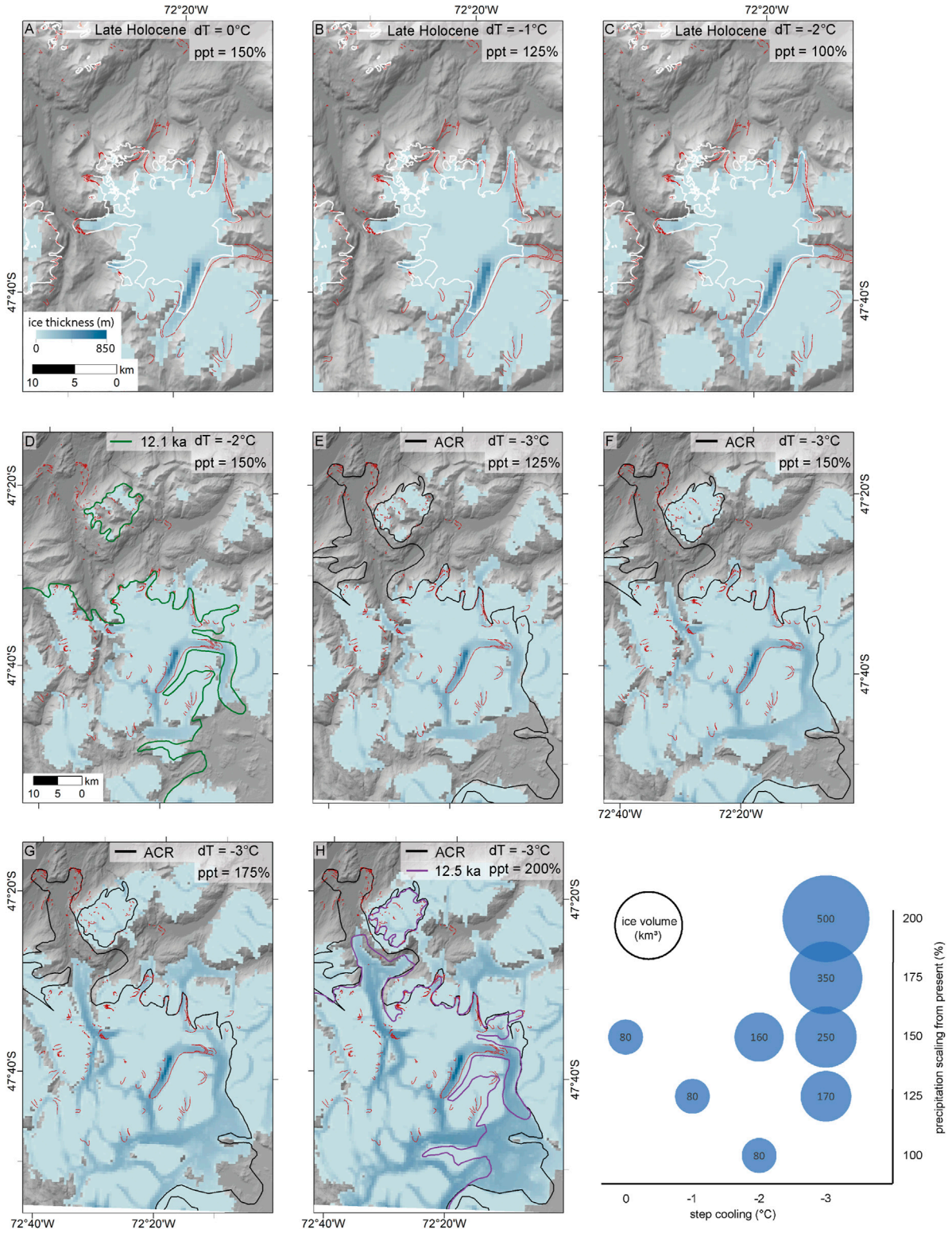

FIGURE 9
Model simulations of the MSL ice cap under combined surface air temperature step cooling of 1–3°C and precipitation scaling of 125%–200% to best fit palaeo ice mass reconstructions from the Late Holocene **(A,B)**, mid-Holocene **(B,C)**, ca 12.1 ka **(D)**, 12.5 ka and the ACR **(E-H)**. Moraines are shown in pink. Scatter plot shows how ice volume changes with different combinations of temperature and precipitation forcing.

(Table 5). Model outputs suggests that ice surface velocities at Glaciar Calluqueo ranged between 250 m a^{-1} and 400 m a^{-1}, similar to the modelled present-day glacier (Figure 6).

During the mid-Holocene (*ca* 5.6 ka) (Sagredo et al., 2016), a negative phase of the SAM brought increased precipitation to central Patagonia. A 0°C offset and 150% precipitation increase forced glacier advance to the mid-Holocene moraines (Figure 9A), which is similar again to the climatic variations suggested by palaeoclimatic ice-core data and Table 5. Modelled ice surface velocity was found to be slightly higher than present day on Glaciar Calluqueo, between 250 m a^{-1} and 600 m a^{-1} at their highest.

4.6.2 Advances during the last glacial-interglacial transition

The best fit model simulation to ice at the 12.1 ka reconstruction of Glaciar Calluqueo (Martin et al., 2022) requires model initialisation of −2°C and 150% precipitation from present, 0.9°C colder and >10% wetter than from the WAIS Divide temperature and ELA precipitation reconstruction (Figure 9D; Table 7). This envelope of palaeoclimatic conditions during the LGIT is the first available from numerical modelling for Patagonian icecaps. Modelled surface ice flowed significantly faster than the present-day, with the fastest ice flow on Glaciar Calluqueo between 1,000 m a^{-1} and 1700 m a^{-1}.

The WAIS-Divide record suggests that surface air temperature at the ACR was up to 3°C colder than present in Antarctica, and Patagonian pollen and charcoal records indicate a cold and wet climate during this period (Moreno, 2004; Whitlock et al., 2007; Villa-Martínez et al., 2012). Model runs at -3°C from present and 200% present-day precipitation are not able to simulate the full extent of Glaciar Calluqueo at the ACR (Figure 9H), producing a glacier 16 km short of the ACR Esmeralda Moraine (*cf.* Davies et al., 2018). However, it does capture the growth of a substantial ice accumulation area in the Barrancos Mountains and Cordon Esmeralda, and gives insights into ice flow and dynamics during the ACR. Although the simulation in the Salto valley underfits, it does show a major advance, with accumulation in the adjacent high grounds, during the ACR. As Glaciar Calluqueo extended further down Pedregoso valley, ice velocities stabilised in comparison with those modelled for 12.1 and 12.5 ka, with maximum velocities between 500 m a^{-1} and 525 m a^{-1}. Ice extending to the southeast of MSL flowed at lower velocities, between 150 m a^{-1} and 250 m a^{-1} at its fastest.

A temperature 3°C cooler and a 200% precipitation change relative to present matches the advance on the eastern side of the massif well, with the outlet glaciers reaching the ACR-dated Belgrano moraines (Mendelová et al., 2020) (*cf.* Figures 1, 9H). The −3°C offset and 150% precipitation increase simulation fits Glaciar Tranquilo in the north of MSL ice cap well as well (Figure 9F). Increasing precipitation to 200% results in an overfit here (Figure 9H), likely due to an overestimation of precipitation as the strong east-west orographic precipitation gradient is not taken into account. Given the northeast orientation of Glaciar Tranquilo's catchment, a lower level of precipitation would be expected than is found within the lapse rate-derived precipitation dataset for the lee side of MSL.

The discrepancies seen between the model simulations of Glaciar Calluqueo and WAIS Divide-ELA climate reconstructions at the ACR are likely because at the ACR, ice was in a period of readvance during overall deglaciation from the LGM. The climate conditions at this point therefore reflect a readvance and stabilisation from an already large ice mass and are not cold enough to force the simulation to form such a significant mass of ice from the smaller modern MSL ice extent.

5 Discussion

5.1 Dynamics of Monte San Lorenzo ice cap

Our study provides a novel modelling approach to the analysis of the components of mass balance of a Patagonian ice cap. We show accumulation at MSL of up to 4.5 m w. e. at high elevations, decreasing to 1 m w. e. on the Glaciar Calluqueo tongue. Ablation in this high through-put system is 18 m w. e. on Glaciar Calluqueo tongue, and decreases to 0.5 m w. e. at the highest elevations. There are few comparative modelling or empirical studies available, but these values fall within the typical range expected east of the watershed. We show high ice velocities (320–340 m a^{-1}), driven by basal sliding. These velocities are in line with observations (Millan et al., 2022). Basal sliding throughout the year has also been suggested at Glacier Perito Moreno from field observations (Skvarca and Naruse, 1997) and from numerical modelling at Glaciar San Rafael (Collao-Barrios et al., 2018). However, at MSL, a basal layer of temperate ice with basal sliding is found only in the ablation areas, with cold-based ice and lower ice velocities at higher elevations. An exception to this occurs on the eastern side of the ice cap, where extremely steep headwalls lead to ice velocities between 80 and 200 m a^{-1}. MSL is sensitive to changes in basal yield shear strength (arising for example from an increase in basal meltwater input), which could result in dynamic thinning of the glacier.

5.2 Glacier sensitivity to climate

The sensitivity of glacier mass balance to changes in various climate variables, and the proportion to which each climate variable impacts glacier mass change, shows a wide spread across the globe (Mackintosh et al., 2017). Accumulation shows its highest sensitivity to temperature at the snow/rain threshold

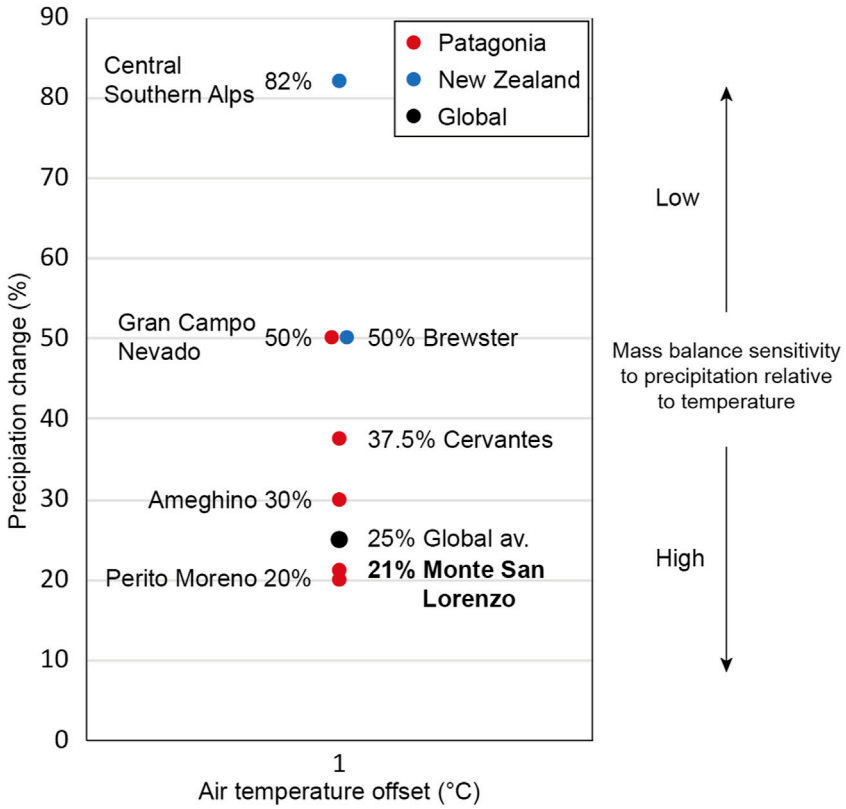

FIGURE 10
Precipitation change equivalent to 1°C change in air temperature at glaciers in Patagonia and New Zealand and a global average (black circle (Oerlemans, 2005),). Red circles are glaciers in Patagonia at Perito Moreno, Ameghino and Cervantes glaciers on the eastern side of the Southern Patagonian Andes (Bippus, 2007) the Gran Campo Nevado ice cap in southern Patagonia (53°S) (Möller et al., 2007) and the MSL ice cap (this study). Blue circles are glaciers in New Zealand's Southern Alps at Brewster Glacier (Anderson et al., 2010) and an average of a collection of glaciers from the central Southern Alps, including Franz Joseph, Fox and Tazman Glaciers (Anderson and Mackintosh, 2012).

(usually between 0 and 3°C) (Anderson and Mackintosh, 2012). This relationship is strongest where precipitation is highest, such as in maritime environments (e.g., Purdie et al., 2008; Cullen and Conway, 2015). Temperate climate and low continentality (the difference in mean temperature between the warmest and coldest month) imply a larger proportion of the year with temperatures high enough for melt (Anderson and Mackintosh, 2012). These factors combined lead to a high mass turnover and result in maritime glaciers having the highest sensitivity to changes in climate (Meier et al., 2018; Oerlemans, 2005; Braithwaite et al., 2002).

Using our numerical model, it is possible to ascertain the relative sensitivity of the ice cap to temperature and precipitation changes. Our sensitivity experiments independently simulating the ice cap under step changes in temperature and precipitation show that a 1°C offset in surface air temperature is equivalent to a 21% change in precipitation in terms of obtaining the same change in ice volume. Glaciers with a higher change in precipitation equivalent to a 1°C change in temperature are less sensitive to precipitation; glaciers where a smaller percentage change in precipitation is required to force an equivalent glacier change to a 1°C change in temperature are more sensitive to precipitation. The global average is 25% precipitation change (Oerlemans, 2005).

We compare our results with other studies from across the Southern Hemisphere mid-latitudes. Here, a 1°C offset in surface air temperature is equivalent to a 20%–83% precipitation change (Figure 10) (Anderson et al., 2006; Bippus, 2007; Möller et al., 2007; Anderson et al., 2010; Anderson and Mackintosh, 2012). More maritime glaciers in New Zealand's Southern Alps and in southern Patagonia are less sensitive to precipitation relative to temperature. For example, at Glaciar Perito Moreno (20% precipitation change equivalent to 1°C temperature change; Bippus, 2007) precipitation has a proportionally greater impact on glacier mass balance relative to temperature than at the more maritime Gran Campo Nevado (50% precipitation change equivalent to 1°C temperature change; Möller et al., 2007).

At the most strongly maritime glaciers, where there is a higher level of precipitation falling close to the snow/rain

threshold temperature, the impact of a small change in temperature on mass balance, by changing the proportion of precipitation that falls as snow or rain, is exacerbated. Glaciers with comparatively higher mass balance sensitivity to precipitation compared with temperature are those with greater continentality, as is the case for MSL, on the eastern side of the Patagonian Andes. Therefore, at MSL, compared with the other Patagonian and New Zealand glaciers studied, and the global average, precipitation plays a greater role in mass balance than temperature.

Further, there are morphological contrasts between the Cervantes, Ameghino, MSL and Perito Moreno glaciers presented in Figure 10. Glaciar Perito Moreno and Glaciar Calluqueo have much higher accumulation area ratios (0.68 at Glaciar Calluqueo) and hence a smaller change in precipitation is needed for an equivalent mass balance change from a 1°C temperature variation. Although the dominant control on glacier mass balance is still temperature due to the strong empirical impact of temperature on accumulation (Anderson and Mackintosh, 2012), the precipitation changes observed at MSL will have a proportionally higher impact on mass balance than for many other glaciers in Patagonia.

5.3 Insights into ice dynamics during the last glacial-Interglacial transition

Empirical reconstructions of palaeo-ice dynamics (e.g., Figure 2), such as PATICE (Davies et al., 2020) or reconstructions of other ice sheets (Hughes et al., 2016; Batchelor et al., 2019; Dalton et al., 2020), rely on spatially limited data to constrain large areas of terrain. These reconstructions mostly rely on moraine limits in valleys and lowlands, with and without chronological control, to understand the extent and timing of former ice limits. They do not account for realistic ice-flow, especially in areas where bedforms such as mega-scale glacial lineations or drumlins are absent (*cf.* Clark et al., 2012). Ice volume and thickness are particularly challenging to constrain from these empirical data (Stokes et al., 2015; Davies, 2021). Numerical modelling provides additional data regarding past ice dynamics, including how glacier morphology evolves under different climates, especially in the upper reaches, where geomorphological data are absent.

In the case of Glaciar Calluqueo, numerical modelling provides information on glacier-tongue bifurcation at the junction of the Pedregoso and Tranquillo valleys. Our simulations showed the ice volume required to damn Río Tranquillo, forming Palaeolake Tranquillo. These simulations also illustrated the growth of multiple glacier accumulation zones across the Barrancos Mountains, with growing glaciers on Cordon Esmeralda that could have contributed ice during the LGIT. This helps to explain why the advance during the ACR was so much larger than that of Glaciar Tranquilo, which has a much smaller accumulation area. We are additionally able to gain insights into former ice velocities and mass balances, providing a deeper understanding of glacier-climate relationships and ice dynamics. These data are unavailable from the geomorphological record. Our numerical modelling experiments therefore add depth to the landform-derived reconstructions previously published in this area (Sagredo et al., 2016; 2018; Garibotti and Villalba, 2017; Davies et al., 2018, 2020; Martin et al., 2019; 2022; Mendelová et al., 2020).

We find that both cooler and wetter climates are needed to force readvances of these glaciers during the LGIT and Holocene, due to their temperate climate and high ablation rates. This supports previous work from proxy data, which shows that cooler, wetter conditions associated with changing Southern Westerly Winds are required to force Holocene advances (Moreno et al., 2018; Kaplan et al., 2020), though there are few direct quantitative records of precipitation available (Kilian and Lamy, 2012). The sensitivity of MSL to precipitation suggests that the rapid recession observed between 12.8 ka, when Glaciar Calluqueo was at the mouth of the valley (*cf.* Glasser et al., 2012) and 12.1 ka (Martin et al., 2022) was likely driven by both post-ACR temperature increase and a decrease in precipitation. At this time, a southward shift to *ca* 55°S in the Southern Westerly Winds is suggested by changing lake levels at Lago Cardiel (Quade and Kaplan, 2017), which would reduce precipitation at MSL (47.5°S). This would have contributed to the glacier's rapid recession.

We are able to provide the first quantitative estimates for temperature and precipitation at key periods during the Late Glacial and Holocene. Firstly, meeting the readvance or stabilisation noted at 12.1 ka for Glaciar Calluqueo requires a cooling of 2°C and precipitation to increase to 150% of current values. An increase in precipitation at this time is likely, as noted by lake-level studies at Lago Cardiel, which increased to its hydrological maximum (136% of current level) by 11.3 ka (Quade and Kaplan, 2017). A readvance of glaciers at this time has been noted in other catchments (Mercer, 1968; 1976; Marden and Clapperton, 1995; Strelin and Malagnino, 2000; Glasser et al., 2012; Harrison et al., 2012; Menounos et al., 2013; Mendelová et al., 2020); however it has been queried whether this readvance was climatically driven or related to base level fall in ice-dammed lakes (Davies et al., 2020). Our modelled data suggests that a climatic driver (cooling and increased precipitation) is needed to force glaciers to readvance or stabilise at ~11 to 12 ka, post-dating the ACR.

5.4 Insights into holocene palaeoclimates

Proxy palaeoclimatic evidence indicates less strong cooling during the Mid-Holocene readvance (5.6 ka) reconstructed for

MSL (Sagredo et al., 2016), and we find that increasing precipitation to 150% of current values is required. There are widespread moraines around this region of Patagonia dating to the mid-Holocene, typically close to and just outside of those deposited during the Late Holocene readvances at 1–2 ka and 0.2–0.5 ka (Mercer, 1976; Fernandez et al., 2012; Nimick et al., 2016; Sagredo et al., 2016; Garibotti and Villalba, 2017; Reynhout et al., 2019; Davies et al., 2020). This period was a time of persistent negative Southern Annular Mode conditions, with an expansion northwards of the Southern Westerly Winds and a cold and wet climate forcing glacier growth (Moreno et al., 2018). This is in agreement with previous climate model simulations, which have suggested that during this mid-Holocene period (4–6 ka), cooling was limited, with changes of −0.2°C in the summer (the key time to influence ablation), −0.5°C in autumn, −0.4°C in winter, and warmer temperatures in the spring (0.2°C) (with respect to current values; Bravo et al., 2015). Bravo et al. (2015) argue that there was limited change in precipitation, but there was a seasonal shift, with more occurring in the principal accumulation season from October to April. While we did not change the seasonality in our sensitivity or palaeoclimate experiments, this would have a similar impact on the glaciers to increasing mean annual precipitation, by providing more accumulation, while summer cooling decreases ablation. Indeed, other studies have inferred increased precipitation at this time (Van Daele et al., 2016), so our reconstruction is in good agreement with results by Bravo et al. (2015) and Van Daele et al. (2016).

Finally, we find that a cooling of 1°C relative to today, together with a precipitation 125% of today's values, is sufficient to force the readvance observed during the Late Holocene (0.2–0.5 ka). A readvance at this time is widely recognised in Patagonia (Masiokas et al., 2009; Davies and Glasser, 2012; Meier et al., 2018; Davies et al., 2020), with widespread deposition of moraines (Kaplan et al., 2016). Tree-ring and modelling-based temperature reconstructions agree with the ice-core record of cooling of 1–2°C at this time (Villalba et al., 2005; Kaplan et al., 2016). Our estimate is, however, one of the first quantified estimates of precipitation change during the Late Holocene in this region of Patagonia.

6 Conclusion

In this study, we used the Parallel Ice Sheet Model (PISM) to model a Patagonian ice cap. We undertook a series of experiments that used systematic iterations of different parameters within the model in order to establish the key controls on the modelled icefield and define the envelope of parameter space within which the results agree most closely with the present-day observed icefield. We were then able to define the palaeoclimatic envelopes that best approximate the mean palaeoclimatic conditions during readvances of the ice cap during the Late Glacial period.

We produced a simulation of the MSL ice cap matching present-day ice distribution, when initialised using the WorldClim2 modelled surface air temperatures and a precipitation dataset built from a tuned lapse rate (1.35 mm m^{-1}). This dataset results in mean annual precipitation at Glaciar Calluqueo, MSL, between 1,200 and 5,500 mm a^{-1}. These values are in line with sparse local measured records and regional modelled climate data.

Sensitivity experiments demonstrate that higher basal shear strength leads to a thicker and longer profile of Glaciar Calluqueo, due to the impact of ablation at low altitudes following rapid initial ice growth. Furthermore, they demonstrate a significant sensitivity of the model to changes in positive degree day snow and ice melt factors, with greater sensitivity to melting of ice in the ablation area than a reduction in mass input through snow melt in the accumulation area.

Cold-based ice, frozen to the bed, occupies higher elevations of the MSL ice cap (> *ca* 1,800 to 2,200 m asl), while temperate, warm-based ice is found at lower elevations in outlet glaciers. Temperate ice flows *via* basal sliding at up to 330 m a^{-1}, with negligible internal ice flow velocity. The simulated ice cap shows high surface mass flux, with ablation at outlet glacier tongues up to 18 m w. e. a^{-1}, and accumulation at highest elevations up to 5.5 m w. e. a^{-1}. Surface mass balance ranges from +4.8 m w. e. a^{-1} to −6.5 m w. e. a^{-1} with a simulated ELA between 1,750 m asl and 2,000 m asl.

Simulations initialised with a varied combination of temperature and precipitation values show that the model matched temperature and precipitation reconstructed from the WAIS Divide ice cores during the latest Holocene readvance. However, greater discrepancy is seen with simulations of greater ice extent, requiring further investigation through higher resolution and transient simulations. The MSL ice cap, situated to the east of the Andean cordillera with high continentality, is more sensitive to precipitation compared with temperature than the markedly maritime glaciers of the NPI and SPI, Gran Campo Nevado and glaciers of New Zealand's Southern Alps. For MSL, a 1°C offset in surface air temperature is equivalent to a 21% change in precipitation. Our data suggest that palaeoenvironmental reconstructions and modelling of smaller ice caps east of the Andes could provide important insights into latitudinal shifts in the South Westerly Winds.

At 47°S, our modelling of Monte San Lorenzo demonstrates that cooler, wetter conditions are needed to drive reconstructed glacier advances at 0.2–0.5 ka, 5.6 ka and 12.1 ka, with temperature offsets of −1°C and 125% of modern precipitation (0.2–0.5 ka), 0°C and 150% precipitation (5.6 ka), and −2°C and 150% precipitation (12.1 ka). This new understanding of glacier sensitivity to temperature and precipitation change improves our ability to quantify the climatic drivers of past and present glacier fluctuations.

Data availability statement

The original contributions presented in the study are included in the article/Supplementary Material, further inquiries can be directed to the corresponding author.

Author contributions

This work was undertaken as part of a studentship awarded to JM at Royal Holloway University of London. The project was conceptualised, initialised and guided by BD and VT; the numerical modelling was undertaken by JM in collaboration with and guided by RJ.

Funding

JM was supported by a Natural Environment Research Council award NE/L002485/1.

Acknowledgments

Jan Leanarts is gratefully thanked for processing the RAMCO 2.3 climatic dataset for use in PISM. Nick Golledge is thanked for his advice and assistance in running PISM. We thank three reviewers for their constructive comments, which helped to improve the manuscript.

Conflict of interest

The authors declare that the research was conducted in the absence of any commercial or financial relationships that could be construed as a potential conflict of interest.

Publisher's note

Supplementary material

The Supplementary Material for this article can be found online at: https://www.frontiersin.org/articles/10.3389/feart.2022.831631/full#supplementary-material

References

Abram, N. J., Mulvaney, R., Vimeux, F., Phipps, S. J., Turner, J., and England, M. H. (2014). Evolution of the Southern Annular Mode during the past millennium. *Nat. Clim. Chang.* 4, 564–569. doi:10.1038/nclimate2235

Anderson, B., Lawson, W., Owens, I., and Goodsell, B. (2006). Past and future mass balance of 'ka roimata o hine hukatere' Franz Josef glacier, New Zealand. *J. Glaciol.* 52, 597–607. doi:10.3189/172756506781828449

Anderson, B., and Mackintosh, A. (2012). Controls on mass balance sensitivity of maritime glaciers in the Southern Alps, New Zealand: The role of debris cover. *J. Geophys. Res.* 117. doi:10.1029/2011jf002064

Anderson, B., Mackintosh, A., Stumm, D., George, L., Kerr, T., Winter-Billington, A., et al. (2010). Climate sensitivity of a high-precipitation glacier in New Zealand. *J. Glaciol.* 56, 114–128. doi:10.3189/002214310791190929

Anderson, B., and Mackintosh, A. (2006). Temperature change is the major driver of late-glacial and Holocene glacier fluctuations in New Zealand. *Geol.* 34, 121–124. doi:10.1130/g22151.1

Arendt, A., and Sharp, M. (1999). *Energy balance measurements on a Canadian high Arctic glacier and their implications for mass balance modelling*. Birmingham, UK: IAHS Publ., 165–172.

Aristarain, A. J., and Delmas, R. J. (1993). Firn-core study from the southern Patagonia ice cap, South America. *J. Glaciol.* 39, 249–254. doi:10.3189/s0022143000015914

Aschwanden, A., Aðalgeirsdóttir, G., and Khroulev, C. (2013). Hindcasting to measure ice sheet model sensitivity to initial states. *Cryosphere* 7, 1083–1093. doi:10.5194/tc-7-1083-2013

Aschwanden, A., Bueler, E., Khroulev, C., and Blatter, H. (2012). An enthalpy formulation for glaciers and ice sheets. *J. Glaciol.* 58, 441–457. doi:10.3189/2012JoG11J088

Aschwanden, A., Fahnestock, M. A., and Truffer, M. (2016). Complex Greenland outlet glacier flow captured. *Nat. Commun.* 7, 10524–10528. doi:10.1038/ncomms10524

Bahr, D. B., Pfeffer, W. T., Sassolas, C., and Meier, M. F. (1998). Response time of glaciers as a function of size and mass balance: 1. Theory. *J. Geophys. Res.* 103, 9777–9782. doi:10.1029/98JB00507

Barcaza, G., Nussbaumer, S. U., Tapia, G., Valdés, J., García, J.-L., Videla, Y., et al. (2017). Glacier inventory and recent glacier variations in the Andes of Chile, South America. *Ann. Glaciol.* 58, 166–180. doi:10.1017/aog.2017.28

Batchelor, C. L., Margold, M., Krapp, M., Murton, D. K., Dalton, A. S., Gibbard, P. L., et al. (2019). The configuration of Northern Hemisphere ice sheets through the Quaternary. *Nat. Commun.* 10, 3713. doi:10.1038/s41467-019-11601-2

Bendle, J. M., and Glasser, N. F. (2012). Palaeoclimatic reconstruction from lateglacial (younger dryas chronozone) cirque glaciers in snowdonia, north wales. *Proc. Geologists'. Assoc.* 123, 130–145. doi:10.1016/j.pgeola.2011.09.006

Bendle, J. M., Palmer, A. P., Thorndycraft, V. R., and Matthews, I. P. (2019). Phased patagonian ice sheet response to southern Hemisphere atmospheric and oceanic warming between 18 and 17 ka. *Sci. Rep.* 9, 4133. doi:10.1038/s41598-019-39750-w

Bippus, G. (2007). Modelling mass balance and climate sensitivity of glaciers of the southern Patagonia icefield. Available at: https://www.uibk.ac.at/acinn/theses/diploma-theses/bippus_gabriele_2007_dipl.pdf.

Blunier, T., Schwander, J., Stauffer, B., Stocker, T., Dällenbach, A., Indermühle, A., et al. (1997). Timing of the antarctic cold reversal and the atmospheric CO2 increase with respect to the younger dryas event. *Geophys. Res. Lett.* 24, 2683–2686. doi:10.1029/97GL02658

Boex, J., Fogwill, C., Harrison, S., Glasser, N. F., Hein, A., Schnabel, C., et al. (2013). Rapid thinning of the late pleistocene patagonian ice sheet followed migration of the southern westerlies. *Sci. Rep.* 3, 2118. doi:10.1038/srep02118

Boulton, G. S., and Jones, A. S. (1979). Stability of temperate ice caps and ice sheets resting on beds of deformable sediment. *J. Glaciol.* 24, 29–43. doi:10.3189/s0022143000014623

Braithwaite, R. J. (2008). Temperature and precipitation climate at the equilibrium-line altitude of glaciers expressed by the degree-day factor for melting snow. *J. Glaciol.* 54, 437–444. doi:10.3189/002214308785836968

Braithwaite, R. J., and Olesen, O. B. (1989). *Calculation of glacier ablation from air temperature, west Greenland*. Dordrecht: Springer, 219–233. doi:10.1007/978-94-015-7823-3_15

Braithwaite, R. J., and Olesen, O. B. (1990). Response of the energy balance on the margin of the Greenland ice sheet to temperature changes. *J. Glaciol.* 36, 217–221. doi:10.3189/S0022143000009461

Bravo, C., Quincey, D. J., Ross, A. N., Rivera, A., Brock, B., Miles, E., et al. (2019). Air temperature characteristics, distribution, and impact on modeled ablation for the South Patagonia Icefield. *J. Geophys. Res. Atmos.* 124, 907–925. doi:10.1029/2018jd028857

Bravo, C., Rojas, M., Anderson, B. M., Mackintosh, A. N., Sagredo, E., and Moreno, P. I. (2015). Modelled glacier equilibrium line altitudes during the mid-Holocene in the southern mid-latitudes. *Clim. Past.* 11, 1575–1586. doi:10.5194/cp-11-1575-2015

Brown, N. E., Hallet, B., and Booth, D. B. (1987). Rapid soft bed sliding of the Puget glacial lobe. *J. Geophys. Res.* 92, 8985–8997. doi:10.1029/jb092ib09p08985

Bueler, E., and Brown, J. (2009). Shallow shelf approximation as a "sliding law" in a thermomechanically coupled ice sheet model. *J. Geophys. Res.* 114, F03008. doi:10.1029/2008jf001179

Carrasco, J., Casassa, G., and Rivera, A. (2002). "Meteorological and climatological aspect of the southern patagonian icefield," in *The patagonian icefields*. Editors G. Casassa, F. V Sepulveda, and R. M. Sinclair (New York: Kluwer-Plenum), 29–41.

Carrivick, J. L., Davies, B. J., James, W. H. M., Quincey, D. J., and Glasser, N. F. (2016). Distributed ice thickness and glacier volume in southern South America. *Glob. Planet. Change* 146, 122–132. doi:10.1016/j.gloplacha.2016.09.010

Chandler, B. M. P., and Lukas, S. (2017). Reconstruction of Loch Lomond Stadial (Younger Dryas) glaciers on Ben More Coigach, north-west Scotland, and implications for reconstructing palaeoclimate using small ice masses. *J. Quat. Sci.* 32, 475–492. doi:10.1002/jqs.2941

Clark, C. D., Hughes, A. L. C., Greenwood, S. L., Jordan, C., and Sejrup, H. P. (2012). Pattern and timing of retreat of the last British-Irish Ice Sheet. *Quat. Sci. Rev.* 44, 112–146. doi:10.1016/j.quascirev.2010.07.019

Collao-Barrios, G., Gillet-Chaulet, F., Favier, V., Casassa, G., Berthier, E., Dussaillant, I., et al. (2018). Ice flow modelling to constrain the surface mass balance and ice discharge of San Rafael Glacier, Northern Patagonia Icefield. *J. Glaciol.* 64, 568–582. doi:10.1017/jog.2018.46

Cuffey, K. M., Clow, G. D., Steig, E. J., Buizert, C., Fudge, T. J., Koutnik, M., et al. (2016). Deglacial temperature history of West Antarctica. *Proc. Natl. Acad. Sci. U. S. A.* 113, 14249–14254. doi:10.1073/pnas.1609132113

Cullen, N. J., and Conway, J. P. (2015). A 22 month record of surface meteorology and energy balance from the ablation zone of Brewster Glacier, New Zealand. *J. Glaciol.* 61, 931–946. doi:10.3189/2015jog15j004

Dalton, A. S., Margold, M., Stokes, C. R., Tarasov, L., Dyke, A. S., Adams, R. S., et al. (2020). An updated radiocarbon-based ice margin chronology for the last deglaciation of the North American Ice Sheet Complex. *Quat. Sci. Rev.* 234, 106223. doi:10.1016/j.quascirev.2020.106223

Davies, B. J., Darvill, C. M., Lovell, H., Bendle, J. M., Dowdeswell, J. A., Fabel, D., et al. (2020). The evolution of the Patagonian Ice Sheet from 35 ka to the present day (PATICE). *Earth. Sci. Rev.* 204, 103152. doi:10.1016/j.earscirev.2020.103152

Davies, B. J. (2021). "Dating glacial landforms II: Radiometric techniques," in *Cryospheric geomorphology* (Elsevier). doi:10.1016/B978-0-12-818234-5.00040-7

Davies, B. J., and Glasser, N. F. (2012). Accelerating shrinkage of patagonian glaciers from the "little ice age" (~AD 1870) to 2011. *J. Glaciol.* 58, 1063–1084. doi:10.3189/2012JoG12J026

Davies, B. J., Thorndycraft, V. R., Fabel, D., and Martin, J. R. V. (2018). Asynchronous glacier dynamics during the antarctic cold reversal in central Patagonia. *Quat. Sci. Rev.* 200, 287–312. doi:10.1016/j.quascirev.2018.09.025

Davies, J. H. (2013). Global map of solid Earth surface heat flow. *Geochem. Geophys. Geosyst.* 14, 4608–4622. doi:10.1002/ggge.20271

Direccion Meteologica de Chile (2001). *Estadistica climatologia tomo III*.

Doughty, A. M., Anderson, B. M., Mackintosh, A. N., Kaplan, M. R., Vandergoes, M. J., Barrell, D. J. A., et al. (2013). Evaluation of lateglacial temperatures in the southern Alps of New Zealand based on glacier modelling at irishman stream, ben ohau range. *Quat. Sci. Rev.* 74, 160–169. doi:10.1016/j.quascirev.2012.09.013

Dussaillant, I., Berthier, E., Brun, F., Masiokas, M., Hugonnet, R., Favier, V., et al. (2019). Two decades of glacier mass loss along the Andes. *Nat. Geosci.* 12, 802–808. doi:10.1038/s41561-019-0432-5

Escobar, F., Fernando, V., and Garin, C. (1992). "Water balance in the Patagonia icefield," in *Glaciological researches in Patagonia, 1990*. Editors R. Naruse and M. Aniya (Japanese Society of Snow and Ice), 109–119.

Fahnestock, M., Scambos, T., Moon, T., Gardner, A., Haran, T., and Klinger, M. (2016). Rapid large-area mapping of ice flow using Landsat 8. *Remote Sens. Environ.* 185, 84–94. doi:10.1016/j.rse.2015.11.023

Falaschi, D., Bolch, T., Rastner, P., Lenzano, M. G., Lenzano, L., Vecchio, A. L. O., et al. (2017). Mass changes of alpine glaciers at the eastern margin of the Northern and Southern Patagonian Icefields between 2000 and 2012. *J. Glaciol.* 63, 258–272. doi:10.1017/jog.2016.136

Falaschi, D., Bravo, C., Masiokas, M., Villalba, R., and Rivera, A. A. A. (2013). First Glacier Inventory and recent changes in glacier area in the Monte san Lorenzo region (47°S), southern patagonian Andes, south America. *Arct. Antarct. Alp. Res.* 45, 19–28. doi:10.1657/1938-4246-45.1.19

Falaschi, D., Lenzano, M. G., Villalba, R., Bolch, T., Rivera, A., and Lo Vecchio, A. (2019). Six decades (1958–2018) of geodetic glacier mass balance in Monte san Lorenzo, patagonian Andes. *Front. Earth Sci.* 7, 326. doi:10.3389/feart.2019.00326

Falaschi, D., Rivera, A., Lo Vecchio Repetto, A., Moragues, S., Villalba, R., Rastner, P., et al. (2021). Evolution of surface characteristics of three debris-covered glaciers in the patagonian Andes from 1958 to 2020. *Front. Earth Sci.* 9. doi:10.3389/feart.2021.671854

Falaschi, D., Tadono, T., and Masiokas, M. (2015). Rock glaciers in the patagonian Andes: An inventory for the Monte san Lorenzo (cerro Cochrane) massif, 47° S. *Geogr. Ann. Ser. A Phys. Geogr.* 97, 769–777. doi:10.1111/geoa.12113

Fernandez, R., Anderson, J., Bertrand, S., and Wellner, J. (2012). Gualas glacier sedimentary record of climate and environmental change, golfo elefantes, western Patagonia (46.5° S). *Holocene* 22, 451–463. doi:10.1177/0959683611425545

Fick, S. E., and Hijmans, R. J. (2017). WorldClim 2: New 1-km spatial resolution climate surfaces for global land areas. *Int. J. Climatol.* 37, 4302–4315. doi:10.1002/joc.5086

Frieler, K., Clark, P. U., He, F., Buizert, C., Reese, R., Ligtenberg, S. R. M., et al. (2015). Consistent evidence of increasing Antarctic accumulation with warming. *Nat. Clim. Chang.* 5, 348–352. doi:10.1038/nclimate2574

Garibotti, I. A., and Villalba, R. (2017). Colonization of mid- and late-Holocene moraines by lichens and trees in the Magellanic sub-Antarctic province. *Polar Biol.* 40, 1739–1753. doi:10.1007/s00300-017-2096-1

Garreaud, R., Lopez, P., Minvielle, M., and Rojas, M. (2013). Large-scale control on the patagonian climate. *J. Clim.* 26, 215–230. doi:10.1175/JCLI-D-12-00001.1

Glasser, N. F., Harrison, S., Schnabel, C., Fabel, D., and Jansson, K. N. (2012). Younger Dryas and early Holocene age glacier advances in Patagonia. *Quat. Sci. Rev.* 58, 7–17. doi:10.1016/j.quascirev.2012.10.011

Golledge, N. R., Mackintosh, A. N. N., Anderson, B. M. M., Buckley, K. M. M., Doughty, A. M. M., Barrell, D. J. A. J. A., et al. (2012). Last glacial maximum climate in New Zealand inferred from a modelled southern Alps icefield. *Quat. Sci. Rev.* 46, 30–45. doi:10.1016/j.quascirev.2012.05.004

Greve, R., and Blatter, H. (2009). *Dynamics of ice sheets and glaciers*. Springer.

Gudmundsson, G. H. (1994). *Converging glacier flow _ A case study: The unteraarglacier. Mitteilungen der Versuchsanstalt Fur wasserbau, hydrol. Und glaziologie an der Eidgenoss.* Hochschule Zurich. Tech.

Haddam, N. A., Siani, G., Michel, E., Kaiser, J., Lamy, F., Duchamp-Alphonse, S., et al. (2018). Changes in latitudinal sea surface temperature gradients along the Southern Chilean margin since the last glacial. *Quat. Sci. Rev.* 194, 62–76. doi:10.1016/j.quascirev.2018.06.023

Harrison, S., Glasser, N. F., Duller, G. A. T., and Jansson, K. N. (2012). Early and mid-holocene age for the tempanos moraines, laguna san Rafael, patagonian Chile. *Quat. Sci. Rev.* 31, 82–92. doi:10.1016/j.quascirev.2011.10.015

Hock, R. (2003). Temperature index melt modelling in mountain areas. *J. Hydrol. X.* 282, 104–115. doi:10.1016/S0022-1694(03)00257-9

Hubbard, A., Hein, A. S., Kaplan, M. R., Hulton, N. R. J., and Glasser, N. (2005). A modelling reconstruction of the last glacial maximum ice sheet and its deglaciation in the vicinity of the northern patagonian icefield, south America. *Geogr. Ann. Ser. A Phys. Geogr.* 87, 375–391. doi:10.1111/j.0435-3676.2005.00264.x

Hughes, A. L. C., Gyllencreutz, R., Lohne, Ø. S., Mangerud, J., and Svendsen, J. I. (2016). The last Eurasian ice sheets–a chronological database and time-slice reconstruction, DATED-1. *Boreas* 45, 1–45. doi:10.1111/bor.12142

Hugonnet, R., McNabb, R., Berthier, E., Menounos, B., Nuth, C., Girod, L., et al. (2021). Accelerated global glacier mass loss in the early twenty-first century. *Nature* 592, 726–731. doi:10.1038/s41586-021-03436-z

Hulton, N. R. J., Purves, R. S., McCulloch, R. D., Sugden, D. E., and Bentley, M. J. (2002). The last glacial maximum and deglaciation in southern south America. *Quat. Sci. Rev.* 21, 233–241. doi:10.1016/S0277-3791(01)00103-2

Hulton, N. R., Sugden, D. E., Payne, A., and Clapperton, C. (1994). Glacier modeling and the climate of Patagonia during the last glacial maximum. *Quat. Res.* 42, 1–19. doi:10.1006/qres.1994.1049

Hutter, K. (1983). *Theoretical glaciology, mathematical approaches to geophysics*. D. D. Reidel.

Inoue, J., Kondo, H., Fujiyoshi, Y., Yamada, T., and Fukami, H. (1987). Summer climate of the northern Patagonia icefield. *Bull. glacier Res.*, 7–14.

Iverson, N. R., Jansson, P., and Hooke, R. L. (1995). *In-situ* measurement of the strength of deforming subglacial till. *J. Glaciol.* 40, 497–503. doi:10.3189/s0022143000012375

James, W. H. M., and Carrivick, J. L. (2016). Automated modelling of spatially-distributed glacier ice thickness and volume. *Comput. Geosci.* 92, 90–103. doi:10.1016/j.cageo.2016.04.007

Jenny, B., Wilhelm, D., and Valero-Garcés, B. (2003). The Southern Westerlies in Central Chile: Holocene precipitation estimates based on a water balance model for Laguna Aculeo (33 50′ S). *Clim. Dyn.* 20, 269–280. doi:10.1007/s00382-002-0267-3

Jouvet, G., Seguinot, J., Ivy-Ochs, S., and Funk, M. (2017). Modelling the diversion of erratic boulders by the Valais Glacier during the last glacial maximum. *J. Glaciol.* 63, 487–498. doi:10.1017/jog.2017.7

Kaplan, M. R., Schaefer, J. M., Strelin, J. A., Denton, G. H., Anderson, R. F., Vandergoes, M. J., et al. (2016). Patagonian and southern south atlantic view of Holocene climate. *Quat. Sci. Rev.* 141, 112–125. doi:10.1016/j.quascirev.2016.03.014

Kaplan, M. R., Strelin, J. A., Schaefer, J. M., Peltier, C., Martini, M. A., Flores, E., et al. (2020). Holocene glacier behavior around the northern Antarctic Peninsula and possible causes. *Earth Planet. Sci. Lett.* 534, 116077. doi:10.1016/j.epsl.2020.116077

Kavan, J., Nývlt, D., Láska, K., Engel, Z., and Kňažková, M. (2020). High-latitude dust deposition in snow on the glaciers of James Ross Island, Antarctica. *Earth Surf. Process. Landforms* 45, 1569–1578. doi:10.1002/esp.4831

Kilian, R., and Lamy, F. (2012). A review of Glacial and Holocene paleoclimate records from southernmost Patagonia (49–55°S). *Quat. Sci. Rev.* 53, 1–23. doi:10.1016/j.quascirev.2012.07.017

Koppes, M., Conway, H., Rasmussen, L. A., and Chernos, M. (2011). Deriving mass balance and calving variations from reanalysis data and sparse observations, Glaciar San Rafael, northern Patagonia, 1950-2005. *Cryosphere* 5, 791–808. doi:10.5194/tc-5-791-2011

Köse, O., Sarıkaya, M. A., Çiner, A., Candaş, A., Yıldırım, C., and Wilcken, K. M. (2022). Reconstruction of last glacial maximum glaciers and palaeoclimate in the central taurus range, Mt. Karanfil, of the eastern mediterranean. *Quat. Sci. Rev.* 291, 107656. doi:10.1016/j.quascirev.2022.107656

Lang, H., and Braun, L. (1990). *On the information content of air temperature in the context of snow melt estimation*. Hydrol. Mt. Areas, 347–354.

Lang, H. (1986). *Forecasting meltwater runoff from snow-covered areas and from glacier basins*. Dordrecht: Springer, 99–127. doi:10.1007/978-94-009-4536-4_5

Leclercq, P. W., Pitte, P., Giesen, R. H., Masiokas, M. H., and Oerlemans, J. (2012). Modelling and climatic interpretation of the length fluctuations of Glaciar Frías (north Patagonian Andes, Argentina) 1639–2009 AD. *Clim. Past.* 8, 1385–1402. doi:10.5194/cp-8-1385-2012

Lenaerts, J. T. M., Van Den Broeke, M. R., van Wessem, J. M., van de Berg, W. J., van Meijgaard, E., van Ulft, L. H., et al. (2014). Extreme precipitation and climate gradients in Patagonia revealed by high-resolution regional atmospheric climate modeling. *J. Clim.* 27, 4607–4621. doi:10.1175/jcli-d-13-00579.1

Li, H., Ng, F., Li, Z., Qin, D., and Cheng, G. (2012). An extended "perfect-plasticity" method for estimating ice thickness along the flow line of mountain glaciers. *J. Geophys. Res.* 117, 1–11. doi:10.1029/2011JF002104

Lowe, J. J., and Hoek, W. Z. (2001). Inter-regional correlation of palaeoclimatic records for the last glacial–interglacial transition: A protocol for improved precision recommended by the INTIMATE project group. *Quat. Sci. Rev.* 20, 1175–1187. doi:10.1016/S0277-3791(00)00183-9

Mackintosh, A. N., Anderson, B. M., and Pierrehumbert, R. T. (2017). Reconstructing climate from glaciers. *Annu. Rev. Earth Planet. Sci.* 45, 649–680. doi:10.1146/annurev-earth-063016-020643

Małecki, J. (2015). Snow accumulation on a small high-arctic glacier svenbreen: Variability and topographic controls. *Geogr. Ann. Ser. A Phys. Geogr.* 97, 809–817. doi:10.1111/geoa.12115

Mansilla, C. A., McCulloch, R. D., and Morello, F. (2016). Palaeoenvironmental change in southern Patagonia during the lateglacial and Holocene: Implications for forest refugia and climate reconstructions. *Palaeogeogr. Palaeoclimatol. Palaeoecol.* 447, 1–11. doi:10.1016/j.palaeo.2016.01.041

Marden, C. J., and Clapperton, C. M. (1995). Fluctuations of the south patagonian ice-field during the last glaciation and the Holocene. *J. Quat. Sci.* 10, 197–209. doi:10.1002/jqs.3390100302

Martin, J. R. V., Davies, B. J., and Thorndycraft, V. R. (2019). Glacier dynamics during a phase of Late Quaternary warming in Patagonia reconstructed from sediment-landform associations. *Geomorphology* 337, 111–133. doi:10.1016/j.geomorph.2019.03.007

Martin, J. R. V., Thorndycraft, V. R., Davies, B. J., and Rodes, A. (2022). Rapid glacier recession at Monte san Lorenzo (Patagonia) in response to abrupt southern Hemisphere warming 13.0–12.0 ka BP. *J. Quat. Sci.* doi:10.1002/jqs.3463

Martin, M. A., Winkelmann, R., Haseloff, M., Albrecht, T., Bueler, E., Khroulev, C., et al. (2011). The potsdam parallel ice sheet model (PISM-PIK) – Part 2: Dynamic equilibrium simulation of the antarctic ice sheet. *Cryosphere* 5, 727–740. doi:10.5194/tc-5-727-2011

Masiokas, M. H., Rivera, A., Espizua, L. E., Villalba, R., Delgado, S., and Aravena, J. C. (2009). Glacier fluctuations in extratropical South America during the past 1000 years. *Palaeogeogr. Palaeoclimatol. Palaeoecol.* 281, 242–268. doi:10.1016/j.palaeo.2009.08.006

Massaferro, J., Larocque-Tobler, I., Brooks, S. J., Vandergoes, M., Dieffenbacher-Krall, A., and Moreno, P. (2014). Quantifying climate change in Huelmo mire (Chile, Northwestern Patagonia) during the Last Glacial Termination using a newly developed chironomid-based temperature model. *Palaeogeogr. Palaeoclimatol. Palaeoecol.* 399, 214–224. doi:10.1016/j.palaeo.2014.01.013

Massaferro, J., and Larocque-Tobler, I. (2013). Using a newly developed chironomid transfer function for reconstructing mean annual air temperature at Lake Potrok Aike, Patagonia, Argentina. *Ecol. Indic.* 24, 201–210. doi:10.1016/j.ecolind.2012.06.017

McCulloch, R. D., Blaikie, J., Jacob, B., Mansilla, C. A., Morello, F., De Pol-Holz, R., et al. (2020). Late glacial and Holocene climate variability, southernmost Patagonia. *Quat. Sci. Rev.* 229, 106131. doi:10.1016/j.quascirev.2019.106131

Meier, W. J.-H., Grießinger, J., Hochreuther, P., and Braun, M. H. (2018). An updated multi-temporal glacier inventory for the Patagonian Andes with changes between the Little Ice Age and 2016. *Front. Earth Sci.* 6, 1–21. doi:10.3389/feart.2018.00062

Mendelová, M., Hein, A. S., Rodes, A., Smedley, R. K., and Xu, S. (2020). Glacier expansion in central Patagonia during the antarctic cold reversal followed by retreat and stabilisation during the younger dryas. *Quat. Sci. Rev.* 227, 106047. doi:10.1016/j.quascirev.2019.106047

Menounos, B., Clague, J. J., Osborn, G., Davis, P. T., Ponce, F., Goehring, B., et al. (2013). Latest Pleistocene and Holocene glacier fluctuations in southernmost Tierra del Fuego, Argentina. *Quat. Sci. Rev.* 77, 70–79. doi:10.1016/j.quascirev.2013.07.008

Mercer, J. H. (1976). Glacial history of southernmost South America. *Quat. Res.* 6, 125–166. doi:10.1016/0033-5894(76)90047-8

Mercer, J. H. (1968). Variations of some patagonian glaciers since the late-glacial. *Am. J. Sci.* 266, 91–109. doi:10.2475/ajs.266.2.91

Millan, R., Mouginot, J., Rabatel, A., and Morlighem, M. (2022). Ice velocity and thickness of the world's glaciers. *Nat. Geosci.* 15, 124–129. doi:10.1038/s41561-021-00885-z

Möller, M., Schneider, C., and Kilian, R. (2007). Glacier change and climate forcing in recent decades at Gran Campo Nevado, southernmost Patagonia. *Ann. Glaciol.* 46, 136–144. doi:10.3189/172756407782871530

Morales, M. S., Cook, E. R., Barichivich, J., Christie, D. A., Villalba, R., LeQuesne, C., et al. (2020). Six hundred years of South American tree rings reveal an increase in severe hydroclimatic events since mid-20th century. *Proc. Natl. Acad. Sci. U. S. A.* 117, 16816–16823. doi:10.1073/pnas.2002411117

Moreno, P. I., François, J. P., Villa-Martínez, R. P., and Moy, C. M. (2009). Millennial-scale variability in Southern Hemisphere westerly wind activity over the last 5000 years in SW Patagonia. *Quat. Sci. Rev.* 28, 25–38. doi:10.1016/j.quascirev.2008.10.009

Moreno, P. I. (2004). Millennial-scale climate variability in northwest Patagonia over the last 15 000 yr. *J. Quat. Sci.* 19, 35–47. doi:10.1002/jqs.813

Moreno, P. I. (2020). Timing and structure of vegetation, fire, and climate changes on the Pacific slope of northwestern Patagonia since the last glacial termination. *Quat. Sci. Rev.* 238, 106328. doi:10.1016/j.quascirev.2020.106328

Moreno, P. I., Vilanova, I., Villa-Martínez, R., Dunbar, R. B., Mucciarone, D. A., Kaplan, M. R., et al. (2018). Onset and evolution of southern annular mode-

like changes at centennial timescale. *Sci. Rep.* 8, 3458. doi:10.1038/s41598-018-21836-6

Murray, T. (1997). Assessing the paradigm shift: Deformable glacier beds. *Quat. Sci. Rev.* 16, 995–1016. doi:10.1016/S0277-3791(97)00030-9

Nielsen, L. T., Aðalgeirsdóttir, G., Gkinis, V., Nuterman, R., and Hvidberg, C. S. (2018). The effect of a Holocene climatic optimum on the evolution of the Greenland ice sheet during the last 10 kyr. *J. Glaciol.* 64, 477–488. doi:10.1017/jog.2018.40

Nimick, D. A., McGrath, D., Mahan, S. A., Friesen, B. A., and Leidich, J. (2016). Latest pleistocene and Holocene glacial events in the colonia valley, northern Patagonia icefield, southern Chile. *J. Quat. Sci.* 31, 551–564. doi:10.1002/jqs.2847

Oehlerich, M., Mayr, C., Gussone, N., Hahn, A., Hölzl, S., Lücke, A., et al. (2015). Lateglacial and Holocene climatic changes in south-eastern Patagonia inferred from carbonate isotope records of Laguna Potrok Aike (Argentina). *Quat. Sci. Rev.* 114, 189–202. doi:10.1016/j.quascirev.2015.02.006

Oerlemans, J. (2005). Extracting a climate signal from 169 glacier records. *Science* 308, 675–677. doi:10.1126/science.1107046

Ohmura, A., Kasser, P., and Funk, M. (1992). Climate at the equilibrium line of glaciers. *J. Glaciol.* 38, 397–411. doi:10.1017/s0022143000002276

Oien, R. P., Rea, B. R., Spagnolo, M., Barr, I. D., and Bingham, R. G. (2021). Testing the area–altitude balance ratio (AABR) and accumulation–area ratio (AAR) methods of calculating glacier equilibrium-line altitudes. *J. Glaciol.*, 68, 357–368. doi:10.1017/jog.2021.100

Osmaston, H. (2005). Estimates of glacier equilibrium line altitudes by the Area×Altitude, the Area×Altitude balance ratio and the Area×Altitude balance index methods and their validation. *Quat. Int.* 138–139, 22–31. doi:10.1016/j.quaint.2005.02.004

Parizek, B. R., and Alley, R. B. (2004). Ice thickness and isostatic imbalances in the ross embayment, west Antarctica: Model results. *Glob. Planet. Change* 42, 265–278. doi:10.1016/J.GLOPLACHA.2003.09.005

Paterson, W. S. B. (1994). *The physics of glaciers*, 480.

Pedro, J. B., Bostock, H. C., Bitz, C. M., He, F., Vandergoes, M. J., Steig, E. J., et al. (2016). The spatial extent and dynamics of the Antarctic Cold Reversal. *Nat. Geosci.* 9, 51–55. doi:10.1038/ngeo2580

Pellitero, R., Rea, B. R., Spagnolo, M., Bakke, J., Hughes, P., Ivy-Ochs, S., et al. (2015). A GIS tool for automatic calculation of glacier equilibrium-line altitudes. *Comput. Geosci.* 82, 55–62. doi:10.1016/j.cageo.2015.05.005

Pellitero, R., Rea, B. R., Spagnolo, M., Bakke, J., Ivy-Ochs, S., Frew, C. R., et al. (2016). GlaRe, a GIS tool to reconstruct the 3D surface of palaeoglaciers. *Comput. Geosci.* 94, 77–85. doi:10.1016/j.cageo.2016.06.008

Peltier, C., Kaplan, M. R., Birkel, S. D., Soteres, R. L., Sagredo, E. A., Aravena, J. C., et al. (2021). The large MIS 4 and long MIS 2 glacier maxima on the southern tip of South America. *Quat. Sci. Rev.* 262, 106858. doi:10.1016/j.quascirev.2021.106858

Porter, P. R., Murray, T., and Dowdeswell, J. A. (1997). Sediment deformation and basal dynamics beneath a glacier surge front: Bakaninbreen, Svalbard. *Ann. Glaciol.* 24, 21–26. doi:10.3189/s0260305500011873

Purdie, H. L., Brook, M. S., and Fuller, I. C. (2008). Seasonal variation in ablation and surface velocity on a temperate maritime glacier: Fox Glacier, New Zealand. *Arct. Antarct. Alp. Res.* 40, 140–147. doi:10.1657/1523-0430(06-032)[purdie]2.0.co;2

Putnam, A. E. E., Schaefer, J. M. M., Denton, G. H. H., Barrell, D. J. A. J. A., Birkel, S. D. D., Andersen, B. G. G., et al. (2013). The last glacial maximum at 44°S documented by a 10Be moraine chronology at lake ohau, southern Alps of New Zealand. *Quat. Sci. Rev.* 62, 114–141. doi:10.1016/j.quascirev.2012.10.034

Quade, J., and Kaplan, M. R. (2017). lake-level stratigraphy and geochronology revisited at Lago (lake) Cardiel, Argentina, and changes in the southern hemispheric westerlies over the last 25 ka. *Quat. Sci. Rev.* 177, 173–188. doi:10.1016/j.quascirev.2017.10.006

Ramos, V. A., Niemeyer, H., Skarmeta, J., and Muñoz, J. (1982). Magmatic evolution of the austral patagonian Andes. *Earth. Sci. Rev.* 18, 411–443. doi:10.1016/0012-8252(82)90047-2

Randolph Glacier Inventory Consortium, Arendt, A., Bliss, A., Bolch, T., Cogley, J. G., Gardner, A., et al. (2017). *Randolph Glacier inventory–a dataset of global glacier outlines: Version 6.0: Technical report, global land ice measurements from space*. Colorado, USA: Digit. Media.

Rasmussen, S. O., Bigler, M., Blockley, S. P., Blunier, T., Buchardt, S. L., Clausen, H. B., et al. (2014). A stratigraphic framework for abrupt climatic changes during the last Glacial period based on three synchronized Greenland ice-core records: Refining and extending the INTIMATE event stratigraphy. *Quat. Sci. Rev.* 106, 14–28. doi:10.1016/j.quascirev.2014.09.007

Rea, B. R. (2009). Defining modern day Area-Altitude Balance Ratios (AABRs) and their use in glacier-climate reconstructions. *Quat. Sci. Rev.* 28, 237–248. doi:10.1016/j.quascirev.2008.10.011

Reynhout, S., Sagredo, E. A., Kaplan, M. R., Aravena, J. C., Martini, M. A., Moreno, P. I., et al. (2019). Holocene glacier fluctuations in Patagonia are modulated by summer insolation intensity and paced by Southern Annular Mode-like variability. *Quat. Sci. Rev.* 220, 178–187. doi:10.1016/j.quascirev.2019.05.029

Ritz, C., Fabre, A., and Letréguilly, A. (1996). Sensitivity of a Greenland ice sheet model to ice flow and ablation parameters: Consequences for the evolution through the last climatic cycle. *Clim. Dyn.* 13, 11–23. doi:10.1007/s003820050149

Rivera, A. (2004). *Mass balance investigations at glaciar Chico, southern Patagonia icefield*. Chile. South. Patagon. Icefield, Chile.

Rodbell, D. T., Smith, J. A., and Mark, B. G. (2009). Glaciation in the Andes during the lateglacial and Holocene. *Quat. Sci. Rev.* 28, 2165–2212. doi:10.1016/j.quascirev.2009.03.012

Sagredo, E. A., Kaplan, M. R., Araya, P. S., Lowell, T. V., Aravena, J. C., Moreno, P. I., et al. (2018). Trans-Pacific glacial response to the Antarctic Cold Reversal in the southern mid-latitudes. *Quat. Sci. Rev.* 188, 160–166. doi:10.1016/j.quascirev.2018.01.011

Sagredo, E. A., Lowell, T. V., Kelly, M. A., Rupper, S., Aravena, J. C., Ward, D. J., et al. (2016). Equilibrium line altitudes along the Andes during the Last millennium: Paleoclimatic implications. *Holocene* 27, 1019–1033. doi:10.1177/0959683616678458

Sagredo, E. A., Rupper, S., and Lowell, T. V. (2014). Sensitivities of the equilibrium line altitude to temperature and precipitation changes along the Andes. *Quat. Res.* 81, 355–366. doi:10.1016/j.yqres.2014.01.008

Sato, A., Takahashi, S., Naruse, R., and Wakahama, G. (1984). Ablation and heat balance of the yukikabe snow patch in the daisetsu mountains, hokkaido, Japan. *Ann. Glaciol.* 5, 122–126. doi:10.3189/1984AoG5-1-122-126

Scambos, T., Fahnestock, M., Moon, T., Gardner, A., and Klinger, M. (2016). *Global land ice velocity extraction from Landsat 8 (Go-LIVE), version 1*, 10. Boulder, Colorado USA: NSIDC Natl. Snow Ice Data Center, N5ZP442B.

Schaefer, M., Machguth, H., Falvey, M., and Casassa, G. (2013). Modeling past and future surface mass balance of the Northern Patagonia Icefield. *J. Geophys. Res. Earth Surf.* 118, 571–588. doi:10.1002/jgrf.20038

Schaefer, M., Machguth, H., Falvey, M., Casassa, G., and Rignot, E. (2015). Quantifying mass balance processes on the southern Patagonia icefield. *Cryosphere* 9, 25–35. doi:10.5194/tc-9-25-2015

Schmidt, L. S., Aðalgeirsdóttir, G., Pálsson, F., Langen, P. L., Guðmundsson, S., and Björnsson, H. (2020). Dynamic simulations of Vatnajökull ice cap from 1980 to 2300. *J. Glaciol.* 66, 97–112. doi:10.1017/jog.2019.90

Schneider, C., Glaser, M., Kilian, R., Santana, A., Butorovic, N., and Casassa, G. (2003). Weather observations across the southern Andes at 53°S. *Phys. Geogr.* 24, 97–119. doi:10.2747/0272-3646.24.2.97

Schneider, C., Kilian, R., and Glaser, M. (2007). Energy balance in the ablation zone during the summer season at the gran Campo Nevado ice cap in the southern Andes. *Glob. Planet. Change* 59, 175–188. doi:10.1016/j.gloplacha.2006.11.033

Schwikowski, M., Schläppi, M., Santibañez, P., Rivera, A., and Casassa, G. (2013). Net accumulation rates derived from ice core stable isotope records of Pío XI glacier, Southern Patagonia Icefield. *Cryosphere* 7, 1635–1644. doi:10.5194/tc-7-1635-2013

Skvarca, P., and Naruse, R. (1997). "Dynamic behavior of glaciar Perito Moreno, southern Patagonia," in *Annals of glaciology*. Editor I. M. Whillans, 24, 268–271.

Stokes, C. R., Tarasov, L., Blomdin, R., Cronin, T. M., Fisher, T. G., Gyllencreutz, R., et al. (2015). On the reconstruction of palaeo-ice sheets: Recent advances and future challenges. *Quat. Sci. Rev.* 125, 15–49. doi:10.1016/j.quascirev.2015.07.016

Strelin, J. A., and Malagnino, E. C. (2000). Late-glacial history of Lago argentino, Argentina, and age of the puerto bandera moraines. *Quat. Res.* 54, 339–347. doi:10.1006/qres.2000.2178

Stuefer, M., Rott, H., and Skvarca, P. (2007). Glaciar Perito Moreno, Patagonia: Climate sensitivities and glacier characteristics preceding the 2003/04 and 2005/06 damming events. *J. Glaciol.* 53, 3–16. doi:10.3189/172756507781833848

Sugden, D. E., Hulton, N. R. J., and Purves, R. S. (2002). Modelling the inception of the Patagonian icesheet. *Quat. Int.* 95, 55–64. doi:10.1016/s1040-6182(02)00027-7

Takeuchi, Y., Naruse, R., and Skvarca, P. (1996). Annual air-temperature measurement and ablation estimate at Moreno Glacier, Patagonia. *Bull. glacier Res.* 14, 23–28.

The PISM authors (2017). PISM, a parallel ice sheet model, manual version 1.0. Available at: https://pism-docs.org/sphinx/manual/.

Thorndycraft, V. R., Bendle, J. M. J. M., Benito, G., Davies, B. J. B. J., Sancho, C., Palmer, A. P. A. P., et al. (2019). Glacial lake evolution and Atlantic-Pacific drainage reversals during deglaciation of the Patagonian Ice Sheet. *Quat. Sci. Rev.* 203, 102–127. doi:10.1016/j.quascirev.2018.10.036

Tonello, M. S., Mancini, M. V., and Seppä, H. (2009). Quantitative reconstruction of Holocene precipitation changes in southern Patagonia. *Quat. Res.* 72, 410–420. doi:10.1016/j.yqres.2009.06.011

Van Daele, M., Bertrand, S., Meyer, I., Moernaut, J., Vandoorne, W., Siani, G., et al. (2016). Late Quaternary evolution of Lago Castor (Chile, 45.6° S): Timing of the deglaciation in northern Patagonia and evolution of the southern westerlies during the last 17 kyr. *Quat. Sci. Rev.* 133, 130–146. doi:10.1016/j.quascirev.2015.12.021

Van Pelt, W. J. J., and Oerlemans, J. (2012). Numerical simulations of cyclic behaviour in the parallel ice sheet model (PISM). *J. Glaciol.* 58, 347–360. doi:10.3189/2012jog11j217

Villa-Martínez, R., Moreno, P. I., and Valenzuela, M. A. (2012). Deglacial and postglacial vegetation changes on the eastern slopes of the central Patagonian Andes (47°S). *Quat. Sci. Rev.* 32, 86–99. doi:10.1016/j.quascirev.2011.11.008

Villalba, R., Masiokas, M. H., Kitzberger, T., and Boninsegna, J. A. (2005). "Biogeographical consequences of recent climate changes in the southern Andes of Argentina," in *Global change and mountain regions* (Springer), 157–166.

Waldmann, N., Ariztegui, D., Anselmetti, F. S., Coronato, A., and Austin, J. A. (2010). Geophysical evidence of multiple glacier advances in Lago Fagnano (54°S), southernmost Patagonia. *Quat. Sci. Rev.* 29, 1188–1200. doi:10.1016/j.quascirev.2010.01.016

Weidemann, S. S., Sauter, T., Malz, P., Jaña, R., Arigony-Neto, J., Casassa, G., et al. (2018). glacier mass changes of lake-terminating grey and Tyndall glaciers at the southern Patagonia icefield derived from geodetic observations and energy and mass balance modeling. *Front. Earth Sci.* 6, 81. doi:10.3389/feart.2018.00081

Weis, M., Greve, R., and Hutter, K. (1999). Theory of shallow ice shelves. *Contin. Mech. Thermodyn.* 11, 15–50. doi:10.1007/s001610050102

Whitlock, C., Moreno, P. I., and Bartlein, P. (2007). Climatic controls of Holocene fire patterns in southern South America. *Quat. Res.* 68, 28–36. doi:10.1016/j.yqres.2007.01.012

Winkelmann, R., Martin, M. A., Haseloff, M., Albrecht, T., Bueler, E., Khroulev, C., et al. (2011). The potsdam parallel ice sheet model (PISM-PIK) – Part 1: Model description. *Cryosphere* 5, 715–726. doi:10.5194/tc-5-715-2011

Yan, Q., Owen, L. A., Wang, H., and Zhang, Z. (2018). Climate constraints on glaciation over high-mountain asia during the last glacial maximum. *Geophys. Res. Lett.* 45, 9024–9033. doi:10.1029/2018GL079168

Žebre, M., Sarıkaya, M. A., Stepišnik, U., Colucci, R. R., Yıldırım, C., Çiner, A., et al. (2021). An early glacial maximum during the last glacial cycle on the northern Velebit Mt. (Croatia). *Geomorphology* 392, 107918. doi:10.1016/j.geomorph.2021.107918

Zemp, M., Huss, M., Thibert, E., Eckert, N., McNabb, R., Huber, J., et al. (2019). Global glacier mass changes and their contributions to sea-level rise from 1961 to 2016. *Nature* 568, 382–386. doi:10.1038/s41586-019-1071-0

Ziemen, F. A., Hock, R., Aschwanden, A., Khroulev, C., Kienholz, C., Melkonian, A., et al. (2016). Modeling the evolution of the juneau icefield between 1971 and 2100 using the parallel ice sheet model (PISM). *J. Glaciol.* 62, 199–214. doi:10.1017/jog.2016.13

Frontiers in Earth Science

Investigates the processes operating within the major spheres of our planet

Advances our understanding across the earth sciences, providing a theoretical background for better use of our planet's resources and equipping us to face major environmental challenges.

Discover the latest Research Topics

See more →

Frontiers

Avenue du Tribunal-Fédéral 34
1005 Lausanne, Switzerland
frontiersin.org

Contact us

+41 (0)21 510 17 00
frontiersin.org/about/contact